Shaker A. Meguid
George J. Weng *Editors*

# Micromechanics and Nanomechanics of Composite Solids

Springer

# Micromechanics and Nanomechanics of Composite Solids

Shaker A. Meguid • George J. Weng
Editors

# Micromechanics and Nanomechanics of Composite Solids

Springer

*Editors*
Shaker A. Meguid
Mechanical and Industrial Engineering
University of Toronto
Toronto, ON, Canada

George J. Weng
Mechanical and Aerospace Engineering
Rutgers University
New Brunswick, NJ, USA

ISBN 978-3-319-52793-2 ISBN 978-3-319-52794-9 (eBook)
DOI 10.1007/978-3-319-52794-9

Library of Congress Control Number: 2017940393



Printed on acid-free paper

This Springer imprint is published by Springer Nature
The registered company is Springer International Publishing AG
The registered company address is: Gewerbestrasse 11, 6330 Cham, Switzerland

# Preface

There exists considerable work involving isotropic and homogeneous solids. Most metallic and polymeric composite materials are heterogeneous in nature. The heterogeneity is the result of the presence of multiphases and interfaces both adhesively and cohesively in these composites. Their effective elastic properties are governed by the joint properties of the different phases, where volume fractions, directionality, inhomogeneity and anisotropy, and varied length and time scales govern these properties. Two major categories exist: composites with microscopic functional reinforcements/alloying elements and composites with nanoscopic reinforcements. The treatments of those two categories of composites are the focus of this work.

This edited book covers micromechanics and nanomechanics as applied to composite solids. Micromechanics employs traditional continuum mechanics techniques to describe the behavior of features in the order of microns. Nanomechanics, on the other hand, considers the atomic/molecular structures by employing molecular mechanics, molecular dynamics, sequential and concurrent coupling of length scales, and atomistic-based continuum techniques, among others. Whether micromechanics or nanomechanics are used in the treatment of composites, a representative unit cell or a representative volume element is typically developed and used to obtain a homogenized determination of the effective macroscopic properties of the composite. Many micromechanics, nanomechanics, and homogenization techniques exist, and it is the intention of this effort to provide the reader with recent advances in these fields. The unique property combinations that result from the introduction of fiber and alloying elements and additives, the interface, and the matrix provide greater opportunities for the development of advanced material technologies to meet the challenges of the next century.

There are three reasons for the surge and interest in micro- and nanomechanics research as applied to composite, functional materials, and granular structures. The first stems from the desire to tailor the properties of engineered materials to suit a specific application(s). The second, from the desire to reduce our carbon print and ensure effective use of resources. And the third, from the current advances in computational micromechanics, nanomechanics, and multiscale modeling techniques.

This book is not an attempt to exhaustively cover all the relevant topics on micromechanics, nanomechanics, and homogenization of heterogeneous solids. Instead, it is dedicated to recent developments in the field and its most exciting aspects. It covers a range of topics that clearly demonstrate the depth, the diversity, and the breadth of this fertile area of research which is governed by size/scale, anisotropy, and morphology dependence of interacting phases that define the bulk properties of the resulting materials. It contains 17 chapters authored/coauthored by some of the most talented and respected researchers in the community. Specifically, it covers the following important topics:

Sequential and concurrent atomistic multiscale modeling of multiphysics problems (Chapter 1), MD modeling of nanoindentaion of multilayered graphene-reinforced nanocomposites (Chapter 2), MD studies of nanocomposites reinforced by defective CNTs (Chapter 3), Electrical conductivity of CNT- and Graphene-Based Nanocomposites (Chapter 4), Mechanical behavior of nanowires with high-order surface stress effects (Chapter 5), Design of nano-inhomogeneities with internal strain in antiplane deformations of Composites (Chapter 6), Ballistic performance of bimodal nanostructured and nanotwin-strengthened metals (Chapter 7), Full-field micromechanics of Precipitated SMAs (Chapter 8), Micromechanics of ferroic functional materials (Chapter 9), Micromechanics of bone modeled as a composite material (Chapter 10), Linear elastic composites containing spheroidal inclusions (Chapter 11), Time-incremental Eshelby-based homogenization scheme for viscoelastic heterogeneous materials (Chapter 12), Local spin effects on bulk properties of granule materials (Chapter 13), Parametric HFGMC micromechanics (Chapter 14), Parameterization of reinforcement phase distribution in continuous FRCs (Chapter 15), Micromechanical modeling of polymeric composites with moisture absorption (Chapter 16), General interface integral equations in elasticity of random structure composites (Chapter 17).

In each chapter, the state of the art in the respective field and the future trends are covered and discussed.

This effort offers an up-to-date coverage of diverse but highly related topics on modeling, characterization, and applications of micromechanics and nanomechanics in advanced and functional materials in a single volume. We believe that it is an excellent resource and it should be of interest to undergraduate and graduate physics and engineering students as well as researchers in academic institutions, government agencies and industries specializing in aerospace, mechanical, electrical, material science, mining, biomedical, and civil engineering. We are confident that the readers will find the information covered in this book current, useful, and informative. We are confident that the readers will find the information covered in this book current, useful, and informative.

Finally, we wish to take this opportunity to sincerely express our gratitude to the authors for their outstanding contributions in addressing many of the exciting new concepts and developments in micromechanics and nanomechanics of composites. Their informative efforts should guide both the experienced and the new-comers

to these fascinating areas of research. We are also indebted to our wives Valerie Meguid and Jackie Li for their affectionate encouragement and support throughout the different stages of this effort.

Shaker A. Meguid, Toronto, Canada
George J. Weng, New Jersey, USA

# Contents

# Contributors

**Jacob Aboudi** Faculty of Engineering, Tel-Aviv University, Tel Aviv, Israel

**Ahmed R. Alian** Mechanics and Aerospace Design Laboratory, Mechanical and Industrial Engineering, University of Toronto, Toronto, ON, Canada

**T. Baxevanis** Department of Mechanical Engineering, University of Houston, Houston, TX, USA

**Stéphane Berbenni** Laboratoire d'Etude des Microstructures et de Mécanique des Matériaux, Université de Lorraine, Metz, France

**Valeriy Buryachenko** Micromechanics and Composites LLC, Dayton, OH, USA

**Tungyang Chen** Department of Civil Engineering, National Cheng Kung University, Tainan, Taiwan

**Min-Sen Chiu** Department of Civil Engineering, National Cheng Kung University, Tainan, Taiwan

**Ming Dai** School of Mechanical Engineering, Changzhou University, Changzhou, China

**M.A.N. Dewapriya** Mechanics and Aerospace Design Laboratory, Mechanical and Industrial Engineering, University of Toronto, Toronto, ON, Canada

**Salvatore Federico** Department of Mechanical and Manufacturing Engineering, The University of Calgary, Calgary, AB, Canada

**Alfio Grillo** DISMA - Dipartimento di Scienze Matematiche "G.L. Lagrange", Politecnico di Torino, Torino, Italy

**Xiang Guo** School of Mechanical Engineering, Tianjin University, Tianjin, China

Tianjin Key Laboratory of Nonlinear Dynamics and Control, Tianjin, China

**Rami Haj-Ali** Faculty of Engineering, Tel-Aviv University, Tel Aviv, Israel

**Muneo Hori** Earthquake Research Institute, The University of Tokyo, Tokyo, Japan

**John E. Huber** Department of Engineering Science, University of Oxford, Oxford, UK

**Tsuyoshi Ichimura** Earthquake Research Institute, The University of Tokyo, Tokyo, Japan

**Iwona Jasiuk** Department of Mechanical Science and Engineering, University of Illinois at Urbana-Champaign, Urbana, IL, USA

**I. Karaman** Department of Materials Science and Engineering, Texas A&M University, College Station, TX, USA

**D.C. Lagoudas** Department of Aerospace Engineering, Texas A&M University, College Station, TX, USA

Department of Materials Science and Engineering, Texas A&M University, College Station, TX, USA

**James D. Lee** Department of Mechanical and Aerospace Engineering, The George Washington University, Washington, DC, USA

**Jiaoyan Li** School of Engineering, Brown University, Providence, RI, USA

**Jian Lu** Department of Mechanical and Biomedical Engineering, City University of Hong Kong, Kowloon Tong, Hong Kong

**Shaker A. Meguid** Mechanics and Aerospace Design Laboratory, Mechanical and Industrial Engineering, University of Toronto, Toronto, ON, Canada

**Yihui Pan** School of Aerospace Engineering and Applied Mechanics, Tongji University, Shanghai, China

**Xudong Peng** Mechanics and Aerospace Design Laboratory, Mechanical and Industrial Engineering, University of Toronto, Toronto, ON, Canada

**Hafid Sabar** Laboratoire de Mécanique Biomécanique Polymères Structures, Ecole Nationale Ingénieurs de Metz, Metz, France

**Tomasz Sadowski** Department of Solid Mechanics, Lublin University of Technology, Lublin, Poland

**Sylwester Samborski** Department of Applied Mechanics, Lublin University of Technology, Lublin, Poland

**Peter Schiavone** Department of Mechanical Engineering, University of Alberta, Edmonton, AB, Canada

**A. Solomou** Department of Aerospace Engineering, Texas A&M University, College Station, TX, USA

**Supprasert Sument** Earthquake Research Institute, The University of Tokyo, Tokyo, Japan

**Leyu Wang** Colleage of Science, George Mason University, Fairfax, VA, USA

**Yang Wang** Department of Mechanical and Aerospace Engineering, Rutgers University, New Brunswick, NJ, USA

**George J. Weng** Mechanical and Aerospace Engineering, Rutgers University, New Brunswick, NJ, USA

**Lalith Wijerathne** Earthquake Research Institute, The University of Tokyo, Tokyo, Japan

**Piotr Wolszczak** Department of Automation, Lublin University of Technology, Lublin, Poland

**Guang Yang** School of Mechanical Engineering, Tianjin University, Tianjin, China

**Zhen Zhang** Department of Mechanical and Aerospace Engineering, The George Washington University, Washington, DC, USA

**Zheng Zhong** School of Aerospace Engineering and Applied Mechanics, Tongji University, Shanghai, China

**Linli L. Zhu** Department of Engineering Mechanics, School of Aeronautics and Astronautics, Zhejiang University, Hangzhou, Zhejiang, China

# Chapter 1
# Sequential and Concurrent Multiscale Modeling of Multiphysics: From Atoms to Continuum

**James D. Lee, Jiaoyan Li, Zhen Zhang, and Leyu Wang**

**Abstract** The multiscale and multi-physics approaches reach a new height for modeling and simulation. It opens up a new opportunity to connect engineering applications with basic science. In this work, a more general governing equation of non-equilibrium molecular dynamics, covering thermo-mechanical-electromagnetic coupling effects, has been derived. This theoretical development of classical molecular dynamics provides a solid foundation for our bottom-up sequential multiscale modeling, from which we calculate material properties including the elastic constants, thermal conductivity, specific heat, and thermal expansion coefficients for thermoelasticity. With these preparations, we further present our newly formulated concurrent multiscale theory. The key challenge in constructing a concurrent multiscale theory hinges at the formulation of the interfacial conditions, which determine the communication between the atomic region and genuine continuum region. Our philosophy of concurrent modeling is that we decompose the solution region into two sub-regions in space and utilize the central difference method with different time steps for different sub-regions to march on in time. For sub-regions where critical physical phenomena, such as crack initiation and propagation, occur, we adopt molecular dynamics with small time step to simulate the material behavior with relatively high resolution. For non-critical regions, we adopt finite element method with relatively large time step to reduce the computational effort. The interfacial condition is constructed naturally by anchoring finite element nodes at centroids of groups. Each group is a cluster of atoms simulated by molecular dynamics. In this way, a concurrent multiscale modeling theory from atoms to genuine continuum is constructed. To test the capability of our theory, we conduct

J.D. Lee (✉) • Z. Zhang
Department of Mechanical and Aerospace Engineering, The George Washington University, Washington, DC 20052, USA
e-mail: jdlee@gwu.edu; chillzz@gwu.edu

J. Li
School of Engineering, Brown University, Providence, RI 02860, USA
e-mail: jiaoyan_li@brown.edu

L. Wang
Colleage of Science, George Mason University, Fairfax, VA 22030, USA
e-mail: lwang28@gmu.edu



S.A. Meguid, G.J. Weng (eds.), *Micromechanics and Nanomechanics of Composite Solids*, DOI 10.1007/978-3-319-52794-9_1

crack propagation simulations with different loading conditions. It was observed that the crack that pre-existed in the continuum region can propagate into the critical atomic region without any fracture criterion.

## 1.1 Introduction

Molecular dynamic (MD) simulation has established itself as a widely employed simulation technique for the study of material behaviors at the nanoscale. Unfortunately, the extension of MD into computational science over a realistic range of length and time is limited, due to the large number of particles involved as well as the complex nature of their interactions. The limitations are also imposed by the requirement of smallness of the time steps, even though one may be primarily interested in events that occur over a much longer time scale. The emergence of multiple length scale and time scale approaches, along with the development of massively parallel computers, remarkably expands the realm of modeling and simulation from nanoscale to microscale.

The past several years have witnessed the explosive growth of interest in multiple length scale theories and simulations. There have been several reviews on multiscale modeling and simulation in the literature, focusing on different aspects. Generally speaking, there are two categories of multiscale modeling methods: sequential and concurrent. The sequential multiscale methodology separates calculation at each scale and passes the results between scales. For instance, almost all conventional MD simulations rely on interatomic potentials obtained from first principles calculations. Material constants in constitutive relation for finite element calculation could be predicted from MD simulation. The idea of sequential multiscale modeling and simulation is straightforward and has shown applicability for systems which are weakly coupled at different scales. The other one, concurrent multiscale methodology integrates calculations and solves the problem simultaneously, and therefore, it is more efficient and more challenge than the sequential one. In a concurrent simulation, the system is often decomposed into several sub-domains characterized by different scales and physics. Different theories are applied to different domains to simulate the material behaviors. A successful concurrent multiscale model seeks a smooth coupling between these sub-domains, interpreted as the construction of interfacial conditions. Although there are a lot of attempts on this important issue, challenges and limitations still exist. The concurrent approach is more desirable for systems in which system behavior at each scale depends strongly on what happens at the higher or lower scales.

We organize the remaining part of this work as follows. In Sect. 1.2, the molecular dynamics simulation of multiphysics is formulated. It includes the introduction of Maxwell's equations and Lorentz force at nanoscale, reformulation of Nosé-Hoover thermostat, proof of the objectivity of *Nosé-Hoover thermal velocity*, and virial stress tensor. In Sect. 1.3, we demonstrate that the material properties of thermoelasticity can be obtained from molecular dynamics simulation through a set of procedures named as *sequential multiscale modeling*. Graphene and Tersoff

potential are used as examples. In Sect. 1.4, we construct a concurrent multiscale theory and formulate the interfacial conditions to bridge the gap between atoms and genuine continuum. It also includes a multiple time scale algorithm and a corresponding numerical procedure. Sample problems are solved and numerical results are discussed. The work ends with discussions on the significance and the achievement of this multiscale theory in Sect. 1.5.

## 1.2 Molecular Dynamics Simulation of Multiphysics

When Molecular Dynamics (MD) was originally conceived (Alder and Wainwright 1959; Rahman 1964), the fundamental idea was to determine the trajectories of atoms or molecules by numerically solving the Newton's equations of motion for a system of interacting particles. To begin with, the general picture in our mind is a material system which consists of many different kinds of atoms. Let the Newton's law be expressed as

$$m^i \dot{\mathbf{v}}^i = \mathbf{f}^i + \boldsymbol{\varphi}^i, \qquad i = [1, 2, 3, ...., N], \tag{1.1}$$

where $N$ is the total number of atoms in the material system; $m^i$ is the mass of *atom i*; $\mathbf{v}^i$ and $\mathbf{f}^i$ are the velocity of *atom i* and the interatomic force acting on *atom i*, respectively; $\boldsymbol{\varphi}^i$ is reserved, in this book chapter, for forces other than interatomic force acting on *atom i*, i.e., $\boldsymbol{\varphi}^i$ could be any combination of applied force, body force including Lorentz force, fictitious force due to the translation and rotation of the coordinate system, and thermal force due to the presence of thermostat.

A detailed formulation of Maxwell's equations and Lorentz force at the atomistic level was given by de Groot and Suttorp (1972). For non-relativistic electromagnetics, $\boldsymbol{\varphi}^i$ was obtained:

$$\boldsymbol{\varphi}^i = q^i \left\{ \mathbf{E}^e + c^{-1} \mathbf{v}^i \times \mathbf{B}^e \right\} + \sum_{j=1, j \neq i}^{N} q^i q^j \frac{\mathbf{r}^{ij}}{\left(r^{ij}\right)^3}, \tag{1.2}$$

where $q^i$ is the electric charge of *atom i*; $\mathbf{E}^e$ and $\mathbf{B}^e$ are the external electric and magnetic fields, respectively; $c$ is the speed of light; $\mathbf{r}^{ij} \equiv \mathbf{r}^i - \mathbf{r}^j$; and $r^{ij} \equiv \|\mathbf{r}^{ij}\|$. It is seen that the last term on the right-hand side of Eq. (1.2) is the Coulomb forces between *atom i* and *atom j*. It is worthwhile to note that, due to the non-relativistic approximation, i.e., $\|\mathbf{v}^i\| << c$, the Lorentz force exists only between charged atom and external $\mathbf{E}^e$ and $\mathbf{B}^e$ fields; between charged atoms themselves, only Coulomb forces exist.

The interatomic force $\mathbf{f}^i$ acting on *atom i* can be expressed as

$$\mathbf{f}^i = -\frac{\partial U}{\partial \mathbf{r}^i}, \tag{1.3}$$

where $U$ is the interatomic potential, a function of the position vectors $(\mathbf{r}^i, i = 1, 2, 3, \ldots, N)$ of all atoms in the system, i.e.,

$$U = U\left(\mathbf{r}^1, \mathbf{r}^2, \mathbf{r}^3, \ldots, \mathbf{r}^N\right). \tag{1.4}$$

It is noticed that, in MD simulation, temperature is a dependent variable. Usually, but not correctly, it was expressed as

$$T = \frac{\sum_{i=1}^{N} m^i \left(\mathbf{v}^i \cdot \mathbf{v}^i\right)}{N_{dof} k_B}, \tag{1.5}$$

where $N_{dof}$ is the number of degrees of freedom of the system and $k_B$ is the Boltzmann constant.

### 1.2.1 Reformulation of Nosé-Hoover Thermostat

The revolutionary Nosé-Hoover dynamics, originally introduced by Nosé (1984a, b) and developed further by Hoover (1985), modified Newtonian dynamics so as to reproduce canonical and isobaric-isothermal ensemble equilibrium systems. However, there is an increasing interest in conducting MD simulations which do not fall within the classification of these classical ensembles. A typical example is a nano material system whose temperature varies spatially and temporally during the simulation with the imposition of a temperature gradient. Clearly, this is a nanoscale heat conduction problem and requires Nonequilibrium Molecular Dynamics (NEMD) with a suitable algorithmic thermostat for the local temperature regulation. Li and Lee (2014a) pointed out the need to reformulate the Nosé-Hoover thermostat to locally regulate the temperatures at many distinct regions without introducing the unphysical linear and angular momenta. In this way, the trajectories of atoms and molecules can be generated more rigorously and accurately by NEMD simulations.

Here, for the reader's convenience, we briefly review the procedures and results of the reformulation of the Nosé-Hoover thermostat. Let's consider the whole specimen is divided into $N_G$ groups; in *group g*, there are $n_g$ atoms, not necessarily of the same kind. Then it is straightforward to calculate the mass, the position of the centroid, and the average velocity of *group g* as follows:

$$m^g \equiv \sum_{i=1}^{n_g} m^i \quad , \quad \overline{\mathbf{r}}^g \equiv \left(\sum_{i=1}^{n_g} m^i \mathbf{r}^i\right) / m^g \quad , \quad \overline{\mathbf{v}}^g \equiv \left(\sum_{i=1}^{n_g} m^i \mathbf{v}^i\right) / m^g. \tag{1.6}$$

Then the relative position and relative velocity can be obtained as

$$\overline{\mathbf{r}}^i \equiv \mathbf{r}^i - \overline{\mathbf{r}}^g \quad , \quad \overline{\mathbf{v}}^i \equiv \mathbf{v}^i - \overline{\mathbf{v}}^g. \tag{1.7}$$

It is noticed that

$$\sum_i m^i \overline{\mathbf{r}}^i = 0 \quad , \quad \sum_i m^i \overline{\mathbf{v}}^i = 0. \tag{1.8}$$

From now on, if there is no ambiguity, we use the abbreviation $\sum_i \equiv \sum_{i=1}^{n_g}$, $\overline{\mathbf{r}} \equiv \overline{\mathbf{r}}^g$, $\overline{\mathbf{v}} \equiv \overline{\mathbf{v}}^g$. The angular momentum (with respect to the centroid) is calculated as

$$\mathbf{H} = \sum_i m^i \overline{\mathbf{r}}^i \times \overline{\mathbf{v}}^i. \tag{1.9}$$

If, in general, a system of $n$ particles has a rigid body rotation about the centroid with an angular velocity $\boldsymbol{\omega}$, then the relative velocity of the $i-th$ particle, $\boldsymbol{\eta}^i$, with respect to the centroid can be calculated as

$$\boldsymbol{\eta}^i = \boldsymbol{\omega} \times \overline{\mathbf{r}}^i. \tag{1.10}$$

The angular momentum due to the rigid body rotation can now be calculated as

$$\overline{\mathbf{H}} = \sum_i m^i \overline{\mathbf{r}}^i \times \boldsymbol{\eta}^i = \sum_i m^i \overline{\mathbf{r}}^i \times \left(\boldsymbol{\omega} \times \overline{\mathbf{r}}^i\right) = \mathbf{J}\boldsymbol{\omega}, \tag{1.11}$$

where the moment of inertia tensor, $\mathbf{J}$, is defined as

$$\mathbf{J} \equiv \sum_i m^i \left\{\left(\overline{\mathbf{r}}^i \cdot \overline{\mathbf{r}}^i\right)\mathbf{I} - \overline{\mathbf{r}}^i \otimes \overline{\mathbf{r}}^i\right\}. \tag{1.12}$$

By equating $\mathbf{H}$ and $\overline{\mathbf{H}}$, one may find the angular velocity of the system:

$$\mathbf{H} = \overline{\mathbf{H}} = \mathbf{J}\boldsymbol{\omega} \quad \Rightarrow \quad \boldsymbol{\omega} = \mathbf{J}^{-1}\mathbf{H}. \tag{1.13}$$

Now we define the *Nosé-Hoover thermal velocity* as

$$\tilde{\mathbf{v}}^i \equiv \mathbf{v}^i - \overline{\mathbf{v}} - \boldsymbol{\eta}^i = \mathbf{v}^i - \overline{\mathbf{v}} - \boldsymbol{\omega} \times \overline{\mathbf{r}}^i = \mathbf{v}^i - \overline{\mathbf{v}} - \left(\mathbf{J}^{-1}\mathbf{H}\right) \times \overline{\mathbf{r}}^i. \tag{1.14}$$

In other words, the *Nosé-Hoover thermal velocity* is the velocity beyond rigid body translation and rotation. Now one may prove the following theorem.

**Theorem 1** *The total linear momentum and angular momentum caused by the Nosé-Hoover thermal velocity are vanishing.*

*Proof*

$$\begin{aligned} \sum_i m^i \tilde{\mathbf{v}}^i &= \sum_i m^i \left(\mathbf{v}^i - \overline{\mathbf{v}} - \boldsymbol{\eta}^i\right) \\ &= \sum_i m^i \mathbf{v}^i - m\overline{\mathbf{v}} - \sum_i m^i \boldsymbol{\omega} \times \overline{\mathbf{r}}^i \\ &= -\boldsymbol{\omega} \times \sum_i m^i \overline{\mathbf{r}}^i = 0, \end{aligned} \tag{1.15}$$

$$\begin{aligned}\sum_i m^i \mathbf{r}^i \times \tilde{\mathbf{v}}^i &= \sum_i m^i \left(\overline{\mathbf{r}}^i + \overline{\mathbf{r}}\right) \times \left(\mathbf{v}^i - \overline{\mathbf{v}} - \boldsymbol{\eta}^i\right) \\ &= \sum_i m^i \overline{\mathbf{r}}^i \times \left(\mathbf{v}^i - \overline{\mathbf{v}} - \boldsymbol{\eta}^i\right) + \overline{\mathbf{r}} \times \sum_i m^i \left(\mathbf{v}^i - \overline{\mathbf{v}} - \boldsymbol{\eta}^i\right) \\ &= \sum_i m^i \overline{\mathbf{r}}^i \times \left(\mathbf{v}^i - \overline{\mathbf{v}} - \boldsymbol{\omega} \times \overline{\mathbf{r}}^i\right) \\ &= \sum_i m^i \overline{\mathbf{r}}^i \times \overline{\mathbf{v}}^i - \sum_i m^i \overline{\mathbf{r}}^i \times \left(\boldsymbol{\omega} \times \overline{\mathbf{r}}^i\right) \\ &= \mathbf{H} - \overline{\mathbf{H}} = 0.\end{aligned} \tag{1.16}$$

Now the temperature of *group g* is calculated as

$$T_g = \frac{1}{N_g^{dof} k_B} \sum_{i=1}^{n_g} m^i \tilde{\mathbf{v}}^i \cdot \tilde{\mathbf{v}}^i, \tag{1.17′}$$

where $N_g^{dof} = 3n_g - 6$ is the number of degrees of freedom of *group g*. It is noticed that, according to Eqs. (1.15) and (1.16), rigid body translation and rotation have no contribution to the calculation of temperature. The subtraction of 6 from $3n_g$ is due to the elimination of linear and angular momenta from the velocity field in the calculation of the *Nosé-Hoover thermal velocity*.

The governing equations for a material system with upgraded Nosé-Hoover thermostats should now be expressed as

$$m^i \dot{\tilde{\mathbf{v}}}^i = \mathbf{f}^i + \boldsymbol{\varphi}^i - \chi_g m^i \tilde{\mathbf{v}}^i, \qquad i \in \textit{group } g, \tag{1.18′}$$

where $-\chi_g m^i \tilde{\mathbf{v}}^i$ is named as the *Nosé-Hoover temperature force*. The role of $\chi_g$ is similar to that of the damping coefficient, except that $\chi_g$ is not a constant—instead it is governed by

$$\dot{\chi}_g = \frac{1}{\tau_g^2 T_g^o} \left(T_g - T_g^o\right), \tag{1.19′}$$

where $\tau_g$ is a specified time constant associated with *group g*; $T_g^o$ is the target temperature of the Nosé-Hoover thermostat. It is noticed that if *group g* doesn't have a thermostat, then it is a special case with $\chi_g = \dot{\chi}_g = 0$. From now on, if there is no ambiguity, we use the general case for description and derivation. Now one can readily prove the following theorem.

**Theorem 2** *The total force and total moment caused by the Nosé-Hoover temperature forces are vanishing.*

*Proof*

$$\sum_{i\in S_g}\left(-\chi_g m^i\tilde{\mathbf{v}}^i\right)=-\chi_g\sum_{i\in S_g}m^i\tilde{\mathbf{v}}^i=0, \tag{1.20}$$

$$\sum_{i\in S_g}\mathbf{r}^i\times\left(-\chi_g m^i\tilde{\mathbf{v}}^i\right)=-\chi_g\sum_{i\in S_g}m^i\mathbf{r}^i\times\tilde{\mathbf{v}}^i=0. \tag{1.21}$$

Together with Theorem 1, it means that the *Nosé-Hoover thermal velocity* doesn't introduce extra linear and angular momenta; the *Nosé-Hoover temperature force* doesn't introduce extra force and moment to the temperature-controlled group either. Actually, these conditions must be imposed whenever a thermostat is applied. Also, it is noticed that, according to Eq. (1.17), (1) the temperature of *group g* can be calculated irrespective of whether that group has a thermostat or not and (2) the temperature depends on the *Nosé-Hoover thermal velocity*, but not on linear or angular momentum.

### 1.2.2 Hamiltonian of the Material System

The *Hamiltonian* of the entire system can be expressed as

$$\begin{aligned}H=&\sum_{g=1}^{N_g}\sum_{i\in g}\left\{\tfrac{1}{2}m^i\mathbf{v}^i\cdot\mathbf{v}^i-\int_0^t\boldsymbol{\varphi}^i(s)\cdot\mathbf{v}^i(s)ds\right\}\\&+\sum_{g=1}^{N_g}\left\{\tfrac{1}{2}Q_g\chi_g^2+\tfrac{Q_g}{\tau_g^2}\int_0^t\chi_g(s)ds\right\}\\&+U\left(\mathbf{r}^1,\mathbf{r}^2,\mathbf{r}^3,....,\mathbf{r}^N\right),\end{aligned} \tag{1.22}$$

where $U$ is the total interatomic potential energy of the entire system and

$$Q_g\equiv N_g^{dof}k_BT_g^o\tau_g^2. \tag{1.23}$$

It is seen that the Hamiltonian, $H$, consists of four parts: (1) the kinetic energy which is the sum of the kinetic energies of all atoms, i.e., $\frac{1}{2}m^i\mathbf{v}^i\cdot\mathbf{v}^i$ $(i=1,2,3,...,N)$, (2) the potential energy $U(\mathbf{r}^1,\mathbf{r}^2,\mathbf{r}^3,....,\mathbf{r}^N)$, which in principle cannot be divided into a summation of subsets, (3) the work done by force $\boldsymbol{\varphi}^i$ $[i=1,2,3,...,N]$, and (4) the sum of thermal energy $E_g$ $[g=1,2,3,...,N_g]$ of all groups, where

$$E_g\equiv\left\{\frac{1}{2}Q_g\chi_g^2+\frac{Q_g}{\tau_g^2}\int_0^t\chi_g(s)ds\right\}. \tag{1.24}$$

One may prove the following theorem.

**Theorem 3** *Hamiltonian is a constant.*

*Proof* If there is no ambiguity, we use the abbreviation $\sum_{i=1}^{N} \equiv \sum_{g=1}^{N_g} \sum_{i \in g}$. Now we differentiate Eq. (1.22) term by term with respect to time as follows:

$$\frac{d}{dt} \sum_{i=1}^{N} \frac{1}{2} m^i \mathbf{v}^i \cdot \mathbf{v}^i = \sum_{i=1}^{N} m^i \dot{\mathbf{v}}^i \cdot \mathbf{v}^i, \tag{1.25}$$

$$-\frac{d}{dt} \sum_{i=1}^{N} \int_0^t \boldsymbol{\varphi}^i(s) \cdot \mathbf{v}^i(s) ds = -\sum_{i=1}^{N} \boldsymbol{\varphi}^i \cdot \mathbf{v}^i, \tag{1.26}$$

$$\begin{aligned} \frac{d}{dt} \sum_{g=1}^{N_g} \left\{ \frac{1}{2} Q_g \chi_g^2 + \frac{Q_g}{\tau_g^2} \int_0^t \chi_g(s) ds \right\} &= \sum_{g=1}^{N_g} \left\{ Q_g \chi_g \dot{\chi}_g + \frac{Q_g \chi_g}{\tau_g^2} \right\} \\ = \sum_{g=1}^{N_g} N_g^{dof} k_B \chi_g T_g &= \sum_{g=1}^{N_g} \sum_{i \in g} \chi_g m^i \tilde{\mathbf{v}}^i \cdot \tilde{\mathbf{v}}^i \\ = \sum_{g=1}^{N_g} \sum_{i \in g} \chi_g m^i \tilde{\mathbf{v}}^i \cdot \mathbf{v}^i &= \sum_{i=1}^{N_g} \chi_g m^i \tilde{\mathbf{v}}^i \cdot \mathbf{v}^i, \end{aligned} \tag{1.27}$$

$$\frac{dU}{dt} = \sum_{i=1}^{N} \frac{\partial U}{\partial \mathbf{r}^i} \cdot \mathbf{v}^i = -\sum_{i=1}^{N} \mathbf{f}^i \cdot \mathbf{v}^i. \tag{1.28}$$

Now we have

$$\dot{H} = \sum_{i=1}^{N} \left\{ m^i \dot{\mathbf{v}}^i - \mathbf{f}^i - \boldsymbol{\varphi}^i + \chi_g m^i \tilde{\mathbf{v}}^i \right\} \cdot \mathbf{v}^i. \tag{1.29}$$

We recall that $m^i \dot{\mathbf{v}}^i - \mathbf{f}^i - \boldsymbol{\varphi}^i + \chi_g m^i \tilde{\mathbf{v}}^i = 0 \quad [i = 1, 2, 3, ..., N]$ is the governing equation for every atom in the system. Thus we have proved Theorem 3. We also notice that

$$\dot{E}_g = N_g^{dof} k_B \chi_g T_g. \tag{1.30}$$

Actually, $\dot{E}_g$ is the flow of energy per unit time out of *group g* due to the action of the Nosé-Hoover thermostat.

### 1.2.3 Objectivity in Molecular Dynamics

The principle of objectivity, sometimes referred to as the principle of material frame-indifference, addresses the invariance attributes of physical quantities and material properties under change of reference frame. This concept of objectivity has been introduced in almost every textbook of continuum mechanics, for example, in *Mechanics of Continua* (Eringen 1980) and *Microcontinuum Field Theories* (Eringen 1999). The idea is very simple: material properties measure in different reference frames are required to be objectively equivalent, i.e., not subject to the motion of the observers. However, in molecular dynamics (MD), sharing common ground with Newtonian mechanics, objectivity was rarely discussed. Recently, Yang et al. (2016) presented detailed discussions about objectivity. Here we briefly describe the concepts, end results, and implications of objectivity. We first recall the two definitions on objectivity given by Eringen (1980) as follows.

**Definition 1.** Two motions $x_k(\mathbf{X}, t)$ and $x_k^*(\mathbf{X}, t^*)$ are called objectively equivalent if and only if

$$\mathbf{x}^*\left(\mathbf{X}, t^*\right) = \mathbf{Q}(t)\mathbf{x}\left(X, t\right) + \mathbf{b}(t), \qquad t^* = t + a, \tag{1.31}$$

where $a$ is a constant time shift, $\mathbf{b}(t)$ is a time-dependent translation, and $\mathbf{Q}(t)$ is time-dependent orthogonal transformations, i.e.,

$$\mathbf{Q}\mathbf{Q}^T = \mathbf{Q}^T\mathbf{Q} = \mathbf{I}, \qquad \det\left(\mathbf{Q}\right) = 1. \tag{1.32}$$

It is seen that $\mathbf{Q}$ consists of all rigid rotations ($\det \mathbf{Q} = +1$). Two objectively equivalent motions differ only in relative frame and time.

**Definition 2.** Any tensorial quantity that obeys the following tensor transformation law is said to be objective or material frame-indifferent.

$$A^*_{abcd....}\left(\mathbf{X}, t^*\right) = Q_{a\alpha}(t)Q_{b\beta}(t)Q_{c\gamma}(t)Q_{d\delta}(t)....A_{\alpha\beta\gamma\delta....}\left(\mathbf{X}, t\right) \tag{1.33}$$

Following Eq. (1.31), one may obtain

$$\mathbf{v}^* = \mathbf{Q}\mathbf{v} + \dot{\mathbf{Q}}\mathbf{x} + \dot{\mathbf{b}} \quad , \quad \mathbf{a}^* = \mathbf{Q}\mathbf{a} + \ddot{\mathbf{Q}}\mathbf{x} + 2\dot{\mathbf{Q}}\mathbf{v} + \ddot{\mathbf{b}} \tag{1.34}$$

which simply says velocity and acceleration are not objective—actually this statement is just a common sense.

Among $N$ atoms, if one picks *atom i* as the reference point, the interatomic potential can be expressed as

$$U = U\left(\mathbf{r}^{i1}, \mathbf{r}^{i2}, \mathbf{r}^{i3}, ....\right) \tag{1.35}$$

From the viewpoint of objectivity, $U$ is a scalar-valued isotropic function of many objective vectors. Following Wang's representative theorem for isotropic functions (Wang 1970), one may rewrite $U$ as a function of lengths and angles:

$$r^{ij} = \left\| \mathbf{r}^{ij} \right\| \quad , \quad \theta^{ijk} \equiv \cos^{-1}\left( \frac{\mathbf{r}^{ij} \cdot \mathbf{r}^{ik}}{r^{ij} r^{ik}} \right). \tag{1.36}$$

In fact, for a two-body potential, e.g., Lennard Jones potential or Buckingham potential, it takes the form

$$U^{(2)} = \frac{1}{2!} \sum_{i,j=1}^{N} U^{ij}\left(r^{ij}\right); \tag{1.37}$$

for a three-body potential, e.g., Tersoff potential (Tersoff 1988, 1989) or Stillinger-Weber potential (Stillinger and Weber 1985),

$$U^{(3)} = \frac{1}{3!} \sum_{i,j,k=1}^{N} U^{ijk}\left(r^{ij}, r^{ik}, \theta^{ijk}\right); \tag{1.38}$$

for a four-body potential, e.g., in UFF (Rappe et al. 1992),

$$U^{(4)} = \frac{1}{4!} \sum_{i,j,k,l=1}^{N} U^{ijkl}\left(r^{ij}, r^{ik}, r^{il}, \theta^{ijk}, \phi, \varphi\right), \tag{1.39}$$

where $\phi$ and $\varphi$ are the torsion angle and inversion angle, respectively. Also, the interatomic force can be obtained as

$$\begin{aligned} \mathbf{f}^{i} &= -\frac{\partial U\left(\mathbf{r}^{i1}, \mathbf{r}^{i2}, \mathbf{r}^{i3}, ....\right)}{\partial \mathbf{r}^{i}} \\ &= -\sum_{j} \frac{\partial U\left(\mathbf{r}^{i1}, \mathbf{r}^{i2}, \mathbf{r}^{i3}, ....\right)}{\partial r^{ij}} \frac{\partial r^{ij}}{\partial \mathbf{r}^{i}} \\ &= -\sum_{j} \frac{\partial U\left(\mathbf{r}^{i1}, \mathbf{r}^{i2}, \mathbf{r}^{i3}, ....\right)}{\partial r^{ij}} \frac{\mathbf{r}^{ij}}{r^{ij}}. \end{aligned} \tag{1.40}$$

Again, it is seen that $\mathbf{f}^{i}$, in Eq. (1.40), obeys Wang's representative theorem and is an objective vector-valued isotropic function.

Although velocity,$\mathbf{v}$, is not objective, one may prove that the *Nosé-Hoover thermal velocity*, $\tilde{\mathbf{v}}$, is objective (Yang et al. 2016), i.e.,

$$\tilde{\mathbf{v}}^{*} = \mathbf{Q}\tilde{\mathbf{v}}. \tag{1.41}$$

Then it is straightforward to conclude that temperature expressed in Eq. (1.17) is objective, but the one expressed in Eq. (1.5) is not. From now on, we name the temperature calculated by Eq. (1.17) as *atomistic temperature.*

Also, we express the virial stress tensor $\mathbf{S}$, which is the counterpart of the Cauchy stress tensor in continuum mechanics, as

$$\mathbf{S} = -\frac{1}{V_\Omega}\sum_{i\in\Omega}\left(m^i\tilde{\mathbf{v}}^i\otimes\tilde{\mathbf{v}}^i + \sum_j \mathbf{r}^i\otimes\mathbf{f}^i\right), \tag{1.42}$$

where $\Omega$ is the region of which one seeks to find the virial stress; $V_\Omega$ is the volume of $\Omega$; $\mathbf{r}^i$ is the position vector of *atom i*; $\mathbf{f}^i$ is all the interatomic force acting on *atom i*; and the summation on *j* means all the interactions between *atom i* and *atom j* should be counted, irrespective of whether *atom j* is in $\Omega$ or not. Now let's examine whether the virial stress expressed in Eq. (1.42) is objective. Since the kinetic part is obviously objective now, let's take a look at the potential part:

$$\begin{aligned}\tilde{S}_{\alpha\beta} = \sum_{i\in\Omega}\sum_j \tilde{\mathbf{r}}^i_\alpha\tilde{\mathbf{f}}^i_\beta &= \sum_{i\in\Omega}\sum_j\left(Q_{\alpha\gamma}\mathbf{r}^i_\gamma + b_\alpha\right)Q_{\beta\delta}\mathbf{f}^i_\delta \\ &= \sum_{i\in\Omega}\sum_j Q_{\alpha\gamma}\mathbf{r}^i_\gamma Q_{\beta\delta}\mathbf{f}^i_\delta + b_\alpha Q_{\beta\delta}\sum_{i\in\Omega}\sum_j \mathbf{f}^i_\delta \\ &= Q_{\alpha\gamma}Q_{\beta\delta}S_{\gamma\delta} + b_\alpha Q_{\beta\delta}\sum_{i\in\Omega}\sum_j \mathbf{f}^i_\delta \\ &= Q_{ik}Q_{jl}S_{kl},\end{aligned} \tag{1.43}$$

which means the virial stress tensor expressed in Eq. (1.42) is objective. It is noticed that the proof indicated in Eq. (1.43) depends on two key points: (1) interatomic force $\mathbf{f}^i$ is objective (which has been shown in Eq. (1.40)) and (2) the total interatomic forces in a close system are zero, i.e.,

$$\sum_{i\in\Omega}\sum_j \mathbf{f}^i = 0. \tag{1.44}$$

What if not all *atom j* are in $\Omega$? For example, there is an *n*-body potential and there are *n* atoms among which one has

$$\sum_{i=1}^n \mathbf{f}^i = 0 \quad \Rightarrow \quad \sum_{i=1}^n \mathbf{r}^i\otimes\mathbf{f}^i \text{ is objective.} \tag{1.45}$$

If *atom i* is one of the *n* atoms, then consider that $\frac{1}{n}\sum_{i=1}^n \mathbf{r}^i\otimes\mathbf{f}^i$ is the contribution of *atom i* to the virial stress of $\Omega$.

So far, we have imposed the principle of objectivity on constitutive relations in molecular dynamics (MD). To capture the full motion of a material body with respect to a non-inertial reference frame (a reference frame accelerates and rotates), the governing equation must account for the motion of the reference frame itself, thus fictitious forces are introduced. *Rectilinear acceleration force*, *centrifugal force*, *Coriolis force*, *Euler force*, etc., are several commonly noticed fictitious forces. Moreover, Einstein pointed out that gravity, too, is a form of fictitious force,

which leads to the birth of *general relativity*. It is regarded that the appearance of fictitious force resolves the discrepancy in different non-inertial reference frames so that motion observed in one frame can be converted to the motion observed in another. As one may observe that acceleration $\mathbf{a} \equiv \dot{\mathbf{v}}$ is not objective (cf. Eq. (1.34)), let $\mathbf{i}$ be the acceleration induced by the fictitious force. The principle of objectivity imposes a requirement:

$$\mathbf{a}^* - \mathbf{i}^* = \mathbf{Q}\,(\mathbf{a} - \mathbf{i})\,. \tag{1.46}$$

For simplicity, we assume there is no fictitious force in the inertia reference frame, which at most moves with constant speed, then Eq. (1.46) simply means

$$\mathbf{i}^* = \ddot{\mathbf{Q}}\mathbf{x} + 2\dot{\mathbf{Q}}\mathbf{v} + \ddot{\mathbf{b}}. \tag{1.47}$$

Yang et al. (2016) further developed the expressions for $\mathbf{a}^*$ and $\mathbf{i}^*$ as

$$\begin{aligned}\mathbf{a}^* = \mathbf{Q}\mathbf{a} &+ [-2\boldsymbol{\omega} \times \mathbf{v}^* - \boldsymbol{\omega} \times (\boldsymbol{\omega} \times \mathbf{x}^*) - \dot{\boldsymbol{\omega}} \times \mathbf{x}^*] \\ &+ [2\boldsymbol{\omega} \times \dot{\mathbf{b}} + \boldsymbol{\omega} \times (\boldsymbol{\omega} \times \mathbf{b}) - \dot{\boldsymbol{\omega}} \times \mathbf{b}] + \ddot{\mathbf{b}},\end{aligned} \tag{1.48}$$

$$\begin{aligned}\mathbf{i}^* = &[-2\boldsymbol{\omega} \times \mathbf{v}^* - \boldsymbol{\omega} \times (\boldsymbol{\omega} \times \mathbf{x}^*) - \dot{\boldsymbol{\omega}} \times \mathbf{x}^*] \\ &+ [2\boldsymbol{\omega} \times \dot{\mathbf{b}} + \boldsymbol{\omega} \times (\boldsymbol{\omega} \times \mathbf{b}) - \dot{\boldsymbol{\omega}} \times \mathbf{b}] + \ddot{\mathbf{b}},\end{aligned} \tag{1.49}$$

where $\Omega_{ij} \equiv \dot{Q}_{ik} Q_{jk}$ and $\omega_k \equiv \frac{1}{2} e_{ijk} \Omega_{ij}$.

## 1.3 Thermoelasticity and Sequential Multiscale Modeling

### *1.3.1 Governing Equations of Thermoelasticity*

In small-strain thermoelasticity (a branch of continuum mechanics), the relevant balance laws and constitutive equations may be expressed as (Eringen 1999; Chen et al. 2006; Boresi et al. 2011)

$$\rho^o \dot{\mathbf{v}} = \nabla \cdot \boldsymbol{\sigma} + \rho^o \boldsymbol{\varphi}, \tag{1.50}$$

$$\rho^o \dot{e} - \boldsymbol{\sigma} : \nabla \mathbf{v} + \nabla \cdot \mathbf{q} - \rho^o h = 0, \tag{1.51}$$

$$\sigma_{ij} = -\beta_{ij} \left(T - T^{ref}\right) + A_{ijkl} e_{kl}, \tag{1.52}$$

$$\rho^o \dot{e} = \rho^o \gamma \dot{T} + A_{ijkl} e_{ij} \dot{e}_{kl}, \tag{1.53}$$

$$q_i = -\kappa_{ij} T_{,j}, \tag{1.54}$$

where $\rho^o$ is the mass density in the reference state, $\mathbf{u}$ is the displacement vector and $\mathbf{v} = \dot{\mathbf{u}}$ is the velocity vector, $\boldsymbol{\sigma}$ is the Cauchy stress tensor, $e$ is the internal energy density, $\mathbf{q}$ is the heat flux, $T$ is the absolute temperature, $T^{ref}$ is the reference temperature, $\mathbf{e}$ is the strain tensor ($\mathbf{e} \approx (\nabla\mathbf{u} + (\nabla\mathbf{u})^T)/2$), $\boldsymbol{\beta}$ is named as the thermal expansion coefficients, $\mathbf{A}$ are the elastic constants, $\boldsymbol{\kappa}$ is the thermal conductivity, $\gamma$ is the specific heat, and $\boldsymbol{\varphi}$ is the body force per unit mass. Notice that, in thermoelasticity, the Cauchy stress is derivable from a scalar-valued Helmholtz free energy density function; stress tensor and strain tensor are both symmetric. Therefore, one has

$$\beta_{ij} = \beta_{ji} \quad , \quad A_{ijkl} = A_{jikl} = A_{ijlk} = A_{klij}. \tag{1.55}$$

It is emphasized that in continuum mechanics (CM), temperature is an independent variable. Therefore, an energy equation, Eq. (1.51), is needed. On the contrary, the Nosé-Hoover thermostat is not needed—all one needs to do is to set temperature-specified boundary conditions. Of course, one may set heat-flux-specified boundary conditions too. Also, the temperature field and displacement field in CM are functions of spatial and temporal variables—that is why we see terms such as $\nabla\cdot\boldsymbol{\sigma}$ , $\nabla\mathbf{u}$ , $\nabla\mathbf{v}$ , $\nabla\cdot\mathbf{q}$ , and$\nabla T$ in Eqs. (1.50) to (1.54). From now on, we refer to the temperature in continuum mechanics as continuum temperature, to distinguish it from atomistic temperature in molecular dynamics.

In finite element analysis, relate the displacement and temperature fields with their nodal values as

$$\begin{array}{lll} u_i = N_{i\alpha}U_\alpha & , & e_{ij} = B_{ij\alpha}U_\alpha \\ T = N_\xi T_\xi & , & T_{,k} = C_{k\xi}T_\xi. \end{array} \tag{1.56}$$

Then it is straightforward to obtain the dynamic finite element equations as

$$\mathbf{M}\ddot{\mathbf{U}} + \mathbf{K}\mathbf{U} = \mathbf{P}\mathbf{T} + \mathbf{F}^1 + \mathbf{F}^2, \tag{1.57$'$}$$

$$\mathbf{G}\dot{\mathbf{T}} + \mathbf{H}\mathbf{T} + T^{ref}\mathbf{P}^{\mathbf{T}}\dot{\mathbf{U}} = -\mathbf{Q}^1 + \mathbf{Q}^2, \tag{1.58$'$}$$

where

$$M_{\alpha\beta} \equiv \int_v \rho^o N_{i\alpha}N_{i\beta}dv = M_{\beta\alpha}, \tag{1.59}$$

$$K_{\alpha\beta} \equiv \int_v A_{ijkl}B_{kl\alpha}B_{ij\beta}dv = K_{\beta\alpha}, \tag{1.60}$$

$$P_{\beta\eta} \equiv \int_v \beta_{ij}N_\eta B_{ij\beta}dv, \tag{1.61}$$

$$G_{\xi\eta} \equiv \int_v \rho^o \gamma N_\xi N_\eta dv = G_{\eta\xi}, \tag{1.62}$$

$$H_{\xi\eta} \equiv \int_v \kappa_{kl} C_{k\xi} C_{l\eta} dv = H_{\eta\xi}, \tag{1.63}$$

$$F_\beta^1 \equiv \int_{s_\sigma} \widehat{\sigma}_i N_{i\beta} ds, \tag{1.64}$$

$$F_\beta^2 \equiv \int_v \rho^o \varphi_i N_{i\beta} dv, \tag{1.65}$$

$$Q_\eta^1 \equiv \int_{s_q} \widehat{q} N_\eta ds, \tag{1.66}$$

$$Q_\eta^2 \equiv \int_v \rho^o h N_\eta dv. \tag{1.67}$$

Now it is noticed that, if one has the values of $\mathbf{A}, \boldsymbol{\beta}, \boldsymbol{\kappa}$, and $\gamma$, then one may proceed to solve Eqs. (1.57) and (1.58) for $\mathbf{U}(\mathbf{X}, t)$ and $T(\mathbf{X}, t)$. If further we can obtain those material properties from *molecular dynamics* (MD) simulation, then this approach would be named as a *sequential multiscale modeling*.

### 1.3.2 Material Constants from Molecular Dynamics Simulation

In Voigt's convention, one may rewrite Eqs. (1.52) and (1.54) as

$$\begin{vmatrix} \sigma_{11} \\ \sigma_{22} \\ \sigma_{33} \\ \sigma_{23} \\ \sigma_{31} \\ \sigma_{12} \end{vmatrix} = - \begin{vmatrix} \beta_{11} \\ \beta_{22} \\ \beta_{33} \\ \beta_{23} \\ \beta_{31} \\ \beta_{12} \end{vmatrix} \left(T - T^{ref}\right) + \begin{vmatrix} A_{1111} & A_{1122} & A_{1133} & A_{1123} & A_{1131} & A_{1112} \\ A_{1122} & A_{2222} & A_{2233} & A_{2223} & A_{2231} & A_{2212} \\ A_{1133} & A_{2233} & A_{3333} & A_{3323} & A_{3331} & A_{3312} \\ A_{1123} & A_{2223} & A_{3323} & A_{2323} & A_{2331} & A_{2312} \\ A_{1131} & A_{2231} & A_{3331} & A_{2331} & A_{3131} & A_{3112} \\ A_{1112} & A_{2212} & A_{3312} & A_{2312} & A_{3112} & A_{1212} \end{vmatrix} \begin{vmatrix} e_{11} \\ e_{22} \\ e_{33} \\ \gamma_{23} \\ \gamma_{31} \\ \gamma_{12} \end{vmatrix}. \tag{1.68}$$

$$\begin{vmatrix} q_1 \\ q_2 \\ q_3 \end{vmatrix} = - \begin{vmatrix} \kappa_{11} & \kappa_{12} & \kappa_{13} \\ \kappa_{21} & \kappa_{22} & \kappa_{23} \\ \kappa_{31} & \kappa_{32} & \kappa_{33} \end{vmatrix} \begin{vmatrix} T_{,1} \\ T_{,2} \\ T_{,3} \end{vmatrix}, \tag{1.69}$$

where $\gamma_{23} = 2e_{23}$, $\gamma_{31} = 2e_{31}$, $\gamma_{12} = 2e_{12}$.

#### 1.3.2.1 Elastic Constants

In a simple strain problem, the deformation can be expressed as

$$\begin{vmatrix} x \\ y \\ z \end{vmatrix} = \begin{vmatrix} 1+e_1 & \gamma_{12} & \gamma_{13} \\ \gamma_{21} & 1+e_2 & \gamma_{23} \\ \gamma_{31} & \gamma_{32} & 1+e_3 \end{vmatrix} \begin{vmatrix} X \\ Y \\ Z \end{vmatrix} \quad \text{or} \quad x_k = F_{kK} X_K, \tag{1.70}$$

which implies the Green's deformation tensor, and Lagrangian strain tensor can be calculated as

$$C_{KL} = F_{kK} F_{kL} \quad , \quad E_{KL} = (C_{KL} - \delta_{KL})/2. \tag{1.71}$$

One may obtain the Lagrangian strains and their small-strain counterparts as follows:

$$E_{11} = 0.5 \left\{ (1+e_1)^2 + \gamma_{21}^2 + \gamma_{31}^2 - 1 \right\} \approx e_1, \tag{1.72}$$

$$E_{22} = 0.5 \left\{ (1+e_2)^2 + \gamma_{12}^2 + \gamma_{32}^2 - 1 \right\} \approx e_2, \tag{1.73}$$

$$E_{33} = 0.5 \left\{ (1+e_3)^2 + \gamma_{13}^2 + \gamma_{23}^2 - 1 \right\} \approx e_3, \tag{1.74}$$

$$\begin{aligned} E_{12} = E_{21} &= 0.5 \{ (1+e_1)\gamma_{12} + (1+e_2)\gamma_{21} + \gamma_{31}\gamma_{32} \} \\ &\approx (\gamma_{12} + \gamma_{21})/2, \end{aligned} \tag{1.75}$$

$$\begin{aligned} E_{13} = E_{31} &= 0.5 \{ (1+e_1)\gamma_{13} + (1+e_3)\gamma_{31} + \gamma_{21}\gamma_{23} \} \\ &\approx (\gamma_{13} + \gamma_{31})/2, \end{aligned} \tag{1.76}$$

$$\begin{aligned} E_{23} = E_{32} &= 0.5 \{ (1+e_2)\gamma_{23} + (1+e_3)\gamma_{32} + \gamma_{12}\gamma_{13} \} \\ &\approx (\gamma_{23} + \gamma_{32})/2. \end{aligned} \tag{1.77}$$

In molecular dynamics (MD) simulation, let the whole specimen have $N$ atoms. There are six independent simple strains that can be created in the following six cases:

(1) Simple tension along the $x$-axis

$$r_1^i \leftarrow (1+e_1)\, r_1^i \quad , \quad i \in [1, 2, 3, ...., N], \tag{1.78}$$

where $\mathbf{r}^i$ is the position vector of *atom i*; $r_2^i$ and $r_3^i$ remain unchanged.

(2) Simple tension along the $y$-axis

$$r_2^i \leftarrow (1+e_2)\, r_2^i. \tag{1.79}$$

(3) Simple tension along $z-$axis

$$r_3^i \leftarrow (1+e_3)\, r_3^i. \tag{1.80}$$

(4) Simple shear on the $x-y$ plane

$$r_1^i \leftarrow r_1^i + \gamma_{12} r_2^i \quad , \quad r_2^i \leftarrow r_2^i + \gamma_{21} r_1^i, \tag{1.81}$$

with $r_3^i$ unchanged.
(5) Simple shear on the $y-z$ plane

$$r_2^i \leftarrow r_2^i + \gamma_{23} r_3^i \quad , \quad r_3^i \leftarrow r_3^i + \gamma_{32} r_2^i, \tag{1.82}$$

with $r_1^i$ unchanged.
(6) Simple shear on the $z-x$ plane

$$r_1^i \leftarrow r_1^i + \gamma_{13} r_3^i \quad , \quad r_3^i \leftarrow r_3^i + \gamma_{31} r_1^i, \tag{1.83}$$

with $r_2^i$ unchanged.
Because these six cases are static cases, the virial stress tensor is reduced to

$$\mathbf{S} = -\frac{1}{V} \sum_{i=1}^{N} \mathbf{r}^i \otimes \mathbf{f}^i, \tag{1.84}$$

where $V$ is the volume of the whole specimen. For each case, we obtain six components of the virial stress, from which the elastic constants are deduced as:

**Case 1**

$$\begin{aligned} &\{A_{1111}, A_{1122}, A_{1133}, A_{1123}, A_{1131}, A_{1112}\} \\ &= \{S_{11}, \mathrm{S}_{22}, \mathrm{S}_{33}, \mathrm{S}_{23}, \mathrm{S}_{31}, \mathrm{S}_{12}\} / e_1. \end{aligned} \tag{1.85}$$

**Case 2**

$$\begin{aligned} &\{A_{1122}, A_{2222}, A_{2233}, A_{2223}, A_{2231}, A_{2212}\} \\ &= \{S_{11}, \mathrm{S}_{22}, \mathrm{S}_{33}, \mathrm{S}_{23}, \mathrm{S}_{31}, \mathrm{S}_{12}\} / e_2. \end{aligned} \tag{1.86}$$

**Case 3**

$$\begin{aligned} &\{A_{1133}, A_{2233}, A_{3333}, A_{3323}, A_{3331}, A_{3312}\} \\ &= \{S_{11}, \mathrm{S}_{22}, \mathrm{S}_{33}, \mathrm{S}_{23}, \mathrm{S}_{31}, \mathrm{S}_{12}\} / e_3. \end{aligned} \tag{1.87}$$

**Case 4**

$$\begin{aligned} &\{A_{1112}, A_{2212}, A_{3312}, A_{2312}, A_{3112}, A_{1212}\} \\ &= \{S_{11}, \mathrm{S}_{22}, \mathrm{S}_{33}, \mathrm{S}_{23}, \mathrm{S}_{31}, \mathrm{S}_{12}\} / \gamma_{12}. \end{aligned} \tag{1.88}$$

**Case 5**

$$\{A_{1123}, A_{2223}, A_{3323}, A_{2323}, A_{2331}, A_{2312}\} = \{S_{11}, S_{22}, S_{33}, S_{23}, S_{31}, S_{12}\}/\gamma_{23}. \tag{1.89}$$

**Case 6**

$$\{A_{1131}, A_{2231}, A_{3331}, A_{2331}, A_{3131}, A_{3112}\} = \{S_{11}, S_{22}, S_{33}, S_{23}, S_{31}, S_{12}\}/\gamma_{31}. \tag{1.90}$$

In general, the stress-strain relation is nonlinear, and we focus our attention to small strain theory; therefore, to evaluate the elastic constants, those specified strains, namely, $e_1$, $e_2$, $e_3$, $\gamma_{12}$, $\gamma_{23}$, and $\gamma_{31}$, should be in the linear elastic range.

### 1.3.2.2 Thermal Conductivity

Now suppose we have several atomic groups lined up in series and let the first group subject to Nosé-Hoover thermostat at atomistic temperature be $T_H$ and let the last group subject to Nosé-Hoover thermostat at atomistic temperature be $T_L$. Those groups in between do not have Nosé-Hoover thermostat. After the system reaches steady state, one may obtain the thermal energies $E_H$ and $E_L$ as

$$E_H \equiv \left\{ \frac{1}{2} Q_H \chi_H^2 + \frac{Q_H}{\tau_H^2} \int_0^t \chi_H(s) ds \right\}, \tag{1.91}$$

$$E_L \equiv \left\{ \frac{1}{2} Q_L \chi_L^2 + \frac{Q_L}{\tau_L^2} \int_0^t \chi_L(s) ds \right\}. \tag{1.92}$$

Because, in MD simulation, atomistic temperature is a statistical quantity and involves a significant amount of noises, one may plot the thermal energies $E_H$ and $E_L$ as functions of time, which can be approximated by two straight lines. Numerically one should obtain

$$\frac{\Delta E_H}{\Delta t} \approx \dot{E}_H = N_H^{dof} k_B \chi_H T_H \quad , \quad \frac{\Delta E_L}{\Delta t} \approx \dot{E}_L = N_L^{dof} k_B \chi_L T_L, \tag{1.93'}$$

where $\dot{E}_H$ and $\dot{E}_L$ should be approximately equal in magnitude but opposite in sign. The heat flux in magnitude is equal to $\dot{E}_H$ and $\dot{E}_L$ divided by the cross-sectional area; the temperature gradient is equal to $\Delta T \Big/ \Delta L$, where $\Delta T = T_H - T_L$ and $\Delta L$ is the distance between the centers of mass of the two atomic groups controlled by Nosé-Hoover thermostats. Following this way, one may find the numerical values of thermal conductivities.

#### 1.3.2.3 Specific Heat and Thermal Expansion Coefficients

We now recall two constitutive equations in small-strain thermoelasticity:

$$\rho^o \dot{e} = \rho^o \gamma \dot{T} + A_{ijkl} e_{ij} \dot{e}_{kl}, \tag{1.53''}$$

$$\sigma_{ij} = -\beta_{ij} T + A_{ijkl} e_{kl}, \tag{1.52''}$$

where $\gamma$ and $\boldsymbol{\beta}$ are the specific heat and thermal expansion coefficients, respectively. In MD simulation, one may consider a group of atoms in relaxed and idealized state, i.e., absolute zero temperature, vanishing interatomic forces, and vanishing virial stresses. Then imagine that this group of atoms is put into a rigid box and prohibited to move out of the box. In this situation, the strain and the strain rate are zero; Eqs. (1.53″) and (1.52″) are rewritten as

$$S_{ij} = -\beta_{ij} T \quad , \quad \dot{e} = \gamma \dot{T}. \tag{1.94}$$

Here we assume that the Cauchy stress tensor in continuum mechanics is equivalent to the virial stress tensor in MD simulation (Subramaniyan and Sun 2008). This may be considered as an approximation. But, without it, it is very difficult, even impossible to bridge the gap between atoms and genuine continuum.

Now let the atomistic temperature of atoms in the box be raised to a specified temperature $T$ by Nosé-Hoover thermostat and, after steady state is reached, one may calculate virial stresses $S_{ij}$ and internal energy density $e$ (sum of potential energy and thermal energy divided by total mass of atoms). It results in

$$\beta_{ij} = -S_{ij}/T \quad , \quad \gamma = \frac{e}{T}. \tag{1.95}$$

## 1.4 Concurrent Multiscale Modeling from Atoms to Genuine Continuum

### *1.4.1 One Specimen, Two Regions*

The basic strategy for concurrent modeling may be described as: divide the entire solution domain into non-critical far field and several critical sub-regions, where stress concentrations, crack initiation and propagation, dislocations, and other critical physical phenomena may occur. We have successfully modeled the critical regions (or atomic regions) by molecular dynamics (MD) simulation and the atom-based-continuum (ABC) region by Coarse-Grained Molecular Dynamics (CGMD) simulation (Li et al. 2012; Li and Lee 2014a, b) in a single theoretical framework. One may extend this approach by dividing the entire solution domain into three parts: atomic region, ABC region, and genuine continuum (GC) region, modeled by continuum theory.

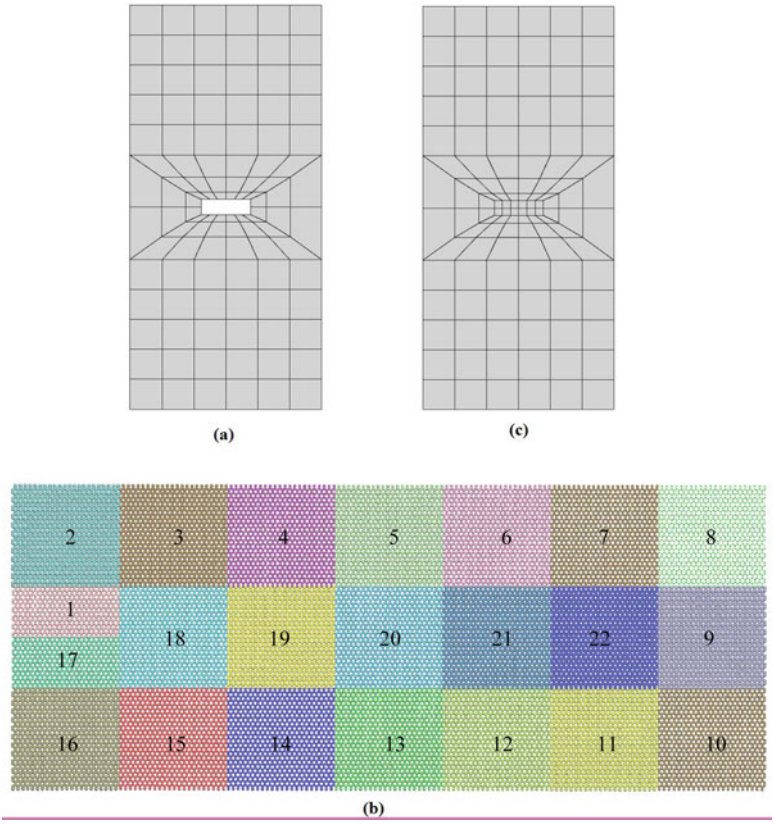


**Fig. 1.1** (**a**) Finite element mesh in the genuine continuum region, (**b**) groups of atoms in the atomic region, (**c**) apparent FE mesh

In this work, just to illustrate the idea, the entire solution domain is divided into two regions: atomic region and GC region. As mentioned in Sect. 1.2, the atomic region is further divided into $N_g$ groups;*group g* has $n_g$ atoms; and the total number of atoms in the atomic region is $N$. Let the first $M_g$ groups have Nosé-Hoover thermostats, $N_g > M_g$. For example, Fig. 1.1b shows $N_g = 22$ and $M_g = 17$. These $M_g$ groups are linked to the first $M_g$ nodes in the GC region (cf. Fig. 1.1a). It is noticed that there are $N_g - M_g = 5$ groups not controlled by thermostats because they are not linked to any node in the GC region. If one had viewed the $N_g$ groups as nodes and inserted them into the finite element (FE) mesh (cf. Fig. 1.1a) of GC, then an apparent FE mesh would have been created as shown in Fig. 1.1c. The basic idea is that there is an *interface* between the atomic region and the continuum region. In the *interface*, each node is corresponding to a group of atoms, not just a single atom (cf. Fig. 1.1a, b).

In this work, we make two major assumptions:

**Assumption 1**
*Each node in the interface is anchored at the mass center of its corresponding group.*

**Assumption 2**
*The sum of heat fluxes into the node and its corresponding group is zero.*

Now the mathematical formulation proceeds as follows: First, for the atomic region, we recall the relevant governing equations as

$$m^i \dot{\mathbf{v}}^i = \mathbf{f}^i + \boldsymbol{\varphi}^i + \mathbf{f}^i_{\text{int}} - \chi_g m^i \tilde{\mathbf{v}}^i, \tag{1.18''}$$

$$\dot{\chi}_g = \frac{1}{\tau_g^2 T_g^c} \left( T_g^a - T_g^c \right), \tag{1.19''}$$

$$T_g^a = \frac{1}{N_g^{dof} k_B} \sum_{i=1}^{n_g} m^i \tilde{\mathbf{v}}^i \cdot \tilde{\mathbf{v}}^i, \tag{1.17''}$$

$$\dot{E}_g = N_g^{dof} k_B \chi_g T_g^a. \tag{1.93''}$$

However, we replace $T_g$ by $T_g^a$ to emphasize that it is the atomistic temperature of *group g* calculated through the *Nosé-Hoover thermal velocity* $\tilde{\mathbf{v}}^i$ in the atomic region; we replace $T_g^o$ by $T_g^c$ to indicate the target temperature of the *group g* is no longer a constant, but the nodal temperature of the corresponding *node g* in the GC region, $g \in [1, 2, 3, \ldots, M_g]$. Especially, it is noticed that we add an interactive term $\mathbf{f}^i_{\text{int}}$ into Eq. (1.18) to indicate the interaction between atoms in *group g* and its corresponding *node g* in the GC region. We employ the velocity Verlet method to solve Eqs. (1.18″) and (1.19″). Detailed formulas will be derived later. The time steps used in the atomic region is denoted by $\Delta t^a$.

For the GC region, we recall and rewrite the finite element equations as

$$\mathbf{M}\ddot{\mathbf{U}} + \mathbf{K}\mathbf{U} = \mathbf{P}\mathbf{T} + \mathbf{F}^1 + \mathbf{F}^2 + \mathbf{F}_{\text{int}}, \tag{1.57''}$$

$$\mathbf{G}\dot{\mathbf{T}} + \mathbf{H}\mathbf{T} + T^{ref}\mathbf{P}^T\dot{\mathbf{U}} = -\mathbf{Q}^1 + \mathbf{Q}^2 + \mathbf{Q}_{\text{int}}. \tag{1.58''}$$

It is seen that, for those nodes anchored in groups of atoms in the atomic region, we add $\mathbf{F}_{\text{int}}$ and $\mathbf{Q}_{\text{int}}$ to the governing equations; for other nodes, $\mathbf{F}_{\text{int}} = \mathbf{Q}_{\text{int}} = 0$. We employ the central difference method to solve Eqs. (1.57″) and (1.58″). Detailed formulas will be derived later. The time steps used in the continuum region is denoted by $\Delta t^c$. The ratio of time steps $N^{time}$, which should be an integer, is defined as

$$N^{time} \equiv \Delta t^c \Big/ \Delta t^a \quad \text{or} \quad \Delta t^c = N^{time} \Delta t^a. \tag{1.96}$$

### 1.4.2 Interfacial Conditions

One needs to impose boundary conditions, either displacement-specified or force-specified, at each component of each node, and, similarly, impose boundary condition, either temperature-specified or heat flow-specified, at each node, at outer boundary of GC region, but not at inner boundary, which is the interface.

At each node/group in the interface, one should have the following two conditions:

$$\sum_{i\in g} \mathbf{f}^i_{\text{int}} + \mathbf{F}^g_{\text{int}} = 0, \tag{1.97}$$

$$Q^g_{\text{int}} = \dot{E}_g = N^{dof}_g k_B \chi_g T^a_g. \tag{1.98}$$

The first condition, Eq. (1.97), simply means the sum of interactive forces of the node/group pair should be vanishing. Recall that $\dot{E}_g$ is the flow of energy per unit time out of *group g* due to the action of the Nosé-Hoover thermostat. Therefore, the second condition simply says $\dot{E}_g$ should be the inward flow of energy per unit time to the corresponding *node g*.

We now rewrite Eqs. (1.18″) and (1.57″), respectively, as

$$m^i \ddot{\mathbf{u}}^i = m^i \dot{\mathbf{v}}^i = \mathbf{f}^i + \boldsymbol{\varphi}^i + \mathbf{f}^i_{\text{int}} - \chi_g m^i \tilde{\mathbf{v}}^i \equiv \overline{\mathbf{f}}^i + \mathbf{f}^i_{\text{int}}, \tag{1.99}$$

$$\mathbf{M}\ddot{\mathbf{U}} = -\mathbf{K}\mathbf{U} + \mathbf{P}\mathbf{T} + \mathbf{F}^1 + \mathbf{F}^2 + \mathbf{F}_{\text{int}} \equiv \overline{\mathbf{F}} + \mathbf{F}_{\text{int}}, \tag{1.100}$$

where $\mathbf{u}^i$ denotes the position vector of *atom i*. In this work, the lumped-mass system is adopted, i.e., the mass matrix $\mathbf{M}$ is diagonalized and, hence, nodal mass is well defined. Similarly, the $\mathbf{G}$ matrix in Eq. (1.58) is also diagonalized. Eq. (1.97″) leads to

$$M^g \ddot{\mathbf{U}}^g + \sum_{i\in g} m^i \ddot{\mathbf{u}}^i = \overline{\mathbf{F}}^g + \sum_{i\in g} \overline{\mathbf{f}}^i. \tag{1.101}$$

Assumption 1, that we made, says *node g* is anchored at the mass center of *group g*. It implies

$$\ddot{\mathbf{U}}^g = \frac{\sum_{i\in g} m^i \ddot{\mathbf{u}}^i}{\sum_{i\in g} m^i} \equiv \frac{\sum_{i\in g} m^i \ddot{\mathbf{u}}^i}{m^g} \equiv \ddot{\mathbf{u}}^g_{avg}. \tag{1.102}$$

To ensure Eq. (1.102), one needs

$$\ddot{\mathbf{u}}^i = \frac{\overline{\mathbf{f}}^i}{m^i} + \ddot{\mathbf{U}}^g - \frac{\sum_{i\in g} \overline{\mathbf{f}}^i}{m^g}. \tag{1.103′}$$

Substituting Eq. (1.102) into Eq. (1.101) results

$$\ddot{\mathbf{U}}^g = \frac{1}{M^g + m^g}\left\{\overline{\mathbf{F}}^g + \sum_{i\in g}\overline{\mathbf{f}}^i\right\}. \tag{1.104′}$$

### 1.4.3 Multiple Time Scale Algorithm

There are two regions, atomic and continuum, and therefore, there are two time scales, $n$ and $m$. Then time $t$ equals

$$t\,(n,m) = n\Delta t^c + m\Delta t^a. \tag{1.105}$$

It is seen that $t(n+1,0) = t(n, N^{time})$. First, suppose at $t(n,0)$ we know $\mathbf{u}^{n,0}$, $\mathbf{a}^{n,0} \equiv \ddot{\mathbf{u}}^{n,0}$, $\chi^{n,0}$,$\mathbf{v}^{n,-\frac{1}{2}} = \dot{\mathbf{u}}^{n,-\frac{1}{2}}$, $\mathbf{U}^{n,0}$, $\mathbf{V}^{n,0} \equiv \dot{\mathbf{U}}^{n,0}$, $\mathbf{A}^{n,0} \equiv \ddot{\mathbf{U}}^{n,0}$, $\mathbf{T}^{n,0}$, and $\dot{\mathbf{T}}^{n,0}$. The numerical procedures to solve Eqs. (1.18″), (1.19″), (1.57″), and (1.58″) are listed in the following.

**Step 1**
Calculate $\mathbf{U}^{n,m}$ and $\mathbf{T}^{n,m}$ $(m = 1, 2, 3, \ldots, N^{time})$.

$$\mathbf{U}^{n,m} = \mathbf{U}^{n,0} + m\Delta t^a \mathbf{V}^{n,0} + 0.5(m\Delta t^a)^2 \mathbf{A}^{n,0}, \tag{1.106}$$

$$\mathbf{T}^{n,m} = \mathbf{T}^{n,0} + m\Delta t^a \dot{\mathbf{T}}^{n,0}. \tag{1.107}$$

Impose boundary conditions at $t(n,m)$ on $\mathbf{U}^{n,m}$ and $\mathbf{T}^{n,m}$. Notice that $\mathbf{U}^{n+1,0} = \mathbf{U}^{n,N^{time}}$ and $\mathbf{T}^{n+1,0} = \mathbf{T}^{n,N^{time}}$.

**Step 2**
Based on *Velocity Verlet Method*, let the velocity and position of each atom be updated as

$$\mathbf{v}^{n,m+1/2} = \mathbf{v}^{n,m-1/2} + \Delta t^a \mathbf{a}^{n,m}, \tag{1.108}$$

$$\mathbf{u}^{n,m+1} = \mathbf{u}^{n,m} + \Delta t^a \mathbf{v}^{n,m+1/2}. \tag{1.109}$$

For each node/group in the interface, identify the position of *node g* as $\mathbf{R}_g = \mathbf{R}_g^o + \mathbf{U}_g$ ($\mathbf{R}_g^o$ denotes the position of *node g* in the reference state and $\mathbf{U}_g$ is the displacement vector obtained from Step 1) and calculate the position of the mass center of *group g* as

$$\mathbf{u}_{avg}^g = \frac{\sum_{i\in g} m^i \mathbf{u}^i}{m^g}. \tag{1.110}$$

Then let every atom in *group g* move according to

$$\mathbf{u}^i \leftarrow \mathbf{u}^i + \mathbf{R}_g - \mathbf{u}^g_{avg}. \tag{1.111}$$

This simply means that Assumption 1 is enforced on the atomic positions at all time $t(n,m)$.

**Step 3**

Calculate $T_g^a$ according to Eq. (1.17″) based on $\mathbf{v}^{n,m+1/2}$(cf. Eq. (108)). Notice that $\tilde{\mathbf{v}}^{n,m+1/2}$ can be obtained from $\mathbf{v}^{n,m+1/2}$ and $\mathbf{u}^{n,m+1}$. Then calculate

$$\dot{\chi}_g^{n,m+1/2} = \frac{1}{\tau_g^2 T_g^{c(n,m+1)}}\left(T_g^a - T_g^{c(n,m+1)}\right), \tag{1.112}$$

$$\chi_g^{n,m+1} = \chi_g^{n,m} + \Delta t^a \dot{\chi}_g^{n,m+1/2}. \tag{1.113}$$

The force acting on all atoms, without counting the interactive force between *node g* and *group g*, can now be calculated as

$$\overline{\mathbf{f}}^{i(n,m+1)} = \mathbf{f}^{i(n,m+1)} + \boldsymbol{\varphi}^{i(n,m+1)} - \chi_g^{n,m+1} m^i \tilde{\mathbf{v}}^{i\left(n,m+\frac{1}{2}\right)}. \tag{1.99″}$$

Then the acceleration is updated as

$$\mathbf{a}^{i(n,m+1)} = \overline{\mathbf{f}}^{i(n,m+1)}/m^i, \tag{1.114}$$

with the understanding that, at $m = N^{time}$, a special treatment (cf. Eqs. (1.102)–(1.104)) needs to be implemented. Repeat the cycle of Steps 2 and Steps 3 for $N^{time}$ times.

**Step 4**

After $m$ reaches $N^{time}$, calculate

$$\mathbf{V}^{n+\frac{1}{2},0} = \mathbf{V}^{n,0} + \Delta t^c \mathbf{A}^{n,0}, \tag{1.115}$$

$$\overline{\mathbf{F}}^{n+1,0} = -\mathbf{K}\mathbf{U}^{n+1,0} + \mathbf{P}\mathbf{T}^{n+1,0} + \mathbf{F}^{1(n+1,0)} + \mathbf{F}^{2(n+1,0)}, \tag{1.116}$$

$$\mathbf{A}^{n+1.0} \equiv \ddot{\mathbf{U}}^{n+1,0} = \overline{\mathbf{F}}^{n+1,0}/\mathbf{M}. \tag{1.117}$$

Here, we notice that (1) because we adopt the lumped-mass system, we can express $\ddot{\mathbf{U}}^{n+1,0} = \overline{\mathbf{F}}^{n+1,0}/\mathbf{M}$ and (2) only for the nodes in the *interface*, we have special treatment as follows:

$$\mathbf{A}^{n+1,0} \equiv \ddot{\mathbf{U}}^{g(n+1,0)} = \frac{1}{M^g + m^g} \left\{ \overline{\mathbf{F}}^{g(n+1,0)} + \sum_{i \in g} \overline{\mathbf{f}}^{i(n+1,0)} \right\}, \tag{1.104''}$$

$$\mathbf{a}^{n+1,0} = \ddot{\mathbf{u}}^{i(n+1,0)} = \frac{\overline{\mathbf{f}}^{i(n+1,0)}}{m^i} + \ddot{\mathbf{U}}^{g(n+1,0)} - \frac{\sum_{i \in g} \overline{\mathbf{f}}^{i(n+1,0)}}{m^g}. \tag{1.103''}$$

Now the velocity vector in the GC region is updated as

$$\mathbf{V}^{n+1,0} = \mathbf{V}^{n+\frac{1}{2},0} + \frac{1}{2} \Delta t^c \mathbf{A}^{n+1,0}. \tag{1.118}$$

**Step 5**
Following Eq. (1.58″), calculate

$$\mathbf{Q}^{n+1,0} \equiv -\mathbf{H}\mathbf{T}^{n+1,0} - T^{ref} \mathbf{P}^T \mathbf{V}^{n+1,0} - \mathbf{Q}^{1(n+1,0)} + \mathbf{Q}^{2(n+1,0)} + \mathbf{Q}_{\text{int}}^{g(n+1,0)}, \tag{1.119}$$

$$\dot{\mathbf{T}}^{n+1,0} = \mathbf{Q}^{n+1,0} / \mathbf{G}, \tag{1.120}$$

where

$$\mathbf{Q}_{\text{int}}^{g(n+1,0)} = N_g^{dof} k_B \chi_g^{n+1,0} \mathbf{T}_g^{a(n+1,0)}. \tag{1.98''}$$

It is seen that, after going from Steps 1 to Steps 5, all the unknown variables are updated as

$$\mathbf{U}^{n,0}, \mathbf{V}^{n,0}, \mathbf{T}^{n,0}, \mathbf{A}^{n,0}, \mathbf{T}^{n,0} \rightarrow \mathbf{U}^{n+1,0}, \mathbf{V}^{n+1,0}, \mathbf{T}^{n+1,0}, \mathbf{A}^{n+1,0}, \mathbf{T}^{n+1,0}, \tag{1.121}$$

$$\mathbf{u}^{n,m}, \mathbf{v}^{n,m-\frac{1}{2}}, \mathbf{a}^{n,m}, \boldsymbol{\chi}^{n,m} \rightarrow \mathbf{u}^{n,m+1}, \mathbf{v}^{n,m+\frac{1}{2}}, \mathbf{a}^{n,m+1}, \boldsymbol{\chi}^{n,m+1}. \tag{1.122}$$

### *1.4.4 Sample Problems and Numerical Results*

For illustrative purposes, the material we studied in this work is graphene. Graphene belongs to a broad family of two-dimensional (2D) materials, characterized by strong covalent in-plane bonds and weak interlayer van der Waals interactions which give them a layered structure. One of the fascinating properties of 2D crystals is their high stretchability and the possibility to use external strain to manipulate their optical and electronic properties, coined as strain engineering. For interested readers, a review article by Roldan et al. (2015) is recommended.

#### 1.4.4.1 Material Constants Obtained from MD Simulations

The interatomic potential for graphene used in this work is the Tersoff potential (Tersoff 1988, 1989), which is a three-body potential. In the continuum region, we model the material as a 2D thermoelastic solid with its material properties obtained from MD simulation (cf. Sect. 1.3). Since graphene is anisotropic, we identify $x_1 - axis \equiv x - axis$ as the one perpendicular to the *armchair* edge and $x_2 - axis \equiv y - axis$ as the one perpendicular to the *zigzag* edge. The material properties may be summarized as follows:

$$\begin{vmatrix} \sigma_{11} \\ \sigma_{22} \\ \sigma_{12} \end{vmatrix} = - \begin{vmatrix} 0.1723 \text{ x } 10^{-6} \\ 0.1710 \text{ x } 10^{-6} \\ 0 \end{vmatrix} \left(T - T^{ref}\right) + \begin{vmatrix} 0.04496 & -0.00792 & 0 \\ -0.00792 & 0.04624 & 0 \\ 0 & 0 & 0.02646 \end{vmatrix} \begin{vmatrix} e_{11} \\ e_{22} \\ \gamma_{12} \end{vmatrix}, \tag{1.123}$$

$$\begin{vmatrix} q_1 \\ q_2 \end{vmatrix} = - \begin{vmatrix} 0.6238 \text{ x } 10^{-7} & 0 \\ 0 & 0.4936 \text{ x } 10^{-7} \end{vmatrix} \begin{vmatrix} T_{,1} \\ T_{,2} \end{vmatrix}, \tag{1.124}$$

$$\gamma = 0.2551 \text{ x } 10^{-9}. \tag{1.125}$$

In this work, we use atomic units, i.e., the dimensions and units of stress, temperature, heat expansion coefficient, heat flux, thermal conductivity, and specific heat are

$$\begin{aligned} &[\sigma] = \tfrac{Hartree}{Bohr^3} \quad , \quad [T] = Kelvin \quad , \quad [\beta] = \tfrac{Hartree}{Bohr^3\ Kelvin} \\ &[q] = \tfrac{Hartree}{\tau\ Bohr^2} \quad , \quad [\kappa] = \tfrac{Hartree}{\tau\ BohrKelvin} \quad , \quad [\gamma] = \tfrac{Hartree}{m_e\ Kelvin}, \end{aligned} \tag{1.126}$$

where

$$\begin{aligned} Hartree &= 4.3597482 \times 10^{-18}\ Joule \\ Bohr &= 5.29177249 \times 10^{-11}\ meter \\ \tau &= 2.418884326555 \times 10^{-17}\ \text{sec}\, ond \\ m_e &= 9.10938291 \times 10^{-31}\ kg. \end{aligned} \tag{1.127}$$

It can be calculated from Eq. (1.123) to obtain the Young's modulus and Poisson's ratio along the $x - axis$ ($y - axis$) as 0.0436 (0.0448) and −0.171 (−0.176), respectively; in other words, graphene is anisotropic and has negative Poisson's ratios if the Tersoff potential is adopted.

#### 1.4.4.2 Material Constants: Comparison with Other Researchers' Work

Frank et al. (2007) measured the Young's modulus of suspended multilayer graphene sheets to be 0.5 TPa (0.01699 Hartree/Bohr$^3$). Lee et al. (Lee et al. 2008) measured the effective Young's modulus of monolayer graphene to be 1 TPa (0.03399 Hartree/Bohr$^3$). Monolayer graphene and multilayer graphene exhibit different material properties. MD simulations can realize a variety of loading cases to calculate the Young's modulus and Poisson's ratio, including nano-indentation, tension, compression, and bending. So far, mechanical properties of graphene have been intensively studied using MD simulations. Table 1.1 is the list of reported values of Young's modulus and Poisson's ratio of graphene through MD simulations. From Table 1.1, we can see that in many works, not only the thickness, but also the size of graphene has effect on material properties.

Yoon et al. (2011) measured the thermal expansion coefficient of single-layer graphene with temperature-dependent Raman spectroscopy in the temperature range between 200 and 400 K. They found the thermal expansion coefficient of single-layer graphene to be negative in the whole temperature range with a room temperature value of $(-8.0 \pm 0.7) \times 10^{-6}$ K$^{-1}$. Shaina et al. (2016) also measured the negative thermal expansion coefficient of graphene and the value is $-3.75 \times 10^{-6}$ K$^{-1}$ for the entire temperature range. It is noticed that the terminology "thermal expansion coefficient" used by Yoon et al. and Shaina et al. is different from that used in this work.

Balandin et al. (2008) measured the thermal conductivity of a suspended single-layer graphene and stated that graphene has excellent thermal conductivity, in the range from $(4.84 \pm 0.44) \times 10^3$ to $(5.30 \pm 0.48) \times 10^3$ W/m/K, i.e., $(1.421 \pm 0.129) \times 10^{-6}$ to $(1.556 \pm 0.141) \times 10^{-6}$ Hartree/$\tau$/Bohr/K, at room temperature. Not only the experiment conducted by Balandin et al. measured the high thermal conductivity of graphene, but also many MD simulations draw the same conclusion even though the value of thermal conductivity varies.

Table 1.2 lists some MD simulation results of thermal conductivity of graphene.

The specific heat of graphite at room temperature is reported to be 0.7 J/g/K (1.4626 x $10^{-10}$ Hartree/$m_e$/K) (Tohei et al. 2006). Fried and Howard (2000) found that at very high temperatures, the specific heat is nearly constant at 2.1 J/g/K (4.3878 x $10^{-10}$ Hartree/$m_e$/K).

Through comparison, the material constants we obtained in our MD simulations are different from other researchers' work, but our values are in the same order. Specially, the thermal expansion coefficient measured by Yoon et al. and Shaina et al. is based on the change of geometry instead of the change of stress, which is not the same as the heat expansion coefficient we use in Eq. (1.123). However, we also obtain a negative value that would lead to the same physical phenomena. In a word, the material constants we obtained are reasonable and are able to drive reliable conclusions.

**Table 1.1** Young's modulus and Poisson's ration of graphene calculated by MD simulations

| Reference | Interatomic potential | Simulation model | Young's modulus (TPa) | Young's modulus (Hartree/Bohr$^3$) | Poisson's ratio |
|---|---|---|---|---|---|
| Zhao et al. (2009) | AIREBO | Graphene nanoribbons under uniaxial tension | 0.99 ± 0.04 | 0.03365 ± 0.00136 | 0.21 ± 0.01 |
| Zheng et al. (2011) | AIREBO | Strengthened folded graphene nanoribbon | 0.725 | 0.02464 | 0.398 |
| Shen and Wu (2012) | modified AIREBO | Bending multilayer graphene | 1.025 | 0.03484 | – |
| Zhang et al. (2012) | AIREBO | Single-layer graphene under tension | 0.995 | 0.03382 | – |
| Pei et al. (2012) | AIREBO | Single-layer graphene under tension | 0.893 (armchair)/0.832 (zigzag) | 0.03035 (armchair)/0.02828 (zigzag) | – |
| Jing et al. (2012) | COMPASS | Single-layer graphene under tension | 1.0322 | 0.03508 | – |
| Neek-Amal and Peeters (2010) | Tersoff–Brenner | Bilayer graphene under indentation | 0.8 | 0.02719 | – |

**Table 1.2** Thermal conductivity of graphene calculated by MD simulations

| Reference | Interatomic potential | Thermal conductivity (W/m/K) | Thermal conductivity ($10^{-7}$ Hartree/τ/Bohr/K) |
|---|---|---|---|
| Guo et al. (2009) | Tersoff | 460 (ac)/590 (zz) | 1.3506 (ac)/1.7322 (zz) |
| Wei et al. (2011a, b) | AIREBO | 140 | 0.4110 |
| Wei et al. (2011a, b) | Tersoff with LJ interaction | 130–290 | 0.3817–0.8514 |
| Guo et al. (2012) | Tersoff | 77.7 | 0.2281 |
| Jiang et al. (2010a, b) | Brenner | 61 | 0.1791 |
| Lindsay et al. (2011) | Tersoff with LJ interaction | 1400–3500 | 4.1104–10.2760 |
| Chen and Kumar (2012) | Optimized Tersoff | 2520 | 7.3986 |

#### 1.4.4.3 Case Studies

The entire specimen is divided into two regions: (1) the finite element mesh of the continuum region has 138 nodes and 108 2D 4-noded plane elements, shown in Fig. 1.1a; (2) the atomic region is further divided into 22 groups, as shown in Fig. 1.1b. There are 528 atoms in *groups* 1 and 17 and 1056 atoms in each of the other 20 groups. There are 22,176 atoms in the atomic region and, equivalently, more than 1.36 million atoms in the continuum region. One may take a close look and find that *group i* and its corresponding *node i*($i = 1, 2, 3, \ldots, 17$) form 17 node/group pairs. For the purpose of presentation, one may consider, and view later, the finite element mesh of the entire specimen has 143 nodes (143 = 138 + 5 groups) and 120 elements (120 = 108 + 2(5 + 1)), as shown in Fig. 1.1c. In this view, one may say this specimen had a crack and the crack tip is located at the centroid of *group* 18. In this work the time steps are set at $\Delta t^a = 20$, $\tau = 0.4838$ fs, and $\Delta t^c = 20\ \Delta t^a$. It is emphasized that, from the concurrent multiscale modeling, one can obtain the positions of the centroids, the atomistic temperatures, and the virial stress tensors of the 22 groups. Therefore, later in the *Tecplot*, one may see the graphic representations of a mixture of Cauchy stress tensors and continuum temperatures at 121 nodes (121 = 138–17) together with virial stress tensors and atomistic temperatures at 22 groups. Of course, one may take another approach, i.e., consider the positions of the centroids and the atomistic temperatures of the 22 groups as if they are the nodal values obtained in a classical finite element analysis. However, this approach is not recommended because it simply defeats the purpose of performing concurrent multiscale modeling.

In this work, we perform the analyses of several cases and present the results as follows:

**Case 1**

The boundary conditions are specified as follows:

Along top edge

$$\begin{aligned} T &= T^{ref} + 50\ K \\ u_y &= \begin{cases} 20\frac{t}{t^r}\ \text{(Bohr)} & , \quad t \le t^r \\ 20\ \ \text{(Bohr)} & , \quad t \ge t^r \end{cases} . \end{aligned} \tag{1.128}$$

Along the bottom edge

$$\begin{aligned} T &= T^{ref} - 50\ K \\ u_y &= \begin{cases} -20\frac{t}{t^r}\ \text{(Bohr)} & , \quad t \le t^r \\ -20\ \ \text{(Bohr)} & , \quad t \ge t^r \end{cases} , \end{aligned} \tag{1.129}$$

where $t^r = 1000\ \ \Delta t^c = 20000\ \ \Delta t^a$ and the reference temperature is set at $T^{ref} = 300\ K$.

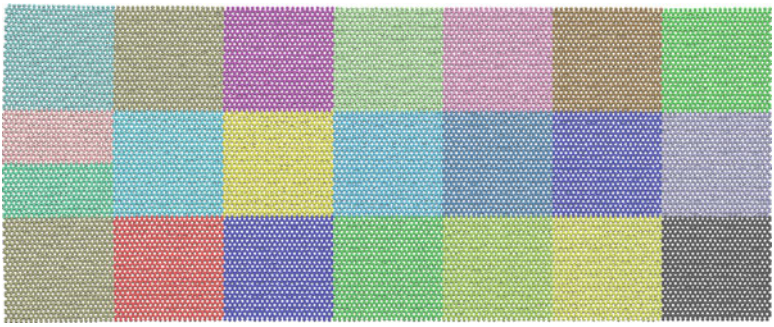

**Fig. 1.2** VMD plot at $t = 2000\ \Delta t^c$

In this work, $\Delta T \equiv T - T^{ref}$ is named as temperature variation; there are temperature gradient and elongation along the $y-axis$. It seems that this is a static problem. But, in principle, there is no static problem in multiscale modeling and, besides, there is no damping built in the theory, except we put in artificial damping in the relaxation stage so that we have an idealized starting point, i.e., nearly zero atomic forces, atomistic temperature, and virial stresses, to begin with.

The positions of 22,176 atoms are shown in the *VMD* plots (Humphrey et al. 1996), Fig. 1.2. Because, relatively speaking, the applied loading (in this case, 20 *Bohr*) is small, there is no crack opening in the atomic region and therefore only one VMD plot is shown at $t = 2000\ \Delta t^c$. The displacements (*Bohr*), continuum and atomistic temperature variations (*Kelvin*), Cauchy stress, and virial stress (*Hartree/Bohr*$^3$) are shown in the *Tecplots*, Fig. 1.3. The matching between atomistic temperatures and continuum temperatures of the 17 node/group pairs is surprisingly good. The averages of virial stress $V_{22}$ over $t \in [1901\ \Delta t^c, 2000\ \Delta t^c]$ for *group* $i$, $i \in [18, 19, 20, 21, 22]$ (cf. Fig. 1.1b) are shown in Fig. 1.4. In fact, the centroid of *group* 18 is the crack tip. Figure 1.4 shows the stress distribution ahead of the crack tip. It is seen that there is no stress singularity, no stress concentration either. In short, the concepts behind *linear elastic fracture mechanics* (LEFM) and *molecular dynamics* (MD) are totally different in this respect.

**Case 2**

The boundary conditions are specified as follows:

Along top edge

$$\begin{aligned} T &= T^{ref} \\ u_y &= 50\tfrac{t}{t^f}\ \ Bohr. \end{aligned} \tag{1.130}$$

Along the bottom edge

$$\begin{aligned} T &= T^{ref} \\ u_y &= -50\tfrac{t}{t^f}\ \ Bohr, \end{aligned} \tag{1.131}$$

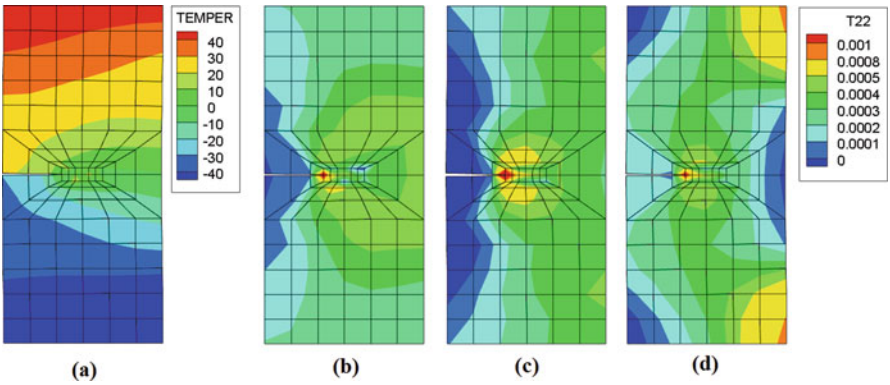


**Fig. 1.3** (**a**) Continuum and atomistic temperature variations at $t = 2000\ \Delta t^c$; Cauchy stress $\sigma_{22}$ and virial stress $S_{22}$ (*Hartree/Bohr*$^3$) at (**b**) $t = 1000\ \Delta t^c$, (**c**) $t = 1500\ \Delta t^c$, (**d**)$t = 2000\ \Delta t^c$

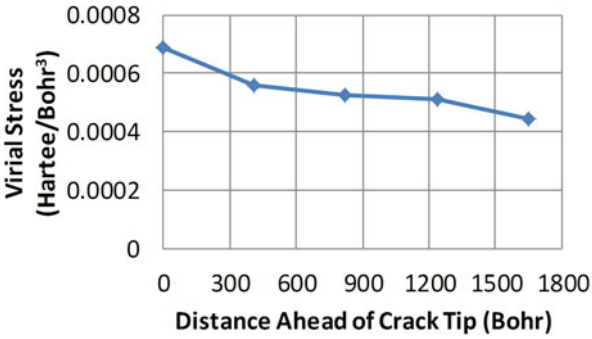


**Fig. 1.4** Virial stress $V_{22}$ in ahead of crack tip

where $t^f = 2000\Delta t^c = 40000\ \Delta t^a$. It means there is no temperature gradient and the elongation is monotonically increasing with respect to time, from $u_y = 0$ at $t = 0$ to $u_y = 50$ *Bohr* at $t = t^f$. The positions of 22,176 atoms at different time steps are shown in the *VMD* plots (Fig. 1.5). Because the elongation is purposefully specified to be very large, one may see the crack opening and crack propagations along multiple fronts.

The displacements, temperatures (continuum and atomistic), and Cauchy and virial stresses are shown in the *Tecplots* (Fig. 1.6). At $t = 1050\ \Delta t^c$, it is seen that the stress is high around *group* 1 and *group* 17. At $t = 1900\ \Delta t^c$, the stress is even higher around the same place. This is because the loading is higher but the crack has not propagated yet. At $t = 2000\ \Delta t^c$, crack fronts reach group 18 (cf. Fig. 1.5c) and it is seen that the high-stress area is shifted to the node corresponding to group 19 (cf. Fig. 1.6c).

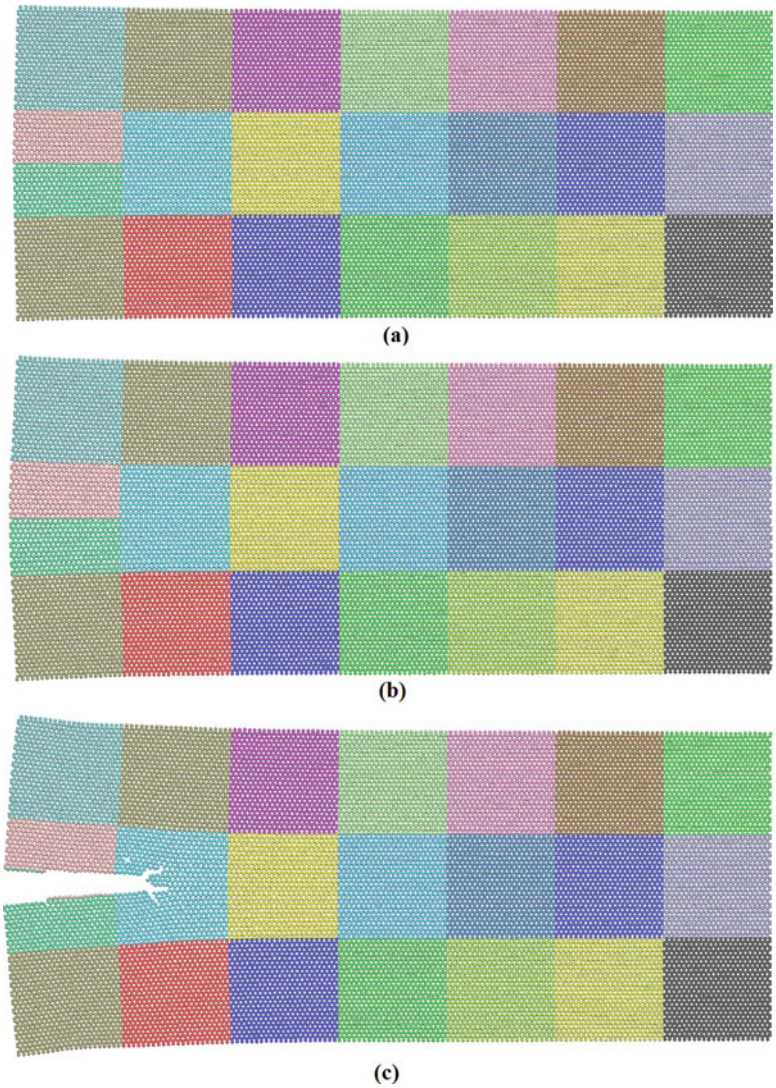


**Fig. 1.5** VMD plots at various time steps: (**a**) $t = 1050\ \Delta t^c$; (**b**) $t = 1900\ \Delta t^c$, right before crack propagates; (**c**) $t = 2000\ \Delta t^c$, crack propagations and branches

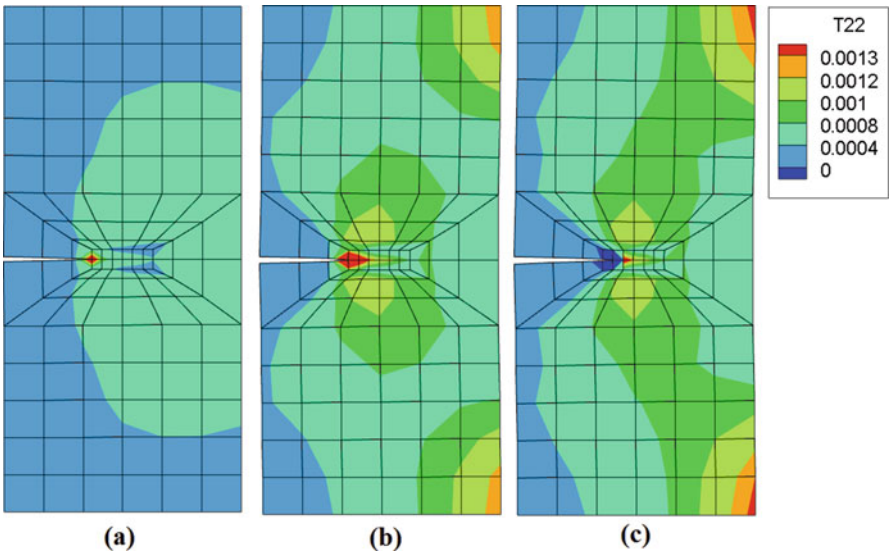


**Fig. 1.6** Cauchy stress $\sigma_{22}$ and virial stress $S_{22}$ ($Hartree/Bohr^3$) at (**a**) $t = 1050\ \Delta t^c$, (**b**) $t = 1900\ \Delta t^c$, (**c**) $t = 2000\ \Delta t^c$

**Case 3**

The boundary conditions are specified as follows:

Along top edge

$$T = T^{ref}$$
$$u_y = \begin{cases} 40\frac{t}{t^r}\ (Bohr) & , \quad t \le t^r \\ 40 + 10\sin\left(2\pi\frac{t-t^r}{\bar{t}}\right)\ (Bohr) & , \quad t \ge t^r \end{cases}. \tag{1.132}$$

Along the bottom edge

$$T = T^{ref}$$
$$u_y = \begin{cases} -40\frac{t}{t^r}\ (Bohr) & , \quad t \le t^r \\ -40 - 10\sin\left(2\pi\frac{t-t^r}{\bar{t}}\right)\ (Bohr) & , \quad t \ge t^r \end{cases}. \tag{1.133}$$

where $t^r = 500\ \Delta t^c = 10000\ \Delta t^a$ and $\bar{t} = 50\ \Delta t^c = 1000 \Delta t^a$. It means there is no temperature gradient and the elongation, after time becomes larger than $t^r$, is a constant plus a sinusoidal function with the period being $\bar{t} = 1000\ \Delta t^a$. It is seen that, from Eqs. (1.132) and (1.133), the time average of $|u_y|$ equals to 40 *Bohr*. The purpose is to simulate the effect of fatigue loading. The positions of 22,176 atoms at different time steps are shown in the *VMD* plots (Fig. 1.7). Because of the fatigue loading with very high frequency, one may also observe the crack opening and crack propagations along multiple fronts. It means, in critical regions, MD simulation can be and should be utilized to investigate problems in fracture mechanics and fatigue

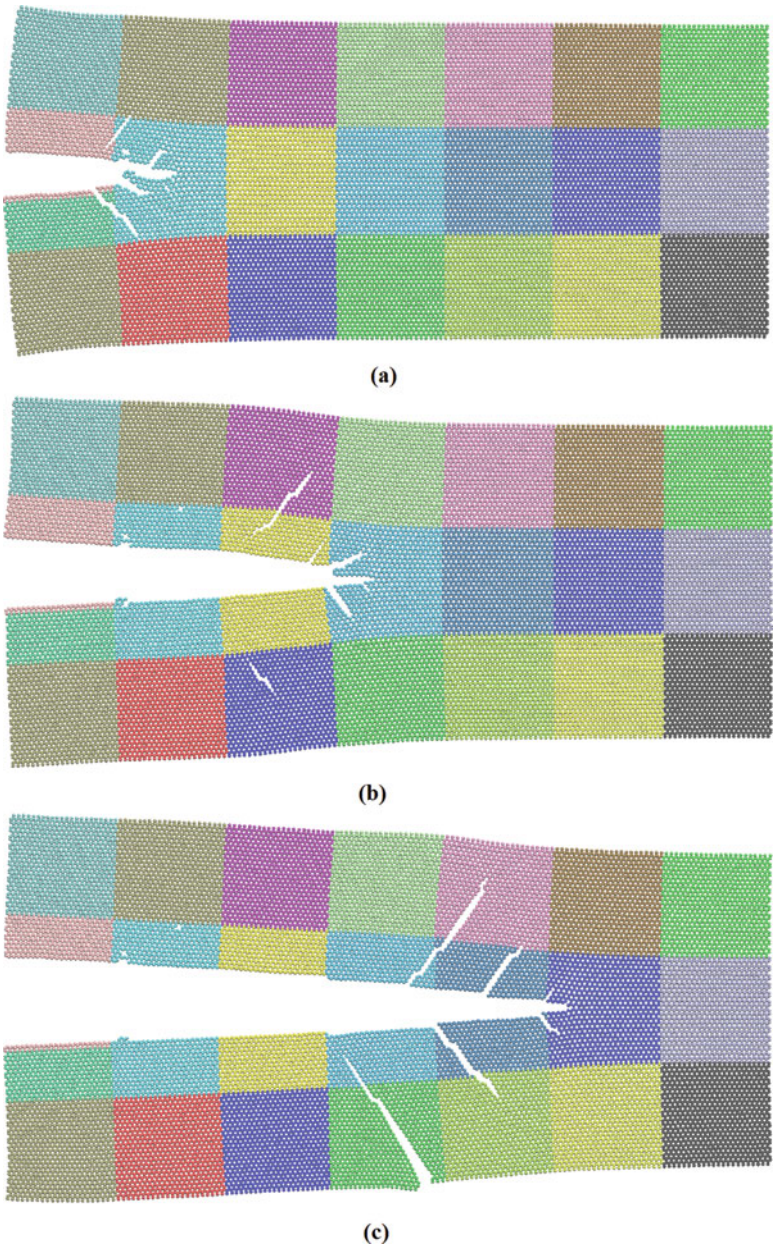


**Fig. 1.7** VMD plots at various time steps: (**a**) $t = 800\ \Delta t^c$, (**b**) $t = 900\ \Delta t^c$, (**c**) $t = 1000\ \Delta t^c$

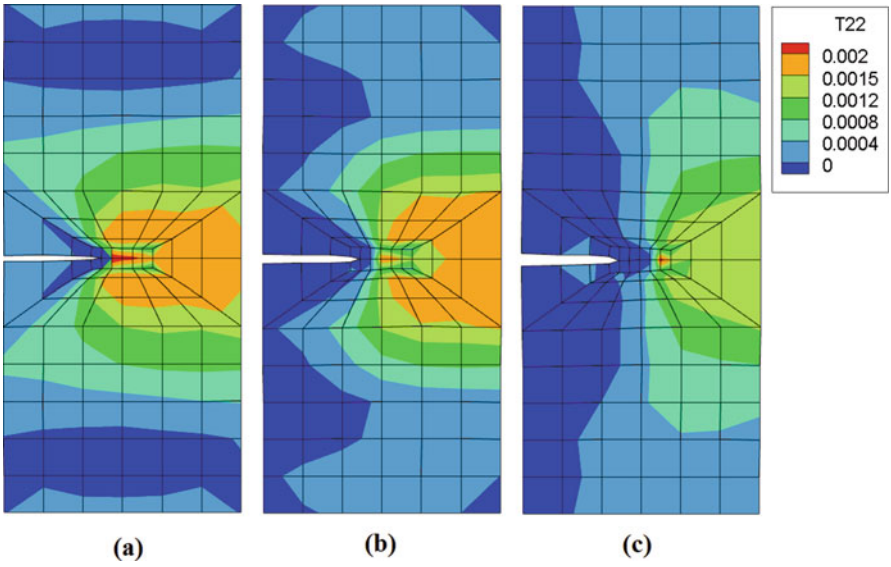


**Fig. 1.8** Cauchy stress $\sigma_{22}$ and virial stress $S_{22}$ ($Hartree/Bohr^3$) at (**a**) $t = 800\ \Delta t^c$, (**b**) $t = 900\ \Delta t^c$, (**c**) $t = 1000\ \Delta t^c$

crack propagation. The displacements, temperatures (continuum and atomistic), virial stresses are shown in the *Tecplots* (Fig. 1.8). Notice that the virial stress **S** evaluated at current volume is equivalent to Cauchy Stress $\boldsymbol{\sigma}$. Similar to Case 2, one may observe that the high-stress area shifts with the propagating crack fronts. As usual, the matching between atomistic temperatures and continuum temperatures of the 17 node/group pairs is surprisingly good. This actually is a verification of the computer software in handling the interfacial conditions.

## 1.5 Discussions

Nowadays, due to the development of massively parallel computers, numerical simulation has emerged as a powerful tool to investigate material and structural behaviors (Oden et al. 2006). Basically, there exist two fundamental physical models, discrete and continuous, that provide foundations for all material modeling. At nano-scale, in molecular dynamics (MD) simulation, the material body is viewed as a collection of atoms moving under the influence of interatomic forces. Unfortunately, due to a large number of particles involved as well as the complex nature of atomistic interactions, the application of MD over a realistic range of length and time scales is not feasible. Even worse, the occurring time of concerned physical event is too far away in the future compared with the small time steps needed in MD simulations. On the other hand, at macro-scale, materials are modeled by continuum

physics, which is simply invalid for material systems at the nanoscale because, to say the least, stress-strain relation cannot replace interatomic potential. Also, it is emphasized that the treatment of temperature is totally different than that in MD. Stress singularity at the crack tip as predicted by linear elastic fracture mechanics (LEFM) simply doesn't exist in MD; crack propagation occurs naturally in MD and doesn't need any criteria. From a practical viewpoint, the simulation of strongly coupled multiscale systems becomes necessary. Therefore, we developed a multiple length/time scale theory connecting atoms to genuine continuum. As indicated in Sect. 1.2, molecular dynamics of multiphysics is adopted for the simulation of atoms in the critical region. The numerical results of sample problems show the distribution of virial stress tensors and atomistic temperature, crack opening and crack propagation with multiple crack fronts, and the motion of individual atoms. Meanwhile, the displacement and temperature fields and their derivables, Cauchy stresses, and heat fluxes in the continuum region are obtained through finite element analysis based on small-strain thermoelasticity. The material properties used in the finite element analysis, including elastic constants, thermal expansion coefficients, thermal conduction coefficients, and specific heat, are obtained from MD simulation—usually named as sequential multiscale modeling. The continuum theory used in this work is thermoelasticity. Of course, it can be generalized. Then the problem is reduced to the finding of needed and specified material properties through sequential multiscale modeling.

The pivot of the concurrent multiscale modeling is hinged at the interfacial conditions, described and formulated in Sect. 1.4. In the interface, there are several atomic groups, each corresponding to a node in the continuum region. For each node/group pair, we assume (1) the sum of heat flow is vanishing, and (2) the sum of interactive force is vanishing and the node is anchored at the centroid of the group (cf. Eqs. (1.97), (1.103), and (1.104)). Assumption 1 is considered as logical and reasonable. The sum of interactive force being zero is also logical and reasonable. Whether one can improve or generalize the assumption "the node is anchored at the centroid of the group" is left as an open question. If one is willing to accept these two assumptions, then the challenge due to the huge differences in length and time scales between the atomic region and continuum region is resolved in principle. For example, in this work, the time steps for MD simulation is set at $\Delta t^a = 20\ \tau = .4838$ fs and the time steps for finite element analysis of the continuum region is set at $\Delta t^c = 20\ \Delta t^a$ , i.e., the time ratio is 20. This ratio can be enlarged. The smallest length scale in the continuum region is the distance between the atomic groups. Beyond that, there is no limitation as far as finite element size is concerned. It is noticed that the interfacial conditions have nothing to do with the material properties. In other words, the material in the atomic region can be different from the material in the continuum region and therefore, this work is readily applicable for nanocomposites.

## References

Alder, B.J., Wainwright, T.E.: Studies in molecular dnamics. I. General method. J. Chem. Phys. **31**(2), 459–466 (1959)

Balandin, A., Ghosh, S., Bao, W., Calizo, I., Teweldebrhan, D., Miao, F., Lau, C.: Superior thermal conductivity of single-layer graphene. Nano Lett. **8**, 902 (2008)

Boresi, A.P., Chong, K.P., Lee, J.D.: Elasticity in Engineering Mechanics. Wiley, New York, NY (2011)

Chen, L., Kumar, S.: Thermal transport in graphene supported on copper. J. Appl. Phys. **112**(4), 043502 (2012)

Chen, Y., Lee, J.D., Eskandarin, A.: Meshless Methods in Solid Mechanics. Springer, New York, NY (2006)

de Groot, S.R., Suttorp, L.G.: Foundations of Electrodynamics. North-Holland Pub. Co., Amsterdam (1972)

Eringen, A.C.: Mechanics of Continua. R. E. Krieger Pub. Co., Malabar, FL (1980)

Eringen, A.C.: Microcontinuum Field Theories I: Foundation and Solids. Springer, New York, NY (1999)

Frank, I., Tanenbaum, D., Van der Zande, A., McEuen, P.: Mechanical property of suspended graphene sheets. J. Vac. Sci. Technol., B. **25**(6), 2558–2561 (2007)

Fried, L., Howard, W.: Explicit Gibbs free energy equation of state applied to the carbon phase diagram. Phys. Rev. B. **61**(13), 8734 (2000)

Guo, Z., Zhang, D., Gong, X.: Thermal conductivity of graphene nanoribbons. Appl. Phys. Lett. **95**(16), 163103 (2009)

Guo, Z., Ding, J., Gong, X.: Substrate effects on the thermal conductivity of epitaxial graphene nanoribbons. Phys. Rev. B. **85**(23), 235429 (2012)

Hoover, W.G.: Canonical dynamics: equilibrium phase-space distributions. Phys. Rev. A. **31**(3), 1695 (1985)

Humphrey, W., Dalke, A., Schulten, K.: VMD—visual molecular dynamics. J. Mol. Graphics. **14**(1), 33–38 (1996)

Jiang, J., Lan, J., Wang, J., Li, B.: Isotopic effects on the thermal conductivity of graphene nanoribbons: localization mechanism. J. Appl. Phys. **107**(5), 054314 (2010a)

Jiang, J., Wang, J., Li, B.: Elastic and nonlinear stiffness of graphene: a simple approach. Phys. Rev. B. **81**(7), 073405 (2010b)

Jing, N., Xue, Q., Ling, C., Shan, M., Zhang, T., Zhou, X., Jiao, Z.: Effect of defects on Young's modulus of graphene sheets: a molecular dynamics simulation. RSC Adv. **2**(24), 9124–9129 (2012)

Lee, C., Wei, X., Kysar, J., Hone, J.: Measurement of the elastic properties and intrinsic strength of monolayer graphene. Science. **321**(5887), 385–388 (2008)

Li, J., Lee, J.D.: Reformulation of the Nose-Hoover thermostat for heat conduction simulation at nanoscale. Acta Mech. **225**, 1223–1233 (2014a)

Li, J., Lee, J.D.: Stiffness-based course-grained miecular dynamics. J. Nanomech. Micromech. **4**, 1–8 (2014b)

Li, J., Wang, X., Lee, J.D.: Multiple time scale algorithm for multiscale modeling. Comput. Model. Eng. Sci. **85**, 463–480 (2012)

Lindsay, L., Broido, D., Mingo, N.: Flexural phonons and thermal transport in multilayer graphene and graphite. Phys. Rev. B. **83**(23), 235428 (2011)

Neek-Amal, M., Peeters, F.: Nanoindentation of a circular sheet of bilayer graphene. Phys. Rev. B. **81**(23), 235421 (2010)

Nosé, S.: A unified formulation of the constant temperature molecular dynamics methods. J. Chem. Phys. **81**, 511–519 (1984a)

Nosé, S.: A molecular dynamics method for simulations in the canonical ensemble. Mol. Phys. **53**, 255–268 (1984b)

Oden, J. T., et al.: Simulation-based engineering science, NSF Blue Ribbon Panel Report (2006), http://www.nsf.gov/pubs/reports/sbes_final_report.pdf

Pei, Q., Zhang, Y., Shenoy, V.: Mechanical properties of graphynes under tension: a molecular dynamics study. Appl. Phys. Lett. **101**(8), 081909 (2012)

Rahman, A.: Correlations in the motion of atoms in liquid argon. Phys. Rev. **136**(2A), A405–A411 (1964)

Rappe, A.K., Casewit, C.J., Colwell, K.S., Goddard, W.A., Skiff, W.M.: UFF, a full period table force field for molecular mechanics and molecular dynamics simulations. J. Am. Chem. Soc. **114**, 10024–10035 (1992)

Roldan, R., Castellanos-Gomez, A., Cappelluti, E., Guinea, F.: Strain engineering in semiconducting two-dimensional crystals. J. Phys. Condens. Matter. **27**, 333201 (2015)

Shaina, P., George, L., Yadav, V., Jaiswal, M.: Estimating the thermal expansion coefficient of graphene: the role of graphene–substrate interactions. J. Phys. Condens. Matter. **28**(8), 085301 (2016)

Shen, Y., Wu, H.: Interlayer shear effect on multilayer graphene subjected to bending. Appl. Phys. Lett. **100**(10), 101909 (2012)

Stillinger, F.H., Weber, T.A.: Computer simulation of local order in condensed phases of silicon. Phys. Rev. B. **31**, 5262 (1985)

Subramaniyan, A.K., Sun, C.T.: Continuum interpretation of virial stress in molecular simulations. Int. J. Solids Struct. **45**(14–15), 4340–4346 (2008)

Tersoff, J.: New empirical approach for the structure and energy of covalent systems. Phys. Rev. B. **37**, 6991–7000 (1988)

Tersoff, J.: Modeling solid-state chemstry: interatomic potentials for multicomponent system. Phys. Rev. B. **39**, 5566–5566 (1989)

Tohei, T., Kuwabara, A., Oba, F., Tanaka, I.: Debye temperature and stiffness of carbon and boron nitride polymorphs from first principles calculations. Phys. Rev. B. **73**(6), 064304 (2006)

Wang, C.C.: A new representation theorem for isotropic functions, Part I and Part II. Arch. Rat. Mech. Anal. **36**, 166–223 (1970)

Wei, Z., Ni, Z., Bi, K., Chen, M., Chen, Y.: In-plane lattice thermal conductivities of multilayer graphene films. Carbon. **49**(8), 2653–2658 (2011b)

Wei, N., Xu, L., Wang, H., Zheng, J.: Strain engineering of thermal conductivity in graphene sheets and nanoribbons: a demonstration of magic flexibility. Nanotechnology. **22**(10), 105705 (2011a)

Yang, Z., Lee, J.D., Eskandarian, A.: Objectivity in molecular dynamics simulations. Int. J. Terraspace Sci. Eng. **8**(1), 79–92 (2016)

Yoon, D., Son, Y., Cheong, H.: Negative thermal expansion coefficient of graphene measured by Raman spectroscopy. Nano Lett. **11**(8), 3227–3231 (2011)

Zhang, Y., Pei, Q., Wang, C.: Mechanical properties of graphynes under tension: a molecular dynamics study. Appl. Phys. Lett. **101**(8), 081909 (2012)

Zhao, H., Min, K., Aluru, N.: Size and chirality dependent elastic properties of graphene nanoribbons under uniaxial tension. Nano Lett. **9**(8), 3012–3015 (2009)

Zheng, Y., Wei, N., Fan, Z., Xu, L., Huang, Z.: Mechanical properties of grafold: a demonstration of strengthened graphene. Nanotechnology. **22**(40), 405701 (2011)

# Chapter 2
# Atomistic Modelling of Nanoindentation of Multilayered Graphene-Reinforced Nanocomposites

**Shaker A. Meguid, Ahmed R. Alian, and M.A.N. Dewapriya**

**Abstract** The force-displacement curves, obtained from a nanoindentation experiment, are generally analysed using continuum contact mechanics models. However, the applicability of these models at the nanoscale is questionable due to several inherited nanoscale phenomena, e.g., discreteness, quantum manifestations, and scale effects. Atomistic simulations such as molecular dynamics could provide better insight into the contact mechanics of nanoscale systems. In this chapter, we present a comprehensive molecular dynamics simulations of the contact behaviour of multilayered graphene-reinforced composite systems. Three aspects of the work were considered. The first was concerned with the force-displacement curves resulting from nanoindentation of a polyethylene matrix reinforced by multilayered graphene sheets. The second is concerned with the associated deformation patterns as well as the atomic adhesion associated with the retraction stage of the indenter. The third is concerned with the reinforcement mechanism and fracture behaviour associated with the increase in the number of graphene sheets and their spatial locations within the composite. The results of our work reveal: (a) strong interlayer interaction of graphene results in higher indentation resistance, (b) indentation resistance of a single-layer graphene-coated polyethylene is about 13-fold of the indentation resistance of pure polyethylene, (c) strong atomic adhesion between the indenter and the graphene prevails at the nanoscale, and (d) the proper choice of interlayer separation is critical in achieving the best performance of multilayered graphene-reinforced nanocomposites.

S.A. Meguid (✉) • A.R. Alian • M.A.N. Dewapriya
Mechanics and Aerospace Design Laboratory, Mechanical and Industrial Engineering, University of Toronto, Toronto, ON, M5S 3G8 Canada
e-mail: meguid@mie.utoronto.ca; arowaey@mie.utoronto.ca; nuwand@mie.utoronto.ca



S.A. Meguid, G.J. Weng (eds.), *Micromechanics and Nanomechanics of Composite Solids*, DOI 10.1007/978-3-319-52794-9_2

## 2.1 Introduction and Background

Nanoindentation tests have been used for material characterization since the 1970s (Pethicai et al. 1983). Recently, these tests have been extensively improved by developing advanced testing instruments and techniques and improved analysis methods (Oliver and Pharr 1992, 2004; Hay et al. 1999; Li and Bhushan 2002). As a result of these recent advances, nanoindentation has now become a vitally important test in characterizing the mechanical properties of various materials ranging from nanocomposites to biological materials (Paul et al. 2014). The focus of the current work is multilayered graphene-reinforced composites.

Due to their better strength-to-weight ratio and stiffness, longer fatigue life, and other superior electro mechanical properties, multilayered composites have proven to be very effective in numerous industries ranging from automotive to biomedical applications (Sinha Ray and Okamoto 2003; Pavlidou and Papaspyrides 2008; Jang and Zhamu 2008). Recent advances in fabricating nanoscale multilayered systems, such as graphene-based multilayered nanocomposites, are pushing the frontiers of conventional nanocomposites research (Raccichini et al. 2014; Richardson et al. 2015). In developing such advanced nanoscale multilayered systems, a thorough understanding of the mechanical behaviour of these systems is essential. This has prompted extensive experimental and theoretical studies of the nanoscale phenomena associated with reinforcement characteristics, contact stresses, force-displacement response, failure criteria, atomic adhesion, and atomic pileup, which are essential in designing high performance nanocomposite systems.

More importantly, however, using graphene in composite materials provides an excellent opportunity to transfer the superior electromechanical properties of graphene, across multiple length scales, up to the macroscopic level. Devices such as electromechanical resonators have been fabricated using both single and multi-layered graphene nanoribbons (Bunch et al. 2007; Chen et al. 2009, 2013). Novel methods for constructing multilayered assembly of graphene have been developed by several groups (Kong et al. 2009; Shen et al. 2009). Recent advances in synthesis of graphene-based multilayered nanostructures are showing promising applications in electrochemical energy storage (Raccichini et al. 2014), solar cells (Wang et al. 2011), and gas sensors (Ji et al. 2010). Such graphene-based layered materials could also be used for structural applications in automotive and aerospace industries. Latest developments in multilayered nanofilm assembly (Richardson et al. 2015) will further accelerate the commercial scale fabrication of multilayered graphene-based composites. In order to understand the mechanics of nanoscale multilayered systems, nanoindentation tests on multilayered silicate/polymer nanocomposites have been conducted by several groups; see, e.g., Bruzaud and Bourmaud (2007) and Aldousiri et al. (2011).

### 2.1.1 Experimental Techniques in Nanoindentation

Nanoindentation tests using atomic force microscopy have been widely used to characterize the material properties at the nanoscale (Gibson 2014; Díez-Pascual et al. 2015). A typical nanoindenter is composed of a force actuator and a displacement sensor to apply a pre-programmed load/displacement profile on the test specimen by using a hard tip (usually made out of diamond). The shape of the indenter tip is often a three-sided Berkovich pyramid because geometric self-similarity of this geometry creates a simple relationship between indentation depth and contact area (Fischer-Cripps 2011). Other commonly used geometries are the three-sided Berkovich pyramidal indenter and the four-sided Vickers pyramidal indenter. The load and the displacement data acquired during the test are plotted against each other, and the mechanical properties including the elastic modulus and the hardness are calculated using analytical models, which will be presented in the next section.

In order to estimate the hardness and stiffness of a material using nanoindentation, it is necessary to accurately determine the contact area between the specimen and the indenter. In early days, the contact area had been estimated by examining the induced residual impression using optical microscopy and image analysis. However, as the dimensions of the indenters began to approach the atomic level, determining of the contact area accurately became extremely challenging. This challenge prompted the development of depth-sensing indentation technique in which both the applied load and the resulting penetration depth are continuously recorded during the indentation process (Doerner and Nix 1986).

In their recent review, Paul et al. (2014) identified several key challenges and recent advances in nanoindentation experiments. Minor et al. (2006) demonstrated the importance of achieving high load resolution (in the range of nN) because the experiments carried out at a very small scale have shown that the initial yielding could occur at extremely low loads even below the force resolution limit. Cross et al. (2006) resolved this problem and succeeded in achieving smaller indenter displacements and force resolution in the range of nN by using atomic force microscopy for their nanoindentation experiments. Controlling surface chemistry and morphology of the test specimen is also very critical in determining the surface characteristics of the material at the nanoscale level (Song and Srolovitz 2006). Preparing the surfaces of the sample and the tip and conducting the indentation experiment in ultra-high vacuum is considered to be the best method to overcome this problem. In addition, indenter characterization becomes increasingly difficult at the atomic level. At this scale, not only the indenter radius but also the crystallographic direction of the tip and the structure of the stepped crystal surface could become important (Paul et al. 2014). Tip characterization can be carried out by scanning and transmission electron microscopy; however these techniques cannot be used to determine the full three-dimensional structure at the atomic scale (Egberts et al. 2009).

In fact, nanoindentation tests have been employed to measure the elastic properties and mechanical strength of graphene (Lee et al. 2008). Recently, Zandiatashbar et al. (2014) conducted nanoindentation tests of graphene to investigate

the effect of defects on the stiffness and the strength of graphene. The obtained load-displacement curves indicated that the strength of graphene with oxygen adatom is ∼14% smaller than the strength of pristine graphene. Shokrieh et al. (2013) conducted nanoindentation and nanoscratch tests to investigate the wear resistance of graphene-based polymer nanocomposites. They found that 0.5 wt% of graphene improved the scratch resistance and the hardness of polymer by 83% and 50%, respectively. By employing nanoindentation tests, Das et al. (2009) demonstrated that 0.6 wt% of multilayered graphene significantly enhances the stiffness (∼70%) and hardness (∼50%) of treated polymers. A more recent experimental study (Flores et al. 2016) has demonstrated that the stiffness of graphene-polyethylene nanocomposites obtained from dynamic nanoindentation measurements is higher than those obtained from quasi-static tensile tests. Furthermore, they found that the hardness decreases with the increase in the strain rate. In addition, they employed grid indentation, which is a very useful method to study the spatial distribution of mechanical properties, to characterize the surface distribution of the elastic modulus of graphene-based nanocomposites.

### *2.1.2 Analytical Modelling of Nanoindentation*

In addition to the experimental developments, substantial advance has also been made in both analytical and numerical modelling of nanoindentation. The classical continuum mechanics has limited applicability at the nanoscale due to the discrete nature of matter and quantum manifestations at the nanoscale (Luan and Robbins 2005; Tapasztó et al. 2012). However, the continuum concepts are computationally efficient and provide reasonable insights into the mechanical behaviour of graphene-based systems (Liu et al. 2011; Zhang et al. 2012; Xu et al. 2012; Dewapriya et al. 2013, 2014; Dewapriya and Rajapakse 2014). On the other hand, when it comes to modelling a complex system such as graphene-based nanocomposites, the accuracy of continuum models is questionable, because they do not take into account the structural configurations and the complex surface morphologies of nanoscopic systems, which are quite important in modelling mechanical properties at the atomic scale (Odegard et al. 2002; Haque and Ramasetty 2005; Dewapriya et al. 2015; Dewapriya and Rajapakse 2016).

Continuum contact mechanics models (Oliver and Pharr 1992; Pharr et al. 1992; Oliver and Pharr 2004) and Hertzian theory (Vlassak and Nix 1994) are widely used to analyse the force-displacement curves obtained from nanoindentation tests. The Oliver–Pharr method extended the initial analysis conducted by Sneddon (1965) on the indentation of an elastic half space by a flat cylindrical punch, which provided a simple relationship between load and displacement. Using the Sneddon's analysis, Oliver and Pharr established a simple method to estimate the elastic modulus and the hardness of a given material by using loading/unloading curve and the geometry of the indenter. According to the Oliver–Pharr simplified model, the hardness $H$ was calculated to be

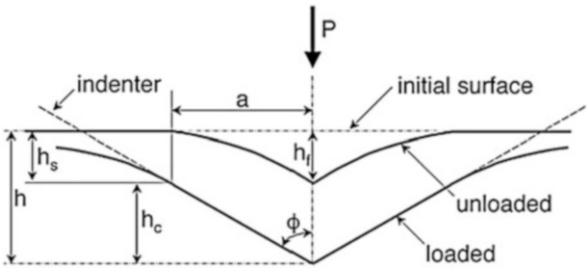


**Fig. 2.1** Schematic representation of loaded and unloaded deformations of a specimen during indentation test (Oliver and Pharr 2004)

$$H = \frac{P_{max}}{A} \tag{2.1}$$

where $P_{max}$ is the peak indentation force and $A$ is the contact area between the indenter and the specimen. The value of $A$ depends on the height $h_c$, which is defined in Fig. 2.1.

The elastic modulus ($E$) of the specimen can be obtained from the relationship

$$\frac{1}{E_r} = \frac{\left(1-\upsilon^2\right)}{E} + \frac{\left(1-\upsilon_i^2\right)}{E_i} \tag{2.2}$$

where $\upsilon$ and $\upsilon_i$ are the Poisson's ratios of the specimen and the indenter, respectively. $E_i$ is the elastic modulus of the indenter and $E_r$ is the reduced modulus, which takes into account the induced elastic deformations in both the indenter and the specimen. The value of $E_r$ is given as

$$E_r = \frac{\sqrt{\pi}}{2\beta}\frac{S}{\sqrt{A}} \tag{2.3}$$

where $S$ is the initial unloading contact stiffness given by the initial slope of the unloading curve. $\beta$ is a dimensionless parameter, and its value depends on the geometry of the indenter. Using finite element models, Sakharova et al. (2009) showed that $\beta$ is 1.034, 1.081, and 1.055 for the axisymmetric conical indenter, the Berkovich pyramidal indenter, and the Vickers pyramidal indenter, respectively.

The model developed by Oliver and Pharr was modified by several researchers in order to overcome its inherited limitations (Oyen and Cook 2003; Tang and Ngan 2003). For example, after several experimental studies demonstrated that the initial portion of the unloading curve is nonlinear (Oliver and Pharr 2004), it was proposed that the unloading curve is better represented by a nonlinear power law in the form

$$P = \alpha\left(h - h_f\right)^m \tag{2.4}$$

where $P$, $h$, and $h_f$ are defined in Fig. 2.1; $\alpha$ and $m$ are power law curve-fitting parameters.

However, it is questionable whether the Oliver–Pharr method can be directly applied to nanoindentation of polymers due to their viscoelastic properties (Gibson 2014). The viscoelastic properties could lead to an inaccurate estimate of the

hardness and the stiffness of the considered polymer. As an example, the creep behaviour of polymers could induce a "nose effect" during the unloading stage, leading to an inaccurate estimation of the contact stiffness (Oyen and Cook 2003; Tang and Ngan 2003). Furthermore, McAllister et al. (2012) and Wang et al. (2016) studied the applicability of the Oliver–Pharr method in analysing the load-displacement curves obtained by nanoindentation of polymers. They conducted both experiments and finite element modelling and found that the Oliver–Pharr method can be applied to polymers with a reasonable accuracy. They also revealed that the viscoelastic effects of polymer can be minimized by using high loading/unloading rate and by holding the load for a relatively longer duration. However, the Oliver–Pharr method has several limitations when it is used at the atomic level (McAllister et al. 2012; Yan et al. 2012).

### *2.1.3 Atomistic Modelling of Nanoindentation*

Atomistic modelling and simulation methods such as quantum mechanics (QM) and molecular dynamics (MD) play an important role in investigating the mechanical behaviour of nanoscale material systems. First principle QM calculations have been used to investigate the deformation at the contact region of a silicon (Si) substrate (Pérez et al. 1995). The simulations revealed that the flow of atoms occurs close to the interstitial position inside the Si substrate and extrusion of Si atoms towards the tip, which was made out of aluminium atoms. This extrusion is induced by non-uniform volumetric strain, and it is stabilized by the adhesive interaction with the tip. QM-based models have been used to investigate several mechanical aspects of graphene such as fracture (Khare et al. 2007a; Xu et al. 2012), edge stress and stability (Huang et al. 2009), bending (Kwon et al. 2012), effect of defects (Robertson et al. 2013), and interface mechanics (Xu and Buehler 2010). However, MD simulations are used to investigate the temperature-dependent properties because QM is not able to simulate systems at finite temperatures.

Molecular dynamics simulations have been widely used to study the mechanics of graphene and carbon nanotube (CNT)-based nanocomposites. Meguid and his collaborators used MD simulations to determine the effective elastic properties of a representative volume element that is comprised of CNT nanofillers (Alian et al. 2016; Alian and Meguid 2016; Alian et al. 2015a; b). Xia et al. (2016) conducted course-grained MD simulations of nanoindentation to study the interphase length scale of a polymer. Beyond the interphase length scale, the elastic modulus can be considered to be similar to the elastic modulus of the bulk polymer. They found that the interphase length scale is several tens of nanometres in the case of nanoindentation measurements and also found that this length scale is sensitive to the indenter radii.

Mathew and Sewell (2016) characterized the thermomechanical response of an energetic molecular crystal (i.e. TATB) by conducting MD simulations of nanoindentation. They observed that the elastic part of the force-displacement curve on the

basal plane is accurately predicted by an analytical solution obtained using Hertzian theory of indentation of an anisotropic half space with a rigid, frictionless parabola of revolution (Vlassak and Nix 1994; Willis 1966), whereas non-Hertzian response is demonstrated on the nonbasal planes. Tavazza et al. (2015) investigated the interaction between a diamond tip and nickel (Ni) substrate using MD simulations. They observed a significant amount of Ni atoms transfer to the diamond tip. This material transfer could have a significant impact on the nanoindentation test results. Rocha et al. (2013) used MD simulations to study the indentation behaviour of high-density polyethylene. Their study revealed that increasing the external force results in a decrease in the viscoelastic recovery and that a larger size indenter, under constant external force, generates increased viscoelastic recovery. MD simulations of nanoindentation tests on crystalline cellulose materials (Wu et al. 2013) and synthetic poly-dopamine (Lin et al. 2014) have been conducted to predict the mechanical properties and structure of those advanced materials.

Li et al. (2012) carried out atomistic simulations of the tensile response of thermoset polymer composites reinforced with multilayered graphene. Their results revealed that regardless of the relative orientation of the multilayered graphene and the composite interface, the strength of the composites under uniaxial tension is higher than the corresponding strength for the bulk polymer. Tan et al. (2013) conducted MD simulations to investigate the nanoindentation of circular monolayer graphene. They found that in the small deflection range, the indenter has a near point contact with graphene, and that the point load model is applicable. If the indenter is large, the size effect of the indenter is evident in the large deflection range, and the sphere-load model, which was developed to study spherical indentation of materials (Begley and Mackin 2004; Scott et al. 2004), should be used. Neek-Amal and Peeters (2010) conducted nanoindentation tests on bilayer graphene and found that Young's modulus is 0.8 TPa, which is less than a single-layer sheet. They also found that Young's modulus at 20 K is 14% less than the value at 300 K. A recent MD simulation of tensile behaviour of multilayered graphene shows that the ultimate tensile strength and Young's modulus of multilayered graphene are insensitive to the number of layers (Zhang and Gu 2013).

In this chapter, we present a detailed molecular dynamics simulations of the contact mechanical behaviour of a multilayered graphene-polyethylene composite resulting from numerical nanoindentation tests. Two aspects of the work are considered. First, we conducted molecular dynamics simulations of nanoindentation tests of single- and multilayered graphene. Second, building upon the knowledge obtained from the first part, we investigated the contact mechanical behaviour of multilayered graphene-reinforced polymer composites by conducting numerical nanoindentation tests. This chapter is organized as follows. In Sect. 2.2, the basics of molecular dynamics simulations are explained. Molecular dynamic modelling of nanoindentation of graphene and graphene-reinforced polymer composite is described in detail in Sect. 2.3, and results are also presented in that section. Finally, the concluding remarks are given in Sect. 2.4.

## 2.2 Basic Concepts of Molecular Dynamics Simulations

The main purpose of MD simulations is to study the time-dependent behaviour of a system by computing the current and the future positions and the velocity of each atom using Newton's equations of motion. This information can be later used to calculate the averaged mechanical properties of the system (Rapaport 1995; van Gunsteren and Berendsen 1990).

The initial position and velocity of each atom of the system must be known at the beginning of the MD simulation. The initial velocities are randomly generated based on the required average temperature of the system. Then, the trajectories of the atoms are determined by solving Newton's equations of motion of the interacting atoms of the system, viz.,

$$\vec{F}_i = m_i \vec{a}_i \tag{2.5}$$

where $\vec{F}_i$, $m_i$, and $\vec{a}_i$ are the respective acting force, mass, and acceleration of atom $i$. The interatomic forces are the gradient of the total potential energy $V$ of the system and is given by

$$\vec{F}_i = -\nabla V\left(\vec{r}\right). \tag{2.6}$$

The velocity $\vec{v}_i$ and the acceleration $\vec{a}_i$ of each atom are the first and second derivatives of the displacement vector $\vec{r}_i$, respectively:

$$\vec{v}_i = \frac{d\vec{r}_i}{dt} \tag{2.7}$$

$$\vec{a}_i = \frac{d\vec{v}_i}{dt} \tag{2.8}$$

Using Eqs. (2.5) to (2.8), we can obtain the following differential equation:

$$-\nabla V\left(\vec{r}\right) = m_i \frac{d^2\vec{r}_i}{dt^2}. \tag{2.9}$$

The most popular algorithm to integrate the resulting equations of motion of the system is the Verlet algorithm (Verlet 1967). In this algorithm, Newton's equations of motion are approximated by a Taylor series expansion as a time series, as follows:

$$\mathrm{r}\left(\mathrm{t}+\delta\mathrm{t}\right) = \mathrm{r}\left(\mathrm{t}\right) + \mathrm{v}\left(\mathrm{t}\right)\ \delta\mathrm{t} + \frac{1}{2}\mathrm{a}\left(\mathrm{t}\right)\ \delta\mathrm{t}^2 + \frac{1}{6}\frac{d^3r(t)}{\mathrm{dt}^3}\ \delta\mathrm{t}^3 + \mathrm{O}\left(\delta\mathrm{t}^4\right) \tag{2.10}$$

$$\mathrm{r}\,(\mathrm{t}-\delta\mathrm{t}) = \mathrm{r}\,(\mathrm{t}) - \mathrm{v}\,(\mathrm{t})\;\delta\mathrm{t} + \frac{1}{2}\mathrm{a}\,(\mathrm{t})\;\delta\mathrm{t}^2 - \frac{1}{6}\frac{d^3 r(t)}{\mathrm{dt}^3}\;\delta\mathrm{t}^3 + \mathrm{O}\left(\delta\mathrm{t}^4\right) \tag{2.11}$$

Adding Eqs. (2.10) and (2.11), and moving the r(t − δt) term to the right-hand side, we can obtain

$$r\,(t+\delta t) = 2r(t) - \mathrm{r}\,(\mathrm{t}-\delta\mathrm{t}) + a(t)\;\delta t^2 + O\left(\delta t^4\right) \tag{2.12}$$

This is the general form of the Verlet algorithm for MD, where δt is the time step of the analysis. The accuracy of this approach increases significantly with the decrease in this time step, because it is a function of the fourth order of δt. The value of a(t) is determined from Eq. (2.9), which depends on the location of the atom. Here, we use the positions from the previous and current time steps and acceleration of the current step to predict the trajectory of the atom. The instantaneous velocity $v(t)$ of each atom can be later calculated using the following Taylor series expansion

$$v(t) = \frac{\mathrm{r}\,(\mathrm{t}+\delta\mathrm{t}) - \mathrm{r}\,(\mathrm{t}-\delta\mathrm{t})}{2\delta\mathrm{t}} + O\left(\delta t^3\right) \tag{2.13}$$

The kinetic energy K(t) and the averaged instantaneous temperature T of the system, based on the equipartition theory, can be calculated using the obtained velocities in the following relations:

$$\mathrm{K}\,(\mathrm{t}) = \frac{1}{2}\sum_{\mathrm{i}} \mathrm{m_i}\;(\mathrm{v_i}\,(\mathrm{t}))^2 \tag{2.14}$$

$$\mathrm{T}\,(\mathrm{t}) = \frac{2}{3}\frac{\mathrm{K}\,(\mathrm{t})}{\mathrm{N}\;\mathrm{K_B}} \tag{2.15}$$

where $\mathrm{K_B}$ is the Boltzmann constant.

The total potential energy of the system can be defined by interatomic potentials or molecular mechanics force fields which describe how the atoms interact with each other (LeSar 2013). The selected interatomic potential or force field for the system under investigation must be very accurate for the quantum mechanical processes and to yield reliable results. These potentials and force fields have been developed by several researchers based on quantum mechanics calculations and then validated by comparing their results with experimental tests (Brenner 2000; LeSar 2013). The general expression for the total atomistic potential energy of the system can be written as a many-body expansion that depends on the position of one, two, three, or more atoms at a time (LeSar 2013), such that

$$V\left(\vec{r}_1, \vec{r}_2, \ldots, \vec{r}_N\right) = \sum_{i}^{N} V_1\left(\vec{r}_i\right) + \sum_{i,j}^{N} V_2\left(\vec{r}_i, \vec{r}_j\right) + \sum_{i,j,k}^{N} V_3\left(\vec{r}_i, \vec{r}_j, \vec{r}_{ik}\right) + \ldots \tag{2.16}$$

where $V_1$ is the one-body term (energy of the isolated atom $i$ due to an external force field such as the electrostatic force), $V_2$ is the two-body term (pair-wise interactions of the atoms $i$ and $j$ such as Lennard-Jones potential (Jones 1924)), $V_3$ is the three-body term (three-body interactions and usually called many-body interactions such as Tersoff and Brenner potentials), $N$ is the number of atoms in the system, and $\vec{r}_i$ is the position vector of atom $i$ (Tersoff 1988; Brenner 1990). In this work, we used an inter atomic many-body potential for hydrocarbons called the Adaptive Intermolecular Reactive Empirical Bond Order (AIREBO) potential (Stuart et al. 2000).

The AIREBO potential consists of three sub-potentials, which are Lennard-Jones potential, the torsional potential, and the reactive empirical bond order (REBO) potential. Lennard-Jones potential incorporates the van der Waals forces, and the torsional potential includes the energy due to torsional interactions between atoms. The REBO potential (Brenner 1990) evaluates energy stored in atomic bonds; the energy stored in a bond between atom $i$ and atom $j$ can be expressed as

$$E_{ij}^{REBO} = f\left(r_{ij}\right)\left[V_{ij}^{R} + b_{ij}V_{ij}^{A}\right] \tag{2.17}$$

where $V_{ij}^{R}$ and $V_{ij}^{A}$ are the repulsive and the attractive potentials, respectively; $b_{ij}$ is the bond order term, which modifies $V_{ij}^{A}$ according to the local bonding environment; $r_{ij}$ is the distance between the atoms $i$ and $j$; $f(r_{ij})$ is the cut-off function, which limits the interatomic interactions to the nearest neighbours. The cut-off function in REBO potential (Brenner 1990), given in Eq. (2.18), limits the interatomic interactions to the nearest neighbours, such that

$$f\left(r_{ij}\right) = \begin{cases} 1, & r_{ij} < R^{(1)} \\ 1 + \cos\left[\frac{\pi\left(r_{ij} - R^{(1)}\right)}{\left(R^{(2)} - R^{(1)}\right)}\right], & R^{(1)} < r_{ij} < R^{(2)} \\ 0, & R^{(2)} < r_{ij} \end{cases} \tag{2.18}$$

where $R^{(1)}$ and $R^{(2)}$ are the cut-off radii, which are determined to be 1.7 and 2 Å, respectively. The values of cut-off radii are defined based on the first and the second nearest neighbouring distances of the relevant hydrocarbon. The cut-off function, however, causes non-physical strain hardening in carbon nanostructures (Shenderova et al. 2000). Therefore, the modified cut-off radii, ranging from 1.9 to 2.2 Å, have been used to eliminate this non-physical strain hardening (Jhon et al. 2014; Zhang et al. 2012; Zhao and Aluru 2010). High strains and fracture of carbon–carbon bonds are possible during nanoindentation test simulations. Therefore, we investigated the influence of the cut-off function on the nanoindentation test results by using a truncated cut-off function $f_t(r_{ij})$, given in Eq. (2.19) (Dewapriya 2012; Dilrukshi et al. 2015).

$$f_t\left(r_{ij}\right) = \begin{cases} 1, & r_{ij} < R \\ 0, & r_{ij} > R \end{cases} \tag{2.19}$$

where the value of $R$ is 2 Å. Similar cut-off functions have been used by Zhang et al. (2012) and Cao and Qu (2013) to simulate the fracture of graphene.

All MD simulations are being conducted under specified conditions. These ensembles are characterized by fixed values of the following thermodynamic variables: potential energy, temperature, pressure, volume, and total number of particles. The most commonly used ensembles in MD simulations are:

- Micro-canonical ensemble: constant number of atoms, volume, and energy (NVE)
- Isothermal-isobaric ensemble: constant number of atoms, temperature, and pressure (NTP)
- Canonical ensemble: constant number of atoms, temperature, and volume (NVT)

There is a common sequence that can be followed to build an MD model and perform a successful simulation. The first step is to build the initial structure of the system using the appropriate software such as Nanoengineer, Materials Studio, Packmol, amongst others. The second step is to optimize this initial structure by changing the location of its atoms relative to each other to reduce the total potential energy of the system and also to release the existing residual stresses. The third step is to assign an initial velocity to each atom based on the targeted average temperature of the system. The fourth step is to equilibrate the minimized structure to obtain the system at targeted initial conditions (pressure, volume, temperature). The final step is to conduct the required analysis and measure the system properties of interest.

## 2.3 Molecular Dynamics Simulation of Graphene-Reinforced Nanocomposites

The main goal of this study is to determine the reinforcement effect of graphene sheets on nanocomposites. In order to understand the reinforcing mechanism of such composites, MD simulations of the numerical nanoindentation test of pure polymer and both single and multilayered graphene structures were conducted. Consequently, numerical nanoindentation tests of multilayered graphene-reinforced systems with different configurations followed. The results of the MD simulations for all the systems considered are presented and compared in order to give insight into the behaviour of these materials at the nanoscale. All MD simulations were performed with large-scale atomic/molecular massively parallel simulator (LAMMPS; Plimpton 1995) using the adaptive intermolecular reactive bond order (AIREBO) potential (Stuart et al. 2000).

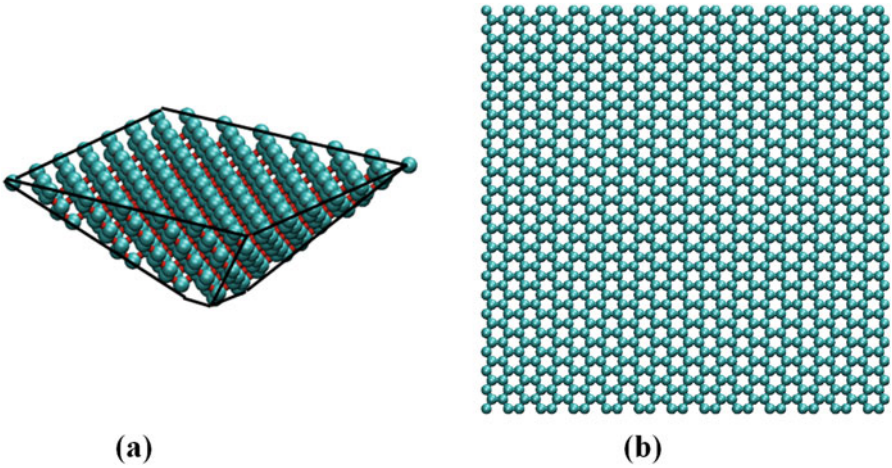


**Fig. 2.2** Preliminary system used for the nanoindentation simulations. (**a**) The pyramid-shaped diamond indenter with dimensions of 24 × 24 × 10 Å and (**b**) the graphene sheet with dimensions of 50 × 50 Å

### *2.3.1 Indentation of a Single Layer of Graphene*

We used a pyramid-type diamond indenter (Vickers indenter) for the nanoindentation simulations. Figure 2.2 shows the diamond indenter and the graphene sheet used for the study. The base of the indenter selected was 24 × 24 Å with a thickness of 10 Å. The indenter tip consists of 9 carbon atoms (3 × 3 atoms). In a graphene sheet, carbon atoms are arranged in a honeycomb lattice, where the carbon–carbon bond length is assumed to be 1.396 Å (Stuart et al. 2000). The dimensions of the graphene target selected were 50 × 50 Å, and it has 1070 carbon atoms. The MD simulations were conducted at a temperature of 300 K with a time step of 0.5 fs. The energy of the system (the graphene target and the indenter) was firstly minimized using the Conjugate Gradient algorithm. The system was considered to be optimized once the change in the total potential energy between subsequent steps is less than $1.0 \times 10^{-10}$ kcal/mol (Alian and Meguid 2017). Then, the minimized system was allowed to reach equilibrium over 50,000 time steps in the constant temperature and volume (NVT) ensemble. Figure 2.3 shows the system reaching equilibrium after some 5 ps.

The initial gap between the indenter tip and the graphene target was selected to be 15 Å as the system reaches its equilibrium. The diamond indenter was brought into contact with the graphene target at a constant speed of 1 Å/ps, and the resisting force on the indenter was calculated at each simulation step and also averaged over an interval of 0.1 ps to reduce the effect of fluctuations on the obtained results. The MD unit cell was equilibrated using the NVT ensemble at 300 K during the indentation process. Four edges of the graphene target were kept fixed during the indentation, and the diamond indenter was considered as a rigid body (i.e. constant

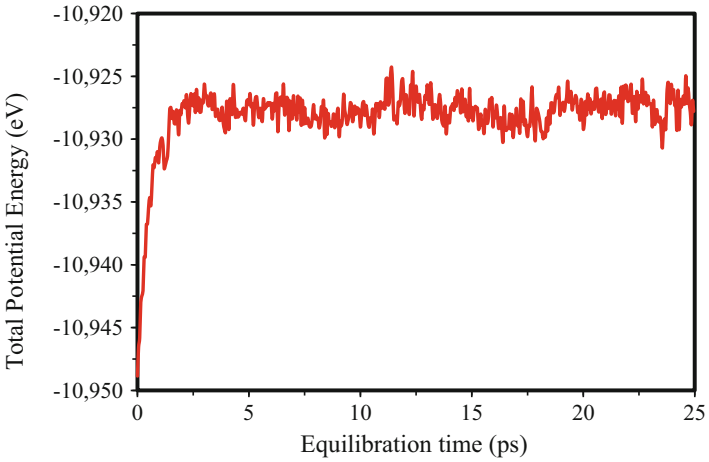


**Fig. 2.3** Variation in potential energy of the simulated system with the equilibration time

speed in $z$ direction and zero speed in $x$ and $y$ directions). The indentation process continued until the graphene sheet was fractured to establish the upper bound of indentation depth and the associated indenter force. Figure 2.4 demonstrates the corresponding deformation and the fracture behaviour of the graphene sheet during the indentation process. The figure shows the severe deformation of the graphene sheet upon fracture revealing its extraordinary out-of-plane flexibility. Interestingly, however, even at fracture, several carbon chains hold the two fractured entities of the graphene together, as shown in Fig. 2.4d. Similar phenomenon had been observed in experiments (Chuvilin et al. 2009; Jin et al. 2009) as well as in MD/QM simulation studies (Hobi et al. 2010). These linear carbon chains represent connected dimers composed of two coordinated carbon atoms. Hobi et al. (2010) revealed that in the absence of such dimers, full rupture of graphene will take place.

Figure 2.5 shows the change in the indenter force versus the total potential energy of the system with the indentation time. The indenter touches the graphene sheet at 3 ps. Fracture of the graphene target occurs at an indentation depth of 20 Å, and the maximum indenter force is 510 nN. It can be seen in the figure that the indenter experiences a significant resisting force even after the fracture of the graphene target.

In MD simulations of nanoscale systems, selection of the system and boundary condition is very critical in obtaining reliable results (Mattoni et al. 2005; Dewapriya 2012). Therefore, we investigated the influence of the graphene sheet size on the resulting indentation force at a fixed indentation depth by modelling square graphene sheets with various dimensions ranging from 50 to 200 Å. The indentation force at an indentation depth of 17 Å was determined and compared for all cases considered; see Fig. 2.6. It can be clearly seen that the indentation force decreases significantly as the sheet size increases. This is due to the additional stiffness provided by the fixed boundaries in the out-of-plane direction of the graphene sheet during the indentation process.

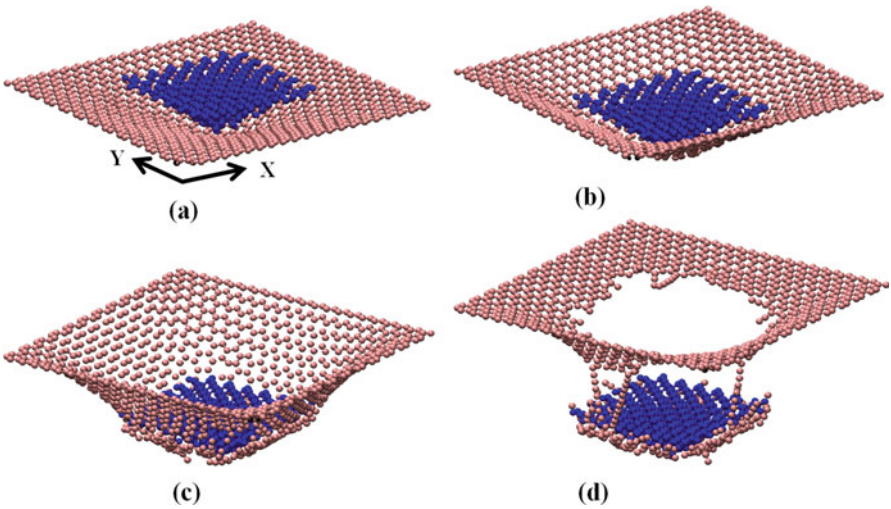


**Fig. 2.4** Snapshots of the graphene-indenter system during indentation. The diamond indenter, shown in blue, was moved downwards (along $-z$ direction) at a constant speed of 1 Å/ps. (**a**) and (**b**) show the deformation of the graphene prior to fracture, and (**c**) and (**d**) show the behaviour of graphene after fracture

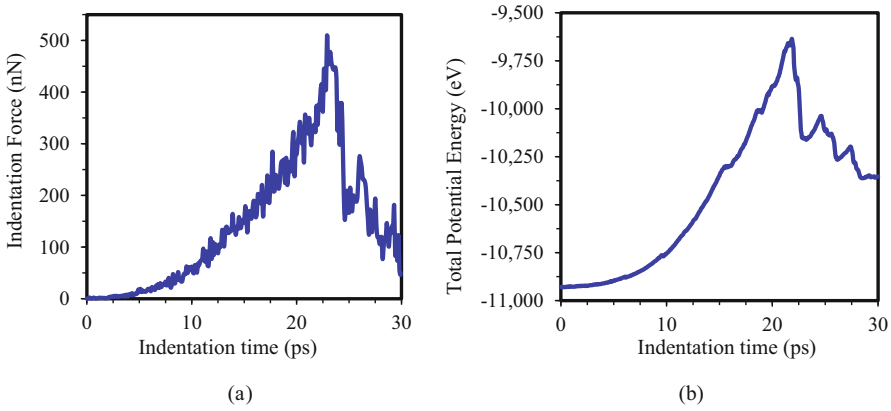


**Fig. 2.5** Time variations of (**a**) indentation force versus time and (**b**) system potential energy versus time

The influence of the cut-off function on the indentation force during the MD simulation is investigated in this section. The original and modified cut-off functions are given in Eqs. (2.18) and (2.19), respectively. Even though the original cut-off function introduced non-physical strain hardening of graphene when simulating a tensile test, our study revealed that the influence of a cut-off function on the indentation force is unnoticeable as shown in Fig. 2.7.

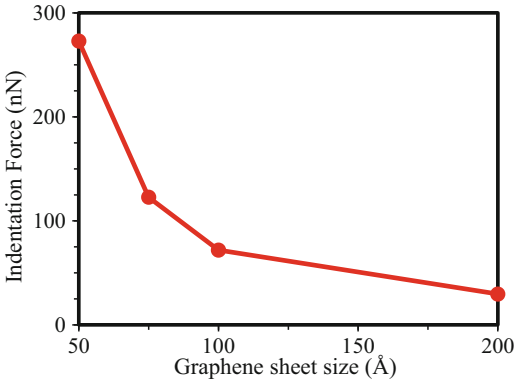


**Fig. 2.6** Effect of graphene sheet size upon the resistance to indentation

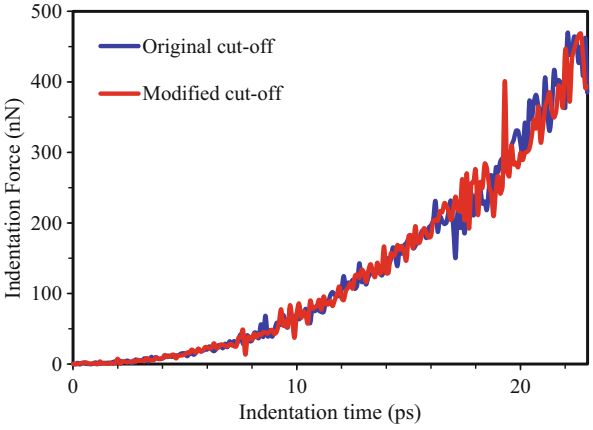


**Fig. 2.7** Effect of the interatomic REBO cut-off function on the indentation force of graphene

### 2.3.2 *Indentation of Multilayers of Graphene Sheets*

Single-layer graphene sheets tend to agglomerate and form a multilayered system (Li et al. 2008; Shen et al. 2009). The interlayer separation in multilayered graphene is assumed to be 3.4 Å (Lu 1997; Ohta 2006). We performed numerical nanoindentation tests on different multilayered graphene systems consisting of a gradually increasing number of layers up to five sheets. A diamond indenter similar to the one used for the aforementioned single sheet studies (see Fig. 2.2a) but with a longer stem was used for the current simulations. All edges of all multilayered graphene sheets were kept fixed during the indentation stage. The procedures of the MD simulation were similar to that of the single-layer studies, which are explained in Sect. 2.3.1. Figure 2.8 shows indentation of a three-layer graphene sheet for an indentation depth of 30 Å.

Figure 2.9 compares the variation in indentation force with the indentation depth for a different number of layers up to an indentation depth of 20 Å. The figure also shows the best fit polynomial for a single-layer graphene, where the force-depth

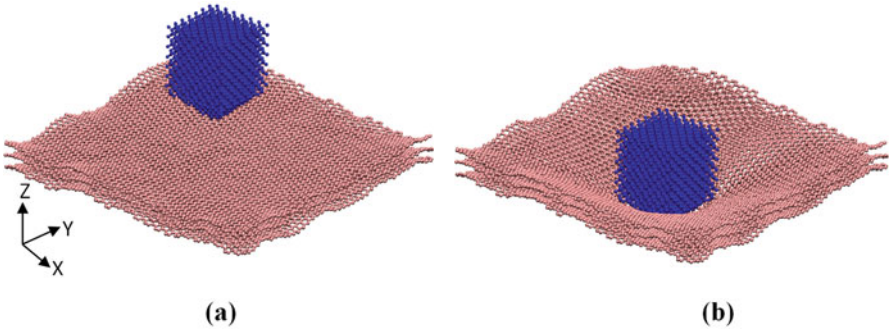


**Fig. 2.8** Nanoindentation of a three-layered graphene sheet (**a**) prior to indentation and (**b**) deformed shape during indentation

**Fig. 2.9** Variation of indentation force with indentation depth for multilayered graphene targets

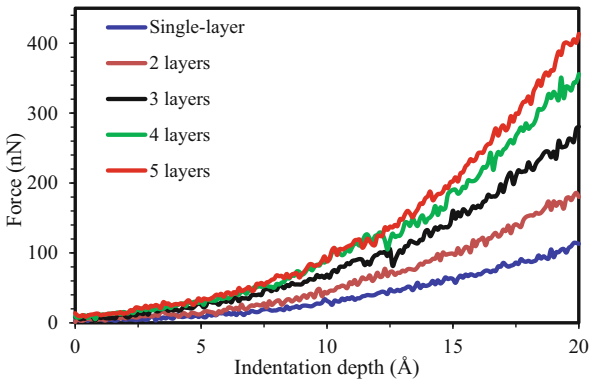


relationship is in the third order as proposed by Lee et al. (2008) and Komaragiri et al. (2005). It can be seen that, at a given indentation depth, the indentation forces of the multilayered graphene cannot be expressed as the linear sum of the indentation force of a single-layer graphene. This is because contact is nonlinear even at the continuum level. In addition, the contact stresses and the resulting contact area are typically unknown a priori.

Figure 2.10 compares the variation of indentation force with the number of graphene sheets at three indentation depths (i.e. 10, 20, and 30 Å). It should be noted that the force is obtained as the average force over 100 time steps in order to obtain more reliable results by reducing the effect of the instantaneous force-time fluctuations. The figure clearly demonstrates an approximately linear relationship between the number of graphene sheets and the indentation force up to five layers. It is also interesting to note that the slope of each curve is different indicating the complexity of the problem.

For example, during the nanoindentation of the five-layered graphene system, all graphene sheets begin to experience some form of fracture around an indentation depth of 27 Å. Figure 2.11a shows the variation in the indentation force during

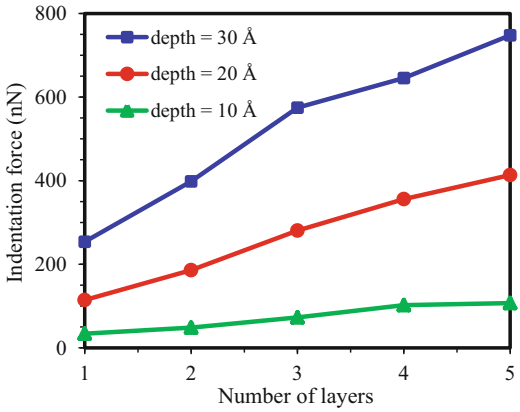


**Fig. 2.10** Variation of the maximum indentation force with the number of graphene sheets of a multilayered system at different indentation depths

the indentation process, at $t = 0$, when the indenter is in contact with the top graphene layer. It can be seen in that figure that the indenter experiences a noticeable indentation force even before it touches the top uppermost layer. This force is generated by the repulsive van der Waals interaction forces. Figure 2.11b–g demonstrate the interaction between graphene and indenter at the times shown in Fig. 2.11a. It can be seen in Fig. 2.11c, d that the atoms in contact with the indenter experience highly concentrated deformation. The fracture of the multilayered graphene sheets starts at a depth of 26.5 Å as shown in Fig. 2.11e. Figure 2.11f shows that three graphene sheets are fractured at a depth of 30 Å. After reaching a depth of 30 Å, the indenter was retracted with the same velocity. Figure 2.11g–i show the interaction between the multilayered graphene targets and the indenter during the retraction stage. It can be seen from these figures that there is a significant adhesion between the fractured graphene sheets and the indenter. Fracture of graphene sheet leads to the generation of carbon atoms with dangling bonds which have very high cohesion with the indenter (Alian et al. 2017).

In the following sections, we investigate the mechanical behaviour of polyethylene with and without the use of multilayered reinforcing graphene sheets.

### *2.3.3 Indentation of Polyethylene*

In this section, we will investigate the response of a pure polymer to nanoindentation tests using MD simulations. The results obtained from this analysis will be used as a reference for comparisons with graphene-reinforced polymer nanocomposites. To model the surrounding matrix, a polyethylene (PE) polymer was selected. The unit cell used for the MD simulations consists of 952 PE chains, in which each chain was formed by 10 $C_2H_4$ units. Planar dimensions ($x$ and $y$) of the PE block are $100 \times 100$ Å and thickness is 50 Å; the density of PE is 0.9 g/cm$^3$. Periodic boundary conditions were applied along $x$ and $y$ directions. In addition, an invisible surface

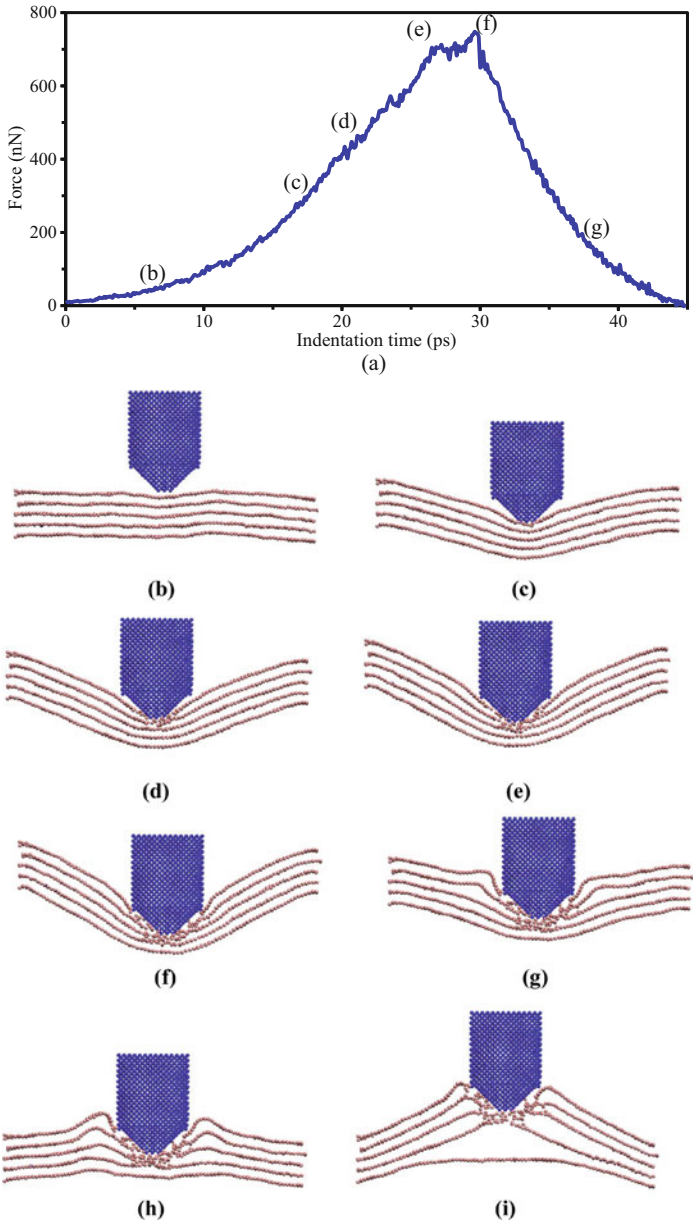


**Fig. 2.11** Nanoindentation of five-layered graphene targets: (**a**) Variation in indentation force with time during the test. (**b**)–(**g**) Interaction between graphene and indenter at times indicated as (**b**)–(**g**) on Fig. 2.11a. Figures (**g**)–(**i**) depict behaviour of the system during retraction stage. In Figs. 2.11b–i, a cross section cut through the centre of the indenter was taken in order to demonstrate the position of the indenter and deformation of the different graphene layers

was created just above the PE block to repel any polymer chains from escaping the top polymer surface, while a layer of thickness 3 Å at the bottom of the PE block was kept fixed. The diamond indenter used in the previous sections was used here as well to perform nanoindentation. The procedures of the MD simulation of the indentation test were similar to that of the multilayered graphene system studies, which is explained in Sect. 2.3.2.

Figure 2.12a shows the variation in indentation force during the numerical nanoindentation test, while Fig. 2.12b–d demonstrate the behaviour of the system at different times during the indentation process. Indentation time was measured from the instance where the indenter touches the top of the equilibrated polyethylene system. It can be seen clearly in Fig. 2.12a that the indentation force rapidly increases during the first 12 ps of the indentation stage. After this initial duration, the indentation force increased slightly before reaching its maximum value at a depth of 30 Å. The recorded maximum indentation force in the case of pure polyethylene was 24.5 nN, which represent 10% of the maximum indentation force of a single-layer graphene at the same indentation depth. It can also be seen in Fig. 2.12a that the indentation force does not decrease immediately after the start of the retraction of the indenter at 30 ps. This phenomenon is attributed to the recovery of the polyethylene chains to their original positions and thus maintains the resisting force. However, the polyethylene chains cannot fully return to their original positions at the rate of indenter retraction. In other words, density of polyethylene around the indenter decreases significantly, which eventually leads to a sudden drop in the indentation force at 32 ps.

In the ensuing section, we investigate the contact behaviour of polyethylene matrix reinforced by a single-layer of graphene.

### *2.3.4 Single-Layer Graphene-Reinforced Polyethylene*

In this section, we investigate the reinforcement effect resulting from adding a single-layer of a graphene sheet on the top of the polyethylene used in Sect. 2.3.3. The difference between the composite and the pure polymer will be presented and discussed thoroughly to determine the improvement in the mechanical properties and performance. Figure 2.13 shows a graphene-reinforced polyethylene system. The equilibrium separation distance between the graphene sheet and the polymer matrix is around 3 Å, which was maintained by the repulsive forces between the graphene sheet and the polyethylene atoms in contact with the sheet. Periodic boundary conditions were applied along the $x$ and the $y$ directions of the system, while the graphene sheet was allowed to stand freely on the polymer block.

Figure 2.14 compares the indentation force vs depth relation of a graphene-reinforced polymer composite with the response of a single-layer graphene and that of pure polyethylene. The maximum indentation force for the graphene and the polyethylene are 254 and 24.5 nN, respectively. When these two materials were put together, the maximum indentation force of the combined system becomes

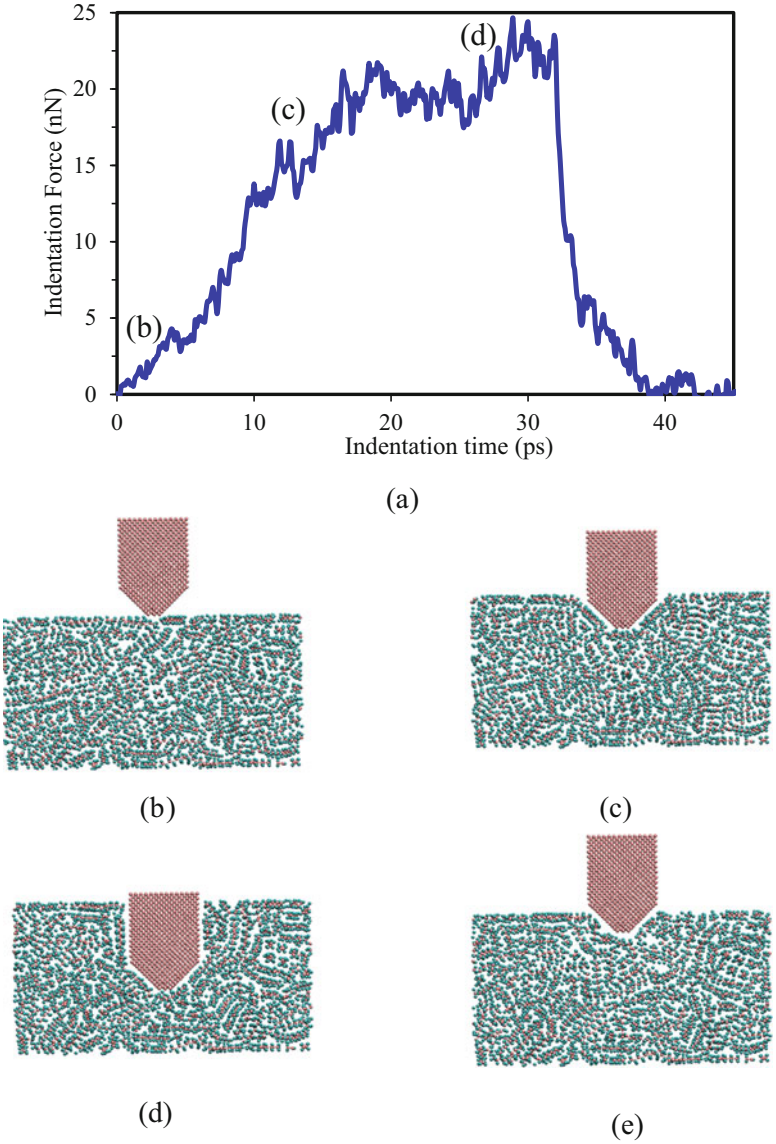


**Fig. 2.12** Nanoindentation of polyethylene: (**a**) Variation of force during indentation and retraction of polyethylene matrix. (**b**)–(**e**) Four stages during nanoindentation of polyethylene. A section going through the centre of the indenter was shown in order to demonstrate the position of the indenter and the relative deformation of polyethylene block. (**b**)–(**d**) demonstrate the deformation of polyethylene at times indicated as (**b**)–(**d**) on (**a**)

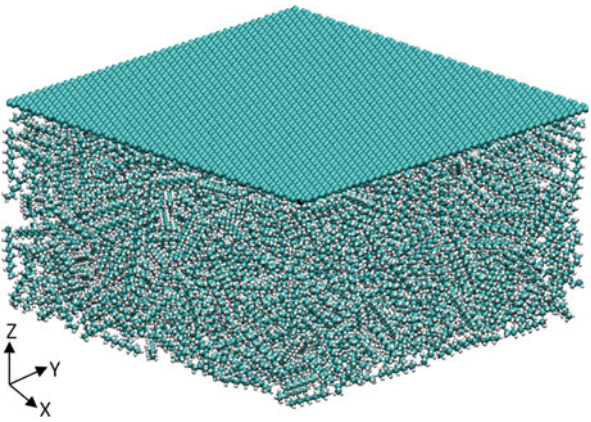


**Fig. 2.13** A single-layer graphene-reinforced polyethylene system, which has 67,985 atoms. Dimensions of the polyethylene block are 100 × 100 × 50 Å

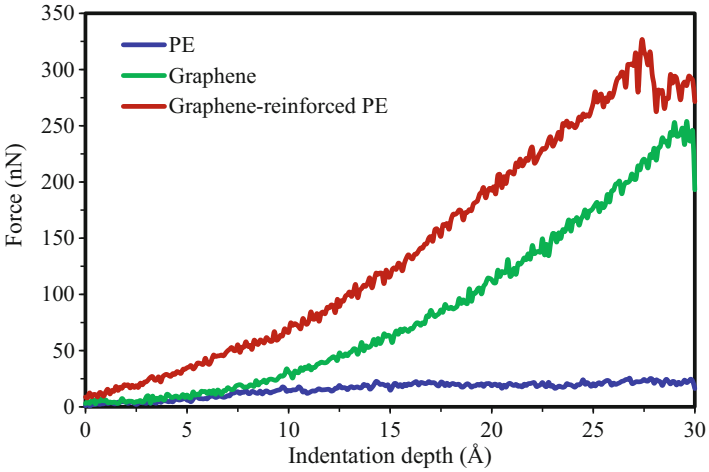


**Fig. 2.14** Force-Indentation response for graphene-reinforced polyethylene together with the individual responses of graphene and polyethylene separately

327 nN, which is 13-fold increase in the maximum indentation force of pure polyethylene. In fact, and more remarkably, the indentation resistance of graphene has also increased by 29%. It can be seen in Fig. 2.14 that the graphene-reinforced polyethylene is much stiffer than the combined individual stiffness of graphene and polyethylene. The polyethylene matrix resists the deformation of the graphene sheet, and the graphene sheet is able to distribute the concentrated force exerted by the indenter through a considerably larger area. As a consequence of these two interacting effects, both the graphene and the polyethylene deforms much less than their individual responses to the indentation force, which results in a higher effective stiffness.

### 2.3.5 *Graphene-Reinforced Multilayered Polyethylene Composites*

Five systems representing PE matrix reinforced with increasing number of graphene sheets that form multilayered structures were considered here. The difference between the response of these systems and the pure polymer to numerical nanoindentation tests will be presented and discussed to determine the improvement in the material performance and also to help designing new nanocomposites with optimized properties. The number of graphene sheets and hence the thickness of the graphene/PE layers range from zero (to represent pure polymer of a thickness of 50 Å) to five layers (to represent a PE layer of 10 Å).

Selecting the system size and boundary conditions properly is very crucial in obtaining accurate and reliable results at a reasonable computational cost. Accordingly, performing MD simulations of large graphene-reinforced polyethylene systems could be computationally very expensive. In order to reduce this burden, we investigated the ability of using smaller structures to model multilayered graphene-reinforced polymer composites. For this purpose, several systems of different sizes were considered to determine the effect of the system size on the obtained properties (i.e. boundary effects). Figure 2.15a–c show the deformation of a multilayered graphene-reinforced polyethylene system during nanoindentation, where the size of the graphene sheets is 50 × 50 Å (designated case A); thickness of individual polyethylene layers is 10 Å, and the system consists of five such layers. Periodic boundary conditions were applied along $x$ and $y$ directions. Indenting/retracting speed of the indenter were 1 Å/ps. It can be seen in Fig. 2.15b that the entire system underwent severe deformation during the indentation process.

The indentation test of a larger system with planar dimensions of 100 × 100 Å (designated case B) was also simulated. Figures 2.15d, e depict snapshots of the larger system before the start of the indentation process at the maximum indentation depth, and after retracting the indenter, respectively. It can be seen in Fig. 2.15e that the boundaries of case A are not severely deformed, and the deformation is mostly localized around the indenter. It is also noticed that the graphene sheet, which was in contact with the indenter, was partially fractured in case B, however the sheet was not fractured in case A. This indicates that even under the same indentation depth, the graphene sheets at the surface of the two system experience totally different levels of deformation. In case A, the entire system (including boundaries) deforms, which can be seen in Fig. 2.15b. However, in case B, the boundaries are slightly deformed as shown in Fig. 2.15e. Therefore, at a given indentation depth, the effective deformation experienced by graphene in case B is higher than that of case A. It can also be seen that there is a significant migration of the polymer chains due to the indentation, which can be clearly seen in Fig. 2.15e. But then, substantial amount of individual polymer chains has come back closer to their original positions during the retraction stage. This polymer migration phenomenon results in a relatively lower density of polyethylene below the indenter. Figure 2.15f demonstrates a significant cohesion between the indenter and the adjacent

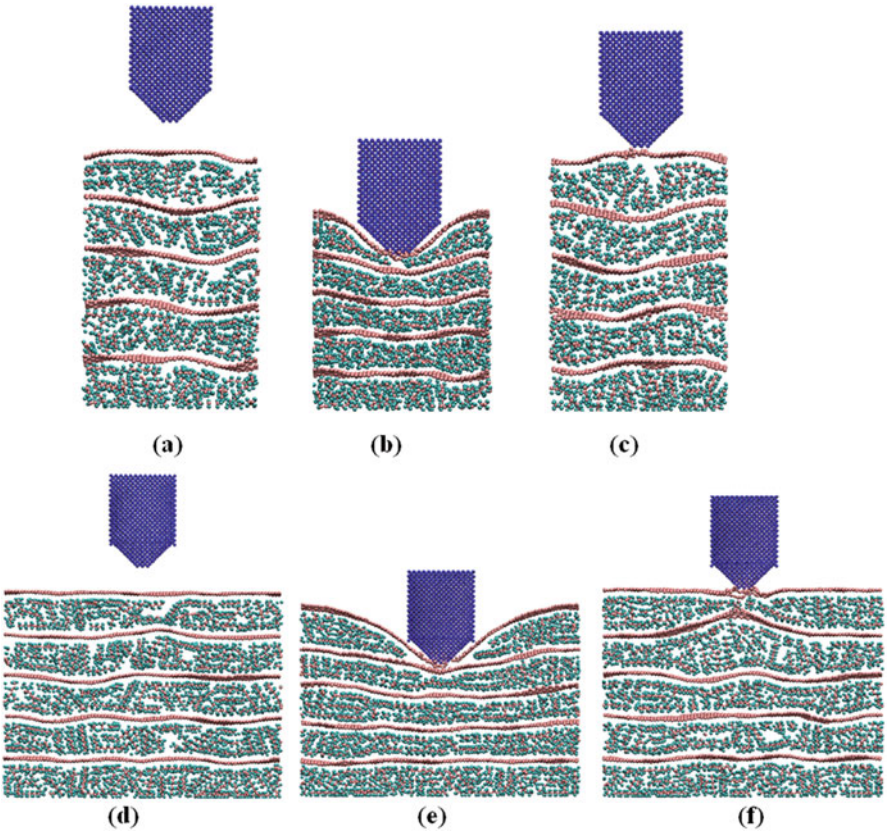


**Fig. 2.15** Deformation of multilayered Graphene-PE systems (Cases A and B) considered during nanoindentation. (**a**)–(**c**) depict case A of indentation of 50 × 50 Å, and (**d**)–(**e**) depict case B of indentation of 100 × 100 Å system with five layers

graphene layer and also between indenter and polymer chains in the multilayered system during the retraction stage. One reason for this cohesion is that the graphene sheet has been partially broken which lead to the formation of several dangling bonds on the graphene sheet at the fractured region. The dangling bonds want to be stabilized by creating covalent bonds. Therefore, carbon atoms with dangling bonds have strong cohesion with the diamond indenter and polymer chains (Alian et al. 2017).

Figure 2.16 compares the indentation forces for Cases A and B. There is a 10% difference in the maximum indentation forces of the 50 × 50 Å and 100 × 100 Å systems, which are 307 and 341 nN, respectively. The loading curve of the 50 × 50 Å system indicates that the system is slightly stiffer than the other one. This could be due to the fact that the boundary effects are dominant in case A, whereas this effect lessens in Case B. All polymer layers of case A deform and exert a resisting force on the indenter, but the deformation is localized in case B.

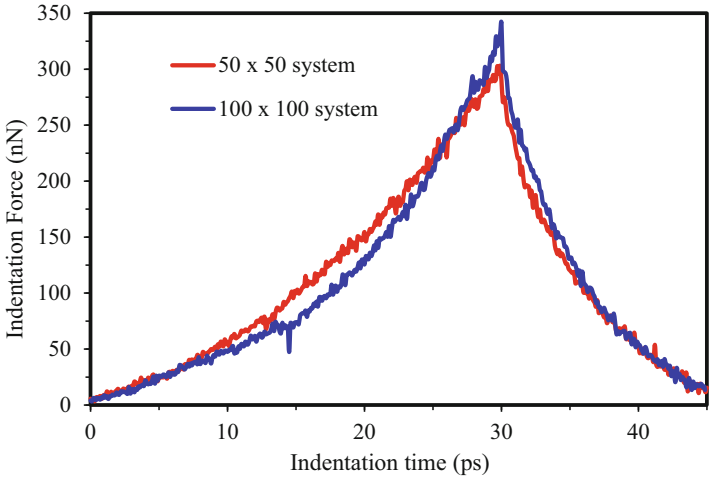


**Fig. 2.16** Comparison of indentation force vs time curves of the two five-layered systems shown on Fig. 2.15

Considering the boundary effects, we decided to use a system with planar dimensions of 100 × 100 Å to further investigate the indentation resistance of graphene-reinforced multilayered systems. Figure 2.17 shows the two-, the three-, and the four-layered systems used in the study. Figure 2.18a compares the variation of indentation force with time in all systems, where the indentation was carried out at a speed of 1 ps/Å until the indentation depth of 30 Å is reached. Time is measured from the instant that the indenter touches the uppermost layers of the graphene sheet. The figure reveals that the behaviour of the single, the two, and the three-layered systems is almost identical except that the fracture of a single layer occurs slightly early around an indentation depth of 27 Å; fracture of other systems is not evident. This identical indentation resistance of these layered systems occurred due to the fact that only the uppermost graphene layer is resisting the indenter and that the interior sub-graphene sheets layers do not exert substantial resisting force to the indenter due to the large interlayer separation distance. As an example, Fig. 2.18b shows the deformation of the three-layered system at the maximum indentation depth, and it demonstrates that the second graphene layer does not experience a significant deformation. Therefore, the second layer does not exert any resisting force during the indenter penetration of the first graphene layer. It can be seen that the four-layered system experienced a significant improvement in the performance, which is due to the contribution of the second graphene layer. Surprisingly, however, the performance of the five-layered graphene system is the weakest amongst all the considered systems, even though it was expected to offer greater resistance to indentation due to the higher number of the multilayered graphene sheets. This weakness is attributed to the inability of the 10 Å polyethylene layers to resist the applied load.

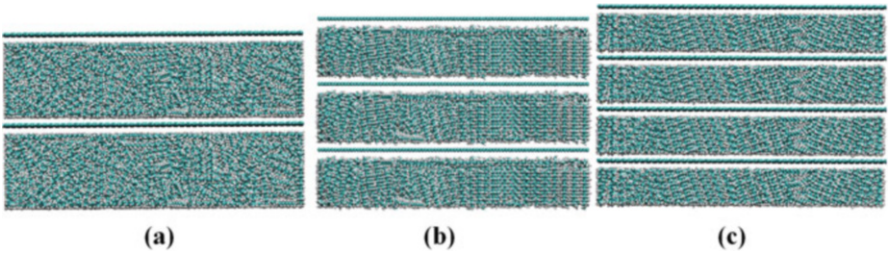


**Fig. 2.17** Multilayered graphene-reinforced polyethylene systems. (**a**) The two-, (**b**) the three-, and (**c**) the four-layered systems

Figure 2.18c shows the maximum indentation force of the studied multilayered systems. These results indicate that there is a slight improvement in the maximum resisting force up to three-layered system, where the interlayer spacing is 16.7 Å. When the spacing is reduced from 16.7 to 12.5 Å, there is a 16.5% improvement of the maximum force. However, this improvement completely vanishes when the spacing was further reduced to 10 Å. This result indicates that proper choice of the interlayer separation distance is critically important in achieving the best performance of multilayered graphene-reinforced composites.

## 2.4 Concluding Remarks

Nanoscale multilayered systems have attracted significant attention in recent research. Graphene has been already proven in its ability to become an exceptional reinforcement for nanocomposites, and graphene-based multilayered systems are believed to be a candidate of the next generation of advanced multifunctional nanocomposites. Recently fabricated graphene-based multilayered nanostructures have demonstrated promising potential for applications in electrochemical energy storage, solar cells, and gas sensors. These multilayered materials could also be used for structural applications in automotive and aerospace industries. Latest developments in multilayered nanofilm assembly will further accelerate the commercial scale fabrication of multilayered graphene-based composites.

In order to design advanced nanoscale multilayered systems with optimized properties, a thorough understanding of the mechanical behaviour of these systems is essential. Even though there is considerable research interest in nanoscale multilayered systems, understanding of their mechanical behaviour is still in its infancy.

Nanoindentation tests using atomic force microscopy have been widely used to characterize the mechanical properties at the nanoscale. The force-displacement data obtained from a nanoindentation test are generally analysed using continuum

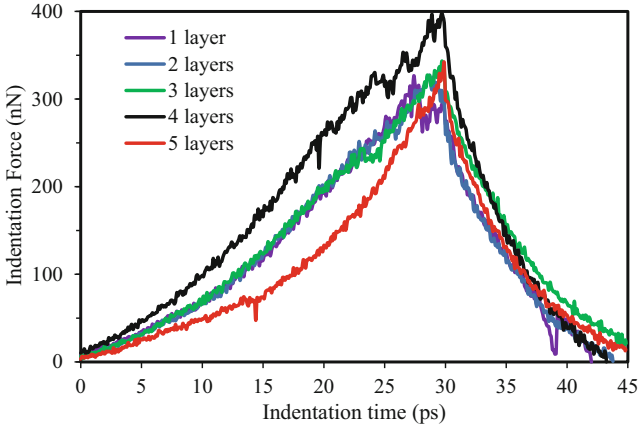


(a)

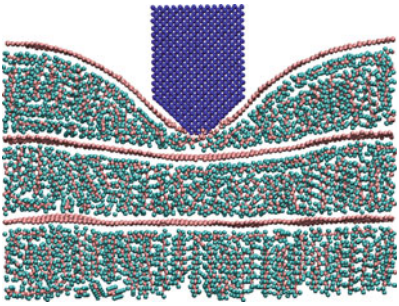

(b)

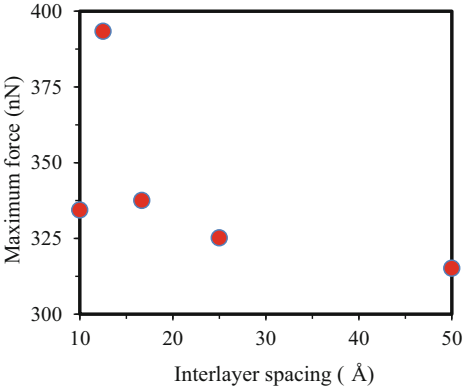


(c)

**Fig. 2.18** Force-indentation depth of multilayered graphene systems: (**a**) variation of indentation force with time of the multilayered graphene-reinforced systems, (**b**) deformed three-layered system at maximum indentation depth (30 Å), and (**c**) maximum indentation force of the multilayered systems when indented up to 30 Å

contact mechanics models. However, the applicability of continuum models at the atomic level is questionable due to the discrete nature of structures at this scale. Our comprehensive molecular dynamics simulations of the nanoindentation of multilayered graphene-reinforced composites provide significant insight into the force-indentation behaviour of these advanced systems. The results of the molecular dynamics simulations reveal that a strong interlayer interaction has a substantial influence on the material response at the nanoscale.

Furthermore, the observed strong atomic adhesion between the multilayered system and the indenter during indentation could not be studied using existing continuum-based models. Similarly, the atomic adhesion results in a unique deformation pattern that develops during the retraction stage of the indenter. In addition, graphene demonstrated an extraordinary reinforcing influence on the force-indentation predictions. For example, indentation resistance of a single-layer graphene-coated polyethylene is about 13-fold of the indentation resistance of a pure polyethylene target. Significant improvement in the indentation resistance of the multilayered graphene-reinforced system was also observed with the increase of the number of graphene layers. However, proper choice of their spatial locations within the composite is crucial in attaining the greatest resistance to indentation by multilayered graphene-reinforced nanocomposites.

**Acknowledgements** The authors wish to thank NSERC and the Discovery Accelerator Supplement for their kind support of this research.

## References

Aldousiri, B., Dhakal, H.N., Onuh, S., Zhang, Z.Y., Bennett, N.: Nanoindentation behaviour of layered silicate filled spent polyamide-12 nanocomposites. Polym. Test. **30**, 688–692 (2011). doi:10.1016/j.polymertesting.2011.05.008

Alian, A.R., Meguid, S.A.: Molecular dynamics simulations of the effect of waviness and agglomeration of CNTs on interface strength of thermoset nanocomposites. Phys. Chem. Chem. Phys. (2017). doi:10.1039/C6CP07464B

Alian, A.R., Meguid, S.A.: Multiscale modeling of nanoreinforced composites. In: Meguid, S.A. (ed.) Advances in Nanocomposites, pp. 1–39. Springer, Cham (2016)

Alian, A.R., Kundalwal, S.I., Meguid, S.A.: Interfacial and mechanical properties of epoxy nanocomposites using different multiscale modeling schemes. Compos. Struct. **131**, 545–555 (2015a). doi:10.1016/j.compstruct.2015.06.014

Alian, A.R., Kundalwal, S.I., Meguid, S.A.: Multiscale modeling of carbon nanotube epoxy composites. Polymer. **70**, 149–160 (2015b). doi:10.1016/j.polymer.2015.06.004

Alian, A.R., El-Borgi, S., Meguid, S.A.: Multiscale modeling of the effect of waviness and agglomeration of CNTs on the elastic properties of nanocomposites. Comput. Mater. Sci. **117**, 195–204 (2016). doi:10.1016/j.commatsci.2016.01.029

Begley, M.R., Mackin, T.J.: Spherical indentation of freestanding circular thin films in the membrane regime. J. Mech. Phys. Solids. **52**, 2005–2023 (2004). doi:10.1016/j.jmps.2004.03.002

Brenner, D.W.: Empirical potential for hydrocarbons for use in simulating the chemical vapor deposition of diamond films. Phys. Rev. B. **42**, 9458–9471 (1990). doi:10.1103/PhysRevB.42.9458

Brenner, D.W.: The art and science of an analytic potential. Phys. Status Solidi B. **217**, 23–40 (2000). doi:10.1002/(SICI)1521-3951(200001)217:1<23::AID-PSSB23>3.0.CO;2-N

Bruzaud, S., Bourmaud, A.: Thermal degradation and (nano)mechanical behavior of layered silicate reinforced poly(3-hydroxybutyrate-co-3-hydroxyvalerate) nanocomposites. Polym. Test. **26**, 652–659 (2007). doi:10.1016/j.polymertesting.2007.04.001

Bunch, J.S., van der Zande, A.M., Verbridge, S.S., Frank, I.W., Tanenbaum, D.M., Parpia, J.M., Craighead, H.G., McEuen, P.L.: Electromechanical resonators from graphene sheets. Science. **315**, 490–493 (2007). doi:10.1126/science.1136836

Cao, A., Qu, J.: Atomistic simulation study of brittle failure in nanocrystalline graphene under uniaxial tension. Appl. Phys. Lett. **102**, 71902 (2013). doi:10.1063/1.4793088

Chen, C., Rosenblatt, S., Bolotin, K.I., Kalb, W., Kim, P., Kymissis, I., Stormer, H.L., Heinz, T.F., Hone, J.: Performance of monolayer graphene nanomechanical resonators with electrical readout. Nat. Nanotechnol. **4**, 861–867 (2009). doi:10.1038/nnano.2009.267

Chen, C., Lee, S., Deshpande, V.V., Lee, G.-H., Lekas, M., Shepard, K., Hone, J.: Graphene mechanical oscillators with tunable frequency. Nat. Nanotechnol. **8**, 923–927 (2013). doi:10.1038/nnano.2013.232

Chuvilin, A., Meyer, J.C., Algara-Siller, G., Kaiser, U.: From graphene constrictions to single carbon chains. New J. Phys. **11**, 83019 (2009). doi:10.1088/1367-2630/11/8/083019

Cross, G.L.W., Schirmeisen, A., Grütter, P., Dürig, U.T.: Plasticity, healing and shakedown in sharp-asperity nanoindentation. Nat. Mater. **5**, 370–376 (2006). doi:10.1038/nmat1632

Das, B., Eswar Prasad, K., Ramamurty, U., Rao, C.N.R.: Nano-indentation studies on polymer matrix composites reinforced by few-layer graphene. Nanotechnology. **20**, 125705 (2009). doi:10.1088/0957-4484/20/12/125705

Dewapriya, M.A.N.: Molecular Dynamics Study of Effects of Geometric Defects on the Mechanical Properties of Graphene. Department of Mechanical Engineering, University of British Columbia, British Columbia (2012)

Dewapriya, M.A.N., Rajapakse, R.K.N.D.: Molecular dynamics simulations and continuum modeling of temperature and strain rate dependent fracture strength of graphene with vacancy defects. J. Appl. Mech. **81**, 081010 (2014). doi:10.1115/1.4027681

Dewapriya, M.A.N., Rajapakse, R.K.N.D.: Development of a homogenous nonlinear spring model characterizing the interfacial adhesion properties of graphene with surface defects. Compos. Part B: Eng. **98**, 339–349 (2016). doi:10.1016/j.compositesb.2016.04.052

Dewapriya, M.A.N., Srikantha Phani, A., Rajapakse, R.K.N.D.: Influence of temperature and free edges on the mechanical properties of graphene. Model. Simul. Mater. Sci. Eng. **21**, 65017 (2013). doi:10.1088/0965-0393/21/6/065017

Dewapriya, M.A.N., Rajapakse, R.K.N.D., Phani, A.S.: Atomistic and continuum modelling of temperature-dependent fracture of graphene. Int. J. Fract. **187**, 199–212 (2014). doi:10.1007/s10704-014-9931-y

Dewapriya, M.A.N., Rajapakse, R.K.N.D., Nigam, N.: Influence of hydrogen functionalization on the fracture strength of graphene and the interfacial properties of graphene-polymer nanocomposite. Carbon. **1**, 6991–7000 (2015). doi:10.1103/PhysRevB.37.6991

Díez-Pascual, A.M., Gómez-Fatou, M.A., Ania, F., Flores, A.: Nanoindentation in polymer nanocomposites. Prog. Mater. Sci. **67**, 1–94 (2015). doi:10.1016/j.pmatsci.2014.06.002

Dilrukshi, K.G.S., Dewapriya, M.A.N., Puswewala, U.G.A.: Size dependency and potential field influence on deriving mechanical properties of carbon nanotubes using molecular dynamics. Theor. Appl. Mech. Lett. **5**, 167–172 (2015). doi:10.1016/j.taml.2015.05.005

Doerner, M.F., Nix, W.D.: A method for interpreting the data from depth-sensing indentation instruments. J. Mater. Res. **1**, 601–609 (1986). doi:10.1557/JMR.1986.0601

Egberts, P., Filleter, T., Bennewitz, R.: A kelvin probe force microscopy of charged indentation-induced dislocation structures in KBr. Nanotechnology. **20**, 264005 (2009). doi:10.1088/0957-4484/20/26/264005

Fischer-Cripps, A.C.: Nanoindentation, Mechanical Engineering Series, 3rd edn. Springer, New York, NY (2011)

Flores, A., Ania, F., Salavagione, H.J., Ellis, G., Saurel, D., Gómez-Fatou, M.A.: Local mechanical properties of graphene/polyethylene-based nanocomposites by depth-sensing indentation. Eur. Polym. J. **74**, 120–129 (2016). doi:10.1016/j.eurpolymj.2015.11.016

Gibson, R.F.: A review of recent research on nanoindentation of polymer composites and their constituents. Compos. Sci. Technol. **105**, 51–65 (2014). doi:10.1016/j.compscitech.2014.09.016

Haque, A., Ramasetty, A.: Theoretical study of stress transfer in carbon nanotube reinforced polymer matrix composites. Compos. Struct. **71**, 68–77 (2005). doi:10.1016/j.compstruct.2004.09.029

Hay, J.C., Bolshakov, A., Pharr, G.M.: A critical examination of the fundamental relations used in the analysis of nanoindentation data. J. Mater. Res. **14**, 2296–2305 (1999). doi:10.1557/JMR.1999.0306

Hobi, E., Pontes, R.B., Fazzio, A., da Silva, A.J.R.: Formation of atomic carbon chains from graphene nanoribbons. Phys. Rev. B. **81**, 201406 (2010). doi:10.1103/PhysRevB.81.201406

Huang, B., Liu, M., Su, N., Wu, J., Duan, W., Gu, B., Liu, F.: Quantum manifestations of graphene edge stress and edge instability: A first-principles study. Phys. Rev. Lett. **102**, 166404 (2009). doi:10.1103/PhysRevLett.102.166404

Jang, B.Z., Zhamu, A.: Processing of nanographene platelets (NGPs) and NGP nanocomposites: a review. J. Mater. Sci. **43**, 5092–5101 (2008). doi:10.1007/s10853-008-2755-2

Jhon, Y.I., Jhon, Y.M., Yeom, G.Y., Jhon, M.S.: Orientation dependence of the fracture behavior of graphene. Carbon. **66**, 619–628 (2014). doi:10.1016/j.carbon.2013.09.051

Ji, Q., Honma, I., Paek, S.-M., Akada, M., Hill, J.P., Vinu, A., Ariga, K.: Layer-by-layer films of graphene and ionic liquids for highly selective gas sensing. Angew. Chem. **122**, 9931–9933 (2010). doi:10.1002/ange.201004929

Jin, C., Lan, H., Peng, L., Suenaga, K., Iijima, S.: Deriving carbon atomic chains from graphene. Phys. Rev. Lett. **102**, 205501 (2009). doi:10.1103/PhysRevLett.102.205501

Jones, J.E.: On the determination of molecular fields. II. From the equation of state of a gas. Proc. R. Soc. Math. Phys. Eng. Sci. **106**, 463–477 (1924). doi:10.1098/rspa.1924.0082

Khare, R., Mielke, S.L., Paci, J.T., Zhang, S., Ballarini, R., Schatz, G.C., Belytschko, T.: Coupled quantum mechanical/molecular mechanical modeling of the fracture of defective carbon nanotubes and graphene sheets. Phys. Rev. B. **75**, 75412 (2007a). doi:10.1103/PhysRevB.75.075412

Alian, A.R., Dewapriya, M.A.N., Meguid, S.A.: Molecular dynamics study of the reinforcement effect of graphene in multilayered polymer nanocomposites. Materials and Design, 2017 (Accepted).

Komaragiri, U., Begley, M.R., Simmonds, J.G.: The mechanical response of freestanding circular elastic films under point and pressure loads. J. Appl. Mech. **72**, 203 (2005). doi:10.1115/1.1827246

Kong, B.-S., Geng, J., Jung, H.-T.: Layer-by-layer assembly of graphene and gold nanoparticles by vacuum filtration and spontaneous reduction of gold ions. Chem. Commun. **2009**, 2174 (2009). doi:10.1039/b821920f

Kwon, S., Ko, J.-H., Jeon, K.-J., Kim, Y.-H., Park, J.Y.: Enhanced nanoscale friction on fluorinated graphene. Nano Lett. **12**, 6043–6048 (2012). doi:10.1021/nl204019k

Lee, C., Wei, X., Kysar, J.W., Hone, J.: Measurement of the elastic properties and intrinsic strength of monolayer graphene. Science. **321**, 385–388 (2008). doi:10.1126/science.1157996

LeSar, R.: Introduction to Computational Materials Science: Fundamentals to Applications. Cambridge University Press, Cambridge; NY (2013)

Li, X., Bhushan, B.: A review of nanoindentation continuous stiffness measurement technique and its applications. Mater. Charact. **48**, 11–36 (2002). doi:10.1016/S1044-5803(02)00192-4

Li, D., Müller, M.B., Gilje, S., Kaner, R.B., Wallace, G.G.: Processable aqueous dispersions of graphene nanosheets. Nat. Nanotechnol. **3**, 101–105 (2008). doi:10.1038/nnano.2007.451

Li, C., Browning, A.R., Christensen, S., Strachan, A.: Atomistic simulations on multilayer graphene reinforced epoxy composites. Compos. Part Appl. Sci. Manuf. **43**, 1293–1300 (2012). doi:10.1016/j.compositesa.2012.02.015

Lin, S., Chen, C.-T., Bdikin, I., Ball, V., Grácio, J., Buehler, M.J.: Tuning heterogeneous poly(dopamine) structures and mechanics: in silico covalent cross-linking and thin film nanoindentation. Soft Matter. **10**, 457–464 (2014). doi:10.1039/C3SM51810H

Liu, Y., Xu, Z., Zheng, Q.: The interlayer shear effect on graphene multilayer resonators. J. Mech. Phys. Solids. **59**, 1613–1622 (2011). doi:10.1016/j.jmps.2011.04.014

Lu, J.P.: Elastic properties of carbon nanotubes and nanoropes. Phys. Rev. Lett. **79**, 1297–1300 (1997). doi:10.1103/PhysRevLett.79.1297

Luan, B., Robbins, M.O.: The breakdown of continuum models for mechanical contacts. Nature. **435**, 929–932 (2005). doi:10.1038/nature03700

Mathew, N., Sewell, T.D.: Nanoindentation of the triclinic molecular crystal 1,3,5-triamino-2,4,6-trinitrobenzene: a molecular dynamics study. J. Phys. Chem. C. **120**, 8266–8277 (2016). doi:10.1021/acs.jpcc.6b01103

Mattoni, A., Colombo, L., Cleri, F.: Atomic scale origin of crack resistance in brittle fracture. Phys. Rev. Lett. **95**, 115501 (2005). doi:10.1103/PhysRevLett.95.115501

McAllister, Q.P., Gillespie, J.W., VanLandingham, M.R.: Nonlinear indentation of fibers. J. Mater. Res. **27**, 197–213 (2012). doi:10.1557/jmr.2011.336

Minor, A.M., Syed Asif, S.A., Shan, Z., Stach, E.A., Cyrankowski, E., Wyrobek, T.J., Warren, O.L.: A new view of the onset of plasticity during the nanoindentation of aluminium. Nat. Mater. **5**, 697–702 (2006). doi:10.1038/nmat1714

Neek-Amal, M., Peeters, F.M.: Nanoindentation of a circular sheet of bilayer graphene. Phys. Rev. B. **81**, 235421 (2010). doi:10.1103/PhysRevB.81.235421

Odegard, G.M., Gates, T.S., Nicholson, L.M., Wise, K.E.: Equivalent-continuum modeling of nano-structured materials. Compos. Sci. Technol. **62**, 1869–1880 (2002). doi:10.1016/S0266-3538(02)00113-6

Ohta, T.: Controlling the electronic structure of bilayer graphene. Science. **313**, 951–954 (2006). doi:10.1126/science.1130681

Oliver, W.C., Pharr, G.M.: An improved technique for determining hardness and elastic modulus using load and displacement sensing indentation experiments. J. Mater. Res. **7**, 1564–1583 (1992). doi:10.1557/JMR.1992.1564

Oliver, W.C., Pharr, G.M.: Measurement of hardness and elastic modulus by instrumented indentation: advances in understanding and refinements to methodology. J. Mater. Res. **19**, 3–20 (2004). doi:10.1557/jmr.2004.19.1.3

Oyen, M.L., Cook, R.F.: Load–displacement behavior during sharp indentation of viscous–elastic–plastic materials. J. Mater. Res. **18**, 139–150 (2003). doi:10.1557/JMR.2003.0020

Paul, W., Oliver, D., Grütter, P.: Indentation-formed nanocontacts: an atomic-scale perspective. Phys. Chem. Chem. Phys. **16**, 8201 (2014). doi:10.1039/c3cp54869d

Pavlidou, S., Papaspyrides, C.D.: A review on polymer–layered silicate nanocomposites. Prog. Polym. Sci. **33**, 1119–1198 (2008). doi:10.1016/j.progpolymsci.2008.07.008

Pérez, R., Payne, M.C., Simpson, A.D.: First principles simulations of silicon nanoindentation. Phys. Rev. Lett. **75**, 4748–4751 (1995). doi:10.1103/PhysRevLett.75.4748

Pethicai, J.B., Hutchings, R., Oliver, W.C.: Hardness measurement at penetration depths as small as 20 nm. Philos. Mag. A. **48**, 593–606 (1983). doi:10.1080/01418618308234914

Pharr, G.M., Oliver, W.C., Brotzen, F.R.: On the generality of the relationship among contact stiffness, contact area, and elastic modulus during indentation. J. Mater. Res. **7**, 613–617 (1992). doi:10.1557/JMR.1992.0613

Plimpton, S.: Fast parallel algorithms for short-range molecular dynamics. J. Comput. Phys. **117**, 1–19 (1995). doi:10.1006/jcph.1995.1039

Raccichini, R., Varzi, A., Passerini, S., Scrosati, B.: The role of graphene for electrochemical energy storage. Nat. Mater. **14**, 271–279 (2014). doi:10.1038/nmat4170

Rapaport, D.C.: The Art of Molecular Dynamics Simulation. Cambridge University Press, Cambridge, NY (1995)

Richardson, J.J., Bjornmalm, M., Caruso, F.: Technology-driven layer-by-layer assembly of nanofilms. Science. **348**, 2491–2491 (2015). doi:10.1126/science.aaa2491

Robertson, A.W., Montanari, B., He, K., Kim, J., Allen, C.S., Wu, Y.A., Olivier, J., Neethling, J., Harrison, N., Kirkland, A.I., Warner, J.H.: Dynamics of single Fe atoms in graphene vacancies. Nano Lett. **13**, 1468–1475 (2013). doi:10.1021/nl304495v

Rocha, J.R., Yang, K.Z., Hilbig, T., Brostow, W., Simoes, R.: Polymer indentation with mesoscopic molecular dynamics. J. Mater. Res. **28**, 3043–3052 (2013). doi:10.1557/jmr.2013.307

Sakharova, N.A., Fernandes, J.V., Antunes, J.M., Oliveira, M.C.: Comparison between Berkovich Vickers and conical indentation tests: a three-dimensional numerical simulation study. Int. J. Solids Struct. **46**, 1095–1104 (2009). doi:10.1016/j.ijsolstr.2008.10.032

Scott, O.N., Begley, M.R., Komaragiri, U., Mackin, T.J.: Indentation of freestanding circular elastomer films using spherical indenters. Acta Mater. **52**, 4877–4885 (2004). doi:10.1016/j.actamat.2004.06.043

Shen, J., Hu, Y., Li, C., Qin, C., Shi, M., Ye, M.: Layer-by-layer self-assembly of graphene nanoplatelets. Langmuir. **25**, 6122–6128 (2009). doi:10.1021/la900126g

Shenderova, O.A., Brenner, D.W., Omeltchenko, A., Su, X., Yang, L.H.: Atomistic modeling of the fracture of polycrystalline diamond. Phys. Rev. B. **61**, 3877–3888 (2000). doi:10.1103/PhysRevB.61.3877

Shokrieh, M.M., Hosseinkhani, M.R., Naimi-Jamal, M.R., Tourani, H.: Nanoindentation and nanoscratch investigations on graphene-based nanocomposites. Polym. Test. **32**, 45–51 (2013). doi:10.1016/j.polymertesting.2012.09.001

Sinha Ray, S., Okamoto, M.: Polymer/layered silicate nanocomposites: a review from preparation to processing. Prog. Polym. Sci. **28**, 1539–1641 (2003). doi:10.1016/j.progpolymsci.2003.08.002

Sneddon, I.N.: The relation between load and penetration in the axisymmetric boussinesq problem for a punch of arbitrary profile. Int. J. Eng. Sci. **3**, 47–57 (1965). doi:10.1016/0020-7225(65)90019-4

Song, J., Srolovitz, D.J.: Adhesion effects in material transfer in mechanical contacts. Acta Mater. **54**, 5305–5312 (2006). doi:10.1016/j.actamat.2006.07.011

Stuart, S.J., Tutein, A.B., Harrison, J.A.: A reactive potential for hydrocarbons with intermolecular interactions. J. Chem. Phys. **112**, 6472 (2000). doi:10.1063/1.481208

Tan, X., Wu, J., Zhang, K., Peng, X., Sun, L., Zhong, J.: Nanoindentation models and Young's modulus of monolayer graphene: a molecular dynamics study. Appl. Phys. Lett. **102**, 71908 (2013). doi:10.1063/1.4793191

Tang, B., Ngan, A.H.W.: Accurate measurement of tip–sample contact size during nanoindentation of viscoelastic materials. J. Mater. Res. **18**, 1141–1148 (2003). doi:10.1557/JMR.2003.0156

Tapasztó, L., Dumitrică, T., Kim, S.J., Nemes-Incze, P., Hwang, C., Biró, L.P.: Breakdown of continuum mechanics for nanometre-wavelength rippling of graphene. Nat. Phys. **8**, 739–742 (2012). doi:10.1038/nphys2389

Tavazza, F., Senftle, T.P., Zou, C., Becker, C.A., van Duin, A.C.T.: Molecular dynamics investigation of the effects of tip–substrate interactions during nanoindentation. J. Phys. Chem. C. **119**, 13580–13589 (2015). doi:10.1021/acs.jpcc.5b01275

Tersoff, J.: Empirical interatomic potential for silicon with improved elastic properties. Phys. Rev. B. **38**, 9902–9905 (1988). doi:10.1103/PhysRevB.38.9902

van Gunsteren, W.F., Berendsen, H.J.C.: Computer simulation of molecular dynamics: methodology, applications, and perspectives in chemistry. Angew. Chem., Int. Ed. Eng. **29**, 992–1023 (1990). doi:10.1002/anie.199009921

Verlet, L.: Computer "experiments" on classical fluids. I. Thermodynamical properties of Lennard-Jones molecules. Phys. Rev. **159**, 98–103 (1967). doi:10.1103/PhysRev.159.98

Vlassak, J.J., Nix, W.D.: Measuring the elastic properties of anisotropic materials by means of indentation experiments. J. Mech. Phys. Solids. **42**, 1223–1245 (1994). doi:10.1016/0022-5096(94)90033-7

Wang, Y., Tong, S.W., Xu, X.F., Özyilmaz, B., Loh, K.P.: Interface engineering of layer-by-layer stacked graphene anodes for high-performance organic solar cells. Adv. Mater. **23**, 1514–1518 (2011). doi:10.1002/adma.201003673

Wang, Z., Gu, P., Zhang, H., Zhang, Z., Wu, X.: Indenter geometrical effects on sub-micro/nano indentation and scratch behaviors of polymeric surfaces. Mech. Adv. Mater. Struct. **23**, 291–300 (2016). doi:10.1080/15376494.2014.955154

Willis, J.R.: Hertzian contact of anisotropic bodies. J. Mech. Phys. Solids. **14**, 163–176 (1966). doi:10.1016/0022-5096(66)90036-6

Wu, X., Moon, R.J., Martini, A.: Crystalline cellulose elastic modulus predicted by atomistic models of uniform deformation and nanoscale indentation. Cellulose. **20**, 43–55 (2013). doi:10.1007/s10570-012-9823-0

Xia, W., Song, J., Hsu, D.D., Keten, S.: Understanding the interfacial mechanical response of nanoscale polymer thin films via nanoindentation. Macromolecules. **49**, 3810–3817 (2016). doi:10.1021/acs.macromol.6b00121

Xu, Z., Buehler, M.J.: Interface structure and mechanics between graphene and metal substrates: a first-principles study. J. Phys. Condens. Matter. **22**, 485301 (2010). doi:10.1088/0953-8984/22/48/485301

Xu, M., Tabarraei, A., Paci, J., Oswald, J., Belytschko, T.: A coupled quantum/continuum mechanics study of graphene fracture. Int. J. Fract. **173**, 163–173 (2012). doi:10.1007/s10704-011-9675-x

Yan, W., Pun, C.L., Simon, G.P.: Conditions of applying Oliver–Pharr method to the nanoindentation of particles in composites. Compos. Sci. Technol. **72**, 1147–1152 (2012). doi:10.1016/j.compscitech.2012.03.019

Zandiatashbar, A., Lee, G.-H., An, S.J., Lee, S., Mathew, N., Terrones, M., Hayashi, T., Picu, C.R., Hone, J., Koratkar, N.: Effect of defects on the intrinsic strength and stiffness of graphene. Nat. Commun. **5**, 3186 (2014). doi:10.1038/ncomms4186

Zhang, Y.Y., Gu, Y.T.: Mechanical properties of graphene: Effects of layer number, temperature and isotope. Comput. Mater. Sci. **71**, 197–200 (2013). doi:10.1016/j.commatsci.2013.01.032

Zhang, B., Mei, L., Xiao, H.: Nanofracture in graphene under complex mechanical stresses. Appl. Phys. Lett. **101**, 121915 (2012). doi:10.1063/1.4754115

Zhao, H., Aluru, N.R.: Temperature and strain-rate dependent fracture strength of graphene. J. Appl. Phys. **108**, 64321 (2010). doi:10.1063/1.3488620

# Chapter 3
# Molecular Dynamics Studies of Load Transfer in Nanocomposites Reinforced by Defective Carbon Nanotube

**Xudong Peng and Shaker A. Meguid**

**Abstract** This chapter is concerned with the development of relatively more accurate numerical simulations than those adopted in the literature to investigate the considerable discrepancies between experimental findings and theoretical predictions of the interfacial shear strength (ISS) of nano-reinforced thermoset composites. Those differences are most likely attributed to the presence of various defects, the possible inaccuracies in the system modeling, and the variance between experiments. In this chapter, we present a review of the literature as well as recent work conducted by the authors focusing on the effect of defects and functionalization on the ISS and buckling behavior of carbon nanotube (CNT)-reinforced composites. Different modeling and calculation techniques pertinent to CNT pull-out tests are presented, and proper selection of the simulation parameters are discussed. Unlike earlier studies, which focused on thermoplastics, in this chapter attention is devoted to CNT-reinforced thermoset polymer composites with different degrees of conversion. Pull-out and compressive load simulations were performed on a representative volume element comprising a single-walled CNT embedded in an epoxy matrix. All MD simulations used the consistent valence forcefield (CVFF) to represent the interatomic potential. Our results revealed that different defects can, to some extent, either enhance or degrade the properties of nanocomposites. The findings of this chapter will assist in improving our understanding of the toughening/weakening mechanisms associated with nanoscopic reinforcement and the load transfer capability in epoxy-based nanocomposites and give an insight into the reasons for the discrepancies in ISS.

X. Peng • S.A. Meguid (✉)
Mechanics and Aerospace Design Laboratory, Mechanical and Industrial Engineering, University of Toronto, Toronto, ON, M5S 3G8, Canada
e-mail: xpeng@mie.utoronto.ca; meguid@mie.utoronto.ca



S.A. Meguid, G.J. Weng (eds.), *Micromechanics and Nanomechanics of Composite Solids*, DOI 10.1007/978-3-319-52794-9_3

## 3.1 Introduction

Since their discovery by Iijima (1991), carbon nanotubes (CNT) have attracted great interest from the mechanics and materials communities because of their promise and potential as reinforcements in polymer-based nanocomposites. These advanced polymer nanocomposites are used in various fields such as light-weight automobile and aerospace engineering, biomedical applications, energy storage devices, and molecular electronics, to name a few. The mechanical properties of CNT-reinforced composites are significantly influenced by the interface condition (cohesion and adhesion) between the CNT and the surrounding matrix. Higher interfacial shear strength (ISS) is an indicator of better stress transfer from the polymer matrix to the embedded nanotube, and hence enhanced reinforcement's effect (Desai and Haque 2005).

### *3.1.1 Interfacial Shear Strength*

Numerous experimental efforts have been devoted to the experimental studies of the ISS of CNT-reinforced composites. Three techniques including CNT pull-out tests (depicted in Fig. 3.1), Raman spectroscopy, and fragmentation tests have been mainly used to determine the ISS experimentally. For example, Lourie and Wagner (1998, 1999) presented transmission electron microscopy (TEM)-based evidence of significant nanotube-polymer interfacial adhesion. They directly observed damage doublets and fracture of nanotubes under tensile stresses, implying strong nanotube-polymer interface. Qian and Dickey (2001) performed in-situ TEM straining studies on MWCNT-polystyrene composite films. Their experiments demonstrated significant load transfer across the nanotube-polystyrene interface by showing crack bridging, sword-in-sheath, and transverse shear fracture mechanisms. However, in a TEM study of an aligned CNT-epoxy composite, Ajayan et al. (1994) indicated the interfacial bonding between an MWCNT and epoxy matrix was weak. Schadler et al. (1998), using Raman spectroscopy, also concluded that the interfacial bonding was very weak when an MWCNT–epoxy composite was

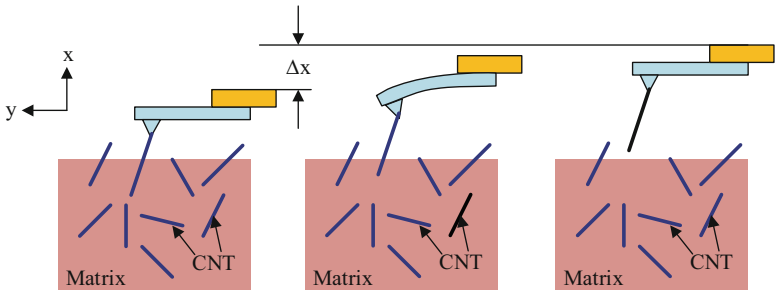


**Fig. 3.1** Schematics of the procedures of CNT pull-out testing

under tension. Advances in high precision instruments at the atomic level have led to quantitative measurements of interface strength. For example, Cooper et al. (2002) calculated the ISS for single-walled CNTs (SWCNTs) and multi-walled CNTs (MWCNTs) embedded in an epoxy matrix based on pull-out experiments using a scanning probe microscope. In both cases, the ISS was found to be in the range of 35–376 MPa. Barber et al. (2003, 2004) employed an atomic force microscope (AFM) to carry out direct CNT pull-out tests. Depending on the nanotube radius, they observed an ISS of 10–130 MPa for MWCNTs embedded in the polyethylene (PE)-butene matrix. Barber et al. (2006) further investigated the effect of functionalization using both pristine and chemically modified MWCNTs in their AFM experiments. They found that for different embedded length, the measured ISS ranges from 10 to 50 MPa for pristine SWCNTs and from 20 to 165 MPa for MWCNTs. Roy et al. (2010) measured the ISS of SWCNT-polyvinyl alcohol composite functionalized with biomolecules using a novel Raman peak shift method. The ISS was found to be larger than 160 MPa. Meguid and Sun (2004) also reported that the homogeneous dispersion of CNTs in an epoxy adhesive can improve the bonding and shear properties of composite interfaces by 1.2 and 1.3 times the pure epoxy adhesive. Xu et al. (2002) added 0.1 wt% MWCNTs into thin epoxy films and observed a 20% increase in the elastic modulus using a shaft-loaded blister test. The ISS was estimated to be between 88 and 280 MPa, based on transmission electron microscopy (TEM) images. Recently, Ganesan et al. (2011, 2014) conducted in-situ pull-out experiments on pristine and fluorinated MWCNTs embedded in an epoxy matrix within an SEM using a nanoindenter assisted micro-device. The average value of ISS for the fluorinated MWCNT–epoxy interface ($19.8 \pm 7.78$ MPa) was found to be larger than that for the pristine MWCNT–epoxy interface ($6.24 \pm 3.6$ MPa). This demonstrated the effect of interfacial adhesion to CNT surface treatments such as sidewall fluorination. Tsuda et al. (2011) used a nano-pull-out testing system installed in an SEM to pull out MWCNTs embedded in a Poly-ether-ether-ketone (PEEK) composite. The ISS of MWCNT-PEEK composite was measured as 3.5–7 MPa, and the ISS of the specimen treated at 573 K under 1 MPa for 1 h increased to 6–14 MPa because of the recovery in interfacial bonding. Newcomb et al. (2014) characterized CNT-polyacrylonitrile (PAN) get-spun composite fibers through Raman spectroscopy by monitoring the Raman band shift during tensile deformation. The as-spun and fully drawn CNT-PAN nanocomposite fibers exhibit the ISS of 13.1 and 30.9 MPa, respectively, while improved CNT dispersion resulted in an ISS of 44.3 MPa. Chen et al. (2013) presented an in-situ nanomechanical single-tube pull-out testing scheme of the ISS between double-walled CNTs (DWCNTs) and polymethyl methacrylate (PMMA). The average ISS was reported to be within 32–68 MPa and the maximum ISS was within 85–372 MPa depending on different nanotube diameters. Chen et al. (2015) further employed the same technique to study both PMMA and epoxy materials. They found that the average ISS of the PMMA and epoxy is $45 \pm 9$ MPa and $130 \pm 34$ MPa, respectively. They further reported that the respective maximum ISS can reach 178 and 282 MPa for PMMA and epoxy considered.

Several analytical works have also been conducted to shed light on the complexities and the marked discrepancies in the reported ISS of CNT-polymer composites. A number of models such as Kelly–Tyson model, shear-lag model, and energy minimization approach previously used for the analysis of carbon fiber composites have been modified for determining the ISS of CNT-reinforced composites. For instance, Wagner et al. (1998) combined fragmentation tests with the Kelly–Tyson model modified for hollow tubes to estimate the efficiency and quality of CNT-urethane composite interfaces. The ISS obtained was to be on the order of 500 MPa and higher. Wagner (2002) further demonstrated that the ISS is dependent on the CNT strength which may be strongly reduced by the presence of defects on CNTs. Xu et al. (2002) further applied the same modified Kelly–Tyson model to theoretically calculate the ISS and found it to be in the range of 88–280 MPa for different diameters MWCNTs. Lau (2003) studied the ISS of SWCNT/MWCNT-reinforced polymer matrix through the uses of local density approximation (Lenosky et al. 1992), elastic shells (Tu and Ou-Yang 2002), and conventional fiber pull-out models (Zhou et al. 1995). The ISS increased to 200 MPa with the increase in nanotubes' wall thickness. Xiao and Zhang (2004) used a modified Cox model (Cox 1952) to investigate the effects of length and diameter of an SWCNT in an epoxy matrix on the load transfer properties. They found that the maximum ISS increases with the decrease in the CNT diameter and that there exists an optimal CNT length at which the ISS reaches its maximum. The maximum ISS was reported to be in the range of 30–100 MPa. Gao and Li (2005) modified the shear-lag model originally proposed by Cox (1952) and used a cylindrical matrix embedded with a capped SWCNT as the representative volume element (RVE) of a nano-reinforced polymer composite. The maximum ISS for different aspect ratios of the RVE was predicted to be about twice as large as the axial normal stress in the matrix. Zhang and Wang (2005) used an analytical method to investigate thermal effects on interfacial stress transfer characteristics of SWCNT/MWCNT polymer composites, based on a thermoelastic theory and conventional fiber pull-out models (Quek 2002). They found that the maximum ISS decreases from as high as 500 MPa with increasing temperature change. Furthermore, other models dedicated to CNT-reinforced composites such as multi-layer structure and structural mechanics approach have been developed to evaluate the ISS. For example, Natsuki et al. (2007) evaluated the ISS of SWCNTs/MWCNTs with composite coatings by means of a multi-layer CNT pull-out model. Their results suggested that the maximum ISS occurred at the pull-out end of CNTs and decreased from as high as 100 MPa with increasing coating thickness as well as CNT wall thickness. Li and Saigal (2007) employed a refined micromechanics model including three concentric cylinders as the RVE for assessing the ISS in CNT-reinforced polymer composites. They reported that the maximum ISS normalized by the axial normal stress in the matrix can range from 0.2 to 1.5 depending on the different volume fractions, aspect ratios, and end gaps. A multiscale model for interfacial stress transfer in SWCNT-reinforced polymer composites was developed by Li and Chou (2003a), which employed the molecular structural mechanics proposed by the same authors (Li and Chou 2003b) to characterize the nanotube and the finite element method to

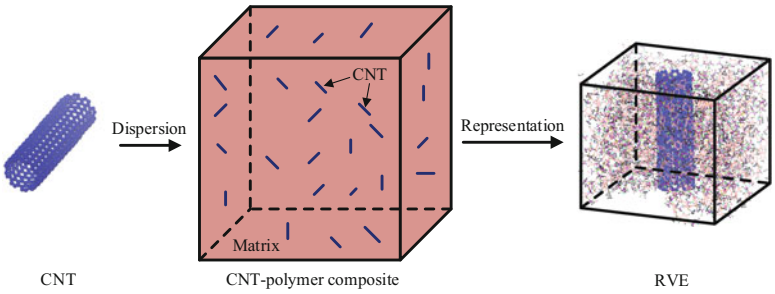


**Fig. 3.2** RVE of CNT-reinforced composites

model the polymer matrix. The maximum ISS normalized by the applied stress is between 0.5 and 3 depending on the different nanotube aspect ratio and interfacial interface.

In addition to existing experimental and analytical investigations, numerous numerical simulations have also been conducted to study the interfacial behavior of CNT-reinforced composites. Molecular mechanics (MM), molecular dynamics (MD) simulations, atomistic-based continuum (ABC), and multiscale modeling technique have been mainly used to determine the ISS of an RVE (refer to Fig. 3.2) comprised of CNT-polymer composites. For instance, Wong et al. (2003) used MD simulations and elasticity calculations to quantify the ISS. They found that the non-bonded interactions, consisting of electrostatic and van der Waals forces, result in respective ISS of 138 and 186 MPa for CNT-epoxy and CNT-polystyrene systems. Gou et al. (2004, 2005) investigated the ISS of individual SWCNTs and CNT ropes via both MM and MD simulations. The ISS was calculated to be 61 and 36 MPa for an SWCNT and a three CNT rope embedded in an epoxy matrix, respectively. Wei (2006) studied the temperature dependent adhesion behavior and the reinforcement effect of CNTs in a polypropylene matrix using MD simulations. He only considered van der Waals (vdW) interactions in the model and established a lower bound ISS of approximately 47 MPa. Liao and Li (2001) used MM to simulate a pull-out process in an SWCNT-polystyrene system and reported that the ISS could be as high as 160 MPa, even without considering the chemical bonding between the nanotube and matrix. Liu et al. (2007) used MD simulations to investigate the influence of noncovalent and covalent functionalization on the interfacial properties of SWCNT-epoxy system. They found that properly designed hybrid system containing both covalent and noncovalent functionalization can increase the ISS to 940 MPa from 170 MPa for a pristine SWCNT-epoxy system. In an MD study of SWCNT-PE composite, Al-Ostaz et al. (2008) used COMPASS forcefield to obtain an ISS of 133 MPa. Li et al. (2011) further conducted pull-out simulations on SWCNT-PE systems. Instead of assuming a uniform distribution of ISS on the entire sidewalls of CNTs, they assumed that the ISS was distributed uniformly within 1 nm from each end of the CNTs but was zero at the middle of the nanotubes. The calculated ISS from this approach ranges from 106.7 to 142 MPa for different CNT diameters.

Xiong and Meguid (2015) investigated the interfacial mechanical characteristics of CNT-reinforced epoxy composites using MD simulations. They found that the ISS varies from 20 to 80 MPa as they studied various parameters, such as epoxy density, length and diameter of the CNT, the CNT-epoxy interfacial thickness, Lennard-Jones (LJ) cutoff distance, and capping conditions of a CNT. Alian et al. (2015a) used a multiscale modeling scheme to study the effect of embedded CNT length, diameter, interfacial thickness, and LJ cutoff distance. Their reported ISS values are also found to be almost identical to those predicted by Wernik et al. (2012) using ABC multiscale modeling technique.

Evidently, numerous experimental, analytical, and numerical studies have been carried out to investigate the ISS of CNT-reinforced composites. However, significant discrepancies exist among these studies. This may be partly due to the complexity of the problem and partly due to the oversimplified numerical models adopted. The simplifications included: (1) the matrix materials are usually assumed to be "frozen" during the pull-out process to avoid excessive degrees of freedom, resulting in an inappropriate estimation of the interfacial thickness and the CNT–matrix interaction energy, (2) the neglect of experimentally observed defects in CNTs, such as vacancies (Meyer et al. 2008), Stone–Wales (SW) (Suenaga et al. 2007), and interstitial atoms (Hashimoto et al. 2004), as depicted in Fig. 3.3, which

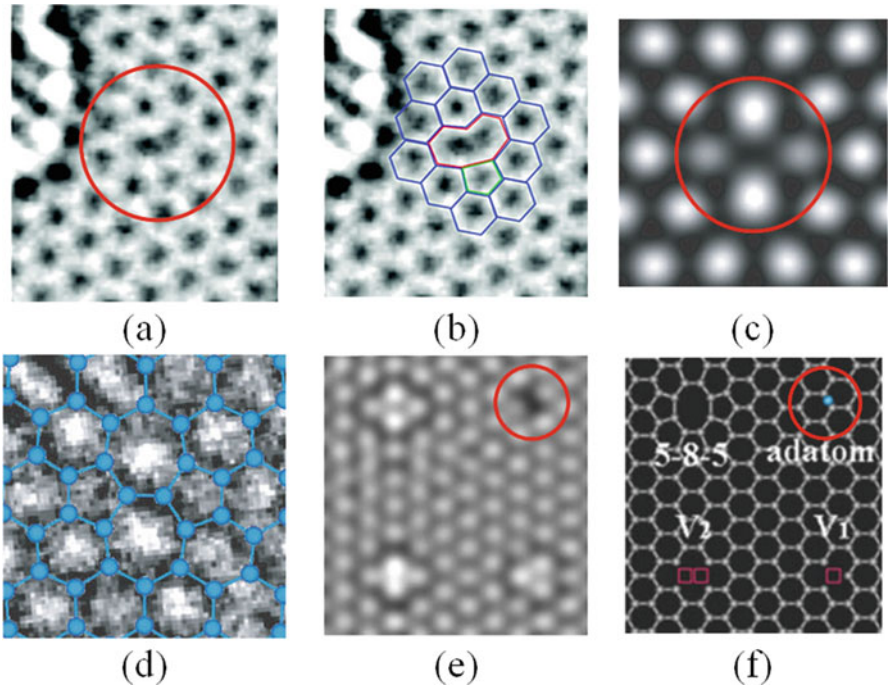


**Fig. 3.3** Intrinsic defects of CNTs: (**a**, **b**) HR-TEM image of single vacancy (Meyer et al. 2008), (**c**, **d**) HR-TEM image of SW defect (Suenaga et al. 2007), (**e**, **f**) HR-TEM image of a single adatom defect (Hashimoto et al. 2004)

are inevitably introduced during CNT synthesis as well as manufacturing (Collins 2010; Charlier 2002; Nardelli et al. 1998), and (3) the neglect of covalent bonding between CNTs and matrix materials. Covalent bonding is usually introduced through surface functionalizations of CNTs (Liu et al. 2005; Spitalsky et al. 2010; Thostenson et al. 2005), which are used to improve the load transferability of nanocomposites.

In addition to the above limitations, most existing numerical models focused their attention on thermoplastic polymers (Chowdhury et al. 2010; Frankland et al. 2002; Xiao et al. 2015; Zheng et al. 2009). Numerical models which can better characterize the interfacial properties of CNT-reinforced thermoset composites systems are scarce. Thermoset materials generally have very different mechanical properties than thermoplastic materials because they comprise three-dimensional networks of bonds (crosslinking). However, to the best of authors' knowledge, there have been no studies performed on the effect of crosslink density on the interfacial properties of CNT-reinforced thermoset composites. The importance of nano-reinforced epoxy composites to many engineering applications as well as the lack of coverage in the literature has motivated the current chapter.

### *3.1.2 Buckling Behavior*

As mentioned in Sect. 3.1.1, considerable experimental and theoretical studies have been carried out to characterize the ISS of CNT-reinforced nanocomposites. However, significant discrepancies exist between experimental and theoretical results. These theoretically obtained values are remarkably different from the experimental data. Apart from the reasons mentioned in Sect. 3.1.1, some researchers attributed the discrepancy of the results to buckled CNTs in nanocomposites.

In particular, the diameters of CNTs are in the range of less than a nanometer for SWCNTs to about 30 nm for MWCNTs while the typical length of CNTs is on the order of microns (Pan et al. 1999; Qian et al. 2000), leading to a large aspect ratio (length to diameter). Because of this large aspect ratio and hollow cylindrical structure, CNTs are prone to buckle under mechanical loads. Buckling can lead to failure in the form of a sudden decline in compressive load carrying capacity and undesirably distorted configuration of structures. Under axial compression, a CNT exhibits shell-like or beam-like buckling depending on its aspect ratio; shell-like buckling appears when the aspect ratio is relatively small, while beam-like buckling appears when the aspect ratio is relatively large. Numerous experimental and theoretical studies have investigated the buckling of CNT-reinforced nanocomposites. Experimental researchers have observed graphs of CNTs in buckled state both as individual nanotubes (Dai et al. 1996; Iijima et al. 1996; Wong et al. 1997) and when embedded in nanocomposites (Schadler et al. 1998; Lourie et al. 1998). A large volume of theoretical work, based on both

continuum-based shell and beam theories (Yakobson et al. 1996; Ru 2000; Wang et al. 2003), and atomistic techniques such as MD (Zhang et al. 2009a; Talukdar et al. 2011; Motevalli et al. 2013; Wang et al. 2014), concentrates on buckling of nanotubes by themselves. However, an increasing number of researchers are interested in the compressive behavior of nanotubes when embedded in composites. For instance, Lourie et al. (1998) coupled the classical Euler model with energy method to examine a CNT buckling behavior within a polymeric matrix. To account for the effect of transverse shear deformation during the CNT buckling, Zhang et al. (2006a) developed Timoshenko beam model, which offers a more precise prediction of the critical buckling stress. Ru (2001) developed an elastic double-walled shell model for the buckling analysis of CNTs in an elastic matrix based on the classical shell theory (Timoshenko 1961). Later, Liew et al. (2005) and Kitipornchai et al. (2005) introduced a Pasternak foundation into Ru's model (Ru 2001). They proposed multi-walled shell model to describe the buckling behavior of MWCNTs that are embedded in a matrix with consideration of the van der Waals (vdW) interactions.

Since CNTs are highly prone to structural defects and buckling, many investigations have focused on buckling of defective CNTs. For example, the MD simulations were employed by Chandra and Namilae (2006) to explore the compressive behavior of SWCNTs in the presence of chemical functionalization and SW defects. They found that functionalization and topological defects have a negative impact on the buckling stress of CNTs. The compressive behavior of SWCNTs and double-walled CNTs in the presence of vacancy defects was examined by Hao et al. (2008) and Xin et al. (2007) using MD simulations. They found that the extent to which vacancy defects weaken the compressive load carrying capacity of CNTs is dependent on the length, chirality, and temperature of the nanotubes as well as the density of the defects and their relative position. Zhang et al. (2009b) conducted an investigation into the buckling behavior of SWCNTs with defects via MD simulations. They revealed that point defects cause a higher reduction in the buckling load than SW defects. Kulathunga et al. (2010) examined the effects of various configurations of vacancy defects on the buckling of SWCNTs by MD simulations in different thermal environments. Their findings revealed that increasing number of missing atoms, asymmetry of vacancy configurations, and asymmetric distribution of vacancy clusters lead to higher deterioration in buckling properties. Ranjbartoreh and Wang (2011) studied the effects of length, radius, chirality, SW defect, and single vacancy defect on the buckling behavior of SWCNTs. Obtained results indicated that the axial stability of SWCNTs decreases significantly due to topological defects and the critical buckling strain was more susceptible to defects than the critical buckling force. Different aspect ratio of defective CNTs on the buckling behavior was investigated by Parvaneh et al. (2009), who showed that single vacancy defects only have a weak impact on the critical buckling load of CNTs with a large aspect ratio at room temperature. Poelma et al. (2012) combined analytical continuum theory with MD to study the effects of vacancy defect position on the CNT critical buckling

load. They concluded that the defects at the ends of the CNT and close to the middle of the CNT significantly reduce the critical buckling load and strain at 1 K. The compressive mechanical properties of SWCNTs with up to 20 randomly distributed vacancies were studied by Cheng et al. (2007) using MD method. It was found that the Young's modulus of the SWCNTs is approximately linearly proportional to the number of vacancies and SWCNTs containing more vacancies have more complicated deformation procedures.

It is evident from the foregoing literature review that there has been no work on the effect of various defects on the buckling of embedded CNTs. To the authors' knowledge, only a few studies have used MD simulations to focus on the buckling of embedded pristine CNTs. For instance, Namilae and Chandra (2006) studied the compressive behavior of CNTs when they are embedded in PE matrix and with interface chemical modifications using MD simulations. It is observed that the buckling load for buckling increases only very marginally for nanotubes embedded in PE matrix compared with neat CNTs. In the case of chemically bonded interfaces, the critical stress for buckling is reduced compared with neat CNTs because of the changes in curvature introduced by chemical bonding. The buckling of SWCNTs embedded in PE matrix was examined by Kulathunga and Ang (2014) via MD method. They found that the embedded CNT has higher buckling stress compared to the freestanding CNT. This stress increment is greater in CNTs with smaller aspect ratio. It is clear that there is an urgent need to carry out a comprehensive research on the buckling of defective CNTs embedded in polymer nanocomposites.

### *3.1.3 Objectives*

It is therefore the objectives of this chapter to:

(1) Provide a critical review of different modeling techniques, CNT pull-out methods, ISS distribution models and discuss recent developments in the field.
(2) Evaluate the ISS of CNT-reinforced thermoset composites and examine the effect of the following parameters on the strength of the interface:
    (a) Defects in embedded CNTs
    (b) Presence of foreign atoms
    (c) Interfacial non-bonded (van der Waals) and bonded (covalent bonding) interactions
    (d) Buckling of embedded CNTs
(3) Investigate which of these parameters either singly or jointly have major effect on the ISS of CNT-reinforced composites.

## 3.2 Fundamental Aspects of MD Simulation Techniques

### *3.2.1 Numerical Simulation Techniques*

CNT pull-out test has been recognized as a standard method for evaluating the ISS of nanocomposites. The force or energy required to debond the CNTs from the surrounding matrix is the output of these tests which are then used to calculate the ISS. The analysis of the ISS of nanocomposites is experimentally conducted using improvised scanning probe microscope (Cooper et al. 2002) and AFM (Barber et al. 2003, 2006), which require high precision instruments to measure the pull-out force because the pull-out forces are usually on the order of nanonewton. These experiments also require high-resolution microscopes such as scanning electron microscope (Barber et al. 2003, 2006) and TEM (Cooper et al. 2002) for imaging the CNTs. The challenge in experiments is manifested from the fact that relatively few experimental works have been published in the literature due to the difficulties of setting up nanoscale experiments and the inability to produce reliable high precision measuring instruments at the atomic scale. Therefore, researchers rely on atomistic-based or continuum-based methods for the ISS analysis of nanocomposites. However, continuum-based approaches such as shear-lag model (Gao and Li 2005) and Kelly–Tyson approach (Xu et al. 2002; Wagner et al. 1998) are less accurate since they do not account for the nanoscopic effects explicitly. It is also difficult to apply continuum methods to CNTs with defects and functional groups. Hence, many researchers resort to atomistic methods such as ABC, MM, and MD simulations to investigate the influence of defects and functionalization on the ISS of nanocomposites.

ABC technique is developed to model CNTs and CNT-reinforced composites by replacing the atomistic structures with equivalent continuum elements. In this technique, in contrast to traditional continuum modeling methods, the discrete nature of the structures on the atomic scale is considered by replacing bonded and non-bonded interactions with continuum elements such as beam, truss, and spring. For example, as illustrated in Fig. 3.4, Wernik and Meguid (2010) used FEA to model CNTs as space frame structures in which beam elements were successfully used to simulate carbon–carbon covalent bond, while nonlinear rotational spring element was used to model non-bonded interactions.

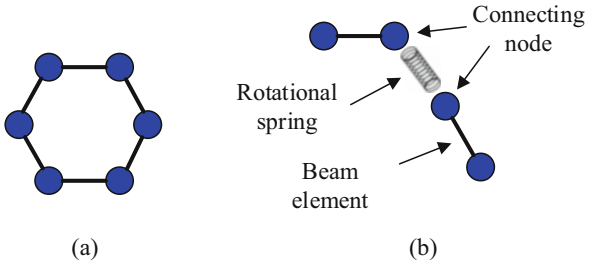


**Fig. 3.4** Atomistic-based continuum representations of (**a**) a hexagonal lattice of the CNT, and (**b**) the connecting structural finite elements used to model the CNT

In MD and MM techniques, the atomic structures of nanocomposites are initially defined. Interactions of atoms in nanocomposites are defined by interatomic potential energy function, which is either obtained from first-principle calculations (Sun 1998), or from experimental results, such as bond energy and atomization energy (Brenner et al. 2002). In general, the interatomic potential energy is a function of the positions of atoms in nanocomposites. Force on each atom is derived from the gradient of the total potential energy in nanocomposites.

In MM, thermodynamic equilibrium is achieved by minimizing the total potential energy of the system by considering the atomic coordinates. The governing equation for MM is given by

$$\frac{\partial U(r)}{\partial r} = 0 \tag{3.1}$$

where U is the total potential energy of the system and r is the position vector of an atom.

MM does not consider time-dependent quantities like velocity, acceleration, and inertia force. Unlike MM, MD is performed by solving Newton's equation of motion for each atom in the system. The governing equations for MD are

$$m_i \frac{d^2 r_i}{dt^2} = F_i \tag{3.2}$$

and

$$F_i = -\frac{\partial U\left(r_1, r_2, \ldots, r_i, \ldots, r_N\right)}{\partial r_i} \tag{3.3}$$

where $r_i$ is the position vector of atom i, N is the total number of atoms, and $F_i$ is the force vector acting on atom i, $m_i$ is the mass of ith atom, and t is the time. Since MM does not consider transient and dynamic quantities, it cannot account for the thermal effect during the CNT pull-out process. In order to determine the ISS accurately under realistic temperature, MD approach is used by the authors in this chapter.

The current MD simulations were carried out using the large-scale atomic/molecular massively parallel simulator (LAMMPS) (Plimpton 1995). The CVFF (Dauber-Osguthorpe et al. 1988) was adopted in the simulations to model all bonded and non-bonded interactions in the CNT-epoxy systems. This forcefield has been widely used by other researchers to study the mechanical properties of CNT-reinforced epoxy composites (Alian et al. 2015a, 2015b; Kumar et al. 2014; Li et al. 2012). The analytic forms ($U_{pot}$) of the energy expressions utilized in the CVFF are given below:

$$U_{pot} = U_{bond} + U_{angle} + U_{dihedral} + U_{improper} + U_{vdW} + U_{Coulomb} \tag{3.4}$$

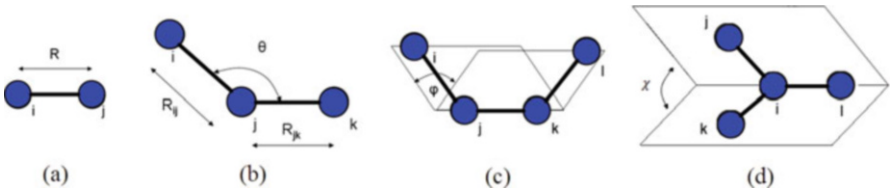


**Fig. 3.5** Schematics of the different bonded CVFF terms: (**a**) bond length, (**b**) bond angle, (**c**) torsion angle, (**d**) inversion angle

where $U_{bond}$, $U_{angle}$, $U_{dihedral}$, $U_{improper}$ are the bonded interactions which represent the respective energy of deformation of bond lengths, bond angles, torsion angles, and inversion angles, $U_{vdW}$ and $U_{Coulomb}$ are the non-bonded interactions which represent the respective van der Waals (vdW) and electrostatic interactions. The components of the potential energy due to the bonded interactions are shown in Fig. 3.5.

## *3.2.2 Molecular Modeling of Pull-Out Simulation*

### 3.2.2.1 Molecular Structure of CNTs with Defects and Functionalization

The molecular structures of five different types of possible defects and one type of CNT functionalization considered are presented in Fig. 3.6. All defects are assumed to form onto the sidewall of an armchair (9, 9) SWCNT. As can be seen in Fig. 3.6a–c, monovacancy, bivacancy, and trivacancy were formed by removing one-, two-, and three-bonded carbon atoms from the pristine SWCNT, respectively. A single adatom presented in Fig. 3.6d is an interstitial defect formed by an extra carbon that is covalently bonded to two adjacent carbon atoms. The SW defect shown in Fig. 3.6e is formed via a 90° rotation of the carbon–carbon bond, transforming four hexagons into two pentagons and heptagons (5-7-7-5). Finally, Fig. 3.6f shows the phenyl functional group ($-C_6H_5$) which is end-grafted to the sidewall of the CNT. The phenyl group contains a benzene ring, which typically exists in epoxy resins. The associated change in geometry of the atoms is that the phenyl group becomes perpendicular to the sidewalls of CNTs and the hybridization of the bonded atom is changed from $sp^2$ to $sp^3$.

Five different defects in CNTs and one case of functionalization were considered in our research; as follows: (1) CNTs with 3, 6, 9, 12, 15, 18 monovacancies; (2) CNTs with 2, 3, 4, 5, 6, 7, 8, 9 bivacancies; (3) CNTs with 1, 2, 3, 4, 5, 6 trivacancies; (4) CNTs with 4, 8, 12 adatoms; (5) CNTs with 5, 10, 15 SW defects; and (6) Functionalized CNTs using 3, 6, 9 phenyl functional groups. The positions of the defects and functionalization were randomly located on the sidewalls of the CNTs. The simulation for each case was repeated three times, and the ISS results were averaged and curve fitted.

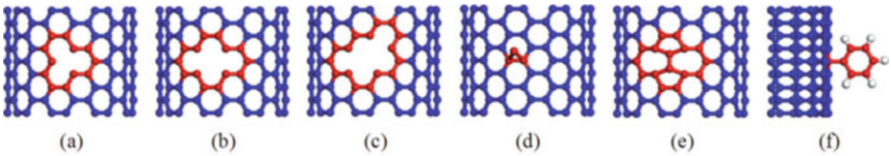


**Fig. 3.6** Geometries of CNTs containing different defects and functionalization: (**a**) monovacancy, (**b**) bivacancy, (**c**) trivacancy, (**d**) single carbon adatom defect, (**e**) SW defect, and (**f**) phenyl group functionalization

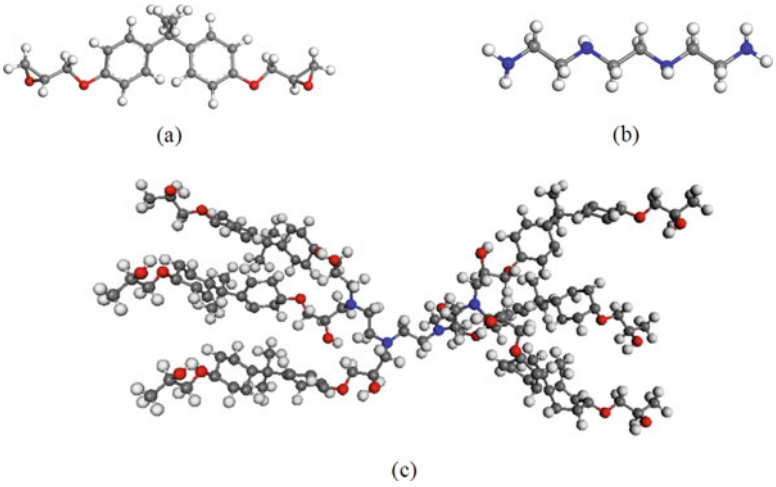


**Fig. 3.7** Chemical structures of (**a**) epoxy resin (DGEBA), (**b**) curing agent (TETA), and (**c**) cured epoxy oligomer (6 DGEBA molecules connected by 1 TETA). (The hydrogen, carbon, oxygen, and nitrogen atoms of the epoxy chain are presented by white, gray, red, and blue colors, respectively)

#### 3.2.2.2 Cured versus Uncured Polymer

The polymer used was a specific two-component epoxy resin based on a diglycidyl ether of bisphenol A (DGEBA) epoxy and triethylene tetramine (TETA) curing agent, which is typically used in the aerospace industry. Different degrees of conversion were introduced by analyzing both uncured and cured epoxy composites. Cured epoxy system was developed during the curing process by forming covalent bonds between the hydrogen atoms in the amine groups of the curing agent and the epoxide groups of the epoxy. As shown in Fig. 3.7, each epoxy oligomer consists of six DGEBA molecules connected by one TETA molecule so that the resin-hardener weight ratio in the epoxy polymer is equal to 100:16.7. Finally, 33 epoxy oligomers were packed into the RVE using Packmol software (Martínez et al. 2009) to obtain an appropriate density, and the final structure of the RVE is visualized by VMD (Humphrey et al. 1996) as shown in Fig. 3.8a. For the uncured epoxy matrix, the

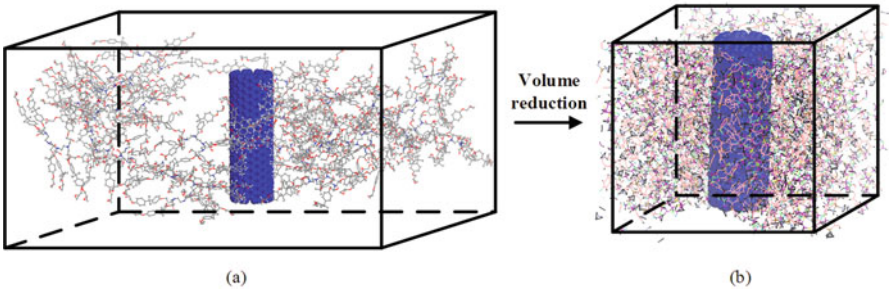


**Fig. 3.8** Preparation of the RVE (**a**) SWCNT embedded in 33 randomly placed cured epoxy oligomers in a simulation box of size 150 × 150 × 45 Å, and (**b**) the compressed SWCNT-epoxy system in a simulation box of size 50 × 50 × 42 Å

same numbers of individual DGEBA and TETA as the cured system were used to generate the RVE. The uncured state means that there is no curing process in the epoxy matrix and no covalent bonds were formed between the DGEBA and TETA.

#### 3.2.2.3 Construction of Nanocomposite RVE

In order to conduct the pull-out simulations of a CNT from an epoxy matrix, an RVE was built to contain an SWCNT embedded at the center of the RVE and the epoxy polymer molecules. In the current MD simulations, periodic boundary conditions were applied in the x- and y-directions, while the z-direction was non-periodic and shrink-wrapped. The time step used in the MD simulations was selected to be 1 fs for all MD simulations, and a cutoff distance of 12 Å was used to model vdW interactions. The main steps involved in preparing both the uncured and cured epoxy composites are as follows:

*Step 1–Volume reduction*: Since Packmol software treats molecules as rigid bodies, the size of the RVE was initially enlarged to accommodate all the epoxy molecules and the CNT atoms. Subsequently, the RVE was compressed gradually through seven steps from its initial dimensions of 150 × 150 × 45 Å to the targeted size of 50 × 50 × 42 Å, resulting in the appropriate density of the RVE. At each stage, the CNT was "frozen," and the coordinates of the epoxy atoms were remapped to fit inside the compressed box. The potential energy of the compressed box was then minimized using the conjugate gradient method. The final compressed box is demonstrated in Fig. 3.8b.

*Step 2–Equilibration*: The compressed box was initially equilibrated for 2 ns in the isothermal-isobaric (NPT) ensemble at 300 K and 1 atm using the Nose–Hoover algorithm to evenly distribute the molecules due to the volume reduction. The equilibrium was ensured by using the following temperature cycle protocol. Two stepwise NPT cycles of heating and cooling (from 400 K to 300 K by a step of 25 K) were performed with each step occupying 10 ps. This was followed by a

simulation in the NPT ensemble for 1 ns at 300 K and 1 atm to generate an epoxy system with an appropriate CNT-matrix interfacial thickness. The final equilibrated density was found to be 0.94 g/cm$^3$, which is slightly less than expected due to the non-periodic boundary in the z-direction of the RVE.

### *3.2.3 Molecular Modeling of Compressive Load Simulation*

#### 3.2.3.1 Molecular Structure of CNTs with Defects

It is expected that defects have an influence on buckling behavior of CNTs, since buckling is very sensitive to geometric imperfections. However, it is crucial to understand the severity of the effect of different defects on the buckling behavior of CNTs. For CNTs with vacancy and SW defect, several factors can be presumed to influence buckling such as the number and location of defects, the number of vacancy clusters, and the distribution of these vacancy clusters. In order to examine the contribution of these factors, the defect configurations given in Fig. 3.9 are investigated. Specifically, vacancies coded as (1A), (2B), and (3A) are symmetric monovacancy, bivacancy, and trivacancy, respectively. Vacancies coded as (2C) and (2B) are asymmetric bivacancy and trivacancy, respectively. Both vacancies coded as (1B) and (1C) contain two monovacancies. The monovacancies (1B) locate exactly opposite to each other while the monovacancies (1C) locate towards one side of the nanotubes. Symmetric and asymmetric SW defects are coded as (1SW-A) and (1SW-B), respectively. Armchair (7, 7), (9, 9) and zigzag (12, 0) SWCNTs with the same aspect ratio of 6.5 were considered here. Two types of armchair SWCNTs were

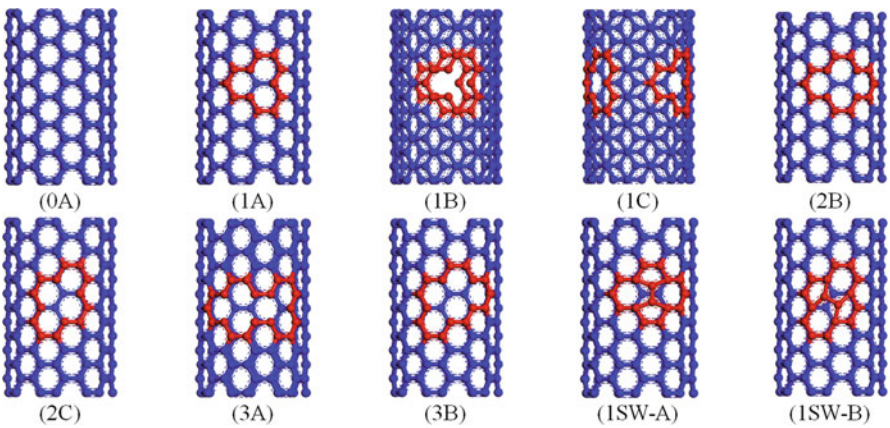


**Fig. 3.9** Defects studied in this research (0A—pristine, 1A—monovacancy, 1B—two symmetrically distributed monovacancies, 1C—asymmetrically distributed two monovacancies, 2B—symmetric bivacancy, 2C—asymmetric bivacancy, 3A—symmetric trivacancy, 3B—asymmetric trivacancy, 1SW-A—symmetric SW defect, 1SW-B—asymmetric SW defect)

repeated to confirm the simulation results, and zigzag (12, 0) SWCNTs were chosen to have similar diameters to armchair (7, 7) SWCNTs. All defects were assumed to form onto the sidewall of SWCNTs. The defects were introduced approximately at the middle of the nanotubes since defects at the mid-length are proven to reduce buckling strain and buckling load to the greatest (Parvaneh et al. 2009; Wang et al. 2008).

#### 3.2.3.2 Construction of Freestanding CNT and Nanocomposite RVE

It should be emphasized that the objective of the present chapter is to investigate the buckling behavior of an embedded CNT within a matrix and not the buckling behavior of the CNT-reinforced nanocomposites. Thus, both freestanding CNTs and CNT-epoxy nanocomposites were prepared here with the view to understand the influence of matrix material on the buckling of defective CNTs. To prepare freestanding armchair (7, 7), (9, 9) and zigzag (12, 0) SWCNTs for compression, the SWCNTs were initially minimized in terms of total potential energy using the conjugate gradient method. This was followed by canonical (NVT) equilibration at 300 K for the duration of 50 ps using a time step of 1 fs. The boundary condition was kept non-periodic in all three directions, and vdW interactions were truncated at a cutoff distance of 12 Å.

For the buckling simulation of embedded CNTs, the epoxy system was the same as the one for the pull-out analysis. In this MD simulation, periodic boundary conditions were applied in x- and y-directions, while periodicity was removed in z-direction. The time step used in the MD simulation was selected to be 1 fs, and a cutoff distance of 12 Å was used to model vdW interactions. The same parameters were followed for different RVEs containing different armchair (7, 7), (9, 9) and zigzag (12, 0) SWCNTs. For example, the main steps involved in preparing the buckling simulation for the (7, 7) pristine SWCNT-epoxy nanocomposites are as follows:

*Step 1–Volume reduction*: Since Packmol software treats molecules as rigid bodies, the size of the RVE was initially enlarged to accommodate all the epoxy molecules and the CNT atoms. Subsequently, the RVE was compressed gradually through seven steps from its initial dimensions of $150 \times 150 \times 62$ Å to the targeted size of $50 \times 50 \times 62$ Å, resulting in the appropriate density of the RVE. At each stage, the CNT was "frozen," and the coordinates of the epoxy atoms were remapped to fit inside the compressed box. The potential energy of the compressed box was then minimized using the conjugate gradient method.

*Step 2–Equilibration*: The compressed box was initially equilibrated for 2 ns in the isothermal-isobaric (NPT) ensemble at 300 K and 1 atm using the Nose–Hoover algorithm to distribute the molecules evenly due to the volume reduction. The equilibrium was ensured by using the following temperature cycle protocol. Two stepwise NPT cycles of heating and cooling (from 400 to 300 K by a step of 25 K) were performed with each step occupying 10 ps. This was followed by a simulation in the NPT ensemble for 1 ns at 300 K and 1 atm to generate an epoxy

system with the appropriate CNT-matrix interfacial thickness. The final equilibrated density of the SWCNT-epoxy RVE was found to be 0.95 g/cm$^3$, which is slightly less than expected due to the non-periodic boundary in the z-direction of the RVE.

## 3.3 Molecular Dynamics Simulation

### *3.3.1 Pull-Out Simulation*

#### 3.3.1.1 CNT Pull-Out Method

The MD pull-out numerical experiments were carried out to determine the ISS of the epoxy nanocomposite systems considered. In the existing pull-out studies, mainly two types of approaches are used to conduct MD pull-out simulations: the displacement pull-out approach (Chen et al. 2015; Li et al. 2011; Zheng et al. 2008, 2009) and the velocity pull-out approach (Wernik et al. 2012, Meguid et al. 2010; Wernik and Meguid 2011). For the displacement pull-out approach, the CNT is pulled out a certain distance. This is followed by an equilibration to ensure that the CNT-polymer system reaches equilibrium prior to the next CNT pull-out. This process is repeated until the CNT is completely out of the matrix. In terms of the velocity pull-out approach, the CNT is pulled out a small distance each step continuously until it is completely out of the matrix. Xiong and Meguid (2015) found that these two approaches produced very similar pull-out results if the simulation parameters were properly adjusted. Hence, in this chapter, we employed only the velocity pull-out approach, thanks to the less time spent on the MD simulations. In order to prevent the simultaneous drift of the epoxy with the CNT in the z-direction during the pull-out process, one edge of the epoxy molecules was constrained (shown in red in Fig. 3.10). The constrained system was further equilibrated in the NVT ensemble at 300 K for 50 ps to avoid the effect of the constraint on the final results. The composition of the RVE prior to the pull-out process of the pristine CNT is listed in Table 3.1. Subsequently, the edge atoms of the CNT, which are marked in green in Fig. 3.10, were pulled out at a uniform velocity of $1 \times 10^{-4}$ Å/fs at 300 K in the NVT ensemble until the CNT was completely pulled out from the matrix. During the pull-out process, the driving forces formed by the CNT edge atoms pulled out the remaining CNT atoms in the z-direction. Since the interactive deformation of the CNT and the epoxy atoms were enabled, our method can accurately capture the effect of each defect and functionalization on the interfacial load transfer mechanisms in a deformable epoxy polymer matrix.

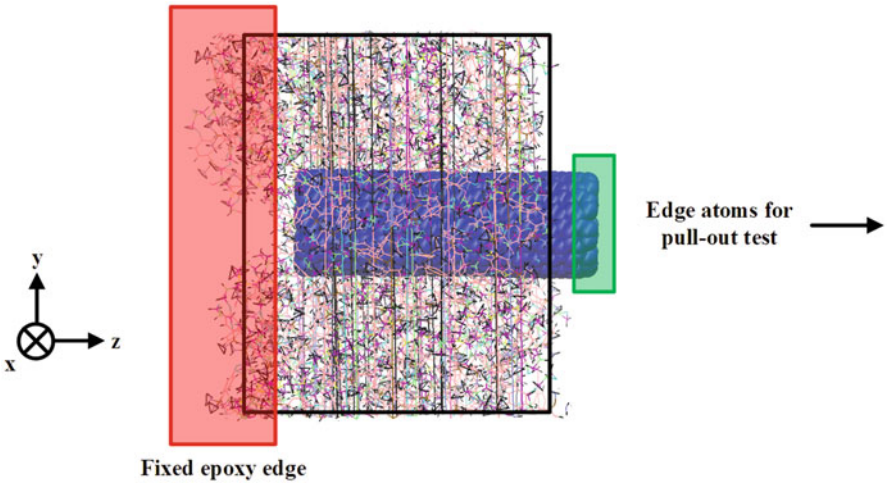


**Fig. 3.10** Setup for pull-out simulation of a CNT from the epoxy matrix

**Table 3.1** Composition of nanocomposite RVE immediately before pristine CNT pull-out simulation

| CNT | | | Epoxy | Composites | | | | |
|---|---|---|---|---|---|---|---|---|
| Chiral vector | Length (Å) | Radius (Å) | No. of chain | X (Å) | Y (Å) | Z (Å) | Density (g/cm$^3$) | Total number of atoms |
| (9,9) | 38.120 | 5.752 | 33 | 52.323 | 52.323 | 51.111 | 0.94 | 11,238 |

### 3.3.1.2 Evaluation of ISS

There are four theories in the literature regarding the location along the CNT where the ISS is the largest. Natsuki et al. (2007) and Zhang and Wang (2005) proposed that the ISS be the largest at the pull-out end of the CNT and decays nearly exponentially with the nanotube depth into the polymer (model A in Fig. 3.11a). In contrast, Gao and Li (2005) suggested that the maximum occurs at both ends of the CNT but that it is zero at the middle of the nanotube (model B in Fig. 3.11b). A similar method was used by Li et al. (2011), where they assumed that the ISS was distributed uniformly within 10 Å from each end of the CNT (model C in Fig. 3.11c). The most common assumption is that the ISS is uniformly distributed along the entire length of the CNT (Gou et al. 2004; Al-Ostaz et al. 2008) (model D in Fig. 3.11d).

In model A, the maximum ISS ($\tau$), which occurs at the nanotube pull-out end, is given as (Cox 1952; Chua and Piggott 1985),

$$\tau = \frac{Fn}{2\pi r^2 \tanh\left(nL/r\right)} \tag{3.5}$$

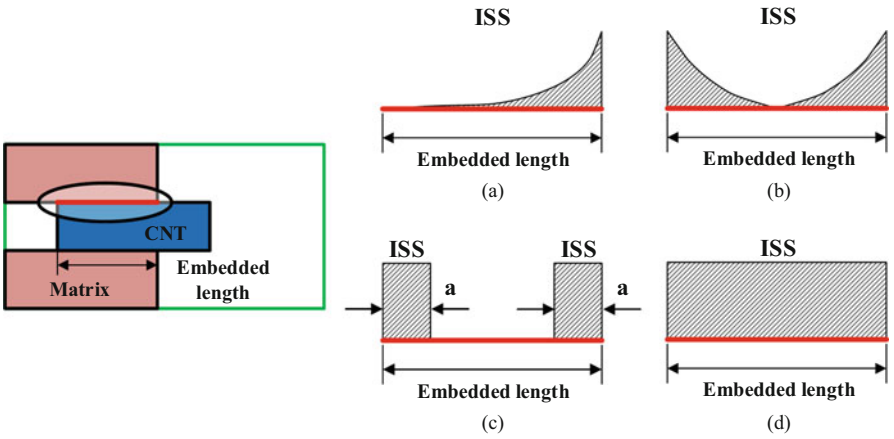


**Fig. 3.11** Different proposed distribution of ISS: (**a**) exponential decay of ISS, (**b**) dominant ISS at CNT ends and decays rapidly, (**c**) uniform distribution of ISS near CNT ends, and (**d**) uniform ISS for the entire length of CNT

where F is the pull-out force, r is the radius of the CNT, L is the embedded initial length of the CNT into the matrix, n is a parameter given by $n = \sqrt{\frac{E_m}{E_{nt}(1+v_m)\log\left(\frac{t}{2r}\right)}}$, in which $E_m$ is the polymer's Young's modulus, $v_m$ is its Poisson's ratio, $E_{nt}$ is the nanotube's Young's modulus, and t is the total thickness of the polymer film. Most numerical simulations used models C and D to estimate the ISS, since it is easy to calculate. In model C, the ISS is defined by,

$$\tau = \frac{F}{4\pi ra} \tag{3.6}$$

which assumes that the ISS is distributed at both ends of the CNT, and where a is the length along the CNT over which the ISS is distributed.

For model D, there are two approaches: force approach and energy approach, to calculate the ISS in the literature. In terms of the force approach, the ISS can be calculated from the pull-out force, as follows:

$$\tau = \frac{F}{2\pi rL} \tag{3.7}$$

The energy approach adopted in Gou et al. (2005), Zheng et al. (2009) and Yang et al. (2015) is the most common approach used to predict the ISS of CNT-reinforced composites. Since the work required to pull the CNT out is attributed to the shear force between the CNT and the matrix, the ISS can be calculated from the pull-out work ($W_{pull-out}$), as follows:

$$W_{pull-out} = \int_0^L 2\pi r\,(L-z)\,\tau_i dz = \pi r L^2 \tau \tag{3.8}$$

where z is the pull-out distance from the initial position to the final position of the CNT.

Hence, in this chapter, we will adopt the energy approach to estimate the ISS. The pull-out work is usually defined as the variations in the potential energy of the entire system after and prior to the pull-out process, as follows:

$$W_{pull-out} = E_{potential}^{final} - E_{potential}^{initial} \tag{3.9}$$

The potential energy of the nanocomposite can be described as follows:

$$E_{total} = E_{cnt} + E_{epoxy} + E_{interaction} \tag{3.10}$$

where $E_{cnt}$, $E_{epoxy}$, and $E_{interaction}$ are the potential energy of the CNT and epoxy as well as the interaction energy between the CNT and epoxy matrix, respectively. However, some researchers (Zheng et al. 2008, 2009; Yang et al. 2015; Jang et al. 2013) argue that the change in the total potential energy includes both the potential energy variations of the CNT and the epoxy which do not contribute to the calculation of ISS. Therefore, in order to obtain more accurate and reliable ISS, the change in the CNT–matrix interaction energy is considered as the pull-out work, as follows:

$$W_{pull-out} = E_{interaction}^{change} = E_{interaction}^{final} - E_{interaction}^{initial} \tag{3.11}$$

Both of these pull-out work definitions are used to calculate the ISS, and their application conditions are discussed in this chapter. Since most of the atoms in the CNTs are electrically neutral and there are no bonded interactions between the CNT and the matrix, the CNT–matrix interaction energy is mostly attributed to non-bonded vdW interactions. Several researchers (Gou et al. 2004, 2005) also determined the interfacial binding energy $\gamma$ between a CNT and the matrix which serves as another reliable indicator of the effect of defects and functionalization on the nanocomposites. The interfacial binding energy $\gamma$ per unit area can be obtained from the interaction energy ($E_{interaction}$) scaled by twice the instantaneous contact area,

$$\gamma = \frac{E_{interaction}}{2A} \tag{3.12}$$

where A is the instantaneous contact area at each pull-out step.

Since the dimensional changes of CNTs containing defects and functional groups influence the ISS, the diameter and length of defective and functionalized CNTs

**Table 3.2** Equilibrium length and radius of CNTs according to different types and numbers of modified sites

| Defect type | No. of defects | 300 K | |
|---|---|---|---|
| | | Radius (Å) | Length (Å) |
| Pristine | | 5.752 | 38.120 |
| Monovacancy | 3 | 5.756 | 38.208 |
| | 6 | 5.762 | 38.297 |
| | 9 | 5.775 | 38.345 |
| | 12 | 5.776 | 38.466 |
| | 15 | 5.794 | 38.507 |
| | 18 | 5.799 | 38.612 |
| Bivacancy | 2 | 5.758 | 38.197 |
| | 3 | 5.752 | 38.201 |
| | 4 | 5.750 | 38.254 |
| | 5 | 5.754 | 38.253 |
| | 6 | 5.762 | 38.254 |
| | 7 | 5.763 | 38.267 |
| | 8 | 5.769 | 38.308 |
| | 9 | 5.782 | 38.323 |
| Trivacancy | 1 | 5.758 | 38.146 |
| | 2 | 5.754 | 38.122 |
| | 3 | 5.749 | 38.272 |
| | 4 | 5.757 | 38.229 |
| | 5 | 5.761 | 38.245 |
| | 6 | 5.761 | 38.183 |
| Adatom | 4 | 5.761 | 38.187 |
| | 8 | 5.772 | 38.258 |
| | 12 | 5.780 | 38.313 |
| SW | 5 | 5.758 | 38.071 |
| | 10 | 5.743 | 38.091 |
| | 15 | 5.758 | 38.006 |
| Phenyl group | 3 | 5.760 | 38.230 |
| | 6 | 5.759 | 38.156 |
| | 9 | 5.766 | 38.182 |

after the equilibration of epoxy systems were used in all of our MD simulations. The new averaged dimensions of CNTs are summarized in Table 3.2. Compared with the pristine CNT, only the length of SW defective CNT decreases, whereas the diameter and length of other CNTs increase.

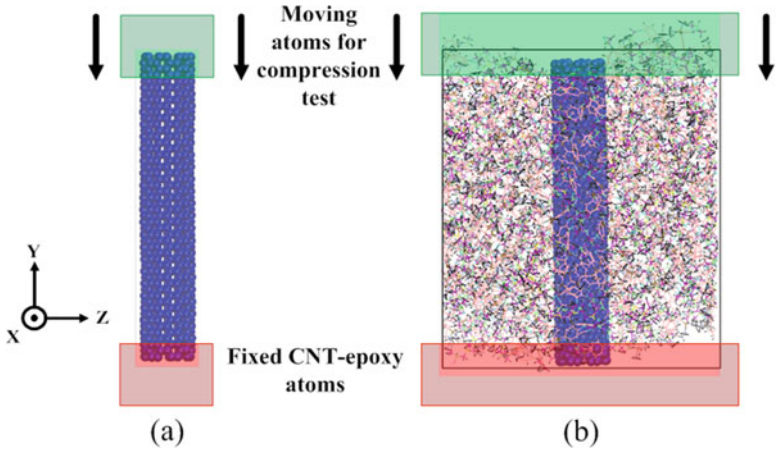


**Fig. 3.12** Setup for the buckling simulations of (**a**) freestanding SWCNT, and (**b**) SWCNT embedded in the epoxy matrix

## *3.3.2 Compressive Load Simulation*

### 3.3.2.1 CNT and RVE Compressive Load Method

The MD compression simulations were carried out to determine the critical buckling strain and buckling load of both freestanding SWCNTs and SWCNT-epoxy nanocomposite systems. To prevent the simultaneous drift of the SWCNT and epoxy atoms in the z-direction during the compression process, we constrained one end of the freestanding SWCNT and the RVE (shown in red in Fig. 3.12). In order to avoid the effect of the constraint on the final results, the constrained systems were further equilibrated in the NVT ensemble at 300 K for 50 ps. The composition of the freestanding SWCNTs and RVEs containing different SWCNTs prior to the compression process is listed in Table 3.3. After the equilibration was complete, an incremental displacement of 0.01 Å was applied on the other end of the freestanding SWCNTs and RVEs, which are marked in green in Fig. 3.12. After each increment, the systems were relaxed for a period to achieve a new equilibrium state while keeping the two ends constrained. The loading was repeated at 300 K in the NVT ensemble until the buckling occurred. Similar to the pull-out simulation, our method can capture the effect of each defect accurately on the buckling behavior of CNTs embedded in a deformable epoxy polymer matrix.

### 3.3.2.2 Evaluation of Buckling Behavior

As for the assessment of buckling behavior, the strain energy-strain and force-displacement curves for the pristine SWCNTs are shown in Fig. 3.13a, b, respec-

**Table 3.3** Composition of freestanding SWCNTs and RVEs containing different SWCNTs immediately before compression simulations

| SWCNT | | | Epoxy | Composites | | | | |
|---|---|---|---|---|---|---|---|---|
| Chiral vector | Length (Å) | Radius (Å) | No. of chain | X (Å) | Y (Å) | Z (Å) | Density (g/cm$^3$) | Total number of atoms |
| (7, 7) | 55.89 | 4.46 | – | – | – | – | – | 700 |
| (9, 9) | 72.11 | 5.73 | – | – | – | – | – | 1152 |
| (12, 0) | 56.68 | 4.39 | – | – | – | – | – | 696 |
| (7, 7) | 55.47 | 4.48 | 44 | 52.47 | 52.47 | 66.79 | 0.95 | 14,868 |
| (9, 9) | 71.70 | 5.75 | 57 | 52.21 | 52.21 | 87.05 | 0.97 | 19,506 |
| (12, 0) | 55.97 | 4.45 | 44 | 52.47 | 52.47 | 67.12 | 0.94 | 14,864 |

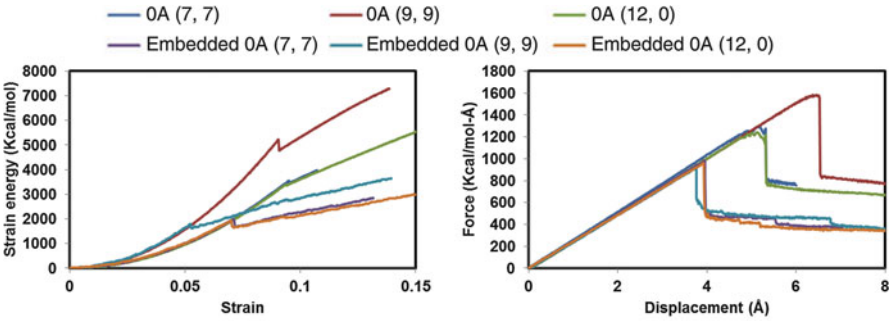


**Fig. 3.13** (**a**) Strain energy-strain curves; (**b**) force-displacement curves for different pristine freestanding and embedded SWCNTs

tively. The critical buckling state is detected by a sudden drop of strain energy or force. This sudden drop is associated with significant structural and geometrical changes of CNTs (shown in Fig. 3.14) corresponding to the release of energy in CNTs. It can be seen in Fig. 3.14 that different pristine SWCNTs with an aspect ratio of 6.5 buckle sideway with the occurrence of a flattening at the center, which is recognized in the literature as being "beam-shell buckling mode." It is a mixture of globalized beam-like buckling for a long and slender CNT and localized shell-like buckling within the atomic layer of a short CNT. In agreement with the findings of Wang et al. (2010, 2014), we conclude that CNTs with aspect ratios more than 6 exhibit beam-shell buckling mode, such as a single beam while preserving its circular cross section with localized shell buckling within the atomic layer. From Fig. 3.13a, it is observed that the strain energy can be approximately expressed as a quadric function of the strain before the singularity happens in each curve, viz.:

$$U = \frac{1}{2} EAL\varepsilon^2 \tag{3.13}$$

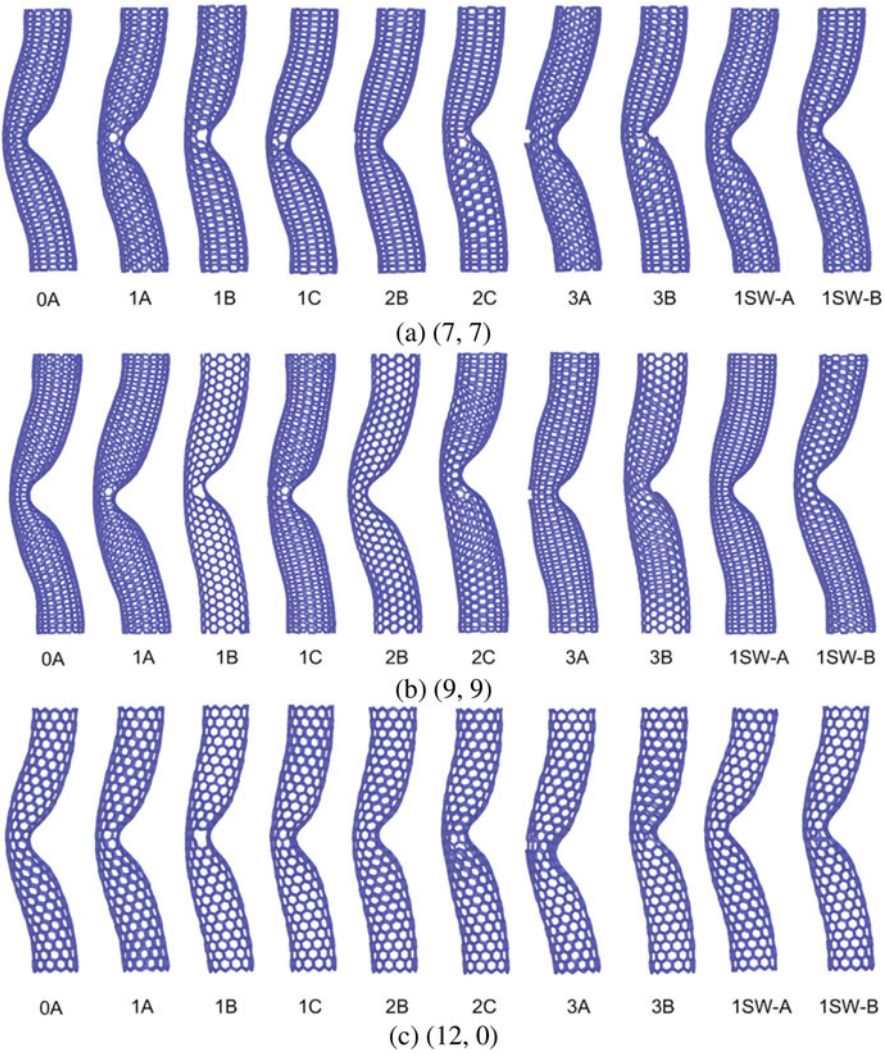


**Fig. 3.14** Buckling mode shapes of the freestanding SWCNTs (**a**) (7, 7), (**b**) (9, 9), and (**c**) (12, 0)

where U, E, A, L, and $\varepsilon$ are the strain energy, Young's modulus, cross-sectional area, original length, and strain of the nanotubes, respectively. This indicates that the SWCNTs sustain elastic deformation under a compressive force in accordance with Hooke's law until bifurcation. Note that in Fig. 3.13a the critical buckling strain is defined as the strain at which the strain energy of the simulated SWCNT registers its first sudden drop in value. We can also see in Fig. 3.13b that the compressive force which the SWCNTs can withstand increases almost linearly with the axial

displacement until the buckling load is reached. Accordingly, this relationship can be formulated as

$$F = \frac{EA}{L}\Delta L \tag{3.14}$$

where F is the compressive force and ΔL is the end-shortening displacement. As it is shown in Fig. 3.13b, there are two values of axial load P at the critical buckling state. The upper value of P at the critical buckling state is defined as the critical buckling load $P_{cr}$ and the corresponding end-shortening displacement is defined as the critical buckling displacement $\Delta_{cr}$. Coincident with the value obtained through strain energy, the critical buckling strain $\varepsilon_{cr}$ can also be calculated by dividing $\Delta_{cr}$ with the original length L of CNT.

## 3.4 Results and Discussions

### *3.4.1 Analysis of Pull-Out Simulation*

#### 3.4.1.1 MD Model Validation

Figure 3.15 shows a snapshot of the respective pull-out process of a pristine CNT from uncured and cured epoxy matrices. We can see that debonding takes place among the uncured epoxy molecules in close proximity to the CNT-matrix interfaces, and that a substantial number of uncured epoxy molecules are attached to the CNT. However, in the cured case, no epoxy molecules are pulled out along

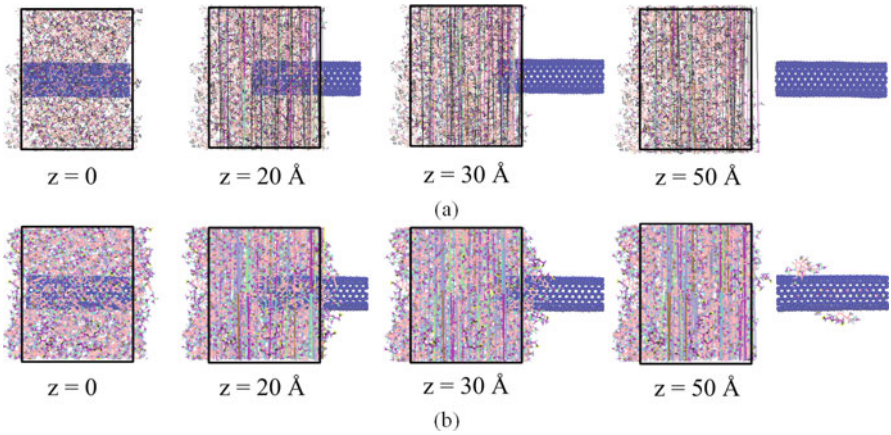


**Fig. 3.15** Schematics of the pull-out processes of pristine CNT embedded in (**a**) uncured epoxy matrix and (**b**) cured epoxy matrix

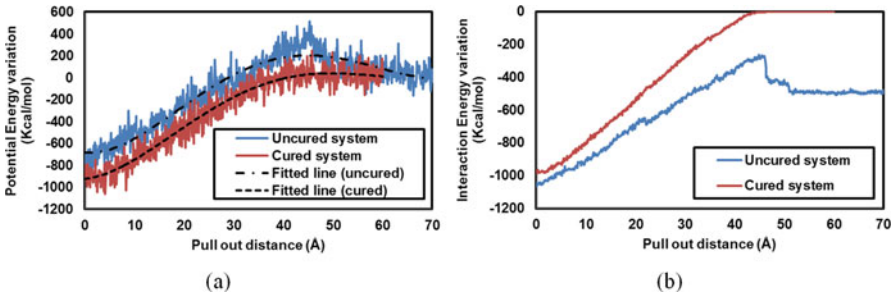


**Fig. 3.16** (**a**) Potential energy and (**b**) interaction energy variations in pristine CNT with pull-out distance

with the CNT. The respective variations in the total potential energy and interaction energy of the uncured and cured CNT-epoxy systems are shown in Fig. 3.16. The zero point of the potential energy is taken as the position where the CNT is pulled out from the matrix completely. Note that the fluctuation in the potential energy of the system is attributed to the rearrangement of molecules in the RVE, and they are fitted using dashed polynomial curves. It can be observed from Fig. 3.16a that the potential energy of the cured system changes from approximately −1000 Kcal/mol to zero at full pull-out, while the corresponding uncured system changes from approximately −700 Kcal/mol to zero again at full pull-out of the CNT from the matrix. This is because the pull-out work is transferred into an increase in the potential energy of the system as the pull-out process proceeds. The reduced level of the change in potential energy of the uncured system can be explained in Fig. 3.15a. The figure shows that some of the uncured molecules are attracted back to the RVE due to vdW forces. And, this happens before the CNT is pulled out completely from the matrix. Since no epoxy molecules are pulled out from the cured epoxy system, the potential energy of the matrix and CNT remains almost constant. This is demonstrated by the very similar variation in the interaction energy of the cured system in Fig. 3.16b. We can also see in Fig. 3.16b that the initial interaction energy magnitude of the uncured system is larger than that of the cured one. However, the final interaction energy of the uncured system does not change to zero as some epoxy molecules are attached on the pull-out CNT.

Based on the change in the total potential energy, the ISS of the uncured and cured epoxy composites was determined to be 198 and 250 MPa, respectively. The higher ISS of the cured system is because the epoxy resin is strengthened by the crosslinked structures developed during the curing process. Since the CNT does not interact with the epoxy matrix after the CNT is pulled out completely, the change in the interaction energy is equal to the initial CNT–matrix interaction energy. By applying the initial interaction energy, we found that the ISS of cured systems is very similar to the ISS based on the total potential energy. However, the ISS of the uncured system becomes 277 MPa, which is unreasonably high because it ignores the energy expended in deforming the polymer during the pull-out test. Thus, we

decide to use the determination based on the total potential energy to calculate the ISS accurately while keeping the ISS based on the initial interaction energy for comparison. The current ISS estimates for the pristine CNTs were found to be in good agreement with those of existing MD pull-out studies with some minor discrepancies due to the use of the different forcefields used in the simulations. For instance, Bohlén and Bolton (2013) used COMPASS forcefield to calculate the ISS via a new approach which assumed that the ISS was distributed uniformly within 10 Å from each end of the SWCNT, but was zero at the middle of the nanotube. The ISS of an SWCNT-polyvinylidene fluoride system resulting from their approach was found to be 214.4 MPa compared with 250 MPa from the current chapter. Chowdhury and Okabe (2007) used MD simulations to examine the effect of polymer matrix density on the ISS. The carbon–carbon interaction in the CNT was modeled using Brenner potential while AMBER potential was used for the polymer matrix. The ISS was calculated to be 245 MPa for an SWCNT-PE composite with a density of 0.97 g/cm$^3$. Chowdhury et al. (2010) then used the same potential to study the effect of vacancy defects on the ISS of SWCNT-PE composites. They reported ISS reaching 300 MPa for a nanocomposite reinforced with pristine SWCNTs.

Figure 3.17 shows the relative concentrations of all atoms and sp$^2$ aromatic carbon atoms monitored as a function of the distance from the center of the CNT before and after crosslinking. We can see in Fig. 3.17a that the relative concentration of all atoms for the uncured matrix near the CNT is higher than the cured one. The increase in the relative concentration is because a less crosslinked structure allows more conformational freedom for the matrix to interact favorably with the CNT. Enhanced conformational flexibility allows a more favorable and denser packing of matrix atoms with the CNT. Moreover, Fig. 3.17b reveals that it is the relative concentration of the sp$^2$ carbon atoms that plays a major role in the CNT–matrix interaction energy. Such factors can improve the initial interaction energy at the CNT-epoxy interface, leading to overestimation of the ISS of the uncured system. Figure 3.18 compares the aromatic ring distribution near the CNT in the uncured

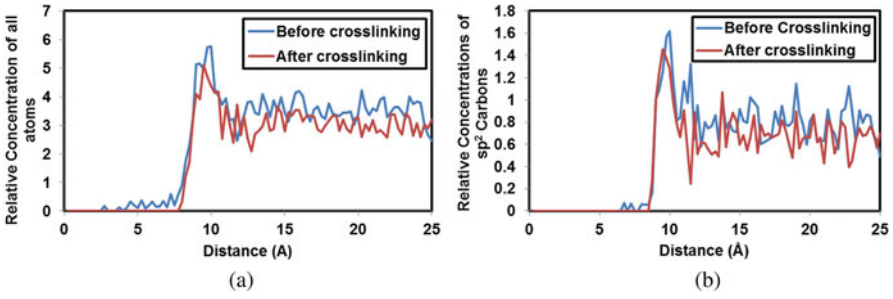


**Fig. 3.17** Spatially averaged concentration profiles versus distance from the center of the CNT before and after curing to 50% conversion (**a**) for all atoms and (**b**) for sp$^2$-hybridized carbon atoms

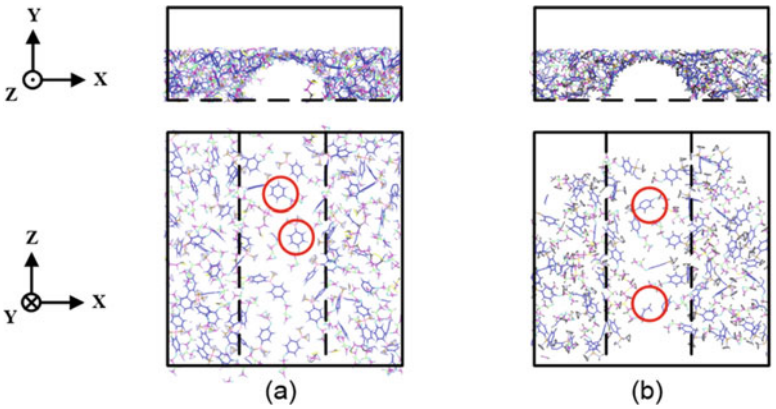


**Fig. 3.18** Aromatic ring distribution near the CNT in (**a**) uncured epoxy matrix and (**b**) cured epoxy matrix

and cured systems schematically. The red circles highlight typical aromatic ring conformation near the CNTs. We can see that aromatic rings in the uncured epoxy matrix are preferentially aligned parallel to the surface of the CNT, which optimizes π-stacking. The curing of the epoxy matrix sterically works against the aromatic rings lying flat on the surface of the CNT, reducing the interaction energy induced by π–π attractions at the CNT-epoxy interface. This chapter examines the relative concentration of the $sp^2$ carbon atoms to investigate the resulting interface properties better.

#### 3.4.1.2 Effect of Vacancy Defects upon ISS

The variations in the ISS of uncured and cured nanocomposite systems containing a defective CNT with different numbers of missing atoms are depicted in Fig. 3.19. This figure reveals that the ISS of the cured systems decreases as the number of missing atoms in the CNTs increases irrespective of the type of these defects. Since the potential energy of the epoxy and CNT does not alter very much for the cured systems, the interaction energy becomes the major contributor to the ISS. The vdW interaction between the CNT and the matrix solely contributes to the interfacial interaction energy. Thus, and as expected, the vdW interaction energy is reduced as a result of increasing number of vacancy defects in the CNT, which will eventually degrade the ISS. From Fig. 3.20a–c, it is clear that the relative concentrations of $sp^2$ carbon atoms near the CNT decrease with the increase in the number of vacancy defects irrespective of the type of defect. An increasing number of vacancy defects decreases the number of $sp^2$ carbon atoms in the CNT, which in turn reduces the ISS induced by π–π attractions. Unlike the cured systems, Fig. 3.19 shows that the number of vacancies in the uncured systems does not affect the ISS. This observation can be explained by the very low shear strength in the uncured

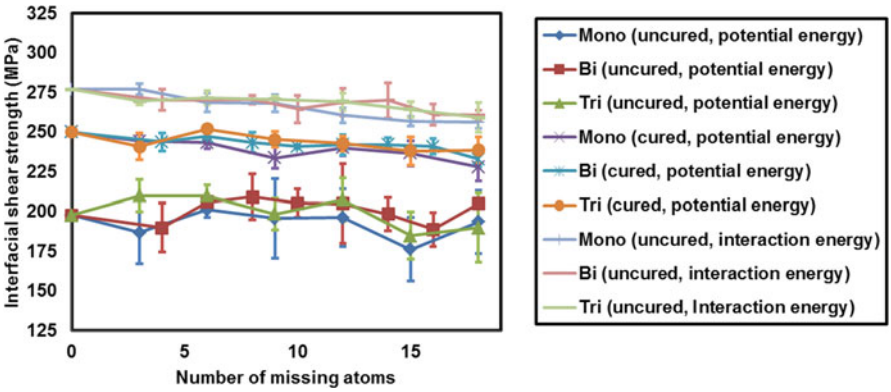


**Fig. 3.19** Variations in ISS with number of missing atoms

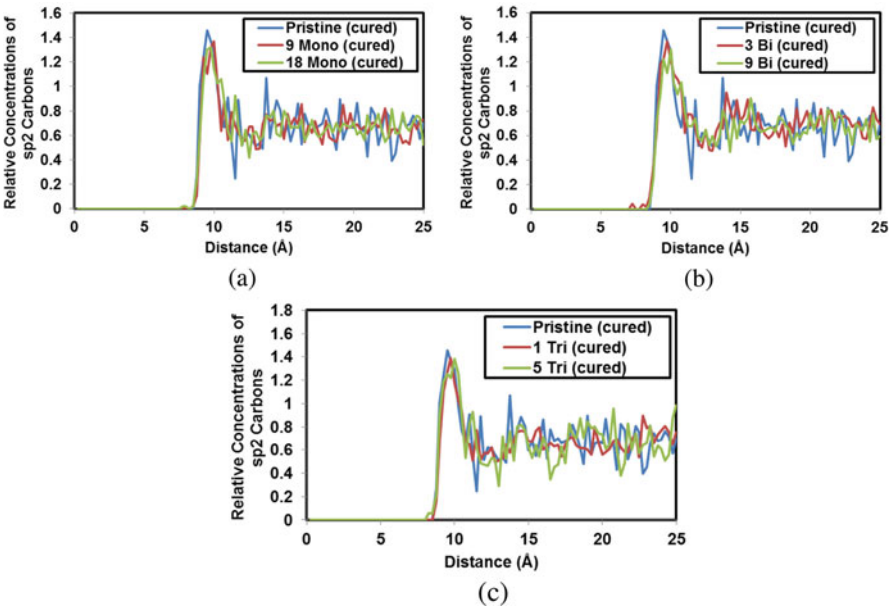


**Fig. 3.20** Relative concentrations of $sp^2$ carbon atoms for (**a**) different monovacancies after curing, (**b**) different bivacancies after curing, and (**c**) different trivacancies after curing

systems. Similar to the uncured pristine CNT system, the debonding takes place initially among the epoxy molecules near the CNT-matrix interface during the pull-out process. Therefore, it is predominantly the uncured epoxy molecules rather than the CNT-epoxy interface that governs the shear strength of the interface. In addition, based on the initial interaction energy, the ISS of the uncured systems in Fig. 3.19 is unreasonably higher than the ISS of the cured systems due to the ignorance of the matrix deformation energy.

Our results in Fig. 3.19 also reveal that for the same number of missing atoms, different types of vacancy defects have almost the same effect on the ISS of the cured systems. We can see that the ISS for various types of vacancies decline at a similar rate and are overlapped for the most part of the curves. Therefore, it can be deduced that the decrease in the ISS is independent of the defect type. The fluctuation of the ISS is possibly due to the different distribution of vacancies within the CNTs and the surrounding epoxy molecules. A total of 18 missing atoms were considered in this chapter, and the average maximum percentage of decrease in the ISS of the cured epoxy matrix was found to be 7.0%.

Our findings generally agree with the earlier work of Yang et al. (2015), but their work used COMPASS forcefield to study SWCNTs embedded in thermoplastic (PE) systems with no crosslinked structures. They reported 4.71% reduction of the ISS for 9 missing atoms. Chowdhury et al. (2010) examined three patterns of vacancy defects with different sizes and distributions; considering up to 8 missing atoms. They found a maximum reduction in ISS of about 5.33%, 5.00%, and 6.00% for one-atom, two-atom, and line vacancies, respectively. Furthermore, the weakened interfacial load transfer ability at the nanotube-matrix interface often leads to a decrease in mechanical properties of nanocomposites. For instance, Xiao and Hou (2006) used MD simulations to investigate the effect of a two-atom vacancy defect on the fracture of CNT-aluminum(AL) composites. As compared with pristine CNT-AL composites, the fracture stress and fracture strain of defected CNT-AL composites reduced by 36% and 57%, respectively. In general, it was found that defected CNT with a small volume fraction cannot reinforce but instead weaken nanocomposite materials. Joshi et al. (2011) investigated the effect of pinhole defects on mechanical properties of wavy CNT-based nanocomposites using RVE as well as Halpin–Tsai equations. They observed that the presence of 7 pinhole defects with each containing 24 atoms on a wavy nanotube can reduce the longitudinal elasticity modulus of the composite by 0.93% when compared with CNT without pinhole defects, and the elasticity modulus decreases with the increase in the number of pinhole defects. Sharma et al. (2014) used MD simulations to study the effects of vacancy defects on SWCNT-polypropylene composites. Results showed that one vacancy defect with 16% SWCNT volume fraction reduces both Young's modulus and shear modulus by 13% and 34%, respectively.

Figure 3.21 exhibits the interfacial binding energy of cured epoxy systems for the respective monovacancy, bivacancy, and trivacancy defects in CNTs obtained from the CNT–matrix interaction energy divided by twice the instantaneous contact area, as defined in Eq. (3.12). In all cases, the magnitude of interfacial binding energy increases gradually as the CNT is pulled out from the matrix. The increase in the interfacial binding energy is due to the reduction in the contact area between the CNT and matrix during the pull-out process. Furthermore, it can be observed that the magnitudes of the interfacial binding energies in the case of vacancy defects in CNTs are initially smaller and then exceed that of pristine CNTs as the pull-out distance of the CNT increases. The snapshots of the pull-out process depicted in Fig. 3.22 reveal that some of the epoxy molecules entered in the vacancy defective CNT

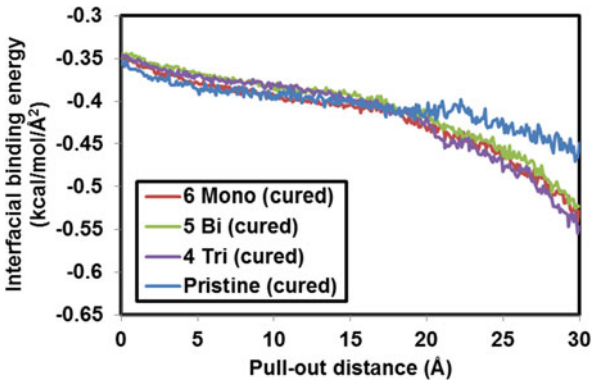


**Fig. 3.21** Variation in interfacial binding energy between vacancy defective CNTs and cured epoxy matrix with pull-out distance

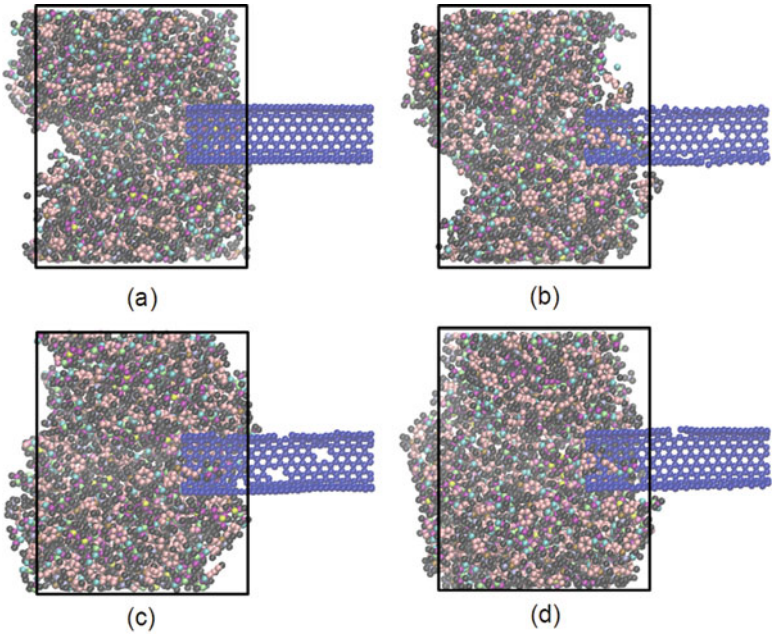


**Fig. 3.22** Cross sections of the pull-out processes for pristine and vacancy defective CNT in cured epoxy matrix at z = 30 Å: (**a**) pristine, (**b**) 6 monovacancy, (**c**) 10 bivacancy, and (**d**) 12 trivacancy

through their uncapped ends, leading to the enhancement of the interaction energy during the pull-out process. This results in a prominent increase in the interfacial binding energy of vacancy defective CNT during the pull-out process.

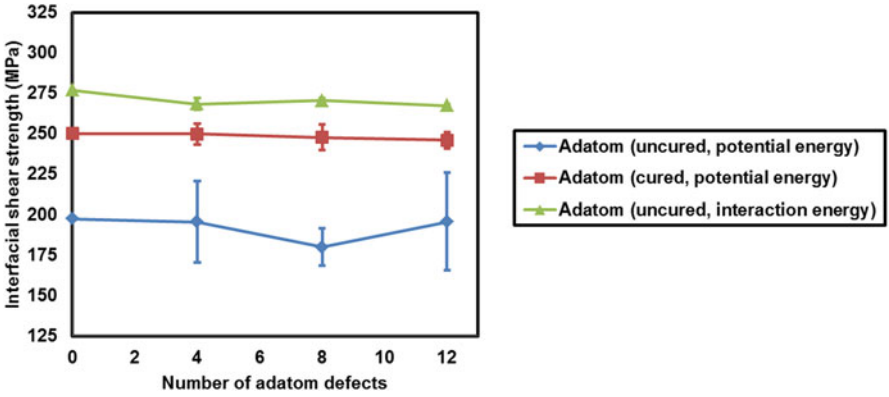


**Fig. 3.23** Variation in ISS with number of adatom defects

**Fig. 3.24** Relative concentrations of $sp^2$ carbon atoms for different adatoms after curing

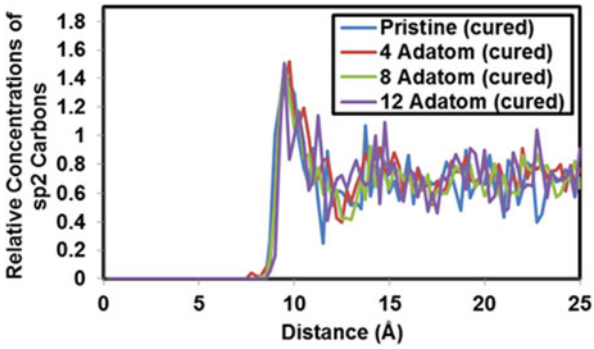


### 3.4.1.3 Effect of Carbon Adatom upon ISS

Unlike the cured cases of vacancy defects, adatom defects have only marginal influence on the ISS of the cured epoxy composites, as depicted in Fig. 3.23. This observation can be explained in terms of the rehybridization and the total number of carbon atoms in the adatom defective CNTs. Newly introduced carbon atoms rehybridize the adjacent carbon atoms and replace 2 $sp^2$ by 3 $sp^3$ carbon atoms. Although adatom defective CNTs have more carbon atoms, the unchanged ISS indicates that the interaction energy due to 3 $sp^3$ carbon atoms is similar to that due to 2 $sp^2$ carbon atoms. As showed in Fig. 3.24, the concentrations of $sp^2$ carbons are almost the same for different number of adatoms in the cured matrix. This also helps to shed light on the marginal influence of adatom defects. Additionally, it is evident from Fig. 3.23 that adatom defective CNTs embedded in the uncured system have very similar ISS, which is analogous to the uncured case of vacancy defects. We can also see that, without considering the matrix deformation energy, the method using the interaction energy still overestimates the ISS as expected.

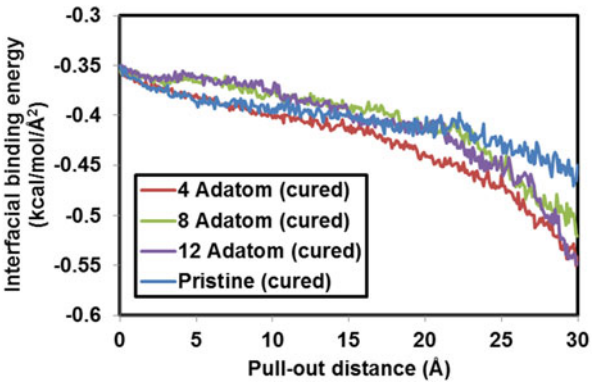


**Fig. 3.25** Variation in interfacial binding energy between adatom defective CNTs and cured epoxy matrix with pull-out distance

Our results are generally consistent with those reported by Yang et al. (2015), but their studies focused on thermoplastic (PE) systems without crosslinked structures. They found that adatom defects marginally increase the ISS by 1.14%, and they further demonstrated that the PE molecules are more effectively adsorbed on the sidewall of the adatom defective CNT than on the pristine CNT. Other researchers also studied the effect of other types of interstitial atoms on nanocomposites. For instance, Pavia and Curtin (2011) used MD simulations of a pull-out test to investigate the degree of interfacial coupling/adhesion between diamond matrix and CNTs. The interfacial behavior was captured using modified REBO potential through interstitial carbon atoms located in the interface, which can form and break bonds with both the matrix and CNT atoms. The total friction force is directly proportional to the number of interstitial carbon atoms along the interface, and the frictional stresses are high, reaching several GPa. Hence, the composite strength and toughness of such materials are expected to be greatly improved relative to materials with no covalent bonds at the interface. Pavia and Curtin (2013) further studied the response of CNT and interface to the matrix crack impingement as a function of the interface strength influenced by the number of interstitial carbon atoms. They simulated an annular crack propagating through a diamond matrix and impinging on the interface with a pristine SWCNT and DWCNT. The results showed that weaker interfaces fail in shear, while stronger interfaces do not fail, and instead the CNT fails once the stress acting on the CNT reaches its tensile strength. The transition from interface debonding to CNT fracture was found to depend on the interface and CNT strength.

Figure 3.25 shows the variations in the interfacial binding energies with the pull-out distance for the cured epoxy matrix. Analogous to the case of vacancy defects, the interfacial binding energies increase with the increase in the pull-out distance, and they further exceed that of pristine CNTs for larger pull-out distances. The prominent increase in the interfacial binding energy can be explained by the fact that carbon adatoms on the sidewalls of the CNTs act like a spike, protruding in the surrounding epoxy molecules, which tends to pull out epoxy molecules of the RVE during the pull-out process, as shown in Fig. 3.26.

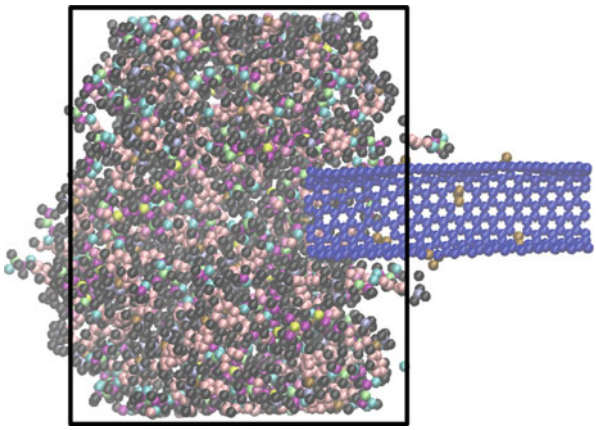

**Fig. 3.26** Cross section of the pull-out process for 12 adatom defective CNT in cured epoxy matrix at $z = 30$ Å

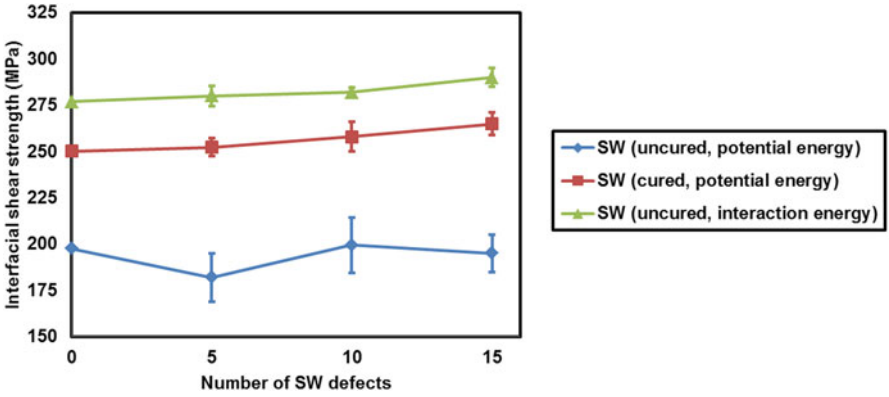


**Fig. 3.27** Variation in ISS with number of SW defects

### 3.4.1.4 Effect of SW Defect upon ISS

In contrast to the vacancy and adatom defects, the ISS of epoxy nanocomposite reinforced with CNTs containing SW defects increases as the number of SW defects increases for the cured epoxy systems, as depicted in Fig. 3.27. Note that the formation of SW defect involves neither missing carbon atoms nor the rehybridization of these atoms in the CNTs. In this case, four hexagons are transformed into two pentagons and two heptagons for a single SW defect. It may be observed from Fig. 3.27 that the increase in the ISS of the cured systems is 6.0%. Since the growth in the number of SW defects increases the concentrations of $sp^2$ carbons near the CNT (Fig. 3.28), it can be concluded that the increase in the ISS results from the increase in $\pi-\pi$ attractions at the CNT-matrix interface. In addition, the ISS in the uncured matrix tends to be unvaried. This again is caused by the relatively low shear strength of the uncured epoxy systems. Due to the lack

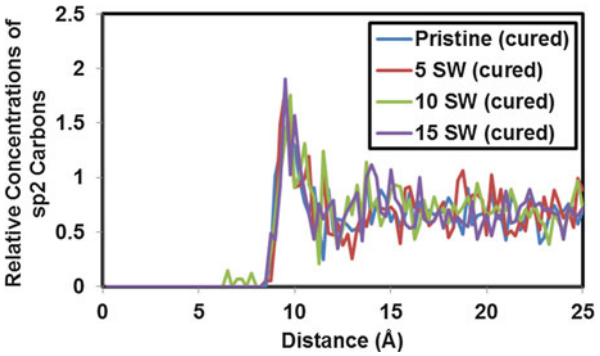


**Fig. 3.28** Relative concentrations of $sp^2$ carbon atoms for different SW defects after curing

of the energy expended in deforming the polymer during the pull-out test, it is expected that the ISS based on the interaction energy for the uncured systems is again overestimated in Fig. 3.27.

Our results are in agreement with the observation made by Yang et al. (2015), though their work was concerned with thermoplastic (PE). They studied the effect of SW defects on the ISS of SWCNT-PE composite and found that the percentage increase in the ISS ranged from 0.71% to 7.14%. Zhou and Shi (2003) helped to explain the increase in the ISS by using a first-principle discrete variational method to estimate the binding energy of foreign atoms attached to CNTs with and without an SW defect. They found that SW defective CNT improves the binding energy magnitude by about 0.5 eV for some foreign atoms compared with the pristine CNT. This would improve the adsorption of the polymer matrix onto the CNTs. However, the overall mechanical properties of SW defective CNT-reinforced composites degrade, since SW defects reduce the mechanical properties of CNTs. For instance, Mahboob and Islam (2013) studied the effect of SW defects on the mechanical properties of composites reinforced with SWCNTs using MD simulations. Their results showed that the longitudinal Young's modulus of the SWCNT-PE composites is strongly dependent on the number of SW defects and CNT volume fraction. They found that SW defects reduce the longitudinal Young's modulus of the SWCNT-PE composites by 12%. Sharma et al. (2014) also used MD simulations to investigate the effect of SW defects on the elastic stiffness of CNT-PP composites. They found that the percentage decrease in moduli is greater for CNTs with SW defects in comparison to vacancy defective CNTs, and one SW defect with 16% SWCNT volume fraction decreases both Young's modulus and shear modulus by 16% and 44%, respectively.

Figure 3.29 shows the variations in the interfacial binding energies for the SW defective CNTs in the cured epoxy matrix against the CNT pull-out distance. Unlike the vacancy and adatom defective cases, the magnitudes of the interfacial binding energies of this case are larger than that of the pristine CNTs, and the energy difference increases with the increase in the pull-out distance. This is attributed to the stronger adhesion effect of SW defective CNTs. Figure 3.30 shows the cross section of the cured CNT-epoxy nanocomposite. It can be observed from Fig. 3.30

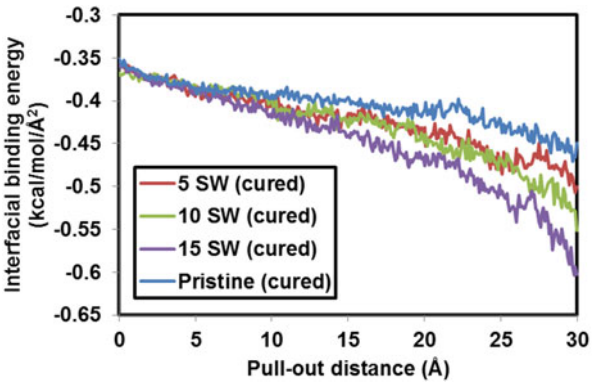


**Fig. 3.29** Variation in interfacial binding energy between SW defective CNTs and cured epoxy matrix with pull-out distance

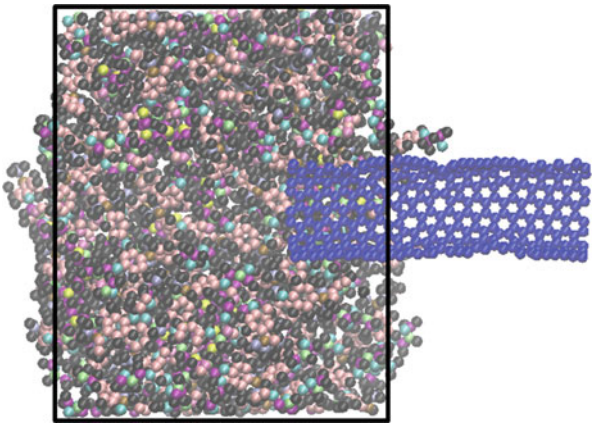

**Fig. 3.30** Cross section of the pull-out process for 12 SW defective CNT in cured epoxy matrix at z = 30 Å

that some epoxy molecules adjacent to the sidewall of SW defective CNT are pulled out together with the CNT leading to an enhanced CNT–matrix interaction energy. This increase in the interaction energy leads to the increased interfacial binding energy difference between SW defective and pristine CNTs.

#### 3.4.1.5 Effect of Phenyl Functional Group upon ISS

In this section, we establish the effect of functionalization on the ISS of CNT-epoxy nanocomposites. Figure 3.31 shows that the ISS increases dramatically with the increase in the number of the phenyl group functionalization on the sidewalls of the CNTs for the cured epoxy composites. Noteworthy is the fact that the carbon atoms of the CNTs are directly bonded to the phenyl group which changes the hybridization from $sp^2$ to $sp^3$, and this formation of the phenyl group functionalization adds more atoms to the original CNTs. Moreover, Fig. 3.32 shows that the relative concentrations of $sp^2$ carbons increase as the number of phenyl groups increases. This also results in the increase in the ISS induced by

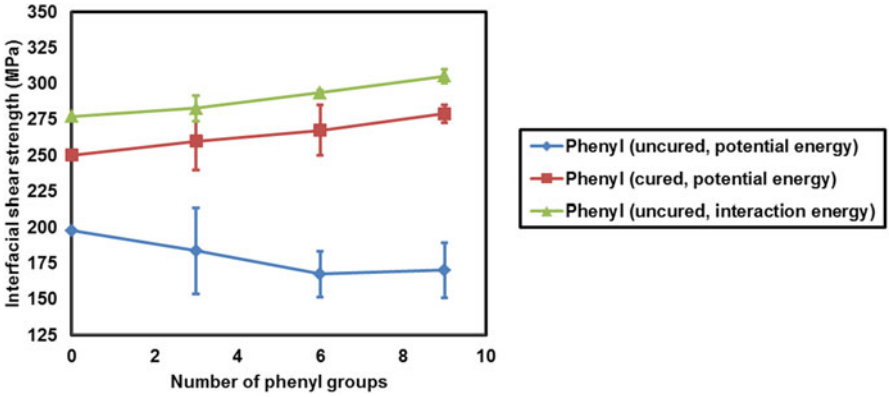


**Fig. 3.31** Variation in ISS with number of phenyl groups

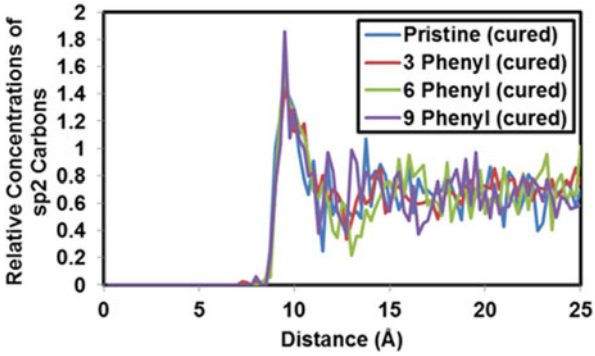


**Fig. 3.32** Relative concentrations of $sp^2$ carbon atoms for different phenyl groups after curing

Ω–Ω attractions. Therefore, the increased ISS is mainly attributed to the additional vdW interactions between the attached phenyl groups and the epoxy molecules. Unsurprisingly, phenyl functional groups do not improve the ISS of the uncured systems due to the same reasons mentioned above. As expected in Fig. 3.31, the negligence of the matrix deformation energy for the uncured systems results in the overestimation of ISS.

It can be observed from Fig. 3.31 that the ISS of the cured epoxy composites increases by 11.5% in comparison with the pristine CNT. Our results are also found to be generally comparable with those reported in the literature despite different matrix materials and simulation techniques (Fig. 3.33). However, most of them only paid attention to cured epoxies or thermoplastics (PE) with no crosslinked structures. For example, Sharma et al. (2015) examined the effect of functionalization using ethylene-di-amine (E-$NH_2$) functional group on the interfacial bonding characteristics of CNT-epoxy composite. They found that the amine functionalized SWCNT increases the ISS twice the pristine SWCNT. Xiao et al. (2015) studied the effects of different functionalization schemes on the interfacial strength of SWCNT-PE systems. They also found that the respective ISS is improved by 8.89%,

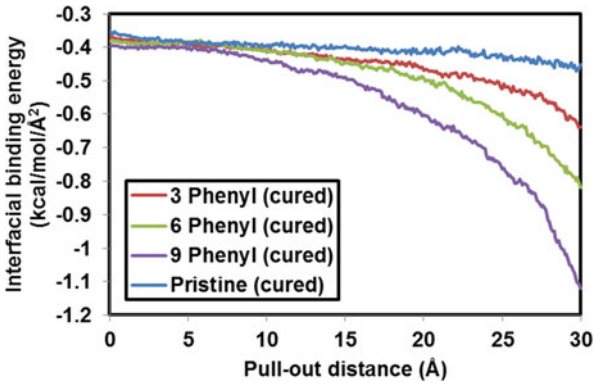


**Fig. 3.33** Variations in interfacial binding energy between functionalized CNTs and cured epoxy matrix with pull-out distance

12.22%, and 31.11% for three types of alkyl groups ($C_5H_{11}/C_{10}H_{21}/C_{15}H_{31}$). Zheng et al. (2008) studied the influence of chemical functionalization on the interfacial bonding characteristics of SWCNT-reinforced polymer composites using MM and MD simulations. The simulations showed that phenyl functional group occupying only 5% of the nanotube carbon atoms drastically increases the ISS by about 1000%. Zheng et al. (2009) also used pull-out simulations to investigate the interfacial bonding characteristics between SWCNTs, on which –COOH, $-CONH_2$, $-C_6H_{11}$, or $-C_6H_5$ groups were chemically attached, and the PE matrix. They found that the ISS for $-C_6H_{11}$ and $-C_6H_5$ functionalized groups increases 3 times and 17 times compared with the pristine SWCNT, whereas the ISS for –COOH and $-CONH_2$ functionalized groups has an almost identical value to that of the pristine SWCNT. Chen et al. (2008) performed MD simulations to study the effect of chemical functionalization on the wrapping ability of the polyphenylacetylene (PPA) polymer chains. They concluded that the SWCNTs modified by methyl or phenyl groups can be well-wrapped by PPA, while the SWCNTs modified by other types of groups such as hydroxyl or –F cannot. The results also indicated that the interaction energy between the SWCNTs and PPA increases with the increase in the concentration of functionalized groups.

Unlike conventional fiber-reinforced polymer composites, CNTs offer large areas for load transfer. However, due to their unique electrical and structural properties, CNTs tend to agglomerate and aggregate and does not bond strongly with their host matrix. Therefore, the potential increase in mechanical properties of CNT-reinforced composites is limited by the degree of interfacial stress transfer. We can see from the above-mentioned results that surface modification of CNTs enhances the nanotube-matrix interfacial bonding. Besides, the modifications can also improve the CNTs' solubility and dispersibility in their nanocomposites by acting as shells to separate CNTs. Many researchers (Park and Bandaru 2010; Zou et al. 2008; Zhu et al. 2004; Tseng et al. 2007; Sun et al. 2008; Chen et al. 2006; Bekyarova et al. 2007) have investigated the effects of CNT functionalization on the mechanical properties of nanocomposites. They found that functionalized CNTs enhance the elastic modulus and tensile strength of nanocomposites, while other structural characteristics such as toughness decrease.

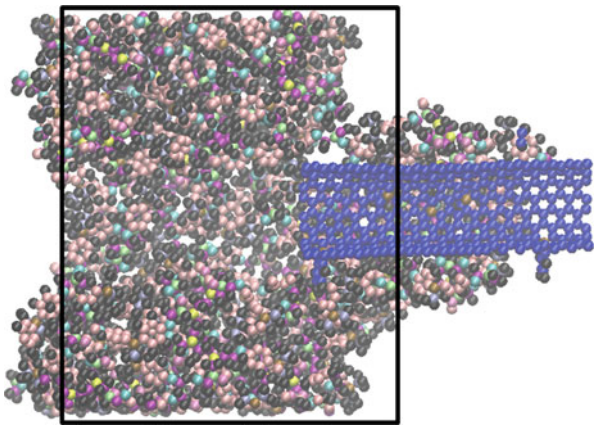

**Fig. 3.34** Cross section of the pull-out process for 9 phenyl group functionalized CNT in cured epoxy matrix at z = 30 Å

The interfacial binding energies of the functionalized CNTs for the cured epoxy systems (depicted in Fig. 3.41) are initially larger and present more prominent energy changes than that of the pristine CNTs as the pull-out process progresses. Similar to the SW defect, the initial larger interfacial binding energy is attributed to the stronger adsorption effect of the functionalized CNTs. Furthermore, the presence of a greater number of phenyl groups introduces additional molecular interactions, leading to a dramatic increase in the interfacial binding energy. It may be observed from Fig. 3.34 that a significant portion of the epoxy molecules are pulled out with the CNT during the pull-out process, indicating a stronger adhesion of the functionalized CNT with the epoxy matrix.

## *3.4.2 Analysis of Compressive Load Simulation*

### 3.4.2.1 Effect of Vacancy Defect upon Freestanding SWCNTs

This section focuses on exploring the effect of different vacancy defects on the buckling behavior of freestanding SWCNTs. Based on the foregoing definitions of Sect. 3.3.2.2, buckling strain and buckling load of the pristine SWCNTs are obtained in Table 3.4. We can see that the armchair SWCNT (7, 7) possesses very similar buckling capacity compared to the zigzag SWCNT (12, 0) with the same length and diameter. However, the buckling strain of the armchair SWCNT (9, 9) is smaller than that of the armchair SWCNT (7, 7) despite the same aspect ratio. The reverse is seen when the buckling load is considered. Our results are consistent with those reported by other researchers. For instance, Wang et al. (2014) used MD simulations to study a broad range of armchair SWCNTs based on AIREBO potential. Their results showed that the buckling strain is in the range of 0.0131–0.0734 and the buckling load varies from 18.6 to 86.8 nN. Zhang et al. (2009c)

**Table 3.4** Comparison of buckling behavior of freestanding defective SWCNTs against the buckling behavior of freestanding pristine SWCNTs

| CNT type | CNT configuration | Buckling strain | % reduction w.r.t. pristine CNT | Buckling load (Kcal/mol-Å) | % reduction w.r.t. pristine CNT |
|---|---|---|---|---|---|
| (7, 7) | 0A | 0.095 | | 1276 (89 nN) | |
| | 1A | 0.091 | 4.3 | 1208 | 5.3 |
| | 1B | 0.084 | 11.3 | 1178 | 7.7 |
| | 1C | 0.090 | 5.0 | 1140 | 10.7 |
| | 2B | 0.094 | 0.7 | 1134 | 11.1 |
| | 2C | 0.090 | 5.8 | 1215 | 4.8 |
| | 3A | 0.092 | 3.0 | 1094 | 14.2 |
| | 3B | 0.085 | 10.2 | 1145 | 10.2 |
| | 1SW-A | 0.093 | 2.5 | 1130 | 11.5 |
| | 1SW-B | 0.092 | 3.5 | 1224 | 4.0 |
| (9, 9) | 0A | 0.091 | | 1560 (108 nN) | |
| | 1A | 0.086 | 4.7 | 1520 | 2.6 |
| | 1B | 0.086 | 5.4 | 1575 | –0.9 |
| | 1C | 0.087 | 4.3 | 1566 | –0.3 |
| | 2B | 0.089 | 1.6 | 1513 | 3.0 |
| | 2C | 0.087 | 3.7 | 1543 | 1.1 |
| | 3A | 0.087 | 4.2 | 1418 | 9.1 |
| | 3B | 0.086 | 4.8 | 1556 | 0.3 |
| | 1SW-A | 0.085 | 6.3 | 1489 | 4.6 |
| | 1SW-B | 0.089 | 1.4 | 1506 | 3.5 |
| (12, 0) | 0A | 0.094 | | 1222 (85 nN) | |
| | 1A | 0.090 | 4.6 | 1199 | 1.8 |
| | 1B | 0.083 | 11.7 | 1148 | 6.0 |
| | 1C | 0.087 | 7.3 | 1104 | 9.7 |
| | 2B | 0.090 | 4.3 | 1163 | 4.8 |
| | 2C | 0.091 | 3.6 | 1174 | 3.9 |
| | 3A | 0.093 | 0.8 | 1122 | 8.2 |
| | 3B | 0.085 | 9.7 | 1117 | 8.6 |
| | 1SW-A | 0.097 | –3.1 | 1021 | 16.4 |
| | 1SW-B | 0.091 | 3.3 | 1138 | 6.8 |

and Wang et al. (2010) also found that the nonlocal cylindrical shell model predicts comparable results compared with MD simulation results for SWCNTs with short aspect ratios ($L/d < 8$). The buckling strain can reach up to 0.1 when the aspect ratio is close to 5. Zhang et al. (2006b) investigated the effect of chirality on the buckling behavior of SWCNTs. They reported that the influence of chirality can be neglected for SWCNTs with relatively larger chiral angles.

Next, we turn our attention to the effect of vacancy defects on the buckling behavior of freestanding CNTs. Fig. 3.35 shows the strain energy-strain and the

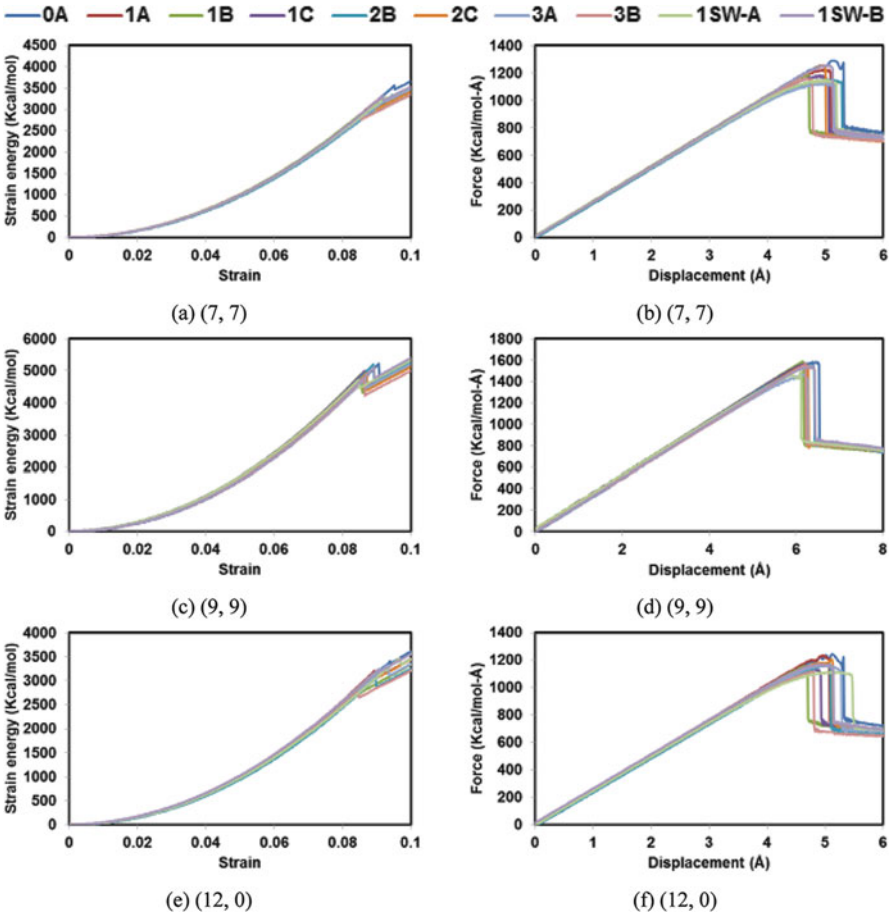


**Fig. 3.35** (**a**, **c**, **e**) Strain energy-strain curves; (**b**, **d**, **f**) force-displacement curves for different freestanding defective SWCNTs

force-displacement curves for the armchairs (7, 7), (9, 9) and zigzag (12, 0) defective SWCNTs. The buckling strain and buckling load obtained based on Fig. 3.35 are compared with the pristine SWCNTs and are tabulated in Table 3.4. The buckling modes of different defective SWCNTs are depicted in Fig. 3.14. It is interesting to observe that the buckling modes of various defective SWCNTs are similar to that of the pristine SWCNTs where one flattening is formed at the mid-length. In order to study the effect of missing atoms, only the symmetric vacancies (1A), (2B), and (3A) are analyzed here. It can also be seen from the results that the monovacancy (1A) has the lowest buckling strain, but increasing the number of missing atoms decreases the buckling load irrespective of the chirality of SWCNTs. It is easy to understand that monovacancy is superior to bivacancy and trivacancy because the defective area induced by the monovacancy is obviously smaller.

However, by taking a closer look at the buckling shapes in Fig. 3.14, monovacancy tends to develop a flattening kink close to the defect, leading to excessive stress concentration. This makes the local buckling occur easily at the defect position.

The vacancies (2B), (2C), (3A), and (3B) are considered next to study the effect of symmetric and asymmetric configurations on the buckling behavior. The results for armchair SWCNTs in Table 3.4 indicate that asymmetric vacancies, compared with symmetric vacancies, cause a higher reduction in the buckling strain but not in the buckling load. This can be explained by Fig. 3.14 that asymmetric vacancies develop flattening kinks near the defect, which expedites the occurrence of the buckling. Those kinks serve to withstand more loads and increase the buckling load accordingly. However, a difference can be observed between armchair and zigzag SWCNTs. For zigzag SWCNTs, asymmetric vacancies reduce both the buckling strain and buckling load, and the buckling behavior is most affected by trivacancies. This may be due to the special bond structure of zigzag CNTs. The third focus here is on the effect of vacancy distribution on the buckling behavior of CNTs. Hence, we studied the nanotubes with vacancies (1B) and (1C). The results in Table 3.4 indicate that the vacancy (1B) has lower buckling strain but higher buckling load than the vacancy (1C). As shown in Fig. 3.14, this again occurs as a result of the positions of kinks relative to the defects. Since the monovacancies in (1B) locate exactly opposite to each other, the kinks tend to develop near the defects, leading to excessive stress concentration. This makes the vacancy (1B) easier to buckle than the vacancy (1C) but allows the vacancy (1B) to withstand higher loads for both armchair and zigzag SWCNTs.

#### 3.4.2.2 Effect of Missing Atoms upon Embedded SWCNTs

In this section, we examine the effect of missing atoms on the buckling behavior of SWCNTs embedded in the epoxy matrix. Embedded pristine SWCNTs are initially taken as a reference to compare with freestanding pristine SWCNTs. Figure 3.13a, b shows the strain energy-strain and the force-displacement curves for the embedded pristine SWCNTs in comparison with pristine stand-alone SWCNTs. Table 3.5 shows the buckling strain and buckling load obtained from Fig. 3.13. Interestingly, the surrounding epoxy matrix significantly reduces resistance to buckling of SWCNTs by up to 43%. The reason for the embedded CNTs to have lower resistance to buckling than their freestanding counterparts is the uneven atomic forces exerted by the surrounding matrix atoms. These atomic forces deform the CNTs unevenly, leading to easier occurrence of buckling. The buckled shapes in Fig. 3.36 show that the embedded pristine CNT displays only pure shell-like buckling modes, where two flattenings referred to as “fins” by Yakobson et al. (1996) that are perpendicular to each other are formed. This is because the atomic forces exerted by the surrounding matrix atoms provide some form of confinement, preventing the CNTs from buckling sideway. The buckling shape transformation may also lead to the reduction in the buckling behavior.

**Table 3.5** Comparison of buckling behavior of embedded defective SWCNTs against the buckling behavior of embedded pristine SWCNTs

| Embedded CNT type | CNT configuration | Buckling strain | % reduction w.r.t. pristine CNT | Buckling load (Kcal/mol-Å) | % reduction w.r.t. pristine CNT |
|---|---|---|---|---|---|
| (7, 7) | 0A | 0.071 | | 979 (68 nN) | |
| | 1A | 0.051 | 28.9 | 710 | 27.5 |
| | 1B | 0.050 | 30.0 | 676 | 30.9 |
| | 1C | 0.053 | 25.0 | 629 | 35.7 |
| | 2B | 0.054 | 24.4 | 712 | 27.3 |
| | 2C | 0.047 | 34.5 | 629 | 35.7 |
| | 3A | 0.057 | 20.1 | 756 | 22.7 |
| | 3B | 0.043 | 40.2 | 576 | 41.2 |
| | 1SW-A | 0.059 | 17.0 | 784 | 19.9 |
| | 1SW-B | 0.052 | 27.4 | 690 | 29.6 |
| (9, 9) | 0A | 0.052 | | 912 (63 nN) | |
| | 1A | 0.043 | 18.4 | 733 | 19.6 |
| | 1B | 0.042 | 19.4 | 733 | 19.6 |
| | 1C | 0.049 | 7.3 | 768 | 15.8 |
| | 2B | 0.044 | 15.9 | 771 | 15.4 |
| | 2C | 0.045 | 15.1 | 762 | 16.4 |
| | 3A | 0.044 | 15.5 | 631 | 30.8 |
| | 3B | 0.043 | 17.9 | 722 | 20.8 |
| | 1SW-A | 0.048 | 7.6 | 866 | 5.1 |
| | 1SW-B | 0.042 | 19.5 | 749 | 17.9 |
| (12, 0) | 0A | 0.070 | | 959 (67 nN) | |
| | 1A | 0.053 | 24.9 | 711 | 25.9 |
| | 1B | 0.042 | 39.7 | 564 | 41.2 |
| | 1C | 0.053 | 24.1 | 680 | 29.1 |
| | 2B | 0.052 | 25.9 | 678 | 29.3 |
| | 2C | 0.049 | 30.6 | 614 | 36.0 |
| | 3A | 0.052 | 26.2 | 656 | 31.6 |
| | 3B | 0.046 | 35.1 | 605 | 36.9 |
| | 1SW-A | 0.056 | 20.7 | 750 | 21.8 |
| | 1SW-B | 0.051 | 26.9 | 699 | 27.2 |

We now proceed to study the buckling of nanotubes with different missing atoms (1A), (2B), and (3A) embedded in the epoxy matrix. Figure 3.37 shows the strain energy-strain and the load-displacement plots for the defective embedded nanotubes discussed above. As demonstrated in Table 3.5, both the buckling strain and buckling load increase as the number of missing atoms increases. The maximum reductions in the buckling strain and buckling load are 29% and 31%, respectively, which is also higher than what we observed in freestanding defective armchair SWCNTs. This may be explained by the buckled shapes depicted in Fig. 3.36; the

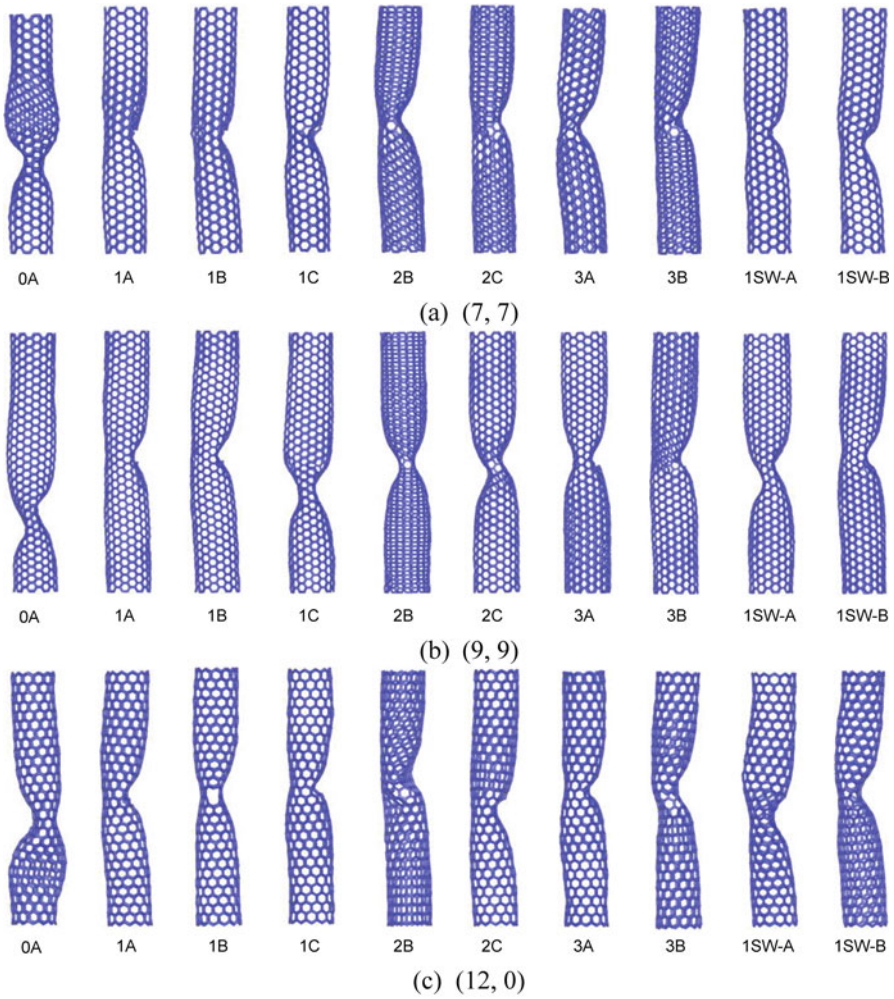


**Fig. 3.36** Buckling mode shapes of the embedded SWCNTs (**a**), (7, 7), (**b**) (9, 9) and (**c**) (12, 0)

first buckling mode occurs only on one side of the SWCNTs near the missing atoms, which are neither beam-like nor shell-like buckling modes. These buckled modes depicted in Fig. 3.36 result in excessive stress concentration for monovacancies, leading to a minima of both the buckling strain and the buckling load. However, an exception can be observed for the (9, 9) SWCNT with the trivacancy (3A) which has the lowest buckling load. A closer look at the buckled shape of (3A) reveals that it displays the shell-like buckling mode due to its longer nanotube. This may contribute to a reduction in the buckling load. In contrast to the embedded defective armchair SWCNTs, Table 3.5 shows that both the buckling strain and buckling load for the embedded defective zigzag SWCNTs decrease with an increasing number of

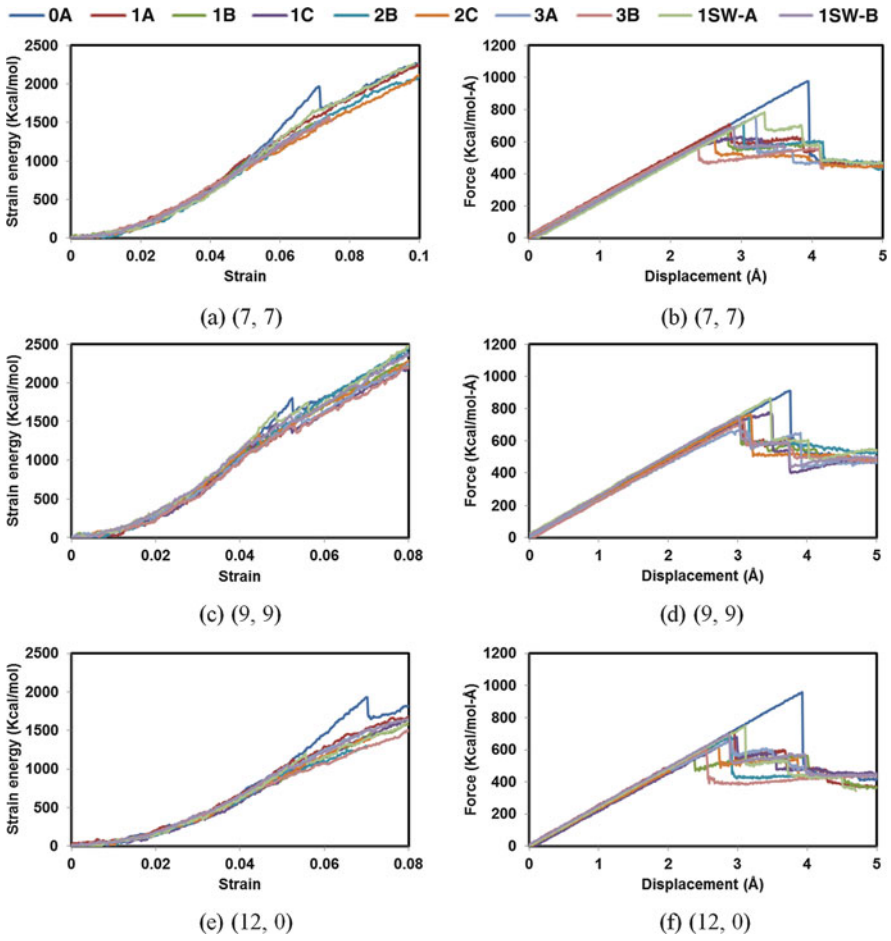


**Fig. 3.37** (**a**, **c**, **e**) Strain energy-strain curves; (**b**, **d**, **f**) force-displacement curves for different embedded defective SWCNTs

missing atoms. This reveals that more missing atoms in zigzag SWCNTs have more negative influence on the buckling behavior despite similar buckling shapes to the embedded defective armchair SWCNTs.

#### 3.4.2.3 Effect of Vacancy Symmetry and Distribution upon Embedded SWCNTs

First, let us focus on the effect of symmetric and asymmetric vacancy configurations (2B), (2C), (3A), and (3B) on the buckling behavior of embedded SWCNTs. It can be seen in Table 3.5 that asymmetric vacancies generally reduce the buckling

behavior of both armchair and zigzag SWCNTs when compared with symmetric vacancies. This is different from corresponding freestanding armchair nanotubes, where the buckling load is increased due to the presence of kinks in asymmetric vacancies. Compared with the symmetric vacancies, asymmetric vacancies further reduce the buckling strain and buckling load by 5–20%. The reason for the discrepancies may be because embedded defective SWCNTs display different buckling modes in Fig. 3.36, where the nanotubes only narrow at one side while keeping their cylindrical shapes at the other side. The position of the narrowing is close to the vacancies. However, due to the longer length in (9, 9) nanotubes, the buckling behavior of the bivacancies (2B) and (2C) is very similar to each other. They tend to buckle in a shell-like way similar to the embedded pristine SWCNTs.

Second, let us devote our attention to the effect of vacancy distribution (1B) and (1C) on the buckling behavior of embedded SWCNTs. Unlike the case of freestanding SWCNTs, both the buckling strain and buckling load of the SWCNTs containing the vacancy (1C) (see Table 3.5) are increased when compared with those of the SWCNTs containing the vacancy (1B) irrespective of the chirality of SWCNTs. This may be due to the different buckling modes presented in Fig. 3.36, which are similar to the previously investigated embedded SWCNTs. It is worth noting that there exists an anomaly for the buckling load of the (7, 7) SWCNT with the vacancy (1C). It is clear from Fig. 3.37b that the (7, 7) SWCNT with the vacancy (1C) does not show an abrupt drop in the load-displacement curve. We can see that the vacancy in the (7, 7) SWCNT helps to delay the occurrence of buckling, which increases the buckling strain, although the buckling load is still relatively low.

#### 3.4.2.4 Effect of SW Defect upon Freestanding and Embedded SWCNTs

As shown in Table 3.4, the SW defects reduce the buckling capacity of SWCNTS in general. Similar to the vacancy symmetry of freestanding SWCNTs, asymmetry results in lower buckling strain but generally requires higher buckling load irrespective of the chirality of SWCNTs. It is noted in Fig. 3.14 that kinks tend to locate close to the asymmetric SW defect (1SW-B). This leads to excessive stress concentration, which expedites the occurrence of the buckling, and the kinks help to withstand more loads, increasing the buckling load.

The second part of this section studies the SW defects (1SW-A) and (1SW-B) of embedded SWCNTs. The embedded SWCNTs containing asymmetric SW defects (1SW-B) have lower buckling strain and buckling load (see Table 3.5) regardless of the chirality of SWCNTs. The maximum decreases in the buckling strain and buckling load are 22% and 30%, respectively, which are higher than the reduction found in their freestanding counterparts. The buckling modes for the embedded SW defective SWCNTs are similar to other embedded SWCNTs. Moreover, if we compare the buckling behavior of SW defective SWCNTs with vacancy defective SWCNTs in Table 3.5, it is evident that the SW defects (1SW-A) have the least effect on the buckling behavior of embedded SWCNTs. By contrast, the degradation effect of embedded SW defective SWCNTs (1SW-B) is very similar to the corresponding embedded vacancy defective SWCNTs.

## 3.5 Conclusions

In the first part of the chapter, we provided a detailed account of the effect of intrinsic defects and functionalization in CNTs upon the interfacial properties of CNT-reinforced composites. Different modeling and calculation techniques pertinent to CNT pull-out tests are presented, and proper selection of the simulation parameters are discussed. The main conclusions of the pull-out studies are summarized as follows:

(1) Deformation energy of defective CNT-reinforced polymers needs to be taken into account to obtain accurate ISS of uncured epoxy polymers.
(2) Among all the defects and functionalization, the influence of vacancy defects on the ISS was found to be significant. Moreover, the influence of the same number of missing atoms on the ISS was found to be almost identical.
(3) Adatom defects have only marginal effect on the ISS. The ISS increased for the cured epoxy systems as the number of SW defects increases.
(4) In the case of phenyl groups, the ISS of the cured systems increases due to the additional vdW interactions generated as a result of functionalization.
(5) Uncured epoxy systems have lower ISS than cured ones, and defects and functionalization do not affect the ISS very much.

The second part of this chapter is to conduct a quantitative analysis of the degradation of buckling behavior due to various types of defects (vacancy and SW defect) using MD simulations. Both freestanding and embedded SWCNTs with different size and chirality ((7, 7), (9, 9), and (12, 0)) were simulated and the results were compared with each other to understand the effect of epoxy matrix atoms. To understand the factors affecting the degree of degradation of buckling behavior, we investigated several defect configurations including the number of missing atoms, symmetry, and vacancy distribution. The main conclusions of the compressive load studies are summarized as follows:

(1) Defects generally either increase or decrease the buckling strain of freestanding and embedded SWCNTs at the same time. However, compared with those of freestanding SWCNTs, the buckling strain and buckling load for embedded SWCNTs are reduced when SWCNTs are confined in an epoxy matrix.
(2) Increasing number of missing atoms generally reduces the buckling load of freestanding SWCNTs; however, a higher number of missing atoms increases the buckling load of embedded armchair SWCNTs because the compressive force is partly supported by the kinks developed during buckling.
(3) The buckling load of freestanding SWCNTs is increased by asymmetric vacancy and SW defects, but the same defects decrease the buckling load of embedded SWCNTs due to different buckling modes.
(4) Freestanding SWCNTs containing asymmetric vacancy distribution have lower buckling load because of the positions of kinks relative to the defects, but the opposite is true for embedded SWCNTs in general.

To sum up our findings, the defective and functionalized CNTs in cured epoxy systems can lead to increased ISS and improved load transferability. However, the presence of defects in the CNTs would ultimately result in a decrease in the effective elastic properties of the nanocomposites. A trade-off between the degradation in the mechanical properties of the defective CNTs and the improvement in the ISS of the resulting multifunctional nanocomposite systems should be carefully considered and addressed. Also, different buckling behaviors are seen between freestanding and embedded CNTs in the presence of various defects. We cannot rely on defect studies focusing only on the buckling of freestanding CNTs when designing CNT-reinforced nanocomposites. It is hoped that the findings in this chapter could contribute to deciding the expected strength from a certain sample of CNT-reinforced nanocomposites, if the degradation of buckling strain and buckling load due to different defects is known. Therefore, this chapter is also believed to be helpful in designing multifunctional nanocomposites.

**Acknowledgements** The authors wish to acknowledge the financial support provided by the Natural Sciences and Engineering Council of Canada (NSERC) and the Discovery Accelerator Supplement.

## References

Ajayan, P., Stephan, O., Colliex, C., Trauth, D.: Aligned carbon nanotube arrays formed by cutting a polymer resin—nanotube composite. Science. **265**, 1212–1212 (1994)
Alian, A., Kundalwal, S., Meguid, S.: Compos. Struct. **131**, 545–555 (2015a)
Alian, A., Kundalwal, S., Meguid, S.: Polymer. **70**, 149–160 (2015b)
Al-Ostaz, A., Pal, G., Mantena, P.R., Cheng, A.: J. Mater. Sci. **43**, 164–173 (2008)
Barber, A.H., Cohen, S.R., Wagner, H.D.: Appl. Phys. Lett. **82**, 4140–4142 (2003)
Barber, A.H., Cohen, S.R., Kenig, S., Wagner, H.D.: Compos. Sci. Technol. **64**, 2283–2289 (2004)
Barber, A.H., Cohen, S.R., Eitan, A., Schadler, L.S., Wagner, H.D.: Adv. Mater. **18**, 83–87 (2006)
Bekyarova, E., Thostenson, E.T., Yu, A., Itkis, M.E., Fakhrutdinov, D., Chou, T.-W., Haddon, R.C.: J. Phys. Chem. C. **111**, 17865–17871 (2007)
Bohlén, M., Bolton, K.: Comput. Mater. Sci. **68**, 73–80 (2013)
Brenner, D.W., Shenderova, O.A., Harrison, J.A., Stuart, S.J., Ni, B., Sinnott, S.B.: J. Phys. Condens. Matter. **14**, 783 (2002)
Chandra, N., Namilae, S.: Mech. Adv. Mater. Struct. **13**, 115–127 (2006)
Charlier, J.-C.: Acc. Chem. Res. **35**, 1063–1069 (2002)
Chen, W., Auad, M.L., Williams, R.J.J., Nutt, S.R.: Eur. Polym. J. **42**, 2765–2772 (2006)
Chen, H., Xue, Q., Zheng, Q., Xie, J., Yan, K.: J. Phys. Chem. C. **112**, 16514–16520 (2008)
Chen, X., Zheng, M., Park, C., Ke, C.: Small. **9**, 3345–3351 (2013)
Chen, X., Zhang, L., Zheng, M., Park, C., Wang, X., Ke, C.: Carbon. **82**, 214–228 (2015)
Cheng, Q., Wang, X.X., Ni, N.G.: Molecular dynamics simulation for compressive mechanics properties of SWCNT with random distributed vacancies. In: Bai, C., Xie, S., Zhu, X. (eds.) Nanoscience and Technology, Pts 1 and 2, pp. 1161–1164 (2007)
Chowdhury, S.C., Okabe, T.: Compos. Part A Appl. Sci. Manufacturing. **38**, 747–754 (2007)
Chowdhury, S.C., Okabe, T., Nishikawa, M.: J. Nanosci. Nanotechnol. **10**, 739–745 (2010)
Chua, P.S., Piggott, M.R.: Compos. Sci. Technol. **22**, 33–42 (1985)
Collins, P.G.: Oxford Handbook of Nanoscience and Technology: Frontiers and Advances (2010)
Cooper, C.A., Cohen, S.R., Barber, A.H., Wagner, H.D.: Appl. Phys. Lett. **81**, 3873–3875 (2002)

Cox, H.L.: British J. Appl. Phys. **3**, 72 (1952)
Dai, H., Hafner, J.H., Rinzler, A.G., Colbert, D.T., Smalley, R.E.: Nature. **384**, 147–150 (1996)
Dauber-Osguthorpe, P., Roberts, V.A., Osguthorpe, D.J., Wolff, J., Genest, M., Hagler, A.T.: Proteins Structure Function Bioinformatics. **4**, 31–47 (1988)
Desai, A.V., Haque, M.A.: Thin-Walled Struct. **43**, 1787–1803 (2005)
Frankland, S., Caglar, A., Brenner, D., Griebel, M.: J. Phys. Chem. B. **106**, 3046–3048 (2002)
Ganesan, Y., Peng, C., Lu, Y., Loya, P.E., Moloney, P., Barrera, E., Yakobson, B.I., Tour, J.M., Ballarini, R., Lou, J.: ACS Appl. Mater. Interfaces. **3**, 129–134 (2011)
Ganesan, Y., Salahshoor, H., Peng, C., Khabashesku, V., Zhang, J., Cate, A., Rahbar, N., Lou, J.: J. Appl. Phys. **115**, 224305 (2014)
Gao, X.L., Li, K.: Int. J. Solids Struct. **42**, 1649–1667 (2005)
Gou, J.H., Minaie, B., Wang, B., Liang, Z.Y., Zhang, C.: Comput. Mater. Sci. **31**, 225–236 (2004)
Gou, J., Liang, Z., Zhang, C., Wang, B.: Compos. Part B Eng. **36**, 524–533 (2005)
Hao, X., Qiang, H., Yao, X.: Compos. Sci. Technol. **68**, 1809–1814 (2008)
Hashimoto, A., Suenaga, K., Gloter, A., Urita, K., Iijima, S.: Nature. **430**, 870–873 (2004)
Humphrey, W., Dalke, A., Schulten, K.: J. Mol. Graph. **14**, 33–38 (1996)
Iijima, S.: Nature. **354**, 56–58 (1991)
Iijima, S., Brabec, C., Maiti, A., Bernholc, J.: J. Chem. Phys. **104**, 2089–2092 (1996)
Jang, C., Lacy, T.E., Gwaltney, S.R., Toghiani, H., Pittman Jr., C.U.: Polymer. **54**, 3282–3289 (2013)
Joshi, U.A., Sharma, S.C., Harsha, S.P.: Comput. Mater. Sci. **50**, 3245–3256 (2011)
Kitipornchai, S., He, X., Liew, K.: J. Appl. Phys. **97**, (2005)
Kulathunga, D.D.T.K., Ang, K.K.: Comput. Mater. Sci. **81**, 233–238 (2014)
Kulathunga, D.D.T.K., Ang, K.K., Reddy, J.N.: J. Phys. Condens. Matter. **22**, (2010)
Kumar, A., Sundararaghavan, V., Browning, A.R.: Modell. Simulation Mater. Sci. Eng. **22**, 025013 (2014)
Lau, K.-T.: Chem. Phys. Lett. **370**, 399–405 (2003)
Lenosky, T., Gonze, X., Teter, M., Elser, V.: Energetics of negatively curved graphitic carbon. Nature. **355**, 333–335 (1992)
Li, C., Chou, T.-W.: J. Nanosci. Nanotechnol. **3**, 423–430 (2003a)
Li, C., Chou, T.-W.: Int. J. Solids Struct. **40**, 2487–2499 (2003b)
Li, K., Saigal, S.: Mater. Sci. Eng. A. **457**, 44–57 (2007)
Li, Y., Liu, Y., Peng, X., Yan, C., Liu, S., Hu, N.: Comput. Mater. Sci. **50**, 1854–1860 (2011)
Li, C., Medvedev, G.A., Lee, E.-W., Kim, J., Caruthers, J.M., Strachan, A.: Polymer. **53**, 4222–4230 (2012)
Liao, K., Li, S.: Appl. Phys. Lett. **79**, 4225–4227 (2001)
Liew, K.M., He, X.Q., Kitipornchai, S.: Proc. R. Soc. Math. Phys. Eng. Sci. **461**, 3785–3805 (2005)
Liu, L., Barber, A.H., Nuriel, S., Wagner, H.D.: Adv. Funct. Mater. **15**, 975–980 (2005)
Liu, J.Q., Xiao, T., Liao, K., Wu, P.: Nanotechnology. **18**, 165701 (2007)
Lourie, O., Wagner, H.D.: Appl. Phys. Lett. **73**, 3527–3529 (1998)
Lourie, O., Wagner, H.: Compos. Sci. Technol. **59**, 975–977 (1999)
Lourie, O., Cox, D., Wagner, H.: Phys. Rev. Lett. **81**, 1638 (1998)
Mahboob, M., Islam, M.Z.: Comput. Mater. Sci. **79**, 223–229 (2013)
Martínez, L., Andrade, R., Birgin, E.G., Martínez, J.M.: J. Comput. Chem. **30**, 2157–2164 (2009)
Meguid, S.A., Sun, Y.: Mater. Des. **25**, 289–296 (2004)
Meguid, S.A., Wernik, J.M., Cheng, Z.Q.: Int. J. Solids Struct. **47**, 1723–1736 (2010)
Meyer, J.C., Kisielowski, C., Erni, R., Rossell, M.D., Crommie, M., Zettl, A.: Nano Lett. **8**, 3582–3586 (2008)
Motevalli, B., Montazeri, A., Liu, J.Z., Rafii-Tabar, H.: Comput. Mater. Sci. **79**, 619–626 (2013)
Namilae, S., Chandra, N.: Compos. Sci. Technol. **66**, 2030–2038 (2006)
Nardelli, M.B., Yakobson, B.I., Bernholc, J.: Phys. Rev. Lett. **81**, 4656 (1998)
Natsuki, T., Wang, F., Ni, Q.Q., Endo, M.: J. Mater. Sci. **42**, 4191–4196 (2007)
Newcomb, B.A., Chae, H.G., Gulgunje, P.V., Gupta, K., Liu, Y., Tsentalovich, D.E., Pasquali, M., Kumar, S.: Polymer. **55**, 2734–2743 (2014)

Pan, Z.W., Xie, S.S., Lu, L., Chang, B.H., Sun, L.F., Zhou, W.Y., Wang, G., Zhang, D.L.: Appl. Phys. Lett. **74**, 3152–3154 (1999)
Park, S.H., Bandaru, P.R.: Polymer. **51**, 5071–5077 (2010)
Parvaneh, V., Shariati, M., Sabed, A.M.M.: Eur. J. Mech. Solids. **28**, 1072–1078 (2009)
Pavia, F., Curtin, W.A.: Acta Mater. **59**, 6700–6709 (2011)
Pavia, F., Curtin, W.A.: J. Mech. Phys. Solids. **61**, 1971–1982 (2013)
Plimpton, S.: J. Comput. Phys. **117**, 1–19 (1995)
Poelma, R.H., Sadeghian, H., Koh, S., Zhang, G.Q.: Microelectronics Reliability. **52**, 1279–1284 (2012)
Qian, D., Dickey, E.C.: J. Microsc. **204**, 39–45 (2001)
Qian, D., Dickey, E.C., Andrews, R., Rantell, T.: Appl. Phys. Lett. **76**, 2868–2870 (2000)
Quek, M.Y.: Int. J. Adhesion Adhesives. **22**, 303–310 (2002)
Ranjbartoreh, A.R., Wang, G.: Nanoscale Res. Lett. **6**, (2011)
Roy, D., Bhattacharyya, S., Rachamim, A., Plati, A., Saboungi, M.-L.: J. Appl. Phys. **107**, 043501 (2010)
Ru, C.: J. Appl. Phys. **87**, 7227–7231 (2000)
Ru, C.: J. Mech. Phys. Solids. **49**, 1265–1279 (2001)
Schadler, L., Giannaris, S., Ajayan, P.: Appl. Phys. Lett. **73**, 3842–3844 (1998)
Sharma, S., Chandra, R., Kumar, P., Kumar, N.: Comput. Mater. Sci. **86**, 1–8 (2014)
Sharma, K., Sen Kaushalyayan, K., Shukla, M.: Comput. Mater. Sci. **99**, 232–241 (2015)
Spitalsky, Z., Tasis, D., Papagelis, K., Galiotis, C.: Prog. Polym. Sci. **35**, 357–401 (2010)
Suenaga, K., Wakabayashi, H., Koshino, M., Sato, Y., Urita, K., Iijima, S.: Nat. Nanotechnol. **2**, 358–360 (2007)
Sun, H.: J. Phys. Chem. B. **102**, 7338–7364 (1998)
Sun, L., Warren, G.L., O'Reilly, J.Y., Everett, W.N., Lee, S.M., Davis, D., Lagoudas, D., Sue, H.J.: Carbon. **46**, 320–328 (2008)
Talukdar, K., Agrawala, R., Mitra, A.K.: New Carbon Mater. **26**, 408–416 (2011)
Thostenson, E.T., Li, C., Chou, T.-W.: Compos. Sci. Technol. **65**, 491–516 (2005)
Timoshenko, S.: Theory of Elastic Stability. McGraw-Hill, New York (1961)
Tseng, C.H., Wang, C.C., Chen, C.Y.: Chem. Mater. **19**, 308–315 (2007)
Tsuda, T., Ogasawara, T., Deng, F., Takeda, N.: Compos. Sci. Technol. **71**, 1295–1300 (2011)
Tu, Z.-C., Ou-Yang, Z.-C.: Phys. Rev. B. **65**, 233407 (2002)
Wagner, H.D.: Chem. Phys. Lett. **361**, 57–61 (2002)
Wagner, H., Lourie, O., Feldman, Y., Tenne, R.: Appl. Phys. Lett. **72**, 188–190 (1998)
Wang, C.Y., Ru, C.Q., Mioduchowski, A.: Int. J. Solids Struct. **40**, 3893–3911 (2003)
Wang, Q., Varadan, V.K., Xiang, Y., Han, Q.K., Wen, B.C.: Int. J. Struct. Stability Dyn. **8**, 357–366 (2008)
Wang, C., Zhang, Y., Xiang, Y., Reddy, J.: Appl. Mech. Rev. **63**, 030804 (2010)
Wang, C., Chowdhury, A.R., Koh, S., Zhang, Y.: Molecular dynamics simulation and continuum shell model for buckling analysis of carbon nanotubes. In: Modeling of Carbon Nanotubes, Graphene and their Composites, pp. 239–273. Springer International Publishing (2014)
Wei, C.Y.: Appl. Phys. Lett. **88**, (2006)
Wernik, J.M., Meguid, S.A.: Acta Mech. **212**, 167–179 (2010)
Wernik, J.M., Meguid, S.A.: Acta Mech. **217**, 1–16 (2011)
Wernik, J.M., Cornwell-Mott, B.J., Meguid, S.A.: Int. J. Solids Struct. **49**, 1852–1863 (2012)
Wong, E.W., Sheehan, P.E., Lieber, C.M.: Science. **277**, 1971–1975 (1997)
Wong, M., Paramsothy, M., Xu, X.J., Ren, Y., Li, S., Liao, K.: Polymer. **44**, 7757–7764 (2003)
Xiao, S., Hou, W.: Phys. Rev. B. **73**, 115406 (2006)
Xiao, K., Zhang, L.: J. Mater. Sci. **39**, 4481–4486 (2004)
Xiao, T., Liu, J., Xiong, H.: Acta Mech. Solida Sin. **28**, 277–284 (2015)
Xin, H., Han, Q., Yao, X.-H.: Carbon. **45**, 2486–2495 (2007)
Xiong, Q.L., Meguid, S.A.: Eur. Polymer J. (2015)
Xu, X., Thwe, M.M., Shearwood, C., Liao, K.: Appl. Phys. Lett. **81**, 2833–2835 (2002)
Yakobson, B.I., Brabec, C.J., Bernholc, J.: Phys. Rev. Lett. **76**, 2511–2514 (1996)

Yang, S., Choi, J., Cho, M.: Compos. Struct. **127**, 108–119 (2015)
Zhang, Y.C., Wang, X.: Int. J. Solids Struct. **42**, 5399–5412 (2005)
Zhang, Y.Y., Wang, C.M., Tan, V.B.C.: J. Eng. Mech. **132**, 952–958 (2006a)
Zhang, Y., Tan, V., Wang, C.: J. Appl. Phys. **100**, 074304 (2006b)
Zhang, Y.Y., Wang, C.M., Tan, V.B.C.: Nanotechnology. **20**, (2009a)
Zhang, Y.Y., Xiang, Y., Wang, C.M.: J. Appl. Phys. **106**, (2009b)
Zhang, Y., Wang, C., Duan, W., Xiang, Y., Zong, Z.: Nanotechnology. **20**, 395707 (2009c)
Zheng, Q., Xue, Q., Yan, K., Gao, X., Li, Q., Hao, L.: Polymer. **49**, 800–808 (2008)
Zheng, Q.B., Xia, D., Xue, Q.Z., Yan, K.Y., Gao, X.L., Li, Q.: Appl. Surf. Sci. **255**, 3534–3543 (2009)
Zhou, L.G., Shi, S.Q.: Carbon. **41**, 613–615 (2003)
Zhou, L.-M., Mai, Y.-W., Ye, L.: Compos. Eng. **5**, 1199–1219 (1995)
Zhu, J., Peng, H., Rodriguez-Macias, F., Margrave, J.L., Khabashesku, V.N., Imam, A.M., Lozano, K., Barrera, E.V.: Adv. Funct. Mater. **14**, 643–648 (2004)
Zou, W., Du, Z.-J., Liu, Y.-X., Yang, X., Li, H.-Q., Zhang, C.: Compos. Sci. Technol. **68**, 3259–3264 (2008)

# Chapter 4
# Electrical Conductivity of Carbon Nanotube- and Graphene-Based Nanocomposites

**Yang Wang and George J. Weng**

**Abstract** Carbon nanotube- and graphene-based polymer nanocomposites are known to have exceptional electrical conductivity even at very low filler loading. In this chapter we present a widely useful composite model for studying this property. This model has the capability of determining both the effective electrical conductivity and the percolation threshold of the nanocomposites. It also embodies several other important elements of the process of conduction, including filler loading, filler agglomeration, anisotropic property of carbon fillers, effect of imperfect interfaces, and the contribution of electron tunneling. The backbone of the model is the effective-medium theory with a perfect interface; it can demonstrate the percolation feature and can also comply with the Hashin-Shtrikman bounds. To study the influence of filler agglomeration, a two-scale approach is further proposed. The imperfect interface is incorporated into the model by the introduction of a thin, weak interface surrounding each inclusion. To account for the effect of electron tunneling, Cauchy's statistical distribution function is further introduced to reflect the increased activity of electron tunneling at and after the percolation threshold. It is demonstrated that the theoretical predictions based on the developed model are in close agreement with available experimental data.

## 4.1 Introduction

With the growth of nanotechnology in recent years, a new kind of nanocomposites has emerged for their enhanced mechanical, thermal, and electrical performance. This class of nanocomposites generally consists of a polymer matrix and various types of carbon fillers, such as graphite, carbon nanofiber, carbon nanotube (CNT), and graphene. Two of the most attractive fillers are carbon nanotubes and graphene.

Y. Wang • G.J. Weng (✉)
Department of Mechanical and Aerospace Engineering, Rutgers University, New Brunswick, NJ 08903, USA
e-mail: yang.wang@rutgers.edu; gjweng@soe.rutgers.edu



S.A. Meguid, G.J. Weng (eds.), *Micromechanics and Nanomechanics of Composite Solids*, DOI 10.1007/978-3-319-52794-9_4

Both are known to possess very high mechanical stiffness and tensile strength, as well as exceptional thermal and electrical conductivity. For electrical conductivity, it can be as high as $10^6$ to $10^7$ S/m for pure CNT and $10^8$ S/m for pure graphene. These values are comparable to the two best kinds of metal conductor, silver and copper, which have $6.30 \times 10^7$ and $5.96 \times 10^7$ S/m, respectively. This remarkable electrical conductivity is due to the microstructure of CNT and graphene. Graphene is an allotrope of carbon that comes in the form of a one-atom-thick two-dimensional layer of $sp^2$-bonded carbon atoms. All atoms are arranged in a honeycomb grid sheet, so that each one of them is bonded with another three (Allen et al. 2010). This two-dimensional single-layered graphene sheet is the basic structural element of other allotropes of carbon. It can be rolled up into a hollow cylindrical structure to get the one-dimensional CNT, while the honeycomb grid for carbon atoms remains unchanged (Geim and Novoselov 2007). Since each carbon atom has four electrons in the outer shell and only three are used to form covalent bonds, there is one remaining electron that is highly mobile and available for electrical conduction. As a consequence, both CNT and graphene are highly conductive. In experiments, their intrinsic electrical conductivities are usually reported on the orders of $10^3$ to $10^5$ S/m. In contrast the electrical conductivity of most polymers is measured on the orders of $10^{-15}$ to $10^{-8}$ S/m. This makes the property contrast between the inclusion and matrix phase on the orders of $10^{12}$ to $10^{18}$. Therefore the electrical conductivity of CNT and graphene-based nanocomposites is a high-contrast problem, and it is significantly different from the classical problem of elastic property in fiber-reinforced composites where the material property contrast is only on the order of $10^2$.

Another great feature for CNT and graphene-based nanocomposites is the percolation phenomenon. As the loading of carbon fillers in the nanocomposites increases, the growth of overall electrical conductivity does not follow a linear rule of mixture. Around certain filler concentrations, its value can grow dramatically for several orders of magnitude, so that the whole composite turns from almost insulating to highly conductive. This rapid growth of overall electrical conductivity around a critical filler concentration is the percolation phenomenon, which usually occurs in composites whose constituent properties have very high contrast. It is also a transitional stage in which the overall property of the composite shifts from the property of matrix phase to that of the inclusion phase, and the onset of this transition is the percolation threshold. At microscopic scale the percolation phenomenon indicates that the conductive fillers are not surrounded by the insulating matrix anymore. Instead they have contact with each other; thus a conductive network is formed and expanded throughout the composite (Nan et al. 2010). The electric current can now flow into this conductive network, without having to bypass the barrier of insulating matrix. Therefore the overall electrical conductivity of the composite is tremendously improved. The value of percolation threshold is mainly governed by the geometrical structure of the composite. One important parameter that characterizes this geometrical structure is the aspect ratio (length-to-diameter ratio) of the inclusion. As mentioned above, graphene has a microstructure of flat sheet so that it can be treated as a spheroid with a very small (usually less than 0.01) aspect ratio, while the aspect ratio of CNT is very large (usually more than

100) due to its long cylinder microstructure. Because of these two kinds of extreme aspect ratios, the percolation thresholds for CNT and graphene fillers are generally very low. This means that we can achieve highly conductive nanocomposites with only a small amount of CNT or graphene loading, which is definitely a desirable characteristic. For example, Gardea and Lagoudas (2014) reported a remarkable 10-order of magnitude increase in the overall electrical conductivity at 0.1 wt.% of pristine CNTs for a CNT/epoxy nanocomposite. He and Tjong (2013) prepared a graphene/polyvinylidene fluoride nanocomposite with a percolation threshold of 0.31 graphene vol.%, while the graphene/polyethylene nanocomposite fabricated by Pang et al. (2010) had an even lower 0.07 vol.%. In short, with high property contrast and extreme aspect ratios, CNTs and graphene are the ideal reinforcements for nanocomposites that can substantially enhance the overall electrical conductivity at very low filler loading.

Because of these geometrical similarities, one can study CNT- and graphene-based nanocomposites together under the same theoretical framework, with only a slight difference being their very long cylinder and thin plate structure. The theoretical study of CNT and graphene-based nanocomposites involves two major issues: (1) the determination of the overall electrical conductivity and (2) the determination of percolation threshold. In retrospect, many investigations have been separately made upon these two issues. For the first one, a simple and widely used empirical model for calculating the effective electrical conductivity, $\sigma_e$, is the scaling law with the dependence on filler concentration $c_1$, as (e.g., Bauhofer and Kovacs 2009)

$$\sigma_e = \sigma_0 \left(c_1 - c_1^*\right)^t, \tag{4.1}$$

where $c_1^*$ is the percolation threshold and $\sigma_0$ and $t$ are the two fitting parameters. This model offers an easy way of curve fitting with the experimental data, but it gives no insights into the physical mechanism of the conduction process. More advanced models that have been developed from the perspective of micromechanics are later brought into the study of electrical conductivity. They can incorporate the issues such as the volume concentration, shape, and orientations of carbon fillers. Among these models, the most widely used ones include the Mori–Tanaka (M–T) method (Mori and Tanaka 1973), the Ponte Castañeda-Willis (PCW) model (Castañeda and Willis 1995), and Bruggeman's effective-medium approach (Bruggeman 1935). A comprehensive development of the M-T method was provided by Weng (1984) and Benveniste (1987) in the elastic context and by Hatta and Taya (1985) and Nan et al. (1997) for thermal conductivity. The PCW model was also originally developed for the elastic properties and was applied to thermal and electrical conductivity by Duan et al. (2006) and Pan et al. (2011), respectively. As the PCW model could easily go out of the Hashin–Shtrikman (H–S) upper bound (Hashin and Shtrikman 1962) beyond certain inclusion concentration, Pan et al. (2011) also suggested using the H–S upper bound to guide the development of electrical conductivity after PCW model hit the bound. The effective-medium approach is a symmetric version of the self-consistent method that is also called the coherent potential approximation. It has a realizable microstructure and treats both the inclusion and matrix on equal, symmetric footing. With spherical inclusions it was first applied by

Landauer (1952) to study the effective electrical conductivity of a metallic mixture with spherical particles. In the mechanical context, it was first developed by Hill (1965) and Budiansky (1965). It should be noted that many notable contributions to the study of electrical conductivity have been made in recent years under the framework of micromechanics. For instance, Xie et al. (2008) adopted another form of the self-consistent method, which relied solely on the average field concentration of the randomly oriented ellipsoids, to compare the electrical conductivity between composites reinforced by CNT and graphene nanosheets. Deng and Zheng (2008) provided an analytical model with the consideration of the percolation probability of CNT inclusions. Seidel and Lagoudas (2009) and Feng and Jiang (2013) both used the composite cylinder method to solve for the electric fields in a microscale representative volume element. All these works have provided significant insights for the physical principle of conduction process and the microstructure of the nanocomposites.

The determination of percolation threshold has also been extensively studied by both numerical methods and some analytical models. Due to the random orientation and distribution of carbon fillers, Monte Carlo (MC) simulations, such as the works by Li and Chou (2007) and Ma et al. (2010), have often been invoked to numerically investigate the percolation threshold. However MC simulation is computationally expensive. There are other theoretical approaches that focus on the geometry of percolation network. For instance, Balberg et al. (1984) considered 3-D randomly oriented sticks combined with their associated average excluded volume, Bao et al. (2013) randomly generated cylinder models in the representative volume and proposed a percolating network recognition scheme with periodic boundary conditions, and Chatterjee (2013) used a polydisperse system of rods with the help of Bethe lattice site percolation model. These models have the merit of providing analytical results for the percolation threshold, but they are under a totally different theoretical framework from the micromechanics theories. Some of the preceding continuum composite models have to borrow the percolation threshold from other numerical results; it implies that such composite models are not self-contained to be able to cover the overall electrical conductivity and percolation threshold simultaneously. This is an issue that we want to avoid here. In what follows, we will show that, in our continuum model, the percolation threshold is an integral part of the continuum theory can be directly derived.

There are some additional problems that affect the overall electrical conductivity and percolation threshold of CNT and graphene-based nanocomposites. We consider three important ones: (1) the filler agglomeration, (2) the imperfect interface effect, and (3) the effect of electron tunneling. The first problem is related to the inhomogeneous dispersion state of carbon fillers in the composite. In certain cases a lot of CNT or graphene fillers tend to cluster together to form many filler agglomerations. Inside each agglomerate, carbon fillers are highly dense, more so than the rest of the composite. This phenomenon can be observed from various TEM images of CNT and graphene-based nanocomposites. It is mainly caused by the different processing routes of CNT and graphene samples. For instance, graphene can be produced by the liquid-phase exfoliation of graphite, or by the thermal reduction of graphite oxide. The former gives more dispersed graphene samples

while the latter results in more graphene agglomerations. Filler agglomerations change the microstructure of the nanocomposites, so it is necessary to investigate its effect on the overall electrical conductivity and percolation threshold. A few experimental results—including those by Martin et al. (2004), Hernández et al. (2009), Aguilar et al. (2010)—have suggested that CNT agglomerations could favor the formation of CNT conductive network and improve the effective electrical conductivity. A theoretical study by Li et al. (2007a, b) has treated CNT agglomerations to be of spherical shape and calculated the percolation threshold based on the corresponding inter-particle distance. However it was not capable of predicting the overall electrical conductivity, so a thorough theoretical analysis of the effect of filler agglomeration was not completed. To this end, we will adopt a two-scale approach as suggested by Barai and Weng (2011) in the study of CNT-based metal plasticity to address the issue of filler agglomeration.

The second problem—the imperfect interface effect—has a long history in the study of composite materials. In general the bonding between the inclusion and matrix is not ideally perfect, and there exists a weak interface that could diminish the overall property of the composite. In the context of thermal conductivity, Dunn and Taya (1993), Duan and Karihaloo (2007), and Nan et al. (1997) have extended the micromechanics formulation to account for the imperfect interface condition. Hashin (2001) also proposed a generalized theory for the imperfect interface of conduction, dielectric behavior, and permeability. A common theoretical treatment for an imperfect interface is to model it as a thin interphase between two constituent phases. Compared with the original inclusion, the interphase has lower electrical conductivity, or in terms of its counterpart, higher electrical resistivity. With a diminishing thickness, the interphase becomes a layer of interface surrounding the original inclusion, so that it turns into a thinly coated inclusion. The overall electrical conductivity of this coated inclusion is lowered due to the interfacial resistance of the interface layer, and this signifies the effect of imperfect interfaces. The last problem on the effect of electron tunneling has received less attention from the continuum perspective. But it has been numerically studied by MC simulations, such as the works by Bao et al. (2012) and Li et al. (2007a, b). MC simulations are highly computational, while our objective is to develop a continuum scheme that could have both simplicity and wide applicability. Electron tunneling is a quantum mechanical effect that electrons can jump from one carbon filler to another adjacent one, over the barrier of an insulating polymer matrix. It gives rise to the tunneling-assisted interfacial conductivity which could enhance the overall electrical conductivity of the nanocomposite. This contribution is incorporated into our model by reducing the interfacial resistance. Finally, considering the probabilistic nature of electron hopping, the reduction of interfacial resistance is further characterized by Cauchy's statistical distribution function. In this way, the effects of imperfect interfaces and electron tunneling can all be taken into account.

In the following we will first introduce the effective-medium theory to determine the overall electrical conductivity of a nanocomposite with a perfect interface. This will be followed with the derivation of percolation threshold. Then the effects of filler agglomeration, imperfect interface, and electron tunneling will be

subsequently added into the model. To verify the applicability of the developed model, three sets of experimental data on CNT and graphene-based nanocomposites will be analyzed and compared with the calculated results.

## 4.2 The Theory

### *4.2.1 Effective-Medium Theory with a Perfect Interface*

The microstructure of CNT and graphene-based nanocomposites can be conceived to be a two-phase composite, with carbon fillers as the inclusions and polymer binder as the matrix. All inclusions are assumed to have spheroidal shapes. CNT inclusions correspond to prolate spheroids with high aspect ratios. Compared with long cylindrical CNTs, a prolate spheroidal CNT will possess almost the same shape when its aspect ratio is sufficiently large. Similarly, graphene inclusions are represented by oblate spheroids with very low aspect ratios, and they can recover the flat sheet graphene model when their aspect ratios are close to zero. The dispersion state of CNT and graphene inclusions is considered to be homogeneous and their orientations are totally random. This microstructure is schematically shown in Fig. 4.1. As the volume concentration of carbon inclusions increases, it becomes possible for them to have contact with each other. Those inclusions in touch can form a percolating path as shown by the red dashed line in Fig. 4.1. All percolating paths together become a conductive network, so that the electrical current can flow in this network without having to bypass the insulating matrix. The formation of the conductive network is exactly the percolation phenomenon at the microscopic scale.

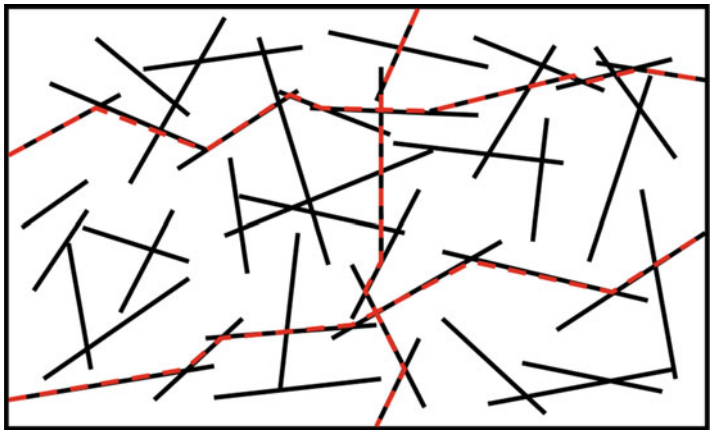

**Fig. 4.1** The microstructure of CNT and graphene-based nanocomposites, showing carbon fillers (*black solid line*) in the effective medium and three percolating paths (one vertical and two horizontal, in *red dashed line*)

To study this phenomenon by micromechanics, we now introduce the effective-medium theory. There are several ways to derive this theory. One of the most attractive ways is to adopt Maxwell's far-field matching (Maxwell 1891) of the scattered fields between the two-phase composite and the homogenized effective medium (Weng 2010). If we denote the moduli tensor of the reference medium in which the scattered fields of the two-phase composite and the homogeneous effective medium are to be evaluated by $\mathbf{L}_r$, the moduli tensor of the effective medium by $\mathbf{L}_e$, and those of the matrix and inclusion phase by $\mathbf{L}_0$ and $\mathbf{L}_1$, respectively, then the scattered tensor $\mathbf{T}_i$ of phase $i$ can be written as

$$\mathbf{T}_i = \left[(\mathbf{L}_i - \mathbf{L}_r)^{-1} + \mathbf{S}_i \mathbf{L}_r^{-1}\right]^{-1}, \tag{4.2}$$

where $\mathbf{S}_i$ is the Eshelby S-tensor (Eshelby 1957) of $i$th phase in the reference medium. Now denote the volume concentrations of the matrix and inclusion phase by $c_0$ and $c_1$, respectively, then Maxwell's far-field matching requires that the scattered fields from the effective medium and the sum of scattered fields from two individual phases are equal, which leads to $\mathbf{T}_e = c_0\mathbf{T}_0 + c_1\mathbf{T}_1$, or

$$\begin{aligned}\left[(\mathbf{L}_e - \mathbf{L}_r)^{-1} + \mathbf{S}_e \mathbf{L}_r^{-1}\right]^{-1} &= c_0\left[(\mathbf{L}_0 - \mathbf{L}_r)^{-1} + \mathbf{S}_0 \mathbf{L}_r^{-1}\right]^{-1} \\ &+ c_1\left[(\mathbf{L}_1 - \mathbf{L}_r)^{-1} + \mathbf{S}_1 \mathbf{L}_r^{-1}\right]^{-1}.\end{aligned} \tag{4.3}$$

In the effective-medium approach, the property of the reference medium $\mathbf{L}_r$ is chosen to be equal to that of the effective medium, $\mathbf{L}_e$, so that the scattered field on the left of Eq. (4.3) automatically vanishes. This leads to the final equation for the effective-medium approach

$$c_0\left[(\mathbf{L}_0 - \mathbf{L}_e)^{-1} + \mathbf{S}_0 \mathbf{L}_e^{-1}\right]^{-1} + c_1\left[(\mathbf{L}_1 - \mathbf{L}_e)^{-1} + \mathbf{S}_1 \mathbf{L}_e^{-1}\right]^{-1} = \mathbf{0}. \tag{4.4}$$

The effective property of this two-phase composite can be obtained by solving Eq. (4.4) for tensor $\mathbf{L}_e$ at any given inclusion volume concentration, $c_1$.

In CNT and graphene-based nanocomposites, the moduli tensor for the electrical conductivity, $\mathbf{L}$, is a second-order tensor, which is defined by

$$J_i = L_{ij}E_j, \tag{4.5}$$

where vector $\mathbf{J}$ and $\mathbf{E}$ are the electric current density and electric field. In addition, due to the microstructure of CNT and graphene, their properties are transversely isotropic, with 3-direction as the symmetric direction, and plane 1–2 as the isotropic plane (they also coincide with the symmetric direction and isotropic plane of the spheroidal model of CNT and graphene inclusion). For the polymer matrix, it has no particular orientation in the microstructure; thus its property is isotropic. As a

result, the moduli tensors for the polymer matrix, $\mathbf{L}_0$, and carbon inclusions, $\mathbf{L}_1$, can be expressed as

$$\mathbf{L}_0 = \begin{bmatrix} \sigma_0 & 0 & 0 \\ 0 & \sigma_0 & 0 \\ 0 & 0 & \sigma_0 \end{bmatrix}, \quad \text{and} \quad \mathbf{L}_1 = \begin{bmatrix} \sigma_1 & 0 & 0 \\ 0 & \sigma_1 & 0 \\ 0 & 0 & \sigma_3 \end{bmatrix}, \tag{4.6}$$

where $\sigma_0$ is the electrical conductivity of the polymer matrix, and $\sigma_1$ and $\sigma_3$ are that of carbon inclusions along the in-plane and normal directions. In general, it is much more conductive along the CNT length and in the graphene plane; thus we have $\sigma_1 \ll \sigma_3$ for CNT inclusions and $\sigma_1 \gg \sigma_3$ for graphene inclusions. It is convenient to introduce a constant $m$ to describe this anisotropy relation as $\sigma_1 = m\sigma_3$, so that $m<1$ for CNT and $m>1$ for graphene. Still both $\sigma_1$ and $\sigma_3$ are much larger than $\sigma_0$, since the polymer is an electrically insulating material. Likewise, the Eshelby S-tensor for the two phases, $\mathbf{S}_0$ and $\mathbf{S}_1$, are also isotropic and transversely isotropic, respectively, such that

$$\mathbf{S}_0 = \begin{bmatrix} S_{00} & 0 & 0 \\ 0 & S_{00} & 0 \\ 0 & 0 & S_{00} \end{bmatrix}, \quad \text{and} \quad \mathbf{S}_1 = \begin{bmatrix} S_{11} & 0 & 0 \\ 0 & S_{11} & 0 \\ 0 & 0 & S_{33} \end{bmatrix}. \tag{4.7}$$

With 3-direction as the symmetric axis of the spheroidal inclusion, the components of $\mathbf{S}_1$ depend on the inclusion aspect ratio, $\alpha$, as

$$S_{11} = S_{22} = \begin{cases} \frac{\alpha}{2\left(1-\alpha^2\right)^{\frac{3}{2}}}\left[\cos^{-1}\alpha - \alpha\left(1-\alpha^2\right)^{\frac{1}{2}}\right], & \alpha < 1 \\ \frac{\alpha}{2\left(\alpha^2-1\right)^{\frac{3}{2}}}\left[\alpha\left(\alpha^2-1\right)^{\frac{1}{2}} - \cosh^{-1}\alpha\right], & \alpha > 1 \end{cases} \tag{4.8}$$

and $S_{33} = 1 - 2S_{11}$ (the sum of all three diagonal components of S-tensor is 1). For the prolate-shaped CNT, its aspect ratio is always larger than 1, and $0<\alpha<1$ corresponds to the oblate shape of graphene. When $\alpha \to \infty$ (long fiber), these components are reduced to $S_{11} = S_{22} = 1/2$ and $S_{33} = 0$, and when $\alpha \to 0$ (thin plate), they are reduced to $S_{11} = S_{22} = 0$ and $S_{33} = 1$. For spherical inclusions, $\alpha = 1$ and each S-tensor component is 1/3. On the other hand, since $\mathbf{S}_0$ is isotropic, it should carry the same diagonal components in all three directions so that $S_{00} = 1/3$. Since the orientations of CNT and graphene inclusions are totally random, the overall nanocomposites must demonstrate isotropic property, and thus $\mathbf{L}_e$ carries the same component $\sigma_e$ in all three directions. At the same time we should also implement the effective-medium approach with its 3-D random version. Denoting the orientational average of a tensor by angular brackets, $\langle\rangle$, the equation for the 3-D random effective-medium approach can be written as

$$c_0\left\langle\left[(\mathbf{L}_0 - \mathbf{L}_e)^{-1} + \mathbf{S}_0\mathbf{L}_e^{-1}\right]^{-1}\right\rangle + c_1\left\langle\left[(\mathbf{L}_1 - \mathbf{L}_e)^{-1} + \mathbf{S}_1\mathbf{L}_e^{-1}\right]^{-1}\right\rangle = \mathbf{0}. \tag{4.9}$$

For any second-order tensor, its orientational average is given by the mean of three diagonal components times the second-order identity tensor, $\delta_{ij}$. Therefore Eq. (4.9) can be simplified from a tensor equation to a scalar equation as

$$c_0 \frac{\sigma_0 - \sigma_e}{\sigma_e + (1/3)(\sigma_0 - \sigma_e)} + c_1 \frac{1}{3}\left[\frac{2(\sigma_1 - \sigma_e)}{\sigma_e + S_{11}(\sigma_1 - \sigma_e)} + \frac{\sigma_3 - \sigma_e}{\sigma_e + S_{33}(\sigma_3 - \sigma_e)}\right] = 0. \tag{4.10}$$

Solving this implicit equation for $\sigma_e$, the effective electrical conductivity of CNT and graphene-based nanocomposites is then obtained.To explain why the effective-medium approach is selected as the backbone of our model, we make a comparison among the effective-medium approach, the M-T method, and the PCW model. Besides, it is helpful to examine these three models in light of the H-S upper and lower bounds. Because these two bounds have been widely used as the maximum and minimum limit for the effective properties of composite materials, any valid estimation of effective properties should stay within the range of them. For simplicity, we make a preliminary study of the effective electrical conductivity of a two-phase composite with isotropic CNT inclusions and polymer matrix (phase 0 for the polymer matrix and phase 1 for the spheroidal CNT inclusion). In this setting, the M-T and PCW results for the effective electrical conductivity can be explicitly written as

$$\frac{\sigma_e^{\mathrm{MT}}}{\sigma_0} = 1 + \frac{c_1 T}{1 - c_1[1 - T/(n-1)]} \quad \text{and} \quad \frac{\sigma_e^{\mathrm{PCW}}}{\sigma_0} = 1 + \frac{c_1 T}{1 - c_1 T/3}, \tag{4.11}$$

where

$$T = \frac{n-1}{3}\left[\frac{2}{1 + (n-1)S_{11}} + \frac{1}{1 + (n-1)S_{33}}\right]. \tag{4.12}$$

It is noted that $S_{11}$ and $S_{33}$ are defined in Eq. (4.8), and $n = \sigma_1/\sigma_0$ is the normalized electrical conductivity of the CNT inclusion. The results for the H-S upper and lower bounds (denoted by "+" and "–" sign) are given by

$$\frac{\sigma_e^{\mathrm{HS}(+)}}{\sigma_0} = 1 + \frac{(1 - c_1)(1 - n)}{(1/3)c_1(1 - n) + n} \quad \text{and}$$
$$\frac{\sigma_e^{\mathrm{HS}(-)}}{\sigma_0} = 1 + \frac{c_1(n-1)}{(1/3)(1 - c_1)(n-1) + 1}. \tag{4.13}$$

Taking $n = 10^{10}$ and the aspect ratio $\alpha = 20$ as the properties of CNT inclusions, we calculate the results of effective electrical conductivity given by these three models and the two H-S bounds and plot them in logarithmic scale in Fig. 4.2. It is seen that the PCW result quickly goes out of the H-S upper bound at a CNT volume concentration of $c_1 < 0.1$. In strict applications, this theory is limited to the range

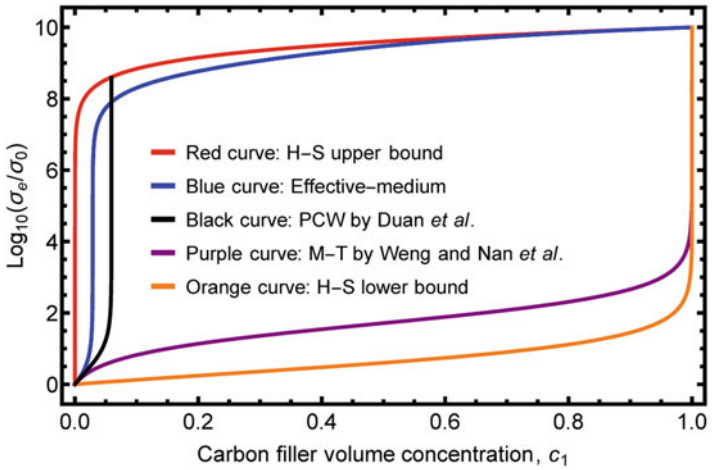


**Fig. 4.2** The examination of the effective-medium approach, the Mori-Tanaka method (Mori and Tanaka 1973) by Weng (1984, 1990) and Nan et al. (1997), and the Ponte Castañeda-Willis method (Castañeda and Willis 1995) by Duan et al. (2006) in light of the Hashin and Shtrikman (1962) bounds

$c_1 < 1/\alpha^2$, which is 0.0025 here, but it can go a bit higher before it hits the H-S upper bound. This shows that the PCW model cannot properly yield the effective electrical conductivity over the entire range of $c_1$. In fact it was originally developed in a mechanical setting where the elastic properties of the inclusion and matrix phase have very little contrast (usually less than 10 times). But the electrical conductivity is an extremely high-contrast problem, which would cause the PCW result to have singularity at certain value of $c_1$. Therefore the PCW model is not suitable to account for a high-contrast, high aspect ratio problem. Both the effective-medium and the M-T results are seen to stay within the bounds, but the M-T result has no early percolation feature. Its curve stays rather flat at low CNT concentration and only when $c_1$ approaches 1 does it start to grow rapidly, which is close to the trend of the H-S lower bound. Only the effective-medium result displays a sharp increase at low CNT concentration and possesses a percolation threshold, which is very close to the H-S upper bound at low volume concentration but is still always lower than it. In the microstructure of CNT or graphene nanocomposites, since a large amount of nanofillers are in contact with each other to form a conductive network, the CNT or graphene inclusions cannot be considered to be directly "embedded" in the polymer matrix any more. They are somewhat embedded in the effective medium, and therefore the effective-medium approach is a very appropriate model to study the effective electrical conductivity.

### 4.2.2 The Percolation Threshold

The percolation threshold of the nanocomposite, $c_1^*$, can be directly derived from Eq. (4.10) (Wang et al. 2014). This is done with the observation that, when the matrix phase is totally insulating ($\sigma_0 = 0$), the effective electrical conductivity $\sigma_e$ is entirely controlled by the conductive network of CNT and graphene inclusions, so the inclusion volume concentration $c_1$ that first gives rise to a non-negative value of $\sigma_e$ represents the percolation threshold, $c_1^*$. With $\sigma_0 = 0$, Eq. (4.10) turns into a quadratic equation for $\sigma_e$, in the following form

$$\mathrm{A}\sigma_e^2 + \mathrm{B}\sigma_e + \mathrm{C} = 0, \tag{4.14}$$

with coefficient A, B, and C all being functions of $c_1$, as

$$\begin{aligned}
\mathrm{A} &= 9\left(1 - S_{33}^2\right) + c_1(1 - 3S_{33})^2, \\
\mathrm{B} &= \sigma_1\left[-3c_1\left(1 - S_{33}\right)\left(5 - 3S_{33}\right) + 9(1 - S_{33})^2\right] + \sigma_3\left[-c_1\left(9S_{33}^2 + 3S_{33} + 2\right)\right. \\
&\quad \left. + 9S_{33}\left(1 + S_{33}\right)\right], \\
\mathrm{C} &= \sigma_1\sigma_3\left[-c_1\left(-9S_{33}^2 + 15S_{33} + 2\right) + 9S_{33}\left(1 - S_{33}\right)\right],
\end{aligned} \tag{4.15}$$

where the relation $2S_{11} + S_{33} = 1$ has been used. As $c_1$ increases from zero, initially all three coefficients are positive, so there is no positive solution for $\sigma_e$ at very low $c_1$. When $c_1$ reaches a critical value, there is a solution $\sigma_e = 0$, and as $c_1$ further increases there is a positive solution for $\sigma_e$. This is the generally sought effective electrical conductivity with a perfectly insulating matrix, whereas the critical value of $c_1$ giving rise to $\sigma_e = 0$ is exactly the percolation threshold, $c_1^*$. This occurs when the coefficient $\mathrm{C} = 0$, and this relation provides the value

$$c_1^* = \frac{9S_{33}\left(1 - S_{33}\right)}{-9S_{33}^2 + 15S_{33} + 2}. \tag{4.16}$$

Since the S-tensor component $S_{33}$ only depends on inclusion aspect ratio, $\alpha$, the percolation threshold is thus a strictly geometrical parameter. To see its effects, we plot its dependence on $\alpha$ in Fig. 4.3, as $\alpha$ increases from almost 0 (graphene-like) to infinity (CNT-like). For CNT- and graphene-based nanocomposites, the percolation thresholds with extreme values of $\alpha$ are further illustrated in the insets. One can see that CNT provides a lower percolation threshold than the graphene with reciprocal aspect ratio. This is consistent with the result predicted by Pan et al. (2011). It can be also seen that the maximum value that $c_1^*$ can attain is exactly 1/3, which corresponds to spherical inclusions, with $\alpha = 1$. This value has been widely reported in the literature.

The percolation threshold $c_1^*$ can also be derived from Eq. (4.10) following a procedure suggested by Gao and Li (2003). In general, the matrix is almost insulating while inclusions are highly conducive. Therefore $\sigma_i$ ($i = 1$ or 3, the

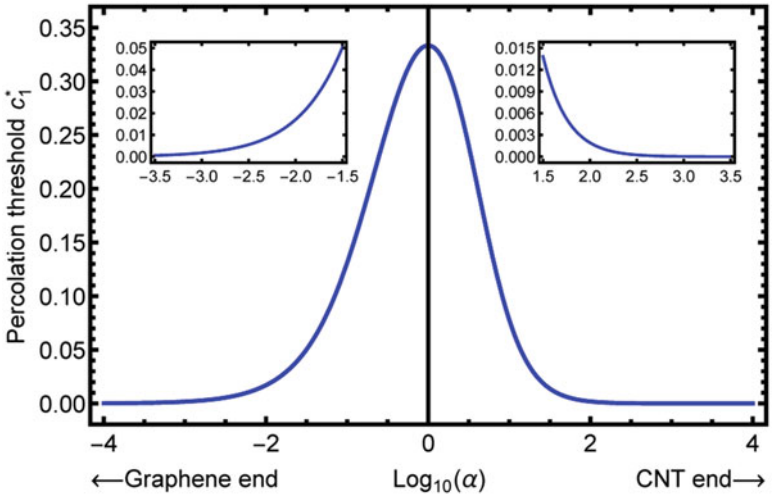


**Fig. 4.3** The dependence of percolation threshold on inclusion aspect ratio. The left-hand side is the graphene side while the right-hand side is the CNT side

same below) are usually several orders of magnitude higher than $\sigma_0$, which makes $\sigma_0/\sigma_i \to 0$. According to the percolation theory, when inclusion concentration $c_1 < c_1^*$, $\sigma_e$ has almost the same order of magnitude as $\sigma_0$, therefore $\sigma_e/\sigma_i \to 0$; but after $c_1^*$, $\sigma_e$ will quickly approach $\sigma_i$, making $\sigma_e/\sigma_0 \to \infty$. Therefore at $c_1 = c_1^*$, $\sigma_e$ is at the transition stage, satisfying both $\sigma_e/\sigma_0 \to \infty$ and $\sigma_e/\sigma_i \to 0$ at the same time. Applying these two conditions to Eq. (4.10) and solving for $c_1^*$, one finds

$$c_1^* = \frac{3/(1-S_0)}{3/(1-S_0) + 1/S_{11} + 1/S_{22} + 1/S_{33}} = \frac{9S_{33}(1-S_{33})}{-9S_{33}^2 + 15S_{33} + 2}, \tag{4.17}$$

which is exactly the same result as Eq. (4.16).

### *4.2.3 The Two-Scale Composite Model for Filler Agglomeration*

In previous sections, we have assumed CNT and graphene-based nanocomposites to be homogeneous. However, the inhomogeneous distribution of CNT and graphene fillers, or filler agglomeration, is inevitable in reality. A good way to study the effect of filler agglomeration is to adopt a two-scale approach as suggested by Barai and Weng (2011) in the study of CNT-based metal plasticity and also by Prasher et al. (2006) and Reinecke et al. (2008) in the context of thermal conductivity. In this approach, the composite is considered to consist of CNT-rich agglomerated regions embedded in a CNT-poor region. To calculate the effective electrical conductivity,

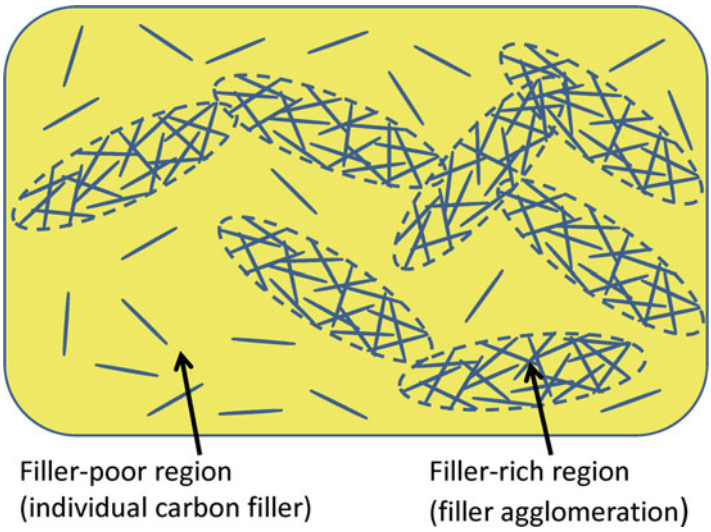


**Fig. 4.4** A schematic plot of the two-scale model of CNT- and graphene-based nanocomposites with filler agglomeration

the effective-medium approach is applied to the filler-rich and filler-poor regions at the smaller scale and then to the whole composite at the larger scale (Wang et al. 2015).

We will begin with establishing the two-scale morphology of the CNT and graphene-based nanocomposites with filler agglomeration. The typical microstructure of such composite is shown in Fig. 4.4. Inside the composite, some CNT or graphene fillers gather together to form the agglomerates, while others exist as individual fillers. Both kinds of fillers are taken to be homogeneously dispersed and randomly oriented in each region. To model such a morphology, we divide the entire volume of the composite into two—one is the filler-rich agglomerate and the other is the filler-poor region. The volume concentrations of the filler-rich and the filler-poor regions are denoted as $c_R$ and $c_P$, respectively, so that

$$c_R + c_P = 1, \tag{4.18}$$

where subscript $R$ stands for "rich" and $P$ for "poor." We assume that the agglomerates are also homogeneously dispersed and randomly oriented and have a shape that can be grossly represented by a spheroid, with an aspect ratio $\alpha_R$. Inside the agglomerate, there is a large amount of carbon fillers residing in the polymer matrix, with the volume concentrations, $c_1^{(R)}$ and $c_0^{(R)}$, respectively, satisfying

$$c_1^{(R)} + c_0^{(R)} = 1, \tag{4.19}$$

where subscripts 1 and 0 stand for carbon fillers and the polymer matrix, respectively. We shall also represent the individual carbon filler by a spheroid with aspect ratio $\alpha$. In the filler-poor region, there are also carbon fillers and the polymer matrix, with the volume concentrations, $c_1^{(P)}$ and $c_0^{(P)}$, respectively, such that

$$c_1^{(P)} + c_0^{(P)} = 1. \tag{4.20}$$

As a result, the total volume concentration of carbon fillers, denoted by $c_1$, is the sum of the filler concentration from both filler-rich and filler-poor regions, and so is the total volume concentration of the matrix, $c_0$. They satisfy

$$\begin{aligned} c_1 &= c_1^{(R)} c_R + c_1^{(P)} c_P, \\ c_0 &= c_0^{(R)} c_R + c_0^{(P)} c_P, \\ c_1 &+ c_0 = 1. \end{aligned} \tag{4.21}$$

It is this $c_1$ that represents the volume concentration of carbon fillers that is commonly measured in experiments. With these definitions, the dispersion state of carbon fillers can be fully described. However, we still need to know how they evolve as $c_1$ increases. Here we choose to study the dependence of $c_R$, $c_1^{(R)}$, and $c_1^{(P)}$, as the other three can be calculated from them. There are two basic requirements for $c_R$, $c_1^{(R)}$, and $c_1^{(P)}$. The first one is that, if there are no carbon fillers in the composite, there should be no filler agglomerates and no individual filler inside the filler-poor region. In other words, when $c_1 = 0$, we must have $c_R = 0$ and $c_1^{(P)} = 0$. The second one is that, if carbon fillers occupy the entire composite, then both the filler-rich and the filler-poor regions are completely filled. This implies that, when $c_1 = 1$, we must have both $c_1^{(R)} = 1$ and $c_1^{(P)} = 1$.

We also need to know how graphene fillers are distributed into the graphene-rich and the graphene-poor regions. For this purpose, we introduce a parameter, $a$ ($0 \le a \le 1$), to represent the volume fraction of graphene inside the graphene-rich region out of the total amount of graphene; it satisfies

$$a = c_1^{(R)} c_R / c_1. \tag{4.22}$$

Essentially, the parameter $a$ specifies how much of the total amount of carbon filler is allocated to the filler-rich region. We also need to specify the dependence of $c_1^{(R)}$ on $c_1$. As the filler agglomerate tends to percolate earlier than the entire composite, $c_1^{(R)}$ can be greater than the percolation threshold of the filler-rich region at low $c_1$. Hence when $c_1 \to 0$, $c_1^{(R)}$ doesn't need to start from 0 but can have a non-zero initial value, represented by another parameter $b$. But this $c_1^{(R)}$ must grow to 1 when $c_1 = 1$. From these two requirements we assume a linear dependence on $c_1$ for $c_1^{(R)}$, as

$$c_1^{(R)} = b + c_1 (1 - b). \tag{4.23}$$

Parameter $b$ also lies between 0 and 1. When $b = 0$, we have $c_1^{(R)} = c_1^{(P)} = c_1$. So there is no distinction among the three and thus the composite is homogeneous. For an agglomerated composite, its $b$ value has to be greater than 0, so that $c_1^{(R)} > c_1$. This implies that carbon fillers are more concentrated inside the filler-rich region, and its percolation condition is reached earlier than that of the overall nanocomposite. It should also be noted that it is the quantity, $c_1^{(R)} c_R$, that specifies the volume fraction of carbon fillers out of the total $c_1$ to reside inside the agglomerates. When $c_1 = 0$, the volume fraction of the filler-rich region is zero, i.e., $c_R = 0$. So even though $c_1^{(R)} \neq 0$ in this situation, there is still no carbon filler in the "filler-rich" region or anywhere else.

With parameters $a$ and $b$, we can then obtain the dependence of $c_R$ and $c_1^{(P)}$ on $c_1$, as

$$\begin{aligned} c_R &= \frac{a}{b + c_1 (1 - b)} c_1, \\ c_1^{(P)} &= \frac{(1 - a)\,[b + c_1 (1 - b)]}{-c_1 a + [b + c_1 (1 - b)]} c_1. \end{aligned} \tag{4.24}$$

The dispersion state of carbon fillers is now completely specified by the two parameters, $a$ and $b$. In the limiting case when $a = 1$, all fillers are allocated to the agglomerates and there is no $c_1^{(P)}$. When $a = 0$, we have $c_R = 0$ and $c_1^{(P)} = c_1$, so the composite is completely specified by the filler-poor region. In both cases the two-scale composite is reduced to only one scale, making it back to a homogeneous composite. With Eqs. (4.23) and (4.24) representing the geometrical foundation of filler agglomeration, we have now fully established the two-scale morphology of CNT and graphene-based nanocomposites.

To evaluate the effective electrical conductivity, the effective-medium approach, as given in Eq. (4.10), is applied to the two scales. At the smaller scale of the filler-rich and filler-poor regions, phase 1 is identified as the individual carbon filler. It has transversely isotropic property with electrical conductivity $\sigma_3$ in the normal direction and $\sigma_1 = \sigma_2$ in the isotropic plane, S-tensor components $S_{11}$ and $S_{33}$ which are determined by its aspect ratio $\alpha$ according to Eq. (4.8), and volume concentration $c_1$ replaced by $c_1^{(R)}$ (for the filler-rich region) or $c_1^{(P)}$ (for the filler-poor region). Phase 0, on the other hand, is identified as the polymer matrix. It has isotropic electrical conductivity $\sigma_0$, S-tensor component 1/3 in all three directions, and volume concentration $c_0$ replaced by $c_0^{(R)}$ (for the filler-rich region) or $c_0^{(P)}$ (for the filler-poor region). On the larger scale of the composite, phase 1 is identified as the filler agglomerates while phase 0 as the filler-poor region. In this case $\sigma_3$ and $\sigma_1$ become the overall electrical conductivity of the filler-rich region in the normal and in-plane direction; $\sigma_0$ becomes the overall electrical conductivity of the filler-poor region; $S_{11}$ and $S_{33}$ are replaced by the S-tensor components of filler agglomerates, $S_{11}^{(R)}$ and $S_{33}^{(R)}$, which are calculated from the aspect ratio of filler agglomerates, $\alpha_R$; and lastly, $c_1$ and $c_0$ become $c_R$ and $c_P$, respectively.

In our two-scale model, the calculation of effective electrical conductivity of the overall nanocomposite takes two steps. In the first place, in both filler-rich and filler-poor regions, carbon fillers are embedded in the polymer matrix (or more strictly speaking, both carbon fillers and the polymer matrix are embedded in the effective medium, as indicated by effective-medium approach). So we use Eq. (4.10) on the smaller scale to obtain the overall electrical conductivity of the filler-rich and filler-poor region, respectively. On the larger scale, it can be regarded that the filler agglomerates are embedded in the filler-poor region. Therefore, we take advantage of the properties of both regions to implement Eq. (4.10) once again, and the effective electrical conductivity of the overall composite, $\sigma_e$, can then be solved.

The percolation threshold will also be affected by the dispersion state of carbon fillers. By using the S-tensor of individual carbon filler, Eq. (4.16) can be used to determine the percolation threshold of the filler-rich region, with $c_1^*$ identified as $c_1^{(R)*}$. $c_1^{(R)*}$ is related to $c_1^*$ of the overall composite through Eq. (4.23), such that

$$c_1^* = \frac{c_1^{(R)*} - b}{1 - b}, \qquad \text{where} \qquad c_1^{(R)*} = \frac{9S_{33}\left(1 - S_{33}\right)}{-9S_{33}^2 + 15S_{33} + 2}. \tag{4.25}$$

Likewise, Eq. (4.16) can also be used to determine the percolation condition of the large-scale overall composite, $c_R^*$, by identifying the S-tensor as that of the filler agglomerate. This $c_R^*$ is related to $c_1^*$ of the composite through Eq. (4.24), such that

$$c_1^* = \frac{bc_R^*}{a - (1 - b)\, c_R^*}, \qquad \text{where} \qquad c_R^* = \frac{9S_{33}^{(R)}\left(1 - S_{33}^{(R)}\right)}{-9S_{33}^{(R)^2} + 15S_{33}^{(R)} + 2}, \tag{4.26}$$

where $S_{33}^{(R)}$ is the S-tensor component of the filler agglomerate that depends on its aspect ratio, $\alpha_R$. For the overall nanocomposite to be in a percolated state, the percolation condition by individual carbon filler inside the filler-rich region as specified by Eq. (4.25) and the percolation condition by the large-scale agglomerates specified by Eq. (4.26) must both be satisfied. So it is the larger of the two $c_1^*$ calculated from these two equations that represents the true percolation threshold of the nanocomposite. But in general it is the second one given by Eq. (4.26) that defines the percolation threshold as the first condition is easier to meet. It is clear from Eq. (4.26) that the percolation threshold $c_1^*$ for the overall, large-scale composite depends on three parameters, $a$, $b$, and $\alpha_R$. Parameter $a$ specifies how much of the total amount of carbon fillers is allocated to the filler-rich agglomerates; parameter $b$ specifies the volume fraction of carbon fillers inside the agglomerate, $c_1^{(R)}$; and parameter $\alpha_R$ specifies the shape of the agglomerates. All of them together describe the dispersion state of carbon fillers.

### 4.2.4 The Interfacial Resistance

In this section we will consider the effect of imperfect interfaces on the effective electrical conductivity. So far we have assumed perfect interface condition between the two phases of CNT and graphene-based nanocomposites, but in real composite materials the interface condition can never be perfect. The effect of imperfect interfaces results in electrical resistance between two phases, which is the interfacial resistance. This makes the transport of electric current more difficult, so that without this additional consideration the calculated $\sigma_e$ could be much higher than the actual value. To address this issue, we first consider the existence of a very thin spheroidal layer of interphase by adding a tiny thickness $t$ to the semi-axes of the spheroidal CNT or graphene inclusion, with an electrical conductivity, $\sigma_i^{\text{int}}$. This layer is taken to surround the spheroidal inclusion, making it similar to a "thinly coated" inclusion. Due to the imperfect condition, $\sigma_i^{\text{int}}$ is usually much lower than the intrinsic conductivity of carbon fillers, $\sigma_i$, so that it is reasonable to assume $\sigma_i^{\text{int}}/\sigma_i \to 0$. Compared to the radius of CNT $R$, or the thickness of the graphene $\lambda$, $t$ is taken to be diminishingly small and we intend to make it approach zero to turn the interphase into an interface. In the limiting case of diminishing thickness ($t \to 0$), the "coated" inclusion and the original inclusion share the same shape, or the same S-tensor. This is a typical inclusion-matrix type of problem; therefore the M-T method is appropriate to calculate the overall electrical conductivity of the coated inclusion, $\sigma_i^c$, as

$$\sigma_i^c = \sigma_i^{\text{int}} \left[ 1 + \frac{\nu \left( \sigma_i - \sigma_i^{\text{int}} \right)}{(1-\nu) S_{ii} \left( \sigma_i - \sigma_i^{\text{int}} \right) + \sigma_i^{\text{int}}} \right], \tag{4.27}$$

where $i = 1$ or 3 (no sum over $i$ in $S_{ii}$), denoting the transverse or axial direction. And $\nu$ is the volume fraction of the original inclusion in the coated inclusion. For a CNT inclusion, by taking the limit $t \to 0$, $\nu$ can be written as

$$\nu = \left( \frac{R}{\alpha} \right) R^2 / \left[ \left( \frac{R}{\alpha} + t \right) (R+t)^2 \right] \approx 1 - \left( \frac{1}{\alpha} + 2 \right) \frac{t}{R}. \tag{4.28}$$

Then, with the assumption $\sigma_i^{\text{int}}/\sigma_i \to 0$, Eq. (4.27) can be rewritten as

$$\sigma_i^c = \frac{\sigma_i}{1 + \rho_i \sigma_i S_{ii} \left( 1/\alpha + 2 \right) / R}. \tag{4.29}$$

Similarly, for a graphene inclusion, $\nu$ is expressed in terms of $\lambda$ and $t$, as

$$\nu = \frac{\lambda}{2} \left( \frac{\lambda}{2\alpha} \right)^2 / \left[ \left( \frac{\lambda}{2} + t \right) \left( \frac{\lambda}{2\alpha} + t \right)^2 \right] \approx 1 - (2 + 4\alpha) \frac{t}{\lambda}. \tag{4.30}$$

and Eq. (4.27) is then rewritten as

$$\sigma_i^{(c)} = \frac{\sigma_i}{1 + \rho_i \sigma_i S_{ii} \left(2 + 4\alpha\right) / \lambda}. \tag{4.31}$$

In Eqs. (4.29) and (4.31), $\rho_i = \lim_{\sigma_i^{\text{int}}/\sigma_i \to 0,\ t \to 0} t/\sigma_i^{\text{int}}$ stands for the interfacial resistivity in the axial or transverse direction. For simplicity, it's convenient to take the property of interface to be isotropic, so that $\rho_i = \rho$. This result is also consistent with the Kapitza resistance in thermal conductivity derived by Nan et al. (1997) and Duan and Karihaloo (2007). This electrical conductivity of coated CNT, $\sigma_i^c$, can then be used to replace the original $\sigma_i$ in Eq. (4.10) of the effective-medium approach to calculate the effective electrical conductivity of imperfectly bonded nanocomposites. In this way, the effect of interfacial resistance has been incorporated into our model.

### 4.2.5 The Tunneling-Assisted Interfacial Conductivity

The interfacial resistivity $\rho$ is an intrinsic property of the interface between carbon fillers and the polymer matrix, and we denote its intrinsic value as $\rho_0$. This quantity contributes to the overall electrical conductivity of the coated CNT, $\sigma_i^c$, through Eq. (4.29) or (4.31). However as the inclusion volume concentration $c_1$ increases, $\rho$ cannot remain constant at $\rho_0$. Electron hopping from one carbon filler to the surface of another one can lead to enhanced electrical conductivity. This phenomenon, that electrons can directly pass though insulating polymer from one CNT to an adjacent one, is the quantum mechanical electron tunneling effect. The outcome is a higher interfacial conductivity, or conversely, a lower interfacial resistivity. It plays an essential role the electrical conduction process, but it is also difficult to analyze due to its complex quantum mechanical nature.

In our continuum model we take this tunneling effect as a statistical process that depends on the volume concentration of carbon fillers. In establishing a probabilistic function, we note that, at dilute filler concentration, the distance between carbon fillers is large and there is little tunneling possibility, so there is a large interfacial resistivity, but around the percolation threshold $c_1^*$, the conductive networks begin to build up and the overall distance between carbon fillers is greatly reduced. As a consequence electron tunneling activity starts to become very intense and $\rho$ begins to decrease. After $c_1^*$, fillers will get even closer, and thus tunneling effect will continue to be at a very high level, so that $\rho$ will stay very low. It turns out that Cauchy's probabilistic model is particularly suited to describe this phenomenon. We will incorporate Cauchy's cumulative distribution function, $F$, which can signify the dramatic increase of interfacial conductivity near $c_1^*$, to describe this tunneling effect. This function is given by

$$F\left(c_1; c_1^*, \gamma\right) = \frac{1}{\pi} \arctan\left(\frac{c_1 - c_1^*}{\gamma}\right) + \frac{1}{2}, \tag{4.32}$$

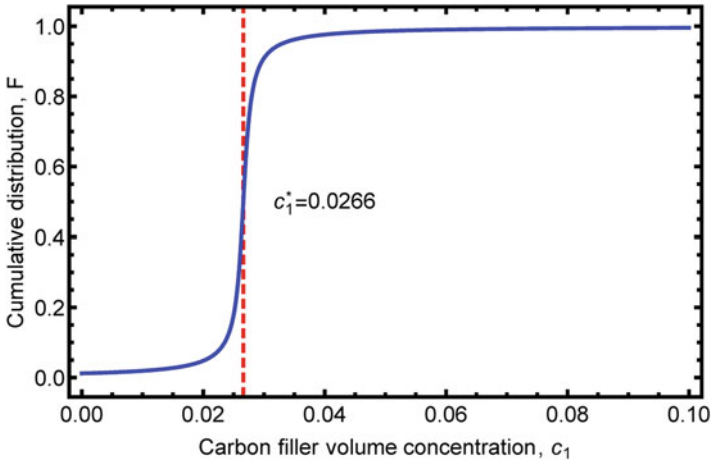


**Fig. 4.5** The illustration of Cauchy's cumulative distribution function in Eq. (4.32), showing an increasing tunneling activity near the percolation threshold

where $\gamma$ is a scale parameter denoting the rate of change for function $F$ around $c_1 = c_1^*$. The nature of function $F$ is illustrated in Fig. 4.5 with $c_1^* = 0.0266$ and $\gamma = 0.001$. It displays a sharp increase around $c_1^*$ and continues to hold afterward. With function $F$, the decrease of interfacial resistivity $\rho$ from $\rho_0$ as $c_1$ increases can be described by

$$\rho = \rho(c_1) = \rho_0 \left[F\left(1; c_1^*, \gamma\right) - F\left(c_1; c_1^*, \gamma\right)\right] / \left[F\left(1; c_1^*, \gamma\right) - F\left(0; c_1^*, \gamma\right)\right]. \tag{4.33}$$

This $c_1$-dependent $\rho$ is the tunneling-assisted interfacial resistivity, which returns to $\rho = \rho_0$ at $c_1 = 0$ and $\rho = 0$ at $c_1 = 1$. The nature of its variation is illustrated in Fig. 4.6 which shows a drastic decrease of interfacial resistivity around $c_1^*$. This tunneling-assisted interfacial resistivity $\rho(c_1)$ now should replace the original interfacial resistivity in Eqs. (4.29) and (4.31) to calculate the electrical conductivity of the coated inclusion $\sigma_i^c$, which in turn will replace $\sigma_i$ in Eq. (4.11) for the effective electrical conductivity, $\sigma_e$, of the overall nanocomposite. In this way, the influence of electron tunneling effect has been incorporated into our continuum model via the tunnel-assisted interfacial resistivity, $\rho(c_1)$. Up to this point we have completed the development of our continuum model for CNT and graphene-based nanocomposites. We now present some calculated results and make comparisons with experimental data.

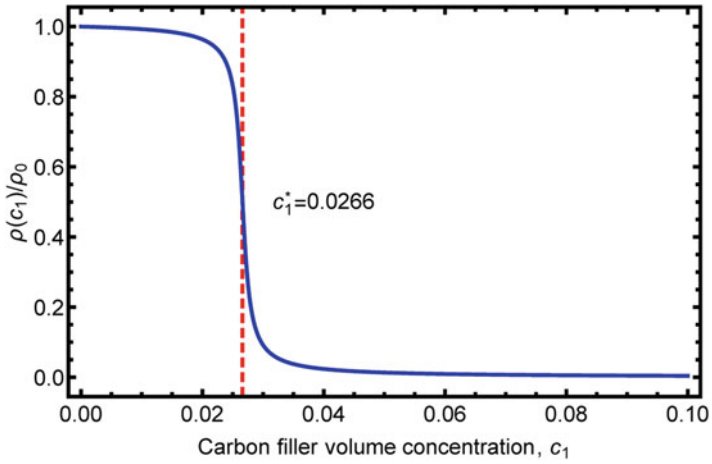


**Fig. 4.6** The illustration of the tunneling-assisted interfacial resistivity in Eq. (4.33), which leads to a sharp drop in resistivity near the percolation threshold

## 4.3 Results and Discussion

### *4.3.1 The Electrical Conductivity of CNT Nanocomposites*

To verify our continuum composite model, we take two steps to study the experimental data of the electrical conductivity of CNT nanocomposites and agglomerated graphene nanocomposites. In the first step, the composite is taken to be homogeneous. We use the effective-medium approach with interfacial resistance and tunneling-assisted interfacial conductivity to study two sets of experimental data by Ngabonziza et al. (2011) and McLachlan et al. (2005) showing notable percolation phenomena. The first set of data involved multi-walled CNTs in the polyimide matrix, while the second set was with single-walled CNTs and also the polyimide matrix. The intrinsic electrical conductivity of CNTs and the matrix are both given in the original papers and are listed in Table 4.1. In our calculations the anisotropic constant $m$, in $\sigma_1 = m\sigma_3$, for the CNT inclusion is assumed to be 0.001 at this moment. All other relevant material constants used in the calculations are also listed in Table 4.1.

#### 4.3.1.1 The Effective Electrical Conductivity of the Coated CNT

With Cauchy's cumulative distribution function $F$, we then use Eq. (4.29) to calculate the increase of the effective electrical conductivity of the coated CNT, $\sigma_i^c$, as $c_1$ increases, to reflect the contribution from the probabilistic electron tunneling process. The results with these two sets of experimental data are shown in Fig. 4.7a, b, respectively, where the upper blue curves are for the axial electrical conductivity

**Table 4.1** Physical values used in the calculation of the effective electrical conductivity of CNT nanocomposites

| Physical values | Ngabonziza et al. 2011 | McLachlan et al. 2005 |
|---|---|---|
| $\sigma_0$ | $2.0 \times 10^{-8}$ S/m | $5.5 \times 10^{-15}$ S/m |
| $\sigma_3$ | $1.943 \times 10^{4}$ S/m | $8.9 \times 10^{3}$ S/m |
| $\sigma_3/\sigma_0$ | $9.715 \times 10^{11}$ | $1.8 \times 10^{18}$ |
| $m$ | $10^{-3}$ | $10^{-3}$ |
| Percolation threshold | 0.0266 | 0.0005 |
| Aspect ratio $\alpha$ | 21 | 213 |
| CNT radius $R$ | 5 nm | 5 nm |
| Interfacial resistivity $\rho_0$ | $4.82 \times 10^{-8}$ m$^2$/S | $7.16 \times 10^{-4}$ m$^2$/S |
| Scale parameter $\gamma$ | 0.003 | 0.0003 |

and the lower red ones for the transverse electrical conductivity. These two sets of data have substantially different percolation thresholds, one at 0.0266 and the other at 0.0005. So the initial, nearly horizontal portion spans over a wider range of $c_1$ in the first set, but following the percolation threshold, both curves display a notable increase due to the stronger electron tunneling effect associated with the conductive network formation.

This characteristic can be made more apparent if we rewrite Eq. (4.29) as

$$\sigma_i^c = \frac{1}{1/\sigma_i + \rho\left(c_1\right) S_{ii}\left(1/\alpha + 2\right)/R}. \tag{4.34}$$

It can be observed that, when $c_1 < c_1^*$, the numerical value of $\rho(c_1)S_{ii}(1/\alpha + 2)/R$ is much larger than $1/\sigma_i$. So in this case the latter can be neglected and we have, approximately, $\sigma_i^c = R/\left[\rho\left(c_1\right) S_{ii}\left(1/\alpha + 2\right)\right]$, which means that $\sigma_i^c$ is now mainly controlled by the interfacial resistivity, rather than the intrinsic electrical conductivity of CNT. As such, the several-orders-of-magnitude difference between the axial conductivity $\sigma_3^c$ and the transverse conductivity $\sigma_1^c$ is only a result of the different components in the S-tensor. S-tensor characterizes the geometric property of CNT, which has a prolate spheroidal shape. Comparing Fig. 4.7a, b, it can be further pointed out that the higher aspect ratio in the second data set also leads to larger difference between $\sigma_3^c$ and $\sigma_1^c$. Therefore we can conclude that the geometry of CNT inclusions plays a very important role in the anisotropy of $\sigma_i^c$.

#### 4.3.1.2 The Effective Electrical Conductivity of CNT Nanocomposites

With the $c_1$-dependent $\sigma_i^c$ to replace the original $\sigma_i$ in Eq. (4.11), the effective electrical conductivity of CNT nanocomposites, $\sigma_e$, can be calculated as a function of CNT concentration $c_1$. The results are plotted in Figs. 4.8 and 4.9, respectively, that correspond to the experiment results of Ngabonziza et al. (2011) and McLachlan et al. (2005). In both figures the highest red curve represents the calculated result

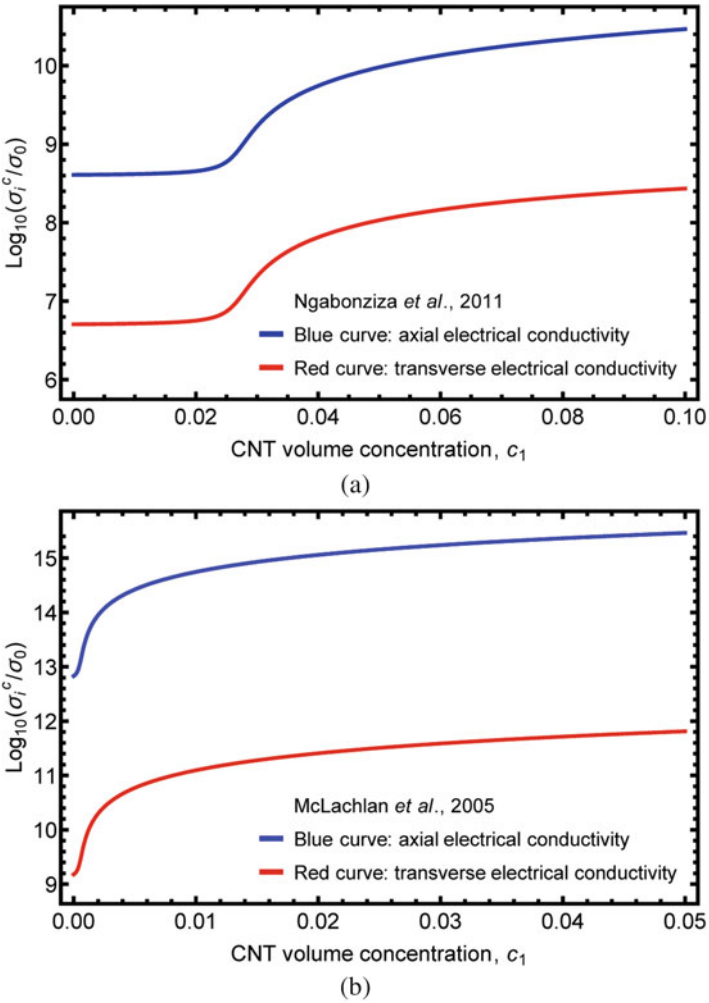


**Fig. 4.7** The electrical conductivity of coated CNT inclusion with the consideration of the interfacial resistance and tunneling-assisted interfacial conductivity: (**a**) by Ngabonziza et al. (2011) data and (**b**) by McLachlan et al. (2005) data

under the assumption of perfect interface between CNT inclusions and the matrix. It is seen that, without accounting for the interfacial resistance, the theoretical predictions are substantially higher than the experimental data. The lowest black curve in each figure represents the case in which the interfacial resistance is included, but the interfacial resistivity $\rho$ is regarded as a constant value $\rho_0$. This curve is seen to be lower than the experimental data, especially after percolation threshold. The middle blue curve represents the case in which $\rho$ is modified to $\rho(c_1)$ according to Eq. (4.33) with the consideration of the additional contribution from

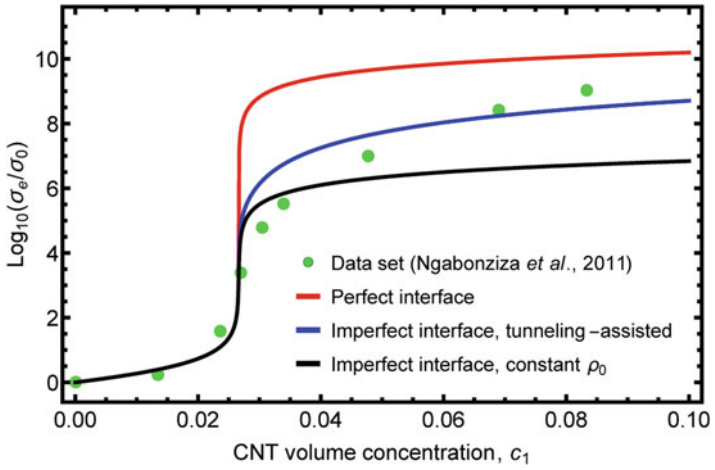


**Fig. 4.8** The effective electrical conductivity of CNT nanocomposites with Ngabonziza et al. (2011) data

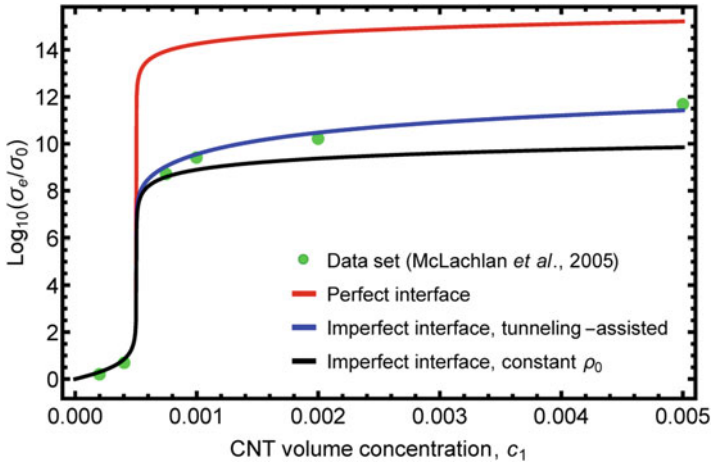


**Fig. 4.9** Effective electrical conductivity of CNT nanocomposites with McLachlan et al. (2005) data

the effect of tunneling-assisted interfacial conductivity. And this curve gives the best predictions for the experimental data. This study clearly confirms the view that the effect of imperfect interface is important and that the tunneling-assisted increase in interfacial conductivity is also a critical component of the theory. It is the combination of the effective-medium approach, interfacial resistance, and tunneling-assisted interfacial conductivity that eventually gives rise to a complete theory for the effective electrical conductivity of CNT nanocomposites.

#### 4.3.1.3 The Effect of CNT Anisotropy

Now with the theory established, we can examine the effect of CNT anisotropy on the effective electrical conductivity. In our previous analysis, the results were obtained based on the assumed value of $m = 10^{-3}$. In fact while the transverse electrical conductivity of CNT is known to be several orders of magnitude lower than the axial one, the precise value of $m$ is not clear yet. Thus further parametric studies are needed to clarify its effect. So we again use the first set of parameters listed in Table 4.1 for the experimental data of Ngabonziza et al. (2011) and consider four cases from isotropic to transversely isotropic, with $m = 1, 10^{-3}, 10^{-8}$, and 0, with the last one meaning that there is only axial electrical conductivity. The results are displayed in Fig. 4.10. From this figure we can immediately conclude that the effective electrical conductivity of overall composite is not sensitive to the value of $m$. Although the transverse electrical conductivity of CNT is lower than its axial one, it still has to be much higher than that of the polymer matrix. So far we have not seen any direct measurement on $\sigma_1$ for CNT, but for graphite sheets the electrical conductivity in the basal plane has been reported to be about 2–3 orders of magnitude higher than that along the normal direction. In this regard the value of $m$ is most likely to lie within the range of $10^{-3} \sim 10^{-2}$, and our assumed value of $10^{-3}$ can be so justified.

#### 4.3.1.4 The Effective Electrical Conductivity with a Totally Insulating Matrix

In CNT nanocomposites, electric current can flow from CNT inclusions to the matrix, or from one CNT to another one in contact. Both ways, plus the direct

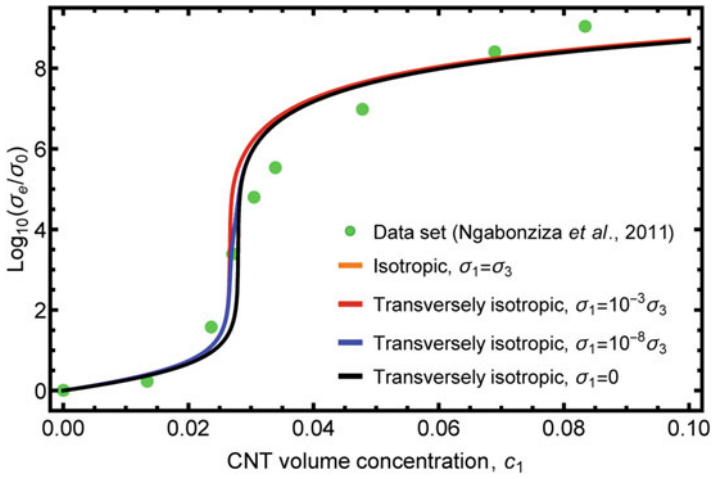


**Fig. 4.10** The effect of CNT anisotropy on the overall electrical conductivity. The orange isotropic curve is entirely overlapped by the red transversely isotropic curve because of their insignificant difference

electron tunneling from one CNT to another, can all contribute to the overall electrical conductivity. So even when the polymer matrix is totally insulating ($\sigma_0 = 0$), a viable continuum composite model should still be able to deliver a non-zero $\sigma_e$ from the last two mechanisms. In fact, even without the electron tunneling process, direct contact between CNT inclusions should still provide a conductive pathway for current flows, and thus the overall electrical conductivity should still exist. Such a capability, however, is lost in both the M-T method and the PCW model, because in both cases each CNT inclusion must be embedded in the polymer matrix. This can be seen from Eq. (4.11) that, if $\sigma_0 = 0$, the effective electrical conductivity will be $\sigma_e = 0$ (to see this, multiply $\sigma_0$ on both sides of the equation). To test such a capability for the effective-medium approach, we take Eq. (4.10) to solve for $\sigma_e$ under the insulating matrix condition. As has been discussed before, initially when $c_1$ is very low, all coefficients A, B, and C in Eq. (4.15) are positive, so there are two negative roots, which should be rejected since the electrical conductivity must be positive. Only when $c_1 > c_1^*$, coefficient C becomes negative, and there is one positive root, which is the effective electrical conductivity we want to solve. The condition of $C = 0$ is a critical point where the root is $\sigma_e = 0$. This analysis indicates that, when $c_1 < c_1^*$, since at this stage all CNT inclusions are isolated by the insulating matrix, there is no overall electrical conductivity. And when $c_1 \geq c_1^*$, the nanocomposite starts to give a non-negative electrical conductivity due to the formation of the conductive network.With the first set of constants taken from Table 4.1, the calculated $\sigma_e$ from $c_1 = c_1^*$ to $c_1 = 0.1$ is shown in Fig. 4.11. A drastic increase of electrical conductivity is observed near the percolation threshold.

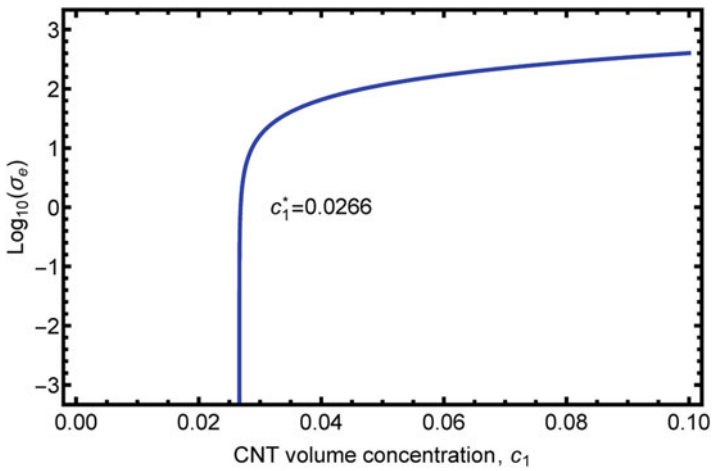


**Fig. 4.11** The examination of the effective-medium approach for the effective electrical conductivity of a composite with a totally insulating matrix

### 4.3.2 The Electrical Conductivity of Agglomerated Graphene Nanocomposites

In the last section our model has been successfully applied to study the electrical conductivity of homogeneous CNT nanocomposites. In this section we will focus on its capability to deal with nanocomposites with filler agglomeration, and we do so by demonstrating that a set of experimental data reported by Tkalya et al. (2014) for the electrical conductivity of agglomerated graphene/polystyrene nanocomposites can be well captured by this theory.

This set of data consists of 4 samples of graphene nanocomposites with different degrees of filler agglomeration, which is reproduced in Fig. 4.12. Note that the electrical conductivity has the unit of S/m, and is shown in logarithmic scale. Among them sample B has the highest percolation threshold of $c_1^* = 0.023$, followed by samples A-HE, A-LC, and A with $c_1^* = 0.015$, 0.012, and 0.010 (note that the original data are in wt.%, and they have been converted to vol.% by considering the density of graphene is twice of that of polystyrene). It is also reported that the different degrees of graphene agglomeration are due to different processing routes. The graphene fillers in sample B are produced by the liquid-phase exfoliation of graphite, which have the most dispersed distribution. In the other three samples, graphene fillers are prepared by the thermal reduction of graphite oxide but with different amount of energy provided during the sonication process. Samples A and A-LC are more agglomerated than sample A-HE, which is in line with the fact that more energy was supplied to sample A-HE during the sonication process. In addition sample A is slightly more agglomerated than sample A-LC, making it the most agglomerated sample among the four. Based on these observations, we assume

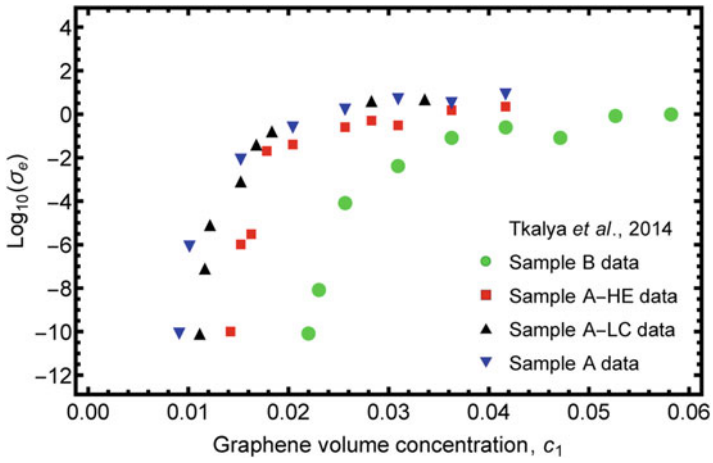


**Fig. 4.12** The experimental data on the electrical conductivity of 4 samples of graphene nanocomposites with various degrees of filler agglomeration, reproduced from Tkalya et al. (2014)

**Table 4.2** Physical values used in the calculations for agglomerated graphene nanocomposite samples B, A-HE, A-LC, and A. The last column gives the percolation threshold for the idealized spherical agglomerates

| | Sample A | Sample A-LC | Sample A-HE | Sample B | Spherical agglomerates |
|---|---|---|---|---|---|
| Parameter $a$ | 0.9 | 0.8 | 0.9 | ... | 0.7 |
| Parameter $b$ | 0.05 | 0.08 | 0.05 | ... | 0.05 |
| Percolation threshold (%) | 1.01 | 1.16 | 1.52 | 2.30 | 4.35 |
| Aspect ratio of agglomerate $\alpha_R$ | 0.1241 | 0.0728 | 0.1399 | ... | 1.0 |
| Thickness of agglomerate $\lambda$ (nm) | 50 | 50 | 50 | ... | 50 |
| Initial interfacial resistivity $\rho_0$ ($m^2$/S) | $5 \times 10^{-8}$ | $1 \times 10^{-7}$ | $6 \times 10^{-7}$ | $5 \times 10^{-7}$ | $5 \times 10^{-7}$ |
| Scale parameter $\gamma$ | 0.03 | 0.003 | 0.01 | 0.001 | 0.01 |

that the amount of graphene agglomeration in sample B is negligible and that the degree of graphene agglomeration increases from sample A-HE, to A-LC, and to A.

In our numerical computations, the in-plane electrical conductivity of graphene is taken to be $\sigma_1 = 8.32 \times 10^4$S/m, which is adopted from Stankovich et al. (2006) (they gave a range of $10^{4.92 \pm 0.52}$S/m), and the electrical conductivity of polystyrene is taken to be $\sigma_0 = 6.09 \times 10^{-12}$S/m, from Srivastava and Mehra (2008). The anisotropic constant $m$, in $\sigma_1 = m\sigma_3$, is taken to be $10^3$ since normal electrical conductivity is weaker for graphene. Other material parameters used here include the aspect ratio of graphene $\alpha = 0.0136$, the thickness of graphene $\lambda = 5$nm, the initial interfacial resistivity $\rho_0 = 5 \times 10^{-7}$m$^2$/S, and scale parameter $\gamma = 0.001$. On the larger scale of the composite consisting of graphene-rich agglomerates and graphene-poor region, the constants used are sample dependent and listed in Table 4.2. Note that the listed $\alpha_R$, $\lambda$, and $\rho_0$ in Table 4.2 pertain to this large-scale property. With these constants, we now show the calculated results.

#### 4.3.2.1 Homogeneously Dispersed Graphene Nanocomposites: Sample B

First we consider the sample B data, which are reproduced in Fig. 4.13. This set of data has a reported percolation threshold of $c_1^* = 0.023$, which can be directly calculated from Eq. (4.16) with the aspect ratio $\alpha = 0.0136$, since this sample has negligible filler agglomerations. We make an initial calculation for the overall electrical conductivity by assuming perfect interfaces (with $\rho = 0$, or $\sigma_i^{(c)} = \sigma_i$). The effective electrical conductivity can be obtained from Eq. (4.10). The calculated result is shown in red line in Fig. 4.13. The comparison between this curve and the experimental data clearly indicates that the calculated electrical conductivity is

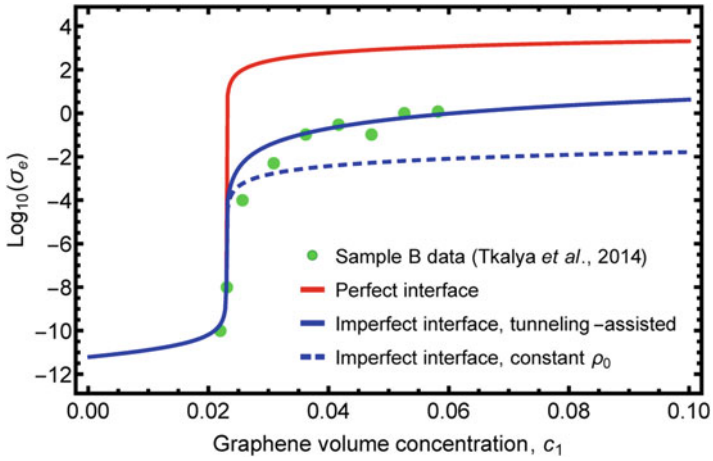


**Fig. 4.13** The theoretical curves for sample B data with perfect and imperfect interfaces

substantially higher than the test data. This is also an indication that the interface condition between graphene and polystyrene cannot be perfect.

In order to understand the effect of imperfect interfaces, we then use the constant interfacial resistivity, $\rho = \rho_0$, to make the calculation. The calculated conductivity is shown in the dashed blue line. When compared with the perfect interface curve, this result clearly shows a substantial drop to an order that is closer to the test data. But the trend of this curve is seen to stay relatively flat after percolation threshold. This is an indication that, without accounting for the additional contribution from the tunneling-assisted interfacial conductivity, the theoretical results become too low, especially after the percolation condition has been reached. When this tunneling effect is implemented through $\rho(c_1)$ in Eq. (4.33), we can see a continuous gain in effective electrical conductivity as shown in the blue line. The outcome is a curve with an added slope, and the theory is then in very close agreement with the experimental data. This consideration strongly points to the need of an imperfect interface with a tunneling-assisted interfacial conductivity.

#### 4.3.2.2 Agglomerated Graphene Nanocomposites: Sample A-HE, A-LC, and A

We now use the two-scale composite model to study the effect of filler agglomeration on the percolation threshold and overall electrical conductivity in samples A-HE, A-LC, and A. These three samples were reported to have an increasing degree of agglomeration, respectively. Their experimental data are reproduced in Figs. 4.14, 4.15, and 4.16, along with theoretical results from the two-scale effective-medium approach. In each case parameters $a$ and $b$ and the aspect ratio of graphene-rich agglomerates, $\alpha_R$, are all involved in the calculation.

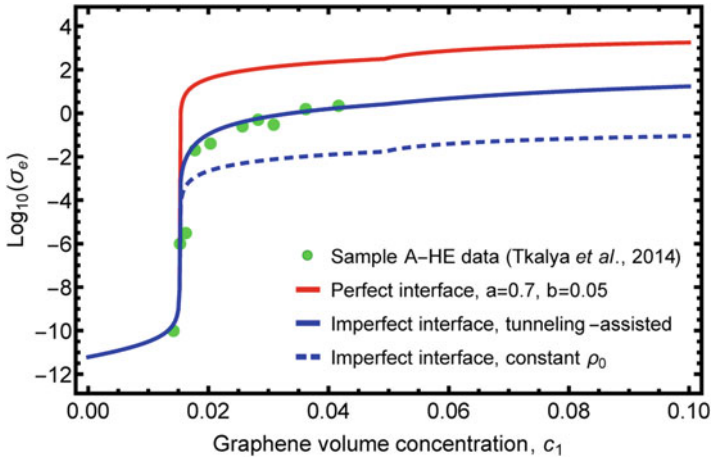


**Fig. 4.14** The theoretical curves for sample A-HE data with perfect and imperfect interfaces

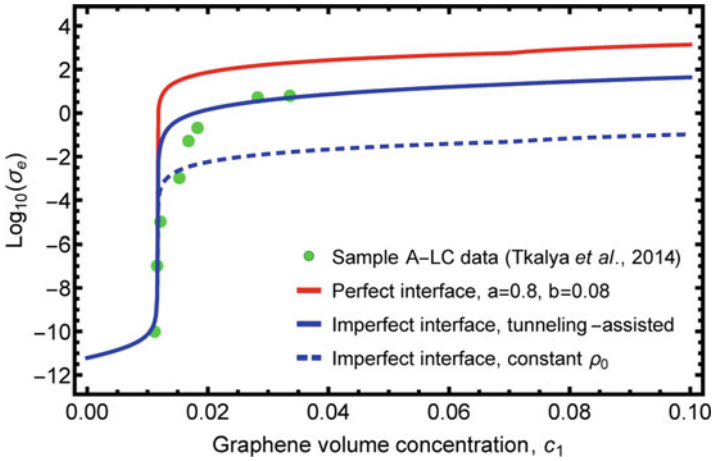


**Fig. 4.15** The theoretical curves for sample A-LC data with perfect and imperfect interfaces

With the constants listed in Table 4.2, the calculated results for these three samples are also plotted in Figs. 4.14, 4.15, and 4.16. As with Fig. 4.13, the red line in each figure represents the calculated conductivity under the assumption of a perfect interface. The three red curves are seen to be notably higher than their respective experimental data. By implementing a constant interfacial resistivity, $\rho = \rho_0$, the calculated conductivity, shown in each dashed blue line, is significantly reduced. These curves, however, all appear to stay relatively flat after the percolation threshold. It is only when the tunneling-assisted interfacial conductivity is also implemented into the interface model can all the reported experimental data be well captured.

In passing it is also noted that there is a kink in the red curve in Fig. 4.14 around $c_1 = 0.05$, and so is in Fig. 4.15 around $c_1 = 0.07$. This slight increase is

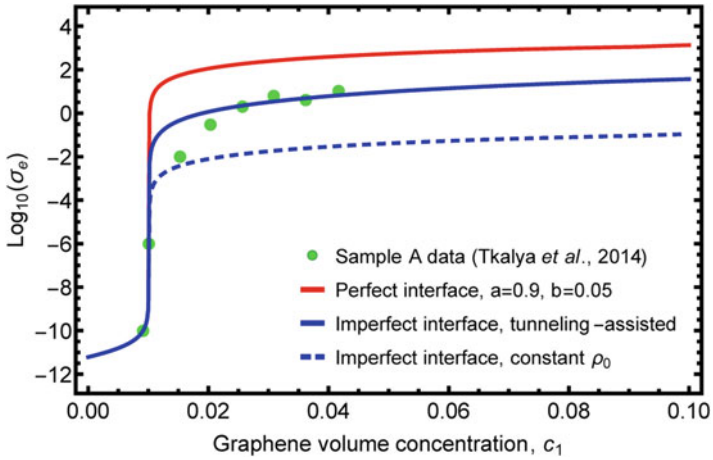


**Fig. 4.16** The theoretical curves for sample A data with perfect and imperfect interfaces

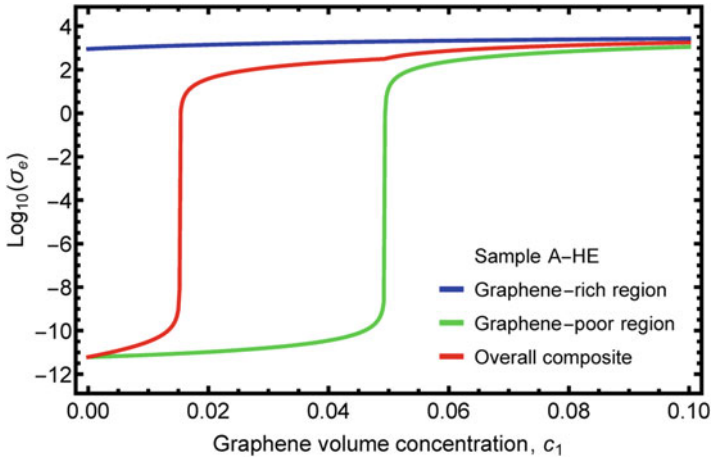


**Fig. 4.17** The effective electrical conductivity of the graphene-rich and graphene-poor regions and the overall composite for sample A-HE

not an artifact of the computational results; it is due to the onset of percolation in the graphene-poor region. To reveal this phenomenon, we plot the effective electrical conductivity of the graphene-rich, and graphene-poor region, and the overall composite altogether in Fig. 4.17. It is clear that the graphene-rich region has been percolated since the beginning, and the graphene-poor region starts to percolate at the highest graphene concentration. The overall composite has the contributions from both two regions, so it has low electrical conductivity in the beginning, but it percolates earlier than the graphene-poor region.

#### 4.3.2.3 The Role of Agglomerate Shape on the Percolation Threshold

The preceding discussions have suggested that filler agglomeration has the primary effect on the percolation threshold, and that interface conditions control the level of overall conductivity post percolation. In the past, it is often said that filler agglomeration tends to increase the percolation threshold, but we have proved and the discussed experiment has also shown that filler agglomeration can decrease the percolation threshold. This is a welcome consequence as high conductivity can be achieved at even lower graphene loading. But it cannot be concluded that graphene agglomeration will always lower the percolation threshold. The percolation threshold $c_1^*$, as shown in Eqs. (4.2) and (4.26), is seen to depend on the three parameters, $a$, $b$, and $\alpha_R$. The first two specify the dispersion state of graphene in the agglomerates, whereas the third one defines the agglomerate shape. For the percolation threshold to decrease, the shape has to be sufficiently oblate (or prolate). If the shape is very rounded or becomes spherical, such a desirable outcome cannot be expected. To show such an effect, we have taken $\alpha_R = 1$ while retaining the other parameters used in the calculation of A-HE to determine the corresponding percolation threshold. The newly calculated value is $c_1^* = 0.044$, which is higher than the percolation threshold of sample B, at $c_1^* = 0.023$. This value is listed in the last column of Table 4.2. So it is possible that the percolation threshold increases with spherical or more rounded agglomerates.

To be sure, the choice of a spherical shape for the agglomerates, $\alpha_R = 1$, does not guarantee that the calculated percolation threshold will always be higher than $c_1^* = 0.023$; it also depends on the dispersion state represented by parameters $a$ and $b$. This can be seen from the consideration of the percolation condition represented by Eq. (4.26). When $\alpha_R = 1$, that is, when $c_R^* = 1/3$, we have $c_1^* = b/[3a - (1 - b)]$. Therefore in order to have $c_1^* > 0.023$, it requires $b/[3a-(1-b)] > 0.023$ or $b > 0.0235(3a-1)$, which is 0.026 when $a = 0.7$. From the last column of Table 4.2, the value of $b$ is 0.05, which is indeed higher than 0.026; therefore the percolation threshold is higher than 0.023. If, instead, a value of $b < 0.026$ is chosen, the overall percolation threshold would become lower than that of the homogeneously dispersed nanocomposites.

It is evident that the dispersion parameters $a$ and $b$, and the agglomerate aspect ratio, $\alpha_R$, all contribute to the final percolation threshold, $c_1^*$, of the agglomerated graphene nanocomposites.

## 4.4 Conclusions

In this chapter, we have developed a continuum composite model to determine the effective electrical conductivity and percolation threshold of CNT and graphene-based nanocomposites. The theoretical framework of our model consists of four major components: (1) the effective-medium approach under perfect interface condition, (2) a two-scale model to account for the effect of filler agglomeration, (3) a diminishing layer of imperfect interface with an interfacial resistivity, and

(4) a statistical function to characterize the increase of interfacial conductivity due to electron tunneling effect. The outcome is a simple and widely useful model that can cover the nanocomposite with perfect and imperfect interfaces, as well as homogeneous and inhomogeneous filler distribution.

Our theories start with the effective-medium approach, which serves as the fundamental equation for the effective electrical conductivity of two-phase CNT and graphene-based nanocomposites. This equation also directly leads to the derivation of percolation threshold. To account for the effect of filler agglomeration, we then establish the two-scale model which divides the whole composite into filler-rich and filler-poor regions. The effective-medium approach is applied to the two-scale composite morphology by first determining the electrical conductivity of the filler-rich and the filler-poor regions and subsequently using their results to determine the overall electrical conductivity of the nanocomposite. Furthermore, the interfacial resistance and tunneling-assisted interfacial resistivity are incorporated in the model to cover the effect of imperfect interfaces and electron tunneling.

We have demonstrated that this model could successfully capture the quantitative behavior of two sets of experimental data of the electrical conductivity of homogeneous CNT nanocomposites. We also studied a set of experimental data of the agglomerated graphene nanocomposites to verify the applicability of our two-scale composite model. In this process, we have further shown how the imperfect interfaces lower the overall electrical conductivity and how the additional tunneling-assisted interfacial conductivity significantly brings it up after the percolation threshold. In addition, we have used the developed model to study the effect of the anisotropic electrical conductivity of carbon fillers in the axial and transverse directions and proved that this effect is insignificant. We have also proved that, even with a perfectly insulating matrix, the effective-medium approach is still capable of delivering non-zero electrical conductivity for the overall nanocomposites after the percolation threshold. In the end we have discussed how the percolation threshold can be influenced by the dispersion state of carbon fillers, as well as the shape of filler agglomerates.

**Acknowledgment** This work was supported by the US National Science Foundation, Mechanics of Materials Program, under grant CMMI-1162431.

## References

Aguilar, J., Bautista-Quijano, J., Avilés, F.: Influence of carbon nanotube clustering on the electrical conductivity of polymer composite films. Express Polym Lett. **4**, 292–299 (2010)

Allen, M.J., Tung, V.C., Kaner, R.B.: Honeycomb carbon: a review of graphene. Chem. Rev. **110**, 132–145 (2010)

Balberg, I., Binenbaum, N., Wagner, N.: Percolation thresholds in the three-dimensional sticks system. Phys. Rev. Lett. **52**, 1465–1468 (1984)

Bao, W.S., Meguid, S.A., Zhu, Z.H., Weng, G.J.: Tunneling resistance and its effect on the electrical conductivity of carbon nanotube nanocomposites. J. Appl. Phys. **111**, 093726 (2012)

Bao, W.S., Meguid, S.A., Zhu, Z.H., Pan, Y., Weng, G.J.: Effect of carbon nanotube geometry upon tunneling assisted electrical network in nanocomposites. J. Appl. Phys. **113**, 234313 (2013)

Barai, P., Weng, G.J.: A theory of plasticity for carbon nanotube reinforced composites. Int. J. Plast. **27**, 539–559 (2011)

Bauhofer, W., Kovacs, J.Z.: A review and analysis of electrical percolation in carbon nanotube polymer composites. Compos. Sci. Technol. **69**, 1486–1498 (2009)

Benveniste, Y.: A new approach to the application of Mori-Tanaka's theory in composite materials. Mech. Mater. **6**, 147–157 (1987)

Bruggeman, D.A.G.: Calculation of various physics constants in heterogenous substances I Dielectricity constants and conductivity of mixed bodies from isotropic substances. Ann. Phys. **24**, 636–664 (1935)

Budiansky, B.: On the elastic moduli of some heterogeneous materials. J. Mech. Phys. Solids. **13**, 223–227 (1965)

Castañeda, P.P., Willis, J.R.: The effect of spatial distribution on the effective behavior of composite materials and cracked media. J. Mech. Phys. Solids. **43**, 1919–1951 (1995)

Chatterjee, A.P.: A percolation-based model for the conductivity of nanofiber composites. J. Chem. Phys. **139**, 224904 (2013)

Deng, F., Zheng, Q.-S.: An analytical model of effective electrical conductivity of carbon nanotube composites. Appl. Phys. Lett. **92**, 071902 (2008)

Duan, H.L., Karihaloo, B.L.: Effective thermal conductivities of heterogeneous media containing multiple imperfectly bonded inclusions. Phys. Rev. B. **75**, 064206 (2007)

Duan, H.L., Karihaloo, B.L., Wang, J., Yi, X.: Effective conductivities of heterogeneous media containing multiple inclusions with various spatial distributions. Phys. Rev. B. **73**, 174203 (2006)

Dunn, M.L., Taya, M.: The effective thermal conductivity of composites with coated reinforcement and the application to imperfect interfaces. J. Appl. Phys. **73**, 1711–1722 (1993)

Eshelby, J.D.: The determination of the elastic field of an ellipsoidal inclusion, and related problems. Proc. R. Soc. London A. **241**, 376–396 (1957)

Feng, C., Jiang, L.: Micromechanics modeling of the electrical conductivity of carbon nanotube (CNT)–polymer nanocomposites. Compos. Part A Appl. Sci. Manuf. **47**, 143–149 (2013)

Gao, L., Li, Z.: Effective medium approximation for two-component nonlinear composites with shape distribution. J. Phys. Condens. Matter. **15**, 4397 (2003)

Gardea, F., Lagoudas, D.C.: Characterization of electrical and thermal properties of carbon nanotube/epoxy composites. Compos. Part B Eng. **56**, 611–620 (2014)

Geim, A.K., Novoselov, K.S.: The rise of graphene. Nat. Mater. **6**, 183–191 (2007)

Hashin, Z.: Thin interphase/imperfect interface in conduction. J. Appl. Phys. **89**, 2261–2267 (2001)

Hashin, Z., Shtrikman, S.: A variational approach to the theory of the effective magnetic permeability of multiphase materials. J. Appl. Phys. **33**, 3125–3131 (1962)

Hatta, H., Taya, M.: Effective thermal conductivity of a misoriented short fiber composite. J. Appl. Phys. **58**, 2478–2486 (1985)

He, L., Tjong, S.C.: Low percolation threshold of graphene/polymer composites prepared by solvothermal reduction of graphene oxide in the polymer solution. Nanoscale Res. Lett. **8**, 1–7 (2013)

Hernández, J.J., García-Gutiérrez, M.C., Nogales, A., Rueda, D.R., Kwiatkowska, M., Szymczyk, A., Roslaniec, Z., Concheso, A., Guinea, I., Ezquerra, T.A.: Influence of preparation procedure on the conductivity and transparency of SWCNT-polymer nanocomposites. Compos. Sci. Technol. **69**, 1867–1872 (2009)

Hill, R.: A self-consistent mechanics of composite materials. J. Mech. Phys. Solids. **13**, 213–222 (1965)

Landauer, R.: The electrical resistance of binary metallic mixtures. J. Appl. Phys. **23**, 779–784 (1952)

Li, C., Chou, T.-W.: Continuum percolation of nanocomposites with fillers of arbitrary shapes. Appl. Phys. Lett. **90**, 174108 (2007)

Li, J., Ma, P.C., Chow, W.S., To, C. K, Tang, B.Z., Kim, J.K.: Correlations between percolation threshold, dispersion state, and aspect ratio of carbon nanotubes. Adv. Funct. Mater. **17**, 3207–3215 (2007b)

Li, C., Thostenson, E.T., Chou, T.-W.: Dominant role of tunneling resistance in the electrical conductivity of carbon nanotube–based composites. Appl. Phys. Lett. **91**, 223114 (2007a)

Ma, H.M., Gao, X.-L., Tolle, T.B.: Monte Carlo modeling of the fiber curliness effect on percolation of conductive composites. Appl. Phys. Lett. **96**, 061910 (2010)

Martin, C.A., Sandler, J.K.W., Shaffer, M.S.P., Schwarz, M.K., Bauhofer, W., Schulte, K., Windle, A.H.: Formation of percolating networks in multi-wall carbon-nanotube–epoxy composites. Compos. Sci. Technol. **64**, 2309–2316 (2004)

Maxwell, J. C. A Treatise on Electricity and Magnetism, Vol. 1, 3rd ed. (Clarendon Press, Oxford, original 1891, reproduced 1982), p. 435–441

McLachlan, D.S., Chiteme, C., Park, C., Wise, K.E., Lowther, S.E., Lillehei, P.T., Siochi, E.J., Harrison, J.S.: AC and DC percolative conductivity of single wall carbon nanotube polymer composites. J. Polym. Sci. Part B Polym. Phys. **43**, 3273–3287 (2005)

Mori, T., Tanaka, K.: Average stress in matrix and average elastic energy of materials with misfitting inclusions. Acta Metall. **21**, 571–574 (1973)

Nan, C.-W., Birringer, R., Clarke, D.R., Gleiter, H.: Effective thermal conductivity of particulate composites with interfacial thermal resistance. J. Appl. Phys. **81**, 6692–6699 (1997)

Nan, C.-W., Shen, Y., Ma, J.: Physical properties of composites near percolation. Annu. Rev. Mater. Res. **40**, 131–151 (2010)

Ngabonziza, Y., Li, J., Barry, C.F.: Electrical conductivity and mechanical properties of multi-walled carbon nanotube-reinforced polypropylene nanocomposites. Acta Mech. **220**, 289–298 (2011)

Pan, Y., Weng, G.J., Meguid, S.A., Bao, W.S., Zhu, Z.-H., Hamouda, A.M.S.: Percolation threshold and electrical conductivity of a two-phase composite containing randomly oriented ellipsoidal inclusions. J. Appl. Phys. **110**, 123715 (2011)

Pang, H., Chen, T., Zhang, G., Zeng, B., Li, Z.-M.: An electrically conducting polymer/graphene composite with a very low percolation threshold. Mater. Lett. **64**, 2226–2229 (2010)

Prasher, R., Evans, W., Meakin, P., Fish, J., Phelan, P., Keblinski, P.: Effect of aggregation on thermal conduction in colloidal nanofluids. Appl. Phys. Lett. **89**, 143119 (2006)

Reinecke, B.N., Shan, J.W., Suabedissen, K.K., Cherkasova, A.S.: On the anisotropic thermal conductivity of magnetorheological suspensions. J. Appl. Phys. **104**, 023507 (2008)

Seidel, G.D., Lagoudas, D.C.: A micromechanics model for the electrical conductivity of nanotube-polymer nanocomposites. J. Compos. Mater. **43**, 917–941 (2009)

Srivastava, N.K., Mehra, R.M.: Study of structural, electrical, and dielectric properties of polystyrene/foliated graphite nanocomposite developed via in situ polymerization. J. Appl. Polym. Sci. **109**, 3991–3999 (2008)

Stankovich, S., Dikin, D.A., Dommett, G.H.B., Kohlhaas, K.M., Zimney, E.J., Stach, E.A., Piner, R.D., Nguyen, S.T., Ruoff, R.S.: Graphene-based composite materials. Nature. **442**, 282–286 (2006)

Tkalya, E., Ghislandi, M., Otten, R., Lotya, M., Alekseev, A., van der Schoot, P., Coleman, J., de With, G., Koning, C.: Experimental and theoretical study of the influence of the state of dispersion of graphene on the percolation threshold of conductive graphene/polystyrene nanocomposites. ACS Appl. Mater. Interfaces. **6**, 15113–15121 (2014)

Wang, Y., Weng, G.J., Meguid, S.A., Hamouda, A.M.: A continuum model with a percolation threshold and tunneling-assisted interfacial conductivity for carbon nanotube-based nanocomposites. J. Appl. Phys. **115**, 193706 (2014)

Wang, Y., Shan, J.W., Weng, G.J.: Percolation threshold and electrical conductivity of graphene-based nanocomposites with filler agglomeration and interfacial tunneling. J. Appl. Phys. **118**, 065101 (2015)

Weng, G.J.: Some elastic properties of reinforced solids, with special reference to isotropic ones containing spherical inclusions. Int. J. Eng. Sci. **22**, 845–856 (1984)

Weng, G.J.: The theoretical connection between Mori-Tanaka's theory and the Hashin-Shtrikman-Walpole bounds. Int. J. Eng. Sci. **28**, 1111–1120 (1990)

Weng, G.J.: A dynamical theory for the Mori–Tanaka and Ponte Castañeda–Willis estimates. Mech. Mater. **42**, 886–893 (2010)

Xie, S.H., Liu, Y.Y., Li, J.Y.: Comparison of the effective conductivity between composites reinforced by graphene nanosheets and carbon nanotubes. Appl. Phys. Lett. **92**, 243121 (2008)

# Chapter 5
# Mechanical Behavior of Nanowires with High-Order Surface Stress Effects

**Min-Sen Chiu and Tungyang Chen**

**Abstract** Surface in solids could behave differently from their bulk part, especially when the size of the solid is on the nanoscale. It has been widely accepted that the continuum mechanics framework along with a suitable implementation of the surface effect, referred to as surface stress model, could serve as a useful tool in the analysis of mechanical behavior of nanosized solids and structures. Here we review the surface stress model briefly and outline recent progress in application to mechanics of nanosolids or nanocomposites. A refined model, termed high-order surface stress model proposed by the authors few years ago, was recapitulated here, particularly for two-dimensional configurations. The distinction between the two frameworks is highlighted from the viewpoint of a simple geometric exposition of mechanics of thin plate and shell. We demonstrate that, by comparison with experimental data, the incorporation of high-order surface stress could be critical in certain situations to capture the trend observed by the experimental observation. Some illustrations are directed to the mechanics of nanowires, including bending and bulking behavior. Future potential subjects along the trend are suggested.

## 5.1 Introduction

For nanostructures or nanoscaled solids, due to their large specific surface-to-volume ratio, surface effects play an important role on the size-dependent physical properties. The subject of surface elasticity, incorporating surface stress effects, has received considerable attention in the last decade. This effect is particularly important for nanosized solids and composites in that they possess large specific surface area. The concept of surface tension in fluids dates back to more than about two centuries ago by the celebrated Young-Laplace (YL) equation (Young 1805; Laplace 1806). Surface tension in fluids is defined as a force per unit length along the perimeter of the interface. Surface stress in solids seems to be first introduced by Gibbs (1928), which is defined through the change in excess free energy when

M.-S. Chiu • T. Chen (✉)
Department of Civil Engineering, National Cheng Kung University, Tainan, 70101 Taiwan
e-mail: visquel88@hotmail.com; tchen@mail.ncku.edu.tw



S.A. Meguid, G.J. Weng (eds.), *Micromechanics and Nanomechanics of Composite Solids*, DOI 10.1007/978-3-319-52794-9_5

the interface is deformed at constant referential area. In contrast to fluids, surface stress may not be isotropic and may depend on the crystallographic parameters of the solids jointed at the interface. This stress is caused by the differences in configuration and in coordination numbers between atoms at the surface and in the bulk. In addition to surface of the domain boundary, surface effects also exist in interfaces between different regions, such as inclusions and the surrounding matrix. Interface stress is also playing the same role as that of surface stress. Using an atomistic calculation analysis, Zhou and Huang (2004) demonstrated that a solid surface can be either elastically softer or stiffer than their bulk counterparts. This surface effect phenomenon has been studied in different disciplines, ranging from material science, physical chemistry, to continuum mechanics (e.g., Nix and Gao 1998; Miller and Shenoy 2000; Thomson et al. 1986; Spaepen 2000; Duan et al. 2005a, b, c; Chen and Dvorak 2006). The aim of this chapter is to give an introductory exposition of the subject and to summarize our recent proposition for the high-order surface stress model, with potential applications in various problems of nanosized solid and composites.

Specifically, we see in this chapter how the high-order surface stress model will influence the solutions significantly for certain boundary value problems. The size-dependent mechanical behavior of nanowires (NWs) will be demonstrated. The difference between the calculations based on the high-order surface stress model and the Gurtin-Murdoch model can be seen remarkably, especially when the scale is in a few nanometers. This framework provides a simple continuum mechanics approach, in place of atomistic analysis or experiments, to analyze the mechanical behavior of nanostructures in a refined manner.

## 5.2 Surface Stresses in Mathematical Descriptions

It is generally thought that the surface stress tensor, $\sigma^s_{\alpha\beta}$, is connected to the deformation-dependent surface energy by the relation $\sigma^s_{\alpha\beta} = \tau^0\delta_{\alpha\beta} + \partial G/\partial\varepsilon^s_{\alpha\beta}$ (Shuttleworth 1950; Cammarata 1994). $\tau^0$ and $\varepsilon^s_{\alpha\beta}$ denote the constant residual surface tension and the strain tensor for surfaces, respectively, and $\delta_{\alpha\beta}$ is the Kronecker delta for surfaces. The Greek indices take on values of interfacial components, taking the numbers of 1–2, while the Latin index numbers indicated later will range from 1 to 3. The index 3 will designate the normal direction of the interface. The interface stresses can be written as a linear constitutive law, $\sigma^s_{\alpha\beta} = \tau^0\delta_{\alpha\beta} + L_{\alpha\beta\gamma\delta}\varepsilon^s_{\gamma\delta}$ (Miller and Shenoy 2000), in which $L_{\alpha\beta\gamma\delta}$ stands for the surface stiffness tensor. Considering isotropic surface property, the linear relationship between surface stress tensor $\sigma^s_{\alpha\beta}$ and surface strain field can be written in the form (Gurtin and Murdoch 1975, 1978; Assadi et al. 2010) $\sigma^s_{\alpha\beta} = \tau^0\delta_{\alpha\beta} + (\mu_s - \tau^0)\left(u^s_{\alpha,\beta} + u^s_{\beta,\alpha}\right) + (\lambda_s + \tau^0)\,u^s_{\gamma,\gamma}\delta_{\alpha\beta} + \tau^0 u^s_{\alpha,\beta}$. In the exposition, $u^s_\alpha$ are the displacement components of the surface, while $\lambda_s$ and $\mu_s$ are surface Lame constants. The effect of residual tension $\tau^0$ is not associated with the deformation

and is sometimes ignored in some relevant studies. For example, Sharma et al. (2003) investigated the elastic state of eigenstrained spherical inhomogeneities with surface effects and interpreted the concentration factor as a function of surface properties and void radius. Sharma and Ganti (2004) presented closed-form expressions of the modified Eshelby's tensor for spherical and cylindrical inclusions incorporating surface effects. Nix and Gao (1998) employed a simple spring model to calculate the excess free energy of interface atoms. They pointed out that this microscopic model is in complete accord with the classical macroscopic interpretation for interface stresses (i.e., $\sigma^s_{\alpha\beta} = \tau^0\delta_{\alpha\beta} + \partial G/\partial\varepsilon^s_{\alpha\beta}$). Gurtin and Murdoch (1975), in their 1975 paper, derived a mathematical framework for an interface between two different solids with interface stresses using the classical membrane theory (see also Gurtin and Murdoch 1978; Landau and Lifshitz 1987; Povstenko 1993; Gurtin et al. 1998; Chen et al. 2006; Ru 2010 for subsequent developments). In the formulation, a surface is assumed to ideally adhere to its counterpart bulk and modeled as a layer of vanishing thickness. This condition was referred to as the generalized Young-Laplace (generalized YL) equation in distinction with its counterpart in fluids. Chen et al. (2006) presented a simple geometrical exposition for the generalized YL equations, which provide a better description on the underlying physical meaning of the YL equation in solids. This approach is based on the notion that the interface stresses can be modeled as in-plane stresses along the tangential planes of the curved surface and the stress vectors on the top and lower faces of the curved surfaces are contributed from its three-dimensional bulk neighborhood. The generalized YL equations were also derived with generally curvilinear coordinates (Weng and Chen 2010), which are better suited for descriptions of some nanostructures, such as nanotubes, in which the grids are not orthonormal.

The modeling of surface/interface stress can be simulated by introducing a vanishingly thin interphase layer between two different regions with relatively high stiffness compared with the adjacent phases. A general rigorous approach is to resolve the elasticity solution for a three-phase configuration and then deduce to a two-phase one through a deliberated asymptotic process. A schematic illustration of the approach is demonstrated in Fig. 5.1. This approach allows us to effectively replace the effect of the thin interphase by equivalent interface conditions without having to resolve the fields within the interphase. Benveniste and Miloh (2001) examined the effects of imperfect soft and stiff interfaces in two-dimensional elasticity. Based on an asymptotic analysis, they showed that, depending on the softness or stiffness of the interphase layer with respect to the neighboring media, there exist seven regimes of interface conditions.

Other derivations can be found in Benveniste (2006a, b) for a three-dimensional thin interphase with anisotropic properties in elasticity as well as higher-order effects in conduction phenomenon. However, all these developments, based on rigorous asymptotic analysis, are indeed mathematically complicated. In summary, the conventional surface stress model is generally referred to as "generalized Young-Laplace (YL) equation," "Gurtin-Murdoch model," or "an $O(h^N)$ interface model with $N = 1$" (Benveniste 2006a, b), i.e., "first-order interface condition" where $h$ is

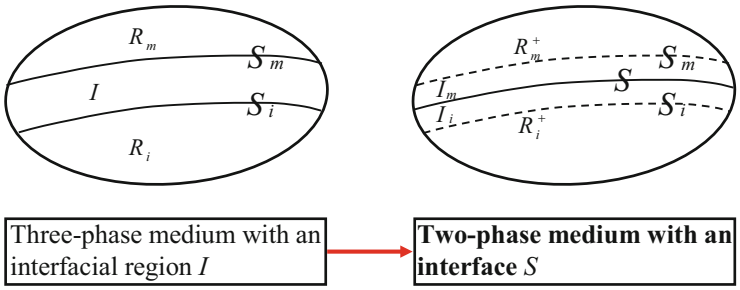


**Fig. 5.1** Surface stress along the interface can be modeled by a thin interphase degenerated into an infinitesimal thickness

the thickness of the interphase layer. Interface or surface stresses incorporating high-order effects may be designated as "an $O(h^N)$ interface model with $N>2$" in which $N$ is an integer. Other relevant researches in this category include Shuttleworth (1950), Bövik (1994), Benveniste and Baum (2007), Ting (2007), and Benveniste and Berdichevsky (2010).

In the following, we introduce some analysis and other aspects of applications related to one-dimensional mechanics problems within the generalized YL model. Nanowires are typical and important nanostructures in sensors, actuators, opto-electronics, and nanoelectromechanical systems (Wang 2009). The size-dependent overall mechanical behavior of NWs has been experimentally observed (Song et al. 2005; Jing et al. 2006; Ni and Li 2006; Ji et al. 2007; Young et al. 2007; Zhu et al. 2009) and theoretically demonstrated based on the Gurtin-Murdoch model (Wang and Feng 2007; He and Lilley 2008a, b; Wang and Feng 2009a, b; Abbasion et al. 2009; Wang and Feng 2010; Jiang and Yan 2010; Farshi et al. 2010; Wang and Yang 2011; Wang and Wang 2011; Yan and Jiang 2011a, b; He and Lilley 2012; Samaei et al. 2012; Zhang et al. 2013; Gao 2015). Considering the first-order interface condition, the stress jump $\bigtriangleup\sigma_{ij}$ across an interface surface is associated with the curvature tensor $\kappa_{\alpha\beta}$ of the surface by the relationship $\triangle\sigma_{ij}n_in_j = \sigma^s_{\alpha\beta}\kappa_{\alpha\beta}$ $(i,j=1,\ 2,\ 3;\ \alpha,\ \beta=1,\ 2)$ in which $n_i$ is the unit vector normal to the interface surface and $\sigma^s_{\alpha\beta}$ is the interface (surface) stress tensor. In one-dimensional problems, the surface constitutive relation $\sigma^s_{\alpha\beta} = \tau^0_{\alpha\beta} + S_{\alpha\beta\gamma\delta}\varepsilon^s_{\alpha\beta}$ can be simplified as $\sigma^s = \tau^0 + E_s\varepsilon^s$ within the framework of Gurtin-Murdoch model, where $\sigma^s$ is the surface stress, $\varepsilon^s$ is the surface strain, $E_s$ is the effective surface Young's modulus, and $\tau^0$ is the constant residual surface tension. For the developments in this line, Wang and Feng (2007) examined the natural frequency of microbeams with surface effect. Wang and Feng (2009a) derived the analytical relation for the axial buckling force of a nanowire under consideration of surface elasticity and residual surface tension effects. The dependence of the surface effects on the overall Young's modulus of bending nanowires in static and resonance has been studied by He and Lilley (2008a, b) for three different boundary conditions. In addition to Euler-Bernoulli beam theory, Timoshenko beam model has also been utilized to investigate the surface effects on the buckling (Wang and Feng 2009b) and free vibration behavior of a nanowire (Wang and Feng 2009b; Abbasion et al. 2009).

Recently, Jiang and Yan (2010) derived explicit solutions for studying the combined effects of shear deformation, surface elasticity, and residual surface tension on the effective stiffness via Timoshenko beam theory as well. It was found that the derivations in some of the above-mentioned one-dimensional researches agree with the experimental measurements well (Lachut and Sader 2007).

## 5.3 High-Order Surface Stresses in Two-Dimensional Configuration

A refined surface stress model, referred to as high-order surface stress model, was recently proposed by the authors (Chen and Chiu 2011). A schematic diagram for the difference between the higher-order interface stress model and the conventional surface stress model is illustrated in Fig. 5.2. For convenience, the concept is illustrated for a two-dimensional configuration. For the conventional surface stress model, only the in-plane surface/interface stress $\sigma_\alpha^s$ is considered in the force balance consideration. While for the high-order surface stress model, in addition to in-plane surface/interface stress $\sigma_\alpha^s$, the surface moment $m_\alpha^s$ is considered at the same time. The surface moment can be viewed as the effect of nonuniformity of the in-plane surface/interface stress across the thickness $h_1$ of the interphase (Fig. 5.2). The approach to introduce $\sigma_\alpha^s$ and $m_\alpha^s$ into the continuum framework is somewhat akin to the classical theories of beams, thin plates, and shells. As shown in Fig. 5.2,

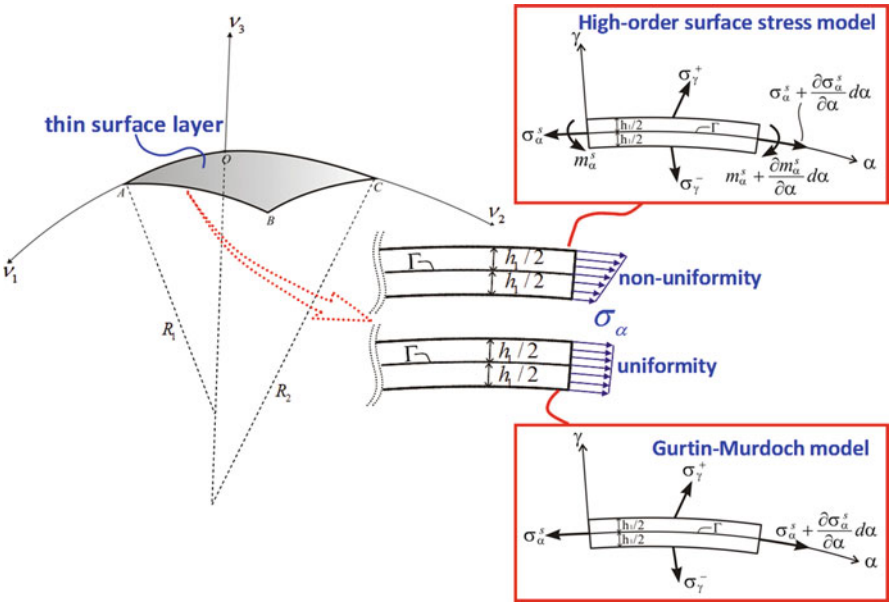


**Fig. 5.2** A schematic illustration of two different surface stress models in two-dimensional configurations: high-order surface stress model and Gurtin-Murdoch model

the stresses $\sigma_\alpha$ along the in-plane direction ($\alpha$-direction) of the layer are replaced by statically equivalent stress resultants and stress moments through the relations $\sigma_\alpha^s = \int_{-h_1/2}^{h_1/2} \sigma_{\alpha\alpha}\ d\gamma, m_\alpha^s = \int_{-h_1/2}^{h_1/2} \sigma_{\alpha\alpha}\gamma\ d\gamma$, and then they are interpreted as surface stress $\sigma_\alpha^s$ and surface moment $m_\alpha^s$, respectively. Of course, when only the in-place surface stress is considered and the effect of $m_\alpha^s$ is omitted from the beginning, this will reduce to the conventional surface stress model based on the membrane theory (generalized YL equation) (Chen et al. 2006).

For the kinematic deformation of the infinitesimally thin layer, based on the Kirchhoff-Love theory of thin shell, the relations were constructed as $\sigma_\alpha^s = E_s\varepsilon_\alpha^0$, $m_\alpha^s = -D_s\kappa_\alpha^0$. We mention that $\varepsilon_\alpha^0$ and $\kappa_\alpha^0$ are, respectively, the strain and the change in curvature on the middle surface of the thin layer. $E_s$ is the surface Young's modulus, defined as $E_s = E_c h_1/(1-{\nu_c}^2)$ here. It is equivalent to the material parameters $\lambda_s + 2\mu_s$ defined in Chen et al. (2007a, b). Note that $h_1$, $E_c$, and $\nu_c$ are the thickness, Young's modulus, and Poisson's ratio of the thin layer, respectively. On the other hand, $D_s$ is the flexure rigidity of the thin surface/interface layer, defined as $D_s = E_c h_1^3/12/\left(1-{\nu_c}^2\right)$.

When the thin layer has a high stiffness compared to its neighboring phases, the effective behavior of the layer can be viewed as a stiff interface. When the stiffness of the thin layer is with magnitudes of high orders $O(h^{-N})$, various kinds of interface conditions can be developed. In addition to the continuity condition for the displacements, $u_\alpha^{(i)}\Big|_\Gamma = u_\alpha^{(m)}\Big|_\Gamma$ and $u_\gamma^{(f)}\Big|_\Gamma = u_\gamma^{(m)}\Big|_\Gamma$, the jump conditions in traction would characterize different degrees of stiff interfaces. These include four types of interface conditions (Benveniste and Miloh 2001; Chen and Chiu 2011).

I. Perfectly bonded interfaces

$$\left[\sigma_{\gamma\alpha}\right]_\Gamma = \left[\sigma_{\gamma\gamma}\right]_\Gamma = 0. \tag{5.1}$$

II. Membrane type interface (the generalized YL equation)

$$\left[\sigma_{\gamma\alpha}\right]_\Gamma = -\left(\frac{\partial\sigma_\alpha^s}{\partial s}\right)_\Gamma, \qquad \left[\sigma_{\gamma\gamma}\right]_\Gamma = -\left(\frac{\sigma_\alpha^s}{R}\right)_\Gamma. \tag{5.2}$$

III. Inextensible membrane type

$$\begin{aligned} &\varepsilon_\alpha^0 = \left.\frac{\partial u_\alpha^0}{\partial s} - \frac{u_\gamma^0}{R}\right|_\Gamma = 0, \\ &\left[\sigma_{\gamma\alpha}\right]_\Gamma - \frac{\partial}{\partial s}\left\{R\left[\sigma_{\gamma\gamma}\right]_\Gamma\right\} = 0. \end{aligned} \tag{5.3}$$

IV. Inextensible classical shell type

$$\begin{aligned} &\varepsilon_\alpha^0 = \left.\frac{\partial u_\alpha^0}{\partial s} - \frac{u_\gamma^0}{R}\right|_\Gamma = 0, \\ &\left[\sigma_{\gamma\alpha}\right]_\Gamma - \frac{\partial}{\partial s}\left\{R\left[\sigma_{\gamma\gamma}\right]_\Gamma\right\} = \left(\frac{1}{R}\frac{\partial m_\alpha^s}{\partial\alpha}\right)_\Gamma + \frac{\partial}{\partial s}\left\{R\frac{\partial^2 m_\alpha^s}{\partial s^2}\right\}. \end{aligned} \tag{5.4}$$

We mention that Type I is the classical perfectly bonded condition and Type II is the conventional surface stress model, or the so-called Gurtin-Murdoch model. Types III and IV represent the stiff interface deduced from the high-order surface stress. It is noted that the inextensible condition $\varepsilon_{\alpha}^{0} = 0$ exists in both Type III and IV. These four kinds of interface conditions demonstrate the mathematical behavior of thin interphase layer between two neighboring media

Benveniste and Miloh (2001) derived the generalized interface conditions using an asymptotic expansion method. With the rigorous approach, Types I–IV here and the rigid type interface condition are termed stiff interfaces. In addition, they also derived two different types of soft interfaces.

### 5.3.1 *Boundary Value Problem: A Circular Inclusion in an Infinite Matrix*

We now illustrate the high-order surface effect by considering the boundary value problem of a circular inclusion in an infinite matrix under a transverse shear deformation applied at the remote boundary. The effect of high-order surface stresses is compared with that of simple surface stress model to exemplify the significance of high-order effects in certain situations. We will also see that the surface stress model and the high-order surface stress model both will have size-dependent behavior, depending on the geometric size of the inclusion. In Fig. 5.3, we suppose that the radius of the circular fiber is denoted by $a$. The effects of various types of interface conditions described in Eqs. (5.1)–(5.4) will be considered along the interface between the fiber and the matrix. It was noted that for high-order interface stresses, namely, Types III and IV, the "inextensible" interface condition needs to prevail (Chen and Chiu 2011). Thus, only the asymmetric deformation mode will be considered to examine the effect of high-order interface

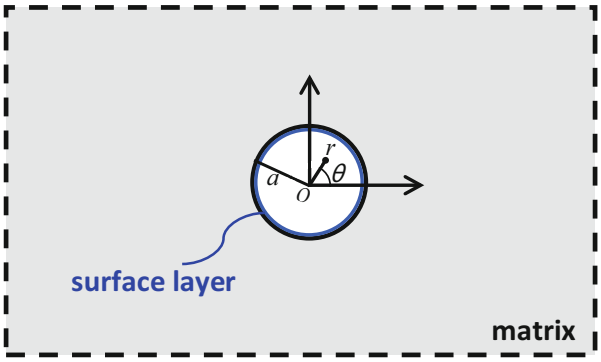


**Fig. 5.3** Schematic illustration of a composite medium composed of the matrix containing circular cavity with radius $a$ under the surface effects resulting from thin surface layer

stresses. The circular cylindrical coordinate is adapted within the mathematical continuum framework. The coordinate variables in Eqs. (5.1)–(5.4) are replaced with $\alpha = \theta$ and $\gamma = r$. Also, in the substitutions of $\partial s = r\partial\theta$ and $1/R = -1/r$, we can obtain the corresponding interface conditions in circular cylindrical coordinate for the present boundary value problem.

As an illustration for high-order interface stress effects, the configuration of a circular cavity in an unbounded isotropic matrix subjected to a remote transverse shear $\sigma_x^m\big|_{r\to\infty} = -\sigma_y^m\big|_{r\to\infty} = \sigma^0$ was studied by Chen and Chiu (2011). The stress concentration factor around the cavity surface was examined. The concentration factor is defined as the ratio of hoop stress on the cavity surface versus the applied stress $\sigma^0$ for the four different types of interfaces. The results were derived in explicit closed forms as

$$\textbf{Type I}: \left.\frac{\sigma_\theta}{\sigma^0}\right|_{r\to a} = -4\cos 2\theta, \tag{5.5}$$

$$\textbf{Type II}: \left.\frac{\sigma_\theta}{\sigma^0}\right|_{r\to a} = -\frac{4km + (E_s/a)(k-m)}{km + (E_s/2a)(2k+m)}\cos 2\theta, \tag{5.6}$$

$$\textbf{Type III}: \left.\frac{\sigma_\theta}{\sigma^0}\right|_{r\to a} = -\frac{2(k-m)}{2k+m}\cos 2\theta, \tag{5.7}$$

$$\textbf{Type IV}: \left.\frac{\sigma_\theta}{\sigma^0}\right|_{r\to a} = \frac{-2m(k-m) + 12\left(D_s/a^3\right)(k-m)}{m(2k+m) + 6\left(D_s/a^3\right)(k+2m)}\cos 2\theta. \tag{5.8}$$

We mention that the stress concentration factor for Type I is exactly the result of perfectly bonded interface given in Timoshenko and Goodier (1970) and that of Type II is identical with the surface stress model previously derived by Chen et al. (2007a). When letting $E_s/a \to 0$ in (5.6), Eq. (5.6) for Type II will reduce to the classical elasticity solution with a concentration factor of $-4$. On the other hand, when $E_s/a$ is a relatively large quantity compared with the orders of $k$ and $m$, then the concentration factor of Eq. (5.6) will approach to Eq. (5.7) for Type III. In addition, in Eq. (5.8), when one has $D_s/a^3 \to 0$, the concentration factor will reduce to that of Eq. (5.7) for Type III. Also, when $D_s/a^3$ is a large quantity compared with other terms in the numerator and denominator of Eq. (5.8), the expression of Eq. (5.8) will reduce to the result of an infinite medium containing a rigid inclusion. We mention that these four types of interface conditions characterize the degree of "stiffness" from the ideal situation (Type I) to the nearly rigid interface (Type IV) in a successive manner (Chen and Chiu 2011).

The stress concentration factor for stress components $\sigma_r$ and $\sigma_{r\theta}$ of an infinite medium containing a circular cavity under different types of interface conditions can also be derived as

$$\textbf{Type I}: \quad \left.\frac{\sigma_r}{\sigma^0}\right|_{r\to a} = 0, \tag{5.9}$$

$$\textbf{Type II}: \quad \left.\frac{\sigma_r}{\sigma^0}\right|_{r\to a} = -\frac{(E_s/a)\,(k+m)}{km + (E_s/2a)\,(2k+m)}\cos 2\theta, \tag{5.10}$$

$$\textbf{Type III}: \quad \left.\frac{\sigma_r}{\sigma^0}\right|_{r\to a} = -\frac{2\,(k+m)}{2k+m}\cos 2\theta, \tag{5.11}$$

$$\textbf{Type IV}: \quad \left.\frac{\sigma_r}{\sigma^0}\right|_{r\to a} = \frac{-2m\,(k+m) + 12\left(D_s/a^3\right)(k+m)}{m\,(2k+m) + 6\,(D_s/a^3)\,(k+2m)}\cos 2\theta, \tag{5.12}$$

$$\text{rigid inclusion}: \quad \left.\frac{\sigma_r}{\sigma^0}\right|_{r\to a} = \frac{2\,(k+m)}{k+2m}\cos 2\theta, \tag{5.13}$$

for the radial stress $\sigma_r$ and

$$\textbf{Type I}: \quad \left.\frac{\sigma_{r\theta}}{\sigma^0}\right|_{r\to a} = 0, \tag{5.14}$$

$$\textbf{Type II}: \quad \left.\frac{\sigma_{r\theta}}{\sigma^0}\right|_{r\to a} = -\frac{2\,(E_s/a)\,(k+m)}{km + (E_s/2a)\,(2k+m)}\sin 2\theta, \tag{5.15}$$

$$\textbf{Type III}: \quad \left.\frac{\sigma_{r\theta}}{\sigma^0}\right|_{r\to a} = -\frac{4\,(k+m)}{2k+m}\sin 2\theta, \tag{5.16}$$

$$\textbf{Type IV}: \quad \left.\frac{\sigma_{r\theta}}{\sigma^0}\right|_{r\to a} = -\frac{4m\,(k+m) + 12\left(D_s/a^3\right)(k+m)}{m\,(2k+m) + 6\,(D_s/a^3)\,(k+2m)}\sin 2\theta, \tag{5.17}$$

$$\text{rigid inclusion}: \quad \left.\frac{\sigma_{r\theta}}{\sigma^0}\right|_{r\to a} = -\frac{2\,(k+m)}{k+2m}\sin 2\theta, \tag{5.18}$$

for the shear stress $\sigma_{r\theta}$. As in the hoop stress $\sigma_\theta$, we see that Eqs. (5.9)–(5.13) for $\sigma_r$ and Eqs. (5.14)–(5.18) for $\sigma_{r\theta}$ also show that these four types of interface conditions characterize the degree of "stiffness" from the ideal situation (Type I) to the nearly rigid interface (Type IV) in a successive manner. Note that here $k_m$ and $m_m$ have been written simply by $k$ and $m$ for simplicity.

## 5.4 High-Order Surface Stresses in Nanowires

In this section, we present the high-order surface stress effect on the mechanical behavior of nanowires. Specifically, the high-order surface stress model developed in Sect. 5.3 was implemented for the static bending and buckling behavior of NWs. In line with the previous related references (Wang and Feng 2007; He and Lilley 2008a, b; Wang and Feng 2009a, b), the effect of surface elasticity as well as the

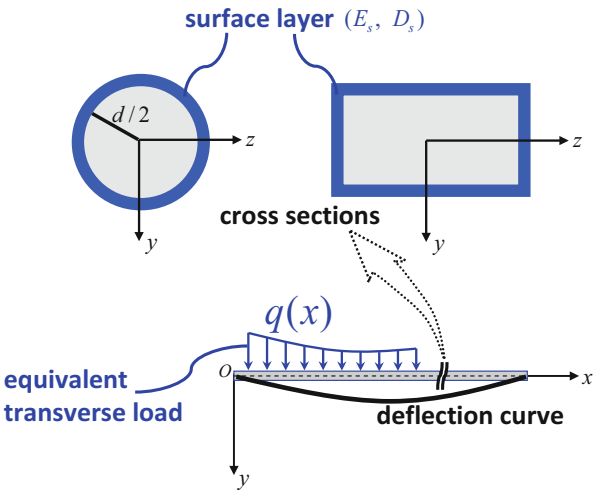


**Fig. 5.4** Cross sections of circular and rectangular nanowires with a surface layer and bending in the $x$-$y$ plane with equivalent distributed transverse load $q(x)$ resulting from surface moments as well as in-plane surface stresses

effect of residual surface tension will be examined. We compare the present results with previous studies based on the Gurtin-Murdoch model and with the existing experimental data. It is demonstrated that the high-order surface stress effect can be significantly pronounced when the dimension is in a few nanometers.

### 5.4.1 *Mechanical Behavior of NWs Based on Euler-Bernoulli Beam Theory*

In the consideration of residual surface tension $\tau_0$, the linear relations between the surface stress and strain and between the surface moment and curvature can be expressed as $\sigma_\alpha^s = \tau_0 + E_s\varepsilon_\alpha^0$ and $m_\alpha^s = -D_s\kappa_\alpha^0$. We mention that $E_s$ is the surface Young's modulus with the dimensions of N/m and $D_s$ is the surface bending stiffness with the dimensions of Nm. Two different cross-sectional shapes, rectangular and circular cross sections, of NWs were considered (Fig. 5.4). The effect of surface stress, based on the Gurtin-Murdoch model, was simulated by an equivalent distributed transverse force $q(x)$ that acts on the NW in bending (Wang and Feng 2007).

Here, the stress jump for high-order surface stress effect also results in a distributed transverse force (Chiu and Chen 2011a). But the surface stress and surface moment will contribute to different terms in the governing differential equation. For bending NWs in the $y$ direction under small deformation with $v$ being the NW transverse displacement (Fig. 5.4), the distributed transverse load for NWs with the high-order surface stress effect could be derived as $q(x) = Hv'' - Kv^{(4)}$(Chiu and Chen 2011a), where $v'' = d^2v/dx^2$ and $v^{(4)} = d^4v/dx^4$. The definitions of $H$ and $K$ can be found in Equation (9) of Chiu and Chen (2011a). For a deformed NW subjected to a compressive force $P$ acting in the longitudinal $x$ direction (Fig. 5.4),

the jump condition resulting from high-order surface stress effect will also give rise to a distributed transverse load $q(x)$ along the NW longitudinal direction. The governing equations based on the high-order surface stress model can be derived as

$$\left[(EI)^* + K\right]\frac{d^4\mathrm{v}}{dx^4} - H_0\frac{d^2\mathrm{v}}{dx^2} = 0 \tag{5.19}$$

for static bending (Chiu and Chen 2011a) and

$$\left[(EI)^* + K\right]\frac{d^4\mathrm{v}}{dx^4} + (P - H_0)\frac{d^2\mathrm{v}}{dx^2} = 0. \tag{5.20}$$

for buckling (Chiu and Chen 2012a). We mention that when neglecting the high-order effect (i.e., $K = 0$), the governing equations in Eqs. (5.19) and (5.20) can be reduced to the corresponding case of static bending (He and Lilley 2008a) and buckling (Wang and Feng 2009a) based on the Gurtin-Murdoch model. Also, when neglecting the surface stress effects (i.e., $K = H_0 = 0$), the results will recover the governing equation of classical beam-column theory (Timoshenko and Gere 1961).

### 5.4.2 *Mechanical Behavior of NWs Based on Timoshenko Beam Theory*

In this section, we will examine the Timoshenko beam (TB) theory incorporating the high-order surface stress effect, in which the shearing deformation could be taken into account. Based on Timoshenko beam theory, the researchers showed that the effect of surface stress within the Gurtin-Murdoch model on the static bending (Jiang and Yan 2010) and buckling (Wang and Feng 2009b) behavior of NWs. Continuing their investigations, the size-dependent buckling (Chiu and Chen 2012b) and static bending (Chiu and Chen 2013) behaviors for NWs based on the high-order surface stress model have been studied. For demonstrations, we record the nondimensional critical compression force (Chiu and Chen 2012b)

$$\frac{P_{cr}}{P_{cr}^0} = \Lambda\left(1 + \frac{6E_s}{Eh} + \frac{2E_s}{Ew} + \frac{24D_s}{Eh^3}\right) + \frac{24}{\eta\pi^2}\frac{\tau_0}{Eh}\left(\frac{L}{h}\right)^2, \tag{5.21}$$

for rectangular sections,

$$\frac{P_{cr}}{P_{cr}^0} = \Lambda\left(1 + \frac{8E_s}{Ed} + \frac{128D_s}{\pi Ed^3}\right) + \frac{128}{\eta\pi^3}\frac{\tau_0}{Ed}\left(\frac{L}{d}\right)^2, \tag{5.22}$$

for circular sections, and the size-dependent effective Young's modulus $E_{\mathrm{eff}}$, based on TB theory was found as

$$E_{\text{eff}} = \frac{\Lambda\left[(EI)^* + K\right]}{I} + \frac{H_0 L^2}{\eta \pi^2 I}. \tag{5.23}$$

Here the definition of the nondimensional parameter $\Lambda$ is (Chiu and Chen 2012b)

$$\Lambda \equiv \frac{\alpha_s GA}{\alpha_s GA + \eta\left(\pi^2/L^2\right)\left[(EI)^* + K\right]}, \tag{5.24}$$

where $G$ is the shear modulus, $A$ is the cross-sectional area of NWs, and $\eta$ is a constant depending on the boundary conditions. It is noted that when neglecting shear deformation ($G \to \infty$) and thus the parameter $\Lambda \to 1$, Eqs. (5.21)–(5.23) will recover the corresponding results of NWs accounting for the high-order surface stress effects based on Euler-Bernoulli beam (EB) theory.

## 5.5 Results and Discussion

### *5.5.1 The Stress Concentration Factor for a Circular Cavity in an Infinite Matrix*

In numerical illustrations, we present analytic solutions for the stress concentration factor in Sect. 5.3. Figure 5.5 shows the maximum value of stress concentration factor for hoop stress $\sigma_\theta$ for different types of interfaces versus the radius $a$ of cavity. Note that the scale of y-axis in the curves of Type I and Type II is different from that of Type III, Type IV, and rigid inclusion. The matrix material is assumed aluminums with the isotropic bulk modulus $K = 75.2$GPa and shear modulus $\mu = 34.7$GPa (Duan et al. 2005b). Note that the relations between elastic constants ($K$, $\mu$) and Hill's moduli ($k$, $m$) are $k = K + \mu/3$ and $m = \mu$ (Hill 1964).

In Figs. 5.6 and 5.7, we also present the maximum value of stress concentration factor for radial stress $\sigma_r$ and shear stress $\sigma_{r\theta}$ shown in Sect. 5.3 versus the radius $a$ of cavities under different types of interfaces. For the numerical calculations in Figs. 5.5, 5.6, and 5.7, the surface material properties for Type II interface conditions on the basis of Gurtin-Murdoch model are considered in two kinds of different free surface properties, $E_s = -8.9465$ N/m for surface A and $E_s = 6.091$ N/m for surface B (Chen et al. 2007a).

For the material parameter $D_s$ of Type IV interface condition which accounts for the high-order surface stress effect, as explained in Chen and Chiu (2011), moderate and reasonable estimated values ranging from $10^2 \times (10^{-18}\text{Nm})$ to $10^4 \times (10^{-18}\text{Nm})$ are adapted for the numerical illustrations.

In Fig. 5.5, we have checked that the numerical results for Type II are the same as that of Chen et al. (2007a), which utilized the Gurtin-Murdoch model based on the variational method to solve this problem. Obviously, we see that the maximum value is size dependent for Type II and Type IV, but not for Type I and Type III. It is

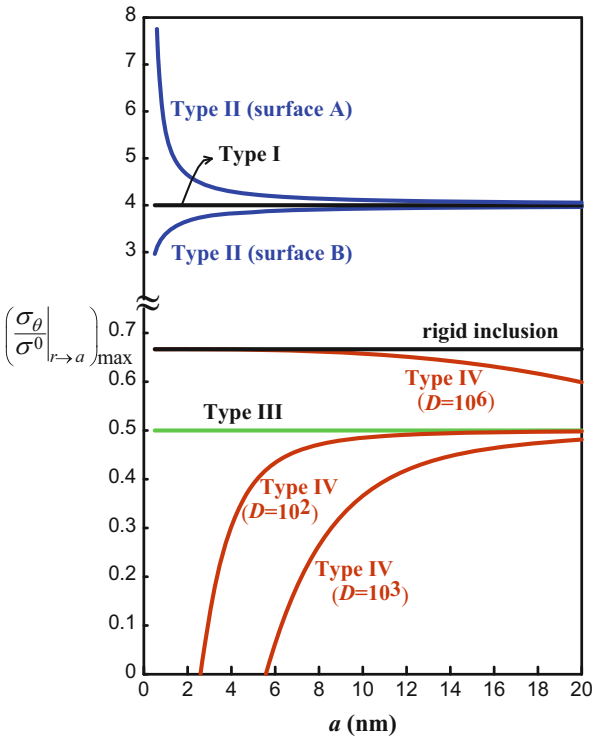


**Fig. 5.5** Maximum value of stress concentration factor for hoop stress $\sigma_\theta$ in different types of interfaces versus the radius $a$ of cavities

interesting to note that the size-dependent behavior for cavity with larger diameter (say $a > 15$ nm) would be still pronounced with the incorporation of high-order surface stress effect (Type IV), while the Type II interface condition has become nearly no size effect.

### 5.5.2 *Mechanical Behavior of NWs*

Figure 5.8 shows the size-dependent effective Young's modulus $E_{\text{eff}}$ numerically. The calculation is based on EB theory incorporating the high-order surface stress effects within the buckling analysis (Chiu and Chen 2012a). We see that the numerical prediction by the theoretical calculation based on the Gurtin-Murdoch model will not be able to capture the general trend of the experimental data, especially when $d \leq 40$ nm. In contrast, the high-order surface stress model will produce a good agreement with the experimental data. This comparison with the experimental data suggests that the effect of surface moments could be crucial in the modeling for mechanical behavior of NWs. In Fig. 5.8, the experimental sample was silicon NWs with fixed-fixed end conditions (Zhu et al. 2009). The surface Young's modulus and residual surface tension were adapted as $E_s = -10.655$N/m and

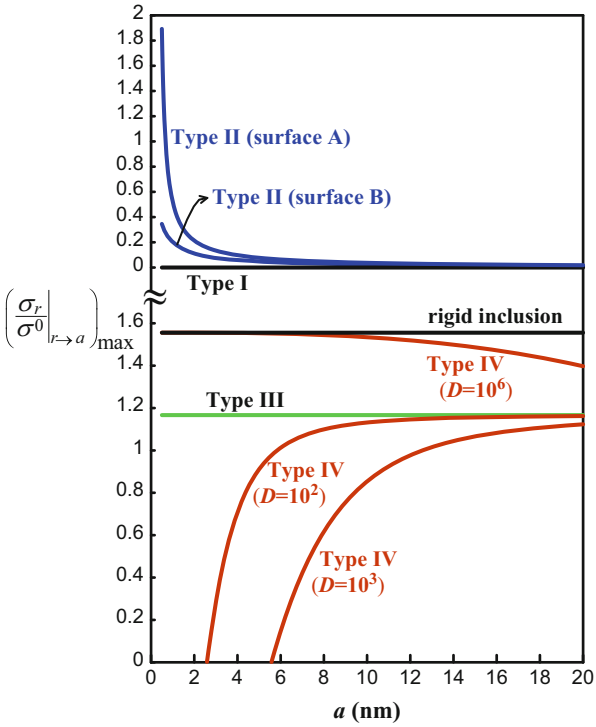


**Fig. 5.6** Maximum value of stress concentration factor for stress component $\sigma_r$ in different types of interfaces versus the radius $a$ of cavity

$\tau_0$=0.6056N/m, respectively (Miller and Shenoy 2000). The high-order material parameter $D_s$ was selected as $D_s = -7 \times 10^4 \times (10^{-18}\text{Nm})$, which has been examined by Chiu and Chen (2012a).

In Fig. 5.9, we demonstrate that the shear deformation of larger NWs, accounting for the framework of TB theory, should not be underestimated. Under the consideration of high-order surface stresses, the size-dependent effective Young's modulus $E_{\text{eff}}$ was theoretically resolved on the basis of static bending analysis (Chiu and Chen 2013). Figure 5.9 presents the numerical solutions of $E_{\text{eff}}$ versus the diameter $d$ for circular NWs. The experimental data in Fig. 5.9 was adapted from Jing et al. (2006), in which fixed-fixed silver NWs were used for observation. We see that when the diameter increases, the solutions considering the shearing effect based on TB theory within the high-order surface stress model will predict more accurate results in comparison with the experimental data than those by EB theory, especially when $d \geq 70$ nm. We mention that the material parameter of high-order effect is used as $D_s = 5 \times 10^4 \times (10^{-18}\text{Nm})$, which was numerically examined by Chiu and Chen (2013).

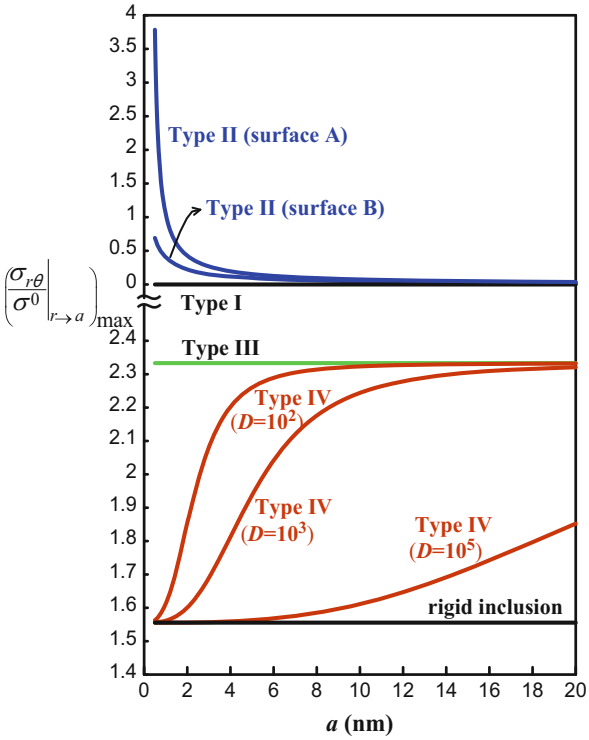


**Fig. 5.7** Maximum value of stress concentration factor for stress component $\sigma_{r\theta}$ in different types of interfaces versus the radius $a$ of cavity

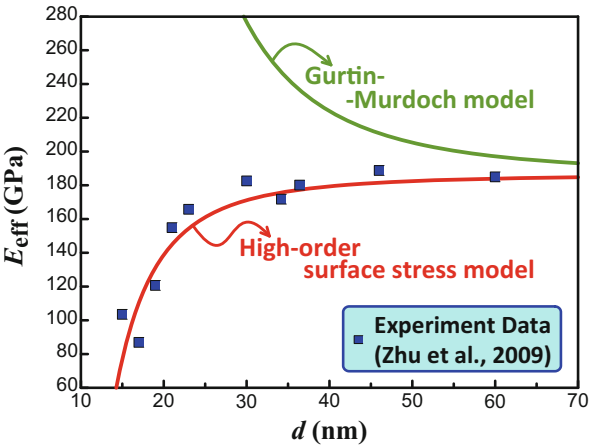


**Fig. 5.8** The size-dependent effective Young's moduli based on the high-order surface stress model and Gurtin-Murdoch model with respect to the diameter $d$ of circular NWs

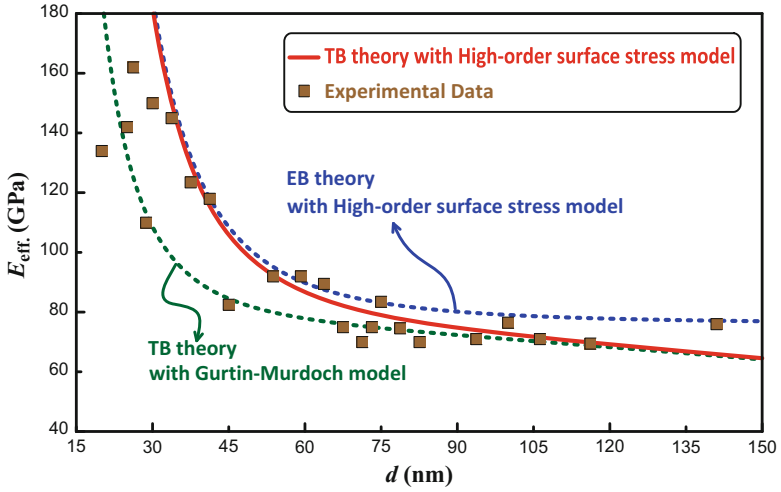


**Fig. 5.9** The difference among three continuum frameworks for the predictions on size dependence of effective Young's modulus. Note that TB theory signifies Timoshenko beam theory and EB theory denotes Euler-Bernoulli beam theory

## 5.6 Conclusions

In this chapter, we have introduced the high-order surface stress model for two-dimensional configurations. Analogous to the classical thin shell theory, this continuum theoretical framework incorporates the in-plane stresses as well as surface moments. The surface moments result in high-order surface effects. We mention that present approach to construct the high-order interface/surface conditions through the classical continuum mechanics and graphical interpretation is mathematically simple. The formulation allows that the in-plane surface stresses could be varying across the thin layer thickness and thus, effectively, it is equivalent to consider an average strain as well as curvature along the interface. In two dimensions, the behavior of interfaces can be grouped into four different types based on the degree of stiffness for the thin layer. We illustrate graphically how these four types of interfaces will influence the stress concentration factor in a successive manner for the boundary value problem of an infinite matrix containing a circular cavity.

In addition, the mechanical behaviors of NWs have been studied based on the high-order surface stress model. Both Timoshenko beam theory and Euler-Bernoulli beam theory have been adopted to incorporate the high-order surface stress effects. We compare the difference between the classical solutions (without surface effects), the calculations based on the high-order surface stress model and conventional surface stress model (Gurtin-Murdoch model). The size-dependent effective Young's modulus of NWs has also been derived. From the investigation of the theoretical calculations and the existing experimental data for the effective

Young's modulus, the effects of higher-order interface stresses between two different materials could be important, especially when the characteristic length is in a few nanometers. Our theoretical framework based on classical continuum mechanics might provide a more direct and simple approach to simulate the mechanical behavior of nanostructures.

We mention that some further studies might be envisaged for engineering applications. The thermal stress effects could be important and sensitive for nanoscaled components and structures. The issue of thermal effects on nanocomposites (Chen 1993; He and Benveniste 2004; Quang and He 2007; Chen et al. 2007b; Quang and He 2009) could be considered using the high-order interface stress model. Another possible extension of the present research can be directed to the subject of mechanics of wrinkling. Andreussi and Gurtin (1977) studied the wrinkling of a free surface and showed that a compressive residual surface tension or negative surface stiffness will result in this behavior. Kornev and Srolovitz (2004) discussed surface stress-driven wrinkling of a free film based on thermodynamics. The ordered patterns of wrinkling in metal thin films deposited on elastomeric polymer can be observed due to thermal effects (Bowden et al. 1998; Huck et al. 2000; Kwon and Lee 2005). Huang (2005) also investigated the wrinkling of a conductive thin film subjected to electric field.

Finally, we note that the high-order interface/surface stress model could be used to examine other related subjects, which have been investigated based on the Gurtin-Murdoch model, such as piezoelectric effects on nanosized structures (Chen 2008; Wang and Feng 2010; Li et al. 2011; Xiao et al. 2011; Yan and Jiang 2011a, b; Samaei et al. 2012; Yan and Jiang 2012; Hadjesfandiari 2013; Dai and Park 2013; Xiao et al. 2013), wave propagation in nanoscaled system (Gurtin and Murdoch 1976; Murdoch 1976; Chakraborty 2010; Li and Lee 2010; Ou and Lee 2012; Liu et al. 2013; Ru et al. 2013), and photonic band structures (Kushwaha et al. 1993; Chen and Wang 2011; Zhen et al. 2012; Liu et al. 2012).

**Acknowledgments** This work was supported by the Ministry of Science and Technology, Taiwan, under grant MOST 104-2221-E-006-152-MY3.

## References

Abbasion, S., Rafsanjani, A., Avazmohammadi, R., Farshidianfar, A.: Free vibration of microscaled Timoshenko beams. Appl. Phys. Lett. **95**, 143122 (2009)

Andreussi, F., Gurtin, M.E.: On the wrinkling of a free surface. J. Appl. Phys. **48**, 3798 (1977)

Assadi, A., Farshi, B., Alinia-Ziazi, A.: Size dependent dynamic analysis of nanoplates. J. Appl. Phys. **107**, 124310 (2010)

Benveniste, Y., Miloh, T.: Imperfect soft and stiff interfaces in two-dimensional elasticity. Mech. Mater. **33**, 309–323 (2001)

Benveniste, Y.: A general interface model for a three-dimensional curved thin anisotropic interphase between two anisotropic media. J. Mech. Phys. Solids. **54**, 708–734 (2006a)

Benveniste, Y.: An interface model of a three-dimensional curved interphase in conduction phenomena. Proc. R. Soc. A. **462**, 1593–1617 (2006b)

Benveniste, Y., Baum, G.: An interface model of a graded three-dimensional anisotropic curved interphase. Proc. R. Soc. A. **463**, 419–434 (2007)
Benveniste, Y., Berdichevsky, O.: On two models of arbitrarily curved three-dimensional thin interphases in elasticity. Int. J. Solids Struct. **47**, 1899–1915 (2010)
Bövik, P.: On the modeling of thin interface layers in elastic and acoustic scattering problems. Q. J. Mech. Appl. Math. **47**, 17–42 (1994)
Bowden, N., Brittain, S., Evans, A.G., Hutchinson, J.W., Whitesides, G.M.: Spontaneous formation of ordered structures in thin films of metals supported on an elastomeric polymer. Nature. **393**, 146–149 (1998)
Cammarata, R.C.: Surface and interface stress effects in thin films. Prog. Surf. Sci. **46**, 1–38 (1994)
Chakraborty, A.: The effect of surface stress on the propagation of Lamb waves. Ultrasonics. **50**, 645–649 (2010)
Chen, T.: Thermoelastic properties and conductivity of composites reinforced by spherically anisotropic particles. Mech. Mater. **14**, 257–268 (1993)
Chen, T., Dvorak, G.J.: Fibrous nanocomposites with interface stress: Hill's and Levin's connections for effective moduli. Appl. Phys. Lett. **88**, 211912 (2006)
Chen, T., Chiu, M.S., Weng, C.N.: Derivation of the generalized Young-Laplace equation of curved interface in nanoscaled solids. J. Appl. Phys. **100**, 074308 (2006)
Chen, T., Dvorak, G.J., Yu, C.C.: Size-dependent elastic properties of unidirectional nanocomposites with interface stresses. Acta Mech. **188**, 39–54 (2007a)
Chen, T., Dvorak, G.J., Yu, C.C.: Solids containing spherical nano-inclusions with interface stresses: effective properties and thermal-mechanical connections. Int. J. Solids Struct. **44**, 941–955 (2007b)
Chen, T.: Exact size-dependent connections between effective moduli of fibrous piezoelectric nanocomposites with interface effects. Acta Mech. **196**, 205–217 (2008)
Chen, A.L., Wang, Y.S.: Size-effect on band structures of nanoscale phononic crystals. Physica E. **44**, 317–321 (2011)
Chen, T., Chiu, M.S.: Effects of higher-order interface stresses on the elastic states of two-dimensional composites. Mech. Mater. **43**, 212–221 (2011)
Chiu, M.S., Chen, T.: Effects of high-order surface stress on static bending behavior of nanowires. Physica E. **44**, 714–718 (2011a)
Chiu, M.S., Chen, T.: Higher-order surface stress effects on buckling of nanowires under uniaxial compression. Procedia Eng. **10**, 397–402 (2011b)
Chiu, M.S., Chen, T.: Effects of high-order surface stress on buckling and resonance behavior of nanowires. Acta Mech. **223**, 1473–1484 (2012a)
Chiu, M.S., Chen, T.: Timoshenko beam model for buckling of nanowires with high-order surface stresses effects. Adv. Mater. Res. **528**, 281–284 (2012b)
Chiu, M.S., Chen, T.: Bending and resonance behavior of nanowires based on Timoshenko beam theory with high-order surface stress effects. Physica E. **54**, 149–156 (2013)
Dai, S., Park, H.S.: Surface effects on the piezoelectricity of ZnO nanowires. J. Mech. Phys. Solids. **61**, 385–397 (2013)
Duan, H.L., Wang, J., Huang, Z.P., Karihaloo, B.L.: Eshelby formalism for nano-inhomogeneities. Proc. R. Soc. A. **461**, 3335–3353 (2005a)
Duan, H.L., Wang, J., Huang, Z.P., Karihaloo, B.L.: Size-dependent effective elastic constants of solids containing nano-inhomogeneities with interface stress. J. Mech. Phys. Solids. **53**, 1574–1596 (2005b)
Duan, H.L., Wang, J., Huang, Z.P., Zhong, Y.: Stress fields of a spheroidal inhomogeneity with an interphase in an infinite medium under remote loadings. Proc. R. Soc. A. **461**, 1055–1080 (2005c)
Farshi, B., Assadi, A., Alinia-ziazi, A.: Frequency analysis of nanotubes with consideration of surface effects. Appl. Phys. Lett. **96**, 093105 (2010)
Gao, X.L.: A new Timoshenko beam model incorporating microstructure and surface energy effects. Acta Mech. **226**, 457–474 (2015)
Gibbs, J.W.: The Collected Works of J. W. Gibbs, vol. 1. Longman, New York (1928)

Gurtin, M.E., Murdoch, A.I.: A continuum theory of elastic material surfaces. Arch. Ration. Mech. Anal. **57**, 291–323 (1975)
Gurtin, M.E., Murdoch, A.I.: Effect of surface stress on wave propagation in solids. J. Appl. Phys. **47**, 4414 (1976)
Gurtin, M.E., Murdoch, A.I.: Surface stress in solids. Int. J. Solids Struct. **14**, 431–440 (1978)
Gurtin, M.E., Weissmüller, J., Larché, F.: A general theory of curved deformable interfaces in solids at equilibrium. Philos. Mag. A. **78**, 1093–1109 (1998)
Hadjesfandiari, A.R.: Size-dependent piezoelectricity. Int. J. Solids Struct. **50**, 2781–2791 (2013)
He, Q.C., Benveniste, Y.: Exactly solvable spherically anisotropic thermoelastic microstructures. J. Mech. Phys. Solids. **52**, 2661–2682 (2004)
He, J., Lilley, C.M.: Surface effect on the elastic behavior of static bending nanowires. Nano Lett. **8**, 1798–1802 (2008a)
He, J., Lilley, C.M.: Surface stress effect on bending resonance of nanowires with different boundary conditions. Appl. Phys. Lett. **93**, 263108 (2008b)
He, Q., Lilley, C.M.: Resonant frequency analysis of Timoshenko nanowires with surface stress for different boundary conditions. Appl. Phys. Lett. **112**, 074322 (2012)
Hill, R.: Theory of mechanical properties of fibre-strengthened materials: I. Elastic behaviour. J. Mech. Phys. Solids **12**, 199–212 (1964)
Huang, R.: Electrically induced surface instability of a conductive thin film on a dielectric substrate. Appl. Phys. Lett. **87**, 151911 (2005)
Huck, W.T.S., Bowden, N., Onck, P., Pardoen, T., Hutchinson, J.W., Whitesides, G.M.: Ordering of spontaneously formed buckles on planar surfaces. Langmuir. **16**, 3497–3501 (2000)
Ji, L.W., Young, S.J., Fang, T.H., Liu, C.H.: Buckling characterization of vertical ZnO nanowires using nanoindentation. Appl. Phys. Lett. **90**, 033109 (2007)
Jiang, L.Y., Yan, Z.: Timoshenko beam model for static bending of nanowires with surface effects. Physica E. **42**, 2274–2279 (2010)
Jing, G.Y., Duan, H.L., Sun, X.M., Zhang, Z.S., Xu, J., Li, Y.D., Wang, X.J., Yu, D.P.: Surface effects on elastic properties of silver nanowires: contact atomic-force microscopy. Phys. Rev. B. **73**, 235409 (2006)
Kornev, K.G., Srolovitz, D.J.: Surface stress-driven instabilities of a free film. Appl. Phys. Lett. **85**, 2487–2489 (2004)
Kushwaha, M.S., Halevi, P., Dobrzynski, L., Djafari-Rouhani, B.: Acoustic band structure of periodic elastic composites. Phys. Rev. Lett. **71**, 2022–2025 (1993)
Kwon, S.J., Lee, H.H.: Theoretical analysis of two-dimensional buckling patterns of thin metal-polymer bilayer on the substrate. J. Appl. Phys. **98**, 063526 (2005)
Lachut, M.J., Sader, J.E.: Effect of surface stress on the stiffness of cantilever plates. Phys. Rev. Lett. **99**, 206102 (2007)
Laplace, P.S.: Traite de mechanique celeste; supplements au Livre X. Euvres Complete Vol. 4. Gauthier-Villars, Paris (1806)
Landau, L.D., Lifshitz, E.M.: Fluid Mechanic, 2nd edn. Pergamon Press, Oxford (1987)
Li, Y., Fang, B., Zhang, J., Song, J.: Surface effects on the wrinkling of piezoelectric films on compliant substrates. J. Appl. Phys. **110**, 114303 (2011)
Li, Y.D., Lee, K.Y.: Size-dependent behavior of Love wave propagation in a nanocoating. Mod. Phys. Lett. B. **24**, 3015–3023 (2010)
Liu, W., Chen, J.W., Liu, Y.Q., Su, X.Y.: Effect of interface/surface stress on the elastic wave band structure of two-dimensional phononic crystals. Phys. Lett. A. **376**, 605–609 (2012)
Liu, H., Liu, H., Yang, J.: Surface effects on the propagation of shear horizontal waves in thin films with nano-scalethickness. Physica E. **49**, 13–17 (2013)
Miller, R.E., Shenoy, V.B.: Size-dependent elastic properties of nanosized structural elements. Nanotechnology. **11**, 139–147 (2000)
Murdoch, A.I.: The propagation of surface waves in bodies with material boundaries. J. Mech. Phys. Solids. **24**, 137–146 (1976)
Ni, H., Li, X.: Young's modulus of ZnO nanobelts measured using atomic force microscopy and nanoindentation techniques. Nanotechnology. **17**, 3591–3597 (2006)

Nix, W.D., Gao, H.: An atomistic interpretation of interface stress. Scr. Mater. **39**, 1653–1661 (1998)
Ou, Z.Y., Lee, D.W.: Effects of interface energy on scattering of plane elastic wave by a nano-sized coated fiber. J. Sound Vib. **331**, 5623–5643 (2012)
Povstenko, Y.Z.: Theoretical investigation of phenomena caused by heterogeneous surface tension in solids. J. Mech. Phys. Solids. **41**, 1499–1514 (1993)
Quang, H.L., He, Q.C.: Size-dependent effective thermoelastic properties of nanocomposites with spherically anisotropic phases. J. Mech. Phys. Solids. **55**, 1889–1921 (2007)
Quang, H.L., He, Q.C.: Estimation of the effective thermoelastic moduli of fibrous nanocomposites with cylindrically anisotropic phases. Arch. Appl. Mech. **79**, 225–248 (2009)
Ru, C.Q.: Simple geometrical explanation of Gurtin-Murdoch model of surface elasticity with clarification of its related versions. Sci. China. **53**, 536–544 (2010)
Ru, Y., Wang, G.F., Su, L.C., Wang, T.J.: Scattering of vertical shear waves by a cluster of nanosized cylindrical holes with surface effect. Acta Mech. **224**, 935–944 (2013)
Samaei, A.T., Bakhtiari, M., Wang, G.F.: Timoshenko beam model for buckling of piezoelectric nanowires with surface effects. Nanoscale Res. Lett. **7**, 201 (2012)
Sharma, P., Ganti, S., Bhate, N.: Effect of surfaces on the size-dependent elastic state of nano-inhomogeneities. Appl. Phys. Lett. **82**, 535–537 (2003)
Sharma, P., Ganti, S.: Size-dependent Eshelby's tensor for embedded nano-inclusions incorporating surface/interface energies. J. Appl. Mech. **71**, 663–671 (2004)
Shuttleworth, R.: The surface tension of solids. Proc. Phys. Soc. A. **63**, 444–457 (1950)
Song, J., Wang, X., Riedo, E., Wang, Z.L.: Elastic property of vertically aligned nanowires. Nano Lett. **5**, 1954–1958 (2005)
Spaepen, F.: Interfaces and stresses in thin films. Acta Mater. **48**, 31–42 (2000)
Ting, T.C.T.: Mechanics of a thin anisotropic elastic layer and a layer that is bonded to an anisotropic elastic body or bodies. Proc. R. Soc. A. **463**, 2223–2239 (2007)
Timoshenko, S.P., Gere, J.M.: Theory of Elastic Stability. McGraw-Hill, New York (1961)
Timoshenko, S.P., Goodier, J.N.: Theory of Elasticity. McGraw-Hill, New York (1970)
Thomson, R., Chuang, T.J., Lin, I.H.: The role of surface stress in fracture. Acat Metall. **34**, 1133–1143 (1986)
Wang, Z.L.: ZnO nanowire and nanobelt platform for nanotechnology. Mater. Sci. Eng.: Rep. **64**, 33–71 (2009)
Wang, G.F., Feng, X.Q.: Effects of surface elasticity and residual surface tension on the natural frequency of microbeams. Appl. Phys. Lett. **90**, 231904 (2007)
Wang, G.F., Feng, X.Q.: Surface effects on buckling of nanowires under uniaxial compression. Appl. Phys. Lett. **94**, 141913 (2009a)
Wang, G.F., Feng, X.Q.: Timoshenko beam model for buckling and vibration of nanowires with surface effects. J. Phys. D: Appl. Phys. **42**, 155411 (2009b)
Wang, G.F., Feng, X.Q.: Effect of surface stresses on the vibration and buckling of piezoelectric nanowires. Europhys. Lett. **91**, 56007 (2010)
Wang, D.H., Wang, G.F.: Surface effects on the vibration and buckling of double-nanobeam-systems. J. Nanomater. **2011**, 518706 (2011)
Wang, G.F., Yang, F.: Postbuckling analysis of nanowires with surface effects. J. Appl. Phys. **109**, 063535 (2011)
Weng, C.N., Chen, T.: General interface conditions in surface elasticity of nanoscaled solids in general curvilinear coordinates. J. Mech. **26**, 81–86 (2010). doi:10.1017/S1727719100003749
Xiao, J.H., Xu, Y.L., Zhang, F.C.: Size-dependent effective electroelastic moduli of piezoelectric nanocomposites with interface effect. Acta Mech. **222**, 59–67 (2011)
Xiao, J.H., Xu, Y.L., Zhang, F.C.: Evaluation of effective electroelastic properties of piezoelectric coated nano-inclusion composites with interface effect under antiplane shear. Int. J. Eng. Sci. **69**, 61–68 (2013)
Yan, Z., Jiang, L.Y.: The vibrational and buckling behaviors of piezoelectric nanobeams with surface effects. Nanotechnology. **22**, 245703 (2011a)

Yan, Z., Jiang, L.Y.: Surface effects on the electromechanical coupling and bending behaviours of piezoelectric nanowires. J. Phys. D: Appl. Phys. **44**, 075404 (2011b)

Yan, Z., Jiang, L.Y.: Vibration and buckling analysis of a piezoelectric nanoplate considering surface effects and in-plane constraints. Proc. R. Soc. A. **468**, 3458–3475 (2012)

Young, T.: Phil.: an essay on the cohesion of fluid. Philos. Trans. R. Soc. Lond. **95**, 65–87 (1805)

Young, S.J., Ji, L.W., Chang, S.J., Fang, T.H., Hsueh, T.J., Meen, T.H., Chen, I.C.: Nanoscale mechanical characteristics of vertical ZnO nanowires grown on ZnO: Ga/glass templates. Nanotechnology. **18**, 225603 (2007)

Zhang, Y., Zhuo, L.J., Zhao, H.S.: Determining the effects of surface elasticity and surface stress by measuring the shifts of resonant frequencies. Proc. R. Soc. A. **469**, 20130449 (2013)

Zhen, N., Wang, Y.S., Zhang, C.Z.: Surface/interface effect on band structures of nanosized phononic crystals. Mech. Res. Commun. **46**, 81–89 (2012)

Zhou, L.G., Huang, H.C.: Are surfaces elastically softer or stiffer? Appl. Phys. Lett. **84**, 1940–1942 (2004)

Zhu, Y., Xu, F., Qin, Q., Fung, W.Y., Lu, W.: Mechanical properties of vapor-liquid-solid synthesized silicon nanowires. Nano Lett. **9**, 3934–3939 (2009)

# Chapter 6
# The Design of Nano-Inhomogeneities with Uniform Internal Strain in Anti-Plane Shear Deformations of Composite Solids

**Ming Dai and Peter Schiavone**

**Abstract** In the micromechanical analysis of composite materials, the objective is to predict the overall behavior of the composite from known properties of its individual constituents. When applied to fibrous composites, stress distributions in a composite material subjected to applied stresses can be modelled using inhomogeneity-matrix systems in which the fibers are represented by inhomogeneities embedded in a foreign matrix material. One of the most important challenges associated with inhomogeneity-matrix systems is concerned with the design of inhomogeneities in which the interior strain distribution remains uniform. The primary motivation for the interest in this class of problems lies in the optimal nature of an interior uniform strain field in that such a field does not give rise to stress peaks within the inhomogeneity and also effectively reduces the stress concentration in the surrounding matrix (it is well known that stress peaks are usually responsible for the mechanical failure of the inhomogeneity-matrix system). The main focus in addressing this challenge has been on designing the shape of the inhomogeneity and the properties of the material interface between the inhomogeneity and its surrounding matrix to achieve the desired uniform strain distribution inside the inhomogeneity. In the emerging area of nanocomposites, however, the presence of appreciable interface energy (known also as the "interface effect") presents formidable challenges in the design of corresponding nano-inhomogeneities with uniform internal strain distributions. In this chapter, we present some new results in this area for anti-plane shear deformations of composite solids. In particular, we demonstrate the existence of a single nano-inhomogeneity with uniform internal strain distribution induced by a screw dislocation as well as that of periodic nano-inhomogeneities with uniform internal strain distributions when the composite is subjected to uniform remote (anti-plane shear) loading. Our method involves the

M. Dai
School of Mechanical Engineering, Changzhou University, Changzhou 213164, China

P. Schiavone (✉)
Department of Mechanical Engineering, University of Alberta, Edmonton, AB T6G 1H9, Canada
e-mail: P.Schiavone@ualberta.ca



S.A. Meguid, G.J. Weng (eds.), *Micromechanics and Nanomechanics of Composite Solids*, DOI 10.1007/978-3-319-52794-9_6

identification of the corresponding unknown shape of the desired inhomogeneity via a conformal mapping whose unknown coefficients are determined from a system of nonlinear equations. Extensive numerical examples are given to verify the correctness of our method and to illustrate the size dependence of the shapes of the inhomogeneities. It is anticipated that these results will find extensive application in the optimal design of fibrous nanocomposites.

## 6.1 Introduction

In the micromechanics of composite materials, it is well known that "stress peaks" inside material inhomogeneities are a significant factor contributing to the possible failure of the composite. To address this problem, researchers have focused on the design of inhomogeneities which achieve uniform internal stress distributions. Such inhomogeneities not only eliminate the possibility of internal stress peaks but are also known to effectively reduce the existing stress concentration in the surrounding matrix.

In early studies, Eshelby (1957) showed that a uniform internal stress distribution can be achieved inside a two-dimensional elliptical inhomogeneity or a three-dimensional ellipsoidal inhomogeneity when the surrounding matrix is subjected to *any* uniform remote elastic loading. Eshelby's results are the main reason why so many researchers in the mechanics of composites have focused primarily on the study of elliptical and ellipsoidal inhomogeneities. Subsequently, Eshelby (1961) conjectured that the converse of his result is also true, that is, that if the field inside an inhomogeneity is uniform for *all* uniform remote loadings, then the inhomogeneity must be of elliptical (two dimensions) or ellipsoidal (three dimensions) shape (see also Horgan (1995) for the case of anti-plane shear deformations). The latter is commonly referred to in the literature as the "Eshelby conjecture" and has evoked much discussion among researchers. For example, Mura and his co-workers (Mura 1997; Mura et al. 1994) claimed they had found a counterexample to Eshelby's conjecture by identifying a star-shaped inhomogeneity enclosing a uniform stress distribution. Unfortunately, Rodin (1996) (see also Markenscoff 1997) disproved Mura's claim by pointing out that *no* polygonal inhomogeneity can ever achieve a uniform internal stress distribution under Eshelby's conditions. In fact, through the use of complex variable methods, a *stronger* version of Eshelby's conjecture has been proved by Sendeckyj (1970) in the case of plane elasticity and by Ru and Schiavone (1996) for anti-plane shear elasticity: if the field inside an inhomogeneity is uniform for a *single* uniform remote loading, then the inhomogeneity must be elliptical. Subsequent discussion of Eshelby's conjecture in the literature has consequently led to two different interpretations of the conjecture:

**Weak Eshelby's conjecture**: If the stress is uniform inside for *all* uniform remote loadings, then the inhomogeneity is an ellipse (2D) or an ellipsoid (3D).

**Strong Eshelby's conjecture**: If the stress is uniform inside for a *single* uniform remote loading, then the inhomogeneity is an ellipse (2D) or an ellipsoid (3D).

Of course, the strong form of Eshelby's conjecture implies the weak form.

Kang and Milton (2008) and Liu (2008) have proved a weak version of the conjecture, while Ammari et al. (2010) proved a somewhat "medium version" of the conjecture lying somewhere between the weak and strong versions. Although the strong Eshelby's conjecture in three-dimensional elasticity has not yet been completely resolved, Liu (2008) has shown that a similar strong conjecture in three-dimensional thermal conductivity fails to be true.

It is important to note that the original Eshelby's conjecture was established for only a single inhomogeneity. In reality, however, composite materials contain a variety of multiple inhomogeneities and the effect of interaction between these inhomogeneities on the mechanical properties of the composite cannot be ignored. In fact, it is unrealistic to expect that elliptical or ellipsoidal inhomogeneities will continue to exhibit the remarkable property of uniform internal fields in the presence of such interactions. Consequently, there has been much interest in the question of existence and construction of multiple (not necessarily elliptical) inhomogeneities enclosing uniform stress fields. Vigdergauz (1994) found that a two-dimensional microstructure consisting of a double-periodic array of inhomogeneities with uniform internal stress fields can achieve a particular optimal elastic property among all other structures with given inhomogeneity volume fraction. Grabovsky and Kohn (1995) gave an explicit formula to construct the "Vigdergauz microstructure" based on the method proposed by Cherepanov (1974) to establish "equally strong" holes. Most recently, the existence of multiple inhomogeneities with uniform internal fields has been further verified and several distinct methods have been dedicated to their design. For example, Liu and his co-workers (Liu et al. 2007; Liu 2008) identified special shapes of multiple inhomogeneities with uniform internal stress or magnetic fields in three dimensions based on a variational inequality. Using the Weierstrass zeta function and Schwarz–Christoffel formula, Kang et al. (2008) established an inhomogeneity pair enclosing uniform internal stress and further revealed an interesting fact that when the internal stress field inside a single inhomogeneity tends towards uniformity, the corresponding shape of the inhomogeneity need not converge to that of an ellipse (such a single inhomogeneity is constructed by adding an extremely narrow bridge between the components of the inhomogeneity pair with uniform internal stress). Wang (2012) introduced a specific mapping function to construct an inhomogeneity pair with uniform internal stress in anti-plane shear piezoelectricity and finite plane elasticity, respectively. Dai et al. (2015a, 2017) derived specific conditions imposed on the uniform internal stress fields, material constants, and remote loadings to guarantee the existence of multiple symmetrical and rotationally symmetric inhomogeneities enclosing uniform stress fields.

The interaction between inhomogeneities is not the only factor which must be taken into account when designing inhomogeneities in the context of Eshelby's result: the interaction between an inhomogeneity and the edge of the surrounding matrix has also great impact on the corresponding shape of the inhomogeneity.

The model of a half plane containing multiple inhomogeneities is widely used to study the interaction between inhomogeneities and the edge of a surrounding matrix. It then becomes natural to ask whether there exist single or multiple inhomogeneities enclosing uniform fields in an elastic half plane with traction-free surface. In fact, the symmetrical inhomogeneity pair constructed in Liu (2008), Kang et al. (2008), Wang (2012), and Dai et al. (2015a, 2017) indeed implies the existence of a single inhomogeneity with uniform internal stress field in a solid subjected to anti-plane shear deformations. As an extension of the results in Dai et al. (2015a, 2017), Dai et al. (2015b) have undertaken a systematic investigation of the construction of single and multiple inhomogeneities with uniform internal stress fields in an elastic half plane and further verified the corresponding existence of multiple inhomogeneities with distinct uniform internal stress distributions. In particular, the symmetrical inhomogeneity pairs established in Dai et al. (2015b) reveal the existence of a single inhomogeneity enclosing uniform internal stress inside a quarter plane with two mutually perpendicular traction-free surfaces. It is worth noting that the results of Dai et al. (2015b) are restricted to anti-plane shear deformations. A complete solution to the analogous but more challenging problem of the existence of inhomogeneities with uniform internal stress field in an elastic half plane subjected to plane deformations remains unresolved.

From the micromechanical analysis of composite materials has emerged the most recent and perhaps most exciting topic of the analysis of nanocomposites. The latter are known to have unique mechanical and multifunctional properties which have led to a wide variety of fascinating applications in engineering and applied science. In the modelling of nanocomposites, material inhomogeneities are considered at the nanoscale where surface to volume ratios become significantly larger and the so-called surface or interface effects can no longer be ignored. Consequently, interface energy and interface tension (here subsequently referred to as "interface effects"—usually neglected at the micro—or higher length scales) can play a significant role in the model of deformation so that the stress field in the vicinity of inhomogeneities exhibits significant size dependence (see, e.g. Sharma et al. 2003). Gurtin and his co-workers (Gurtin and Murdoch 1975; Gurtin et al. 1998) developed a general framework to account for interface effects by modelling the interface as a separate elastic membrane, perfectly bonded to the surrounding bulk material but having distinct material properties. In the context of the Gurtin–Murdoch model, it turns out that the displacement in the bulk material is continuous across the interface while the traction is discontinuous with jump across the interface related to its curvature and the strain gradient of the bulk material at the interface. Based on the Gurtin–Murdoch model, it has been shown that in the presence of interface effects, a general elliptical inhomogeneity can no longer achieve a uniform internal stress field in either anti-plane shear deformations or plane deformations (see Tian and Rajapakse 2007a; Luo and Wang 2009). Interestingly enough, the *circular* inhomogeneity does continue to admit a uniform internal stress field in the presence of interface effects (see Sharma and Ganti 2004; Fang and Liu 2006; Tian and Rajapakse 2007b). Sharma and Ganti (2004) further asserted that *only* circular and spherical inhomogeneities can enjoy the property of uniform internal stress in

the presence of interface effects. In sharp contrast to Sharma and Ganti (2004), however, Dai and Gao (2016) have recently identified noncircular shapes of a single inhomogeneity which continues to achieve uniform internal stress in the presence of interface effects when the composite is subjected to anti-plane shear deformations.

In this chapter, the word *nano-inhomogeneity* (an inhomogeneity at the nanoscale) will be taken to be synonymous with a material inhomogeneity in the presence of interface effects. Many significant problems in the area of continuum-based modelling and analysis of nanocomposites remain unresolved. This can be attributed directly to the formidable mathematical difficulties associated with the introduction of interface effects into the model of deformation. In this chapter, we present some new results in this area, in particular, concerning nano-inhomogeneities with uniform stress fields in which interface effects are fully incorporated into the model of deformation.

The chapter is organized as follows. In Sect. 6.2, we present the basic equations for an inhomogeneity-matrix system which incorporates interface effects in a composite subjected to anti-plane shear deformations. Based on the method developed by Dai and Gao (2016), in Sect. 6.3 we identify distinct shapes of a single nano-inhomogeneity achieving uniform internal fields induced by a screw dislocation. In Sect. 6.4, we develop a new method to verify the existence of periodic nano-inhomogeneities which enclose uniform internal stress fields in anti-plane shear deformations of the nanocomposite.

## 6.2 Basic Equations

We refer to the $(x_1, x_2)$ Cartesian coordinate system and consider an inhomogeneity embedded in a foreign matrix subjected to anti-plane shear deformations. We incorporate interface effects into the inhomogeneity-matrix system so that our analysis accommodates the behavior of nano-inhomogeneities as defined in Sect. 6.1. The notations $S_0$ and $S_1$ will be used to denote the regions occupied by the matrix and the inhomogeneity, respectively, while the curve $L$ represents the interface between the inhomogeneity and the matrix. Based on the Gurtin–Murdoch theory (see Gurtin and Murdoch 1975; Gurtin et al. 1998), the out-of-plane displacement $w$ and the anti-plane shear stresses $(\sigma_{13}, \sigma_{23})$ within the inhomogeneity and matrix satisfy

$$\frac{\partial^2 w^{(j)}}{\partial x_1^2} + \frac{\partial^2 w^{(j)}}{\partial x_2^2} = 0, j = 0, 1; \tag{6.1}$$

$$\sigma_{13}^{(j)} = G_j \frac{\partial w^{(j)}}{\partial x_1}, \sigma_{23}^{(j)} = G_j \frac{\partial w^{(j)}}{\partial x_2}, j = 0, 1, \tag{6.2}$$

where $G$ refers to the shear modulus and the use of the subscript $j = 0,1$ or superscript $(j) = 0,1$ denotes the respective quantity in $S_0$ and $S_1$. Despite the

presence of interface effects, the displacement $w$ remains continuous across the interface, i.e.,

$$w^{(1)} = w^{(0)}, \text{ on } L, \tag{6.3}$$

but the shear traction $\sigma_{n3}$ becomes discontinuous with jump across the interface described by

$$\sigma_{n3}^{(1)} - \sigma_{n3}^{(0)} = G_s \frac{d\sigma_{t3}^{(S)}}{ds}, \text{ on } L, \tag{6.4}$$

where $\sigma_{t3}^{(S)}$ denotes the interfacial shear stress (the subscript $t$ is used here to denote the direction of the tangent to the curve $L$), $ds$ is the arc length of an infinitesimal element of the curve $L$ along its tangent, and $G_s$ is the (interface) shear modulus on $L$. In the Gurtin–Murdoch model, the elastic interfacial region is assumed to be perfectly bonded to the surrounding bulk material so that the interfacial shear stress $\sigma_{t3}^{(S)}$ can be represented as

$$\sigma_{t3}^{(S)} = G_s \frac{dw^{(1)}}{ds}, \text{ on } L. \tag{6.5}$$

The general solution to Eqs. (6.1) and (6.2) can be written in the form (see Muskhelishvili 1975)

$$w^{(j)} = \text{Im}\left[f_j(z)\right], j = 0, 1; \tag{6.6}$$

$$\sigma_{23}^{(j)} + i\sigma_{13}^{(j)} = G_j f_j'(z), j = 0, 1, \tag{6.7}$$

where $f_j(z)$ ($z = x_1 + ix_2, j = 0,1$) denote complex potentials defined in the regions $S_j$ ($j = 0,1$), respectively, and the symbol $i$ denotes the usual imaginary unit. In particular, the shear traction $\sigma_{n3}^{(j)}$ ($j = 0,1$) on the interface $L$ can be written in terms of $f_j(z)$ ($j = 0,1$) as

$$\sigma_{n3}^{(j)} = -G_j \text{Re}\left[f_j'(t)\frac{dt}{ds}\right], t \in L, j = 0, 1, \tag{6.8}$$

where $dt$ is an infinitesimal element of the curve $L$ along its tangent and $ds$ is the arc length of $dt$. Using Eqs. (6.6) and (6.8), the interface conditions (6.3) and (6.4) with (6.5) become

$$\text{Im}\left[f_0(t)\right] = \text{Im}\left[f_1(t)\right], t \in L, \tag{6.9}$$

$$G_0 \text{Re}\left[f_0(t)\right] - G_1 \text{Re}\left[f_1(t)\right] = G_s \text{Im}\left[f_1'(t)\frac{dt}{ds}\right], t \in L. \tag{6.10}$$

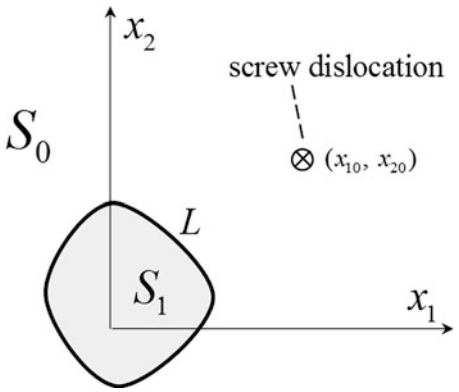


**Fig. 6.1** An inhomogeneity interacting with a screw dislocation in an infinite matrix

Combining Eqs. (6.9) and (6.10) yields

$$f_0(t) = \frac{1 + G_1/G_0}{2} f_1(t) + \frac{G_1/G_0 - 1}{2} \overline{f_1(t)} + \frac{G_s}{G_0} \mathrm{Im}\left[ f_1'(t) \frac{dt}{ds} \right], t \in L. \quad (6.11)$$

In what follows, the integrated form (6.11) of the interface condition will be utilized in the design of inhomogeneities which achieve uniform internal strain fields in the presence of interface effects.

## 6.3 Single Inhomogeneity with Interface Effects that Achieves Uniform Internal Strain Induced by a Screw Dislocation

As shown in Fig. 6.1, we consider a single inhomogeneity interacting with a screw dislocation (at the point $(x_{10}, x_{20})$) embedded in an infinite matrix. Most recently, Wang and Schiavone (2016) verified the existence of inhomogeneities with uniform internal strain fields induced by screw dislocations in the absence of interface effects (i.e., in the case of a perfectly bonded interface). The analogous problem in the presence of interface effects, however, remains unresolved. We address this issue here by deriving and solving a system of equations with respect to the parameters which define the unknown shape of the inhomogeneity.

### *6.3.1 Analysis*

Consider an elastic inhomogeneity with prescribed uniform internal strain field embedded in an infinite matrix interacting with a screw dislocation (with Burgers

vector $b_z$ located at the point $(x_{10}, x_{20})$) (see Fig. 6.1). The corresponding complex potentials $f_0(z)$ and $f_1(z)$ take the form

$$f_0(z) = \frac{b_z}{2\pi} \log(z - z_0) + g_0(z), z_0 = x_{10} + ix_{20}, \tag{6.12}$$

$$f_1(z) = \Gamma_1 z, \tag{6.13}$$

where $\Gamma_1$ is a known complex constant determined by the prescribed uniform internal strain field and $g_0(z)$ is an unknown holomorphic function defined in the infinite region $S_0$. Substituting Eqs. (6.12) and (6.13) into Eq. (6.11), we obtain

$$g_0(t) = At + B\bar{t} + \frac{G_s}{G_0} \mathrm{Im}\left[\Gamma_1 \frac{dt}{ds}\right] - \frac{b_z}{2\pi} \log(t - z_0), t \in L, \tag{6.14}$$

with

$$A = (1 + G_1/G_0)\,\Gamma_{1/2}, B = (G_1/G_0 - 1)\,\overline{\Gamma}_{1/2}. \tag{6.15}$$

Introduce a conformal mapping from the infinite region $S_0$ in the $z$-plane to the exterior of the unit circle in the $\xi$-plane (Muskhelishvili 1975),

$$z = \omega(\xi) = R\left(\xi + \sum_{j=1}^{+\infty} a_j \xi^{-j}\right), |\xi| \geq 1, \tag{6.16}$$

which, in particular, associates the shape $L$ of the inhomogeneity in the $z$-plane with the unit circle (denoted by $\sigma = e^{i\theta}, 0 \leq \theta \leq 2\pi$) in the $\xi$-plane. In the mapping (6.16), the real constant $R$ characterizes the size of the inhomogeneity and is prescribed in advance leaving the complex coefficients $a_j$ $(j = 1 \ldots +\infty)$, which determine the actual shape of the inhomogeneity, as the only remaining unknowns. In the context of mapping (6.16), noting that

$$t = \omega(\sigma), \frac{dt}{ds} = \frac{i\sigma\omega'(\sigma)}{|\omega'(\sigma)|}, (t \in L) \tag{6.17}$$

it follows from Eq. (6.14) that

$$g_0(\omega(\sigma)) = A\omega(\sigma) + B\overline{\omega(\sigma)} + \frac{G_s}{G_0} \mathrm{Re}\left[\Gamma_1 \frac{\sigma\omega'(\sigma)}{|\omega'(\sigma)|}\right] - \frac{b_z}{2\pi} \log[\omega(\sigma) - z_0]. \tag{6.18}$$

In order to ensure the existence of the function $g_0(z)$ holomorphic in the infinite region $S_0$ (which is equivalent to ensuring the existence of the function $g_0(\omega(\xi))$ holomorphic outside the unit circle in the $\xi$-plane), the boundary value $g_0(\omega(\sigma))$

(see Eq. (6.18)) of the function $g_0(\omega(\xi))$ on the unit circle in the $\xi$-plane should satisfy the following necessary and sufficient condition (Muskhelishvili 1975):

$$\frac{1}{2\pi}\int_0^{2\pi} g_0\left(\omega\left(\sigma\right)\right)\sigma^{-k}d\theta = 0, \sigma = e^{i\theta}, k = 1, 2, .... \tag{6.19}$$

Using Eq. (6.16) and defining

$$b_k = \frac{1}{2\pi}\int_0^{2\pi} \mathrm{Re}\left[\Gamma_1\frac{\sigma\omega'\left(\sigma\right)}{|\omega'\left(\sigma\right)|}\right]\sigma^{-k}d\theta, \sigma = e^{I\theta}, k = 1, 2, ... \tag{6.20}$$

$$d_k = \frac{1}{4\pi^2}\int_0^{2\pi} \log\left[\omega\left(\sigma\right) - z_0\right]\sigma^{-k}d\theta, \sigma = e^{i\theta}, k = 1, 2, ... \tag{6.21}$$

the condition (6.19) results in

$$A\delta_k^1 + B\overline{a}_k + \gamma b_k - \frac{b_z}{R}d_k = 0, k = 1, 2, ... \tag{6.22}$$

with

$$\gamma = \frac{G_s}{G_0 R}, \tag{6.23}$$

$$\delta_k^1 = \begin{cases} 1, k = 1 \\ 0, k = 2, 3, ... \end{cases} \tag{6.24}$$

in which the parameters $A$, $B$, $\gamma$, $R$, and $b_z$ are all known while the unknown coefficients $a_j$ ($j = 1 \ \ldots \ + \infty$) introduced from the mapping (6.16) will determine the actual shape of the inhomogeneity. Here, it should be noted that each step in the derivation leading to Eq. (6.22) is necessary and sufficient so that we can state categorically that once Eq. (6.22) admits a solution for the coefficients $a_j$ ($j = 1 \ \ldots \ + \infty$) introduced from the mapping (6.16), the resulting shape of the inhomogeneity is the one which achieves the corresponding uniform internal strain field as a result of the influence of the corresponding dislocation. Instead of examining analytically whether Eq. (6.22) admits a solution, we employ the Newton–Raphson method to solve the truncated form of Eq. (6.22). In fact, we can truncate the infinite series from the mapping (6.16) to a finite order polynomial in $N$ unknown coefficients $a_j$ ($j = 1 \ \ldots \ N$), which can be obtained numerically from the corresponding truncated nonlinear Eq. (6.22) for $k = 1 \ \ldots \ N$. In particular, the Jacobi matrix in the corresponding Newton–Raphson iteration can be obtained using

$$\left.\begin{aligned}\frac{d\left(\frac{\omega'(\sigma)}{|\omega'(\sigma)|}\right)}{d\mathrm{Re}(a_j)} &= R\frac{-j\sigma^{-j-1}|\omega'(\sigma)|^2+j\omega'(\sigma)\mathrm{Re}\left[\sigma^{j+1}\omega'(\sigma)\right]}{|\omega'(\sigma)|^3},\\ \frac{d\left(\frac{\omega'(\sigma)}{|\omega'(\sigma)|}\right)}{d\mathrm{Im}(a_j)} &= R\frac{-ij\sigma^{-j-1}|\omega'(\sigma)|^2+j\omega'(\sigma)\mathrm{Im}\left[\sigma^{j+1}\omega'(\sigma)\right]}{|\omega'(\sigma)|^3},\end{aligned}\right\} j=1...N, \tag{6.25}$$

$$\left.\begin{aligned}\frac{d\log[\omega(\sigma)-z_0]}{d\mathrm{Re}(a_j)} &= \frac{R\sigma^{-j}}{\omega(\sigma)-z_0},\\ \frac{d\log[\omega(\sigma)-z_0]}{d\mathrm{Im}(a_j)} &= \frac{iR\sigma^{-j}}{\omega(\sigma)-z_0},\end{aligned}\right\} j=1...N, \tag{6.26}$$

with detailed implementation of the Newton–Raphson iteration scheme available in Dai and Gao (2016). We proceed with the assertion that if the Newton–Raphson method always results in convergent solutions (shapes of desired inhomogeneities) with increasing values of $N$, then the original Eq. (6.22) (not truncated) indeed admits solutions which, in turn, identify inhomogeneities with the desired property, i.e., which achieve uniform internal strain fields in the presence of interface effects when subjected to the influence of a screw dislocation.

It is expected that the values of $A$ and $B$ (determined by the prescribed uniform internal strain field $\Gamma_1$, see Eq. (6.15)) greatly influence the existence of solutions to Eq. (6.22). Consequently, the uniform internal strain field prescribed inside the inhomogeneity should be chosen judiciously. However, since there are no known standard shapes of inhomogeneity capable of achieving uniform internal fields in the presence of interface effects, we proceed by simply prescribing the uniform internal strain field inside the unknown inhomogeneity using the average internal strain field (induced by a screw dislocation) inside, for example, a circular inhomogeneity. In this case, the average internal strain field is obtained as (based on Fang and Liu (2006))

$$\Gamma_1^{average} = \frac{-b_z}{\pi z_0\left(1+G_1/G_0+\gamma\right)}, \tag{6.27}$$

where $\gamma$ is given by Eq. (6.23) with $R$ representing the radius of the circular inhomogeneity. The prescribed uniform internal strain field inside the unknown inhomogeneity is then defined by introducing a perturbation into Eq. (6.27) as follows:

$$\Gamma_1 = \Gamma_1^{average}(1+\eta) = \frac{-b_z(1+\eta)}{\pi z_0\left(1+G_1/G_0+\gamma\right)}, \tag{6.28}$$

where $\eta$ is a complex parameter. In particular, we can see from Eqs. (6.20)–(6.22) that the actual shape (ignoring the orientation) of the inhomogeneity with prescribed uniform internal strain field defined by Eq. (6.28) is determined by only the parameter $\gamma$ corresponding to the size-dependent interface effects (see Eq. (6.23)), the perturbation parameter $\eta$ (see Eq. (6.28)), and the relative distance $|z_0|/R$ between the dislocation and the inhomogeneity itself. Consequently, in the following numerical examples, for the sake of convenience, the dislocation will always occupy a position on the positive $x$-axis.

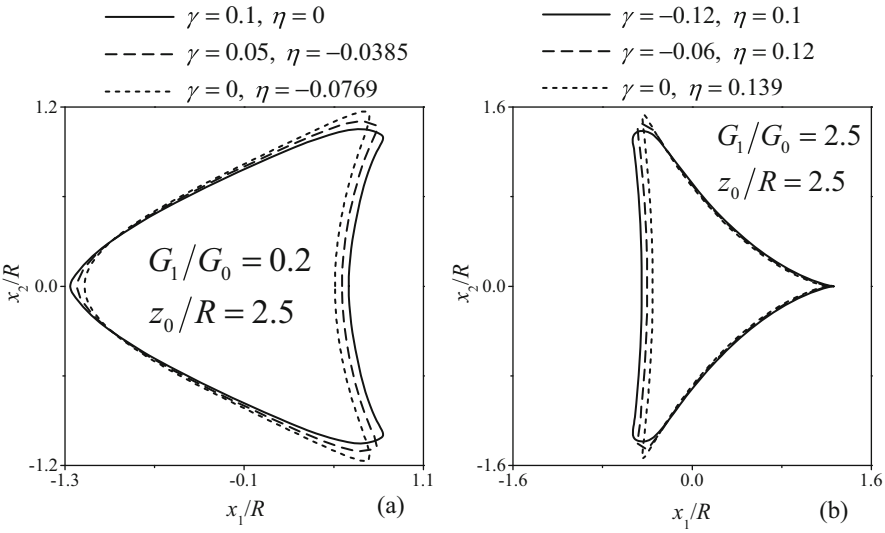


**Fig. 6.2** Effect of dislocation on the shape of an inhomogeneity with interface effects that achieves a uniform internal strain field for real $\eta$ with increasing size of the inhomogeneity

### 6.3.2 *Numerical Examples*

Previous studies have shown that the interfacial shear modulus $G_s$ is of the order of 1 N/m (see Ruud et al. 1993; Josell et al. 1999) and may take positive or negative values depending on the crystallographic orientation (see Miller and Shenoy 2000; Shenoy 2005), while the shear modulus $G_0$ of the matrix is of the order of 10 GPa. Consequently, the parameter $G_s/G_0$ is of the order of $10^{-10}$ m and we can see from the parameter $\gamma$ defined in Eq. (6.23) that incorporation of interface effects will impact the shape of the inhomogeneity with uniform internal strain field only when the inhomogeneity size $R$ decreases towards the nanoscale. In the following examples, we adopt the dimensionless parameters $\gamma$, $\eta$, and $z_0/R$ to identify the shape of the desired inhomogeneity with interface effects which achieves a prescribed uniform internal strain field under the influence of a screw dislocation.

The size-dependent phenomenon of the elastic field inside a nano-inhomogeneity with interface effect is well reported in the literature. Here, our numerical results will show that the shape of a nano-inhomogeneity which achieves a uniform internal strain field under the influence of a dislocation is also size dependent. Figures 6.2 and 6.3 illustrate this size dependence when the inhomogeneity increases in size from the nanoscale to the macroscale.

Note that the shapes shown in Figs. 6.2 and 6.3 for different sizes of inhomogeneity are normalized by their respective inhomogeneity size to facilitate comparisons. In Figs. 6.2 and 6.3, all of the inhomogeneities of different sizes are able to achieve the same uniform internal strain field under the same relative distance between

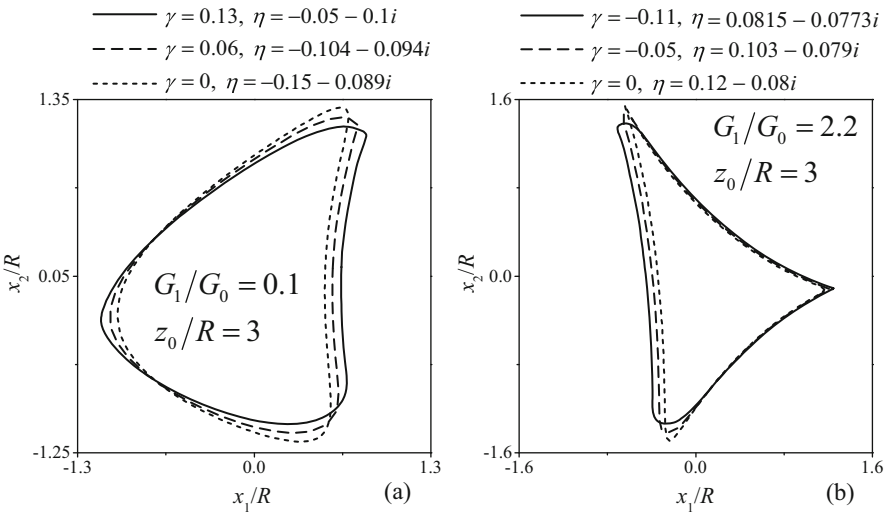


**Fig. 6.3** Effect of dislocation on the shape of an inhomogeneity with interface effects that achieves a uniform internal strain field for complex $\eta$ with increasing size of the inhomogeneity

inhomogeneity and dislocation. It follows that the clear size dependence of the shape of the inhomogeneity is due mainly to the size-dependent interface effects determined by $\gamma$ (see Eq. (6.23)). It is interesting to note from Figs. 6.2 and 6.3 that soft and hard inhomogeneities seem to be repelled and attracted, respectively, by the dislocation to achieve a uniform internal strain field.

It is clear that the distance between the inhomogeneity and the dislocation has a significant impact on the shape of an inhomogeneity able to sustain a uniform internal strain field. It is of particular interest, therefore, to examine the effect of the dislocation on the shape of the inhomogeneity in terms of the convergence of related procedures with increasing distance between the inhomogeneity and the dislocation. Shown in Figs. 6.4 and 6.5 is the convergence of the shape of the nano-inhomogeneity that achieves a uniform internal strain field when the distance between the inhomogeneity and the dislocation increases.

In Fig. 6.4, we can see that the shape of the nano-inhomogeneity which achieves a uniform internal strain field for $\eta = 0$ converges to a circle with increasing distance between the inhomogeneity and the dislocation. This is actually not surprising given that (as shown by Fang and Liu (2006)) the internal strain field inside a circular nano-inhomogeneity induced by a dislocation tends towards a uniform field (given by the average internal strain field (6.27)) with increasing distance between the inhomogeneity and the dislocation. The general reason why the inhomogeneity shape achieving a uniform internal strain field converges when the distance between the inhomogeneity and dislocation increases can perhaps be explained as follows. For a sufficiently large distance between the inhomogeneity and the dislocation, the

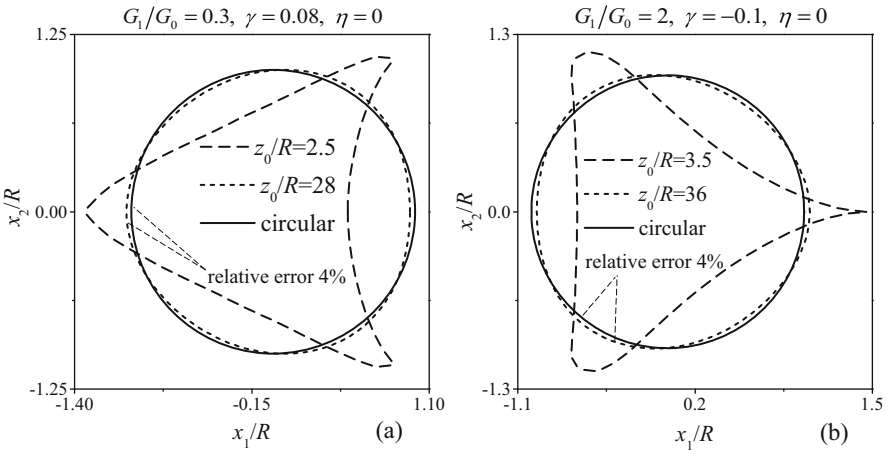


**Fig. 6.4** Convergence of the shape of a nano-inhomogeneity which achieves a uniform internal strain field for $\eta = 0$ with increasing distance between the dislocation and the inhomogeneity

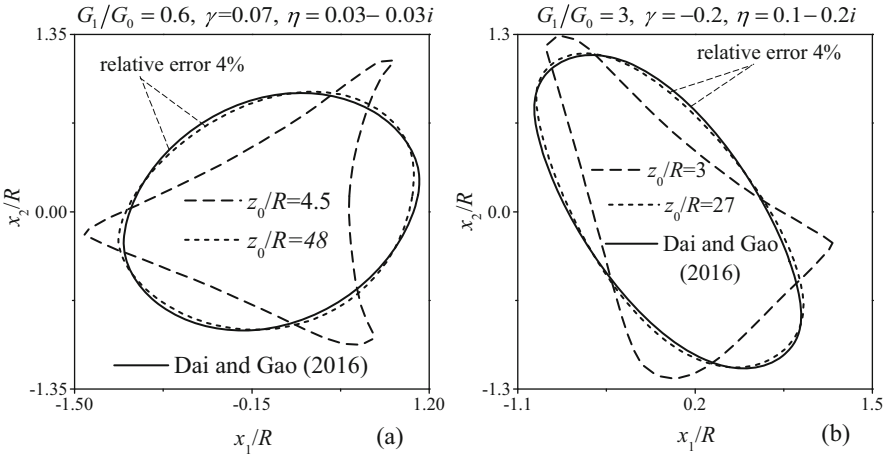


**Fig. 6.5** Convergence of the shape of a nano-inhomogeneity that achieves a uniform internal strain field for complex $\eta$ with increasing distance between the inhomogeneity and the dislocation

logarithmic term related to the dislocation in the boundary condition (6.14) has the following first-order asymptotic form:

$$\log(t - z_0) = \log(-z_0) - \sum_{j=1}^{+\infty} \frac{t^j}{j z_0^j} \approx \log(-z_0) - \frac{t}{z_0},\ |z_0| \gg |t|\,. \tag{6.29}$$

From Eq. (6.29), we see that, with increasing distance between the inhomogeneity and the dislocation, the effect of the dislocation on the shape of the

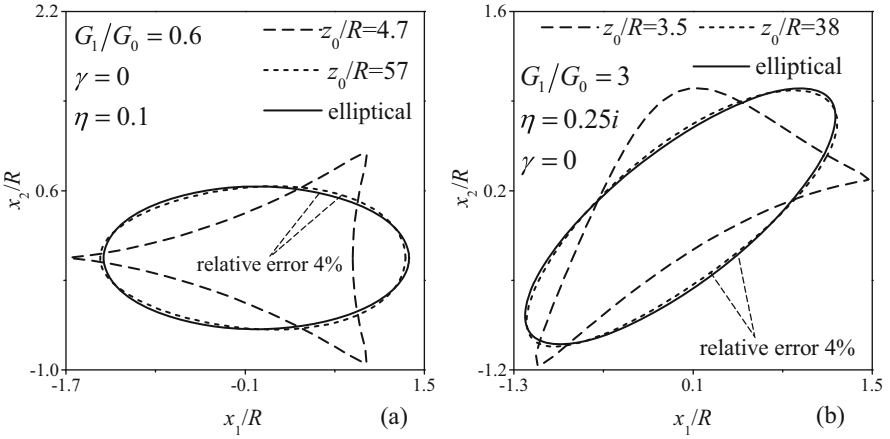


**Fig. 6.6** Convergence of the shape of an inhomogeneity without interface effect which achieves a uniform internal strain field with increasing distance between the dislocation and the inhomogeneity

inhomogeneity approximates the equivalent effect of a uniform remote loading on the shape of the inhomogeneity. Consequently, we can see in Fig. 6.5 that the shape of a nano-inhomogeneity with uniform internal strain field induced by a screw dislocation is indeed consistent with that of a nano-inhomogeneity with the same uniform internal strain field under uniform remote anti-plane shear loadings (see Dai and Gao 2016) when the distance between the inhomogeneity and the dislocation is sufficiently large. Here, an additional example (in which interface effects are ignored—see Fig. 6.6) is given to verify this reasoning.

It is seen quite clearly that when the distance between the inhomogeneity and the dislocation increases, the non-elliptical inhomogeneity that achieves a uniform internal strain field under the influence of a dislocation, in the absence of interface effects, does indeed converge to the corresponding case of an equivalent elliptical inhomogeneity subjected to the corresponding uniform remote strain field $\frac{-b_z}{2\pi z_0}$. Moreover, by comparing Figs. 6.5 and 6.6, it is found that for a given margin of relative error, the presence of interface effects will accelerate the convergence of the shape of the inhomogeneity.

## 6.4 Periodic Inhomogeneities with Interface Effects That Achieve Uniform Internal Strain Fields

In the presence of interface effects, the design of a single inhomogeneity with uniform internal strain field in anti-plane shear deformations has been well studied by Dai and Gao (2016). In a real composite with relatively high inhomogeneity volume

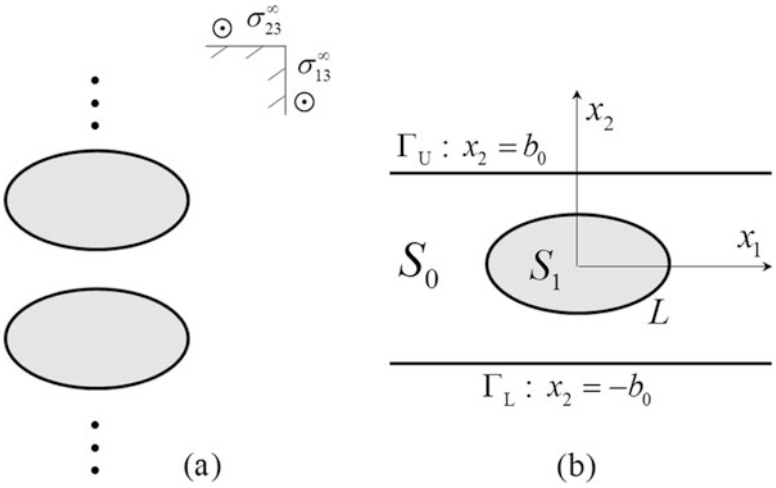


**Fig. 6.7** Periodic inhomogeneities with interface effects embedded in an infinite matrix under a uniform remote anti-plane shear loading

fraction, however, the interaction among inhomogeneities cannot be neglected so that the optimal shapes constructed by Dai and Gao (2016) are no longer relevant in this context. In this section, we develop a new method to construct optimal shapes of periodic inhomogeneities with uniform internal strain fields. As shown in Fig. 6.7a, we consider a composite containing an array of elastic inhomogeneities periodically distributed along the $x_2$-direction under uniform remote anti-plane shear loadings $\sigma_{13}^{\infty}$ and $\sigma_{23}^{\infty}$. The composite is subjected to anti-plane shear deformations and the interface between each inhomogeneity and its surrounding matrix is assumed to incorporate interface effects as described earlier. Our objective is again to determine the shape of the inhomogeneities enclosing uniform internal strain fields prescribed within a certain admissible range leaving the shape of the inhomogeneities as the only remaining unknown. To illustrate this investigation, we consider a representative strip of the composite which contains a single inhomogeneity as shown in Fig. 6.7b. In Fig. 6.7b, we denote the lower and upper edges of the strip parallel to the $x_2$-axis by $\Gamma_L$ and $\Gamma_U$, respectively, the inhomogeneity–matrix interface is again denoted by $L$, and the regions occupied by the matrix and the inhomogeneity by $S_0$ and $S_1$, respectively.

### *6.4.1 Solution Procedure*

The complex potentials for the matrix and inhomogeneity (with uniform internal strain) in the strip (defined in $S_0$ and $S_1$, respectively) take the form

$$f_0(z) = \Gamma_0 z + g_0(z), \Gamma_0 = \frac{\sigma_{23}^{\infty} + i\sigma_{13}^{\infty}}{G_0}, \tag{6.30}$$

$$f_1(z) = \Gamma_1 z, \tag{6.31}$$

where $g_0(z)$ is an unknown holomorphic function in $S_0$ while the uniform internal strain given by $\Gamma_1/2$ can be prescribed within a certain admissible range to guarantee the existence of the desired shape of inhomogeneity. Substituting Eqs. (6.30) and (6.31) into Eq. (6.11), we obtain

$$g_0(t) = At + B\bar{t} + \frac{G_s}{G_0}\mathrm{Im}\left[\Gamma_1 \frac{dt}{ds}\right], t \in L, \tag{6.32}$$

with

$$A = (1 + G_1/G_0)\,\Gamma_{1/2} - \Gamma_0, B = (G_1/G_0 - 1)\,\overline{\Gamma}_{1/2}. \tag{6.33}$$

In addition to the interface condition (6.32) on $L$, the periodicity of stress on the edges $\Gamma_{\mathrm{L}}$ and $\Gamma_{\mathrm{U}}$ of the strip requires

$$g_0\left(t_L\right) = g_0\left(t_U\right), \left(t_L = \bar{t}_U, t_{\mathrm{L}} \in \Gamma_{\mathrm{L}}, t_{\mathrm{U}} \in \Gamma_{\mathrm{U}}\right). \tag{6.34}$$

Here, we mention that the holomorphic function $g_0(z)$ can take the boundary values (6.32) and (6.34) only for very specific curves $L$. In what follows, we determine these particular curves $L$ by demonstrating the existence of $g_0(z)$ satisfying the boundary conditions (6.32) on $L$ and (6.34) on the edges $\Gamma_{\mathrm{L}}$ and $\Gamma_{\mathrm{U}}$.

First, we introduce two mappings as (see Dai et al. 2016a)

$$z = \rho(\eta) = \frac{b_0 \log \eta}{\pi} - ib_0, \tag{6.35}$$

$$\eta = \omega(\xi) = \eta_0 + R\left(\xi + \sum_{j=1}^{+\infty} a_j \xi^{-j}\right), |\xi| \geq 1. \tag{6.36}$$

As shown in Fig. 6.8, Eq. (6.35) maps the region $S_0$ in the $z$-plane to the region $S_\eta$ in the $\eta$-plane ($b_0$ is the semi-height of the strip in the physical plane, see Fig. 6.7b) and, in particular, it associates the edges $\Gamma_{\mathrm{L}}$ and $\Gamma_{\mathrm{U}}$ of the strip in the $z$-plane with the upper and lower limits of the ray $\Gamma_\eta$ in the $\eta$-plane, respectively. Consequently, in the context of the mapping (6.35), it follows from the boundary condition (6.34) that the function $g_0(\rho(\eta))$ defined in the region $S_\eta$ is continuous across the ray $\Gamma_\eta$ in the $\eta$-plane so that the existence of the holomorphic function $g_0(z)$ in the region $S_0$ satisfying boundary conditions (6.32) and (6.34) is now equivalent to the existence

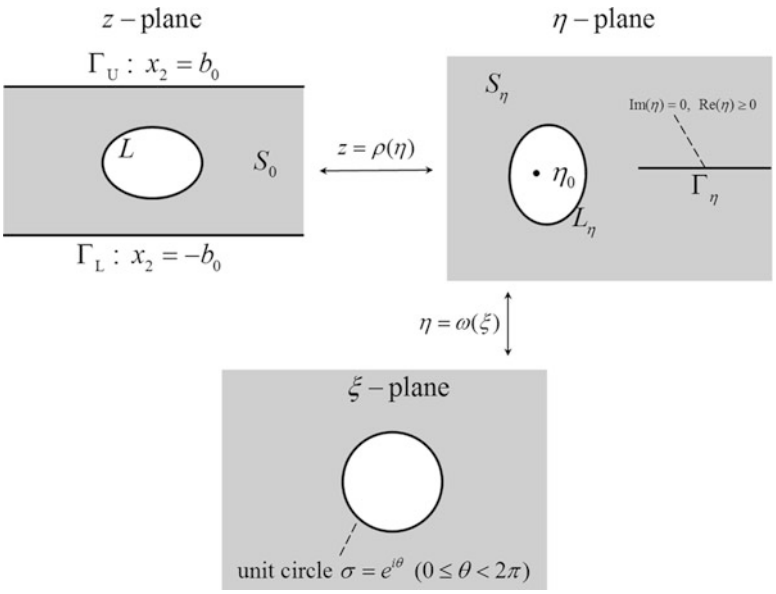


**Fig. 6.8** Particular conformal mappings from the physical strip to imaginary planes

of the holomorphic function $g_0(\rho(\eta))$ in the region $S_\eta$ with the following boundary value:

$$g_0\left(\rho\left(\eta\right)\right) = \frac{b_0\left(A\log\eta + B\overline{\log\eta}\right)}{\pi} + \frac{G_s}{G_0}\mathrm{Im}\left[\Gamma_1\frac{d\eta/\eta}{|d\eta/\eta|}\right] + i\left(B-A\right)b_0,\ \eta \in L_\eta. \tag{6.37}$$

We again note that Eq. (6.36) maps the region $S_\eta$ in the $\eta$-plane to the exterior of the unit circle (denoted by $\sigma = e^{i\theta}$, $0 \le \theta \le 2\pi$) in the $\xi$-plane (Muskhelishvili 1975) as shown in Fig. 6.8. In Eq. (6.36), the point $\eta_0$ surrounded by the curve $L_\eta$, the real constant $R$, and the complex coefficients $a_j$ $(j = 1\ \ldots\ +\infty)$ determines the overall location and the size and shape of the curve $L_\eta$ in the $\eta$-plane, respectively. Here, the mapping (6.36) implies that the existence of the holomorphic function $g_0(\rho(\eta))$ in the region $S_\eta$ with boundary value (6.37) is equivalent to the existence of the holomorphic function $g_0(\rho(\omega(\xi)))$ outside the unit circle in the $\xi$-plane with the following boundary value on the unit circle:

$$\begin{aligned} g_0\left(\rho\left(\omega\left(\sigma\right)\right)\right) = {} & \frac{b_0\left(A\log\omega(\sigma) + B\overline{\log\omega(\sigma)}\right)}{\pi} \\ & + \lambda b_0 \mathrm{Im}\left[i\Gamma_1\sigma W/\left|W\right|\right] + i\left(B-A\right)b_0, \end{aligned} \tag{6.38}$$

with

$$\lambda = \frac{G_s}{G_0 b_0},\ W = \frac{\omega'\left(\sigma\right)}{\omega\left(\sigma\right)}. \tag{6.39}$$

In order to ensure the existence of the holomorphic function $g_0(\rho(\omega(\xi)))$ outside the unit circle in the $\xi$-plane, its boundary value (6.38) on the unit circle should satisfy the following necessary and sufficient condition (Muskhelishvili 1975):

$$\frac{1}{2\pi}\int_0^{2\pi} g_0\left(\rho\left(\omega\left(\sigma\right)\right)\right)\sigma^{-k}d\theta = 0, \sigma = e^{i\theta}, k = 1, 2, .... \tag{6.40}$$

Introducing

$$P_k = \frac{1}{2\pi}\int_0^{2\pi} \log\left[\omega\left(\sigma\right)\right]\sigma^{-k}d\theta, k = 1, 2, ... \tag{6.41}$$

$$Q_k = \frac{1}{2\pi}\int_0^{2\pi} \overline{\log\left[\omega\left(\sigma\right)\right]}\sigma^{-k}d\theta, k = 1, 2, ... \tag{6.42}$$

$$T_k = \frac{1}{2\pi}\int_0^{2\pi} \mathrm{Im}\left[i\Gamma_1\sigma W/\left|W\right|\right]\sigma^{-k}d\theta, k = 1, 2, ... \tag{6.43}$$

it follows from Eq. (6.40) that

$$\frac{A}{B}P_k + Q_k + \frac{\pi\lambda}{B}T_k = 0, k = 1, 2, .... \tag{6.44}$$

Here, we note that Eq. (6.44) is a system of nonlinear equations with respect to the coefficients $a_j$ ($j = 1 \ \ldots \ +\infty$) introduced in the mapping (6.36). In what follows, we first prescribe the parameters $\eta_0$ and $R$ in the mapping (6.36) and truncate the mapping into a polynomial involving a finite number of coefficients $a_j$ ($j = 1 \ \ldots \ N$), which are then determined from the truncated Eq. (6.44) for $i = 1 \ \ldots \ N$ using the Newton–Raphson method. This then determines the actual shape $L$ of the inhomogeneity in the physical plane. Using the formulae

$$\frac{d\log\omega\left(\sigma\right)}{da_j} = \frac{R\sigma^{-j}}{\omega\left(\sigma\right)}, j = 1...N, \tag{6.45}$$

$$\left.\begin{array}{l} \frac{d(W/|W|)}{d\mathrm{Re}\left(a_j\right)} = \frac{D_j|W| - W\mathrm{Re}\left(W\overline{D}_j\right)/|W|}{|W|^2}, \\ \frac{d(W/|W|)}{d\mathrm{Im}\left(a_j\right)} = \frac{i\cdot D_j|W| - W\mathrm{Im}\left(W\overline{D}_j\right)/|W|}{|W|^2}, \\ D_j = R\frac{-j\sigma^{-j-1}\omega(\sigma) - \sigma^{-j}\omega'(\sigma)}{(\omega(\sigma))^2}, \end{array}\right\} j = 1...N, \tag{6.46}$$

it is relatively straightforward to calculate the Jacobi matrix in the Newton–Raphson iteration of the truncated Eq. (6.44) (for details on the implementation of the Newton–Raphson iteration in this context, we refer the reader to Dai and Gao (2016)). In addition, it follows from Eqs. (6.35), (6.36), and (6.41)–(6.44) that the final shapes of the periodic inhomogeneities with interface effects achieving uniform internal strain fields in the physical plane are determined by only the remote loading,

the ratio of shear moduli $G_1/G_0$, the ratio $A/B$ (see Eq. (6.33)), the parameter $\lambda$ characterizing the interface effects (see Eq. (6.39)), and the ratio $|\eta_0|/R$ (see Eq. (6.36)).

### 6.4.2 Numerical Examples

In each of the following examples, we use the parameters

$$g = A/B, \alpha = |\eta_0|/R, \lambda = \frac{G_s}{G_0 b_0}, \tag{6.47}$$

to identify the shapes of the desired periodic inhomogeneities. Here, for most composites with periodic nanostructures, the corresponding parameters $\lambda$ in Eq. (6.47) have order $10^{-2}$ (see Ruud et al. 1993; Josell et al. 1999). In particular, the uniform internal strain field inside the inhomogeneities appears to be associated with the parameter $g$ in Eq. (6.47) by (Dai et al. 2017)

$$\Gamma_1 = 2\frac{(1 + G_1/G_0)\,\Gamma_0 + g\,(G_1/G_0 - 1)\,\overline{\Gamma}_0}{(1 + G_1/G_0)^2 - |g|^2 (G_1/G_0 - 1)^2}. \tag{6.48}$$

Figures 6.9 and 6.10 show the variation of the shape of the desired periodic inhomogeneities (enclosing uniform internal strain fields in the presence of interface effects) with increasing size of the inhomogeneities. In Figs. 6.9 and 6.10, we maintain unchanged the ratio of the period (given by $2b_0$) of the composite to the inhomogeneity size (in the $x_2$-direction) to demonstrate the clear size dependence of interface effects on the shape of the inhomogeneity. Consequently, the increasing size of the inhomogeneities in Figures 6.9 and 6.10 is determined by the decreasing parameter $|\lambda|$ (see Eq. (6.47)).

It can be seen quite clearly in Figs. 6.9 and 6.10 that the presence of interface effects induces a significant impact on the shape of periodic inhomogeneities with uniform internal strain fields. In the absence of interface effects, Dai et al. (2016a) have shown that the shape of periodic inhomogeneities with uniform internal strain fields is independent of the remote loading, whereas in the presence of interface effects, Figs. 6.9a and 6.10a show that such inhomogeneity shapes become strongly dependent on the remote loading. In addition, the accuracy of our present method is verified in Figs. 6.9 and 6.10 by the fact that the shapes obtained in the presence of interface effects using our method for a relatively large size (around a few hundreds of nanometers corresponding to $\lambda$ of the order of $10^{-3}$) of inhomogeneity are consistent with the shapes identified in the simpler case (Cherepanov 1974; Dai et al. 2016a) when the inhomogeneity–matrix interfaces are perfectly bonded.

In addition to the size-dependent shape of periodic inhomogeneities achieving uniform internal strain in the presence of interface effects, it is also of particular interest to see the variation of the shape of such inhomogeneities when the period

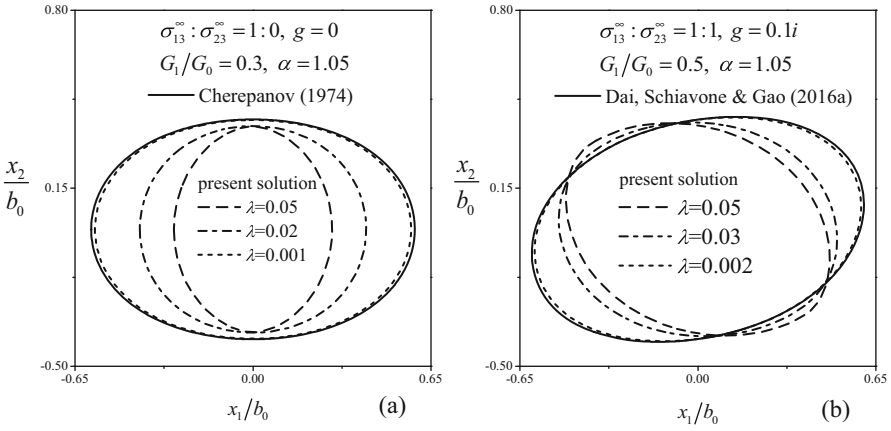


**Fig. 6.9** Periodic soft inhomogeneities with interface effects that achieve uniform internal strain fields with increasing size

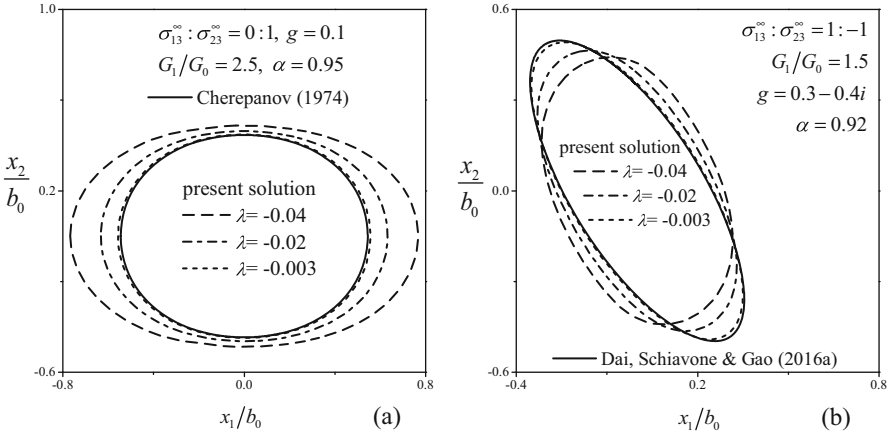


**Fig. 6.10** Periodic hard inhomogeneities with interface effects that achieve uniform internal strain fields with increasing size

of the composite increases. Figures 6.11 and 6.12 show the convergence of the shape of such periodic inhomogeneities with increasing period of the composite. In particular, in Figs. 6.11 and 6.12, we maintain the size of the inhomogeneities (in the $x_2$-direction) unchanged overall when the period of the composite increases.

It is shown in Figs. 6.11 and 6.12 that the convergent shape of the corresponding periodic inhomogeneities which achieve uniform internal fields in the presence of interface effects with increasing period of the composite is typically non-elliptical. This verifies the fact that in the presence of the interface effect, a single inhomogeneity with uniform internal strain field exists but is no longer elliptical (see also Dai and Gao 2016). Moreover, we note in Figs. 6.11 and 6.12 that

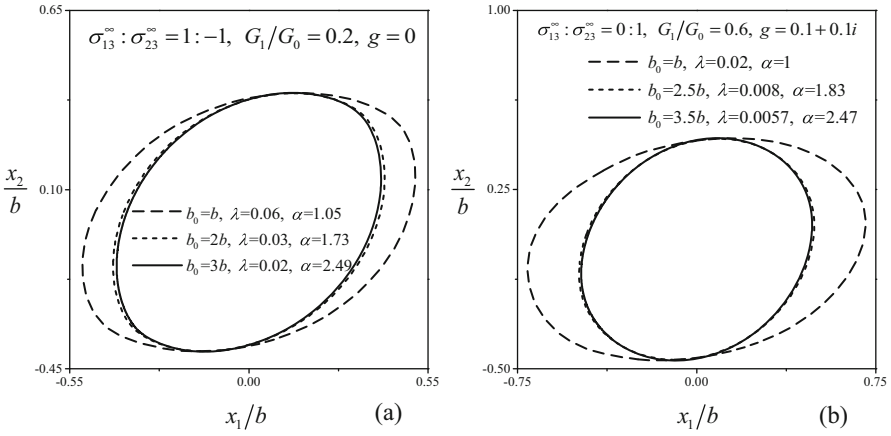


**Fig. 6.11** Periodic soft inhomogeneities with interface effects that achieve uniform internal strain fields with increasing period of the composite

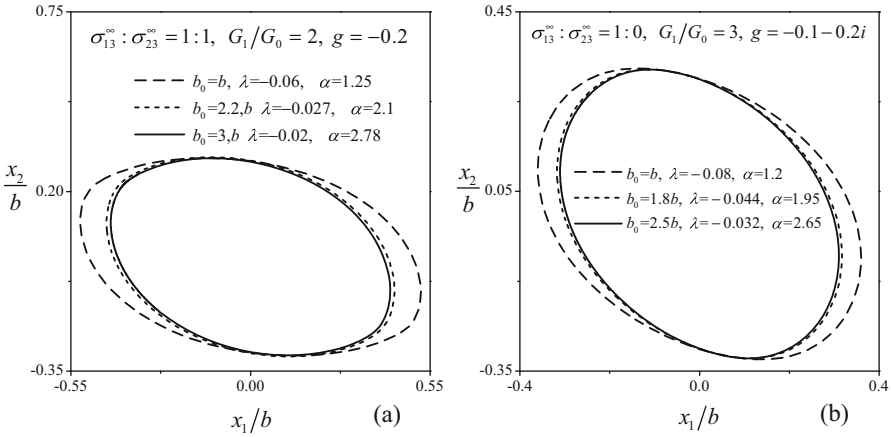


**Fig. 6.12** Periodic hard inhomogeneities with interface effects that achieve uniform internal strain fields with increasing period of the composite

the shape of periodic inhomogeneities with uniform internal strain fields can be treated approximately as that of a single inhomogeneity with the same uniform internal strain field using identical remote loading and identical bulk and interface parameters when the period of the composite exceeds roughly seven times the size of the inhomogeneities.

Since the shape of the periodic inhomogeneities has to change to maintain the prescribed uniform internal strain field as the inhomogeneity size and the period of the composite vary, it is expected that the stress field inside the matrix will also vary with increasing inhomogeneity size and period of the composite. The effects of the size of periodic inhomogeneities (with interface effects) enclosing a given uniform

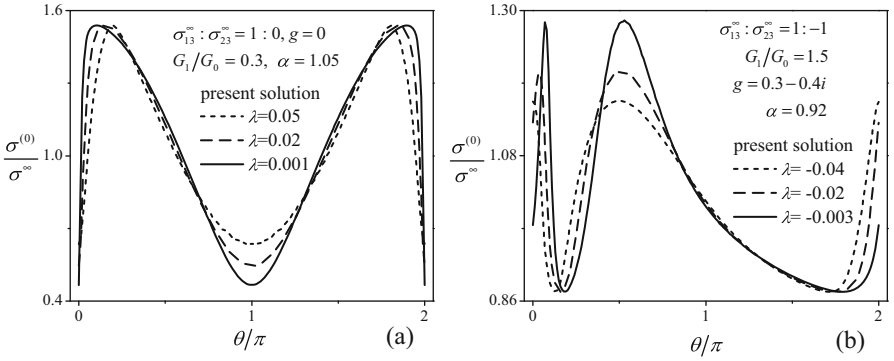


**Fig. 6.13** Size-dependent resultant interfacial shear stresses in the matrix surrounding periodic inhomogeneities with interface effects and given uniform internal strain field

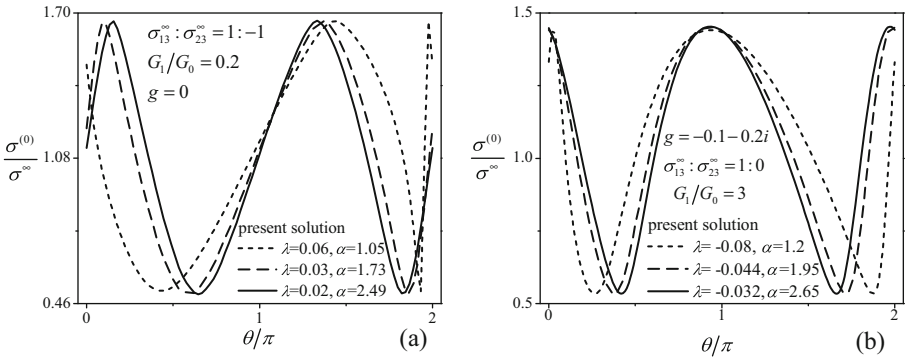


**Fig. 6.14** Influence of the period of the composite on resultant interfacial shear stresses in the matrix surrounding periodic inhomogeneities with interface effects and given uniform internal strain field

strain field and the period of the composite on the resultant interfacial stress in the matrix are shown in Figs. 6.13 and 6.14. In Figs. 6.13 and 6.14, the resultant interfacial stress $\sigma^{(0)}$ and the resultant remote stress $\sigma^{\infty}$ are defined by

$$\sigma^{(0)}=\sqrt{\left(\sigma_{13}^{(0)}\right)^2+\left(\sigma_{23}^{(0)}\right)^2},\sigma^{\infty}=\sqrt{\left(\sigma_{13}^{\infty}\right)^2+\left(\sigma_{23}^{\infty}\right)^2}, \tag{6.49}$$

and the abscissa $\theta$ refers to the amplitude of a certain point on the unit circle (denoted by $\sigma$) in the $\xi$-plane (here, the entire unit circle corresponds to the entire interface in the physical plane—see mappings (6.35) and (6.36)). We can see in Figs. 6.13 and 6.14 that, compared with the period of the composite, the size of the inhomogeneity plays a dominant role in the interfacial stress concentration in the matrix. In particular, the results shown in Fig. 6.14 suggest that for nanocomposites with periodic inhomogeneities, it is possible to maintain the prescribed

uniform stress field inside the inhomogeneities and the bounds of the stress field inside the matrix by changing only the shape of the inhomogeneities when the period of the composite decreases and therefore the interaction among the inhomogeneities themselves becomes stronger.

## 6.5 Conclusions

We incorporate interface effects to examine the existence of a single inhomogeneity able to achieve uniform internal strain under the influence of a screw dislocation as well as the existence of periodic inhomogeneities capable of sustaining uniform internal strain fields when subjected to uniform remote anti-plane shear loadings. We transform the original problem of the existence of such inhomogeneities into an equivalent problem of the existence of a holomorphic function defined in an infinite plane with hole(s) occupying the same position(s) as those of the corresponding inhomogeneities. We define the shape of the inhomogeneities using a conformal mapping with unknown coefficients from which we derive a system of nonlinear equations with respect to these coefficients which are subsequently determined numerically. We present a variety of examples to demonstrate our method and illustrate the shapes of such inhomogeneities. We summarize the main findings as follows:

1. Whether or not interface effects are included in the model of deformation, we have demonstrated the existence of a single inhomogeneity which achieves a uniform internal strain field induced by a screw dislocation in an infinite elastic solid subjected to anti-plane shear deformations. In particular, the shape of such an inhomogeneity is dependent on the inhomogeneity size (in the case of an inhomogeneity with interface effects) and the specific uniform internal strain field.
2. When the distance between the inhomogeneity and the dislocation increases, our method continues to converge to the shape of an inhomogeneity (with or without interface effects) which achieves a uniform internal strain field. When interface effects are absent, we obtain clear convergence to the corresponding elliptical inhomogeneity.
3. A consequence of the above conclusion (2) is that there indeed exist noncircular nano-inhomogeneities (as defined above) that achieve uniform internal strain fields in an elastic solid subjected to uniform remote anti-plane shear.
4. In anti-plane shear deformations, there indeed exist periodic inhomogeneities incorporating interface effects able to achieve uniform internal strain fields under uniform remote (anti-plane shear) loadings.
5. In the presence of interface effects, the shapes of periodic inhomogeneities with uniform internal strain fields are strongly dependent on the inhomogeneity size (especially at the nanoscale) and the remote loading.
6. When the period of the inhomogeneity-matrix system is roughly larger than seven times the size of the inhomogeneities, the shapes of periodic inhomogeneities

with uniform internal strain fields can be treated essentially in the same way as that of a single inhomogeneity with the same uniform strain field using identical inhomogeneity size, bulk and interface constants, and remote loading.

7. The shape of periodic inhomogeneities with interface effects can be varied to maintain both the prescribed uniform stress field inside the inhomogeneities and the upper and lower bounds of the stress field inside the matrix when the period of the inhomogeneity-matrix system decreases.

We conclude by noting that the analogous investigations in plane elasticity (incorporating interface effects) present formidable challenges and are currently part of the authors' subsequent investigations in this area. Finally, the authors would like to mention that the results in Sects. 6.3 and 6.4 of this chapter form the basis of two papers recently submitted for publication (see Dai et al. 2016b, c).

**Acknowledgments** Dai appreciates the support of the China Scholarship Council. Schiavone thanks the Natural Sciences and Engineering Research Council of Canada for their support through a Discovery Grant (Grant # RGPIN 155112).

## References

Ammari, H., Capdeboscq, Y., Kang, H., Lee, H., Milton, G.W., Zribi, H.: Progress on the strong Eshelby's conjecture and extremal structures for the elastic moment tensor. J. Math. Pure Appl. **94**, 93–106 (2010)

Cherepanov, G.P.: Inverse problems of the plane theory of elasticity. J. Appl. Math. Mech. **38**, 915–931 (1974)

Dai, M., Ru, C.Q., Gao, C.F.: Uniform strain fields inside multiple inclusions in an elastic infinite plane under anti-plane shear. Math. Mech. Solids. **22**, 114–128 (2017)

Dai, M., Gao, C.F., Ru, C.Q.: Uniform stress fields inside multiple inclusions in an elastic infinite plane under plane deformation. Proc. R. Soc. A. **471**, 20140933 (2015a)

Dai, M., Ru, C.Q., Gao, C.F.: Non-elliptical inclusions that achieve uniform internal strain fields in an elastic half-plane. Acta Mech. **226**, 3845–3863 (2015b)

Dai, M., Gao, C.F.: Non-circular nano-inclusions with interface effects that achieve uniform internal strain fields in an elastic plane under anti-plane shear. Arch. Appl. Mech. **86**, 1295–1309 (2016)

Dai, M., Schiavone, P., Gao, C.F.: Periodic inclusions with uniform internal hydrostatic stress in an infinite elastic plane. Z. Angew. Math. Mech. **96**, 1374–1380 (2016a)

Dai, M., Schiavone, P., Gao, C.F.: Nano-inclusion with uniform internal strain induced by a screw dislocation. Arch. Mech. **68**, 243–257 (2016b)

Dai, M., Schiavone, P., Gao, C.F.: Uniform strain fields inside periodic inclusions incorporating interface effects in anti-plane shear. Acta Mech. **227**, 2795–2803 (2016c)

Eshelby, J.D.: The determination of the elastic field of an ellipsoidal inclusion and related problems. Proc. R. Soc. Lond. A. **241**, 376–396 (1957)

Eshelby, J.D.: Elastic inclusions and inhomogeneities. Prog. Solid Mech. **2**, 87–140 (1961)

Fang, Q.H., Liu, Y.W.: Size-dependent elastic interaction of a screw dislocation with a circular nano-inhomogeneity incorporating interface stress. Scr. Mater. **55**, 99–102 (2006)

Grabovsky, Y., Kohn, R.V.: Microstructures minimizing the energy of a two phase elastic composite in two space dimensions. II: the Vigdergauz microstructure. J. Mech. Phys. Solids. **43**, 949–972 (1995)

Gurtin, M.E., Murdoch, A.I.: A continuum theory of elastic material surfaces. Arch. Ration. Mech. Anal. **57**, 291–323 (1975)
Gurtin, M.E., Weissmüller, J., Larche, F.: A general theory of curved deformable interfaces in solids at equilibrium. Philos. Mag. A. **78**, 1093–1109 (1998)
Horgan, C.O.: Anti-plane shear deformations in linear and nonlinear solid mechanics. SIAM Rev. **37**, 53–81 (1995)
Josell, D., Bonevich, J.E., Shao, I., Cammarata, R.C.: Measuring the interface stress: Silver/nickel interfaces. J. Mater. Res. **14**, 4358–4365 (1999)
Kang, H., Milton, G.W.: Solutions to the Pólya–Szegö conjecture and the weak Eshelby conjecture. Arch. Ration. Mech. Anal. **188**, 93–116 (2008)
Kang, H., Kim, E., Milton, G.W.: Inclusion pairs satisfying Eshelby's uniformity property. SIAM J. Appl. Math. **69**, 577–595 (2008)
Liu, L., James, R.D., Leo, P.H.: Periodic inclusion—matrix microstructures with constant field inclusions. Metall. Mater. Trans. A. **38**, 781–787 (2007)
Liu, L.P.: Solutions to the Eshelby conjectures. Proc. R. Soc. Lond. A. **464**, 573–594 (2008)
Luo, J., Wang, X.: On the anti-plane shear of an elliptic nano inhomogeneity. Eur. J. Mech. A/Solids. **28**, 926–934 (2009)
Markenscoff, X.: On the shape of the Eshelby inclusions. J. Elasticity. **49**, 163–166 (1997)
Miller, R.E., Shenoy, V.B.: Size-dependent elastic properties of nanosized structural elements. Nanotechnology. **11**, 139–147 (2000)
Mura, T., Shodja, H.M., Lin, T.Y., Safadi, A., Makkawy, A.: The determination of the elastic field of a pentagonal star shaped inclusion. Bull. Tech. Univ. Istanbul. **47**, 267–280 (1994)
Mura, T.: The determination of the elastic field of a polygonal star shaped inclusion. Mech. Res. Commun. **24**, 473–482 (1997)
Muskhelishvili, N.I.: Some Basic Problems of the Mathematical Theory of Elasticity. Noordhoff, Groningen (1975)
Rodin, G.: Eshelby's inclusion problem for polygons and polyhedra. J. Mech. Phys. Solids. **44**, 1977–1995 (1996)
Ru, C.Q., Schiavone, P.: On the elliptic inclusion in anti-plane shear. Math. Mech. Solids. **1**, 327–333 (1996)
Ruud, J.A., Witvrouw, A., Spaepen, F.: Bulk and interface stresses in silver-nickel multilayered thin films. J. Appl. Phys. **74**, 2517–2523 (1993)
Sendeckyj, G.P.: Elastic inclusion problems in plane elastostatics. Int. J. Solids Struct. **6**, 1535–1543 (1970)
Sharma, P., Ganti, S., Bhate, N.: Effect of surfaces on the size-dependent elastic state of nano-inhomogeneities. Appl. Phys. Lett. **82**, 535–537 (2003)
Sharma, P., Ganti, S.: Size-dependent Eshelby's tensor for embedded nano-inclusions incorporating surface/interface energies. ASME J. Appl. Mech. **71**, 663–671 (2004)
Shenoy, V.B.: Atomistic calculations of elastic properties of metallic fcc crystal surfaces. Phys. Rev. B. **71**, 094104 (2005)
Tian, L., Rajapakse, R.: Elastic field of an isotropic matrix with a nanoscale elliptical inhomogeneity. Int. J. Solids Struct. **44**, 7988–8005 (2007a)
Tian, L., Rajapakse, R.: Analytical solution for size-dependent elastic field of a nanoscale circular inhomogeneity. ASME J. Appl. Mech. **74**, 568–574 (2007b)
Vigdergauz, S.: Two-dimensional grained composites of extreme rigidity. ASME J. Appl. Mech. **61**, 390–394 (1994)
Wang, X.: Uniform fields inside two non-elliptical inclusions. Math. Mech. Solids. **17**, 736–761 (2012)
Wang, X., Schiavone, P.: Two inhomogeneities of irregular shape with internal uniform stress fields interacting with a screw dislocation. C. R. Mec. **344**, 532–538 (2016)

# Chapter 7
# Ballistic Performance of Bimodal Nanostructured and Nanotwin-Strengthened Metals

**Xiang Guo, Guang Yang, George J. Weng, Linli L. Zhu, and Jian Lu**

**Abstract** Bimodal nanostructured (NS) metals and coarse-grained (CG) metals strengthened by nanotwinned (NT) regions are two kinds of novel NS metals with high strength and good ductility. They are potential candidates for bullet-proof material. In this work, numerical simulations based on the strain gradient plasticity model and the Johnson–Cook failure criterion are conducted to investigate the effects of microstructural attributes on their ballistic performance. We find that microstructures can significantly affect limit velocity and maximum displacement of the specimens and that regular distribution of the second phase is helpful to improve the overall performance. For the bimodal NS metals, it is found that, under the condition of same distribution, the second phase needs to have a longer projection perpendicular to the impact direction to achieve better performance. For the CG metals strengthened by NT regions, it is found that microstructures with array arrangement of NT regions have higher limit velocities and smaller relative displacements. It is believed that this study could provide insights into the development of advanced NS metals for ballistic protection.

X. Guo (✉)
School of Mechanical Engineering, Tianjin University, Tianjin 300072, China

Tianjin Key Laboratory of Nonlinear Dynamics and Control, Tianjin 300072, China
e-mail: xiangguo@tju.edu.cn

G. Yang
School of Mechanical Engineering, Tianjin University, Tianjin 300072, China

G.J. Weng
Department of Mechanical and Aerospace Engineering, Rutgers University, New Brunswick, NJ 08903, USA
e-mail: gjweng@soe.rutgers.edu

L.L. Zhu
Department of Engineering Mechanics, School of Aeronautics and Astronautics, Zhejiang University, Hangzhou 310027, Zhejiang, China

J. Lu
Department of Mechanical and Biomedical Engineering, City University of Hong Kong, Kowloon Tong, Hong Kong



S.A. Meguid, G.J. Weng (eds.), *Micromechanics and Nanomechanics of Composite Solids*, DOI 10.1007/978-3-319-52794-9_7

## 7.1 Introduction

The study of target-plate materials has attracted much attention in recent years. Several categories of structural materials including ceramics, Kevlar/epoxy composite, Kevlar fiber and $Al_2O_3$ powder-reinforced composites, and carbon nanotube-based composites have been studied and optimized for target-plate applications (Kaufmann et al. 2003; Kumar et al. 2010; Talib et al. 2012; Kulkarni et al. 2013). Besides them, several others are also appealing. A category of potential candidates is nanostructured (NS) metals. NS metals have been a hot topic due to their excellent mechanical properties. Strengthening effect by grain refinement can be described by the Hall–Petch relation (Hall 1951; Petch 1953). However, with their strength increasing, a drawback is that the overall ductility tends to deteriorate (Dao et al. 2007; Jerusalem and Radovitzky 2009). For bullet-proof performance, both high strength and good ductility are necessary (Zhang et al. 2007). Improving the strength of NS metals without markedly losing their ductility remains a challenge. Two strategies corresponding to two different kinds of novel NS metals are available to bypass this restriction.

The first is bimodal NS metals, which have nano-grained (NG) phase as the matrix and coarse-grained (CG) inclusions as the toughening phase. They exhibit high strength and also good ductility (Tellkamp et al. 2001; Wang et al. 2002; Witkin et al. 2003; Yang et al. 2010). Some experimental investigations further revealed their good ballistic performance (Newbery et al. 2006). Ballistic performance is closely correlated to fracture behavior and toughening mechanisms. The enhanced ductility and fracture toughness of various bimodal NS metals could be attributed to two mechanisms: (1) crack blunting, crack bridging, and debonding and (2) strain hardening in the CG inclusions (Zhang et al. 2007). But experiments alone have their inevitable intrinsic limitations because exact distribution and shape of the second phase are difficult to reproduce during fabrication. The overall mechanical responses are tricky to predict (Ma 2006). This makes an accompanied numerical study an urgent need.

The second is CG metals strengthened by nanotwinned (NT) regions. They are fabricated by a novel combination of dynamic plastic deformation (DPD) and thermal annealing. The DPD process is preferable for face-centered cubic metals to form nanotwins. Subsequent annealing recrystallizes the nano-grains and dislocation structures into coarse grains, while the NT regions remain. As a result, a CG structure with NT regions is fabricated. The composite with NT regions embedded in the CG metals can achieve excellent combination of strength and ductility (Li et al. 2008b; Xiao et al. 2011; Yan et al. 2012). In general, the presence of NT regions contributes to the overall high strength, while good ductility is attributed to the recrystallized coarse grains. However, few reports can be found on the ballistic performance of NT metals. Among these limited studies, Frontan et al. (2012) reported inferior energy absorption but better deformation resistance for an NT ultrafine crystal steel versus the CG steel. Other than this, no studies appear to be available in the literature.

Indeed much needs to be known for the ballistic performance of the above two kinds of novel NS metals. This is especially so since the effects of microstructural attributes such as the distribution and shape of the second phase remain unclear. This is the goal of this chapter. Here, the strain gradient plasticity model will be adopted to describe the constitutive relations of the NG and NT phases, and the Johnson–Cook plasticity model together with the Johnson–Cook failure criterion will be employed to study their performance. Our interest is on the microstructural dependence of their ballistic performance. We will use the finite-element calculation to reveal the details of the simulations.

## 7.2 Specimen Configuration and Idealized Microstructures

Specimens with a length $L$ and a thickness 0.06 mm are subjected to a ballistic impact. The bullet with a diameter 0.1 mm impacts the central zone of the specimen along the negative direction of Y axis, as shown in Fig. 7.1. Linear reduced-integration elements with characteristic size 5 μm are used for the bullet. Condition of plane strain is assumed to prevail. For a bimodal NS Cu specimen, $L$ is 1.5 mm. The left is clamped and the right is also clamped except that its movement along the X direction is free. Triangular elements with characteristic size 1 μm are used for the central zone and 3 μm for the other zones. For a CG Cu specimen strengthened by NT regions, $L$ is 2.9 mm. Both edges of the specimen are free. The central zone consists of three repeated microstructures and the other zones are homogenized phase. Triangular elements with characteristic size 0.5 μm are used for the central zone and 10 μm for the other zones.

To study the influences of microstructural attributes, 12 microstructures in Fig. 7.2 are used, with the matrix phase in green and the second phase in red. They have the same volume fraction (∼21%) but different distribution and shape of the

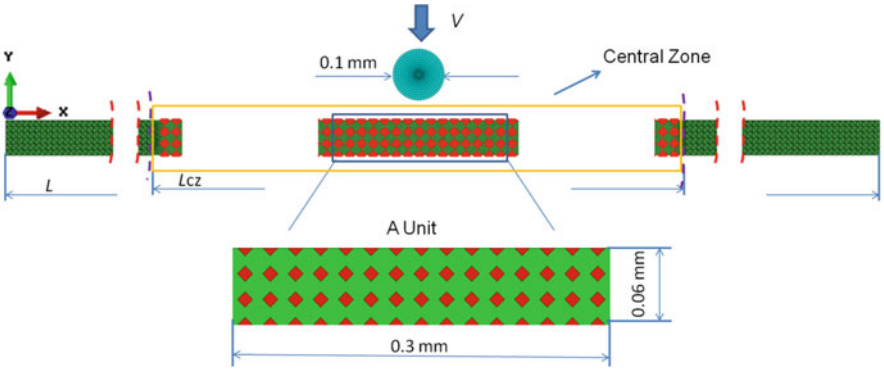


**Fig. 7.1** Specimen configuration and a sampled microstructure under impact

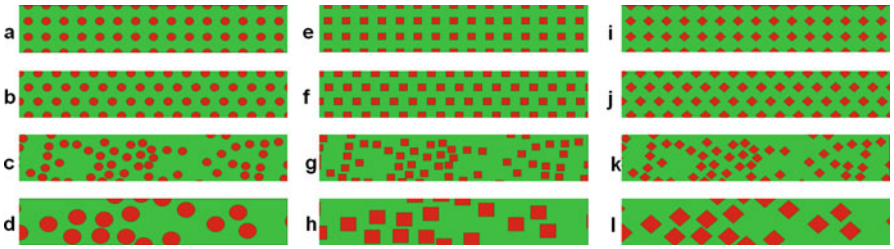


**Fig. 7.2** 12 microstructures (Guo et al. 2014a)

second phase. They are divided into three groups (Guo et al. 2014a). The first one includes (a)–(d), which are named microstructures A, B, C, and D, respectively. Microstructure A (Fig. 7.2a) consists of arrays of uniform inclusions, while B (Fig. 7.2b) has a staggered distribution. Both microstructures C and D (Fig. 7.2c and d) have randomly distributed circular inclusions but the size is smaller in C. The circular inclusions in A, B, and C have a radius of 5 μm, and those in D a radius of 10 μm. They will be called circular particle series. Replacing each circular inclusion in microstructures A, B, C, and D with a square inclusion in situ, we have Fig. 7.2e–h. These four configurations are named microstructures AR, BR, CR, and DR, respectively, and they will be called series R. Rotating each square inclusion in microstructures AR, BR, CR, and DR by 45°, we obtain microstructures in Fig. 7.2i–l. These are named AR-45, BR-45, CR-45, and DR-45, respectively, and they will be called series R-45. We call microstructures A, AR, and AR-45 series A; microstructures B, BR, and BR-45 series B; microstructures C, CR, and CR-45 series C; and microstructures D, DR, and DR-45 series D. Microstructure with regularly distributed CG inclusions refers to that in series A and B. For the bimodal NS Cu, the matrix in green is the NG Cu, while the second phase (the toughening phase) in red is the CG Cu. For the CG Cu strengthened by NT regions, the matrix in green is the CG Cu, while the second phase (the strengthening phase) in red is the NT Cu.

## 7.3 Constitutive Relations and Failure Criterion of the NG and NT Phases

In the bimodal NS metals, the influence of grain boundaries (GBs) should be considered since its volume fraction increases significantly in the NG phase. The geometrically necessary dislocations (GNDs) are mainly stored in the regions near the GBs. Similarly, in the CG metals strengthened by NT regions, the GNDs usually pile up along the twin boundaries (TBs) and GBs as illustrated in Fig. 7.3. Thus the dislocation pile-up zones (DPZ) near the internal boundaries with prominent strain gradients appear in the NT regions. Therefore, the mechanism-based strain gradient

plasticity model is adopted to consider the contribution of the GNDs in either phase (Zhu et al. 2011; Zhu and Lu 2012).

The strain rate tensor $\dot{\boldsymbol{\varepsilon}}$ can be decomposed into elastic and plastic parts:

$$\dot{\boldsymbol{\varepsilon}} = \dot{\boldsymbol{\varepsilon}}^{\mathbf{e}} + \dot{\boldsymbol{\varepsilon}}^{\mathbf{p}}. \tag{7.1}$$

$\dot{\boldsymbol{\varepsilon}}^{\mathbf{e}}$ can be expressed by the elastic compliance tensor $\mathbf{M}$ and the stress rate $\dot{\boldsymbol{\sigma}}$ as

$$\dot{\boldsymbol{\varepsilon}}^{\mathbf{e}} = \mathbf{M} : \dot{\boldsymbol{\sigma}}. \tag{7.2}$$

$\dot{\boldsymbol{\varepsilon}}^{\mathbf{p}}$ is proportional to the deviatoric stress $\boldsymbol{\sigma}'$ according to the $J_2$-plasticity flow rule:

$$\dot{\boldsymbol{\varepsilon}}^{\mathrm{p}} = \frac{3\dot{\varepsilon}_{\mathrm{e}}^{\mathrm{p}}}{2\sigma_{\mathrm{e}}}\boldsymbol{\sigma}', \tag{7.3}$$

where $\sigma_{ij}' = \sigma_{ij} - \sigma_{kk}\delta_{ij}/3$ $(i,j = 1,2,3)$, $\sigma_{\mathrm{e}} = \sqrt{3\sigma_{ij}'\sigma_{ij}'/2}$ is von Mises stress, and $\dot{\varepsilon}_{\mathrm{e}}^{\mathrm{p}} = \sqrt{2\dot{\varepsilon}_{ij}^{\mathrm{p}}\dot{\varepsilon}_{ij}^{\mathrm{p}}/3}$, the equivalent plastic strain rate. $\dot{\varepsilon}_{\mathrm{e}}^{\mathrm{p}}$ can be determined by a power law (Huang et al. 2004)

$$\dot{\varepsilon}_{\mathrm{e}}^{\mathrm{p}} = \dot{\varepsilon}_{\mathrm{e}}\left[\frac{\sigma_{\mathrm{e}}}{\sigma_{\mathrm{flow}}}\right]^{m_0}, \tag{7.4}$$

where $\dot{\varepsilon}_{\mathrm{e}} = \sqrt{2\dot{\varepsilon}_{ij}'\dot{\varepsilon}_{ij}'/3}$ is the equivalent strain rate, $\dot{\varepsilon}_{ij}' = \dot{\varepsilon}_{ij} - \dot{\varepsilon}_{kk}\delta_{ij}/3$, $m_0$ is the strain rate-sensitivity parameter, and $\sigma_{\mathrm{flow}}$ the flow stress of the NG or NT phase.

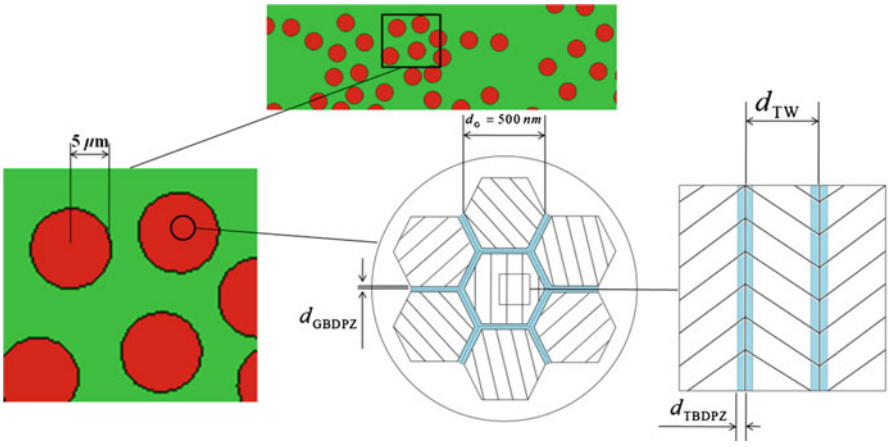


**Fig. 7.3** Hierarchical structure of CG Cu strengthened by NT regions

### 7.3.1 Flow Stress and Johnson–Cook Plasticity Model and Failure Criterion of the NG Phase

The dislocation density due to the GBDPZ near grain boundaries, $\rho_{GB}$, is used to consider the contribution of the GB on the flow stress in Taylor's model, as (Nix and Gao 1998)

$$\sigma_{flow} = M\alpha\mu b\sqrt{\rho_I + \rho_{GB}}. \tag{7.5}$$

Here, $M$, $\alpha$, $\mu$, and $b$ are the Taylor factor, the Taylor constant, shear modulus, and the Burgers vector, respectively, and $\rho_I$ is the dislocation density due to dislocations in the nano-grain interior. By a balance between the athermal storage and the annihilation of dislocations, $\rho_I$ can be formulated into (Kocks and Mecking 2003)

$$\frac{\partial\rho_I}{\partial\varepsilon_e^p} = M\left(\frac{k}{d_G} + k_1\sqrt{\rho_I} - k_2\rho_I\right), \tag{7.6}$$

where $\varepsilon_e^p$ is the equivalent plastic strain, $k = 1/b$; $d_G$ the nano-grain size, $k_1 = \psi/b$; $\psi$ a coefficient, $k_2 = k_2'\left(\dot{\varepsilon}_e^p/\dot{\varepsilon}_0'\right)^{-1/n_0}$; $k_2'$ a constant; $\dot{\varepsilon}_0'$ a reference strain rate; and $n_0$ a dynamic recovery constant. On the other hand, $\rho_{GB}$ can be formulated by $\eta^{GB}$—the strain gradient due to the GBDPZ as

$$\rho_{GB} = k^{GB}\frac{\eta^{GB}}{b}, \tag{7.7}$$

where $k^{GB} = 6d_{GBDPZ}/d_G$ with $d_{GBDPZ}$ the GBDPZ thickness. Young's modulus of the NG Cu is taken to be the same as that of the CG Cu (Chen et al. 2003; Li et al. 2008a). We can obtain $\sigma_{flow}$ numerically.

Johnson and Cook (1983) described a competition among strain hardening, strain rate hardening, and thermal softening as

$$\sigma_e = \left[A + B\left(\varepsilon_e^p\right)^n\right]\left[1 + C\ln\left(\frac{\dot{\varepsilon}_e^p}{\dot{\varepsilon}_0}\right)\right]\left[1 - \left(\frac{T - T_r}{T_m - T_r}\right)^m\right] \quad (T_r \le T \le T_m), \tag{7.8}$$

where $A$, $B$, $C$, $m$, and $n$ are material parameters, $\dot{\varepsilon}_0$ a reference strain rate, $T$ the temperature, $T_r$ the room temperature, and $T_m$ the melting temperature of Cu. Using the strain gradient plasticity model with the calibrated parameters, we can obtain the constitutive relation of the NG Cu with $d_G$ 23 nm at the reference plastic strain rate and under the room temperature. Therefore, a relation $\sigma_e\left(\dot{\varepsilon}_e^p = \dot{\varepsilon}_0, T = T_r\right) = A + B\left(\varepsilon_e^p\right)^n$ is used to fit it, and the fitting results are listed in Guo et al. (2014b). This fitting equation, which is also known as the modified Ludwik equation, is also adopted to describe the constitutive relation of the CG phase.

Johnson and Cook (1985) related a damage parameter $D$ with the equivalent plastic strain increment $\mathrm{d}\varepsilon_{\mathrm{e}}^{\mathrm{p}}$ in a linear incremental fashion as

$$D = \int \frac{1}{\varepsilon_{\mathrm{f}}} \mathrm{d}\varepsilon_{\mathrm{e}}^{\mathrm{p}} = \int \left\{ \left[ d_1 + d_2 e^{d_3 \frac{p}{\sigma_{\mathrm{e}}}} \right] \left[ 1 + d_4 \ln \left( \frac{\dot{\varepsilon}_{\mathrm{e}}^{\mathrm{p}}}{\dot{\varepsilon}_0} \right) \right] \left[ 1 + d_5 \frac{T - T_{\mathrm{r}}}{T_{\mathrm{m}} - T_{\mathrm{r}}} \right] \right\}^{-1} \mathrm{d}\varepsilon_{\mathrm{e}}^{\mathrm{p}}, \tag{7.9}$$

where $\varepsilon_{\mathrm{f}}$ is the failure strain, $d_1$ to $d_5$ are material constants, and $p$ is the hydrostatic pressure. An element is taken to fail when $D$ reaches 1. If loading state does not change too abruptly, $d_2 = d_3 = 0$ is considered as a good approximation (Dabboussi and Nemes 2005; Frontan et al. 2012). Then $d_1$ in Eq. (7.9) can be interpreted as the failure strain at the reference plastic strain rate and under the room temperature. Therefore, $d_1$ is taken as 0.13 for the NG Cu with $d_{\mathrm{G}}$ 23 nm (Guduru et al. 2007). $d_4$ is taken as 0.014 and $d_5$ as 1.12. Due to the high strain rate, the deformation can be assumed adiabatic.

### 7.3.2 *Flow Stress and Johnson–Cook Plasticity Model and Failure Criterion of NT Phase*

Based on the Taylor's model, the flow stress of the NT Cu can be expressed as (Nix and Gao 1998)

$$\sigma_{\mathrm{flow}} = M\alpha\mu b\sqrt{\rho_{\mathrm{I}} + \rho_{\mathrm{GB}} + \rho_{\mathrm{TB}}}, \tag{7.10}$$

where $\rho_{\mathrm{TB}}$ denotes the dislocation density due to the TBDPZ near twin boundaries. The strain gradient due to the full and partial dislocations in the TBDPZ can be expressed as (Zhu et al. 2011)

$$\eta^{\mathrm{TB}} = \frac{\phi^{\mathrm{TB}} \left( n_{\mathrm{F}}^{\mathrm{TB}} + n_{\mathrm{P}}^{\mathrm{TB}} / \sqrt{3} \right) b}{d_{\mathrm{TBDPZ}} d_{\mathrm{G}}}, \tag{7.11}$$

where $d_{\mathrm{TBDPZ}}$ the TBDPZ thickness, $\phi^{\mathrm{TB}}$ a geometric factor, $n_{\mathrm{F}}^{\mathrm{TB}}$ the number of full dislocations, and $n_{\mathrm{P}}^{\mathrm{TB}}$ that of partial dislocations. The density of full dislocations due to the TBDPZ in the unit cell is formulated into (Zhu et al. 2011)

$$\rho_{\mathrm{TB}} = \frac{12N_0}{\pi d_{\mathrm{G}}^2} + \frac{12n_{\mathrm{P}}^{\mathrm{TB}}}{\sqrt{3}\pi d_{\mathrm{G}}} \frac{1}{d_{\mathrm{TW}}} - \frac{\sqrt{3}\phi_0}{\pi} \frac{1}{d_{\mathrm{TW}}^2}, \tag{7.12}$$

where $N_0$ is the maximum number of full dislocations in the grain and independent of twin spacing ($d_{\mathrm{TW}}$), and $\phi_0$ is another geometric parameter. When $d_{\mathrm{TW}}$ decreases below a critical value, the third term on the right-hand side of Eq. (7.12) will

dominate so that the softening will occur. For the ultrafine-grains, the intragrain dislocation-mediated interaction dominates. According to Kocks and Mecking (2003), $\rho_I$ obeys an evolution law described by Eq. (7.6). On the other hand, according to Eq. (7.7), the dislocation density due to the GBDPZ is related to the associated strain gradient (Zhu et al. 2011).

By comparing (1) the predictions of the above strain gradient plasticity model for the NT Cu with (2) the experiments of the NT Cu with $d_G$ 500 nm and six $d_{TW}$ (Lu et al. 2009), $d_{GBDPZ}$, $d_{TBDPZ}$, and $\eta^{GB}$ can be calibrated (Zhu et al. 2011). With the calibrated results, the constitutive relations of the NT phase at the reference strain rate and under the room temperature can be obtained. Therefore, a similar fitting technique can be used to obtain constitutive parameters of the NT phase in the Johnson–Cook plasticity model in Eq. (7.8) (Guo et al. 2014a). One can find that the model can capture the trend of the yield strength that it increases with $d_{TW}$ decreasing from 96 to 15 nm and then decreases with $d_{TW}$ decreasing from 15 to 4 nm.

Similarly, the Johnson–Cook failure criterion, Eq. (7.9), is employed to relate the damage parameter with the equivalent plastic strain increment. $d_2 = d_3 = 0$ is accepted so $d_1$ can be extracted from the experiments of Lu et al. (2009). Here, $d_4$ is taken as 0.014 and $d_5$ as 1.12 for the NT Cu. The deformation is also assumed adiabatic.

## 7.4 Results and Discussion

The above numerical framework, combining the strain gradient plasticity model with the Johnson–Cook failure criterion, is applied to study the ballistic performance of the bimodal NS Cu and the CG Cu strengthened by NT regions. The 12 microstructures in Fig. 7.2 and the constitutive and failure parameters obtained in Sect. 3 are used.

### *7.4.1 Ballistic Performance of the Bimodal NS Cu*

#### 7.4.1.1 Effects of Microstructure

Microstructures are subjected to an impact by a bullet at a velocity of 180 m/s. After a microstructure is impacted, it will reach a maximum displacement $d$ and then rebound. The whole process of microstructure displacement from zero to $d$ includes four stages: i) first impact, ii) separation of the bullet and the microstructure, iii) second impact, and iv) bullet velocity reduction till zero (Guo et al. 2015).

We first examine the influence of distribution of CG inclusions. Figure 7.4a–d illustrates von Mises stress contours in microstructures A, B, C, and D, respectively. In microstructure A, the microcrack is arrested by a CG inclusion in the 2$^{nd}$ row

and another crack initiates at the bottom of the CG inclusion. Maximum stress occurs between adjacent CG inclusions. The CG phase separates the NG phase uniformly, leading to uniformly distributed intense stress regions. Furthermore, CG inclusions do not exhibit large plastic deformation and remain almost circular, implying its ability to bear a more severe impact. In microstructure B, intense stress distributes around the diamond edges. Since it has fewer CG inclusions along the impact direction compared with microstructure A, the area of zones distributing intense stress is smaller and its ability to resist the impact is weaker. Furthermore, small plastic deformation occurs in the CG inclusions, indicating that it can also withstand severe impact. In microstructure C, with its deflection increasing, the CG inclusions near its bottom are stretched until they fail. The microcrack is arrested by a CG inclusion in the middle of the specimen when its displacement reaches $d$ and all other CG inclusions along the impact direction fail. As the microcrack penetrates CG inclusions, they resist its rapid propagation and play a bridging role. This bridging process improves the ductility and is the main source of enhanced performance. However, due to the random distribution of CG inclusions, the high strength of the NG phase cannot be fully exploited, and thus its performance is reduced. In microstructure D, a microcrack is blocked by two larger CG inclusions, and its length is shorter than that in microstructure C. Intense stress only occurs at the phase boundaries. CG inclusions are greatly stretched and large plastic deformation occurs. The CG inclusions also play a bridging role. Because of the larger size of CG inclusions, its performance is better than microstructure C. Both microstructures C and D do not fully exploit the good properties of the constituent phases, so their performances are inferior to those of microstructures A and B. Figure 7.4e–h shows stress contours in microstructures AR, BR, CR, and DR, respectively. Each CG inclusion is square. Figure 7.4i–l illustrates stress contours in microstructures AR-45, BR-45, CR-45, and DR-45, respectively. Each CG inclusion is oblique square. The detailed analyses on the distribution of intensive stress regions and propagation of microcracks have been conducted in Guo et al. (2015). Generally, microstructures AR-45 and BR-45 with regularly distributed inclusions are better than CR-45 and DR-45 with randomly distributed inclusions.

To examine the shape effects, we return to Fig. 7.4a, e, and i, which illustrate stress contours in microstructures A, AR, and AR-45, respectively. These 3 microstructures in series A have the same regular distribution but different shapes of CG inclusions. During the impact, the duration of withstanding intense stress without failure is longest in microstructure AR-45, followed by A and then AR. The NG region can effectively distribute intense stress in microstructure AR-45, which makes the microcrack arrested by 2$^{nd}$ row of the CG inclusions and implies its excellent performance. Microstructure A is weaker than AR-45, because its slightly poorer ability to distribute intense stress, which leads to partially broken CG inclusion in the 2$^{nd}$ row and the initiation of a microcrack at the bottom of the CG inclusion. In microstructure AR, CG inclusions in the 2$^{nd}$ row are sheared and microcrack propagates. Another microcrack takes a shorter time to penetrate an entire CG inclusion from the bottom and is blocked by a CG inclusion in the third row. Figure 7.4b, f, and j illustrates stress contours in microstructures B, BR, and

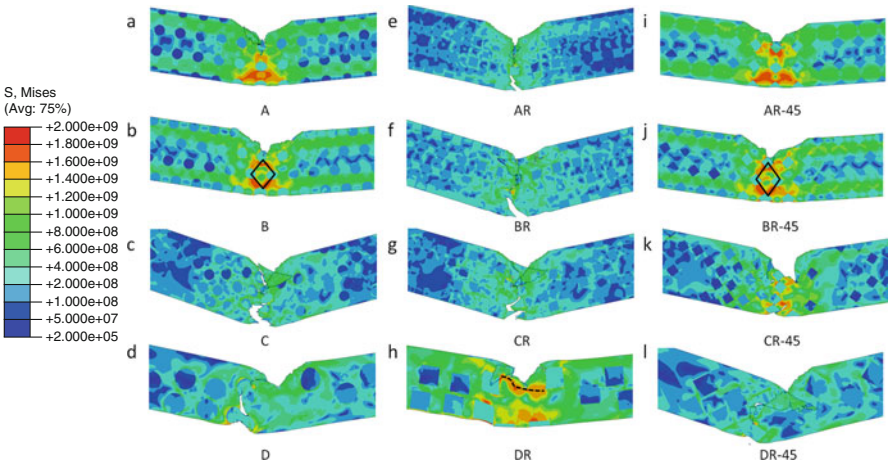


**Fig. 7.4** Stress contours in 12 microstructures with displacement reaching their $d$ (stress in Pa) (Guo et al. 2015)

BR-45, respectively. The ballistic performance of microstructures BR, B, and BR-45 increases monotonically. This shows that microstructures with the same distribution but various shapes of CG inclusions have significantly different performance. A microstructure with oblique square CG inclusions is the best, followed by that with circular ones and then that with square ones. In the direction perpendicular to the impact, the projection of each CG inclusion decreases in the order of oblique square, circle, and square. Therefore, not only the area of zones distributing intense stress is the largest but also the duration to resist the rapid crack propagation is the longest in microstructure with oblique square CG inclusions. Microstructure with square CG inclusions is the opposite. Figure 7.4c, g, and k illustrates stress contours in microstructures C, CR, and CR-45, respectively. Figure 7.4d, h, and l shows stress contours in microstructures D, DR, and DR-45, respectively. The CG inclusions with larger deformation deviate from the impact direction. Consequently, the projection of the CG inclusion is not dominant, and microstructure DR is the best while DR-45 the worst. It can also be found that series D is better than series C because it has larger CG inclusions and thus bridging is dominant in Series D (Guo et al. 2015).

#### 7.4.1.2 Multiple Ballistic Indexes

To further study the intrinsic mechanisms, quantitative analyses are presented, and the impact velocity is still 180 m/s.

The smaller the $d$ is, the better ballistic performance of the microstructure is. The displacements of microstructures in circular particle series, with CG inclusions the same shape but different distribution, are illustrated in Fig. 7.5. It is noted that

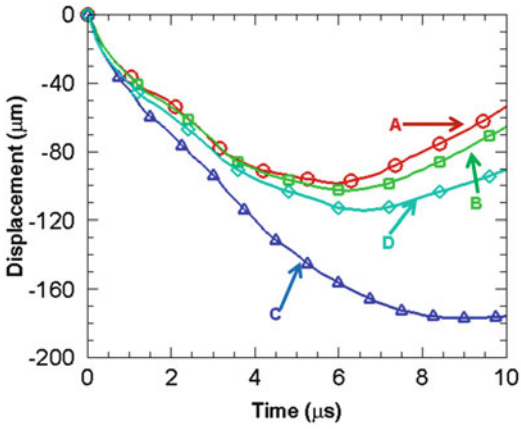


**Fig. 7.5** Microstructure displacements for circular particle series

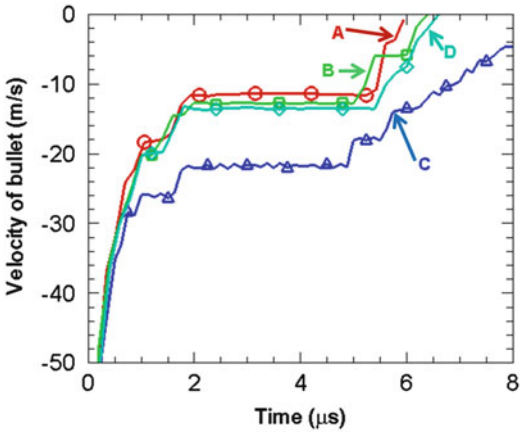


**Fig. 7.6** History of bullet velocity for circular particle series

$d_A < d_B < d_D < d_C$. We can calculate the average of $d$ for each series. It is the smallest in series R-45 and the largest in series R, further indicating that series R-45 is better than R. The displacements of microstructures with CG inclusions the same distribution but different shape can also be obtained. We find that $d_{AR\text{-}45} < d_A < d_{AR}$, $d_{BR\text{-}45} < d_B < d_{BR}$, $d_{CR\text{-}45} < d_{CR} < d_C$, and $d_{DR} < d_D < d_{DR\text{-}45}$. Series A has the smallest average of $d$, followed by series B, D, and series C; thus the performance decreases correspondingly.

The velocity of the bullet has a large reduction after the 1st impact, suggesting it is the main stage to consume the kinetic energy of the bullet. Therefore, its residual velocity after the 1st impact, $V_R$, can well characterize the ballistic performance of microstructure. Furthermore, the shorter the duration to reduce velocity of the bullet to zero, the better the performance of microstructure. Figure 7.6 shows history of bullet velocity in case of circular particle series. After the 1st impact, $V_R$ for microstructures A, B, and D almost coincide and are smaller than that for microstructure C, which indicates its worst performance. The overall duration to


**Fig. 7.7** Limit velocities of 12 microstructures

reduce velocity of the bullet increases in the order of microstructures A, B, D, and C, implying that microstructure A is the optimal and C the worst. We can also obtain the history of the bullet velocity for microstructures with CG inclusions of the same distribution but different shape. History of the bullet velocity almost coincides in the 1st and 2nd stages and deviates in the third and fourth stages in case of series A and B. Velocity of the bullet reduces till zero at a highest rate for microstructures AR-45 and BR-45, contrary to that for microstructures AR and BR in series A and B, respectively. In series C, microstructure CR-45 is still the best. History of the bullet velocity for series D differs from that for the other three series, i.e., microstructure DR is the best.

Limit velocity of the specimen is defined as the minimum impact velocity of the bullet rendering microstructure fail in the 1st bending and bouncing. The higher the limit velocity, the better the ballistic performance of the microstructure. The limit velocity of the single phase—NG structure with the same computational configuration—is also calculated. Figure 7.7 shows that limit velocity of the NG structure (190 m/s) is lower than that of the bimodal microstructures, which indicates that the bimodal microstructures can enhance the performance. Limit velocities of microstructures in series A and B are higher than those of microstructures in series C and D. In the cases of series A, B, and C, the highest limit velocity occurs in microstructures AR-45, BR-45, and CR-45, respectively. Why the limit velocity of microstructure DR-45 is lowest in series D is relevant to the larger area of the single CG inclusion (Guo et al. 2015).

## *7.4.2 Ballistic Performance of CG Metals Strengthened by NT Regions*

### 7.4.2.1 Effects of Microstructure

The failure pattern of microstructure changes significantly with twin spacing $d_{TW}$. It relies on the contrast of mechanical properties between two phases. When $d_{TW}$ is small ($\leq$15 nm), the NT phase has higher strength and better ductility. Microcrack initiates in CG matrix first and propagates continuously, eventually leading to the

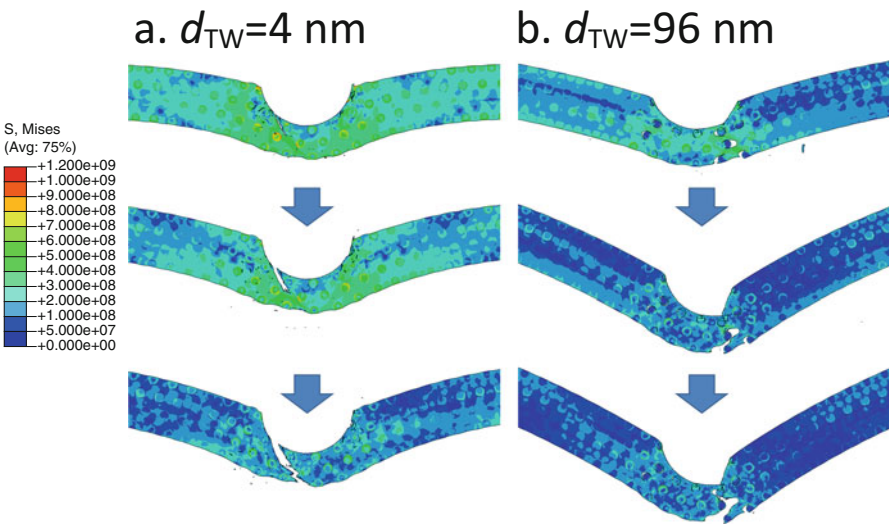


**Fig. 7.8** Failure process of microstructure B (stress in Pa)

failure of the microstructure. However, intense stress occurs in the NT phase only. Therefore, matrix failure is the main failure pattern in these cases. When $d_{TW}$ is larger ($\geq$35 nm), both the strength and ductility of the NT phase are relatively poor. Microcracks initiate at the interfaces and propagate continuously along them. For some NT regions, the entire interface almost debonds, making strengthening effect of the NT phase negligible. In the impact zone, the material essentially behaves as a porous CG Cu as though the NT regions do not exist. Microcrack initiation, coalescence, and propagation at adjacent interfaces lead to the failure of microstructure. Therefore, interface debonding is the main failure pattern in these cases. The above two failure patterns are similar with those when the specimen is subjected to uniaxial tension (Guo et al. 2014a). Figure 7.8 illustrates the failure processes of microstructure B when $d_{TW}$ is 4 and 96 nm, and the impact velocities are 325 and 240 m/s, respectively. It shows two totally different failure processes. Interface debonding can cause more severe damage than matrix failure. It lies in the fact that once large-scale interface debonding occurs, more microcracks initiate, so microcracks coalescence and rapid propagation is prone to occur, making the overall performance deteriorate dramatically.

During the impact, the specimen dissipates a part of kinetic energy of the bullet and obtains the kinetic energy at the same time. Eventually, the bullet has a residual kinetic energy. The energy balance tells that (Yang et al. 2015)

$$\frac{1}{2}m_b V_i^2 = E_i = \frac{1}{2}m_b V_r^2 + E_d + E_k + E_p \tag{7.13a}$$

and

$$K = E_k + \frac{1}{2}m_b V_r^2 \tag{7.13b}$$

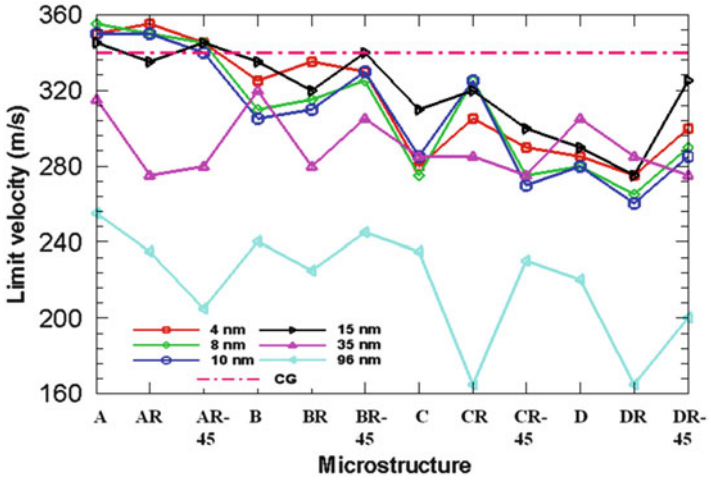


**Fig. 7.9** Limit velocities of CG structure and 12 microstructures

where $m_b$, $V_i$, and $V_r$ are the mass, the initial velocity, and the residual velocity of the bullet, respectively. $E_i$ and $K$ are the initial and residual kinetic energy of the system, respectively. $E_d$ and $E_p$ are the dissipated and absorbed energies by the specimen and bullet, respectively. $E_k$ is the kinetic energy transferred to the specimen and the debris. Here, $E_k$ is relatively small and $E_p$ is negligible generally, so $E_d$ can be expressed as:

$$E_d = E_i - K \tag{7.14}$$

Limit velocity of the specimen, $V_L$, is defined as the minimum impact velocity of the bullet rendering specimen completely fail. All limit velocities of 12 microstructures with 6 $d_{TW}$ are illustrated in Fig. 7.9. We can find that, when $d_{TW} \leq 15$ nm, $V_L$ of microstructures A and AR-45 is in the range of 340–355 m/s. For microstructures AR and BR, $V_L$ is the highest when $d_{TW} = 4$ nm. For microstructures B, BR-45, C, CR-45, and DR-45, $V_L$ is the highest when $d_{TW} = 15$ nm. For microstructure CR, $V_L$ is the highest when $d_{TW}$ is 8 and 10 nm. For microstructures D and DR, $V_L$ is the highest when $d_{TW} = 35$ nm. In general, all limit velocities are the lowest when $d_{TW} = 96$ nm, originating from the fact that both the strength and ductility of NT region are the worst in this case. Generally, all microstructures have the highest limit velocity when $d_{TW} \leq 35$ nm. 35 nm is the critical $d_{TW}$ where the failure pattern changes. It indicates that the effect of $d_{TW}$ on the ballistic performance is essentially that on the failure pattern of microstructure. Interface debonding can cause more severe damage than matrix failure, and thus smaller twin spacing is conducive to the promotion of performance.

We select circular particle series with $d_{TW} = 4$ nm to investigate the effect of the distribution of NT regions. Figure 7.10 shows initial impact velocities versus

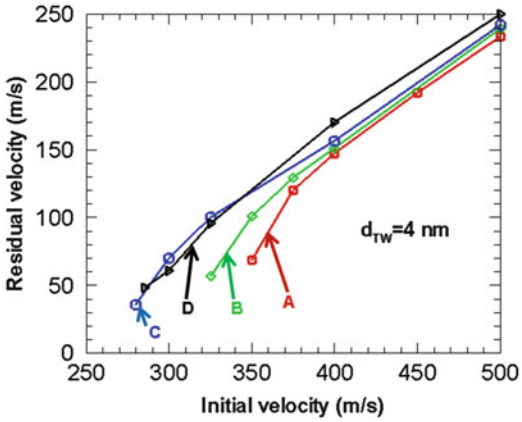


**Fig. 7.10** The residual velocity of bullet in the cases of microstructures in circular particle series

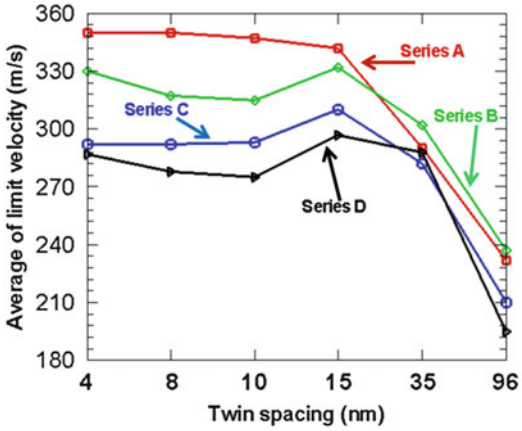


**Fig. 7.11** The average of $V_L$ in series A, B, C, and D

residual velocities of the bullet. The difference between the initial impact velocity and the residual velocity of the bullet is defined as $V_d$, namely, $V_d = V_i - V_r$. From Fig. 7.10, it is noticeable that microstructure A has the highest limit velocity, followed by microstructures B, D, and C. In addition, four curves have the same trend, and with the increase of the impact velocity, the slope of each curve gradually reduces. In a smaller range of impact velocity (close to $V_L$) for a microstructure, $V_d$ is relatively high when $V_i = V_L$, and it increases with $V_i$. This indicates that the dependence of $V_d$ on the impact velocity is prominent. Under the same impact velocity, the residual velocity of the bullet in the case of microstructure A is the lowest, followed by that in the cases of microstructures B, D, and C. Therefore, more impact energy is dissipated by microstructure A, which further indicates that A is the best while C and D are the worst (Yang et al. 2015).

Figure 7.11 illustrates the average of $V_L$ ($\bar{V}_L$) in series A, B, C, and D with 6 $d_{TW}$. It is found that all $\bar{V}_L$ in series A are the highest and prominently larger than those in other series when $d_{TW} \leq 15$ nm. All $\bar{V}_L$ in series B are the highest when $d_{TW} \geq 35$ nm. All of the maximum $\bar{V}_L$ occur in the series whose microstructures have

the regular distribution of NT regions. $\bar{V}_L$ in series C and D is lower. Especially in series D, $\bar{V}_L$ is the lowest except the case with $d_{TW} = 35$ nm. On the one hand, under the condition of the same volume fraction, the smaller the NT regions is, the more uniform the distribution is. Therefore, microstructure C is more ductile than D (Guo et al. 2014a). When the abrasion effect of the target plate on the bullet is neglected, its ballistic performance depends heavily on its ductility (Guo et al. 2015). On the other hand, smaller particles lead to greater strengthening effect (Suh et al. 2009). Since the NT regions is smaller in series A, B, and C than that in series D, the former is stronger than the latter. Microstructures in series D are affected by the distribution and size of NT regions. Both the poor ductility and strength lead to their worse performance.

#### 7.4.2.2 Comparison with Single Phase CG Structure

We also calculate $V_L$ of the single phase CG structure with the same configuration as 340 m/s. Due to its better ductility, its limit velocity is higher than limit velocities of 12 microstructures except those in series A. All structures are impacted by a bullet at a velocity of 240 m/s ($E_i = 1.761$ J/m). The energy dissipation capacities of the specimens obtained by Eq. (7.14), are shown in Fig. 7.12. It is found that the CG structure dissipates more energy than other microstructures. Frontan et al. (2012) investigated nanocrystalline and nanotwinned ultrafine steels experimentally and found that they exhibited a lower energy dissipation capacity than their CG counterpart. Our results agree with their findings. In addition, for each $d_{TW}$, the microstructures in series A dissipate the most energy. Each microstructure dissipates the most energy when $d_{TW} = 4$ or 8 nm.

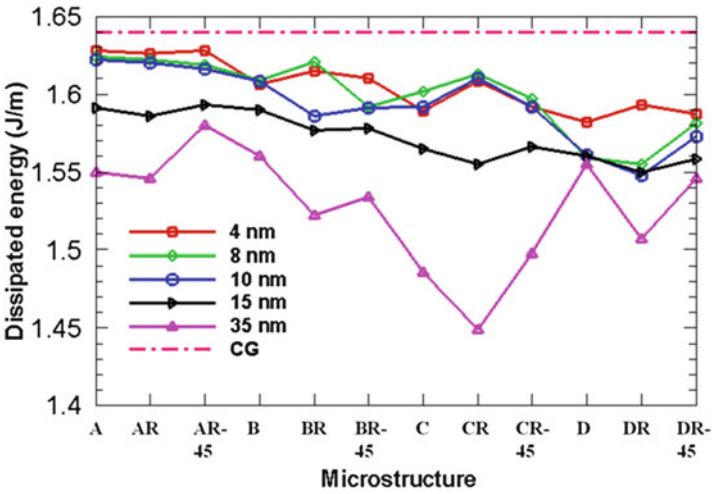


**Fig. 7.12** The dissipated energy by the specimens

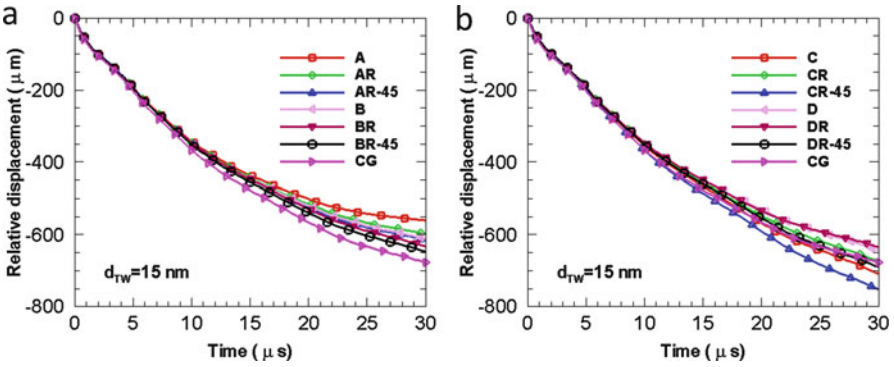


**Fig. 7.13** The relative displacements for microstructures in (**a**) series A and B, and (**b**) series C and D

After impacted by a bullet at a velocity of 240 m/s, each structure bends without complete failure. The central zone of the specimen has a higher velocity, while the ends have a lower velocity, which makes the specimen obtain a relative displacement, $d_r$. Figure 7.13 illustrates their $d_r$ when $d_{TW} = 15$ nm. The curves almost coincide first, but as bending increases, the $d_r$ of 12 microstructures differs from that of the CG structure. The $d_r$ of microstructures in series A, B, and D are less than that of the CG structure gradually. For microstructures in series C, the $d_r$ of microstructure C and the CG structure are almost same. However, $d_r$ of microstructures CR and CR-45 is smaller and larger than that of the CG structure, respectively.

We obtain the relative displacements of the 12 microstructures with $d_{TW} = 4$, 8, 10, and 35 nm when $V_i = 240$ m/s. It is found that with the specimen bending, the $d_r$ of microstructures in series B, C, and D are larger than that of the CG structure. For microstructures in series A, all of their $d_r$ are smaller than that of the CG structure except when $d_{TW} = 35$ nm. The differences of the $d_r$ between microstructures in series A and the CG structure are at least larger than the thickness of the specimen when $t = 30$ μs. Some study pointed out the importance of the clearance between helmet and skull (Sarron et al. 2004). In addition, limit velocities of the microstructures in series A with the above 4 $d_{TW}$ are higher than that of the CG structure. Although the energy dissipation capacities of the microstructures in series A are lower than that of the CG structure, their smaller relative displacements make them suitable for helmets and other personal protective equipments.

## 7.5 Conclusions

In this chapter, numerical simulations via the strain gradient plasticity model and the Johnson–Cook failure criterion have been carried out to study the effects of microstructural attributes on the ballistic performance of two kinds of NS metals. It

is found that a regular distribution of the second phase can lead to a better overall performance than a random distribution.

In case of the bimodal NS metals, under the condition of same distribution of CG inclusions, the longer the projection perpendicular to the impact direction, the better the ballistic performance. Therefore, series R-45 is better than circular particle series and series R. For the microstructures with randomly distributed CG inclusions, the bridging effect is more prominent in series D with larger CG inclusions, so series D is better than series C with smaller CG inclusions.

In case of the CG metals strengthened by NT regions, most microstructures have better ballistic performance when $d_{TW} < 35$ nm. Microstructures with array arrangement of the NT regions (series A) have higher limit velocities and smaller relative displacements, making them attractive for target-plate applications such as helmets and other personal protective equipments.

Relations between microstructural attributes and ballistic performance have been established. Insights have been provided in the selection of the NS metals and the design of novel NS metals with tailored ballistic performance.

**Acknowledgments** This work is supported by the Major Program of National Natural Science Foundation of China: NSFC 51590892. X. Guo acknowledges the support from National Natural Science Foundation of China (Project no. 11372214). G.J. Weng thanks the support of NSF Mechanics of Materials Program under CMMI-1162431. L.L. Zhu acknowledges the support from National Natural Science Foundation of China (Project no. 11472243).

## References

Chen, J., Wang, W., Qian, L.H., Lu, K.: Critical shear stress for onset of plasticity in a nanocrystalline Cu determined by using nanoindentation. Scr. Mater. **49**, 645–650 (2003)

Dabboussi, W., Nemes, J.A.: Modeling of ductile fracture using the dynamic punch test. Int. J. Mech. Sci. **47**, 1282–1299 (2005)

Dao, M., Lu, L., Asaro, R., Hosson, J.D., Ma, E.: Toward a quantitative understanding of mechanical behavior of nanocrystalline metals. Acta Mater. **55**, 4041–4065 (2007)

Frontan, J., Zhang, Y., Dao, M., Lu, J., Galvez, F., Jerusalem, A.: Ballistic performance of nanocrystalline and nanotwinned ultrafine crystal steel. Acta Mater. **60**, 1353–1367 (2012)

Guduru, R.K., Murty, K.L., Youssef, K.M., Scattergood, R.O., Koch, C.C.: Mechanical behavior of nanocrystalline copper. Mater. Sci. Eng. A. **463**, 14–21 (2007)

Guo, X., Ji, R., Weng, G.J., Zhu, L.L., Lu, J.: Computer simulation of strength and ductility of nanotwin-strengthened coarse-grained metals. Modell. Simul. Mater. Sci. Eng. **22**, 075014 (2014a)

Guo, X., Ji, R., Weng, G.J., Zhu, L.L., Lu, J.: Micromechanical simulation of fracture behavior of bimodal nanostructured metals. Mater. Sci. Eng. A. **618**, 479–489 (2014b)

Guo, X., Yang, G., Weng, G.J., Zhu, L.L.: Numerical simulation of ballistic performance of bimodal nanostructured metals. Mater. Sci. Eng. A. **630**, 13–26 (2015)

Hall, E.O.: The deformation and ageing of mild steel: III. Discussion of results. Proc. Phys. Soc. Lond. B. **64**, 747–753 (1951)

Huang, Y., Qu, S., Hwang, K.C., Li, M., Gao, H.J.: A conventional theory of mechanism-based strain gradient plasticity. Int. J. Plast. **20**, 753–782 (2004)

Jerusalem, A., Radovitzky, R.: A continuum model of nanocrystalline metals under shock loading. Modell. Simul. Mater. Sci. Eng. **17**, 025001 (2009)

Johnson, G.R., Cook, W.H.: A constitutive model and data for metals subjected to large strains, high strain rates and high temperatures. In: Proceedings of the 7th International Symposium on Ballistics, The Hague, The Netherlands (1983)

Johnson, G.R., Cook, W.H.: Fracture characteristics of three metals subjected to various strains, strain rates, temperatures and pressures. Eng. Fract. Mech. **21**, 31–48 (1985)

Kaufmann, C., Cronin, D., Worswick, M., Pageau, G., Beth, A.: Influence of material properties on the ballistic performance of ceramics for personal body armour. Shock Vib. **10**, 51–58 (2003)

Kocks, U.F., Mecking, H.: The physics and phenomenology of strain hardening. Prog. Mater. Sci. **48**, 171–273 (2003)

Kulkarni, S.G., Gao, X.L., Horner, S.E., Zheng, J.Q., David, N.V.: Ballistic helmets—Their design, materials, and performance against traumatic brain injury. Compos. Struct. **101**, 313–331 (2013)

Kumar, S., Gupta, D.S., Singh, I., Sharma, A.: Behavior of kevlar/epoxy composite plates under ballistic impact. J. Reinf. Plast. Compos. **29**, 2048–2064 (2010)

Li, W.L., Tao, N.R., Lu, K.: Fabrication of a gradient nano-micro-structured surface layer on bulk copper by means of a surface mechanical grinding treatment. Scr. Mater. **59**, 546–549 (2008a)

Li, Y.S., Zhang, Y., Tao, N.R., Lu, K.: Effect of thermal annealing on mechanical properties of a nanostructured copper prepared by means of dynamic plastic deformation. Scr. Mater. **59**, 475–478 (2008b)

Lu, L., Chen, X., Huang, X., Lu, K.: Revealing the maximum strength in nanotwinned copper. Science. **323**, 607–610 (2009)

Ma, E.: Eight routes to improve the tensile ductility of bulk nanostructured metals and alloys. JOM. **58**, 49–53 (2006)

Newbery, A.P., Nutt, S.R., Lavernia, E.J.: Multi-scale Al 5083 for military vehicles with improved performance. JOM. **58**, 56–61 (2006)

Nix, W.D., Gao, H.J.: Indentation size effects in crystalline materials: a law for strain gradient plasticity. J. Mech. Phys. Solids. **46**, 411–425 (1998)

Petch, N.J.: The cleavage strength of polycrystals. J. Iron Steel Inst. **174**, 25–28 (1953)

Sarron, J.C., Dannawi, M., Faure, A., Calliou, J., Cunha, J.D., Robert, R.: Dynamic effects of a 9 mm missile on cadaveric skull protected by aramid, polyethylene or aluminum plate: an experimental study. J. Trauma. **57**, 236–242 (2004)

Suh, Y.S., Joshi, S.P., Ramesh, K.T.: An enhanced continuum model for size-dependent strengthening and failure of particle-reinforced composites. Acta Mater. **57**, 5848–5861 (2009)

Talib, A.R.A., Abbud, L.H., Ali, A., Mustapha, F.: Ballistic impact performance of Kevlar-29 and $Al_2O_3$ powder/epoxy targets under high velocity impact. Mater. Des. **35**, 12–19 (2012)

Tellkamp, V.L., Lavernia, E.J., Melmed, A.: Mechanical behavior and microstructure of a thermally stable bulk nanostructured Al alloy. Metall. Mater. Trans. A. **32**, 2335–2343 (2001)

Wang, Y., Chen, M., Zhou, F., Ma, E.: High tensile ductility in a nanostructured metal. Nature. **419**, 912–915 (2002)

Witkin, D.V., Lee, Z., Rodriguez, R., Nutt, S., Lavernia, E.J.: Al–Mg alloy engineered with bimodal grain size for high strength and increased ductility. Scr. Mater. **49**, 297–302 (2003)

Xiao, G.H., Tao, N.R., Lu, K.: Strength–ductility combination of nanostructured Cu–Zn alloy with nanotwin bundles. Scr. Mater. **65**, 119–122 (2011)

Yan, F.K., Liu, G.Z., Tao, N.R., Lu, K.: Strength and ductility of 316 L austenitic stainless steel strengthened by nano-scale twin bundles. Acta Mater. **60**, 1059–1071 (2012)

Yang, D.K., Hodgson, P.D., Wen, C.E.: Simultaneously enhanced strength and ductility of titanium via multimodal grain structure. Scr. Mater. **63**, 941–944 (2010)

Yang, G., Guo, X., Weng, G.J., Zhu, L.L., Ji, R.: Simulation of ballistic performance of coarse-grained metals strengthened by nanotwinned regions. Modell. Simul. Mater. Sci. Eng. **23**, 085009 (2015)

Zhang, H.T., Ye, J.C., Joshi, S.P., Schoenung, J.M., Chin, E.S.C., Gazonas, G.A., Ramesh, K.T.: Superlightweight nanoengineered aluminum for strength under impact. Adv. Eng. Mater. **9**, 355–359 (2007)

Zhu, L.L., Lu, J.: Modelling the plastic deformation of nanostructured metals with bimodal grain size distribution. Int. J. Plast. **30–31**, 166–184 (2012)

Zhu, L.L., Ruan, H.H., Li, X.Y., Dao, M., Gao, H.J., Lu, J.: Modeling grain size dependent optimal twin spacing for achieving ultimate high strength and related high ductility in nanotwinned metals. Acta Mater. **59**, 5544–5557 (2011)

# Chapter 8
# Full-Field Micromechanics of Precipitated Shape Memory Alloys

**T. Baxevanis, A. Solomou, I. Karaman, and D.C. Lagoudas**

**Abstract** A full-field micromechanics approach is developed to predict the effective thermomechanical response of precipitation-hardened near-equiatomic Ni-rich NiTi alloys on the basis of composition and heat treatment. The microscale-informed model takes into account the structural effects of the precipitates (precipitate volume fraction, elastic properties, and coherency stresses due to the lattice mismatch between the precipitates and the matrix) on the reversible martensitic transformation under load as well as the chemical effects resulting from the Ni depletion of the matrix during precipitate growth. The post-aging thermomechanical response is predicted based on finite element simulations on representative microstructures, using the response of the solutionized material and time–temperature–martensitic transformation temperature maps. The predictions are compared with experiments for materials of different initial compositions and heat treatments and reasonably good agreement is demonstrated. The proposed methodology can be in principle extended to predict the post-aging thermomechanical response of other shape memory alloy systems as well.

T. Baxevanis
Department of Mechanical Engineering, University of Houston, Houston, TX 77204, USA

A. Solomou
Department of Aerospace Engineering, Texas A&M University, College Station, TX 77843, USA

I. Karaman
Department of Materials Science and Engineering, Texas A&M University, College Station, TX 77843, USA

D.C. Lagoudas (✉)
Department of Aerospace Engineering, Texas A&M University, College Station, TX 77843, USA

Department of Materials Science and Engineering, Texas A&M University, College Station, TX 77843, USA
e-mail: lagoudas@tamu.edu



S.A. Meguid, G.J. Weng (eds.), *Micromechanics and Nanomechanics of Composite Solids*, DOI 10.1007/978-3-319-52794-9_8

## 8.1 Introduction

Shape Memory Alloys (SMAs) are used in many engineering and biomedical applications, as they can recover deformations of approximately 10%, due to their capacity to undergo thermal and/or stress-induced martensitic phase transformations (Lagoudas, 2008). The ability of SMAs to recover this deformation at high stresses marks them as superb high-work-density actuators (Benefan et al., 2014) and makes them desirable for applications involving devices such as couplers and vibration dampeners in the aerospace (Hartl and Lagoudas, 2007; Calkins and Mabe, 2010), civil (Ozbulut et al., 2011; Song et al., 2006; Dong et al., 2011), and petroleum (Anderson et al., 1999) industries and in MEMS (Bellouard, 2008) and biomedical devices such as stents (Machado and Savi, 2003; Duerig et al., 1999; Morgan, 2004) and implants (Bansiddhi et al., 2008; Elahinia et al., 2012). The unique SMA properties are the result of a reversible martensitic transformation from a high-temperature/low-stress austenitic phase to a low-temperature/high-stress martensitic phase. As the austenite phase has a higher-symmetry crystallographic structure (typically cubic) and martensite exhibits a lower-symmetry structure (e.g., monoclinic or tetragonal) the resulting phase transformation is accompanied by the aforementioned inelastic deformations.

Different applications have their own requirements for material properties as the environments and loading conditions may differ; however, in many applications, emphasis is primarily placed upon phase transition temperatures and attainable transformation strain. In this respect, the ability to create material systems which result in material properties tailored to meet specific, application-driven requirements is desirable. As pointed out by Ashby and Bréchet (2003) the development of tailored material systems is usually accomplished in one of the two ways. First is the identification and manufacture of distinctly new alloys or material systems. The second approach is the creation of hybrid or composite materials that combine the properties of the two (or more) existing materials. With respect to SMAs, this second methodology has been heavily investigated since the late 1980s and has led to the production of a wide set of polymer, metal, and ceramic matrix composites—SMA composites that cover a large application space. A recent review by Lester et al. (2015) discusses the various composites that have been developed as well as some of the modeling approaches undertaken to investigate these materials. In terms of the former approach, shape memory polymers (Ratna and Karger-Kocsis, 2008; Leng et al., 2011), magnetic shape memory alloys (Pons et al., 2008; Karaca et al., 2009), and high-temperature SMAs (Firstov et al., 2006; Ma et al., 2010) have been shown to cover engineering design spaces traditional SMAs cannot reach.

Although, the various aforementioned efforts have created a set of material systems that operate in conditions in which traditional SMAs are not suited, often, however, designing materials to meet application needs requires more subtle tuning and tailoring of the response characteristics. One way of accomplishing this is by controlling the formation of precipitates in macroscopically homogenous SMA material systems. Aging of Ni-rich NiTi SMAs can be used to achieve a range

of phase transition temperatures and improve thermomechanical cyclic stability through the precipitation of mostly $Ni_4Ti_3$ particles, depleting Ni from the NiTi matrix. The corresponding changes in microstructure drastically alter the material's thermomechanical response (Zarinejad et al., 2009; Allafi et al., 2002; Karaca et al., 2013; Sehitoglu et al., 2000, 2001a,b; Karaman et al., 2005). Originally characterized by Nishida et al. (1986) and Saburi et al. (1986), such precipitates are known to reduce transformation-induced plasticity (TRIP) and quickly stabilize the actuation response after a few cycles (Eggeler et al., 2004) as opposed to hundreds of cycles for many homogenous materials. Their transformation temperatures are known to shift dramatically, and their transformation strain decreases with small changes in Ni content for Ni-rich stoichiometries (Otsuka, 2002; Tang, 1997; Frenzel et al., 2010). Such material parameters are key design targets for applications and are therefore considered important components of the final characterized response.

Currently, there is no way to accurately predict how the thermomechanical response of such materials will change after precipitation heat treatments, necessitating that if a material is subjected to a new heat treatment, it must be characterized again to determine its new properties. Presently, precipitation-hardened SMA material properties are only known for a few initial compositions and aging paths due to the high cost and preparation time required to produce and characterize the materials. Therefore, numerical models able to predict changes in the material behavior brought about by precipitation without requiring lengthy and costly processing and experimental procedures are highly desirable.

*Precipitation in Ni-Rich NiTi SMAs*—the evolution of precipitates in a supersaturated solution during aging can be divided into two different regimes: nucleation and coarsening. During the initial stages of aging, the precipitate evolution is nucleation dominated, and the formation of new precipitates continuously decreases the mean distance between precipitates. During the subsequent coarsening regime, Ostwald ripening becomes the dominant process during which smaller particles are consumed by larger ones. During coarsening, the volume fraction and composition of the matrix remain relatively constant (Geng et al., 2015; Madras and McCoy, 2004), which means that after coarsening, the mean interparticle distance becomes larger.

The formation of $Ni_4Ti_3$ particles via precipitation heat treatments in a Ni-rich NiTi alloy is known to affect the transformation behavior through a variety of mechanisms, which are summarized in the following:

- The transformation temperatures are highly dependent on the Ni content (Frenzel et al., 2010) and can be changed by up to 100 °C with a 1 at.% change in Ni content on the Ni-rich side of the stoichiometry. The formation of Ni-rich precipitates depletes the Ni content of the matrix, resulting in compositional inhomogeneity that leads to local differences in the phase transition temperatures (Stroz et al., 1988). The Ni content immediately surrounding the precipitates is lower than that of the matrix, and thus these regions transform at higher temperatures (Allafi et al., 2002).

- Coherent precipitates exist in a local stress field arising from the lattice mismatch with the surrounding matrix; these local stresses can increase the transformation temperatures of the matrix relative to the precipitate-free regions (Bataillard et al., 1998).
- Coherent non-transforming precipitates experience shear loading during the transformation of the matrix. As a result, elastic energy is stored in the precipitates and the transformation temperatures are decreased (Hornbogen, 1985).
- The fraction of compound twins to type I and II twins in martensite changes with interparticle distance. In solutionized materials and overaged materials with large interparticle distances, the elastic shear can be accommodated solely by type I and II twinning. However, as the interparticle distance decreases, the density of compound (001) twins increases, and eventually only compound twins are observed (Nishida et al., 1988). Since compound twins are highly dense in comparison to type I and II twins, with a greater surface area, the energy barrier associated with the formation and motion of compound twins is higher than that of type I and II twins. This corresponds to an increase in hysteresis and a decrease in the temperature needed to begin austenitic to martensitic transformation (Panchenko et al., 2008).

*Modeling precipitation effects in NiTi SMAs*—Micromechanics-based simulations can be used to complement experimental efforts in exploring the influence of precipitation on the thermomechanical response and structural behavior of SMA material systems, thereby accelerating their development cycle for specific applications. There are two prominent methodologies which may be utilized to approach the problem, termed mean-field and full-field methods. Both methods use particle volume fraction, aspect ratio, and orientations as their main defining geometric factors, and since particle size is not used directly, size effects are not captured through these methods except in the description of the material constitutive behaviors. Methodologies considering only the phase-averaged response of the various constituents are defined to be mean-field approaches while full-field methods are those in which the position-dependent field values are determined and then averaged for the effective macroscopic response. The mean-field approaches typically draw on the seminal result of Eshelby (1957) to account for the presence of multiple inhomogeneities while the latter category utilizes numerical techniques like the finite element method to solve representative computational domains—unit cells (UC) for periodic materials and representative volume elements (RVEs) for statistically homogeneous materials (Pindera et al., 2009). The latter approach is gaining in popularity as the level of available computational power and utilization of distributed computing methods continue to increase. Such analyses are able to simulate the effect of microstructural processes on the effective macroscopic response that may not be fully captured by mean-field approaches, such as the effect of Ni depletion during precipitation in Ni-rich NiTi SMAs.

There are various RVE definitions used in the mechanics of *random* heterogeneous materials (Hill, 1963; Huet, 1999; Kanit et al., 2003; Drugan and Willis, 1996). The classical RVE is defined as the smallest material volume of which the

response does not depend on the applied boundary conditions (Hill, 1963; Huet, 1999). In another definition, based on the knowledge of the statistical nature of the microstructure, the RVE can be regarded as a volume $V$ sufficiently large to be statistically representative of the material, i.e., it includes a sampling of all microstructural heterogeneities that occur in the material (Kanit et al., 2003). Drugan and Willis (1996) defined an RVE as "the smallest material volume element of the composite for which the usual spatially constant (overall modulus) macroscopic constitutive representation is a sufficiently accurate model to represent mean constitutive response." Therefore, it can be concluded that there is, a priori, no systematic quantification of the RVE sizes and that results will depend on many combinations of factors (material structure, volume fraction of heterogeneities, etc.). The intrinsic difficulty of simultaneously satisfying homogeneous displacement and traction boundary conditions, necessary in fulfilling the RVE requirement for subvolumes with random microstructures, has led to the concept of periodization of random media. Numerical estimates of the effective properties of random heterogeneous materials are more accurate when periodic boundary conditions are applied than when homogeneous strain or stress boundary conditions are considered (Kanit et al., 2003).

*Proposed model*—in this chapter, a full-field micromechanics methodology to predict changes in an SMA's thermomechanical response due to the aging of Ni-rich NiTi material systems is described (Baxevanis et al., 2014). Moreover, predictions of actuation responses obtained from the proposed methodology are compared to experimentally produced and characterized material (50.8 at.% Ni). Comparisons are made for two aging paths to determine the model's accuracy.

The employed model takes into account chemical changes due to the depletion of Ni from the matrix associated with $Ni_4Ti_3$ precipitate formation and growth that may not be fully captured by mean-field approaches, in contrast to the works of Collard et al. (2008) and Collard and Ben Zineb (2012), as well as the structural changes associated with the precipitation process. The RVEs contain randomly distributed non-overlapping precipitates, which are assumed to have reached their equilibrium size, shape, and resulting volume fraction. The precipitates are assumed to behave as linear elastic isotropic solids, while for the matrix material, isotropic elastic and transformation constitutive behavior appropriate for polycrystalline materials is assumed as a result of random texture. The constitutive behavior of the matrix does not account for TRIP (Bo and Lagoudas, 1999a; Arghavani et al., 2010), minor loops (Bo and Lagoudas, 1999b), thermomechanical coupling (Morin et al., 2011), or reorientation (Popov and Lagoudas, 2007; Auricchio et al., 2014; Arghavani et al., 2010), that are outside the scope of the present study. More representative of the actual microstructure, RVEs would consist of polycrystalline ensembles with random texturing and populations of precipitates within each of the crystals oriented in four different orientations with respect to the orientation of the crystal (Zhou et al., 2010). A point-wise representation of the Ni concentration fields surrounding distinct precipitates in a finite element polycrystalline ensemble requires large RVEs and subgranular constitutive models (Patoor et al., 2006; Manchiraju and Anderson, 2010; Yu et al., 2013, 2014; Cisse et al., 2016) with a

heavy computational burden that inhibits extensive study of multiple realizations of the microstructure. Moreover, such polycrystalline averaging makes decoupling the texture and precipitate effects on the effective response difficult. It should also be noted that the present work mainly focuses on the NiTi concentrations and heat treatments that solely form $Ni_4Ti_3$ precipitates. Ni-rich NiTi SMAs may also form $Ni_3Ti_2$ and $Ni_3Ti$ precipitates, which are usually not as beneficial as the $Ni_4Ti_3$ precipitates in terms of stabilizing the shape memory response.

## 8.2 Modeling Approach

### *8.2.1 Computational Procedure*

In this subsection, the key components of the numerical calculations are described: the method for creating the heterogeneous microstructure using precipitate information; the approach used to determine the coherency fields induced adjacent to the precipitates to replicate lattice coherency; the procedure used to obtain the resulting Ni concentration fields due to Ni-depletion from the matrix during precipitation; and finally the details of the finite element analyses for modeling the macroscopic response under specific thermomechanical loading paths.

#### 8.2.1.1 Microstructure Generation

The RVEs are cubes of dimensions $L \times L \times L$, which contain a dispersion of non-overlapping identical precipitates. The precipitates are assumed to have fully grown into the matrix and reached an equilibrium state, taking up their final observed volume fraction in the NiTi matrix, which is dependent on the heat-treatment conditions. The grown precipitates are oblate spheroids with a specified major to minor axis ratio, $\lambda$. Given a total precipitate volume fraction, $v$, and number of precipitates, $N$, the radius of the major ellipsoid axis, $r$, may be calculated as $r = L\left[v3\lambda/(4\pi N)\right]^{1/3}$. Although precipitates are known to form in 4 orientations along the [111] habit planes in NiTi SMAs, the random grain orientations of the polycrystalline ensemble are assumed to smear out such directionality. Thus, the precipitates are randomly placed and oriented in the matrix, minimizing directional dependence on effective properties. To place the precipitates, translation vectors and rotation angles are randomly generated and then geometries are tested for precipitate—precipitate overlap using coordinate rotation matrices and a volume query feature in Abaqus. A new precipitate is accepted if it falls within the cube's boundary and the distance between its surface and all previously generated precipitates is greater than $0.05r$. Enforcing such a minimum distance allows for an adequate finite element discretization of the space between neighboring inclusions. This condition, also checked for the distance between the surface of the new

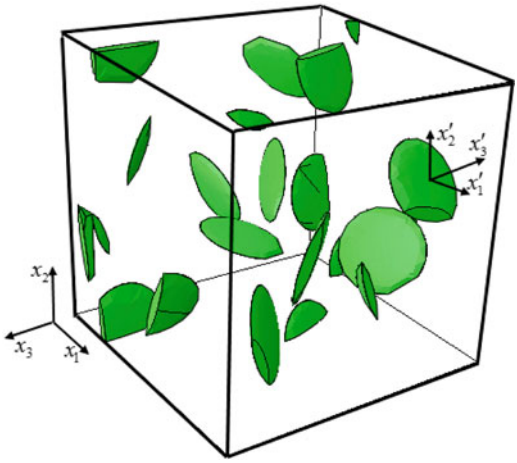


**Fig. 8.1** "Spheroids in box" morphology showing a periodic cubic cell containing a random distribution of 12 oblate spheroids. The volume fraction of the spheroids is 2% and the precipitate major to minor axis ratio, $\lambda$, is equal to 8

precipitate and the cube's surfaces, prevents some clustering effects, as the average stress within an inclusion is influenced by the minimal distance between inclusions. If any of these conditions are not met, new center translation vectors and rotation angles are generated, and the process is repeated. When the predetermined volume fraction of precipitates is reached, placement is stopped. A resulting "spheroids in box" morphology is shown in Fig. 8.1.

#### 8.2.1.2 Coherency Fields

Eigenstrains, $\varepsilon_{ij}^{Ni_4Ti_3}$, corresponding to the lattice mismatch between the precipitates and austenitic phase are introduced into the precipitates to develop the coherency stress and strain fields. These eigenstrains are introduced into the precipitates by assuming an additive decomposition of strains into elastic and stress-free strains of the form $\varepsilon_{ij}^{Ni_4Ti_3}\Delta t$, where $\Delta t$ is a parameter that changes continuously in the numerical calculations from its initial value 0 to its final value 1. The initial shape and volume fraction of the precipitates is such that the precipitates assume their observed shape and volume fraction at the end of the simulation process, in which periodic boundary conditions are used:

$$\begin{aligned} u_i(x_1, x_2, 0) - u_i^3 &= u_i(x_1, x_2, L), \\ u_i(x_1, 0, x_3) - u_i^2 &= u_i(x_1, L, x_3), \\ u_i(0, x_2, x_3) - u_i^1 &= u_i(L, x_2, x_3), \end{aligned} \tag{8.1}$$

where $u_i$ stands for the displacement vector in the different RVE faces and the vectors $u_i^3$, $u_i^2$, and $u_i^1$ depend on the loading applied to the cell. These conditions are applied using an Abaqus plug-in developed by Lejeunes and Bourgeois (2011),

which takes a periodic mesh and, given the two faces to be paired as well as the vector of periodicity, creates appropriate equation constraints in Abaqus for each minimally interdependent set of nodes in the manner described in Li and Wongsto (2004).

#### 8.2.1.3 Ni Concentration Fields

The Ni concentration, $c$, in the RVE is given by

$$c = vc_{Ni_4Ti_3} + (1 - v)c_A, \tag{8.2}$$

where $c_{Ni_4Ti_3}$ and $c_A$ represent the Ni concentrations of the precipitates and austenitic matrix, respectively. Since $c_{Ni_4Ti_3}$ is constant, only diffusion in the austenitic matrix needs to be considered. Initially, the matrix material is set to the homogeneous concentration before precipitation, and the development of the Ni concentration field is simulated using Fick's approximation:

$$\dot{c}_A = D_A \nabla^2 c_A, \tag{8.3}$$

where the dot denotes differentiation with respect to time and $D_A$, the temperature-dependent diffusivity coefficient.

Periodic boundary conditions are used on the RVE faces for solving the diffusion equation (8.3):

$$\begin{aligned} c_A(x_1, x_2, 0) &= c_A(x_1, x_2, L), \\ c_A(x_1, 0, x_3) &= c_A(x_1, L, x_3), \\ c_A(0, x_2, x_3) &= c_A(L, x_2, x_3), \end{aligned} \tag{8.4}$$

handled as described in Sect. 8.2.1.2, while $c_A$ is set equal to its equilibrium value for a given aging temperature on the precipitate boundaries.

#### 8.2.1.4 Simulations of the Effective Thermomechanical Response

The macroscopic actuation response is obtained by subjecting the RVEs to a thermal cycle under a constant uniaxial load (see Fig. 8.2), i.e., the diffused material with coherent precipitates is loaded uniaxially to a predetermined level and subsequently thermally cycled to induce forward and reverse phase transformation, from austenite to martensite and back, in order to obtain its actuation response.

Periodic boundary conditions are applied in all cases through equation constraints in Abaqus, as is done for the finite element calculations determining the coherency stress and Ni concentration fields. The effective thermomechanical

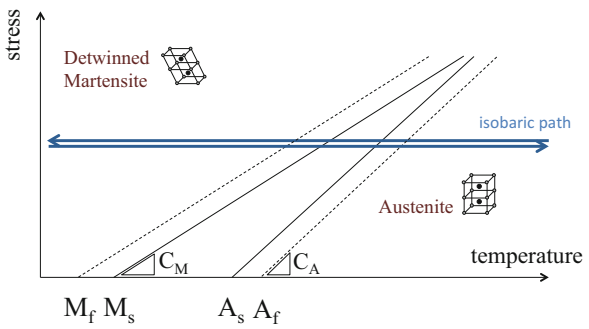


**Fig. 8.2** Stress-temperature phase diagram. The *blue arrows* represent a loading path, a thermal cycle under constant mechanical load. The nomenclature used in the figure is explained in the Appendix

response of the RVEs is presented in terms of the volume average stress and total strain over the RVE, defined, respectively, as

$$\Sigma_{ij} = \frac{1}{\Omega}\int_{\Omega} \sigma_{ij} dV, \quad E_{ij} = \frac{1}{\Omega}\int_{\Omega} \varepsilon_{ij} dV, \tag{8.5}$$

where $\sigma_{ij}$ and $\varepsilon_{ij}$ are the Cartesian components of the stress and strain and $\Omega$ is the RVE volume. Note that the effective elastic and transformation strains are not necessarily the volume averages of the corresponding local strains. In the calculations, these strains are resolved from the boundary displacements that correspond to the volume average of the total strains.

A standard RVE is discretized with ∼55,000 quadratic 10-node tetrahedral elements with integration at four Gauss points and hourglass control (C3D10M in Abaqus 2009). This tetrahedron exhibits minimal volumetric locking during transformation and captures strain gradients in the matrix better than the standard 10-node tetrahedron due to its three extra internal degrees of freedom. The high-performance computing cluster EOS at Texas A&M University was used to run the majority of the simulations. The appropriateness of the simulations' mesh density was checked by discretizing one model using ∼150,000 elements and comparing the overall strain–temperature response with the one obtained with the standard discretization.

The accuracy of the numerical simulations is checked by generating RVEs of various particle numbers and examining their actuation response for different dispersions of the precipitates in each case. Kanit et al. (2003) showed that the effective physical properties of a heterogeneous material can be determined either by a few measurements on large RVE volumes (large number of particles for a given volume fraction) or by many realizations for small volumes of material. The number of realizations needed for a given RVE volume is less for periodic boundary conditions than for homogeneous stress or strain boundary conditions. However, the mean values computed on small RVE volumes may not represent the effective response for the composite material even when using periodic boundary conditions and a sufficient number of realizations. Here, the average thermomechanical

**Table 8.1** Constitutive model parameters for solutionized $Ni_{50.8}Ti$ material

| Parameter | Value | Parameter | Value |
|---|---|---|---|
| $E^A$ [GPa] | 68 | $H_{sat}$ | 0.051 |
| $E^M$ [GPa] | 43 | $k$ [MPa$^{-1}$] | 0.05 |
| $\nu^A = \nu^M$ | 0.33 | $C^A$ [MPa K$^{-1}$] | 6.0 |
| | | $C^M$ [MPa K$^{-1}$] | 6.0 |
| | | $n_1 = n_{...} = n_4$ | 0.3 |

response of microstructures obtained from 5 different dispersions of 12 precipitates is considered below as representative of the material-at-large (Baxevanis et al., 2014).

### 8.2.2 *Insight into the Computational Results*

In the numerical results below, the precipitates are assumed elastic, while the Lagoudas et al. (2012) constitutive model is used to simulate the response of the matrix (see Appendix). The values of the precipitates' Young's modulus, $E_p = 107$ GPa, and Poisson's ratio, $\nu_p = 0.39$, are extracted from the first principle calculations presented in Wagner and Windl (2009). The parameters describing the constitutive response of the matrix are given in Table 8.1. The phase transition temperatures that are further needed as input in the matrix constitutive model are assumed to vary with Ni content. Once the Ni content distribution in the matrix is evaluated, phase transition temperatures are individually assigned to each integration station in the matrix by using a least square fit of the experimental data in Table 8.2 relating the Ni content in unprecipitated NiTi material systems to phase transition temperatures. The Ni concentration in the precipitates is $c_{Ni_4Ti_3} = 56.8\%$ at. and the diffusivity coefficient is $D_A = 5.48 \times 10^{-9} \exp\left(\frac{-103{,}000\,\mathrm{J/mol}}{\mathrm{R}T}\right) \mathrm{m^2\,s^{-1}}$ between temperatures $T = 773\,\mathrm{K}$ and $T = 1173\,\mathrm{K}$ (Zhou et al., 2010). The eigenstrains corresponding to the lattice mismatch between the precipitates and austenitic phase imposed into the precipitates are given as

$$\varepsilon_{ij}^{Ni_4Ti_3} = \begin{bmatrix} -0.00417 & 0 & 0 \\ 0 & -0.00417 & 0 \\ 0 & 0 & -0.0257 \end{bmatrix}, \tag{8.6}$$

with respect to local coordinate systems $(x_1', x_2', x_3')$ taken such that their origins are located at the center of the precipitates, where the coordinate axis $x_3'$ is extending along the direction of the minor axis, and $x_1'$ and $x_2'$ lie in the plane perpendicular to $x_3'$ (Fig. 8.1). The values of the eigenstrains are determined using experimental data on the lattice constants of the austenitic-B2 and $Ni_3Ti_4$-rhombohedral unit cells (Zhou et al., 2010).

**Table 8.2** Characteristic martensitic phase transition temperatures of the solutionized NiTi alloys with different compositions (Frenzel et al., 2010)

| $c_{Ni}$ | $M_s$ (K) | $M_f$ (K) | $A_s$ (K) | $A_f$ (K) |
|---|---|---|---|---|
| 49.99 | 338.7 | 311.7 | 352.1 | 380.2 |
| 50.19 | 325.8 | 296.1 | 337.1 | 365.8 |
| 50.39 | 302.1 | 275.9 | 319.4 | 339.3 |
| 50.59 | 290.2 | 263.4 | 302.0 | 324.6 |
| 50.80 | 272.1 | 245.3 | 284.2 | 308.3 |
| 50.86 | 266.0 | 237.9 | 277.9 | 301.3 |
| 51.0 | 246.1 | 222.4 | 245.5 | 268.0 |
| 51.10 | 226.9 | 207.5 | 240.9 | 254.0 |
| 51.21 | 210.9 | 181.4 | 226.4 | 242.0 |

#### 8.2.2.1 Coherency Stress, Ni concentration, and Mechanical Fields

The coherency stress field in an RVE with 2% precipitate volume fraction, resulting by introducing the eigenstrains given in (8.6) into the precipitates with a major to minor axis ratio, $\lambda = 8$, is shown in Fig. 8.3. All RVE figures show a section cut of the inside of the cube for illustration purposes. Note that the values of the von Mises stress get as high as 480 MPa adjacent to the precipitates. In Fig. 8.4, the Ni concentration profile for the same RVE is shown. Although the variation of Ni concentration in the matrix caused by the presence of precipitates is relatively small, it may have a significant effect on the martensitic transformations, since a 0.1% at. difference in Ni-rich NiTi alloys can lead up to a 20 K change in the phase transition temperatures, $M_f$, $M_s$, $A_s$, and $A_f$ (Table 8.2). Above 50% at. Ni, the phase transition temperatures fall down drastically with increasing Ni content. Under 50% at. Ni, there is no relation between Ni concentration and transformation transition temperatures, and constant values of the phase transition temperatures are observed. A comparison between the Ni concentration surrounding a single precipitate and experimental measurements reported in Schryvers et al. (2006) is presented in Fig. 8.5. These concentration values are obtained by taking a precipitate relatively away from the others and measuring the Ni content radially outward along the minor axis of the ellipsoid. It is seen that although simplifications were made for simulating the diffusion process, including the calculation of Ni concentration without accounting for the elastic energy or sub-granular anisotropy, the simulated results are in reasonable agreement with the experimental ones. The phase transition temperature distributions resulting from assigning phase transition temperatures to each integration station in the matrix using a least square fit of the experimental data in Table 8.2 are also presented in Fig. 8.4.

The martensite volume fraction and von Mises effective stress field during forward transformation (cooling) under a constant uniaxial load of 200 MPa are shown in Fig. 8.6. The heterogeneity of transformation and stress is clearly visible in these figures. Microstructural stress concentrations and low levels of Ni content around precipitates lead to the formation of martensite earlier than in matrix regions away from precipitates (Fig. 8.6a). Martensitic regions first grow in between $Ni_4Ti_3$

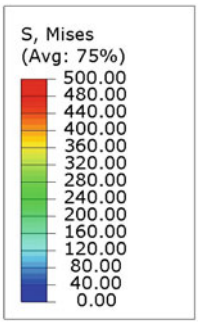


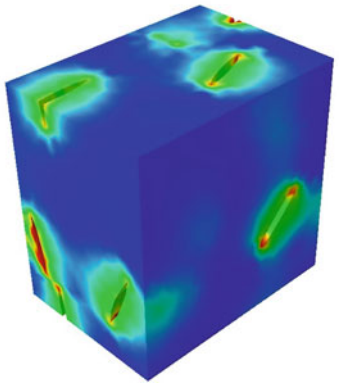

**Fig. 8.3** von Mises coherency stress field [MPa]. The volume fraction of precipitates is 2% and the precipitate major to minor axis ratio, $\lambda$, is equal to 8

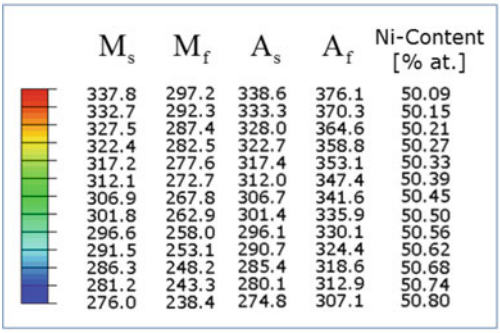


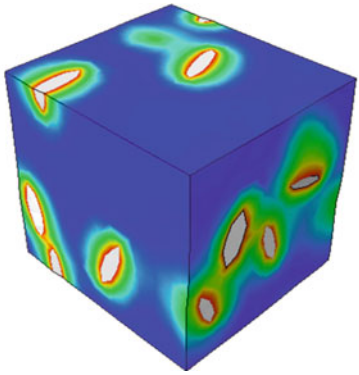

**Fig. 8.4** Distribution of phase transition temperatures $M_f$, $M_s$, $A_s$, and $A_f$ [K] and Ni concentration (% at.) field for the SMA matrix material. The volume fraction of precipitates is 2% and the precipitate major to minor axis ratio, $\lambda$, is equal to 8. The different colors represent sets ($M_f$, $M_s$, $A_s$, $A_f$, Ni content %at.) of phase transition temperature values

precipitates before the cross spreading of martensite occurs in line with the results of Kröger et al. (2008). The process of phase transformation relaxes stresses near precipitates (Fig. 8.6b) until the majority of transformation completes. Then precipitates become stress concentrators due to their higher Young's modulus as before the initiation of phase transformation. During heating under constant load, at equal levels of effective strain, the martensite volume fraction and von Mises effective stress fields are very similar to the ones presented in Fig. 8.6.

#### 8.2.2.2 Effective Thermomechanical Response

The effects of precipitation on the thermomechanical response obtained from the model during a thermal cycle under constant uniaxial load are examined next.

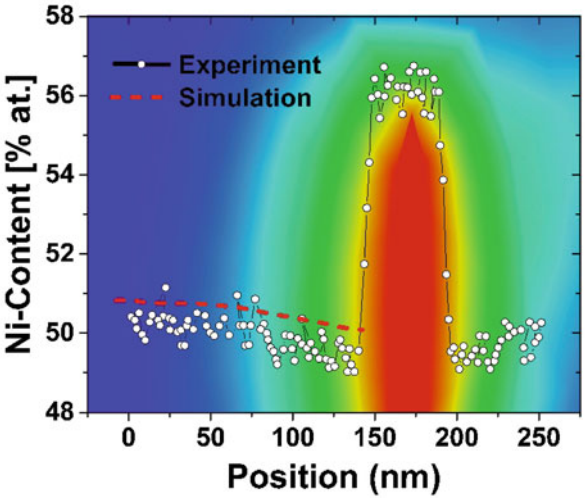


**Fig. 8.5** Ni content close to a precipitate as measured experimentally (Schryvers et al., 2006) with simulation results overlaid

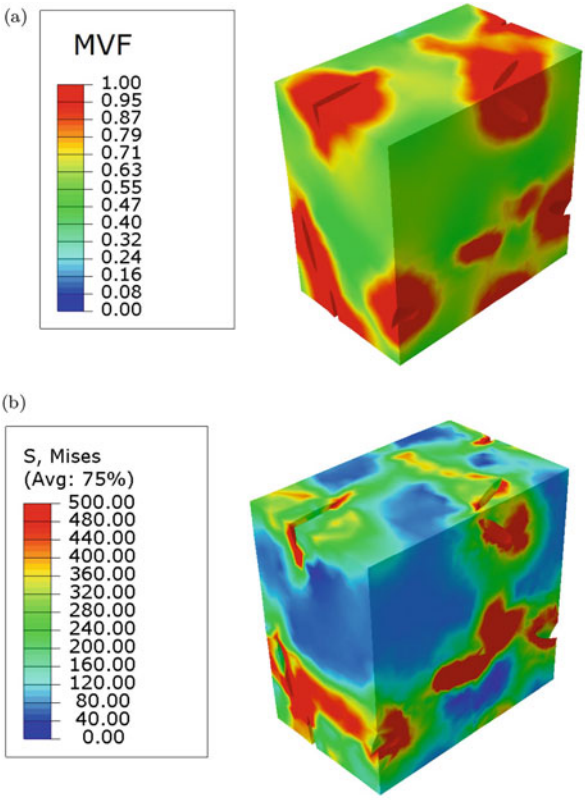


**Fig. 8.6** Mechanical fields during forward phase transformation (cooling) under constant uniaxial load. The volume fraction of precipitates is 2% and the precipitate major to minor axis ratio, $\lambda$, is equal to 8. The periodic boundary conditions result in martensitic islands and stress relaxation in regions of the RVE opposite from precipitates. (**a**) Martensite volume fraction. (**b**) von Mises stress [Mpa]

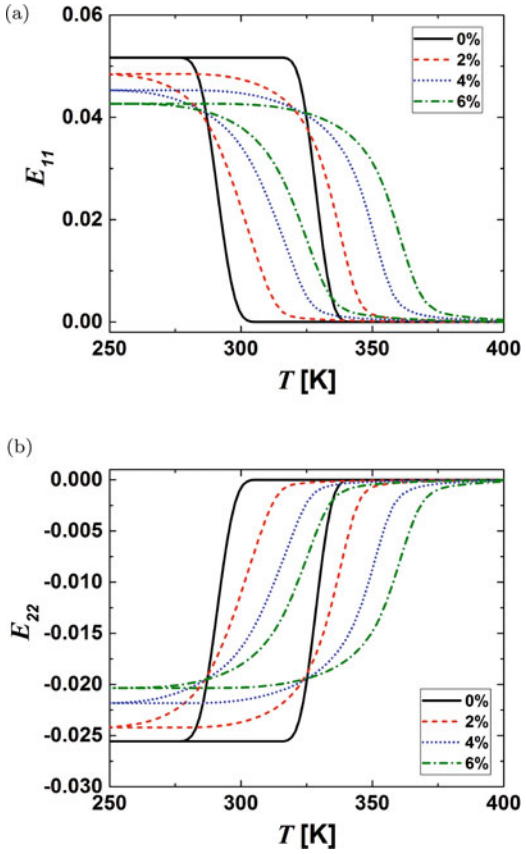


**Fig. 8.7** Comparison of the effective strain vs temperature responses of 0%, 2%, 4%, and 6% volume fraction precipitated materials for a thermal cycle under a constant uniaxial loading at 200 MPa. The precipitate major to minor axis ratio is equal to 8. (**a**) Effective strain in the direction of loading vs temperature response. (**b**) Effective strain in the transverse to loading direction vs temperature response

*Precipitate volume fraction*—As shown in Fig. 8.7, which displays the effective strain–temperature response of thermally cycled material systems with different precipitate volume fractions, the formation of elastic precipitates at the expense of transformable material decreases the maximum transformation strain. Moreover, the heterogeneous nature of the precipitated microstructure is shown to significantly alter the effective strain–temperature hysteresis loop by shifting the phase transition temperatures to higher values. Additionally, a more gradual or "smooth" transition from the elastic response to the transformation response (and vice versa) is evident and in accordance to experimental observations. Also, from Fig. 8.7, it is shown that the higher the volume fraction of precipitation, the more pronounced the aforementioned effects. For instance, the 6% case results in smaller maximum transformation strains, a more gradual transition between the elastic and the transformation response, and higher martensitic-start and austenitic-finish temperatures than the 4 and 2% cases.

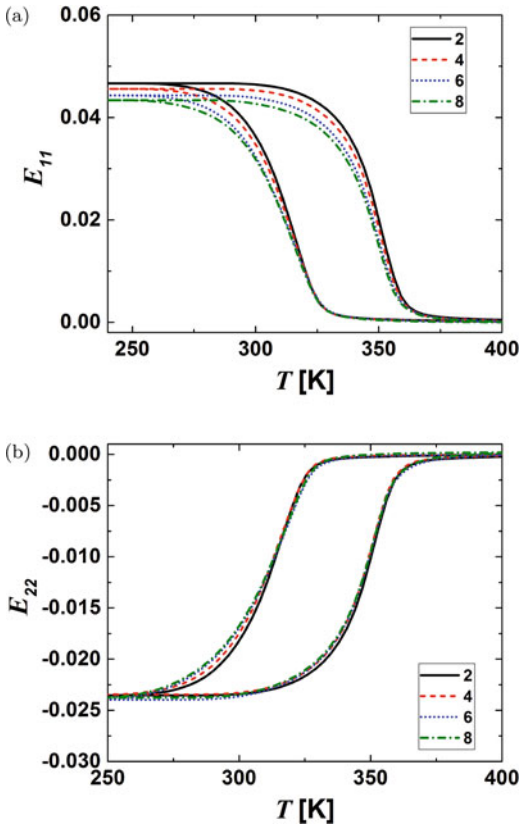


**Fig. 8.8** Comparison of the effective strain vs temperature responses for precipitated materials with precipitate major to minor axis ratio $\lambda = 2, 4, 6$, and 8 for a thermal cycle under a constant uniaxial loading at 200 MPa. The precipitate volume fraction is 2%. (**a**) Effective strain in the direction of loading vs temperature response. (**b**) Effective strain in the transverse to loading direction vs temperature response

*Coherency stresses and precipitate volume fraction*—In Fig. 8.8, which displays the effective strain–temperature response of thermally cycled material systems with different precipitate major to minor axis ratios, $\lambda$, for a precipitate volume fraction equal to 4%, $\lambda$ has a second-order effect on the thermomechanical response of the precipitated microstructures which becomes negligible for precipitate volume fractions below 2%. Similarly, the effect of coherency stresses arising at the interface between the precipitates and the austenitic matrix due to their lattice mismatch on the effective thermomechanical response is negligible, the reason being that it is the low Ni content close to the precipitates that drives the martensitic transformation which in turn relaxes the coherency stresses (Fig. 8.9).

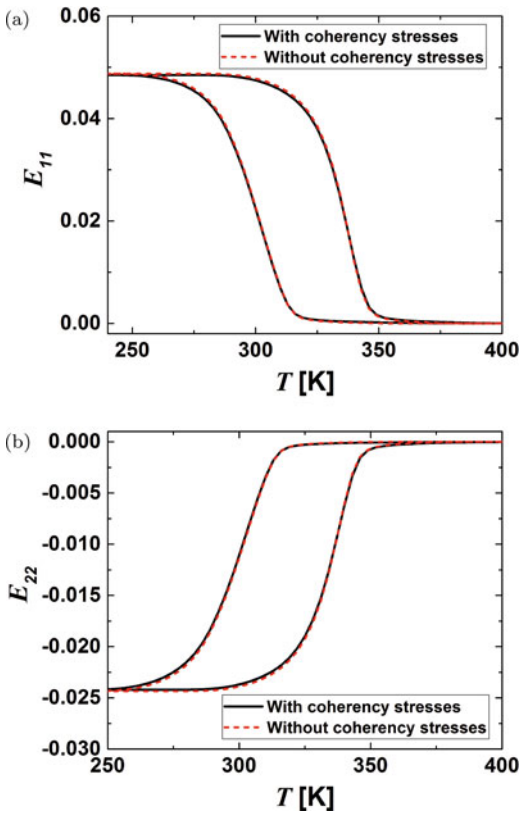


**Fig. 8.9** Comparison of the effective strain vs temperature responses for precipitated materials with and without accounting for the coherency stresses due to the lattice mismatch between precipitates and B2 matrix for a thermal cycle under a constant uniaxial loading at 200 MPa. The precipitate volume fraction is 4% and the precipitate major to minor axis ratio, $\lambda$, is equal to 8. (**a**) Effective strain in the direction of loading vs temperature response. (**b**) Effective strain in the transverse to loading direction vs temperature response

## 8.3 Prediction of the Effective Response of Precipitated NiTi

In this section, the model described in the preceding sections is used to *predict* the effective thermomechanical response of precipitated NiTi knowing only the homogenized parameters and aging path. First, the experimental characterization of the materials[1] is briefly presented.

To test the ability of the developed model to predict the effect of precipitation, NiTi specimens with a nominal composition of $Ni_{50.8}Ti$ were prepared via vacuum induction melting. The initial homogenized, nominally precipitate-free specimens were produced via solution treating at 800 °C for 1 h and water quenching. Specimens for both digital scanning calorimetry (DSC) and tensile testing were prepared and then subjected to a variety of additional aging treatments to characterize the impact of precipitate formation. Specifically, to construct the TTT diagram of

[1]The authors would like to acknowledge and thank Brian Franco and the other members of the Microstructural Engineering of Structural and Active Materials (MESAM) Research Group at Texas A & M University for preparing and characterizing the experimental specimens.

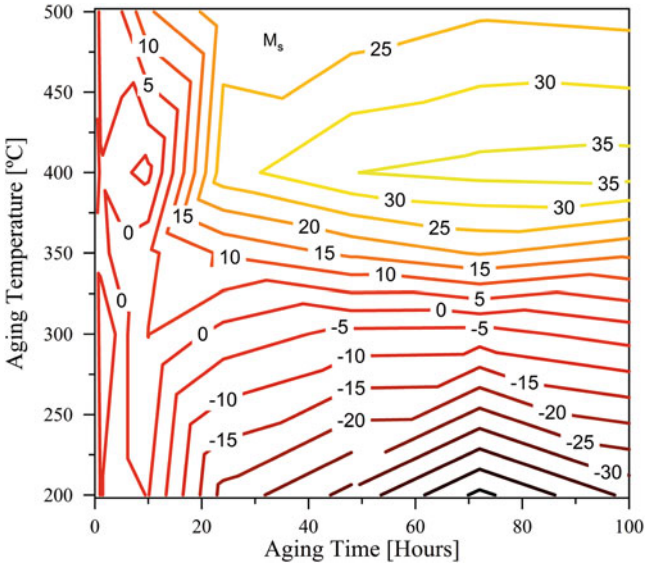


**Fig. 8.10** Contour plot showing the effect of aging time and aging temperature on martensitic transformation start temperature (TTT diagram) in $Ni_{50.8}Ti$. Each contour represents a line of constant $M_s$. Individual data points are measured from systematic DSC experiments, after which Voronoi interpolation is used to produce the *contour lines*

interest, separate DSC specimens were aged for between 30 min and 100 h at temperature increments of 200 and 500 °C. The martensitic-start temperatures were then measured and correlated with the processing conditions to construct the TTT diagram (Fig. 8.10).

To predict the effective thermomechanical responses of precipitated NiTi (1) the calibrated response of the solutionized (matrix) material and (2) a representation of the material microstructure are needed. With respect to the former, the thermomechanical response of the solutionized material is used to calibrate the SMA constitutive model. These parameters are summarized in Table 8.1. A comparison between model calibration and the experimental data of the response of $Ni_{50.8}Ti$ solutionized material subjected to thermal actuation under constant bias loads is presented in Fig. 8.11. The dashed curves represent experimental data at a given bias load, while the solid ones represent the simulations. Good agreement between the results can be noted supporting the proposition that this model can be used for the response of the matrix material. Regarding the representation of the microstructure, an estimate of the precipitate volume fraction is needed. This estimate is obtained using relations between transformation temperatures and atomic composition obtained from highly pure NiTi materials given in Frenzel et al. (2010) and listed in Table 8.2. Specifically, the martensitic-start temperature, $M_s$, of the aged material system is approximated on the basis of heat treatment using

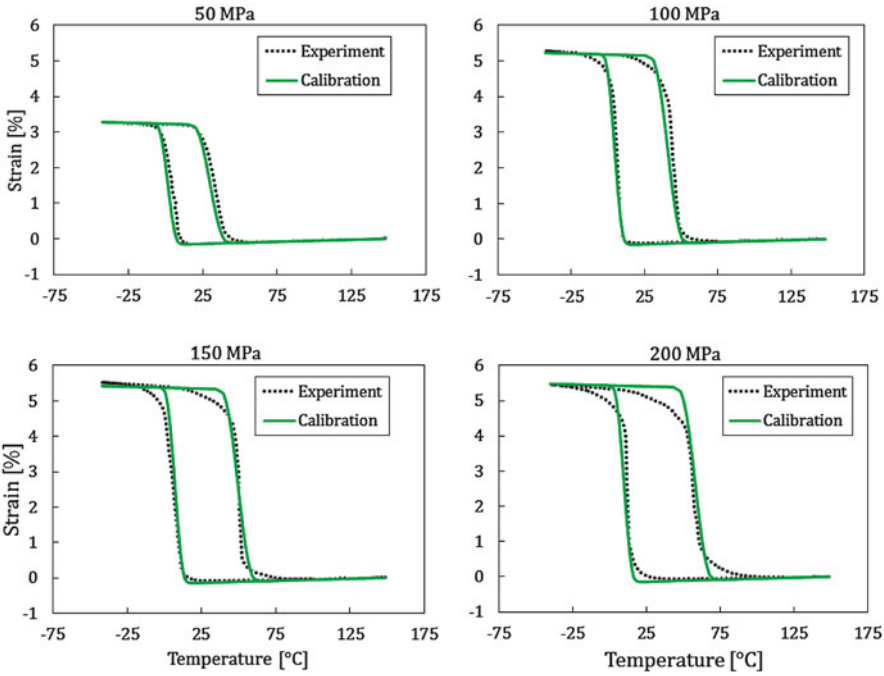


**Fig. 8.11** Strain vs temperature plots for $Ni_{50.8}Ti$ solutionized material subjected to thermal cycle under constant bias loads. *Dashed curves* represent experimental data at a given bias load (given in MPa), while *solid* ones represent the simulations

time–temperature–martensite transformation (TTT) maps such as those in Fig. 8.10 and used for providing an estimate of the Ni content of the matrix material after precipitation heat treatment. The estimate is based on the assumption that the average Ni content of the matrix material would be equal to the Ni content of a solutionized material with the same martensitic-start temperature. The difference between the Ni content of the initial solutionized material and estimated average Ni content of the matrix in the aged material reveals how much Ni is consumed to form the precipitates. Then, it is a simple matter of algebraic manipulation to obtain the precipitate volume fraction in the material, as the Ni content of the $Ni_4Ti_3$ precipitates is a known constant. The expression for the precipitate volume fraction is given as follows:

$$v = (c_{\text{sm}} - c_{\text{am}})/(c_{\text{Ni}_4\text{Ti}_3} - c_{\text{am}}) \tag{8.7}$$

where $c_{\text{sm}}$ is the concentration of Ni in the solutionized material, and $c_{\text{am}}$ is the average Ni content in the aged material matrix. In the following comparison of model predictions against experimental data, the value $\lambda = 6$ is adopted for the calculations. As discussed in Sect. 8.2.2.2, the precipitate major to minor axis ratio, $\lambda$, has a second-order effect on the thermomechanical response of the precipitated microstructures.

**Table 8.3** Ni-rich NiTi SMA sample conditions, studied in this work, with detailed initial compositions, processing conditions, and estimation of final precipitate volume fraction

| Initial composition [Niat.%] | Aging temp. [°C] | Aging time [h] | Estimated precipitate VF [%] |
|---|---|---|---|
| 50.8 | 300 | 100 | 1.7 |
| 50.8 | 500 | 24 | 4.2 |

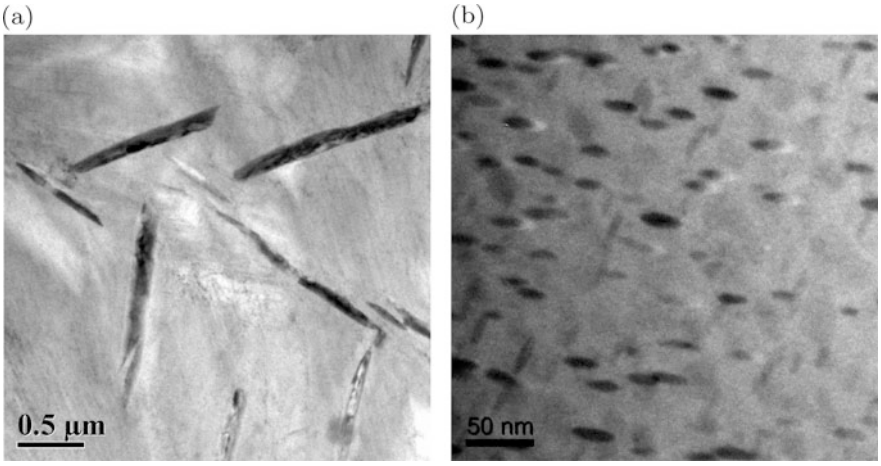


**Fig. 8.12** TEM micrographs of the $Ni_{50.8}Ti$ material. The apparent precipitate size in the material aged at 500 °C for 24 h is on the order of 1 μm. Since Ostwald ripening is a diffusional process, the lower aging temperature (300 °C vs 500 °C) delays the onset of coarsening, leading to the small precipitate size and interparticle distance shown in Figure 8.12b (Madras and McCoy, 2004). (**a**) Aged at 500 °C for 24 h. (**b**) Aged at 300 °C for 100 h. Note the image-scale difference between the two images

The model predictions are compared to the experimental results for two differently heat-treated materials. These material systems are subjected to thermal cycles with bias loads of 200 MPa and below in order to minimize the effects of TRIP which heavily influence transformation responses above this load level. The compositions of the materials tested and their processing conditions are listed in Table 8.3 along with their estimated precipitate volume fractions, while their microstructures are shown in Fig. 8.12. The experimental data regarding the thermomechanical response reveals that the heterogeneous nature of the precipitated microstructure decreases the maximum transformation strain, alters significantly the effective strain–temperature hysteresis loops, and shifts the phase transition temperatures to higher values versus the solutionized response, as seen in the Figs. 8.14 through 8.15.

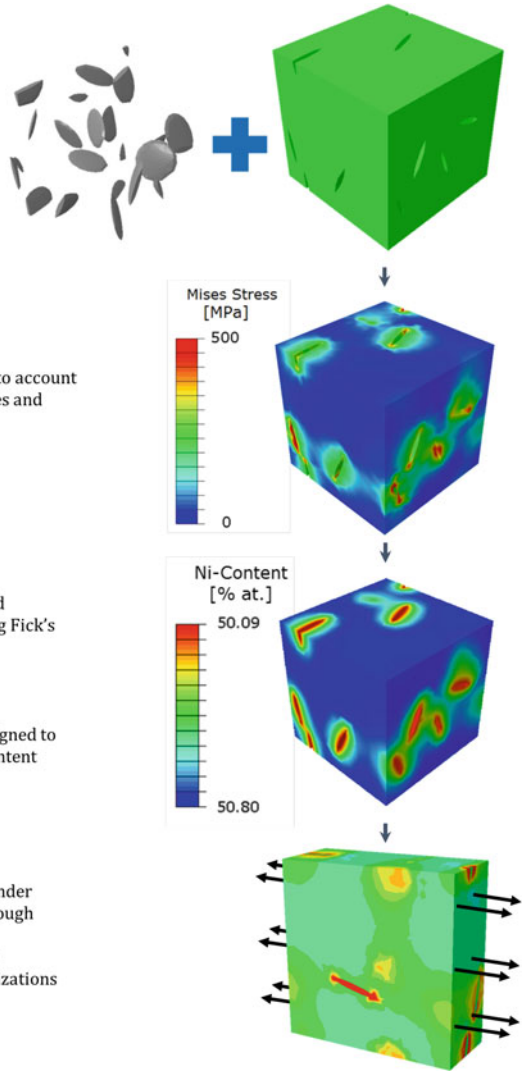


**Fig. 8.13** Computational procedure

The computational procedure is reviewed in Fig. 8.13. The predictions of the strain–temperature response of the thermally cycled $Ni_{50.8}Ti$ material aged at 300 °C for 100 h subject to bias loads of 100, 150, and 200 MPa are compared against experimental data in Fig. 8.14. The predictions are able to reproduce quantitatively all the aforementioned precipitation-induced changes in the thermomechanical response. These include changes in transformation temperature due to matrix compositional change and applied stress, increases in the width of transformation intervals (i.e., $M_s - M_f$), and reduction in transformation strain. The model does not

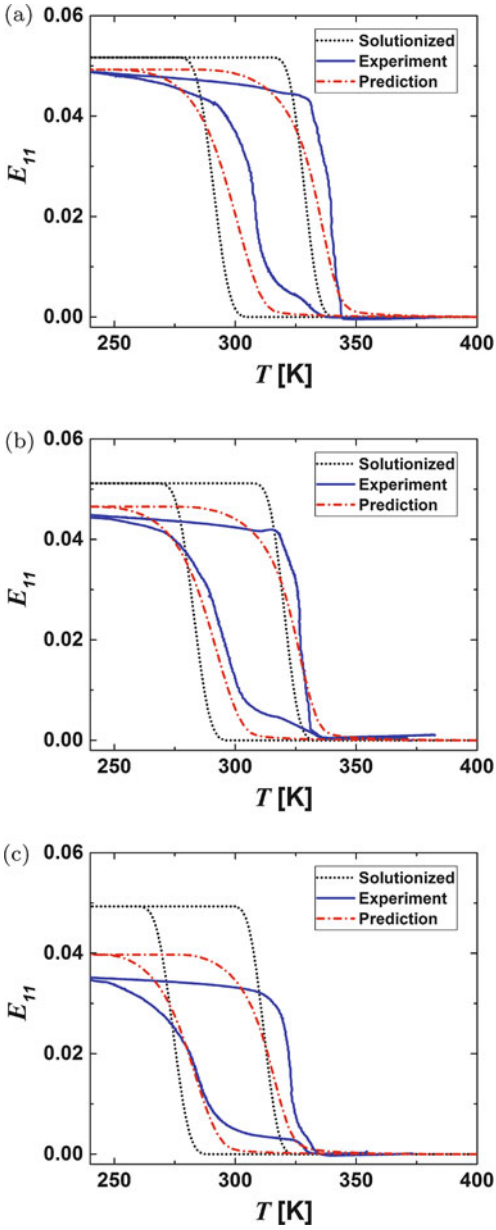


**Fig. 8.14** Comparison of the predicted and experimental results of the material with an initial composition of $Ni_{50.8}Ti$ aged at 300 °C for 100 h. The estimated volume fraction of the precipitates is about 1.7%. (**a**) 200 MPa; (**b**) 150 MPa; (**c**) 100 MPa

predict the transition region at the onset of martensitic transformation that is caused by the R phase transformation. Since the transformation strain associated with the R-phase is relatively small, the details of such transformations are neglected in the present modeling effort for the sake of simplicity. In the case of thermally cycled $Ni_{50.8}Ti$ material aged at 500 °C for 24 h (Fig. 8.15), the predicted transformation strain is in good agreement with experiments, while the predicted austenitic-start and -finish temperatures, $A_s$ and $A_f$, respectively, are overestimated, the martensitic-start, $M_s$, and -finish, $M_f$, temperatures are underestimated, and consequently the strain–temperature slopes are underestimated as well.

## 8.4 Discussion

As already mentioned, the model in its present form can only capture volume fraction, aspect ratio, and orientations as the main precipitate defining geometric quantities, i.e., to the extent that the constructed RVEs are truly representative of the material microstructure, but not microstructural size effects. Size effects arise mostly from the interparticle distance and the surface to volume fraction ratio of the precipitates. Small interparticle distance between the precipitates can reduce the martensitic transformation temperatures and sometimes fully suppress transformation (Hornbogen, 1985) and also enlarge the transformation hysteresis (Franco, 2014). However, the role of microstructural size effects on martensitic transformation and its energetics are currently not fully understood at a level that can be incorporated into micromechanics and continuum-level materials modeling. In addition, the model does not capture the transition from type I and type II martensite twin formation in the solutionized NiTi SMAs to mostly $(001)_M$-type compound twin formation and thus the associated changes in the thermomechanical responses in precipitation-hardened NiTi SMAs. For example, compound twins in martensite via the B2-R-B19′ transformation sequence, as observed here, lead to lower transformation strains than type II twins formed in the B2-B19′ transformation (Sehitoglu et al., 2001c).

In general, the model underestimates austenitic-start and -finish temperatures and overestimates the martensitic-start and -finish ones, the transformation hardening, and attainable maximum transformation strain. Overall, the effective thermomechanical response is shown to be in good agreement with experiments, although, it seems that a single-parameter (that of martensite volume fraction) description of phase transformation cannot fully capture the structural and compositional effects of precipitates on the complexity of the martensitic microstructures formed (e.g., type and number of active martensitic variants, detwinning, etc.) and the observable macroscopic thermomechanical response. As mentioned above, the type of twins formed in martensite significantly influences the transformation strain. However, the model assumes the same twinning type, transformation sequence, and transformation strain in the matrix of precipitation-hardened NiTi and the solution-treated NiTi samples, overestimating the attainable transformation strain in comparison with the

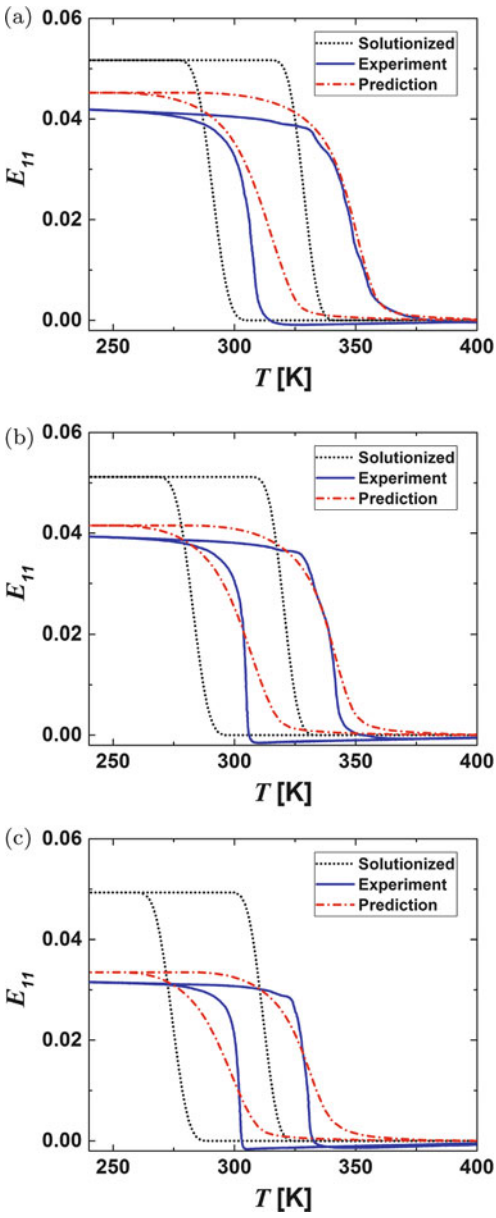


**Fig. 8.15** Comparison of the predicted and experimental results of the material with an initial composition of $Ni_{50.8}Ti$ aged at 500 °C for 24 h. The estimated volume fraction of the precipitates is about 4.2%. (**a**) 200 MPa; (**b**) 150 MPa; (**c**) 100 MPa

experiments. The model seems to capture well the phase transition temperatures and thus the hysteresis for relatively small interparticle distances (Fig. 8.14); however, there is a deviation between predictions and the experimental data for relatively large interparticle distances (Fig. 8.15). The differences in the experimentally observed transformation hysteresis under stress between the two processing conditions should be attributed partly to size effects. Size effects are known to impact the dissipated energy due to phase transformation that in turn impacts the widening of the thermal hysteresis and the reverse transformation interval (Franco, 2014; Hamilton et al., 2004). Moreover, in almost all cases, the slopes of the predicted strain–temperature curves are lower than the experimentally observed ones, i.e., the predicted transformation hardening is higher than the measured one, irrespective of the interparticle distance and precipitate volume fraction. The observed discrepancy can be attributed again to the differences in the detwinning behavior of compound twins and type II twins in martensite. In overaged cases, where the Ostwald ripening drastically reduces the precipitate surface to volume fraction ratio, the effect of compositional gradients becomes less prevalent and the matrix can be considered to be essentially homogeneously transforming in a very small temperature interval.

In summary, despite its shortcomings, the current modeling framework can provide an, at least first-order, approximation of the thermomechanical response of virtually heat-treated Ni-rich NiTi SMAs, without actually performing the heat-treatment experiments and associated thermomechanical characterization. According to the results, smaller approximated precipitate volume fractions yield better predictions. For precipitate volume fractions up to about 2% that can still alter the thermomechanical response substantially, the predictions are almost as good as simulations of a model that has been calibrated from the response of the specific microstructure. Moreover, with the effective response of the RVEs described, a homogenized SMA material can be determined by calibrating the same SMA model used previously for the matrix material based on the RVE effective response. Such a homogenized constitutive model is necessary, and critical, for predicting the structural response of SMA components with such precipitated materials. In this way, the influences of the microstructure may be brought up to the structural scale.

Continuing efforts may focus on three distinct areas. The first is associated with the modeling of the precipitate formation. Efforts may be directed towards phase field simulations for estimating the precipitate volume fraction and shape for specific heat treatments, an estimation which now relies on precipitation time–temperature–martensitic transformation temperature maps. Such simulations will also estimate the shape of precipitates that are currently assumed to be oblate spheroids with an a priori specified major to minor axis ratio irrespective of the aging process. The second area is associated with a higher-fidelity modeling capable of addressing spatial correlations and complex interactions occurring at different length scales. Multiscale micromechanical computational research capable of incorporating more detailed physics and potentially non-local interactions stemming from microstructural features of different sizes, such as precipitate and grains, and compositional gradients is needed to investigate these interactions. Although computational resources continue to come online, making increasingly large problems

tractable, the third effort could be in developing multiscale mean-field approaches or surrogate models that can be utilized in addressing the *inverse* problem of application-driven design of processing conditions to determine optimized material responses.

**Acknowledgements** This material is based upon work supported by the Air Force Office of Scientific Research under Grant No. FA9550-12-1-0218. The authors would like to acknowledge the crucial work of Austin Cox in developing and implementing the predictive model presented in this chapter.

## Appendix: Constitutive Law for Polycrystalline SMAs

The model is developed within the framework of continuum thermodynamics and adopts the classical rate-independent small-strain flow theory for the evolution equations of the transformation strains (Lagoudas et al., 1996, 2012; Lagoudas, 2008). This model is used to describe the response of both precipitated and unprecipitated polycrystalline SMAs.

By utilizing infinitesimal strains and assuming an additive strain rate decomposition, the increments of the total strain tensor components, $d\varepsilon_{ij}$, are given as

$$d\varepsilon_{ij} = S_{ijkl} d\sigma_{kl} + dS_{ijkl}\sigma_{kl} + d\varepsilon^t_{ij}, \tag{8.8}$$

where $\sigma_{ij}$ and $\varepsilon^t_{ij}$ are the Cartesian components of the stress and transformation strain tensor, respectively, and $S_{ijkl}$ represents the "current" compliance tensor. Standard Einstein notation is used with summation over repeated indices assumed. The "current" compliance tensor varies with the martensite volume fraction, $\xi$, as $S_{ijkl} = (1-\xi)S^A_{ijkl} + \xi S^M_{ijkl}$, where $S^A_{ijkl}$ and $S^M_{ijkl}$ are the components of the compliance tensor of the polycrystalline SMA material in the austenitic and martensitic phase, respectively. The assumption of elastic isotropy for both the austenitic and martensitic phases results in $S^\alpha_{ijkl} = \frac{1+\nu_\alpha}{2E_\alpha}(\delta_{il}\delta_{jk} + \delta_{ik}\delta_{jl}) - \frac{\nu_\alpha}{E_\alpha}\delta_{ij}\delta_{kl}$, where the index $\alpha$ stands for A and M in the cases of pure austenite and martensite, respectively. The Young's modulus and Poisson's ratios of the SMA's two phases are denoted $E_\alpha$ and $\nu_\alpha$, respectively, and $\delta_{ij}$ is Kronecker's delta.

An evolution equation of the transformation strain is defined so that it is related to the evolution of martensite volume fraction $\xi$,

$$d\varepsilon^t_{ij} = \Lambda_{ij} d\xi, \quad \Lambda_{ij} = \begin{cases} \Lambda^{fwd}_{ij}, & d\xi > 0, \\ \Lambda^{rev}_{ij}, & d\xi < 0, \end{cases} \tag{8.9}$$

where, $\Lambda_{ij}$, the components of the direction tensor, are defined as

$$\Lambda_{ij}^{fwd} = \frac{3}{2}\frac{H^{cur}}{\sigma}\sigma'_{ij}, \quad \Lambda_{ij}^{rev} = \frac{\varepsilon_{ij}^{t}}{\xi}. \tag{8.10}$$

Here, $H^{cur}$ is the uniaxial transformation strain magnitude for complete transformation, $\sigma = \sqrt{\frac{3}{2}\sigma'_{ij}\sigma'_{ij}}$ is the Mises equivalent effective stress, and $\sigma'_{ij} = \sigma_{ij} - \sigma_{kk}\delta_{ij}/3$ are the stress deviator components. Forward transformation generates transformation strain in the direction of the deviatoric stress, which motivates the selected $J_2$ form of the direction tensor. During reverse phase transformation, it is assumed that the direction and magnitude of the transformation strain recovery is governed by the average orientation of martensite at transformation reversal (the cessation of forward transformation, be it partial or full). This definition ensures a zero transformation strain for every state with a null martensite volume fraction.

During transformation, the stress tensor components should remain on the transformation surface:

$$\Phi = 0, \quad \Phi = \begin{cases} \Phi^{fwd} = \pi^{fwd} - Y_0, \ d\xi > 0, \\ \Phi^{rev} = -\pi^{rev} - Y_0, \ d\xi < 0, \end{cases} \tag{8.11}$$

with $\pi^{fwd}$, $\pi^{rev}$ being the thermodynamic driving forces for forward and reverse transformation, respectively, and $Y_0$ being the critical value of the thermodynamic force to both initiate and sustain forward and reverse phase transformation.

The thermodynamic driving force for forward transformation is written as

$$\pi^{fwd} = \sigma_{ij}\Lambda_{ij}^{fwd} + \frac{1}{2}\Delta S_{ijkl}\sigma_{ij}\sigma_{kl} + \rho\Delta s_0 T - \rho\Delta u_0 - f^{fwd}, \tag{8.12}$$

and for reverse transformation

$$\pi^{rev} = \sigma_{ij}\Lambda_{ij}^{rev} + \frac{1}{2}\Delta S_{ijkl}\sigma_{ij}\sigma_{kl} + \rho\Delta s_0 T - \rho\Delta u_0 - f^{rev}. \tag{8.13}$$

$f^{fwd}$ and $f^{rev}$ are functions describing the transformation hardening behavior during forward and reverse phase transformation, respectively. $s_0$ and $u_0$ are the specific entropy and internal energy, respectively, $\rho$ is the density, and $\Delta$ denotes the difference in property between the martensitic and the austenitic states.

### *Variation of the Transformation Strain Magnitude*

The transformation strain magnitude, $H^{cur}$, is a function of the stress state since precipitated polycrystalline SMA materials do not exhibit a constant maximum attainable transformation strain at all stress levels (Bo and Lagoudas, 1999c; Bo et al., 1999). A saturated value of maximum attainable transformation strain, $H_{sat}$,

is reached at a high-stress level, which is dependent on the SMA material and the processing conditions. Following this observation, $H^{cur}$ is represented by the following decaying exponential function:

$$H^{cur}(\sigma) = H_{sat}\left(1 - e^{-k\sigma}\right). \tag{8.14}$$

The parameter $k$ controls the rate at which $H^{cur}$ exponentially evolves from 0 to $H_{sat}$.

### *Description of a "Smooth" Thermomechanical Response*

In precipitated polycrystalline SMAs, local transformation initiates in a non-uniform manner, resulting in an experimentally observed gradual transition from the elastic to transformation response and vice versa. To capture the gradual transformation initiation and completion response, the hardening functions are given as general power laws in terms of $\xi$ with real components:

$$f^{fwd}(\xi) = \frac{1}{2}\alpha_1\left[1 + \xi^{n_1} - (1-\xi)^{n_2}\right] + \alpha_3, \tag{8.15}$$

$$f^{rev}(\xi) = \frac{1}{2}\alpha_2\left[1 + \xi^{n_3} - (1-\xi)^{n_4}\right] - \alpha_3, \tag{8.16}$$

where, $\alpha_i$ $(i = 1, 2, 3)$ are coefficients that assume real number values and $n_i$ $(i = 1, 2, 3)$ are exponents that assume real numbers in the interval $(0, 1]$. If $n_1$ and/or $n_3$ take values less than 1, the forward and/or reverse phase transformations, respectively, are initiated in a "smooth" gradual fashion. Similarly, if $n_2$ and/or $n_4$ take values less than 1, the forward and/or reverse phase transformations, respectively, are completed in a "smooth" gradual fashion.

### *Calibration of the Model*

Given the above constitutive relations, the following model parameters must be calibrated: (1) the elastic parameters of the precipitated polycrystalline SMA in the austenitic and martensitic states, (2) parameters contained in the functional form of the maximum transformation strain $H^{cur}(\sigma)$, and (3) six model parameters ($\rho\Delta s_0$, $\rho\Delta u_0$, $\alpha_1$, $\alpha_2$, $\alpha_3$, $Y_0$) that are characteristic of the martensitic transformation. The common material properties that are used to calibrate the model are $E_A$, $E_M$, $\nu_A$, $\nu_M$, $H_{sat}$, $M_s$, $M_f$, $A_s$, $A_f$, $C_M$, and $C_A$. $M_s$, $M_f$, $A_s$, and $A_f$ are the martensitic-start, martensitic-finish, austenitic-start, and austenitic-finish temperatures at zero load, respectively, and $C_M$ and $C_A$ are the forward and reverse transformation slopes in the stress-temperature phase diagram, respectively (Fig. 8.2). The elastic constants can

be calculated directly from nominally isothermal stress–strain curves where loads are applied at temperatures outside the transformation regions. The parameters for $H^{cur}(\sigma)$ can be calibrated directly from material testing under thermal variations at a constant applied load, where the value of $k$ in particular is chosen to best fit the experimental trend. The remaining six parameters are calibrated by considering the conditions under which forward transformation begins and ends in the stress-temperature space (Lagoudas, 2008). The hardening coefficients $n_1 - n_4$ do not have an associated material property but are directly chosen to best fit the four corners of the transformation hysteresis plots.

## References


Abaqus: Analysis User's Manual. Dassault Systèmes of America Corporation, Woodlands Hills (2009)

Allafi, J., Ren, X., Eggeler, G.: The mechanism of multistage martensitic transformations in aged Ni-rich NiTi shape memory alloys. Acta Mater. **50**(4), 793–803 (2002)

Anderson, A., Pedersen, D., Sivertsen, A., Sangesland, S.: Detailed study of shape memory alloys in oil well applications. Technical Report, SINTEF Petroleum Research, Trondheim, Norway (1999)

Arghavani, J., Auricchio, F., Naghdabadi, R., Reali, A., Sohrabpour, S.: A 3-D phenomenological constitutive model for shape memory alloys under multiaxial loadings. Int. J. Plast. **26**(7), 976–991 (2010)

Ashby, M.F., Bréchet, Y.J.M.: Designing hybrid materials. Acta Mater. **53**, 5801–5821 (2003)

Auricchio, F., Bonetti, E., Scalet, G., Ubertini, F.: Theoretical and numerical modeling of shape memory alloys accounting for multiple phase transformations and martensite reorientation. Int. J. Plast. **59**, 30–54 (2014)

Bansiddhi, A., Sargeant, T.D., Stupp, S.I., Dunand, D.C.: Porous NiTi for bone implants: a review. Acta Biomater. **4**, 773–782 (2008)

Bataillard, L., Bidaux, J.E., Gotthard, R.: Interaction between microstructure and multiple-step transformation in binary NiTi alloys using in-situ transmission electron microscopy observations. Philos. Mag. A **78**(2), 327–344 (1998)

Baxevanis, T., Cox, A., Lagoudas, D.C.: Micromechanics of precipitated near-equiatomic Ni-rich NiTi shape memory alloys. Acta Mech. **65**, 1167–1185 (2014)

Bellouard, Y.: Shape memory alloys for microsystems: a review from a material perspective. Mater. Sci. Eng. A **481–482**, 582–589 (2008)

Benefan, O., Brown, J., Calkins, F.T., Kumar, P., Stebner, A.P., Turner, T.L., Vaidyanathan, R., Webster, J., Young, M.L.: Shape memory alloy actuator design: CASMART collaborative best practices and case studies. Int. J. Mech. Mater. Design **10**, 1–42 (2014)

Bo, Z., Lagoudas, D.: Thermomechanical modeling of polycrystalline SMAs under cyclic loading, Part I: theoretical derivations. Int. J. Eng. Sci. **37**(9), 1089–1140 (1999a)

Bo, Z., Lagoudas, D.: Thermomechanical modeling of polycrystalline SMAs under cyclic loading, Part IV: modeling of minor hysteresis loops. Int. J. Eng. Sci. **37**(9), 1205–1249 (1999b)

Bo, Z., Lagoudas, D.C.: Thermomechanical modeling of polycrystalline SMAs under cyclic loading, Part I: theoretical derivations. Int. J. Eng. Sci. **37**(9), 1089–1140 (1999c)

Bo, Z., Lagoudas, D.C., Miller, D.: Material characterization of SMA actuators under nonproportional thermomechanical loading. J. Eng. Mater. Technol. Trans. ASME **121**(1), 75–85 (1999)

Calkins, F.T., Mabe, J.H.: Shape memory alloy based morphing aerostructures. J. Mech. Des. **132**, 111012 (2010)

Cisse, C., Zaki, W., Ben Zineb, T.: A review of constitutive models and modeling techniques for shape memory alloys. Int. J. Plast. **76**, 244–284 (2016)

Collard, C., Ben Zineb, T.: Simulation of the effect of elastic precipitates in SMA materials based on a micromechanical model. Compos. Part B **43**(6), 2560–2576 (2012)

Collard, C., Ben Zineb, T., Patoor, E., Ben Salah, M.O.: Micromechanical analysis of precipitate effects on shape memory alloys behaviour. Mater. Sci. Eng. A **481–482**(1–2 C), 366–370 (2008)

Dong, J., Cai, C.S., Okeil, A.M.: Overview of potential and existing applications of shape memory alloys in bridges. J. Bridg. Eng. **16**, 305–315 (2011)

Drugan, W.J., Willis, J.R.: A micromechanics-based nonlocal constitutive equation and estimates of representative volume element size for elastic composites. J. Mech. Phys. Solids **44**(4), 497–524 (1996)

Duerig, T., Pelton, A., Stöckel, D.: An overview of NiTiNOL medical applications. Mater. Sci. Eng. A **273–275**, 149–160 (1999)

Eggeler, G., Hornbogen, E., Yawny, A., Heckmann, A., Wagner, M.: Structural and functional fatigue of NiTi shape memory alloys. Mater. Sci. Eng. A **378**(1–2), 24–33 (2004)

Elahinia, M.H., Hashemi, M., Tabesh, M., Bhaduri, S.B.: Manufacturing and processing of NiTi implants: a review. Prog. Mater. Sci. **57**, 911–946 (2012)

Eshelby, J.D.: The determination of the elastic field of an ellipsoidal inclusion, and related problems. Proc. R. Soc. Lond. Ser. A Math. Phys. Sci. **241**(1226), 376–396 (1957)

Firstov, G.S., Van Humbeeck, J., Koval, Y.N.: High temperature shape memory alloys problems and prospects. J. Intell. Mater. Syst. Struct. **17**, 1041 (2006)

Franco, B.E.: Engineering the martensitic transformation hysteresis of Ni-rich NiTi alloys. Master's Thesis, Texas A&M University (2014)

Frenzel, J., George, E.P., Dlouhy, A., Somsen, C., Wagner, M.F.X., Eggeler, G.: Influence of Ni on martensitic phase transformations in NiTi shape memory alloys. Acta Mater. **58**(9), 3444–3458 (2010)

Geng, Y., Lee, D., Xu, X., Nagasako, M., Jin, M., Jin, X., Omori, T., Kainuma, R.: Coherency of ordered $\gamma$' precipitates and thermoelastic martensitic transformation in FeNiCoAlTaB alloys. J. Alloys Compd. **628**, 287–292 (2015)

Hamilton, R., Sehitoglu, H., Chumlyakov, Y., Maier, H.: Stress dependence of the hysteresis in single crystal NiTi alloys. Acta Mater. **52**, 3383–3402 (2004)

Hartl, D.J., Lagoudas, D.: Aerospace applications of shape memory alloys. Proc. Inst. Mech. Eng. Part G J. Aerosp. Eng. **221**(Special Issue), 535–552 (2007)

Hill, R.: Elastic properties of reinforced solids: Some theoretical principles. J. Mech. Phys. Solids **11**(5), 357–372 (1963)

Hornbogen, E.: The effect of variables on martensitic-transformation temperatures. Acta Metall. **33**(4), 595–601 (1985)

Huet, C.: Coupled size and boundary-condition effects in viscoelastic heterogeneous and composite bodies. Mech. Mater. **31**(12), 787–829 (1999)

Kanit, T., Forest, S., Galliet, I., Mounoury, V., Jeulin, D.: Determination of the size of the representative volume element for random composites: statistical and numerical approach. Int. J. Solids Struct. **40**(13–14), 3647–3679 (2003)

Karaca, H., Karaman, I., Basaran, B., Ren, Y., Chumlyakov, Y., Maier, H.: Magnetic field-induced phase transformation in NiMnCoIn magnetic shape-memory alloys - a new actuation mechanism with large work output. Adv. Funct. Mater. **19**, 983–998 (2009)

Karaca, H.E., Saghaian, S.M., Ded, G., Tobe, H., Basaran, B., Maier, H.J., Noebe, R.D., Chumlyakov, Y.I.: Effects of nanoprecipitation on the shape memory and material properties of an Ni-rich NiTiHf high temperature shape memory alloy. Acta Mater. **61**(19), 7422–7431 (2013)

Karaman, I., Kulkarni, A.V., Luo, Z.P.: Transformation behavior and unusual twinning in a NiTi shape memory alloy ausformed using equal channel angular extrusion. Philos. Mag. **85**, 1729–1745 (2005)

Kröger, A., Dziaszyk, S., Frenzel, J., Somsen, C., Dlouhy, A., Eggeler, G.: Direct transmission electron microscopy observations of martensitic transformations in Ni-rich NiTi single crystals during in situ cooling and straining. Mater. Sci. Eng. A **481–482**(1–2 C), 452–456 (2008)

Lagoudas, D. (ed.): Shape Memory Alloys: Modeling and Engineering Applications. Springer, New York (2008)

Lagoudas, D., Bo, Z., Qidwai, M.A.: A unified thermodynamic constitutive model for SMA and finite element analysis of active metal matrix composites. Mech. Comput. Mater. Struct. **4**, 153–179 (1996)

Lagoudas, D., Hartl, D., Chemisky, Y., Machado, L., Popov, P.: Constitutive model for the numerical analysis of phase transformation in polycrystalline shape memory alloys. Int. J. Plast. **32–33**, 155–183 (2012)

Lejeunes, S., Bourgeois, S., et al.: Une Toolbox Abaqus pour le calcul de propriétés effectives de milieux hétérogènes, in: 10e colloque national en calcul des structures, http://www.lma.cnrs-mrs.fr/spip.php?article171 (2011)

Leng, J., Lan, X., Liu, Y., Du, S.: Shape-memory polymers and their composites: stimulus methods and applications. Prog. Mater. Sci. **56**, 1077–1135 (2011)

Lester, B.T., Baxevanis, T., Chemisky, Y., Lagoudas, D.C.: Review and perspectives: shape memory alloy composite systems. Acta Mech. **226**(12), 3907–3960 (2015)

Li, S., Wongsto, A.: Unit cells for micromechanical analyses of particle-reinforced composites. Mech. Mater. **36**, 543–572 (2004)

Ma, J., Karaman, I., Noebe, R.D.: Medical applications of shape memory alloys. Int. Mater. Rev. **55**(5), 257–315 (2010)

Machado, L., Savi, M.: Medical applications of shape memory alloys. Braz. J. Med. Biol. Res. **36**, 683–691 (2003)

Madras, G., McCoy, B.J.: Temperature effects on the transition from nucleation and growth to Ostwald ripening. Chem. Eng. Sci. **59**(13), 2753–2765 (2004)

Manchiraju, S., Anderson, P.: Coupling between martensitic phase transformations and plasticity: a microstructure-based finite element model. Int. J. Plast. **26**(10), 1508–1526 (2010)

Morgan, N.B.: Medical shape memory alloy applications – the market and its products. Mater. Sci. Eng. A **378**, 16–23 (2004)

Morin, C., Moumni, Z., Zaki, W.: A constitutive model for shape memory alloys accounting for thermomechanical coupling. Int. J. Plast. **27**(5), 748–767 (2011)

Nishida, M., Wayman, C.M., Kainuma, R., Honma, T.: Further electron microscopy studies of the $Ti_{11}Ni_{14}$ phase in an aged Ti–52at%Ni shape memory alloy. Scr. Metall. **20**(6), 899–904 (1986)

Nishida, M., Wayman, C.M., Chiba, A.: Electron-microscopy studies of the martensitic-transformation in an aged Ti-51 at. % Ni shape memory alloy. Metallography **21**(3), 275–291 (1988)

Otsuka, K., Ren, X.: Factors affecting the ms temperature and its control in shape-memory alloys. Mater. Sci. Forum **177**, 394–395 (2002)

Ozbulut, O.E., Hurlebaus, S., Desroches, R.: Seismic response control using shape memory alloys: a review. J. Intell. Mater. Syst. Struct. **22**, 1531 (2011)

Panchenko, E.Y., Chumlyakov, Y.I., Kireeva, I.V., Ovsyannikov, A.V., Sehitoglu, H., Karaman, I., Maier, Y.H.J.: Effect of disperse $Ti_3Ni_4$ particles on the martensitic transformations in titanium nickelide single crystals. Phys. Metals Metall. **106**(6), 577–589 (2008)

Patoor, E., Lagoudas, D., Entchev, P., Brinson, L., Gao, X.: Shape memory alloys, part I: general properties and modeling of single crystals. Mech. Mater. **38**(5–6), 391–429 (2006)

Pindera, M.-J., Khatam, H., Drago, A., Bansal, Y.: Micromechanics of spatially uniform heterogeneous media: a critical review and emerging approaches. Compos. Part B Eng. **40**(5), 349–378 (2009)

Pons, J., Cesari, E., Seguí, C., Masdeu, F., Santamarta, R.: Ferromagnetic shape memory alloys: alternatives to Ni-Mn-Ga. Materials Sci. Eng. A **481–482**, 57–65 (2008)

Popov, P., Lagoudas, D.: A 3-D constitutive model for shape memory alloys incorporating pseudoelasticity and detwinning of self-accommodated martensite. Int. J. Plast. **23**(10–11), 1679–1720 (2007)

Ratna, D., Karger-Kocsis, J.: Recent advances in shape memory polymers and composites: a review. J. Mater. Sci. **43**, 254–269 (2008)

Saburi, T., Nenno, S., Fukuda, T.: Crystal structure and morphology of the metastable X phase in shape memory Ti-Ni alloys. J. Less Common Met. **125**(0), 157–166 (1986)

Schryvers, D., Tirry, W., Yang, Z.: Measuring strain fields and concentration gradients around $Ni_4Ti_3$ precipitates. Mater. Sci. Eng. A **438–440**, 485–488 (2006)

Sehitoglu, H., Karaman, I., Anderson, R., Zhang, X., Gall, K., Maier, H.J., Chumlyakov, Y.: Compressive response of NiTi single crystals. Acta Mater. **48**(13), 3311–3326 (2000)

Sehitoglu, H., Anderson, R., Karaman, I., Gall, K., Chumlyakov, Y.: Cyclic deformation behavior of single crystal NiTi. Mater. Sci. Eng. A **314**(1–2), 67–74 (2001a)

Sehitoglu, H., Jun, J., Zhang, X., Karaman, I., Chumlyakov, Y., Maier, H.J., Gall, K.: Shape memory and pseudoelastic behavior of 51.5% Ni-Ti single crystals in solutionized and overaged state. Acta Mater. **49**(17), 3609–3620 (2001b)

Sehitoglu, H., Karaman, I., Zhang, X., Viswanath, A., Chumlyakov, Y., Maier, H.J.: Strain-temperature behavior of NiTiCu shape memory single crystals. Acta Mater. **49**(17), 3621–3634 (2001c)

Song, G., Ma, N., Li, H.-N.: Applications of shape memory alloys in civil structures. Eng. Struct. **28**, 1266–1274 (2006)

Stroz, D., Kwarciak, J., Morawiec, H.: Effect of aging on martensitic-transformation in NiTi shape memory alloy. J. Mater. Sci. **23**(11), 4127–4131 (1988)

Tang, W.: Thermodynamic study of the low-temperature phase B19′ and the martensitic transformation in near-equiatomic Ti-Ni shape memory alloys. Metall. Mater. Trans. A **28**(3), 537–544 (1997)

Wagner, M.F.-X., Windl, W.: Elastic anisotropy of $Ni_4Ti_3$ from first principles. Scr. Mater. **60**(4), 207–210 (2009)

Yu, C., Kang, G., Kan, Q., Song, D.: A micromechanical constitutive model based on crystal plasticity for thermo-mechanical cyclic deformation of NITI shape memory alloys. Int. J. Plast. **44**, 161–191 (2013)

Yu, C., Kang, G., Kan, Q.: Crystal plasticity based constitutive model of niti shape memory alloy considering different mechanisms of inelastic deformation. Int. J. Plast. **54**, 132–162 (2014)

Zarinejad, M., Liu, Y., Tong, Y.X.: Transformation temperature changes due to second phase precipitation in NiTi-based shape memory alloys. Intermetallics **17**(11), 914–919 (2009)

Zhou, N., Shen, C., Wagner, M.-X., Eggeler, G., Mills, M., Wang, Y.: Effect of $Ni_4Ti_3$ precipitation on martensitic transformation in Ti-Ni. Acta Mater. **58**, 6685–6694 (2010)

# Chapter 9
# Micromechanics of Ferroic Functional Materials

**John E. Huber**

**Abstract** This chapter introduces a range of ferroic functional materials including ferroelectrics, ferroelastics, and ferromagnets. Coupling among the different types of ferroic order results in multiferroic behavior that is of importance in transducers and memory devices. The physical laws governing each type of material are compared, noting the closely analogous governing equations. However, attention is also given to the differences in behavior that can necessitate distinct modeling approaches. The general form of the Eshelby tensor for coupled ferroics is introduced, and the methods for estimating the properties of composites, including self-consistent and Mori–Tanaka schemes, are briefly described. The chapter then focuses on the analysis of a commonly encountered arrangement of microstructure: a composite laminate comprising distinct crystal variants of the same physical phase. Rules are presented for determining how laminates can form with a minimum energy arrangement of layers, and methods are described for estimating the resulting material properties of the composite. An application to the microstructure of freestanding polycrystalline thin films is described.

## 9.1 Introduction

*Ferroics* are materials that exhibit any one or more of the properties of *ferroelectricity*, *ferroelasticity*, or *ferromagnetism* (Aizu 1970; Schmid 1994). They are of importance in the development of smart material systems and functional devices. Included in this class of materials are *ferroelectrics* that possess a remanent polarization, which can be reversed by the application of electric field. Also included are the *ferroelastic materials* that possess distinct, symmetry-related crystal variants with differing states of stress-free strain. These materials can be deformed by converting one crystal variant into another and the process may be reversed allowing cyclic straining. The resulting effect is named *ferroelasticity* by analogy with ferroelectricity and ferromagnetism. *Ferromagnetic* materials possess a remanent

J.E. Huber (✉)
Department of Engineering Science, University of Oxford, Parks Road, Oxford, OX1 3PJ, UK
e-mail: John.Huber@eng.ox.ac.uk



S.A. Meguid, G.J. Weng (eds.), *Micromechanics and Nanomechanics of Composite Solids*, DOI 10.1007/978-3-319-52794-9_9

magnetization that can be reversed by the application of magnetic field. Each of the aforementioned material types has the capacity to be ordered in a way that stores a permanent state—a polarization, strain, or magnetization—and for that state to be altered by the application of external fields. This leads to applications in switching and memory devices. Ferroic order is sometimes taken to include other orderings, such as ferrimagnetism or ferrielectricity, wherein the presence of positive and negative magnetization or polarization produces a partial balance, and antiferromagnetism or antiferroelectricity, where there is complete balance eliminating the macroscopic magnetization or polarization. Ferrotoroidicity, the possession of a circulation of magnetization, has been ascribed as a further form of ferroic order (Van Aken et al. 2007). However, as this ordering is relatively rare, this chapter will focus on the three main types of ferroic order and relations between them.

Where more than one ferroic order is present, and especially where there is coupling between ferroic orders, a material may be called *multiferroic*. The term is sometimes reserved for materials exhibiting both ferroelectricity and ferromagnetism, coupled through the magnetoelectric effect, such that electric fields can induce magnetization and magnetic fields can induce polarization. However, the broader definition involves the pairing of any two or more ferroic orders. Using this broader definition of multiferroicity, most ferroelectrics are multiferroic since they typically display both ferroelectricity and ferroelasticity. Similarly, *magnetic shape memory alloys* display both conventional ferromagnetic behavior and ferroelasticity in the form of shape memory. These materials are intrinsically multiferroic: multiple ferroic orders are present in a single phase. However, strong coupling between ferroelectricity and ferromagnetism in a single phase is relatively rare (Eerenstein et al. 2006). Instead, composites of ferroelectric and ferromagnetic materials can achieve strong magnetoelectric coupling mediated by continuity of displacement at the interface between phases (Nan et al. 2008). Effectively, application of a magnetic field can cause magnetization and strain in the ferromagnetic phase, and the coupling of strain into the ferroelectric phase can modify polarization. This composite route to strong magnetoelectric coupling is important because of the potential applications in memory devices where combinations of electrical and magnetic read–write operations may be desirable.

Returning to the main ferroic orders, their interrelations are shown in Fig. 9.1. Commonly, the presence of a ferroic order implies symmetry that allows useful coupled effects. Hence, ferroelectrics are typically piezoelectric (though not all piezoelectrics are ferroelectric) and so forth. The strong couplings give rise to applications where transduction between electrical, magnetic and mechanical energy occurs. Then the primary role of the material is not structural and these materials are referred to as *functional*. This chapter deals with *ferroic functional materials*, which display ferroic order and coupling that may be used for applications such as sensing, actuation, transduction, memory devices, and others. In each case, the ferroic order results from a symmetry breaking phase transition, normally a high-temperature symmetric phase with no ferroic order transforming upon cooling into a low-symmetry phase with ferroic order. In both ferroelectrics and ferromagnetics,

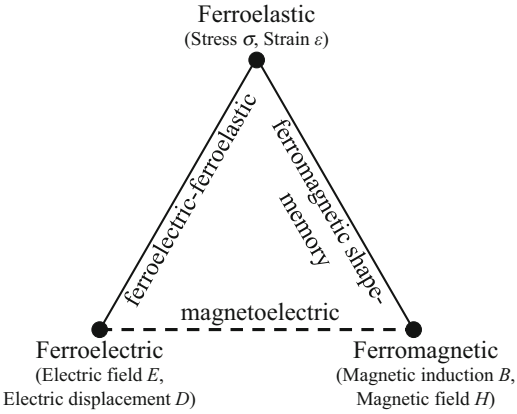


**Fig. 9.1** The main ferroic orders and relations among them

the transition temperature is called the Curie temperature $T_C$. The corresponding transition in shape memory alloys is an austenite–martensite transformation, producing a low-temperature martensite phase with several symmetry-related crystal variants.

As well as introducing the three main ferroic orders, Fig. 9.1 also introduces the field variables associated with each type of ferroic material at uniform and constant temperature. In ferroelasticity, the key variables are mechanical stress $\sigma$ and strain $\varepsilon$; ferroic ordering allows for a remanent strain $\varepsilon^R$to be present. The corresponding variables in ferroelectricity are electric field $E$ and electric displacement $D$ with remanent polarization $P^R$ being an electric displacement at zero electric field due to ordering. In ferromagnets, magnetic induction $B$ (also called magnetic flux) and magnetic field $H$ are the field variables, with a remanent magnetization $M$ describing the state when applied fields are absent.

## 9.2 Governing Equations, Constitutive Equations, and Material Description

Let us first consider the physical laws that govern ferroic materials and the specific forms of these laws relevant to quasi-static conditions. Mechanical equilibrium and Gauss' law for electric and magnetic fields provide closely analogous equations for the divergence of stress, electric displacement, and magnetic induction:

$$\sigma_{ij,j} = -b_i \tag{9.1}$$

$$D_{i,i} = q \tag{9.2}$$

$$B_{i,i} = 0 \tag{9.3}$$

Here $b_i$ is the body force density including inertial forces and $q$ is the free charge density. Indicial notation is used to indicate Cartesian tensors, with commas indicating spatial derivatives. In the absence of free charge and body forces, Eqs. (9.1)–(9.3) become equivalent except for the second-order tensorial nature of stress contrasting with electric displacement and magnetic induction, which are vectors. It should be noted that while ferroelectrics are always insulators, or at best weakly semiconducting, ferromagnets and ferroelastic shape memory alloys are commonly conducting. Therefore, care should be taken in the treatment of free charge in composites containing these materials. Theories of magneto-electro-elastic materials nevertheless often neglect free charge as this provides a convenient formulation.

Further relations allow the conjugate quantities $(\varepsilon, D, H)$ to be expressed as gradients, defining strain as the symmetrized gradient of displacement $u_i$,

$$\varepsilon_{ij} = \left(u_{i,j} + u_{j,i}\right)/2 \tag{9.4}$$

and noting that for quasi-static conditions both electric and magnetic fields are irrotational, in consequence of Maxwell's equations:

$$E_i = -\phi_{,i} \tag{9.5}$$

$$H_i = -\varphi_{,i} \tag{9.6}$$

Here $\phi$ is the electric potential and φ the magnetic potential. So far, the mechanical, electrical, and magnetic equations are closely analogous. We next turn to the definitions of the remanent quantities associated with ferroic order. These variables indicate the material state in the absence of external loads. Here it is desirable to decompose the strain into a reversible part $\varepsilon_{ij}^{\text{rev}}$due to the application of loads (which may be mechanical, electrical, or magnetic loads) and a remanent part due to ferroelastic ordering. Then

$$\varepsilon_{ij} = \varepsilon_{ij}^{\text{rev}} + \varepsilon_{ij}^{\text{R}} \tag{9.7}$$

The analogous gradient variable in ferroelectricity is the electric field as defined in Eq. (9.5). However, ferroic ordering does not provide a permanent electric field, but instead a polarization that is the moment of charge resulting from structural displacement of ions and polarization of individual ions. The polarization contributes to the total electric displacement. Hence, naming the reversible part of electric displacement $D_i^{\text{rev}}$, we could write

$$D_i = D_i^{\text{rev}} + P_i^{\text{R}} \tag{9.8}$$

However, the conventional concept of material polarization includes all of the electric displacement that is due to the presence of the material, excepting only that part which would be present in vacuum with the same electric field; thus,

$$D_i = \varepsilon_0 E_i + P_i \tag{9.9}$$

where $\varepsilon_0$ is the permittivity of free space. The polarization so defined includes both the remanent part of polarization, $P_i^{\mathrm{R}}$, and that part of $D_i^{\mathrm{rev}}$ due to the presence of the material itself—that is, all except the part due to the permittivity of free space.

For magnetic materials, it is conventional to make a similar division with magnetic field and magnetization, in the form

$$B_i = \mu_0 \left(H_i + M_i\right) \tag{9.10}$$

where $\mu_0$ is the permeability of free space. However, there is no analogous expression for stress and strain because they are unrelated (or undefined) in free space.

Constitutive relations for the materials may be developed by considering energy. An increment of internal energy $U$ is produced when external loads do work on the material:

$$dU = \sigma_{ij} d\varepsilon_{ij} + E_i dD_i + H_i dB_i \tag{9.11}$$

Notice that positive work increments are driven not only by stress (which is divergence free) changing the strain (which is a gradient variable) but also by electric field and magnetic field (both are gradient variables) changing the electric displacement and magnetic induction (divergence free). This positive work description thus produces a mixture of gradient terms and divergence-free terms as the independent variables which is inconvenient for solving boundary value problems. A commonly used alternative (Alshits et al. 1992) is achieved through the Legendre transform

$$\Psi = U - E_i D_i - H_i B_i \tag{9.12}$$

such that

$$d\Psi = \sigma_{ij} d\varepsilon_{ij} - D_i dE_i - B_i dH_i \tag{9.13}$$

Taking $\Psi$, known as the electromagnetic enthalpy (Soh and Liu 2005), to be a function of $\varepsilon_{ij}$, $E_i$, and $H_i$, the stress, electric displacement, and magnetic induction may be derived as

$$\sigma_{ij} = \frac{\partial \Psi}{\partial \varepsilon_{ij}}; \quad D_i = -\frac{\partial \Psi}{\partial E_i}; \quad B_i = -\frac{\partial \Psi}{\partial H_i} \tag{9.14}$$

Expanding $\Psi$ as a power series and showing second-order terms gives

$$\Psi = \frac{1}{2}C_{ijkl}\varepsilon_{ij}\varepsilon_{kl} + \frac{1}{2}\kappa_{ij}E_iE_j + \frac{1}{2}\mu_{ij}H_iH_j - e_{ikl}E_i\varepsilon_{kl} - q_{ikl}H_i\varepsilon_{kl} - \lambda_{ik}E_iH_k + \cdots \tag{9.15}$$

The linear material coefficients are $C_{ijkl}$, the elastic modulus; $\kappa_{ij}$, the dielectric permittivity tensor; $\mu_{ij}$, the magnetic permeability tensor; $e_{ikl}$, the piezoelectric tensor; $q_{ikl}$, the piezomagnetic tensor; and $\lambda_{ik}$, the magnetoelectric tensor.

For small changes in $\varepsilon_{ij}$, $E_i$ and $H_i$ about a reference state, linear constitutive equations can be derived from Eq. (9.15):

$$\sigma_{ij} = C_{ijkl}\varepsilon_{kl} - e_{kij}E_k - q_{kij}H_k \tag{9.16}$$

$$D_i = e_{ikl}\varepsilon_{kl} + \kappa_{ik}E_k + \lambda_{ik}H_k \tag{9.17}$$

$$B_i = q_{ikl}\varepsilon_{kl} + \lambda_{ik}E_k + \mu_{ik}H_k \tag{9.18}$$

The appearance of minus signs in Eq. (9.15) is somewhat arbitrary but the non-symmetric form of Eqs. (9.16)–(9.18) is not. However, expressing the electric and magnetic fields as gradients produces a symmetrized form that can be represented by the compact notation

$$\Sigma_{iJ} = L_{iJKl}Z_{Kl} \qquad (i,l = 1\ldots3; J,K = 1\ldots5) \tag{9.19}$$

where $\Sigma_{iJ}$ contains the elements of $\sigma_{ij}$ for $J = 1,2,3$, $D_i$ for $J = 4$, and $B_i$ when $J = 5$. Similarly, $Z_{Kl}$ contains the elements of $\varepsilon_{kl}$ for $K = 1,2,3$, $\phi_{,l}$ for $K = 4$, and $\varphi_{,l}$ when $K = 5$. Summation over the indices is conducted for $i,l = 1\ \ldots\ 3$ and $J,K = 1\ \ldots\ 5$. Then $L_{iJKl}$ is symmetric and contains the various material coefficients.

## 9.3 Eshelby Tensor and Estimates of Composite Properties

The Eshelby tensor (Eshelby 1957) relates the transformation strain of a transforming ellipsoidal inclusion to the strain experienced by the inclusion when constrained by surrounding matrix material. Thus, for an elastic, transforming medium undergoing a stress-free transformation strain (or eigenstrain) $\varepsilon_{ij}^{\mathrm{T}}$, the total strain experienced by a transforming ellipsoidal inclusion embedded in a surrounding matrix of the same material is

$$\varepsilon_{ij} = S_{ijkl}\varepsilon_{kl}^{\mathrm{T}} \tag{9.20}$$

Eshelby showed that the strain is uniform within the inclusion. The coupled problem including electrical terms (Wang 1992; Dunn and Taya 1993) and magnetic terms (Li and Dunn 1998; Li 2000) is analogous, allowing a fully coupled Eshelby tensor to be defined in the form

$$Z_{Kl} = S^{\mathrm{MEE}}_{KlMn}\, Z^{\mathrm{T}}_{Mn} \tag{9.21}$$

where the superscript MEE identifies the Eshelby tensor for magneto-electro-elastic materials. Methods for computing the components of $S^{\mathrm{MEE}}_{KlMn}$ and applications have given by several authors, following procedures analogous to those of Eshelby (Huang and Kuo 1997; Huang et al. 1998).

The significance of the Eshelby tensor for estimating the properties of composites arises because by varying the material properties and proportions of the ellipsoid, the interaction of diverse forms of composite phases with the surrounding medium can be estimated. Cylindrical fibers, spherical inclusions, and laminar platelets are all special cases of ellipsoidal inclusions. Hence, the average properties of composites can be estimated.

A simple but powerful means of estimating composite properties is provided by the *self-consistent* estimate (Hill 1965). In the case of composites of ferroic or multiferroic phases, the self-consistent estimate arises by treating each phase of the composite as an inclusion embedded in a matrix that has the average properties of the overall composite. Each individual phase (or inclusion) has its own moduli, so that locally

$$\Sigma_{iJ} = L_{iJKl} Z_{Kl} \tag{9.22}$$

while denoting volume averages over the whole composite with an overbar and the overall properties of the composite by $L^{\mathrm{o}}_{iJKl}$:

$$\overline{\Sigma}_{iJ} = L^{\mathrm{o}}_{iJKl} \overline{Z}_{Kl} \tag{9.23}$$

Any deviation $\Sigma_{iJ} - \overline{\Sigma}_{iJ}$ in the local fields is related to the corresponding deviation $Z_{Kl} - \overline{Z}_{Kl}$ using the Eshelby inclusion model. This prescribes that for ellipsoidal inclusions in a matrix with overall properties $L^{\mathrm{o}}_{iJKl}$,

$$\Sigma_{iJ} - \overline{\Sigma}_{iJ} = -L^{\mathrm{o}}_{iJKl} \left( I_{iJKl} - \left( S^{\mathrm{o}}_{KlMn} \right)^{-1} \right) \left( Z_{Kl} - \overline{Z}_{Kl} \right) = -L^{*}_{iJKl} \left( Z_{Kl} - \overline{Z}_{Kl} \right) \tag{9.24}$$

where $I_{iJKl}$ is a collection of identity tensors defined such that $\mathbf{LI} = \mathbf{IL} = \mathbf{L}$ and the inverse $\left( S^{\mathrm{o}}_{KlMn} \right)^{-1}$ is chosen such that $\mathbf{S}^{-1}\mathbf{S} = \mathbf{S}\mathbf{S}^{-1} = \mathbf{I}$. Equation (9.24) also defines the constraint tensor $L^{*}_{iJKl}$. Combining Eqs. (9.22)–(9.24) provides the relationship

$$\left( \mathbf{L} + \mathbf{L}^{*} \right) \mathbf{Z} = \left( \mathbf{L}^{\mathrm{o}} + \mathbf{L}^{*} \right) \overline{\mathbf{Z}} \tag{9.25}$$

where indices have been omitted for brevity. Hence,

$$\boldsymbol{\Sigma} = \mathbf{L}\left(\mathbf{L} + \mathbf{L}^*\right)^{-1}\left(\mathbf{L}^{\mathrm{o}} + \mathbf{L}^*\right)\overline{\mathbf{Z}} \tag{9.26}$$

Averaging over all inclusions and hence over the entire volume of the composite gives

$$\overline{\boldsymbol{\Sigma}} = \left(\overline{\mathbf{L}(\mathbf{L} + \mathbf{L}^*)^{-1}\left(\mathbf{L}^{\mathrm{o}} + \mathbf{L}^*\right)}\right)\overline{\mathbf{Z}} \tag{9.27}$$

Thus, the overall properties $\mathbf{L}^{\mathrm{o}}$of the composite could be estimated by the average

$$\mathbf{L}^{\mathrm{o}} = \overline{\mathbf{L}(\mathbf{L} + \mathbf{L}^*)^{-1}\left(\mathbf{L}^{\mathrm{o}} + \mathbf{L}^*\right)} \tag{9.28}$$

but for the inconvenient fact that both $\mathbf{L}^{\mathrm{o}}$ itself and $\mathbf{L}^*$, which depends on $\mathbf{L}^{\mathrm{o}}$ through the Eshelby tensor, appear on the right-hand side. All is not lost as $\mathbf{L}^{\mathrm{o}}$ can still be computed by using a simple first guess such as $\overline{\mathbf{L}}$ and iteration of Eq. (9.28) until a consistent set of moduli for the composite is found. This self-consistent estimate works well under a wide range of conditions.

An alternative approach, also based on the mean stress and strain fields in the composite and valued for its close relationship with bounds derived from variational approaches, is the mean field method of Mori and Tanaka (Mori and Tanaka, 1973; Weng 1990). The application to ferroic materials with magneto-electro-elastic coupling has been explored by several authors (Huang and Kuo 1997; Lee et al. 2005). The Mori–Tanaka method is generally developed for composites with an identifiable matrix within which there is a volume fraction $f$ of inhomogeneities that modify the mean fields. Consideration of the disturbance to the mean field caused by inhomogeneities leads to the estimate

$$\mathbf{L}^{\mathrm{o}} = \mathbf{L}^{\mathrm{m}}\left(\mathbf{I} + f\mathbf{V}^{-1}\left(\mathbf{L} - \mathbf{L}^{\mathrm{m}}\right)\right) \tag{9.29}$$

where $\mathbf{L}^{\mathrm{o}}$ is the overall tensor of moduli of the composite, $\mathbf{L}^{\mathrm{m}}$ and $\mathbf{L}$ are the corresponding moduli in the matrix and inhomogeneities, respectively, and $\mathbf{V}$ is given by (Huang and Kuo 1997)

$$\mathbf{V} = (1 - f)\left(\mathbf{L} - \mathbf{L}^{\mathrm{m}}\right)\mathbf{S} + \mathbf{L}^{\mathrm{m}} \tag{9.30}$$

The Mori–Tanaka method has the advantage of providing explicit expressions for the moduli of the composite and has been shown to agree well with generalized self-consistent methods and variational bounds for a range of material properties and inclusion geometries (Christensen 1990).

The estimates of the linear properties of composites discussed so far are of use for a wide range of ferroic materials and indicate, for example, that strong magnetoelectric coupling can be produced in certain composites, even when none of the individual phases has such coupling. However, these methods do not deal

with the remanent states produced by the symmetry-related ferroic crystal variants, which will be considered in the remaining sections.

## 9.4 Ferroic Crystal Variants and Domains

In a typical ferroic material, the transformation from a high-symmetry state to a lower-symmetry state with multiple, symmetry-related crystal variants produces the ferroic properties. For example, the ferroelectric barium titanate, $BaTiO_3$, has cubic perovskite crystal structure above the Curie temperature but has tetragonal structure immediately below the Curie temperature. The tetragonal state has a spontaneous polarization of each unit cell, along the crystallographic c-axis, in the absence of externally applied electric fields. Similarly, the magnetic shape memory alloy $Ni_2MnGa$ transforms from cubic to tetragonal and develops spontaneous magnetization along the c-axis. While several shape memory alloys exhibit cubic–tetragonal transformations, a wide variety of other crystal systems are found (James and Hane 2000). Among the most widely used shape memory alloys are the nickel-titanium alloys exhibiting a cubic–monoclinic transformation. Nevertheless, the tetragonal system is instructive and relatively easy to study and so will be used in examples here.

In most general terms, we can consider a ferroic material with magneto-electro-elastic linear properties and capability for all three ferroic orders, resulting in spontaneous strain, polarization, and magnetization. Pure single-phase materials with all of these properties are rare, but by developing the theory most generally the relations between the different types of materials found in practice will become evident. Let the low-symmetry phase have $N$ distinct variants, $I = 1 \ldots N$, each with its own spontaneous strain $\boldsymbol{\varepsilon}^I$, spontaneous polarization $\mathbf{P}^I$, and magnetization $\mathbf{M}^I$. Then in a region of material comprising the $I$th variant, the linear constitutive equations, Eqs. (9.16)–(9.18), can be modified to read

$$\sigma_{ij} = C_{ijkl}\left(\varepsilon_{kl} - \varepsilon_{kl}^I\right) - e_{kij}E_k - q_{kij}H_k \tag{9.31}$$

$$D_i - P_i^I = e_{ikl}\left(\varepsilon_{kl} - \varepsilon_{kl}^I\right) + \kappa_{ik}E_k + \lambda_{ik}H_k \tag{9.32}$$

$$B_i - \mu_{ik}M_k^I = q_{ikl}\left(\varepsilon_{kl} - \varepsilon_{kl}^I\right) + \lambda_{ik}E_k + \mu_{ik}H_k \tag{9.33}$$

At first sight, it may appear that the crystal variants could be randomly distributed over the volume of a ferroic crystal with free variation from unit cell to unit cell. Such a balanced distribution of spontaneous states could reduce energy by avoiding the generation of a macroscopic strain, polarization, or magnetization. However, ferroic ordering arises when, as is commonly the case, there is also an energy penalty associated with adjacent cells having different values of the spontaneous state. This energy penalty is due to elastic energy in the ferroelastic

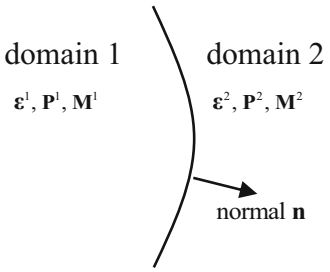


**Fig. 9.2** The interface between a pair of ferroic domains

case, dipole–dipole interaction energy for ferroelectrics, and exchange energy in magnetic materials. There is then competition between a macroscopic driving force towards a balanced average and a microscopic driving force towards uniformity. The result is the formation of *domains* that are regions of uniform spontaneous strain, polarization, or magnetization (Tagantsev et al. 2010). The size and form of these domains are determined by energetic considerations and vary greatly, but the appearance of domain patterns is so widespread as to be considered a defining feature of ferroics (Van Aken et al. 2007). Since the domains can comprise distinct crystal variants, a ferroic material can be thought of as a composite of domains.

It is instructive to consider the conditions that pertain to the interfaces between adjacent domains. These interfaces are known as *domain walls* when they separate domains within a single phase. Figure 9.2 shows an interface, which may generally be curved, with local normal direction $\mathbf{n}$, separating domains numbered 1 and 2. Then, in the absence of body forces or charges, the governing equations, Eqs. (9.1)–(9.3), imply that the local stress, electric displacement, and magnetic induction must have no jump in normal component:

$$\left(\Sigma^1_{iJ} - \Sigma^2_{iJ}\right) n_i = 0 \tag{9.34}$$

Similarly, the irrotational nature of the gradient terms requires that

$$\left(Z^1_{Kl} - Z^2_{Kl}\right) t_l = 0 \tag{9.35}$$

where $t_l$ is any vector tangent to the interface, such that $n_l t_l = 0$. Equations (9.34) and (9.35) can be used to specify *compatibility* conditions for the interface in terms of the spontaneous state of the crystal variants ($\boldsymbol{\varepsilon}^I$,$\mathbf{P}^I$,$\mathbf{M}^I$) for minimum energy. The pair of crystal variants meets with a minimum energy arrangement if the elastic stress, electric field, and magnetic field are zero in both variants. Using this condition and Eqs. (9.31)–(9.33) results in

$$\boldsymbol{\varepsilon} = \boldsymbol{\varepsilon}^I \tag{9.36}$$

$$\mathbf{D} = \mathbf{P}^I \tag{9.37}$$

$$\mathbf{B} = \boldsymbol{\mu}\mathbf{M}^I \tag{9.38}$$

meaning that each variant adopts one of the $N$ undisturbed spontaneous states.

Of course, the zero-field condition may not be possible in the presence of external loading, or there may be no spatial arrangement of the crystal variants that can achieve this condition. However, in the absence of applied loading and given that there are many possible arrangements the material might adopt, it is reasonable to suppose that Eqs. (9.36)–(9.38) may hold pointwise if there is an arrangement which allows it. This is to treat the mixture of crystal variants as a minimizer of energy. Using Eqs. (9.34) and (9.35), the consequences of Eqs. (9.36)–(9.38) may be written as

$$\left(\boldsymbol{\varepsilon}^1 - \boldsymbol{\varepsilon}^2\right) \cdot \mathbf{t} = 0 \tag{9.39}$$

$$\left(\mathbf{P}^1 - \mathbf{P}^2\right) \cdot \mathbf{n} = 0 \tag{9.40}$$

$$\left(\mathbf{M}^1 - \mathbf{M}^2\right) \cdot \mathbf{n} = 0 \tag{9.41}$$

In Eq. (9.41), it has been assumed that the magnetic permeability tensor $\boldsymbol{\mu}$ is the same in both domains; more generally, it is the product $\boldsymbol{\mu}\mathbf{M}$ whose normal component is continuous. Equation (9.39) can conveniently be rewritten in terms of the interface normal $\mathbf{n}$ as

$$\boldsymbol{\varepsilon}^1 - \boldsymbol{\varepsilon}^2 = \mathbf{n} \otimes \mathbf{a} + \mathbf{a} \otimes \mathbf{n} \tag{9.42}$$

where $\mathbf{a}$ can be chosen as any vector to satisfy the equation and $\mathbf{n} \otimes \mathbf{a}$ indicates the outer product $n_i a_j$. Equation (9.42) is the well-known Hadamard condition for continuity of displacement at an interface, and Eqs. (9.40)–(9.42) collectively provide compatibility conditions for an interface between low-energy domains in ferroic materials. The consequences of these conditions have been widely explored in the various types of ferroic material (Ball and James 1987; Bhattacharya 2003; Shu and Bhattacharya 2001; Tsou and Huber 2010; De Simone and James 2002).

It is worth noting that, in the presence of stress, electric field, and magnetic field, the invariants and principal directions of both the strain and polarization can be modified. This arises because both quantities are structural in nature, being affected by the location and arrangement of atoms or ions. Magnetization, however, typically has a fixed or very nearly fixed magnitude, determined by spin states. Then only the direction of magnetization can be varied away from one of the spontaneous states at an energy cost known as the magnetocrystalline anisotropy energy.

Suppose that the spontaneous states of the crystal variants are known. Then, for a particular pair of crystal variants meeting at an interface, Eqs. (9.40)–(9.42) specify conditions for an interface orientation that can give minimum energy of the

domains. Taking into account the symmetry of the strain tensor, Eqs. (9.40)–(9.42) provide 12 equations for the 3 components of $\mathbf{n}$, and so the problem of finding a low-energy interface is strongly overdetermined: at first sight, it may seem unlikely that any such interface can form. However, in most ferroic phases, the symmetry-related crystal variants do admit low-energy domain arrangements. It has been shown (Ball and James 1987) that Eq. (9.42) may have no solutions, or at most two distinct solutions for $\mathbf{n}$. It very often arises that one of these solutions will satisfy Eq. (9.40) or (9.41). Thus, it is often the case that ferroic domains in materials with ferroelastic ordering are separated by planar domain walls with a well-defined orientation. The case where $\boldsymbol{\varepsilon}^1 = \boldsymbol{\varepsilon}^2$, such that Eq. (9.42) is trivially satisfied for any $\mathbf{n}$, is also of importance in ferromagnetic and ferroelectric materials. Then the domain wall orientation is constrained only by Eq. (9.40) or (9.41) which is easily satisfied, giving rise to a continuous set of solutions for $\mathbf{n}$ in the plane normal to $\mathbf{P}^1 - \mathbf{P}^2$ or $\mathbf{M}^1 - \mathbf{M}^2$. The resulting domain walls are wavy, developable surfaces commonly found in both ferroelectric and ferromagnetic materials.

The domain walls themselves comprise narrow regions of material with steep gradients in some combination of strain, electrical polarization, and magnetization. They have finite width, again determined by energetic considerations. In ferroelastic and ferroelectric materials, domain walls can be almost atomically sharp and widths less than 10 nm are common. Ferromagnetic domain walls are usually thicker, 10–100 nm being typical. Provided that the domain size is much greater than this, it is common to neglect the domain wall energy, so that Eqs. (9.40)–(9.42) can be treated as the main constraint on the formation of domain patterns.

The presence of domain pairs whose domain walls have unique orientation in ferroics has far-reaching consequences. A mixture of such domains can then take on only one form, namely, alternating layers of the two crystal variants in the form of a laminate. Closer consideration of such laminates is given in Sects. 9.5 and 9.6.

For the moment, let us explore further the consequences of the kind of field-free minimum energy patterns of domains for which Eqs. (9.36)–(9.38) hold. Consider now deforming the outer surface of a body of ferroic material occupying a volume $V$ into a shape consistent with uniform straining. That is, for each point $\mathbf{x}$ on the surface, the displacement $\mathbf{u}(\mathbf{x})$ should be

$$u_i(\mathbf{x}) = \varepsilon^{\mathrm{o}}_{ij} x_j \tag{9.43}$$

for some overall imposed strain $\varepsilon^{\mathrm{o}}_{ij}$. It is easy to show that the pointwise strain then averages to $\varepsilon^{\mathrm{o}}_{ij}$, that is,

$$\overline{\varepsilon}_{ij} = \frac{1}{V}\int_V \varepsilon_{ij}(\mathbf{x})\,\mathrm{d}V = \varepsilon^{\mathrm{o}}_{ij} \tag{9.44}$$

Thus, an average strain can be imposed by controlling surface displacements. Similar arguments apply to electric field, which can be controlled using surface voltages. However, it is not straightforward to impose an average electric displacement

or magnetic induction; care must then be taken into account for the space outside $V$. In the case of electric displacement, a uniform $D_i^{\mathrm{o}}$ can be compensated at the boundary of $V$ by placing free charge on the boundary with density $D_i^{\mathrm{o}} n_i^{\mathrm{V}}$ where $n_i^{\mathrm{V}}$is the outward surface normal of $V$. The external electric displacement is then zero. However, imposing this charge density on the surface of $V$ does not guarantee $\overline{D}_i = D_i^{\mathrm{o}}$ because there could be electric fields both internal and external to $V$. This contrasts with the mechanical case, where external stresses can often be assumed to be zero. If the material can adopt a polarization state that matches $D_i^{\mathrm{o}}$ at no cost in energy, then this state minimizes energy overall by eliminating electric field. The magnetic case is less straightforward as there is no magnetic analogue for charge. An external magnetic field $H_i^{\mathrm{o}}$can be imposed outside $V$. Once again, if the material can adopt a magnetization state aligned with $H_i^{\mathrm{o}}$, this can minimize energy. There thus arises the question of what states of average strain, polarization, and magnetization can be achieved by mixtures of the crystal variants within $V$. If Eqs. (9.36)–(9.38) hold, and neglecting inhomogeneity in $\boldsymbol{\mu}$, the macroscopic strain, polarization, and magnetization are given by simple volume averages. Then, regardless of the detailed arrangement of the crystal variants, it is only their overall volume fractions $f^I$ that affect the average, giving

$$\boldsymbol{\varepsilon}^{\mathrm{o}} = \sum_{I=1}^{N} f^I \boldsymbol{\varepsilon}^I \tag{9.45}$$

$$\mathbf{P}^{\mathrm{o}} = \sum_{I=1}^{N} f^I \mathbf{P}^I \tag{9.46}$$

$$\mathbf{M}^{\mathrm{o}} = \sum_{I=1}^{N} f^I \mathbf{M}^I \tag{9.47}$$

To make the discussion more concrete, take the example of the magnetic shape memory alloy $Ni_2MnGa$. The martensitic phase has tetragonal structure with $c < a$ and magnetization aligned with the $\pm c$ axis (Webster et al. 1984; Pons et al. 2000; Kiefer and Lagoudas 2005). The variants are thus 6 in number with the spontaneous magnetization states

$$\begin{aligned} &\mathbf{M}^1 = m_0 \mathbf{e}_1; \;\; \mathbf{M}^2 = -m_0 \mathbf{e}_1; \;\; \mathbf{M}^3 = m_0 \mathbf{e}_2; \\ &\mathbf{M}^4 = -m_0 \mathbf{e}_2; \;\; \mathbf{M}^5 = m_0 \mathbf{e}_3; \;\; \mathbf{M}^6 = m_0 \mathbf{e}_3 \end{aligned} \tag{9.48}$$

where $m_0$ is the magnitude of spontaneous magnetization and $\mathbf{e}_1, \mathbf{e}_2, \mathbf{e}_3$ are unit vectors along the crystallographic axes. The corresponding spontaneous strain states are

$$\boldsymbol{\varepsilon}^1 = \boldsymbol{\varepsilon}^2 = \mathbf{I}\varepsilon_a + (\varepsilon_c - \varepsilon_a)(\mathbf{e}_1 \otimes \mathbf{e}_1) \tag{9.49}$$

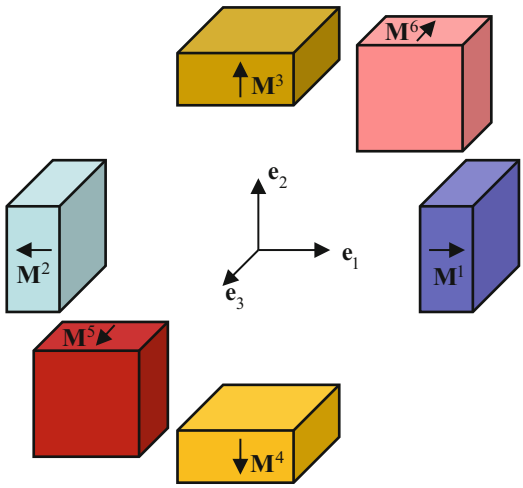


**Fig. 9.3** Tetragonal martensite variants with magnetization aligned to the *c*-axis

$$\boldsymbol{\varepsilon}^3 = \boldsymbol{\varepsilon}^4 = \mathbf{I}\varepsilon_a + (\varepsilon_c - \varepsilon_a)\,(\mathbf{e}_2 \otimes \mathbf{e}_2) \tag{9.50}$$

$$\boldsymbol{\varepsilon}^5 = \boldsymbol{\varepsilon}^6 = \mathbf{I}\varepsilon_a + (\varepsilon_c - \varepsilon_a)\,(\mathbf{e}_3 \otimes \mathbf{e}_3) \tag{9.51}$$

where $\mathbf{I}$ is the $3 \times 3$ identity matrix, $\varepsilon_a$ is the (positive) $a$-axis strain, and $\varepsilon_c$ is the (negative) $c$-axis strain. The alloy is not ferroelectric. The six variants are illustrated schematically in Fig. 9.3.

Given a macroscopic magnetization $\mathbf{M}^{\mathrm{o}}$ and strain $\boldsymbol{\varepsilon}^{\mathrm{o}}$, is there a set of volume fractions $f^I$ of the 6 variants that will achieve this average by a composite of domains? This is a constrained linear algebra problem. Due to the symmetry of strain, Eq. (9.45) provides 6 linear equations and Eq. (9.47) provides a further 3. Additionally,

$$\sum f^I = 1 \tag{9.52}$$

as the volume fractions must sum to unity, providing one further equation. Since, in the tetragonal case, the strain matrices are all diagonal in form, any off-axis terms in $\boldsymbol{\varepsilon}^{\mathrm{o}}$ must be zero. Furthermore, the variants each have the same volume of unit cell, so that $\varepsilon^{\mathrm{o}}_{11} + \varepsilon^{\mathrm{o}}_{22} + \varepsilon^{\mathrm{o}}_{33} = \varepsilon_c + 2\varepsilon_a$ is required. Assuming that these conditions on $\boldsymbol{\varepsilon}^{\mathrm{o}}$ are satisfied, there remain only two independent equations derived from Eq. (9.45), so that there are in total 6 equations for the 6 unknown $f^I$:

$$\begin{bmatrix} \varepsilon_c & \varepsilon_c & \varepsilon_a & \varepsilon_a & \varepsilon_a & \varepsilon_a \\ \varepsilon_a & \varepsilon_a & \varepsilon_c & \varepsilon_c & \varepsilon_a & \varepsilon_a \\ m_0 & -m_0 & 0 & 0 & 0 & 0 \\ 0 & 0 & m_0 & -m_0 & 0 & 0 \\ 0 & 0 & 0 & 0 & m_0 & -m_0 \\ 1 & 1 & 1 & 1 & 1 & 1 \end{bmatrix} \begin{bmatrix} f^1 \\ f^2 \\ f^3 \\ f^4 \\ f^5 \\ f^6 \end{bmatrix} = \begin{bmatrix} \varepsilon_{11}^{\mathrm{o}} \\ \varepsilon_{22}^{\mathrm{o}} \\ M_1^{\mathrm{o}} \\ M_2^{\mathrm{o}} \\ M_3^{\mathrm{o}} \\ 1 \end{bmatrix} \tag{9.53}$$

The constraint $f^I \geq 0$ must be added. The resulting system of equations has solutions provided that the prescribed macroscopic state ($\mathbf{M}^{\mathrm{o}}$, $\boldsymbol{\varepsilon}^{\mathrm{o}}$) lies within the convex hull determined by the spontaneous states of the set of variants. In the case illustrated by Eq. (9.53), a unique set of $f^I$ can be found for a given ($\mathbf{M}^{\mathrm{o}}$, $\boldsymbol{\varepsilon}^{\mathrm{o}}$), but more generally the $f^I$ may not be unique, so that a prescribed macroscopic state could be achieved with different volume fractions (see Tsou and Huber (2010) for further discussion). Of course, if ($\mathbf{M}^{\mathrm{o}}$, $\boldsymbol{\varepsilon}^{\mathrm{o}}$) is outside the convex hull, there is no solution.

What can be said about the linear elastic, electrical, and magnetic properties of the composite of domains? Knowledge of the volume fractions will provide only bounds on the various moduli, and these may be far apart; estimates could also be made using the self-consistent or Mori–Tanaka schemes. However, a specific evaluation of the moduli would require knowledge of how the domains were arranged. So we may ask: once the volume fractions are known, is there a specific arrangement of domains that satisfies the compatibility conditions? This question is discussed further in Sect. 9.5.

## 9.5 Laminates of Ferroic Crystal Variants

A mixture of two crystal variants with a unique orientation of interface normal, as shown in Fig. 9.4, is a laminate. This pattern of microstructure is widespread in ferroics, and there have been many studies of the properties of ferroic laminates (Kessler and Balke 2001; Weng and Wong 2009; Li and Liu 2004; Li and Ma 2008; De Simone and James 2002; Tsou et al. 2013) including estimates of the elastic, electrical, and magnetic moduli.

Next, following a procedure similar to that of Li and Liu (2004), consider the magneto-electro-elastic moduli of such a composite of domains. The laminate structure enforces continuity of stress, electric displacement, and magnetic induction components normal to the interfaces, as well as strain, electric field, and magnetic field components tangential to the interfaces. This allows a straightforward and exact evaluation of the moduli of the composite. First, rotate coordinates into a system where the $x_3$ coordinate axis is normal to the interface. In this coordinate system, the linear constitutive equation, Eq. (9.19), for each crystal variant, and for the composite of layers, can be rewritten in the form

$$\begin{bmatrix} \boldsymbol{\Sigma}^{\perp} \\ \boldsymbol{\Sigma}^{\parallel} \end{bmatrix} = \begin{bmatrix} \mathbf{P} & \mathbf{Q} \\ \mathbf{Q}^{\mathrm{T}} & \mathbf{R} \end{bmatrix} \begin{bmatrix} \mathbf{Z}^{\perp} \\ \mathbf{Z}^{\parallel} \end{bmatrix} \tag{9.54}$$

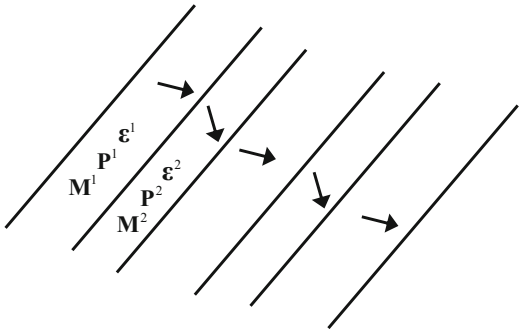


**Fig. 9.4** A laminate comprising alternating layers of two crystal variants

where $\boldsymbol{\Sigma}^{\perp} = [\sigma_{31}, \sigma_{32}, \sigma_{33}, D_3, B_3]^{\mathrm{T}}$ contains the components of $\Sigma_{iJ}$ which are continuous across the interface and thus uniform in the laminate. Meanwhile, $\boldsymbol{\Sigma}^{\parallel}$ contains the remaining components of $\Sigma_{iJ}$, which may be discontinuous at the interface. Similarly, $\mathbf{Z}^{\parallel} = [\varepsilon_{11}, \varepsilon_{22}, \varepsilon_{12}, -E_1, -E_2, -H_1, -H_2]^{\mathrm{T}}$ contains those components of $Z_{Kl}$ which are continuous across the interface and thus uniform in the laminate. The remaining components of $Z_{Kl}$ are contained in $\mathbf{Z}^{\perp}$. The various components of $L_{iJKl}$ are arranged into the sub-matrices $\mathbf{P}$, $\mathbf{Q}$, and $\mathbf{R}$, which thus contain the material moduli for a crystal variant in the rotated coordinate system. We seek corresponding moduli $\mathbf{P}^{\mathrm{o}}$, $\mathbf{Q}^{\mathrm{o}}$, and $\mathbf{R}^{\mathrm{o}}$ for the laminate. Let superscript 1 or 2 indicate the field variables in the first or second layer, respectively. Now, since $\boldsymbol{\Sigma}^{\perp 1} = \boldsymbol{\Sigma}^{\perp 2} = \boldsymbol{\Sigma}^{\perp}$ and $\mathbf{Z}^{\parallel 1} = \mathbf{Z}^{\parallel 2} = \mathbf{Z}^{\parallel}$, it can easily be shown that

$$\mathbf{Z}^{\perp} = \overline{\mathbf{P}^{-1}}\,\boldsymbol{\Sigma}^{\perp} - \overline{\mathbf{P}^{-1}\mathbf{Q}}\,\mathbf{Z}^{\parallel} \tag{9.55}$$

and

$$\boldsymbol{\Sigma}^{\parallel} = \overline{\mathbf{Q}^{\mathrm{T}}\mathbf{P}^{-1}}\,\boldsymbol{\Sigma}^{\perp} + \overline{\mathbf{R} - \mathbf{Q}^{\mathrm{T}}\mathbf{P}^{-1}\mathbf{Q}}\,\mathbf{Z}^{\parallel} \tag{9.56}$$

Overbars indicate volume averaging over the two variants in the laminate. Inverting Eq. (9.55) gives

$$\boldsymbol{\Sigma}^{\perp} = \left(\overline{\mathbf{P}^{-1}}\right)^{-1}\mathbf{Z}^{\perp} + \left(\overline{\mathbf{P}^{-1}}\right)^{-1}\overline{\mathbf{P}^{-1}\mathbf{Q}}\,\mathbf{Z}^{\parallel} \tag{9.57}$$

And substituting into Eq. (9.56) gives

$$\boldsymbol{\Sigma}^{\parallel} = \overline{\mathbf{Q}^{\mathrm{T}}\mathbf{P}^{-1}}\left(\overline{\mathbf{P}^{-1}}\right)^{-1}\mathbf{Z}^{\perp} + \left(\overline{\mathbf{Q}^{\mathrm{T}}\mathbf{P}^{-1}}\left(\overline{\mathbf{P}^{-1}}\right)^{-1}\overline{\mathbf{P}^{-1}\mathbf{Q}} + \overline{\mathbf{R} - \mathbf{Q}^{\mathrm{T}}\mathbf{P}^{-1}\mathbf{Q}}\right)\mathbf{Z}^{\parallel} \tag{9.58}$$

From Eqs. (9.57) and (9.58), the overall properties of the laminate can be identified as

$$\mathbf{P}^{\mathrm{o}} = \left(\overline{\mathbf{P}^{-1}}\right)^{-1} \tag{9.59}$$

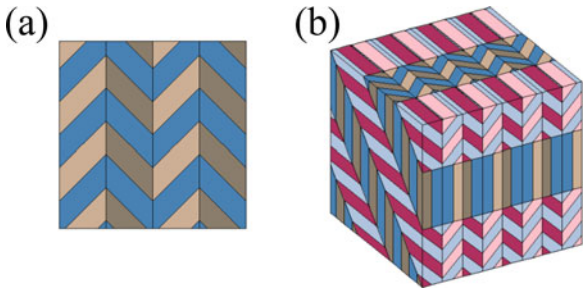


**Fig. 9.5** Laminates of (**a**) rank-2 and (**b**) rank-3. Colors indicate distinct crystal variants

$$\mathbf{Q}^{\mathrm{o}} = \left(\overline{\mathbf{P}^{-1}}\right)^{-1}\overline{\mathbf{P}^{-1}\mathbf{Q}} \tag{9.60}$$

$$\mathbf{R}^{\mathrm{o}} = \overline{\mathbf{Q}^{\mathrm{T}}\mathbf{P}^{-1}}\left(\overline{\mathbf{P}^{-1}}\right)^{-1}\overline{\mathbf{P}^{-1}\mathbf{Q}} + \overline{\mathbf{R} - \mathbf{Q}^{\mathrm{T}}\mathbf{P}^{-1}\mathbf{Q}} \tag{9.61}$$

Once $\mathbf{P}^{\mathrm{o}}$, $\mathbf{Q}^{\mathrm{o}}$, and $\mathbf{R}^{\mathrm{o}}$ are found, it is a straightforward matter to reassemble $L^{\mathrm{o}}_{iJKl}$ in the rotated coordinate system and then rotate back into global coordinates.

A remarkable feature of many ferroic crystals is that the material can form higher-rank laminates by layering together regions of simple laminate. Examples of such higher-rank laminates are illustrated in Fig. 9.5. In Fig. 9.5a, the laminate is of rank-2 and is formed by layering together two simple laminates. The more complicated example in Fig. 9.5b is of rank-3, formed by layering together two distinct laminates, each of rank-2. A cube-shaped section of the rank-3 lamination is illustrated in perspective to show the complicated three-dimensional arrangement of the layers. Using a hierarchical framework, arbitrarily complicated laminates can be analyzed mathematically. However, it is rare in practice to find laminations of rank greater than 3 in real materials.

The laminates in Fig. 9.5 show fairly coarse sub-layers within each layer for the purpose of illustration. However, the sub-layers can be much finer. If the sub-layers are many times finer than their resulting composite layers, each composite layer can be treated as a homogenized medium for the purposes of estimating overall properties. Equations (9.59)–(9.61) can then be used in a hierarchical procedure: First, an estimate is made of the homogenized properties of a lamination made of individual crystal variants. Then, several such layers are each treated as the laminae building up a more complicated lamination. In this way, it is possible to estimate the moduli of an arbitrarily complex laminate. Note that the results are now only approximate: the sub-layers would need to be of vanishing thickness to make the estimate exact.

In the context of the more complicated laminates of the kind shown in Fig. 9.5, it is of interest to explore whether the compatibility equations, Eqs. (9.40)–(9.42), can be satisfied at the many interfaces that form. By construction, it can be shown that for every macroscopic state ($\boldsymbol{\varepsilon}^{\mathrm{o}}$,$\mathbf{P}^{\mathrm{o}}$,$\mathbf{M}^{\mathrm{o}}$) that can be reached through Eqs. (9.45)–(9.47) with all volume fractions $f^I$ satisfying $\sum f^I = 1$ and $f^I \geq 0$ (i.e., for

any macroscopic state in the convex hull of the spontaneous states of the variants), there is a pattern of lamination satisfying the compatibility conditions in at least an approximate, layer-wise manner. Specifically, the compatibility conditions will be satisfied for every interface in the finest laminations, and then layer to layer, treating each composite layer as a homogenized medium with an average state ($\overline{\boldsymbol{\varepsilon}}$,$\overline{\mathbf{P}}$,$\overline{\mathbf{M}}$). A construction that achieves compatibility in this way has been given for ferroelastic martensites by Bhattacharya (1993) and readily extends to ferroelectrics (Li and Liu 2004) and ferromagnetics (De Simone and James 2002). However, the problem of finding the set of macroscopic states that can be achieved while satisfying the compatibility conditions exactly at every interface remains unsolved.

## 9.6 Applications in Polycrystalline Films

In this section, a brief discussion is given of the application of the theory of compatibility to relaxed states in freestanding polycrystalline thin films of ferroic materials. Previous sections have dealt with composites of ferroic domains with a common crystallographic orientation. In a polycrystal, the grain boundaries introduce interfaces that can have arbitrary orientation relative to the adjacent crystal lattices and also allow arbitrary relative rotations of crystal axes between grains. Typically, the compatibility constraints on grains in random polycrystals are so severe that stress-free states are unlikely and complex energy-minimizing patterns form (Bhattacharya 1993). However, in polycrystalline thin films and lamellae, the out-of-plane constraints can be relaxed, giving the material greater freedom to adopt a stress-free configuration (Shu 2000). For simplicity, the example given here neglects constraint imposed by a substrate, consistent with the situation of a freestanding, unconstrained region of thin film. The methods are readily extended to other cases. Consider, then, the problem of finding a stress-free state in a ferroic lamella extracted as a section from a polycrystalline material. The theory will be developed here with reference to ferroelastic martensite.

First, examine a junction of grains in a ferroelastic lamina. A group of $N$ such grains, $i = 1 \cdots N$, fit together around a junction in this thin lamella that is taken to lie in the $x-y$ plane. The grain boundary between pairs of grains $(i,j)$ has vector normal direction $\mathbf{n}_{ij}$ and tangential direction $\mathbf{t}_{ij}$ in the plane of the lamella. Here subscripts label only the grain numbers and are not tensorial indices—summation over repeated indices will not be implied unless stated explicitly. Each grain has its crystallographic axes rotated relative to reference $(x, y, z)$ coordinates by rotation matrix $\mathbf{R}_i$ and undergoes a transformation strain $\boldsymbol{\varepsilon}_i$ belonging to the set of stress-free spontaneous states, or mixtures of such martensitic variants. Figure 9.6 illustrates such an arrangement of grains, with reference coordinates in grain number 1. Can the resulting group of grains fit together without stress? How will the individual grains organize their microstructure to minimize energy?

Suppose that the polycrystal is initially formed above the transformation temperature, but on cooling each grain undergoes a transformation strain that is uniform on the scale of the grain (though not on finer scales), with the grain comprising a

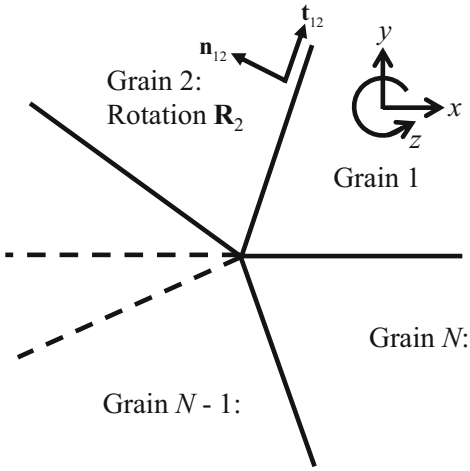


**Fig. 9.6** Configuration of grains around a junction

mixture of the stress-free transformation strains that correspond to the spontaneous states of individual crystal variants. Then the transformation strain may be written, in the local coordinates of the grain, as

$$\boldsymbol{\varepsilon}_i' = \sum_k f_{ik} \boldsymbol{\varepsilon}_k^0 \tag{9.62}$$

where $\boldsymbol{\varepsilon}_k^0$ is the transformation strain of the $k$th crystal variant and $f_{ik}$ is the volume fraction of that variant in the $i$th grain. In reference coordinates, this becomes

$$\boldsymbol{\varepsilon}_i = \sum_k f_{ik} \mathbf{R}_i \boldsymbol{\varepsilon}_k^0 \mathbf{R}_i^{\mathrm{T}} \tag{9.63}$$

Where adjacent grains meet, the compatibility condition given by Eq. (9.42),

$$\boldsymbol{\varepsilon}_i - \boldsymbol{\varepsilon}_j = \mathbf{a}_{ij} \otimes \mathbf{n}_{ij} + \mathbf{n}_{ij} \otimes \mathbf{a}_{ij} \tag{9.64}$$

can be used to ensure continuity of displacement. For materials that exhibit ferroelectricity or ferromagnetism, Eqs. (9.40) and (9.41) would also apply. Out-of-plane components of the electric displacement and magnetization may also be constrained depending on the surface conditions, or external conditions. If Eq. (9.64) is satisfied for some choice of vector $\mathbf{a}_{ij}$, then the grain boundary is a compatible interface in the stress-free state. While Eq. (9.64) is suitable for full three-dimensional constraint, the case of a thin lamella is less constrained provided that the grains are much larger than the lamellar thickness. This is because out-of-plane displacements are unconstrained. In fact, only a single displacement component is of relevance in the lamellar case: displacement in the plane of the lamella and in the direction along the grain boundary. Continuity requires no jump of displacement along the boundary as it is crossed. A condition for matching displacement components along the boundary

is achieved by considering Eq. (9.64) resolved in the $\mathbf{t}_{ij}$ direction:

$$\mathbf{t}_{ij} \cdot \left(\boldsymbol{\varepsilon}_i - \boldsymbol{\varepsilon}_j\right) \cdot \mathbf{t}_{ij} = \mathbf{t}_{ij} \cdot \left(\mathbf{a}_{ij} \otimes \mathbf{n}_{ij} + \mathbf{n}_{ij} \otimes \mathbf{a}_{ij}\right) \cdot \mathbf{t}_{ij} = 0 \tag{9.65}$$

The compatibility conditions for the grains of the lamella become a set of $N$ equations of the form

$$\mathbf{t}_{12} \cdot \boldsymbol{\varepsilon}_1 \cdot \mathbf{t}_{12} - \mathbf{t}_{12} \cdot \boldsymbol{\varepsilon}_2 \cdot \mathbf{t}_{12} = 0 \tag{9.66}$$

Defining scalar $l_{ijk}$ as the linear strain in grain $i$ along the boundary with grain $j$ due to the $k$th crystal variant,

$$l_{ijk} = \mathbf{t}_{ij} \cdot \left(\mathbf{R}_i \boldsymbol{\varepsilon}_k^0 \mathbf{R}_i^{\mathrm{T}}\right) \cdot \mathbf{t}_{ij} \tag{9.67}$$

The $N$ compatibility conditions then take the form

$$\sum_k f_{ik} l_{ijk} - f_{jk} l_{jik} = 0 \tag{9.68}$$

where only the $N$ pairings $(i,j)$ for which grain boundaries exist are included in the sum. Note that the formulation is readily extended to consider the more general problem of a group of grains in a polycrystalline lamella by allowing all $(i,j)$ pairings that represent grain boundaries present in the polycrystal. For the present problem, the equations entailed by Eqn. (9.68) form a closed chain of connections between adjacent grains around a single junction and ignore any constraint external to that group. Equation (9.68) expresses the compatibility conditions explicitly in terms of the volume fractions of the crystal variants, and the following additional constraints apply:

$$\sum_k f_{ik} = 1 \tag{9.69}$$

and

$$f_{ik} \geq 0 \tag{9.70}$$

Equation (9.69) produces $N$ linear equations, and Eq. (9.70) is a set of $mN$ inequalities in a system with $m$ crystal variants and $N$ grains. Equations (9.68) and (9.69) provide $2N$ linear relations for the $mN$ volume fractions in the individual grains. Thus, the system of linear equations is underdetermined except in the case $m = 2$. For tetragonal martensite, $m = 3$, and so there exists a space of solutions of the form

$$f_{ik} = \sum_{j=0}^{N} \alpha^j f_{ik}^j \tag{9.71}$$

with $\alpha^0 = 1$, $f_{ik}^0$ a particular solution, and the $f_{ik}^j$ $(j > 0)$ comprising a basis for the solution space. The $\alpha^j$ $(j = 1 \ldots N)$ are arbitrary and provide the $N$ degrees of freedom of the solution. By further imposing the inequality constraints, Eq. (9.70), the $\alpha^j$ values may be restricted to those that give feasible volume fractions. Uniqueness of solutions is not guaranteed and indeed is unlikely in practical examples. Note that additional closure conditions on the relative rotations of the grains have been neglected: on making a complete circuit of the central junction of grains, the final grain must meet the initial grain at the fixed initial boundary. This condition is likely to be of importance in fully three-dimensional examples such as films with grain diameter less than the film thickness, or bulk polycrystals. In a thin, unconstrained lamina, small mismatches may be accommodated by out-of-plane bending at relatively low energetic cost.

For computation, it is convenient to prepare the linear algebra problem in the form

$$\mathbf{L}\mathbf{f} = \mathbf{k}; \quad \mathbf{f} \geq 0 \tag{9.72}$$

where $\mathbf{L}$ is the $2N \times mN$ matrix of coefficients

$$\begin{bmatrix}
l_{121} & \cdots & l_{12m} & -l_{211} & \cdots & -l_{21m} & 0 & \cdots & 0 \\
0 & \cdots & 0 & l_{231} & \cdots & l_{23m} & -l_{321} & \cdots & 0 \\
\vdots & & & \ddots & & & & & \\
-l_{1N1} & \cdots & -l_{1Nm} & & & & & & l_{N1m} \\
1 & \cdots & 1 & 0 & \cdots & 0 & & \cdots & 0 \\
0 & \cdots & 0 & 1 & \cdots & 1 & & \cdots & 0 \\
\vdots & & & \ddots & & & & & \vdots \\
0 & & & & & & & \cdots & 1
\end{bmatrix} \tag{9.73}$$

while $\mathbf{f}$ and $\mathbf{k}$ are column matrices of length $mN$ and $2N$, respectively, given by

$$\mathbf{f} = \begin{bmatrix} f_{11} \\ f_{12} \\ \vdots \\ f_{1m} \\ f_{21} \\ \vdots \\ f_{Nm} \end{bmatrix}, \quad \mathbf{k} = \begin{bmatrix} 0 \\ \vdots \\ 0 \\ 1 \\ \vdots \\ 1 \end{bmatrix} \tag{9.74}$$

The first $N$ rows of Eq. (9.72) provide the compatibility equations, while rows $N+1 \cdots 2N$ ensure that the volume fractions sum to unity in each grain. Inverting this system of equations, including the inequalities in Eq. (9.72), is readily achieved using active set methods.

Calculation of example cases indicates that, for a single junction of grains and a ferroic material with more than two variants, it is normally possible to find a stress-free state. Extending this to a polycrystal with $J$ junctions, each surrounded by, on average, $N$ grains, and with $G$ grains in total, the linear equations number $JN + G$ for the $mG$ unknown volume fractions. In a large region of polycrystalline lamina, let the average number of sides on each grain be $s$ such that $J \sim Gs/N$ and $N \sim 2s/(s-2)$ on average. Then there are approximately $(s+1)/m$ equations per unknown. For realistic values of $s$ and tetragonal martensite, $m = 3$, the problem is overdetermined. Thus, stress-free states in which the microstructure is uniform within each grain are unlikely. The situation is worse in bulk polycrystals, where grains may typically have 14 neighbors. An energy-minimizing solution will then involve more complicated microstructure, wherein grains break up into regions with differing mixtures of crystal variants and hence different average states of spontaneous strain. It is commonly observed that grains in ferroic polycrystals show such microstructure, with several sub-grain regions in which bundles of domains form laminated patterns.

## 9.7 Conclusion

This chapter has presented several models of ferroic materials, treating these materials as composites comprising individual ferroic phases or crystal variants. The close analogy between the divergence-free field variables (stress, electric displacement, magnetic induction) and irrotational variables (strain, electric field, magnetic field) allows several methods from the theory of composites to be generalized easily to multiferroic materials. However, some care is needed in recognizing aspects of the ferroic orders that need distinct modeling approaches. Applications in energy-minimizing laminated composites have been described, including the exact evaluation of the moduli of hierarchical laminates and the compatibility conditions that pertain to crystals and polycrystals of ferroic materials. The methods provide a starting point for the analysis of ferroic composites and their properties.

**Acknowledgments** The author gratefully acknowledges valuable discussions and contributions from Prof. B. Kiefer, Prof. N. T. Tsou, Dr. M. Arredondo-Arechavala, and K. Holsgrove.

## References


Aizu, K.: Possible species of ferromagnetic, ferroelectric, and ferroelastic crystals. Phys. Rev. B. **2**, 754–772 (1970)

Alshits, V.I., Darinskii, A.N., Lothe, J.: On the existence of surface waves in half-infinite anisotropic elastic media with piezoelectric and piezomagnetic properties. Wave Motion. **16**, 265–283 (1992)

Ball, J.M., James, R.D.: Fine phase mixtures as minimizers of energy. Arch. Ration. Mech. Anal. **11**, 13–52 (1987)

Bhattacharya, K.: Comparison of the geometrically nonlinear and linear theories of martensitic transformation. Continuum Mech. Thermodyn. **5**, 205–242 (1993)

Bhattacharya, K.: Why it forms and how it gives rise to the shape-memory effect. In: Microstructure of Martensite. Oxford University Press, Oxford (2003)

Christensen, R.M.: A critical evaluation for a class of micro-mechanics models. J. Mech. Phys. Solids. **38**, 379–404 (1990)

De Simone, A., James, R.D.: A constrained theory of magnetoelasticity. J. Mech. Phys Solids. **50**, 283–320 (2002)

Dunn, M.L., Taya, M.: An analysis of piezoelectric composite materials containing ellipsoidal inhomogeneities. Proc. R. Soc. London A. **443**, 265–287 (1993)

Eerenstein, W., Mathur, N.D., Scott, J.F.: Multiferroic and magnetoelectric materials. Nature. **442**, 759–765 (2006)

Eshelby, J.D.: The determination of the elastic field of an ellipsoidal inclusion, and related problems. Proc. R. Soc. London A. **241**, 376–396 (1957)

Hill, R.: A self-consistent mechanics of composite materials. J. Mech. Phys. Solids. **13**, 213–222 (1965)

Huang, J.H., Kuo, W.-S.: The analysis of piezoelectric/piezomagnetic composite materials containing ellipsoidal inclusions. J. Appl. Phys. **81**, 1378–1386 (1997)

Huang, J.H., Chiu, Y.-H., Liu, H.-K.: Magneto-electro-elastic Eshelby tensors for a piezoelectric -piezomagnetic composite reinforced by ellipsoidal inclusions. J. Appl. Phys. **83**, 5364–5370 (1998)

James, R.D., Hane, K.F.: Martensitic transformations and shape-memory materials. Acta Mater. **48**, 197–222 (2000)

Kessler, H., Balke, H.: On the local and average energy release in polarization switching phenomena. J. Mech. Phys. Solids. **49**, 953–978 (2001)

Kiefer, B., Lagoudas, D.C.: Magnetic field-induced martensitic variant reorientation in magnetic shape memory alloys. Philos. Mag. **85**, 4289–4329 (2005)

Lee, J., Boyd, J.G., Lagoudas, D.C.: Effective properties of three-phase electro-magneto-elastic composites. Int. J. Eng. Sci. **43**, 790–825 (2005)

Li, J.Y.: Magnetoelectroelastic multi-inclusion and inhomogeneity problems and their applications in composite materials. Int. J. Eng. Sci. **38**, 1993–2011 (2000)

Li, J.Y., Dunn, M.L.: Anisotropic coupled-field inclusion and inhomogeneity problems. Philos. Mag. A. **77**, 1341–1350 (1998)

Li, J.Y., Liu, D.: On ferroelectric crystals with engineered domain configurations. J. Mech. Phys. Solids. **52**, 1719–1742 (2004)

Li, J.Y., Ma, Y.F.: Magnetoelastic modeling of magnetization rotation and variant rearrangement in ferromagnetic shape memory alloys. Mech. Mater. **40**, 1022–1036 (2008)

Mori, T., Tanaka, K.: Average stress in matrix and average elastic energy of materials with misfitting inclusions. Acta Metall. **21**, 571–574 (1973)

Nan, C.-W., Bichurin, M.I., Dong, S., Viehland, D., Srinivasan, G.: Multiferroic magnetoelectric composites: historical perspective, status, and future directions. J. Appl. Phys. **103**, 031101 (2008)

Pons, J., Chernenko, V.A., Santamarta, R., Cesari, E.: Crystal structure of martensitic phases in Ni-Mn-Ga shape memory alloys. Acta Mater. **48**, 3027–3038 (2000)

Schmid, H.: Multi-ferroic magnetoelectrics. Ferroelectrics. **162**, 317–338 (1994)
Shu, Y.C.: Heterogeneous thin films of martensitic materials. Arch. Ration. Mech. Anal. **153**, 39–90 (2000)
Shu, Y.C., Bhattacharya, K.: Domain patterns and macroscopic behaviour of ferroelectric materials. Philos. Mag. B. **81**, 2021–2054 (2001)
Soh, A.K., Liu, J.X.: On the constitutive equations of magnetoelectroelastic solids. J. Intell. Mater. Syst. Struct. **16**, 597–602 (2005)
Tagantsev, A.K., Cross, L.E., Fousek, J.: Domains in Ferroic Crystals and Thin Films. Springer, New York (2010)
Tsou, N.T., Huber, J.E.: Compatible domain structures and the poling of single crystal ferroelectrics. Mech. Mater. **42**, 740–753 (2010)
Tsou, N.T., Huber, J.E., Cocks, A.C.F.: Evolution of compatible laminate domain structures in ferroelectric single crystals. Acta Mater. **61**, 670–682 (2013)
Van Aken, B.B., Rivera, J.-P., Schmid, H., Fiebig, M.: Observation of ferrotoroidic domains. Nature. **449**, 702–705 (2007)
Wang, B.: Three-dimensional analysis of an ellipsoidal inclusion in a piezoelectric material. Int. J. Solids Struct. **29**, 293–308 (1992)
Webster, P.J., Ziebeck, K.R.A., Town, S.L., Peak, M.S.: Magnetic order and phase transformation in $Ni_2MnGa$. Philos. Mag. B. **49**, 295–310 (1984)
Weng, G.J.: The theoretical connection between Mori-Tanaka's theory and the Hashin-Shtrikman-Walpole bounds. Int. J. Eng. Sci. **28**, 1111–1120 (1990)
Weng, G.J., Wong, D.T.: Thermodynamic driving force in ferroelectric crystals with a rank-2 laminated domain pattern, and a study of enhanced electrostriction. J. Mech. Phys. Solids. **57**, 571–597 (2009)

# Chapter 10
# Micromechanics of Bone Modeled as a Composite Material

**Iwona Jasiuk**

**Abstract** In this chapter, we present an overview of modeling of bone as a composite material. First, we describe bone's complex hierarchical structure spanning from the nanoscale to macroscale and summarize bone's mechanical properties and biological characteristics which include self-healing, adaptation, and regeneration. Then, we summarize nanomechanics and micromechanics modeling of bone. Effective medium theories such as Mori–Tanaka, self-consistent, and generalized self-consistent methods are used to model the elastic response of bone, while a finite element method is used to more precisely account for bone architecture and to simulate inelastic effects. Challenges in bone modeling include bone's composite and hierarchical structure, lack of scale separations, scale and size effects, interfaces, porosity spanning across structural scales, and complex constitutive laws (anisotropic, nonlinear, Cosserat, time dependent, piezoelectric, poroelastic). Variability in bone properties due to the anatomic location, species, age, gender, and method of storage makes validation of theoretical models challenging. Finally, lessons learned from nature on bone structure–property relations can be applied to design stiff, strong, tough, and lightweight bioinspired materials.

## 10.1 Introduction

### *10.1.1 Characteristics of Biological Materials*

Engineers have traditionally studied materials such as metals, ceramics, polymers, and their composites. Natural, including biological, materials are another class of materials which offer new opportunities for analysis and discovery (Fratzl and Weinkamer 2007; Chen et al. 2008; Meyers et al. 2008; Meyers et al. 2011; Meyers et al. 2013). Examples of biological materials are bone, cartilage, muscle, tendon, ligament, skin, brain tissue, enamel, dentin, and others. General characteristics of

I. Jasiuk (✉)
Department of Mechanical Science and Engineering, University of Illinois at Urbana-Champaign, Urbana, IL 61801, USA
e-mail: ijasiuk@illinois.edu



S.A. Meguid, G.J. Weng (eds.), *Micromechanics and Nanomechanics of Composite Solids*, DOI 10.1007/978-3-319-52794-9_10

biological materials are that they self-assemble and self-organize from atomic level into complex hierarchical, composite, often porous, and fluid-filled structures (Cui et al. 2007; Bar-On and Wagner 2013). They are multifunctional, adapt to the environment, and can often self-heal (Meyers et al. 2008; Weinkamer and Fratzl 2011). They range from soft and highly deformable tissues such as skin to hard mineralized materials such as bone. Knowledge of biological materials is needed for various medical applications and to design new bioinspired synthetic materials (Munch et al. 2008; Studart 2012; Mirkhalaf et al. 2013; Libonati et al. 2014; Naleway et al. 2015).

### *10.1.2 Hierarchical Composite Structure of Bone*

In this chapter, we focus on the mechanics of bone. Bone is a multifunctional biological material, which has a structural role in the body by providing the frame, facilitating movement, and protecting organs. In addition, it stores minerals, manufactures blood, maintains PH of blood, and detoxifies the body. As a structural material, bone has excellent mechanical properties when healthy as it is stiff, strong, tough, and lightweight (Rho et al. 1998; Weiner and Wagner 1998; Launey et al. 2010; Ural and Vashishth 2014). In addition, by being a biological material, bone is in a constant state of remodeling as old or damaged tissues are being continuously replaced by a new bone. This allows bone to continuously change to adapt to its environment (stronger bone is built when subjected to exercise) and to self-heal (e.g., healing of bone fractures) (Weinkamer and Fratzl 2011; Zimmermann and Ritchie 2015).

The superior mechanical properties of bone are due to bone's composite and hierarchical structure (Weiner and Traub 1992; Lakes 1993; Rho et al. 1998; Olszta et al. 2007; Hamed et al. 2010, 2012a, b). Bone consists of a soft organic phase with collagen type I and non-collagenous proteins, 33–43% by volume (vol%), a stiff inorganic phase with hydroxyapatite crystals, 32–44 vol%, and water-filled pores, 15–25 vol%. Collagen and water provide bone its ductility and toughness, and minerals give it high stiffness and strength, while porosity makes it lightweight.

Bone self-assembles from atoms into a complex hierarchical structure up to a whole bone level, as shown in Fig. 10.1. In this paper, we distinguish six structural levels: macroscale, mesoscale, microscale, sub-microscale, nanoscale, and sub-nanoscale following (Rho et al. 1998; Hamed et al. 2010). These choices are not unique and other choices have been proposed in the literature (Weiner and Traub 1992; Katz et al. 2007). This is due to the fact that bone structure changes continuously with length scale, i.e., bone does not have clear scale separations.

At the macroscale, bone is made of dense cortical (also called compact) bone which forms an outer shell of whole bone and a spongy trabecular (also called cancellous) bone which fills ends of bone. Cortical bone, in the form of a hollow shaft, provides stiffness and strength and superior bending and torsion resistance while trabecular bone absorbs energy. Such structure achieves optimal structural performance while being lightweight.

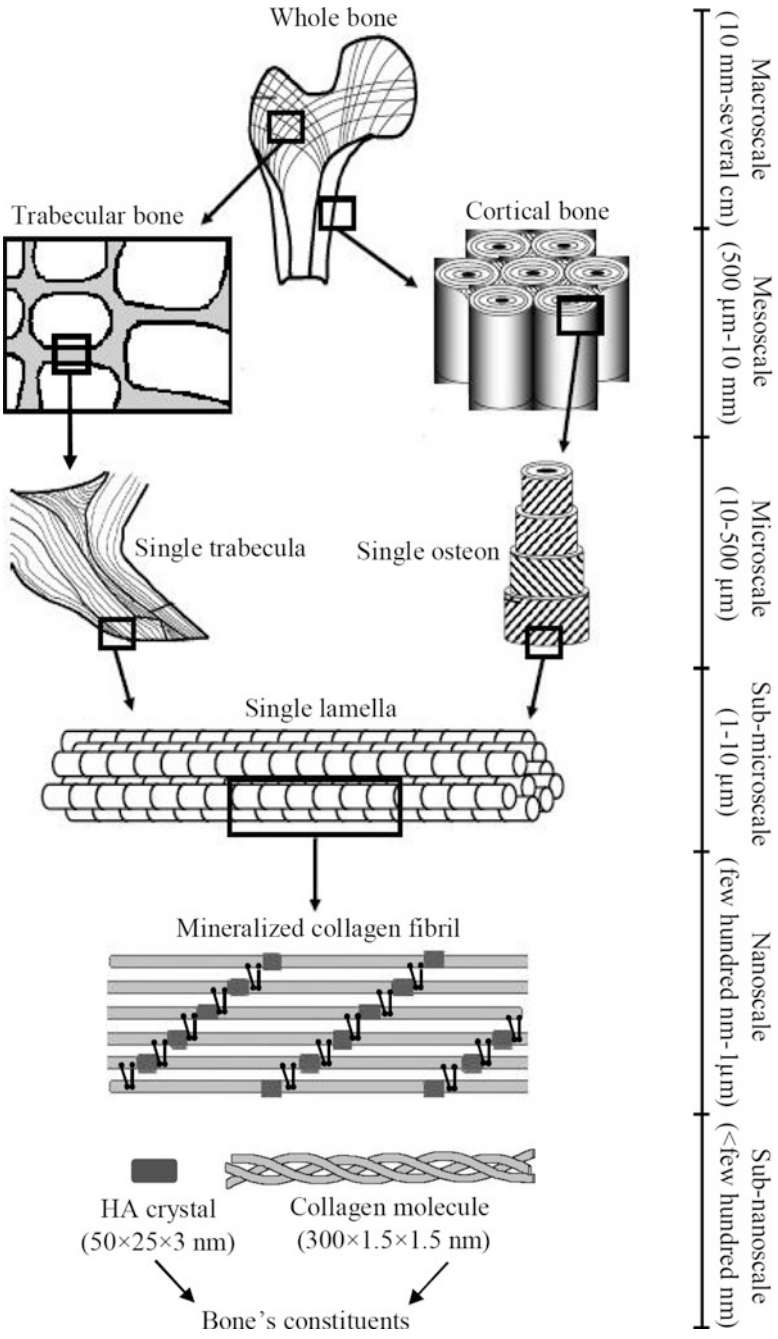


**Fig. 10.1** Hierarchical structure of bone (Hamed and Jasiuk 2013)

At the mesoscale, cortical bone (with 5–10% porosity) consists of concentric hollow cylinders, called osteons, embedded in an interstitial bone which is made of old osteons. The outer shell of cortical bone is made of softer periosteum and circumferential bone. Trabecular bone, present mainly at bone's ends, has a highly porous structure (20–95% porosity) with porosity increasing in the direction away from the cortical bone giving it a functionally graded structure. Its architecture consists of randomly arranged rodlike or platelike struts, called trabeculae, which give it a foamlike appearance.

At the microscale level, bone is made of lamellar structures, resembling those of laminated composite materials. These include osteonal, interstitial, and circumferential bone types in cortical bone and trabecular pockets forming trabecular struts in trabecular bone.

At the sub-microscale, a single lamella, which is few microns thick, is made of preferentially oriented mineralized collagen fibrils.

At the nanoscale, the mineralized collagen fibril consists of tropocollagen molecules and nanosized minerals. It is considered a basic building block of bone. The tropocollagen molecules, which have a triple-helix structure, about one nanometer (nm) in diameter and 300 nm in length, are crosslinked with each other and arranged in a staggered way with gap and overlap zones and assembled into collagen fibrils which are 50–100 nm in diameters and microns in length. The gap and overlap zones in collagen fibrils result in a characteristic banded pattern which is visible under a transmission electron microscope. The minerals are in the shape of platelets and they are about 25 nm by 50–100 nm and few nanometers thick. Crystals are believed to be infused within the gaps, to fit between collagen molecules (intrafibrillar crystals) and to form cores outside the collagen fibrils (extrafibrillar crystals). There is still a lack of consensus on the percentages of minerals within and outside the collagen fibrils and their precise arrangements. Also, the role of non-collagenous proteins is not fully understood, but it is believed that they reside at collagen–crystal and crystal–crystal interfaces. Most of the models of bone at the nanoscale assume the matrix-fiber geometry with collagen being a matrix and crystals being inclusions (Fratzl et al. 2004). More recent studies observed that bone with organic phase removed still has a self-standing structure, which implies that crystals form a continuous phase (Chen et al. 2011; Hamed et al. 2015).

### *10.1.3 Overview on Modeling of Bone*

Thus, bone is a complex natural nanocomposite material having distinct features at different structural scales. There are several geometric models proposed to represent bone at the nanoscale. Most popular is a matrix-inclusion model which assumes that isolated minerals are embedded in a collagen matrix (Fratzl et al. 2004). More recent propositions involve assumptions of bi-continuous collagen–mineral phases (Chen et al. 2011). At the sub-microscale, a single lamella can be represented as a collection of preferentially aligned fibers (mineralized collagen fibrils) and extrafibrillar minerals and pores (osteocytes

and canaliculi canals). At the microscale, bone resembles a laminated composite material forming various lamellar structures (osteonal, interstitial, and circumferential bone) and trabecular struts. At the mesoscale, cortical bone can be considered as a hybrid composite material consisting of osteons and resorption cavities embedded in an interstitial bone, while trabecular bone can be modeled as a random or periodic foam.

Various computational approaches have been proposed to model bone. They can be classified into the following four categories: (a) approximate analytical models based on strength of materials theories, (b) analytical models based on micromechanics theories, (c) computational models using mainly a finite element method, and (d) atomic level simulations utilizing molecular dynamics (Hamed and Jasiuk 2012; Sabet et al. 2016).

Each approach has its advantages and limitations. Strength of materials models are approximate and they can provide quick estimates. Micromechanical approaches involve more rigorous mechanics formulations but they also utilize simplified geometric models. They have been used to estimate the elastic properties of bone. Computational models have addressed more complex geometries and have been used to model damage, plasticity, and fracture of bone. In particular, the finite element models, using images obtained by computed and micro-computed tomography (CT and micro-CT), provide a powerful tool to account precisely for bone's complex geometries and architectures. Molecular dynamics simulations have been used to predict the mechanical properties of bone's main constituents (collagen and crystals) and to provide insights on interfaces between them.

Numerous models have been proposed for modeling of bone at different structural scales. For a review of the literature on characterization and elastic modeling of bone, the reader is referred to a recent review paper (Novitskaya et al. 2011). Elastic modeling of bone at the nanoscale is summarized in Hamed and Jasiuk (2012). Modeling of bone fracture and strength at different structural scales is summarized in Sabet et al. (2016).

In the next section, we present a hierarchical approach for modeling the elastic properties of bone. It involves successive steps spanning from the nanoscale to the mesoscale. Effective elastic properties are computed analytically at each structural level by using a "bottom-up" approach in which the effective properties computed at a lower level serve as the inputs for a next higher up level. In the analysis, we employ micromechanics theories and a classical lamination theory. $\mathbf{C}$ and $\Phi$ denote, respectively, a stiffness tensor and a volume fraction of phases. The analysis follows our formulations presented in Hamed et al. (2010, 2012a, b, 2015).

## 10.2 Elastic Hierarchical Modeling of Bone

In this section, we present a representative approach to model the elastic properties of bone in order to illustrate how micromechanics methods can be used to study this biological material. This example also provides a framework for modeling other mineralized tissues. Note that scale definitions are not unique, effective medium choices are not unique, and there are various assumptions made on bone geometry at the defined length scales. Different modeling steps are summarized in Fig. 10.2.

### *10.2.1 Nanoscale*

At the nanoscale, the mineralized collagen fibril is modeled as a bi-continuous composite material, following (Chen et al. 2011). We use a self-consistent method (Hill 1963; Budiansky 1965) to account for the two interpenetrating phases: collagen fibrils and hydroxyapatite crystals. In this model, there is no matrix and both phases are represented as inclusions. For simplicity, we assume that the bone constituents are linear elastic and isotropic. The properties used in the analysis and their volume fractions are given in Table 10.1. Note that there are a wide range of values reported in the literature as summarized in Table 1 in Hamed et al. (2010), so input choices are not unique.

Collagen fibrils are modeled as cylinders with an aspect ratio of 1000:1:1 following the dimensions reported in the literature 100 μm length and 100 nm diameter of collagen fibrils (Olszta et al. 2007; Hang and Barber 2011), while platelet-like crystals are represented as ellipsoidal inclusions with an aspect ratio of 50:25:3 (Robinson 1952) which are aligned in the direction of a long axis of the collagen fibril. Again, these aspect ratios reflect representative values. The effective stiffness tensor of a mineralized collagen fibril, $\mathbf{C}_{fib}$, is computed in terms of stiffness tensors of wet collagen, $\mathbf{C}_{wcol}$, and hydroxyapatite, $\mathbf{C}_{wHA}$, as follows:

$$\begin{aligned}\mathbf{C}_{fib} = &\Big\{ \Phi_{wcol}\mathbf{C}_{wcol} : \Big[\mathbf{I} + \mathbf{S}_{fib}^{cyl} : \mathbf{C}_{fib}^{-1} : \left(\mathbf{C}_{wcol} - \mathbf{C}_{fib}\right)\Big]^{-1} \\ &+ \Phi_{wHA}\mathbf{C}_{wHA} : \Big[\mathbf{I} + \mathbf{S}_{fib}^{ellipse} : \mathbf{C}_{fib}^{-1} : \left(\mathbf{C}_{wHA} - \mathbf{C}_{fib}\right)\Big]^{-1} \Big\} \\ &: \Big\{ \Phi_{wcol}\Big[\mathbf{I}+\mathbf{S}_{fib}^{cyl} : \mathbf{C}_{fib}^{-1} : \left(\mathbf{C}_{wcol}-\mathbf{C}_{fib}\right)\Big]^{-1} \\ &+\Phi_{wHA}\Big[\mathbf{I}+\mathbf{S}_{fib}^{ellipse} : \mathbf{C}_{fib}^{-1} : \left(\mathbf{C}_{wHA}-\mathbf{C}_{fib}\right)\Big]^{-1}\Big\}^{-1},\end{aligned} \tag{10.1}$$

**Table 10.1** Elastic properties and volume fractions of bone constituents used in modeling

| Material | Young's modulus (GPa) | Poisson's ratio | Volume fraction (%) |
|---|---|---|---|
| Collagen | 1.5 (Hall 1951; Currey 1969) | 0.28 (Nikolov and Raabe 2008) | 41 |
| Hydroxyapatite (HA) | 114 (Katz and Ukraincik 1971; Gilmore and Katz 1982) | 0.23 (Snyders et al. 2007) | 42 |
| Non-collagenous proteins (NCPs) | 1 (Nikolov and Raabe 2008) | 0.45 (Nikolov and Raabe 2008) | 4 |
| | Bulk modulus (GPa) | Poisson's ratio | Volume fraction (%) |
| Water | 2.3 | 0.49 | 13 |

where the expressions for $\mathbf{C}_{wcol}$ and $\mathbf{C}_{wHA}$ are given in the next paragraph. Subscripts in Eq. (10.1), "wcol," "HA," and "fib," represent, respectively, the wet collagen, interfibrillar hydroxyapatite, and mineralized collagen fibril. The fourth-order Eshelby tensor (Eshelby 1959) $\mathbf{S}_0^r$ accounts for the shape of phase r in a matrix with a stiffness tensor $\mathbf{C}_0$, with 0 being a generic subscript.

Furthermore, the superscripts "cyl" and "ellipse" refer to the cylindrical and ellipsoidal shapes of collagen fibrils and hydroxyapatite crystals, respectively. Note that the effective stiffness tensor of the mineralized collagen fibril, $\mathbf{C}_{fib}$, is not isotropic since hydroxyapatite crystals are assumed to be aligned in the direction of collagen fibrils. Thus, the components of the Eshelby tensor need to be evaluated numerically by considering the problem of an ellipsoidal inclusion embedded in an anisotropic matrix using the approach of Gavazzi and Lagoudas (1990). $\mathbf{C}_{fib}$ is computed by solving Eq. (10.1) iteratively, with the Eshelby tensors $\mathbf{S}_{fib}^{cyl}$ and $\mathbf{S}_{fib}^{ellipse}$ being updated at each iteration.

Water and non-collagenous proteins (NCPs) also influence the mechanical properties of bone, and solid phases are immersed in fluid (Yoon and Cowin 2008). Thus, in Eq. (10.1), we use the properties of wet collagen while the minerals are represented as a porous HA foam filled with water and NCPs (Fritsch and Hellmich 2007).

We compute the effective elastic properties of wet collagen, $\mathbf{C}_{wcol}$, following the approach of Fritsch and Hellmich (2007). More specifically, we use the Mori–Tanaka scheme (Mori and Tanaka 1973; Benveniste 1987), with the crosslinked collagen molecules modeled as a matrix and the voids (filled with water and NCPs) represented as inclusions as shown in Fig. 10.2b

$$\mathbf{C}_{wcol} = \mathbf{C}_{col} + \Phi_w \left\{ (\mathbf{C}_w - \mathbf{C}_{col}) : \left[ \mathbf{I} + \mathbf{S}_{col}^{sph} : \mathbf{C}_{col}{}^{-1} : (\mathbf{C}_w - \mathbf{C}_{col}) \right]^{-1} \right\} : \left\{ \Phi_{col}\mathbf{I} + \Phi_w \left[ \mathbf{I} + \mathbf{S}_{col}^{sph} : \mathbf{C}_{col}{}^{-1} : (\mathbf{C}_w - \mathbf{C}_{col}) \right]^{-1} \right\}^{-1}. \tag{10.2}$$

Secondly, we obtain the stiffness of the interfibrillar hydroxyapatite, $\mathbf{C}_{wHA}$, using the Mori-Tanaka method, as follows

$$\mathbf{C}_{wHA} = \mathbf{C}_{HA} + \Phi_w \left\{ (\mathbf{C}_w - \mathbf{C}_{HA}) : \left[ \mathbf{I} + \mathbf{S}_{HA}^{sph} : \mathbf{C}_{HA}{}^{-1} : (\mathbf{C}_w - \mathbf{C}_{HA}) \right]^{-1} \right\} : \left\{ \Phi_{HA}\mathbf{I} + \Phi_w \left[ \mathbf{I} + \mathbf{S}_{HA}^{sph} : \mathbf{C}_{HA}{}^{-1} : (\mathbf{C}_w - \mathbf{C}_{HA}) \right]^{-1} \right\}^{-1}. \tag{10.3}$$

In Eqs. (10.3) and (10.4), the subscripts "col," "w," and "HA" denote, respectively, the dry collagen, water and NCPs, and hydroxyapatite crystals. The superscript "sph" refers to the spherical shape of voids. Furthermore, we assume equal water volume fractions in wet collagen composite and hydroxyapatite foam. In addition, 75% of the total hydroxyapatite crystals are taken as interfibrillar and the remaining 25% are extrafibrillar (Hamed et al. 2010). Again, these choices are not unique, as there is still no clear consensus on these percentages.

The nanoscale model, presented in this section and captured in Fig. 10.2b–c, applies to both cortical and trabecular bone. Alternatively, one can use molecular dynamics, finite element method, or other micromechanics theories. A comprehensive review of literature on elastic modeling of bone at the nanoscale is presented in Hamed and Jasiuk (2012).

### *10.2.2 Sub-microscale*

At the sub-microstructural level, we use two modeling steps: (1) mineralized collagen fibrils interacting with an extrafibrillar hydroxyapatite matrix and (2) the matrix of step 1 combined with lacunar cavities to form a single lamella, following (Hamed et al. 2010).

Several experimental studies reported on the presence of extrafibrillar hydroxyapatite crystals on the outer surface of mineralized collagen fibrils (Katz and Li 1973; Prostak and Lees 1996; Sasaki and Sudoh 1997; Sasaki et al. 2002) and noted that these crystals are randomly dispersed (Lees et al. 1994; Fratzl et al. 1996; Benezra Rosen et al. 2002) (Fig. 10.3). Therefore, the extrafibrillar hydroxyapatite is modeled here as a HA foam with intercrystalline pores, filled with water and NCPs (Hellmich et al. 2004; Fritsch et al. 2006; Fritsch and Hellmich 2007; Fritsch et al. 2009). The effective stiffness tensor of this extrafibrillar foam, $\mathbf{C}_{Efoam}$, was evaluated using the self-consistent scheme with two interpenetrating phases, HA crystals and pores, as

$$\begin{aligned}\mathbf{C}_{Efoam} = &\left\{\Phi_w\mathbf{C}_w : \left[\mathbf{I} + \mathbf{S}^{sph}_{Ifoam} : \mathbf{C}^{-1}_{Ifoam} : \left(\mathbf{C}_w - \mathbf{C}_{Efoam}\right)\right]^{-1}\right.\\ &\left. + \Phi_{HA}\mathbf{C}_{HA} : \left[\mathbf{I} + \mathbf{S}^{sph}_{Ifoam} : \mathbf{C}^{-1}_{Ifoam} : \left(\mathbf{C}_{HA} - \mathbf{C}_{Efoam}\right)\right]^{-1}\right\}\\ &: \left\{\Phi_w\left[\mathbf{I} + \mathbf{S}^{sph}_{Efoam} : \mathbf{C}^{-1}_{Efoam} : \left(\mathbf{C}_w - \mathbf{C}_{Efoam}\right)\right]^{-1}\right.\\ &\left. +\Phi_{HA}\left[\mathbf{I} + \mathbf{S}^{sph}_{Efoam} : \mathbf{C}^{-1}_{Efoam} : \left(\mathbf{C}_{HA} - \mathbf{C}_{Efoam}\right)\right]^{-1}\right\}^{-1},\end{aligned} \tag{10.4}$$

where the subscript "Efoam" denotes the extrafibrillar HA foam. The resulting stiffness tensor is isotropic due to the random arrangement of extrafibrillar HA crystals in the foam. Also, for simplicity, both phases, HA crystals and voids, are assumed to be spherical in shape, following (Hellmich and Ulm 2002).

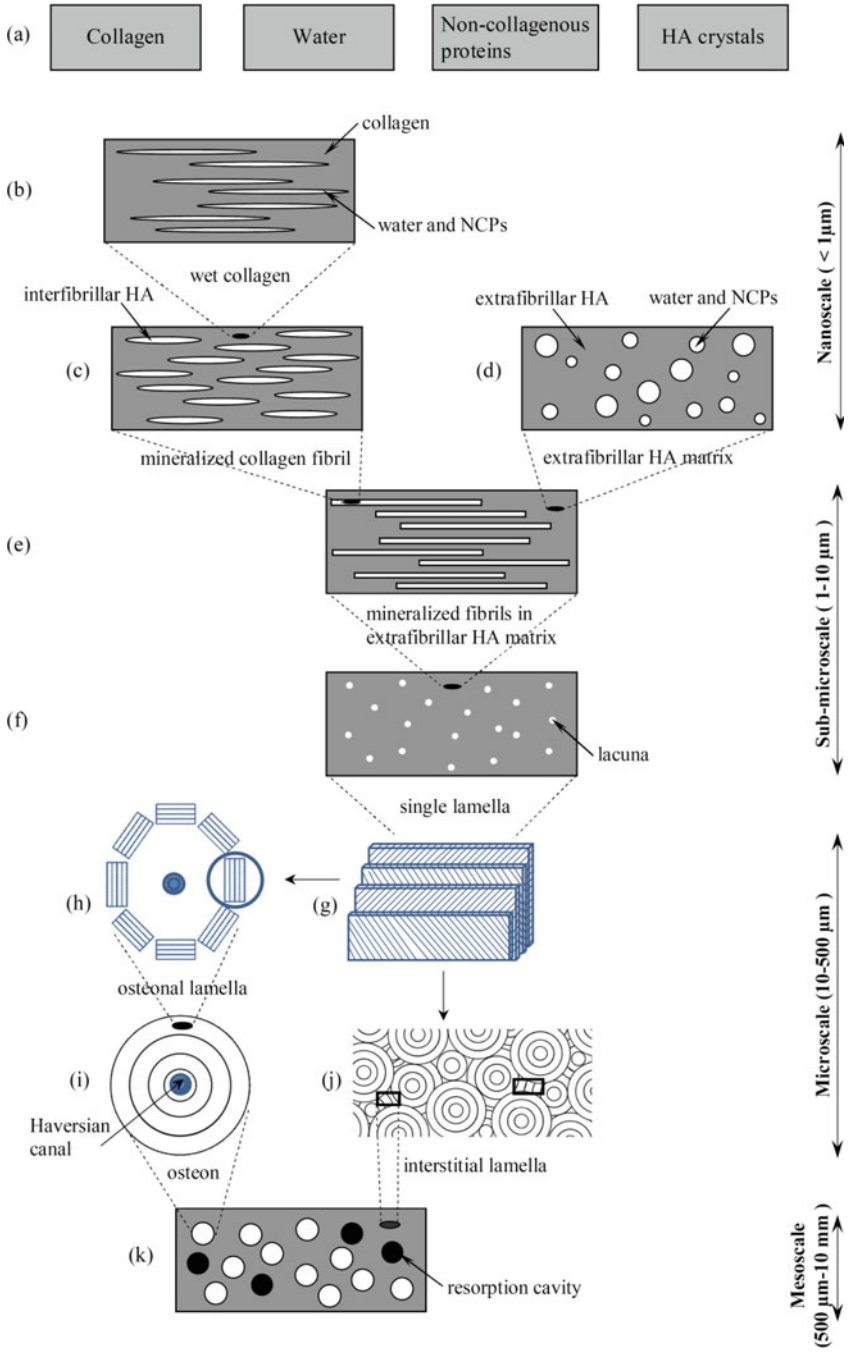


**Fig. 10.2** Homogenization steps used in modeling the elastic properties of cortical bone following Hamed et al. (2010)

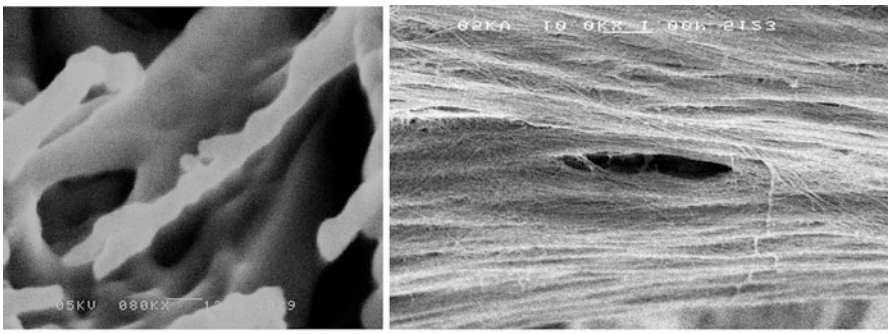


**Fig. 10.3** Scanning electron microscopy images of bone at the nanoscale and sub-microscale. (**a**) The nanoscale with a mineralized collagen fibril (length bar is 125 nm) and (**b**) the sub-microscale with single lamella with preferentially aligned mineralized collagen fibrils and a lacuna cavity which houses a bone sensing cell (osteocyte)

Mineralized collagen fibrils, with the elastic properties obtained in Eq. (10.2), and the extrafibrillar HA foam, with the elastic properties obtained in Eq. (10.5), form two bi-continuous phases, resulting in coated fibrils. The self-consistent method is used to predict the effective elastic stiffness tensor of coated fibrils, $\mathbf{C}_{cfib}$, as

$$\begin{aligned}\mathbf{C}_{cfib} = &\left\{\Phi_{fib}\mathbf{C}_{fib} : \left[\mathbf{I} + \mathbf{S}^{cyl}_{cfib} : \mathbf{C}^{-1}_{cfib} : \left(\mathbf{C}_{fib} - \mathbf{C}_{cfib}\right)\right]^{-1}\right. \\ &\left. + \Phi_{Efoam}\mathbf{C}_{Efoam} : \left[\mathbf{I} + \mathbf{S}^{sph}_{cfib} : \mathbf{C}^{-1}_{cfib} : \left(\mathbf{C}_{Efoam} - \mathbf{C}_{cfib}\right)\right]^{-1}\right\} \\ &: \left\{\Phi_{fib}\left[\mathbf{I} + \mathbf{S}^{cyl}_{cfib} : \mathbf{C}^{-1}_{cfib} : \left(\mathbf{C}_{fib} - \mathbf{C}_{cfib}\right)\right]^{-1}\right. \\ &\left. + \Phi_{Efoam}\left[\mathbf{I} + \mathbf{S}^{sph}_{cfib} : \mathbf{C}^{-1}_{cfib} : \left(\mathbf{C}_{Efoam} - \mathbf{C}_{cfib}\right)\right]^{-1}\right\}^{-1}.\end{aligned} \tag{10.5}$$

In Eq. (10.6), the subscript "cfib" denotes the coated fibrils consisting of mineralized collagen fibrils coated with the extrafibrillar HA foam. The superscripts "cyl" and "sph" denote, respectively, the cylindrical shape of fibrils and spherical shape of voids in extrafibrillar HA foam. Here again, two bi-continuous phases are assumed, modeled as two different types of inclusions and no matrix.

A single lamella is represented as a material with coated fibrils as a matrix, with properties given in Eq. (10.6), containing ellipsoidal cavities, lacunae, which house bone cells osteocytes. The subscript "lac" denotes the ellipsoidal lacunae, with an aspect ratio of 5:2:1 following their approximate $25 \times 10 \times 5$ $\mu m^3$ dimension (Remaggi et al. 1998; Yoon and Cowin 2008). The osteocytes are stimuli sensing cells in bone which play a key role in bone remodeling. The major axes of lacunae

are assumed to be oriented along the long axis of bone. The effective elastic stiffness tensor of a single lamella, $\mathbf{C}_{lamella}$, is computed by using the Mori–Tanaka scheme as

$$\mathbf{C}_{lamella} = \mathbf{C}_{cfib} + \Phi_{lac}\left\{\left(\mathbf{C}_{lac} - \mathbf{C}_{cfib}\right) : \left[\mathbf{I} + \mathbf{S}_{cfib}^{ellipse} : \mathbf{C}_{cfib}^{-1} : \left(\mathbf{C}_{lac} - \mathbf{C}_{cfib}\right)\right]^{-1}\right\} : \left\{\Phi_{cfib}\mathbf{I} + \Phi_{lac}\left[\mathbf{I} + \mathbf{S}_{cfib}^{ellipse} : \mathbf{C}_{cfib}^{-1} : \left(\mathbf{C}_{lac} - \mathbf{C}_{cfib}\right)\right]^{-1}\right\}^{-1}. \tag{10.6}$$

In our model, the effect of canaliculi on elastic properties of the single lamella is neglected. Canaliculi are canals, about 50–100 nm in diameter, which connect lacunae and form an intricate network. They transport nutrients and waste in bone.

Again, the presented model applies to cortical and trabecular bones. Other models of bone at the sub-microscale have been reported in the literature but they are rather limited. They include predictions obtained using other micromechanics approaches (Yoon and Cowin 2008), finite element models (Hamed and Jasiuk 2013), and finite element beam network method (Jasiuk and Ostoja-Starzewski 2004). They are summarized in our review paper (Novitskaya et al. 2011) and in our more recent study (Hamed et al. 2015).

In Jasiuk and Ostoja-Starzewski (2004), mineralized collagen fibrils were represented as three-dimensional Timoshenko beam finite elements as shown in Fig. 10.4a. The inputs included dimensions of rectangular cross sections of fibrils and their lengths, the fiber volume fraction, and fiber orientations. Rigid or flexible connections were assumed at fiber contacts as shown in Fig. 10.4b, and the boundary value problem was solved under displacement boundary conditions. The elastic stiffness tensor was computed by equating the elastic strain energy stored in a discrete fiber network and the energy of the approximating homogeneous medium.

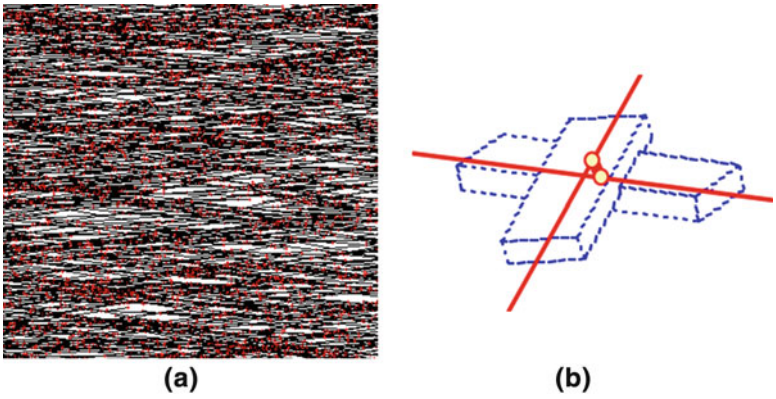


**Fig. 10.4** Finite element beam network approach to model a single lamella in bone. (**a**) Randomly oriented fibers with preferential orientation shown in *black* with fiber connections shown by *red dots* and (**b**) detail of the fiber–fiber connection (rigid or flexible)

Anisotropic stiffness tensor was obtained as a function of fiber volume fraction, aspect ratio, and orientation.

### *10.2.3 Microscale*

At the microscale level, the lamellae in bone are arranged in orthogonal, rotated, or twisted plywood-like patterns (Weiner and Wagner 1998). In our model, we consider a twisted pattern which involves continuous rotation of lamellae and use the properties obtained in Eq. (10.7). There is still no consensus in the literature on the number of lamellae and their orientations in osteons and other lamellar bone types. Also, those orientations vary spatially. In our analysis, we choose the 0° starting angle for the innermost layer and we assume that the mineralized collagen fibrils complete a 180° turn from the innermost to the outermost layer. It was reported that if the layers are not orthogonal to each other, then the angle change between successive layers does not significantly influence the results (Cheng et al. 2008).

The elastic stiffness tensor of osteonal lamella is obtained using a composite laminate theory following the approach of Sun and Li (1988) developed for laminated composite materials. Details on applying this method to an osteonal lamella are given in Hamed et al. (2010).

The properties of an interstitial lamella are obtained using the same approach as for the osteonal lamella. The interstitial bone is more mineralized than the osteons and thus more stiff (Burr et al. 1988; Guo et al. 1998). To capture such behavior, one can use a higher mineral content for an interstitial lamella as compared to an osteonal lamella (Hamed et al. 2010).

Similar approach can be used to obtain the elastic properties of lamellar bone in trabecular bone forming trabecular pockets as discussed in Hamed et al. (2012a).

Next, we compute the effective properties of an osteon forming a basic building block of cortical bone. The osteon is modeled as a hollow cylinder with the osteonal lamella being a solid part and the Haversian canal being a cylindrical void. The osteon has an outer diameter of about 250 μm and is approximately 1 cm long, while the inner diameter (Haversian canal) is approximately 50 μm (Cowin 2001). The volume fraction of the Haversian canals is about 4%. Using the elastic properties of an osteonal lamella, a generalized self-consistent method (Christensen and Lo 1979) is used to calculate the effective elastic constants of an osteon, $\mathbf{C}_{ost}$, following the approach of Dong and Guo (2006).

### *10.2.4 Mesoscale Level*

The mesoscale level represents cortical and trabecular bone levels. Here again, one can use micromechanics analysis or finite element models to model these two bone types.

First, focus on the modeling of cortical bone. The hybrid Mori–Tanaka scheme (Taya and Chou 1981), with an interstitial lamellar bone being a matrix and osteons and resorption cavities being two different types of inclusions, is used to compute the elastic stiffness tensor of cortical bone. The osteons and the resorption sites are assumed to be cylindrical in shape with an aspect ratio of 4:1:1, following the 1 cm length and 250 μm diameter of osteons (Cowin 2001), and aligned along the long axis of the bone. The volume fraction of osteons is assumed to be 70%. Resorption cavities form during bone remodeling process and in time new osteons are built in their place. The subscripts "inters," "ost," and "v" denote, respectively, the interstitial lamella, the osteons, and the voids.

Then, the transversely isotropic effective stiffness tensor of the cortical bone, $\mathbf{C}_{bone}$, is computed as

$$\begin{aligned}\mathbf{C}_{bone} = &\left\{\Phi_{inters}\mathbf{C}_{inters} + \Phi_{ost}\mathbf{C}_{ost} : \left[\mathbf{I} + \mathbf{S}^{cyl}_{inters} : \mathbf{C}^{-1}_{inters} : (\mathbf{C}_{ost} - \mathbf{C}_{inters})\right]^{-1}\right.\\ &\left. + \Phi_v\mathbf{C}_v : \left[\mathbf{I} + \mathbf{S}^{cyl}_{inters} : \mathbf{C}^{-1}_{inters} : (\mathbf{C}_v - \mathbf{C}_{inters})\right]^{-1}\right\} :\\ &\left\{\Phi_{inters} + \Phi_{ost}\left[\mathbf{I} + \mathbf{S}^{cyl}_{inters} : \mathbf{C}^{-1}_{inters} : (\mathbf{C}_{ost} - \mathbf{C}_{inters})\right]^{-1}\right.\\ &\left. + \Phi_v\left[\mathbf{I} + \mathbf{S}^{cyl}_{inters} : \mathbf{C}^{-1}_{inters} : (\mathbf{C}_v - \mathbf{C}_{inters})\right]^{-1}\right\}^{-1}.\end{aligned} \tag{10.7}$$

Trabecular bone has a random and highly porous structure with porosity ranging from 20 to over 90 vol%. Effective medium theories in general do not provide reliable estimates for materials with high porosity. Thus, alternate simplified strength of materials-based approaches have been used. For example, trabecular bone has been modeled as an idealized open-cell foam. Among other models, a simple anisotropic cell, which has a length of $l$ in $x_1$ and $x_2$ directions and a height of $h$ in the $x_3$ direction, has been used. The degree of anisotropy in such a model is defined as $D = h/l$. Young's modulus of trabecular bone in the $x_3$ direction, $E_3$, was obtained by Huber and Gibson (1988) as

$$\frac{E_3}{E_{trabecula}} = CD\left(\frac{\rho_{bone}}{\rho_{trabecula}}\right) \tag{10.8}$$

where $E_{trabecula}$ is Young's modulus of a single trabecula as obtained at the microscale, $\rho_{bone}$ and $\rho_{trabecula}$ are, respectively, densities of trabecular bone and solid trabeculae, and $C$ is a constant of proportionality. Gibson (1985) proposed two types of models for trabecular bone: an open cell (with rodlike elements) at relative densities smaller than 0.2 and a closed cell (with platelike elements) at relative densities greater than 0.2. The power $n = 2$ for an open cell and $n = 3$ for a closed cell (Gibson 1985). The relative density, $\rho_{bone}/\rho_{trabecula}$, is equal to the

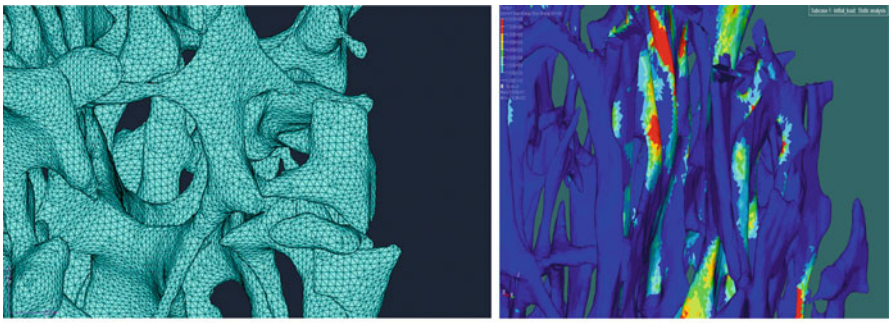


**Fig. 10.5** Finite element model of trabecular bone: (**a**) finite element mesh and (**b**) strain energy density (Hamed et al. 2012a)

bone volume fraction. Young's modulus of trabecular bone in the direction $x_1$ or $x_2$, $E_1 = E_2$, was determined as (Huber and Gibson 1988)

$$\frac{E_1}{E_3} = \frac{1 + 1/D^3}{2D^2}. \tag{10.9}$$

The modeling results obtained at this scale, namely, $E_1$ and $E_3$, represent the elastic moduli of trabecular bone. We utilized this approach for simplicity in Hamed et al. (2015).

However, the mechanical properties of trabecular bone are dependent not only on relative density but also on its architecture. Micro-computed tomography (micro-CT) is a powerful technique that can capture trabecular bone structure. This technique gave rise to micro-CT-based finite element modeling of trabecular bone. Elastic and inelastic properties have been obtained using this approach (Gross et al. 2012; Hambli 2013; Park et al. 2013; Panyasantisuk et al. 2015; Baumann et al. 2016; Gong et al. 2016; Schwiedrzik et al. 2016). An illustration of such an approach is given in Fig. 10.5 with more details in Hamed et al. (2012a).

Numerical results on effective elastic properties of bone, using a similar approach, were reported for cortical bone in Hamed et al. (2010, 2012b) and for trabecular bone in Hamed et al. (2012a, 2015). Very good agreement was found with measurements on bovine bone using experimentally obtained inputs. Cortical bone properties range from 15 to 25 GPa, depending on age, species, and anatomical location, while trabecular bone properties are much lower, ranging from 200 MPa to 1 GPa, depending on porosity.

In this section, we illustrated how micromechanics theories can be used to model the elastic properties of bone. Effective medium theories choices, selected scales, and geometric models used at each scale as well as materials inputs, which are not fully known, they all make this problem computationally and experimentally challenging.

## 10.3 Trabecular Bone Anisotropy

An important issue to consider when modeling trabecular bone is to account for its anisotropy. Trabecular bone is considered to be orthotropic. Cowin (1985) introduced a fabric tensor (second-order tensor) to capture the characteristics of microstructure of porous materials. In the formulation, it is assumed that the base material is isotropic and the anisotropy arises from the pore architecture. Cowin showed that the cases of three, two, and one distinct eigenvalues of the fabric tensor correspond to orthotropy, transverse isotropy, and isotropy of the material, respectively. This concept has been successfully applied to trabecular bone. Computation of fabric tensor allows to determine orthogonal symmetrical planes in trabecular bone. By determining those directions, the problem becomes simpler for computations as only nine elastic constants are needed to define trabecular bone properties. Fabric tensor has been incorporated in computational models of elastic stiffness tensor of bone (VanRietbergen et al. 1996; Odgaard et al. 1997; Zysset et al. 1998; Kabel et al. 1999; Homminga et al. 2003; Maquer et al. 2015; Moreno et al. 2016) and has been used to construct anisotropic yield/failure criteria in bone (Pietruszczak et al. 1999; Doblare et al. 2001; Garcia et al. 2009; Charlebois et al. 2010).

## 10.4 Modeling of Plasticity, Damage, and Fracture of Bone

Predictions of bone fracture and strength are of high scientific and clinical interest. In Sect. 10.2, we focused on the elastic properties of bone (stiffness). As mentioned in the "Introduction," bone is also strong and tough. These properties are again due to bone's composite and hierarchical structure, which includes complex architecture, various interfaces, and hierarchical porosity. There are a number of comprehensive reviews that have addressed the underlying mechanisms of bone fracture toughness and strength (Ritchie et al. 2005, 2006; Gao 2006; Gupta and Zioupos 2008; Launey et al. 2010; Ural and Vashishth 2014; Zimmermann et al. 2015).

Following Launey et al. (2010), high toughness of bone results from a mutual competition between intrinsic (local damage and plasticity) and extrinsic (crack-tip shielding) toughening mechanisms as shown in Fig. 10.6. At the sub-nanoscale, the molecular uncoiling and intermolecular sliding of tropocollagen molecules are present, and at the nanoscale, slipping at interfaces and microcracking of collagen take place within the mineralized collagen fibrils. At the sub-microscale (single lamella level), microcracking and fibrillar sliding are observed in the fibril arrays. Also, breaking of sacrificial bonds formed by non-collagenous proteins contributes to increasing the energy dissipation capacity of bone at the interface of fibril arrays, together with crack bridging by collagen fibrils. At larger length scales (the microscale and higher), the primary sources of toughening are extrinsic and they result from extensive crack deflections due to lamellar layering and

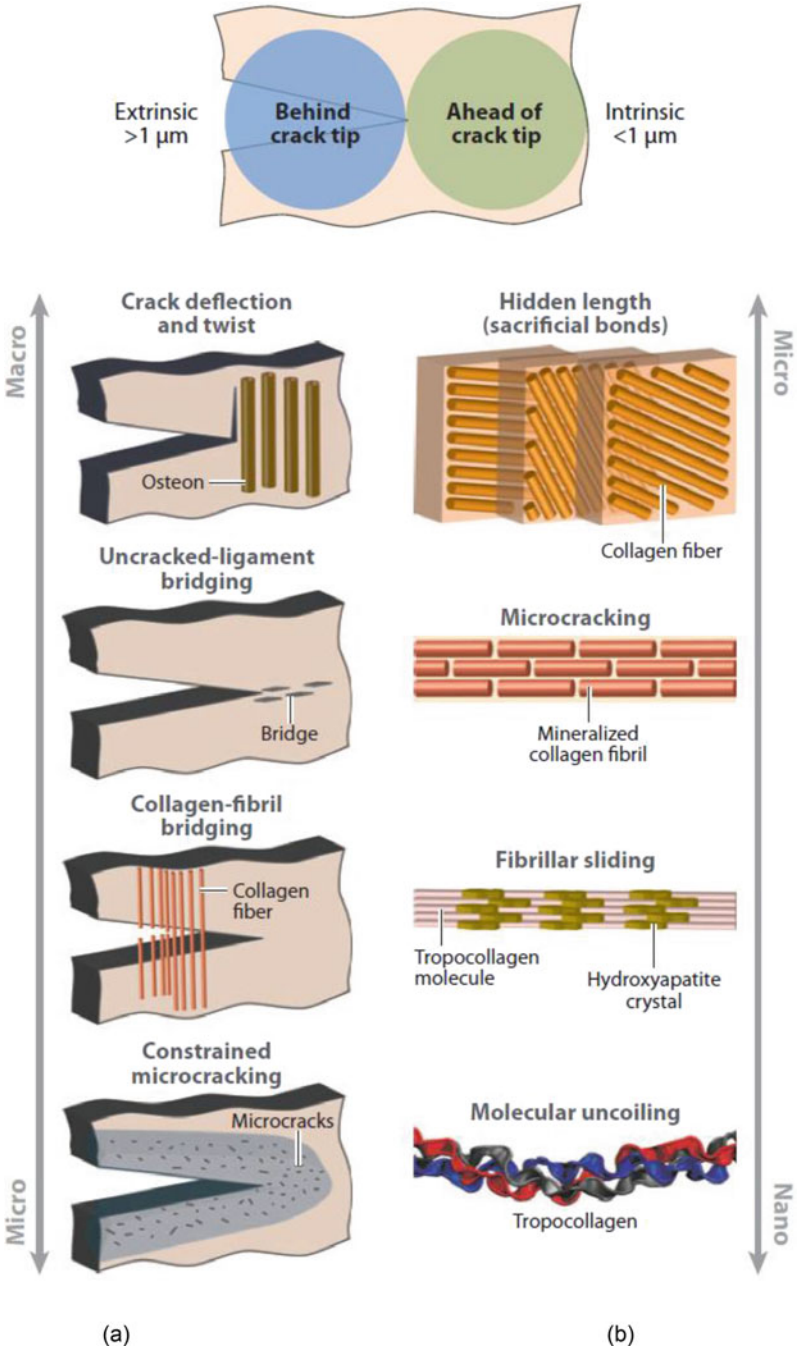


**Fig. 10.6** Bone toughness mechanism at different structural scales (Launey et al. 2010)

interfaces between them (such as cement lines around osteons) and crack bridging by uncracked ligaments. It is important to note that damage zones filled with microcracks stimulate bone remodeling, resulting in damaged bone being replaced by a newly formed bone. Such a continuous process of bone resorption and formation allows bone to adapt to new loads and create thicker bone when loads are increased. When the applied force is too large and/or bone remodeling process does not have enough time to replace new bone, the macrocracks will form resulting in the whole bone fracture.

Various models have been proposed to model bone damage, plasticity, and fracture. A comprehensive literature review on various modeling approaches applied at different structural scales is given in our recent review paper (Sabet et al. 2016). The open issues are as follows. Most of the models address only one or two structural scales, while bone fracture is a multiscale phenomenon. Also, no comprehensive multiscale models exist that address the fracture processes in bone across scales. Many studies considered idealized, two-dimensional representations of bone. Since crack initiation and growth are sensitive to microstructures, three-dimensional models would provide more accurate predictions. Also, spatial inhomogeneity and randomness are rarely accounted for, while fracture is a stochastic phenomenon. The bone structure and properties are still not fully characterized especially at smaller scales (nanoscale and below) in both healthy and diseased bone. Open issues remain on the collagen–HA crystal arrangements and interfaces. Most models assume isotropic properties for collagen and HA crystals, while these constituents are anisotropic. One reason is simplicity and the other is that the anisotropic properties are not readily available in the literature. Also, accurate constitutive laws of bone's constituents and bone at different scales up to failure are needed. Finally, insights gained from theoretical and experimental studies on bone fracture and strength should be more closely linked to clinical practice, as they have potential to provide more accurate predictions of bone fracture risk in patients. The key challenge is to be able to incorporate clinically measured parameters in the computational models. There are some exciting advances which involve patient-specific models computed using tomography images in a finite element method to predict bone stiffness and strength (Giambini et al. 2016; Rossman et al. 2016).

There are several other challenges that will be discussed next. The transition between different structural scales is continuous rather than discrete. Do we have a representative volume element (RVE) at each structural scale? Studies on the effects of scale and boundary conditions on bone properties, in particular fracture and strength, are needed.

## 10.5 Apparent Properties

In the micromechanics analyses, described in Sect. 10.2, we assumed the existence of a representative volume element (RVE). The RVE is defined as a representative region such that it is much larger than the microstructural dimensions (inclusions) and the predicted properties are independent of applied uniform

boundary conditions. However, in bone in general, we do not have an RVE. For example, at the nanoscale level, the mineralized collagen fibril is about 50–200 nm in diameter, while the size of mineral crystals is on average $50 \times 25 \times 3$ nm$^3$. Thus, these dimensions are of comparable size. This is also visible in Fig. 10.2, which illustrates collagen fibrils and HA crystals (which are the irregular shapes on collagen fibers). Another example is a trabecular bone at the mesoscale level. Trabecular bone has a spatially changing structure and porosity so only a relatively small region can be selected with constant porosity for testing or computations. Also, the trabecular bone region is limited in size. The typical dimensions of studied trabecular bone compression specimens are 2–4 mm in diameter and about twice that in height, while the voids in trabecular bone may reach up to 0.5 mm. Thus, specimen's dimensions are of comparable sizes to microstructural features (pores) and the samples are smaller than the RVE.

When the size of a specimen is smaller than the RVE size, then experimental results depend on boundary conditions and the so-called apparent properties will be measured. Similarly, computationally, when the size of a region used for computations is smaller than the RVE, then the computed results will depend on boundary conditions unless one models a periodic microstructure and applies periodic boundary conditions. However, trabecular bone, for example, has a highly irregular structure, and thus periodic boundary conditions cannot be used. One can follow the approach of Huet (1990), who showed that when the size of the specimen is smaller than the RVE, the effective properties of composite are bound from above by the properties obtained by applying kinematic (displacement with uniform strain) boundary conditions and are bound from below by the properties obtained using static (tractions with uniform stress) boundary conditions. When the size of the specimen increases, these bounds will come closer and the results will converge when the RVE size is reached.

These findings of Huet (1990) can be described mathematically as follows. The apparent elastic properties are dependent on the size of a window (or specimen size) and boundary conditions which give rise to a hierarchy of bounds

$$\boldsymbol{C}^R \equiv \left(\boldsymbol{S}^R\right)^{-1} \equiv \left\langle \boldsymbol{S}_1^t \right\rangle^{-1} \leq \left\langle \boldsymbol{S}_{\delta'}^t \right\rangle^{-1} \leq \left\langle \boldsymbol{S}_{\delta}^t \right\rangle^{-1} \leq \boldsymbol{C}^{eff} \leq \left\langle \boldsymbol{C}_{\delta}^d \right\rangle \leq \left\langle \boldsymbol{C}_{\delta'}^d \right\rangle \leq \left\langle \boldsymbol{C}_1^d \right\rangle \equiv \boldsymbol{C}^V \tag{10.10}$$

where $\forall \delta' < \delta$, $\delta = d/L$ denotes the relative size of the window, $d$ is the size of the microstructure, $L$ is the size of the window, and $\langle\rangle$denotes ensemble averages. The inequality between any two tensors implies

$$\boldsymbol{C} \geq \boldsymbol{D} \quad \Longleftrightarrow \quad (\boldsymbol{C} - \boldsymbol{D}) : a : a \geq 0, \quad \textit{for any tensor} \quad a_{ij} \neq 0$$

In Eq. (10.10), $\boldsymbol{C}$ is the fourth-order stiffness tensor $C_{ijkl}$ and $\boldsymbol{S}$ is the compliance tensor $S_{ijkl}$, where $\boldsymbol{S}^{-1} = \boldsymbol{C}$. The superscripts $R$ and $V$ denote Voigt and Reuss bounds, respectively, while the superscripts $t$ and $d$ imply traction and displacement boundary conditions, respectively. Following Eq. (10.10), the effective properties

are bounded from above and below by the apparent elastic moduli obtained using displacement and traction boundary conditions, respectively. The larger is the window size $\delta$, the closer are the bounds. When $\delta$ reaches the size of the RVE, the bounds merge and the effective properties are obtained.

Mixed boundary conditions (combination of displacements and tractions) will give apparent properties which are between the two bounds but will not give effective properties until the RVE size is reached:

$$\left\langle \boldsymbol{S}_{\delta}^{tt} \right\rangle^{-1} \leq \left\langle \boldsymbol{C}_{\delta}^{dt} \right\rangle \leq \left\langle \boldsymbol{C}_{\delta}^{dd} \right\rangle \tag{10.11}$$

Several studies addressed the apparent properties of trabecular bone both experimentally and computationally. They include experimental studies of BeVill et al. (2007) and Chevalier et al. (2007) and computational studies of Yeni and Fyhrie (2001), Wang et al. (2009), Gross et al. (2012), Park et al. (2013), Panyasantisuk et al. (2015), and Gong et al. (2016), among others.

In our exploratory computational study (Wang et al. 2009), we modeled trabecular bone, for simplicity, as two- and three-dimensional periodic networks and calculated the apparent orthotropic elastic properties of such idealized models as a function of boundary conditions (displacement, traction, and mixed), window size, and choice of a unit cell. We also obtained effective elastic moduli by applying periodic boundary conditions to obtain effective elastic stiffness tensor. We found that effective results are bound from above by the apparent elastic properties obtained using displacement boundary conditions and from below by apparent properties computed using traction boundary conditions as expected and apparent elastic mixed boundary conditions were very close to effective ones. In addition, we found that for materials like bone, which has one hard phase and one very soft phase (bone marrow, which is often modeled as void), these bounds are far apart and converge slowly. Also, the rate of convergence depends on a choice of the periodic unit cell. These results point out to challenges in obtaining effective properties of trabecular bone.

More advanced studies addressing the effects of window size and boundary conditions on apparent properties of bone, accounting for actual trabecular bone geometries, were done by Yeni and Fyhrie (2001) and Panyasantisuk et al. (2015).

## 10.6 Bone as a Cosserat Material

The concept of apparent properties which arises due to the fact that the size of tested samples or region used for computations may be smaller than the RVE was discussed in Sect. 10.5. In this section, we address a related problem. When dimensions of materials are comparable in size to the length of the microstructural features, such as pores in trabecular bone, then higher-order effects are present. Classical continuum mechanics theories do not include intrinsic length scales and

give first-order approximations for materials behavior. Higher-order continuum theories such as micropolar, strain gradient, or non-local theories aim to account for such phenomena. Micropolar theory, also called the Cosserat theory, is a generalized continuum theory in which not only a force-stress is defined (from force vector) but also a couple-stress (from moment vector) is defined. In terms of kinematics, at a point, not only a translation but also a rotation is defined. Such enriched constitutive equations allow to better capture the mechanical behavior of heterogeneous materials like bone.

First experimental evidence of bone behaving like a Cosserat material is due to Lakes and his coworkers. These experiments on bone showed a stiffening effect in bending and torsion in bone (Lakes 1982; Yang and Lakes 1982; Park and Lakes 1986), and tougher notched bone than predicted by classical fracture mechanics theory (Nakamura and Lakes 1988; Lakes et al. 1990).

Several more recent studies aimed to predict Cosserat or couple-stress (special case of Cosserat theory) constants of trabecular bone. They include studies of Yoo and Jasiuk (2006), Tekoglu and Onck (2008), Fatemi et al. (2002), Onck (2002), and Fatemi et al. (2003).

## 10.7 Bone as a Viscoelastic Material

Bone is also a viscoelastic material. Characteristics of viscoelastic materials include an increase in strain with time under a constant stress (creep), a decrease in stress with time under a constant strain (relaxation), when properties depend on rate of application of the load and when hysteresis occurs under cyclic load, when acoustic waves experience attenuation, and rebound of an object following an impact is less than 100%. The viscoelastic constitutive law accounting for time effect is given as

$$\sigma_{ij}(t) = \int_0^t C_{ijkl}\,(t-\tau)\,\frac{\partial \varepsilon_{kt}}{\partial \tau} d\tau \tag{10.12}$$

Viscoelastic constants involve storage and loss moduli. In bone viscoelastic damping, tan δ, exhibits a broad minimum at frequencies 1 to 100 Hz which are associated with normal activities. Thus, viscoelasticity is not a shock-absorbing mechanism. Interestingly, bone exhibits substantial damping at low frequencies and substantial creep at high frequencies. Tan δ has an intermediate value between that of polymers and metals (δ is 0.01 at 1–10 Hz). Viscoelasticity of bone has been studied by a number of researchers both experimentally and theoretically. These studies date back to early works of Lakes and Katz (1974a, b), and Lakes et al. (1979) as well as more recent studies (Garner et al. 2000; Buechner and Lakes 2003; Ojanen et al. 2015). Most of these papers focus on the overall viscoelastic response of bone rather than micromechanics analyses of bone. An interesting micromechanics study of viscoelasticity of fluid-filled materials like bone or concrete was done by Hellmich

and his coworkers (Eberhardsteiner et al. 2014; Shahidi et al. 2014). These studies addressed the effects of fluid-filled interfaces on viscoelastic properties of materials. In Sandino et al. (2015), they reported that "interface results in exponentially decaying macroscopic viscoelastic phenomena, with both creep and relaxation times increasing with increasing interface size and viscosity, as well as with decreasing elastic stiffness of the solid matrix; while only the relaxation time decreases with increasing interface density."

## 10.8 Conclusions

In this study, we presented an overview on micromechanics modeling of bone. This subject is broad so this study only captures selected topics in this area. Bone is a highly complex composite material, with numerous challenges to model it. There are still many open topics for mechanicians to explore.

**Acknowledgments** The author gratefully acknowledges the support from the National Science Foundation (NSF), the CMMI Program Grant 09-27909, and the DMR Program Grant 15-07169. The findings, conclusions, and recommendations expressed in this manuscript are those of the authors and do not necessarily reflect the views of the NSF.

## References

Bar-On, B., Wagner, H.D.: Structural motifs and elastic properties of hierarchical biological tissues–a review. J. Struct. Biol. **183**(2), 149–164 (2013)

Baumann, A.P., Shi, X., Roeder, R.K., Niebur, G.L.: The sensitivity of nonlinear computational models of trabecular bone to tissue level constitutive model. Comput. Methods Biomech. Biomed. Engin. **19**(5), 465–473 (2016)

Benezra Rosen, V., Hobbs, L.W., Spector, M.: The ultrastructure of anorganic bovine bone and selected synthetic hydroxyapatites used as bone graft substitute materials. Biomaterials. **23**(3), 921–928 (2002)

Benveniste, Y.: A new approach to the application of Mori-Tanaka theory in composite materials. Mech. Mater. **6**(2), 147–157 (1987)

BeVill, G., Easley, S.K., Keaveny, T.M.: Side-artifact errors in yield strength and elastic modulus for human trabecular bone and their dependence on bone volume fraction and anatomic site. J. Biomech. **40**(15), 3381–3388 (2007)

Budiansky, B.: On elastic moduli of some heterogeneous materials. J. Mech. Phys. Solids. **13**(4), 223–227 (1965)

Buechner, P.M., Lakes, R.S.: Size effects in the elasticity and viscoelasticity of bone. Biomech. Model. Mechanobiol. **1**(4), 295–301 (2003)

Burr, D.B., Schaffler, M.B., Frederickson, R.G.: Composition of the cement line and its possible mechanical role as a local interface in human compact bone. J. Biomech. **21**, 939–945 (1988)

Charlebois, M., Pretterklieber, M., Zysset, P.K.: The role of fabric in the large strain compressive behavior of human trabecular bone. J. Biomech. Eng.: Trans. ASME. **132**(12), 121006 (2010)

Chen, P.Y., Lin, A.Y.M., Lin, Y.S., Seki, Y., Stokes, A.G., Peyras, J., Olevsky, E.A., Meyers, M.A., McKittrick, J.: Structure and mechanical properties of selected biological materials. J. Mech. Behav. Biomed. Mater. **1**(3), 208–226 (2008)

Chen, P.-Y., Toroian, D., Price, P.A., McKittrick, J.: Minerals form a continuum phase in mature cancellous bone. Calcif. Tissue Int. **88**(5), 351–361 (2011)

Cheng, L., Wang, L., Karlsson, A.M.: Image analyses of two crustacean exoskeletons and implications of the exoskeletal microstructure on the mechanical behavior. J. Mater. Res. **23**, 2854–2872 (2008)

Chevalier, Y., Pahr, D., Allmer, H., Charlebois, M., Zysset, P.: Validation of a voxel-based FE method for prediction of the uniaxial apparent modulus of human trabecular bone using macroscopic mechanical tests and nanoindentation. J. Biomech. **40**(15), 3333–3340 (2007)

Christensen, R.M., Lo, K.H.: Solutions for effective shear properties in three phases sphere and cylinder models. J. Mech. Phys. Solids. **27**, 315–330 (1979)

Cowin, S.C.: The relationship between the elasticity tensor and the fabric tensor. Mech. Mater. **4**(2), 137–147 (1985)

Cowin, S.C.: Bone Mechanics Handbook. CRC Press, Boca Raton (2001)

Cui, F.-Z., Li, Y., Ge, J.: Self-assembly of mineralized collagen composites. Mater. Sci. Eng. R. **57**(1-6), 1–27 (2007)

Currey, J.D.: Relationship between stiffness and mineral content of bone. J. Biomech. **2**(4), 477–480 (1969)

Doblare, M., Garcia, J.M., Gracia, L.: An anisotropic bone remodelling model based on continuum damage mechanics (2001)

Dong, X.N., Guo, X.E.: Prediction of cortical bone elastic constants by a two-level micromechanical model using a generalized self-consistent method. J. Biomech. Eng. **128**, 309–316 (2006)

Eberhardsteiner, L., Hellmich, C., Scheiner, S.: Layered water in crystal interfaces as source for bone viscoelasticity: arguments from a multiscale approach. Comput. Methods Biomech. Biomed. Engin. **17**(1), 48–63 (2014)

Eshelby, J.D.: The elastic field outside an ellipsoidal inclusion. Proc. R. Soc. London A. **252**, 561–569 (1959)

Fatemi, J., Van Keulen, F., Onck, P.R.: Generalized continuum theories: application to stress analysis in bone. Meccanica. **37**(4–5), 385–396 (2002)

Fatemi, J., Onck, P.R., Poort, G., Van Keulen, F.: Cosserat moduli of anisotropic cancellous bone: a micromechanical analysis. J. Phys. IV. **105**, 273–280 (2003)

Fratzl, P., Weinkamer, R.: Nature's hierarchical materials. Prog. Mater. Sci. **52**(8), 1263–1334 (2007)

Fratzl, P., Schreiber, S., Boyde, A.: Characterization of bone mineral crystals in horse radius by small-angle X-ray scattering. Calcif. Tissue Int. **58**(5), 341–346 (1996)

Fratzl, P., Gupta, H.S., Paschalis, E.P., Roschger, P.: Structure and mechanical quality of the collagen-mineral nano-composite in bone. J. Mater. Chem. **14**(14), 2115–2123 (2004)

Fritsch, A., Hellmich, C.: 'Universal' microstructural patterns in cortical and trabecular, extracellular and extravascular bone materials: micromechanics-based prediction of anisotropic elasticity. J. Theor. Biol. **244**(4), 597–620 (2007)

Fritsch, A., Dormieux, L., Hellmich, C.: Porous polycrystals built up by uniformly and axisymmetrically oriented needles: homogenization of elastic properties. C R Mec. **334**, 151–157 (2006)

Fritsch, A., Hellmich, C., Dormieux, L.: Ductile sliding between mineral crystals followed by rupture of collagen crosslinks: experimentally supported micromechanical explanation of bone strength. J. Theor. Biol. **260**, 230–252 (2009)

Gao, H.: Application of fracture mechanics concepts to hierarchical biomechanics of bone and bone-like materials. Int. J. Fract. **138**(1–4), 101–137 (2006)

Garcia, D., Zysset, P.K., Charlebois, M., Curnier, A.: A three-dimensional elastic plastic damage constitutive law for bone tissue. Biomech. Model. Mechanobiol. **8**(2), 149–165 (2009)

Garner, E., Lakes, R., Lee, T., Swan, C., Brand, R.: Viscoelastic dissipation in compact bone: implications for stress-induced fluid flow in bone. J. Biomech. Eng.: Trans. ASME. **122**(2), 166–172 (2000)

Gavazzi, A.C., Lagoudas, D.C.: On the numerical evaluation of Eshelby's tensor and its application to elastoplastic fibrous composites. Comput. Mech. **7**(1), 13–19 (1990)
Giambini, H., Qin, X., Dragomir-Daescu, D., An, K.-N., Nassr, A.: Specimen-specific vertebral fracture modeling: a feasibility study using the extended finite element method. Med. Biol. Eng. Comput. **54**(4), 583–593 (2016)
Gibson, L.J.: The mechanical behavior of cancellous bone. J. Biomech. **18**(5), 317–328 (1985)
Gilmore, R.S., Katz, J.L.: Elastic properties of apatites. J. Mater. Sci. **17**(4), 1131–1141 (1982)
Gong, H., Wang, L., Fan, Y., Zhang, M., Qin, L.: Apparent- and tissue-level yield behaviors of L4 vertebral trabecular bone and their associations with microarchitectures. Ann. Biomed. Eng. **44**(4), 1204–1223 (2016)
Gross, T., Pahr, D.H., Peyrin, F., Zysset, P.K.: Mineral heterogeneity has a minor influence on the apparent elastic properties of human cancellous bone: a SR mu CT-based finite element study. Comput. Methods Biomech. Biomed. Engin. **15**(11), 1137–1144 (2012)
Guo, X.E., Liang, L.C., Goldstein, S.A.: Micromechanics of osteonal cortical bone fracture. J. Biomech. Eng. **120**, 112–117 (1998)
Gupta, H.S., Zioupos, P.: Fracture of bone tissue: the 'hows' and the 'whys'. Med. Eng. Phys. **30**(10), 1209–1226 (2008)
Hall, R.H.: Variations with pH of the tensile properties of collagen fibres. J. Soc. Leather Trades Chem. **35**, 195–210 (1951)
Hambli, R.: Micro-CT finite element model and experimental validation of trabecular bone damage and fracture. Bone. **56**(2), 363–374 (2013)
Hamed, E., Jasiuk, I.: Elastic modeling of bone at nanostructural level. Mater. Sci. Eng. R. **73**(3–4), 27–49 (2012)
Hamed, E., Jasiuk, I.: Multiscale damage and strength of lamellar bone modeled by cohesive finite elements. J. Mech. Behav. Biomed. Mater. **28**, 94–110 (2013)
Hamed, E., Lee, Y., Jasiuk, I.: Multiscale modeling of elastic properties of cortical bone. Acta Mech. **213**(1–2), 131–154 (2010)
Hamed, E., Jasiuk, I., Yoo, A., Lee, Y., Liszka, T.: Multi-scale modelling of elastic moduli of trabecular bone. J. R. Soc. Interface. **9**(72), 1654–1673 (2012a)
Hamed, E., Novitskaya, E., Li, J., Chen, P.Y., Jasiuk, I., McKittrick, J.: Elastic moduli of untreated, demineralized and deproteinized cortical bone: validation of a theoretical model of bone as an interpenetrating composite material. Acta Biomater. **8**(3), 1080–1092 (2012b)
Hamed, E., Novitskaya, E., Li, J., Jasiuk, I., McKittrick, J.: Experimentally-based multiscale model of the elastic moduli of bovine trabecular bone and its constituents. Mater. Sci. Eng. C. **54**, 207–216 (2015)
Hang, F., Barber, A.H.: Nano-mechanical properties of individual mineralized collagen fibrils from bone tissue. J. R. Soc. Interface. **8**, 500–505 (2011)
Hellmich, C., Ulm, F.J.: Micromechanical model for ultrastructural stiffness of mineralized tissues. J. Eng. Mech. **128**, 898–908 (2002)
Hellmich, C., Barthelemy, J.F., Dormieux, L.: Mineral-collagen interactions in elasticity of bone ultrastructure—a continuum micromechanics approach. Eur. J. Mech. A. **23**(5), 783–810 (2004)
Hill, R.: Elastic properties of reinforced solids- Some theoretical principles. J. Mech. Phys. Solids. **11**(5), 357–372 (1963)
Homminga, J., McCreadie, B.R., Weinans, H., Huiskes, R.: The dependence of the elastic properties of osteoporotic cancellous bone on volume fraction and fabric. J. Biomech. **36**(10), 1461–1467 (2003)
Huber, A.T., Gibson, L.J.: Anisotropy of foams. J. Mater. Sci. **23**, 3031–3040 (1988)
Huet, C.: Application of variational concepts to size effects in elastic heterogeneous bodies. J. Mech. Phys. Solids. **38**, 813–841 (1990)
Jasiuk, I., Ostoja-Starzewski, M.: Modeling of bone at a single lamella level. Biomech. Model. Mechanobiol. **3**(2), 67–74 (2004)
Kabel, J., van Rietbergen, B., Odgaard, A., Huiskes, R.: Constitutive relationships of fabric, density, and elastic properties in cancellous bone architecture. Bone. **25**(4), 481–486 (1999)

Katz, E.P., Li, S.: Structure and function of bone collagen fibrils. J. Mol. Biol. **80**(1), 1–15 (1973)
Katz, J.L., Ukraincik, K.: On the anisotropic elastic properties of hydroxyapatite. J. Biomech. **4**(3), 221–227 (1971)
Katz, J.L., Misra, A., Spencer, P., Wang, Y., Bumrerraj, S., Nomura, T., Eppell, S.J., Tabib-Azar, M.: Multiscale mechanics of hierarchical structure/property relationships in calcified tissues and tissue/material interfaces. Mater. Sci. Eng. C. **27**(3), 450–468 (2007)
Lakes, R.S.: Dynamical study of couple stress effects in human compact bone. J. Biomech. Eng.: Trans. ASME. **104**(1), 6–11 (1982)
Lakes, R.: Materials with structural hierarchy. Nature. **361**(6412), 511–515 (1993)
Lakes, R.S., Katz, J.L.: Interrelationship among viscoelastic functions for anisotropic solids–applications to calcified tissues and related systems. J. Biomech. **7**(3), 259–270 (1974a)
Lakes, R.S., Katz, J.L.: Transformation of the viscoelastic functions of calcified tissues and interfacial bio materials into a common representation. J. Biol. Phys. **2**(4), 193–204 (1974b)
Lakes, R.S., Katz, J.L., Sternstein, S.S.: Viscoelastic properties of wet cortical bone: 1. Torsional and biaxial studies. J. Biomech. **12**(9), 657 (1979)
Lakes, R.S., Nakamura, S., Behiri, J.C., Bonfield, W.: Fracture mechanics of bone with short cracks. J. Biomech. **23**(10), 967–975 (1990)
Launey, M.E., Buehler, M.J., Ritchie, R.O.: On the mechanistic origins of toughness in bone. Annu. Rev. Mater. Res. **40**, 25–53 (2010)
Lees, S., Prostak, K.S., Ingle, V.K., Kjoller, K.: The loci of mineral in turkey leg tendon as seen by atomic-force microscope and electron microscopy. Calcif. Tissue Int. **55**(3), 180–189 (1994)
Libonati, F., Colombo, C., Vergani, L.: Design and characterization of a biomimetic composite inspired to human bone. Fatigue Fract. Eng. Mater. Struct. **37**(7), 772–781 (2014)
Maquer, G., Musy, S.N., Wandel, J., Gross, T., Zysset, P.K.: Bone volume fraction and fabric anisotropy are better determinants of trabecular bone stiffness than other morphological variables. J. Bone Miner. Res. **30**(6), 1000–1008 (2015)
Meyers, M.A., Chen, P.-Y., Lin, A.Y.-M., Seki, Y.: Biological materials: structure and mechanical properties. Prog. Mater. Sci. **53**(1), 1–206 (2008)
Meyers, M.A., Chen, P.-Y., Lopez, M.I., Seki, Y., Lin, A.Y.M.: Biological materials: a materials science approach. J. Mech. Behav. Biomed. Mater. **4**(5), 626–657 (2011)
Meyers, M.A., McKittrick, J., Chen, P.-Y.: Structural biological materials: critical mechanics-materials connections. Science. **339**(6121), 773–779 (2013)
Mirkhalaf, M., Zhu, D., Barthelat, F.: Biomimetic hard materials. Engineered Biomimicry, Elsevier, pp. 59–79 (2013)
Moreno, R., Smedby, O., Pahr, D.H.: Prediction of apparent trabecular bone stiffness through fourth-order fabric tensors. Biomech. Model. Mechanobiol. **15**(4), 831–844 (2016)
Mori, T., Tanaka, K.: Average stress in matrix and average elastic energy of materials with misfitting inclusions. Acta Metall. **21**(5), 571–574 (1973)
Munch, E., Launey, M.E., Alsem, D.H., Saiz, E., Tomsia, A.P., Ritchie, R.O.: Tough, bio-inspired hybrid materials. Science. **322**(5907), 1516–1520 (2008)
Nakamura, S., Lakes, R.S.: Finite element analysis of stress concentration around a blunt crack in a Cosserat elastic solid. Comput. Methods Appl. Mech. Eng. **66**(3), 257–266 (1988)
Naleway, S.E., Porter, M.M., McKittrick, J., Meyers, M.A.: Structural design elements in biological materials: application to bioinspiration. Adv. Mater. **27**(37), 5455–5476 (2015)
Nikolov, S., Raabe, D.: Hierarchical modeling of the elastic properties of bone at submicron scales: the role of extrafibrillar mineralization. Biophys. J. **94**(11), 4220–4232 (2008)
Novitskaya, E.E., Chen, P.-Y., Hamed, E., Li, J., Lubarda, V., Jasiuk, I., McKittrick, J.: Recent advances on the measurement and calculation of the elastic moduli of cortical and trabecular bone: a review. Theor. Appl. Mech. J. **38**(3), 209–303 (2011)
Odgaard, A., Kabel, J., vanRietbergen, B., Dalstra, M., Huiskes, R.: Fabric and elastic principal directions of cancellous bone are closely related. J. Biomech. **30**(5), 487–495 (1997)
Ojanen, X., Isaksson, H., Toyras, J., Turunen, M.J., Malo, M.K.H., Halvari, A., Jurvelin, J.S.: Relationships between tissue composition and viscoelastic properties in human trabecular bone. J. Biomech. **48**(2), 269–275 (2015)

Olszta, M.J., Cheng, X.G., Jee, S.S., Kumar, R., Kim, Y.Y., Kaufman, M.J., Douglas, E.P., Gower, L.B.: Bone structure and formation: a new perspective. Mater. Sci. Eng. R. **58**(3–5), 77–116 (2007)

Onck, P.R.: Cosserat modeling of cellular solids. C. R. Mec. **330**(11), 717–722 (2002)

Panyasantisuk, J., Pahr, D.H., Gross, T., Zysset, P.K.: Comparison of mixed and kinematic uniform boundary conditions in homogenized elasticity of femoral trabecular bone using microfinite element analyses. J. Biomech. Eng. **137**(1), 011002 (2015)

Park, H.C., Lakes, R.S.: Cosserat micromechanics of human bone–strain redistribution by a hydration sensitive constituent. J. Biomech. **19**(5), 385–397 (1986)

Park, S., Chae, S.-W., Park, J., Han, S.-H., Hong, J., Kim, Y.E.: Finite element modeling to estimate the apparent material properties of trabecular bone. Int. J. Precis. Eng. Manuf. **14**(8), 1479–1485 (2013)

Pietruszczak, S., Inglis, D., Pande, G.N.: A fabric-dependent fracture criterion for bone. J. Biomech. **32**(10), 1071–1079 (1999)

Prostak, K.S., Lees, S.: Visualization of crystal-matrix structure. In situ demineralization of mineralized turkey leg tendon and bone. Calcif. Tissue Int. **59**(6), 474–479 (1996)

Remaggi, F., Cane, V., Palumbo, C., Ferretti, M.: Histomorphometric study on the osteocyte lacuno-canalicular network in animals of different species. I. Woven-fibered and parallel fibered bones. Ital. J. Anat. Embryol. **103**, 145–155 (1998)

Rho, J.-Y., Kuhn-Spearing, L., Zioupos, P.: Mechanical properties and the hierarchical structure of bone. Med. Eng. Phys. **20**(2), 92–102 (1998)

Ritchie, R.O., Kinney, J.H., Kruzic, J.J., Nalla, R.K.: A fracture mechanics and mechanistic approach to the failure of cortical bone. Fatigue Fract. Eng. Mater. Struct. **28**(4), 345–371 (2005)

Ritchie, R.O., Nalla, R.K., Kruzic, J.J., Ager III, J.W., Balooch, G., Kinney, J.H.: Fracture and ageing in bone: toughness and structural characterization. Strain. **42**(4), 225–232 (2006)

Robinson, R.: An electron microscopic study of the crystalline inorganic component of bone and its relationship to the organic matrix. J. Bone Joint Surg. **344**, 389–435 (1952)

Rossman, T., Kushvaha, V., Dragomir-Daescu, D.: QCT/FEA predictions of femoral stiffness are strongly affected by boundary condition modeling. Comput. Methods Biomech. Biomed. Engin. **19**(2), 208–216 (2016)

Sabet, F.A., Najafi, A.R., Hamed, E., Jasiuk, I.: Modelling of bone fracture and strength at different length scales: a review. Interface Focus. **6**(1), 20150055 (2016)

Sandino, C., McErlain, D.D., Schipilow, J., Boyd, S.K.: The poro-viscoelastic properties of trabecular bone: a micro computed tomography-based finite element study. J. Mech. Behav. Biomed. Mater. **44**, 1–9 (2015)

Sasaki, N., Sudoh, Y.: X-ray pole figure analysis of apatite crystals and collagen molecules in bone. Calcif. Tissue Int. **60**(4), 361–367 (1997)

Sasaki, N., Tagami, A., Goto, T., Taniguchi, M., Nakata, M., Hikichi, K.: Atomic force microscopic studies on the structure of bovine femoral cortical bone at the collagen fibril-mineral level. J. Mater. Sci. Mater. Med. **13**(3), 333–337 (2002)

Schwiedrzik, J., Gross, T., Bina, M., Pretterklieber, M., Zysset, P., Pahr, D.: Experimental validation of a nonlinear FE model based on cohesive-frictional plasticity for trabecular bone. Int. J. Numer. Methods Biomed. Eng. **32**(4), e02739 (2016)

Shahidi, M., Pichler, B., Hellmich, C.: Viscous interfaces as source for material creep: a continuum micromechanics approach. Eur. J. Mech. A: Solids. **45**, 41–58 (2014)

Snyders, R., Music, D., Sigumonrong, D., Schelnberger, B., Jensen, J., Schneider, J.M.: Experimental and ab initio study of the mechanical properties of hydroxyapatite. Appl. Phys. Lett. **90**(19), 193902 (2007)

Studart, A.R.: Towards High-Performance Bioinspired Composites. Adv. Mater. **24**(37), 5024–5044 (2012)

Sun, C.T., Li, S.: Three-dimensional effective elastic constants for thick laminates. J. Compos. Mater. **22**, 629–639 (1988)

Taya, M., Chou, T.W.: On two kinds of ellipsoidal inhomogeneities in an infinite elastic body: an application to a hybrid composite. Int. J. Solids Struct. **17**, 553–563 (1981)
Tekoglu, C., Onck, P.R.: Size effects in two-dimensional Voronoi foams: a comparison between generalized continua and discrete models. J. Mech. Phys. Solids. **56**(12), 3541–3564 (2008)
Ural, A., Vashishth, D.: Hierarchical perspective of bone toughness–from molecules to fracture. Int. Mater. Rev. **59**(5), 245–263 (2014)
VanRietbergen, B., Odgaard, A., Kabel, J., Huiskes, R.: Direct mechanics assessment of elastic symmetries and properties of trabecular bone architecture. J. Biomech. **29**(12), 1653–1657 (1996)
Wang, C., Feng, L., Jasiuk, I.: Scale and boundary conditions effects on the apparent elastic moduli of trabecular bone modeled as a periodic cellular solid. J. Biomech. Eng.: Trans. ASME. **131**(12), 121008 (2009)
Weiner, S., Traub, W.: Bone structure–from angstroms to microns. FASEB J. **6**(3), 879–885 (1992)
Weiner, S., Wagner, H.D.: The material bone: structure mechanical function relations. Annu. Rev. Mater. Sci. **28**, 271–298 (1998)
Weinkamer, R., Fratzl, P.: Mechanical adaptation of biological materials–the examples of bone and wood. Mater. Sci. Eng. C. **31**(6), 1164–1173 (2011)
Yang, J.F.C., Lakes, R.S.: Experimental study of micropolar and couple stress elasticity in compact bone in bending. J. Biomech. **15**(2), 91–98 (1982)
Yeni, Y.N., Fyhrie, D.P.: Finite element calculated uniaxial apparent stiffness is a consistent predictor of uniaxial apparent strength in human vertebral cancellous bone tested with different boundary conditions. J. Biomech. **34**(12), 1649–1654 (2001)
Yoo, A., Jasiuk, I.: Couple-stress moduli of a trabecular bone idealized as a 3D periodic cellular network. J. Biomech. **39**(12), 2241–2252 (2006)
Yoon, Y.J., Cowin, S.C.: The estimated elastic constants for a single bone osteonal lamella. Biomech. Model. Mechanobiol. **7**(1), 1–11 (2008)
Zimmermann, E.A., Ritchie, R.O.: Bone as a structural material. Adv. Healthcare Mater. **4**(9), 1287–1304 (2015)
Zimmermann, E.A., Busse, B., Ritchie, R.O.: The fracture mechanics of human bone: influence of disease and treatment. BonekEy Rep. **4**, 743 (2015)
Zysset, P.K., Goulet, R.W., Hollister, S.J.: A global relationship between trabecular bone morphology and homogenized elastic properties. J. Biomech. Eng.: Trans. ASME. **120**(5), 640–646 (1998)

# Chapter 11
# Linear Elastic Composites with Statistically Oriented Spheroidal Inclusions

**Salvatore Federico and Alfio Grillo**

**Abstract** The purpose of this chapter is to critically review some results that our groups obtained in previous works, which were devoted to the investigation of the elastic properties of composite materials with a statistical distribution of spheroidal inclusions. These studies were motivated by our interest in the description of mechanical properties of fibre-reinforced biological tissues (such as articular cartilage), starting from the internal structure of these tissues. After an introduction to tensor algebra, which defines the notation and clarifies the mathematical framework adopted in the chapter, we present, in a covariant setting inspired by Differential Geometry, Walpole's representation of isotropic and transversely isotropic second- and fourth-order tensors, along with its properties. Hence, starting from Eshelby's seminal work on the problem of an inclusion in an infinite matrix, we briefly review the theories developed by Hill, Walpole and Weng for the determination of the overall elasticity tensor of materials with one or more inclusion phases. Then, we discuss in detail the cases of composite materials with aligned spheroidal inclusions and with statistically oriented spheroidal inclusions. Emphasis is put on extending Walpole's formula to the case of inclusions aligned according to some probability density of orientation, both in the transversely isotropic and the isotropic case.

Dedicated to the memory of Prof. Gaetano Giaquinta (1945–2016)

S. Federico (✉)
Department of Mechanical and Manufacturing Engineering, The University of Calgary, 2500 University Drive NW, Calgary, AB, Canada T2N1N4
e-mail: salvatore.federico@ucalgary.ca

A. Grillo
DISMA - Dipartimento di Scienze Matematiche "G.L. Lagrange", Politecnico di Torino, Corso Duca degli Abruzzi 24, Torino I-10124, Italy
e-mail: alfio.grillo@polito.it



S.A. Meguid, G.J. Weng (eds.), *Micromechanics and Nanomechanics of Composite Solids*, DOI 10.1007/978-3-319-52794-9_11

## 11.1 Introduction

From the 1950s to the 1970s, Eshelby published several papers (e.g., Eshelby, 1951, 1957, 1975) that turned out to be of fundamental importance in the development of the theory of materials with defects or inclusions. In this chapter, we are particularly interested in his work on the ellipsoidal inclusion (Eshelby, 1957), which is at the basis of the theory of materials reinforced by one or more phases of ellipsoidal inclusions, whose shape ranges from flat discs (which could represent cracks, if assigned a null elasticity tensor) to spherical inclusions to fibre-like inclusions.

The theory for the determination of the elasticity tensor of a composite material with inclusions has been developed by, among others, Hill (1963, 1965), Hashin (1963) and Walpole (1966a,b, 1969). The case of aligned inclusions has been thoroughly studied by Weng and his group (Weng, 1984, 1990; Qiu and Weng, 1990). A few cases of composites with non-aligned inclusions have been studied in the 1980s. The first work we are aware of is that by Chou and Nomura (1981), who studied a short-fibre composite in which the directions of alignment of the fibres lay on the surface of a cone. Tandon and Weng (1986), Weng (1990) and Qiu and Weng (1990) studied the case of randomly oriented spheroidal inclusions.

In this chapter, we report our method of solution for the general case of statistically oriented inclusions and, in particular, for the case of probability density being transversely isotropic with respect to a given direction. This is the core of one of our first works (Federico et al., 2004), which here we would like to present from a more mature point of view (12 years are not so few...) and in a more general setting. Furthermore, we take this chance to correct a few imprecisions in our original work and in some subsequent ones.

Originally, we were motivated by our interest in modelling articular cartilage as a composite comprised of a proteoglycan matrix with spheroidal inclusions, representing the chondrocytes (i.e., cartilage cells) and collagen fibres (Federico et al., 2005). This method was able to predict the elastic behaviour of articular cartilage only for a given type of deformation (i.e., either in compression or in tension). Indeed, the method had been conceived to model "pure" linear elasticity rather than to capture the tension-compression asymmetry caused by the fact that the collagen fibres bear load when extended but almost no load when contracted. Such non-linear effect was highlighted by Soltz and Ateshian (2000), who modelled cartilage by means of the *conewise linear elastic model* developed by Curnier et al. (1995), which adopts different elasticity tensors in tension and compression. However, considering the sign of deformation explicitly in the original paper (Federico et al., 2004) and its application to articular cartilage (Federico et al., 2005) would have prevented direct averaging integration of the elasticity tensors over all possible directions. In fact, this difficulty emerged also in our subsequent non-linear works (see Federico, 2015, and the references therein). Despite the limitations of our early paper (Federico et al., 2004), its methods have served as the basis for several other projects in our research groups, both in the linear and non-linear settings (see, again, Federico, 2015, for an account of all works in this "family").

## 11.2 Theoretical Background

We shall exclusively deal with the theory of small deformations, and therefore we shall make no distinction between reference and current configuration of a deformable body, which we shall simply regard as an open subset $\mathcal{B}$ of the physical space $\mathcal{S}$. Consequently, we shall not make distinction between uppercase and lowercase symbols as typically done in modern continuum mechanics (see, e.g., Marsden and Hughes, 1983) and shall exclusively use lowercase indices. However, we decided to keep the distinction between vector and covector quantities, which is reflected in the distinction between contravariant and covariant indices, respectively. The rationale for this choice is twofold. First, we believe that, even when Cartesian coordinates are used and the difference between vectors and covectors fades under orthogonal transformations (and *exclusively* under orthogonal transformations), it is good practice to keep the distinction, from a didactical point of view. Second, the theory of composite materials has traditionally been developed under the tacit assumption of Cartesian coordinates, and our own past work is no exception; thus, we found appealing the idea of attempting to systematically employ a covariant formalism instead.

We start by presenting the description of the physical space $\mathcal{S}$ as an affine space. Then, we introduce our general notation for tensors and tensor spaces, the metric tensor and contractions of tensors. We continue by introducing the symmetries of second- and fourth-order tensors and the material symmetries of isotropy and transverse isotropy, along with the corresponding representations of second- and fourth-order tensors satisfying these symmetries. In particular, we present Walpole's formalism for the representation of transversely isotropic fourth-order tensors. Finally, we briefly recall some key relations from the theory of linear elasticity.

### *11.2.1 Affine Spaces, Open Subsets and Tangent Spaces*

We cannot but agree with, e.g., Marsden and Hughes (1983) or Epstein (2010), when they say that *differentiable manifolds* are the most general and most appropriate setting for the description of mechanics. However, in many cases, the much simpler structure of *affine space* is sufficient for a reasonably rigorous presentation. An affine space is in fact a *trivial* differentiable manifold (i.e., a differentiable manifold that can be covered by a single chart) and is the minimal structure that allows to develop differential calculus and to attach vectors and tensors at any point in space.

An affine space consists of a set $\mathcal{S}$, called the *point space*; a vector space $\mathcal{V}$, called the *modelling* space; and a map $\mathcal{F} : \mathcal{S} \times \mathcal{S} \to \mathcal{V}$ that, for every pair of points $x, y$ in $\mathcal{S}$, yields a vector in $\mathcal{V}$ denoted $\mathcal{F}(x, y) = y - x = \boldsymbol{w}$, called the *oriented segment* from $x$ to $y$. The map $\mathcal{F}$ must be anti-commutative, i.e., $[x-y] = -[y-x]$, and must satisfy the triangle rule, i.e., $y - x = [y - z] + [z - x]$, and the axiom of arbitrary origin, i.e., for every $x \in \mathcal{S}$ and $\boldsymbol{w} \in \mathcal{V}$ there exists one, and only one, $y \in \mathcal{S}$, such

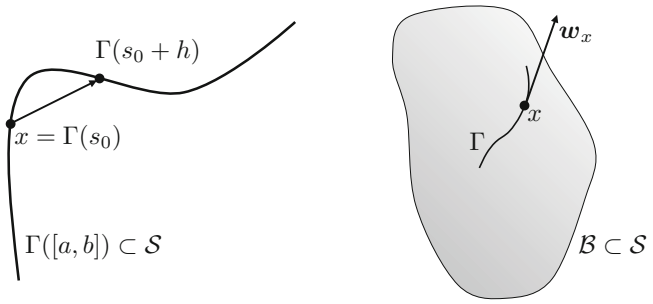


**Fig. 11.1** *Left*: The geometrical definition of tangent vector at a point $x$ in the affine space $\mathcal{S}$ as the tangent at $x$ to a curve passing by $x$, obtained as the limit of the secant passing by $x$. *Right*: A body $\mathcal{B}$ is an open subset of the physical space $\mathcal{S}$, which is considered as an affine space. Considering all regular curves $\Gamma$ passing by $x \in \mathcal{B}$, the tangent space $T_x\mathcal{B}$ is the set of the tangent vectors $\boldsymbol{w}_x$ that are each tangent at $x$ to one of the curves $\Gamma$

that $y - x = \boldsymbol{w}$. At every point $x \in \mathcal{S}$, the set of all vectors emanating from $x$ is defined by

$$T_x\mathcal{S} = \{\boldsymbol{w}_x = y - x : y \in \mathcal{S}\}, \tag{11.1}$$

where the notation $\boldsymbol{w}_x$ means that "$\boldsymbol{w}$ is attached at $x$". The space $T_x\mathcal{S}$ is a vector space called *tangent space* of $\mathcal{S}$ at point $x$. The *tangent bundle* of $\mathcal{S}$, denoted by $T\mathcal{S}$, is defined as the disjoint union of all tangent spaces $T_x\mathcal{S}$ for all $x \in \mathcal{S}$.

The definition of tangent space given in Eq. (11.1), however, applies exclusively to affine spaces and *not* to subsets of an affine space. This is crucial because deformable bodies are often seen as open subsets $\mathcal{B} \subset \mathcal{S}$. The problem for the case of a subset is that, if $x \in \mathcal{B}$, there exist tangent vectors $\boldsymbol{w}_x \in T_x\mathcal{B}$ such that $y = x + \boldsymbol{w}_x$ does *not* belong to $\mathcal{B}$, i.e., the "tip of the arrow" lies outside $\mathcal{B}$ (see the example in Fig. 11.1, right). Therefore, in order to properly define the tangent space $T_x\mathcal{B}$ at a point $x \in \mathcal{B}$, we need to use the definition inherited from differential geometry. In this definition, the tangent space $T_x\mathcal{S}$ is the set of all vectors that are tangent at $x$ to all possible regular curves $\Gamma : [a, b] \to \mathcal{S} : s \mapsto \Gamma(s)$ such that $\Gamma(s_0) = x$, with $s_0 \in ]a, b[$, i.e., the vectors

$$\boldsymbol{w}_x = \lim_{h\to 0} \frac{\Gamma(s_0 + h) - \Gamma(s_0)}{h} = \Gamma'(s_0) \in T_x\mathcal{S}, \tag{11.2}$$

in which the numerator of the limit is the difference between point $\Gamma(s_0 + h)$ and $\Gamma(s_0)$, which is a vector *secant* to $\Gamma$, and the limit is precisely the tangent at $x$ (Fig. 11.1, left). For the case of an affine space $\mathcal{S}$, this definition of tangent space $T_x\mathcal{S}$ coincides with that in Eq. (11.1). However, although the definition in Eq. (11.1) does not make sense for an open subset $\mathcal{B}$, that in Eq. (11.2) can be automatically inherited by $T_x\mathcal{B}$ just by saying that $x \in \mathcal{B}$ and the curves $\Gamma$ are such that $\Gamma : [a, b] \to \mathcal{B} : s \mapsto \Gamma(s)$, with $\Gamma(s_0) = x$, and $s_0 \in ]a, b[$.

Usually, the affine space of classical mechanics is constructed by assuming that both the point space and the modelling space are $\mathbb{R}^3$ and is often denoted by $\mathbb{E}^3$. Here, we shall assume that $\mathcal{S} \equiv \mathbb{E}^3$.

### *11.2.2 Tensors*

For our purposes, we shall refer to tensors on the tangent bundle $T\mathcal{B}$ of a material body $\mathcal{B}$, but these definitions are completely general and could be used in the tangent bundle $T\mathcal{S}$ of the physical space $\mathcal{S}$ or even in a generic vector space $\mathcal{V}$ of dimension $n$. Whenever we give examples, we use second- or fourth-order tensors, which are the types of tensors that are relevant in the subsequent sections of this chapter. This section is largely based on a previous work on non-linear elasticity (Federico, 2015) and is adapted to the setting of the small-displacement theory.

A *covector*, or *linear form*, or *one-form* is a linear map

$$\boldsymbol{\varphi} : T\mathcal{B} \to \mathbb{R} : \boldsymbol{u} \mapsto \boldsymbol{\varphi}\, \boldsymbol{u} \equiv \boldsymbol{\varphi}(\boldsymbol{u}), \tag{11.3}$$

where we use simple juxtaposition to indicate the action of the covector $\boldsymbol{\varphi}$ on the vector $\boldsymbol{u}$. The space of all covectors on the tangent bundle $T\mathcal{B}$ is the *dual* of $T\mathcal{B}$ and is denoted $T^\star\mathcal{B}$ and called *cotangent bundle*. If one looks at a point $x \in \mathcal{B}$, the dual of the tangent space $T_x\mathcal{B}$ is the *cotangent space* $T_x^\star\mathcal{B}$. It is possible to prove that, given a basis $\{\boldsymbol{e}_i\}_{i=1}^3$ in $T\mathcal{B}$, the covectors $\{\boldsymbol{e}^i\}_{i=1}^3$, defined by

$$\boldsymbol{e}^i\, \boldsymbol{u} \equiv \boldsymbol{e}^i(\boldsymbol{u}) = u^i, \tag{11.4}$$

constitute a basis for the cotangent bundle $T^\star\mathcal{B}$. The basis $\{\boldsymbol{e}^i\}_{i=1}^3$ is called the *dual basis* of $\{\boldsymbol{e}_i\}_{i=1}^3$. Each of the basis covectors $\boldsymbol{e}^i$ has a very precise geometrical meaning, as it associates, with every vector $\boldsymbol{u}$, the $i$-th component $u^i$ of $\boldsymbol{u}$ with respect to the vector basis $\{\boldsymbol{e}_i\}_{i=1}^3$, and, for this reason, the basis covectors $\boldsymbol{e}^i$ are often called *projections*. The definition in Eq. (11.4) implies

$$\boldsymbol{e}^i\, \boldsymbol{e}_j \equiv \boldsymbol{e}^i(\boldsymbol{e}_j) = \delta^i{}_j, \tag{11.5}$$

where $\delta^i{}_j$ is the Kronecker symbol. If, in the definition (11.3) of covector, we express vector $\boldsymbol{u}$ in the basis $\{\boldsymbol{e}_i\}_{i=1}^3$, we have

$$\boldsymbol{\varphi}\, \boldsymbol{u} = \boldsymbol{\varphi}(u^i\, \boldsymbol{e}_i) = u^i\, \boldsymbol{\varphi}\, \boldsymbol{e}_i = u^i\, \varphi_i \tag{11.6}$$

where

$$\varphi_i = \boldsymbol{\varphi}\, \boldsymbol{e}_i \equiv \boldsymbol{\varphi}(\boldsymbol{e}_i). \tag{11.7}$$

Using the definition of basis covector, it follows that the covector $\boldsymbol{\varphi}$ can be decomposed as a linear combination of the basis covectors $\{\boldsymbol{e}^i\}_{i=1}^3$, i.e., as

$$\boldsymbol{\varphi} = \varphi_i \, \boldsymbol{e}^i, \tag{11.8}$$

where the coefficients $\varphi_i$ take the meaning of components of $\boldsymbol{\varphi}$ with respect to $\{\boldsymbol{e}^i\}_{i=1}^3$.

In finite dimension, which is the case we are interested in, the relation between a vector space and its dual is symmetric in the sense that $T\mathcal{B}$ can be identified with the bi-dual space $T^{\star\star}\mathcal{B}$ (the set of all linear maps from $T^\star\mathcal{B}$ into $\mathbb{R}$). Therefore, the vectors of $T\mathcal{B}$ can be made to act on the covectors of $T^\star\mathcal{B}$ as linear forms, and the action of a vector $\boldsymbol{u}$ on a covector $\boldsymbol{\varphi}$ is identical to that of $\boldsymbol{\varphi}$ on $\boldsymbol{u}$

$$\boldsymbol{\varphi}\,\boldsymbol{u} = \varphi_i \, u^i = u^i \varphi_i = \boldsymbol{u}\boldsymbol{\varphi}. \tag{11.9}$$

Consequently, the basis vectors $\{\boldsymbol{e}_i\}_{i=1}^3$ are the projections in $T^\star\mathcal{B}$, i.e.,

$$\boldsymbol{e}_i \, \boldsymbol{\varphi} = \boldsymbol{\varphi}\, \boldsymbol{e}_i \; = \varphi_i. \tag{11.10}$$

We also say that the expression $\boldsymbol{\varphi}\,\boldsymbol{u} = \boldsymbol{u}\,\boldsymbol{\varphi} = u^i \, \varphi_i$ is the *contraction* of $\boldsymbol{\varphi}$ and $\boldsymbol{u}$.

A *tensor* of order $r + s = m$ on the tangent bundle $T\mathcal{B}$ is a *multilinear form*, i.e., a map of the type

$$\mathbb{T} : \underbrace{T^\star\mathcal{B} \times \ldots \times T^\star\mathcal{B}}_{r \text{ times}} \times \underbrace{T\mathcal{B} \times \ldots \times T\mathcal{B}}_{s \text{ times}} \to \mathbb{R}, \tag{11.11a}$$

$$\mathbb{T} : (\boldsymbol{\varphi}^1, \ldots \boldsymbol{\varphi}^r, \boldsymbol{u}_1, \ldots \boldsymbol{u}_s) \mapsto \mathbb{T}(\boldsymbol{\varphi}^1, \ldots \boldsymbol{\varphi}^r, \boldsymbol{u}_1, \ldots \boldsymbol{u}_s), \tag{11.11b}$$

that is linear in each of the $r + s$ arguments separately. The space of all tensors of the type in Eq. (11.11) is denoted $[T\mathcal{B}]^r{}_s$, a notation that will be justified later on [Eq. (11.17)].

The *tensor product* of the $r$ vectors $\boldsymbol{v}_1, \ldots, \boldsymbol{v}_r$ in $T\mathcal{B}$ and the $s$ covectors $\boldsymbol{\psi}^1, \ldots, \boldsymbol{\psi}^s$ in $T^\star\mathcal{B}$ is the tensor $\boldsymbol{v}_1 \otimes \ldots \otimes \boldsymbol{v}_r \otimes \boldsymbol{\psi}^1 \otimes \ldots \otimes \boldsymbol{\psi}^s$ in $[T\mathcal{B}]^r{}_s$ such that, for every $\boldsymbol{\varphi}^1, \ldots, \boldsymbol{\varphi}^r$ in $T^\star\mathcal{B}$ and for every $\boldsymbol{u}_1, \ldots, \boldsymbol{u}_s$ in $T\mathcal{B}$,

$$[\boldsymbol{v}_1 \otimes \ldots \otimes \boldsymbol{v}_r \otimes \boldsymbol{\psi}^1 \otimes \ldots \otimes \boldsymbol{\psi}^s](\boldsymbol{\varphi}^1, \ldots, \boldsymbol{\varphi}^r, \boldsymbol{u}_1, \ldots, \boldsymbol{u}_s) = \boldsymbol{v}_1(\boldsymbol{\varphi}^1) \; \ldots \; \boldsymbol{v}_r(\boldsymbol{\varphi}^r) \; \boldsymbol{\psi}^1(\boldsymbol{u}_1) \; \ldots \; \boldsymbol{\psi}^s(\boldsymbol{u}_s). \tag{11.12}$$

The tensor $\boldsymbol{v}_1 \otimes \ldots \otimes \boldsymbol{v}_r \otimes \boldsymbol{\psi}^1 \otimes \ldots \otimes \boldsymbol{\psi}^s$ is said to have $r$ *vector legs* $\boldsymbol{v}_1, \ldots, \boldsymbol{v}_r$ and $s$ *covector legs* $\boldsymbol{\psi}^1, \ldots, \boldsymbol{\psi}^s$.

With the definition of tensor product of vectors and covectors, and using multilinearity, we can derive the component expression of any tensor $\mathbb{T}$ in $[T\mathcal{B}]^r{}_s$ with respect to a given basis $\{\boldsymbol{e}_i\}_{i=1}^n$ and dual basis $\{\boldsymbol{e}^i\}_{i=1}^n$. Indeed, we have

$$\begin{aligned}\mathbb{T}(\boldsymbol{\varphi}^1,\ldots,\boldsymbol{\varphi}^r,\boldsymbol{u}_1,\ldots,\boldsymbol{u}_s) &= \mathbb{T}(\varphi^1_{i_1}\,\boldsymbol{e}^{i_1},\ldots,\varphi^r_{i_r}\,\boldsymbol{e}^{i_r},u^{j_1}_1\,\boldsymbol{e}_{j_1},\ldots,u^{j_s}_s\,\boldsymbol{e}_{j_s})\\ &= \varphi^1_{i_1}\,\ldots\,\varphi^r_{i_r}\,u^{j_1}_1\,\ldots\,u^{j_s}_s\,\mathbb{T}(\boldsymbol{e}^{i_1},\ldots,\boldsymbol{e}^{i_r},\boldsymbol{e}_{j_1},\ldots,\boldsymbol{e}_{j_s})\\ &= \varphi^1_{i_1}\,\ldots\,\varphi^r_{i_r}\,u^{j_1}_1\,\ldots\,u^{j_s}_s\,\mathrm{T}^{i_1\ldots i_r}{}_{j_1\ldots j_s},\end{aligned}\tag{11.13}$$

where

$$\mathrm{T}^{i_1\ldots i_r}{}_{j_1\ldots j_s} = \mathbb{T}(\boldsymbol{e}^{i_1},\ldots,\boldsymbol{e}^{i_r},\boldsymbol{e}_{j_1},\ldots,\boldsymbol{e}_{j_s})\tag{11.14}$$

are the components of $\mathbb{T}$. By analogy with the indices of vectors and covectors, the indices $i_1\,\ldots\,i_r$ are called *contravariant* and the indices $j_1\,\ldots\,j_s$ are called *covariant*. Using Eqs. (11.4), (11.10) and (11.12), we obtain

$$\begin{aligned}&\mathbb{T}(\boldsymbol{\varphi}^1,\ldots,\boldsymbol{\varphi}^r,\boldsymbol{u}_1,\ldots,\boldsymbol{u}_s)\\ &= \varphi^1_{i_1}\,\ldots\,\varphi^r_{i_r}\,u^{j_1}_1\,\ldots\,u^{j_s}_s\,\mathrm{T}^{i_1\ldots i_r}{}_{j_1\ldots j_s}\\ &= \boldsymbol{e}_{i_1}(\boldsymbol{\varphi}^1)\ldots\boldsymbol{e}_{i_r}(\boldsymbol{\varphi}^r)\,\boldsymbol{e}^{j_1}(\boldsymbol{u}_1)\ldots\boldsymbol{e}^{j_s}(\boldsymbol{u}_s)\,\mathrm{T}^{i_1\ldots i_r}{}_{j_1\ldots j_s}\\ &= \mathrm{T}^{i_1\ldots i_r}{}_{j_1\ldots j_s}\,[\boldsymbol{e}_{i_1}\otimes\ldots\otimes\boldsymbol{e}_{i_r}\otimes\boldsymbol{e}^{j_1}\otimes\ldots\otimes\boldsymbol{e}^{j_s}](\boldsymbol{\varphi}^1,\ldots,\boldsymbol{\varphi}^r,\boldsymbol{u}_1,\ldots,\boldsymbol{u}_s).\end{aligned}\tag{11.15}$$

By dropping the arguments $\boldsymbol{\varphi}^1,\ldots,\boldsymbol{\varphi}^r,\boldsymbol{u}_1,\ldots,\boldsymbol{u}_s$ on both sides of Eq. (11.15), we obtain the component representation of $\mathbb{T}$ in the *tensor basis* $\{\boldsymbol{e}_{i_1}\otimes\ldots\otimes\boldsymbol{e}_{i_r}\otimes\boldsymbol{e}^{j_1}\otimes\ldots\otimes\boldsymbol{e}^{j_s}\}^n_{i_1,\ldots,i_r,j_1,\ldots,j_s=1}$ of the tensor space $[T\mathcal{B}]^r{}_s$ as

$$\mathbb{T} = \mathrm{T}^{i_1\ldots i_r}{}_{j_1\ldots j_s}\,\boldsymbol{e}_{i_1}\otimes\ldots\otimes\boldsymbol{e}_{i_r}\otimes\boldsymbol{e}^{j_1}\otimes\ldots\otimes\boldsymbol{e}^{j_s}.\tag{11.16}$$

A tensor $\mathbb{T}$ in $[T\mathcal{B}]^r{}_s$ is said to have $r$ vector legs and $s$ covector legs, and $[T\mathcal{B}]^r{}_s$ can be represented as the *tensor product of spaces* (Bishop and Goldberg, 1968)

$$[T\mathcal{B}]^r{}_s = \underbrace{T\mathcal{B}\otimes\ldots\otimes T\mathcal{B}}_{r\text{ times}}\otimes\underbrace{T^\star\mathcal{B}\otimes\ldots\otimes T^\star\mathcal{B}}_{s\text{ times}}.\tag{11.17}$$

With a widely accepted abuse of terminology, we shall often refer to a tensor in $[T\mathcal{B}]^r{}_s$ as being "$r$ times contravariant and $s$ times covariant" although, rigorously speaking, the adjectives contravariant and covariant refer to tensor *indices* and tensor *components*.

Since a tensor leg can be a vector or a covector, there are $2^m$ possible spaces of tensors of order $m$. For instance, there is only one type of space of zero-order tensors (scalars in $[T\mathcal{B}]^0_0 \equiv \mathbb{R}$), two types of spaces of first-order tensors (vectors in $[T\mathcal{B}]^1_0 \equiv T\mathcal{B}$ and covectors in $[T\mathcal{B}]^0_1 \equiv T^\star\mathcal{B}$), four types of spaces of second-order tensors and sixteen types of spaces of fourth-order tensors. The table below summarises the situation and reports some examples of the 16 types of fourth-order tensors. Here, we shall exclusively deal with the first four types of fourth-order tensors.

| Order | Types | Spaces | Components | Notes |
|---|---|---|---|---|
| 0 | $2^0$ | $[T\mathcal{B}]_0^0 \equiv \mathbb{R}$ | $a$ | Scalars |
| 1 | $2^1$ | $[T\mathcal{B}]_0^1 \equiv T\mathcal{B}$ | $a^i$ | Vectors |
| | | $[T\mathcal{B}]_1^0 \equiv T^\star\mathcal{B}$ | $a_i$ | Covectors |
| 2 | $2^2$ | $[T\mathcal{B}]_0^2$ | $a^{ij}$ | "Contravariant" |
| | | $[T\mathcal{B}]_2^0$ | $a_{ij}$ | "Covariant" |
| | | $[T\mathcal{B}]^1{}_1$ | $a^i{}_j$ | "Mixed" |
| | | $[T\mathcal{B}]_1{}^1$ | $a_i{}^j$ | "Mixed" |
| 4 | $2^4$ | $[T\mathcal{B}]_0^4$ | $\mathrm{A}^{ijkl}$ | "Contravariant" |
| | | $[T\mathcal{B}]_4^0$ | $\mathrm{A}_{ijkl}$ | "Covariant" |
| | | $[T\mathcal{B}]^2{}_2$ | $\mathrm{A}^{ij}{}_{kl}$ | "Mixed" |
| | | $[T\mathcal{B}]_2{}^2$ | $\mathrm{A}_{ij}{}^{kl}$ | "Mixed" |
| | | ... | ... | |
| | | $[T\mathcal{B}]^1{}_1{}^1{}_1$ | $\mathrm{A}^i{}_j{}^k{}_l$ | |
| | | $[T\mathcal{B}]_1{}^1{}_1{}^1$ | $\mathrm{A}_i{}^j{}_k{}^l$ | |
| | | ... | ... | |

### *11.2.3 Tensor Contractions and Tensor as Linear Maps*

So far, we have seen tensors as multilinear maps, whose legs are all contracted at the same time with vectors or covector arguments, as appropriate. However, one could contract part of the legs of a tensor with all or part of the legs of another tensor. In this work, we are going to see single and double contractions.

Given a tensor whose last leg is a vector and another tensor whose first leg is a covector, or vice versa, we call *single contraction* the contraction of the last leg of the first tensor with the first leg of the second tensor and denote it by simple juxtaposition. For instance, for a "contravariant" second-order tensor $\boldsymbol{a}$ in $[T\mathcal{B}]_0^2$ and a "covariant" second-order tensor $\boldsymbol{c}$ in $[T\mathcal{B}]_2^0$, the contraction $\boldsymbol{a}\,\boldsymbol{c}$ has components $a^{ij}c_{jk}$. The same type of contraction occurs between, e.g., a "mixed" tensor $\boldsymbol{l}$ in $[T\mathcal{B}]^1{}_1$ and a vector $\boldsymbol{u}$ in $T\mathcal{B}$, and the single contraction is the usual $\boldsymbol{l}\,\boldsymbol{u}$ with components $l^i{}_j\,u^j$.

The double contraction of two tensors works similarly to the simple contraction, except that one contracts the last two legs of the first tensor and the first two legs of the second tensor. As with the single contraction, the contracting legs must be of opposite type. Double contraction is denoted by a colon. For example, for a fourth-order tensor $\mathbb{T}$ in $[T\mathcal{B}]^2{}_2$ and a second-order tensor $\boldsymbol{a}$ in $[T\mathcal{B}]_0^2$, the double contraction $\mathbb{T} : \boldsymbol{a}$ has components $\mathrm{T}^{ij}{}_{kl}a^{kl}$.

Tensors can also be regarded as linear maps between tensor spaces. For instance, a "mixed" second-order tensor, i.e., a tensor $\boldsymbol{l}$ in $[T\mathcal{B}]^1{}_1$ could be seen as the linear map $\boldsymbol{l} : T\mathcal{B} \to T\mathcal{B} : \boldsymbol{u} \mapsto \boldsymbol{l}\,\boldsymbol{u}$ (in components, $l^i{}_j\,u^j$). Similarly, a "contravariant" fourth-order tensor $\mathbb{T}$ in $[T\mathcal{B}]_0^4$ could be regarded as the linear map $\mathbb{T} : [T\mathcal{B}]_2^0 \to [T\mathcal{B}]_0^2 : \boldsymbol{c} \mapsto \mathbb{T} : \boldsymbol{c}$ (in components, $\mathrm{T}^{ijkl}c_{kl}$). Rigorously speaking, a tensor seen as a linear map between two tensor spaces should be somehow notationally

distinguished from its multilinear form counterpart. However, since context and, above all, index notation prevent any possible confusion, the customary practice is to use the same symbol $\mathbb{T}$ for the tensor employed in both manners.

### 11.2.4 Metric Tensor and Scalar Products

The physical space $\mathcal{S}$ is assumed to be equipped with a metric tensor $\boldsymbol{g}$, which is inherited by the body $\mathcal{B}$. A metric tensor is a symmetric and positive definite tensor in $[T\mathcal{B}]^0_2$, such that, for every pair of vectors $\boldsymbol{u}$ and $\boldsymbol{v}$ in $T\mathcal{B}$,

$$\boldsymbol{g}(\boldsymbol{u},\boldsymbol{v}) \equiv \boldsymbol{u}\,\boldsymbol{g}\,\boldsymbol{v} \equiv \langle \boldsymbol{u},\boldsymbol{v}\rangle \equiv \boldsymbol{u}.\boldsymbol{v} = u^i\, g_{ij}\, v^j. \tag{11.18}$$

Symmetry means that $\langle \boldsymbol{u},\boldsymbol{v}\rangle = \langle \boldsymbol{v},\boldsymbol{u}\rangle$, and positive definiteness means that, for every $\boldsymbol{u} \neq \boldsymbol{0}$, $\langle \boldsymbol{u},\boldsymbol{u}\rangle > 0$. The equivalent notations $\boldsymbol{g}(\boldsymbol{u},\boldsymbol{v}) \equiv \boldsymbol{u}\,\boldsymbol{g}\,\boldsymbol{v} \equiv \langle \boldsymbol{u},\boldsymbol{v}\rangle \equiv \boldsymbol{u}.\boldsymbol{v}$ denote the *scalar product* of the vectors $\boldsymbol{u}$ and $\boldsymbol{v}$. The metric tensor induces the *Euclidean norm* $\|\boldsymbol{u}\| = \sqrt{\boldsymbol{g}(\boldsymbol{u},\boldsymbol{u})} \equiv \sqrt{\langle \boldsymbol{u},\boldsymbol{u}\rangle}$. A basis $\{\boldsymbol{e}_i\}_{i=1}^3$ is called *orthonormal* with respect to $\boldsymbol{g}$ if $\boldsymbol{g}(\boldsymbol{e}_i,\boldsymbol{e}_j) \equiv \langle \boldsymbol{e}_i,\boldsymbol{e}_j\rangle = \delta_{ij}$, i.e., if the matrix representation of the metric tensor is the identity. Positive definiteness of $\boldsymbol{g}$ also implies invertibility, and the inverse is the tensor $\boldsymbol{g}^{-1}$ valued in $[T\mathcal{B}]^2_0$ such that, for every pair of covectors $\boldsymbol{\varphi}$ and $\boldsymbol{\psi}$ in $T^\star\mathcal{B}$,

$$\boldsymbol{g}^{-1}(\boldsymbol{\varphi},\boldsymbol{\psi}) \equiv \boldsymbol{\varphi}\,\boldsymbol{g}^{-1}\,\boldsymbol{\psi} \equiv \langle \boldsymbol{\varphi},\boldsymbol{\psi}\rangle \equiv \boldsymbol{\varphi}.\boldsymbol{\psi} = \varphi_i\,(\boldsymbol{g}^{-1})^{ij}\,\psi_j. \tag{11.19}$$

When considered as a linear map $\boldsymbol{g} : T\mathcal{B} \to T^\star\mathcal{B}$, the metric tensor $\boldsymbol{g}$ is said to be used to "lower contravariant indices", by mapping the vector $\boldsymbol{u}$ into the associated covector $\boldsymbol{u}^\flat = \boldsymbol{g}\,\boldsymbol{u}$, with components $u_i = g_{ij}u^j$. Analogously, the inverse metric tensor $\boldsymbol{g}^{-1}$, seen as the linear map $\boldsymbol{g}^{-1} : T^\star\mathcal{B} \to T\mathcal{B}$, is said to "raise covariant indices", by mapping the covector $\boldsymbol{\varphi}$ into the associated vector $\boldsymbol{\varphi}^\sharp = \boldsymbol{g}^{-1}\boldsymbol{\varphi}$, with components $\varphi^i = (\boldsymbol{g}^{-1})^{ij}\varphi_j$. The metric tensor and its inverse can be used to lower and rise, respectively, the indices of tensors of any order. For instance, given the "contravariant" fourth-order tensor $\mathbb{T}$ in $[T\mathcal{B}]^4_0$, its "covariant" associated tensor is denoted $\mathbb{T}^\flat$ and has components $\mathrm{T}_{ijkl} = g_{ip}\,g_{jq}\,g_{kr}\,g_{ls}\,\mathrm{T}^{pqrs}$. In particular, if we raise the indices of the metric tensor $\boldsymbol{g}$ itself by means of the inverse metric tensor $\boldsymbol{g}^{-1}$, we have the important identity

$$\boldsymbol{g}^\sharp = \boldsymbol{g}^{-1}\boldsymbol{g}\,\boldsymbol{g}^{-1} = \boldsymbol{g}^{-1}, \qquad g^{il} = (\boldsymbol{g}^{-1})^{ij}\,g_{jk}\,(\boldsymbol{g}^{-1})^{kl} = (\boldsymbol{g}^{-1})^{il}. \tag{11.20}$$

The scalar product induced by the metric tensor $\boldsymbol{g}$ can be extended to pairs of tensors of the same type of any order, by contracting each pair of homologous indices by means of the metric tensor or its inverse, as appropriate. For instance, given two tensors $\mathbb{T}$ and $\mathbb{Z}$ in $[T\mathcal{B}]^1{}_1{}^1{}_1$, their scalar product is $\langle \mathbb{T},\mathbb{Z}\rangle = \mathrm{T}^i{}_j{}^k{}_l\,g_{ip}\,g^{jq}\,g_{kr}\,g^{ls}\,\mathrm{Z}^p{}_q{}^r{}_s$.

Finally, we use a single low dot to indicate that the metric tensor (or its inverse) is involved in the contraction of two tensors such that the last leg of the first tensor

and the first leg of the second tensor are of the same type. For instance, given two "contravariant" tensors $\boldsymbol{a}, \boldsymbol{b}$ in $[T\mathcal{B}]^2_0$, the expression $\boldsymbol{a}.\boldsymbol{b}$ stands for $\boldsymbol{a}\,\boldsymbol{g}\,\boldsymbol{b}$, which has components $(\boldsymbol{a}.\boldsymbol{b})^{il} = a^{ij}\, g_{jk}\, b^{kl}$.

### 11.2.5 Symmetries of Second- and Fourth-Order Tensors

For a "covariant" second-order tensor $\boldsymbol{c}$ in $[T\mathcal{B}]^0_2$, the *transpose* is defined as the tensor $\boldsymbol{c}^T$ in $[T\mathcal{B}]^0_2$ such that, for every pair of vectors $\boldsymbol{u}, \boldsymbol{v}$ in $T\mathcal{B}$, $\boldsymbol{u}\,\boldsymbol{c}\,\boldsymbol{v} = \boldsymbol{v}\,\boldsymbol{c}^T\boldsymbol{u}$, which in components reads $u^i\, c_{ij}\, v^j = v^j\, (\boldsymbol{c}^T)_{ji}\, u^i$, implying $(\boldsymbol{c}^T)_{ji} = c_{ij}$. The transpose of a "contravariant" second-order tensor is defined analogously. For the case of a "mixed" tensor $\boldsymbol{a}$ in $[T\mathcal{B}]^1{}_1$, the transpose is the tensor $\boldsymbol{a}^T$ in $[T\mathcal{B}]_1{}^1$ such that, for every vector $\boldsymbol{v}$ in $T\mathcal{B}$ and every covector $\boldsymbol{\varphi}$ in $T^\star\mathcal{B}$, $\boldsymbol{\varphi}\,\boldsymbol{a}\,\boldsymbol{v} = \boldsymbol{v}\,\boldsymbol{a}^T\boldsymbol{\varphi}$, which in components reads $\varphi_i\, a^i{}_j\, v^j = v_j\, (\boldsymbol{a}^T)_j{}^i\, u^i$, implying $(\boldsymbol{a}^T)_j{}^i = a^i{}_j$. Note that, while a "covariant" and its transpose, or a "contravariant" tensor and its transpose, belong to the *same* space, a "mixed" tensor and its transpose belong to *different* spaces.

A "covariant" second-order tensor $\boldsymbol{c}$ in $[T\mathcal{B}]^0_2$ is called symmetric if $\boldsymbol{c} = \boldsymbol{c}^T$, which, in components, means $c_{ij} = c_{ji}$. The symmetry of a "contravariant" tensor $\boldsymbol{a}$ in $[T\mathcal{B}]^2_0$ is defined analogously. For the case of a "mixed" tensor, speaking about equality of the tensor and its transpose has no meaning, as they belong to *different* spaces. Thus, symmetry of a "mixed" tensor $\boldsymbol{l}$ in $[T\mathcal{B}]^1{}_1$ is defined in terms of the symmetry of its "covariant" counterpart $\boldsymbol{l}^\flat = \boldsymbol{g}\,\boldsymbol{l}$ or, equivalently, in terms of the symmetry of its "contravariant" counterpart $\boldsymbol{l}^\sharp = \boldsymbol{l}\,\boldsymbol{g}^{-1}$; indeed, we have that $\boldsymbol{l}^\sharp$ is symmetric if and only if $\boldsymbol{l}^\flat$ is such.

When a fourth-order tensor is viewed as a linear map between spaces of second-order tensors, its transpose can be defined in a way similar to that of a second-order tensor. For the purposes of our presentation, let us restrict our attention to "covariant" tensors in $[T\mathcal{B}]^0_4$, "contravariant" tensors in $[T\mathcal{B}]^4_0$ and "mixed" tensors in $[T\mathcal{B}]^2{}_2$ and $[T\mathcal{B}]_2{}^2$ (actually, the transpose of fourth-order tensors of any other type is defined exactly in the same way, but we do not need these tensors here). For instance, the transpose of $\mathbb{A}$ in $[T\mathcal{B}]^4_0$ is defined as the tensor $\mathbb{A}^T$ in $[T\mathcal{B}]^4_0$ such that, for every $\boldsymbol{c}, \boldsymbol{d}$ in $[T\mathcal{B}]^0_2$, the identity $\boldsymbol{c} : \mathbb{A} : \boldsymbol{d} = \boldsymbol{d} : \mathbb{A}^T : \boldsymbol{c}$ holds. In components, this reads $c_{ij}\, \mathrm{A}^{ijkl}\, d_{kl} = d_{kl}\, [\mathbb{A}^T]^{klij}\, c_{ij}$, i.e., $[\mathbb{A}^T]^{klij} = \mathrm{A}^{ijkl}$.

Fourth-order tensors admit a variety of symmetries. Here we are interested in those called *major* and *minor* symmetry. A "contravariant" fourth-order tensor $\mathbb{A}$ in $[T\mathcal{B}]^4_0$ is said to have *major symmetry* (or *diagonal symmetry*) if $\mathbb{A}^T = \mathbb{A}$. The same definition holds for a "covariant" tensor $\mathbb{B}$ in $[T\mathcal{B}]^0_4$. The case of "mixed" tensors is of course a little more complicated. We are interested in the case of a "mixed" tensor $\mathbb{T}$ in $[T\mathcal{B}]^2{}_2$ or in $[T\mathcal{B}]_2{}^2$. The major symmetry of such tensor is checked by looking at the major symmetry of either its "contravariant" counterpart $\mathbb{T}^\sharp$ or of its "covariant" counterpart $\mathbb{T}^\flat$, as $\mathbb{T}^\sharp$ is major-symmetric if, and only if, $\mathbb{T}^\flat$ is major-symmetric. Another important symmetry of fourth-order tensors is called *minor symmetry* (or *pair symmetry*), and it is straightforward to define for tensors in which the two legs (indices) within the first pair and within the second pair are of the same type, i.e., for

tensors in $[T\mathcal{B}]^4_0$, $[T\mathcal{B}]^0_4$, $[T\mathcal{B}]^2{}_2$ and $[T\mathcal{B}]_2{}^2$. For instance, a tensor $\mathbb{A}$ in $[T\mathcal{B}]^4_0$ is said to possess minor symmetry on the first pair of legs (indices) if, for every $\boldsymbol{c}$ in $[T\mathcal{B}]^0_2$, one has $\boldsymbol{c} : \mathbb{A} = \boldsymbol{c}^T : \mathbb{A}$, and on the second pair of legs (indices) if $\mathbb{A} : \boldsymbol{c} = \mathbb{A} : \boldsymbol{c}^T$. In components, these symmetries read $\mathrm{A}^{ijkl} = \mathrm{A}^{jikl}$ and $\mathrm{A}^{ijkl} = \mathrm{A}^{ijlk}$, respectively. If a tensor enjoys minor symmetry on both the first and the second pair of legs, we simply say that it "enjoys minor symmetry". When there is no danger of confusion, we say that a fourth-order tensor is *symmetric* if it enjoys both major and minor symmetry.[1]

### 11.2.6 Isotropic Second- and Fourth-Order Tensors

Isotropy is the invariance of a material property under any arbitrary rotation. A "mixed" second-order tensor $\boldsymbol{l}$ in $[T\mathcal{B}]^1{}_1$ is isotropic if, and only if, it is proportional to the identity tensor $\boldsymbol{i}$, i.e., if $\boldsymbol{l} = l\,\boldsymbol{i}$ (in components, $l^i{}_j = l\,\delta^i{}_j$). A "contravariant" tensor $\boldsymbol{a}$ in $[T\mathcal{B}]^2_0$ is said to be isotropic if the associated "mixed" tensor $\boldsymbol{a}\,\boldsymbol{g}$ is isotropic, which implies that $\boldsymbol{a} = a\,\boldsymbol{g}^{-1}$ (i.e., $a^{ij} = a\,g^{ij}$). Similarly, a "covariant" tensor $\boldsymbol{c}$ in $[T\mathcal{B}]^0_2$ is said to be isotropic if such is the associated "mixed" tensor $\boldsymbol{g}^{-1}\boldsymbol{c}$, from which $\boldsymbol{c} = c\,\boldsymbol{g}$ (i.e., $c_{ij} = c\,g_{ij}$). We remark that, as a consequence of the definition of isotropic second-order tensor, it follows that any isotropic second-order tensor is symmetric.

Let us consider the subspace $([T\mathcal{B}]^2{}_2, \mathrm{Sym})$ of $[T\mathcal{B}]^2{}_2$ of all tensors with major and minor symmetry. Since tensors in $[T\mathcal{B}]^2{}_2$ are "mixed", major symmetry of a tensor $\mathbb{T}$ is understood in the sense of Sect. 11.2.5, i.e., in relation to the symmetry of the "contravariant" counterpart $\mathbb{T}^\sharp$ or of the symmetry of the "covariant" counterpart $\mathbb{T}^\flat$. The *symmetric identity* in $([T\mathcal{B}]^2{}_2, \mathrm{Sym})$ is defined with the help of the special tensor products $\underline{\otimes}$ and $\overline{\otimes}$ introduced by Curnier et al. (1995) as

$$\mathbb{I} = \tfrac{1}{2}(\boldsymbol{i} \,\underline{\otimes}\, \boldsymbol{i} + \boldsymbol{i} \,\overline{\otimes}\, \boldsymbol{i}), \qquad \mathrm{I}^{ij}{}_{kl} = \tfrac{1}{2}(\delta^i{}_k\delta^j{}_l + \delta^i{}_l\delta^j{}_k), \tag{11.21}$$

where $\boldsymbol{i}$, with components $\delta^i{}_j$, is the identity second-order tensor in $[T\mathcal{B}]^1{}_1$. Since $\mathbb{I}$ is the identity, it is invariant under rotations and is therefore clearly isotropic. The symmetric identity is such that, for every *symmetric* second-order tensor $\boldsymbol{a}$ in $[T\mathcal{B}]^2_0$, $\mathbb{I} : \boldsymbol{a} = \boldsymbol{a}$.

The tensor basis of the subspace $([T\mathcal{B}]^2{}_2, \mathrm{Sym}, \mathrm{Iso})$ of the symmetric *and* isotropic tensors is found by decomposing the symmetric identity into (Walpole, 1981, 1984; Federico, 2012)

$$\mathbb{I} = \mathbb{K} + \mathbb{M}, \tag{11.22}$$

[1] In our past works, we have called a fourth-order tensor with both major and minor (diagonal- and pair-) symmetry "fully symmetric", but we are not going to use this nomenclature here, as it can be confusing. Indeed, what is normally called fully or completely symmetric is a tensor that is invariant under *any* permutation of the indices.

where

$$\mathbb{K} = \tfrac{1}{3}\,\boldsymbol{g}^{-1}\otimes\boldsymbol{g}, \qquad \mathrm{K}^{ij}{}_{kl} = \tfrac{1}{3}\,g^{ij}g_{kl}, \tag{11.23a}$$

$$\mathbb{M} = \mathbb{I} - \mathbb{K}, \qquad \mathrm{M}^{ij}{}_{kl} = \tfrac{1}{2}(\delta^{i}{}_{k}\delta^{j}{}_{l} + \delta^{i}{}_{l}\delta^{j}{}_{k}) - \tfrac{1}{3}\,g^{ij}g_{kl}, \tag{11.23b}$$

are the *spherical operator* and the *deviatoric operator*, such that, for every symmetric tensor $\boldsymbol{a}$ in $[T\mathcal{B}]^2_0$, $\mathbb{K} : \boldsymbol{a} = \frac{1}{3}\,\mathrm{tr}(\boldsymbol{a})\,\boldsymbol{g}^{-1}$ is the spherical part of $\boldsymbol{a}$, and $\mathbb{M} : \boldsymbol{a} = \boldsymbol{a} - \frac{1}{3}\,\mathrm{tr}(\boldsymbol{a})\,\boldsymbol{g}^{-1}$ is the deviatoric part of $\boldsymbol{a}$, where $\mathrm{tr}(\cdot)$ is the natural trace operator, such that $\mathrm{tr}(\boldsymbol{a}) = \boldsymbol{g} : \boldsymbol{a} = g_{ij}\,a^{ij}$. The tensors $\{\mathbb{K}, \mathbb{M}\}$ constitute the basis of the space $([T\mathcal{B}]^2{}_2, \mathrm{Sym}, \mathrm{Iso})$ of the symmetric and isotropic tensors. We remark that *all* isotropic fourth-order tensors enjoy minor symmetry (Jog, 2006) and that there exist isotropic fourth-order tensors which do *not* enjoy major symmetry (the additional basis tensor is the *skew-symmetriser* $\mathbb{W} = \frac{1}{2}(\boldsymbol{i} \underline{\otimes} \boldsymbol{i} - \boldsymbol{i} \overline{\otimes} \boldsymbol{i})$; see Jog, 2006).

The bases of the spaces $([T\mathcal{B}]^4_0, \mathrm{Sym}, \mathrm{Iso})$ and $([T\mathcal{B}]^0_4, \mathrm{Sym}, \mathrm{Iso})$ are obtained by raising and lowering, respectively, the indices of $\{\mathbb{K}, \mathbb{M}\}$, or by decomposing the "contravariant" symmetric identity $\mathbb{I}^\sharp$ and the "covariant" symmetric identity $\mathbb{I}^\flat$, respectively. The resulting tensors are (Federico, 2012)

$$\mathbb{I}^\sharp = \tfrac{1}{2}(\boldsymbol{g}^{-1} \underline{\otimes} \boldsymbol{g}^{-1} + \boldsymbol{g}^{-1} \overline{\otimes} \boldsymbol{g}^{-1}), \quad \mathrm{I}^{ijkl} = \tfrac{1}{2}(g^{ik}g^{jl} + g^{il}g^{jk}), \tag{11.24a}$$

$$\mathbb{K}^\sharp = \tfrac{1}{3}\,\boldsymbol{g}^{-1}\otimes\boldsymbol{g}^{-1}, \qquad \mathrm{K}^{ijkl} = \tfrac{1}{3}\,g^{ij}g^{kl}, \tag{11.24b}$$

$$\mathbb{M}^\sharp = \mathbb{I}^\sharp - \mathbb{K}^\sharp, \qquad \mathrm{M}^{ijkl} = \tfrac{1}{2}(g^{ik}g^{jl} + g^{il}g^{jk}) - \tfrac{1}{3}\,g^{ij}g^{kl}, \tag{11.24c}$$

and

$$\mathbb{I}^\flat = \tfrac{1}{2}(\boldsymbol{g} \underline{\otimes} \boldsymbol{g} + \boldsymbol{g} \overline{\otimes} \boldsymbol{g}), \qquad \mathrm{I}_{ijkl} = \tfrac{1}{2}(g_{ik}g_{jl} + g_{il}g_{jk}), \tag{11.25a}$$

$$\mathbb{K}^\flat = \tfrac{1}{3}\,\boldsymbol{g}\otimes\boldsymbol{g}, \qquad \mathrm{K}_{ijkl} = \tfrac{1}{3}\,g_{ij}g_{kl}, \tag{11.25b}$$

$$\mathbb{M}^\flat = \mathbb{I}^\flat - \mathbb{K}^\flat, \qquad \mathrm{M}_{ijkl} = \tfrac{1}{2}(g_{ik}g_{jl} + g_{il}g_{jk}) - \tfrac{1}{3}\,g_{ij}g_{kl}. \tag{11.25c}$$

The tensors $\{\mathbb{K}^\sharp, \mathbb{M}^\sharp\}$ and $\{\mathbb{K}^\flat, \mathbb{M}^\flat\}$ constitute the bases of the spaces $([T\mathcal{B}]^4_0, \mathrm{Sym}, \mathrm{Iso})$ and $([T\mathcal{B}]^0_4, \mathrm{Sym}, \mathrm{Iso})$, respectively. It is important to recall how to obtain the representation of a symmetric isotropic tensor, and we show this in the case that is most important for our purposes, i.e., that of a "contravariant" tensor. A symmetric isotropic tensor $\mathbb{T}$ in $([T\mathcal{B}]^4_0, \mathrm{Sym}, \mathrm{Iso})$ can be shown to admit the representation (Walpole, 1981, 1984)

$$\mathbb{T} = \langle \mathbb{T}, \mathbb{K}^\sharp \rangle\, \mathbb{K}^\sharp + \tfrac{1}{5}\langle \mathbb{T}, \mathbb{M}^\sharp \rangle\, \mathbb{M}^\sharp, \tag{11.26}$$

where

$$\langle \mathbb{T}, \mathbb{K}^\sharp \rangle = \mathrm{T}^{ijkl}\, g_{ip}\, g_{jq}\, g_{kr}\, g_{ls} \left(\tfrac{1}{3}\, g^{pq}\, g^{rs}\right) = \tfrac{1}{3}\,\mathrm{T}^{i}{}_{i}{}^{k}{}_{k}, \tag{11.27a}$$

$$\langle \mathbb{T}, \mathbb{M}^\sharp \rangle = \mathrm{T}^{ijkl}\, g_{ip}\, g_{jq}\, g_{kr}\, g_{ls} \left(\tfrac{1}{2}(g^{pr}\, g^{qs} + g^{ps}\, g^{qr}) - \tfrac{1}{3}\, g^{pq}\, g^{rs}\right) = \mathrm{T}^{ij}{}_{ij} - \tfrac{1}{3}\,\mathrm{T}^{i}{}_{i}{}^{k}{}_{k}. \tag{11.27b}$$

Note that, in the second of Eq. (11.27), we obtain a term $\frac{1}{2}(\mathrm{T}^{ij}{}_{ij} + \mathrm{T}^{ij}{}_{ji})$, which reduces to $\mathrm{T}^{ij}{}_{ij}$ because of the minor symmetry of $\mathbb{T}$. We remark that, if $\mathbb{T}$ is a generic, not necessarily symmetric and isotropic tensor in $[T\mathcal{B}]^4_0$, the right-hand side of Eq. (11.26) yields the *projection* of $\mathbb{T}$ onto the isotropic subspace $([T\mathcal{B}]^4_0, \mathrm{Sym}, \mathrm{Iso})$ of $[T\mathcal{B}]^4_0$, i.e.,

$$\mathbb{T}_{\mathrm{iso}} = \langle \mathbb{T}, \mathbb{K}^\sharp \rangle \, \mathbb{K}^\sharp + \tfrac{1}{5} \langle \mathbb{T}, \mathbb{M}^\sharp \rangle \, \mathbb{M}^\sharp \neq \mathbb{T}, \tag{11.28}$$

where the coefficients on the right-hand side are found in precisely the same way as in Eq. (11.27).

A thorough analysis of the properties of *idempotence* and *orthogonality* (Walpole, 1981, 1984) enjoyed by the tensors of each of the bases $\{\mathbb{K}, \mathbb{M}\}$, $\{\mathbb{K}^\sharp, \mathbb{M}^\sharp\}$ and $\{\mathbb{K}^\flat, \mathbb{M}^\flat\}$ is discussed in a previous work (Federico, 2012), in the same covariant formalism used here. The idempotence and orthogonality of isotropic basis tensors implies that multiplication and inversion of isotropic tensors are performed by multiplying and inverting the individual scalars of the decomposition (11.26).

### 11.2.7 Transversely Isotropic Second- and Fourth-Order Tensors

The set

$$\mathbb{S}^2\mathcal{B} = \{\boldsymbol{m} \in T\mathcal{B} : \|\boldsymbol{m}\| = 1\}, \tag{11.29}$$

where $\|\boldsymbol{m}\| = \sqrt{\boldsymbol{m}.\boldsymbol{m}}$ is the Euclidean norm of vector $\boldsymbol{m}$, is the subset of all *unit* vectors in the tangent bundle $T\mathcal{B}$ and is called the (bundle) *unit sphere* in the body $\mathcal{B}$. When the point $x$ is fixed, one speaks about the *unit sphere* $\mathbb{S}^2_x\mathcal{B} = \{\boldsymbol{m} \in T_x\mathcal{B} : \|\boldsymbol{m}\| = 1\}$ at $x$. Transverse isotropy with respect to $\boldsymbol{m}$ is defined as the symmetry (i.e., the invariance) with respect to rotations about $\boldsymbol{m}$. The direction identified by $\boldsymbol{m}$ is called *symmetry axis*, and the class of equivalence of the planes orthogonal to $\boldsymbol{m}$ is called *transverse plane*.

The subspace of $[T\mathcal{B}]^2_0$ of all second-order "contravariant" symmetric tensors with transverse isotropy with respect to a direction $\boldsymbol{m}$ is denoted $([T\mathcal{B}]^2_0, \boldsymbol{m})$. The basis of $([T\mathcal{B}]^2_0, \boldsymbol{m})$ is given by (Walpole, 1981, 1984; Federico, 2012)

$$\boldsymbol{a} = \boldsymbol{m} \otimes \boldsymbol{m}, \tag{11.30a}$$

$$\boldsymbol{t} = \boldsymbol{g}^{-1} - \boldsymbol{a}, \tag{11.30b}$$

where $\boldsymbol{t}$ is the complement of tensor $\boldsymbol{a}$ to $\boldsymbol{g}^{-1}$, which serves as the "contravariant identity" in $[T\mathcal{B}]^2_0$. Evidently, both $\boldsymbol{a}$ and $\boldsymbol{t}$ are invariant under reflections $\boldsymbol{m} \mapsto -\boldsymbol{m}$, i.e., the sense of $\boldsymbol{m}$ is irrelevant. Tensors $\boldsymbol{a}$ and $\boldsymbol{t}$ take the geometrical meaning of *axial projection operator* and *transverse projection operator*, respectively. Indeed,

contraction of $\boldsymbol{a}$ and $\boldsymbol{t}$, by means of the metric tensor $\boldsymbol{g}$, with a vector $\boldsymbol{v}$ in $T\mathcal{B}$ yields the axial and transverse *vectorial* components of $\boldsymbol{v}$, respectively, as[2]

$$\boldsymbol{v}_{\parallel} = \boldsymbol{a}.\boldsymbol{v} = (\boldsymbol{m}.\boldsymbol{v})\boldsymbol{m}, \tag{11.31a}$$

$$\boldsymbol{v}_{\perp} = \boldsymbol{t}.\boldsymbol{v} = \boldsymbol{v} - (\boldsymbol{m}.\boldsymbol{v})\boldsymbol{m}. \tag{11.31b}$$

In the jargon of composite and fibre-reinforced materials, tensor $\boldsymbol{a}$ is often called the *structure tensor* or *fabric tensor* of direction $\boldsymbol{m}$. Tensor $\boldsymbol{t}$ is often simply called *projector* (Bonet and Wood, 2008; Gurtin et al., 2010). It is sometimes convenient to explicitly indicate the dependence of $\boldsymbol{a}$ and $\boldsymbol{t}$ on the direction $\boldsymbol{m}$, in which case we say that $\{\boldsymbol{a}(\boldsymbol{m}), \boldsymbol{t}(\boldsymbol{m})\}$ is the basis of the space $([T\mathcal{B}]^2_0, \boldsymbol{m})$. As seen in the case of isotropy, transversely isotropic second-order tensors are necessarily symmetric.

The basis of the subspace of $[T\mathcal{B}]^4_0$ of all tensors with transverse isotropy with respect to direction $\boldsymbol{m}$, denoted $([T\mathcal{B}]^4_0, \boldsymbol{m})$, has been obtained in two different versions by Walpole (1981, 1984). Initially, Walpole (1981) used a tensor basis allowing for a representation in the form of a $6\times 1$ array, which has been extensively used by other authors (Weng, 1990; Qiu and Weng, 1990; Bhattacharyya and Weng, 1994; Wu and Herzog, 2002; Federico et al., 2004, 2005). Later, Walpole (1984) perfected the representation, with new normalisation constants for the basis tensors, which allows for an extremely convenient representation in an array constituted by a $2\times 2$ matrix and 2 scalars (Walpole (1984) has also provided similar representations for all other symmetry groups). This later representation (Walpole, 1984) has been used in more recent works (Federico, 2015; Federico et al., 2015), developed within a covariant framework, and we do so in this chapter too.

The basis of $([T\mathcal{B}]^4_0, \boldsymbol{m})$ proposed by Walpole (1984) is obtained (similarly to that proposed in the older work; Walpole, 1981) by means of suitable tensor products, as

$$\mathbb{U}_{11} = \boldsymbol{a}\otimes\boldsymbol{a}, \qquad (\mathbb{U}_{11})^{ijkl} = a^{ij}\,a^{kl}, \tag{11.32a}$$

$$\mathbb{U}_{12} = \tfrac{\sqrt{2}}{2}\,\boldsymbol{a}\otimes\boldsymbol{t}, \qquad (\mathbb{U}_{12})^{ijkl} = \tfrac{\sqrt{2}}{2}\,a^{ij}\,t^{kl}, \tag{11.32b}$$

$$\mathbb{U}_{21} = \tfrac{\sqrt{2}}{2}\,\boldsymbol{t}\otimes\boldsymbol{a}, \qquad (\mathbb{U}_{21})^{ijkl} = \tfrac{\sqrt{2}}{2}\,t^{ij}\,a^{kl}, \tag{11.32c}$$

$$\mathbb{U}_{22} = \tfrac{1}{2}\,\boldsymbol{t}\otimes\boldsymbol{t}, \qquad (\mathbb{U}_{22})^{ijkl} = \tfrac{1}{2}\,t^{ij}\,t^{kl}, \tag{11.32d}$$

$$\mathbb{V}_1 = \tfrac{1}{2}\,(\boldsymbol{t}\underline{\otimes}\boldsymbol{t} + \boldsymbol{t}\overline{\otimes}\boldsymbol{t} - \boldsymbol{t}\otimes\boldsymbol{t}), \qquad (\mathbb{V}_1)^{ijkl} = \tfrac{1}{2}\,(t^{ik}\,t^{jl} + t^{il}\,t^{jk} - t^{ij}\,t^{kl}), \tag{11.32e}$$

$$\mathbb{V}_2 = \tfrac{1}{2}\,(\boldsymbol{a}\underline{\otimes}\boldsymbol{t} + \boldsymbol{a}\overline{\otimes}\boldsymbol{t} + \boldsymbol{t}\underline{\otimes}\boldsymbol{a} + \boldsymbol{t}\overline{\otimes}\boldsymbol{a}), \qquad (\mathbb{V}_2)^{ijkl} = \tfrac{1}{2}\,(a^{ik}\,t^{jl} + a^{il}\,t^{jk} + t^{ik}\,a^{jl} + t^{il}\,a^{jk}). \tag{11.32f}$$

The transversely isotropic basis in Eq. (11.32) is denoted $\{\mathbb{U}_{\alpha\beta}, \mathbb{V}_{\gamma}\}^2_{\alpha,\beta,\gamma=1}$ and, when it is convenient to explicitly indicate the dependence of the basis tensors

[2] In two of our past works [Eq. (2.8) in Federico and Grillo (2012), and Eq. (96) in Federico (2015)], we regrettably forgot to set the font in bold for the parallel and transverse components of a vector $\boldsymbol{v}$ with respect to a direction $\boldsymbol{m}$, and we may have therefore given the misleading impression that we were referring to scalar components when, in fact, we meant to speak about *vectorial* components.

on the direction $\boldsymbol{m}$, one says that $\{\mathbb{U}_{\alpha\beta}(\boldsymbol{m}), \mathbb{V}_\gamma(\boldsymbol{m})\}_{\alpha,\beta,\gamma=1}^{2}$ is the basis of the space $([T\mathcal{B}]_0^4, \boldsymbol{m})$. A tensor $\mathbb{T}$ in $([T\mathcal{B}]_0^4, \boldsymbol{m})$ is expressed as

$$\mathbb{T} = \overline{\mathbb{T}}^{\alpha\beta}\mathbb{U}_{\alpha\beta} + \overline{\mathbb{T}}^{\gamma}\mathbb{V}_\gamma, \tag{11.33}$$

where Einstein's summation convention is understood for $\alpha, \beta, \gamma \in \{1, 2\}$ and the components $\overline{\mathbb{T}}^{\alpha\beta}$ and $\overline{\mathbb{T}}^{\gamma}$ are obtained by the scalar product of $\mathbb{T}$ with each of the basis tensors, with some normalisation constants[3]:

$$\overline{\mathbb{T}}^{\alpha\beta} = \langle \mathbb{T}, \mathbb{U}_{\alpha\beta} \rangle, \qquad \overline{\mathbb{T}}^{\gamma} = \tfrac{1}{2} \langle \mathbb{T}, \mathbb{V}_\gamma \rangle. \tag{11.34}$$

In the basis of Eq. (11.32) the tensors $\mathbb{U}_{\alpha\beta}$ constitute an algebra isomorphic to that of $2 \times 2$ matrices (Walpole, 1984), which allows for grouping the Walpole components $\overline{\mathbb{T}}^{\alpha\beta}$ and $\overline{\mathbb{T}}^{\gamma}$ of Eq. (11.34) into the array

$$\overline{\mathbb{T}} = \left\{ \begin{bmatrix} \overline{\mathbb{T}}^{11} & \overline{\mathbb{T}}^{12} \\ \overline{\mathbb{T}}^{21} & \overline{\mathbb{T}}^{22} \end{bmatrix}, \overline{\mathbb{T}}^{1}, \overline{\mathbb{T}}^{2} \right\} = \{[\overline{\mathbb{T}}^{\alpha\beta}], \overline{\mathbb{T}}^{\gamma}\}, \tag{11.35}$$

which we call *Walpole array representation* of tensor $\mathbb{T}$. Note the compact notation $\overline{\mathbb{T}} = \{[\overline{\mathbb{T}}^{\alpha\beta}], \overline{\mathbb{T}}^{\gamma}\}$.

It is precisely for the form of the array in Eq. (11.35) that we find Walpole's formalism (Walpole, 1984) to be very convenient. Indeed, *all* operations on transversely isotropic tensors in $([T\mathcal{B}]_0^4, \boldsymbol{m})$ can be performed by working on the $2\times2$ matrix and the two scalars of the Walpole array of each tensor. Linear combination of tensors in $([T\mathcal{B}]_0^4, \boldsymbol{m})$ can be obtained via the linear combination of the matrices and the individual scalars. Given a tensor $\mathbb{T}$ with Walpole array $\overline{\mathbb{T}} = \{[\overline{\mathbb{T}}^{\alpha\beta}], \overline{\mathbb{T}}^{\gamma}\}$, the Walpole array of the transpose $\mathbb{T}$ is obtained by simply transposing the $2 \times 2$ matrix, i.e., $\overline{\mathbb{T}^T} = \overline{\mathbb{T}}^T = \{[\overline{\mathbb{T}}^{\alpha\beta}]^T, \overline{\mathbb{T}}^{\gamma}\}$. Moreover, since $\mathbb{U}_{12}^T = \mathbb{U}_{21}$, major (diagonal) symmetry of a tensor $\mathbb{T}$ is attained if $\overline{\mathbb{T}}^{12} = \overline{\mathbb{T}}^{21}$, in which case $\mathbb{T}$ has only 5 independent components, rather than the 6 independent components of the general case.[4] We also remark that positive definiteness of a tensor $\mathbb{T}$ in $([T\mathcal{B}]_0^4, \boldsymbol{m})$ can be checked extremely simply: $\mathbb{T}$ is positive definite if, and only if, the $2 \times 2$ matrix $[\overline{\mathbb{T}}^{\alpha\beta}]$ is positive definite and the two scalars $\overline{\mathbb{T}}^{\gamma}$ are strictly positive. We remark that

[3] In some previous works (Federico, 2010a,b), we used the normalisation constants of the later work by Walpole (1984) but kept the formalism with the $6 \times 1$ array formalism of the earlier work by Walpole (1981). We candidly admit that this was an infelicitous choice on our part. Also, because of an incautious copy-and-paste operation from the definitions of the basis tensors, we reported (see Appendices in Federico, 2010a,b) the wrong coefficients for the scalar products in Eq. (11.34).

[4] In our original work (see text immediately following Eq. (20) in Federico et al., 2004), we had stated that $\mathbb{U}_{11}$, $\mathbb{U}_{22}$, $\mathbb{V}_1$ and $\mathbb{V}_2$ (called $\mathbb{B}_2$, $\mathbb{B}_1$, $\mathbb{B}_3$ and $\mathbb{B}_4$, respectively, in Federico et al., 2004) span the whole space of major- and minor-symmetric (transversely isotropic) tensors, which is of course incorrect, as we should have added also $\frac{1}{2}(\mathbb{U}_{12} + \mathbb{U}_{21})$ (corresponding to $\frac{1}{2}(\mathbb{B}_5 + \mathbb{B}_6)$ in Federico et al., 2004).

*all* transversely isotropic fourth-order tensors [i.e., tensors of the space $([T\mathcal{B}]^4_0, \boldsymbol{m})$, spanned by the basis in Eq. (11.32)] enjoy minor symmetry.

At this point, one may wonder how to treat transversely isotropic fourth-order tensors of type other than those in $([T\mathcal{B}]^4_0, \boldsymbol{m})$, for instance, the tensors in $([T\mathcal{B}]^0_4, \boldsymbol{m})$, among which there are the inverses (when they exist) of those in $([T\mathcal{B}]^4_0, \boldsymbol{m})$. Fortunately, the representation with Walpole's array of Eq. (11.39) is *independent* of the type of fourth-order tensor at hand. For instance, if we transform a tensor $\mathbb{T}$ in $([T\mathcal{B}]^4_0, \boldsymbol{m})$ into its "covariant" counterpart $\mathbb{T}^\flat$ in $([T\mathcal{B}]^0_4, \boldsymbol{m})$, we have

$$\mathbb{T} = \overline{\mathbb{T}}^{\alpha\beta}\mathbb{U}_{\alpha\beta} + \overline{\mathbb{T}}^{\gamma}\mathbb{V}_{\gamma} \mapsto \mathbb{T}^\flat = \overline{\mathbb{T}}^{\alpha\beta}\mathbb{U}^\flat_{\alpha\beta} + \overline{\mathbb{T}}^{\gamma}\mathbb{V}^\flat_{\gamma}, \tag{11.36}$$

i.e., the transformation takes place on the basis tensors, leaving the Walpole components *untouched*. Thus, the double contraction of, e.g., a tensor $\mathbb{T}$ in $([T\mathcal{B}]^2{}_2, \boldsymbol{m})$ and a tensor $\mathbb{Z}$ in $([T\mathcal{B}]^4_0, \boldsymbol{m})$ is obtained by keeping in mind that the resulting tensor belongs to $([T\mathcal{B}]^4_0, \boldsymbol{m})$, and by performing the ordinary row-by-column product of the two matrices, and the multiplication of the homologous scalars, i.e.,

$$\overline{\mathbb{T} : \mathbb{Z}} = \left\{ \begin{bmatrix} \overline{\mathbb{T}}^{11} & \overline{\mathbb{T}}^{12} \\ \overline{\mathbb{T}}^{21} & \overline{\mathbb{T}}^{22} \end{bmatrix} \begin{bmatrix} \overline{\mathbb{Z}}^{11} & \overline{\mathbb{Z}}^{12} \\ \overline{\mathbb{Z}}^{21} & \overline{\mathbb{Z}}^{22} \end{bmatrix}, \overline{\mathbb{T}}^1\overline{\mathbb{Z}}^1, \overline{\mathbb{T}}^2\overline{\mathbb{Z}}^2 \right\}. \tag{11.37}$$

Also, it is now clear how to represent the inverse (when it exists) of a tensor $\mathbb{T}$ in $([T\mathcal{B}]^4_0, \boldsymbol{m})$. Indeed, the inverse of an invertible tensor $\mathbb{T}$ in $([T\mathcal{B}]^4_0, \boldsymbol{m})$ is the tensor $\mathbb{T}^{-1}$ in $([T\mathcal{B}]^0_4, \boldsymbol{m})$ such that $\mathbb{T} : \mathbb{T}^{-1} = \mathbb{I}$ and $\mathbb{T}^{-1} : \mathbb{T} = \mathbb{I}^T$, and has Walpole array representation

$$\overline{\mathbb{T}^{-1}} \equiv \overline{\mathbb{T}}^{-1} = \left\{ \begin{bmatrix} \overline{\mathbb{T}}^{11} & \overline{\mathbb{T}}^{12} \\ \overline{\mathbb{T}}^{21} & \overline{\mathbb{T}}^{22} \end{bmatrix}^{-1}, \frac{1}{\overline{\mathbb{T}}^1}, \frac{1}{\overline{\mathbb{T}}^2} \right\}. \tag{11.38}$$

In an orthonormal basis $\{\boldsymbol{e}_i\}_{i=1}^3$, such that $\boldsymbol{e}_1 = \boldsymbol{m}$, the components of the Walpole array $\overline{\mathbb{T}} = \{[\overline{\mathbb{T}}^{\alpha\beta}], \overline{\mathbb{T}}^{\gamma}\}$ of a tensor $\mathbb{T}$ are related to the conventional components $\mathrm{T}^{ijkl}$ by

$$\overline{\mathbb{T}} = \left\{ \begin{bmatrix} \mathrm{T}^{1111} & \sqrt{2}\,\mathrm{T}^{1122} \\ \sqrt{2}\,\mathrm{T}^{2211} & 2\,\mathrm{T}^{2222} - 2\,\mathrm{T}^{2323} \end{bmatrix}, 2\,\mathrm{T}^{2323}, 2\,\mathrm{T}^{1212} \right\}. \tag{11.39}$$

Since an isotropic tensor is transversely isotropic with respect to any direction $\boldsymbol{m}$, it is possible to express it in Walpole's transversely isotropic representation. In particular, the "contravariant" fourth-order identity and the spherical and deviatoric operators in $[T\mathcal{B}]^4_0$, defined in Eq. (11.24), have Walpole array representations

$$\overline{\mathbb{I}^\sharp} = \left\{ \begin{bmatrix} 1 & 0 \\ 0 & 1 \end{bmatrix}, 1, 1 \right\}, \tag{11.40a}$$

$$\overline{\mathbb{K}^\sharp} = \left\{ \begin{bmatrix} \frac{1}{3} & \frac{\sqrt{2}}{3} \\ \frac{\sqrt{2}}{3} & \frac{2}{3} \end{bmatrix}, 0,\ 0 \right\}, \tag{11.40b}$$

$$\overline{\mathbb{M}^\sharp} = \left\{ \begin{bmatrix} \frac{2}{3} & -\frac{\sqrt{2}}{3} \\ -\frac{\sqrt{2}}{3} & \frac{1}{3} \end{bmatrix}, 1,\ 1 \right\}. \tag{11.40c}$$

Thus, a generic symmetric isotropic tensor $\mathbb{T}$ in $([T\mathcal{B}]_0^4, \mathrm{Sym}, \mathrm{Iso})$, which is written as

$$\mathbb{T} = 3\,k\,\mathbb{K}^\sharp + 2\,m\,\mathbb{M}^\sharp, \tag{11.41}$$

in the symmetric isotropic basis $\{\mathbb{K}^\sharp, \mathbb{M}^\sharp\}$ admits the representation

$$\overline{\mathbb{T}} = \left\{ \begin{bmatrix} k + \frac{4}{3}m & \sqrt{2}\,(k - \frac{2}{3}m) \\ \sqrt{2}\,(k - \frac{2}{3}m) & 2\,(k + \frac{4}{3}m) - 2\,m \end{bmatrix}, 2\,m,\ 2\,m \right\}, \tag{11.42}$$

where the coefficients $3\,k$ and $2\,m$ in Eq. (11.41) echo those typical of isotropic linear elasticity [see Eq. (11.54)] and are found as shown in Eq. (11.26).

### *11.2.8 Basic Relations of the Theory of Linear Elasticity*

Linear elasticity can be developed as an independent branch of Mathematical Physics (see, e.g., the text by Gurtin, 1972), or can be retrieved by linearising the general Theory of (Non-Linear) Elasticity (a covariant procedure is presented in the text by Marsden and Hughes, 1983). Linear Elasticity has a strong pedagogical character. Indeed, it often allows to find either analytical solutions or solutions in closed form to many problems of engineering relevance. Moreover, in many circumstances, it suffices to determine first-order approximations that, with relatively low computational costs, provide solutions to real-world problems even in the cases in which engineering materials undergo finite deformations. Perhaps because of these advantages, Linear Elasticity is what is usually taught to the vast majority of the students in structural/mechanical Engineering or Physics during their undergraduate studies. Linear Elasticity is so diffused that some call it "Classical Elasticity" and that, still today, quite many understand "Linear Elasticity", when they hear the word "Elasticity". One can choose to present the linear theory of elasticity either, and equivalently, by starting from stress or from energy. We choose the latter and we present this approach after having briefly introduced displacement, strain and stress.

In a body $\mathcal{B}$, the *displacement* is the vector field

$$\boldsymbol{u} : \mathcal{B} \to T\mathcal{B} : x \mapsto \boldsymbol{u}(x) \in T_x\mathcal{B}, \tag{11.43}$$

whose gradient (also called *covariant derivative*) is called *displacement gradient*,

$$\boldsymbol{h} = \operatorname{grad} \boldsymbol{u}, \qquad h^i{}_j = u^i{}_{|j}, \tag{11.44}$$

where the vertical bar denotes covariant differentiation.[5] The *infinitesimal strain* is the "covariant" second-order tensor field

$$\boldsymbol{\epsilon} : \mathcal{B} \to [T\mathcal{B}]^0_2 : x \mapsto \boldsymbol{\epsilon}(x) \in [T_x\mathcal{B}]^0_2, \tag{11.45}$$

defined as the symmetric part of the "covariant" displacement gradient tensor $\boldsymbol{h}^\flat = \boldsymbol{g}\,\boldsymbol{h}$ (with components $h_{ij} = g_{ip}h^p{}_j$), i.e.,

$$\boldsymbol{\epsilon} = \tfrac{1}{2}\,(\boldsymbol{h}^\flat + \boldsymbol{h}^{\flat T}), \qquad \epsilon_{ij} = \tfrac{1}{2}\,(h_{ij} + h_{ji}). \tag{11.46}$$

The *Cauchy stress* is defined as a "contravariant" second-order tensor field[6]

$$\boldsymbol{\sigma} : \mathcal{B} \to [T\mathcal{B}]^2_0 : x \mapsto \boldsymbol{\sigma}(x) \in [T_x\mathcal{B}]^2_0. \tag{11.47}$$

In the absence of external body forces and neglecting inertia, the balance of linear momentum reduces to the vanishing of the divergence of the Cauchy stress, i.e.,

$$\operatorname{div} \boldsymbol{\sigma} = \boldsymbol{0}, \qquad \sigma^{ij}{}_{|j} = 0. \tag{11.48}$$

Often, the balance of angular momentum is invoked to obtain the condition of symmetry of the Cauchy stress:

$$\boldsymbol{\sigma} = \boldsymbol{\sigma}^T, \qquad \sigma^{ij} = \sigma^{ji}. \tag{11.49}$$

Balance of linear and angular momentum constitute a system of 6 equations in 12 unknowns (the 3 components of the displacement and the 9 components of the Cauchy stress) or, equivalently, of 3 independent equations in 9 unknowns (the 3 components of the displacement and the 6 independent components of the Cauchy stress). In order to be able to close the system, the need arises for 6 additional relations, called *constitutive laws*, expressing the stress tensor as a function of the strain tensor.

[5] In Cartesian coordinates, covariant differentiation of a vector or tensor field reduces to the regular partial derivative and one writes, e.g., for a vector field, $u^i{}_{,j}$.

[6] In the general, large-deformation setting of continuum mechanics, the Cauchy stress is defined as a *spatial* tensor field, valued in $[T\mathcal{S}]^2_0$. In the small-deformation theory, however, the distinction between reference configuration (or body $\mathcal{B}$) and current configuration fades out, and it is legitimate to define also tensors, which by their nature would be spatial, in the body $\mathcal{B}$ rather than in the space $\mathcal{S}$. In contrast, it is natural to define the infinitesimal strain $\boldsymbol{\epsilon}$ as a tensor field valued in $[T\mathcal{B}]^0_2$, since it can be thought of as the linearisation of the *material* Green-Lagrange strain $\boldsymbol{E}$.

A material is said to obey a linear elastic constitutive law if there exists a quadratic function of the infinitesimal strain,

$$W(x) = \hat{W}(\boldsymbol{\epsilon}(x), x) = \tfrac{1}{2}\,\boldsymbol{\epsilon}(x) : \mathbb{L}(x) : \boldsymbol{\epsilon}(x) = \tfrac{1}{2}\,\epsilon_{ij}(x)\,\mathrm{L}^{ijkl}(x)\,\epsilon_{kl}(x), \tag{11.50}$$

called (quadratic) *elastic potential* ($W : \mathcal{B} \to \mathbb{R} : x \mapsto W(x)$ denotes the *scalar field*, while $\hat{W}$ denotes the corresponding *constitutive function*), such that the stress can be obtained as the derivative of $\hat{W}$ with respect to the strain, i.e.,

$$\boldsymbol{\sigma}(x) = \frac{\partial \hat{W}}{\partial \boldsymbol{\epsilon}}(\boldsymbol{\epsilon}(x), x) = \mathbb{L}(x) : \boldsymbol{\epsilon}(x), \qquad \sigma^{ij}(x) = \frac{\partial \hat{W}}{\partial \epsilon_{ij}}(\boldsymbol{\epsilon}(x), x) = \mathrm{L}^{ijkl}(x)\,\epsilon_{kl}(x). \tag{11.51}$$

The "contravariant" fourth-order tensor field

$$\mathbb{L} : \mathcal{B} \to [T\mathcal{B}]^4_0 : x \mapsto \mathbb{L}(x) \in [T_x\mathcal{B}]^4_0 \tag{11.52}$$

is called the *linear elasticity tensor* and does *not* depend on $x$ if the body is *homogeneous*. Equation (11.50) and the symmetry of $\boldsymbol{\epsilon}$ imply that the elasticity tensor $\mathbb{L}$ enjoys both major and minor symmetry. In order to guarantee the positiveness of the elastic potential, which implies the positivity of the internal work (or deformation work), one normally requires the positive definiteness of the elasticity tensor $\mathbb{L}$. The positive definiteness of $\mathbb{L}$ in turn implies its invertibility. Note that the inverse of the "contravariant" elasticity tensor $\mathbb{L}$, which is also called *stiffness elasticity tensor*, is the "covariant" *compliance elasticity tensor* $\mathbb{L}^{-1}$, which is a tensor field valued in $[T\mathcal{B}]^0_4$.

For a transversely isotropic elasticity tensor $\mathbb{L}$, Walpole's representation takes the form [see Eq. (11.39)]

$$\overline{\mathbb{L}} = \left\{ \begin{bmatrix} n & \sqrt{2}\,\ell \\ \sqrt{2}\,\ell & 2\,c \end{bmatrix}, 2\,\mu_t,\ 2\,\mu_a \right\}, \tag{11.53}$$

where (see Hill, 1964) $n$ is the *modulus in uniaxial strain* (also called *p-wave modulus* or also, in the literature on articular cartilage, *aggregate modulus*: see Holmes and Mow, 1990), $c$ is the *plane-strain bulk modulus* (in the transverse plane of transverse isotropy), $\ell$ is the *cross modulus* (transversely isotropic analogue of the first Lamé's constant $\lambda = \kappa - \frac{2}{3}\,\mu$ of isotropic linear elasticity: see Spencer, 1984), $\mu_t$ is the shear modulus in the transverse plane, and $\mu_a$ is the shear modulus in any plane containing the axis of symmetry $\boldsymbol{m}$ of transverse isotropy.

An isotropic elasticity tensor $\mathbb{L}$ can be represented in the basis $\{\mathbb{K}^\sharp, \mathbb{M}^\sharp\}$ of symmetric isotropic tensors in $[T\mathcal{B}]^4_0$ as [see Eq. (11.41)]

$$\mathbb{L} = 3\,\kappa\,\mathbb{K}^\sharp + 2\,\mu\,\mathbb{M}^\sharp, \tag{11.54}$$

where $\kappa$ and $\mu$ are the bulk modulus and shear modulus, respectively. Using Eq. (11.42) for the expression of an isotropic tensor in Walpole's transversely isotropic array, we can represent the isotropic elasticity tensor of Eq. (11.54) as

$$\overline{\mathbb{L}} = \left\{ \begin{bmatrix} \kappa + \frac{4}{3}\mu & \sqrt{2}\,(\kappa - \frac{2}{3}\mu) \\ \sqrt{2}\,(\kappa - \frac{2}{3}\mu) & 2\,(\kappa + \frac{4}{3}\mu) - 2\,\mu \end{bmatrix}, 2\,\mu,\, 2\,\mu \right\}, \tag{11.55}$$

in which it is possible to recognise the first Lamé's constant $\lambda = \kappa - \frac{2}{3}\mu$ and the modulus in uniaxial strain $n = \kappa + \frac{4}{3}\mu = \lambda + 2\,\mu$. In terms of the Lamé's moduli $\lambda$ and $\mu$, the Walpole array reads

$$\overline{\mathbb{L}} = \left\{ \begin{bmatrix} \lambda + 2\,\mu & \sqrt{2}\,\lambda \\ \sqrt{2}\,\lambda & 2(\lambda + 2\,\mu) - 2\,\mu \end{bmatrix}, 2\,\mu,\, 2\,\mu \right\}, \tag{11.56}$$

where $(\lambda + 2\,\mu) - \mu = \lambda + \mu$ is the isotropic equivalent of the plane-strain bulk modulus $c$ of transverse isotropy [Eq. (11.53)].

## 11.3 Composite Materials with Aligned Inclusions

We first recall the definitions of *Eshelby's fourth-order tensor* $\mathbb{S}$ introduced by Eshelby (1957) and of the closely related *strain concentration tensor* $\mathbb{A}$, which arises in the case of inclusions with material properties different from those of the matrix. Finally, we introduce composite materials with inclusions as described by the works of Hill (1963, 1965) and Walpole (1966a,b, 1969) and focus on the case of aligned inclusions.

### *11.3.1 Eshelby's Inclusion and Fourth-Order Tensor*

Eshelby (1957) studied the problem of an inclusion in an infinite matrix, and in particular the case of an ellipsoidal inclusion. Eshelby constructed the inclusion problem in several steps (Eshelby, 1957, last paragraph of page 376), which we report in our own words, following a previous work (Alhasadi and Federico, 2017):

1. A cavity is cut in a body $\mathcal{B}$ and a *transformation strain* $\boldsymbol{\epsilon}^*$ is applied to the geometry of the region $\mathcal{D}$ occupied by the cavity, which is thus mapped into the new region $\mathcal{D}^*$; the remaining region $\mathcal{M} = \mathcal{B} \setminus \mathcal{D}$ is called *matrix*.
2. The transformed region $\mathcal{D}^*$ is now "filled" with a material, which could be the same as that of the matrix, with elasticity tensor $\mathbb{L}_0$, or another one, with elasticity tensor $\mathbb{L}_1$. The transformed region $\mathcal{D}^*$, now assigned with certain elastic properties, constitutes the *inclusion*, which *no longer fits* the original cavity $\mathcal{D}$.

3. In order to make the inclusion occupying the transformed region $\mathcal{D}^*$ fit again into the original cavity $\mathcal{D}$, tractions are applied on the boundary of the inclusion, so that it attains a strain $-\boldsymbol{\epsilon}^*$, and then it is put back into the cavity.
4. Once the inclusion is back in place, the tractions on the boundary are removed, and so the inclusion and the surrounding matrix relax, causing a *cancelling strain* or *constrained strain* $\boldsymbol{\epsilon}^c$, which is *discontinuous* across the boundary of the inclusion.

At the end of this sequence of operations, and in the absence of external tractions applied on the boundary of the body $\mathcal{B}$, the *residual* strain due to the *geometrical* misfit is

$$\boldsymbol{\epsilon}^b = \boldsymbol{\epsilon}^c, \qquad \text{in } \mathcal{M}, \tag{11.57a}$$

$$\boldsymbol{\epsilon}^b = \boldsymbol{\epsilon}^c - \boldsymbol{\epsilon}^*, \qquad \text{in } \mathcal{D}, \tag{11.57b}$$

where we emphasise again that the cancelling strain $\boldsymbol{\epsilon}^c$ is *discontinuous* across the boundary of $\mathcal{D}$ and thus must be studied and described *piecewise*.

In the absence of the inclusion, i.e., if the body $\mathcal{B}$ were perfectly homogeneous (elasticity tensor equal to $\mathbb{L}_0$ everywhere) and without any region with geometrical misfit (identically vanishing transformation strain $\boldsymbol{\epsilon}^*$), the cancelling strain would vanish identically, and the application of traction forces on the boundary of $\mathcal{B}$ would cause a stress state described by the continuous field $\boldsymbol{\sigma}^a$ everywhere in $\mathcal{B}$, which in turn would cause the continuous strain field

$$\boldsymbol{\epsilon}^a = \mathbb{L}_0^{-1} : \boldsymbol{\sigma}^a, \quad \text{everywhere in } \mathcal{B}. \tag{11.58}$$

In the presence of both inclusion and external tractions, the linearity of the problem allows to write the total strain as the superposition of that in Eq. (11.57), which was obtained in the absence of external applied tractions, and of that in Eq. (11.58), which was obtained in the absence of inclusion, as

$$\boldsymbol{\epsilon} = \boldsymbol{\epsilon}^a + \boldsymbol{\epsilon}^b = \boldsymbol{\epsilon}^a + \boldsymbol{\epsilon}^c, \qquad \text{in } \mathcal{M}, \tag{11.59a}$$

$$\boldsymbol{\epsilon} = \boldsymbol{\epsilon}^a + \boldsymbol{\epsilon}^b = \boldsymbol{\epsilon}^a + \boldsymbol{\epsilon}^c - \boldsymbol{\epsilon}^* \qquad \text{in } \mathcal{D}. \tag{11.59b}$$

For the case of an ellipsoidal inclusion, it is clear that it remains an ellipsoid if, and only if, the transformation strain $\boldsymbol{\epsilon}^*$ is uniform (Eshelby, 1957). In this case, also the cancelling strain $\boldsymbol{\epsilon}^c$ in the inclusion is uniform, and it is possible to relate it to the transformation strain $\boldsymbol{\epsilon}^*$ by means of the relation (Eshelby, 1957)

$$\boldsymbol{\epsilon}^c = \mathbb{S} : \boldsymbol{\epsilon}^*, \quad \text{in } \mathcal{D}, \tag{11.60}$$

where the tensor $\mathbb{S}$ in $[T\mathcal{B}]_2{}^2$ is the *fourth-order Eshelby tensor*, which depends on ratios of the elastic constants of the matrix and on the geometry of the inclusion. For an isotropic matrix, there is only one independent ratio of elastic constants,

which is usually chosen to be the Poisson's ratio $\nu_0$ (e.g., Qiu and Weng, 1990). For the case of spheroidal inclusions, i.e., revolution ellipsoids, the only independent geometrical ratio is that of the major to the minor semi-axis (e.g., Qiu and Weng, 1990). Note that the fourth-order Eshelby tensor can be seen as the linear operator $\mathbb{S} : [\mathcal{TB}]^0_2 \to [\mathcal{TB}]^0_2$ mapping the transformation strain into the cancelling strain. In components, Eq. (11.60) reads

$$\epsilon^c_{ij} = \mathrm{S}_{ij}{}^{kl}\, \epsilon^*_{kl}, \quad \text{in } \mathcal{D}. \tag{11.61}$$

We remark that the Eshelby tensor $\mathbb{S}$ has minor symmetry on each pair of legs, but it lacks major symmetry (i.e., its "contravariant" counterpart $\mathbb{S}^\sharp$, with components $(\mathbb{S}^\sharp)^{ijkl} \equiv \mathrm{S}^{ijkl} = g^{ip}\, g^{jq}\, \mathrm{S}_{pq}{}^{kl}$, and its "covariant" counterpart $\mathbb{S}^\flat$, with components $(\mathbb{S}^\flat)_{ijkl} \equiv \mathrm{S}_{ijkl} = \mathrm{S}_{ij}{}^{rs}\, g_{rk}\, g_{sl}$, lack major symmetry). Therefore, assuming an isotropic matrix, for the case of an ellipsoidal inclusion with three distinct semi-axes, $\mathbb{S}$ is a non-major-symmetric orthotropic tensor with 12 independent components and, for the case of a spheroidal inclusion with two equal semi-axes (i.e., a revolution ellipsoid), it is a non-major-symmetric transversely isotropic tensor with 6 independent components.

There are three possible inclusion problems:

- The "homogeneous inclusion", with geometrical misfit caused by a transformation strain $\boldsymbol{\epsilon}^*$, but material properties identical to those of the matrix, i.e., $\mathbb{L}_0 = \mathbb{L}_1$;
- The "inhomogeneous inclusion", with no geometrical misfit, i.e., $\boldsymbol{\epsilon}^* = \mathbf{0}$, but material properties different from those of matrix, i.e., $\mathbb{L}_0 \neq \mathbb{L}_1$;
- The "general inclusion", with both geometrical misfit, i.e., $\boldsymbol{\epsilon}^* \neq \mathbf{0}$, and material properties different from those of matrix, i.e., $\mathbb{L}_0 \neq \mathbb{L}_1$.

The "homogeneous" case is the fundamental one, and indeed the "inhomogeneous" and the "general" cases are solved by reducing the effect of the different material properties to an *equivalent transformation strain* (Eshelby, 1957; Mura, 1987; Alhasadi and Federico, 2017). In this work, we shall restrict our attention to the "inhomogeneous" case. Thus, we shall exclusively deal with inclusions with no geometrical misfit with the matrix but with material properties different from those of the matrix.

### *11.3.2 Strain Concentration Tensor*

The *strain concentration tensor* arises in the cases of the "inhomogeneous" inclusion and "general" inclusion and is the object that captures the difference in material properties between matrix and inclusion within the method of the *equivalent transformation strain*, which is that fictitious transformation strain that

has the same effect on the stress and strain fields that the mismatch in material properties has. This method is, again, described in detail by Eshelby (1957), and we also mention the classical book by Mura (1987).

The standard derivation of the strain concentration tensor is done in the case of the "inhomogeneous inclusion", and we report its expression (for the details, see, e.g., Weng, 1984, 1990; Alhasadi and Federico, 2017)

$$\mathbb{A} = \left[\mathbb{I}^T + \mathbb{S} : [\mathbb{L}_0^{-1} : \mathbb{L}_1 - \mathbb{I}^T]\right]^{-1}, \quad \text{in } \mathcal{D}, \tag{11.62}$$

which clearly depends on the Eshelby tensor, $\mathbb{S}$, and the elasticity tensors of matrix and inclusion, $\mathbb{L}_0$ and $\mathbb{L}_1$. Like $\mathbb{S}$, tensor $\mathbb{A}$ is in $[T\mathcal{B}]_2{}^2$ and is endowed with minor, but not major, symmetry. Its component expression is

$$(\mathbb{A}^{-1})_{ij}{}^{kl} = (\mathbb{I}^T)_{ij}{}^{kl} + \mathrm{S}_{ij}{}^{pq}\,[(\mathbb{L}_0^{-1})_{pqrs}\,(\mathbb{L}_1)^{rskl} - (\mathbb{I}^T)_{pq}{}^{kl}], \quad \text{in } \mathcal{D}. \tag{11.63}$$

Note the use of the *transpose* of the symmetric identity $\mathbb{I}$. Indeed, since the symmetric identity $\mathbb{I}$ belongs to $[T\mathcal{B}]^2{}_2$, it is necessary here to use its transpose $\mathbb{I}^T$, which belongs to $[T\mathcal{B}]_2{}^2$, in order to be able to sum it to the other tensors. This distinction is unnecessary in Cartesian coordinates, and indeed in all papers and books we are aware of, including our own past works, one finds the expression in Eq. (11.62) written with $\mathbb{I}$.

The strain concentration tensor gives the cancelling strain in the inclusion as

$$\boldsymbol{\epsilon}^c = \left(\mathbb{A} - \mathbb{I}^T\right) : \boldsymbol{\epsilon}^a, \quad \text{in } \mathcal{D}, \tag{11.64}$$

with components

$$\epsilon_{ij}^c = \left(\mathrm{A}_{ij}{}^{kl} - (\mathbb{I}^T)_{ij}{}^{kl}\right)\,\epsilon_{kl}^a, \quad \text{in } \mathcal{D}. \tag{11.65}$$

It is important to note the structural similarity between Eqs. (11.60) and (11.64). However, it is even more important to emphasise that, while in the case of the "homogeneous inclusion" [Eq. (11.60)], the cancelling strain $\boldsymbol{\epsilon}^c$ is a constant once the transformation strain $\boldsymbol{\epsilon}^*$ is assigned, in the case of the "inhomogeneous inclusion", the cancelling strain $\boldsymbol{\epsilon}^c$ is *linearly related* to the applied strain $\boldsymbol{\epsilon}^a$. Indeed, since there is no geometrical misfit ($\boldsymbol{\epsilon}^* = \mathbf{0}$), the cancelling strain $\boldsymbol{\epsilon}^c$ is identically zero when no tractions are applied, i.e., when the applied strain $\boldsymbol{\epsilon}^a$ is zero.

By adding the applied strain $\boldsymbol{\epsilon}^a$ to either side of Eq. (11.64), we obtain the total strain in the "inhomogeneous" inclusion as

$$\boldsymbol{\epsilon} = \boldsymbol{\epsilon}^a + \boldsymbol{\epsilon}^c = \mathbb{A} : \boldsymbol{\epsilon}^a, \quad \text{in } \mathcal{D}, \tag{11.66}$$

with component expression

$$\epsilon_{ij} = \epsilon_{ij}^a + \epsilon_{ij}^c = \mathrm{A}_{ij}{}^{kl}\,\epsilon_{kl}^a, \quad \text{in } \mathcal{D}. \tag{11.67}$$

Equation (11.66) gives $\mathbb{A}$ in $[\mathcal{TB}]_2{}^2$ its physical meaning of *strain concentration tensor*: it can indeed be seen as the linear operator $\mathbb{A} : [\mathcal{TB}]_2^0 \to [\mathcal{TB}]_2^0$ that maps the applied strain $\boldsymbol{\epsilon}^a$ that would be attained in the absence of inclusion into the strain $\boldsymbol{\epsilon}$ *actually attained* by the inclusion.

### *11.3.3 Composites with Spheroidal Inclusions and the Aligned Case*

In the 1960s, Hill (1963, 1965), Hashin (1963) and Walpole (1966a,b, 1969) gave fundamental contributions to the development of techniques for the evaluation of the overall elasticity tensor (overall elastic moduli, in the terminology of the time) of a composite starting from the elasticity tensors of the individual constituents of the composite. A composite differs from the system of Eshelby's inclusion problem in that an inclusion is no longer a solitary *singularity* in an infinite matrix, but is one of many other inclusions, which could be of the same or of different type.

The problem of the evaluation of the overall elasticity tensor for a composite with one or more families of inclusions is therefore tackled by means of the concept of *representative element of volume* or, with the customary acronym, REV. The REV could be defined as the smallest region whose material properties are equivalent to those of the whole composite. We quote the definition of REV given by Hill (1963):

> This phrase [*representative element of volume*] will be used when referring to a sample that (a) is structurally entirely typical of the whole mixture on average, and (b) contains a sufficient number of inclusions for the apparent overall moduli to be effectively independent of the surface values of traction and displacement, so long as these values are "macroscopically uniform". That is, they fluctuate about a mean with a wavelength small compared with the dimensions of the sample, and the effects of such fluctuations become insignificant within a few wavelengths of the surface. The contribution of this surface layer to any average can be made negligible by taking the sample large enough.

Thus, the REV that we consider must contain a sufficient number of inclusions for the overall elasticity tensor (or the collection of the "apparent elastic moduli", in Hill's words) to be representative of that of the whole composite.

The composite is assumed to be comprised of $N+1$ phases, with phase 0 referring to the matrix and phases $r \in \{1, \dots, N\}$ referring to the $r$-th inclusion families. The inclusions are assumed to be *perfectly fitted* (Walpole, 1966a) in the matrix, which, in Eshelby's terminology, means that they are "inhomogeneous inclusions", i.e., inclusions with *no geometrical misfit* with the matrix, but with elastic properties *different* from those of the matrix. It is important to emphasise that, in order to be able to apply Eshelby's theory as described in Sects. 11.3.1 and 11.3.2, which is based on an *inclusion in an infinite matrix*, we must make sure that each inclusion is far enough from its prime neighbours, and the interactions among inclusions can be neglected. This is achieved by imposing a reasonably low *volumetric fraction* for each of the inclusion phases. The volumetric fraction of each phase is defined as

$$\phi_r = \frac{\Omega_r}{\Omega}, \tag{11.68}$$

where $\Omega$ is the volume of the REV, and $\Omega_r$ is the volume of the portion of the REV occupied by phase $r$. The volumetric fractions obey the constraint

$$\sum_{r=0}^{N} \phi_r = 1. \tag{11.69}$$

The strain concentration tensor seen in Sect. 11.3.2 has been extensively used in the determination of the overall elastic properties of composite materials with inclusions (see, e.g., Hill, 1963; Walpole, 1966a,b, 1969; Weng, 1984, 1990; Qiu and Weng, 1990). In the formalism introduced by Walpole (1966a,b, 1969) and Weng (1990), the overall elasticity tensor $\mathbb{L}$ reads

$$\mathbb{L} = \left[\sum_{r=0}^{N} \phi_r \mathbb{L}_r : \mathbb{A}_r\right] : \left[\sum_{r=0}^{N} \phi_r \mathbb{A}_r\right]^{-1}, \tag{11.70}$$

where $\mathbb{L}_r$ is the elasticity tensor of phase $r$ and

$$\mathbb{A}_r = \left[\mathbb{I}^T + \mathbb{S}_r : [\mathbb{L}_0^{-1} : \mathbb{L}_r - \mathbb{I}^T]\right]^{-1} \tag{11.71}$$

is the strain concentration tensor of the $r$-th phase, in which $\mathbb{S}_r$ is the Eshelby fourth-order tensor relative to the $r$-th phase, depending on the shape of the inclusions of phase $r$ and the elastic constants of the matrix. Note that the strain concentration tensor $\mathbb{A}_0$ of the matrix is identically equal to the transpose $\mathbb{I}^T$ of the symmetric identity. Indeed, *since the matrix is not an inclusion embedded in itself*, from Eq. (11.71) we have

$$\mathbb{A}_0 = \left[\mathbb{I}^T + \mathbb{S}_0 : [\mathbb{L}_0^{-1} : \mathbb{L}_0 - \mathbb{I}^T]\right]^{-1} = \left[\mathbb{I}^T + \mathbb{S}_0 : \mathbb{O}\right]^{-1} = \mathbb{I}^T, \tag{11.72}$$

where $\mathbb{O}$ is the zero tensor, regardless of the value of the tensor $\mathbb{S}_0$.[7]

We remark that Eq. (11.70) is analogical to that of the centre of mass of a system of particles, i.e.,

$$x_G = \frac{\sum_{r=0}^{N} m_r x_r}{\sum_{r=0}^{N} m_r}. \tag{11.73}$$

[7] On one occasion, we had stated that $\mathbb{S}_0$ reduces to the identity $\mathbb{I}^T$ (paragraph following Eq. (35) in Federico et al., 2004) and, on another occasion, that it reduces to the zero tensor $\mathbb{O}$ (paragraph following Eq. (12) in Federico, 2010a). Both statements are incorrect, as this $\mathbb{S}_0$ is really arbitrary. One can think to obtain $\mathbb{A}_0$ by imagining to have an inclusion with an arbitrary ellipsoidal shape and an elasticity tensor $\mathbb{L}_0'$, which defines a corresponding $\mathbb{S}_0$, and then by performing the limit $\mathbb{L}_0' \to \mathbb{L}_0$. This yields $\mathbb{A}_0 \to \mathbb{I}^T$ regardless of the value of $\mathbb{S}_0$.

In this analogy, Eq. (11.70) provides the "barycentric elasticity tensor" of a composite, in which the "masses" are the products $\phi_r \, \mathbb{A}_r$ and the "moment arms" are the elasticity tensors $\mathbb{L}_r$.

In principle, Eq. (11.70) applies to any composite with ellipsoidal inclusions. However, for ellipsoidal inclusion families with different semi-axis ratios, different alignment of the semi-axes and different alignment of the directions or planes of material symmetry, the overall elasticity tensor could be completely anisotropic. Equation (11.70) becomes immediately usable in the case of transverse isotropy with respect to a given direction $\boldsymbol{m}_0$, which is obtained when:

(A1) The matrix is either isotropic or transversely isotropic with respect to direction $\boldsymbol{m}_0$.
(A2) All inclusions in all families have their axis of symmetry oriented in direction $\boldsymbol{m}_0$, are spheroidal (i.e., are revolution ellipsoids) and are either isotropic or transversely isotropic with respect to $\boldsymbol{m}_0$.

When the two conditions (A1) and (A2) are satisfied, all tensors featuring in Eq. (11.70) are transversely isotropic in direction $\boldsymbol{m}_0$ and can be represented using Walpole's formalism (Walpole, 1981, 1984) presented in Sect. 11.2.7. This is the procedure followed by Weng (1990) and Qiu and Weng (1990), leading to the Walpole array representation

$$\overline{\mathbb{L}} = \left[\sum\nolimits_{r=0}^{N} \phi_r \, \overline{\mathbb{L}_r : \mathbb{A}_r}\right] \left[\sum\nolimits_{r=0}^{N} \phi_r \, \overline{\mathbb{A}_r}\right]^{-1} . \tag{11.74}$$

Qiu and Weng (1990) also noted that the lack of major symmetry of the strain concentration tensors $\mathbb{A}_r$ causes in general the lack of major symmetry of the overall elasticity tensor obtained via Eq. (11.70), except in the perfectly isotropic case mentioned above and when the aligned inclusion phases have all the same shape. Thus, the transversely isotropic overall elasticity tensor found from Eq. (11.70) when the conditions (A1) and (A2) are satisfied has Walpole representation

$$\overline{\mathbb{L}} = \left\{ \begin{bmatrix} n & \sqrt{2}\,\ell \\ \sqrt{2}\,\ell' & 2\,c \end{bmatrix}, 2\,\mu_t, \, 2\,\mu_a \right\} , \tag{11.75}$$

where, in contrast with Eq. (11.53), $\ell' \neq \ell$. A "brute force" solution to this problem was proposed by Wu and Herzog (2002), who took the (major) symmetric part of the overall elasticity tensor $\mathbb{L}$ of Eq. (11.75), i.e.,

$$\mathbb{L}_{\text{sym}} = \tfrac{1}{2}(\mathbb{L} + \mathbb{L}^T), \qquad (\mathbb{L}_{\text{sym}})^{ijkl} = \tfrac{1}{2}(\mathrm{L}^{ijkl} + \mathrm{L}^{klij}), \tag{11.76}$$

which, in terms of the symmetrised cross modulus to be used in the Walpole representation $\overline{\mathbb{L}_{\text{sym}}}$ of $\mathbb{L}_{\text{sym}}$, reads

$$\ell_{\text{sym}} = \tfrac{1}{2}(\ell + \ell'). \tag{11.77}$$

Finally, we note that, if the matrix is isotropic and all inclusions in all families are spherical and isotropic, isotropy is retrieved as a trivial particular case of transverse isotropy.

## 11.4 Composite Materials with Statistically Oriented Inclusions

In this section, we report, in the more recent notation presented in Sect. 11.2 (Federico, 2010a, 2015; Federico et al., 2015), our results for the general case of a composite with statistically oriented spheroidal inclusions, in which the orientation obeys a given probability density (Federico et al., 2004).

### *11.4.1 Generalised Walpole's Formula*

In order to univocally identify the orientation of an ellipsoid, we need three parameters, e.g., the three Euler angles. In the case of a spheroid, by virtue of the rotational symmetry, only two parameters are required, and those could be, e.g., two Euler angles or, equivalently, the unit vector describing the direction of the axis of symmetry of the spheroid. We shall restrict our attention to the case of *spheroidal* inclusions. A phase of statistically oriented spheroidal inclusions (i.e., inclusions all sharing the same geometry and elastic properties, but having different orientations) can be thought of as an infinity of phases, each oriented in a certain direction, so that the summation in Eq. (11.70) becomes an integral on the unit sphere $\mathbb{S}^2\mathcal{B}$. In this integral, at every point $x$ in the body $\mathcal{B}$, the weighing function is a probability density

$$\psi : \mathbb{S}^2\mathcal{B} \to \mathbb{R}_0^+ : \boldsymbol{m} \mapsto \psi(\boldsymbol{m}), \tag{11.78}$$

which describes the probability to find, at each point $x$ in $\mathcal{B}$, an inclusion oriented in direction $\boldsymbol{m}$. In the case of inhomogeneous bodies, $\psi$ depends explicitly on the point $x$ in the body. In the present formulation, however, for the sake of a lighter notation, this dependence is omitted but understood. The probability density $\psi$ must be normalised over the sphere and must be invariant for reflections $\boldsymbol{m} \mapsto -\boldsymbol{m}$, i.e.,

$$\int_{\mathbb{S}^2\mathcal{B}} \psi(\boldsymbol{m}) = 1, \tag{11.79a}$$

$$\psi(-\boldsymbol{m}) = \psi(\boldsymbol{m}). \tag{11.79b}$$

For any function $f$ defined on the unit sphere $\mathbb{S}^2\mathcal{B}$ and valued in a tensor space of any order (including order zero, i.e., scalar functions), we denote by[8]

$$\langle\langle f \rangle\rangle = \int_{\mathbb{S}^2\mathcal{B}} \psi(\boldsymbol{m}) f(\boldsymbol{m}) \tag{11.80}$$

its *directional average*. Note that we do not explicitly indicate the area element (more precisely, the *area two-form*; see Epstein, 2010; Segev, 2013) in the integral. If the function $f$ to be averaged enjoys the same symmetry as $\psi$, i.e., $f(-\boldsymbol{m}) = f(\boldsymbol{m})$, it is possible to restrict the integral to the *north hemisphere*, defined by

$$\mathbb{S}^{2+}\mathcal{B} = \{\boldsymbol{m} \in \mathbb{S}^2\mathcal{B} : \boldsymbol{m}.\boldsymbol{m}_0 \geq 0\}, \tag{11.81}$$

where $\boldsymbol{m}_0 \in \mathbb{S}^2\mathcal{B}$ is the chosen *polar direction*. Naturally, since the integral is performed on *half* the domain (the north hemisphere $\mathbb{S}^{2+}\mathcal{B}$ is *half* of the sphere $\mathbb{S}^2\mathcal{B}$), one has to take *twice* the value of the integral (alternatively, one could re-normalise the probability density).

When the sum in Eq. (11.70) becomes an integral, we need to transform the variables according to

$$\phi_r \quad \mapsto \quad \phi_1\, \psi(\boldsymbol{m}), \tag{11.82a}$$

$$\mathbb{L}_r \quad \mapsto \quad \mathbb{L}_1(\boldsymbol{m}), \tag{11.82b}$$

$$\mathbb{A}_r \quad \mapsto \quad \mathbb{A}_1(\boldsymbol{m}), \tag{11.82c}$$

i.e., we can call the collection of all inclusions "phase 1" and identify all orientations in $\mathbb{S}^2\mathcal{B}$ by means of the probability density $\psi$. Equation (11.70) then becomes

$$\mathbb{L} = [\phi_0\, \mathbb{L}_0 + \phi_1 \langle\langle \mathbb{L}_1 : \mathbb{A}_1 \rangle\rangle] : \left[\phi_0\, \mathbb{I}^T + \phi_1 \langle\langle \mathbb{A}_1 \rangle\rangle\right]^{-1}, \tag{11.83}$$

where the terms relative to the matrix account for the fact that the strain concentration tensor $\mathbb{A}_0$ reduces to the transpose $\mathbb{I}^T$ of the symmetric identity [Eq. (11.72)], and we used the definition (11.80) of directional average in

$$\langle\langle \mathbb{L}_1 : \mathbb{A}_1 \rangle\rangle = \int_{\mathbb{S}^2\mathcal{B}} \psi(\boldsymbol{m})\, \mathbb{L}_1(\boldsymbol{m}) : \mathbb{A}_1(\boldsymbol{m}), \tag{11.84}$$

$$\langle\langle \mathbb{A}_1 \rangle\rangle = \int_{\mathbb{S}^2\mathcal{B}} \psi(\boldsymbol{m})\, \mathbb{A}_1(\boldsymbol{m}). \tag{11.85}$$

[8] Note that, in some previous works (Federico et al., 2004; Federico, 2010a), we used the symbol $\langle f \rangle$ for the integral in Eq. (11.80) in the case of isotropic probability $\psi(\boldsymbol{m}) = 1/4\pi$ and called $\langle f \rangle$ the "average of $f$" . We do not adopt this meaning of "average" here and, much more generally, we use "directional average" for the integral in Eq. (11.80) with *any* probability density $\psi$.

In the most general case, the composite is comprised of matrix (subscript 0), $N_a$ inclusion phases, all aligned in a definite direction (subscript $r \in \{1, \dots N_a\}$), and $N_p$ inclusion phases with statistical orientation (subscript $r \in \{1, \dots N_p\}$). Thus, the overall elasticity tensor reads

$$\mathbb{L} = \left[\phi_0 \, \mathbb{L}_0 + \sum\nolimits_{r=1}^{N_a} \phi_r \, \mathbb{L}_r : \mathbb{A}_r + \sum\nolimits_{s=1}^{N_p} \phi_s \langle\langle \mathbb{L}_s : \mathbb{A}_s \rangle\rangle\right] : \left[\phi_0 \, \mathbb{I}^T + \sum\nolimits_{r=1}^{N_a} \phi_r \, \mathbb{A}_r + \sum\nolimits_{s=1}^{N_p} \phi_s \langle\langle \mathbb{A}_s \rangle\rangle\right]^{-1}, \tag{11.86}$$

where, for each phase $s$,

$$\langle\langle \mathbb{L}_s : \mathbb{A}_s \rangle\rangle = \int_{\mathbb{S}^2\mathcal{B}} \psi_s(\boldsymbol{m}) \, \mathbb{L}_s(\boldsymbol{m}) : \mathbb{A}_s(\boldsymbol{m}), \tag{11.87}$$

$$\langle\langle \mathbb{A}_s \rangle\rangle = \int_{\mathbb{S}^2\mathcal{B}} \psi_s(\boldsymbol{m}) \, \mathbb{A}_s(\boldsymbol{m}) \tag{11.88}$$

are the directional averages of the product $\mathbb{L}_s : \mathbb{A}_s$ and of the strain concentration tensor $\mathbb{A}_s$, respectively, and $\psi_s$ is the probability density describing the orientation.

In both the case of Eq. (11.83) with one phase of statistically oriented inclusions and the general case of Eq. (11.86), it is important to remark that all inclusions in the same phase $s$ have identical geometry and mechanical properties, which means that, for every pair of directions $\boldsymbol{m}_\alpha$ and $\boldsymbol{m}_\beta$, there are suitable rotation tensors $\boldsymbol{Q}$ and $\boldsymbol{R}$ (which coincide if the axes of geometrical symmetry coincide with the axes of material symmetry) such that

$$\mathbb{L}_s(\boldsymbol{m}_\alpha) = (\boldsymbol{Q} \underline{\otimes} \boldsymbol{Q}) : \mathbb{L}_s(\boldsymbol{m}_\beta) : (\boldsymbol{Q}^T \underline{\otimes} \boldsymbol{Q}^T), \tag{11.89a}$$

$$\mathbb{A}_s(\boldsymbol{m}_\alpha) = (\boldsymbol{R}^{-T} \underline{\otimes} \boldsymbol{R}^{-T}) : \mathbb{A}_s(\boldsymbol{m}_\beta) : (\boldsymbol{R}^T \underline{\otimes} \boldsymbol{R}^T). \tag{11.89b}$$

### *11.4.2 Transversely Isotropic Case: Preliminaries*

In the general system with statistically oriented inclusions described by Eq. (11.86), transverse isotropy in direction $\boldsymbol{m}_0$ is obtained with weaker conditions than those of the aligned case seen in Sect. 11.3.3. Specifically, while condition (S1) below is identical to condition (A1), condition (S2) below echoes (A2) but is valid only for the aligned phases $r \in \{1, \dots, N_a\}$, and a new condition (S3) must be stated for the statistically oriented phases $s \in \{1, \dots, N_p\}$:

(S1) The matrix is either isotropic or transversely isotropic with respect to $\boldsymbol{m}_0$.
(S2) All inclusions in all aligned families $r \in \{1, \dots, N_a\}$ have their axis of symmetry oriented in direction $\boldsymbol{m}_0$, are spheroidal (i.e., are revolution ellipsoids) and are either isotropic or transversely isotropic with respect to $\boldsymbol{m}_0$.

(S3) All inclusions in all statistically oriented families $s \in \{1, \ldots, N_p\}$ are spheroidal, are either isotropic or transversely isotropic with respect to their axis of geometrical symmetry, and the probability densities $\psi_s$ are all transversely isotropic with respect to direction $\boldsymbol{m}_0$, i.e., $\psi_s(\boldsymbol{Q}\boldsymbol{m}) = \psi_s(\boldsymbol{m})$, where $\boldsymbol{Q}$ is an orthogonal tensor such that $\boldsymbol{Q}\boldsymbol{m}_0 = \pm\boldsymbol{m}_0$.

Indeed, under the hypotheses (S1)–(S3), all elasticity tensors $\mathbb{L}_0$ and $\mathbb{L}_r$, the transpose $\mathbb{I}^T$ of the symmetric identity, all strain concentration tensors $\mathbb{A}_r$ and all directional averages $\langle\langle \mathbb{L}_s : \mathbb{A}_s \rangle\rangle$ and $\langle\langle \mathbb{A}_s \rangle\rangle$ in Eq. (11.86) are transversely isotropic with respect to $\boldsymbol{m}_0$, which implies the transverse isotropy of the overall elasticity tensor $\mathbb{L}$. Thus, all tensors in Eq. (11.86) can be decomposed in Walpole's transversely isotropic basis of Eq. (11.32) relative to direction $\boldsymbol{m}_0$, i.e., $\{\mathbb{U}_{\alpha\beta}(\boldsymbol{m}_0), \mathbb{V}_\gamma(\boldsymbol{m}_0)\}^2_{\alpha,\beta,\gamma=1}$, so that all tensor contractions and inversions can be performed conveniently exploiting Walpole's array formalism, in which Eq. (11.86) takes the form

$$\overline{\mathbb{L}} = \left[\phi_0\,\overline{\mathbb{L}_0} + \sum\nolimits_{r=1}^{N_a} \phi_r\,\overline{\mathbb{L}_r : \mathbb{A}_r} + \sum\nolimits_{s=1}^{N_p} \phi_s\,\overline{\langle\langle \mathbb{L}_s : \mathbb{A}_s \rangle\rangle}\right] \left[\phi_0\,\overline{\mathbb{I}^T} + \sum\nolimits_{r=1}^{N_a} \phi_r\,\overline{\mathbb{A}_r} + \sum\nolimits_{s=1}^{N_p} \phi_s\,\overline{\langle\langle \mathbb{A}_s \rangle\rangle}\right]^{-1}, \tag{11.90}$$

where the Walpole array $\overline{\mathbb{I}^T}$ is equal to $\overline{\mathbb{I}}$, identically.

The decomposition in the transversely isotropic basis $\{\mathbb{U}_{\alpha\beta}(\boldsymbol{m}_0), \mathbb{V}_\gamma(\boldsymbol{m}_0)\}^2_{\alpha,\beta,\gamma=1}$ is straightforward for $\mathbb{L}_0$, $\mathbb{I}^T$, $\mathbb{L}_r$ and $\mathbb{A}_r$, which are all transversely isotropic in direction $\boldsymbol{m}_0$ by hypothesis, but requires some additional work for the directional averages $\langle\langle \mathbb{L}_s : \mathbb{A}_s \rangle\rangle$ and $\langle\langle \mathbb{A}_s \rangle\rangle$. Even though Eq. (11.90) requires the determination of the Walpole components of $\langle\langle \mathbb{A}_s \rangle\rangle$ in $[T\mathcal{B}]_2{}^2$, we shall decompose its "contravariant" counterpart $\langle\langle \mathbb{A}_s^\sharp \rangle\rangle$ in $[T\mathcal{B}]_0^4$, for which the formulae (11.34) are applied. This can be done because, as seen in Sect. 11.4.3, $\langle\langle \mathbb{A}_s^\sharp \rangle\rangle$ and $\langle\langle \mathbb{A}_s \rangle\rangle$ have the same Walpole array (see Sect. 11.2.7). We recall that $\langle\langle \mathbb{A}_s^\sharp \rangle\rangle$ is obtained from $\langle\langle \mathbb{A}_s \rangle\rangle$ by raising the first pair of indices of $\mathbb{A}_s$ through $\mathbb{I}^\sharp$ (the "contravariant" symmetric identity defined in Eq. (11.24a)), i.e., by computing $\mathbb{A}_s^\sharp = \mathbb{I}^\sharp : \mathbb{A}_s$, and averaging the resulting expression: $\langle\langle \mathbb{A}_s^\sharp \rangle\rangle = \langle\langle \mathbb{I}^\sharp : \mathbb{A}_s \rangle\rangle = \mathbb{I}^\sharp : \langle\langle \mathbb{A}_s \rangle\rangle = \langle\langle \mathbb{A}_s \rangle\rangle^\sharp$. Note that the equality $\langle\langle \mathbb{A}_s^\sharp \rangle\rangle = \langle\langle \mathbb{A}_s \rangle\rangle^\sharp$ stems from the fact that directional averaging and raising of indices commute with each other.

The whole problem of inclusions oriented according to a given transversely isotropic probability density reduces to the evaluation of the Walpole array of the directional average of the $2\,s$ tensors $\langle\langle \mathbb{L}_s : \mathbb{A}_s \rangle\rangle$ and $\langle\langle \mathbb{A}_s \rangle\rangle$. This latter problem is solved once we are able to evaluate the Walpole array of the directional average of a generic tensor $\mathbb{T}$, which is the topic of Sect. 11.4.3. We conclude this section by noting that isotropy is retrieved if the inclusions in the "aligned" phases are spherical and isotropic, and if the probability density is imposed to be isotropic, which means that the inclusions of the statistical phases are oriented randomly. Under this latter hypothesis, the inclusions of the statistically oriented phases are allowed to be of spheroidal shape and either isotropic or transversely isotropic with respect to the direction of their axis of geometrical symmetry.

### 11.4.3 Transversely Isotropic Case: Average of a Function of the Direction

Let

$$\mathbb{T} : \mathbb{S}^2\mathcal{B} \to [T\mathcal{B}]^4_0 : \boldsymbol{m} \mapsto \mathbb{T}_s(\boldsymbol{m}) \in ([T\mathcal{B}]^4_0, \boldsymbol{m}), \tag{11.91}$$

be a $([T\mathcal{B}]^4_0, \boldsymbol{m})$-valued function, $\boldsymbol{m}_0$ a direction in $\mathbb{S}^2\mathcal{B}$ and $\psi$ a probability density with transverse isotropy with respect to $\boldsymbol{m}_0$. Our purpose is to study the directional average

$$\langle\langle \mathbb{T} \rangle\rangle = \int_{\mathbb{S}^2\mathcal{B}} \psi(\boldsymbol{m})\, \mathbb{T}(\boldsymbol{m}). \tag{11.92}$$

First, we note that, since the probability density $\psi$ is transversely isotropic with respect to $\boldsymbol{m}_0$, then $\langle\langle \mathbb{T} \rangle\rangle$ belongs to $([T\mathcal{B}]^4_0, \boldsymbol{m}_0)$, and we have the identity

$$\langle\langle \mathbb{T} \rangle\rangle = \overline{\langle\langle \mathbb{T} \rangle\rangle}^{\alpha\beta}\, \mathbb{U}_{\alpha\beta}(\boldsymbol{m}_0) + \overline{\langle\langle \mathbb{T} \rangle\rangle}^{\gamma}\, \mathbb{V}_{\gamma}(\boldsymbol{m}_0), \tag{11.93}$$

where $\{\mathbb{U}_{\alpha\beta}(\boldsymbol{m}_0), \mathbb{V}_{\gamma}(\boldsymbol{m}_0)\}^2_{\alpha,\beta,\gamma=1}$ is the basis of $([T\mathcal{B}]^4_0, \boldsymbol{m}_0)$, and

$$\overline{\langle\langle \mathbb{T} \rangle\rangle}^{\alpha\beta} = \langle \langle\langle \mathbb{T} \rangle\rangle, \mathbb{U}_{\alpha\beta}(\boldsymbol{m}_0) \rangle, \qquad \overline{\langle\langle \mathbb{T} \rangle\rangle}^{\gamma} = \tfrac{1}{2} \langle \langle\langle \mathbb{T} \rangle\rangle, \mathbb{V}_{\gamma}(\boldsymbol{m}_0) \rangle, \tag{11.94}$$

according to Eq. (11.34). Second, if we decompose $\mathbb{T}(\boldsymbol{m})$ in the basis $\{\mathbb{U}_{\mu\nu}(\boldsymbol{m}), \mathbb{V}_{\pi}(\boldsymbol{m})\}^2_{\mu,\nu,\pi=1}$ of the space $([T\mathcal{B}]^4_0, \boldsymbol{m})$ of transversely isotropic tensors with respect to $\boldsymbol{m}$, the directional average in Eq. (11.92) becomes

$$\begin{aligned}
\langle\langle \mathbb{T} \rangle\rangle &= \int_{\mathbb{S}^2\mathcal{B}} \psi(\boldsymbol{m}) \left[ \overline{\mathbb{T}}^{\mu\nu}\, \mathbb{U}_{\mu\nu}(\boldsymbol{m}) + \overline{\mathbb{T}}^{\pi}\, \mathbb{V}_{\pi}(\boldsymbol{m}) \right] \\
&= \overline{\mathbb{T}}^{\mu\nu} \int_{\mathbb{S}^2\mathcal{B}} \psi(\boldsymbol{m})\, \mathbb{U}_{\mu\nu}(\boldsymbol{m}) + \overline{\mathbb{T}}^{\pi} \int_{\mathbb{S}^2\mathcal{B}} \psi(\boldsymbol{m})\, \mathbb{V}_{\pi}(\boldsymbol{m}) \\
&= \overline{\mathbb{T}}^{\mu\nu}\, \langle\langle \mathbb{U}_{\mu\nu} \rangle\rangle + \overline{\mathbb{T}}^{\pi}\, \langle\langle \mathbb{V}_{\pi} \rangle\rangle,
\end{aligned} \tag{11.95}$$

where the Walpole components $\overline{\mathbb{T}}^{\mu\nu}$ and $\overline{\mathbb{T}}^{\pi}$ *do not* depend on the direction $\boldsymbol{m}$ and can be therefore factorised out of the integral.

Now, we note that the directional averages $\langle\langle \mathbb{U}_{\mu\nu} \rangle\rangle$ and $\langle\langle \mathbb{V}_{\pi} \rangle\rangle$ are of the same type as the average $\langle\langle \mathbb{T} \rangle\rangle$ in Eq. (11.92) and thus are transversely isotropic in direction $\boldsymbol{m}_0$. Therefore, we can use Eq. (11.93) to write $\langle\langle \mathbb{U}_{\mu\nu} \rangle\rangle$ and $\langle\langle \mathbb{V}_{\pi} \rangle\rangle$ as

$$\langle\langle \mathbb{U}_{\mu\nu} \rangle\rangle = \overline{\langle\langle \mathbb{U}_{\mu\nu} \rangle\rangle}^{\alpha\beta}\, \mathbb{U}_{\alpha\beta}(\boldsymbol{m}_0) + \overline{\langle\langle \mathbb{U}_{\mu\nu} \rangle\rangle}^{\gamma}\, \mathbb{V}_{\gamma}(\boldsymbol{m}_0), \tag{11.96a}$$

$$\langle\langle \mathbb{V}_{\pi} \rangle\rangle = \overline{\langle\langle \mathbb{V}_{\pi} \rangle\rangle}^{\alpha\beta}\, \mathbb{U}_{\alpha\beta}(\boldsymbol{m}_0) + \overline{\langle\langle \mathbb{V}_{\pi} \rangle\rangle}^{\gamma}\, \mathbb{V}_{\gamma}(\boldsymbol{m}_0). \tag{11.96b}$$

In this way, the problem of evaluating the directional average $\langle\langle \mathbb{T} \rangle\rangle$ of the tensor-valued function $\mathbb{T}(\boldsymbol{m})$ is reduced to finding the averages $\langle\langle \mathbb{U}_{\mu\nu} \rangle\rangle$ and $\langle\langle \mathbb{V}_{\pi} \rangle\rangle$ of $\mathbb{U}_{\mu\nu}(\boldsymbol{m})$ and $\mathbb{V}_{\pi}(\boldsymbol{m})$. Since the scalar product by a tensor that is independent of the direction $\boldsymbol{m}$ and integration over all directions $\boldsymbol{m}$ commute, we have

$$\overline{\langle\langle \mathbb{U}_{\mu\nu} \rangle\rangle}^{\alpha\beta} = \left\langle \left( \int_{\mathbb{S}^2\mathcal{B}} \psi(\boldsymbol{m})\, \mathbb{U}_{\mu\nu}(\boldsymbol{m}) \right), \mathbb{U}_{\alpha\beta}(\boldsymbol{m}_0) \right\rangle = \int_{\mathbb{S}^2\mathcal{B}} \psi(\boldsymbol{m})\, \langle \mathbb{U}_{\mu\nu}(\boldsymbol{m})\,,\, \mathbb{U}_{\alpha\beta}(\boldsymbol{m}_0) \rangle, \tag{11.97a}$$

$$\overline{\langle\langle \mathbb{U}_{\mu\nu} \rangle\rangle}^{\gamma} = \frac{1}{2} \left\langle \left( \int_{\mathbb{S}^2\mathcal{B}} \psi(\boldsymbol{m})\, \mathbb{U}_{\mu\nu}(\boldsymbol{m}) \right), \mathbb{V}_{\gamma}(\boldsymbol{m}_0) \right\rangle = \frac{1}{2} \int_{\mathbb{S}^2\mathcal{B}} \psi(\boldsymbol{m})\, \langle \mathbb{U}_{\mu\nu}(\boldsymbol{m})\,,\, \mathbb{V}_{\gamma}(\boldsymbol{m}_0) \rangle, \tag{11.97b}$$

$$\overline{\langle\langle \mathbb{V}_{\pi} \rangle\rangle}^{\alpha\beta} = \left\langle \left( \int_{\mathbb{S}^2\mathcal{B}} \psi(\boldsymbol{m})\, \mathbb{V}_{\pi}(\boldsymbol{m}) \right), \mathbb{U}_{\alpha\beta}(\boldsymbol{m}_0) \right\rangle = \int_{\mathbb{S}^2\mathcal{B}} \psi(\boldsymbol{m})\, \langle \mathbb{V}_{\pi}(\boldsymbol{m})\,,\, \mathbb{U}_{\alpha\beta}(\boldsymbol{m}_0) \rangle, \tag{11.97c}$$

$$\overline{\langle\langle \mathbb{V}_{\pi} \rangle\rangle}^{\gamma} = \frac{1}{2} \left\langle \left( \int_{\mathbb{S}^2\mathcal{B}} \psi(\boldsymbol{m})\, \mathbb{V}_{\pi}(\boldsymbol{m}) \right), \mathbb{V}_{\gamma}(\boldsymbol{m}_0) \right\rangle = \frac{1}{2} \int_{\mathbb{S}^2\mathcal{B}} \psi(\boldsymbol{m})\, \langle \mathbb{V}_{\pi}(\boldsymbol{m})\,,\, \mathbb{V}_{\gamma}(\boldsymbol{m}_0) \rangle. \tag{11.97d}$$

This procedure reduces the number of integrals to be evaluated from $6 \times 81 = 486$ [indeed, each of the 6 tensors $\langle\langle \mathbb{U}_{\mu\nu} \rangle\rangle$, $\langle\langle \mathbb{V}_{\pi} \rangle\rangle$, with $\mu, \nu, \pi \in \{1, 2\}$, has 81 components] to $6 \times 6 = 36$ (or $16 + 8 + 8 + 4 = 36$, if one looks at the four equations (11.97)), i.e., 6 independent components for each of the 6 averages $\{\langle\langle \mathbb{U}_{\mu\nu} \rangle\rangle, \langle\langle \mathbb{V}_{\pi} \rangle\rangle\}_{\mu\nu\pi=1}^{2}$. Moreover, this procedure eliminates many integrals, which vanish because of the transverse isotropy of the system with respect to $\boldsymbol{m}_0$ and could give numerical problems as they could be highly oscillatory (Federico et al., 2004). As we shall show in Sect. 11.4.4, these integrals can be expressed in spherical coordinates as a function of the co-latitude and longitude angles taken from a reference frame in which the polar axis is the overall direction of symmetry $\boldsymbol{m}_0$.

Using Eqs. (11.93), (11.95) and (11.96), we obtain the expression of the directional average $\langle\langle \mathbb{T} \rangle\rangle$ in the basis $\{\mathbb{U}_{\alpha\beta}(\boldsymbol{m}_0), \mathbb{V}_{\gamma}(\boldsymbol{m}_0)\}_{\alpha,\beta,\gamma=1}^{2}$ as

$$\begin{aligned} \langle\langle \mathbb{T} \rangle\rangle = {} & \overline{\mathbb{T}}^{\mu\nu} \left( \overline{\langle\langle \mathbb{U}_{\mu\nu} \rangle\rangle}^{\alpha\beta}\, \mathbb{U}_{\alpha\beta}(\boldsymbol{m}_0) + \overline{\langle\langle \mathbb{U}_{\mu\nu} \rangle\rangle}^{\gamma}\, \mathbb{V}_{\gamma}(\boldsymbol{m}_0) \right) \\ & + \overline{\mathbb{T}}^{\pi} \left( \overline{\langle\langle \mathbb{V}_{\pi} \rangle\rangle}^{\alpha\beta}\, \mathbb{U}_{\alpha\beta}(\boldsymbol{m}_0) + \overline{\langle\langle \mathbb{V}_{\pi} \rangle\rangle}^{\gamma}\, \mathbb{V}_{\gamma}(\boldsymbol{m}_0) \right), \end{aligned} \tag{11.98}$$

which can be rearranged into the final expression

$$\langle\langle \mathbb{T} \rangle\rangle = \left( \overline{\mathbb{T}}^{\mu\nu} \overline{\langle\langle \mathbb{U}_{\mu\nu} \rangle\rangle}^{\alpha\beta} + \overline{\mathbb{T}}^{\pi} \overline{\langle\langle \mathbb{V}_{\pi} \rangle\rangle}^{\alpha\beta} \right) \mathbb{U}_{\alpha\beta}(\boldsymbol{m}_0) + \left( \overline{\mathbb{T}}^{\mu\nu} \overline{\langle\langle \mathbb{U}_{\mu\nu} \rangle\rangle}^{\gamma} + \overline{\mathbb{T}}^{\pi} \overline{\langle\langle \mathbb{V}_{\pi} \rangle\rangle}^{\gamma} \right) \mathbb{V}_{\gamma}(\boldsymbol{m}_0). \tag{11.99}$$

The Walpole array form of Eq. (11.99) is

$$\overline{\langle\langle \mathbb{T} \rangle\rangle} = \left\{ \left[ \overline{\mathbb{T}}^{\mu\nu} \overline{\langle\langle \mathbb{U}_{\mu\nu} \rangle\rangle}^{\alpha\beta} + \overline{\mathbb{T}}^{\pi} \overline{\langle\langle \mathbb{V}_{\pi} \rangle\rangle}^{\alpha\beta} \right], \overline{\mathbb{T}}^{\mu\nu} \overline{\langle\langle \mathbb{U}_{\mu\nu} \rangle\rangle}^{\gamma} + \overline{\mathbb{T}}^{\pi} \overline{\langle\langle \mathbb{V}_{\pi} \rangle\rangle}^{\gamma} \right\}. \quad (11.100)$$

### 11.4.4 Transversely Isotropic Case: Solution in the Polar Parametrisation

Assuming that the symmetry axis $\boldsymbol{m}_0$ of the transverse isotropy coincides with vector $\boldsymbol{e}_1$ of an orthonormal basis $\{\boldsymbol{e}_i\}_{i=1}^3$, the generic direction $\boldsymbol{m}$ can be expressed as a function

$$\boldsymbol{m}(\theta, \varphi) = \cos\theta\ \boldsymbol{e}_1 + \sin\theta\ \cos\varphi\ \boldsymbol{e}_2 + \sin\theta\ \sin\varphi\ \boldsymbol{e}_3, \quad (11.101)$$

where $\theta$ is the *co-latitude*, measured from the polar direction $\boldsymbol{m}_0 \equiv \boldsymbol{e}_1$, and $\varphi$ is the *longitude*, measured from the plane spanned by $\boldsymbol{e}_1$ and $\boldsymbol{e}_2$ (see Fig. 11.2). Using the polar parametrisation of the sphere, the probability density $\psi$ can be written as

$$\varrho(\theta) = \psi(\boldsymbol{m}(\theta, \varphi)), \quad (11.102)$$

where the new function $\varrho$ does *not* depend on the latitude angle $\varphi$ because of the transverse isotropy of $\psi$. In the polar parametrisation, the directional average (11.80) of a generic function $f$ becomes

$$\langle\langle f \rangle\rangle = \int_0^{2\pi} \left[ \int_0^{\pi} \varrho(\theta) f(\boldsymbol{m}(\theta, \varphi))\ \sin\theta\ \mathrm{d}\theta \right] \mathrm{d}\varphi. \quad (11.103)$$

We recall the symmetry of $\psi$ for reflections $\boldsymbol{m} \mapsto -\boldsymbol{m}$ and note that it is inherited by $\varrho$ as a symmetry in $\theta$ about the value $\pi/2$, i.e., $\varrho(\theta) = \varrho(\pi - \theta)$. Thus, for functions $f$ invariant under reflections $\boldsymbol{m} \mapsto -\boldsymbol{m}$ (such as all our fourth-order tensors, which depend on $\boldsymbol{m}$ via the structure tensor $\boldsymbol{a} = \boldsymbol{m} \otimes \boldsymbol{m}$), we can also write

$$\langle\langle f \rangle\rangle = 2 \int_0^{2\pi} \left[ \int_0^{\pi/2} \varrho(\theta) f(\boldsymbol{m}(\theta, \varphi))\ \sin\theta\ \mathrm{d}\theta \right] \mathrm{d}\varphi, \quad (11.104)$$

which is equivalent to integrating $\psi$ over the *north hemisphere* $\mathbb{S}^{2+}\mathcal{B}$ as in Eq. (11.81). For our purposes, the generic function $f$ has to be replaced by the integrands in Eq. (11.97).

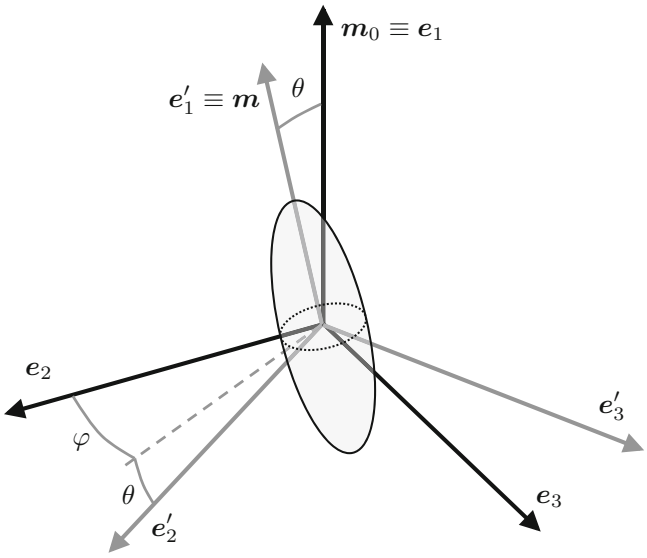


**Fig. 11.2** Representation of the generic direction $\boldsymbol{e}_1' \equiv \boldsymbol{m}$ of the axis of symmetry of a spheroidal inclusion in terms of the co-latitude angle $\theta$ and the longitude angle $\varphi$. The co-latitude $\theta$ is calculated from the global direction of symmetry $\boldsymbol{e}_1 \equiv \boldsymbol{m}_0$, and the longitude $\varphi$ is calculated from the plane spanned by $\boldsymbol{e}_1$ and $\boldsymbol{e}_2$

### *11.4.5 Some Relevant Particular Cases*

The most "classical" particular cases of transversely isotropic probability density $\psi$ are the case of probability density converging to the Dirac delta, describing orientation in one direction; the case of in-plane random orientation, in which all directions within the same plane are equally probable; and the case of random orientation, yielding an isotropic solution. In the solutions that we report below, in order to minimise the possibility of making mistakes with the tedious integrals (11.97), we employed *Wolfram Mathematica*.

The case of alignment in one definite direction can be tackled by means of a parametric probability density peaked at $\theta = 0$, which can be made to converge, in the sense of distributions (see, e.g., Kolmogorov and Fomin, 1999), to a Dirac delta, which is the approach we used in the past (Federico et al., 2004). However, quite trivially, one can directly say that, if all inclusions are oriented in the same direction, Eq. (11.86) reduces to the Walpole solution (11.70) which Weng (1990) and Qiu and Weng (1990) used for aligned inclusions [and which we reported in the form of a Walpole array in Eq. (11.74)].

The case of random orientation in a plane can also be solved with a parametric probability density peaked at $\theta = \pi/2$ that converges, in the sense of distributions, to a Dirac delta (Federico et al., 2004). However, we can follow a simpler method. Rather than averaging the function $f(\boldsymbol{m}(\cdot, \cdot))$ with values $f(\boldsymbol{m}(\theta, \varphi))$ of

Eq. (11.103) on the whole unit sphere $\mathbb{S}^2\mathcal{B}$, we average the function $f(\boldsymbol{m}(\pi/2,\cdot))$ with values $f(\boldsymbol{m}(\pi/2,\varphi))$ on the equatorial unit circumference $(\mathbb{S}^1\mathcal{B},\boldsymbol{m}_0)$, i.e., the circumference laying on the plane orthogonal to the direction of overall symmetry $\boldsymbol{m}_0$ (which is the plane spanned by $\boldsymbol{e}_2$ and $\boldsymbol{e}_3$ in Fig. 11.2). This boils down to transforming the integral in Eq. (11.103) into

$$\langle\langle f\rangle\rangle = \int_0^{2\pi} \frac{1}{2\pi} f(\boldsymbol{m}(\pi/2,\varphi))\,\sin(\pi/2)\,\mathrm{d}\varphi = \frac{1}{2\pi}\int_0^{2\pi} f(\boldsymbol{m}(\pi/2,\varphi))\,\mathrm{d}\varphi, \tag{11.105}$$

where $1/2\pi$ is the constant value of the probability density on the equatorial unit circumference $(\mathbb{S}^1\mathcal{B},\boldsymbol{m}_0)$ and equals the reciprocal of the amplitude of the interval $[0,2\pi]$ within which the longitude $\varphi$ varies. Considering Eq. (11.105), the components of the directional averages $\langle\langle\mathbb{U}_{\mu\nu}\rangle\rangle$ and $\langle\langle\mathbb{V}_\pi\rangle\rangle$ in Eq. (11.97) can be obtained and represented via the Walpole arrays

$$\overline{\langle\langle\mathbb{U}_{11}\rangle\rangle} = \frac{1}{8}\left\{\begin{bmatrix}0&0\\0&4\end{bmatrix},2,\,0\right\}, \qquad \overline{\langle\langle\mathbb{U}_{12}\rangle\rangle} = \frac{1}{8}\left\{\begin{bmatrix}0&0\\4&2\sqrt{2}\end{bmatrix},-\sqrt{2},\,0\right\}, \tag{11.106a}$$

$$\overline{\langle\langle\mathbb{U}_{21}\rangle\rangle} = \frac{1}{8}\left\{\begin{bmatrix}0&4\\0&2\sqrt{2}\end{bmatrix},-\sqrt{2},\,0\right\}, \qquad \overline{\langle\langle\mathbb{U}_{22}\rangle\rangle} = \frac{1}{8}\left\{\begin{bmatrix}4&2\sqrt{2}\\2\sqrt{2}&2\end{bmatrix},1,\,0\right\}, \tag{11.106b}$$

$$\overline{\langle\langle\mathbb{V}_1\rangle\rangle} = \frac{1}{8}\left\{\begin{bmatrix}4&-2\sqrt{2}\\-2\sqrt{2}&2\end{bmatrix},1,\,4\right\}, \qquad \overline{\langle\langle\mathbb{V}_2\rangle\rangle} = \frac{1}{8}\left\{\begin{bmatrix}0&0\\0&0\end{bmatrix},4,\,4\right\}. \tag{11.106c}$$

For the case of random orientation, we follow the approach we used in the past (Federico et al., 2004), with some minor notational and procedural differences. When the probability density is given by $\psi(\boldsymbol{m}(\theta,\varphi)) = \varrho(\theta,\varphi) = 1/4\pi$ (random orientation), the integral in Eq. (11.92) *must* coincide with its isotropic projection [see Eq. (11.28)], i.e., must necessarily be isotropic. Thus, we have the identity

$$\langle\langle\mathbb{T}\rangle\rangle = \int_{\mathbb{S}^2\mathcal{B}} \psi(\boldsymbol{m})\,\mathbb{T}(\boldsymbol{m}) \equiv \left[\int_{\mathbb{S}^2\mathcal{B}} \psi(\boldsymbol{m})\,\mathbb{T}(\boldsymbol{m})\right]_{\mathrm{iso}} = \langle\langle\mathbb{T}\rangle\rangle_{\mathrm{iso}}. \tag{11.107}$$

Since the operation of isotropic projection (11.28) and the averaging integral commute, we can also write

$$\langle\langle\mathbb{T}\rangle\rangle = \int_{\mathbb{S}^2\mathcal{B}} \psi(\boldsymbol{m})\,\mathbb{T}(\boldsymbol{m}) \equiv \int_{\mathbb{S}^2\mathcal{B}} \psi(\boldsymbol{m})\,[\mathbb{T}(\boldsymbol{m})]_{\mathrm{iso}} = \langle\langle\mathbb{T}_{\mathrm{iso}}\rangle\rangle. \tag{11.108}$$

Moreover, the dependence on $\boldsymbol{m}$ in $[\mathbb{T}(\boldsymbol{m})]_{\mathrm{iso}}$ *must* disappear, as $[\mathbb{T}(\boldsymbol{m})]_{\mathrm{iso}}$ is isotropic. Thus, we can replace $[\mathbb{T}(\boldsymbol{m})]_{\mathrm{iso}}$ by $[\mathbb{T}(\boldsymbol{m}_0)]_{\mathrm{iso}}$, where $\boldsymbol{m}_0$ is an *arbitrary*

direction, and factorise $[\mathbb{T}(\boldsymbol{m}_0)]_{\text{iso}}$ *outside* of the integral sign to obtain the final expression

$$\langle\langle \mathbb{T} \rangle\rangle = [\mathbb{T}(\boldsymbol{m}_0)]_{\text{iso}} \,, \tag{11.109}$$

where we used the normalisation to one of the probability densities. Since $\mathbb{T}(\boldsymbol{m}_0) = \overline{\mathbb{T}}^{\alpha\beta}\, \mathbb{U}_{\alpha\beta}(\boldsymbol{m}_0) + \overline{\mathbb{T}}^{\gamma}\, \mathbb{V}_{\gamma}(\boldsymbol{m}_0)$, we can use linearity and write

$$\langle\langle \mathbb{T} \rangle\rangle = \overline{\mathbb{T}}^{\alpha\beta}\, \left[\mathbb{U}_{\alpha\beta}(\boldsymbol{m}_0)\right]_{\text{iso}} + \overline{\mathbb{T}}^{\gamma}\, \left[\mathbb{V}_{\gamma}(\boldsymbol{m}_0)\right]_{\text{iso}} . \tag{11.110}$$

The isotropic projections $\left[\mathbb{U}_{\alpha\beta}(\boldsymbol{m}_0)\right]_{\text{iso}}$ and $\left[\mathbb{V}_{\gamma}(\boldsymbol{m}_0)\right]_{\text{iso}}$ can be written either in the isotropic basis $\{\mathbb{K}^\sharp, \mathbb{M}^\sharp\}$ or in Walpole's transversely isotropic representation as seen in Eq. (11.42). In the former case, we have

$$[\mathbb{U}_{11}]_{\text{iso}} = \frac{1}{3}\,\mathbb{K}^\sharp + \frac{2}{15}\,\mathbb{M}^\sharp, \qquad [\mathbb{U}_{12}]_{\text{iso}} = \frac{\sqrt{2}}{3}\,\mathbb{K}^\sharp - \frac{\sqrt{2}}{15}\,\mathbb{M}^\sharp, \tag{11.111a}$$

$$[\mathbb{U}_{21}]_{\text{iso}} = \frac{\sqrt{2}}{3}\,\mathbb{K}^\sharp - \frac{\sqrt{2}}{15}\,\mathbb{M}^\sharp, \qquad [\mathbb{U}_{22}]_{\text{iso}} = \frac{2}{3}\,\mathbb{K}^\sharp + \frac{1}{15}\,\mathbb{M}^\sharp, \tag{11.111b}$$

$$[\mathbb{V}_{1}]_{\text{iso}} = 0\,\mathbb{K}^\sharp + \frac{2}{5}\,\mathbb{M}^\sharp, \qquad [\mathbb{V}_{2}]_{\text{iso}} = 0\,\mathbb{K}^\sharp + \frac{2}{5}\,\mathbb{M}^\sharp, \tag{11.111c}$$

and, in the latter, we have

$$\overline{[\mathbb{U}_{11}]_{\text{iso}}} = \frac{1}{15}\left\{\begin{bmatrix} 3 & \sqrt{2} \\ \sqrt{2} & 4 \end{bmatrix}, 2, 2\right\}, \qquad \overline{[\mathbb{U}_{12}]_{\text{iso}}} = \frac{1}{15}\left\{\begin{bmatrix} \sqrt{2} & 4 \\ 4 & 3\sqrt{2} \end{bmatrix}, -\sqrt{2}, -\sqrt{2}\right\}, \tag{11.112a}$$

$$\overline{[\mathbb{U}_{21}]_{\text{iso}}} = \frac{1}{15}\left\{\begin{bmatrix} \sqrt{2} & 4 \\ 4 & 3\sqrt{2} \end{bmatrix}, -\sqrt{2}, -\sqrt{2}\right\}, \qquad \overline{[\mathbb{U}_{22}]_{\text{iso}}} = \frac{1}{15}\left\{\begin{bmatrix} 4 & 3\sqrt{2} \\ 3\sqrt{2} & 7 \end{bmatrix}, 1, 1\right\}, \tag{11.112b}$$

$$\overline{[\mathbb{V}_{1}]_{\text{iso}}} = \frac{1}{15}\left\{\begin{bmatrix} 4 & -2\sqrt{2} \\ -2\sqrt{2} & 2 \end{bmatrix}, 6, 6\right\}, \qquad \overline{[\mathbb{V}_{2}]_{\text{iso}}} = \frac{1}{15}\left\{\begin{bmatrix} 4 & -2\sqrt{2} \\ -2\sqrt{2} & 2 \end{bmatrix}, 6, 6\right\}. \tag{11.112c}$$

## 11.5 Discussion

In this chapter, we summarised and discussed in detail some selected results from previous studies of ours, with the purpose of rephrasing in a more efficient, consequent, and formally correct way the linear elastic formulation of our picture of composite materials with statistically oriented spheroidal inclusions.

After presenting the covariant formulation of the linear algebra of isotropic and transversely isotropic second- and fourth-order tensors, we addressed some fundamental aspects of composite materials with aligned inclusions, which required to review Eshelby's inclusion problem, Eshelby's fourth-order tensor $\mathbb{S}$ and the strain concentration tensor $\mathbb{A}$. Within this framework, we discussed the conditions, pertaining the geometry of the inclusions and their orientation as well as the material symmetries of the matrix, which lead to a globally transversely isotropic (or, in some special cases, isotropic) composite. Then, we considered composite materials with statistically oriented inclusions. To this end, we introduced the probability density describing the probability that the symmetry axis of an inclusion is in a given direction and generalised Walpole's formula (11.70) (Walpole, 1966a,b, 1969; Weng, 1990) to the case of transversely isotropic materials with respect to a symmetry axis $\boldsymbol{m}_0$ [cf. Eq. (11.99)]. In order to achieve this and to minimise the number of integrals to be performed, we translated the directional averaging of tensor functions depending on the direction into Walpole's formalism and obtained Eq. (11.100), which determines the Walpole array of the directional average of a given fourth-order tensor $\mathbb{T}$. Finally, we showed some explicit calculations for the relevant cases of isotropy and transverse isotropy.

It is important to emphasise the difference in terms of conditions necessary to obtain transverse isotropy between Walpole's original formula and the generalised one. Walpole's original formula (11.70) necessitates only the two conditions (A1) and (A2) seen in Sect. 11.3.3 to be applicable to transversely isotropic materials, in the Walpole array form of Eq. (11.74). In contrast, the generalised Walpole's formula (11.86) considers $N_a$ families of aligned inclusions and $N_p$ families of statistically oriented fibres, and the three conditions (S1)–(S3) of Sect. 11.4.2 are needed. While condition (S1) is identical to the "old" condition (A1), and (S2) echoes condition (A2), but only for the $N_a$ aligned phases, a new condition (S3) needs to be stated for the $N_p$ statistically oriented families (i.e., the $N_p$ probability densities $\psi_s$ must be transversely isotropic with respect to $\boldsymbol{m}_0$).

The theory of composite materials with statistical orientation of the inclusions is a rich research field in which very diverse scientific interests converge. The trigger of our studies has been the mechanical characterisation of soft biological tissues. These are highly organised media, endowed with a complex internal structure, whose mechanical properties are vastly influenced by the presence and orientation of collagen fibres. Tendons and ligaments are typical examples of tissues in which the collagen fibres are aligned, and blood vessels and articular cartilage are examples of tissues in which the collagen fibres have statistical orientation. Collagen fibres can indeed be viewed as inclusions that provide structural reinforcement to the non-fibrous extracellular matrix and modulate several important bio-chemo-mechanical processes, which involve, for instance, the flow of interstitial fluids as well as the diffusive-reactive dynamics of the chemical species populating the tissues (nutrients and outputs of chemical reactions). These processes are associated with both second- and fourth-order tensor quantities that, depending on the (either statistical or not) arrangement of the fibres, can be represented by using the methods outlined in Sects. 11.3 and 11.4. In the case of statistical orientation, the directional

average defined in Eq. (11.92) takes a tensor describing how a given quantity is associated with the spatial direction $\boldsymbol{m}$ of local fibre alignment and returns the overall tensor quantity defined in one point of the tissue. This allows for obtaining microstructurally based constitutive laws and puts in evidence how the evolution of the tissue's internal structure yields an evolution of the averaged tensor quantity $\langle\langle \mathbb{T} \rangle\rangle$ associated with the considered material property.

In two previous papers of ours (Grillo et al., 2012, 2015), we proposed a theory of remodelling in fibre-reinforced materials, where by "remodelling" we mean here the structural reorganisation of a body, be it a tissue or a non-biological material. In this theory, the evolution of the internal structure of a given medium was described by the time change of the probability density $\psi$ featuring in the averaging integral (11.92). Under the hypothesis that the evolution of $\psi$ does not modify the transverse isotropy of the material with respect to the direction $\boldsymbol{m}_0$ (in fact, this requires $\psi$ to evolve by maintaining itself transversely isotropic, i.e., by maintaining itself independent of the longitude angle, in the spherical coordinate setting of Sect. 11.4.4), the use of Walpole's notation in Eq. (11.100) makes it possible to isolate the effect of remodelling on the averaged tensor quantity $\langle\langle \mathbb{T} \rangle\rangle$, expressed in terms of the array $\overline{\langle\langle \mathbb{T} \rangle\rangle}$. Indeed, while the averaged tensors of the Walpole's basis for transverse isotropy with respect to the generic direction $\boldsymbol{m}$, i.e., $\langle\langle \mathbb{U}_{\mu\nu} \rangle\rangle$ and $\langle\langle \mathbb{V}_{\pi} \rangle\rangle$, evolve in time as they are driven by the time change of $\psi$, the components $\overline{\mathbb{T}}^{\mu\nu}$ and $\overline{\mathbb{T}}^{\pi}$ do not. In turn, since the direction $\boldsymbol{m}_0$ is assumed to be preserved by the considered remodelling process, only the arrays $\{[\overline{\langle\langle \mathbb{U}_{\mu\nu} \rangle\rangle}^{\alpha\beta}], \overline{\langle\langle \mathbb{U}_{\mu\nu} \rangle\rangle}^{\gamma}\}$, $\{[\overline{\langle\langle \mathbb{V}_{\pi} \rangle\rangle}^{\alpha\beta}], \overline{\langle\langle \mathbb{V}_{\pi} \rangle\rangle}^{\gamma}\}$ vary in time. In conclusion, by adopting Walpole's arrays, it is possible to study the influence of remodelling on a global property, expressed by the averaged fourth-order tensor $\langle\langle \mathbb{T} \rangle\rangle$ (e.g., the fourth-order elasticity tensor of the considered medium), by looking at the evolution of the components of the averages of the Walpole's basis tensors $\mathbb{U}_{\mu\nu}$ and $\mathbb{V}_{\pi}$. This subject is among the topics of our current investigations.

**Acknowledgements** At the time in which we originally conceived the methods presented in this chapter, back in 2003 (see Federico et al., 2004), we were quite younger and less experienced than we are now, and we received help from several senior colleagues, whom we would like to acknowledge again. We are grateful to Prof. L.J. Walpole (East Anglia University) and Prof. G.J. Weng (Rutgers University) for the precious suggestions and crucial references they provided and to Prof. F. Santoro (Liceo Scientifico Archimede, Messina) for the invaluable tutorials on the use of *Wolfram Mathematica*. We would also like to thank Prof. W. Herzog (The University of Calgary) for his guidance and contributions to the original work (Federico et al., 2004). Finally, we would like to acknowledge the contribution of Mr. M.F. Alhasadi (The University of Calgary) to the material contained in Sects. 11.3.1 and 11.3.2, which is a revisitation of the classical work by Eshelby and of the derivation of the strain concentration tensor, developed as part of his PhD thesis work (see Alhasadi and Federico, 2017).

This work has been supported in part by the Natural Science and Engineering Research Council of Canada, through the NSERC Discovery Programme (Salvatore Federico); Alberta Innovates Technology Futures (Canada), through the New Faculty Programme (Salvatore Federico); Alberta Innovates Health Solutions (Canada), through the Sustainability Programme (Salvatore Federico); the *Politecnico di Torino* (Italy) (Alfio Grillo); and the *Fondazione Cassa di Risparmio di Torino* (Italy), through the *La Ricerca dei Talenti* (HR Excellence in Research) programme (Alfio Grillo).

## In Memoriam

This work is dedicated to the memory of our maestro and mentor Prof. Gaetano Giaquinta (Catania, Italy, 25 November 1945 – 13 August 2016). Professor Giaquinta was professor of structure of matter at the Università di Catania (Italy) and was our teacher of physics and Alfio's PhD supervisor. He had a profound influence on our scientific as well as humanistic formation, as he taught us how to look at things in life. Among the many other things, his input for the original work that we are revisiting in this chapter has been of fundamental importance. It is not possible to properly express our gratitude to Prof. Giaquinta for all he has meant, means and will mean in our lives.

## References

Alhasadi, M.F., Federico, S.: Relation between Eshelby stress and Eshelby fourth-order tensor within an ellipsoidal inclusion. Acta Mech. **228**, 1045–1069 (2017)

Bhattacharyya, A., Weng, G.J.: Plasticity of isotropic composites with randomly oriented and packeted inclusions. Int. J. Plast. **10**, 553–578 (1994)

Bishop, R.L., Goldberg, S.I.: Tensor Analysis on Manifolds. Prentice-Hall, NJ (1968)

Bonet, J., Wood, R.D.: Nonlinear Continuum Mechanics for Finite Element Analysis, 2nd edn. Cambridge University Press, Cambridge (2008)

Chou, T.W., Nomura, S.: Fibre orientation effects on the thermoelastic properties of short-fibre composites. Fibre Sci. Technol. **14**, 279–291 (1981)

Curnier, A., He, Q.-C., Zysset, P.: Conewise linear elastic materials. J. Elast. **37**, 1–38 (1995)

Epstein, M.: The Geometrical Language of Continuum Mechanics. Cambridge University Press, Cambridge (2010)

Eshelby, J.D.: The force on an elastic singularity. Philos. Trans. R. Soc. A **244**, 87–112 (1951)

Eshelby, J.D.: The determination of the elastic field of an ellipsoidal inclusion, and related problems. Proc. R. Soc. Lond. A **241**, 376–396 (1957)

Eshelby, J.D.: The elastic energy-momentum tensor. J. Elast. **5**, 321–335 (1975)

Federico, S.: On the linear elasticity of porous materials. Int. J. Mech. Sci. **52**, 175–182 (2010a)

Federico, S.: Volumetric-distortional decomposition of deformation and elasticity tensor. Math. Mech. Solids **15**, 672–690 (2010b)

Federico, S.: Covariant formulation of the tensor algebra of non-linear elasticity. Int. J. Non-Linear Mech. **47**, 273–284 (2012)

Federico, S.: Porous materials with statistically oriented reinforcing fibres. In: Dorfmann, L., Ogden, R.W. (eds.) Nonlinear Mechanics of Soft Fibrous Materials. CISM Courses and Lectures No. 559, International Centre for Mechanical Sciences, pp. 49–120. Springer, Berlin (2015)

Federico, S., Grillo, A.: Elasticity and permeability of porous fibre-reinforced materials under large deformations. Mech. Mater. **44**, 58–71 (2012)

Federico, S., Grillo, A., Herzog, W.: A transversely isotropic composite with a statistical distribution of spheroidal inclusions: a geometrical approach to overall properties. J. Mech. Phys. Solids **52**, 2309–2327 (2004)

Federico, S., Grillo, A., La Rosa, G., Giaquinta, G., Herzog, W.: A transversely isotropic, transversely homogeneous microstructural-statistical model of articular cartilage. J. Biomech. **38**, 2008–2018 (2005)

Federico, S., Grillo, A., Imatani, S.: The linear elasticity tensor of incompressible materials. Math. Mech. Solids **20**, 643–662 (2015)

Grillo, A., Federico, S., Wittum, G.: Growth, mass transfer, and remodeling in fiber-reinforced, multi-constituent materials. Int. J. Non-Linear Mech. **47**, 388–401 (2012)
Grillo, A., Wittum, G., Tomic, A., Federico, S.: Remodelling in statistically oriented fibre-reinforced composites and biological tissues. Math. Mech. Solids **20**, 1107–1129 (2015)
Gurtin, M.E.: The linear theory of elasticity. In: Truesdell, C.A. (ed.) Handbuch der Physik, vol. IVa/2. Springer, Berlin (1972)
Gurtin, M.E., Fried, E., Anand, L.: The Mechanics and Thermodynamics of Continua. Cambridge University Press, Cambridge (2010)
Hashin, Z.: Theory of mechanical behavior of heterogeneous media. Appl. Mech. Rev. **17**, 1–9 (1963)
Hill, R.: Elastic properties of reinforced solids: some theoretical principles. J. Mech. Phys. Solids **11**, 357–372 (1963)
Hill, R.: Theory of mechanical properties of fibre-strengthened materials - I. Elastic behaviour. J. Mech. Phys. Solids **12**, 199–212 (1964)
Hill, R.: A self-consistent mechanics of composite materials. J. Mech. Phys. Solids **13**, 213–222 (1965)
Holmes, M.H., Mow, V.C.: The nonlinear characteristics of soft gels and hydrated connective tissues in ultrafiltration. J. Biomech. **23**, 1145–1156 (1990)
Jog, C.S.: A concise proof of the representation theorem for fourth-order isotropic tensors. J. Elast. **85**, 119–124 (2006)
Kolmogorov, A.N., Fomin, S.V. Elements of the Theory of Functions and Functional Analysis. Dover, New York (1999)
Marsden, J.E., Hughes, T.J.R.: Mathematical Foundations of Elasticity. Prentice-Hall, Englewood Cliff, NJ (1983)
Mura, T.: Micromechanics of Defects in Solids. Martinus Nijhoff, The Hague (1987)
Qiu, Y.P., Weng, G.J.: On the application of Mori-Tanaka's theory involving transversely isotropic spheroidal inclusions. Int. J. Eng. Sci. **28**, 1121–1137 (1990)
Segev, R.: Notes on metric independent analysis of classical fields. Math. Methods Appl. Sci. **36**, 497–566 (2013)
Soltz, M.A., Ateshian, G.A.: A conewise linear elasticity mixture model for the analysis of tension-compression nonlineartiy in articular cartilage. J. Biomech. Eng. **122**, 576–586 (2000)
Spencer, A.J.M.: Constitutive theory for strongly anisotropic solids. In: Spencer, A.J.M. (ed.) Continuum Theory of the Mechanics of Fibre-Reinforced Composites. CISM Courses and Lectures No. 282, International Centre for Mechanical Sciences, pp. 1–32. Springer, Wien (1984)
Tandon, G.P., Weng, G.J.: Average stress in the matrix and effective moduli of randomly oriented composites. Compos. Sci. Technol. **27**, 111–132 (1986)
Walpole, L.J.: On bounds for the overall elastic moduli of inhomogeneous systems - I. J. Mech. Phys. Solids **14**, 151–162 (1966a)
Walpole, L.J.: On bounds for the overall elastic moduli of inhomogeneous systems - II. J. Mech. Phys. Solids **14**, 289–301 (1966b)
Walpole, L.J.: On the overall elastic moduli of composite materials. J. Mech. Phys. Solids **17**, 235–251 (1969)
Walpole, L.J.: Elastic behavior of composite materials: theoretical foundations. Adv. Appl. Mech. **21**, 169–242 (1981)
Walpole, L.J.: Fourth-rank tensors of the thirty-two crystal classes: multiplication tables. Proc. R. Soc. Lond. A **391**, 149–179 (1984)
Weng, G.J.: Some elastic properties of reinforced solids, with special reference to isotropic ones containing spherical inclusions. Int. J. Eng. Sci. **22**, 845–856 (1984)
Weng, G.J.: The theoretical connection between Mori-Tanaka's theory and the Hashin-Shtrikman-Walpole bounds. Int. J. Eng. Sci. **28**, 1111–1120 (1990)
Wu, J.Z., Herzog, W.: Elastic anisotropy of articular cartilage is associated with the micro-structures of collagen fibers and chondrocytes. J. Biomech. **35**, 931–942 (2002)

# Chapter 12
# A Time-Incremental Eshelby-Based Homogenization Scheme for Viscoelastic Heterogeneous Materials

**Stéphane Berbenni and Hafid Sabar**

**Abstract** A time-incremental Eshelby-based homogenization scheme for Maxwellian heterogeneous materials is proposed and discussed. This is based on the exact solution of the heterogeneous Eshelby ellipsoidal inclusion problem obtained in the time domain. In contrast with hereditary methods, the effective behavior and the evolution laws of the averaged stresses per phase are solved incrementally in the time domain without the need of inverse Laplace or Laplace–Carson transforms. This is made through a time differential equation to exactly solve a volume term in the integral equation that was generally approximated in previous internal variable methods. The present formulation works for any arbitrary anisotropic ellipsoidal Maxwellian inclusion embedded in an isotropic Maxwellian matrix without any other restrictive assumptions. In order to show the interest of the present approach, a Mori–Tanaka homogenization scheme is applied to two-phase composites using the developed strain rate concentration equations. The results are reported and discussed in comparisons with other existing methods, including hereditary approaches and more recent internal variable approaches, in order to show the efficiency of the present time-incremental homogenization scheme.

## 12.1 Introduction

Materials like composites, metals, or polymers exhibit time-dependent behaviors which, from the homogenization point of view, may require the use of linear viscoelastic properties (Christensen, 1969; Laws and McLaughlin, 1978). Generally,

S. Berbenni (✉)
Laboratoire d'Etude des Microstructures et de Mécanique des Matériaux, Université de Lorraine, UMR CNRS 7239, 57045 Metz, France
e-mail: stephane.berbenni@univ-lorraine.fr

H. Sabar
Laboratoire de Mécanique Biomécanique Polymères Structures, Ecole Nationale Ingénieurs de Metz, 57078 Metz, France
e-mail: sabar@enim.fr



S.A. Meguid, G.J. Weng (eds.), *Micromechanics and Nanomechanics of Composite Solids*, DOI 10.1007/978-3-319-52794-9_12

the coupling between elastic and inelastic deformations renders micromechanical homogenization schemes particularly complex even in the case of linear viscoelastic heterogeneous materials. For instance, it was highlighted that the overall behavior of aggregates with Maxwellian constituents is no longer Maxwellian (Suquet, 1987; Rougier et al., 1993; Li and Weng, 1994). This is due to the differential nature of constitutive equations which involves different orders of time-derivation mechanical fields. In past decades, several approaches were proposed to solve linear viscoelastic problems.

Riemann–Stieltjes integral-based "hereditary" homogenization approaches using Laplace–Carson transforms and the correspondence principle (see, e.g., Mandel 1966) were first developed in the case of non-aging linear viscoelastic materials. The inclusion problem was first solved (Hashin, 1969; Laws and McLaughlin, 1978) and further introduced in different homogenization schemes: Mori–Tanaka (Wang and Weng, 1992; Li and Weng, 1994, 1997; Brinson and Lin, 1998; Pierard and Doghri, 2006), Hashin–Shtrickman (DeBotton and Tevet-Deree, 2004), or self-consistent (Laws and McLaughlin, 1978; Weng, 1993; Turner and Tomé, 1993; Rougier et al., 1993, 1994; Masson and Zaoui, 1999; Brenner et al., 2002) estimates, among others. The overall properties of composites in the time domain are then obtained by the Laplace or Laplace–Carson inversion either analytically in simple cases (Hashin, 1969; Rougier et al., 1993; Wang and Weng, 1992; Li and Weng, 1994), or, numerically in major cases (Laws and McLaughlin, 1978; Levesque et al., 2007) which demands large CPU time and memory.

A more efficient homogenization strategy is based on "incremental internal variables approaches," whereby the stress history is recorded through the inelastic strains of the individual constituents. The hereditary approaches give the solution in the transformed (Laplace or Laplace–Carson) domain, whereas the internal variables formulations directly provide the solution in the time domain. Time is implicitly present in these formulations through the inelastic strains. Thus, these fields are defined as "internal variables." One of the main advantages of developing such approaches in addition to CPU time and memory lies in examining complex loading paths in time domains and aging behaviors.

First, internal variables self-consistent and Mori–Tanaka approximations for heterogeneous linear and non-linear viscoelastic materials were developed in Weng (1981), Kouddane et al. (1993), Molinari et al. (1997), Paquin et al. (1999), Sabar et al. (2002), and Molinari (2002). The first developments were carried out by Weng (1981) in the 1980s who adapted Kröner's (1961) elastoplastic self-consistent model to the case of elasto-viscoplasticity. However, similarly to the original proposition of Kröner's (1961), internal stresses are overestimated with this method. In the 1990s, an "additive" interaction law for the Eshelby's inclusion problem was derived for Maxwellian local viscoelastic behavior by Molinari et al. (Kouddane et al., 1993; Molinari et al., 1997; Molinari, 2002). This interaction law was written in terms of strain rates and was postulated as the superposition of elastic and inelastic interaction laws. It was applied to the non-linear elasto-viscoplastic Eshelby's inclusion problem using a "tangent" formulation with some applications to the Mori–Tanaka and self-consistent estimates in Mercier and Molinari (2009). The

"translated fields" method was developed for linear and non-linear viscoelasticity in Paquin et al. (1999) and in Sabar et al. (2002) starting from the integral equation of the heterogeneous elasto-viscoplastic problem. Good predictions were found in Paquin et al. (1999) in comparison with the exact "1-site" self-consistent solution of Rougier et al. (1994). The "translated fields" approach of Paquin et al. (1999) was recently extended to treat linear viscoelastic composites with the Mori–Tanaka scheme in Mercier et al. (2012), where it was compared to the "additive" interaction law and Fast Fourier Transform (FFT) calculations. A very rich but complex interaction law was obtained with the "translated fields" method in Mercier et al. (2012). The extensions of the "translated fields" method to non-linear viscoelastic composites and polycrystals with an "affine" formulation were recently reported by Berbenni and Capolungo (2015) and by Mareau and Berbenni (2015), respectively. The results of this extended "translated fields" method were successfully compared to the ones obtained by the "affine" hereditary approach developed by Masson and Zaoui (1999) for the same non-linear polycrystal Mareau and Berbenni (2015). Another approach based on a "sequential" linearization technique was recently developed by Kowalczyk-Gajewska and Petryk (2011). This technique is based on the sequential resolution of purely elastic and purely viscoplastic interaction laws. Different "variants" of the technique were proposed for sequential linearization, and the aforementioned "additive" interaction law was retrieved as a specific "variant." Lastly, a self-consistent internal variables approach for two-phase linear isotropic viscoelastic composites was also proposed by Coulibaly and Sabar (2011) and successfully compared to the exact results of Hashin (1969) and Rougier et al. (1994) for two-phase composites. Variational approaches were developed by Lahellec and Suquet (2007a,b) and by Brassard et al. (2012). An incremental internal variables approach was first developed in linear viscoelasticity by Lahellec and Suquet (2007a) and extended to non-linear viscoelasticity also by Lahellec and Suquet (2007b). These authors used two potentials (free energy density and dissipation potential) with an implicit time discretization scheme based on a variational method. Their theory was applied to both Maxwell and Kelvin–Voigt rheological models. The FFT technique was also reported in Lahellec and Suquet (2007a,b) as "exact" reference solutions to assess the variational approach. Recently, another variational approach was developed in Brassard et al. (2012) for non-linear two-phase elasto-viscoplastic composites using a "secant" linearization scheme and a Mori–Tanaka approximation. A method inspired from the collocation method was first developed by Ricaud and Masson (2009). Interestingly, this approach is based on an equivalence between the collocation method and an internal variables formulation to obtain the exact effective behavior for a two-phase microstructure in the cases of Voigt, Reuss, and Mori–Tanaka estimates. Exact analytical results were provided in Ricaud and Masson (2009) in the case of two-phase elastically homogeneous Maxwellian linear viscoelastic composites. These solutions will be used in the sequel to assess the present internal variables formulation with a Mori–Tanaka estimate. The extension of Ricaud and Masson (2009) method to the case of linear viscoelastic polycrystals with a self-consistent procedure was recently reported in Masson et al. (2012). It is noteworthy that Ricaud and Masson (2009)

homogenization scheme was also applied to aging linear viscoelasticity. A different homogenization scheme for aging linear viscoelastic matrix-inclusion composite materials using the Volterra operator and working in the time domain was developed by Sanahuja (2013) for isotropic phases and spherical inclusions. This scheme was recently extended by Lavergne et al. (2016) to ellipsoidal inclusions and assuming isotropic aging viscoelastic matrices with time-independent Poisson ratio.

The objective of this chapter is to present and discuss a recent internal variables approach first introduced by Berbenni et al. (2015) based on an incremental Eshelby-based homogenization scheme for viscoelastic heterogeneous materials operating in the time domain. Section 12.2 introduces the constitutive equations and the exact time-incremental internal variables formulation in the case of micro-heterogeneous linear viscoelastic Maxwellian behavior. The integral equation can be simplified by considering isotropic viscoelastic properties for the reference medium without other more restrictive assumptions. Then, the incremental internal variables approach is set up through a time differential equation related to the "volume" term in the integral equation. In Sect. 12.3, the viscoelastic Eshelby's inclusion problem is exactly solved through incremental strain rate concentration laws and through incremental interaction laws that do not contain any approximation. Based on the strain rate concentration equations of the Eshelby problem, a time-incremental internal variables homogenization Mori–Tanaka scheme is derived in Sect. 12.4 for linear viscoelastic two-phase composites and an isotropic distribution of phases. Then, this homogenization scheme is applied to different cases, including comparisons with other Mori–Tanaka homogenization schemes for two-phase Maxwellian composites: (1) the exact analytical derivations from Li and Weng (1994) using a hereditary approach and Laplace transform inversion, (2) Ricaud and Masson (2009) exact formulation for compressible viscoelastic phases with homogeneous elasticity, and (3) the approximate models based on the "translated fields" method (Paquin et al., 1999; Berbenni and Capolungo, 2015; Mareau and Berbenni, 2015) or based on the "additive" interaction law (Kouddane et al., 1993; Molinari et al., 1997; Molinari, 2002; Mercier and Molinari, 2009).

## 12.2 Time-Incremental Formulation

### *12.2.1 Constitutive Equations*

A heterogeneous linear viscoelastic medium $V$ with boundary $\partial V$ is considered with Maxwellian constituents characterized by linear elastic moduli $\underset{\approx}{c}$ (elastic compliances $\underset{\approx}{s} = \underset{\approx}{c}^{-1}$) and linear inelastic moduli $\underset{\approx}{b}$ (inelastic compliances $\underset{\approx}{m} = \underset{\approx}{b}^{-1}$). For linear viscoelasticity, $\underset{\approx}{m}$ and $\underset{\approx}{b}$ are constant (i.e., time independent). Here, non-linear viscoelasticity, where $\underset{\approx}{m}$ and $\underset{\approx}{b}$ are time- and stress-dependent, is disregarded. The problem is treated within the framework of quasi-static equilibrium with

infinitesimal strains and no volume forces. Thus, for a given applied homogeneous strain rate $\dot{\underset{\sim}{\varepsilon}}^0$, field equations of the linear viscoelastic (Maxwellian) problem are given by

$$\begin{aligned}
&\dot{\underset{\sim}{\sigma}} = \underset{\approx}{b} : \left(\dot{\underset{\sim}{\varepsilon}} - \underset{\approx}{s} : \dot{\underset{\sim}{\sigma}}\right) \text{ or } \dot{\underset{\sim}{\sigma}} = \underset{\approx}{c} : \left(\dot{\underset{\sim}{\varepsilon}} - \underset{\approx}{m} : \underset{\sim}{\sigma}\right) \\
&\underline{div}\,\dot{\underset{\sim}{\sigma}} = 0 \\
&\underline{div}\,\underset{\sim}{\sigma} = 0 \\
&\dot{\underset{\sim}{\varepsilon}} = \nabla^s \underline{\dot{u}} \\
&\underline{\dot{u}}^d = \dot{\underset{\sim}{\varepsilon}}^0 \cdot \underline{x} \text{ on } \partial V
\end{aligned} \tag{12.1}$$

where $\dot{\underset{\sim}{\varepsilon}}$ is the total strain rate with linearized kinematics, $\underset{\sim}{\sigma}$ is the Cauchy stress, and $\dot{\underset{\sim}{\varepsilon}}^e = \underset{\approx}{s} : \dot{\underset{\sim}{\sigma}}$ (resp. $\dot{\underset{\sim}{\varepsilon}}^v = \underset{\approx}{m} : \underset{\sim}{\sigma}$) is the elastic (resp. inelastic) strain rate. In Eq. (12.1), $\underline{u}$ is the unknown displacement field, $\nabla^s$ denotes the symmetrized gradient operator, $\underline{div}$ denotes the divergence operator, and the symbols "." and ":" denote simple and contracted products, respectively.

The heterogeneous elastic moduli $\underset{\approx}{c}$ (resp. compliances $\underset{\approx}{s}$) and the heterogeneous viscous moduli $\underset{\approx}{b}$ (resp. compliances $\underset{\approx}{m}$) can be written in terms of spatial fluctuations $\underset{\approx}{\delta c}$ (resp. $\underset{\approx}{\delta s}$) and $\underset{\approx}{\delta b}$ (resp. $\underset{\approx}{\delta m}$) as follows:

$$\underset{\approx}{c} = \underset{\approx}{c}^0 + \underset{\approx}{\delta c}; \underset{\approx}{s} = \underset{\approx}{s}^0 + \underset{\approx}{\delta s}; \underset{\approx}{b} = \underset{\approx}{b}^0 + \underset{\approx}{\delta b}; \underset{\approx}{m} = \underset{\approx}{m}^0 + \underset{\approx}{\delta m} \tag{12.2}$$

where $\underset{\approx}{c}^0$, $\underset{\approx}{s}^0$, $\underset{\approx}{b}^0$, and $\underset{\approx}{m}^0$ denote the elastic moduli, elastic compliances, viscous moduli, and viscous compliances of the homogeneous reference medium. Using the classic Green's function technique and previous constitutive equations yields

$$\dot{\underset{\sim}{\varepsilon}} = \dot{\underset{\sim}{\varepsilon}}^0 + \underset{\approx}{\Gamma}^{c^0} \star \underset{\approx}{c}^0 : \underset{\sim}{R} + \underset{\approx}{\Gamma}^{c^0} \star \underset{\approx}{c}^0 : \underset{\approx}{m}^0 : \underset{\sim}{\sigma} \tag{12.3}$$

or

$$\dot{\underset{\sim}{\varepsilon}} = \dot{\underset{\sim}{\varepsilon}}^0 + \underset{\approx}{\Gamma}^{b^0} \star \underset{\approx}{b}^0 : \underset{\sim}{R} + \underset{\approx}{\Gamma}^{b^0} \star \underset{\approx}{b}^0 : \underset{\approx}{s}^0 : \dot{\underset{\sim}{\sigma}} \tag{12.4}$$

where $\star$ denotes spatial convolution and $\underset{\sim}{R}$ contains the fluctuations of both elastic and inelastic compliances and is given by

$$\underset{\sim}{R} = \underset{\approx}{\delta s} : \dot{\underset{\sim}{\sigma}} + \underset{\approx}{\delta m} : \underset{\sim}{\sigma} \tag{12.5}$$

The fourth-order tensor $\underset{\approx}{\Gamma}^{c^0}$ (resp. $\underset{\approx}{\Gamma}^{b^0}$) is the modified Green tensor associated with $\underset{\approx}{c}^0$ (resp. $\underset{\approx}{b}^0$) as defined in Kröner (1990):

$$\Gamma^*_{ijkl}(\underline{x}-\underline{x}') = -\frac{1}{2}\left(G^*_{ik,jl}(\underline{x}-\underline{x}') + G^*_{jk,il}(\underline{x}-\underline{x}')\right) \tag{12.6}$$

where $\underset{\sim}{G}^*$ is the Green tensor (see Mura 1987) associated with $* = c^0$ and $* = b^0$, and $\underline{x}$ and $\underline{x}'$ are position vectors.

### 12.2.2 Time-Incremental Internal Variables Formulation

For the rest of the paper, we assume the case of a homogeneous reference medium with isotropic elastic and viscous properties, where $k^0$ and ${k_v}^0$ are the elastic and inelastic bulk moduli of the reference medium, and $\mu^0$ and ${\mu_v}^0$ are its elastic and inelastic shear moduli, such that

$$\begin{aligned}
\underset{\approx}{c}^0 : \underset{\approx}{m}^0 : \underset{\sim}{\sigma} &= \left(\frac{k^0}{{k_v}^0} - \frac{\mu^0}{{\mu_v}^0}\right)\sigma_m \underset{\sim}{\delta} + \frac{\mu^0}{{\mu_v}^0}\underset{\sim}{\sigma} \\
\underset{\approx}{b}^0 : \underset{\approx}{s}^0 : \underset{\sim}{\dot{\sigma}} &= \left(\frac{{k_v}^0}{k^0} - \frac{{\mu_v}^0}{\mu^0}\right)\dot{\sigma}_m \underset{\sim}{\delta} + \frac{{\mu_v}^0}{\mu^0}\underset{\sim}{\dot{\sigma}}
\end{aligned} \tag{12.7}$$

where $\sigma_m$ is the spherical part of $\underset{\sim}{\sigma}$ (i.e., hydrostatic pressure $\sigma_m = \frac{1}{3}\sigma_{kk}$).

For any statically admissible stress field verifying, Eq. (12.1), traction vector continuity at perfectly bonded interfaces and homogeneous boundary conditions, the modified Green operators associated with the homogeneous reference elastic and viscous media have the following property (Kunin, 1983; Kröner, 1990):

$$\underset{\approx}{\Gamma}^{c^0} \star \underset{\sim}{\sigma} = 0 \text{ and } \underset{\approx}{\Gamma}^{b^0} \star \underset{\sim}{\dot{\sigma}} = 0 \tag{12.8}$$

Using Eqs. (12.7) and (12.8), Eq. (12.3) can be recast:

$$\underset{\sim}{\dot{\varepsilon}} = \underset{\sim}{\dot{\varepsilon}}^0 + \underset{\approx}{\Gamma}^{c^0} \star \underset{\approx}{c}^0 : \underset{\sim}{R} + \beta \underset{\sim}{\sigma}^* \tag{12.9}$$

with

$$\beta = \frac{3}{3k^0 + 4\mu^0}\left(\frac{k^0}{{k_v}^0} - \frac{\mu^0}{{\mu_v}^0}\right) \tag{12.10}$$

and Eq. (12.4) simplifies to

$$\underset{\sim}{\dot{\varepsilon}} = \underset{\sim}{\dot{\varepsilon}}^0 + \underset{\approx}{\Gamma}^{b^0} \star \underset{\approx}{b}^0 : \underset{\sim}{R} + \gamma \underset{\sim}{\dot{\sigma}}^* \tag{12.11}$$

with

$$\gamma = \frac{3}{3{k_v}^0 + 4{\mu_v}^0}\left(\frac{{k_v}^0}{k^0} - \frac{{\mu_v}^0}{\mu^0}\right) \tag{12.12}$$

and where

$$\sigma_{ij}^{*}\left(\underline{x}\right) = -\frac{1}{4\pi}\int_{V}\left(\frac{1}{|\underline{x}-\underline{x}'|}\right)_{,ij}\sigma_m\left(\underline{x}'\right)\,dV' \tag{12.13}$$

with $\sigma_{ij}^{*}\left(\underline{x}\right) \to 0$ when $|\underline{x}| \to \infty$.

In Eq. (12.13), $\underset{\sim}{\sigma}^{*}$ is a volume term that is difficult to solve using only the integral form described in Eq. (12.9) or Eq. (12.11). Therefore, an incremental time differential equation is now proposed to solve $\underset{\sim}{\sigma}^{*}$. Then, $\underset{\sim}{\sigma}^{*}$ is incrementally computed using Eq. (12.13) as follows:

$$\dot{\sigma}_{ij}^{*}\left(\underline{x}\right) = -\frac{1}{4\pi}\int_{V'}\left(\frac{1}{|\underline{x}-\underline{x}'|}\right)_{,ij}\dot{\sigma}_m\left(\underline{x}'\right)\,dV' \tag{12.14}$$

In Eq. (12.14), the rate of $\sigma_m\left(\underline{x}\right)$ is obtained using the first constitutive laws in Eq. (12.1) together with Eq. (12.9) or Eq. (12.11), and using Eq. (12.13) (see Berbenni et al. (2015) for details). Finally, the following time differential equation is obtained for $\underset{\sim}{\sigma}^{*}$:

$$\begin{aligned}\dot{\sigma}_{ij}^{*}\left(\underline{x}\right) = &-\frac{{\alpha^c}^0}{4\pi}\int_{V}\left|\underline{x}-\underline{x}'\right|_{,ijkl}R_{kl}\left(\underline{x}'\right)\,dV' \\ &+\frac{3{\alpha^c}^0}{2\pi}\int_{V}\left(\frac{1}{|\underline{x}-\underline{x}'|}\right)_{,ij}R_m\left(\underline{x}'\right)\,dV' - \frac{{\alpha^c}^0}{{\alpha^b}^0}\sigma_{ij}^{*}\left(\underline{x}\right)\end{aligned} \tag{12.15}$$

where

$${\alpha^c}^0 = \frac{3k^0\mu^0}{3k^0 + 4\mu^0} \tag{12.16}$$

$${\alpha^b}^0 = \frac{3{k_v}^0{\mu_v}^0}{3{k_v}^0 + 4{\mu_v}^0} \tag{12.17}$$

Equation (12.15) together with Eq. (12.9) or Eq. (12.11) represents the two exact equations of the present incremental internal variables approach that are to be solved simultaneously in a given time step. In the following, the Eshelby's inclusion problem is solved in the context of arbitrary anisotropic ellipsoidal Maxwellian inclusion embedded in an infinite isotropic Maxwellian matrix.

## 12.3 Viscoelastic Ellipsoidal Eshelby Inclusion

### *12.3.1 Strain Rate Concentration Equations*

Here, we consider the whole volume $V$ constituted of an ellipsoidal inclusion $I$ with volume $V_I$ embedded in an infinite matrix (here considered as the homogeneous reference medium) subjected to $\underset{\sim}{\dot{\varepsilon}}^0$ at remote boundaries. The inclusion and the matrix follow a Maxwellian behavior with uniform respective linear elastic $\underset{\approx}{c}^I$, $\underset{\approx}{c}^0$ and inelastic $\underset{\approx}{b}^I$, $\underset{\approx}{b}^0$ moduli (and conversely uniform respective linear elastic $\underset{\approx}{s}^I$, $\underset{\approx}{s}^0$ and inelastic $\underset{\approx}{m}^I$, $\underset{\approx}{m}^0$ compliances). In the following, only the infinite homogeneous reference medium (0) is restricted to be isotropic. Thus, the spatial fluctuations of elastic and linear inelastic properties are given by $\underset{\approx}{\delta c}^I = \underset{\approx}{c}^I - \underset{\approx}{c}^0$, $\underset{\approx}{\delta s}^I = \underset{\approx}{s}^I - \underset{\approx}{s}^0$, $\underset{\approx}{\delta b}^I = \underset{\approx}{b}^I - \underset{\approx}{b}^0$, and $\underset{\approx}{\delta m}^I = \underset{\approx}{m}^I - \underset{\approx}{m}^0$.

By denoting $\underset{\sim}{\dot{\varepsilon}}^I$ the spatial average of $\underset{\sim}{\dot{\varepsilon}}$ over the ellipsoidal inclusion $V_I$, $\underset{\sim}{\dot{\varepsilon}}^I$ is obtained from Eq. (12.9):

$$\underset{\sim}{\dot{\varepsilon}}^I = \underset{\sim}{\dot{\varepsilon}}^0 + \underset{\approx}{T}^{c^{0I}} : \underset{\approx}{c}^0 : \underset{\sim}{R}^I + \beta \underset{\sim}{\sigma}^{*I} \tag{12.18}$$

or from Eq. (12.11),

$$\underset{\sim}{\dot{\varepsilon}}^I = \underset{\sim}{\dot{\varepsilon}}^0 + \underset{\approx}{T}^{b^{0I}} : \underset{\approx}{b}^0 : \underset{\sim}{R}^I + \gamma \underset{\sim}{\dot{\sigma}}^{*I} \tag{12.19}$$

where for any $\underline{x} \in V_I$, the fourth-order tensors $\underset{\approx}{T}^{c^{0I}}$ and $\underset{\approx}{T}^{b^{0I}}$ defined as

$$\begin{aligned} \underset{\approx}{T}^{c^{0I}} &= \int_{V_I} \underset{\approx}{\Gamma}^{c^0}\left(\underline{x} - \underline{x}'\right) dV' \\ \underset{\approx}{T}^{b^{0I}} &= \int_{V_I} \underset{\approx}{\Gamma}^{b^0}\left(\underline{x} - \underline{x}'\right) dV' \end{aligned} \tag{12.20}$$

are uniform tensors due to the Eshelby's property for ellipsoidal inclusions (Eshelby, 1957). In Eqs. (12.18) and (12.19), $\underset{\sim}{\sigma}^{*I}$ is the spatial average of $\underset{\sim}{\sigma}^*$ over $V_I$ and $\underset{\sim}{R}^I$ is given by

$$\underset{\sim}{R}^I = \underset{\approx}{\delta s}^I : \underset{\sim}{\dot{\sigma}}^I + \underset{\approx}{\delta m}^I : \underset{\sim}{\sigma}^I \tag{12.21}$$

where $\underset{\sim}{\sigma}^I$ is the spatial average of $\underset{\sim}{\sigma}$ over $V_I$.

Using Eq. (12.21) together with the constitutive laws in Eq. (12.1), Eq. (12.18) can be rewritten as

$$\underset{\sim}{\dot{\varepsilon}}^{I} = \underset{\approx}{A}^{c^{0I}} : \underset{\sim}{\dot{\varepsilon}}^{0} + \underset{\approx}{A}^{c^{0I}} : \underset{\approx}{T}^{c^{0I}} : \left( \underset{\approx}{c}^{I} : \underset{\approx}{m}^{I} - \underset{\approx}{c}^{0} : \underset{\approx}{m}^{0} \right) : \underset{\sim}{\sigma}^{I} + \beta \underset{\approx}{A}^{c^{0I}} : \underset{\sim}{\sigma}^{*I} \tag{12.22}$$

and Eq. (12.19) can be rewritten as

$$\underset{\sim}{\dot{\varepsilon}}^{I} = \underset{\approx}{A}^{b^{0I}} : \underset{\sim}{\dot{\varepsilon}}^{0} + \underset{\approx}{A}^{b^{0I}} : \underset{\approx}{T}^{b^{0I}} : \left( \underset{\approx}{b}^{I} : \underset{\approx}{s}^{I} - \underset{\approx}{b}^{0} : \underset{\approx}{s}^{0} \right) : \underset{\sim}{\dot{\sigma}}^{I} + \gamma \underset{\approx}{A}^{b^{0I}} : \underset{\sim}{\dot{\sigma}}^{*I} \tag{12.23}$$

The strain rate concentration tensors $\underset{\approx}{A}^{c^{0I}}$ and $\underset{\approx}{A}^{b^{0I}}$ are given by

$$\begin{aligned} \underset{\approx}{A}^{c^{0I}} &= \left( \underset{\approx}{I} + \underset{\approx}{T}^{c^{0I}} : \delta \underset{\approx}{c}^{I} \right)^{-1} \\ \underset{\approx}{A}^{b^{0I}} &= \left( \underset{\approx}{I} + \underset{\approx}{T}^{b^{0I}} : \delta \underset{\approx}{b}^{I} \right)^{-1} \end{aligned} \tag{12.24}$$

Using Eq. (12.15), $\underset{\sim}{\sigma}^{*I}$ is the solution of the following time differential equation:

$$\dot{\sigma}_{ij}^{*I} = -\frac{\alpha^{c^0}}{4\pi} \psi^{I}_{,ijkl} R^{I}{}_{kl} + \frac{3\alpha^{c^0}}{2\pi} \phi^{I}_{,ij} R_{m}{}^{I} - \frac{\alpha^{c^0}}{\alpha^{b^0}} \sigma_{ij}^{*I} \tag{12.25}$$

In Eq. (12.25), $\phi^I$ and $\psi^I$ are harmonic and bi-harmonic potential functions (Ferrers, 1877; Dyson, 1891; Eshelby, 1957) related to the ellipsoidal inclusion $V_I$. $\phi^I_{,ij}$ and $\psi^I_{,ijkl}$ are given by Eq. 11.35 (p. 85) in Mura (1987):

$$\phi^{I}_{,ij} = \int_{V_I} \left( \frac{1}{|\underline{x} - \underline{x}'|} \right)_{,ij} dV' \quad \psi^{I}_{,ijkl} = \int_{V_I} |\underline{x} - \underline{x}'|_{,ijkl} \, dV' \tag{12.26}$$

which are uniform when $\underline{x} \in V_I$. The expressions of $\phi^I_{,ij}$ and $\psi^I_{,ijkl}$ for a general ellipsoidal inclusion are given in classic books in micromechanics (Mura, 1987). $\phi^I_{,ij}$ and $\psi^I_{,ijkl}$ are contained in $\underset{\approx}{T}^{c^{0I}}$, resp. $\underset{\approx}{T}^{b^{0I}}$, as follows:

$$T^{c^{0I}}_{ijkl} = -\frac{1}{8\pi\mu^0} \left( \phi^{I}_{,jl}\delta_{ik} + \phi^{I}_{,il}\delta_{jk} \right) + \frac{3k^0 + \mu^0}{8\pi\mu^0 \left(3k^0 + 4\mu^0\right)} \psi^{I}_{,ijkl} \tag{12.27}$$

$$T^{b^{0I}}_{ijkl} = -\frac{1}{8\pi\mu_v{}^0} \left( \phi^{I}_{,jl}\delta_{ik} + \phi^{I}_{,il}\delta_{jk} \right) + \frac{3k_v{}^0 + \mu_v{}^0}{8\pi\mu_v{}^0 \left(3k_v{}^0 + 4\mu_v{}^0\right)} \psi^{I}_{,ijkl} \tag{12.28}$$

Furthermore, the elastic (resp. inelastic) Eshelby tensors $\underset{\approx}{S}^{c^0}$ (resp. $\underset{\approx}{S}^{b^0}$) for elastic (resp. inelastic) reference media are defined as $\underset{\approx}{S}^{c^{0I}} = \underset{\approx}{T}^{c^{0I}} : \underset{\approx}{c}^{0}$ and $\underset{\approx}{S}^{b^{0I}} = \underset{\approx}{T}^{b^{0I}} : \underset{\approx}{b}^{0}$.

### 12.3.2 Interaction Laws

The interaction law for an arbitrary anisotropic and ellipsoidal inclusion $V_I$ embedded in an infinite matrix can be obtained from Eq. (12.18) or from Eq. (12.19) and by using the constitutive law in Eq. (12.1). Using Eq. (12.1), and after algebraic manipulations, $\underset{\sim}{R}^I$ defined in Eq. (12.21) can also be rewritten as follows:

$$\underset{\sim}{R}^I = \underset{\sim}{\dot{\varepsilon}}^I - \underset{\sim}{\dot{\varepsilon}}^0 - \underset{\approx}{s}^0 : \left(\underset{\sim}{\dot{\sigma}}^I - \underset{\sim}{\dot{\sigma}}^0\right) - \underset{\approx}{m}^0 : \left(\underset{\sim}{\sigma}^I - \underset{\sim}{\sigma}^0\right) \tag{12.29}$$

Thus, using Eq. (12.18) together with Eq. (12.29) leads to a first form of the interaction law for the linear viscoelastic Eshelby problem:

$$\underset{\sim}{\dot{\sigma}}^I - \underset{\sim}{\dot{\sigma}}^0 = \left(\underset{\approx}{c}^0 - \left(\underset{\approx}{T}^{c^{0I}}\right)^{-1}\right) : \left(\underset{\sim}{\dot{\varepsilon}}^I - \underset{\sim}{\dot{\varepsilon}}^0\right) - \underset{\approx}{c}^0 : \underset{\approx}{m}^0 : \left(\underset{\sim}{\sigma}^I - \underset{\sim}{\sigma}^0\right) + \beta \left(\underset{\approx}{T}^{c^{0I}}\right)^{-1} : \underset{\sim}{\sigma}^{*I} \tag{12.30}$$

where $\underset{\sim}{\sigma}^0$ is the uniform remote stress at the boundaries. Using Eq. (12.19) together with Eq. (12.29), a second form of the interaction law can be written for the linear viscoelastic Eshelby problem as follows:

$$\underset{\sim}{\sigma}^I - \underset{\sim}{\sigma}^0 = \left(\underset{\approx}{b}^0 - \left(\underset{\approx}{T}^{b^{0I}}\right)^{-1}\right) : \left(\underset{\sim}{\dot{\varepsilon}}^I - \underset{\sim}{\dot{\varepsilon}}^0\right) - \underset{\approx}{b}^0 : \underset{\approx}{s}^0 : \left(\underset{\sim}{\dot{\sigma}}^I - \underset{\sim}{\dot{\sigma}}^0\right) + \gamma \left(\underset{\approx}{T}^{b^{0I}}\right)^{-1} : \underset{\sim}{\dot{\sigma}}^{*I} \tag{12.31}$$

Equations (12.30) and (12.31) are two forms for the interaction law that are written for the same Maxwellian linear viscoelastic inclusion problem where all the averaged terms are exactly defined. In both equations, the third terms in the second members are new in comparison with other previous approximations starting from the same constitutive equations as Eq. (12.1) and using the Green's function technique as in Kouddane et al. (1993), Molinari et al. (1997), Paquin et al. (1999), Molinari (2002), Mercier and Molinari (2009), Mercier et al. (2012), Berbenni and Capolungo (2015), and Mareau and Berbenni (2015). These terms describe the complex spatio temporal integral nature of elastic–inelastic accommodations within the heterogeneous viscoelastic material. Here, they are fully defined through isotropic elastic and inelastic constants of the matrix and the evolution of $\underset{\sim}{\sigma}^{*I}$. Note that only the viscoelastic properties of the infinite matrix are isotropic, not the ones related to the inclusion. In Berbenni et al. (2015), the exactness of the interaction law was shown for an arbitrary anisotropic and ellipsoidal inclusion $V_I$ embedded in an infinite matrix with isotropic properties in comparison with the exact hereditary approach obtained with the Riemann–Stieltjes integral-based technique (Laws and McLaughlin, 1978).

## 12.4 Homogenization and Results for Two-Phase Composite Materials

### *12.4.1 Homogenization for Two-Phase Composite Materials*

In the case of two-phase composite materials, the Representative Volume Element (RVE) is constituted of several inclusions (phase $I$) with volume fraction $f$ embedded in a matrix phase $M$ with volume fraction $(1-f)$. The RVE is subjected at its boundary $\partial V$ to the homogeneous macroscopic strain rate here denoted $\underset{\sim}{\dot{E}}$ satisfying

$$f\,\underset{\sim}{\dot{\varepsilon}}^{I} + (1-f)\,\underset{\sim}{\dot{\varepsilon}}^{M} = \underset{\sim}{\dot{E}} \tag{12.32}$$

The Mori–Tanaka scheme (Mori and Tanaka, 1973; Weng, 1984; Benveniste, 1987) is based on choosing the infinite homogeneous reference medium 0 as the matrix phase $M$ (i.e., $0 = M$). This popular scheme is very well suited to estimate the effective properties of two-phase composites with an isotropic distribution of phases, provided the volume fraction $f$ of inclusions is not too large (generally not larger than 0.2). Based on Eq. (12.22), the strain rate in the phase $I$ is given by

$$\underset{\sim}{\dot{\varepsilon}}^{I} = \underset{\approx}{A}^{c^M I} : \underset{\sim}{\dot{\varepsilon}}^{M} + \underset{\approx}{A}^{c^M I} : \underset{\approx}{T}^{c^M I} : \left(\underset{\approx}{c}^{I} : \underset{\approx}{m}^{I} - \underset{\approx}{c}^{M} : \underset{\approx}{m}^{M}\right) : \underset{\sim}{\sigma}^{I} + \beta \underset{\approx}{A}^{c^M I} : \underset{\sim}{\sigma}^{*I} \tag{12.33}$$

where from Eq. (12.25), $\underset{\sim}{\sigma}^{*I}$ is the solution of the following time differential equation:

$$\dot{\sigma}_{ij}^{*I} = -\frac{\alpha^{c^M}}{4\pi}\psi^{I}_{,ijkl}R^{I}{}_{kl} + \frac{3\alpha^{c^M}}{2\pi}\phi^{I}_{,ij}R_m{}^{I} - \frac{\alpha^{c^M}}{\alpha^{b^M}}\sigma_{ij}^{*I} \tag{12.34}$$

and from Eq. (12.24),

$$\underset{\approx}{A}^{c^M I} = \left(\underset{\approx}{I} + \underset{\approx}{T}^{c^M I} : \underset{\approx}{\delta c}^{I}\right)^{-1} \tag{12.35}$$

with $\underset{\approx}{\delta c}^{I} = \underset{\approx}{c}^{I} - \underset{\approx}{c}^{M}$. Using Eq. (12.33) together with Eq. (12.32) gives the strain rate in the matrix phase $M$:

$$\begin{aligned}\underset{\sim}{\dot{\varepsilon}}^{M} = {} & \underset{\approx}{B}^{c^M I} : \underset{\sim}{\dot{E}} - f\underset{\approx}{B}^{c^M I} : \underset{\approx}{A}^{c^M I} : \underset{\approx}{T}^{c^M I} : \left(\underset{\approx}{c}^{I} : \underset{\approx}{m}^{I} - \underset{\approx}{c}^{M} : \underset{\approx}{m}^{M}\right) : \underset{\sim}{\sigma}^{I} \\ & - f\beta\underset{\approx}{B}^{c^M I} : \underset{\approx}{A}^{c^M I} : \underset{\sim}{\sigma}^{*I}\end{aligned} \tag{12.36}$$

where $\underset{\approx}{B}^{c^M I}$ is defined as

$$\underset{\approx}{B}^{c^M I} = \left[(1-f)\,\underset{\approx}{I} + f\underset{\approx}{A}^{c^M I}\right]^{-1} \tag{12.37}$$

In the case of spherical inclusions, $\underset{\approx}{T}^{c^M I}$ is given by

$$\underset{\approx}{T}^{c^M I} = \frac{1}{3k^M + 4\mu^M} \underset{\approx}{J} + \frac{3\left(k^M + 2\mu^M\right)}{5\mu^M\left(3k^M + 4\mu^M\right)} \underset{\approx}{K} \tag{12.38}$$

and the expressions of $\phi^I_{,ij}$ and $\psi^I_{,ijkl}$ [Eq. (12.26)] are simplified to the following expressions (Walpole, 1981; Mura, 1987):

$$\phi^I_{,ij} = -\frac{4\pi}{3}\delta_{ij} \quad \psi^I_{,ijkl} = -\frac{8\pi}{15}\left(\delta_{ij}\delta_{kl} + \delta_{ik}\delta_{jl} + \delta_{il}\delta_{jk}\right) \tag{12.39}$$

Therefore, the explicit forms of $\underset{\approx}{A}^{c^M I}$ and $\underset{\approx}{B}^{c^M I}$ follow from Eq. (12.38) together with Eq. (12.35) and Eq. (12.37), respectively. Furthermore, Eq. (12.34) for spherical inclusions simplifies to

$$\dot{\sigma}^{*I}_{ij} = \frac{4}{15}\alpha^{c^M}\left(R_{ij}{}^I - 6R_m{}^I\delta_{ij}\right) - \frac{\alpha^{c^M}}{\alpha^{b^M}}\sigma^{*I}_{ij} \tag{12.40}$$

Therefore, the average stress rates in each phase $\dot{\underset{\sim}{\sigma}}^I$ and $\dot{\underset{\sim}{\sigma}}^M$ are obtained from Eqs. (12.33) and (12.36) and from the constitutive laws [Eq. (12.1)]. Lastly, the overall stress $\underset{\sim}{\Sigma}$ of the composite is incrementally obtained from the stress rate averaging rule:

$$\dot{\underset{\sim}{\Sigma}} = f\dot{\underset{\sim}{\sigma}}^I + (1-f)\dot{\underset{\sim}{\sigma}}^M \tag{12.41}$$

In the following applications and for simplicity, both phases (inclusions and matrix) will have isotropic properties and the inclusions will be supposed to be spherical.

## *12.4.2 Results and Discussion*

### 12.4.2.1 Comparison with a Hereditary Approach

A first type of application is to show that the present time-incremental Eshelby-based homogenization scheme is able to easily retrieve the same results as the ones obtained from hereditary approaches using the correspondence principle and inverse Laplace or Laplace–Carson transforms. One of the main shortcomings of these approaches compared to the present approach derived in the time domain is that simple analytical solutions remain limited to particular cases even for a composite constituted of two phases with a Maxwellian behavior and isotropic properties. As an example, let us consider the case developed by Li and Weng (1994) who used a Mori–Tanaka scheme for two-phase composites under constant strain rate loading

in the case where the spherical inclusions with a volume fraction $f = 0.2$ are elastic, and the inelastic (viscous) behavior of the matrix phase is supposed to be pressure independent. Starting from the effective bulk and shear moduli in the transformed Laplace domain, Eqs. 5.5 and 5.6 in Li and Weng (1994) were obtained by Laplace inversion. By considering Eqs. (12.32) to (12.41) of the present model, the exact solutions for purely hydrostatic and purely deviatoric loadings are easily retrieved. As an illustration for the application of the present exact time-incremental approach to this specific case, the materials parameters used for this comparison are reported in Table 12.1. Figure 12.1a shows the evolution of the overall hydrostatic stress $\Sigma_{kk}$ as a function of the overall dilatational strain $E_{kk}$, whereas Fig. 12.1b displays the evolution of the overall (deviatoric) shear stress $\Sigma_{12}$ as a function of the overall shear strain $E_{kk}$, for both applied $\dot{E}_{kk}$ and $\dot{E}_{12}$ equal to $10^{-4}\,\mathrm{s}^{-1}$. The different asymptotic states at large times were also checked to be consistent with the expressions given by Li and Weng (1994) (see their Eqs. 5.7 and 5.8). For large times or large strains, the shear stress tends to a saturation stress whereas the dilatational stress response is characterized by a constant tangent modulus equal to the effective elastic bulk modulus of the composite.

#### 12.4.2.2 Comparison with Another Exact Internal Variable Approach

In the case of linear Maxwellian compressible two-phase composites with homogeneous elastic properties, exact solutions were recently derived by Ricaud and Masson (2009) using a Mori–Tanaka homogenization scheme. Their approach is based on an internal variable formulation inspired from the collocation method. The evolution laws of the average stresses in both phases were obtained with inverse Laplace–Carson transforms in Ricaud and Masson (2009), knowing the overall behavior from the internal variables evolutions. For comparison, in the present method, the average phase behaviors and the effective behavior are directly obtained from Eqs. (12.32) to (12.41) in the time domain without the need of Laplace–Carson inversions. The inclusions are assumed spherical with a volume fraction of $f = 0.2$. In order to assess the present model in comparison with Ricaud and Masson (2009) solutions, four cases are considered as reported in Table 12.2. The common parameters in all cases are the elastic shear moduli $\mu^I = \mu^M = 50{,}000\,\mathrm{MPa}$ and the inelastic shear modulus of the matrix ${\mu_v}^M = 10{,}000\,\mathrm{MPa\,s}$. Both phases have the same elastic properties like in Ricaud and Masson (2009). The inclusions are also considered with mechanical contrasts 100 (cases 1 and 2), resp 1/100 (cases 3 and 4), with respect to the matrix on the bulk/shear elastic/inelastic moduli. In "case 1" and "case 3," the phase behaviors are assumed compressible elastic (uniform elastic Poisson ratio: $\nu_e = 0.05$) and incompressible inelastic (uniform inelastic Poisson ratio $\nu_v \sim 0.5$). In the "case 2 " and the "case 4," a full compressible viscoelasticity in both phases is assumed with constants $\nu_e = 0.05$ and $\nu_v = 0.3$.

**Table 12.1** Materials parameters for the introduced two-phase composite with elastic inclusions and Maxwellian matrix for comparison with the hereditary formulation of Li and Weng (1994)

| Inclusions (elastic) | $k^I$ (MPa) | $\mu^I$ (MPa) |
|---|---|---|
| | 58,666.66 | 35,200 |

| Matrix (viscoelastic Maxwell) | $k^M$ (MPa) | $\mu^M$ (MPa) | ${k_v}^M$ (MPa s) | ${\mu_v}^M$ (MPa s) |
|---|---|---|---|---|
| | 3633.33 | 1211.11 | $\infty$ | 480,000 |

For the simulations, the volume fraction of inclusions is set to $f = 0.2$

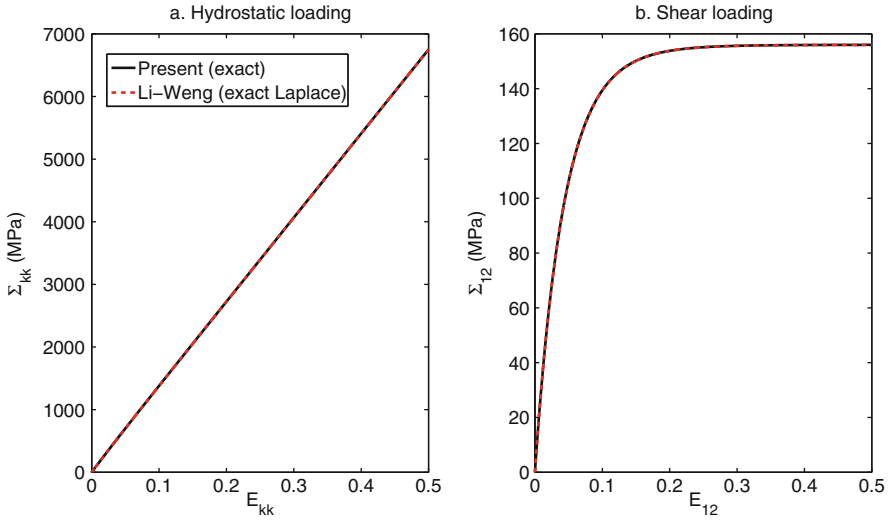


**Fig. 12.1** Overall stress–strain responses of a two-phase composite with spherical elastic inclusions of volume fraction $f = 0.2$ and with a matrix phase exhibiting a Maxwell behavior such that the bulk viscoelastic modulus is restricted to the bulk elastic modulus (see Table 12.1). (**a**) Overall hydrostatic stress $\Sigma_{kk}$ as a function of $E_{kk}$ for an applied dilatational strain rate $\dot{E}_{kk} = 10^{-4}\,\mathrm{s}^{-1}$, (**b**) Overall shear stress $\Sigma_{12}$ as a function of $E_{12}$ for an applied shear strain rate $\dot{E}_{12} = 10^{-4}\,\mathrm{s}^{-1}$. The present model exactly matches the Li and Weng (1994)'s analytical solutions which are superimposed to the present's model responses

**Table 12.2** Materials parameters introduced for the first illustrations (comparisons with Ricaud and Masson (2009) approach): compressible elasticity/incompressible inelasticity (cases 1 and 3), compressible elasticity/inelasticity (cases 2 and 4)

| Case | $k^I = k^M$ (MPa) | ${k_v}^M$ (MPa s) | ${k_v}^I$ (MPa s) | ${\mu_v}^I$ (MPa s) |
|---|---|---|---|---|
| Case 1 | 38,890 | $\infty$ | $\infty$ | 1,000,000 |
| Case 2 | 38,890 | 21,666.66 | 2,166,666 | 1,000,000 |
| Case 3 | 38,890 | $\infty$ | $\infty$ | 100 |
| Case 4 | 38,890 | 21,666.66 | 216.6666 | 100 |

A uniaxial tension–compression test is simulated with the following prescribed macroscopic strain rate, $\underset{\sim}{\dot{E}} = \dot{E}_{11} \begin{pmatrix} 1 & 0 & 0 \\ 0 & -0.5 & 0 \\ 0 & 0 & -0.5 \end{pmatrix}$, with $\dot{E}_{11} = 10^{-4}\,\mathrm{s}^{-1}$ for tension and $\dot{E}_{11} = -10^{-4}\,\mathrm{s}^{-1}$ for compression. For comparisons of the overall responses given by the present internal variables approach with the Ricaud and Masson (2009) solutions, Eqs. 10 and 18 and Table 1 in Ricaud and Masson (2009) are used.

Figure 12.2 shows the overall stress $\Sigma_{11}$ cyclic responses up to $t = 20\,\mathrm{s}$ for cases 1 and 2 (high mechanical contrast of 100 with the matrix) as functions of $E_{11}$ (Fig. 12.2a) and physical time $t$ (Fig. 12.2b). It was checked that both present and Ricaud and Masson (2009) models give the same responses (the

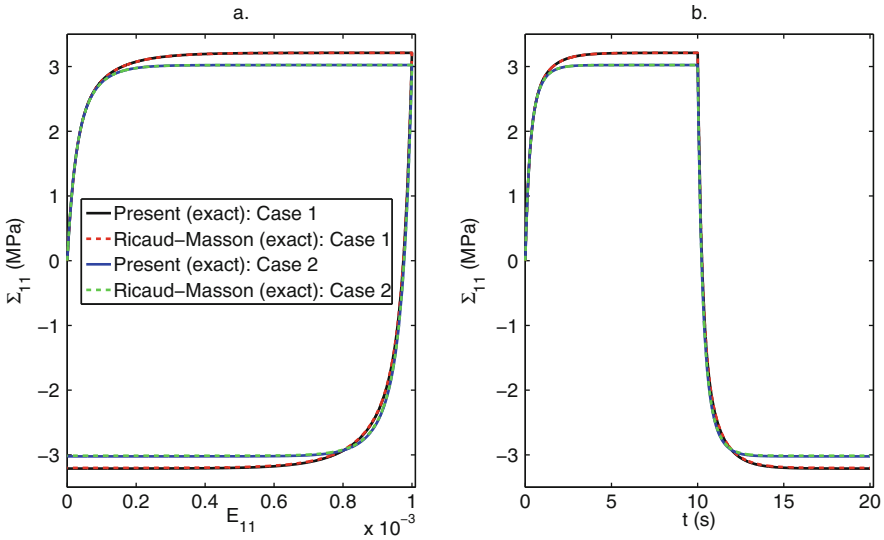


**Fig. 12.2** Cases 1 and 2 (see Table 12.2 for materials parameters): overall tension–compression uniaxial stress $\Sigma_{11}$ responses predicted by the present linear homogenization Mori–Tanaka approach based on the exact interaction law for Eshelby's inclusion problem [Eqs. (12.32)–(12.41)] or by Ricaud and Masson (2009) Mori–Tanaka approach, as functions of applied macroscopic strain $E_{11}$ (**a**) and physical time $t$ (**b**). The present model exactly matches Ricaud and Masson (2009) solutions which are superimposed to the present's model responses

curves for both models are superimposed) regarding the transient regimes between overall elastic and inelastic states and the asymptotic state during tension and compression. In particular, the differences between compressible elasticity only and fully compressible viscoelasticity are well captured by the present model, especially when the loading changes from tension to compression.

For cases 3 and 4 (high mechanical contrast of 1/100 with respect to the matrix), Fig. 12.3 verifies that both present and Ricaud and Masson (2009) models also give the same responses up to $t = 10\,\mathrm{s}$ (the curves for both models are superimposed) regarding the transient regimes between overall elastic and inelastic states and the (inelastic) asymptotic states during tension and compression. As a function of materials properties, the composite responses have different transient and asymptotic states which are observable in Figs. 12.2 and 12.3. The effect of elastic or viscoelastic compressibility is observed in the same way with both models. The present formulation also well captures the stress history due to materials properties in the transient effective behavior during the reverse compression loading that are more important than during the first tensile stage.

In order to refine the analysis, the time evolutions of the uniaxial phase average stresses $\sigma_{11}^I$ and $\sigma_{11}^M$ corresponding to cases 1 to 4 are reported in Figs. 12.4 and 12.5

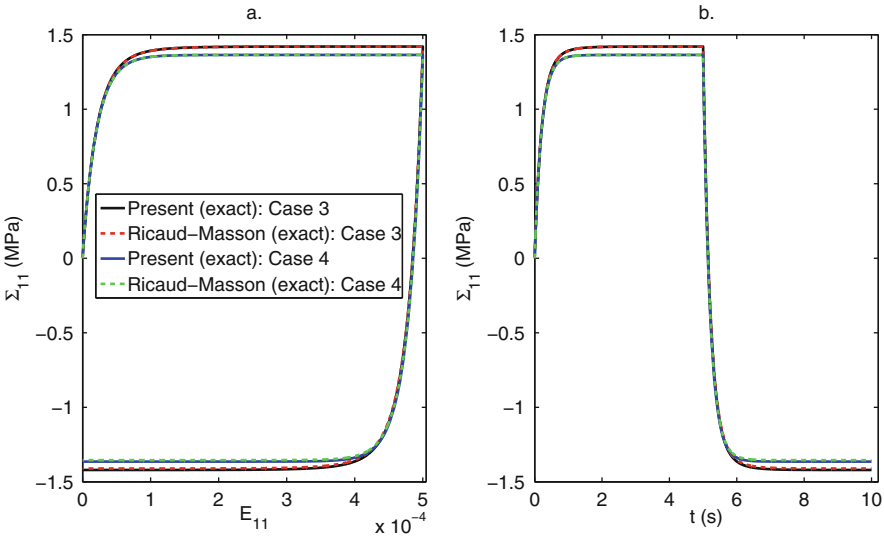


**Fig. 12.3** Cases 3 and 4 (see Table 12.2 for materials parameters): overall tension–compression uniaxial stress $\Sigma_{11}$ responses predicted by the present linear homogenization Mori–Tanaka approach based on the exact interaction law for Eshelby's inclusion problem [Eqs. (12.32)–(12.41)] or by Ricaud and Masson (2009) Mori–Tanaka approach, as functions of applied macroscopic strain $E_{11}$ (**a**) and physical time $t$ (**b**). The present model matches exactly Ricaud and Masson (2009) solutions which are superimposed to the present's model responses

to see the differences due to two different mechanical contrasts on the phase responses, i.e., 100 in Figs. 12.4a and 12.5a and $1/100$ in Figs. 12.4b and 12.5b.

#### 12.4.2.3 Comparisons with the "Translated Fields" Method and the "Additive Law"

For comparisons with previous internal variable models containing approximations like the "translated fields" method (Paquin et al., 1999; Mercier et al., 2012; Berbenni and Capolungo, 2015) and the "additive interaction" law (Kouddane et al., 1993; Molinari et al., 1997; Molinari, 2002), a third application of the present time-incremental Eshelby-based model is now focused on heterogeneous and compressible elasticity in addition to heterogeneous incompressible inelasticity for inclusions stiffer than the matrix (case A) or the matrix stiffer than the inclusions (case B). Interestingly, such a case was recently treated by Kowalczyk-Gajewska and Petryk (2011) with different approximate models (see their Fig. 4) and using inverse Laplace–Carson to find the exact time evolution of the strain rate in the spherical inclusion. This application can be performed assuming a diluted concentration of Eshelby inclusions, i.e., in the limiting case where $f \to 0$ using the present Mori–Tanaka homogenization scheme. The common materials properties

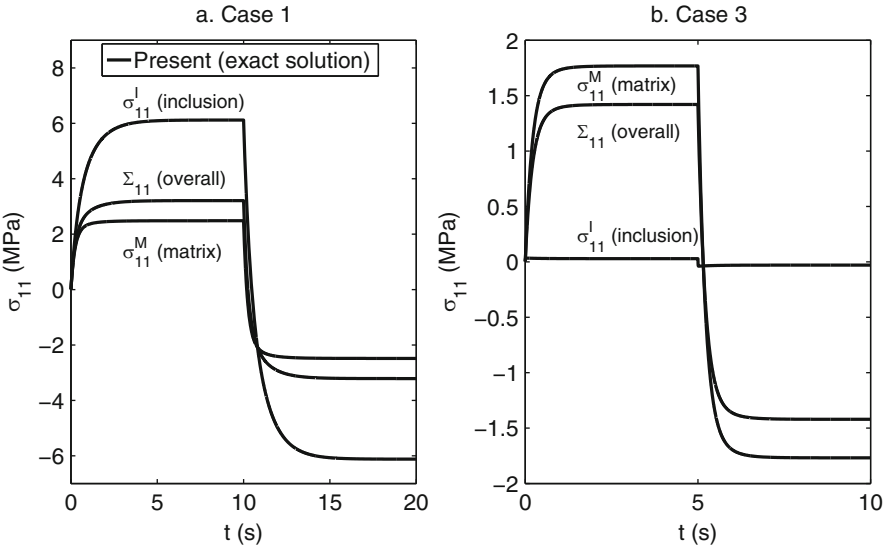


**Fig. 12.4** Tension–compression simulations in case 1 (**a**) and in case 3 (**b**) (see Table 12.2 for materials parameters): time evolution of uniaxial overall stress $\Sigma_{11}$ and phase average stress $\sigma_{11}$ responses predicted by the homogenization Mori–Tanaka approach based on the exact interaction law [Eqs. (12.32)–(12.41)]

describe elastic compressible properties for the matrix and inclusions with the same elastic Poisson ratios ${\nu_e}^I = {\nu_e}^M = 0.05$, an elastic Young's modulus for the matrix of $E^M = 200\,\text{MPa}$, and an incompressible inelasticity for the matrix given by ${\mu_v}^M = 1/3\,\text{MPa s}$. The other parameters are introduced to account for different mechanical contrasts. More specifically, two different elastic Young's moduli and inelastic shear moduli ratios are considered in Table 12.3.

Following Kowalczyk-Gajewska and Petryk (2011), a uniaxial tension–compression test is simulated with the following applied strain rate $\underset{\sim}{\dot{E}} = \dot{E}_{11}\begin{pmatrix}1 & 0 & 0\\ 0 & -0.5 & 0\\ 0 & 0 & -0.5\end{pmatrix}$ with $\dot{E}_{11} = 1\,\text{s}^{-1}$ for tension and $\dot{E}_{11} = -1\,\text{s}^{-1}$ for compression. Figure 12.6 reports the axial strain rate $\dot{\varepsilon}^I_{11}$ evolution in the inclusion along the tension–compression axis as a function of time $t$ obtained with the present model for "case A" (Fig. 12.5a) and for "case B" (Fig. 12.6b) according to the parameters given in Table 12.3. By comparing such evolutions with the exact solutions obtained by the correspondence principle and Laplace–Carson inversion, both approaches give the same results. In particular, for "case B," Fig. 12.6b displays a peak strain rate at the onset of the tensile and compression stages with the present exact solution which is not really captured by the "translated fields" method and by the "additive interaction" law (see Fig. 12.6b). As reported in Kowalczyk-Gajewska and Petryk (2011), the "translated fields" method and the

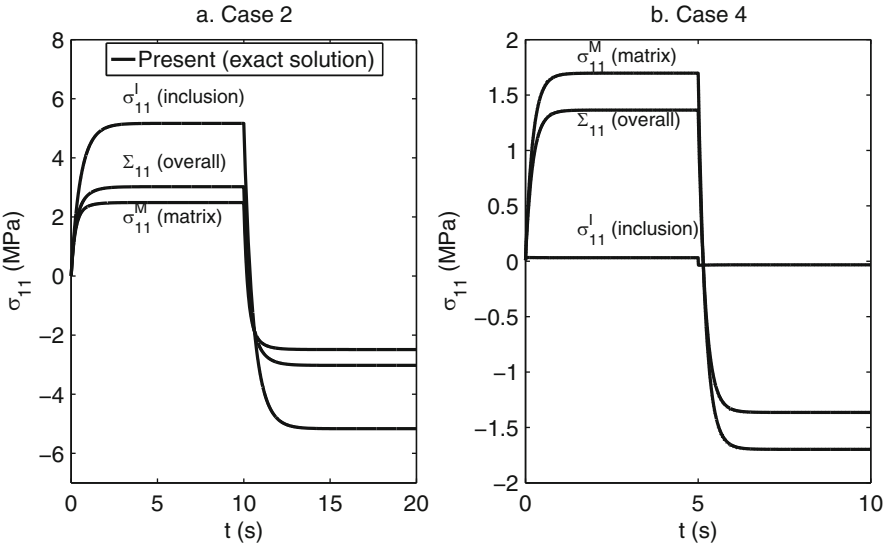


**Fig. 12.5** Tension–compression simulations in case 2 (**a**) and in case 4 (**b**) (see Table 12.2 for materials parameters): time evolution of uniaxial overall stress $\Sigma_{11}$ and phase average stress $\sigma_{11}$ responses predicted by the homogenization Mori–Tanaka approach based on the exact interaction law [Eqs. (12.32)–(12.41)]

**Table 12.3** Materials parameters introduced for the third application for comparisons with approximate models

| Case | $E^I/E^M$ | ${\mu_v}^I/{\mu_v}^M$ |
|---|---|---|
| Case A: inclusions stiffer than matrix | 3 | 10 |
| Case B: matrix stiffer than inclusions | 1/3 | 1/10 |

"additive interaction" law were the best approximate models for this application. This application demonstrates the advantage of the present model to obtain the exact strain rate evolution in the inclusion without the need of Laplace–Carson inversion. The present approach also improves the predictions of previous approximate models that were seen to be unable to match the exact solutions.

## 12.5 Conclusions

A time-incremental internal variables homogenization scheme for Maxwellian linear viscoelastic heterogeneous materials has been presented. The formulation is based on isotropic elastic and inelastic homogeneous reference media associated with the strain rate integral equation. The complete solution is obtained through the introduction of the variable $\underset{\sim}{\sigma}^*$, which reflects a volume term in the integral equation

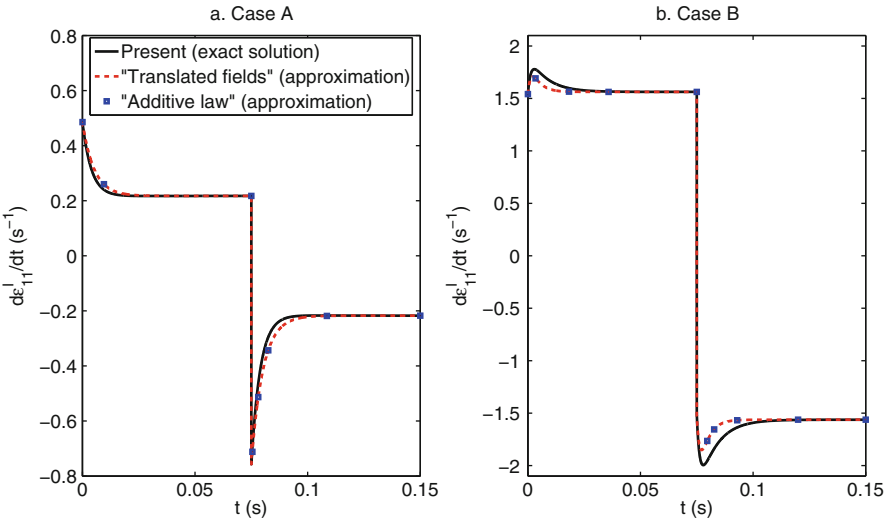


**Fig. 12.6** Time evolution of axial strain rate $\dot{\varepsilon}^I_{11}$ in the inclusion along the tension–compression axis predicted by the present linear homogenization Mori–Tanaka approach based on the exact interaction law for Eshelby's inclusion problem [Eqs. (12.32)–(12.41)] in "case A" (**a**) and in "case B" (**b**). For both cases, the present model (*solid lines*) matches exactly the inverse Laplace–Carson solutions reported in Kowalczyk-Gajewska and Petryk (2011). For comparisons, the time evolutions of $\dot{\varepsilon}^I_{11}$ given by the approximate "translated fields" method (*dashed lines*) and "additive interaction" law (*points*) are reported

of the heterogeneous viscoelastic problem. This variable is exactly solved by a time differential equation. The major advantage of the present internal variables formulation compared to previous internal variables approaches containing approximations is the derivation of the exact interaction laws for the Eshelby ellipsoidal inclusion problem. In the case of a homogenization Mori–Tanaka scheme for an isotropic distribution of phases, the present internal variables formulation may be considered as another alternative way to fasten some numerical calculations in structures made of linear viscoelastic composites. The present time-incremental internal variables approach can be applied to aging linear viscoelastic behaviors without any major difficulty in contrast with Riemann–Stieltjes integral-based hereditary homogenization approaches. The extensions to more refined homogenization schemes taking into account ellipsoidal distributions of phases (Ponte Castañeda and Willis, 1995; Zheng, 2001) are left for future work. Furthermore, the present framework can be extended to other types of rheological models in linear viscoelasticity, such as Kelvin–Voigt, Burgers, and Generalized Maxwell models.

## References


Benveniste, Y.: A new approach to the application of Mori-Tanaka's theory in composite materials. Mech. Mater. **6**(2), 147–157 (1987)

Berbenni, S., Capolungo, L.: A Mori-Tanaka homogenization scheme for non-linear elasto-viscoplastic heterogeneous materials based on translated fields: an affine extension. C. R. Mecanique **343**, 95–106 (2015)

Berbenni, S., Dinzart, F., Sabar, H.: A new internal variables homogenization scheme for linear viscoelastic materials based on an exact Eshelby interaction law. Mech. Mater. **81**, 110–124 (2015)

Brassard, L., Stainier, L., Doghri, I., Delannay, L.: Homogenization of elasto-(visco)plastic composites based on an incremental variational principle. Int. J. Plast. **36**, 86–112 (2012)

Brenner, R., Masson, R., Castelnau, O., Zaoui, A.: A "quasi-elastic" affine formulation for the homogenised behaviour of nonlinear viscoelastic polycrystals and composites. Eur. J. Mech. A. Solids **21**, 943–960 (2002)

Brinson, L.C., Lin, W.S.: Comparison of micromechanics methods for effective properties of multiphase viscoelastic composites. Compos. Struct. **41**, 353–367 (1998)

Christensen, R.M.: Viscoelastic properties of heterogeneous media. J. Mech. Phys. Solids **17**, 23–41 (1969)

Coulibaly, M., Sabar, H.: Micromechanical modeling of linear viscoelastic behavior of heterogeneous materials. Arch. Appl. Mech. **81**, 345–359 (2011)

DeBotton, G., Tevet-Deree, L.: The response of a fiber-reinforced composite with a viscoelastic matrix phase. J. Compos. Mater. **38**, 1255–1277 (2004)

Dyson, F.: The potentials of ellipsoids of variable densities. Q. J. Pure Appl. Math. **25**, 259–288 (1891)

Eshelby, J.D.: The determination of the elastic field of an ellipsoidal inclusion and related problems. Proc. R. Soc. Lond. A **241**, 376–396 (1957)

Ferrers, N.: On the potentials of ellipsoids, ellipsoidal shells, elliptic laminae and elliptic rings of variable densities. Q. J. Pure Appl. Math. **14**, 1–22 (1877)

Hashin, Z.: The inelastic inclusion problem. Int. J. Eng. Sci. **7**, 11–36 (1969)

Kouddane, R., Molinari, A., Canova, G.R.: Self-consistent modelling of heterogeneous viscoelastic and elastoplastic materials. In: Teodosiu C., Raphanel J-.L., Sidoroff F. (eds.) Mecamat 91: Large Plastic Deformations, Fundamentals and Application to Metal Forming, pp. 129–141. Balkema, Rotterdam (1993)

Kowalczyk-Gajewska, K., Petryk, H.: Sequential linearization method for viscous/elastic heterogeneous materials. Eur. J. Mech. A Solids **30**, 650–664 (2011)

Kröner, E.: Zur plastischen Verformung des Vielkristalls. Acta Metall. **9**, 155–161 (1961)

Kröner, E.: Modified Green functions in the theory of heterogeneous and/or anisotropic linearly elastic media. In: Weng G.J., Taya M., Abe H. (eds.) Micromechanics and Inhomogeneity. The Toshio Mura 65th Anniversary Volume, pp. 197–211. Springer, New York (1990)

Kunin, I.A.: Elastic media with microstructure II: three-dimensional models. In: Kröner E. (ed.) Springer Series in Solid-State Sciences 44. Springer, Berlin (1983)

Lahellec, N., Suquet, P.: Effective behavior of linear viscoelastic composites: a time-integration approach. Int. J. Solids Struct. **44**, 507–529 (2007)

Lahellec, N., Suquet, P.: On the effective behavior of non linear inelastic composites: I. Incremental variational principles. J. Mech. Phys. Solids **55**, 1932–1963 (2007)

Lavergne, F., Sab, K., Sanahuja, J., Bornert, M., Toulemonde, C.: Homogenization schemes for aging linear viscoelastic matrix-inclusion composite materials with elongated inclusions. Int. J. Solids Struct. **80**, 545–560 (2016)

Laws, N., McLaughlin, R.: Self-consistent estimates for the viscoelastic creep compliance of composite materials. Proc. R. Soc. Lond. A **359**, 251–273 (1978)

Levesque, M., Gilchrist, M.D., Bouleau, N., Derrien, K., Baptiste, D.: Numerical inversion of the Laplace-Carson transform applied to homogenization of randomly reinforced linear viscoelastic media. Comput. Mech. **40**, 771–789 (2007)

Li, J., Weng, G.J.: Strain-rate sensitivity, relaxation behavior and complex moduli of a class of isotropic viscoplastic composites. ASME J. Eng. Mater. Tech. **116**, 495–504 (1994)

Li, J., Weng, G.J.: A secant-viscosity approach to the time-dependent creep of an elastic-viscoplastic composite. J. Mech. Phys. Solids **45**(7), 1069–1083 (1997)

Mandel, J.: Cours de Mécanique des Milieux Continus. Gauthiers-Villars, Paris (1966)

Mareau, C., Berbenni, S.: An affine formulation for the self-consistent modeling of elasto-viscoplastic heterogeneous materials based on the translated field method. Int. J. Plast. **64**, 134–150 (2015)

Masson, R., Zaoui, A.: Self-consistent estimates for the rate-dependent elastoplastic behaviour of polycrystalline materials. J. Mech. Phys. Solids **47**, 1543–1568 (1999)

Masson, R., Brenner, R., Castelnau, O.: Incremental homogenization approach for ageing viscoelastic polycrystals. C. R. Mecanique **340**, 378–386 (2012)

Mercier, S., Molinari, A.: Homogenization of elastic-viscoplastic heterogeneous materials: self-consistent and Mori-Tanaka schemes. Int. J. Plast. **25**, 1024–1048 (2009)

Mercier, S., Molinari, A., Berbenni, S., Berveiller, M.: Comparison of different homogenization approaches for elastic-viscoplastic materials. Model. Simul. Mater. Sci. Eng. **20**, 024004 (2012)

Molinari, A.: Averaging models for heterogeneous viscoplastic and elastic-viscoplastic materials. ASME J. Eng. Mater. Tech. **124**, 62–70 (2002)

Molinari, A., Ahzi, S., Kouddane, R.: On the self-consistent modelling of elastic-plastic behavior of polycrystals. Mech. Mater. **26**, 43–62 (1997)

Mori, T., Tanaka, K.: Average stress in matrix and average elastic energy of materials with misfitting inclusions. Acta Metall. **21**, 571–574 (1973)

Mura, T.: Micromechanics of Defects in Solids. Kluwer Academic, Dordrecht (1987)

Paquin, A., Sabar, H., Berveiller, M.: Integral formulation and self-consistent modelling of elasto-viscoplastic behavior of heterogeneous materials. Arch. Appl. Mech. **69**, 14–35 (1999)

Pierard, O., Doghri, I.: An enhanced affine formulation and the corresponding numerical algorithms for the mean-field homogenization of elasto-viscoplastic composites. Int. J. Plast. **22**, 131–157 (2006)

Ponte Castañeda, P., Willis, J.R.: The effect of spatial distribution on the effective behavior of composite materials and cracked media. J. Mech. Phys. Solids **43**, 1919–1951 (1995)

Ricaud, J.M., Masson, R.: Effective properties of linear viscoelastic heterogeneous media: internal variables formulation and extension to ageing behaviours. Int. J. Solids Struct. **46**, 1599–1606 (2009)

Rougier, Y., Stolz, C., Zaoui, A.: Representation spectrale en viscoelasticite lineaire des materiaux heterogenes. C. R. Acad. Sci. Paris Ser. II **316**, 1517–1522 (1993)

Rougier, Y., Stolz, C., Zaoui, A.: Self-consistent modelling of elastic-viscoplastic polycrystals. C. R. Acad. Sci. Paris Ser. IIb **318**, 145–151 (1994)

Sabar, H., Berveiller, M., Favier, V., Berbenni, S.: A new class of micro-macro models for elastic-viscoplastic heterogeneous materials. Int. J. Solids Struct. **39**, 3257–3276 (2002)

Sanahuja, J.: Effective behavior of aging linear viscoelastic composites: homogenization approach. Int. J. Solids Struct. **50**, 2846–2856 (2013)

Suquet, P.: Elements of homogenization for inelastic solid mechanics. In: Sanchez-Palencia E., Zaoui A. (eds.) Homogenization Techniques for Composite Media, pp. 193–278. Springer, Berlin (1987)

Turner, P.A., Tomé, C.N.: Self-consistent modeling of visco-elastic polycrystals: application to irradiation creep and growth. J. Mech. Phys. Solids **41**(7), 1191–1211 (1993)

Walpole, L.J.: Elastic behavior of composite materials: theoretical foundations. Adv. Appl. Mech. **21**, 169–242 (1981)

Wang, Y.M., Weng, G.J.: The influence of inclusion shape on the overall viscoelastic behavior of composites. ASME J. Appl. Mech. **59**(3), 510–518 (1992)

Weng, G.J.: Self-consistent determination of time-dependent behavior of metals. ASME J. Appl. Mech. **48**, 41–46 (1981)

Weng, G.J.: Some elastic properties of reinforced solids with special reference to isotropic ones containing spherical inclusions. Int. J. Eng. Sci. **22**(7), 845–856 (1984)

Weng, G.J.: A self-consistent relation for the time-dependent creep of polycrystals. Int. J. Plast. **9**, 181–198 (1993)

Zheng, Q.S., Du, D.X.: An explicit and universally applicable estimate for the effective properties of multiphase composite which accounts for inclusion distribution. J. Mech. Phys. Solids **49**, 2765–2788 (2001)

# Chapter 13
# Effects of Local Spin on Overall Properties of Granule Materials

**Muneo Hori, Jian Chen, Supprasert Sument, Lalith Wijerathne, and Tsuyoshi Ichimura**

**Abstract** This paper proposes continuumnization of a set of rigid body spherical particles which are regularly arranged and connected by springs. Continuumnization converts translation and spin of all particles to spatially varying functions, together with derivation of material properties from spring constants. It is shown that a function of particles' spin tends to vanish in the limit as the radius of the particles goes to zero. The governing equations of the functions of translation and spin are studied for a symmetric assembly of rigid body particles. The characteristic equation of the governing equations shows the presence of high-frequency modes of spin, as well as waves which correspond to P- and S-waves of ordinary continuum.

## 13.1 Introduction

Soil is a typical granular material, as it consists of particles of various sizes and configurations (Sahimi and Arbabi, 1992). Each particle behaves like a rigid body, but the assembly of the particles exhibits complicated behavior. For instance, damping property of soil is unique as it does not depend on the frequency; while most of materials show linear dependence of the damping parameter on the frequency, the damping parameter of soil is little sensitive to the frequency. Accounting for this property is an essential element in accurately analyzing amplification processes of seismic waves in surface ground layers.

M. Hori (✉) • S. Sumentt • L. Wijerathne • T. Ichimura
Earthquake Research Institute, The University of Tokyo, 1-1-1 Yayoi, Bunkyo, Tokyo 113-0031, Japan
e-mail: hori@eri.u-tokyo.ac.jp; sumenti@eri.u-tokyo.ac.jp; lalith@eri.u-tokyo.ac.jp; ichimura@eri.u-tokyo.ac.jp

J. Chen
RIKEN Advanced Institute of Computational Science, 7-1-26 Minatoshima-Minami, Chuo, Kobe, Hyogo 650-0047, Japan
e-mail: jcheni@riken.jp



S.A. Meguid, G.J. Weng (eds.), *Micromechanics and Nanomechanics of Composite Solids*, DOI 10.1007/978-3-319-52794-9_13

Besides for phenomenological investigation, it is of interest to study the mechanism that induces complicated material properties such as damping, paying an attention to the fact that soil is an assembly of rigid body particles. A fundamental question is

why does a material of such simple microstructures exhibit complicated material properties?

We focus on spin of a particle to answer this question. As a rigid body, each particle has translation and spin. Particles' translation induces deformation of the assembly as the configuration of the assembly changes. However, the effects of particles' spin a on the assembly deformation are not observable as each particle appears to stand still when it just spins around its center; see Fig. 13.1. When neighboring particles spin, a certain frictional work is made on the interface and some portion of the energy stored in the assembly is consumed. Therefore, we can expect that there ought to be certain effects of particles' spin on the overall properties, even though particles' spin does not induce observable deformation.

In this paper, we investigate the effects of particles' spin on overall behaviors of the particle assembly. An ordinary method of micromechanics might not be suitable for this investigation, because the particles' spin does not induce deformation of the

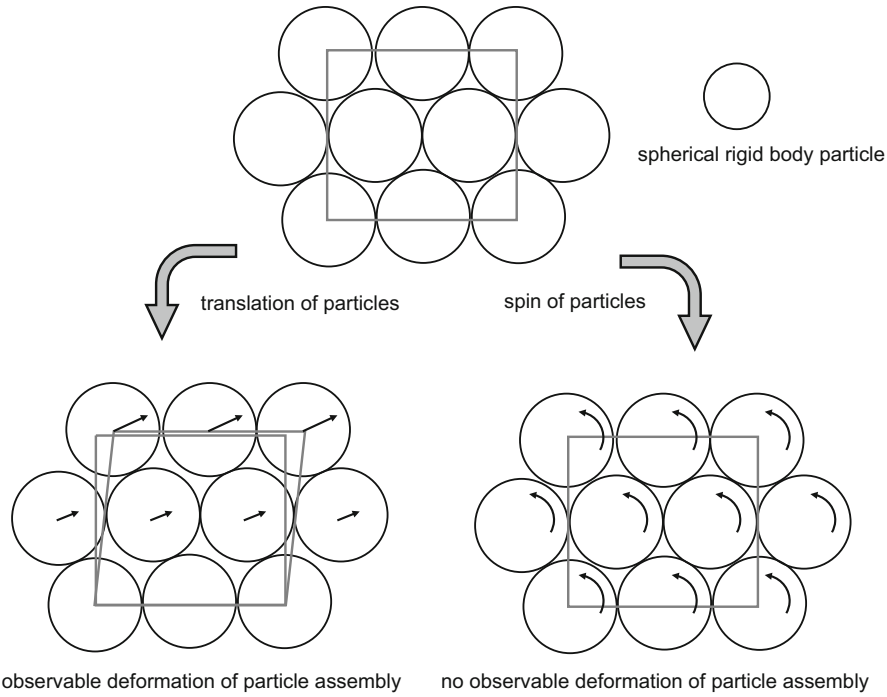


**Fig. 13.1** Observable and no observable deformation of particle assembly in case of particles' translation and spin

assembly. We thus introduce a new approach which considers the limiting case as the particle size goes to zero and converts particles' motion to spatially varying functions. The limit of the particle assembly is regarded as a continuum. This approach is called continuumnization in this paper (Hori et al., 2016).

The objective of this paper is to provide basic formulation of continuumnization of a particle assembly for the estimation of overall properties of the assembly. The contents of this paper are organized as follows: First, we make a brief literature survey on microstructure models which use a particle assembly in Sect. 13.2. We formulate continuumnization in Sect. 13.3, converting particles' translation and spin to smooth functions and deriving governing equations for the functions. In Sects. 13.4 and 13.5, respectively, the natures of the continuumnized functions and the material properties that appear in the governing equations are studied; vanishing of continuumnized spin in the limit as the particle radius goes to zero is shown in Sect. 13.5. Finally, the characteristic equation of the governing equations is studied in Sect. 13.6, to derive the material properties which include wave velocity and to analyze damping of the particle assembly due to spin.

## 13.2 Literature Survey

An assembly of rigid body particles is used as a model of microstructure of granular materials such as soil (Sahimi and Arbabi, 1992) and damaged rock (Cundall and Strack, 1979; Potyondy and Cundall, 2004). It is intuitively clear to use this model for the granular materials as the assembly resembles a set of granules. Regarding the effects of granules' spin on the material properties, there are a few researches (Chang and Ma, 1992); considering spin often results in the model of *micro-polar* materials (Mindlin and Tiersten, 1962; Eringen, 1978; Kunin, 1982; Kuhn, 2003), which presumes the presence of nonsymmetric stress, coupled stress, or local torque.

We should mention the Cosserat theory (Cosserat and Cosserat, 1909) which has been used for the micro-polar materials; this theory is relevant to local torque. In the particle assembly, the presence of local torque must be taken for granted as it is induced by the corresponding spin of the particles; see also (Kroner and Datta, 1970; Nowacki, 1974; Mustoe, 1992). However, we have to point out that the spin vanishes in the limit as the size of particles goes to zero. This implies that the local torque vanishes as well, if it is induced by the spin.

Although it is not a granular material, concrete employs a particle assembly as a material model; concrete is a composite of mortar and aggregates of various sizes, but an assembly of irregularly shaped particles is used as a material model when concrete is separated by numerous micro-cracks which are initiated in mortar (Lilliu and van Mier, 2003; Liu et al., 2007). The major concern of concrete is to treat micro-cracks which reduce the concrete strength and induce large deformation (Zubelewicz and Bazant, 1987; Cusatis et al., 2003; Kozicki and Tejchman, 2008). It is thus natural to use a particle assembly in which particles

of irregular configuration are connected by nonlinear and nonhomogeneous springs. Failure analysis of concrete using the particle assembly is found in literature (Kawai, 1978; Schlangen and Garboczi, 1997).

The research achievements mentioned above share the mathematical treatment called *homogenization*. For a material with microstructure, homogenization studies the relation among the volume average of strain and stress in order to estimate the overall material properties. The volume integral that is used to compute the volume average of strain and stress is converted to surface integral of displacement and force, respectively, and homogenization could be regarded as mathematical abstraction of material sample experiment in which material properties are measured as the relation between displacement and force which are measured on the sample surface.

In closing this section, we point out that there are various works which use a particle assembly or a lattice model in modern physics (Buxton et al., 2001). The target of such works (Lemieux et al., 1985; Ray and Chakrabarti, 1985) is a disordered system which is a model of microstructure of a heterogeneous material. Although it does not provide a practical solution to engineering problems, the lattice model (Sahimi and Goddard, 1986; Beale and Srolovitz, 1988; Curtin and Scher, 1990; Monette and Anderson, 1994; Ostoja-Starzewski et al., 1996; Karihaloo et al., 2003) is used to study elasticity as well as local failure of composites and polycrystals.

## 13.3 Continuumnization for Rigid Body Grid

### *13.3.1 Motion and Force of Particle Assembly*

We start from a simple particle assembly, which is called a *rigid body grid* (Hori et al., 2016). The grid consists of spherical rigid body particles of identical radius which are regularly arranged; see Fig. 13.2; Walton studied the case for randomly packed spheres (Walton, 1987). We denote by $P^\alpha$ and $\mathbf{x}^\alpha$, respectively, the $\alpha$th particle and its center. There is an infinitesimally short spring that connects one particle to another neighboring particle. Since the grid consists of regularly arranged spheres, the number of the spring directions is finite, and a set of the spring directions is denoted by $\{\mathbf{n}^I\}$. The two tangential directions associated with $\mathbf{n}^I$ are denoted by $\mathbf{t}^I$ and $\mathbf{s}^I$, and $(\mathbf{n}^I, \mathbf{t}^I, \mathbf{s}^I)$ forms a right-hand triad. We assume that all springs share the same normal and tangential spring constants, $k$ and $h$, respectively; the spring constant in the $\mathbf{n}^I$-direction is $k$ and that in the $\mathbf{t}^I$- or $\mathbf{s}^I$-direction is $h$. Recall that the spring constants are rigorously computed (Walton, 1987) for two contacting spheres of the same radius if the spheres are linearly and isotropically elastic.

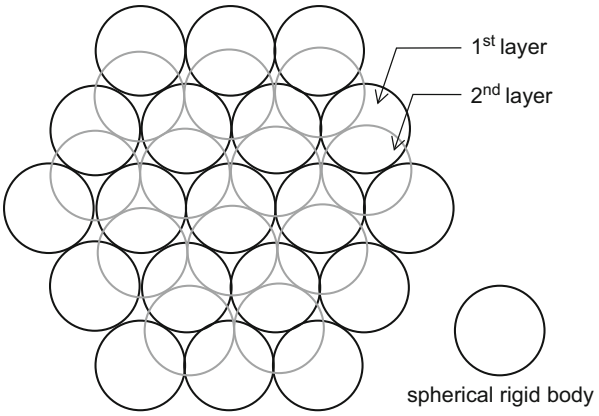


**Fig. 13.2** Rigid body grid

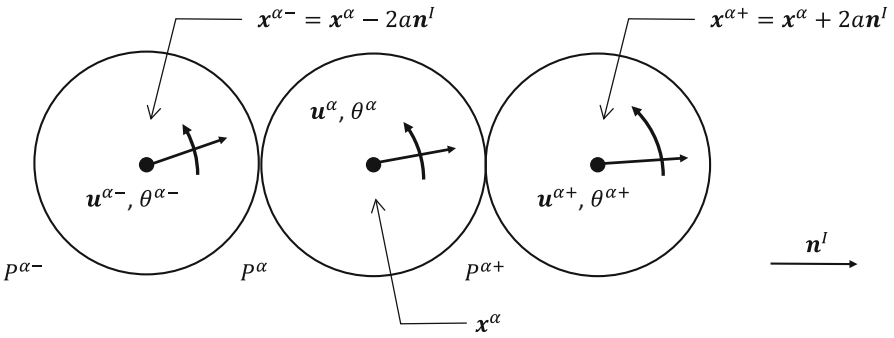


**Fig. 13.3** Neighboring particles of $P^{\alpha}$ and $P^{\alpha\pm}$

A particle $P^{\alpha}$ is connected to two particles by the spring in the $\mathbf{n}^I$-direction. We denote them by $P^{\alpha\pm}$; the superscript $+$ or $-$ stands for the positive or negative $\mathbf{n}^I$-direction, respectively; see Fig. 13.3. We introduce translation and spin of $P^{\alpha}$, denoted by $\mathbf{u}^{\alpha}(t)$ and $\boldsymbol{\theta}^{\alpha}(t)$ with $t$ being time, respectively. We assume that $\mathbf{u}^{\alpha}$ and $\boldsymbol{\theta}^{\alpha}$ are infinitesimally small and that the axis of rotation always passes $\mathbf{x}^{\alpha}$. Denoting by $\mathbf{u}^{\alpha+}$ and $\boldsymbol{\theta}^{\alpha+}$ translation and spin of $P^{\alpha+}$, we calculate the relative displacement of $P^{\alpha}$ and $P^{\alpha+}$ at their contacting point, $\mathbf{x}^{\alpha} + a\mathbf{n}^I$, as

$$\Delta\mathbf{u}^{\alpha+} = \mathbf{u}^{\alpha+} - \mathbf{u}^{\alpha} + \boldsymbol{\theta}^{\alpha+} \times (-a\mathbf{n}^I) - \boldsymbol{\theta}^{\alpha} \times (a\mathbf{n}^I);$$

$\boldsymbol{\theta}^{\alpha} \times (a\mathbf{n}^I)$ gives displacement due to spin, since $\boldsymbol{\theta}^{\alpha}$ is infinitesimally small; see Fig. 13.4. We rewrite $\Delta\mathbf{u}^{+}$ as

$$\Delta\mathbf{u}^{\alpha+} = \mathbf{u}^{\alpha+} - \mathbf{u}^{\alpha} - (\boldsymbol{\theta}^{\alpha+} + \boldsymbol{\theta}^{\alpha}) \times (a\mathbf{n}^I). \tag{13.1}$$

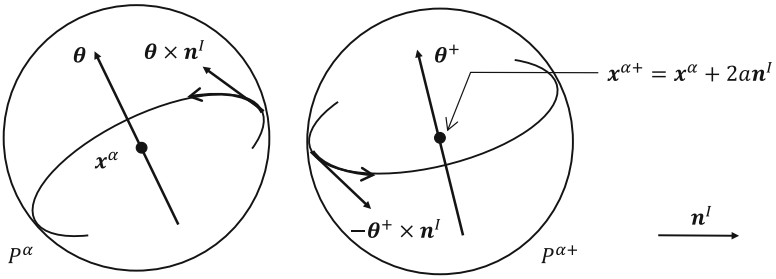


**Fig. 13.4** Relative displacement due to spin, $\boldsymbol{\theta}$ and $\boldsymbol{\theta}^+$, of neighboring particles of $P^\alpha$ and $P^{\alpha+}$

Similarly, we calculate the relative displacement of $P^{\alpha-}$ and $P^\alpha$ at their contacting point as

$$\Delta\mathbf{u}^{\alpha-} = \mathbf{u}^{\alpha-} - \mathbf{u}^\alpha + (\boldsymbol{\theta}^{\alpha-} + \boldsymbol{\theta}^\alpha) \times (a\mathbf{n}). \tag{13.2}$$

Note that the sign of the second term in the right side is $+$.

Since $(\mathbf{n}^I, \mathbf{t}^I, \mathbf{s}^I)$ forms a right-hand triad, an outer product of $\boldsymbol{\theta}^\alpha \times \mathbf{n}^I$ satisfies

$$(\boldsymbol{\theta}^\alpha \times \mathbf{n}^I) \cdot \mathbf{n}^I = 0, \quad (\boldsymbol{\theta}^\alpha \times \mathbf{n}^I) \cdot \mathbf{t}^I = \boldsymbol{\theta}^\alpha \cdot \mathbf{s}^I, \quad (\boldsymbol{\theta}^\alpha \times \mathbf{n}^I) \cdot \mathbf{s}^I = -\boldsymbol{\theta}^\alpha \cdot \mathbf{t}^I.$$

The force provided by the spring that connects $P^\alpha$ and $P^{\alpha+}$ is computed as

$$\mathbf{f}^{\alpha+} = k\,(\Delta\mathbf{u}^{\alpha+} \cdot \mathbf{n}^I)\mathbf{n}^I + h\left((\Delta\mathbf{u}^{\alpha+} \cdot \mathbf{t}^I)\mathbf{t}^I + (\Delta\mathbf{u}^{\alpha+} \cdot \mathbf{s}^I)\mathbf{s}^I\right)$$

or

$$\begin{aligned}\mathbf{f}^{\alpha+} = {} & k\left((\mathbf{u}^{\alpha+} - \mathbf{u}^\alpha) \cdot \mathbf{n}^I\right)\mathbf{n}^I + h\left((\mathbf{u}^{\alpha+} - \mathbf{u}^\alpha) \cdot \mathbf{t}^I - a(\boldsymbol{\theta}^{\alpha+} + \boldsymbol{\theta}^\alpha) \cdot \mathbf{s}^I\right)\mathbf{t}^I \\ & + h\left((\mathbf{u}^{\alpha+} - \mathbf{u}^\alpha) \cdot \mathbf{s}^I + a(\boldsymbol{\theta}^{\alpha+} + \boldsymbol{\theta}^\alpha) \cdot \mathbf{t}^I\right)\mathbf{s}^I.\end{aligned} \tag{13.3}$$

Similarly, the spring that connects $P^\alpha$ and $P^{\alpha-}$ provides the following force:

$$\begin{aligned}\mathbf{f}^{\alpha-} = {} & k\left((\mathbf{u}^{\alpha-} - \mathbf{u}^\alpha) \cdot \mathbf{n}^I\right)\mathbf{n}^I + h\left((\mathbf{u}^{\alpha-} - \mathbf{u}^\alpha) \cdot \mathbf{t}^I + a(\boldsymbol{\theta}^{\alpha-} + \boldsymbol{\theta}^\alpha) \cdot \mathbf{s}^I\right)\mathbf{t}^I \\ & + h\left((\mathbf{u}^{\alpha-} - \mathbf{u}^\alpha) \cdot \mathbf{s}^I - a(\boldsymbol{\theta}^{\alpha-} + \boldsymbol{\theta}^\alpha) \cdot \mathbf{t}^I\right)\mathbf{s}^I.\end{aligned} \tag{13.4}$$

### *13.3.2 Equation of Motion and Euler's Momentum Equation*

As explained, the $\alpha$th particle $P^\alpha$ has a pair of springs in the $\mathbf{n}^I$-direction at $\mathbf{x}^\alpha + (a\mathbf{n}^I)$ and $\mathbf{x}^\alpha \pm (a\mathbf{n}^I)$, and $P^\alpha$ is subjected to the springs' forces of $\mathbf{f}^\pm$ of Eqs. (13.3) and (13.4). The equation of motion of $P^\alpha$ is thus expressed as

$$M\,\ddot{\mathbf{u}}^\alpha = \sum_I \mathbf{f}^{\alpha+} + \mathbf{f}^{\alpha-}, \tag{13.5}$$

where dot stands for temporal derivative ($\ddot{\mathbf{u}}^\alpha = \frac{\partial^2 \mathbf{u}^\alpha}{\partial t^2}$) and $M$ is the mass of $P^\alpha$. Recall that $\mathbf{f}^{\alpha\pm}$ is the force provided by the springs in the $\mathbf{n}^I$-direction, although the superscript $I$ is omitted. Similarly, Euler's momentum equation of $P^\alpha$ is

$$I\,\ddot{\boldsymbol{\theta}}^\alpha = \sum_I (a\mathbf{n}^I) \times \mathbf{f}^{\alpha+} + (-a\mathbf{n}^I) \times \mathbf{f}^{\alpha-}, \tag{13.6}$$

where $I$ is the momentum of inertia of $P^\alpha$.

Substituting Eqs. (13.3) and (13.4) into Eqs. (13.5) and (13.6), we have

$$\begin{aligned} M\ddot{\mathbf{u}}^\alpha = \sum k \Big( &(\mathbf{u}^{\alpha+} - 2\mathbf{u}^\alpha + \mathbf{u}^{\alpha-}) \cdot \mathbf{n}^I \Big) \mathbf{n}^I \\ &+ h \Big( (\mathbf{u}^{\alpha+} - 2\mathbf{u}^\alpha + \mathbf{u}^{\alpha-}) \cdot \mathbf{t}^I - a(\boldsymbol{\theta}^{\alpha+} - \boldsymbol{\theta}^{\alpha-}) \cdot \mathbf{s}^I \Big) \mathbf{t}^I \\ &+ h \Big( (\mathbf{u}^{\alpha+} - 2\mathbf{u}^\alpha + \mathbf{u}^{\alpha-}) \cdot \mathbf{s}^I + a(\boldsymbol{\theta}^{\alpha+} - \boldsymbol{\theta}^{\alpha-}) \cdot \mathbf{t} \Big) \mathbf{s}^I, \end{aligned} \tag{13.7}$$

and

$$\begin{aligned} I\ddot{\boldsymbol{\theta}}^\alpha = \sum ah \Big( &(\mathbf{u}^{\alpha+} - 2\mathbf{u}^\alpha + \mathbf{u}^{\alpha-}) \cdot \mathbf{t}^I - a(\boldsymbol{\theta}^{\alpha+} + 2\boldsymbol{\theta}^\alpha + \boldsymbol{\theta}^{\alpha-}) \cdot \mathbf{s}^I \Big) \mathbf{s}^I \\ &- ah \Big( \big( (\mathbf{u}^{\alpha+} - \mathbf{u}^\alpha) + (\mathbf{u}^{\alpha-} - \mathbf{u}^\alpha) \big) \cdot \mathbf{s}^I + a(\boldsymbol{\theta}^{\alpha+} + 2\boldsymbol{\theta}^\alpha + \boldsymbol{\theta}^{\alpha-}) \cdot \mathbf{t}^I \Big) \mathbf{t}^I. \end{aligned} \tag{13.8}$$

Equations (13.7) and (13.8) form a set of ordinary differential equations for $\{\mathbf{u}^\alpha, \boldsymbol{\theta}^\alpha\}$.

### 13.3.3 Continuumnization of Translation and Spin

We consider a smooth function, $\mathbf{u}(\mathbf{x}, t)$, which satisfies

$$\mathbf{u}(\mathbf{x}, t) = \mathbf{u}^\alpha(t) \quad \text{at } \mathbf{x} = \mathbf{x}^\alpha.$$

We approximate $\mathbf{u}^{\alpha+} - \mathbf{u}^\alpha$ using this smooth function as

$$\mathbf{u}^{\alpha+}(t) - \mathbf{u}^\alpha(t) \approx (2a\mathbf{n}) \cdot (\nabla \mathbf{u}(\mathbf{x}^\alpha, t)),$$

where $\nabla\mathbf{u}$ is the gradient of $\mathbf{u}$. In a Cartesian coordinate $(x_1, x_2, x_3)$, the components[1] of the gradient are $(\nabla \mathbf{u})_{ij} = \frac{\partial u_j}{\partial x_i}$. By definition, $\mathbf{n} \cdot \nabla$ is interpreted as the derivative of $\mathbf{u}$ in the $\mathbf{n}$-direction; $\nabla \cdot \mathbf{n}$ is expressed as $\sum_i n_i \frac{\partial}{\partial x_i}$. In the limit as the spherical

[1]Note that while the ordinary definition of the gradient is $(\nabla \mathbf{u})_{ij} = \frac{\partial u_i}{\partial x_j}$, we define the gradient component in this way in order to make the expression of $\nabla \cdot \mathbf{n}$ consistent.

particle radius $a$ goes to 0, the error of the above approximation tends to vanish. We call this $\mathbf{u}(\mathbf{x}, t)$ a *continuumnized* displacement of $\{\mathbf{u}^\alpha(t)\}$.

In a similar manner, we introduce a continuumnized spin, $\boldsymbol{\theta}(\mathbf{x}, t)$, which satisfies

$$\boldsymbol{\theta}(\mathbf{x}, t) = \boldsymbol{\theta}^\alpha(t) \quad \text{at } \mathbf{x} = \mathbf{x}^\alpha.$$

Unlike translation, a continuumnized spin vanishes at $a = 0$, which will be shown in Sect. 13.5. However, for a nonzero value of $a$, it is possible to assume the presence of $\boldsymbol{\theta}(\mathbf{x}, t)$ that is associated with $\{\boldsymbol{\theta}^\alpha\}$, and $\boldsymbol{\theta}^{\alpha+} - \boldsymbol{\theta}^\alpha$ is approximated as

$$\boldsymbol{\theta}^{\alpha+}(t) - \boldsymbol{\theta}^{\alpha-}(t) \approx (4a\mathbf{n}) \cdot (\nabla\boldsymbol{\theta}(\mathbf{x}^\alpha, t)).$$

Again, the error of this approximation tends to vanish in the limit as $a$ goes to 0; as will be shown in Sect. 13.5, $\boldsymbol{\theta}$ itself vanishes in this limit, though.

In terms of the continuumnized $\mathbf{u}$ and $\boldsymbol{\theta}$, Eqs. (13.7) and (13.8) are approximately expressed as

$$M\ddot{\mathbf{u}}(\mathbf{x}, t) \approx a^3\big(\nabla \cdot (\mathbf{c} : \nabla\mathbf{u}(\mathbf{x}, t)) + \mathbf{q}^t : \nabla\boldsymbol{\theta}(\mathbf{x}, t)\big), \tag{13.9}$$

and

$$I\ddot{\boldsymbol{\theta}}(\mathbf{x}, t) \approx -a^3\big(\mathbf{r} \cdot \boldsymbol{\theta}(\mathbf{x}, t) + \mathbf{q} : \nabla\mathbf{u}(\mathbf{x}, t)\big), \tag{13.10}$$

where

$$\begin{aligned}
\mathbf{c} &= \sum \frac{k}{a}\,\mathbf{n}^I \otimes \mathbf{n}^I \otimes \mathbf{n}^I \otimes \mathbf{n}^I + \frac{h}{a}\left(\mathbf{n}^I \otimes \mathbf{t}^I \otimes \mathbf{n}^I \otimes \mathbf{t}^I + \mathbf{n}^I \otimes \mathbf{s}^I \otimes \mathbf{n}^I \otimes \mathbf{s}^I\right), \\
\mathbf{q} &= \sum \frac{h}{a}\left(\mathbf{t}^I \otimes \mathbf{n}^I \otimes \mathbf{s}^I - \mathbf{s}^I \otimes \mathbf{n}^I \otimes \mathbf{t}^I\right), \\
\mathbf{r} &= \sum \frac{h}{a}\left(\mathbf{t}^I \otimes \mathbf{t}^I + \mathbf{s}^I \otimes \mathbf{s}^I\right).
\end{aligned} \tag{13.11}$$

As is seen, $\mathbf{c}$, $\mathbf{q}$, or $\mathbf{r}$ is a fourth-, third-, or second-order tensor that is determined in terms of $k$ and $h$, respectively; the superscript $t$ stands for transpose ($q^t_{ijk} = q_{kji}$). The identical equations hold for all $\mathbf{x}^\alpha$'s of the rigid body grid. That is, continuumnization derives coupled partial differential equations for $\mathbf{u}(\mathbf{x}, t)$ and $\boldsymbol{\theta}(\mathbf{x}, t)$ from a set of ordinary differential equations of $\{\mathbf{u}^\alpha(t)\}$ and $\{\boldsymbol{\theta}^\alpha(t)\}$. In Fig. 13.5, we present a schematic view of continuumnization of a rigid body grid; a schematic view of homogenization that considers the volume average of strain and stress is presented for the comparison with continuumnization.

## 13.4 Nature of Material Properties for Continuumnized Functions

The three tensors $(\mathbf{c}, \mathbf{q}, \mathbf{r})$ of Eq. (13.11) are regarded as material properties as they relate translation and spin (or their derivative) to stress or local torque. We seek to interpret these three tensors.

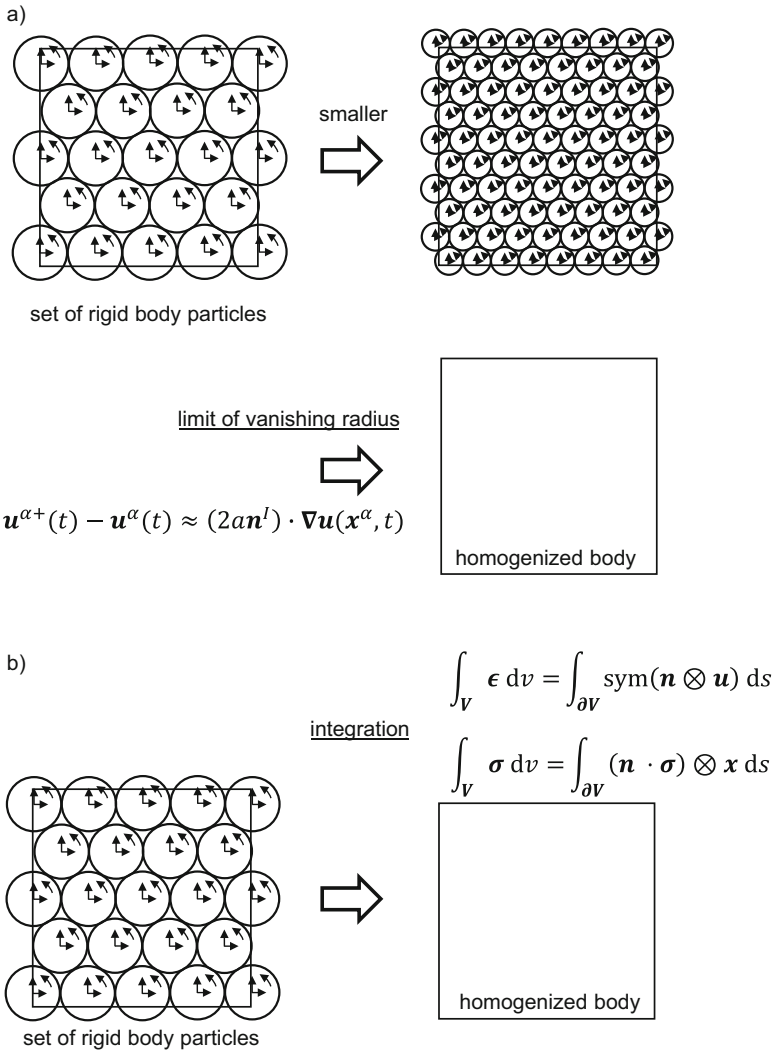


**Fig. 13.5** Schematic view of continuumnization of motion. (**a**) Continuumnization and (**b**) homogenization

First, we study $\mathbf{c}$, decomposing it into two parts which include $k$ and $h$, i.e., $\mathbf{c} = \mathbf{c}^k + \mathbf{c}^h$ with

$$\mathbf{c}^k = \sum \frac{k}{a}\, \mathbf{n} \otimes \mathbf{n}^I \otimes \mathbf{n} \otimes \mathbf{n},$$

$$\mathbf{c}^h = \sum \frac{h}{a} \left( \mathbf{n} \otimes \mathbf{t} \otimes \mathbf{n} \otimes \mathbf{t} + \mathbf{n} \otimes \mathbf{s} \otimes \mathbf{n} \otimes \mathbf{s} \right).$$

Here, for simplicity, the superscript $I$ is omitted. The components of $\mathbf{c}^k$ in the Cartesian coordinate system satisfy $c^k_{ijkl} = c^k_{jikl} = c^k_{ijlk} = c^k_{klij}$, but those of $\mathbf{c}^h$ satisfy only $c^h_{ijkl} = c^h_{klij}$. Hence, $\mathbf{c}^k$ is regarded as an ordinary elasticity tensor in the sense that it operates the symmetric part of $\nabla\mathbf{u}$ and produces a symmetric second-order tensor, while $\mathbf{c}^h$ operates the whole $\nabla\mathbf{u}$ and produces a nonsymmetric second-order tensor. Whether symmetric or nonsymmetric, the second-order tensor produced by $\mathbf{c}^{k,h}$ is regarded as stress in the sense that its divergence ($\nabla \cdot (\mathbf{c}^{k,h} : \nabla\mathbf{u})$) appears in the equation of motion.

Next, we study $\mathbf{r}$, which relates spin $\boldsymbol{\theta}$ to local torque. Precisely speaking, $I\ddot{\boldsymbol{\theta}}$ is linearly related to $-\mathbf{r}\cdot\boldsymbol{\theta}$ in Eq. (13.10), which means that $\mathbf{r}\cdot\boldsymbol{\theta}$ works to decrease $\ddot{\boldsymbol{\theta}}$. By definition of Eq. (13.11), $\mathbf{r}$ includes only shear spring constant, $h$, in it. The shear springs that are connected to the particle resist the spin of the particle, and $\mathbf{r}$ corresponds to this resistance.

Finally, we study $\mathbf{q}$ which appears in both Eqs. (13.9) and (13.10); this $\mathbf{q}$ provides coupling effects between $\mathbf{u}$ and $\boldsymbol{\theta}$. In Eq. (13.9), the components of the term that includes $\mathbf{q}$ are written as

$$\sum_{j,k} a^3 q_{ikj}\frac{\partial\theta_k}{\partial x_j} = \sum_j a^3 \frac{\partial}{\partial x_j}\left(\sum_k q_{ikj}\theta_k\right) \quad \text{for } i = 1,\ 2,\ 3.$$

Hence, $\sum q_{ikj}\theta_k$ is regarded as stress (of second-order tensor) in the sense that its divergence appears in the equation of motion. In Eq. (13.10), the components of the term that includes $\mathbf{q}$ are written as

$$\sum_{k,l} q_{ikl}\frac{\partial u_l}{\partial x_k} = \sum_{p,q}\varepsilon_{ipq}\sum_{k,l} c^h_{pqkl}\frac{\partial u_l}{\partial x_k} \quad \text{for } i = 1,\ 2,\ 3,$$

where $\varepsilon_{ipq}$ is permutation symbol. As is seen, this term is local torque that is produced by the antisymmetric part of $\nabla\mathbf{u}$ via $\mathbf{c}^h$.

It is shown that the three tensors $(\mathbf{c}, \mathbf{q}, \mathbf{r})$ are regarded as material property in the sense that they relate $\nabla\mathbf{u}$ and $\boldsymbol{\theta}$ to stress and local torque; stress is not symmetric, and the antisymmetric part influences spin. The stress and local torque are derived as continuumnization of the spring force, $\mathbf{f}^{\alpha\pm}$, of Eqs. (13.3) and (13.4). That is, we can assume the presence of $\boldsymbol{\sigma}(\mathbf{x}, t)$ which satisfies

$$\pm\mathbf{n}^I \cdot \boldsymbol{\sigma}(\mathbf{x} \pm a\mathbf{n}^I, t) = \mathbf{f}^{\alpha\pm}(t) \quad \text{at } \mathbf{x} = \mathbf{x}^\alpha.$$

This $\boldsymbol{\sigma}$ is related to $\nabla\mathbf{u}$ and $\boldsymbol{\theta}$ via $\mathbf{c}$ and $\mathbf{q}$, respectively. We introduce local torque, $\boldsymbol{\tau}$, as

$$\boldsymbol{\tau}(\mathbf{x}, t) = \sum (a\mathbf{n}^I) \times \mathbf{f}^{\alpha+}(t) + (-a\mathbf{n}^I) \times \mathbf{f}^{\alpha-}(t) \quad (\text{at } \mathbf{x} = \mathbf{x}^\alpha).$$

Note that the antisymmetric part of $\mathbf{c}^h : \nabla\mathbf{u}$ contributes local torque, too, where $\mathbf{c}^h$ changes its form to be $\mathbf{q}$.

We can provide more transparent presentation of $(\mathbf{c}, \mathbf{q}, \mathbf{r})$ using a Lagrangian of a rigid body grid. Denoting this Lagrangian by $\mathcal{L}$, we define $\mathcal{L}$ as

$$\begin{aligned}\mathcal{L}[\{\mathbf{u}^\alpha\}, \{\boldsymbol{\theta}^\alpha\}] = \sum_\alpha & \frac{1}{2} M |\dot{\mathbf{u}}^\alpha|^2 + \frac{1}{2} I |\dot{\boldsymbol{\theta}}^\alpha|^2 \\ & - \frac{1}{4} k \left( (\Delta \mathbf{u}^+ \cdot \mathbf{n})^2 + (\Delta \mathbf{u}^- \cdot \mathbf{n})^2 \right) \\ & + \frac{1}{4} h \left( (\Delta \mathbf{u}^+ \cdot \mathbf{t})^2 + (\Delta \mathbf{u}^+ \cdot \mathbf{s})^2 + (\Delta \mathbf{u}^- \cdot \mathbf{t})^2 + (\Delta \mathbf{u}^- \cdot \mathbf{s})^2 \right). \end{aligned} \tag{13.12}$$

Note that the energy stored in a spring is divided by 2, because it is shared by two neighboring particles. If continuumnized $\mathbf{u}$ and $\boldsymbol{\theta}$ are used, the right side of Eq. (13.12) is replaced by the volume integration, and $\mathcal{L}$ becomes

$$\mathcal{L}[\mathbf{u}, \boldsymbol{\theta}] = \int \frac{1}{2} \frac{M}{a^3} |\dot{\mathbf{u}}|^2 + \frac{1}{2} \frac{I}{a^3} |\dot{\boldsymbol{\theta}}|^2 - \frac{1}{2} \nabla \mathbf{u} : \mathbf{c} : \nabla \mathbf{u} - \boldsymbol{\theta} \cdot \mathbf{q} : \nabla \mathbf{u} - \frac{1}{2} \boldsymbol{\theta} \cdot \mathbf{r} \cdot \boldsymbol{\theta} \, \mathrm{d}v. \tag{13.13}$$

Energy stored in the springs is replaced by an energy density which is computed by $\nabla \mathbf{u}$ and $\boldsymbol{\theta}$.

## 13.5 Vanishing of Spin

As pointed out in preceding sections, it is not natural to introduce a field of spin, $\boldsymbol{\theta}(\mathbf{x}, t)$, which is not considered in continuum mechanics. In view of kinematics, local spin inevitably produces discontinuity everywhere, and hence the presence of local spin is not acceptable. In view of dynamics, vanishing of local angular momentum, or symmetry of stress, is proved by considering equilibrium; for instance, when a cube of edge length $a$ is considered, the angular momentum vanishes as the speed of $a^5$, while the torque caused by traction on the opposite faces vanishes as the speed of $a^3$, and this leads to vanishing of local angular momentum.

In Sect. 13.3, applying the same mathematical procedure of associating particle displacement, $\{\mathbf{u}^\alpha(t)\}$, to the continuumnized displacement, $\mathbf{u}(\mathbf{x}, t)$, we can associate particle spin, $\{\boldsymbol{\theta}^\alpha(t)\}$, to the continuumnized spin, $\boldsymbol{\theta}(\mathbf{x}, t)$. We need to show that $\boldsymbol{\theta}(\mathbf{x}, t)$ vanishes in the limit as $a$ goes to 0, so that the continuumnized fields are consistent with continuum mechanics.

First, we examine the limit of Eq. (13.8) as $a$ goes to 0. Dropping the third term that includes $\boldsymbol{\theta}$, we write this equation as

$$\frac{M}{a^3} \ddot{\mathbf{u}}(\mathbf{x}, t) = \nabla \cdot (\mathbf{c} : \nabla \mathbf{u}(\mathbf{x}, t)).$$

By definition, the physical dimensions of $M/a^3$ and $\mathbf{c}$ are density and elasticity, respectively. This equation is regarded as a wave equation that uses two constant $\frac{M}{a^3}$

and $\mathbf{c}$. In the limit as $a$ goes to 0, $M/a^3$ remains finite. Hence, we can assume that $\mathbf{c}$ remains finite, so that the solution of this wave equation is not trivial.

Next, we examine the limit of Eq. (13.10). Dropping the second term that includes $\mathbf{u}$, we write this equation as

$$\frac{I}{a^5} I\ddot{\boldsymbol{\theta}}(\mathbf{x}, t) = -\frac{1}{a^2}\mathbf{r} \cdot \boldsymbol{\theta}(\mathbf{x}, t). \tag{13.14}$$

The physical dimensions of $\frac{I}{a^5}$ and $\mathbf{r}$ are density and elasticity, respectively. Just like $\frac{M}{a^3}$, $\frac{I}{a^5}$ remains finite in the limit as $a$ goes to 0, and $\mathbf{r}$ remains finite since $\mathbf{c}$ remains finite. If $\boldsymbol{\theta}/a^2$ remains finite, $\ddot{\boldsymbol{\theta}}$ is finite but $\boldsymbol{\theta}$ vanishes. That is,

$$\lim_{a \to 0} \boldsymbol{\theta}(\mathbf{x}, t) = \mathbf{0}.$$

If $\boldsymbol{\theta}$ remains finite, the right side of Eq. (13.14) diverges as the speed of $a^{-2}$, and hence the left side or $\boldsymbol{\theta}(\mathbf{x}, t)$ tends to vibrate at an increasing frequency. The average of such high-frequency vibration vanishes if the average is taken with respect to time. That is,

$$\lim_{a \to 0} \frac{1}{T} \int_0^T \boldsymbol{\theta}(\mathbf{x}, t)\, \mathrm{d}t = 0$$

for a fixed $T$. Therefore, we can conclude that $\boldsymbol{\theta}$ vanishes in the limit as $a$ goes to 0, except for components which vibrate at high frequencies and have zero average in time.

The vanishing of $\boldsymbol{\theta}(\mathbf{x}, t)$ in the limit $a$ goes to 0 implies that the second term in the right side of Eq. (13.10), $\mathbf{q} : \nabla\mathbf{u}(\mathbf{x}, t)$, vanishes as well. Indeed, this is true since $\mathbf{q} : \nabla\mathbf{u}(\mathbf{x}, t)$ equals the antisymmetric part of $\mathbf{c} : \nabla\mathbf{u}$, as shown in the preceding section. This is well understood; as mentioned, stress in continuum mechanics is symmetric so that local torque vanishes. In the limit as $a$ goes to 0, Euler's momentum equation, Eq. (13.10), becomes trivial in the sense that all the terms in the equation vanish.

## 13.6 Characteristic Equation of Continuumnized Function

We consider a three-dimensional rigid body grid. As shown in Fig. 13.6, this grid has six spring directions, $\{\mathbf{n}^I\}$ for $I = 1, \cdots, 6$. We take a Cartesian coordinate, $(x_1, x_2, x_3)$, so that $\{\mathbf{n}^1, \mathbf{n}^2, \mathbf{n}^3\}$ lie on the $x_1, x_2$-plane. Two tangential directions, $\mathbf{t}^I$ and $\mathbf{s}^I$, which are associated with $\mathbf{n}^I$ are suitably chosen. To simplify notation, we define

$$\rho^M = \frac{M}{a^3}, \quad \rho^I = \frac{I}{a^5}, \quad k' = \frac{k}{a} \quad \text{and} \quad h' = \frac{h}{a};$$

the physical dimension of $\rho^M$ and $\rho^I$ is density and that of $k'$ and $h'$ is elasticity.

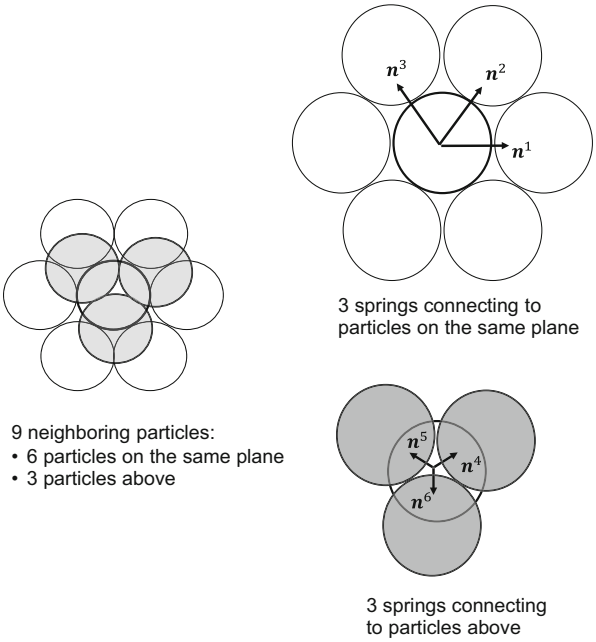


**Fig. 13.6** Six springs connecting particles

The three tensors defined in Eq. (13.11) are readily computable. The fourth-order tensor $\mathbf{c}$ has an isotropic part as

$$\frac{4(k'-h')}{25}\mathbf{I}^1 + \frac{4(2k'+3h')}{25}\mathbf{I}^2,$$

where the components of $\mathbf{I}^{1,2}$ in the Cartesian coordinate are $I^1_{ijkl} = \delta_{ij}\delta_{kl}$ and $I^2_{ijkl} = \frac{1}{2}(\delta_{ik}\delta_{jl} + \delta_{il}\delta_{jk})$, with $\delta_{ij}$ being Kronecker's delta. The remaining part, denoted by $\mathbf{c}^*$, is

$$\frac{4h'}{5}\mathbf{I}^3,$$

where the components of $\mathbf{I}^3$ are $I^3_{ijkl} = \frac{1}{2}(\delta_{ik}\delta_{jl} - \delta_{il}\delta_{jk})$; note that $\mathbf{I}^2$ and $\mathbf{I}^3$ are an identity tensor for a second-order symmetric tensor and a second-order antisymmetric tensor, respectively. The third-order tensor $\mathbf{q}$ and the second-order tensor $\mathbf{r}$ are isotropic, as their components are

$$q_{ijk} = 2h'\varepsilon_{jik} \quad \text{and} \quad r_{ij} = 4h'\delta_{ij} \quad (\text{for } i,j = 1,2,3).$$

Recall that $\varepsilon_{ijk}$ and $\delta_{ij}$ are the permutation symbol and Kronecker's delta, respectively.

We rewrite the coupled partial differential equations of $\mathbf{u}$ and $\boldsymbol{\theta}$, Eqs. (13.9) and (13.10), applying Fourier transform with the kernel of $\exp(\imath(\boldsymbol{\xi}\cdot\mathbf{x}-\omega t))$ to $\mathbf{u}$ and $\boldsymbol{\theta}$. The resulting equations are given as

$$\left(\omega^2[M]+[K]\right)[U]=[0] \tag{13.15}$$

where $[U]$ is a six-dimensional vector, consisting of the Fourier transformation of $[u_1,u_2,u_3,\theta_1,\theta_2,\theta_3]^T$, $[M]$ is a six-by-six diagonal matrix of

$$[M]=\begin{bmatrix}\rho^M&0&0&0&0&0\\0&\rho^M&0&0&0&0\\0&0&\rho^M&0&0&0\\0&0&0&\rho^I&0&0\\0&0&0&0&\rho^I&0\\0&0&0&0&0&\rho^I\end{bmatrix}, \tag{13.16}$$

and $[K]$ is a six-by-six matrix of

$$[K]=\begin{bmatrix}\frac{4(3k'+2h')}{25}(\xi_2^2+\xi_3^2)&\frac{8(k'-h')}{25}\xi_1\xi_2&\frac{8(k'-h')}{25}\xi_1\xi_3&0&2\imath h'\xi_3&-2\imath h'\xi_2\\\frac{8(k'-h')}{25}\xi_2\xi_1&\frac{4(3k'+2h')}{25}(\xi_3^2+\xi_1^2)&\frac{8(k'-h')}{25}\xi_2\xi_3&-2\imath h'\xi_3&0&2\imath h'\xi_1\\\frac{8(k'-h')}{25}\xi_3\xi_1&\frac{8(k'-h')}{25}\xi_3\xi_2&\frac{4(3k'+2h')}{25}(\xi_1^2+\xi_2^2)&2\imath h'\xi_2&-2\imath h'\xi_1&0\\0&-2\imath h'\xi_3&2\imath h'\xi_2&-4h'&0&0\\2\imath h'\xi_3&0&-2\imath h'\xi_1&0&-4h'&0\\-2\imath h'\xi_2&2\imath h'\xi_1&0&0&0&-4h'\end{bmatrix}. \tag{13.17}$$

Note that $[K]$ is symmetric; recall that the governing equations can be derived from the Lagrangian of Eq. (13.13).

### 13.6.1 Characteristic Equation

Now, we study the characteristic equation of Eq. (13.15), which is given as vanishing of the determinant of $\omega^2[M]+[K]$. That is,

$$\begin{aligned}&(25\rho^M\omega^2-4(3k'+2h')\xi^2)(\rho^I\omega^2+4h'\tfrac{1}{a^2})\\&\quad\left(25\rho^M\rho^I+4(25\rho^Mh'\tfrac{1}{a^2}-\rho^I(k'+4h')\xi^2)\omega^2+4h'(4k'-9h')\xi^2\tfrac{1}{a^2}\right)^2=0.\end{aligned} \tag{13.18}$$

This is a polynomial equation of $\omega$ for a given $\boldsymbol{\xi}$.

The first solution of Eq. (13.18) is given as

$$\omega^2 = \frac{4(3k' + 2h')}{25\rho^M}\xi^2. \tag{13.19}$$

This solution accompanies an eigenvector of $[\xi_1, \xi_2, \xi_3, 0, 0, 0]^T$, which is a translation wave (or spin-free wave) parallel to the wave number vector, $\boldsymbol{\xi}$. The wave velocity of this translation wave is independent from the wave number and given as $\frac{4(3k'+2h')}{25\rho^M}$. Therefore, this translation wave corresponds to a P-wave of a material which is linearly isotropically elastic. We have to emphasize that continuumnization enables us to compute a wave velocity for a rigid body grid; it is not possible to compute wave velocity for such a discrete system in which spring transfers stress without causing any delay.

For the second solution of Eq. (13.18),

$$\omega^2 = -\frac{4h'}{\rho^I a^2}, \tag{13.20}$$

the accompanied eigenvector is $[0, 0, 0, \xi_1, \xi_2, \xi_3]^T$, which is a spin wave (or translation-free wave) parallel to $\boldsymbol{\xi}$. This $\omega$ does not depend on $\boldsymbol{\xi}$ but depends on $\frac{1}{a^2}$. This spin wave is the one that is discussed in the preceding section, which vibrates at increasing frequency when $a$ goes to 0. Furthermore, since $\omega$ is a purely imaginary number, this spin wave vanishes exponentially. It is concluded that the spin wave of $\omega^2 = -\frac{4h'}{\rho^I a^2}$ is local and vibrates at high frequency for small $a$.

The remaining solutions of Eq. (13.18) accompany eigenvectors in which translation and spin are mixed. If we set $\boldsymbol{\xi}$ as $[\xi_1, \xi_2, \xi_3] = [\xi, 0, 0]$, we can derive the following four-by-four matrix from $\omega^2[M] + [K]$ that correspond to the remaining solution of Eq. (13.18):

$$\det \begin{bmatrix} \rho^M\omega^2 - \frac{4(k'+4h')}{25}\xi^2 & 0 & 0 & -2\imath h'\xi \\ 0 & \rho^M\omega^2 - \frac{4(k'+4h')}{25}\xi^2 & -2\imath h'\xi & 0 \\ 0 & 2\imath h'\xi & 4h' + \rho^I a^2\omega^2 & 0 \\ -2\imath h'\xi & 0 & 0 & 4h' + \rho^I a^2\omega^2 \end{bmatrix} = 0;$$

note that this matrix is for a four-dimensional vector of $[u_2, u_3, \theta_2, \theta_3]^T$. The four solutions are

$$\omega^2 = \frac{2(k' + 4h')}{25\rho^M}\xi^2 - \frac{2h'}{\rho^I}a^2 \pm \sqrt{\left(\frac{2(k'+4h')}{25\rho^M}\right)^2\xi^4 + \frac{4h'(2k'-17h')}{25\rho^M\rho^I}\xi^2 a^{-2} + \left(\frac{2h'}{\rho^I}\right)^2 a^{-4}}. \tag{13.21}$$

The accompanied eigenvectors are of the following form:

$$\begin{bmatrix} u_2 \\ u_3 \\ \theta_2 \\ \theta_3 \end{bmatrix} = \begin{bmatrix} 1 \\ 0 \\ 0 \\ -\dfrac{2\imath h'\xi}{4h' + \rho^I a^2 \omega^2} \end{bmatrix} \quad \text{or} \quad \begin{bmatrix} 0 \\ 1 \\ \dfrac{2\imath h'\xi}{4h' + \rho^I a^2 \omega^2} \\ 0 \end{bmatrix}.$$

Note that for $a$ satisfying $a\xi \ll 1$, Eq. (13.21) yields

$$\omega^2 \approx \frac{2(k' + 4h')}{25\rho^M}\xi^2 \quad \text{and} \quad \frac{h'(9h' - 4k')}{(k' + 4h')\rho^I}a^{-2}.$$

The first solution has a wave velocity $\frac{2(k'+4h')}{25\rho^M}$ that is independent from the wave number and corresponds to a S-wave of linearly isotropic elastic material. The ratio of the spin component to the translation component of the corresponding eigenvectors is $\frac{2}{4h'}\xi$. Hence, spin components do not vanish for these four solutions even in the limit as $a$ goes to 0.

In Table 13.1, we summarize the characteristics of the four kinds of the solutions of the characteristic equations, Eq. (13.18), in the limit as $a$ goes to 0. As shown, if the wave length is sufficiently compared with the particle radius, the continuumnized fields produce both P- and S-waves. While the P-wave is spin free, the S-wave accompanies spin and the amplitude could be large. The large amplitude of spin exceeds the assumption of infinitesimally small deformation or we have to treat spin and displacement more rigorously as explained in Sect. 13.5.

**Table 13.1** Four kinds of solutions of characteristic equation in the limit as $a$ goes to 0

| | $\omega^2$ | Eigenvector | Characteristics |
|---|---|---|---|
| 1 | $\frac{4(3k'+2h')}{25\rho^M}\xi^2$ | $[1,0,0,0,0,0]^t$ | Corresponds to P-wave |
| | | | Has a wave velocity of $\frac{4(3k'+2h')}{25\rho^M}$ |
| 2 | $-\frac{4h'}{\rho^I}\frac{1}{a^2}$ | $[0,0,0,1,0,0]^t$ | Increases at a speed of $\frac{1}{a^2}$ w.r.t. $a$ |
| | | | Independent from wave length |
| | | | Decays exponentially |
| 3 | $\frac{2(k'+4h')}{25\rho^M}\xi^2$ | $\left[0,1,0,0,0,-\frac{\imath}{2}\xi\right]^t$ | Coupling of translation and spin |
| | | | Corresponds to S-wave |
| | | | Has a wave velocity of $\frac{2(k'+4h')}{25\rho^M}$ |
| 4 | $\frac{h'(9h'-4k')}{(k'+4h')\rho^I}\frac{1}{a^2}$ | $\left[0,1,0,0,0\frac{2(k'+4h')\imath}{25h'}\xi\right]^t$ | Coupling of translation and spin |
| | | | Increases at a speed of $\frac{1}{a^2}$ w.r.t. a |
| | | | Independent from wave length |

### 13.6.2 Remaining of Local Torque in the Limit as a Goes to 0

It is interesting to note that $\mathbf{c}^*$, the remaining of $\mathbf{c}$ subtracted by the fourth-order isotropic part, maps rotation, or the antisymmetric part of displacement gradient, to the antisymmetric part of stress. That is, defining by

$$\omega_{ij} = \frac{1}{2}\left(\frac{\partial u_2}{\partial x_1} - \frac{\partial u_1}{\partial x_2}\right)$$

$\mathbf{c}^*$ maps this $\boldsymbol{\omega}$ to $\frac{2h'}{5}\boldsymbol{\omega}$; recall that $\mathbf{c}^*$ is isotropic in the present case. The antisymmetric part of stress is produced by the spin, $\boldsymbol{\theta}$, via $\mathbf{q}$. Denoting the antisymmetric part by $\boldsymbol{\tau}$, we thus have its nonzero components as

$$\tau_{ij} = \frac{2h'}{5}\omega_{ij} + \sum_k 2h'\varepsilon_{ijk}\theta_k \quad \text{for } i,j = 1,2,3. \tag{13.22}$$

The gradient of this $\mathbf{m}$ appears in the equation of motion, Eq. (13.9), while $4h'\theta_i + \sum_{k,j} 2h'\varepsilon_{jki}\omega_{ij}$ appears in Euler's momentum equation, Eq. (13.10); this term corresponds to local torque.

As mentioned in the preceding section, $\boldsymbol{\theta}$ vanishes in the limit as $a$ goes to 0. However, the rotation, $\boldsymbol{\omega}$, does not vanish, because it is the antisymmetric part of the displacement gradient. Local torque or the antisymmetric part of stress that is produced by the continuumnized fields remains nonzero in the limit, even though local torque due to spin vanishes. Remaining of local torque in the limit is contracting to continuum mechanics in which stress is proved to be symmetric and to have no antisymmetric part.

We should not make any extra condition for $\mathbf{u}$ so that $\boldsymbol{\omega}$ vanishes. A possible solution of making $\boldsymbol{\tau}$ vanish is to consider a certain set of *admissible* springs which make $\mathbf{c}^*$ so that $\mathbf{c}^* : \boldsymbol{\omega}$ vanishes in the limit. We should emphasize that the spring set shown in Fig. 13.2 is not admissible. Indeed, it is not easy to find such an admissible spring set for a rigid body grid which has regularly arranged particles of identical radius. We may thus have to consider an assembly of heterogeneous spherical rigid body particles to find an admissible spring set.

## 13.7 Concluding Remarks

In this paper, we present continuumnization of a rigid body grid, which consists of regularly arranged particles. Continuumnization results in a set of smooth functions of displacement and spin that correspond to particles' translation and spin, respectively. Assuming that spin is infinitesimally small, we derive a set of coupled differential equations for these continuumnized functions. The wave velocity of the rigid body grid can be computed by solving these equations. It is

shown that continuumnized spin function vanishes in the limit as the particle radius goes to zero, as expected. Also, it is shown that for nonzero value of particle radius, the continuumnized spin plays a role of damping for translation wave due to its nonlinearity.

The above remarks are made based on the study of a two-dimensional rigid body grid. Further studies are essential to clarify the vanishing of the continuumnized spin in the limit as the particles' radius goes to 0 in a general 3D setting. Also, more rigorous treatment of spin is needed to clarify the nonlinear effects of spin on translation, which is interpreted as damping in the present study.

In closing this paper, we point out a possibility of continuumnization as a new tool of analyzing a microstructure model, which could be an alternative of conventional tool of homogenization. The idea of taking the limit as the size of microconstituents might be interesting and worth being investigated. In mathematical viewpoint, the procedure of continuumnization, generating differential equations from a set of discretized equations, is opposite to finite difference that generates a set of discretized equations from differential equations.

**Acknowledgments** This work was supported by JSPS KAKENHI Grant Number 25220908. Part of the results was obtained by using the K computer at the RIKEN Advanced Institute for Computational Science.

## References

Beale, P.D., Srolovitz, D.J.: Elastic fracture in random materials. Phys. Rev. B **37**(10), 5500–5507 (1988)

Buxton, G.A., Care, C.M., Cleaver, D.J.: A lattice spring model of heterogeneous materials with plasticity. Model. Simul. Mater. Sci. Eng. **9**(6), 485–497 (2001)

Chang, C.S., Ma, L.: Elastic material constants for isotropic granular solids with particle rotation. Int. J. Solids Struct. **29**, 1001–1018 (1992)

Cosserat, E., Cosserat, F.: Theorie des Corps deformables. A. Hermann et Fils, Paris (1909) [in French]

Cundall, P.A., Strack, O.D.L.: Discrete numerical model for granular assemblies. Geotechnique **29**(1), 47–65 (1979)

Curtin, W.A., Scher, H.: Mechanics modeling using a spring network. J. Mater. Res. **5**, 554–562 (1990)

Cusatis, G., Bazant, Z.P., Cedolin, L.: Confinement-shear lattice model for concrete damage in tension and compression: I. Theory. J. Eng. Mech. **129**(12), 1439–1448 (2003)

Eringen, A.C.: Non-local continuum mechanics and some application. In: Barut, A.O. (ed.) Nonlinear Equations in Physics and Mathematics, pp. 271–318. Riedel, Dordrecht (1978)

Hori, M., Wijerathene, L., Chen, J., Ichimura, T.: Continuumnization of regularly arranged rigid bodies. J. Jpn. Soc. Civ. Eng. **4**(1), 38–45 (2016)

Karihaloo, B.L., Shao, P.F., Xiao, Q.Z.: Lattice modelling of the failure of particle composites. Eng. Fract. Mech. **70**(17), 2385–2406 (2003)

Kawai, T.: New discrete models and their application to seismic response analysis of structures. Nucl. Eng. Des. **48**(1), 207–229 (1978)

Kozicki, J., Tejchman, J.: Modelling of fracture process in concrete using a novel lattice model. Granul. Matter **10**(5), 377–388 (2008)

Kroner, E., Datta, B.K.: Non-local theory of elasticity for a finite inhomogeneous medium: a derivation from lattice theory. In: Simmons, J.A., de Wit, R., Bullough, R. (eds.) Fundamental Aspects of Dislocation Theory. National Bureau of Standards Special Publication 317, vol. II, pp. 737–74. National Bureau of Standards, Washington (1970)

Kuhn, M.: Discussion on the asymmetry of stress in granular media. Int. J. Solids Struct. **40**, 1805–1807 (2003)

Kunin, I.A.: Elastic Media with Microstructure 1. One-Dimensional Models. Springer, New York (1982)

Lemieux, M.A., Breton, P., Tremblay, A.M.S.: Unified approach to numerical transfer matrix methods for disordered systems: applications to mixed crystals and to elasticity percolation. J. Phys. Lett. **46**, 1–7 (1985)

Lilliu, G., van Mier, J.G.M.: 3D lattice type fracture model for concrete. Eng. Fract. Mech. **70**, 927–941 (2003)

Liu, J.X., Deng, S.C., Zhang, J., Liang, N.G.: Lattice type of fracture model for concrete. Theor. Appl. Fract. Mech. **48**(3), 269–284 (2007)

Mindlin, R.D., Tiersten, H.F.: Effects of couple-stresses in linear elasticity. Arch. Ration. Mech. Anal. **11**, 415–448 (1962)

Monette, L., Anderson, M.P.: Elastic and fracture properties of the two-dimensional triangular and square lattices. Model. Simul. Mater. Sci. Eng. **2**(1), 53–66 (1994)

Mustoe, G.G.W.: Generalized formulation of the discrete element method. Eng. Comput. **9**(2), 181–190 (1992)

Nowacki, W.: The linear theory of micropolar elasticity. In: Nowacki, W., Olszak, W. (eds.) Micropolar Elasticity, pp. 1–43. Springer, New York (1974)

Potyondy, D.O., Cundall, P.A.: A bonded-particle model for rock. Int. J. Rock Mech. Min. Sci. **41**(8), 1329–1364 (2004)

Ostoja-Starzewski, M., Sheng, P.Y., Alzebdeh, K.: Spring network models in elasticity and fracture of composites and polycrystals. Comput. Mater. Sci. **7**(1–2), 82–93 (1996)

Ray, P., Chakrabarti, B.K.: A microscopic approach to the statistical fracture analysis of disordered brittle solids. Solid State Commun. **53**(5), 4770–479 (1985)

Sahimi, M., Arbabi, S.: Percolation and fracture in disordered solids and granular media: approach to a fixed point. Phys. Rev. Lett. **68**(5), 608–11 (1992)

Sahimi, M., Goddard, J.D.: Elastic percolation models for cohesive mechanical failure in heterogeneous systems. Phys. Rev. B **33**, 7848–7851 (1986)

Schlangen, E., Garboczi, E.J.: Fracture simulations of concrete using lattice models: computational aspects. Eng. Fract. Mech. **57**, 319–332 (1997)

Walton, K.: The effective elastic modulus of a random packing of spheres. J. Mech. Phys. Solids **35**, 213–226 (1987)

Zubelewicz, A., Bazant, Z.P.: Interface element modeling of fracture in aggregate composites. J. Eng. Mech. **113**(11), 1619–1630 (1987)

# Chapter 14
# The Parametric HFGMC Micromechanics

**Rami Haj-Ali and Jacob Aboudi**

**Abstract** The parametric high-fidelity generalized method of cells (HFGMC) is thoroughly developed and reviewed starting from the HFGMC formulation with regular array of subcells. The HFGMC is shown to be an effective micromechanical analysis method for linear, nonlinear, and multi-physics problems involving heterogeneous materials with periodic microstructure. This chapter deals with two (2D) and three-dimensional (3D) HFGMC applied for multiphase periodic composites suited for nonlinear and evolving damage. A new average virtual work formulation is also introduced in order to generate a symmetric stiffness matrix formulation for the nonlinear iterative solution of the HFGMC system of equations. This approach allows the application of classical direct iterative solution techniques and tremendously enhances the computational efficiency. A review of noteworthy recent HFGMC applications for composite materials is also given. The HFGMC micromechanics is well suited for integrating the nonlinear and damage response of composites and predicting the fiber-matrix spatial local fields including progressive damage effects.

## 14.1 Introduction

The high-fidelity generalized method of cells (HFGMC) is a micromechanical model that is capable to predict the behavior of composites which poses periodic microstructure. This periodicity character enables the identification of a repeating unit cell (RUC) on which the micromechanics analysis is performed. The HFGMC developed from the method of cells (MOC) in which the repeating unit cell of the composite is divided into four subcells. Aboudi (1982) is the first article in which MOC has been presented, and a comprehensive treatment and a host of applications can be found in the monograph (Aboudi, 1991). The MOC was followed by the generalized method of cells (GMC) (Paley and Aboudi, 1992), where an arbitrary

R. Haj-Ali (✉) • J. Aboudi
Faculty of Engineering, Tel-Aviv University, Ramat Aviv, Tel Aviv 69978, Israel
e-mail: rami98@tau.ac.il; aboudi@eng.tau.ac.il



S.A. Meguid, G.J. Weng (eds.), *Micromechanics and Nanomechanics of Composite Solids*, DOI 10.1007/978-3-319-52794-9_14

number of cells can be used to model the RUC. In both MOC and GMC, the displacement vector field is based on a linear expansion. This is generalized to a second-order expansion (Aboudi et al., 2001; Aboudi, 2001), which explains the term HFGMC as a subsequent extension to its predecessors, MOC and GMC. A detailed presentation of these three methods together with many applications can be found in Aboudi et al. (2013) where their applications on thermoelastic, inelastic, viscoelastic, and smart materials, including analysis at finite strain, are presented, including multiscale implementations.

Several extensions of the HFGMC have been conducted. Thus, Haj-Ali and Aboudi (2009) provided total and incremental formulation of the HFGMC for the micromechanical analysis of nonlinear multiphase materials. An iterative procedure has been developed to minimize the residual error and satisfy the HFGMC governing equations in their total form. In addition, the overall system of algebraic equations has been assembled in a compact matrix form utilizing the relevant equations for a set of two feed-forward interfaces sweeping the entire array of subcells resulting in enhanced computational efficiency.

The original HFGMC formulations have been performed in conjunction with orthogonal array of subcells used to depict the geometry of the phases (regular array). This limitation requires a relatively large number of subcells if the objective is to accurately capture refined geometrical features and the spatial variations of the local solution fields. Despite this limitation, the previous applications have demonstrated the effectiveness of the method to generate the local solution fields by using a sufficiently large number of rectangular subcells. It should be emphasized that a small number of rectangular subcells is sufficient to generate the effective linear and nonlinear response for the overall composite with high accuracy. In fact, this is one of the advantages of using the HFGMC in a multiscale (local–global) analysis of composite structures with selective geometrical refinement for the microstructure.

A natural extension that overcomes the limitations of the regular orthogonal array is to employ a parametric mapping. This is a common practice, which has been used in many science and engineering fields; it involves the solution of the governing equations using classical coordinate transformation in conjunction with the well-known Jacobian of the transformation. To this end, Haj-Ali and Aboudi (2010) used linear geometrical mapping of the subcells to map the geometry of the phases of a composite with doubly periodic microstructure. This linear and parametric geometric mapping can be applied for a unit cell with general phase geometry using arbitrary quadrilateral cell shapes that are transformed to an auxiliary uniform square shape (parent coordinates). In Haj-Ali and Aboudi (2013), this parametric HFGMC has been generalized to the analysis of composites with triply periodic microstructure. Haj-Ali and Aboudi (2013) showed that the average displacement vectors at the edges (or faces) of the subcell can be expressed in terms of the expansion coefficients to form an independent subset of the subcell's face-based variables. In addition, the bilinear polynomial terms were related to the quadratic coefficients of the displacements. Thus, there was no need for the additional moment

of equilibrium relation suggested in Haj-Ali and Aboudi (2010). The parametric HFGMC follows the same physical assumptions and variables as the original formulation and the regular array HFGMC which can be obtained as a special case of the parametric formulation.

In a recent publication (Haj-Ali and Aboudi 2016), a new average virtual work integral form is proposed for the HFGMC method which allows for the definition of a generalized internal resisting force vector along with its corresponding symmetric stiffness matrix. Unlike the nodal displacement-based finite element, this proposed HFGMC and its weak form have been cast in terms of the work-conjugate average displacement and traction vectors, defined on the surfaces (faces) of the subcells. This allowed direct interface continuity relations between the hexahedral subcells. The resulting symmetric stiffness matrix forms a great advantage of this parametric HFGMC formulation since for symmetric matrices, well-established incremental solution techniques exist.

This chapter is organized as follows. In Sect. 14.2, the doubly periodic HFGMC for nonlinear composites with regular array is presented in which an iterative procedure is developed to minimize the residual error and satisfy the HFGMC governing equations in their total form. In Sect. 14.3, the doubly periodic parametric HFGMC is discussed, followed in Sect. 14.4 by a full generalization to the triply periodic HFGMC parametric micromechanical model. A new average virtual work multilevel formulation of the HFGMC model is presented in Sect. 14.5. This average virtual work formulation enables significant computational advantages. This chapter is concluded by an application section where references to several implementations and examples are given.

## 14.2 Nonlinear Doubly Periodic HFGMC Formulation: Regular Array

The principal HFGMC micromechanical framework for periodic multiphase composites has been fully described by Aboudi et al. (2013). In this section, we present a different version suitable for the analysis of nonlinear and inelastic composites. Towards that end, an iterative incremental formulation is presented along with stress correction and update. This leads to satisfying the overall HFGMC nonlinear equations by minimizing the residual error vector.

The HFGMC framework is based on the homogenization technique of composites with periodic microstructure as shown in Fig. 14.1 for the 2D case. The repeating unit volume of such a composite, Fig. 14.2, is divided into an arbitrary number of rectangular cells, labeled by the indices $(\beta\gamma)$, each of which may contain a distinct nonlinear homogeneous material. The dimensions of the cell along the 2 and 3 axes are denoted by $h_\beta$ and $l_\gamma$, respectively. In the present doubly periodic case of continuous fibers, a local coordinate system $(y_2^{(\beta)}, y_3^{(\gamma)})$ is introduced in each cell whose origin is located at its center (see Fig. 14.2).

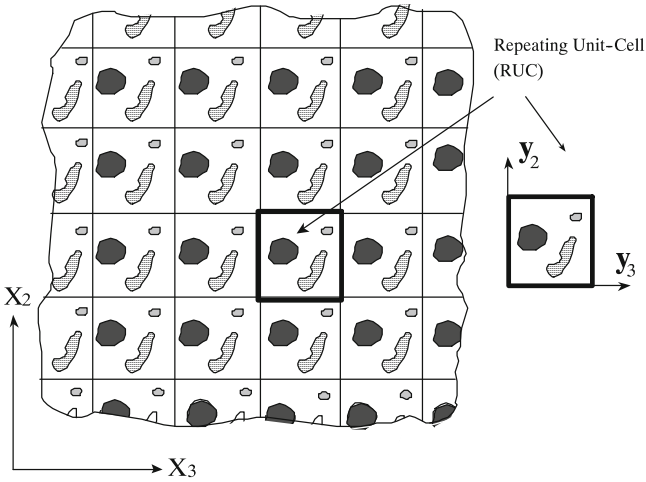


**Fig. 14.1** Schematic illustration of a unidirectional periodic array in the global $x_2 - x_3$ plane of multiphase composite media with its repeating unit cell (RUC), defined with respect to its $y_2 - y_3$ local coordinate system

The displacement vector in the subcell $(\beta\gamma)$ is given , e.g., Aboudi et al. (2013), by the quadratic higher-order polynomial form

$$\mathbf{u}^{(\beta\gamma)} = \bar{\boldsymbol{\epsilon}} \cdot \mathbf{x} + \mathbf{W}_{(00)}^{(\beta\gamma)} + y_2^{(\beta)} \mathbf{W}_{(10)}^{(\beta\gamma)} + y_3^{(\gamma)} \mathbf{W}_{(01)}^{(\beta\gamma)} + \frac{1}{2}(3y_2^{(\beta)2} - \frac{h_\beta^2}{4})\mathbf{W}_{(20)}^{(\beta\gamma)} + \frac{1}{2}(3y_3^{(\gamma)2} - \frac{l_\gamma^2}{4})\mathbf{W}_{(02)}^{(\beta\gamma)} \tag{14.1}$$

where $\bar{\boldsymbol{\epsilon}}$ is the remote applied average strain. The microvariable vectors, $\mathbf{W}_{(mn)}^{(\beta\gamma)}$, represent the surface-averaged displacement in the case of $m = n = 0$, which together with the additional higher-order unknown microvariables should be determined.

The spatial strain vector at each subcell can be easily brought in the form

$$\boldsymbol{\epsilon}^{(\beta\gamma)} \equiv \{\epsilon_{11}, \epsilon_{22}, \epsilon_{33}, 2\epsilon_{12}, 2\epsilon_{13}, 2\epsilon_{23}\}^{(\beta\gamma)} \tag{14.2}$$

After some algebraic manipulations, it is possible to represent the strain vector in the form

$$\boldsymbol{\epsilon}^{(\beta\gamma)} = \bar{\boldsymbol{\epsilon}} + P_{(10)}\mathbf{W}_{(10)}^{(\beta\gamma)} + P_{(01)}\mathbf{W}_{(01)}^{(\beta\gamma)} + P_{(20)}\mathbf{W}_{(20)}^{(\beta\gamma)} y_2^{(\beta)} + P_{(02)}\mathbf{W}_{(02)}^{(\beta\gamma)} y_3^{(\gamma)} \tag{14.3}$$

After some algebraic manipulations, it is possible to establish the matrix coefficients of the spatial expansion of the strain vectors, where

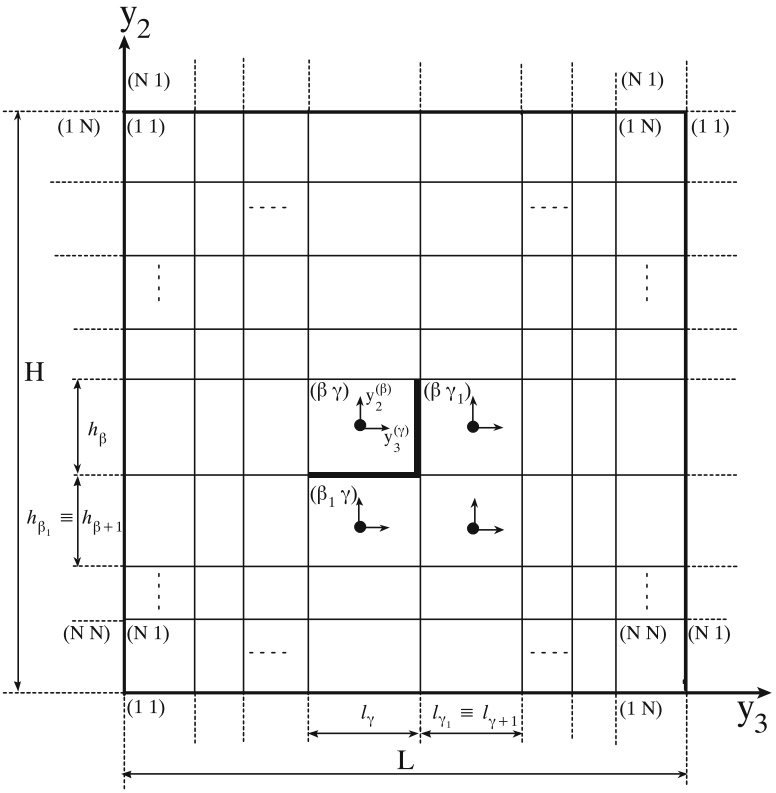


**Fig. 14.2** General arrangement of cells and their geometry and coordinate systems for the HFGMC-RUC model. Mirrored cells–interfaces are illustrated to enforce the periodic boundary conditions

$$P_{(10)} = \begin{bmatrix} 0\,0\,0 \\ 0\,0\,0 \\ 0\,0\,1 \\ 0\,0\,0 \\ 1\,0\,0 \\ 0\,1\,0 \end{bmatrix}, \quad P_{(01)} = \begin{bmatrix} 0\,0\,0 \\ 0\,1\,0 \\ 0\,0\,0 \\ 1\,0\,0 \\ 0\,0\,0 \\ 0\,0\,1 \end{bmatrix} \tag{14.4}$$

and $P_{(20)} = 3P_{(10)}$, $P_{(02)} = 3P_{(01)}$.

The volume average of the strain in the subcell $(\beta\gamma)$ can be consequently represented by

$$\bar{\boldsymbol{\epsilon}}^{(\beta\gamma)} = \bar{\boldsymbol{\epsilon}} + P_{(10)}\mathbf{W}_{(10)}^{(\beta\gamma)} + P_{(01)}\mathbf{W}_{(01)}^{(\beta\gamma)} \tag{14.5}$$

The strain concentration matrix $\mathbf{B}^{(\beta\gamma)}$ of the subcell, which relates the subcell strain average to the externally applied strain, can be expressed in an incremental form by

$$\Delta\bar{\boldsymbol{\epsilon}}^{(\beta\gamma)} \equiv \boldsymbol{B}^{(\beta\gamma)}\Delta\bar{\boldsymbol{\epsilon}} = \left[\mathbf{I} + P_{(10)}\hat{\mathbf{D}}_{(10)}^{(\beta\gamma)} + P_{(01)}\hat{\mathbf{D}}_{(01)}^{(\beta\gamma)}\right]\Delta\bar{\boldsymbol{\epsilon}} \tag{14.6}$$

with $\mathbf{I}$ being the identity matrix. Furthermore, one can easily identify

$$\hat{\mathbf{D}}_{(10)}^{(\beta\gamma)}\Delta\bar{\boldsymbol{\epsilon}} = \Delta\mathbf{W}_{(10)}^{(\beta\gamma)}, \quad \hat{\mathbf{D}}_{(01)}^{(\beta\gamma)}\Delta\bar{\boldsymbol{\epsilon}} = \Delta\mathbf{W}_{(01)}^{(\beta\gamma)} \tag{14.7}$$

where $\hat{\mathbf{D}}_{(mn)}^{(\beta\gamma)}$ are dependent on the solution of the overall governing equations of the RUC.

The spatial form of the stress vector can be expected to be a linear polynomial order. Thus, it is possible to express the stress as follows:

$$\boldsymbol{\sigma}^{(\beta\gamma)} = \bar{\boldsymbol{\sigma}}^{(\beta\gamma)} + \boldsymbol{\sigma}_{(10)}^{(\beta\gamma)} y_2^{(\beta)} + \boldsymbol{\sigma}_{(01)}^{(\beta\gamma)} y_3^{(\gamma)} \tag{14.8}$$

where $\bar{\boldsymbol{\sigma}}^{(\beta\gamma)}$ is the average stress in the subcell $(\beta\gamma)$ and $\boldsymbol{\sigma}_{(mn)}^{(\beta\gamma)}$ are higher-order stresses which can be directly expressed in terms of the stress moments defined by

$$\mathbf{S}_{(mn)}^{(\beta\gamma)} = \frac{1}{h_\beta l_\gamma}\int_{-h_\beta/2}^{h_\beta/2}\int_{-l_\gamma/2}^{l_\gamma/2}\boldsymbol{\sigma}^{(\beta\gamma)}(y_2^{(\beta)})^m(y_3^{(\gamma)})^n\, dy_2^{(\beta)}\, dy_3^{(\gamma)} \tag{14.9}$$

These moments were first employed in the original derivation of the HFGMC (see Aboudi et al. 2013). Hence, the present form of the stress vector is equivalent to the original derivation:

$$\boldsymbol{\sigma}_{(10)}^{(\beta\gamma)} = \frac{12}{h_\beta^2}\mathbf{S}_{(10)}^{(\beta\gamma)}, \quad \boldsymbol{\sigma}_{(01)}^{(\beta\gamma)} = \frac{12}{l_\gamma^2}\mathbf{S}_{(01)}^{(\beta\gamma)} \tag{14.10}$$

The strong form of the equilibrium equations $\nabla\cdot\boldsymbol{\sigma} = \mathbf{0}$ is satisfied in an average volumetric sense:

$$L_2\boldsymbol{\sigma}_{(10)}^{(\beta\gamma)} + L_3\boldsymbol{\sigma}_{(01)}^{(\beta\gamma)} = 0 \tag{14.11}$$

where $L_2$ and $L_3$ are given by the Boolean matrices:

$$L_2 = \begin{bmatrix} 0&0&0&1&0&0\\ 0&1&0&0&0&0\\ 0&0&0&0&0&1 \end{bmatrix}, \quad L_3 = \begin{bmatrix} 0&0&0&0&1&0\\ 0&0&0&0&0&1\\ 0&0&1&0&0&0 \end{bmatrix} \tag{14.12}$$

For the general case of a nonlinear material in the subcell $(\beta\gamma)$, the incremental form of its constitutive relation is given by

$$\Delta\boldsymbol{\sigma}^{(\beta\gamma)} = \mathbf{C}^{(\beta\gamma)}\Delta\boldsymbol{\epsilon}^{(\beta\gamma)} \tag{14.13}$$

where $\mathbf{C}^{(\beta\gamma)}$ is the instantaneous fourth-order tangent stiffness tensor that is defined based on the specific nonlinear material within the subcell.

The increment of the spatial stress polynomial is

$$\Delta\boldsymbol{\sigma}^{(\beta\gamma)} = \Delta\bar{\boldsymbol{\sigma}}^{(\beta\gamma)} + \Delta\boldsymbol{\sigma}^{(\beta\gamma)}_{(10)} y_2^{(\beta)} + \Delta\boldsymbol{\sigma}^{(\beta\gamma)}_{(01)} y_3^{(\gamma)} \tag{14.14}$$

The above incremental stress form can be expressed by the incremental strain given by Eq. (14.3). The last two relations can be identified by comparison with Eq. (14.14). Thus,

$$\begin{aligned}
\Delta\bar{\boldsymbol{\sigma}}^{(\beta\gamma)} &= \mathbf{C}^{(\beta\gamma)}\Delta\bar{\boldsymbol{\epsilon}} + \mathbf{C}^{(\beta\gamma)}P_{(10)}\Delta\mathbf{W}^{(\beta\gamma)}_{(10)} + \mathbf{C}^{(\beta\gamma)}P_{(01)}\Delta\mathbf{W}^{(\beta\gamma)}_{(01)} \\
\Delta\boldsymbol{\sigma}^{(\beta\gamma)}_{(10)} &= \mathbf{C}^{(\beta\gamma)}P_{(20)}\Delta\mathbf{W}^{(\beta\gamma)}_{(20)} \\
\Delta\boldsymbol{\sigma}^{(\beta\gamma)}_{(01)} &= \mathbf{C}^{(\beta\gamma)}P_{(02)}\Delta\mathbf{W}^{(\beta\gamma)}_{(02)}
\end{aligned} \tag{14.15}$$

where $\Delta\bar{\boldsymbol{\sigma}}^{(\beta\gamma)}$ is the incremental average stress in the subcell. These relations are employed in the equilibrium equations, Eq. (14.11), resulting into

$$L_2\mathbf{C}^{(\beta\gamma)}P_{(20)}\Delta\mathbf{W}^{(\beta\gamma)}_{(20)} + L_3\mathbf{C}^{(\beta\gamma)}P_{(02)}\Delta\mathbf{W}^{(\beta\gamma)}_{(02)} = 0 \tag{14.16}$$

An alternate compact form of the above equation can be written as

$$A^{(\beta\gamma)}_{2(20)}\Delta\mathbf{W}^{(\beta\gamma)}_{(20)} + A^{(\beta\gamma)}_{3(02)}\Delta\mathbf{W}^{(\beta\gamma)}_{(02)} = 0 \tag{14.17}$$

where

$$A^{(\beta\gamma)}_{i(mn)} \equiv L_i\mathbf{C}^{(\beta\gamma)}P_{(mn)}, \quad (mn) \neq (00) \tag{14.18}$$

and

$$A^{(\beta\gamma)}_{i(00)} \equiv L_i\mathbf{C}^{(\beta\gamma)} \tag{14.19}$$

Next, the traction and displacement continuity are imposed on an integral basis over the interfaces. Consider the two interfaces between the neighboring cells $(\beta\gamma)$ and $(\beta_1\gamma)$, and $(\beta\gamma)$ and $(\beta\gamma_1)$, where $\beta_1 = \beta+1$ and $\gamma_1 = \gamma+1$; the displacement continuity conditions are given by

$$\int_{-l_\gamma/2}^{l_\gamma/2} \left[ \mathbf{u}^{(\beta\gamma)}\big|_{y_2^{(\beta)}=-h_\beta/2} - \mathbf{u}^{(\beta_1\gamma)}\big|_{y_2^{(\beta_1)}=h_{\beta_1}/2} \right] dy_3^{(\gamma)} = \mathbf{0} \tag{14.20}$$

with $\beta = 1,\ldots,N_\beta - 1$ and $\gamma = 1,\ldots,N_\gamma$. Similarly, the displacement continuity at the interface whose normal is in the $y_3$-direction is

$$\int_{-h_\beta/2}^{h_\beta/2} \left[ \mathbf{u}^{(\beta\gamma)}\big|_{y_3^{(\gamma)}=l_\gamma/2} - \mathbf{u}^{(\beta\gamma_1)}\big|_{y_3^{(\gamma_1)}=-l_{\gamma_1}/2} \right] dy_2^{(\beta)} = \mathbf{0} \tag{14.21}$$

with $\beta = 1, \ldots, N_\beta$ and $\gamma = 1, \ldots, N_\gamma - 1$. The needed displacement periodicity conditions are

$$\int_{-l_\gamma/2}^{l_\gamma/2} \left[ \mathbf{u}^{(1\gamma)}|_{y_2^{(1)}=h_1/2} - \mathbf{u}^{(N_\beta\gamma)}|_{y_2^{(N_\beta)}=-h_{N_\beta}/2} \right] dy_3^{(\gamma)} = \mathbf{0} \tag{14.22}$$

with $\gamma = 1, \ldots, N_\gamma$.

$$\int_{-h_\beta/2}^{h_\beta/2} \left[ \mathbf{u}^{(\beta 1)}|_{y_3^{(1)}=-l_1/2} - \mathbf{u}^{(\beta N_\gamma)}|_{y_3^{(N_\gamma)}=l_{N_\gamma}/2} \right] dy_2^{(\beta)} = \mathbf{0} \tag{14.23}$$

with $\beta = 1, \ldots, N_\beta$.

The two traction continuity conditions are

$$\int_{-l_\gamma/2}^{l_\gamma/2} \left[ L_2\boldsymbol{\sigma}^{(\beta\gamma)}|_{y_2^{(\beta)}=-h_\beta/2} - L_2\boldsymbol{\sigma}^{(\beta_1\gamma)}|_{y_2^{(\beta_1)}=h_{\beta_1}/2} \right] dy_3^{(\gamma)} = \mathbf{0} \tag{14.24}$$

with $\beta = 1, \ldots, N_\beta - 1$ and $\gamma = 1, \ldots, N_\gamma$.

$$\int_{-h_\beta/2}^{h_\beta/2} \left[ L_3\boldsymbol{\sigma}^{(\beta\gamma)}|_{y_3^{(\gamma)}=l_\gamma/2} - L_3\boldsymbol{\sigma}^{(\beta\gamma_1)}|_{y_3^{(\gamma_1)}=-l_{\gamma 1}/2} \right] dy_2^{(\beta)} = \mathbf{0} \tag{14.25}$$

with $\beta = 1, \ldots, N_\beta$ and $\gamma = 1, \ldots, N_\gamma - 1$. The average traction periodicity conditions are

$$\int_{-l_\gamma/2}^{l_\gamma/2} \left[ L_2\boldsymbol{\sigma}^{(1\gamma)}|_{y_2^{(1)}=h_1/2} - L_2\boldsymbol{\sigma}^{(N_\beta\gamma)}|_{y_2^{(N_\beta)}=-h_{N_\beta}/2} \right] dy_3^{(\gamma)} = \mathbf{0} \tag{14.26}$$

with $\gamma = 1, \ldots, N_\gamma$.

$$\int_{-h_\beta/2}^{h_\beta/2} \left[ L_3\boldsymbol{\sigma}^{(\beta 1)}|_{y_3^{(1)}=-l_1/2} - L_3\boldsymbol{\sigma}^{(\beta N_\gamma)}|_{y_3^{(N_\gamma)}=l_{N_\gamma}/2} \right] dy_2^{(\beta)} = \mathbf{0} \tag{14.27}$$

with $\beta = 1, \ldots, N_\beta$. It should be emphasized that the periodicity relations, Eqs. (14.22)–(14.23) and (14.26)–(14.27), are satisfied by mirroring and extending the cells near the periodic interfaces as shown in Fig. 14.2. Therefore, Eqs. (14.20)–(14.21) and (14.24)–(14.25) are equivalent to the periodic relations by using the proposed mirroring technique. For example, the continuity equations can be applied to satisfy the periodicity conditions by simply performing the shifting operation: $(\beta = N_\beta + 1, \gamma) \Longrightarrow (1, \gamma)$. Thus, Eqs. (14.20)–(14.21) and Eqs. (14.24)–(14.25) can be applied using the outlined mirroring procedure to enforce the periodicity conditions as well.

The resulting four incremental displacement and traction continuity conditions, Eqs. (14.20)–(14.21) and Eqs. (14.24)–(14.25), can be expressed as

$$\left[\Delta \mathbf{W}^{(\beta\gamma)}_{(00)} - \frac{h_\beta}{2}\Delta \mathbf{W}^{(\beta\gamma)}_{(10)} + \frac{h_\beta^2}{4}\Delta \mathbf{W}^{(\beta\gamma)}_{(20)}\right] - \left[\Delta \mathbf{W}^{(\beta_1\gamma)}_{(00)} + \frac{h_{\beta_1}}{2}\Delta \mathbf{W}^{(\beta_1\gamma)}_{(10)} + \frac{h_{\beta_1}^2}{4}\Delta \mathbf{W}^{(\beta_1\gamma)}_{(20)}\right] = \mathbf{0} \quad (14.28)$$

$$\left[\Delta \mathbf{W}^{(\beta\gamma)}_{(00)} + \frac{l_\gamma}{2}\Delta \mathbf{W}^{(\beta\gamma)}_{(01)} + \frac{l_\gamma^2}{4}\Delta \mathbf{W}^{(\beta\gamma)}_{(02)}\right] - \left[\Delta \mathbf{W}^{(\beta\gamma_1)}_{(00)} - \frac{l_{\gamma_1}}{2}\Delta \mathbf{W}^{(\beta\gamma_1)}_{(01)} + \frac{l_{\gamma_1}^2}{4}\Delta \mathbf{W}^{(\beta\gamma_1)}_{(02)}\right] = \mathbf{0} \quad (14.29)$$

$$\left[\mathbf{A}^{(\beta\gamma)}_{2(10)}\Delta \mathbf{W}^{(\beta\gamma)}_{(10)} + \mathbf{A}^{(\beta\gamma)}_{2(01)}\Delta \mathbf{W}^{(\beta\gamma)}_{(01)} - \frac{h_\beta}{2}\mathbf{A}^{(\beta\gamma)}_{2(20)}\Delta \mathbf{W}^{(\beta\gamma)}_{(20)}\right] - \left[\mathbf{A}^{(\beta_1\gamma)}_{2(10)}\Delta \mathbf{W}^{(\beta_1\gamma)}_{(10)} + \mathbf{A}^{(\beta_1\gamma)}_{2(01)}\Delta \mathbf{W}^{(\beta_1\gamma)}_{(01)} + \frac{h_{\beta_1}}{2}\mathbf{A}^{(\beta_1\gamma)}_{2(20)}\Delta \mathbf{W}^{(\beta_1\gamma)}_{(20)}\right] = \left[\mathbf{A}^{(\beta_1\gamma)}_{2(00)} - \mathbf{A}^{(\beta\gamma)}_{2(00)}\right]\Delta\bar{\boldsymbol{\epsilon}} \quad (14.30)$$

$$\left[\mathbf{A}^{(\beta\gamma)}_{3(10)}\Delta \mathbf{W}^{(\beta\gamma)}_{(10)} + \mathbf{A}^{(\beta\gamma)}_{3(01)}\Delta \mathbf{W}^{(\beta\gamma)}_{(01)} + \frac{l_\gamma}{2}\mathbf{A}^{(\beta\gamma)}_{3(02)}\Delta \mathbf{W}^{(\beta\gamma)}_{(02)}\right] - \left[\mathbf{A}^{(\beta\gamma_1)}_{3(10)}\Delta \mathbf{W}^{(\beta\gamma_1)}_{(10)} + \mathbf{A}^{(\beta\gamma_1)}_{3(01)}\Delta \mathbf{W}^{(\beta\gamma_1)}_{(01)} - \frac{l_{\gamma_1}}{2}\mathbf{A}^{(\beta\gamma_1)}_{3(02)}\Delta \mathbf{W}^{(\beta\gamma_1)}_{(02)}\right] = \left[\mathbf{A}^{(\beta\gamma_1)}_{3(00)} - \mathbf{A}^{(\beta\gamma)}_{3(00)}\right]\Delta\bar{\boldsymbol{\epsilon}} \quad (14.31)$$

The overall vector of incremental variables of each $(\beta\gamma)$ subcell can be ordered as

$$\Delta \mathbf{X}^{(\beta\gamma)} \equiv \left\{\Delta \mathbf{W}_{(10)}, \Delta \mathbf{W}_{(01)}, \Delta \mathbf{W}_{(00)}, \Delta \mathbf{W}_{(20)}, \Delta \mathbf{W}_{(02)}\right\}^{(\beta\gamma)} \quad (14.32)$$

Figure 14.3 illustrates the common interfaces between a subcell $(\beta\gamma)$ and its neighboring subcells. As previously discussed, it is sufficient to consider the continuity conditions at the two interfaces $y_2 = h_\beta/2$ and $y_3 = l_\gamma/2$ (illustrated by bold lines in Fig. 14.3). Sweeping these two interfaces in the regular array of subcells yields writing all interface and periodic conditions of the entire RUC.

The incremental formulation previously carried out is due to the nonlinearity of the total form of the equations. This linearization procedure necessitates a consistent definition of a residual vector $\boldsymbol{R}^{(\beta\gamma)}$ for the corresponding total form of the governing equations. These are arranged in the following order: traction continuity, Eqs. (14.30)–(14.31), internal equilibrium equations for the cell, Eq. (14.17),

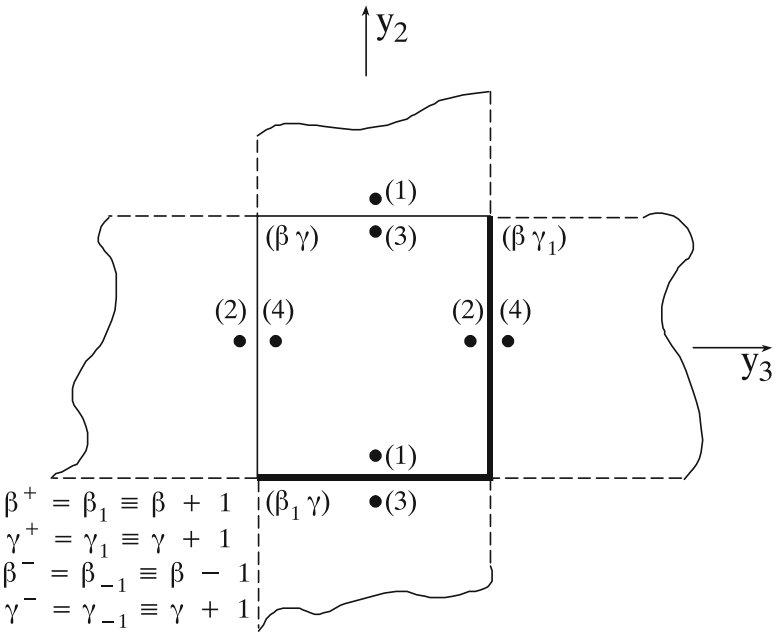


**Fig. 14.3** One-cell configuration with its neighboring cells showing its two primary "feed-forward" interfaces along with the location for the stress integration points

followed by the displacement continuity, Eqs. (14.28)–(14.29). The increment of the residual vector can be written for the above principal two interfaces in the form

$$\begin{aligned}\Delta \boldsymbol{R}^{(\beta\gamma)} &\equiv \left\{\Delta \mathbf{R}_{\sigma},\ \Delta \mathbf{R}_{E},\ \Delta \mathbf{R}_{u}\right\}^{(\beta\gamma)} \\ &= \mathbf{T}_1^{(\beta\gamma)}\Delta \mathbf{X}^{(\beta\gamma)} + \mathbf{T}_2^{(\beta_1\gamma)}\Delta \mathbf{X}^{(\beta_1\gamma)} + \mathbf{T}_3^{(\beta\gamma_1)}\Delta \mathbf{X}^{(\beta\gamma_1)} \\ &- \mathbf{D}_1^{(\beta\gamma)}\Delta \bar{\boldsymbol{\epsilon}} - \mathbf{D}_2^{(\beta_1\gamma)}\Delta \bar{\boldsymbol{\epsilon}} - \mathbf{D}_3^{(\beta\gamma_1)}\Delta \bar{\boldsymbol{\epsilon}}\end{aligned} \tag{14.33}$$

The matrix $\mathbf{T}_1^{(\beta\gamma)}$ operates on the incremental microvariable vector $\Delta \mathbf{X}^{(\beta\gamma)}$ and provides the incremental traction and displacement at the two interfaces within the cell $(\beta\gamma)$. Its structure is given by

$$\mathbf{T}_1^{(\beta\gamma)} = \begin{bmatrix} \mathbf{A}_{2(10)} & \mathbf{A}_{2(01)} & \mathbf{0} & -\frac{h_\beta}{2}\mathbf{A}_{2(20)} & \mathbf{0} \\ \mathbf{A}_{3(10)} & \mathbf{A}_{3(01)} & \mathbf{0} & \mathbf{0} & \frac{l_\gamma}{2}\mathbf{A}_{3(02)} \\ \mathbf{0} & \mathbf{0} & \mathbf{0} & \mathbf{A}_{2(20)} & \mathbf{A}_{3(02)} \\ -\frac{h_\beta}{2}\mathbf{I} & \mathbf{0} & \mathbf{I} & \frac{h_\beta^2}{4}\mathbf{I} & \mathbf{0} \\ \mathbf{0} & \frac{l_\gamma}{2}\mathbf{I} & \mathbf{I} & \mathbf{0} & \frac{l_\gamma^2}{4}\mathbf{I} \end{bmatrix}^{(\beta\gamma)} \tag{14.34}$$

Similarly, the matrices $\mathbf{T}_2^{(\beta_1\gamma)}$ and $\mathbf{T}_3^{(\beta\gamma_1)}$ operate on the incremental microvariable vectors $\Delta\mathbf{X}^{(\beta_1\gamma)}$ and $\Delta\mathbf{X}^{(\beta\gamma_1)}$ of the adjacent subcells, respectively. They provide the incremental traction and displacement on the other side of the two interfaces. The matrix $\mathbf{T}_3^{(\beta\gamma_1)}$ defines the incremental displacement and stress within the subcell $(\beta\gamma_1)$ needed to complete the continuity conditions at the common interface of the adjacent subcell $(\beta\gamma)$. These two matrices are of the form

$$\mathbf{T}_2^{(\beta_1\gamma)} = \begin{bmatrix} -\mathbf{A}_{2(10)} & -\mathbf{A}_{2(01)} & \mathbf{0} & -\frac{h_\beta}{2}\mathbf{A}_{2(20)} & \mathbf{0} \\ \mathbf{0} & \mathbf{0} & \mathbf{0} & \mathbf{0} & \mathbf{0} \\ \mathbf{0} & \mathbf{0} & \mathbf{0} & \mathbf{0} & \mathbf{0} \\ -\frac{h_\beta}{2}\mathbf{I} & \mathbf{0} & -\mathbf{I} & -\frac{h_\beta^2}{4}\mathbf{I} & \mathbf{0} \\ \mathbf{0} & \mathbf{0} & \mathbf{0} & \mathbf{0} & \mathbf{0} \end{bmatrix}^{(\beta_1\gamma)} \tag{14.35}$$

$$\mathbf{T}_3^{(\beta\gamma_1)} = \begin{bmatrix} \mathbf{0} & \mathbf{0} & \mathbf{0} & \mathbf{0} & \mathbf{0} \\ -\mathbf{A}_{3(10)} & -\mathbf{A}_{3(01)} & \mathbf{0} & \mathbf{0} & \frac{l_{\gamma 1}}{2}\mathbf{A}_{3(02)} \\ \mathbf{0} & \mathbf{0} & \mathbf{0} & \mathbf{0} & \mathbf{0} \\ \mathbf{0} & \mathbf{0} & \mathbf{0} & \mathbf{0} & \mathbf{0} \\ \mathbf{0} & \frac{l_{\gamma 1}}{2}\mathbf{I} & -\mathbf{I} & \mathbf{0} & -\frac{l_\gamma^2}{4}\mathbf{I} \end{bmatrix}^{(\beta\gamma_1)} \tag{14.36}$$

The $\mathbf{D}_i$ matrices provide the contribution of the applied global strain field to the local stress differences of the adjacent subcells that are connected to the two corresponding interfaces. The structures of the $\mathbf{D}_i$ matrices are given by

$$\mathbf{D}_1^{(\beta\gamma)} = \begin{bmatrix} -\mathbf{A}_{2(00)} \\ -\mathbf{A}_{3(00)} \\ 0 \\ 0 \\ 0 \\ 0 \end{bmatrix}^{(\beta\gamma)} \quad \mathbf{D}_2^{(\beta_1\gamma)} = \begin{bmatrix} \mathbf{A}_{2(00)} \\ 0 \\ 0 \\ 0 \\ 0 \\ 0 \end{bmatrix}^{(\beta_1\gamma)} \quad \mathbf{D}_3^{(\beta\gamma_1)} = \begin{bmatrix} 0 \\ \mathbf{A}_{3(00)} \\ 0 \\ 0 \\ 0 \\ 0 \end{bmatrix}^{(\beta\gamma_1)} \tag{14.37}$$

internal equilibrium equations for the cell, followed by the displacement continuity, Eqs. (14.28)–(14.29).

The incremental displacement continuity, Eqs. (14.28)–(14.29), and the equilibrium equations, Eq. (14.17), expressed in terms of the microvariables resulted in a set of homogeneous algebraic equations. This fact is useful for condensation purposes of the overall system of equations as will be shown later. The system of the incremental (tangential) governing equations is obtained by assembling the contributions of the repeated two-interface conditions from all the subcells. This is done by utilizing the derived forms given by Eq. (14.33). Figure 14.4 shows the contribution from the subcell $(\beta\gamma)$ to the RUC incremental coupled system of equations. The structure of the entire RUC vector of variables is

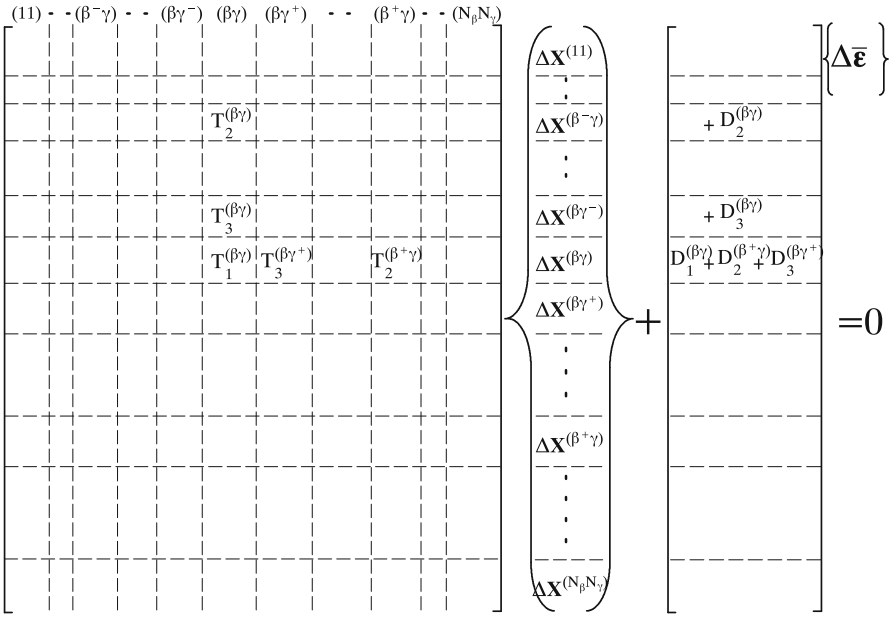


**Fig. 14.4** Overall tangential system of equations for the HFGMC-RUC model indicating the contribution of cell $(\beta\gamma)$ to the system and showing a row of complete equations for this cell

$$\Delta\mathbf{X} = \left\{ \Delta\mathbf{X}^{(11)}, \Delta\mathbf{X}^{(12)}, \ldots, \Delta\mathbf{X}^{(N_\beta N_\gamma)} \right\} \tag{14.38}$$

Alternatively, it is possible to collect the two-interface contributions to the governing system of equations (assembly) on a subcell-by-subcell basis. In this case, all indicted matrices will be solely computed from the subcells' stiffnesses and assembled on a column basis.

A dramatic reduction of the computational effort can be achieved by employing a local condensation procedure. To this end, the homogeneous and nonhomogeneous equations at the subcell level can be grouped into homogeneous and nonhomogeneous parts. This repartitioned system has the form

$$\begin{bmatrix} \mathbf{A}_{\sigma\sigma} & \mathbf{A}_{\sigma u} \\ \mathbf{A}_{u\sigma} & \mathbf{A}_{uu} \end{bmatrix} \begin{Bmatrix} \Delta\mathbf{X}_\sigma \\ \Delta\mathbf{X}_u \end{Bmatrix} = \begin{bmatrix} \mathbf{D} \\ \mathbf{0} \end{bmatrix} \{ \Delta\bar{\boldsymbol{\epsilon}} \} \tag{14.39}$$

The matrix $\mathbf{A}_{\sigma\sigma}$ is involved in the lumped traction continuity and the equilibrium equations. The matrix $\mathbf{A}_{uu}$ in Eq. (14.39) is part of the displacement continuity (homogeneous equations). On the other hand, the off-diagonal mixed terms $\mathbf{A}_{\sigma u}$ and $\mathbf{A}_{u\sigma}$ emerge from repartitioning the system of equations. The vector of variables can then be partitioned into two corresponding parts: $\Delta\mathbf{X}_\sigma$ and $\Delta\mathbf{X}_u$.

The solution for the entire RUC system can be represented symbolically as

$$\Delta \mathbf{X} = \mathbf{A}^{-1}\mathbf{D}\Delta\bar{\boldsymbol{\epsilon}} \equiv \hat{\mathbf{D}}\Delta\bar{\boldsymbol{\epsilon}} \tag{14.40}$$

where the above left-hand-side square matrix $\mathbf{A}$ has the dimension $15N_\beta N_\gamma \times 15N_\beta N_\gamma$ in a non-condensed form, i.e., with no microvariable equivalences performed between adjacent interfaces for problem size reduction. Alternately, by performing a simple condensation procedure, the dimension of the reduced system is $6N_\beta N_\gamma \times 6N_\beta N_\gamma$.

The RUC effective tangential stiffness matrix for the periodic composite medium defines the effective incremental stress–strain relation $\Delta\bar{\boldsymbol{\sigma}} = \mathbf{C}^*\Delta\bar{\boldsymbol{\epsilon}}$. It can be obtained from the RUC solution for the microvariables in Eq. (14.39). This solution, in turn, allows determining the influence matrices $\mathbf{B}^{(\beta\gamma)}$ for each subcell that relate the incremental form of Eqs. (14.5)–(14.7). The needed matrices $\hat{\mathbf{D}}^{(\beta\gamma)}_{(10)}$ and $\hat{\mathbf{D}}^{(\beta\gamma)}_{(01)}$ can be identified from $\hat{\mathbf{D}}$ in Eq. (14.40) which can be partitioned as follows:

$$\hat{\mathbf{D}}^{(\beta\gamma)} = \begin{bmatrix} \hat{\mathbf{D}}_{(10)} \\ \hat{\mathbf{D}}_{(01)} \\ \hat{\mathbf{D}}_{(00)} \\ \hat{\mathbf{D}}_{(20)} \\ \hat{\mathbf{D}}_{(02)} \end{bmatrix}^{(\beta\gamma)} \tag{14.41}$$

Consequently, the effective tangential stiffness of the composite at each strain level can be readily evaluated as follows:

$$\mathbf{C}^* = \frac{1}{HL}\sum_{\beta=1}^{N_\beta}\sum_{\gamma=1}^{N_\gamma} h_\beta l_\gamma \mathbf{C}^{(\beta\gamma)}\mathbf{B}^{(\beta\gamma)} \equiv \sum_{\beta=1}^{N_\beta}\sum_{\gamma=1}^{N_\gamma} h_\beta l_\gamma \mathbf{B}^{T(\beta\gamma)}\mathbf{C}^{T(\beta\gamma)} \tag{14.42}$$

which shows the symmetry of the stiffness of the composite.

The contribution to the overall RUC residual vector from a characteristic subcell $(\beta\gamma)$ needs to be defined. This is an important aspect of any nonlinear iterative solution method of the RUC nonlinear system of equations. The residual vector is composed from the total (rather than incremental) interfacial displacements, equilibrium, and traction conditions. It is evaluated at each iteration from the trial microvariables. These field variables are evaluated at both sides of the neighboring cells as illustrated in Fig. 14.3. The locations of the numerical integration points are indicated by the solid circles. It should be noted that the displacement residuals are explicitly zero and can be used for condensation of the microvariables (unknowns). The contribution to the residual vector from subcell $(\beta\gamma)$ is given by

$$\mathbf{R}^{(\beta\gamma)} = \begin{bmatrix} \int [L_2\boldsymbol{\sigma}^{(\beta\gamma)} - L_2\boldsymbol{\sigma}^{(\beta_1\gamma)}]dy_3^{(\gamma)} \\ \int [L_3\boldsymbol{\sigma}^{(\beta\gamma)} - L_3\boldsymbol{\sigma}^{(\beta\gamma_1)}]dy_2^{(\beta)} \\ L_2\boldsymbol{\sigma}^{(\beta\gamma)}_{(10)} - L_3\boldsymbol{\sigma}^{(\beta\gamma)}_{(01)} \\ 0 \\ 0 \end{bmatrix} \longrightarrow \begin{bmatrix} L_2\boldsymbol{\sigma}^{(\beta\gamma)_1} - L_2\boldsymbol{\sigma}^{(\beta_1\gamma)_3} \\ L_3\boldsymbol{\sigma}^{(\beta\gamma)_2} - L_3\boldsymbol{\sigma}^{(\beta\gamma_1)_4} \\ L_2\boldsymbol{\sigma}^{(\beta\gamma)}_{(10)} - L_3\boldsymbol{\sigma}^{(\beta\gamma)}_{(01)} \\ 0 \\ 0 \end{bmatrix} \tag{14.43}$$

where the first two rows define the traction continuities in a total form, whereas the third row stands for the total form of the equilibrium equations in the subcell. The last equality of Eq. (14.43) expresses the transition from the mathematical definition of the residual vector to its numerical form. The higher-order stress terms are derived from the total stresses evaluated at the numerical integration points:

$$\boldsymbol{\sigma}_{(10)}^{(\beta\gamma)} = \frac{1}{h_\beta}\left(\boldsymbol{\sigma}^{(\beta\gamma)_3} - \boldsymbol{\sigma}^{(\beta\gamma)_2}\right); \quad \boldsymbol{\sigma}_{(01)}^{(\beta\gamma)} = \frac{1}{l_\gamma}\left(\boldsymbol{\sigma}^{(\beta\gamma)_2} - \boldsymbol{\sigma}^{(\beta\gamma)_4}\right) \tag{14.44}$$

The subcell's contribution to the residual vector, $\mathbf{R}^{(\beta\gamma)}$, is used in the process of assembling the overall residual vector of the HFGMC-RUC model $\mathbf{R}_{HFGMC}$ given by

$$\mathbf{R}_{HFGMC} = \left\{\mathbf{R}^{(11)}, .., \mathbf{R}^{(\beta\gamma)}, .., \mathbf{R}^{(N_\beta N_\gamma)}\right\} \tag{14.45}$$

The iterative solution technique (e.g., Newton–Raphson) aims to minimize the residual vector where the exact solution should yield each term to zero. This is numerically satisfied by requiring that residual norm to be sufficiently small. In addition, another cycle of iterations may be needed in the case where a mixed remote stress and strain combination is applied (e.g., a uniaxial transverse loading defined by $\bar{\epsilon}_{22} \neq 0$ and $\bar{\sigma}_{ij} = 0$ for all other components). In this case, an additional global residual vector, $\mathbf{R}_G$, must be introduced (for the above uniaxial transverse loading, $\mathbf{R}_G = \{\bar{\sigma}_{11}, \bar{\sigma}_{33}, \bar{\sigma}_{23}, \bar{\sigma}_{13}, \bar{\sigma}_{12}\}$). Thus, two separate conditions for the residual vectors, $\mathbf{R}_G = \mathbf{0}$ and $\mathbf{R}_{HFGMC} = \mathbf{0}$, should be satisfied simultaneously at each incremental loading.

## 14.3 Nonlinear Doubly Periodic Parametric HFGMC Formulation

In this section, the governing equations of doubly periodic parametric HFGMC are presented (Levi-Sasson et al. 2015). They form a special case of the general triply periodic equations that are presented in the next section.

Consider a doubly periodic composite described with respect to global coordinates $x_2$ and $x_3$ (see Fig. 14.5a). A RUC is identified which is described with respect to local coordinates $y_2$ and $y_3$ as shown in Fig. 14.5b. The RUC is discretized into an arbitrary number of subcells as illustrated in Fig. 14.5c. The micromechanical analysis of triply periodic composites has been presented by Haj-Ali and Aboudi (2013). Presently, the corresponding analysis for doubly periodic composites is summarized in the following. A characteristic subcell is shown in Fig. 14.5d. The parametric doubly periodic HFGMC-2D is formulated in the parent $(r, s)$ domain, Fig. 14.5e, in which a subcell is represented by a square shape with boundaries located between $-1 \leq r, s \leq 1$. A linear transformation from the parent domain $(r, s)$ to the physical domain $(y_2, y_3)$ can be selected to define this mapping:

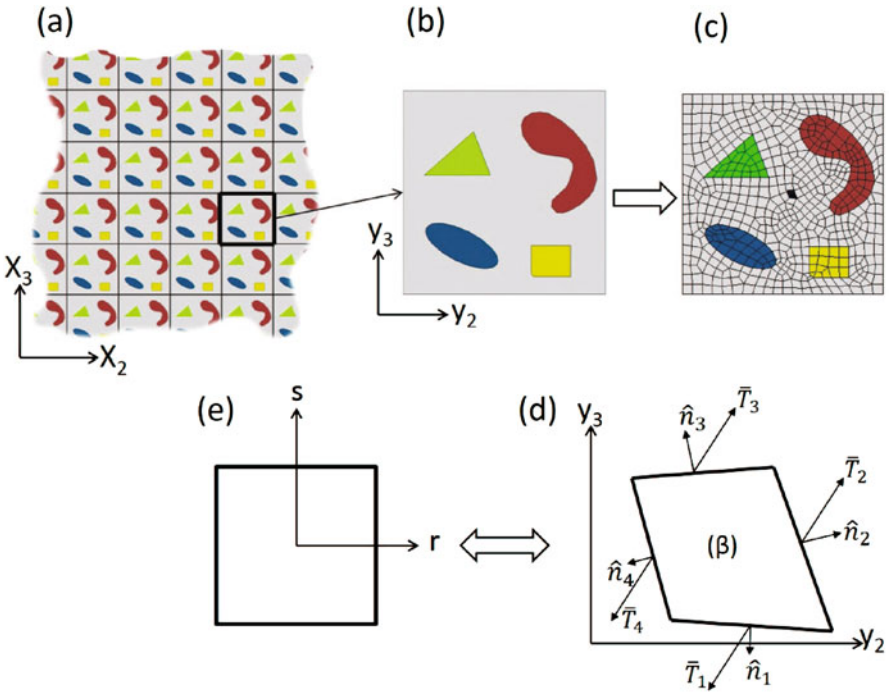


**Fig. 14.5** Schematic representation of doubly periodic composite. (**a**) A RUC can be identified and (**b**) isolated. (**c**) A RUC is divided into subcells. The mapping of a subcell from the physical to the parametrical coordinate system is illustrated in (**d**), and (**e**) $\bar{\boldsymbol{T}}_i$ and $\widehat{n}_i$ are the traction applied on face i and its normal vector, respectively

$$y_i(r,s) = \sum_{k=1}^{4} H_k(r,s) y_i^{(k)} \tag{14.46}$$

$$H_1 = \frac{1}{4}(1-r)(1-s), \quad H_2 = \frac{1}{4}(1+r)(1-s)$$

$$H_3 = \frac{1}{4}(1+r)(1+s), \quad H_4 = \frac{1}{4}(1-r)(1+s)$$

where $k$ indicates a corner of a subcell, $r$ and $s$ are the uniform parametric coordinate system of the parent domain, and $y_i^{(k)}$ is the coordinate of the $k$th corner in the physical domain. The Jacobian is defined by

$$\boldsymbol{J} = \begin{vmatrix} \dfrac{\partial y_2}{\partial r} & \dfrac{\partial y_3}{\partial r} \\ \dfrac{\partial y_2}{\partial s} & \dfrac{\partial y_3}{\partial s} \end{vmatrix} \tag{14.47}$$

While a 2D geometry of the doubly periodic medium is used, a three-dimensional displacement polynomial is defined for each subcell as follows (Haj-Ali and Aboudi 2013):

$$\begin{aligned}\mathbf{u} = \boldsymbol{\epsilon}^0 \cdot \mathbf{x} + \mathbf{W}_0 + \frac{1}{2}(\mathbf{W}_2 - \mathbf{W}_4)r + \frac{1}{2}(\mathbf{W}_3 - \mathbf{W}_1)s \\ + \frac{1}{4}(\mathbf{W}_2 + \mathbf{W}_4 - 2\mathbf{W}_0)(3r^2 + rs - 1) \\ + \frac{1}{4}(\mathbf{W}_1 + \mathbf{W}_3 - 2\mathbf{W}_0)(3s^2 + rs - 1)\end{aligned} \tag{14.48}$$

where $\mathbf{W}_i$ are micromechanical unknowns to be determined in the following. In this equation, the expression for the displacement $\boldsymbol{\epsilon}^0 \cdot \mathbf{x}$ includes the remote strain field applied on the composite, $\mathbf{W}_0$ can be associated with a center microvariable, and $\mathbf{W}_i$ $(i = 1, 2, 3, 4)$ are directly related to the average displacement of the $i$th subcell face. It should be emphasized that the micromechanical unknowns (microvariables) are related to the faces of the subcells. This allows, in part, to reduce the computing effort of solving the resulting set of equations.

The HFGMC enforces displacement and traction continuity in an average manner on the faces between adjacent subcells. To that goal, the displacement and traction are averaged on each face in every subcell. These averages are determined by integration over a face path. Thus, the average displacement $\bar{\boldsymbol{u}}^{(\beta_k)}$ of the $k$th face in subcell $\beta$ is given by

$$\bar{\boldsymbol{u}}^{(\beta_k)} = \frac{1}{l_k}\int_{l_k} \boldsymbol{u}^{(\beta)}(\boldsymbol{y})dl_k = \frac{1}{2}\int_{-1}^{1} \boldsymbol{u}^{(\beta)}(\xi_k)d\xi_k, \quad k = 1, 2, 3, 4 \tag{14.49}$$

where $l_k$ indicates the path of the $k$th face in the physical domain and $\xi_k$ denotes the integration variable along the $k$th face in the parent domain. By performing this integration, the following relations are obtained:

$$\begin{aligned}\bar{\boldsymbol{u}}^{(\beta_1)} &= \mathbf{W}_1^{(\beta)}, \quad \bar{\boldsymbol{u}}^{(\beta_2)} = \mathbf{W}_2^{(\beta)} \\ \bar{\boldsymbol{u}}^{(\beta_3)} &= \mathbf{W}_3^{(\beta)}, \quad \bar{\boldsymbol{u}}^{(\beta_4)} = \mathbf{W}_4^{(\beta)}\end{aligned} \tag{14.50}$$

The expression for the average traction $\bar{\boldsymbol{T}}^{(\beta_k)}$ on the $k$th face of a subcell $\beta$, following from the definition of the traction $\boldsymbol{T} = \boldsymbol{\sigma} \cdot \boldsymbol{n}$, is

$$\bar{\boldsymbol{T}}^{(\beta_k)} = \frac{1}{l_k}\int_{l_k} \boldsymbol{\sigma}^{(\beta)}(\boldsymbol{y}) \cdot \boldsymbol{n}^{(\beta_k)}dl_k = \frac{1}{2}\int_{-1}^{1} \boldsymbol{\sigma}^{(\beta)}(r, s) \cdot \boldsymbol{n}^{(\beta_k)}d\xi_k, \quad k = 1, 2, 3, 4 \tag{14.51}$$

where $\boldsymbol{\sigma}^{(\beta)}$ is the stress field within subcell $\beta$ and $n^{(\beta_k)}$ is the normal vector to the $k$th face. Traction vectors and normal vectors are schematically illustrated in Fig. 14.5d.

The strain components in a subcell are given as a sum of the remote strain $\epsilon_{ij}^0$ applied on the RUC and local strains:

$$\boldsymbol{\epsilon}_{ij}^{(\beta)}(\boldsymbol{y}(r,s)) = \epsilon_{ij}^0 + \frac{1}{2}\left(\frac{\partial u_i}{\partial y_j} + \frac{\partial u_j}{\partial y_i}\right) \tag{14.52}$$

Substituting Eq. (14.48) into (14.52) results in

$$\boldsymbol{\epsilon}^{(\beta)} = \boldsymbol{\epsilon}^0 + \boldsymbol{A}^{(\beta)}\boldsymbol{W}^{(\beta)} \tag{14.53}$$

where $\boldsymbol{W}^{(\beta)}$ is the vector of the micromechanical unknowns of subcell $\beta$, also termed as microvariables. By applying contracted notation, the dimensions of $\boldsymbol{\epsilon}^{(\beta)}$, $\boldsymbol{\epsilon}^{(0)}$, $\boldsymbol{W}^{(\beta)}$, and $\boldsymbol{A}^{(\beta)}$ are $6 \times 1$, $6 \times 1$, $15 \times 1$, and $6 \times 15$, respectively. It should be noted that the coefficient matrix $\boldsymbol{A}^{(\beta)}$ includes data about the geometry and the elements of the Jacobian of the transformation.

The linear stress–strain relation for a material within a subcell is governed by Hooke's law $\boldsymbol{\sigma}^{(\beta)} = \boldsymbol{C}^{(\beta)}\boldsymbol{\epsilon}^{(\beta)}$, with $\boldsymbol{C}^{(\beta)}$ being the stiffness matrix of the material. It follows from Eqs. (14.53) and (14.51) that the average traction can be expressed in the form

$$\bar{\boldsymbol{T}}^{(\beta_k)} = \frac{1}{2}\int_{-1}^{1} \boldsymbol{N}^{(\beta_k)}\boldsymbol{C}^{(\beta)}\left[\boldsymbol{\epsilon}^0 + \boldsymbol{A}^{(\beta)}\boldsymbol{W}^{(\beta)}\right] d\xi_k = \boldsymbol{N}^{(\beta_k)}\boldsymbol{C}^{(\beta)}\left[\boldsymbol{\epsilon}^0 + \bar{\boldsymbol{A}}^{(\beta_k)}\boldsymbol{W}^{(\beta)}\right] \tag{14.54}$$

where the matrix $\boldsymbol{N}^{(\beta_k)}$ is composed of the components of the normal to the $k$th face of subcell $\beta$ which is given as follows:

$$\boldsymbol{N}^{(\beta_k)} = \begin{bmatrix} 0 & 0 & 0 & 0 & n_3 & n_2 \\ 0 & n_2 & 0 & n_3 & 0 & 0 \\ 0 & 0 & n_3 & n_2 & 0 & 0 \end{bmatrix}^{(\beta_k)} \tag{14.55}$$

and $\bar{\boldsymbol{A}}^{(\beta_k)}$ is defined by

$$\bar{\boldsymbol{A}}^{(\beta_k)} = \frac{1}{2}\int_{-1}^{1} \boldsymbol{A}^{(\beta)} d\xi_k \tag{14.56}$$

The displacement and traction continuity conditions are imposed in an average manner along the interface of adjacent subcells. As to the periodicity of displacement and traction, they are implemented at two matched subcells at the opposite sides of the RUC. Thus, the continuity and periodicity equations are given by

$$\begin{aligned} \bar{\boldsymbol{u}}^{(\beta_k)} &= \bar{\boldsymbol{u}}^{(\gamma_m)} \\ \bar{\boldsymbol{T}}^{(\beta_k)} &= \bar{\boldsymbol{T}}^{(\gamma_m)} \end{aligned} \tag{14.57}$$

In the current parametric implementation, imposing the periodicity conditions requires identical distribution of subcells along the opposite sides of the RUC. This requirement is not a limitation since periodicity is an inherent property of the HFGMC due to the periodic microstructure character of the composite.

Another set of equations is obtained by enforcing the equilibrium equations in the average sense, on each subcell, which yield

$$\int_S \nabla \cdot \boldsymbol{\sigma}^{(\beta)} dS = \int_l \boldsymbol{\sigma}^{(\beta)} \cdot \boldsymbol{n} dl = \sum_{k=1}^{4} \int_{l_k} \boldsymbol{N}^{(\beta_k)} \boldsymbol{\sigma}^{(\beta)} dl_k = \sum_{k=1}^{4} l_k \bar{\boldsymbol{T}}^{(\beta_k)} = \boldsymbol{0} \tag{14.58}$$

The total number of unknown components in $\boldsymbol{W}$ is 15 times the number of subcells $N_{sc}$. For each subcell, only two faces contribute independent sets of equations. Therefore, displacement, traction continuity, and periodicity provide $2\times 3N_{sc}$ equations. The equilibrium equations provide $3N_{sc}$ independent relations. In summary, the total number of equations is $15N_{sc}$ and it is equal to the total number of unknowns for the general case where no static condensation of the microvariables is carried out.

The overall set of equations can be represented in the form

$$\boldsymbol{A}\boldsymbol{W} = \boldsymbol{D}\boldsymbol{\epsilon}^{\boldsymbol{0}} \tag{14.59}$$

where $\boldsymbol{A}$ is a sparse matrix of size $15N_{sc}\times 15N_{sc}$ and $\boldsymbol{D}$ is a matrix of size of $15N_{sc}\times 6$ that relate the external remote strain to the traction and equilibrium equations.

Equation (14.59) can be arranged as follows:

$$\begin{bmatrix} \bar{\boldsymbol{u}}^{(\beta_k)} - \bar{\boldsymbol{u}}^{(\gamma_m)} \\ \bar{\boldsymbol{T}}^{(\beta_k)} - \bar{\boldsymbol{T}}^{(\gamma_m)} \\ \nabla \cdot \boldsymbol{\sigma}^{(\beta)} \end{bmatrix} \begin{Bmatrix} \boldsymbol{W}^1 \\ \vdots \\ \boldsymbol{W}^{N_{sc}} \end{Bmatrix} = \begin{bmatrix} \boldsymbol{0} \\ \boldsymbol{D}_{trac} \\ \boldsymbol{D}_{eq} \end{bmatrix} \boldsymbol{\epsilon}^{\boldsymbol{0}} \tag{14.60}$$

where $\boldsymbol{D}_{trac}$ and $\boldsymbol{D}_{eq}$ are the appropriate decomposition of $\boldsymbol{D}$. In this formulation, the part with the homogeneous equations expresses the interface displacement continuity. A further look at Eqs. (14.50) and (14.57) allows the static condensation of the face displacement microvariables' continuity on both sides of the shared faces. Therefore, the reduced number of unknowns is decreased to $9N_{sc}$ which significantly decreases the computational effort.

Once the set of equations of the HFGMC is solved for the microvariables, the strain concentration tensor $\boldsymbol{G}^{(\beta)}$ can be readily established. This concentration tensor relates the external remote strain $\boldsymbol{\epsilon}^0$, applied on the composite, to the local average strain $\bar{\boldsymbol{\epsilon}}^{(\beta)}$ within subcell $\beta$:

$$\begin{aligned} \bar{\boldsymbol{\epsilon}}^{(\beta)} &= \frac{1}{S_\beta} \int_{S_\beta} \boldsymbol{\epsilon}(\boldsymbol{y}) dS = \boldsymbol{\epsilon}^0 + \frac{1}{2S_\beta} \int_{S\beta} \left( \nabla_{\boldsymbol{y}} \boldsymbol{u} + \boldsymbol{u} \nabla_{\boldsymbol{y}} \right) dS \\ &= \boldsymbol{\epsilon}^0 + \frac{1}{2S_\beta} \int_l \left( \boldsymbol{u} \otimes \boldsymbol{n} + \boldsymbol{n} \otimes \boldsymbol{u} \right) dl = \boldsymbol{\epsilon}^0 + \frac{1}{2S_\beta} \sum_{k=1}^{4} l_k \left( \bar{\boldsymbol{u}} \otimes \boldsymbol{n} + \boldsymbol{n} \otimes \bar{\boldsymbol{u}} \right)^{(\beta_k)} \\ &\equiv \boldsymbol{G}^{(\beta)} : \boldsymbol{\epsilon}^0 \end{aligned} \tag{14.61}$$

where $S_\beta$ is the surface area of subcell $\beta$, $\boldsymbol{u}$ is the displacement field, and $\boldsymbol{n}$ is the normal to the perimeter $l$.

The effective RUC stiffness matrix $\boldsymbol{C}^*$ that relates between the global average stress and strain can be determined from

$$\boldsymbol{C}^* = \frac{1}{S_{total}} \sum_{\beta=1}^{N_{sc}} S_\beta \boldsymbol{C}^{(\beta)} \boldsymbol{G}^{(\beta)} \tag{14.62}$$

where $S_{total}$ is the total area of the RUC and $\boldsymbol{C}^{(\beta)}$ is the local stiffness matrix of subcell $\beta$.

## 14.4 Nonlinear Triply Periodic Parametric HFGMC Formulation

The parametric HFGMC method is cast herein in its most general 3D form with nonlinear formulation. The previous doubly periodic parametric HFGMC can be shown to be a special case of the current generalization. The parametric HFGMC presently developed is well suited for nonlinear and damage behaviors as shown by Haj-Ali and Aboudi (2016). Figure 14.6 is used to schematically illustrate a general triply periodic multiphase heterogeneous material. A global Cartesian coordinate system $(x_1, x_2, x_3)$ is used for the periodic composite. A 3D repeating unit cell (RUC) can be identified and described by using the local coordinate system $(y_1, y_2, y_3)$. In the parametric HFGMC theory, the RUC can be divided into an arbitrary 3D array of hexahedral cells, often denoted as subcells. Figure 14.6 shows the RUC domain which is discretized into a general assembly of hexahedral subcells to represent the different phase geometries. The current formulation extends the linear parametric HFGMC formulation (Haj-Ali and Aboudi, 2010, 2013) to analyze nonlinear RUC of triply periodic composites. Figure 14.7 shows a one general hexahedral subcell isolated in its physical coordinates $(y_1, y_2, y_3)$. This subcell is mapped to a uniform parametric coordinate system $(r, s, t)$:

$$y_i(r, s, t) = \sum_{k=1}^{8} H_k(r, s, t) y_{ki}, \qquad i = 1, 2, 3 \tag{14.63}$$

where $y_i$, $i = 1, 2, 3$, are the coordinates of a general point within the subcell $(\beta)$ mapped from the parent parametric coordinates to the physical RUC coordinates. The coordinates $y_{ki}$ are located at the corners (vertices) of the subcell. The parametric geometric transformation is considered independent from the displacement field and can be linear or quadratic.

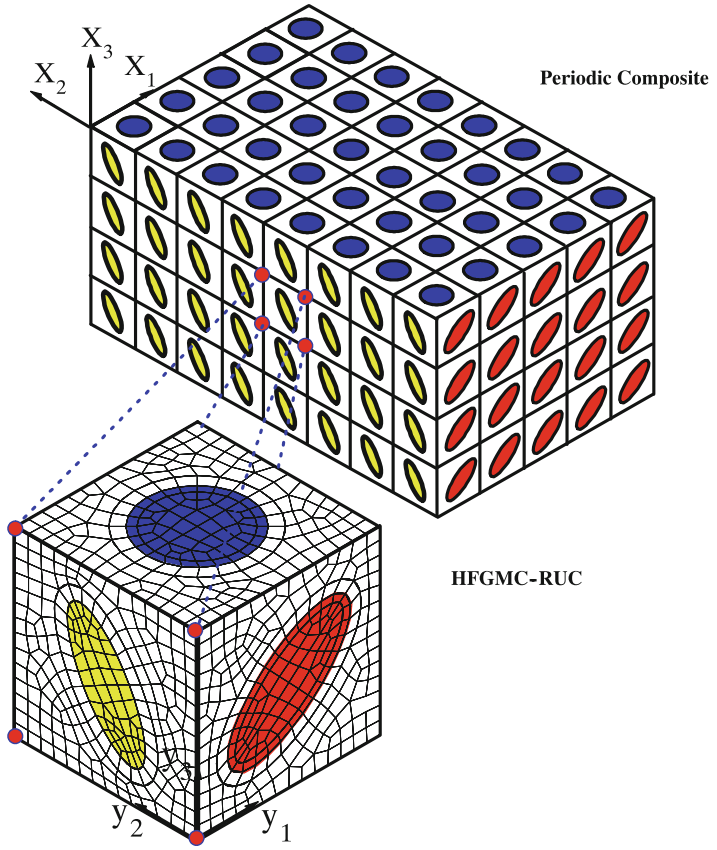


**Fig. 14.6** Schematic illustration of a triply periodic array in the global $(X_1, X_2, X_3)$ space of a multiphase composite with its repeating unit cell (RUC) having arbitrary-shaped hexahedral subcells, defined with respect to its $(y_1, y_2, y_3)$ local coordinate system

In the present HFGMC-3D formulation, the complete quadratic form of the displacement expansion in the subcell is given by

$$\mathbf{u} = \mathbf{u}^0 + \mathbf{W}_{000} + \mathbf{W}_{100}r + \mathbf{W}_{010}s + \mathbf{W}_{001}t + \mathbf{W}_{110}rs + \mathbf{W}_{101}rt + \mathbf{W}_{011}st + \frac{1}{2}\mathbf{W}_{200}(3r^2 - 1) + \frac{1}{2}\mathbf{W}_{020}(3s^2 - 1) + \frac{1}{2}\mathbf{W}_{002}(3t^2 - 1) \tag{14.64}$$

where the applied remote global-scale displacement field is given by $\boldsymbol{u}^0 \equiv \boldsymbol{\epsilon}^0 \cdot \mathbf{x}$ or $\boldsymbol{u}^0 \equiv \boldsymbol{u}^0_{ij} \cdot \mathbf{x}$.

This full quadratic expansion was initially used by Haj-Ali and Aboudi (2010) in the case of a general parametric HFGMC for doubly periodic composites. Knowing that the bilinear terms did not contribute to the subcell average displacements at the surfaces, Haj-Ali and Aboudi (2010) treated these bilinear terms as internal

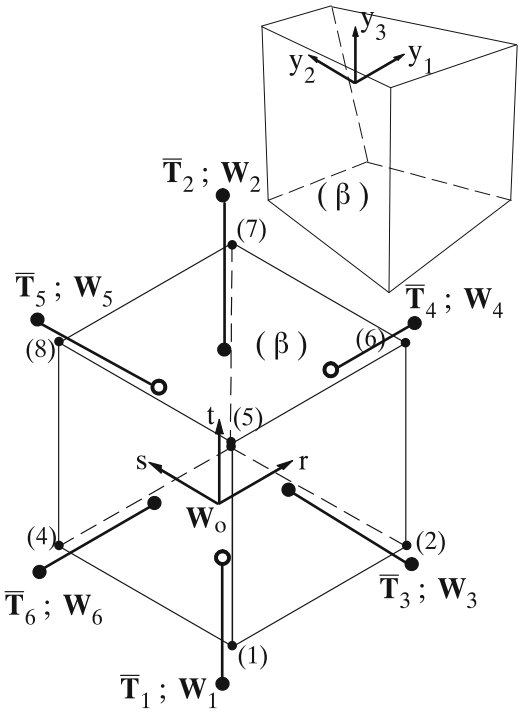


**Fig. 14.7** A hexahedral-shaped subcell in its physical and natural coordinates. The numbering for the faces are shown. The average traction and displacement vectors for each face are illustrated

subcell variables that can be determined with the help of average moments of equilibrium equations. Later, Haj-Ali and Aboudi (2013) defined the bilinear terms as internal dependent variables by two alternate solution cases, the first by completely eliminating these terms from the polynomial expansion, denoted as the trivial case:

$$\boldsymbol{W}_{110} = \boldsymbol{W}_{011} = \boldsymbol{W}_{101} = \boldsymbol{0} \tag{14.65}$$

The second nontrivial solution case can also be obtained to preserve the polynomial symmetry and frame indifference, yet retaining the complete quadratic expansion. Consequently, this nontrivial case is expressed by

$$\begin{aligned} \boldsymbol{W}_{110} &= \frac{1}{2}\left(\boldsymbol{W}_{200} + \boldsymbol{W}_{020}\right) \\ \boldsymbol{W}_{011} &= \frac{1}{2}\left(\boldsymbol{W}_{020} + \boldsymbol{W}_{002}\right) \\ \boldsymbol{W}_{101} &= \frac{1}{2}\left(\boldsymbol{W}_{200} + \boldsymbol{W}_{002}\right) \end{aligned} \tag{14.66}$$

Therefore, the displacement expansion of the parametric HFGMC in the general 3D case has the form

$$\begin{aligned}\mathbf{u} = \boldsymbol{u}^0 + \mathbf{W}_0 + \frac{1}{2}(\boldsymbol{W}_4 - \boldsymbol{W}_6)\, r + \frac{1}{2}(\boldsymbol{W}_5 - \boldsymbol{W}_3)\, s + \frac{1}{2}(\boldsymbol{W}_2 - \boldsymbol{W}_1)\, t \\ + \frac{1}{4}(\boldsymbol{W}_4 + \boldsymbol{W}_6 - 2\boldsymbol{W}_0)\left(3r^2 + rs + rt - 1\right) \\ + \frac{1}{4}(\boldsymbol{W}_3 + \boldsymbol{W}_5 - 2\boldsymbol{W}_0)\left(3s^2 + rs + st - 1\right) \\ + \frac{1}{4}(\boldsymbol{W}_1 + \boldsymbol{W}_2 - 2\boldsymbol{W}_0)\left(3t^2 + rt + st - 1\right)\end{aligned} \tag{14.67}$$

The above form can be exclusively expressed in terms of the face-average displacement vectors at the six subcell faces, $\boldsymbol{W}_k, k = 1..6$, and one internal displacement variable, $\boldsymbol{W}_0$ (see Haj-Ali and Aboudi 2013, 2016). Hence, Eq. (14.67) is derived from Eq. (14.64) by using Eq. (14.66) and

$$\begin{aligned}\boldsymbol{W}_{000} &= \boldsymbol{W}_7 \\ \boldsymbol{W}_{100} &= \frac{1}{2}(\boldsymbol{W}_4 - \boldsymbol{W}_6) \\ \boldsymbol{W}_{010} &= \frac{1}{2}(\boldsymbol{W}_5 - \boldsymbol{W}_3) \\ \boldsymbol{W}_{001} &= \frac{1}{2}(\boldsymbol{W}_2 - \boldsymbol{W}_4) \\ \boldsymbol{W}_{200} &= \frac{1}{2}(\boldsymbol{W}_4 + \boldsymbol{W}_6 - 2\boldsymbol{W}_7) \\ \boldsymbol{W}_{020} &= \frac{1}{2}(\boldsymbol{W}_3 + \boldsymbol{W}_5 - 2\boldsymbol{W}_7) \\ \boldsymbol{W}_{002} &= \frac{1}{2}(\boldsymbol{W}_1 + \boldsymbol{W}_2 - 2\boldsymbol{W}_7)\end{aligned} \tag{14.68}$$

The six subcell face-average total displacement vectors are expressed by

$$\begin{aligned}\bar{\boldsymbol{u}}^{(\beta_k)} &\equiv \frac{1}{A_k}\int_{A_k} \boldsymbol{u}^{(\beta)}(\mathbf{y})\, dA_k \\ &= \frac{1}{4}\int_{-1}^{1}\int_{-1}^{1} \boldsymbol{u}^{(\beta)}(\xi_k, \eta_k)\, d\xi_k d\eta_k = \bar{\boldsymbol{u}}^{0,(\beta_k)} + W_k, \quad k = 1, 2, .., 6\end{aligned} \tag{14.69}$$

where $(\xi_k,\eta_k)$ are the surface parametric integration variables of the $k$th edge, denoted by $(\beta_k)$.

In order to establish expressions for the spatial displacement gradients and the strain or stress components, the displacement gradients with respect to the physical coordinates $\boldsymbol{y}$ are derived using the inverse Jacobian of the parametric geometry, Eq. (14.63), defined by

$$\boldsymbol{J} \equiv \frac{\partial\left(y_1, y_2, y_3\right)}{\partial\left(r, s, t\right)} = \begin{bmatrix} \frac{\partial y_1}{\partial r} & \frac{\partial y_2}{\partial r} & \frac{\partial y_3}{\partial r} \\ \frac{\partial y_1}{\partial s} & \frac{\partial y_2}{\partial s} & \frac{\partial y_3}{\partial s} \\ \frac{\partial y_1}{\partial t} & \frac{\partial y_2}{\partial t} & \frac{\partial y_3}{\partial t} \end{bmatrix} \tag{14.70}$$

Its inverse is denoted by $\hat{\boldsymbol{J}} \equiv \boldsymbol{J}^{-1} = \partial\left(r, s, t\right)/\partial\left(y_1, y_2, y_3\right)$ and used to relate the micro-displacement derivatives as

$$\boldsymbol{d}^{(\beta)}_{W(9\times1)} \equiv \begin{Bmatrix} \boldsymbol{u}_{,y_1} \\ \boldsymbol{u}_{,y_2} \\ \boldsymbol{u}_{,y_3} \end{Bmatrix}^{(\beta)} = \left[\hat{\boldsymbol{J}}\right]^{(\beta)} \begin{Bmatrix} \boldsymbol{u}_{,r} \\ \boldsymbol{u}_{,s} \\ \boldsymbol{u}_{,t} \end{Bmatrix}^{(\beta)} \tag{14.71}$$

The right-hand-side vector can be simply obtained using the displacement form, Eq. (14.67). It is important to emphasize that the Jacobian depends on the shape functions used for the parametric mapping in Eq. (14.63). Thus, the proposed parametric HFGMC is general and can have linear (subparametric) or quadratic mapping in the case where a higher accurate geometry is needed. Other parametric reconstruction attempts of the original HFGMC with orthogonal subcells (see discussions by Haj-Ali and Aboudi 2012, 2013) have proposed a linear 2D mapping with constant average Jacobian. This may introduce significant errors and restrict the discretization of the RUC to be performed with subcell geometries close to paralleloid or rectangular shapes. The 2D and 3D parametric HFGMC (Haj-Ali and Aboudi 2010, 2013, 2016) have no restrictions on the Jacobian and currently employ linear transformation using general quadrilateral 2D or hexahedral 3D shapes.

Similar to the displacement gradients with respect to $(y_i)$ in Eq. (14.71), at this stage, we also treat the global displacement gradients over the subcell $(\beta)$ as independent, even though these are usually prescribed uniformly for all the subcells. The vector form of the subcell global gradients is expressed as

$$\boldsymbol{d}^{(\beta)}_{U(9\times1)} \equiv \begin{Bmatrix} \boldsymbol{u}^0{}_{,x_1} \\ \boldsymbol{u}^0{}_{,x_2} \\ \boldsymbol{u}^0{}_{,x_3} \end{Bmatrix}^{(\beta)} = \begin{Bmatrix} u^0{}_{i,1} \\ u^0{}_{i,2} \\ u^0{}_{i,3} \end{Bmatrix}^{(\beta)} \equiv \boldsymbol{U}_0{}^{(\beta)}{}_{(9\times1)} \tag{14.72}$$

The full displacement gradient vector, $\boldsymbol{d}^{(\beta)}$, is a linear combination of the local and global counterparts, i.e.,

$$\boldsymbol{d}^{(\beta)} = \boldsymbol{d}_U{}^{(\beta)} + \boldsymbol{d}_W{}^{(\beta)} \equiv \boldsymbol{I}_{(9\times9)}\boldsymbol{U}_0{}^{(\beta)}{}_{(9\times1)} + \boldsymbol{A}_W{}^{(\beta)}{}_{(9\times21)}\boldsymbol{W}^{(\beta)}{}_{(21\times1)} \tag{14.73}$$

The nonzero terms of the $\boldsymbol{A}_W{}^{(\beta)}$ matrix are listed in the appendix in terms of the Jacobian inverse matrix, $\hat{\boldsymbol{J}}$. These are given for an $(r, s, t)$ point in the parent coordinates. The matrix is evaluated numerically for the needed integral forms at select integration points.

The total vector of the displacement microvariables for each subcell can be organized in the order

$$\boldsymbol{W}^{(\beta),T} = \{W_{1i}, W_{2i}, W_{3i}, W_{4i}, W_{5i}, W_{6i}, W_{0i}\}^{(\beta)}_{(1\times 21)} \quad i = 1, 2, 3 \tag{14.74}$$

The small strain tensor in a given subcell $(\beta)$ is defined by

$$\epsilon_{ij}^{(\beta)}(\boldsymbol{y}(r, s, t)) = \epsilon_{ij}^{0} + \frac{1}{2}\left(\frac{\partial u_i}{\partial y_j} + \frac{\partial u_j}{\partial y_i}\right) \tag{14.75}$$

The corresponding strain vector form is expressed as

$$\boldsymbol{\epsilon}^{(\beta)} = \boldsymbol{I}_B \boldsymbol{U}_0{}^{(\beta)} + \boldsymbol{I}_B \boldsymbol{A}_W{}^{(\beta)} \boldsymbol{W}^{(\beta)} \equiv \boldsymbol{I}_B \boldsymbol{U}_0{}^{(\beta)} + \boldsymbol{B}_W \boldsymbol{W}^{(\beta)} \tag{14.76}$$

where the strain vector notation $\boldsymbol{\epsilon}$ is defined by

$$\boldsymbol{\epsilon}^T \equiv \{\epsilon_{11}, \epsilon_{22}, \epsilon_{33}, 2\epsilon_{12}, 2\epsilon_{13}, 2\epsilon_{23}\} \tag{14.77}$$

Therefore, the matrix $\boldsymbol{I}_B$ has the Boolean structure

$$\boldsymbol{I}_B = \begin{bmatrix} 1\,0\,0\,0\,0\,0\,0\,0\,0 \\ 0\,0\,0\,0\,1\,0\,0\,0\,0 \\ 0\,0\,0\,0\,0\,0\,0\,0\,1 \\ 0\,0\,0\,0\,0\,1\,0\,1\,0 \\ 0\,0\,1\,0\,0\,0\,1\,0\,0 \\ 0\,1\,0\,1\,0\,0\,0\,0\,0 \end{bmatrix} \tag{14.78}$$

and $\boldsymbol{B}_W{}^{(\beta)}$ is the matrix that relates the spatial strain components to the displacement microvariables and the $\boldsymbol{I}_B$ takes the form of a direct global strain-gradient matrix. The combined size of the two vectors, $\boldsymbol{W}^{(\beta)}$ and $\boldsymbol{U}_0{}^{(\beta)}$, includes all 30 displacement variables of each subcell $(\beta)$.

The average traction vector $\bar{\boldsymbol{T}}^{(\beta_k)}$ on the six faces (sides) of the hexahedral subcell is given by

$$\bar{\boldsymbol{T}}^{(\beta_k)} = \frac{1}{A_k}\int_{S_k} \boldsymbol{\sigma}^{(\beta)}(\boldsymbol{y}) \cdot \boldsymbol{n}^{(\beta_k)} dS_k \;=\; \frac{1}{4}\int_{-1}^{1}\int_{-1}^{1} \boldsymbol{\sigma}^{(\beta)}(r, s, t) \cdot \boldsymbol{n}^{(\beta_k)} d\xi_k d\eta_k, \quad k = 1, 2, .., 6 \tag{14.79}$$

where $\boldsymbol{n}^{(\beta_k)}$ is the unit normal vector to the $k$th side of subcell $(\beta)$. The stress field, $\boldsymbol{\sigma}^{(\beta)}$, is given by

$$\boldsymbol{\sigma}^{(\beta)} = \boldsymbol{C}^{(\beta)} : \boldsymbol{\epsilon}^{(\beta)} \tag{14.80}$$

assuming a tangential or linear stress–strain relation of the subcell, with $\boldsymbol{C}^{(\beta)}$ being the stiffness of the material in the subcell. Since the current geometry is interpolated using linear mapping, the normal vector $\boldsymbol{n}^{(\beta_k)}$ to each of the six faces is constant. The established spatial strains in the subcell are used to obtain the corresponding stresses. The latter are used in the expression for the average tractions, Eq. (14.79). This provides

$$\begin{aligned}\bar{\boldsymbol{T}}^{(\beta_k)} &= \frac{1}{4}\int_{-1}^{1}\int_{-1}^{1} \boldsymbol{N}^{(\beta_k)}\boldsymbol{C}^{(\beta)}\left[\boldsymbol{I}_B\boldsymbol{U}_0^{(\beta)} + \boldsymbol{B}_W{}^{(\beta)}\boldsymbol{W}^{(\beta)}\right] d\xi_k d\eta_k \\ &= \boldsymbol{N}^{(\beta_k)}\boldsymbol{C}^{(\beta)}\left[\boldsymbol{I}_B\boldsymbol{U}_0^{(\beta)} + \bar{\boldsymbol{B}}_W^{(\beta_k)}\boldsymbol{W}^{(\beta)}\right]\end{aligned} \tag{14.81}$$

with

$$\boldsymbol{N}^{(\beta_k)} = \begin{bmatrix} n_1 & 0 & 0 & 0 & n_3 & n_2 \\ 0 & n_2 & 0 & n_3 & 0 & n_1 \\ 0 & 0 & n_3 & n_2 & n_1 & 0 \end{bmatrix}^{(\beta_k)} \tag{14.82}$$

and

$$\bar{\boldsymbol{B}}_W^{(\beta_k)} = \frac{1}{4}\boldsymbol{I}_B\int_{-1}^{1}\int_{-1}^{1}\boldsymbol{A}^{(\beta)}d\xi_k d\eta_k \tag{14.83}$$

As mentioned above, in the linear parametric mapping case, the $\boldsymbol{N}^{(\beta_k)}$ matrix is constant.

Following the original HFGMC formulation, we impose the displacement and traction continuity between the subcells. These conditions are enforced in an average integral sense. In addition, periodicity conditions are imposed between the boundary subcells of the RUC by requiring that the displacements and tractions be equal at these mirrored interfaces. The third major requirement of the HFGMC method is the intra-subcell equilibrium applied in a volumetric average form. In the following, the above transformed expressions for the average displacements and tractions, Eqs. (14.69) and (14.81), respectively, can be used to impose the HFGMC equations. The displacement and traction continuity conditions can be written as

$$\bar{\boldsymbol{u}}^{(\beta_k)} = \boldsymbol{W}_k{}^{(\beta)} = \bar{\boldsymbol{u}}^{(\gamma_m)} = \boldsymbol{W}_m{}^{(\gamma)}, \qquad \bar{\boldsymbol{T}}^{(\beta_k)} = \bar{\boldsymbol{T}}^{(\gamma_m)} \tag{14.84}$$

where $(\beta_k)$ denotes the $k$th interface (side) of subcell $(\beta)$ and $(\gamma_m)$ is the neighboring $m$th interface side of subcell $(\gamma)$. The displacement and traction periodicity conditions are imposed as in Eq. (14.84) but with subcells $(\beta)$ and $(\gamma)$ located on the opposite sides of the RUC.

The equilibrium equations for each subcell are imposed in an average volumetric sense in conjunction with the divergence theorem. This allows to utilize the previously derived expressions for the average tractions as follows:

$$\int_V \nabla \cdot \boldsymbol{\sigma}\, dV = \int_S \boldsymbol{\sigma} \cdot \boldsymbol{n} dS = \sum_{k=1}^{6} \int_{S_k} \boldsymbol{N}^{(\beta_k)} \boldsymbol{\sigma}^{(\beta)} dS_k = \sum_{k=1}^{6} A_k \bar{\boldsymbol{T}}^{(\beta_k)} = \boldsymbol{0} \quad (14.85)$$

where $V$ and $S$ are the volume and surface of the $(\beta)$ subcell, respectively, and $A_k$ is the area of the $k$th side.

The above formulation completes the nonlinear theoretical derivation of the general three-dimensional parametric HFGMC micromechanical method. The assembly of the derived $21 \times N_c$ HFGMC governing equations of the RUC is solved to obtain the unknown 21 microvariables for each cell. This is assuming that the global displacement gradients are known $\boldsymbol{U}_0{}^{(\beta)} = \boldsymbol{U}_0$ and no static condensation, i.e., all the microvariables of the subcells are retained as independent variables. In general, the equations can be symbolically grouped into three parts:

$$\begin{bmatrix} \mathbf{1}_u^{(+)} - \mathbf{1}_u^{(-)} \\ \mathbf{I}_T^{(+)} + \mathbf{I}_T^{(-)} \\ \sum \mathbf{I}_T \end{bmatrix} \{\mathbf{W}\} + \begin{bmatrix} \mathbf{0} \\ \mathbf{D}_T^{(+)} - \mathbf{D}_T^{(-)} \\ \sum \mathbf{D}_T \end{bmatrix} \{\boldsymbol{I}_B \boldsymbol{U}_0\} = \begin{Bmatrix} \mathbf{0} \\ \mathbf{0} \\ \mathbf{0} \end{Bmatrix} \quad (14.86)$$

where the first part (row) represents the average continuity and periodicity of the displacements, the second represents the continuity of the tractions in a similar fashion, and the third part represents the equilibrium equations for all the subcells. The above system of equations is solved for a given externally applied strain, $\boldsymbol{\epsilon}^0 = \boldsymbol{I}_B \boldsymbol{U}_0$, to obtain the cell microvariables. See Haj-Ali and Aboudi (2013, 2016) for more discussions of the solution approach for the above equations in the linear and nonlinear cases, respectively, and how to obtain the effective elastic properties of the multiphase composite.

## 14.5 HFGMC with Average Virtual Work Formulation

A new average virtual work is derived with associated generalized residuals and a symmetric stiffness for the RUC system needed for the nonlinear iterative solution. This is a new alternate solution approach to the one presented in the previous section. The aim herein is to replace the above direct HFGMC nonsymmetric system of equations, Eqs. (14.84)–(14.86), with a symmetric incremental system and its associated residual error vector. To that end, we define an average virtual work, expressed at the local level in terms of the subcell face-average virtual displacement microvariables associated with the average face tractions. At the overall global level, we use the average virtual work defined through the remote virtual strains and their associated average stresses. The subcell external and internal average virtual work balance is expressed by

$$\delta \boldsymbol{U}_0{}^{(\beta),T}\boldsymbol{f}_{\boldsymbol{U}}{}^{(\beta)} + \delta \boldsymbol{W}^{(\beta),T}\boldsymbol{f}_{\boldsymbol{W}}{}^{(\beta)} = \int_V \delta \boldsymbol{\epsilon}^{(\beta),T}\boldsymbol{\sigma}^{(\beta)} dV$$
$$= \int_V (\delta \boldsymbol{U}_0{}^{(\beta),T}\boldsymbol{I}_B{}^{(\beta),T} + \delta \boldsymbol{W}^{(\beta),T}\boldsymbol{B}_W{}^{(\beta),T})\boldsymbol{\sigma}^{(\beta)} dV \tag{14.87}$$

The generalized internal resisting force vector of the subcell can be identified with its two parts as

$$\boldsymbol{f}_{\boldsymbol{U}}{}^{(\beta)} = \int_V \boldsymbol{I}_B{}^{(\beta),T}\boldsymbol{\sigma}^{(\beta)} dV \;\; ; \;\; \boldsymbol{f}_{\boldsymbol{W}}{}^{(\beta)} = \int_V \boldsymbol{B}_W{}^{(\beta),T}\boldsymbol{\sigma}^{(\beta)} dV \tag{14.88}$$

It is interesting to note that the part of the internal resisting vector $\boldsymbol{f}_{\boldsymbol{U}}{}^{(\beta)}$ is the contribution of the subcell to the RUC average overall stress, which is also a work conjugate to the global displacement gradients, while the $\boldsymbol{f}_{\boldsymbol{W}}{}^{(\beta)}$ part is a work-conjugate force to the local average micro-displacement vectors at the interfaces of the subcell. We use Eqs. (14.76) and (14.80) substituted in (14.84) and take the derivatives of the generalized internal force vectors with respect to the subcell's variables in order to obtain the stiffness matrix. The results are written by dropping the $(\beta)$ symbol since the following derived expressions apply to one or the entire number of RUC subcells (by assembly). Hence,

$$\boldsymbol{f}_{\boldsymbol{U}} = \int_V \boldsymbol{I}_B^T C(\boldsymbol{I}_B \boldsymbol{U}_0 + \boldsymbol{B}_W \boldsymbol{W}) dV \;\; ; \;\; \boldsymbol{f}_{\boldsymbol{W}} = \int_V \boldsymbol{B}_W^T C(\boldsymbol{I}_B \boldsymbol{U}_0 + \boldsymbol{B}_W \boldsymbol{W}) dV \tag{14.89}$$

The resulting stiffness matrix that relates the overall generalized force vector, $\boldsymbol{f} = (\boldsymbol{f}_{\boldsymbol{W}}, \boldsymbol{f}_{\boldsymbol{U}})$, and the overall variables of the subcells (RUC), $(\boldsymbol{W}, \boldsymbol{U}_{\boldsymbol{0}})$, is symbolically expressed by

$$\boldsymbol{K} = \begin{bmatrix} \int_V \boldsymbol{B}_{\boldsymbol{W}}{}^T C \boldsymbol{B}_{\boldsymbol{W}} dV & \int_V \boldsymbol{B}_{\boldsymbol{W}}{}^T C \boldsymbol{I}_{\boldsymbol{B}} dV \\ \int_V \boldsymbol{I}_{\boldsymbol{B}}{}^T C \boldsymbol{B}_{\boldsymbol{W}} dV & \int_V \boldsymbol{I}_{\boldsymbol{B}}{}^T C \boldsymbol{I}_{\boldsymbol{B}} dV \end{bmatrix} \tag{14.90}$$

The stiffness matrix of the HFGMC is symmetric. In the case of nonlinear material response, the incremental derivation of the above generalized average virtual work is straightforward. The equilibrium residual of the entire RUC system can be expressed in a general manner, with imposing the interface continuity and periodicity on the displacement microvariables, by

$$\boldsymbol{R} \equiv \boldsymbol{P} - \boldsymbol{f} = \begin{Bmatrix} \boldsymbol{P}_{\boldsymbol{W}} \\ \boldsymbol{P}_{\boldsymbol{U}} \end{Bmatrix} - \begin{Bmatrix} \int_V \boldsymbol{B}_{\boldsymbol{W}}{}^T \boldsymbol{\sigma} \\ \int_V \boldsymbol{I}_{\boldsymbol{B}}{}^T \boldsymbol{\sigma} \end{Bmatrix} = \{0\} \tag{14.91}$$

The solution for the overall system equilibrium equations for the RUC in the nonlinear case can follow one of the classical Newton methods in computational

mechanics to solve Eq. (14.91) incrementally and in an iterative manner. In general, the $\boldsymbol{P}_W$ is not directly prescribed in a typical RUC because the external surfaces are usually occupied using periodicity conditions over the conjugate microvariables $\boldsymbol{W}$, unless it has free internal surfaces with pressure-type loading. The applied generalized force $\boldsymbol{P}_U$ is equal to the average RUC stress with a unit volume. The incremental system of equations at time $\boldsymbol{t}$ is

$$\begin{bmatrix} \int_V \boldsymbol{B_W}^T \boldsymbol{C}_t \boldsymbol{B_W} dV & \int_V \boldsymbol{B_W}^T \boldsymbol{C}_t \boldsymbol{I_B} dV \\ \int_V \boldsymbol{I_B}^T \boldsymbol{C}_t \boldsymbol{B_W} dV & \int_V \boldsymbol{I_B}^T \boldsymbol{C}_t \boldsymbol{I_B} dV \end{bmatrix}^{(t)} \begin{Bmatrix} \boldsymbol{\Delta W} \\ \boldsymbol{\Delta U_0} \end{Bmatrix}^{(t+\Delta t)} = \{\boldsymbol{R}\}^{(t+\Delta t)} \quad (14.92)$$

The use of incremental nonlinear HFGMC equilibrium-based formulation, Eq. (14.92), with the generalized internal resisting vector, Eq. (14.89), instead of the average traction continuity relations and average equilibrium, Eq. (14.86), respectively, provides an enhanced computational advantage. This is manifested by using the symmetric stiffness matrix and well-established incremental solution techniques for the overall nonlinear system of equations.

The HFGMC linear geometric mapping and quadratic displacement interpolation (subparametric formulation) have been proposed, e.g., Haj-Ali and Aboudi (2010, 2013, 2016). The current nonlinear formulation simplifies the numerical integration and puts the HFGMC at an equal footing in terms of the computational effort compared to the nodal displacement-based FE. Both the FE and the parametric HFGMC require similar computational efforts expressed by symmetric stiffness assembly and iterative direct solution of the overall system of equations. Therefore, it is possible for the first time to give an exact answer to the computational time required for the HFGMC solution compared to the FE analysis. The classical FE quadratic brick (hexahedral) element is usually composed of 20 nodes with a total of 60 degrees of freedom (variables). The HFGMC employs a quadratic subcell with a maximum of 30 variables including the micro-displacements and the average displacement gradients (having them as independent even though these prescribed variables can be statically condensed). Therefore, one would accurately estimate that the required HFGMC computational time will not exceed 50% of the FE computations.

It is important to draw the distinctions between the proposed parametric HFGMC and the classical displacement-based finite element (FE) method, where a common misconception has been to link the HFGMC to FE. In the FE formulation, the displacement continuity between two adjacent and connected elements is satisfied in a pointwise manner by sharing the same nodal degrees of freedom at both sides. However, the HFGMC quadratic displacement expansion is nonconforming and the displacement continuity is only satisfied in an average sense between adjacent subcells. The latter is an approximation that allows the HFGMC to explicitly use additional stress variables in the formulation and directly apply average traction continuity. This approach can facilitate cohesive damage modeling that can be easily implemented (see Haj-Ali and Aboudi 2010). In addition, the remote fields in the HFGMC are directly tied to the micromechanical formulation by using

both the remote average strain and local displacement microvariables. This allows additional advantage in applying direct periodicity conditions over global and local microvariables (and their conjugates) of the RUC, where in the FE formulation is imposed only through displacement total variables. The latter differences are illustrated in comparing the HFGMC to the FE for the analysis of a relatively wide range of cases (see Haj-Ali and Aboudi 2013). The current nonlinear solution formulation of the overall system of equations, however, is very analogous to that in FE method, realized by defining the stiffness assembly and generalized internal resisting forces.

## 14.6 Applications

Many applications of the HFGMC with regular array have been presented in Aboudi et al. (2013). These include applications on elastic, inelastic, smart composites, and finite strain HFGMC micromechanical analysis. Further implementation of the HFGMC method for composites with nonlinear effects has been presented by Haj-Ali and Aboudi (2009, 2010). The later implicit formulation developed iterative procedure to minimize the residual error that satisfies the HFGMC governing equations suitable for applied finite strain increments.

The HFGMC model has been applied by Gilat and Aboudi (2013) for the prediction of the inelastic behavior of periodic microstructural auxetic arrays that can generate negative values of Poisson's ratios. Experimental evaluation of the mechanical properties of reinforced carbon nanotubes and comparisons by the HFGMC predictions has been presented by Ben David et al. (2013).

The effects of fiber misalignment (Bednarcyk et al. 2014) and clustering (Bednarcyk et al. 2015) have been investigated by employing the HFGMC model. The damping properties of unidirectional, laminated, and woven composites by employing a multiscale HFGMC micromechanics have been recently presented by Bednarcyk et al. (2016). In Levi-Sasson et al. (2015), failure envelopes for laminated composites have been predicted by the parametric HFGMC, in conjunction with continuum damage implemented separately for the fiber and matrix subcells. The predicted failure envelopes compared well with results available in the literature and with well-known anisotropic failure criteria.

The microplane constitutive modeling theory has been integrated within the parametric HFGMC by Haj-Ali and Aboudi (2016) to represent the nonlinear and strain softening of the matrix subcells. To this end, the nonlinear micromechanical formulation of both the HFGMC and the microplane theories has been both developed and integrated in a nested fashion.

*Smart Composites* The HFGMC has also been implemented for the prediction of the behavior of smart composites. Thus, piezoresistive composites which are capable of measuring the changes in electrical resistance caused by the application of mechanical deformation have been analyzed by Haj-Ali et al. (2014) by employing the HFGMC micromechanics model.

Magnetostrictive materials are capable of generating elastic strain as result of the application of magnetic field. In Aboudi et al. (2014), the HFGMC analysis has been formulated for the analysis of magnetostrictive composites in which one of the phases behaves as a magnetostrictive material whose constitutive response is nonlinear.

Multiferroic materials exhibit magnetoelectric effect such that the application of a magnetic field induces an electric polarization, whereas the application of electric field induces magnetization. The induced mechanical deformation can be utilized for sensing and actuation.

The HFGMC micromechanics has been implemented by Jin and Aboudi (2015) for the prediction of the macroscopic behavior of multiferroic composites. These composites consist of a magnetostrictive and piezoelectric phases.

A new class of thermoelectric (TE) composite materials and devices has been recently introduced as a promising technology for harvesting a large number of otherwise wasted thermal heat sources into electric energy. These material systems are based on the application of thermal gradient in order to produce a flow of electrical current to be utilized in practice. The micromechanical HFGMC has been extended by Aboudi and Haj-Ali (2016) to account for the three-way coupled thermal-electrical-mechanical effects that include the Seebeck, Peltier, and Joule heat.

*Finite Strain HFGMC* Composite materials that are subjected to large deformations have been analyzed by generalizing the HFGMC formulation to finite strain. Such a finite strain HFGMC analysis has been recently presented by Aboudi (2015) for the modeling and prediction of the effective behavior of dielectric elastomers with embedded dielectric particles.

The concept of an energy limiter, according to which the amount of energy that can be accumulated by the material during deformation is finite, has been introduced by Volokh (see, e.g., Volokh 2013).This concept has been incorporated with the constitutive relation itself which has been designated for the description of the material response. As a result, enhanced finite strain constitutive equations are obtained which provide the critical values of the strain energy at which failure of the material occurs and at which its static stability is lost. This approach has been recently utilized by Aboudi and Volokh (2015) by developing a finite strain HFGMC micromechanical analysis for composites undergoing large deformations that is capable of the prediction of the occurrence of the loss of its static stability.

Aneurysms are abnormal dilatation of vessels in the vascular system that are prone to rupture. The latter approach for the micromechanical determination by HFGMC of loss of initial failure of composites undergoing large deformations has been utilized by Volokh and Aboudi (2016) for the prediction of aneurysm rupture.

## Appendix

In this appendix, the nonzero components of the matrix relating the spatial microdisplacement gradients to the displacement microvariables are listed. The terms are

$$
\begin{aligned}
A_W(1,1) &= 1/4\,\hat{J}_{1,1}t + 1/4\,\hat{J}_{1,2}t - 1/2\,\hat{J}_{1,3} + 1/4\,\hat{J}_{1,3}r + 1/4\,\hat{J}_{1,3}s + 3/2\,\hat{J}_{1,3}t \\
A_W(1,4) &= 1/4\,\hat{J}_{1,1}t + 1/4\,\hat{J}_{1,2}t + 1/2\,\hat{J}_{1,3} + 1/4\,\hat{J}_{1,3}r + 1/4\,\hat{J}_{1,3}s + 3/2\,\hat{J}_{1,3}t \\
A_W(1,7) &= 1/4\,\hat{J}_{1,1}s - 1/2\,\hat{J}_{1,2} + 1/4\,\hat{J}_{1,2}r + 3/2\,\hat{J}_{1,2}s + 1/4\,\hat{J}_{1,2}t + 1/4\,\hat{J}_{1,3}s \\
A_W(1,10) &= 1/2\,\hat{J}_{1,1} + 3/2\,\hat{J}_{1,1}r + 1/4\,\hat{J}_{1,1}s + 1/4\,\hat{J}_{1,1}t + 1/4\,\hat{J}_{1,2}r + 1/4\,\hat{J}_{1,3}r \\
A_W(1,13) &= 1/4\,\hat{J}_{1,1}s + 1/2\,\hat{J}_{1,2} + 1/4\,\hat{J}_{1,2}r + 3/2\,\hat{J}_{1,2}s + 1/4\,\hat{J}_{1,2}t + 1/4\,\hat{J}_{1,3}s \\
A_W(1,16) &= -1/2\,\hat{J}_{1,1} + 3/2\,\hat{J}_{1,1}r + 1/4\,\hat{J}_{1,1}s + 1/4\,\hat{J}_{1,1}t + 1/4\,\hat{J}_{1,2}r + 1/4\,\hat{J}_{1,3}r \\
A_W(1,19) &= -3\,\hat{J}_{1,1}r - \hat{J}_{1,2}r - \hat{J}_{1,3}r - \hat{J}_{1,1}s - 3\,\hat{J}_{1,2}s - \hat{J}_{1,3}s - \hat{J}_{1,1}t - \hat{J}_{1,2}t - 3\,\hat{J}_{1,3}t \\
A_W(2,2) &= 1/4\,\hat{J}_{1,1}t + 1/4\,\hat{J}_{1,2}t - 1/2\,\hat{J}_{1,3} + 1/4\,\hat{J}_{1,3}r + 1/4\,\hat{J}_{1,3}s + 3/2\,\hat{J}_{1,3}t \\
A_W(2,5) &= 1/4\,\hat{J}_{1,1}t + 1/4\,\hat{J}_{1,2}t + 1/2\,\hat{J}_{1,3} + 1/4\,\hat{J}_{1,3}r + 1/4\,\hat{J}_{1,3}s + 3/2\,\hat{J}_{1,3}t \\
A_W(2,8) &= 1/4\,\hat{J}_{1,1}s - 1/2\,\hat{J}_{1,2} + 1/4\,\hat{J}_{1,2}r + 3/2\,\hat{J}_{1,2}s + 1/4\,\hat{J}_{1,2}t + 1/4\,\hat{J}_{1,3}s \\
A_W(2,11) &= 1/2\,\hat{J}_{1,1} + 3/2\,\hat{J}_{1,1}r + 1/4\,\hat{J}_{1,1}s + 1/4\,\hat{J}_{1,1}t + 1/4\,\hat{J}_{1,2}r + 1/4\,\hat{J}_{1,3}r \\
A_W(2,14) &= 1/4\,\hat{J}_{1,1}s + 1/2\,\hat{J}_{1,2} + 1/4\,\hat{J}_{1,2}r + 3/2\,\hat{J}_{1,2}s + 1/4\,\hat{J}_{1,2}t + 1/4\,\hat{J}_{1,3}s \\
A_W(2,17) &= -1/2\,\hat{J}_{1,1} + 3/2\,\hat{J}_{1,1}r + 1/4\,\hat{J}_{1,1}s + 1/4\,\hat{J}_{1,1}t + 1/4\,\hat{J}_{1,2}r + 1/4\,\hat{J}_{1,3}r \\
A_W(2,20) &= -3\,\hat{J}_{1,1}r - \hat{J}_{1,2}r - \hat{J}_{1,3}r - \hat{J}_{1,1}s - 3\,\hat{J}_{1,2}s - \hat{J}_{1,3}s - \hat{J}_{1,1}t - \hat{J}_{1,2}t - 3\,\hat{J}_{1,3}t \\
A_W(3,3) &= 1/4\,\hat{J}_{1,1}t + 1/4\,\hat{J}_{1,2}t - 1/2\,\hat{J}_{1,3} + 1/4\,\hat{J}_{1,3}r + 1/4\,\hat{J}_{1,3}s + 3/2\,\hat{J}_{1,3}t \\
A_W(3,6) &= 1/4\,\hat{J}_{1,1}t + 1/4\,\hat{J}_{1,2}t + 1/2\,\hat{J}_{1,3} + 1/4\,\hat{J}_{1,3}r + 1/4\,\hat{J}_{1,3}s + 3/2\,\hat{J}_{1,3}t \\
A_W(3,9) &= 1/4\,\hat{J}_{1,1}s - 1/2\,\hat{J}_{1,2} + 1/4\,\hat{J}_{1,2}r + 3/2\,\hat{J}_{1,2}s + 1/4\,\hat{J}_{1,2}t + 1/4\,\hat{J}_{1,3}s \\
A_W(3,12) &= 1/2\,\hat{J}_{1,1} + 3/2\,\hat{J}_{1,1}r + 1/4\,\hat{J}_{1,1}s + 1/4\,\hat{J}_{1,1}t + 1/4\,\hat{J}_{1,2}r + 1/4\,\hat{J}_{1,3}r \\
A_W(3,15) &= 1/4\,\hat{J}_{1,1}s + 1/2\,\hat{J}_{1,2} + 1/4\,\hat{J}_{1,2}r + 3/2\,\hat{J}_{1,2}s + 1/4\,\hat{J}_{1,2}t + 1/4\,\hat{J}_{1,3}s \\
A_W(3,18) &= -1/2\,\hat{J}_{1,1} + 3/2\,\hat{J}_{1,1}r + 1/4\,\hat{J}_{1,1}s + 1/4\,\hat{J}_{1,1}t + 1/4\,\hat{J}_{1,2}r + 1/4\,\hat{J}_{1,3}r \\
A_W(3,21) &= -3\,\hat{J}_{1,1}r - \hat{J}_{1,2}r - \hat{J}_{1,3}r - \hat{J}_{1,1}s - 3\,\hat{J}_{1,2}s - \hat{J}_{1,3}s - \hat{J}_{1,1}t - \hat{J}_{1,2}t - 3\,\hat{J}_{1,3}t \\
A_W(4,1) &= 1/4\,\hat{J}_{2,1}t + 1/4\,\hat{J}_{2,2}t - 1/2\,\hat{J}_{2,3} + 1/4\,\hat{J}_{2,3}r + 1/4\,\hat{J}_{2,3}s + 3/2\,\hat{J}_{2,3}t \\
A_W(4,4) &= 1/4\,\hat{J}_{2,1}t + 1/4\,\hat{J}_{2,2}t + 1/2\,\hat{J}_{2,3} + 1/4\,\hat{J}_{2,3}r + 1/4\,\hat{J}_{2,3}s + 3/2\,\hat{J}_{2,3}t \\
A_W(4,7) &= 1/4\,\hat{J}_{2,1}s - 1/2\,\hat{J}_{2,2} + 1/4\,\hat{J}_{2,2}r + 3/2\,\hat{J}_{2,2}s + 1/4\,\hat{J}_{2,2}t + 1/4\,\hat{J}_{2,3}s \\
A_W(4,10) &= 1/2\,\hat{J}_{2,1} + 3/2\,\hat{J}_{2,1}r + 1/4\,\hat{J}_{2,1}s + 1/4\,\hat{J}_{2,1}t + 1/4\,\hat{J}_{2,2}r + 1/4\,\hat{J}_{2,3}r \\
A_W(4,13) &= 1/4\,\hat{J}_{2,1}s + 1/2\,\hat{J}_{2,2} + 1/4\,\hat{J}_{2,2}r + 3/2\,\hat{J}_{2,2}s + 1/4\,\hat{J}_{2,2}t + 1/4\,\hat{J}_{2,3}s
\end{aligned}
$$

$$
\begin{aligned}
A_W(4,16) &= -1/2\,\hat{J}_{2,1} + 3/2\,\hat{J}_{2,1}r + 1/4\,\hat{J}_{2,1}s + 1/4\,\hat{J}_{2,1}t + 1/4\,\hat{J}_{2,2}r + 1/4\,\hat{J}_{2,3}r \\
A_W(4,19) &= -3\,\hat{J}_{2,1}r - \hat{J}_{2,2}r - \hat{J}_{2,3}r - \hat{J}_{2,1}s - 3\,\hat{J}_{2,2}s - \hat{J}_{2,3}s - \hat{J}_{2,1}t - \hat{J}_{2,2}t - 3\,\hat{J}_{2,3}t \\
A_W(5,2) &= 1/4\,\hat{J}_{2,1}t + 1/4\,\hat{J}_{2,2}t - 1/2\,\hat{J}_{2,3} + 1/4\,\hat{J}_{2,3}r + 1/4\,\hat{J}_{2,3}s + 3/2\,\hat{J}_{2,3}t \\
A_W(5,5) &= 1/4\,\hat{J}_{2,1}t + 1/4\,\hat{J}_{2,2}t + 1/2\,\hat{J}_{2,3} + 1/4\,\hat{J}_{2,3}r + 1/4\,\hat{J}_{2,3}s + 3/2\,\hat{J}_{2,3}t \\
A_W(5,8) &= 1/4\,\hat{J}_{2,1}s - 1/2\,\hat{J}_{2,2} + 1/4\,\hat{J}_{2,2}r + 3/2\,\hat{J}_{2,2}s + 1/4\,\hat{J}_{2,2}t + 1/4\,\hat{J}_{2,3}s \\
A_W(5,11) &= 1/2\,\hat{J}_{2,1} + 3/2\,\hat{J}_{2,1}r + 1/4\,\hat{J}_{2,1}s + 1/4\,\hat{J}_{2,1}t + 1/4\,\hat{J}_{2,2}r + 1/4\,\hat{J}_{2,3}r \\
A_W(5,14) &= 1/4\,\hat{J}_{2,1}s + 1/2\,\hat{J}_{2,2} + 1/4\,\hat{J}_{2,2}r + 3/2\,\hat{J}_{2,2}s + 1/4\,\hat{J}_{2,2}t + 1/4\,\hat{J}_{2,3}s \\
A_W(5,17) &= -1/2\,\hat{J}_{2,1} + 3/2\,\hat{J}_{2,1}r + 1/4\,\hat{J}_{2,1}s + 1/4\,\hat{J}_{2,1}t + 1/4\,\hat{J}_{2,2}r + 1/4\,\hat{J}_{2,3}r \\
A_W(5,20) &= -3\,\hat{J}_{2,1}r - \hat{J}_{2,2}r - \hat{J}_{2,3}r - \hat{J}_{2,1}s - 3\,\hat{J}_{2,2}s - \hat{J}_{2,3}s - \hat{J}_{2,1}t - \hat{J}_{2,2}t - 3\,\hat{J}_{2,3}t \\
A_W(6,3) &= 1/4\,\hat{J}_{2,1}t + 1/4\,\hat{J}_{2,2}t - 1/2\,\hat{J}_{2,3} + 1/4\,\hat{J}_{2,3}r + 1/4\,\hat{J}_{2,3}s + 3/2\,\hat{J}_{2,3}t \\
A_W(6,6) &= 1/4\,\hat{J}_{2,1}t + 1/4\,\hat{J}_{2,2}t + 1/2\,\hat{J}_{2,3} + 1/4\,\hat{J}_{2,3}r + 1/4\,\hat{J}_{2,3}s + 3/2\,\hat{J}_{2,3}t \\
A_W(6,9) &= 1/4\,\hat{J}_{2,1}s - 1/2\,\hat{J}_{2,2} + 1/4\,\hat{J}_{2,2}r + 3/2\,\hat{J}_{2,2}s + 1/4\,\hat{J}_{2,2}t + 1/4\,\hat{J}_{2,3}s \\
A_W(6,12) &= 1/2\,\hat{J}_{2,1} + 3/2\,\hat{J}_{2,1}r + 1/4\,\hat{J}_{2,1}s + 1/4\,\hat{J}_{2,1}t + 1/4\,\hat{J}_{2,2}r + 1/4\,\hat{J}_{2,3}r \\
A_W(6,15) &= 1/4\,\hat{J}_{2,1}s + 1/2\,\hat{J}_{2,2} + 1/4\,\hat{J}_{2,2}r + 3/2\,\hat{J}_{2,2}s + 1/4\,\hat{J}_{2,2}t + 1/4\,\hat{J}_{2,3}s \\
A_W(6,18) &= -1/2\,\hat{J}_{2,1} + 3/2\,\hat{J}_{2,1}r + 1/4\,\hat{J}_{2,1}s + 1/4\,\hat{J}_{2,1}t + 1/4\,\hat{J}_{2,2}r + 1/4\,\hat{J}_{2,3}r \\
A_W(6,21) &= -3\,\hat{J}_{2,1}r - \hat{J}_{2,2}r - \hat{J}_{2,3}r - \hat{J}_{2,1}s - 3\,\hat{J}_{2,2}s - \hat{J}_{2,3}s - \hat{J}_{2,1}t - \hat{J}_{2,2}t - 3\,\hat{J}_{2,3}t \\
A_W(7,1) &= 1/4\,\hat{J}_{3,1}t + 1/4\,\hat{J}_{3,2}t - 1/2\,\hat{J}_{3,3} + 1/4\,\hat{J}_{3,3}r + 1/4\,\hat{J}_{3,3}s + 3/2\,\hat{J}_{3,3}t \\
A_W(7,4) &= 1/4\,\hat{J}_{3,1}t + 1/4\,\hat{J}_{3,2}t + 1/2\,\hat{J}_{3,3} + 1/4\,\hat{J}_{3,3}r + 1/4\,\hat{J}_{3,3}s + 3/2\,\hat{J}_{3,3}t \\
A_W(7,7) &= 1/4\,\hat{J}_{3,1}s - 1/2\,\hat{J}_{3,2} + 1/4\,\hat{J}_{3,2}r + 3/2\,\hat{J}_{3,2}s + 1/4\,\hat{J}_{3,2}t + 1/4\,\hat{J}_{3,3}s \\
A_W(7,10) &= 1/2\,\hat{J}_{3,1} + 3/2\,\hat{J}_{3,1}r + 1/4\,\hat{J}_{3,1}s + 1/4\,\hat{J}_{3,1}t + 1/4\,\hat{J}_{3,2}r + 1/4\,\hat{J}_{3,3}r \\
A_W(7,13) &= 1/4\,\hat{J}_{3,1}s + 1/2\,\hat{J}_{3,2} + 1/4\,\hat{J}_{3,2}r + 3/2\,\hat{J}_{3,2}s + 1/4\,\hat{J}_{3,2}t + 1/4\,\hat{J}_{3,3}s \\
A_W(7,16) &= -1/2\,\hat{J}_{3,1} + 3/2\,\hat{J}_{3,1}r + 1/4\,\hat{J}_{3,1}s + 1/4\,\hat{J}_{3,1}t + 1/4\,\hat{J}_{3,2}r + 1/4\,\hat{J}_{3,3}r \\
A_W(7,19) &= -3\,\hat{J}_{3,1}r - \hat{J}_{3,2}r - \hat{J}_{3,3}r - \hat{J}_{3,1}s - 3\,\hat{J}_{3,2}s - \hat{J}_{3,3}s - \hat{J}_{3,1}t - \hat{J}_{3,2}t - 3\,\hat{J}_{3,3}t \\
A_W(8,2) &= 1/4\,\hat{J}_{3,1}t + 1/4\,\hat{J}_{3,2}t - 1/2\,\hat{J}_{3,3} + 1/4\,\hat{J}_{3,3}r + 1/4\,\hat{J}_{3,3}s + 3/2\,\hat{J}_{3,3}t \\
A_W(8,5) &= 1/4\,\hat{J}_{3,1}t + 1/4\,\hat{J}_{3,2}t + 1/2\,\hat{J}_{3,3} + 1/4\,\hat{J}_{3,3}r + 1/4\,\hat{J}_{3,3}s + 3/2\,\hat{J}_{3,3}t \\
A_W(8,8) &= 1/4\,\hat{J}_{3,1}s - 1/2\,\hat{J}_{3,2} + 1/4\,\hat{J}_{3,2}r + 3/2\,\hat{J}_{3,2}s + 1/4\,\hat{J}_{3,2}t + 1/4\,\hat{J}_{3,3}s \\
A_W(8,11) &= 1/2\,\hat{J}_{3,1} + 3/2\,\hat{J}_{3,1}r + 1/4\,\hat{J}_{3,1}s + 1/4\,\hat{J}_{3,1}t + 1/4\,\hat{J}_{3,2}r + 1/4\,\hat{J}_{3,3}r \\
A_W(8,14) &= 1/4\,\hat{J}_{3,1}s + 1/2\,\hat{J}_{3,2} + 1/4\,\hat{J}_{3,2}r + 3/2\,\hat{J}_{3,2}s + 1/4\,\hat{J}_{3,2}t + 1/4\,\hat{J}_{3,3}s \\
A_W(8,17) &= -1/2\,\hat{J}_{3,1} + 3/2\,\hat{J}_{3,1}r + 1/4\,\hat{J}_{3,1}s + 1/4\,\hat{J}_{3,1}t + 1/4\,\hat{J}_{3,2}r + 1/4\,\hat{J}_{3,3}r \\
A_W(8,20) &= -3\,\hat{J}_{3,1}r - \hat{J}_{3,2}r - \hat{J}_{3,3}r - \hat{J}_{3,1}s - 3\,\hat{J}_{3,2}s - \hat{J}_{3,3}s - \hat{J}_{3,1}t - \hat{J}_{3,2}t - 3\,\hat{J}_{3,3}t
\end{aligned}
$$

$$A_W(9,3) = 1/4\,\hat{J}_{3,1}t + 1/4\,\hat{J}_{3,2}t - 1/2\,\hat{J}_{3,3} + 1/4\,\hat{J}_{3,3}r + 1/4\,\hat{J}_{3,3}s + 3/2\,\hat{J}_{3,3}t$$

$$A_W(9,6) = 1/4\,\hat{J}_{3,1}t + 1/4\,\hat{J}_{3,2}t + 1/2\,\hat{J}_{3,3} + 1/4\,\hat{J}_{3,3}r + 1/4\,\hat{J}_{3,3}s + 3/2\,\hat{J}_{3,3}t$$

$$A_W(9,9) = 1/4\,\hat{J}_{3,1}s - 1/2\,\hat{J}_{3,2} + 1/4\,\hat{J}_{3,2}r + 3/2\,\hat{J}_{3,2}s + 1/4\,\hat{J}_{3,2}t + 1/4\,\hat{J}_{3,3}s$$

$$A_W(9,12) = 1/2\,\hat{J}_{3,1} + 3/2\,\hat{J}_{3,1}r + 1/4\,\hat{J}_{3,1}s + 1/4\,\hat{J}_{3,1}t + 1/4\,\hat{J}_{3,2}r + 1/4\,\hat{J}_{3,3}r$$

$$A_W(9,15) = 1/4\,\hat{J}_{3,1}s + 1/2\,\hat{J}_{3,2} + 1/4\,\hat{J}_{3,2}r + 3/2\,\hat{J}_{3,2}s + 1/4\,\hat{J}_{3,2}t + 1/4\,\hat{J}_{3,3}s$$

$$A_W(9,18) = -1/2\,\hat{J}_{3,1} + 3/2\,\hat{J}_{3,1}r + 1/4\,\hat{J}_{3,1}s + 1/4\,\hat{J}_{3,1}t + 1/4\,\hat{J}_{3,2}r + 1/4\,\hat{J}_{3,3}r$$

$$A_W(9,21) = -3\,\hat{J}_{3,1}r - \hat{J}_{3,2}r - \hat{J}_{3,3}r - \hat{J}_{3,1}s - 3\,\hat{J}_{3,2}s - \hat{J}_{3,3}s - \hat{J}_{3,1}t - \hat{J}_{3,2}t - 3\,\hat{J}_{3,3}t$$

## References


Aboudi, J.: A continuum theory for fiber-reinforced elastic viscoplastic composites. Int. J. Eng. Sci. **20**, 605–621 (1982)

Aboudi, J.: Mechanics of Composite Materials: A Unified Micromechanical Approach. Elsevier, Amsterdam (1991)

Aboudi, J.: Micromechanical analysis of fully coupled electro-magneto-thermo-elastic multiphase composites. Smart Mater. Struct. **10**, 867–877 (2001)

Aboudi, J.: Micro-electromechanics of soft dielectric matrix composites. Int. J. Solids Struct. **64–65**, 30–41 (2015)

Aboudi, J., Haj-Ali, R.: A fully coupled thermal-electrical-mechanical micromodel for multi-phase periodic thermoelectrical composite materials and devices. Int. J. Solids Struct. **80**, 84–95 (2016)

Aboudi, J., Volokh, K.Y.: Failure prediction of unidirectional composites undergoing large deformations. J. Appl. Mech. **82**, 071004 (2015)

Aboudi, J., Pindera, M-J., Arnold, S.M.: Linear thermoelastic higher-order theory for periodic multiphase materials. J. Appl. Mech. **68**, 697–707 (2001)

Aboudi, J., Arnold, S.M., Bednarcyk, B.A.: Micromechanics of Composite Materials: A Generalized Multiscale Analysis Approach. Elsevier, Oxford (2013)

Aboudi, J., Zheng, X., Jin, K.: Micromechanics of magnetostrictive composites. Int. J. Eng. Sci. **81**, 82–99 (2014)

Bednarcyk, B.A., Aboudi, J., Arnold, S.M.: The effect of general statistical fiber misalignment on predicted damage initiation in composites. Compos. Part B **66**, 97–108 (2014)

Bednarcyk, B.A., Aboudi, J., Arnold, S.M.: Analysis of fiber clustering in composite materials using high-fidelity multiscale micromechanics. Int. J. Solids Struct. **69–70**, 311–327 (2015)

Bednarcyk, B.A., Aboudi, J., Arnold, S.M.: Enhanced composite damping through engineered interfaces. Int. J. Solids Struct. **92–93**, 91–104 (2016)

Ben David, O., Banks-Sills, L., Aboudi, J., Fourman, V., Eliasy, R., Simhi, T., Shlayer, A. Raz, O.: Evaluation of the Mechanical Properties of PMMA Reinforced with Carbon Nanotubes - Experiments and Modeling. Exper. Mech. **54**, 175–186 (2013)

Gilat, R., Aboudi, J.: Behavior of elastoplastic auxetic microstructural arrays. Materials **6**, 726–737 (2013)

Haj-Ali. R., Aboudi, J.: Nonlinear micromechanical formulation of the high fidelity generalized method of cells. Int. J. Solids Struct. **46**, 2577–2592 (2009)

Haj-Ali. R., Aboudi, J.: Formulation of the high-fidelity generalized method of cells with arbitrary cell geometry for refined micromechanics and damage in composites. Int. J. Solids Struct. **47**, 3447–3461 (2010)

Haj-Ali. R., Aboudi, J.: Discussion paper: has renaming the high fidelity generalized method of cells been justified? Int. J. Solids Struct. **49**, 2051–2058 (2012)

Haj-Ali, R., Aboudi, J.: A new and general formulation of the parametric HFGMC micromechanical method for two and three-dimensional multi-phase composites. Int. J. Solids Struct. **50**(6), 907–919 (2013)

Haj-Ali, R., Aboudi, J.: Integrated microplane model with the HFGMC micromechanics for nonlinear analysis of composite materials with evolving damage. Int. J. Solids Struct. **90**, 129–143 (2016)

Haj-Ali., R., Zemer, H., El-Hajjar, R., Aboudi, J.: Piezoresistive fiber-reinforced composites: a coupled nonlinear micromechanical-microelectrical modeling approach. Int. J. Solids Struct. **51**, 491–503 (2014)

Jin, K., Aboudi, J.: Macroscopic behavior prediction of multiferroic composites. Int. J. Eng. Sci. **94**, 226–241 (2015)

Levi-Sasson, A., Aboudi, J., Matzenmiller, A., Haj-Ali, R.: Failure envelops for laminated composites by the parametric HFGMC. Compos. Struct. **140**, 378–389 (2015)

Paley, M., Aboudi, J.: Micromechanical analysis of composites by the generalized cells model. Mech. Mater **14**, 127–139 (1992)

Volokh, K.Y.: Review of the energy limiters approach to modeling failure of rubber. Rubber Chem. Tech. **86**, 470–487 (2013)

Volokh, K.Y., Aboudi, J.: Aneurysm strength can decrease under calcification. J. Mech. Behav. Biomed. Mater. **57**, 164–174 (2016)

# Chapter 15
# On Parameterization of the Reinforcement Phase Distribution in Continuous Fiber-Reinforced Composites

**Piotr Wolszczak, Sylwester Samborski, and Tomasz Sadowski**

**Abstract** This chapter discusses a problem of parameterization of irregular reinforcement distribution in uniaxial fiber-reinforced composites (CFRC) expressed as an area ratio of the matrix surrounding a single fiber to its perimeter. The distribution parameter, $G_{AB}$, was applied in the analysis of possible relationships between the microgeometry and mechanical properties of glass-epoxy composites with random distribution of continuous fibers. Test specimens were made in a repeatable process production of the girders of helicopter blades and were tested in bending during the short beam shear tests (SBST), as well as their basic mechanical properties (e.g., the flexural modulus $E_f$, taking into account shear effects) were determined. The relationship between the SBST results and the theoretical topology of regular CFRC structures was presented: the square (K) and the hexagonal (H) type. The K theoretical model of fiber distribution corresponded with experimental results. It was concluded that the measure of irregular reinforcement distribution ($G_{AB}$) could be used to estimate the flexural elastic modulus $E_f$ of unidirectional CFRC composites.

P. Wolszczak
Department of Automation, Lublin University of Technology, Nadbystrzycka 36, 20-618, Lublin, Poland

S. Samborski
Department of Applied Mechanics, Lublin University of Technology, Nadbystrzycka 36, 20-618 Lublin, Poland

T. Sadowski (✉)
Department of Solid Mechanics, Lublin University of Technology, Nadbystrzycka 36, 20-618 Lublin, Poland
e-mail: t.sadowski@pollub.pl



S.A. Meguid, G.J. Weng (eds.), *Micromechanics and Nanomechanics of Composite Solids*, DOI 10.1007/978-3-319-52794-9_15

## 15.1 Introduction

The reinforcement distribution in continuous fiber-reinforced composites (CFRC) can be highly anisotropic, which favors nonuniform stress distribution and can lead to matrix cracking or delamination. This adverse property weakens the reliability of such materials, despite their obvious merits from the engineering structures design point of view, such as high strength-to-mass ratio and a possibility of tailoring their mechanical characteristics. The mechanical properties of the CFRC composites depend on relative volume, size, and shape of the composite components (fibers). There is also an evidence that just the interface is largely responsible for the strength of composites. The reason for this is high degree of cross-linking in polymeric matrix. The uniformity of fiber distribution in unidirectional composites is crucial for the strength of a composite due to the orientation mechanism of the polymer. The technological irregularity of fiber distribution affects initiation of microdefects and decreases the composite strength. The analysis of theoretical models of reinforcement arrangement presented in the literature indicates that non-normal distribution of the topological elements increases the risk of transverse crack (delamination) onset and propagation inside the material subjected to mechanical loading e.g. Banerjee and Sankar (2014), Bienias et al. (2011), Sadowski and Samborski (2008), Postek and Sadowski (2011), Sadowski and Golewski (2008), Birsan et al. (2012), Sadowski and Golewski (2012a,b).

The irregularities of fiber arrangement in unidirectional composites are a consequence of manual treatment of the material during the manufacturing process. In practice, the analysis of fiber distribution in manually molded composites, the semi-empirical Halpin–Tsai approach, provides sufficient accuracy of the results for typical shape of fiber cross-section. Development of composite technology in nanoscale requires quality control for a weakly disordered system of fibers. Every manual methods of composite fabrication technology can be developed with the new distribution factors characterizing the irregularities of fiber arrangement Bieniaś et al. (2012), Talreja (2014), Megnis and Varna (2003), Torquato (1997), Jones(1999), Halpin and Kardos (1976), Bochenek and Pyrz (2004).

It seems to be important to examine the effect of the thickness of matrix layer surrounding a single fiber in a composite. Basic geometrical and topological parameters of fiber distribution should be considered and a representative measure for characterizing of the composite's fiber distribution should be established. Next the obtained solution could be applied to an estimation of selected strength characteristics. In the case of a moderately or strongly disordered system of fibers, morphological parameters of the microstructure could be replaced by their equivalent counterparts in the conjugated polygonal tessellation model. The topological properties of fibers in the polygonal tessellation model are related to morphological examination of the microstructure Pyrz (2000), Werwer et al. (1998), Banerjee and Sankar (2014), Yazdanbakhsh et al. (2011), Grasley and Yazdanbakhsh (2011), Sun et al. (2009), Pyrz and Bochenek (1998), Kurzydłowski and Ralph (1995), Wada and Fukuda (1999), Raghavan and Ghosh (2005).

The topological and the morphological properties of the unidirectional composite microstructure can be characterized by:

- Neighbor distances and orientations in all points of the observed area of the composite cross-section
- Areas of Dirichlet polygons conjugate to fibers
- Micromorphological parameters
- Degree of contiguity, etc.

In this chapter, a statistical analysis of several geometrical and topological properties of microstructures is presented, which allow for the most important composite microgeometry parameters substantially related to the overall mechanical composite properties. In particular the flexural modulus, $E_f$, was determined in shear strength experiments (SBST), whereas some new geometrical parameters were selected by formulation of discriminant functions for the composite cross-section. Namely, the geometrical parameters of microstructure were used for comparing irregular fiber patterns of the real composite to the regular and periodic microstructural models. Regular models were based on the K and the H patterns. In general, the patterns can be applied to the description of a complex nonhomogeneous internal structure, common in real composites Pyrz (2000), Kurzydłowski and Ralph (1995), Yu et al. (2015).

## 15.2 Experiments

### *15.2.1 Specimens and Experimental Tests*

The technology of specimens preparation consists of the E-glass fibers (10 μm diameter) arrangement in the epoxy resin matrix and curing the molded composite in environmental chamber at 60°C for 5–6 h. The operations were made manually in repeatable production conditions, the same as those for the girders of helicopter blades, with the relative volume of the glass fibers varied among the specimens (the average value was 51%).

The following tests were performed: three-point bending test (3-PBT), according to the ISO 14125 Standard and the SBST, according to the ISO 14130. The tests allowed to characterize mechanical properties of the analyzed composite. The tests were destructive and gave the following characteristics: the force at yield point $F_l$, the maximum force $F_{max}$, the maximum elastic deformation in shear test $L_1$, the maximum deflection in shear test $L_2$, and the beam deflection angle φ; the analysis was, however, limited to the elastic response of the composites.

The value of modulus of elasticity $E_f$ can be calculated with the following equation:

$$E_f = \frac{F_{max} L^3}{4BH^3 f} \tag{15.1}$$

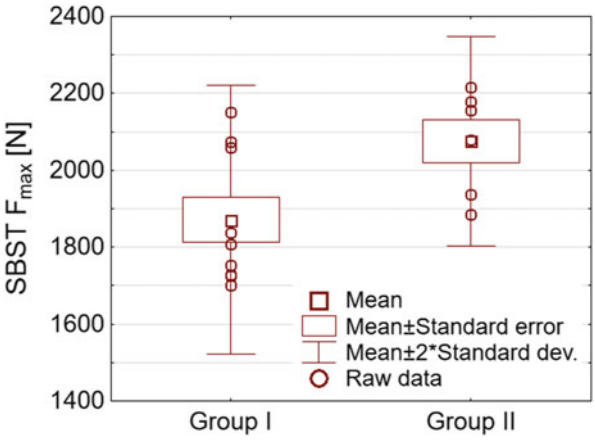


**Fig. 15.1** The maximum force $F_{max}$ [N] values obtained during the tests (SBST) for two subgroups of specimens

where:

$F_{max}$—the maximal force corresponding to the elastic limit measured in the SBST, *B, H, L*—the width, the thickness, and the specimen length, respectively, and $f$—the beam deflection at its midpoint with respect to its length.

The specimens used in the research constituted the homogeneous group of specimens manufactured in the aircraft factory with respect to the volume fraction, as well as the diameter distribution of glass fibers. After performing the strength tests, from that homogeneous group of specimens two subgroups emerged in accordance with the strength tests' results (Fig. 15.1). These two subgroups (numbered I and II) had similar glass fiber content, as well as the fiber diameter, but their strength was different.

The authors aimed at answering the question, if the property that differentiated the subgroups of specimens was the irregularity of the fiber arrangement and how important were the design (glass fiber content, fiber diameter) and the technological factors (number of flaws, e.g., fibers being in mutual contact or breaks in the interface, delaminations, etc.).

### *15.2.2 Microscopic Photographing and Image Processing*

The microscopic analysis was focused at the regions near the specimens' edges, where the mechanical load reached the highest value. Additionally, the irregular distribution of fibers and their agglomeration caused local concentration of the stress field. The cross-sectional analysis was performed with 40 photographs, and the average viewing area was 3.67 $mm^2$. The average cross-sectional area of the specimen in the bending test was 45 $mm^2$ ($3 \times 15$ mm). The exemplary microscopic fragment of cross-sections of the composite sample is presented in Fig. 15.2a. Figure 15.2 shows the processing steps of microstructure photographs analysis having in target determination of tessellation and calculation of factors characterizing distribution of fibers Wolszczak and Cechowicz (2011).

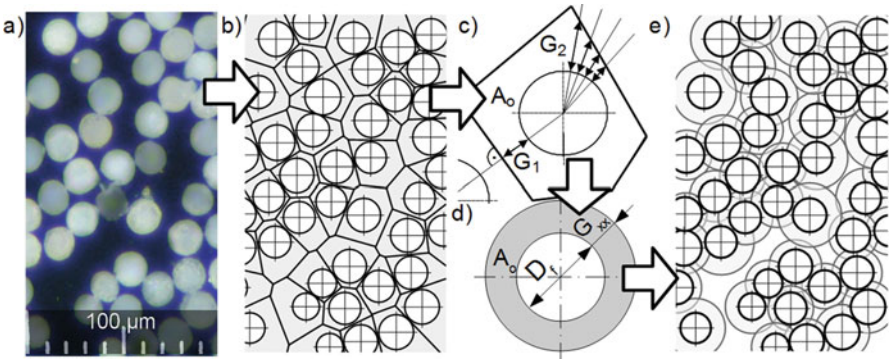


**Fig. 15.2** Processing steps in the microscopic analysis: the composite specimen cross-section (a fragment of the photograph) (**a**), the geometry image with tessellation polygons (**b**), the way of measurement of the thickness of matrix layer surrounding a fiber (**c**), the ring of matrix surrounding the fiber (**d**), and the geometrical model of the composite with the fields of matrix surrounding individual fibers, represented as the rings (**e**)

The microscopic analysis of the cross-section images allowed estimation of all distribution kinds of the fibers reinforcing the composite. In order to detect the edges of circle-shaped inclusions (fibers) and generation of the geometric image of a composite cross-section, a special computer software was elaborated by the first author. The software enables calculating all the measures characterizing the distribution of reinforcement phase in the composite. The geometry image (consisted of the coordinates and the diameters of circles) as well as the polygon tessellation enables determination of the factors characterizing the shape of the matrix sheath for each single fiber Chang et al. (2014), Samborski (2016).

### *15.2.3 Average Matrix Thickness of the Layer Surrounding a Single Fiber as the Measure of Fiber Distribution*

The surface area ($A_o$) of the matrix sheath surrounding any individual fiber was extracted with the tessellation method and could be represented as an equivalent of the area in the form of a ring of the thickness $G_{xx}$ (Fig. 15.2d). The ring area is the difference between the tessellation polygon and the circle area of the fiber cross-section:

$$A_o = \frac{\pi}{4}\left[\left(D_f + 2G_{XX}\right)^2 - D_f^2\right] \tag{15.2}$$

where
$D_f$—fiber diameter, and $G_{xx}$—thickness of the ring surrounding a fiber (the gray ring in Fig. 15.2c).

A set of characteristic parameters for matrix sheath surrounding a single fiber (see Fig. 15.2c) were defined, including:

- $G_1$—the local thickness of the matrix measured on sections connecting the centers of the neighboring fibers
- $G_2(\theta)$—the local thickness of the matrix measured along the circumference of the fiber at constant angular intervals ($\Delta\theta = 5°$)
- $G_{AD}$—the average film thickness $G_2$ calculated from the matrix area ($A_o$), derived from the formula (15.2) and the fiber diameter ($D_f$), according to the formula:

$$\overline{G}_2 \approx G_{AD} = \frac{1}{2}\left(\sqrt{D_f^2 + 4\frac{A_o}{\pi}} - D_f\right) \tag{15.3}$$

- $G_{AB}$—the quotient of the separated matrix area $A_o$ by the circuit fiber:

$$G_{AB} = \frac{A_o}{\pi D_f} \tag{15.4}$$

## 15.3 Statistical Analysis

### *15.3.1 Geometric Measures Influencing the Flexural Elastic Modulus $E_f$*

As a result of microscopic observations (Fig. 15.2a), the following measures characterizing the structure of the composite were collected:

- The relative volume of glass fibers—$V_f$ and the fiber diameter—$D_f$, characterizing the macrostructure
- The relative volume of gas bubbles—$V_{gb}$
- The topological entropy—$S$ and the minimum distance between the fibers—$G_{1min}$, characterizing the relative fiber position
- The matrix sheath thickness around the fibers—$G_2$, $G_{AB}$, $G_{AD}$
- The ratio of the areas of the tessellation polygon $A_c$ and the fiber $A_f$, i.e., $A_c/A_f$
- Additional set of variables containing the properties directly emerging from the polygon tessellation, such as:
  - The number of polygon sides—$n$
  - The polygon perimeter—$B_c$
  - The polygon area—$A_c$

for the calculation of the $G_{AB}$ and $G_{AD}$ measures and the topological entropy $S$.

In order to determine whether the properties of the composite microgeometry were associated with the flexural modulus $E_f$ or other strength parameters, the

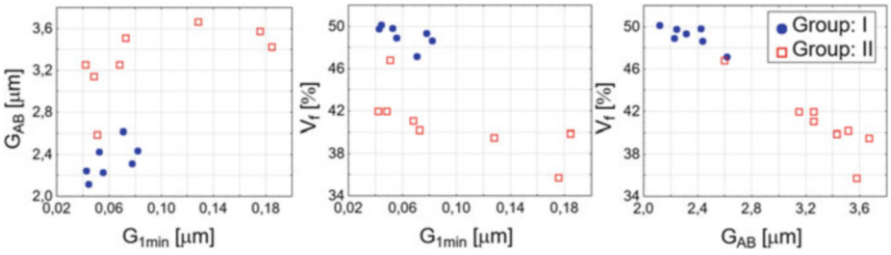


**Fig. 15.3** Individual specimens of groups I and II located in the space specified with the average values of $V_f$,$G_{AB}$, and $G_{1min}$

calculation of basic statistics was performed. In particular, fitting the theoretical parameter distributions to the experimental results and the Student's t-test evaluating variation of the mean values of the elastic modulus $E_f$ were done.

For determination of the geometric characteristics of composite cross-sections compatible with the results of the SBST tests, the discriminant analysis and the regression analysis were performed. The calculations took into account 40 images for each specimen. The discriminant analysis had in target determination of the geometrical measures responsible for the variability of the flexural strength (related to $F_{max}$), which enabled classification of the composite morphological quality into two subgroups (I and II). The regression analysis allowed to determine approximately linear relationship between the specified variables for estimation of the flexural elastic modulus $E_f$ value and for choosing the most substantive characteristics.

Three characteristics (the averaged values $\overline{G}_{AB}$, $\overline{G}_{1\,\mathrm{min}}$, and $\overline{V}_f$) were incorporated into the model during the discriminant analysis. Location of the specimens in the space formed by these three characteristics are shown in Fig. 15.3.

The discriminant function for the specimens from the subgroups I and II characterized by the vectors [$V_f$, $G_{AB}$, $G_{1min}$] has the form:

$$D1 = 14,357 + 1,649\, G_{AB} - 16,944\, G_{1\,\mathrm{min}} - 0,396\, V_f \tag{15.5}$$

The chi-square test used to calculate the significance level of the discriminant function gave the $p$-value below 0.0001 and the coefficient of canonical analysis, R, reached a high value (0.915), which proved that there is a strong correlation of the discriminant function with the separated subgroups of specimens.

When the specimens' vector was used for calculation with the classification function (Eq. 15.5), the results confirmed the discriminant ability of the classification function. The average percentage of the correct classification of the specimens to the original subgroups I and II was over 93%. Also, the calculation of the individual specimens' distance from the groups' centroids and the classification based on probabilities of sample association with the respective subgroup were consistent with the classification function. The standardized discriminant function coefficients revealed the effect of geometrical characteristics on the diversity of two subgroups

**Table 15.1** Discriminant function coefficients and factorial structure's coefficients of geometrical characteristics

| | $G_{AB}$ | $G_{1min}$ | $V_f$ | |
|---|---|---|---|---|
| Discriminant function coefficients | | | | 5.515 |
| | 0448 | −0746 | −0945 | |
| Factor structure coefficients | 0837 | 0188 | −0810 | |

**Table 15.2** Discriminant analysis results: coefficients of linear regression and standard error values

| Characteristics | Constant | $G_{AB}$ | $G_{1min}$ | $V_f$ |
|---|---|---|---|---|
| Estimated values | 93.82 | −20.52 | 77.74 | −0.0076 |
| Standard errors | 115.4 | 13.7 | 50.9 | 1.69 |

(I and II). On the other hand, the values of the factorial structure's coefficients demonstrate the individual contribution of these variables to the development of the discriminant function (Table 15.1).

As shown in Table 15.1, the coefficients of the standardized discriminant function determined the effect of each variable on the diversity of the subgroups I and II. The $V_f$ parameter reached the highest value of the standardized coefficient equal −0.945. Concurrently, the volume fraction of glass fiber ($V_f$) confirmed the theoretical correlation with $G_{AB}$. Accordingly, the coefficient of $G_{AB}$ had opposite sign to $V_f$, which meant that the contribution of the $G_{AB}$ variable was reduced by $V_f$. Therefore the factorial structure's coefficients were analyzed (Table 15.1). Although the values of the discriminant function's coefficients for $G_{AB}$ and $V_f$ reached similar values, the coefficient for $G_{AB}$ was bigger. The significant impact of the variability of volume fraction of glass fiber $V_f$ makes it difficult to analyze importance of the fiber arrangement characteristics. A lack of any significant effect of the fiber diameter is a confirmation of the experiment plan of receiving specimens of the same fiber diameter.

Verification of effect of the three characteristics—$G_{1min}$, $G_{AB}$, $V_f$—on the value of flexural modulus $E_f$ was carried out using the multiple regression analysis (MRA) method. The experimental results were compared with those obtained theoretically for the function $E_f$ ($G_{1min}$, $G_{AB}$, $V_f$). In Table 15.2, there are shown the coefficients of linear regression and the respective standard errors calculated in discriminant analysis.

On the base of the obtained discriminant function coefficients a cumulative proportion values were calculated which explained 74% of the variance of the subgroups I and II, with the correlation coefficient $R = 0.86$. The significance of the coefficients is consistent with the results of the discriminant analysis and is easy to be interpreted.

It was observed that an increase in the value of the average thickness $\overline{G}_{AB}$ of the matrix sheath at the fibers in the composite causes a decrease of the flexural elastic modulus $E_f$. It may be connected with a decrease of the volume fraction of glass fibers $V_f$ or an increase of the shrinkage areas (lower fiber content regions).

The improvement of the elasticity of the composite expressed by $E_f$ is caused by the increase of the minimum distance between fibers $G_{1min}$.

The analysis of influence of geometrical characteristics on the value of the flexural elastic modulus $E_f$ using the unidirectional composites produced in the factory allows the conclusion that the most important characteristics of the composite microgeometry are the following:

- The contractual average matrix sheath thickness for a single fiber, $G_{AB}$
- The minimum matrix sheath thickness for a single fiber, $G_{1min}$
- The volume fraction of glass fiber, $V_f$

highlighted during statistical analysis of strength tests and microscopic measurements' results. These certainly should be complemented by:

- The fiber diameter, $D_f$
- The standard deviation, $S_{VGab}$, of the thickness $G_{AB}$

The thickness $G_{AB}$ plays the most important role in the assessment of the flexural modulus $E_f$, but it does not provide exact quantitative information about possible composite microstructure inhomogeneities, such as the number of fibers being in contact. The significance of the average minimum distance between neighboring fibers, $G_{1min}$, is probably due to the existence of local stress concentration regions, where microdefects initiate at the advanced stage of the composite deformation.

### *15.3.2 Comparison of the Real Composite Cross-Sections and the Theoretical Models*

The authors investigated the applicability of two base regular micromechanical models: K (square arrangement of fibers) and H (hexagonal arrangement of fibers) for estimation of mechanical properties of CFRC composites. Figure 15.4 presents an implementation of both models with a constant fiber diameter ($D_f = const.$) and a constant distance ($a = const.$) between the fibers. It was assumed that the maximum fiber volume fraction $V_{fmax}$ (when $G_{AB} \rightarrow$ min) was 79% for the K fiber distribution model and 91% for H type structure.

The experimental data (average fiber diameter $\overline{D}_f = 10\ \mu m$) were compared with theoretical models ($D_f = 10\ \mu m = const$). Figure 15.5a presents the correlation of averaged matrix sheath thicknesses $G_{AB}$ and $G_{AD}$, divided by the fiber diameter $D_f$ for each individual fiber versus the local glass fiber volume fraction, $V_f$. The theoretical square model, K outcomes (continuous lines) quite precisely replicate the characteristics of real fibers with their surroundings. Figure 15.5b shows the correlation of the matrix sheath thickness as a function of the matrix surface area, $A_o$, enclosed in the tessellation polygon. One can conclude that the increase of $A_o$ induces the increase of the spacing between fibers ($a$). The values of thickness $G_{AB}$ are higher than $G_{AD}$ and $G_{1min}$ with increasing the area $A_o$. The relationship between the thickness $G_{AB}$ and the area $A_o$ is linear, while the dependency of $G_{1min}$, $G_{2max}$, and $G_{AD}$ thicknesses are nonlinear.

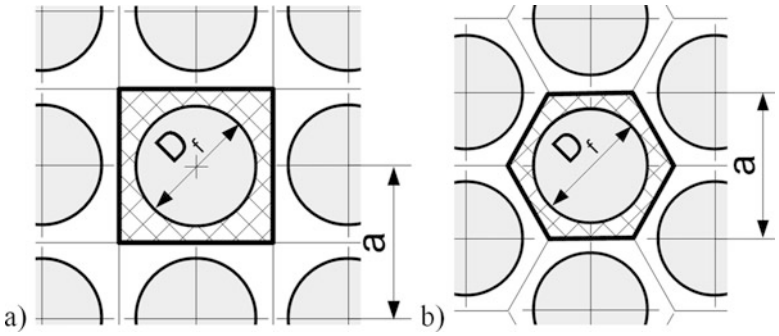


**Fig. 15.4** Theoretical arrangements of fibers: the K (*square*) model (**a**) and the H (hexagonal) model (**b**)

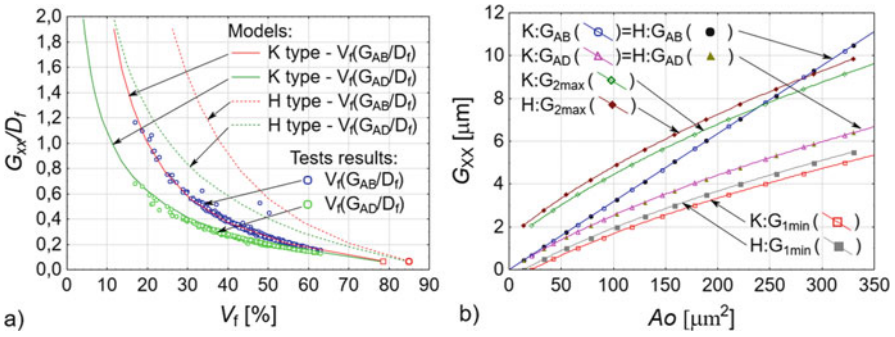


**Fig. 15.5** Relationship between experimental results and theoretical *square* model (K): (**a**)$V_f$ vs $G_{AB}/D_f$ and $G_{AD}/D_f$ in a single tessellation polygon, as experimental results and theoretical models of K (*square—continuous lines*) and H (hexagonal—*dotted line*) types. (**b**) The dependency of the matrix thickness surrounding a single fiber (calculated with different methods) and area of matrix for the regular K (*square*) and H (hexagonal) models

Figure 15.6 shows the distribution of thicknesses $G_{AB}$ and $G_{AD}$ in function of the matrix area $A_o$ determined for any single fiber for the real specimens and the adequate curves obtained with the regular model K. The function approximated by the least squares (LS) method of experimental thickness $G_{AB}$ to $A_o$ (the continuous line) is localized near a theoretical curve. It represented the regular square model (K). The microgeometrical characteristics $G_{1min}$ and $G_{2max}$ plotted for the theoretical square model create the upper and lower limits for experimentally obtained thicknesses $G_{AB}$ and $G_{AD}$.

## 15.4 Summary and Conclusions

The chapter presents microscopic observations of polymer-matrix composite cross-section specimens obtained from industrial process production and their mechanical shear testing in bending (SBST). For characterizing the composite's microgeometry,

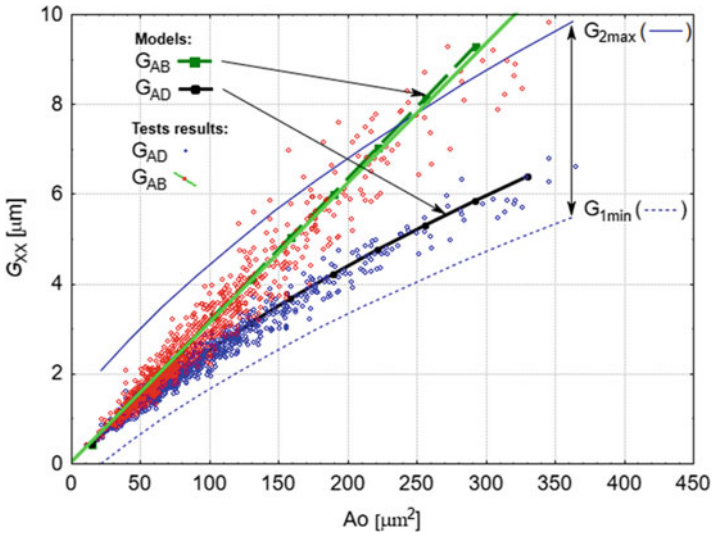


**Fig. 15.6** Dependency of the matrix sheath at a single fiber (calculated with different methods) on the area $A_o$ in experiment and theoretical square model (*K*type)

the new measures were proposed. The performed experiment led to the following findings:

The unidirectional composite material can be classified to different classes of strength characterized by the flexural elastic modulus $E_f$ using geometric features of the microstructure, including: the average fiber diameter $D_f$, matrix sheath thickness average $G_{AB}$ and its standard deviation $S_{VGab}$, the minimum matrix thickness $G_{1min}$, and the volume fraction of the glass fibers $V_f$.

The fiber distribution uniformity proved to be the most important and was best represented by the $G_{AB}$ parameter. In the range of variation of the variables considered in the experiment, the set of three characteristics form a linear function that allows to predict the flexural elastic modulus $E_f$.

The real thickness of matrix sheath surrounding a fiber, separated by tessellation, was consistent (assuming $D_f = \text{const.}$) with the values calculated with the theoretical square model (K).

## References

Banerjee, S., Sankar, B.V.: Mechanical properties of hybrid composites using finite element method based micromechanics. Compos. Part B Eng. **58**, 318–327 (2014)

Bieniaś, J., Dębski, H., Surowska, B., Sadowski, T.: Analysis of microstructure damage in carbon/epoxy composites. Comput. Mater. Sci. **64**, 168–172 (2012)

Bîrsan, M., Altenbach, H., Sadowski, T., Eremeyev, V.A., Pietras, D.: Deformation analysis of functionally graded beams by the direct approach. Compos. Part B. **43**, 1315–1328 (2012)

Bochenek, B., Pyrz, R.: Reconstruction of random microstructures - a stochastic optimization problem. Comput. Mater. Sci. **31**, 93–112 (2004)
Chang, S.-H., Parinov, I., Topolov, V.Y.: Advanced Materials Physics, Mechanics and Applications. Springer, Cham, Heidelberg, New York, Dordrecht, London (2014)
Halpin, J.C., Kardos, J.C.: The Halpin-Tsai equation. A review. Polym. Eng. Sci. **16**, 344–352 (1976)
Jones, R.M.: Mechanics of Composite Materials. Taylor and Francis Inc., Philadelphia/Levittown/London (1999)
Kurzydłowski, K.J., Ralph, B.: The Quantitative Description of the Microstructure of Materials. CRC, London (1995)
Megnis, M., Varna, J.: Micromechanics based modeling of nonlinear viscoplastic response of unidirectional composite. Comput. Mater. Sci. **63**, 19–31 (2003)
Postek, E., Sadowski, T.: Assessing the influence of porosity in the deformation of metal-ceramic composites. Compos. Interfaces **18**, 57–76 (2011)
Pyrz, R., Bochenek, B.: Topological disorder of microstructure and its relation to the stress field. Int. J. Solids Struct. **19**, 2413–2427 (1998)
Pyrz, R.: Morphological characterization of microstructures. In: Kelly, A., Zweben, C. (eds.) Comprehensive Composite Materials, pp. 465–478. Elsevier Science, Oxford (2000)
Raghavan, P., Ghosh, S.: A continuum damage mechanics model for unidirectional composites undergoing interfacial debonding. Mech. Mater. **37**, 955–979 (2005)
Sadowski, T., Golewski, G.: Effect of aggregate kind and graining on modelling of plain concrete under compression, Comput. Mat. Sci. **43**, 119–126 (2008)
Sadowski, T., Golewski, P.: The influence of quantity and distribution of cooling channels of turbine elements on level of stresses in the protective layer TBC and the efficiency of cooling, Comput. Mater. Sci. **52**, 293–297 (2012a)
Sadowski, T., Golewski, P.: Detection and numerical analysis of the most efforted places in turbine blades under real working conditions, Comput. Mater. Sci. **64**, 285–288 (2012b)
Sadowski, T., Samborski, S.: Development of damage state in porous ceramics under compression. Comput. Mater. Sci. **43**, 75–81 (2008)
Samborski, S.: Numerical analysis of the DCB test configuration applicability to mechanically coupled Fiber Reinforced Laminated Composite beams. Compos. Struct. **152**, 477–487 (2016) of communication. AT&T Technol. J. **27**, 379–423, 623–656 (1948)
Sun, L., Gibson, R.F., Gordaninejad, F., Suhr, J.: Energy absorption capability of nanocomposites: A review. Compos. Sci. Technol. **69**, 2392–2409 (2009)
Talreja R. Multiscale modeling of damage in composite materials. In: Sadowski, T., Trovalusci, P. (eds.) CISM International Centre for Mechanical Sciences, Courses and Lectures Vol. 556: Multiscale modeling of complex materials. Phenomenological, theoretical and computational aspects, pp. 179–209. Springer, Wien Heidelberg New York Dodrecht London (2014), p. 539. Clarendon Press. Oxford. Great Britain (1938)
Torquato, S.: Exact expression for the effective elastic tensor of disordered composites. Phys. Rev. Lett. **79**, 681 (1997)
Wada, A., Fukuda, H.: Approximate upper and lower bounds for the strength of unidirectional composites. Compos. Sci. Technol. **59**, 89–95 (1999)
Werwer, M., Cornec, A., Schwalbe, K.-H.: Local strain fields and global plastic response of continuous fiber reinforced metal-matrix composites under transverse loading. Comput. Mater. Sci. **12**, 124–136 (1998)
Wolszczak, P., Cechowicz, R.: Examination of the influence of shear micro geometrical properties on transverse elasticity the modulus of roving composite materials used in critical constructions. Composite Materials For Structural Performance: Towards Higher Limits. Book Series: Riso International Symposium on Material Science, pp. 487–496. (2011)
Yazdanbakhsh, A., Grasleyb, Z., Tysonc, B., Al-Rub, R.K.A.: Dispersion quantification of inclusions in composites. Compos. Part A. **42**, 75–83 (2011)
Yu, Y., Zhang, B., Tang, Z., Qi, G.: Stress transfer analysis of unidirectional composites with randomly distributed fibers using finite element method. Compos. Part B. **69**, 278–285 (2015)

# Chapter 16
# Micromechanical Modeling of Polymeric Composite Materials with Moisture Absorption

**Yihui Pan and Zheng Zhong**

**Abstract** Natural fiber reinforced composites and wood cell wall are two typical polymeric composite materials that can uptake large amounts of water in the humid environment. This chapter presents a micromechanical scheme to study the mechanical degradation of these polymeric composites induced by moisture absorption that takes place in the matrix and/or the reinforcing phase. The moisture absorption and the mechanical degradation are two thermodynamic processes correlated with each other. Taking both processes into consideration, a modified Mori–Tanaka method with introduced damage variables is proposed. The moisture absorption and the mechanical degradation are, respectively, described by eigenstrains and damage variables. After specifying this model with different inclusion shapes, the overall swelling deformation and the mechanical degradation of the randomly oriented and the unidirectional straight fiber reinforced polymeric composites are studied. The theoretical predictions are compared with the experimental results from other literature and a good agreement is obtained.

## 16.1 Introduction

The micromechanical framework based on the inclusion method has been successfully used in predicting effective properties of composite materials (Aboudi 1991; Milton 2002; Nemat-Nasser and Hori 1999; Torquato 2002; Watt et al. 1976). Accompanying the development of micromechanical models, more and more specific characteristics of materials and structures can be analyzed and interpreted from a microscopic level, such as imperfect interfaces between the inhomogeneity and the matrix (Benveniste and Miloh 2001; Qu 1993; Zheng et al. 2000; Zhong and Meguid 1997). In recent years, with increasing environmental awareness from the general public, numerous efforts have been devoted to natural fiber reinforced composites (NFRCs) (Dhakal et al. 2007). For the current micromechanical framework, it comes

Y. Pan • Z. Zhong (✉)
School of Aerospace Engineering and Applied Mechanics, Tongji University, Shanghai 200092, China
e-mail: 083633@tongji.edu.cn; zhongk@tongji.edu.cn



S.A. Meguid, G.J. Weng (eds.), *Micromechanics and Nanomechanics of Composite Solids*, DOI 10.1007/978-3-319-52794-9_16

to a new challenge to predict the material properties of NFRCs since the material properties and the stress state of NFRCs dynamically evolve with the swelling strain in the humid environment. The similar phenomena of moisture absorption and mechanical degradation can also been found in the wood cell wall which is the microstructure of natural fibers (Smith 2003). Hence, in this chapter, we attempt to establish a novel micromechanical framework to take both moisture absorption and mechanical degradation into consideration, before which such hydrophilic polymeric materials as wood cell wall and NFRCs will be introduced briefly below.

There are three constituent materials in the wood cell wall: cellulose microfibril (CMF, $40-50$ wt%), hemicellulose (25 wt%), and lignin ($20-30$ wt%) (Smith 2003). The CMFs, with tensile modulus along longitudinal direction as high as $120-170$ GPa, show little affinity to moisture absorption in its crystal region and almost maintain its original mechanical properties in a humid environment above fiber saturation point (FSP) (Kojima and Yamamoto 2005; Tashiro and Kobayashi 1991). By contrast, the hemicellulose with elastic modulus as low as 2 GPa is strongly hydrophilic which has remarkable softening effects on its mechanical properties. Such softening phenomenon becomes more obvious after more water uptake. For instance, the elastic modulus of hemicellulose decreases even to 20 MPa when it is fully saturated (Salmén 2004).

The wood cell wall is the microstructure of the $S_2$ layer of natural fibers. Hence, the composites reinforced by natural fibers (NFRCs) also exhibit strong hydrophilicity and remarkable mechanical degradation. In the humid environment, the difference of the chemical potential of water inside and outside can motivate the water to flow into or out of the composites. Moreover, microcracks and voids destroy or reduce interface compatibility and further lead to the interface debonding between natural fibers and matrix (Cheung et al. 2009; Hu et al. 2010; Sgriccia et al. 2008). Both fiber aging and interface damage induce the mechanical degradation of NFRCs such as the reduction of elastic moduli (Song et al. 2011).

As is seen above, both wood cell wall and NFRCs can be treated as an eigenstrain problem that is induced by moisture absorption. Meanwhile, such moisture absorption further causes mechanical degradation of the composites. One should especially note that in the wood cell wall, the CMFs as reinforcement with circular cylindrical shape are enclosed by a matrix composed of hemicellulose and lignin, so that they can be modeled as long fiber reinforced composites under the micromechanical framework based on the inclusion method. For NFRCs, the inhomogeneity (natural fiber) is hydrophilic and the matrix is usually hydrophobic (Cheung et al. 2009). However, for wood cell wall, the difference is that the inhomogeneity (CMF) is hydrophobic while the matrix (hemicellulose) is hydrophilic. For biodegradable polymer-natural fiber biocomposites, both the matrix and the inhomogeneity uptake waters in the humid environment (Alvarez et al. 2004). According to continuum damage mechanics (Chow and Wang 1987), the loss of moduli in inhomogeneities and/or matrix can be treated as a damage process caused by moisture absorption. Hence damage variables are introduced into the existing micromechanical framework to describe the loss of moduli.

To introduce damage mechanism into the classic Mori–Tanaka scheme is an effective way to predict the overall properties of the composites undergoing damage. The damage can occur in the reinforcement phase or matrix phase. Mochida et al. (1991) treated the damaged particles (reinforcement phase) as voids to describe the damage generation in the composites. Ravichandran and Liu (1995) further introduced two damage variables into the Mori–Tanaka method to describe the transition of particles into voids. In this case, the material properties of the reinforcement phase changes with the evolution of damage variables. Another effort on the Mori–Tanaka method considering damage is to study the degradation of the matrix phase (Desrumaux et al. 2001; Meraghni and Benzeggagh 1995). However, the existing damage mechanism contributes to the generation of voids or cracks that are caused by mechanical loadings, rather than the initial eigenstrains (i.e., swelling strains considered in this chapter). In view of the correlated processes of moisture absorption and mechanical degradation in polymeric composites, a novel modified Mori–Tanaka scheme with damage variables is established in this chapter. The evolutions of these damage variables depend on the swelling strain. And then this model is applied to study the problem of biodegradable polymer-natural fiber biocomposites, NFRCs, and wood cell wall.

The present chapter is organized as follows. A modified Mori–Tanaka scheme with damage variables is established in Sect. 16.2, in which both matrix and inhomogeneity uptake water and undergo mechanical degradation. In Sect. 16.3, the randomly oriented straight natural fiber reinforced composites are studied and a comparison between theoretical and experimental results of the sisal fiber reinforced polypropylene matrix is given. In Sect. 16.4, the proposed micromechanical model is employed to predict the modulus loss of wood cell wall, and the predicted tensile moduli along the cell axis are compared with the available experimental results under different MFAs and moisture contents. Finally in Sect. 16.5, we draw the conclusions.

## 16.2 Micromechanical Framework

For composites, the reinforcing fibers or particles can be treated as inhomogeneities (denoted as $\Omega$) which are embedded in an infinite matrix (denoted as $\mathrm{D}-\Omega$). Both the inhomogeneity and the matrix are hydrophilic and free of any initial stress. The inhomogeneity and the matrix are subject to free swelling strains, $\boldsymbol{\varepsilon}^{fs}$ and $\boldsymbol{\varepsilon}^{ms}$, respectively, in a humid environment. The governing equations and boundary conditions for this problem are given as

$$\begin{cases} \nabla\cdot\boldsymbol{\sigma}^{(i)}=0 \quad \boldsymbol{\varepsilon}^{(i)}=\frac{1}{2}\left(\nabla\mathbf{u}^{(i)}+\mathbf{u}^{(i)}\nabla\right) & \text{in } \mathrm{D} \\ \boldsymbol{\sigma}^{(1)}=\mathbf{C}^{(1)}:\left(\boldsymbol{\varepsilon}^{(1)}-\boldsymbol{\varepsilon}^{fs}\right) & \text{in } \Omega \\ \boldsymbol{\sigma}^{(2)}=\mathbf{C}^{(2)}:\left(\boldsymbol{\varepsilon}^{(2)}-\boldsymbol{\varepsilon}^{ms}\right) & \text{in } \mathrm{D}-\Omega \\ \left[\boldsymbol{\sigma}^{(1)}-\boldsymbol{\sigma}^{(2)}\right]\cdot\mathbf{n}=0 \text{ and } \mathbf{u}^{(1)}=\mathbf{u}^{(2)} & \text{on } \partial\Omega \\ \boldsymbol{\sigma}^{(2)}=0 & \mathbf{x}\to\infty \end{cases} \tag{16.1}$$

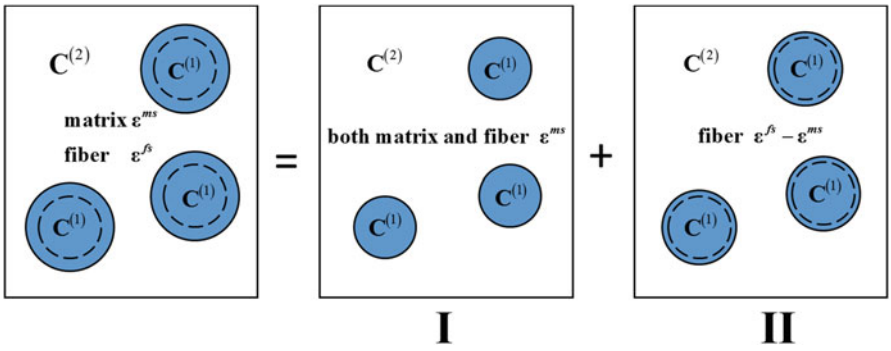


**Fig. 16.1** The original problem and two decomposed sub-problems

where, and throughout the chapter, a colon between two tensors denotes a contraction (inner product) over two indices; $\boldsymbol{\sigma}^{(i)}$, $\boldsymbol{\varepsilon}^{(i)}$, $\mathbf{u}^{(i)}$, and $\mathbf{C}^{(i)}(i=1,2)$ are, respectively, the stress, the strain, the displacement, and the stiffness of inhomogeneities (labeled by the superscript "1") and the matrix (labeled by the superscript "2"). $\partial\Omega$ denotes the interface between $\Omega$ and $\mathrm{D}-\Omega$, $\mathbf{n}$ is the outward unit normal on the interface, and $\nabla = \mathbf{i}_m \frac{\partial}{\partial x_m}$ is the Hamilton operator with $\mathbf{i}_m$ being the unit vector.

The initial eigenstrain is distributed differently in the inhomogeneities and the matrix, so it is difficult to solve Eq. (16.1) directly by a classic eigenstrain problem. Hence, the original problem described by Eq. (16.1) is further decomposed into two sub-problems as illustrated in Fig. 16.1, which can be solved by employing the Eshelby formula for the classic inclusion problem.

In sub-problem I, a swelling strain $\boldsymbol{\varepsilon}^{ms}$ is uniformly distributed both in the inhomogeneities and the matrix, without any other external mechanical loads, so that the governing equations and boundary conditions for sub-problem I can be written as

$$\begin{cases} \nabla\cdot\boldsymbol{\sigma}^{(i),\mathrm{I}}=0 \quad \boldsymbol{\varepsilon}^{(i),\mathrm{I}}=\frac{1}{2}\left(\nabla\mathbf{u}^{(i),\mathrm{I}}+\mathbf{u}^{(i),\mathrm{I}}\nabla\right) & \text{in } \mathrm{D} \\ \boldsymbol{\sigma}^{(1),\mathrm{I}}=\mathbf{C}^{(1)}:\left(\boldsymbol{\varepsilon}^{(1),\mathrm{I}}-\boldsymbol{\varepsilon}^{ms}\right) & \text{in } \Omega \\ \boldsymbol{\sigma}^{(2),\mathrm{I}}=\mathbf{C}^{(2)}:\left(\boldsymbol{\varepsilon}^{(2),\mathrm{I}}-\boldsymbol{\varepsilon}^{ms}\right) & \text{in } \mathrm{D}-\Omega \\ \left[\boldsymbol{\sigma}^{(1),\mathrm{I}}-\boldsymbol{\sigma}^{(2),\mathrm{I}}\right]\cdot\mathbf{n}=0 \text{ and } \mathbf{u}^{(1),\mathrm{I}}=\mathbf{u}^{(2),\mathrm{I}} & \text{on } \partial\Omega \\ \boldsymbol{\sigma}^{(2),\mathrm{I}}=0 & \mathbf{x}\to\infty \end{cases} \tag{16.2}$$

where the superscript "I" stands for physical quantities in the sub-problem I.

Obviously, the stresses $\boldsymbol{\sigma}^{(1),\mathrm{I}}=\boldsymbol{\sigma}^{(2),\mathrm{I}}=0$ and the strains $\boldsymbol{\varepsilon}^{(1),\mathrm{I}}=\boldsymbol{\varepsilon}^{(2),\mathrm{I}}=\boldsymbol{\varepsilon}^{ms}$ satisfy all the governing equations and boundary conditions of sub-problem I.

As for sub-problem II, an initial eigenstrain $\boldsymbol{\varepsilon}^{fs}-\boldsymbol{\varepsilon}^{ms}$ is imposed only in the inhomogeneities, and the matrix is free of any external mechanical loads and initial eigenstrains. Therefore, the governing equations and the boundary conditions for sub-problem II are given as

$$\begin{cases} \nabla \cdot \boldsymbol{\sigma}^{(i),\mathrm{II}} = 0 \quad \boldsymbol{\varepsilon}^{(i),\mathrm{II}} = \frac{1}{2}\left(\nabla \mathbf{u}^{(i),\mathrm{II}} + \mathbf{u}^{(i),\mathrm{II}} \nabla\right) & \text{in D} \\ \boldsymbol{\sigma}^{(1),\mathrm{II}} = \mathbf{C}^{(1)} : \left(\boldsymbol{\varepsilon}^{(1),\mathrm{II}} - \boldsymbol{\varepsilon}^{fs} + \boldsymbol{\varepsilon}^{ms}\right) & \text{in } \Omega \\ \boldsymbol{\sigma}^{(2),\mathrm{II}} = \mathbf{C}^{(2)} : \boldsymbol{\varepsilon}^{(2),\mathrm{II}} & \text{in D} - \Omega \\ \left[\boldsymbol{\sigma}^{(1),\mathrm{II}} - \boldsymbol{\sigma}^{(2),\mathrm{II}}\right] \cdot \mathbf{n} = 0 \text{ and } \mathbf{u}^{(1),\mathrm{II}} = \mathbf{u}^{(2),\mathrm{II}} & \text{on } \partial\Omega \\ \boldsymbol{\sigma}^{(2),\mathrm{II}} = 0 & \mathbf{x} \to \infty \end{cases} \tag{16.3}$$

where the superscript "II" denotes physical quantities in the sub-problem II.

Accordingly, the stress and the displacement of the original problem are the superposition of those of sub-problems I and II, namely,

$$\begin{cases} \boldsymbol{\sigma}^{(1)} = \boldsymbol{\sigma}^{(1),\mathrm{I}} + \boldsymbol{\sigma}^{(1),\mathrm{II}} \\ \boldsymbol{\sigma}^{(2)} = \boldsymbol{\sigma}^{(2),\mathrm{I}} + \boldsymbol{\sigma}^{(2),\mathrm{II}} \end{cases} \quad \begin{cases} \mathbf{u}^{(1)} = \mathbf{u}^{(1),\mathrm{I}} + \mathbf{u}^{(1),\mathrm{II}} \\ \mathbf{u}^{(2)} = \mathbf{u}^{(2),\mathrm{I}} + \mathbf{u}^{(2),\mathrm{II}} \end{cases} \tag{16.4}$$

It is difficult to obtain an exact solution for stress and strain fields in the inhomogeneities and the matrix in sub-problem II. Instead, some approximate models can be used to estimate the average stress or strain in the inhomogeneity and the matrix by considering in part the interaction between matrix and inhomogeneities. In this chapter, based on the Mori–Tanaka method, the average stresses in the matrix and the inhomogeneity (i.e., $\{\boldsymbol{\sigma}^{(1),\mathrm{II}}\}$ and $\{\boldsymbol{\sigma}^{(2),\mathrm{II}}\}$) of sub-problem II can be derived from an equivalent eigenstrain problem, as illustrated in Fig. 16.2. Here the denotation "$\{\bullet\}$" denotes the volume average of any physical quantity "$\bullet$".

By means of the Mori–Tanaka method, the inhomogeneity with stiffness $\mathbf{C}^{(1)}$ is considered to be embedded in an infinite matrix with stiffness $\mathbf{C}^{(2)}$, subject to a remote stress field $\{\boldsymbol{\sigma}^{(2),\mathrm{II}}\}$. And the strain $\boldsymbol{\varepsilon}^{fs} - \boldsymbol{\varepsilon}^{ms}$ illustrated in Fig. 16.2 can be treated as an initial eigenstrain. Hence, the sub-problem II can be further decomposed into two sub-problems as shown in Fig. 16.2: (1) a homogeneous infinite body with uniform stress field $\{\boldsymbol{\sigma}^{(2),\mathrm{II}}\}$, denoted as the sub-problem $\mathrm{II}_1$, and (2) an

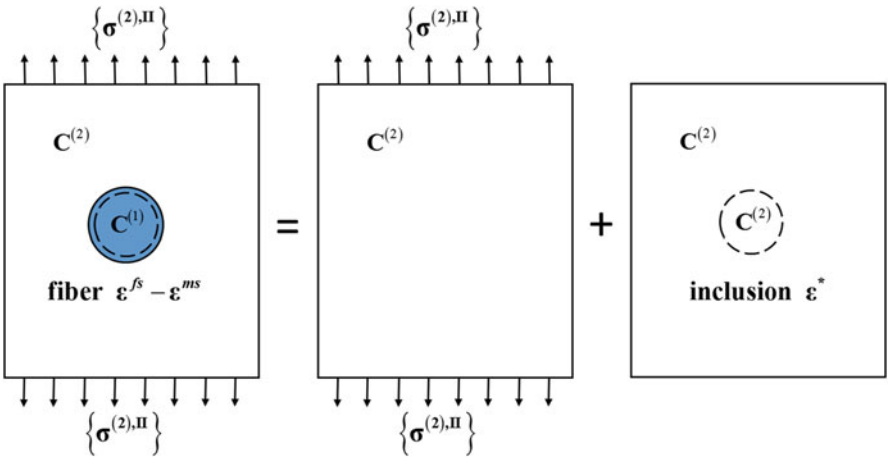


**Fig. 16.2** The equivalent inclusion method for sub-problem II

infinite matrix containing an inclusion (both have stiffness $\mathbf{C}^{(2)}$) with an equivalent eigenstrain $\boldsymbol{\varepsilon}^*$ induced by the mismatch of the stiffness between fibers and matrix, denoted as $\mathrm{II}_2$. The relevant treatments and solutions to sub-problem II have been studied in our previous paper for moisture absorption only taking place in the inhomogeneity (Pan and Zhong 2015) and only in the matrix (Pan and Zhong 2016).

Let us choose a representative volume element (RVE) of the composite for consideration. The stresses in the matrix and the fiber do not vanish because of the interaction between these two materials with mismatch properties under moisture absorption, even though no other external loads exist. The average stress $\{\boldsymbol{\sigma}^{\mathrm{II}}\}$ in a RVE of the composite for sub-problem II can be written as

$$\left\{\boldsymbol{\sigma}^{\mathrm{II}}\right\} = f\left\{\boldsymbol{\sigma}^{(1),\mathrm{II}}\right\} + (1-f)\left\{\boldsymbol{\sigma}^{(2),\mathrm{II}}\right\} = 0 \tag{16.5}$$

where $f$ is the volume fraction of the inhomogeneity. The real stress and strain in the inhomogeneity are uniform for a uniform equivalent eigenstrain $\boldsymbol{\varepsilon}^*$, so that we have $\boldsymbol{\sigma}^{(1),\mathrm{II}} = \{\boldsymbol{\sigma}^{(1),\mathrm{II}}\}$ and $\boldsymbol{\varepsilon}^{(1),\mathrm{II}} = \{\boldsymbol{\varepsilon}^{(1),\mathrm{II}}\}$. Furthermore, if the inhomogeneities are randomly oriented, the volume average $\{\bullet\}$ should be substituted by orientation average $\langle\bullet\rangle$. It is noted that $\{\boldsymbol{\sigma}^{(1),\mathrm{II}}\} = \langle\boldsymbol{\sigma}^{(1),\mathrm{II}}\rangle$ if the fibers with the same geometry are uniformly distributed in the matrix.

The stress in the inhomogeneity can be written as

$$\boldsymbol{\sigma}^{(1),\mathrm{II}} = \mathbf{C}^{(1)} : \left(\boldsymbol{\varepsilon}^{(1),\mathrm{II}} - \boldsymbol{\varepsilon}^{fs} + \boldsymbol{\varepsilon}^{ms}\right) \tag{16.6}$$

Based on the equivalent inclusion method as shown in Fig. 16.2, the stress in the inhomogeneity can also be given as

$$\boldsymbol{\sigma}^{(1),\mathrm{II}} = \mathbf{C}^{(2)} : \left(\boldsymbol{\varepsilon}^{(1),\mathrm{II}} - \boldsymbol{\varepsilon}^{*}\right) \tag{16.7}$$

The equivalence between Eqs. (16.6) and (16.7) holds when

$$\mathbf{C}^{(1)} : \left(\boldsymbol{\varepsilon}^{(1),\mathrm{II}} - \boldsymbol{\varepsilon}^{fs} + \boldsymbol{\varepsilon}^{ms}\right) = \mathbf{C}^{(2)} : \left(\boldsymbol{\varepsilon}^{(1),\mathrm{II}} - \boldsymbol{\varepsilon}^{*}\right) = \mathbf{C}^{(2)} : \left(\boldsymbol{\varepsilon}^{(1),\mathrm{II}_2} - \boldsymbol{\varepsilon}^{*}\right) + \left\{\boldsymbol{\sigma}^{(2),\mathrm{II}}\right\} \tag{16.8}$$

The real strain in the inhomogeneity for sub-problem II is related to the equivalent eigenstrain $\boldsymbol{\varepsilon}^*$ for ellipsoidal inclusions as (Eshelby 1957)

$$\boldsymbol{\varepsilon}^{(1),\mathrm{II}} - \left[\mathbf{C}^{(2)}\right]^{-1} : \left\{\boldsymbol{\sigma}^{(2),\mathrm{II}}\right\} = \mathbf{S} : \boldsymbol{\varepsilon}^* \quad \text{or} \quad \boldsymbol{\varepsilon}^{(1),\mathrm{II}_2} = \mathbf{S} : \boldsymbol{\varepsilon}^* \tag{16.9}$$

where $\mathbf{S}$ is the Eshelby tensor whose explicit forms are presented for different shapes of the inclusion in Mura's monograph (Mura 1987).

Substituting Eqs. (16.7) and (16.9) into (16.5), we derive the average stresses in the sub-problem II as

$$\left\{\boldsymbol{\sigma}^{(1),\mathrm{II}}\right\} = (1-f)\,\mathbf{C}^{(2)} : (\mathbf{S} - \mathbf{I}) : \boldsymbol{\varepsilon}^* \tag{16.10}$$

$$\left\{\boldsymbol{\sigma}^{(2),\mathrm{II}}\right\} = -f\mathbf{C}^{(2)} : (\mathbf{S} - \mathbf{I}) : \boldsymbol{\varepsilon}^{*} \tag{16.11}$$

where $\mathbf{I}$ is the fourth-order identity tensor.

Further substituting Eqs. (16.9) and (16.11) into (16.8) leads to the equivalent eigenstrain $\boldsymbol{\varepsilon}^{*}$ as

$$\boldsymbol{\varepsilon}^{*} = \left[\mathbf{C}^{(1)} : (\mathbf{S} - f\mathbf{S} + f\mathbf{I}) - (1-f)\,\mathbf{C}^{(2)} : (\mathbf{S} - \mathbf{I})\right]^{-1} : \mathbf{C}^{(1)} : \left(\boldsymbol{\varepsilon}^{fs} - \boldsymbol{\varepsilon}^{ms}\right) \tag{16.12}$$

For the conventional micromechanical schemes of composite materials, the material properties of each constituent material remain unchanged. However, this is not true for the hydrophilic composites in the humid environment. The stiffness of the fibers and the matrix may undergo significant mechanical degradation due to water uptake, namely,

$$\mathbf{C}^{(1)} = \mathbf{M}^{-1}\left(\boldsymbol{\varepsilon}^{fs}\right) : \mathbf{C}_{0}^{(1)} : \mathbf{M}^{-\mathrm{T}}\left(\boldsymbol{\varepsilon}^{fs}\right) \tag{16.13}$$

$$\mathbf{C}^{(2)} = \mathbf{M}^{-1}\left(\boldsymbol{\varepsilon}^{ms}\right) : \mathbf{C}_{0}^{(2)} : \mathbf{M}^{-\mathrm{T}}\left(\boldsymbol{\varepsilon}^{ms}\right) \tag{16.14}$$

where the subscript "0" denotes original physical quantities of the material without moisture absorption, and the damage effect tensor of fourth-order $\mathbf{M}$ is here assumed to depend on the swelling strain $\boldsymbol{\varepsilon}^{fs}$ and $\boldsymbol{\varepsilon}^{ms}$ due to moisture absorption. $\mathbf{M}^{-1}$ is the inverse of $\mathbf{M}$, and $\mathbf{M}^{-\mathrm{T}}$ is the transpose of $\mathbf{M}^{-1}$ with respect to the first pair and the second pair of subscripts, i.e., $(\mathbf{M}^{-\mathrm{T}})_{ijkl} = (\mathbf{M}^{-1})_{klij}$.

Obviously, we have $\mathbf{M}(0) = \mathbf{I}$ for the material will keep its virgin properties if no swelling strain is exerted on it. As for NFRCs, the matrix shows a low capacity of water uptake and little change of their mechanical properties (i.e., $\boldsymbol{\varepsilon}^{ms} = 0$), but the fibers will dramatically alter their mechanical properties. In the wood cell wall, the inhomogeneities are almost hydrophobic (i.e., $\boldsymbol{\varepsilon}^{fs} = 0$), while the matrix composed of hemicellulose is strongly hydrophilic. The above two problems can be regarded as special cases of the present micromechanical framework.

Since the moisture absorption does not induce the shear components of $\boldsymbol{\varepsilon}^{fs}$ and $\boldsymbol{\varepsilon}^{ms}$, the damage effect tensor is only related to the bulk inelastic strain $\varepsilon_{kk}^{fs}$ and $\varepsilon_{kk}^{ms}$, i.e., $\mathbf{M}\left(\boldsymbol{\varepsilon}^{fs}\right) = \mathbf{M}\left(\varepsilon_{kk}^{fs}\right)$. After the inhomogeneities and the matrix are fully saturated with the equilibrium bulk strains $\varepsilon_{kk}^{f\infty}$ and $\varepsilon_{kk}^{m\infty}$ achieving, the matrix and fibers are considered to undergo fully mechanical degradation.

Substituting Eq. (16.11) into (16.9) yields

$$\boldsymbol{\varepsilon}^{(1),\mathrm{II}} = (\mathbf{S} - f\mathbf{S} + f\mathbf{I}) : \boldsymbol{\varepsilon}^{*} \tag{16.15}$$

By means of Eq. (16.11) and the relation $\{\boldsymbol{\sigma}^{(2),\mathrm{II}}\} = \mathbf{C}^{(2)} : \{\boldsymbol{\varepsilon}^{(2),\mathrm{II}}\}$, the average strain of the matrix for sub-problem II is derived as

$$\left\{\boldsymbol{\varepsilon}^{(2),\mathrm{II}}\right\} = -f\,(\mathbf{S} - \mathbf{I}) : \boldsymbol{\varepsilon}^{*} \tag{16.16}$$

The real overall average strain $\{\boldsymbol{\varepsilon}\}$ of the composites can be calculated from Eq. (16.4), as follows:

$$\{\boldsymbol{\varepsilon}\} = \left\{\boldsymbol{\varepsilon}^{\mathrm{I}}\right\} + \left\{\boldsymbol{\varepsilon}^{\mathrm{II}}\right\} = \boldsymbol{\varepsilon}^{ms} + \left[f\boldsymbol{\varepsilon}^{(1),\mathrm{II}} + (1-f)\left\{\boldsymbol{\varepsilon}^{(2),\mathrm{II}}\right\}\right] \tag{16.17}$$

Substituting Eqs. (16.12), (16.15), and (16.16) into (16.17), the average strain $\{\boldsymbol{\varepsilon}\}$ can be further written as

$$\{\boldsymbol{\varepsilon}\} = \boldsymbol{\varepsilon}^{ms} + \left[f\left(\mathbf{S} - f\mathbf{S} + f\mathbf{I}\right) : \boldsymbol{\varepsilon}^{*} - f\left(1-f\right)\left(\mathbf{S}-\mathbf{I}\right) : \boldsymbol{\varepsilon}^{*}\right] = \boldsymbol{\varepsilon}^{ms} + f\boldsymbol{\varepsilon}^{*} \tag{16.18}$$

There are many micromechanical models for estimating overall properties of a composite (Nemat-Nasser and Hori 1999). Here we employ the Mori–Tanaka method (Mori and Tanaka 1973) because of its simplicity and accuracy even at a high volume fraction of reinforcements (Shi et al. 2004). One may refer to these literatures (Benveniste 1987; Chen et al. 1992; Karris 1989) for the detailed applications of the Mori–Tanaka method in various composite materials. The effective stiffness of a composite material based on the Mori–Tanaka method is expressed as

$$\mathbf{C} = \left[(1-f)\,\mathbf{C}^{(2)} + f\left\langle \mathbf{C}^{(1)} : \mathbf{A}\right\rangle\right] : \left[(1-f)\,\mathbf{I} + f\left\langle \mathbf{A}\right\rangle\right]^{-1} \tag{16.19}$$

with the strain concentration tensor given as

$$\mathbf{A} = \mathbf{I} + \mathbf{S} : \left(\mathbf{C}^{(1)} : \mathbf{S} - \mathbf{C}^{(2)} : \mathbf{S} + \mathbf{C}^{(2)}\right)^{-1} : \left(\mathbf{C}^{(2)} - \mathbf{C}^{(1)}\right) \tag{16.20}$$

where the notation " $\langle\bullet\rangle$ " means the average of a physical quantity over all possible orientations, which should not be confused with the volume average " $\{\bullet\}$ ".

Finally, from Eqs. (16.18) and (16.19), we can establish a relationship between the macroscopic strain $\{\boldsymbol{\varepsilon}\}$ and the effective stiffness $\mathbf{C}$ of the composite once $\boldsymbol{\varepsilon}^{*}$, $\mathbf{C}^{(1)}$, and $\mathbf{C}^{(2)}$ are all determined for any given $\boldsymbol{\varepsilon}^{fs}$ and $\boldsymbol{\varepsilon}^{ms}$, which can be used to evaluate the mechanical degradation of the composites since the macroscopic deformation of the composite is more convenient to measure.

## 16.3 Modeling Moisture-Induced Damage in NFRCs (Pan and Zhong 2015)

Natural fibers have such advantages over traditional glass fibers as high specific strength and modulus, economic viability, low density, reduced tool wear, enhanced energy recovery, reduced dermal and respiratory irritation, and good biodegradability (Dhakal et al. 2007). Hence, NFRCs have gradually become promising engineering materials in recent years, particularly in such fields as aerospace, leisure, construction, sport, packaging, and automotive industries (Pandey et al. 2010).

However, the hydrophilic nature of natural fibers causes fiber aging since their internal structure exhibits remarkable changes by absorbing large amounts of water when NFRCs are used in the humid environment (Arbelaiz et al. 2005).

For NFRCs, only natural fibers absorb water, while the matrix is resistant to the water. Based on the general framework proposed in Sect. 16.2, we have

$$\boldsymbol{\varepsilon}^{ms} = 0 \quad \text{and} \quad \boldsymbol{\varepsilon}^{fs} = \boldsymbol{\varepsilon}^{s} \tag{16.21}$$

Then the solution to the sub-problem I is obtained as $\boldsymbol{\sigma}^{(1),\mathrm{I}} = \boldsymbol{\sigma}^{(2),\mathrm{I}} = 0$ and $\boldsymbol{\varepsilon}^{(1),\mathrm{I}} = \boldsymbol{\varepsilon}^{(2),\mathrm{I}} = 0$. In the following subsection, the solution to the sub-problem II is further determined by considering different shapes of inclusions.

### *16.3.1 Randomly Oriented Straight Inhomogeneity*

To simulate the randomly oriented straight natural fiber reinforced composites, the isotropic straight natural fibers (inhomogeneities) with random orientations are considered to be embedded in an isotropic matrix. The traditional micromechanical analyses of randomly oriented composites have been studied in detail in these literatures (Qiu and Weng 1991; Tandon and Weng 1986), to which some key conclusions are herein referred. The stiffness of each isotropic constituent material can be expressed by two elastic constants (e.g., the shear modulus $\mu^{(i)}$ and the bulk modulus $\kappa^{(i)}$), namely,

$$C^{(i)}_{mnpq} = \kappa^{(i)}\delta_{mn}\delta_{pq} + \mu^{(i)}\left(\delta_{mp}\delta_{nq} + \delta_{mq}\delta_{np} - \frac{2}{3}\delta_{mn}\delta_{pq}\right) \tag{16.22}$$

Here $\delta_{mn}$ is the Kronecker delta. The notation $i = 1, 2$ represents the physical quantities of the fiber and the matrix, respectively.

For the randomly oriented straight inhomogeneity, two Euler angles are introduced to characterize its orientation, as illustrated in Fig. 16.3. In this case, the strain concentration tensor $\mathbf{A}$ in Eq. (16.20) is a function of the Euler angles $\alpha$ and $\beta$, i.e., $\mathbf{A} = \mathbf{A}(\alpha, \beta)$. If the inclusions have completely random orientations, the Mori–Tanaka estimation (16.19) can be calculated by an average through the integration over the two Euler angles, as follows (Shi et al. 2004):

$$\langle \bullet \rangle = \frac{1}{2\pi}\int_0^{2\pi}\int_0^{\pi/2} (\bullet \cdot \sin\alpha)\,\mathrm{d}\alpha\mathrm{d}\beta \tag{16.23}$$

By using the Eshelby tensor of a circular cylindrical inclusion with infinite length in an isotropic matrix, the Mori–Tanaka estimation of the bulk modulus $\kappa$ and the shear modulus $\mu$ can be derived from Eq. (16.19) with (16.23), as follows:

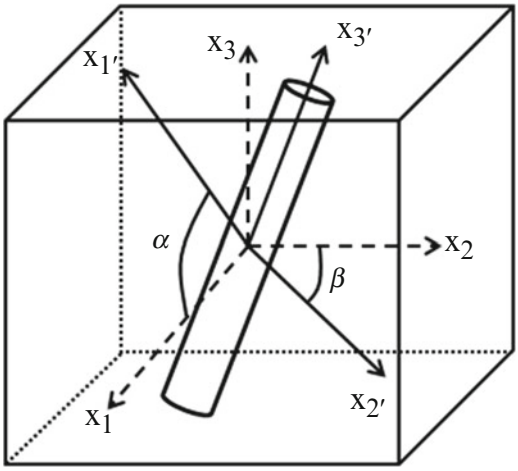


**Fig. 16.3** The orientation of the randomly oriented straight inhomogeneity represented by two Euler angles

$$\kappa = \kappa^{(2)} + \frac{f\left(\kappa^{(1)} - \kappa^{(2)}\right)\left(3\kappa^{(2)} + \mu^{(1)} + 3\mu^{(2)}\right)}{3\left(1-f\right)\kappa^{(1)} + 3f\kappa^{(2)} + 3\mu^{(2)} + \mu^{(1)}}$$
$$\mu = \mu^{(2)} - \frac{f\left(\mu^{(1)} - \mu^{(2)}\right)\left(4\mu^{(2)}\delta_1 + 3\kappa^{(1)}\delta_2\right)}{3\kappa^{(2)}\left(\mu^{(1)} + \mu^{(2)}\right)\eta_1 - \mu^{(2)}\eta_2 + 3\kappa^{(1)}\left(\eta_3 - \eta_4\right)} \tag{16.24}$$

Equation (16.24) is derived under the condition that the inclusion is isotropic. It can be reduced from the results of the papers (Qiu and Weng 1991; Shi et al. 2004; Tandon and Weng 1986), in which the inclusion is transversely isotopic. Furthermore,

$$E = \frac{9\kappa\mu}{3\kappa + \mu} \tag{16.25}$$

with

$$\delta_1 = 3\kappa^{(2)}\left[3\left(\mu^{(1)}\right)^2 + 10\mu^{(1)}\mu^{(2)} + 7\left(\mu^{(2)}\right)^2\right] + 2\mu^{(2)}\left[9\left(\mu^{(1)}\right)^2 + 23\mu^{(1)}\mu^{(2)} + 8\left(\mu^{(2)}\right)^2\right]$$

$$\delta_2 = 3\kappa^{(2)}\left[\left(\mu^{(1)}\right)^2 + 10\mu^{(1)}\mu^{(2)} + 9\left(\mu^{(2)}\right)^2\right] + \mu^{(2)}\left[7\left(\mu^{(1)}\right)^2 + 52\mu^{(1)}\mu^{(2)} + 21\left(\mu^{(2)}\right)^2\right]$$

$$\eta_1 = 5\left(f-1\right)\left(\mu^{(1)}\right)^2 + 4\left(2f-5\right)\mu^{(1)}\mu^{(2)} - \left(15+13f\right)\left(\mu^{(2)}\right)^2$$

$$\eta_2 = -35\left(f-1\right)\left(\mu^{(1)}\right)^3 + \left(145-73f\right)\left(\mu^{(1)}\right)^2\mu^{(2)} + \left(125+59f\right)\mu^{(1)}\left(\mu^{(2)}\right)^2 + \left(15+49f\right)\left(\mu^{(2)}\right)^3$$

$$\eta_3 = 3\kappa^{(2)}\left(\mu^{(1)} + \mu^{(2)}\right)\left[\left(-5+4f\right)\mu^{(1)} - \left(5+4f\right)\mu^{(2)}\right]$$

$$\eta_4 = \mu^{(2)}\left[-7\left(-5+4f\right)\left(\mu^{(1)}\right)^2 + 4\left(10+3f\right)\mu^{(1)}\mu^{(2)} + \left(5+16f\right)\left(\mu^{(2)}\right)^2\right]$$

For an isotropic elastic natural fiber with moisture absorption, we assume that the damaged natural fiber is still isotopic after moisture absorption. Only natural fibers absorb water (i.e., $\boldsymbol{\varepsilon}^{fs} = \boldsymbol{\varepsilon}^{s}$ and $\boldsymbol{\varepsilon}^{ms} = 0$), and thereby the damage effect tensor $\mathbf{M}$ for natural fibers in Eq. (16.13) is an isotopic tensor taking the following form as

$$M_{mnpq}\left(\varepsilon_{kk}^{s}\right) = \frac{\sqrt{\mathrm{A}\left(\varepsilon_{kk}^{s}\right)}}{3}\delta_{mn}\delta_{pq} + \frac{\sqrt{\mathrm{B}\left(\varepsilon_{kk}^{s}\right)}}{2}\left(\delta_{mp}\delta_{nq} + \delta_{mq}\delta_{np} - \frac{2}{3}\delta_{mn}\delta_{pq}\right) \tag{16.26}$$

where $\mathsf{A}$ and $\mathsf{B}$ are two degradation parameters depending on the fiber swelling expansion $\varepsilon_{kk}^{s}$ induced by moisture absorption.

Substituting Eq. (16.26) into Eq. (16.22) and then into (16.13), the degradation of the stiffness $\mathbf{C}^{(1)}$ is obtained as

$$\begin{aligned} C_{mnpq}^{(1)} &= \frac{\kappa_0^{(1)}}{\mathrm{A}\left(\varepsilon_{kk}^{s}\right)}\delta_{mn}\delta_{pq} + \frac{\mu_0^{(1)}}{\mathrm{B}\left(\varepsilon_{kk}^{s}\right)}\left(\delta_{mp}\delta_{nq} + \delta_{mq}\delta_{np} - \frac{2}{3}\delta_{mn}\delta_{pq}\right) \\ &= \kappa^{(1)}\delta_{mn}\delta_{pq} + \mu^{(1)}\left(\delta_{mp}\delta_{nq} + \delta_{mq}\delta_{np} - \frac{2}{3}\delta_{mn}\delta_{pq}\right) \end{aligned} \tag{16.27}$$

where $\kappa_0^{(1)}$ and $\mu_0^{(1)}$ are two initial moduli of the natural fiber. The degradation parameters $\mathsf{A}$ and $\mathsf{B}$ are tentatively assumed to take power forms as $\mathrm{A} = \left(1 + \varepsilon_{kk}^{s}\right)^{\alpha}$ and $\mathrm{B} = \left(1 + \varepsilon_{kk}^{s}\right)^{\beta}$. Here $\alpha$ and $\beta$ are two positive material constants of the natural fiber.

Accordingly, the degraded bulk modulus and the shear modulus can be written as

$$\kappa^{(1)} = \frac{\kappa_0^{(1)}}{\left(1 + \varepsilon_{kk}^{s}\right)^{\alpha}} \qquad \mu^{(1)} = \frac{\mu_0^{(1)}}{\left(1 + \varepsilon_{kk}^{s}\right)^{\beta}} \tag{16.28}$$

Obviously, $\kappa^{(1)}$ and $\mu^{(1)}$ are monotonously decreasing functions of $\varepsilon_{kk}^{s}$. Note that Eq. (16.28) satisfies the basic condition that there is no modulus loss when $\varepsilon_{kk}^{s} = 0$. Furthermore, when $\alpha = \beta$, Poisson's ratio $\upsilon^{(1)}$ is considered to keep constant since $\kappa^{(1)}/\kappa_0^{(1)} = \mu^{(1)}/\mu_0^{(1)}$.

If the initial eigenstrain is assumed to be isotropic, then we have $\varepsilon_{11}^{s} = \varepsilon_{22}^{s} = \varepsilon_{33}^{s}$ and other components $\varepsilon_{ij}^{s} = 0$. Here the fiber direction is along the $x_3$ axis. For a straight circular cylindrical fiber with infinite length, the real strain $\varepsilon_{33}^{(1)}$ equals to 0. Decomposing the isotropic stiffness into the shear and the bulk parts, the following equations can be deduced from Eq. (16.8):

$$\kappa^{(1)}\left(\varepsilon_{kk}^{(1)} - \varepsilon_{kk}^{s}\right) = \kappa^{(2)}\left(\varepsilon_{kk}^{(1),\mathrm{II}_2} - \varepsilon_{kk}^{*}\right) + \frac{1}{3}\left\{\sigma_{kk}^{(2)}\right\} \tag{16.29}$$

$$\lambda^{(1)}\left(\varepsilon_{kk}^{(1)} - \varepsilon_{kk}^{s}\right) - 2\mu^{(1)}\varepsilon_{33}^{s} = \lambda^{(2)}\left(\varepsilon_{kk}^{(1),\mathrm{II}_2} - \varepsilon_{kk}^{*}\right) - 2\mu^{(2)}\varepsilon_{33}^{*} + \left\{\sigma_{33}^{(2)}\right\} \tag{16.30}$$

where $\lambda^{(i)} = \kappa^{(i)} - 2\mu^{(i)}/3$ is the Lame elastic coefficient.

By means of the Eshelby relation given by Eq. (16.9) for circular cylindrical inclusions of infinite length embedded in an isotropic matrix, the following equations can be derived as:

$$\varepsilon_{kk}^{(1),\mathrm{II}_2} = \frac{\varepsilon_{kk}^*}{2\left(1-\upsilon^{(2)}\right)} + \frac{\left(2\upsilon^{(2)}-1\right)\varepsilon_{33}^*}{2\left(1-\upsilon^{(2)}\right)} \tag{16.31}$$

where $\upsilon^{(2)}$ is Poisson's ratio of the matrix.

After the average operation by Eq. (16.23), the average matrix stress $\{\boldsymbol{\sigma}^{(2)}\}$ is calculated from Eq. (16.11) as

$$\begin{aligned} &\left\{\sigma_{11}^{(2)}\right\} = \left\{\sigma_{22}^{(2)}\right\} = \left\{\sigma_{33}^{(2)}\right\} = \frac{f\varepsilon_{11}^s\left(3\lambda^{(1)}+2\mu^{(1)}\right)\left(\mu^{(1)}+3\mu^{(2)}\right)}{3\lambda^{(1)}-(f-3)\mu^{(1)}-3(f-1)\mu^{(2)}} \\ &\left\{\sigma_{kk}^{(2)}\right\} = 3\left\{\sigma_{33}^{(2)}\right\} \end{aligned} \tag{16.32}$$

Once the swelling bulk strain $\varepsilon_{33}^s$ ($\varepsilon_{kk}^s = 3\varepsilon_{33}^s$) is given, the other nine unknowns $\varepsilon_{kk}^*$, $\varepsilon_{33}^*$, $\varepsilon_{kk}^{(1)}$, $\kappa^{(1)}$,$\mu^{(1)}$, $\kappa$, $\mu$, $\left\{\sigma_{kk}^{(2)}\right\}$, and $\left\{\sigma_{33}^{(2)}\right\}$ can be completely determined from Eqs. (16.24), (16.28), (16.29), (16.30), (16.31), and (16.32). Further making use of Eqs. (16.18) and (16.19), a theoretical relationship between the overall elastic modulus of the composite $E$ and the average bulk strain $\{\varepsilon_{kk}\}$ is established. In order to validate this model, the theoretical prediction of $E$ is compared with the corresponding experimental results (Chow et al. 2007) of randomly oriented straight sisal fiber (with the density $\rho_f = 1.48$ g/cm$^3$) reinforced polypropylene (with the density $\rho_m = 0.81$ g/cm$^3$).

In the experiment (Chow et al. 2007), three composite samples with different fiber contents were used: sample A (fiber content $f_1 = 0.057$), sample B ($f_2 = 0.120$), and sample C ($f_3 = 0.189$). Before submerging these samples into water for moisture absorption, the initial Young's moduli $E_0$ of the composite were measured and the results are 2.65 GPa, 2.99 GPa, and 3.39 GPa for Sample A, Sample B, and Sample C, respectively. Poisson's ratio of the polypropylene matrix is taken as $\upsilon^{(2)} = \upsilon_0^{(2)} = 0.33$ (Garg 1982). Since Poisson's ratio of sisal fibers, usually no more than 0.35, has little effect on the mechanical behavior of the composites (José da Silva et al. 2012), we take $\upsilon^{(1)} = \upsilon_0^{(1)} = 0.25$ for theoretical computation. Here we consider that the moisture absorption does not influence Poisson's ratio of the natural fiber, because its compositions: cellulose, hemicellulose, and lignin (Saheb and Jog 1999) keep constant Poisson's ratios under moisture absorption (Salmén 2004).

Fitting the experimental data of the initial Young's modulus $E_0$ of the composite (as shown in Fig. 16.4) through Eqs. (16.24) and (16.25) based on the least square method, we can derive $E_0^{(1)} = 15.03$ GPa for natural fiber and $E_0^{(2)} = E_0 = 2.37$ GPa for polypropylene matrix, see Appendix A. Accordingly, $\kappa_0^{(1)} = 10.02$ GPa, $\mu_0^{(1)} = 6.01$ GPa, $\kappa_0^{(2)} = \kappa^{(2)} = 2.32$ GPa, $\mu_0^{(2)} = \mu^{(2)} = 0.89$ GPa.

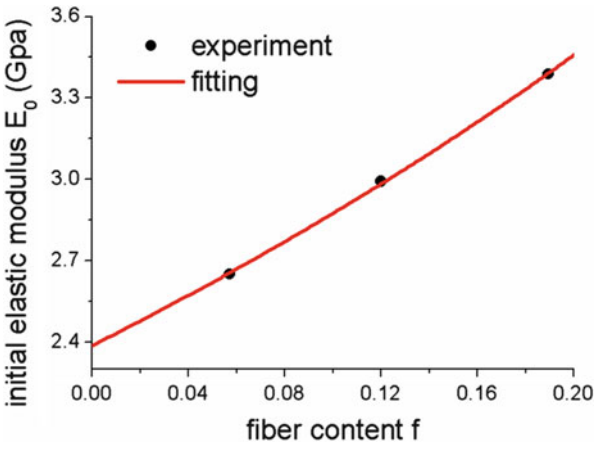


**Fig. 16.4** The fitting results of the initial elastic modulus $E_0$ of the composite

If the swelling of the composites is subject to no external loads, just as the above experimental case, seven unknowns $\kappa^{(1)}$, $\mu^{(1)}$, $\varepsilon_{kk}^{(1)}$, $\varepsilon_{33}^{*}$, $\varepsilon_{kk}^{*}$, $\left\{\sigma_{kk}^{(2)}\right\}$, and $\left\{\sigma_{33}^{(2)}\right\}$ are obtained by solving Eqs. (16.28), (16.29), (16.30), (16.31), and (16.32) simultaneously given the swelling bulk strain $\varepsilon_{kk}^{s}$. Furthermore, the bulk, shear, and Young's moduli $\kappa$, $\mu$, and $E$ of the composites are determined using Eqs. (16.24) and (16.25). Owing to lack of experimental data to determine the material parameters $\alpha$ and $\beta$ as introduced in Eq. (16.28), we try and error, and finally set $\alpha = \beta = 11.5$ in the calculation of the modulus loss ($E$) varying with the bulk strain $\{\varepsilon_{kk}\}$ for Sample A, Sample B, and Sample C. As shown in Fig. 16.5, the theoretical predictions agree well with the corresponding experimental results of modulus loss, which validates the proposed micromechanical model. It can also be found that Young's modulus drops remarkably with the increase of moisture content measured by the bulk strain $\{\varepsilon_{kk}\}$ of the composites.

### *16.3.2 Unidirectional Circular Cylindrical Inhomogeneity*

To simulate the unidirectional natural fiber reinforced composites, the isotropic circular cylindrical natural fibers (inhomogeneities) with a uniform orientation are considered to be embedded in an isotropic matrix with Young's modulus $E^{(2)}$ and Poisson's ratio $\upsilon^{(2)}$. Young's modulus and Poisson's ratio of the natural fiber are denoted by $E^{(1)}$ and $\upsilon^{(1)}$, respectively. Due to the unidirectional reinforcement, the composite is transversely isotropic with respect to the reinforcing direction that is assumed herein along the $x_3$-axis. And then the corresponding overall stiffness $\mathbf{C}$ of the composite can be expressed as

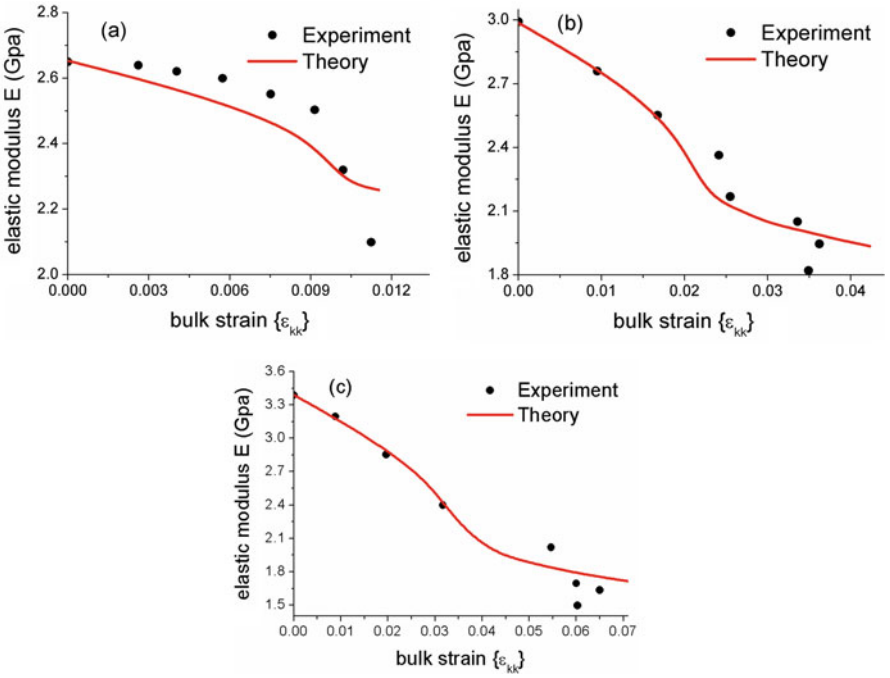


**Fig. 16.5** The comparison of Young's modulus $E$ of the composite between theoretical and experimental results in the case of randomly oriented straight fibers; (**a**) Sample A, (**b**) Sample B, (**c**) Sample C

$$[\mathbf{C}] = \begin{bmatrix} k+m & k-m & l & 0 & 0 & 0 \\ & k+m & l & 0 & 0 & 0 \\ & & n & 0 & 0 & 0 \\ & & & p & 0 & 0 \\ & & & & p & 0 \\ \textit{symmetric} & & & & & m \end{bmatrix} \tag{16.33}$$

where $k$, $l$, $m$, $n$, and $p$ are the Hill's elastic moduli (Hill 1965); $k$ is the plane-strain bulk modulus normal to the fiber direction, $n$ is the uniaxial tension modulus in the reinforcing direction ($x_3$ -axis), $l$ is the associated cross modulus, $m$ and $p$ are the shear moduli in planes normal and parallel to the reinforcing direction, respectively.

Based on the unidirectional inclusion of circular cylindrical shape, the Mori–Tanaka estimation, Eq. (16.19), can be used to determine the five Hill's elastic moduli, among which three are given, as follows:

$$\begin{aligned} l = & \frac{\mu^{(2)}\left[(6-18f)\,\kappa^{(1)} + 9\,(f-1)\,\kappa^{(2)} + 2\mu^{(1)} + 6f\mu^{(1)}\right]}{\eta} \\ & - \frac{3\kappa^{(2)}\left(3\kappa^{(1)} + \mu^{(1)} - 3f\mu^{(1)}\right) + 6\,(f-1)\left(\mu^{(2)}\right)^2}{\eta} \end{aligned} \tag{16.34}$$

$$n = \frac{12(f-1)\left(\mu^{(2)}\right)^2 - 3\kappa^{(1)}\left[3\kappa^{(2)} - 9(f-1)f\left(\mu^{(1)} - \mu^{(2)}\right) + 4\mu^{(2)}\right]}{\eta} - \frac{3(1-3f)^2\kappa^{(2)}\mu^{(1)} - (1+3f)\left[9(f-1)\kappa^{(2)} - 4\mu^{(1)}\right]\mu^{(2)}}{\eta} \tag{16.35}$$

$$k = \frac{-3\kappa^{(2)}\left[\mu^{(1)} + 3\mu^{(2)} - 3f\mu^{(2)}\right] - 3\kappa^{(1)}\left[3\kappa^{(2)} + \mu^{(2)} + 3f\mu^{(2)}\right]}{\eta} - \frac{\mu^{(2)}\left[\mu^{(1)} + 3f\mu^{(1)} + 3\mu^{(2)} - 3f\mu^{(2)}\right]}{\eta} \tag{16.36}$$

with

$$\eta = 9(f-1)\kappa^{(1)} - 3\left[\mu^{(1)} + 3\mu^{(2)} + f\left(3\kappa^{(2)} - \mu^{(1)} + \mu^{(2)}\right)\right] \tag{16.37}$$

Equations (16.34)–(16.37) can be reduced from the result from the papers (Qiu and Weng 1990; Shi et al. 2004). Then the tensile modulus $E_3$ of the composite in the reinforcing direction can be obtained as (Hill 1965)

$$E_3 = n - \frac{l^2}{k} \tag{16.38}$$

If we assume the damaged natural fiber is still isotropic after moisture absorption, the moisture absorption is considered not influenced by Poisson's ratio of natural fibers, as follows:

$$\frac{\kappa^{(1)}}{\kappa_0^{(1)}} = \frac{\mu^{(1)}}{\mu_0^{(1)}} = \frac{\lambda^{(1)}}{\lambda_0^{(1)}} \tag{16.39}$$

which indicates that the two degradation parameters in Eq. (16.28) are identical, i.e., $\alpha = \beta$.

Since the stress and the strain of every inhomogeneity are identical for unidirectional natural fiber composites subject to no external loads except for moisture absorption, the relations $\{\boldsymbol{\varepsilon}^{(1)}\} = \boldsymbol{\varepsilon}^{(1)}$ and $\{\boldsymbol{\sigma}^{(1)}\} = \boldsymbol{\sigma}^{(1)}$ hold. Furthermore, we have $\varepsilon_{11}^{(1)} = \varepsilon_{22}^{(1)}$ and $\varepsilon_{12}^{(1)} = \varepsilon_{23}^{(1)} = \varepsilon_{31}^{(1)} = \varepsilon_{33}^{(1)} = 0$, such that Eq. (16.8) can be particularized into two scalar equations:

$$2\left(\lambda^{(1)} + \mu^{(1)}\right)\left(\varepsilon_{11}^{(1)} - \varepsilon_{11}^{s}\right) - \lambda^{(1)}\varepsilon_{33}^{s} = (1-f)\left[2\left(\lambda^{(2)} + \mu^{(2)}\right)\left(\varepsilon_{11}^{(1),\mathrm{II}_2} - \varepsilon_{11}^{*}\right) - \lambda^{(2)}\varepsilon_{33}^{*}\right] \tag{16.40}$$

$$2\lambda^{(1)}\left(\varepsilon_{11}^{(1)}-\varepsilon_{11}^{s}\right)-\left(\lambda^{(1)}+2\mu^{(1)}\right)\varepsilon_{33}^{s}=(1-f)\left[2\lambda^{(2)}\left(\varepsilon_{11}^{(1),\mathrm{II}_2}-\varepsilon_{11}^{*}\right)\left(\lambda^{(2)}+2\mu^{(2)}\right)\varepsilon_{33}^{*}\right] \tag{16.41}$$

From the Eshelby relation (16.9), the real strain of the fiber can be expressed as

$$\varepsilon_{11}^{(1),\mathrm{II}_2}=S_{1111}\varepsilon_{11}^{*}+S_{1122}\varepsilon_{22}^{*}+S_{1133}\varepsilon_{33}^{*} \tag{16.42}$$

Now that the relation $\varepsilon_{11}^{*}=\varepsilon_{22}^{*}$ holds when the composite swells without external loads, Eq. (16.42) can be further simplified by considering the circular cylindrical shape as

$$\varepsilon_{11}^{(1),\mathrm{II}_2}=\frac{\varepsilon_{11}^{*}}{2\left(1-\upsilon^{(2)}\right)}+\frac{\upsilon^{(2)}\varepsilon_{33}^{*}}{2\left(1-\upsilon^{(2)}\right)} \tag{16.43}$$

Hence, the Hill's moduli $l$, $n$, and $k$ can be solved from Eqs. (16.34)–(16.36), (16.39), (16.40), (16.41), and (16.43) when the free swelling strain $\varepsilon_{11}^{s}=\varepsilon_{22}^{s}=\varepsilon_{33}^{s}$ is given. In what follows, the tensile modulus $E_3$ along the reinforcing direction can be obtained through Eq. (16.38). To illustrate the degradation effect of moisture absorption on the tensile modulus $E_3$, a numerical example is given by comparing $E_3$ of the virgin composite with that of the swollen one. Particularly, the effects of the matrix stiffness on the mechanical degradation of the composite are taken into consideration by introducing the relative stiffness, namely,

$$\gamma=\frac{E_0^{(1)}}{E^{(2)}}=\frac{\left(1+\upsilon^{(1)}\right)\mu_0^{(1)}}{\left(1+\upsilon^{(2)}\right)\mu^{(2)}} \tag{16.44}$$

which takes the following values: 10 (stiff), 20 (moderate), and 30 (soft).

Given the initial eigenstrain $\varepsilon_{11}^{s}=\varepsilon_{22}^{s}=\varepsilon_{33}^{s}=0.05$, the material parameter $\alpha=\beta=9$, the initial Young's modulus $E_0^{(1)}=50$ GPa, and Poisson's ratios $\upsilon^{(1)}=\upsilon_0^{(1)}=0.25$, $\upsilon^{(2)}=\upsilon_0^{(2)}=0.3$, the tensile moduli of the virgin and the swollen composites along the reinforcing direction are theoretically predicted under different fiber contents and shown in Fig. 16.6. It can be seen that the tensile modulus $E_3$, no matter the virgin or the swollen composite, increases with the fiber content. A further comparison reveals that $E_3$ of the swollen composite is much smaller than that of the virgin one and such difference is enlarged with the increase of fiber content.

Other than the mechanical degradation, the swelling deformation of composites described by the lateral strain $\varepsilon_{11}$ is studied as well, and the corresponding results are plotted in Fig. 16.7. One can find that $\varepsilon_{11}$ almost increases linearly with the fiber content. It is also demonstrated that the soft matrix leads to a large real strain $\varepsilon_{11}$ of the composite, from which it is concluded that the stiff matrix can effectively reduce the moisture absorption of the composites.

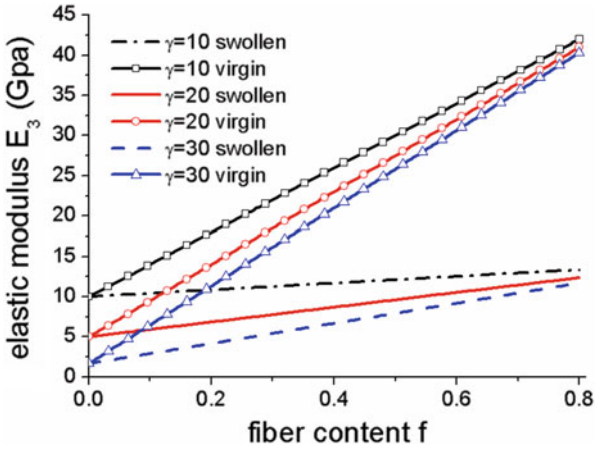


**Fig. 16.6** A comparison of the elastic modulus $E_3$ of the composite between the virgin and the fully swollen in the different cases of $\gamma = 10$, 20, and 30.

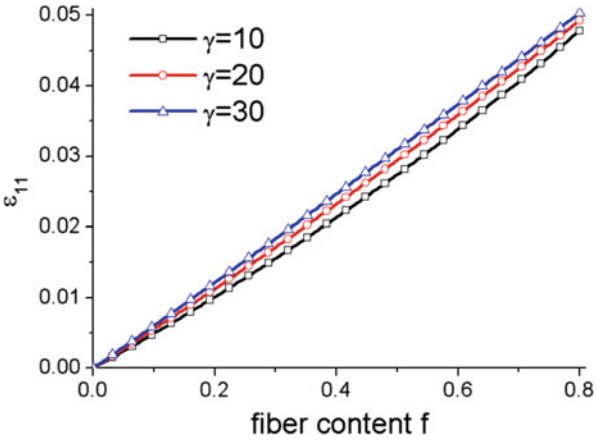


**Fig. 16.7** The strain $\varepsilon_{11}$ of the composite as a function of the fiber content in the different cases of $\gamma = 10$, 20, and 30

## 16.4 Modeling Modulus Loss of the Wood Cell Wall (Pan and Zhong 2016)

### *16.4.1 Backgrounds*

The wood fiber has been used as reinforcement in various natural wood composites since they are environment-friendly and have high specific modulus and strength. Despite rather good knowledge about mechanical modeling of wood composites on macroscopic scale (Hazarika et al. 2014; Okereke et al. 2014; Pan and Zhong 2014; Qing and Mishnaevsky 2009; Srubar 2015), little effort is devoted to theoretical analysis of the wood cell wall from a microscopic level. Existing researches on this topic mainly focus on experimental studies (Eder et al. 2013; Kojima and Yamamoto 2005; Saavedra Flores et al. 2014). Therefore, a deep understanding of the wood cell wall structure is of great importance in modeling the wood cell wall.

In fact, other than the moisture content, the microfibril angle (MFA) defined as the orientation of the specific microfibril with respect to the longitudinal cell axis also plays an important role in mechanical properties of the wood cell wall (Saavedra Flores et al. 2014). The cell wall structure usually consists of several layers with different MFAs (Hofstetter et al. 2007), among which the $S_2$ layer occupying $80-90\%$ of the total volume of the wood cell wall is the thickest and dominates its mechanical properties (Hofstetter et al. 2005).

There are several computational analyses of the wood cell wall structure, for example, the finite element simulation of its extensibility (Saavedra Flores et al. 2014) and the multi-scale numerical model of its creep behavior (Saavedra Flores et al. 2011). However, the moisture-dependent properties are rarely taken into consideration in the existing theoretical or computational analyses.

Note that the analysis of moisture-dependent properties of the wood cell wall is very similar to that of natural fiber composites, in which the inhomogeneity is hydrophilic and the matrix is usually hydrophobic (Cheung et al. 2009). Hence, general micromechanical framework presented in Sect. 16.2 can be further reduced to study the case in which the matrix uptakes water. Further considering the inhomogeneity is resistant to the water, we have

$$\boldsymbol{\varepsilon}^{ms} = \boldsymbol{\varepsilon}^{s} \quad \text{and} \quad \boldsymbol{\varepsilon}^{fs} = 0 \tag{16.45}$$

Then the solution to the sub-problem I is obtained as $\boldsymbol{\sigma}^{(1),\mathrm{I}} = \boldsymbol{\sigma}^{(2),\mathrm{I}} = 0$ and $\boldsymbol{\varepsilon}^{(1),\mathrm{I}} = \boldsymbol{\varepsilon}^{(2),\mathrm{I}} = \boldsymbol{\varepsilon}^{s}$. In the following subsection, we further determine the solution to the sub-problem II.

### *16.4.2 Unidirectional Circular Cylindrical Inhomogeneity*

The microstructure of the wood cell wall is shown in Fig. 16.8, which is composed of hemicellulose, lignin, and cellulose microfibril (CMF) aligned along a given direction ($x_3$ -axis). The microfibril angle (MFA) $\varphi$ is defined as the angle between $x_3$ -axis and the cell axis ($x_3'$ -axis). The microstructure of the wood cell wall is analog to that of a long fiber reinforced composite (Salmén 2004), so that the CMFs can be treated as transversely isotropic inhomogeneities (denoted as $\Omega$) of infinite length. The inhomogeneities are orientated unidirectionally and embedded in an infinite matrix (denoted as $\mathrm{D}-\Omega$) that is composed of hemicellulose and lignin. The inhomogeneities are assumed to be hydrophobic and free of any initial strain and stress, while the matrix is strongly hydrophilic and subject to a swelling strain $\boldsymbol{\varepsilon}^{s}$ in a humid environment.

In this subsection, the above theoretical model is applied to simulate the wood cell wall that contains a large number of unidirectional CMFs embedded in the matrix composed of hemicellulose and lignin. This microstructure is modeled by

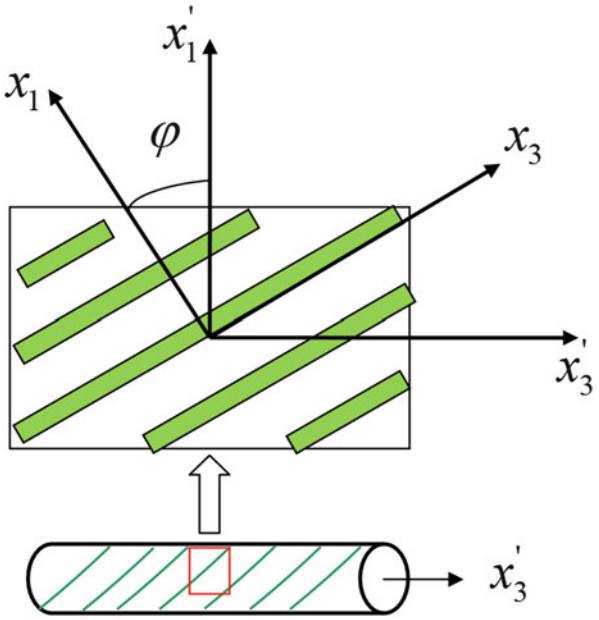


**Fig. 16.8** The illustration of the cell wall structure and the plane problem described by the global and local coordinates

unidirectional circular cylindrical inhomogeneities (transversely isotropic) enclosed by an infinite isotropic matrix. The reinforcing direction of the CMF is along the $x_3'$ -axis, so that the stiffness $\mathbf{C}^{(1)}$ of the CMF can be expressed by Hill's representation (Hill 1965) in which $k^{(1)}$ is the plane-strain bulk modulus normal to the fiber direction, $n^{(1)}$ is the uniaxial tensile modulus in the reinforcing direction ($x_3'$ -axis), $l^{(1)}$ is the associated cross modulus, and $m^{(1)}$ and $p^{(1)}$ are the shear moduli in planes normal and parallel to the reinforcing direction, respectively.

For experimental measurements, other five elastic coefficients are more convenient in use, given as follows:

$$E_3^{(1)} = -\frac{\left(l^{(1)}\right)^2 - k^{(1)}n^{(1)}}{k^{(1)}},\quad E_1^{(1)} = \frac{4\left[\left(l^{(1)}\right)^2 m^{(1)} - k^{(1)}m^{(1)}n^{(1)}\right]}{\left(l^{(1)}\right)^2 - k^{(1)}n^{(1)} - m^{(1)}n^{(1)}},\quad G_{13}^{(1)} = p^{(1)}$$
$$\upsilon_{12}^{(1)} = -\frac{-\left(l^{(1)}\right)^2 + k^{(1)}n^{(1)} - m^{(1)}n^{(1)}}{\left(l^{(1)}\right)^2 - k^{(1)}n^{(1)} - m^{(1)}n^{(1)}},\quad \upsilon_{13}^{(1)} = -\frac{2l^{(1)}m^{(1)}}{\left(l^{(1)}\right)^2 - k^{(1)}n^{(1)} - m^{(1)}n^{(1)}} \tag{16.46}$$

where $E_3^{(1)}$, $E_1^{(1)}$ are, respectively, the tensile moduli along and transverse to the reinforcing direction, $\upsilon_{12}^{(1)}$ and $\upsilon_{13}^{(1)}$ are two Poisson's ratios, and $G_{13}^{(1)}$ is the shear modulus parallel to the reinforcing direction.

The stiffness of the isotropic matrix can be written in terms of the shear modulus $\mu^{(2)}$ and the bulk modulus $\kappa^{(2)}$:

$$C^{(2)}_{mnpq} = \kappa^{(2)}\delta_{mn}\delta_{pq} + \mu^{(2)}\left(\delta_{mp}\delta_{nq} + \delta_{mq}\delta_{np} - \frac{2}{3}\delta_{mn}\delta_{pq}\right) \tag{16.47}$$

where $\delta_{mn}$ is the Kronecker delta.

The swelling expansion coefficients of the wood cell wall are different in three orthogonal directions. The expansion coefficient along the CMF is smaller than those along other two orthogonal directions (Jakob et al. 1996), so that we assume $\varepsilon^s_{11} = \varepsilon^s_{22} > 0$, $\varepsilon^s_{33} = \rho\varepsilon^s_{11} > 0$ $(0 \le \rho < 1)$ and other $\varepsilon^s_{ij} = 0$. Accordingly, the following two equations can be derived from Eq. (16.8):

$$2k^{(1)}\left(\varepsilon^{(1),\mathrm{II}}_{11} + \varepsilon^s_{11}\right) + \rho l^{(1)}\varepsilon^s_{11} = (1-f)\left[2\left(\lambda^{(2)} + \mu^{(2)}\right)\left(\varepsilon^{(1),\mathrm{II}_2}_{11} - \varepsilon^*_{11}\right) - \lambda^{(2)}\varepsilon^*_{33}\right] \tag{16.48}$$

and

$$2l^{(1)}\left(\varepsilon^{(1),\mathrm{II}}_{11} + \varepsilon^s_{11}\right) + \rho n^{(1)}\varepsilon^s_{11} = (1-f)\left[2\lambda^{(2)}\left(\varepsilon^{(1),\mathrm{II}_2}_{11} - \varepsilon^*_{11}\right) - \left(\lambda^{(2)} + 2\mu^{(2)}\right)\varepsilon^*_{33}\right] \tag{16.49}$$

If we further assume that the damage of the matrix induced by moisture absorption is isotropic, then the damage effect tensor $\mathbf{M}$ in Eq. (16.14) can be written as an isotopic tensor taking the following form (Pan and Zhong 2015)

$$M_{mnpq}\left(\varepsilon^s_{kk}\right) = \frac{\sqrt{\mathrm{A}\left(\varepsilon^s_{kk}\right)}}{3}\delta_{mn}\delta_{pq} + \frac{\sqrt{\mathrm{B}\left(\varepsilon^s_{kk}\right)}}{2}\left(\delta_{mp}\delta_{nq} + \delta_{mq}\delta_{np} - \frac{2}{3}\delta_{mn}\delta_{pq}\right) \tag{16.50}$$

where $\mathsf{A}$ and $\mathsf{B}$ are two degradation parameters depending on the swelling expansion $\varepsilon^s_{kk}$ induced by moisture absorption.

Substituting Eq. (16.26) into (16.22) and then into (16.47), the stiffness $\mathbf{C}^{(2)}$ with the effect of mechanical degradation is obtained as

$$\begin{aligned} C^{(2)}_{mnpq} &= \frac{\kappa^{(2)}_0}{\mathrm{A}\left(\varepsilon^s_{kk}\right)}\delta_{mn}\delta_{pq} + \frac{\mu^{(2)}_0}{\mathrm{B}\left(\varepsilon^s_{kk}\right)}\left(\delta_{mp}\delta_{nq} + \delta_{mq}\delta_{np} - \frac{2}{3}\delta_{mn}\delta_{pq}\right) \\ &= \kappa^{(2)}\delta_{mn}\delta_{pq} + \mu^{(2)}\left(\delta_{mp}\delta_{nq} + \delta_{mq}\delta_{np} - \frac{2}{3}\delta_{mn}\delta_{pq}\right) \end{aligned} \tag{16.51}$$

where $\kappa^{(2)}_0$ and $\mu^{(2)}_0$ are two initial bulk and shear modulus of the matrix. We adopt a power form to describe the mechanical degradation of these moduli, so that degradation parameters are written as $\mathrm{A} = \left(1 + \varepsilon^s_{kk}\right)^{\alpha}$ and $\mathrm{B} = \left(1 + \varepsilon^s_{kk}\right)^{\beta}$. Here $\alpha$ and $\beta$ are two positive material constants of the matrix, which should be derived or fitted from experimental data.

Equation (16.51) can be rewritten into a more compact form describing the degradation of the bulk and the shear modulus as

$$\frac{\kappa^{(2)}}{\kappa_0^{(2)}} = \frac{1}{\left(1+\varepsilon_{kk}^s\right)^{\alpha}} \qquad \frac{\mu^{(2)}}{\mu_0^{(2)}} = \frac{1}{\left(1+\varepsilon_{kk}^s\right)^{\beta}} \tag{16.52}$$

As can be seen, $\kappa^{(2)}$ and $\mu^{(2)}$ are monotonously decreasing with the initial bulk strain $\varepsilon_{kk}^s$. If $\varepsilon_{kk}^s = 0$, we have $\kappa^{(2)}(0) = \kappa_0^{(2)}$ and $\mu^{(2)}(0) = \mu_0^{(2)}$, without any modulus loss. Especially when $\alpha = \beta$, the Poisson's ratio $\upsilon^{(2)}$ is considered to keep constant since $\kappa^{(2)}/\kappa_0^{(2)} = \mu^{(2)}/\mu_0^{(2)}$.

By expanding the Eshelby relation (16.9), the real strain $\varepsilon_{11}^{(1),\mathrm{II}_2}$ in sub-problem $\mathrm{II}_2$ is expressed as

$$\varepsilon_{11}^{(1),\mathrm{II}_2} = S_{1111}\varepsilon_{11}^* + S_{1122}\varepsilon_{22}^* + S_{1133}\varepsilon_{33}^* \tag{16.53}$$

When the external loads are absent, the swelling condition $\varepsilon_{11}^s = \varepsilon_{22}^s$ leads to $\varepsilon_{11}^* = \varepsilon_{22}^*$ and $\varepsilon_{11}^{(1),\mathrm{II}} = \varepsilon_{22}^{(1),\mathrm{II}}$. By employing these relations and further substituting the Eshelby tensor of circular cylindrical shape into Eq. (16.42), we derive

$$\varepsilon_{11}^{(1),\mathrm{II}_2} = \frac{\varepsilon_{11}^*}{2\left(1-\upsilon^{(2)}\right)} + \frac{\upsilon^{(2)}\varepsilon_{33}^*}{2\left(1-\upsilon^{(2)}\right)} \tag{16.54}$$

In Eqs. (16.48), (16.49), (16.52), and (16.54), the four unknowns $\varepsilon_{11}^{(1),\mathrm{II}}$, $\varepsilon_{11}^*$, $\varepsilon_{33}^*$, and $\mathbf{C}^{(2)}$ can be solved simultaneously, given the stiffness $\mathbf{C}^{(1)}$ and $\mathbf{C}_0^{(2)}$ of the constituent materials and the swelling strain $\varepsilon_{11}^s$. Thereafter, the overall average strain $\varepsilon_{11}$ of the wood cell wall can be obtained from Eq. (16.18), as follows:

$$\varepsilon_{11} = (1-f)\left(C^{(2)}\right)_{11ij}^{-1} C_{ijkl}^{(1)}\left(\varepsilon_{kl}^{(1),\mathrm{II}} + \varepsilon_{kl}^s\right) + (1-f)\,\varepsilon_{11}^* - (1-f)\,\varepsilon_{11}^{(1),\mathrm{II}_2} + f\varepsilon_{11}^{(1),\mathrm{II}} + \varepsilon_{11}^s \tag{16.55}$$

Considering the unidirectional inclusions of circular cylindrical shape, the Mori–Tanaka prediction of the overall stiffness of the wood cell wall given by Eq. (16.19) can be expanded equivalently into five independent equations (Qiu and Weng 1990; Shi et al. 2004) to yield the five Hill's elastic moduli of the wood cell wall, as follows:

$$l = \frac{E^{(2)}\left\{2fl^{(1)} + (1-f)\left(E^{(2)} + 2k^{(1)}\right)\upsilon^{(2)} - 2\left[fl^{(1)} - (1-f)\,k^{(1)}\right]\left(\upsilon^{(2)}\right)^2\right\}}{\left(1+\upsilon^{(2)}\right)\eta} \tag{16.56}$$

$$n = \frac{E^{(2)}\left\{2(1-f)^2 k^{(1)}\left(1-\upsilon^{(2)}\right)+f\left[n^{(1)}\left(1+f-2\upsilon^{(2)}\right)+4\,(1-f)\,l^{(1)}\upsilon^{(2)}\right]\right\}}{\eta}$$

$$+\frac{2f\,(1-f)\left[k^{(1)}n^{(1)}-\left(l^{(1)}\right)^2\right]\left(1+\upsilon^{(2)}\right)^2\left(1-2\upsilon^{(2)}\right)}{\left(1+\upsilon^{(2)}\right)\eta}$$

$$+\frac{(1-f)\left(E^{(2)}\right)^2\left[1+f-(1-f)\,\upsilon^{(2)}\right]}{\left(1+\upsilon^{(2)}\right)\eta} \tag{16.57}$$

$$k = \frac{E^{(2)}\left\{E^{(2)}\,(1-f)+2k^{(1)}\left(1+\upsilon^{(2)}\right)\left[1+f\left(1-2\upsilon^{(2)}\right)\right]\right\}}{\left(1+\upsilon^{(2)}\right)\eta} \tag{16.58}$$

with

$$\eta = E^{(2)}\left(1+f-2\upsilon^{(2)}\right)-2\,(1-f)\,k^{(1)}\left[-1+\upsilon^{(2)}+2\left(\upsilon^{(2)}\right)^2\right] \tag{16.59}$$

The other five elastic coefficients of the wood cell wall, $E_1$, $E_3$, $G_{31}$, $\upsilon_{12}$, and $\upsilon_{13}$, can be calculated using Eq. (16.46).

### *16.4.3 Results and Discussions*

In this subsection, the theoretically predicted tensile modulus $E_3'$ along the cell axis of the wood cell wall is compared with available experimental data (Kojima and Yamamoto 2005) to illustrate the practical application of the proposed micromechanical framework.

The wood cell wall has layer structures, in which the $S_2$ layer is the thickest and most influential on the mechanical behaviors of the wood cell wall (Saavedra Flores et al. 2011). Hence the $S_2$ layer is particularly studied, taken as a plane stress problem. Two sets of plane coordinate systems are introduced: the local coordinate system $(x_1-x_3)$ and the global one $(x_1'-x_3')$, with the $x_3'$ -axis lying along the cell axis and the $x_3$ -axis along the CMF direction of the $S_2$ layer, as depicted in Fig. 16.8, so that the constitutive relation can be described, respectively, in these two coordinate systems, as follows:

$$\begin{cases}\tilde{\boldsymbol{\varepsilon}} = \tilde{\mathbf{D}}\cdot\tilde{\boldsymbol{\sigma}} \\ \tilde{\boldsymbol{\varepsilon}}' = \tilde{\mathbf{D}}'\cdot\tilde{\boldsymbol{\sigma}}'\end{cases} \tag{16.60}$$

where $\tilde{\boldsymbol{\sigma}} = \{\sigma_{33},\sigma_{11},\sigma_{31}\}^{\mathrm{T}}$ and $\tilde{\boldsymbol{\varepsilon}} = \{\varepsilon_{33},\varepsilon_{11},\varepsilon_{31}\}^{\mathrm{T}}$ are stresses and strains in the local coordinate system, while $\tilde{\boldsymbol{\sigma}}' = \{\sigma_{33}',\sigma_{11}',\sigma_{31}'\}^{\mathrm{T}}$ and $\tilde{\boldsymbol{\varepsilon}}' = \{\varepsilon_{33}',\varepsilon_{11}',\varepsilon_{31}'\}^{\mathrm{T}}$ are stresses and strains in the global coordinate system. $\tilde{\mathbf{D}}$ and $\tilde{\mathbf{D}}'$ are the plane

compliance tensors defined, respectively, in the local and the global coordinate systems. Here $\tilde{\mathbf{D}}$ is given as

$$\left[\tilde{\mathbf{D}}\right] = \begin{bmatrix} \frac{1}{E_3} & -\frac{\upsilon_{13}}{E_1} & 0 \\ -\frac{\upsilon_{31}}{E_3} & \frac{1}{E_1} & 0 \\ 0 & 0 & \frac{1}{G_{31}} \end{bmatrix} \tag{16.61}$$

where $E_1$, $E_3$, $G_{31}$, $\upsilon_{13}$, $\upsilon_{31}$ are, respectively, the tensile moduli along $x_1$ and $x_3$ directions, the shear modulus, and two Poisson's ratios. Note that the plane compliance tensor $\tilde{\mathbf{D}}$ is symmetric with the relation $\upsilon_{13}/E_1 = \upsilon_{31}/E_3$ held. After a rotation operation of the local compliance tensor, the global compliance tensor is derived as

$$\tilde{\mathbf{D}}' = \mathbf{A} \cdot \tilde{\mathbf{D}} \cdot \mathbf{R} \cdot \mathbf{A}^{-1} \cdot \mathbf{R}^{-1} \tag{16.62}$$

with the rotation tensor $\mathbf{A}$ and $\mathbf{R}$ given as

$$[\mathbf{A}] = \begin{bmatrix} \cos^2\varphi & \sin^2\varphi & -\sin\varphi\cos\varphi \\ \sin^2\varphi & \cos^2\varphi & \sin\varphi\cos\varphi \\ 2\sin\varphi\cos\varphi & -2\sin\varphi\cos\varphi & \cos^2\varphi - \sin^2\varphi \end{bmatrix} \tag{16.63}$$

$$[\mathbf{R}] = \begin{bmatrix} 1 & 0 & 0 \\ 0 & 1 & 0 \\ 0 & 0 & 2 \end{bmatrix} \tag{16.64}$$

Here $\mathbf{R}$ is called the Reuter matrix (Reddy 2004) taking into account the relationship between the engineering strains $\gamma_{31}$ and the shear strain $\varepsilon_{31}$, namely, $\gamma_{31} = 2\varepsilon_{31}$.

Hence the tensile modulus $E_3'$ along the cell axis is calculated from Eq. (16.62) as

$$E_3' = \left(\tilde{\mathbf{D}}'\right)^{-1}_{11} = \frac{E_1 G_{31}\cos^4\varphi + E_1\left(E_3 - 2G_{31}\upsilon_{31}\right)\cos^2\varphi\sin^2\varphi + E_3 G_{31}\sin^4\varphi}{E_3 E_1 G_{31}} \tag{16.65}$$

where the elastic coefficients $E_1$, $E_3$, $G_{31}$, $\upsilon_{31}$ are related to the Hill's elastic coefficients by Eq. (16.46). Furthermore, these Hill's coefficients can be calculated from the elastic coefficients of the constituents using Eqs. (16.56)–(16.59).

Since all the Poisson's ratios of the CMF and the matrix remain constant (Salmén 2004) during moisture absorption, Eq. (16.52) is reduced to

$$\frac{E^{(2)}}{E_0^{(2)}} = \frac{1}{\left(1 + \varepsilon_{kk}^s\right)^{\alpha}} \tag{16.66}$$

when $\alpha = \beta$. Here $\varepsilon_{kk}^s = (2 + \rho)\,\varepsilon_{11}^s$ $(0 \le \rho < 1)$.

In the subsequent calculations, we set $\rho = 0$ for simplicity and take the elastic coefficients of the fiber (CMF) and the matrix (hemicelluloses) from the literature (Salmén 2004): $E_0^{(2)} = 1.4$ GPa, $\upsilon_0^{(2)} = 0.2$, $E_1^{(1)} = 27.2$ GPa, $E_3^{(1)} = 134$ GPa, $G_{13}^{(1)} = 4.4$ GPa, and $\upsilon_{12}^{(1)} = \upsilon_{13}^{(1)} = 0.1$.

Accordingly, by virtue of Eq. (16.65), the tensile modulus $E_3'$ can be obtained as a function of the swelling bulk strain $\varepsilon_{kk}^s$, the MFA $\varphi$, the CMF content $f$, and the material parameter $\alpha$, i.e.,

$$E_3' = E_3'\left(\varepsilon_{kk}^s; \varphi, f, \alpha\right) \tag{16.67}$$

where $\varphi$, $f$, and $\alpha$ are three intrinsic parameters of the wood cell wall, which can be derived from experimental measurements. Although the analytical expression of Eq. (16.67) is too long to be presented here, it can be easily operated in the symbolic computation software (e.g., Mathematica 7.0 used in the present chapter).

In the experiment conducted by Kojima and Yamamoto (2005), four samples of wood cell wall were tested, with identical CMF content but different MFAs ($\varphi = 12.0°$, 20.4°, 29.8°, and 44.1°). In their article, the moisture absorption of a sample was described by the relative humidity (RH), $\theta = 0$, 0.76, and 1, rather than the moisture content. However, this is not a problem because they are correlated with each other. Furthermore, the RH can be equivalently represented by the swelling bulk stain $\varepsilon_{kk}^s$ because the samples with an identical RH have the same swelling bulk strain $\varepsilon_{kk}^s$. Thus, the swelling strain $\varepsilon_{kk}^s$, rather than $\theta$, is employed in the subsequent analysis. For each sample, the tensile modulus $E_3'$ was measured for different RHs and listed in Table 16.1.

The CMF content $f$ is obtained by fitting the experimental data according to Eq. (16.67) when setting $\varepsilon_{kk}^s = 0$, as shown in Fig. 16.9. The theoretical prediction is $f = 0.83$, a little bigger than that of previous estimation $f = 0.65 - 0.75$ (Astley and Donald 2001). The four experimental points in Fig. 16.9 are derived from four samples in the case RH = 0, listed at the first row in Table 16.1. From Fig. 16.9, the tensile modulus $E_3'$ decreases with the increase of the MFA, confirming the expectation that the reinforcing effect of CMF is gradually reduced when the alignment of CMFs deviates from the cell axis.

Next the parameter $\alpha$ will be determined. Since $\alpha$ is identical for all four samples, we try and error, and finally set $\alpha = 5.5$ in the prediction of $E_3'$. For convenience, the experimental data listed in Table 16.1 are denoted as $E_3'\big|_{\varphi,\theta}$. The swelling strain

**Table 16.1** The experimentally measured $E_3'$ with different MFAs and moisture contents

| | $\varphi = 12.0°$ | $\varphi = 20.4°$ | $\varphi = 29.8°$ | $\varphi = 44.1°$ |
|---|---|---|---|---|
| $E_3'\big\|_{\theta=0}$ (GPa) | 46.2 | 13.9 | 14.1 | 7.3 |
| $E_3'\big\|_{\theta=0}$ (GPa) | 22.0 | 9.7 | 5.8 | 4.1 |
| $E_3'\big\|_{\theta=0}$ (GPa) | 18.9 | 6.2 | 3.6 | 2.0 |

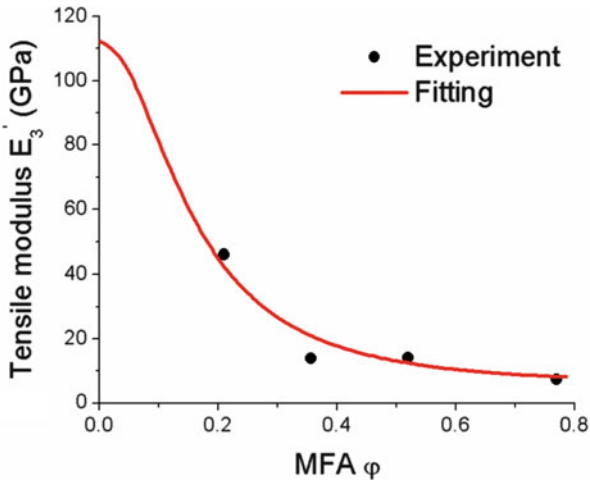


**Fig. 16.9** The fitting result of $E_3'$ varying with $\varphi$ under the condition $\theta = 0$

$\varepsilon_{kk}^s\big|_\theta$ under a given $\theta$ should be identical for all samples. Using Eq. (16.67) with $f = 0.83$ , the swelling strain $\varepsilon_{kk}^s$ is obtained when $\varphi$, $\alpha$, and $E_3'$ are given. For example, for the case $\theta = 0$, given the experimental data $E_3'\big|_{\varphi,\theta=0}$ of four samples, the swelling strain $\varepsilon_{kk}^s\big|_{\varphi,\theta=0}$ can be obtained. Due to model and experimental errors, the four values of $\varepsilon_{kk}^s\big|_{\varphi,\theta=0}$ have a little difference. Hence, it is reasonable to use the average value to determine the swelling strain $\varepsilon_{kk}^s\big|_{\theta=0}$ at $\theta = 0$, namely,

$$\varepsilon_{kk}^s\big|_{\theta=0} = \frac{1}{4}\left(\varepsilon_{kk}|_{\varphi=12.0°,\theta=0} + \varepsilon_{kk}|_{\varphi=20.4°,\theta=0} + \varepsilon_{kk}|_{\varphi=29.8°,\theta=0} + \varepsilon_{kk}|_{\varphi=44.1°,\theta=0}\right) \tag{16.68}$$

In the same way, other two swelling strains $\varepsilon_{kk}^s\big|_{\theta=0.76}$ and $\varepsilon_{kk}^s\big|_{\theta=1}$ can also be determined. Substituting $\varepsilon_{kk}^s\big|_{\theta=0}$, $\varepsilon_{kk}^s\big|_{\theta=0.76}$, and $\varepsilon_{kk}^s\big|_{\theta=1}$ into Eq. (16.55), the average strain $\varepsilon_{11}$ of the wood cell wall with different moisture contents is derived as

$$\varepsilon_{11}|_{\theta=0} = 2.62 \times 10^{-3}\,\varepsilon_{11}|_{\theta=0.76} = 1.45 \times 10^{-2}\,\varepsilon_{11}|_{\theta=1} = 1.93 \times 10^{-2}$$

Then the tensile moduli $E_3'$ versus $\varepsilon_{11}$ of four samples are plotted as scatter points in Fig. 16.10. It is seen that the tensile modulus $E_3'$ decreases with the increase of the average strain $\varepsilon_{11}$ under a given MFA.

Now Eqs. (16.55) and (16.67) can be used together to predict the relation between the tensile moduli of $E_3'$ and the strain $\varepsilon_{11}$ under a given $\varphi$. As shown in Fig. 16.10, the theoretical predictions agree well with the experimental results. Although there are only three experimental points in each figure, one may still find that the proposed model successfully captures the variation trends of $E_3'$. After comparing all four figures, it is also found that $E_3'$ decreases with the increase of the MFA.

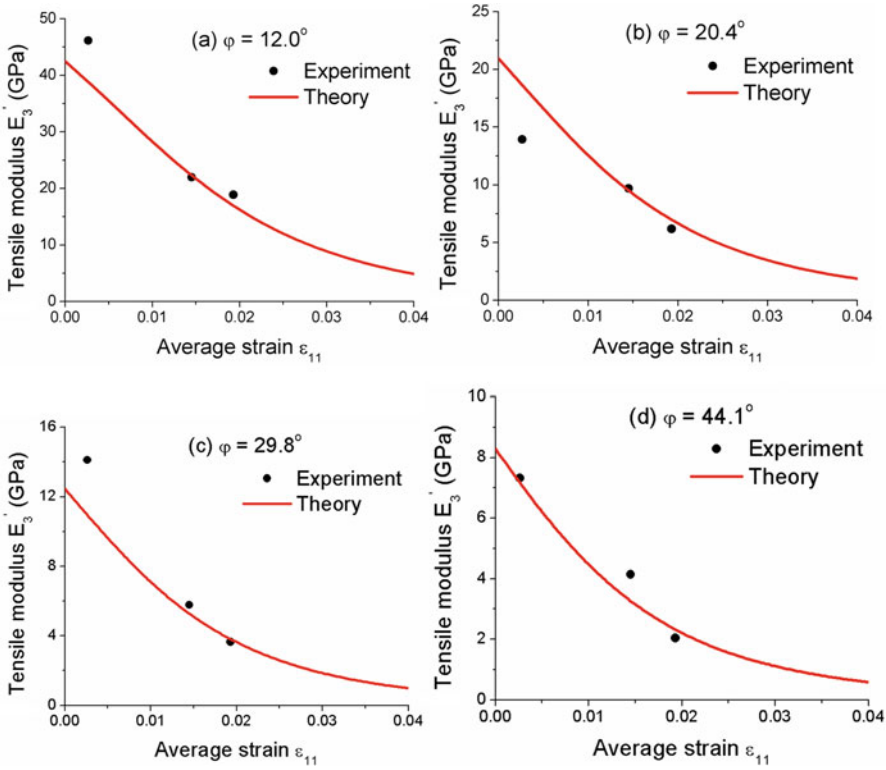


**Fig. 16.10** The theoretical predictions of $E_3'$ under: (**a**) $\varphi = 12.0°$, (**b**) $\varphi = 20.4°$, (**c**) $\varphi = 29.8°$, and (**d**) $\varphi = 44.1°$

It is worthy to note that the properties of the wood cell will change remarkably with the moisture content below FSP that is critical for the wood cell. The tensile modulus $E_3'$ measured by Kojima and Yamamoto (2005) showed that the modulus exhibits a remarkable change for the RH from 76% to 100% (see Table 16.1). This implies that the RH corresponding to the FSP of the studied wood is in between 76 and 100%.

As expected, the proposed micromechanical model effectively predicts the modulus loss of the wood cell wall induced by moisture absorption. For different MFAs, the predicted tensile modulus decreases with the strain induced by moisture content below FSP. This decreasing trend is remarkable at smaller strains, slows down for bigger strains, and eventually goes to a stable state corresponding to the FSP of the wood (see Fig. 16.10). Although the present model has been validated through laboratory testing examples, it can be easily applied in real applications.

The present micromechanical approach also provides additional insights to the mechanical behavior of the wood cell wall by establishing a relation between the macro-scale tensile modulus and the microstructure parameter such as the MFA (see Fig. 16.9).

**Table 16.2** A comparison between the present model and other models of the wood cell wall

| | Matrix | Inhomogeneity | Random distribution | Modulus loss |
|---|---|---|---|---|
| Our model | Hemicellulose and lignin | CMF | No | Yes |
| Cave (1968, 1969) | Hemicellulose and lignin | CMF | Yes | No |
| Hofstetter et al. (2005, 2007) | Polymer network | Lignin, hemicellulose, CMF, and water | No | No |

Other theoretical models have been proposed to study the elastic properties (Cave 1968; Hofstetter et al. 2005), the visco-elastic properties (Kojima and Yamamoto 2004, 2005), and the hysteresis between loading and unloading cycles (Saavedra Flores et al. 2011) of the wood cell wall. A rough comparison between these models with the present micromechanical model elaborated on the modulus loss of the wood cell wall due to moisture absorption is tabulated in Table 16.2.

More specifically, the hemicellulose and lignin is treated similarly as a matrix with the reinforcing CMF in Cave's model (Cave 1968, 1969). The difference from our model is that the MFA $\varphi$ in Cave's model is assumed to have a Gaussian distribution (Cave 1968, 1969)

$$g(\varphi) = \frac{1}{s\sqrt{2\pi}} \exp\left[-\frac{(M-\varphi)^2}{2}\right] \tag{16.69}$$

where $s$ and $M$ are, respectively, the standard deviation and the mean value of $\varphi$. Although the Gaussian distribution of the MFA $\varphi$ presents a more reasonable distribution of the CMF in the wood cell wall, the difficulties rise from the identification of two more parameters $s$ and $M$.

Another micromechanical model was developed by Hofstetter et al. (2005, 2007) based on a four-step homogenization scheme from nano-scale to macro-scale to simulate the wood cell wall, the softwood, and the hardwood. This micromechanical analysis is very complicated, which limits its practical use in the prediction of material properties of the wood cell wall.

Unfortunately, neither Cave's model nor the model proposed by Hofstetter et al. considers the modulus loss induced by moisture absorption. However, the present model introduces damage variables into the Mori–Tanaka micromechanical scheme to deal with modulus loss of the wood cell wall induced by moisture absorption, with which the hemicellulose and lignin is taken together as a matrix, while the CMF is treated as the inhomogeneity.

Different from the Cave's model and the model proposed by Hofstetter et al., our micromechanical analysis is not based directly on the classic eigenstrain problem (i.e., Eshelby inclusion problem). In order to study the eigenstrain occurring in the matrix, two eigenstrain sub-problems were established. This analytical framework

is newly developed in the micromechanical analysis of the wood cell wall. Last but not least, the analytical prediction of the modulus loss in the wood cell wall demonstrates more advantage in the practical applications than implementing finite element analysis (Saavedra Flores et al. 2011).

## 16.5 Conclusions

A micromechanical model is established to study the overall mechanical degradation of polymeric composites that absorb water both in the matrix and the homogeneity. Damage variables are introduced into the Mori–Tanaka framework to describe the mechanical degradation. The original problem of moisture absorption is decomposed into two sub-problems in which an equivalent eigenstrain problem is constructed. Based on the proposed modified Mori–Tanaka scheme, the moisture absorption and the mechanical degradation of NFRCs and wood cell wall are theoretically predicted. The analysis of NFRCs can be reduced from the proposed micromechanical model with only inhomogeneity absorbing water, as well as only matrix absorbing water for wood cell wall. Theoretical predictions are in good agreement with experimental results of sisal fiber reinforced composites and wood cell wall.

**Acknowledgments** This work was supported by National Natural Science Foundation of China (Project No. 11572227).

## Appendix A

The bulk and the shear moduli of natural fiber and matrix are, respectively, expressed as

$$\begin{cases} \kappa^{(i)} = \frac{E^{(i)}}{3\left(1-2\upsilon^{(i)}\right)} \\ \mu^{(i)} = \frac{E^{(i)}}{2\left(1+\upsilon^{(i)}\right)} \end{cases} \qquad (i = 1, 2) \tag{16.A.1}$$

In our theoretical predictions, Poison's ratios are $\upsilon^{(1)} = \upsilon_0^{(1)} = 0.25 = 1/4$ for sisal fiber and $\upsilon^{(2)} = \upsilon_0^{(2)} = 0.33 \approx 1/3$ for polypropylene matrix. Substituting Eq. (16.A.1) into (16.24), we arrive at

$$\kappa = E^{(2)} + \frac{f\left(2E^{(1)}/3 - E^{(2)}\right)\left(3E^{(2)} + 2E^{(1)}/5 + 9E^{(2)}/8\right)}{2\left(1-f\right)E^{(1)} + 3fE^{(2)} + 9E^{(2)}/8 + 2E^{(1)}/5}$$

$$\mu = \frac{3E^{(2)}}{8} - \frac{f\left(2E^{(1)}/5 - 3E^{(2)}/8\right)\left(3E^{(2)}\delta_1/2 + 2E^{(1)}\delta_2\right)}{3E^{(2)}\left(2E^{(1)}/5 + 3E^{(2)}/8\right)\eta_1 - 3E^{(2)}\eta_2/8 + 2E^{(1)}\left(\eta_3 - \eta_4\right)} \tag{16.A.2}$$

As seen in Eq. (16.A.2), the bulk and shear moduli of the composite are expressed by Young's moduli of the fiber and the matrix (i.e., $E^{(1)}$ and $E^{(2)}$).

By means of Eqs. (16.25) and (16.A.2), we can fit the experimental data of $(E_0, f)$ (the scatter points in Fig. 16.4) by the commercial software Mathematica 7.0 with the command *FindFit* to obtain the moduli $E_0^{(1)} = 15.03$ GPa and $E_0^{(2)} = 2.37$ GPa, as shown in Fig. 16.4. The fitting procedure is based on the least square method. The square of the residuals $R$ between the results of theoretical predictions and experimental data should be minimized such as

$$\begin{cases} R = \sum_{i=1}^{n}\left[E\left(E_0^{(1)}, E_0^{(2)}, f\right) - E_0\right]^2 \\ \dfrac{\partial R}{\partial E_0^{(1)}} = 0 \\ \dfrac{\partial R}{\partial E_0^{(2)}} = 0 \end{cases} \tag{16.A.3}$$

from which the two material parameters$E_0^{(1)}$ and $E_0^{(2)}$ are finally determined.

## References


Aboudi, J.: Mechanics of Composite Materials – A Unified Micromechanical Approach. Elsevier, Amsterdam (1991)

Alvarez, V., Fraga, A., Vazquez, A.: Effects of the moisture and fiber content on the mechanical properties of biodegradable polymer–sisal fiber biocomposites. J. Appl. Polym. Sci. **91**, 4007–4016 (2004)

Arbelaiz, A., Fernández, B., Ramos, J.A., Retegi, A., Llano-Ponte, R., Mondragon, I.: Mechanical properties of short flax fibre bundle/polypropylene composites: influence of matrix/fibre modification, fibre content, water uptake and recycling. Compos. Sci. Technol. **65**, 1582–1592 (2005)

Astley, O.M., Donald, A.M.: A small-angle X-ray scattering study of the effect of hydration on the microstructure of flax fibers. Biomacromolecules. **2**, 672–680 (2001)

Benveniste, Y.: A new approach to the application of Mori-Tanaka's theory in composite materials. Mech. Mater. **6**, 147–157 (1987)

Benveniste, Y., Miloh, T.: Imperfect soft and stiff interfaces in two-dimensional elasticity. Mech. Mater. **33**, 309–323 (2001)

Cave, I.: The anisotropic elasticity of the plant cell wall. Wood Sci. Technol. **2**, 268–278 (1968)
Cave, I.: The longitudinal Young's modulus of *Pinus radiata*. Wood Sci. Technol. **3**, 40–48 (1969)
Chen, T., Dvorak, G.J., Benveniste, Y.: Mori-Tanaka estimates of the overall elastic moduli of certain composite materials. ASME Trans. Ser. E J. Appl. Mech. **59**, 539–546 (1992)
Cheung, H.-Y., Ho, M.-P., Lau, K.-T., Cardona, F., Hui, D.: Natural fibre-reinforced composites for bioengineering and environmental engineering applications. Compos. Part B. **40**, 655–663 (2009)
Chow, C., Wang, J.: An anisotropic theory of elasticity for continuum damage mechanics. Int. J. Fract. **33**, 3–16 (1987)
Chow, C., Xing, X., Li, R.: Moisture absorption studies of sisal fibre reinforced polypropylene composites. Compos. Sci. Technol. **67**, 306–313 (2007)
Desrumaux, F., Meraghni, F., Benzeggagh, M.: Generalised Mori-Tanaka scheme to model anisotropic damage using numerical Eshelby tensor. J. Compos. Mater. **35**, 603–624 (2001)
Dhakal, H., Zhang, Z., Richardson, M.: Effect of water absorption on the mechanical properties of hemp fibre reinforced unsaturated polyester composites. Compos. Sci. Technol. **67**, 1674–1683 (2007)
Eder, M., Arnould, O., Dunlop, J.W., Hornatowska, J., Salmén, L.: Experimental micromechanical characterisation of wood cell walls. Wood Sci. Technol. **47**, 163–182 (2013)
Eshelby, J.D.: The determination of the elastic field of an ellipsoidal inclusion, and related problems. Proc. R. Soc. Lond. Ser. A. Math. Phys. Sci. **241**, 376–396 (1957)
Garg, S.K.: Assessment of the intrinsic birefringence of partially oriented poly (ethylene terephthalate) yarns. J. Appl. Polym. Sci. **27**, 2857–2867 (1982)
Hazarika, A., Mandal, M., Maji, T.K.: Dynamic mechanical analysis, biodegradability and thermal stability of wood polymer nanocomposites. Compos. Part B. **60**, 568–576 (2014)
Hill, R.: A self-consistent mechanics of composite materials. J Mech. Phys. Solids. **13**, 213–222 (1965)
Hofstetter, K., Hellmich, C., Eberhardsteiner, J.: Development and experimental validation of a continuum micromechanics model for the elasticity of wood. Eur. J. Mech. A Solids. **24**, 1030–1053 (2005)
Hofstetter, K., Hellmich, C., Eberhardsteiner, J.: Micromechanical modeling of solid-type and plate-type deformation patterns within softwood materials. A review and an improved approach. Holzforschung. **61**, 343–351 (2007)
Hu, R.-H., Sun, M.-Y., Lim, J.-K.: Moisture absorption, tensile strength and microstructure evolution of short jute fiber/polylactide composite in hygrothermal environment. Mater. Des. **31**, 3167–3173 (2010)
Jakob, H., Tschegg, S., Fratzl, P.: Hydration dependence of the wood-cell wall structure in *Picea abies*. A small-angle X-ray scattering study. Macromolecules. **29**, 8435–8440 (1996)
José da Silva, L., Hallak Panzera, T., Luis Christoforo, A., Miguel Pereira Dur, L., Antonio Rocco Lahr, F.: Numerical and experimental analyses of biocomposites reinforced with natural fibres. Int. J. Mater. Eng. **2**, 43–49 (2012)
Karris, A.: An examination of the Mori-Tanaka effective medium—approximation for multiphase composites. J. Appl. Mech. **56**, S3 (1989)
Kojima, Y., Yamamoto, H.: Effect of microfibril angle on the longitudinal tensile creep behavior of wood. J. Wood Sci. **50**, 301–306 (2004)
Kojima, Y., Yamamoto, H.: Effect of moisture content on the longitudinal tensile creep behavior of wood. J. Wood Sci. **51**, 462–467 (2005)
Meraghni, F., Benzeggagh, M.: Micromechanical modelling of matrix degradation in randomly oriented discontinuous-fibre composites. Compos. Sci. Technol. **55**, 171–186 (1995)
Milton, G.W.: The Theory of Composites. Cambridge University Press, Cambridge (2002)
Mochida, T., Taya, M., Obata, M.: Effect of damaged particles on the stiffness of a particle/metal matrix composite. JSME Int. J. Ser. 1 Solid Mech. Strength Mater. **34**, 187–193 (1991)
Mori, T., Tanaka, K.: Average stress in matrix and average elastic energy of materials with misfitting inclusions. Acta Metall. **21**, 571–574 (1973)
Mura, T.: Micro-Mechanics of Defects in Solids. Springer (1987)

Nemat-Nasser, S., Hori, M.: Micromechanics: Overall Properties of Heterogeneous Materials, 2nd edn. Elsevier, Amsterdam (1999)
Okereke, M., Akpoyomare, A., Bingley, M.: Virtual testing of advanced composites, cellular materials and biomaterials: A review. Compos. Part B. **60**, 637–662 (2014)
Pan, Y., Zhong, Z.: A nonlinear constitutive model of unidirectional natural fiber reinforced composites considering moisture absorption. J. Mech. Phys. Solids. **69**, 132–142 (2014)
Pan, Y., Zhong, Z.: A micromechanical model for the mechanical degradation of natural fiber reinforced composites induced by moisture absorption. Mech. Mater. (2015)
Pan, Y., Zhong, Z.: Micromechanical modeling of the wood cell wall considering moisture absorption. Compos. Part B. **91**, 27–35 (2016)
Pandey, J.K., Ahn, S.H., Lee, C.S., Mohanty, A.K., Misra, M.: Recent advances in the application of natural fiber based composites. Macromol. Mater. Eng. **295**, 975–989 (2010)
Qing, H., Mishnaevsky Jr., L.: 3D hierarchical computational model of wood as a cellular material with fibril reinforced, heterogeneous multiple layers. Mech. Mater. **41**, 1034–1049 (2009)
Qiu, Y., Weng, G.: On the application of Mori-Tanaka's theory involving transversely isotropic spheroidal inclusions. Int. J. Eng. Sci. **28**, 1121–1137 (1990)
Qiu, Y., Weng, G.: The influence of inclusion shape on the overall elastoplastic behavior of a two-phase isotropic composite. Int. J. Solids Struct. **27**, 1537–1550 (1991)
Qu, J.: The effect of slightly weakened interfaces on the overall elastic properties of composite materials. Mech. Mater. **14**, 269–281 (1993)
Ravichandran, G., Liu, C.: Modeling constitutive behavior of particulate composites undergoing damage. Int. J. Solids Struct. **32**, 979–990 (1995)
Reddy, J.N.: Mechanics of laminated composite plates and shells: theory and analysis. CRC Press (2004)
Saavedra Flores, E., de Souza Neto, E., Pearce, C.: A large strain computational multi-scale model for the dissipative behaviour of wood cell-wall. Comput. Mater. Sci. **50**, 1202–1211 (2011)
Saavedra Flores, E., DiazDelaO, F., Friswell, M., Ajaj, R.: Investigation on the extensibility of the wood cell-wall composite by an approach based on homogenisation and uncertainty analysis. Compos. Struct. **108**, 212–222 (2014)
Saheb, D.N., Jog, J.: Natural fiber polymer composites: a review. Adv. Polym. Technol. **18**, 351–363 (1999)
Salmén, L.: Micromechanical understanding of the cell-wall structure. C. R. Biol. **327**, 873–880 (2004)
Sgriccia, N., Hawley, M.C., Misra, M.: Characterization of natural fiber surfaces and natural fiber composites. Compos. A Appl. Sci. Manuf. **39**, 1632–1637 (2008)
Shi, D.-L., Feng, X.-Q., Huang, Y.Y., Hwang, K.-C., Gao, H.: The effect of nanotube waviness and agglomeration on the elastic property of carbon nanotube-reinforced composites. J. Eng. Mater. Technol. **126**, 250 (2004)
Smith, I.: Fracture and Fatigue in Wood. Wiley (2003)
Song, J.-H., Mun, S.-D., Kim, C.-S.: Mechanical properties of sisal natural fiber composites according to strain rate and absorption ratio. Polym. Compos. **32**, 1174–1180 (2011)
Srubar, W.V.: An analytical model for predicting the freeze–thaw durability of wood–fiber composites. Compos. Part B. **69**, 435–442 (2015)
Tandon, G., Weng, G.: Average stress in the matrix and effective moduli of randomly oriented composites. Compos. Sci. Technol. **27**, 111–132 (1986)
Tashiro, K., Kobayashi, M.: Theoretical evaluation of three-dimensional elastic constants of native and regenerated celluloses: role of hydrogen bonds. Polymer. **32**, 1516–1526 (1991)
Torquato, S.: Random Heterogeneous Materials: Microstructure and Macroscopic Properties. Springer (2002)
Watt, J.P., Davies, G.F., O'Connell, R.J.: The elastic properties of composite materials. Rev. Geophys. **14**, 541–563 (1976)
Zheng, S., Denda, M., Weng, G.: Interfacial partial debonding and its influence on the elasticity of a two-phase composite. Mech. Mater. **32**, 695–709 (2000)
Zhong, Z., Meguid, S.: On the elastic field of a spherical inhomogeneity with an imperfectly bonded interface. J. Elast. **46**, 91–113 (1997)

# Chapter 17
# General Interface Integral Equations in Elasticity of Random Structure Composites

**Valeriy Buryachenko**

**Abstract** One considers linearly elastic composite media, which consist of a homogeneous matrix containing a statistically homogeneous random set of aligned homogeneous heterogeneities of a noncanonical shape. The new general integral equations connecting the stress and strain fields in the point being considered with the stress and strain fields in the surrounding points are obtained for the random fields of heterogeneities. The method is based on a recently developed centering procedure where the notion of a *perturbator* is introduced in terms of boundary interface integrals that makes it possible to reconsider basic concepts of micromechanics such as effective field hypothesis, quasi-crystalline approximation, and the hypothesis of "ellipsoidal symmetry." The results of this reconsideration are quantitatively estimated for some modeled composite reinforced by aligned homogeneous heterogeneities of a noncanonical shape. Some new effects are detected that are impossible in the framework of a classical background of micromechanics.

## 17.1 Introduction

The prediction of the behavior of composite materials in terms of the mechanical properties of constituents and their microstructure is a central problem of micromechanics, which is evidently reduced to the estimation of stress fields in the constituents. Appropriate, but by no means exhaustive, references for the estimation of effective elastic moduli of statistically homogeneous media are provided by the reviews Willis (1981), Mura (1987), Nemat-Nasser and Hori (1993), Torquato (2002), Milton (2002), Buryachenko (2007), and Dvorak (2013). It appears today that variants of the effective medium method (Kröner, 1958; Hill, 1965) and the Mori-Tanaka method (MTM, see Mori and Tanaka 1973; Benveniste 1987) are the most popular and widely used methods. Recently, a new method, namely the multiparticle effective field method (MEFM), was put forward and developed (see for references Buryachenko 2007). The MEFM is based on the theory of functions

V. Buryachenko (✉)
Micromechanics and Composites LLC, 2520 Hingham Lane, Dayton, OH 45459, USA
e-mail: buryach@aol.com



S.A. Meguid, G.J. Weng (eds.), *Micromechanics and Nanomechanics of Composite Solids*, DOI 10.1007/978-3-319-52794-9_17

of random variables and Green's functions. This way, the interaction of different inclusions is taken into account.

The stress distributions inside a single (or a few) inclusion inside an infinite matrix are assumed to be found and incorporated into one or another general framework of analytical micromechanics for self-consistent estimations of a so-called effective field (see for details Buryachenko 2007). However, all mentioned methods are based on the effective field hypothesis (EFH **H1**, even if the term "effective field hypothesis" was not indicated) according to which each inclusion is located inside a homogeneous so-called effective field (see for references Buryachenko 2007). This concept has directed a development of micromechanics over the last 60 years and made a contribution to their progress incompatible with any another concept. The idea of effective field dating back to Mossotti (1850) was added by the hypothesis of "ellipsoidal symmetry" for the distribution of inclusions attributed to Willis (1977). In the framework of a new background of micromechanics (NBM) proposed (see for references Buryachenko 2014, 2015) and based on the new general integral equations (GIEs), it was demonstrated that the effective field hypothesis **H1** is a central one and that other concepts play a satellite role in providing the conditions for the application of the effective field hypothesis. Moreover, it was also proven that all mentioned hypotheses are not particularly necessary and can be relaxed.

However, the NBM was formulated in terms of perturbations of the stress fields introduced by the interacting inclusions, while these perturbations in both the inside and the vicinity of the inclusions were estimated by either the finite element analysis (FEA) or the volume integral equation method. Obtaining analytical solutions is not feasible in general even for a finite number of interacting particles, so various numerical methods have been developed, mostly based on the finite element analysis (FEA, see, e.g., Zienkiewicz and Taylor 1994; Fish and Belytschko 2007) and boundary integral equation (BIE, see, e.g., Brebbia et al. 1984; Balas et al. 1988; Mukherjee and Liu 2013) technique. A distinct advantage of the BIE over the FEA is that the BIEs require meshing only on the boundary surface of the computational domain as opposed to the entire 3-D domain for FEA. In the BIE, singular forces distributed, for example, on the surface of particles, depend on the external field, thus yielding an integral equation for the singularity strengths.

It is interesting to develop some alternative so-called meshless methods (see Fasshauer 2006, for an overview and historical background on the subject) of the local boundary integral equation, boundary knot method, boundary collocation method, nondimensional dynamic influence functions method, and method of fundamental solutions (MFS proposed by Kupradze and Aleksidze 1964) belonging to the BIE methods for solving boundary value problems, which can be recognized as a discrete type of the indirect boundary element method with a concentrated source instead of distribution (see for references Belytschko et al. 1996; Goldberg and Chen 1998; Atluri 2004; Chen and Tanaka 2002). The MFS belonging to the BIE technique shares the same advantages as the BIE methods over domain discretization methods. Moreover, the MFS has certain attractive advantages over the boundary element method (BEM), since it is truly meshless (which requires neither domain nor boundary mesh structure), simple to program, and is able to take into account sharp changes in geometry. The MFS and related methods over

the last years have found extensive application in computing solutions to a broad range of problems (Fairweather and Karageorghis, 1998; Chen et al., 2008). A few disadvantages are that the positioning of the source points is preassigned and also that the resulting system of algebraic equations is ill-conditioned, which leads to the oscillation of the convergence curve of the numerical solution when a large number of source points are used. In such a case, the Tikhonov regularization can be used to mitigate the ill-conditioned effect (see Lin et al. 2011; Marin 2005).

Thus, the stress distributions inside a single inclusion inside an infinite matrix are assumed to be found. This solution then is incorporated into the new GIE without any additional assumptions such as some sort of "effective field hypothesis" **H1** and the hypothesis of "ellipsoidal symmetry" for the distribution of inclusions attributed to Willis (1977).

The paper is organized as follows. In Sect. 17.2 we present the basic field equations of linear elasticity, notations, and statistical description of the composite microstructure as well as the Green functions used in the BIE and the volume integral equations (VIE) methods. A new concept of the interface polarization tensors exploited in the effective properties representations is introduced in Sect. 17.3. The new general integral equations (GIEs) are proposed in Sect. 17.4 for the case of statistically homogeneous structures of composite materials. These equations are obtained by a centering procedure of subtraction from both sides of a known initial integral equation the statistical averages obtained without any auxiliary assumptions such as EFH implicitly exploited in the known centering methods. In Sect. 17.5, one presents the method of fundamental solution (MFS) adapted to the solution for one homogeneous noncanonical inclusion inside the infinite homogeneous matrix. Classical assumptions of micromechanics are reformulated in Sect. 17.6 in terms of interface operators. In Sect. 17.7 the solutions of the GIEs are proposed and expressed through the interface average variables. In particular, the GIE is solved in the framework of the quasi-crystalline approximation but without basic hypotheses of classical micromechanics such as both the old version of the EFH and ellipsoidal symmetry assumption. In Sect. 17.8 we show the results of the implemented numerical simulations and we analyze the improvements introduced by the new approach with respect to the classic ones and demonstrate the corrections of popular propositions obtained in the framework of the old background of micromechanics.

## 17.2 Preliminaries

### *17.2.1 Basic Equations*

Let a linear elastic body occupy an open bounded domain $w \subset R^d$ with a smooth boundary $\Gamma_0$ and with an indicator function $W$ and space dimensionality $d$ ($d = 2$ and $d = 3$ for 2-$D$ and 3-$D$ problems, respectively). The domain $w$ contains a homogeneous matrix $v^{(0)}$ and a statistically homogeneous set $X = (v_i, V_i, \mathbf{x}_i)$ of inclusions $v_i$ with indicator functions $V_i$ and centers $\mathbf{x}_i$ bounded by the closed

smooth surfaces $\Gamma_i := \partial v_i$ $(i = 1, 2, \ldots)$ defined by the relations $\Gamma_i(\mathbf{x}) = 0$ $(\mathbf{x} \in \Gamma_i)$, $\Gamma_i(\mathbf{x}) > 0$ $(\mathbf{x} \in v_i)$, and $\Gamma_i(\mathbf{x}) < 0$ $(\mathbf{x} \notin v_i)$. It is assumed that the inclusions can be grouped into component (phase) $v^{(1)} = \cup v_i$ $(i = 1, 2, \ldots)$ with identical mechanical and geometrical properties (such as the shape, size, orientation, and microstructure of inclusions). For the sake of definiteness, in the 2-*D* case we will consider a plane-strain problem. At first, no restrictions are imposed on the elastic symmetry of the phases or on the geometry of the inclusions.[1]

The problem is governed by the local equations of elastostatics of composites:

$$\nabla \boldsymbol{\sigma}(\mathbf{x}) = \mathbf{0}, \tag{17.1}$$

$$\boldsymbol{\sigma}(\mathbf{x}) = \mathbf{L}(\mathbf{x})\boldsymbol{\varepsilon}(\mathbf{x}), \quad \text{or} \quad \boldsymbol{\varepsilon}(\mathbf{x}) = \mathbf{M}(\mathbf{x})\boldsymbol{\sigma}(\mathbf{x}), \tag{17.2}$$

$$\boldsymbol{\varepsilon}(\mathbf{x}) = \nabla \overset{s}{\otimes} \mathbf{u}, \quad \nabla \times \boldsymbol{\varepsilon}(\mathbf{x}) \times \nabla = \mathbf{0}, \tag{17.3}$$

where $(.)^{\top}$ denotes transposition; $\otimes$ and $\times$ are the tensor and vector products, respectively; and the operator $\mathbf{a} \overset{s}{\otimes} \mathbf{b}$ represents the symmetric part of the second-order tensor, that is $\mathbf{a} \overset{s}{\otimes} \mathbf{b} = (\mathbf{a} \otimes \mathbf{b} + \mathbf{b} \otimes \mathbf{a})/2$. $\mathbf{L}(\mathbf{x})$ and $\mathbf{M}(\mathbf{x}) \equiv \mathbf{L}(\mathbf{x})^{-1}$ are the known stiffness and compliance fourth-order tensors, and the common notation for contracted products has been employed.

In particular, for isotropic constituents, the stiffness tensor $\mathbf{L}$ is given in terms of the local bulk modulus $k$ and the shear modulus $\mu$: $\mathbf{L} = (dk, 2\mu) \equiv dk\mathbf{N}_1 + 2\mu\mathbf{N}_2$, $\mathbf{N}_1 = \boldsymbol{\delta} \otimes \boldsymbol{\delta}/d$, $\mathbf{N}_2 = \mathbf{I} - \mathbf{N}_1$ $(d = 2 \text{ or } 3)$; $\boldsymbol{\delta}$ and $\mathbf{I}$ are the unit second-order and fourth-order tensors. For the fiber composites it is the plane-strain bulk modulus $k_{[2]}$—instead of the 3-D bulk modulus $k_{[3]}$—that plays the significant role: $k_{[2]} = k_{[3]} + \mu_{[3]}/3$, $\mu_{[2]} = \mu_{[3]}$. The tensors $\mathbf{g}$ $(\mathbf{g} = \mathbf{L}, \mathbf{M})$ of material properties are piecewise constant and decomposed as $\mathbf{g} \equiv \mathbf{g}^{(0)} + \mathbf{g}_1(\mathbf{x}) = \mathbf{g}^{(0)} + \mathbf{g}_1^{(1)}(\mathbf{x})$, where $\mathbf{g}^{(0)} = \text{const}$, $\mathbf{g}(\mathbf{x}) \equiv \mathbf{g}^{(0)}$ at $\mathbf{x} \in v^0$ and $\mathbf{g}_1^{(1)}(\mathbf{x}) \equiv \mathbf{g}_1^{(1)}$ is a homogeneous function of the $\mathbf{x} \in v^{(1)}$:

$$\mathbf{L}_1^{(1)}(\mathbf{x}) = \mathbf{L}_1^{(1)} \equiv \text{const. at } \mathbf{x} \in v^{(1)}. \tag{17.4}$$

The upper index $^{(m)}$ indicates the components and the lower index $i$ indicates the individual inclusions; $v^{(0)} = w \backslash v$, $v \equiv v^{(1)}$, $V(\mathbf{x}) = V^{(1)} = \sum V_i(\mathbf{x})$, and $V^{(1)}(\mathbf{x})$ and $V_i(\mathbf{x})$ are the indicator functions of $v^{(1)}$ and $v_i$, respectively.

The introduction of jumps of material properties allows one to define the stress $\boldsymbol{\tau}$ and strain $\boldsymbol{\eta}$ polarization tensors by two equivalent ways $(\mathbf{x} \in R^d)$:

$$\boldsymbol{\tau}(\mathbf{x}) = \mathbf{L}_1(\mathbf{x})\boldsymbol{\varepsilon}(\mathbf{x}), \quad \boldsymbol{\eta}(\mathbf{x}) = \mathbf{M}_1(\mathbf{x})\boldsymbol{\sigma}(\mathbf{x}), \quad \boldsymbol{\tau} = -\mathbf{L}^{(0)}\boldsymbol{\eta}, \tag{17.5}$$

$$\boldsymbol{\tau}(\mathbf{x}) = \boldsymbol{\sigma}(\mathbf{x}) - \mathbf{L}^{(0)}\boldsymbol{\varepsilon}(\mathbf{x}), \quad \boldsymbol{\eta}(\mathbf{x}) = \boldsymbol{\varepsilon}(\mathbf{x}) - \mathbf{M}^{(0)}\boldsymbol{\sigma}(\mathbf{x}), \tag{17.6}$$

[1] It is known that for 2-*D* problems the plane-strain state is only possible for material symmetry no lower than orthotropic (see, e.g., Lekhnitskii 1963) that will be assumed hereafter in 2-*D* case.

which are simply a notational convenience and vanish inside the matrix $\boldsymbol{\tau}(\mathbf{x}) \equiv \boldsymbol{\eta}(\mathbf{x}) \equiv \mathbf{0}$ $(\mathbf{x} \in v^{(0)})$. It is interesting that the polarization tensors (17.5) (see, e.g., Willis 1981) are attributed to Hashin and Shtrikman (1962) and Hill (1963) who introduced, in fact, these notions in the equivalent form (17.6). For both the local and nonlocal elasticity theory, Eqs. (17.5) and (17.6) are also equivalent; however, the form (17.6) is preferable for subsequent manipulation because Eq. (17.6) does not explicitly use the constitutive equation (17.2) for the heterogeneities $\mathbf{x} \in v$.

We assume that the phases are perfectly bonded, so that the displacements and the traction components are continuous across the interphase boundaries, that is, $[[\boldsymbol{\sigma}\mathbf{n}^{\text{int}}]] = \mathbf{0}$ and $[[\mathbf{u}]] = \mathbf{0}$ on the interface boundary $\Gamma = \cup\Gamma_i$ $(i = 1, 2, \ldots)$ where $\mathbf{n}^{\text{int}}$ is the normal vector on $\Gamma$ and $[[(.)]]$ is the jump operator. The traction $\mathbf{t}(\mathbf{x}) = \boldsymbol{\sigma}(\mathbf{x})\mathbf{n}(\mathbf{x})$ acting on any plane with the normal $\mathbf{n}(\mathbf{x})$ through the point $\mathbf{x}$ can be represented in terms of displacements $\mathbf{t}(\mathbf{x}) = \hat{\mathbf{t}}(\mathbf{n}, \nabla)\mathbf{u}(\mathbf{x})$, where $\hat{t}_{ik}(\mathbf{n}, \nabla) = L_{ijkl}n_j(\mathbf{x})\partial/\partial x_l$ is the conormal derivative operator. The boundary conditions at the interface boundaries will be considered together with the homogeneous boundary conditions:

$$\mathbf{u}^{\Gamma_0}(\mathbf{x}) = \boldsymbol{\varepsilon}^{\Gamma_0}\mathbf{x}, \ \boldsymbol{\varepsilon}^{\Gamma_0} \equiv \text{const.}, \ \mathbf{x} \in \Gamma_0, \tag{17.7}$$

$$\mathbf{t}^{\Gamma_0}(\mathbf{x}) = \boldsymbol{\sigma}^{\Gamma_0}\mathbf{n}^{\Gamma_0}(\mathbf{x}), \ \ \boldsymbol{\sigma}^{\Gamma_0} = \text{const.}, \ \mathbf{x} \in \Gamma_0, \tag{17.8}$$

where $\boldsymbol{\varepsilon}^{\Gamma_0}(\mathbf{x}) = \frac{1}{2}\big[\nabla\mathbf{u}^{\Gamma_0}(\mathbf{x}) + (\nabla\mathbf{u}^{\Gamma_0}(\mathbf{x}))^{\top}\big]$, $\mathbf{x} \in \Gamma_0$, and $\boldsymbol{\sigma}^{\Gamma_0}$ are the given constant symmetric tensors of the macroscopic strain and stress, respectively. We will consider the interior problem when the body occupies the interior domain with respect to the boundary $\Gamma_0$.

### *17.2.2 Statistical Description of Random Structure Composites*

It is assumed that the representative macrodomain $w$ contains a statistically large number of realizations $\alpha$ of inclusions $v_i \in v^{(1)}$ $(i = 1, 2, \ldots)$ of the constituent $v^{(1)}$ (providing validity of the standard probability theory technique). A random parameter $\alpha$ belongs to a sample space $\mathscr{A}$, over which a probability density $p(\alpha)$ is defined (see, e.g., Willis 1981). For any given $\alpha$, any random function $\mathbf{g}(\mathbf{x}, \alpha)$ (e.g., $\mathbf{g} = V, \boldsymbol{\sigma}, \boldsymbol{\varepsilon}$) is defined explicitly as one particular member, with label $\alpha$, of an ensemble realization. Then the mean, statistical (or ensemble) average is defined by the angle brackets enclosing the quantity $\mathbf{g}$:

$$\langle\mathbf{g}\rangle(\mathbf{x}) = \int_{\mathscr{A}} \mathbf{g}(\mathbf{x}, \alpha)p(\alpha)d\alpha. \tag{17.9}$$

No confusion will arise below in the notation of the random quantity $\mathbf{g}(\mathbf{x}, \alpha)$ if the label $\alpha$ is dropped for the compactness of expressions unless such indication is necessary. One treats two material length scales (see, e.g., Torquato 2002): the macroscopic scale $L$, characterizing the extent of $w$, and the microscopic scale $a$,

related with the heterogeneities $v_i$. Moreover, one supposes that the applied field varies on a characteristic length scale $\Lambda$. The limit of our interests for both the material scales and field one is presented in an asymptotic sense:

$$L \gg \Lambda \geq a, \tag{17.10}$$

as the scale of microstructure $a$ relative to the macroscale $L$ tends to zero. All the random quantities under discussion are described by statistically homogeneous random fields. For the alternative description of the random structure of a composite material, let us introduce a conditional probability density $\varphi(v_i, \mathbf{x}_i | v_1, \mathbf{x}_1)$, which is a probability density to find the $i$-th heterogeneity with the center $\mathbf{x}_i$ in the domain $v_i$ with fixed heterogeneity $v_1$ with the centers $\mathbf{x}_1$. The notation $\varphi(v_i, \mathbf{x}_i | ; v_1, \mathbf{x}_1)$ denotes the case $\mathbf{x}_i \neq \mathbf{x}_1$.

To prevent the overlapping of different inclusions, $\varphi(v_i, \mathbf{x}_i | ; v_m, \mathbf{x}_m) = 0$, for values of $\mathbf{x}_i$ lying inside the "excluded volumes," $\cup v^0_{mi}$, where $v^0_{mi} \supset v_m$, with indicator function $V^0_{mi}$ as the "excluded volumes" of $\mathbf{x}_i$ with respect to $v_m$ (it is usually assumed that $v^0_{mi} \equiv v^0_m$) and $\varphi(v_i, \mathbf{x}_i | ; v_m, \mathbf{x}_m) \to \varphi(v_i, \mathbf{x}_i)$ as $|\mathbf{x}_i - \mathbf{x}_m| \to \infty$ (since no long-range order is assumed). $\varphi(v_i, \mathbf{x})$ is a number density, $n(\mathbf{x}) = n$ of component $v \ni v_i$ at the point $\mathbf{x}$ and $c^{(1)}$ is the concentration, that is, the volume fraction of the component $v_i \in v$: $c^{(1)} = \langle V \rangle = \overline{v}_i n$, $\overline{v}_i = \text{mes } v_i$ $(i = 1, 2, \ldots)$, $c^{(0)}(\mathbf{x}) = 1 - \langle V \rangle$. Hereafter, if the pair distribution function $g(\mathbf{x}_i - \mathbf{x}_m) \equiv \varphi(v_i, \mathbf{x}_i | ; v_m, \mathbf{x}_m)/n^{(k)}$ depends on $\mathbf{x}_m - \mathbf{x}_i$ only through $|\mathbf{x}_m - \mathbf{x}_i|$, it is called the radial distribution function (RDF, see for references and details Buryachenko et al., 2012). The notations $\langle (.) \rangle (\mathbf{x})$ and $\langle (.) | v_1, \mathbf{x}_1 \rangle (\mathbf{x})$ will be used for the average and for the conditional average taken for the ensemble of a statistically homogeneous field $X = (v_i)$ at the point $\mathbf{x}$, on the condition that there are inclusions at the points $\mathbf{x}_1$. The notation $\langle \mathbf{(f)} \rangle_i (\mathbf{x})$ of the variable $\mathbf{f}(\mathbf{x})$ (e.g., $\mathbf{f}(\mathbf{x}) = \boldsymbol{\sigma}(\mathbf{x}), \boldsymbol{\varepsilon}(\mathbf{x})$ defined in the domain at $\mathbf{x} \in v_i$) means the statistical average over an ensemble realization of surrounding inclusions at the fixed $v_i$, whereas $\langle (\cdot) \rangle_{(i)}$ indicates the volume average over an inclusion $v_i$ in a single realization and $\langle (.) \rangle_i \equiv \langle \langle (.) \rangle_{(i)} \rangle$. No confusion will arise from our use of the same notations $\langle \mathbf{(f)} \rangle_{(i)}$ and $\langle \mathbf{(f)} \rangle_i$ for the surface averages over the interfaces $\Gamma_i$ if the variable $\mathbf{f(s)}$ (e.g., $\mathbf{f(s)} = \mathbf{t(s)}$) is defined at the interface $\mathbf{s} \in \Gamma_i$. The subdomains $v_i$ $(i = 1, \ldots)$ are called floating subdomains if they do not touch the boundary $\Gamma_0$. In such a case, the body $w$ is considered as one cut out from an infinite random medium and the inclusions $v_i$ intersected with the boundary $\Gamma_0$ are replaced by the matrix material.

### *17.2.3 Green's Function and Related Tensors*

One introduces the infinite body Green's function $\mathbf{G}^{(k)}$ of the Navier equation with homogeneous elastic modulus tensor $\mathbf{L}^{(k)}$, defined by

$$\nabla \left\{ \mathbf{L}^{(k)} [\nabla \otimes \mathbf{G}^{(k)}(\mathbf{x})] \right\} = -\boldsymbol{\delta} \delta(\mathbf{x}), \tag{17.11}$$

of order $O\big( \int |\mathbf{x}|^{1-d} d|\mathbf{x}| \big)$ as $|\mathbf{x}| \to \infty$ and vanishing at infinity ($|\mathbf{x}| \to \infty$) in 3-D.

We will use the tensors of the fundamental stresses, tractions (called also Kupradze tensor), and strains

$$\mathbf{D}^{(m)}(\mathbf{x}-\mathbf{s}) = \mathbf{L}^{(m)}\nabla\mathbf{G}^{(m)}(\mathbf{x}-\mathbf{s}), \quad \mathbf{T}^{(m)}(\mathbf{x},\mathbf{s}) = -\mathbf{n}^{\Gamma}(\mathbf{x})\mathbf{D}^{(m)}(\mathbf{x}-\mathbf{s}),$$
$$\mathscr{E}^{(m)}(\mathbf{x}-\mathbf{s}) = \nabla\mathbf{G}^{(m)}(\mathbf{x}-\mathbf{s}), \tag{17.12}$$

and $\mathbf{S}^{(m)}(\mathbf{x},\mathbf{s}) = \mathbf{L}^{(m)}\nabla\mathbf{T}^{(m)\top}(\mathbf{x},\mathbf{s})$. In particular, for an isotropic medium we reproduce the compact representation of the mentioned Green functions valid for both 2-D and 3-D cases (see also, e.g., Balas et al., 1989; Torquato, 2002):

$$G_{ij}(r) = Cr\big[(3-4\bar{\nu})\gamma(|\mathbf{x}|)\delta_{ij} + n_i n_j\big], \tag{17.13}$$

$$T_{ij}(\mathbf{x},\mathbf{s}) = -2\mu C\big[\big((1-2\bar{\nu})\delta_{ij} + dn_i n_j\big)n_k n_k^{\Gamma}(\mathbf{x}) + (1-2\bar{\nu})(n_i n_j^{\Gamma}(\mathbf{x}) - n_j n_i^{\Gamma}(\mathbf{x}))\big], \tag{17.14}$$

$$D_{ijk}(r) = -2\mu C[(1-2\bar{\nu})(\delta_{ik}n_j + \delta_{jk}n_i - \delta_{ij}n_k) + dn_i n_j n_k], \tag{17.15}$$

$$\mathscr{E}_{ijk}(r) = -C[(3-4\bar{\nu})\delta_{ij}n_k - \delta_{ik}n_j - \delta_{jk}n_i + dn_i n_j n_k], \tag{17.16}$$

$$S_{ijk}(\mathbf{x},\mathbf{s}) = 4\mu^2 C/r\Big\{d\big[(1-2\bar{\nu})\delta_{ij}n_k + \bar{\nu}(\delta_{ik}n_j + \delta_{jk}n_i) - (d+2)n_i n_j n_k\big] \times n_m n_m^{\gamma}(\mathbf{x}) - (1-4\bar{\nu})\delta_{ij}n_k^{\Gamma}(\mathbf{x}) + d\bar{\nu}n_k[n_i n_j^{\Gamma}(\mathbf{x}) + n_j n_i^{\Gamma}(\mathbf{x})] + (1-2\bar{\nu})[dn_i n_j n_k^{\Gamma}(\mathbf{x}) + \delta_{ik}n_j^{\Gamma}(\mathbf{x}) + \delta_{jk}n_i^{\Gamma}(\mathbf{x})]\Big\}, \tag{17.17}$$

respectively, where

$$\gamma(r) = \begin{cases} -\ln r & \text{for } d=2, \\ r^{-1} & \text{for } d=3, \end{cases} \quad \bar{\nu} = \begin{cases} \nu, & \text{for 3-D and plane strain,} \\ \frac{\nu}{1+\nu}, & \text{for plane stress problems.} \end{cases} \tag{17.18}$$

Here, $C = [4\omega_d\mu(1-\bar{\nu})r^{d-1}]^{-1}$, $\omega_d$ is the surface area of the unit sphere in $R^d$, and the tensors $\mathbf{T}(\mathbf{x},\mathbf{s})$ and $\mathbf{S}(\mathbf{x},\mathbf{s})$ are defined at the surface $\mathbf{s}\in S$ with the unit outward normal $\mathbf{n}^{\Gamma} = (n_1^{\Gamma},\ldots,n_d^{\Gamma})^{\top}$ at $\mathbf{s}\in S$, $r \equiv |\mathbf{x}-\mathbf{s}|$, $r_{,i} = r_i/r = n_i$.

For an isolated ellipsoidal inclusion $v_i$ inside an infinite homogeneous matrix, we will also exploit the Green tensors for the strains and stresses,

$$\mathbf{U}^{(m)}(\mathbf{x}) = \nabla\nabla\mathbf{G}(\mathbf{x}), \quad \boldsymbol{\Gamma}^{(m)}(\mathbf{x}) = -\mathbf{L}^{(m)}[\mathbf{I}\delta(\mathbf{x}) + \nabla\nabla\mathbf{G}(\mathbf{x})\mathbf{L}^{(m)}], \tag{17.19}$$

respectively, related with the internal $\mathbf{S}_i$ and external $\mathbf{S}_i(\mathbf{x})$ ($\mathbf{x}\notin v_i$) (Eshelby, 1957) tensors for the inclusion $v_i$:

$$\mathbf{S}_i = \mathbf{P}_i\mathbf{L}^{(0)} \equiv \text{const.}, \quad \mathbf{S}_i(\mathbf{x}) = -\int \mathbf{U}(\mathbf{x}-\mathbf{y})V_i(\mathbf{y})d\mathbf{y}\mathbf{L}^{(0)}, \tag{17.20}$$

$$\mathbf{S}_i = \mathbf{I} - \mathbf{M}^{(0)}\mathbf{Q}_i \equiv \text{const.}, \quad \mathbf{S}_i(\mathbf{x}) = \mathbf{I} + \mathbf{M}^{(0)}\int \boldsymbol{\Gamma}(\mathbf{x}-\mathbf{y})V_i(\mathbf{y})d\mathbf{y}, \tag{17.21}$$

for $\mathbf{x}\in v_i$ and $\mathbf{x}\notin v_i$, respectively.

## 17.3 Effective Properties and Interface polarization Tensors

For statistically homogeneous media and homogeneous boundary conditions, the effective stiffness $\mathbf{L}^*$ and effective compliance $\mathbf{M}^*$ governed by the expectation of Eq. (17.2),

$$\langle \boldsymbol{\sigma} \rangle = \mathbf{L}^* \langle \boldsymbol{\varepsilon} \rangle, \quad \langle \boldsymbol{\varepsilon} \rangle = \mathbf{M}^* \langle \boldsymbol{\sigma} \rangle, \tag{17.22}$$

are defined by general relations

$$\mathbf{L}^* = \langle \mathbf{L}\mathbf{A}^* \rangle, \quad \mathbf{M}^* = \langle \mathbf{M}\mathbf{B}^* \rangle, \tag{17.23}$$

where $\mathbf{A}^*(\mathbf{x})$ and $\mathbf{B}^*(\mathbf{x})$ are the local strain and stress concentrator factors, respectively, obtained under pure mechanical loading $\boldsymbol{\varepsilon}(\mathbf{x}) = \mathbf{A}^*(\mathbf{x})\boldsymbol{\varepsilon}^{\Gamma}$ (17.7) and $\boldsymbol{\sigma}(\mathbf{x}) = \mathbf{B}^*(\mathbf{x})\boldsymbol{\sigma}^{\Gamma}$ (17.8), respectively. By the use of the decomposition of the material tensor $\mathbf{g}$ ($\mathbf{g} = \mathbf{L}, \mathbf{M}$), Eq. (17.23) can be recast in an equivalent form:

$$\mathbf{L}^* = \mathbf{L}^{(0)} + \langle \mathbf{L}_1 \mathbf{A}^* V \rangle, \quad \mathbf{M}^* = \mathbf{M}^{(0)} + \langle \mathbf{M}_1 \mathbf{B}^* V \rangle. \tag{17.24}$$

The effective properties (17.24) can also be expressed through the averaged polarization concentration factors $\mathbf{R}^{\epsilon *}(\mathbf{x})$ and $\mathbf{R}^{\sigma *}(\mathbf{x})$,

$$\mathbf{L}^* = \mathbf{L}^{(0)} + \mathbf{R}^{\epsilon *}, \quad \mathbf{R}^{\epsilon *}(\mathbf{x}) \langle \boldsymbol{\varepsilon} \rangle = \boldsymbol{\tau}(\mathbf{x}), \tag{17.25}$$

$$\mathbf{M}^* = \mathbf{M}^{(0)} + \mathbf{R}^{\sigma *}, \quad \mathbf{R}^{\sigma *}(\mathbf{x}) \langle \boldsymbol{\sigma} \rangle = \boldsymbol{\eta}(\mathbf{x}) \tag{17.26}$$

for the homogeneous boundary conditions (17.7) and (17.8), respectively.

The effective properties evaluations (17.25) and (17.26) are based on the estimations of the average polarization tensors $\boldsymbol{\tau}$ ($17.5_1$) and $\boldsymbol{\eta}$ ($17.5_2$) averaged over the inclusion volume $v$. However, the representations $\boldsymbol{\tau}$ ($17.6_1$) and $\boldsymbol{\eta}$ ($17.6_2$) allow one to use only interface averages of some transformations of these tensors. So, we introduce new notions of the stress $\boldsymbol{\tau}^s(\mathbf{s})$ and strain $\boldsymbol{\eta}^s(\mathbf{s})$ *interface polarization tensors*

$$\boldsymbol{\tau}^s(\mathbf{s}) = \mathbf{t}(\mathbf{s}) \overset{S}{\otimes} \mathbf{s} - \mathbf{L}^{(0)}[\mathbf{u}(\mathbf{s}) \otimes \mathbf{n}(\mathbf{s})], \tag{17.27}$$

$$\boldsymbol{\eta}^s(\mathbf{s}) = \mathbf{u}(\mathbf{s}) \overset{S}{\otimes} \mathbf{n}(\mathbf{s}) - \mathbf{M}^{(0)}[\mathbf{s} \otimes \mathbf{t}(\mathbf{s})], \tag{17.28}$$

defining at the inclusion interface $\mathbf{s} \in \Gamma$. The volume averages of the strains and stresses inside inclusions can be expressed through the averages over the inclusion boundaries by the use of the Gauss's theorem:

$$\langle \boldsymbol{\varepsilon} V \rangle = \frac{1}{\bar{w}} \int_{\Gamma} \mathbf{u}(\mathbf{s}) \overset{S}{\otimes} \mathbf{n}(\mathbf{s}) \, d\mathbf{s}, \tag{17.29}$$

$$\langle \boldsymbol{\sigma} V \rangle = \frac{1}{\bar{w}} \int_{\Gamma} \mathbf{t}(\mathbf{s}) \overset{S}{\otimes} \mathbf{s} \, d\mathbf{s}, \tag{17.30}$$

where in Eq. (17.30) one used the equality $\nabla(\mathbf{s} \otimes \boldsymbol{\sigma}) = \boldsymbol{\sigma}$. Then the effective properties (17.25) and (17.26) can be expressed through the boundary integrals

$$\mathbf{L}^* = \mathbf{L}^{(0)} + \mathbf{S}^{\epsilon *}, \quad \mathbf{S}^{\epsilon *}\langle \boldsymbol{\varepsilon} \rangle := \frac{1}{\bar{w}} \int_{\Gamma} \boldsymbol{\tau}^s(\mathbf{s}) d\mathbf{s}, \tag{17.31}$$

$$\mathbf{M}^* = \mathbf{M}^{(0)} + \mathbf{S}^{\sigma *}, \quad \mathbf{S}^{\sigma *}\langle \boldsymbol{\sigma} \rangle := \frac{1}{\bar{w}} \int_{\Gamma} \boldsymbol{\eta}^s(\mathbf{s}) d\mathbf{s}, \tag{17.32}$$

for the boundary conditions (17.7) and (17.8), respectively. The representation (17.31) for a particular case of the isotropic matrix is reduced to the corresponding equation proposed in Russel and Acrivos (1972) and Chen and Acrivos (1978).

A comparison of Eqs. (17.25) and (17.26) and Eqs. (17.31) and (17.32), respectively, yields a conclusion that the averages of the volume polarization tensors $\boldsymbol{\tau}(\mathbf{x})$ ($17.6_1$) and $\boldsymbol{\eta}(\mathbf{x})$ ($17.6_2$) and the averages of the interface polarization tensors $\boldsymbol{\tau}^s(\mathbf{s})$ (17.27) and $\boldsymbol{\eta}^s(\mathbf{s})$ (17.28), respectively, are coincident with each other:

$$\mathbf{R}^{\epsilon *} = \mathbf{S}^{\epsilon *}, \quad \mathbf{R}^{\sigma *} = \mathbf{S}^{\sigma *}, \tag{17.33}$$

although $\boldsymbol{\tau}(\mathbf{x})$, $\boldsymbol{\eta}(\mathbf{x})$, and $\boldsymbol{\tau}^s(\mathbf{s})$, $\boldsymbol{\eta}^s(\mathbf{s})$, respectively, cannot be compared directly because of the different domains of definition. Equalities (17.33) define a physical meaning and injectivity of the notions of the interface polarization tensors $\boldsymbol{\tau}^s(\mathbf{s})$ (17.27) and $\boldsymbol{\eta}^s(\mathbf{s})$ (17.28).

## 17.4 General Integral Equations

### *17.4.1 Perturbators for a Single Inclusion Inside a Macrodomain*

For notational convenience, in parallel with Eqs. (17.1) and (17.2), we consider the equivalent local boundary value problems

$$\nabla[\mathbf{L}^{(k)} \nabla \mathbf{u}_k(\mathbf{x})] = \mathbf{0} \tag{17.34}$$

for the connected subdomains $\mathbf{x} \in v^{(k)}$ $(k = 0, 1)$ with the natural coupling conditions (called transmission conditions) across all local coupling boundaries $\mathbf{s} \in \Gamma_{km}$:

$$\mathbf{u}_k(\mathbf{s}) = \mathbf{u}_m(\mathbf{s}), \ \mathbf{t}_k(\mathbf{s}) + \mathbf{t}_m(\mathbf{s}) = \mathbf{0} \text{ for } \mathbf{s} \in \Gamma_{km}. \tag{17.35}$$

Here, $\mathbf{u}_k$ is the restriction of $\mathbf{u}$ to $v^k$ and $\mathbf{n}_k$ is the outward normal to $v^{(k)}$ $(k, m = 0, 1)$. According to the essence of the boundary decomposition method reducing

the solution of the original boundary value problem (17.2) to the solutions of local boundary problems (17.34) and (17.35), we can use the different discretization techniques for the solution of Eqs. (17.34) and (17.35) (see for details Toselli and Widlund, 2005; Hsiao et al., 2002). The boundary decomposition method assumes that each heterogeneity $v_k$ can be considered as embedded into the infinite homogeneous matrix and subjected to the effective fields (formally considered as the remote fields) $\overline{\mathbf{u}}(\mathbf{x})$ and $\overline{\boldsymbol{\sigma}}(\mathbf{x})$ ($\mathbf{x} \in v_k$) produced by all surrounding heterogeneities $X \setminus v_k$ and boundary conditions (no restrictions are imposed on the inhomogeneity of these random effective fields).

Let us assume that the domain $w$ contains one heterogeneity $v_k \subset w$. We define the *perturbators* $\mathscr{L}_k^{\theta}(\mathbf{x}-\mathbf{x}_k, \boldsymbol{\zeta})$ and $\mathscr{L}_k^{\chi}(\mathbf{x}-\mathbf{x}_k, \boldsymbol{\chi})$ as the perturbations of the corresponding fields introduced by the heterogeneity $v_k$ subjected to the effective fields $\overline{\boldsymbol{\vartheta}}(\mathbf{x})$ and $\overline{\boldsymbol{\chi}}(\mathbf{x})$, respectively:

$$\mathscr{L}_k^{\theta}(\mathbf{x}-\mathbf{x}_k, \boldsymbol{\zeta}) = \mathscr{L}_k^{\theta}(\mathbf{x}-\mathbf{x}_k, \overline{\boldsymbol{\vartheta}}) \equiv \boldsymbol{\vartheta}(\mathbf{x}) - \overline{\boldsymbol{\vartheta}}(\mathbf{x}), \tag{17.36}$$

$$\mathscr{L}_k^{\chi}(\mathbf{x}-\mathbf{x}_k, \boldsymbol{\chi}) = \mathscr{L}_k^{\chi}(\mathbf{x}-\mathbf{x}_k, \overline{\boldsymbol{\chi}}) \equiv \boldsymbol{\chi}(\mathbf{x}) - \overline{\boldsymbol{\chi}}(\mathbf{x}). \tag{17.37}$$

Hereafter, for the contraction of calculations, we introduce the substitutions

$$(\boldsymbol{\varepsilon}, \boldsymbol{\sigma}) \leftrightarrow \boldsymbol{\vartheta}, \quad (\boldsymbol{\tau}, \boldsymbol{\eta}) \leftrightarrow \boldsymbol{\zeta}, \tag{17.38}$$

indicating that for each duplet $\boldsymbol{\vartheta} = \boldsymbol{\varepsilon}, \boldsymbol{\zeta} = \boldsymbol{\tau}$ and $\boldsymbol{\vartheta} = \boldsymbol{\sigma}, \boldsymbol{\zeta} = \boldsymbol{\eta}$, Eq. (17.36) and the subsequent equations with the variables $\boldsymbol{\vartheta}$ and $\boldsymbol{\zeta}$ are reduced to the corresponding equations for the strain field $\boldsymbol{\varepsilon}$ and stress $\boldsymbol{\sigma}$. In a similar manner, one introduces a duplet

$$(\mathbf{u}, \mathbf{t}) \leftrightarrow \boldsymbol{\chi}, \tag{17.39}$$

which is used in Eq. (17.37) for both variables $\mathbf{u}$ and $\mathbf{t}$ simultaneously. In so doing, the perturbators $\mathscr{L}_k^{\theta}(\mathbf{x}-\mathbf{x}_k, \boldsymbol{\zeta})$ and $\mathscr{L}_k^{\chi}(\mathbf{x}-\mathbf{x}_k, \boldsymbol{\chi})$ are defined by the volume $\boldsymbol{\zeta}(\mathbf{x})$ ($\mathbf{x} \in v_i$) and boundary $\boldsymbol{\chi}(\mathbf{s})$ ($\mathbf{s} \in \Gamma_i$) values of the corresponding fields. Strictly speaking, the perturbators $\mathscr{L}_k^{\theta}(\mathbf{x}-\mathbf{x}_k, \boldsymbol{\zeta})$ ($17.36_1$) and $\mathscr{L}_k^{\chi}(\mathbf{x}-\mathbf{x}_k, \boldsymbol{\chi})$ ($17.37_1$) are just the notations of some problem which is destined to be solved, while the perturbators $\mathscr{L}_k^{\theta}(\mathbf{x}-\mathbf{x}_k, \overline{\boldsymbol{\vartheta}})$ ($17.36_2$) and $\mathscr{L}_k^{\chi}(\mathbf{x}-\mathbf{x}_k, \overline{\boldsymbol{\chi}})$ ($17.37_2$) are the solutions of this problem.

Let us consider the well-known integral representation formulae of the strains and the stresses ($\mathbf{x} \in R^d$, $\mathbf{y} \in v_k$):

$$\begin{aligned} \boldsymbol{\varepsilon}(\mathbf{x}) &= \overline{\boldsymbol{\varepsilon}}(\mathbf{x}) + \int \mathbf{U}(\mathbf{x}-\mathbf{y})\boldsymbol{\tau}(\mathbf{y})d\mathbf{y}, \\ \boldsymbol{\sigma}(\mathbf{x}) &= \overline{\boldsymbol{\sigma}}(\mathbf{x}) + \int \boldsymbol{\Gamma}(\mathbf{x}-\mathbf{y})\boldsymbol{\eta}(\mathbf{y})d\mathbf{y}, \end{aligned} \tag{17.40}$$

where the Green's functions $\mathbf{U}(\mathbf{x}-\mathbf{y})$ and $\boldsymbol{\Gamma}(\mathbf{x}-\mathbf{y})$ are defined by Eq. (17.20). In such a case, the perturbators $\mathscr{L}^{\epsilon}(\mathbf{x}-\mathbf{x}_k, \boldsymbol{\tau})$ and $\mathscr{L}^{\sigma}(\mathbf{x}-\mathbf{x}_k, \boldsymbol{\eta})$ can be expressed through the Green's functions:

$$\mathscr{L}^{\epsilon}(\mathbf{x}-\mathbf{x}_k,\boldsymbol{\tau}) = \int \mathbf{U}(\mathbf{x}-\mathbf{y})\boldsymbol{\tau}(\mathbf{y})d\mathbf{y},$$

$$\mathscr{L}^{\sigma}(\mathbf{x}-\mathbf{x}_k,\boldsymbol{\eta}) = \int \boldsymbol{\Gamma}(\mathbf{x}-\mathbf{y})\boldsymbol{\eta}(\mathbf{y})d\mathbf{y}. \tag{17.41}$$

The displacement and stress fields for the elastostatic problem inside and outside the heterogeneity $v_k \in v^{(1)}$ subjected to the remote fields $\overline{\mathbf{u}}(\mathbf{x})$, $\overline{\boldsymbol{\sigma}}(\mathbf{x})$ (see, e.g., Parton and Perlin 1982; Balas et al. 1989) can also be expressed through the boundary integrals [rather than the volume ones as in Eq. (17.40)]:

$$\mathbf{k}(\mathbf{x})\mathbf{u}(\mathbf{x}) = e\overline{\mathbf{u}}(\mathbf{x}) + \int_{\Gamma_k}\Big[\mathbf{G}^{(m)}(\mathbf{x}-\mathbf{s})\mathbf{t}(\mathbf{s}) - \mathbf{T}^{(m)\top}(\mathbf{x},\mathbf{s})\mathbf{u}(\mathbf{s})\Big]d\mathbf{s}, \tag{17.42}$$

$$\mathbf{k}(\mathbf{x})\boldsymbol{\sigma}(\mathbf{x}) = e\overline{\boldsymbol{\sigma}}(\mathbf{x}) + \int_{\Gamma_k}\Big[\mathbf{D}^{(m)}(\mathbf{x}-\mathbf{s})\mathbf{t}(\mathbf{s}) - \mathbf{S}^{(m)}(\mathbf{x},\mathbf{s})\mathbf{u}(\mathbf{s})\Big]d\mathbf{s}, \tag{17.43}$$

for the external ($e = 1$, $\mathbf{x} \in \Gamma_k^- = \Gamma_{0k}$, $m = 0$) and internal ($e = 0$, $\mathbf{x} \in \Gamma_k^+ = \Gamma_{k0}$, $m = 1$) problems, respectively. Equation (17.43) for the stress components was obtained by differentiating the integral representations of displacements (17.42) and substituting them into Hooke's law (17.2) that leads to the representations (17.12). Hereafter, the superscripts $^-$ and $^+$ denote the limiting values of parameters involved in the outside and inside of the inclusion $v_i$, respectively, near the inclusion boundary $\mathbf{x} \in \Gamma_k$; $\mathbf{k}(\mathbf{x}) = (1 - e(\mathbf{x}))\boldsymbol{\delta}$ for $\mathbf{x} \in R^d \setminus \Gamma_k$ and $\mathbf{k}(\mathbf{x}) = \boldsymbol{\delta}/2$ for $\mathbf{x}$ belonging to the smooth boundary $\Gamma_k$ at point $\mathbf{x} \in \Gamma_k$. Here the traction $\mathbf{t}(\mathbf{s})$ acting on any plane with the outward normal vector $\mathbf{n}(\mathbf{s})$ on $\Gamma_i$ from $v_i$ through the point $\mathbf{s} \in \Gamma_i$ can be represented in terms of displacements $\mathbf{t}(\mathbf{s}) = \hat{\mathbf{t}}(\mathbf{n},\nabla)\mathbf{u}(\mathbf{s})$, where $\hat{t}_{ik}(\mathbf{n},\nabla) = L^{(k)}_{ijkl}n_j(\mathbf{x})\partial/\partial x_l$ is the conormal derivative operator.

The interface perturbators $\mathscr{L}^{\chi}(\mathbf{x}-\mathbf{x}_k,\boldsymbol{\chi})$ can be found from Eq. (17.43) in a similar manner as the volume perturbators $\mathscr{L}^{\theta}(\mathbf{x}-\mathbf{x}_k,\boldsymbol{\zeta})$ were found from Eq. (17.40). Namely, we introduce the single- and double-layer operators $\mathscr{G}$, $\mathscr{T}$, $\mathscr{D}$, and $\mathscr{S}$ with the kernels $\mathbf{G}(\mathbf{x}-\mathbf{s})$, $\mathbf{T}^{\top}(\mathbf{x},\mathbf{s})$, $\mathbf{D}(\mathbf{x}-\mathbf{s})$, and $\mathbf{S}(\mathbf{x},\mathbf{s})$, respectively ($\mathbf{x} \in R^d$):

$$(\mathscr{G}\mathbf{t})(\mathbf{x}) = \int_{\Gamma_k}\mathbf{G}(\mathbf{x},\mathbf{s})\mathbf{t}(\mathbf{s})d\mathbf{s}, \quad (\mathscr{T}\mathbf{u})(\mathbf{x}) = \int_{\Gamma_k}\mathbf{T}^{\top}(\mathbf{x},\mathbf{s})\mathbf{u}(\mathbf{s})d\mathbf{s}, \tag{17.44}$$

$$(\mathscr{D}\mathbf{t})(\mathbf{x}) = \int_{\Gamma_k}\mathbf{D}(\mathbf{x},\mathbf{s})\mathbf{t}(\mathbf{s})d\mathbf{s}, \quad (\mathscr{S}\mathbf{u})(\mathbf{x}) = \int_{\Gamma_k}\mathbf{S}^{\top}(\mathbf{x},\mathbf{s})\mathbf{u}(\mathbf{s})d\mathbf{s}. \tag{17.45}$$

Then Eqs. (17.44) and (17.45) can be presented in the matrix operator form

$$\begin{pmatrix}\mathbf{ku}\\ \mathbf{k}\boldsymbol{\sigma}\end{pmatrix} - \begin{pmatrix}e\overline{\mathbf{u}}\\ e\overline{\boldsymbol{\sigma}}\end{pmatrix} = \begin{pmatrix}-\mathscr{T}^{(m)} & \mathscr{G}^{(m)}\\ -\mathscr{S}^{(m)} & \mathscr{D}^{(m)}\end{pmatrix}\begin{pmatrix}\mathbf{u}\\ \mathbf{t}\end{pmatrix} \tag{17.46}$$

that leads to the obvious matric representation for the perturbator $\mathscr{L}_i^{\chi}(\mathbf{x}-\mathbf{x}_i,\boldsymbol{\chi})$ found from the solution of the conventional BIE (17.42) presented for both the

matrix and inclusion in the matrix forms by the substitution method (see, e.g., Dong et al. 2003; Yao et al. 2004; Wang and Yao 2005). Construction of the perturbator $\mathscr{L}_i^{\chi}(\mathbf{x}-\mathbf{x}_i,\boldsymbol{\chi})$ by the MFS will be performed in Sect. 17.5.

Analytical representations for the operators $\mathscr{L}_k^{\theta}(\mathbf{x}-\mathbf{x}_k,\overline{\boldsymbol{\vartheta}})$ and $\mathscr{L}_k^{\chi}(\mathbf{x}-\mathbf{x}_k,\overline{\boldsymbol{\chi}})$ are only known for the particular canonical shapes of particle and specific effective fields (see, e.g., Pozrikidis 2011; Parnell 2016). So, for a homogeneous effective field ($\mathbf{x}\in v_i$)

$$\overline{\boldsymbol{\vartheta}}(\mathbf{x})\equiv \text{const.} \tag{17.47}$$

and the ellipsoidal homogeneous inclusion $v_k$, the operators $\mathscr{L}_k^{\theta}(\mathbf{x}-\mathbf{x}_k,\boldsymbol{\zeta})$ and $\mathscr{L}_k^{\theta}(\mathbf{x}-\mathbf{x}_k,\overline{\boldsymbol{\vartheta}})$ are reduced to the tensorial multiplication:

$$\mathscr{L}_k^{\theta}(\mathbf{x}-\mathbf{x}_k,\boldsymbol{\zeta})=\mathscr{L}_k^{\zeta}(\mathbf{x}-\mathbf{x}_k)\langle\boldsymbol{\zeta}\rangle_i,\quad \mathscr{L}_k^{\theta}(\mathbf{x}-\mathbf{x}_k,\overline{\boldsymbol{\vartheta}})=\mathscr{L}_k^{\theta}(\mathbf{x}-\mathbf{x}_k)\overline{\boldsymbol{\vartheta}} \tag{17.48}$$

In particular, for $\boldsymbol{\vartheta}=\boldsymbol{\sigma}$, $\boldsymbol{\zeta}=\boldsymbol{\eta}$ (the case $\boldsymbol{\vartheta}=\boldsymbol{\varepsilon}$, $\boldsymbol{\zeta}=\boldsymbol{\tau}$ can be considered in a similar manner):

$$\mathscr{L}_k^{\zeta}(\mathbf{x}-\mathbf{x}_k)=\mathbf{T}_k^{\sigma}(\mathbf{x}-\mathbf{x}_k)\equiv-(\overline{v}_i)^{-1}\begin{cases}\mathbf{Q}_i & \text{for } \mathbf{x}\in v_i,\\ \mathbf{Q}_i(\mathbf{x}) & \text{for } \mathbf{x}\notin v_i,\end{cases} \tag{17.49}$$

$$\mathscr{L}_k^{\theta}(\mathbf{x}-\mathbf{x}_k)=\mathbf{T}_k^{\sigma}(\mathbf{x}-\mathbf{x}_k)\mathbf{R}_i^{\sigma}, \tag{17.50}$$

where $\mathbf{R}_i^{\sigma}=\bar{v}_i\mathbf{M}_1^{(i)}(\mathbf{I}+\mathbf{Q}_i\mathbf{M}_1^{(i)})^{-1}$ and $\mathbf{Q}_i=\mathbf{L}^{(0)}(\mathbf{I}-\mathbf{S}_i)$ and $\mathbf{Q}_i(\mathbf{x})=\mathbf{L}^{(0)}(\mathbf{I}-\mathbf{S}_i(\mathbf{x}))$ are expressed in terms of both the internal $\mathbf{S}_i$ and external $\mathbf{S}_i(\mathbf{x})$ ($\mathbf{x}\notin v_i$) (Eshelby, 1957) tensors (17.21) (see also for references and details Buryachenko 2007).

For the inhomogeneous loading $\overline{\boldsymbol{\vartheta}}(\mathbf{x})\not\equiv$const. and noncanonical shape (or inhomogeneous structure) of the inclusion, the operator concentration factors for the values $\boldsymbol{\sigma}(\mathbf{x})$ and $\boldsymbol{\eta}(\mathbf{x})$ ($\mathbf{x}\in v_k$) can be expressed through the perturbator $\mathscr{L}^{\theta}(\mathbf{x}-\mathbf{x}_k,\overline{\boldsymbol{\vartheta}})$ ($\boldsymbol{\vartheta}=\boldsymbol{\sigma}$, $\boldsymbol{\zeta}=\boldsymbol{\eta}$):

$$\boldsymbol{\sigma}(\mathbf{x})=\mathscr{B}_k^{\sigma}(\overline{\boldsymbol{\sigma}})(\mathbf{x}),\quad \bar{v}_k\boldsymbol{\eta}(\mathbf{x})=\mathscr{R}_k^{\sigma}(\overline{\boldsymbol{\sigma}})(\mathbf{x}), \tag{17.51}$$

where

$$\mathscr{B}_k^{\sigma}(\overline{\boldsymbol{\sigma}})(\mathbf{x})=\mathscr{L}^{\theta}(\mathbf{x}-\mathbf{x}_k,\overline{\boldsymbol{\vartheta}})+\mathbf{I}\overline{\boldsymbol{\sigma}}(\mathbf{x}),\quad \mathscr{R}_k^{\sigma}(\overline{\boldsymbol{\sigma}})(\mathbf{x})=\bar{v}_k\mathbf{M}_1^{(k)}\mathscr{B}_k^{\sigma}(\overline{\boldsymbol{\sigma}})(\mathbf{x}). \tag{17.52}$$

For the homogeneous effective field $\overline{\boldsymbol{\vartheta}}(\mathbf{x})\equiv$const. (17.47) and a general case of the inclusion, in view of the linearity of the problem, there exist constant fourth- and second-rank tensors $\mathbf{B}_i(\mathbf{x})$, $\mathbf{R}_i(\mathbf{x})$, such that ($\mathbf{x}\in R^d$)

$$\boldsymbol{\sigma}(\mathbf{x})=\mathbf{B}_i(\mathbf{x})\overline{\boldsymbol{\sigma}}(\mathbf{x}_i),\quad \mathbf{L}_i^{\sigma}(\mathbf{x}-\mathbf{x}_i)=\mathbf{B}_i(\mathbf{x})-\mathbf{I},\quad \bar{v}_i\boldsymbol{\eta}(\mathbf{x})=\mathbf{R}_i(\mathbf{x})\overline{\boldsymbol{\sigma}}(\mathbf{x}_i), \tag{17.53}$$

where $v_i \subset v^{(1)}$ and $\mathbf{R}_i(\mathbf{x}) = \bar{v}_i \mathbf{M}_1^{(1)}(\mathbf{x})\mathbf{B}_i(\mathbf{x})$. According to Eshelby's (1957) theorem for the ellipsoidal inclusion $v_i$, there is the following relation between the averaged tensors (17.53) $\mathbf{R}_i = \overline{v}_i \mathbf{Q}_i^{-1}(\mathbf{I} - \mathbf{B}_i)$, where $\mathbf{g}_i \equiv \langle \mathbf{g}(\mathbf{x}) \rangle_{(i)}$ ($\mathbf{g}$ stands for $\mathbf{B}_i, \mathbf{R}_i$). For example, for the homogeneous ellipsoidal domain $v_i$ (17.4) we obtain ($\mathbf{x} \in v_i$)

$$\mathbf{B}_i(\mathbf{x}) \equiv \mathbf{B}_i = \left(\mathbf{I} + \mathbf{Q}_i \mathbf{M}_1^{(i)}\right)^{-1}, \quad \mathbf{R}_i = \bar{v}_i \mathbf{M}_1^{(i)}(\mathbf{I} + \mathbf{Q}_i \mathbf{M}_1^{(i)})^{-1}. \tag{17.54}$$

In the general case of coated inclusions $v_i$, the tensors $\mathbf{B}_i(\mathbf{x})$ can be found by the transformation method by Dvorak and Benveniste (1992) (see for references and details Buryachenko 2007).

The concentration operators for the interface variables $\boldsymbol{\chi}(\mathbf{s})$ and $\boldsymbol{\eta}^s(\mathbf{s})$ can be expressed in a similar manner:

$$\boldsymbol{\chi}(\mathbf{s}) = \mathscr{B}_k^{\chi}(\overline{\boldsymbol{\chi}})(\mathbf{s}), \quad \bar{v}_k \boldsymbol{\eta}^s(\mathbf{s}) = \mathscr{R}_k^{\chi}(\overline{\boldsymbol{\chi}})(\mathbf{s}), \tag{17.55}$$

where $\mathscr{B}_k^{\chi}(\overline{\boldsymbol{\chi}})(\mathbf{s}) = \mathscr{L}^{\chi}(\mathbf{x} - \mathbf{x}_k, \overline{\boldsymbol{\chi}}) + \mathbf{I}\overline{\boldsymbol{\chi}}(\mathbf{s})$. It should be mentioned that even for the homogeneous volume effective fields (17.47), the interface effective fields $\overline{\boldsymbol{\chi}}(\mathbf{s})$ ($\mathbf{s} \in v_k$) are inhomogeneous ones, for example, for the boundary condition $\overline{\boldsymbol{\sigma}} \equiv \boldsymbol{\sigma}^{\Gamma}$ (17.8)

$$\overline{\boldsymbol{\chi}}(\mathbf{s}) = (\mathbf{M}^{(0)}\boldsymbol{\sigma}^{\Gamma}(\mathbf{s} - \mathbf{x}_k), \boldsymbol{\sigma}^{\Gamma}\mathbf{n}^{\Gamma_k}(\mathbf{s}))^{\top}, \tag{17.56}$$

and, therefore, the operators in the right-hand sides of Eq. (17.55) are not reduced to the tensorial convolution with the interface effective field $\overline{\boldsymbol{\chi}}(\mathbf{s})$ as in their counterpart (17.48) for the volume effective field $\overline{\boldsymbol{\sigma}}$. However, homogeneity of the volume field $\overline{\boldsymbol{\sigma}}$ in Eq. (17.56) allows one to get another version of splitting the operator $\mathscr{L}^{\chi}(\mathbf{x} - \mathbf{x}_k, \overline{\boldsymbol{\chi}})$:

$$\mathscr{L}^{\chi}(\mathbf{x} - \mathbf{x}_k, \overline{\boldsymbol{\chi}}) = \mathbf{L}^{\chi\sigma}(\mathbf{x} - \mathbf{x}_k)\overline{\boldsymbol{\sigma}} \tag{17.57}$$

with a similar splitting of the operators $\mathscr{B}_k^{\chi}(\overline{\boldsymbol{\chi}})(\mathbf{s})$ and $\mathscr{R}_k^{\chi}(\overline{\boldsymbol{\chi}})(\mathbf{s})$ (17.55).

The estimation of the perturbators $\mathscr{L}_k^{\theta}(\mathbf{x} - \mathbf{x}_k, \overline{\boldsymbol{\vartheta}})$ (17.36) and $\mathscr{L}_k^{\chi}(\mathbf{x} - \mathbf{x}_k, \overline{\boldsymbol{\chi}})$ (17.37) can be done by any available numerical method, such as the volume integral equation (VIE), boundary integral equation method (BIEM), FEM, hybrid FEM-BIEM, multipole expansion method, complex potential method, and others (see for references Buryachenko 2007; Ghosh 2011; Liu et al. 2011; Kushch 2013; Sejnoha and Zeman 2013). Each method has advantages and disadvantages and it is crucial for the analyst to be aware of their range of applications. In particular, the VIE method for the ideal contact conditions enables one to restrict discretization to the inclusions only (in contrast to the FEA), and an inhomogeneous structure of inclusions (see, e.g., Chen et al. 1990; Jayaraman and Reifsnider 1992; You et al. 2006) presents no problem in the framework of the same numerical scheme (compared to the standard BIE methods). The VIE method (see Buryachenko

2010b) has well-developed routines for the solution of integral equations (such as the iteration method and the quadrature schemes) and allows one to analyze arbitrary inhomogeneous fields $\boldsymbol{\varepsilon}^0(\mathbf{x})$ and $\boldsymbol{\sigma}^0(\mathbf{x})$. However, the VIE method is quite time-consuming and no optimized commercial software exists for its application. From other side, the FEM is supported by well-developed commercial software (see, e.g., ABAQUS 2001) and gives strong advantages in terms of CPU-time. The FEA is especially effective for estimations of perturbators at the constant fields $\boldsymbol{\varepsilon}^0, \boldsymbol{\sigma}^0 =$const (see for references, e.g., Buryachenko 2014). In the current paper, one will express the perturbators $\mathscr{L}_k^{\theta}(\mathbf{x}-\mathbf{x}_k, \boldsymbol{\zeta})$ (17.36) and $\mathscr{L}_k^{\chi}(\mathbf{x}-\mathbf{x}_k, \boldsymbol{\chi})$ (17.37) by the use of MFS (Sect. 17.6), which have the advantages described in the Introduction.

### 17.4.2 General Integral Equation for a Microinhomogeneous Infinite Medium

Let us consider an arbitrary random realization $\alpha$ of inclusions in the domain $w$ described by an analog of Eq. (17.36) generalized to any number of inhomogeneities. Then the centering method (see for details Buryachenko 2014) subtracting from both sides of the mentioned equation their statistical averages leads to the *general integral equation* (GIE) ($\mathbf{x} \in v_i$)

$$\boldsymbol{\vartheta}(\mathbf{x}, \alpha) = \langle \boldsymbol{\vartheta} \rangle(\mathbf{x}) + \int_w [\mathscr{L}_k^{\theta}(\mathbf{x}-\mathbf{x}_k, \boldsymbol{\zeta}) V_k^{\delta}(\mathbf{x}_k, \alpha) - \langle \mathscr{L}_k^{\theta}(\mathbf{x}-\mathbf{x}_k, \boldsymbol{\zeta}) \rangle(\mathbf{x}_k)] d\mathbf{x}_k. \quad (17.58)$$

Equation (17.58) is only obtained at the internal points $\mathbf{x} \in w$ of the macrodomain $w$ at a sufficient distance from the boundary:

$$a \ll |\mathbf{x} - \mathbf{s}|, \ \forall \mathbf{s} \in \Gamma_0. \quad (17.59)$$

For no *long-range* order assumed, the function $\varphi(v_j, \mathbf{x}_j|; v_i, \mathbf{x}_i) - \varphi(v_j, \mathbf{x}_j)$ decays at infinity sufficiently rapidly and guarantees an absolute convergence of the integral involved. Therefore, for $\mathbf{x} \in w$ far enough from the boundary $\Gamma_0$ (17.59), the right-hand side integral in (17.58) does not depend on the shape and size of the domain $w$, and it can be replaced by the integrals over the whole space $R^d$; the domain integration $R^d$, as well as the label $\alpha$, will be omitted hereafter for simplicity of notations.

In a similar manner, the GIE expressed through the perturbator $\mathscr{L}_k^{\chi}(\mathbf{x} - \mathbf{x}_k, \boldsymbol{\chi})$ can be obtained. Indeed, the tensors $\overline{\mathbf{u}}(\mathbf{x})$ (17.37) and $\boldsymbol{\sigma}(\mathbf{x})$ can be defined by the boundary integral equations (BIE, see, e.g., Brebbia et al. 1984; Balas et al. 1989) on the boundary $\Gamma_0$ of the domain $w$:

$$\begin{pmatrix} \overline{\mathbf{u}} \\ \overline{\boldsymbol{\sigma}} \end{pmatrix} = \begin{pmatrix} -\mathscr{T}^{(m)} & \mathscr{G}^{(m)} \\ -\mathscr{S}^{(m)} & \mathscr{D}^{(m)} \end{pmatrix} \begin{pmatrix} \mathbf{u}^{\Gamma_0} \\ \mathbf{t}^{\Gamma_0} \end{pmatrix} \quad (17.60)$$

The representation (17.60) is valid for both the Dirichlet or the Neumann boundary value problems as well as for mixed boundary-value problems. For simplicity, we will consider only internal points $\mathbf{x} \in w$ of the macrodomain $w$ at a sufficient distance from the boundary (17.59). The Cauchy data $[\mathbf{u}^{\Gamma_0}(\mathbf{s}), \mathbf{t}^{\Gamma_0}(\mathbf{s})]$ at the smooth surface $\mathbf{s} \in \Gamma_0$ can be found, for example, from the conventional BIE taking the limit $\mathbf{x} \to \Gamma_0$,

$$\mathbf{k}(\mathbf{s})\mathbf{u}_0(\mathbf{s}) = \int_{\Gamma_0} \Big[\mathbf{G}(\mathbf{s}-\boldsymbol{\zeta})\mathbf{t}^{\Gamma_0}(\boldsymbol{\zeta}) - \mathbf{T}^{\top}(\mathbf{s},\boldsymbol{\zeta})\mathbf{u}^{\Gamma_0}(\boldsymbol{\zeta})\Big]d\boldsymbol{\zeta} + \mathscr{L}_k^u(\mathbf{s}-\mathbf{x}_k,\boldsymbol{\tau}), \quad (17.61)$$

at the boundary conditions (17.7) and (17.8); here, $\mathbf{k}(\mathbf{x})$ is the free term coefficient (see, e.g., Cruse 1974) and $\mathscr{L}_k^u(\mathbf{s}-\mathbf{x}_k,\boldsymbol{\tau})$ is defined by Eq. (17.36) at $\boldsymbol{\vartheta} = \mathbf{u}$.

Let us consider an arbitrary random realization $\alpha$ of inclusions in the domain $w$:

$$\boldsymbol{\chi}(\mathbf{s},\alpha) = \boldsymbol{\chi}_0(\mathbf{s},\alpha) + \int \mathscr{L}_k^{\chi}(\mathbf{s}-\mathbf{x}_k,\boldsymbol{\chi})V_k^{\delta}(\mathbf{x}_k,\alpha)d\mathbf{x}_k, \quad (17.62)$$

where $\boldsymbol{\chi}_0(\mathbf{s})$ is defined analogously to Eq. (17.60) with the replacement $(\overline{\mathbf{u}},\overline{\boldsymbol{\sigma}})^{\top} \to \boldsymbol{\chi}_0(\mathbf{s})$ where the Cauchy data $(\mathbf{u}^{\Gamma_0}(\mathbf{s},\alpha), \mathbf{t}^{\Gamma_0}(\mathbf{s},\alpha))$ at $\mathbf{s} \in \Gamma_0$ depend on the total impacts of all perturbators $\mathscr{L}_k^u(\mathbf{s}-\mathbf{x}_k,\alpha)$ [analogously to Eq. (17.61)] presented in the form of the volume integrals similar to (17.41). For the sake of simplicity, Eq. (17.62) was obtained for a particular case of floating heterogeneities with $\boldsymbol{\tau}(\mathbf{s},\alpha), \boldsymbol{\eta}(\mathbf{s},\alpha) \equiv \mathbf{0}$ $(\mathbf{s} \in \Gamma_0)$; a general case of inclusion location $\varphi(v_i,\mathbf{x}_i)$ can be analyzed analogously to Buryachenko (2014).

Now, we apply the centering method initially proposed in a particular form by Shermergor (1977) for statistically homogeneous media subjected to homogeneous boundary conditions. However, the centering method allows for generalization to the statistically inhomogeneous cases describing by Eq. (17.62) by subtracting from both sides of Eq. (17.62) their statistical averages that lead to

$$\boldsymbol{\chi}(\mathbf{s},\alpha) = \langle\boldsymbol{\chi}\rangle(\mathbf{s},\alpha) + \int [\mathscr{L}_k^{\chi}(\mathbf{s}-\mathbf{x}_k,\boldsymbol{\chi})V_k^{\delta}(\mathbf{x}_k,\alpha) - \langle\mathscr{L}_k^{\chi}(\mathbf{s}-\mathbf{x}_k,\boldsymbol{\chi})]d\mathbf{x}_k + \mathscr{L}^{\Gamma_0}. \quad (17.63)$$

On the right-hand side of Eq. (17.63), assuming traction boundary conditions ($\Gamma_0 \equiv \Gamma_t$) (17.10), the integrals $\mathscr{L}^{\Gamma_0} := (\mathscr{L}_u^{\Gamma_0}, \mathscr{L}_t^{\Gamma_0})^{\top}$ over the external surface $\Gamma_0$,

$$\mathscr{L}_u^{\Gamma_0} = -\int_{\Gamma_0} \Big[\mathbf{T}^{\top}(\mathbf{x}-\mathbf{s})\mathbf{u}^{\Gamma_0}(\mathbf{s},\alpha) - \langle\mathbf{T}^{\top}(\mathbf{x}-\mathbf{s})\mathbf{u}^{\Gamma_0}\rangle(\mathbf{s})\Big]d\mathbf{s}, \quad (17.64)$$

$$\mathscr{L}_t^{\Gamma_0} = -\int_{\Gamma_0} \Big[\mathbf{n}\mathbf{S}^{\top}(\mathbf{x}-\mathbf{s})\mathbf{u}^{\Gamma_0}(\mathbf{s},\alpha) - \langle\mathbf{n}\mathbf{S}^{\top}(\mathbf{x}-\mathbf{s})\mathbf{u}^{\Gamma_0}\rangle(\mathbf{s})\Big]d\mathbf{s}, \quad (17.65)$$

vanish at the sufficient distance $\mathbf{x}$ (assumed hereafter) from the boundary $\Gamma_0$ (17.59), when the validity of separation of length scale Eq. (17.12) holds. The boundary integral in Eqs. (17.64) and (17.65) can be different from zero in a "boundary layer" region close to the surface $\mathbf{s} \in \Gamma_0$ where boundary data $[\mathbf{u}^{\Gamma_0}(\mathbf{s}), \mathbf{t}^{\Gamma_0}(\mathbf{s})]$ not prescribed by the boundary conditions depend on perturbations introduced by all inhomogeneities, and, therefore, $\mathbf{u}^{\Gamma_0}(\mathbf{x}) = \mathbf{u}^{\Gamma_0}(\mathbf{x},\alpha)$, $\mathbf{t}^{\Gamma_0}(\mathbf{x}) = \mathbf{t}^{\Gamma_0}(\mathbf{x},\alpha)$.

Let us consider the first integral in Eq. (17.64) (the integral (17.65) can be estimated in a similar manner). If $|\mathbf{x}-\mathbf{s}|$, $\mathbf{s}\in\Gamma_0$, is large enough, then at the portion of the smooth surface $d\mathbf{s}\approx|\mathbf{x}-\mathbf{s}|^{d-1}d\boldsymbol{\omega}^s$ with a small solid angle $d\boldsymbol{\omega}^s$, the tensor $\mathbf{T}^\top(\mathbf{x}-\mathbf{s})|\mathbf{x}-\mathbf{s}|^{d-1}$ depends only on the solid angle $\boldsymbol{\omega}^s$ variables and slowly varies on the portion of the surface $d\mathbf{s}$; in this sense, the tensor $\mathbf{T}^\top(\mathbf{x}-\mathbf{s})$ is called a "slow" variable of the solid angle $\boldsymbol{\omega}^s$ while $\mathbf{u}^{\Gamma_0}(\mathbf{s},\alpha)$ in Eq. (17.64) is a rapidly oscillating function on $d\mathbf{s}$ and is called a "fast" variable. Therefore, we can use a rigorous theory of "separate" integration of "slow" and "fast" variables, according to which (freely speaking) the operation of surface integration may be regarded as averaging [see for details, e.g., Filatov and Sharov (1979) and its applications Shermergor (1977)]. As a consequence of established separation of "slow" and "fast" variables, no confusion arises in interpreting of estimations of averaged items $\langle(.)\rangle(\mathbf{S})$ depending on macrocoordinate $\mathbf{S}\in\Gamma_0$, while the corresponding unaveraged items depend on microcoordinates $\mathbf{s}\in\Gamma_0$. Indeed, the slow variable $\mathbf{T}^\top(\mathbf{x}-\mathbf{s})$ can be consistent (after the first separation of the fast and slow variables) with the macrocoordinate $\mathbf{S}\in\Gamma_0$ as $\mathbf{T}^\top(\mathbf{x}-\mathbf{S})$, while the fast variable $\mathbf{u}^{\Gamma_0}(\mathbf{s},\alpha)$ is in agreement with the microcoordinate $\mathbf{s}\in\Gamma_0$ that makes it possible to present the integrand in the first integral (17.64) in the formal form $\mathbf{T}^\top(\mathbf{x}-\mathbf{S})\Big[\mathbf{u}^{\Gamma_0}(\mathbf{s},\alpha)-\langle\mathbf{u}^{\Gamma_0}\rangle(\mathbf{S})\Big]$, leading (after additional separation of the fast and slow variables) to the vanishing of an integral from the term in the square brackets for a statistically large number of random events $\alpha$. If there is no *long-range* order and the function $\varphi(v_j,\mathbf{x}_j|;v_i,\mathbf{x}_i)-\varphi(v_j,\mathbf{x}_j)$ decays at infinity (as $|\mathbf{x}_i-\mathbf{x}_j|\to\infty$) sufficiently rapidly,[2] then the first surface integral (17.64) becomes zero. The vanishing of other integral in the representation (17.65) can be proven in a similar manner.

The volume integral in (17.63) converge absolutely for both the statistically homogeneous and inhomogeneous random set $X$ of heterogeneities. Indeed, even for the the functional graded materials (FGMs), the integrand in the square brackets in (17.63) is of order $O(|\mathbf{x}-\mathbf{y}|^{-2d+1})$ as $|\mathbf{x}-\mathbf{y}|\to\infty$, and the integrals in Eq. (17.63) converges absolutely. For no *long-range* order assumed, the function $\varphi(v_j,\mathbf{x}_j|;v_i,\mathbf{x}_i)-\varphi(v_j,\mathbf{x}_j)$ decays at infinity sufficiently rapidly and guarantees an absolute convergence of the integral involved. Therefore, for $\mathbf{x}\in w$ far enough from the boundary $\Gamma_0$ (17.59) (that provides vanishing of the integral in Eq. (17.63)), the right-hand side integral in (17.63) does not depend on the shape and size of the domain $w$, and it can be replaced by the integral over the whole space $R^d$. With this assumption Eq. (17.63) takes the form

$$\boldsymbol{\chi}(\mathbf{s})=\langle\boldsymbol{\chi}\rangle(\mathbf{s})+\int[\mathscr{L}_k^{\chi}(\mathbf{s}-\mathbf{x}_k,\boldsymbol{\chi})V_k^{\delta}(\mathbf{x}_k)-\langle\mathscr{L}_k^{\chi}(\mathbf{s}-\mathbf{x}_k,\boldsymbol{\chi})\rangle(\mathbf{x}_k)]d\mathbf{x}_k,\quad(17.66)$$

where the domain integration $R^d$ and the label $\alpha$ are omitted hereafter for simplicity of notation.

[2]Exponential decreasing of this function was obtained by Willis (1978) for spherical inclusions; Hansen and McDonald (1986), Torquato and Lado (1992) proposed a faster decreasing function for aligned fibers of circular cross-section.

The term "general" is used with respect to Eqs. (17.58) and (17.66) in the sense that we did not accept any assumptions related with either the estimation of perturbators $\mathscr{L}_k^{\theta}(\mathbf{x}-\mathbf{x}_k, \boldsymbol{\zeta})$ (17.36) and $\mathscr{L}_k^{\chi}(\mathbf{x}-\mathbf{x}_k, \boldsymbol{\chi})$ (17.37) or the microstructure of heterogeneous medium (such as statistical homogeneity). In so doing, we only consider the physical phenomena described in Sect. 17.2.

### 17.4.3 Infinite Coupled System of General Integral Equations

Let the inclusions $v_1, \ldots, v_n$ be fixed and we define two sorts of effective fields, $\overline{\boldsymbol{\chi}}_i(\mathbf{x})$ and $\widetilde{\boldsymbol{\chi}}_{1,\ldots,n}(\mathbf{x})$ $(i = 1, \ldots, n;\ \mathbf{x} \in v_1, \ldots, v_n)$, by the use of the rearrangement of Eq. (17.60) in the following operator forms (an analogous case of this manipulation approach for the perturbator $\mathscr{L}_k^{\theta}(\mathbf{x}-\mathbf{x}_k, \boldsymbol{\vartheta})$ (17.36) is given in Buryachenko 2015a) $(\mathbf{x} \in \Gamma_i)$:

$$
\begin{aligned}
\boldsymbol{\chi}(\mathbf{x}) &= \overline{\boldsymbol{\chi}}_i(\mathbf{x}) + \mathscr{L}_i^{\chi}(\mathbf{x}-\mathbf{x}_i, \boldsymbol{\chi}),\\
\overline{\boldsymbol{\chi}}_i(\mathbf{x}) &= \widetilde{\boldsymbol{\chi}}_{1,\ldots,n}(\mathbf{x}) + \sum_{j\neq i}^{n} \mathscr{L}_j^{\chi}(\mathbf{x}-\mathbf{x}_j, \boldsymbol{\chi}),\\
\widetilde{\boldsymbol{\chi}}_{1,\ldots,n}(\mathbf{x}) &= \langle \boldsymbol{\chi} \rangle(\mathbf{x}) + \int [\mathscr{L}_k^{\chi}(\mathbf{x}-\mathbf{x}_k, \boldsymbol{\chi}) V^{\delta}(\mathbf{x}_k|; v_1, \mathbf{x}_1; \ldots; v_n, \mathbf{x}_n)\\
&\quad - \langle \mathscr{L}_k^{\chi}(\mathbf{x}-\mathbf{x}_k, \boldsymbol{\chi}) \rangle(\mathbf{x}_k)] d\mathbf{x}_k,
\end{aligned}
\tag{17.67}
$$

respectively, for $\mathbf{x} \in \Gamma_i$, $i = 1, 2, \ldots, n$; here, $V^{\delta}(\mathbf{x}_k|; v_1, \mathbf{x}_1; \ldots; v_n, \mathbf{x}_n) = \sum_m \delta(\mathbf{x}_k - \mathbf{x}_m) - \sum_{i=1}^{n} \delta(\mathbf{x}_k - \mathbf{x}_i)$ is a random delta function of heterogeneity centers $\mathbf{x}_m$ $(m = 1, 2, \ldots)$ under the condition that $\mathbf{x}_k \neq \mathbf{x}_i$, $\mathbf{x}_i \neq \mathbf{x}_j$ if $i \neq j$ $(i, j = 1, \ldots, n)$. The definitions of the effective fields $\overline{\boldsymbol{\chi}}_i(\mathbf{x})$, $\widetilde{\boldsymbol{\chi}}_{1,2,\ldots,n}(\mathbf{x})$ as well as their statistical averages $\langle \overline{\boldsymbol{\chi}}_i \rangle(\mathbf{x})$, $\langle \widetilde{\boldsymbol{\chi}}_{1,2,\ldots,n} \rangle(\mathbf{x})$ are nothing more than a notation convenience for different terms of the infinite system (17.62).

Then, considering some conditional statistical averages of the GIE (17.60) leads to an infinite system of integral equations $(\mathbf{x} \in \Gamma_j,\ j = 1, 2 \ldots n)$:

$$
\begin{aligned}
&\langle \boldsymbol{\chi} | v_1, \mathbf{x}_1; \ldots; v_n, \mathbf{x}_n \rangle(\mathbf{x}) - \sum_{i=1}^{n} \langle \mathscr{L}_i^{\chi}(\mathbf{x}-\mathbf{x}_i, \boldsymbol{\chi}) | v_1, \mathbf{x}_1; \ldots; v_n, \mathbf{x}_n \rangle_i\\
&= \langle \boldsymbol{\chi} \rangle(\mathbf{x}) + \int \big\{ \langle \mathscr{L}_j^{\chi}(\mathbf{x}-\mathbf{x}_j, \boldsymbol{\chi} | ; v_1, \mathbf{x}_1; \ldots; v_n, \mathbf{x}_n \rangle_j \varphi(v_j, \mathbf{x}_j | ; v_1, \mathbf{x}_1, \ldots, v_n, \mathbf{x}_n)\\
&- \langle \mathscr{L}_j^{\chi}(\mathbf{x}-\mathbf{x}_j, \boldsymbol{\chi}) \rangle(\mathbf{x}_j) \big\} d\mathbf{x}_j.
\end{aligned}
\tag{17.68}
$$

Since $\mathbf{x} \in \Gamma_1, \ldots, \Gamma_n$ in the $n$-th line of the system can take the values inside the inclusion interfaces $\Gamma_1, \ldots, \Gamma_n$, the $n$-th line actually contains $n$ equations. Statistical averaging $\langle (\cdot) \rangle_i$ stands for the averaging over all the surrounding

heterogeneities at the fixed $v_i$, while the average $\langle(\cdot)\rangle(\mathbf{x}_j)$ implies the averaging over all possible locations of $v_i$ with possible dependence of this average on the macrocoordinate $\mathbf{x}_i$ as for FGMs.

A comparison of Eqs. (17.68) and (17.37) shows that the operator $\mathscr{L}_k^{\chi}(\mathbf{x}-\mathbf{x}_k, \boldsymbol{\chi})$ has the physical interpretation of perturbations introduced by a single heterogeneity $v_k$ in the infinite homogeneous matrix (the infinite size of the matrix can be approximated with the length of 40 inclusion diameters (see Chapter 4 in Buryachenko 2007) subjected to the effective field $\overline{\boldsymbol{\chi}}_k(\mathbf{x})$, where at first no restrictions are imposed on the inhomogeneities of effective fields.

The introduction of the effective field (17.37) makes it possible to define another sort of the perturbators ($17.37_2$). In such a case, the GIEs (17.68) can be transformed to the new GIEs in terms of effective fields ($\mathbf{x} \in \Gamma_k,\ j = 1, 2, \ldots, n$):

$$\langle\overline{\boldsymbol{\chi}}|v_1, \mathbf{x}_1; \ldots; v_n, \mathbf{x}_n\rangle(\mathbf{x}) - \sum_{i\neq k}^{n}\langle\mathscr{L}_i^{\chi}(\mathbf{x}-\mathbf{x}_i, \overline{\boldsymbol{\chi}})|v_1, \mathbf{x}_1; \ldots; v_n, \mathbf{x}_n\rangle_i$$

$$= \langle\boldsymbol{\chi}\rangle(\mathbf{x}) + \int \big\{\langle\mathscr{L}_j^{\chi}(\mathbf{x}-\mathbf{x}_j, \overline{\boldsymbol{\chi}})|; v_1, \mathbf{x}_1; \ldots; v_n, \mathbf{x}_n\rangle_j \varphi(v_j, \mathbf{x}_j|; v_1, \mathbf{x}_1, \ldots, v_n, \mathbf{x}_n)$$

$$- \langle\mathscr{L}_j^{\chi}(\mathbf{x}-\mathbf{x}_j, \overline{\boldsymbol{\chi}})\rangle(\mathbf{x}_j)\big\} d\mathbf{x}_j. \tag{17.69}$$

The GIEs (17.67), (17.68), and (17.69) can be considered as the general operator equations where the operators $\mathscr{L}_j^{\chi}(\mathbf{x}-\mathbf{x}_j, \boldsymbol{\chi})$ and $\mathscr{L}_j^{\chi}(\mathbf{x}-\mathbf{x}_j, \overline{\boldsymbol{\chi}})$ can be found by any available numerical method. It is implied that the variable $\boldsymbol{\chi}$ denotes the duplet $\boldsymbol{\chi} = (\mathbf{u}, \mathbf{t})^{\top}$ (17.39) of the displacement and traction used in the BIEs. However, Eq. (17.69) holds also for $\boldsymbol{\chi}(\mathbf{s}) = \mathbf{u}(\mathbf{s})$ and $\boldsymbol{\chi}(\mathbf{s}) = \mathbf{t}(\mathbf{s})$ ($\mathbf{s} \in \partial v$) if the corresponding perturbators are found (see, e.g., Sect. 17.4). Buryachenko (2010a, 2015) proved the absolute convergence of GIE for the volume inclusion perturbators (17.36) that holds also for the interface inclusion perturbators (17.37). Indeed, for the porous materials ($\boldsymbol{\chi}(\mathbf{s}) = \mathbf{u}(\mathbf{s}),\ \mathbf{s} \in \partial v$) the integrand of Eq. (17.69) is of order $O(|\mathbf{x} - \mathbf{x}_j|^{2d-1})$ as $|\mathbf{x} - \mathbf{x}_j| \to \infty$, while for the composite materials (CMs) reinforced by the rigid inclusions ($\boldsymbol{\chi}(\mathbf{s}) = \mathbf{t}(\mathbf{s}),\ \mathbf{s} \in \partial v$), the integrand of Eq. (17.69) tends to zero with $|\mathbf{x} - \mathbf{x}_j| \to \infty$ as $O(|\mathbf{x} - \mathbf{x}_j|^{2d})$.

## 17.5 Method of Fundamental Solutions (MFS)

### *17.5.1 The Scheme of the Method of Fundamental Solutions (MFS)*

The estimation of the effective properties (17.31) and (17.32) through the boundary integrals over the inclusion interfaces $\Gamma_i$ is performed by substitutions of the corresponding integrals for a single representative inclusion $v_i$ into one or another micromechanical model (some of them will be considered in Sect. 17.8). Any solution $\mathbf{u}$ of the homogeneous partial differential equations (17.1)–(17.3) is

given for $\mathbf{x} \in w$ by the representation formulae (17.44) and (17.45). The boundary integral equations (17.44) and (17.45) can be regarded as a continuous form of the discrete Method of Fundamental Solutions (MFS), which approximates the solution within a given elastic domain $v$ as a finite linear combination of fundamental solutions generated by a set of virtual sources positioned outside the domain (to avoid singularities). Through these equations, the strains and stresses at any domain point can be easily obtained making use of classic elasticity equations.

Although an estimation of the operator $\mathscr{L}_i^{\chi}(\mathbf{x} - \mathbf{x}_i, \overline{\boldsymbol{\chi}}_i)$ for a single particle $v_i$ can be performed by the different BIEMs, we consider the Method of Fundamental Solutions (MFS), which is a straightforward method that allows one to approach the solution of Eqs. (17.1)–(17.3) for the known fundamental solutions. The solution is treated as a series of the fundamental solutions with singularities located outside the computational domain of the problem under consideration. The unknown coefficients of the series of the fundamental solutions are regarded as the strengths or the densities of the corresponding fundamental solutions. Namely, let the domains $v_i$ and $\hat{v}_i^{(1)}$ be open subsets in $R^d$ separated by the smooth boundary $\Gamma_i$ (see, e.g., Smyrlis 2009). We say that $\hat{v}_i^{(1)}$ with the smooth pseudo-boundary $\hat{\Gamma}_i^{(1)} := \partial \hat{v}_i^{(1)}$ embraces $v_i$ if $(v_i \cup \Gamma_i) \subset \hat{v}_i^{(1)}$. In a similar manner, one can define a pseudo-boundary $\hat{\Gamma}_i^{(0)} := \partial \hat{v}_i^{(0)}$ of an open subset $\hat{v}_i^{(0)}$ embracing the open domain $R^d \backslash (v_i \cup \Gamma_i)$. So, the grey regions in Figs. 17.1a, b are the inclusion $v_i$ with the boundary $\Gamma_i = \partial v_i$. The $\hat{\Gamma}_i^{(1)}$ and $\hat{\Gamma}_i^{(0)}$ are constructed from $\Gamma_i = \partial v_i$ by a homothetic transformation. (17.75) (Fig. 17.1a) and by a normal direction choice for the source points (17.76) (Fig. 17.1b), which will be considered later.

We place $m$ points of the admissible singularities (or sources) $\{\mathbf{y}_s^k\}_{s=1}^S$ corresponding to the external ($k = 0$) and internal ($k = 1$) problems on the prescribed pseudo-boundary surfaces $\hat{\Gamma}_i^{(0)}$ and $\hat{\Gamma}_i^{(1)}$, respectively. A slight modification of Alves and Silvestre (2004) (see also Martins and Rebelo 2013) results shows that it is possible to approach the boundary conditions for the displacement approximated by linear combinations of the corresponding fundamental solutions. Let the effective

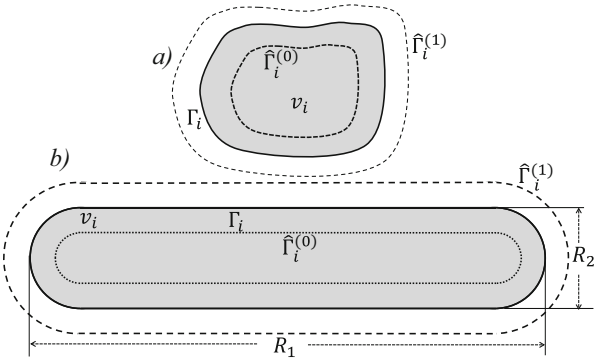


**Fig. 17.1** The boundary $\Gamma_i = \partial v_i$ and the pseudo-boundaries $\hat{\Gamma}_i^{(0)}$ and $\hat{\Gamma}_i^{(1)}$ constructed by Eqs. (17.75) (**a**) and (17.76) (**b**), which will be considered later

field $\overline{\mathbf{u}}(\mathbf{x})$ be prescribed in the collocation points $\{\mathbf{x}_j\}_{j=1}^{S} \in \Gamma_i$. Then the strength of FSs $\mathbf{f}_i^{(k)} = (\mathbf{f}_{is|1}^{(k)}, \ldots, \mathbf{f}_{is|d}^{(k)})^\top$ $(s = 1, \ldots, S)$ holds a $dm \times dm$ linear system of equations $(j = 1, \ldots, d,\ l = 1, \ldots, S)$:

$$\sum_{s=1}^{S}\sum_{q=1}^{d} f_{isq}^{(1)} G_{jq}^{(1)}(\mathbf{r}_{ls}^{1}) = \sum_{s=1}^{S}\sum_{q=1}^{d} f_{isq}^{(0)} G_{jq}^{(0)}(\mathbf{r}_{ls}^{0}) + \overline{u}_j(\mathbf{x}_l), \tag{17.70}$$

where $\mathbf{r}_{ls}^{k} = (\mathbf{x}_l - \mathbf{y}_s^k)$ and $|\mathbf{r}_{ls}^{k}|$ is the distance between the collocation point (the field point), $\mathbf{x}_l$, and the location of the FSs (the source point), $\mathbf{y}_s^k \in \hat{\Gamma}_i^{(k)}$ $(k = 0, 1)$. In a similar manner, the traction boundary conditions (17.35$_2$) can be obtained directly by taking the summation of the traction FSs with the same strength $\mathbf{f}_i^{(k)} = (\mathbf{f}_{is|1}^{(k)}, \ldots, \mathbf{f}_{is|d}^{(k)})^\top$ (17.70) over the source points $\mathbf{y}_s^k \in \hat{\Gamma}_i^{(k)}$ outside the boundary $\Gamma_i$ $(j, q = 1, \ldots, d;\ s = 1, \ldots, S;\ k = 0, 1)$:

$$\sum_{s=1}^{S}\sum_{q=1}^{d} f_{isq}^{(1)} T_{jq}^{(1)}(\mathbf{r}_{ls}^{1}) = \sum_{s=1}^{S}\sum_{q=1}^{d} f_{isq}^{(0)} T_{jq}^{(0)}(\mathbf{r}_{ls}^{0}) + \overline{t}_j(\mathbf{x}_l), \tag{17.71}$$

where $\overline{\mathbf{t}} = \overline{\boldsymbol{\sigma}}\mathbf{n}^{\Gamma_i}(\mathbf{x}_l)$. We assumed in the system (17.72) and (17.71) that the numbers of both the field points $\{\mathbf{x}_l\}_{l=1}^{S}$ and source ones $\{\mathbf{y}_s^k\}_{s=1}^{S}$ $(k = 0, 1)$ coincide. In such a case, the strength of the FSs, $\mathbf{f}_i$, is determined uniquely, provided that the corresponding coefficient matrix is nonsingular. If $\overline{\mathbf{u}}(\mathbf{x})$ is prescribed in more points $\mathbf{x}_1, \ldots, \mathbf{x}_n \in \Gamma_i$, with $n > S$, the system (17.72) and (17.71) is overdetermined, and the strength can be chosen by the discrete least-squares method (see Alves and Silvestre 2004; Smyrlis 2009), which is not considered in more detail in the current paper.

Once the strength of the FS, $\mathbf{f}_i^{(k)}$, is found by solving the system (17.70) and (17.71) at $\{\mathbf{x}_l\}_{l=1}^{S} \in \Gamma_i$, the displacement vector in both the inclusion $v_i$ and matrix $R^d \backslash v_i$ is then calculated straightforwardly by using the left-hand side and right-hand side, respectively, of Eq. (17.72) with values of replaced radius-vectors $\mathbf{x}_l \to \mathbf{x}_s$ corresponding to the location of a point $\mathbf{x}_s$. All other field variables can be obtained directly by taking the summation of the same strength $\mathbf{f}_i^{(k)}$ (17.72) and (17.71) of the corresponding FSs over the source points $\mathbf{y}_s^k \in \hat{\Gamma}_i^{(k)}$ $(k = 0, 1)$ outside the boundary $\Gamma_i$, for example, the displacement, traction, and stress induced by $S$ FSs can be estimated by the equations $(j, l = 1, \ldots, d)$:

$$u_j(\mathbf{x}_r) = \sum_{s=1}^{S}\sum_{q=1}^{d} f_{isq}^{(k)} G_{jq}^{(k)}(\mathbf{r}_{rs}^{k}) + \overline{u}_j(\mathbf{x}_r)\delta_{k0}, \tag{17.72}$$

$$t_j(\mathbf{x}_r) = \sum_{s=1}^{S}\sum_{q=1}^{d} f_{isq}^{(k)} T_{jq}^{(k)}(\mathbf{r}_{rs}^{k}) + \overline{t}_j(\mathbf{x}_r)\delta_{k0}, \tag{17.73}$$

$$\sigma_{jl}(\mathbf{x}_r) = \sum_{s=1}^{S} \sum_{q=1}^{d} f_{isq}^{(k)} D_{jlq}^{(k)}(\mathbf{r}_{rs}^{k}) + \overline{\sigma}_{jl}(\mathbf{x}_r)\delta_{k0} \tag{17.74}$$

for $\mathbf{x}_s \in v_i$ $(k = 1)$ and $\mathbf{x}_s \in (R^d \backslash v_i)$ $(k = 0)$, respectively.

A specific feature of the MFS is some freedom in choosing the source points with respect to the accuracy of the numerical solution. Young et al. (2006) (see also Alves and Silvestre 2004) estimated an excellent accuracy of the MFS for the positions of the source points $\mathbf{y}$ in the computational domain through the field points $\mathbf{x}_l$ $(l = 1, \ldots, S)$ by a homothety transformation:

$$\mathbf{y}_l = \mathbf{x}_i + b(\mathbf{x}_l - \mathbf{x}_i), \tag{17.75}$$

where $\mathbf{x}_i$ is a homothetic center coinciding with the particle center. Once the parameters $0 < b < 1$ and $1 < b$ for $k = 1$ and $k = 0$, respectively, are chosen, the distribution of the source points is determined. The pseudo-boundaries $\hat{\Gamma}_i^{(0)}$ and $\hat{\Gamma}_i^{(1)}$ in Fig. 17.1a are obtained from the boundary $\hat{\Gamma}_i$ of the grey inclusion $v_i$ by the homothety transformation (17.75).

However, for the thin inclusions with the thickness $2h^a$ (e.g., for the triaxial ellipsoid with distinct semiaxis lengths $a_1 > a_2 \gg a_3$, $h^a = a_3$) the distances $D(\mathbf{y}_l, \Gamma_i)$ [defining the matrix coefficients $G_{jq}^{(k)}(\mathbf{r}_{ls}^1)$ (17.70) and $T_{jq}^{(k)}(\mathbf{r}_{ls}^1)$ (17.71)] are essentially differ one from another points $\mathbf{x}_i$. Here, $D(\mathbf{y}_l, \Gamma_i)$ denotes the Euclidean distance between $\mathbf{y}_l$ and the boundary of $v_i$, or in other words, the radius of the largest inscribed sphere (or disk) with center $\mathbf{y}_l$. Because of this, for the thin inclusions, the following allocations of the source points $(k = 0, 1)$

$$\mathbf{y}_l^k = \mathbf{x}_l + (2k - 1)d_k \mathbf{n}^{\Gamma_i}(\mathbf{x}_l) \tag{17.76}$$

with $d = D(\mathbf{y}_l, \Gamma_i) = 10 - 30\% h^a$ are preferable.

The algorithm of the normal direction choice for the source points (17.76) proposed by Alves and Antunes (2005) was accomplished by so-called glocal choice for the coefficient $d_k$ $(k = 0, 1)$ recently presented in Alves (2009). A simplest choice of a constant $d_k$ is a non-optimal one that works in most cases. In such a case, the pseudo-boundaries $\hat{\Gamma}^{(1)}$ and $\hat{\Gamma}^{(0)}$ can be presented as the boundaries of Minkowski addition and subtraction,

$$\hat{v}^{(1)} = v_i \oplus b(\mathbf{0}, d_0), \quad \hat{v}^{(0)} = v_i \ominus b(\mathbf{0}, d_1),$$

respectively, of the domain $v_i$, where $b(\mathbf{0}, d_k)$ $(k = 0, 1)$ stands the ball of radius $d_k$ centered at the origin $\mathbf{0}$. As an example, a grey cross section of a spherocylinder (or a capsule) with the aspect ratio $\alpha = R_2/R_1$ is presented in Fig. 17.1b. The pseudo-boundaries $\hat{\Gamma}_i^{(0)}$ and $\hat{\Gamma}_i^{(1)}$ in Fig. 17.1b are obtained from the boundary $\hat{\Gamma}_i$ of the grey inclusion $v_i$ by the normal direction choice for the source points (17.76) with $d_1 = R_2/2$ and $d_0 = R_2/2$, respectively. In so doing, the aspect

ratios of the domains with the pseudo-boundaries $\hat{\Gamma}_i^{(1)}$ and $\hat{\Gamma}_i^{(0)}$ are $(2\alpha + 1)/3$ and $(2\alpha - 1)$, while the aspect ratios of the corresponding domains obtained by the homothety transform (17.76) do not change and equal $\alpha$.

Alves (2009) (see also Alves and Antunes 2005) analyzed the optimization of more general stresslet allocation techniques for convex and concave regions. However, a more detailed consideration of the optimization of FSs allocation substantially reducing computational time for the elastic problem solution is beyond the scope of the current study.

### *17.5.2 The Matrix Representation of the MFS*

The construction and solution of the linear algebraic system (17.70) is straightforward (see, e.g., Young et al. 2006; Karageorghis and Smyrlis 2007). However, we consider it in more detail for the 2-D domain $v_i$. The singularities $Y_s^0 = (y_{s|1}^0, y_{s|2}^0)$ and $Y_s^1 = (y_{s|1}^1, y_{s|2}^1)$ $(p = 1, \dots, P)$ are fixed on the boundaries $\hat{\Gamma}_i^{(0)}$ of $\hat{v}_i^{(0)}$ and $\hat{\Gamma}_i^{(1)}$ of $\hat{v}_i^{(1)}$, respectively. A set of $P$ collocation points $X_s = (x_{s|1}, x_{s|2})$ $(s = 1, \dots, S)$ is chosen on $\Gamma_i$. Then the system (17.70) can be presented in the matrix form

$$\mathbf{Af} = \begin{pmatrix} \mathbf{A}_{11} & \mathbf{A}_{1,2} & \dots & \mathbf{A}_{1,S} \\ \mathbf{A}_{2,1} & \mathbf{A}_{2,2} & \dots & \mathbf{A}_{2,S} \\ \vdots & \vdots & \ddots & \vdots \\ \mathbf{A}_{S,1} & \mathbf{A}_{S,2} & \dots & \mathbf{A}_{S,S} \end{pmatrix} \begin{pmatrix} \mathbf{f}_1 \\ \mathbf{f}_2 \\ \vdots \\ \mathbf{f}_S \end{pmatrix} = \begin{pmatrix} \mathbf{g}_1 \\ \mathbf{g}_2 \\ \vdots \\ \mathbf{g}_S \end{pmatrix} = \mathbf{g}, \tag{17.77}$$

where the $4P \times 4P$ matrix $\mathbf{A}$ with the submatrices

$$\mathbf{A}_{\alpha,\beta} = \begin{pmatrix} \mathbf{A}_{\alpha,\beta}^{1,1} & \mathbf{A}_{\alpha,\beta}^{1,2} \\ \mathbf{A}_{\alpha,\beta}^{2,1} & \mathbf{A}_{\alpha,\beta}^{2,2} \end{pmatrix} \tag{17.78}$$

are defined through the submatrices

$$\mathbf{A}_{\alpha,\beta}^{1,\delta+1} = (-1)^{\delta+1}\mathbf{G}^{(\delta)}(|X_\alpha - Y_\beta^\delta|) \in R^{2\times 2}, \tag{17.79}$$

$$\mathbf{A}_{\alpha,\beta}^{2,\delta+1} = (-1)^{\delta+1}\mathbf{T}^{(\delta)}(|X_\alpha - Y_\beta^\delta|) \in R^{2\times 2}, \tag{17.80}$$

and

$$\mathbf{f}_s = (\mathbf{f}_s^{(0)}, \mathbf{f}_s^{(1)})^\top = (f_{s|1}^{(0)}, f_{s|2}^{(0)}, f_{s|1}^{(1)}, f_{s|2}^{(1)})^\top \in R^4, \tag{17.81}$$

$$\mathbf{g}_s = (\mathbf{g}_s^{(0)}, \mathbf{g}_s^{(1)})^\top = (g_{s|1}^{(0)}, g_{s|2}^{(0)}, g_{s|1}^{(1)}, g_{s|2}^{(1)})^\top \in R^4, \tag{17.82}$$

where $f_{s|j}^{(\delta)} = f_{s|j}^{(\delta)}(Y_s^\delta)$, $g_{s|j}^{(\delta)} = \overline{u}_{s|j}\delta_{0\delta} + \overline{t}_{s|j}\delta_{1\delta}$, and $j = 1, 2$; $s, \alpha, \beta = 1, \dots, S$; $\delta = 0, 1$. It is observed for $d = 2, 3$ that accurate numerical results could be

obtained when the source points for the pseudo-boundary $\hat{\Gamma}_i^{(0)}$ of the submerged stresslets are located off the boundary at about 70–90% (17.75) of the distance from the center (see for details Young et al. 2006).

However, the MFS coefficient matrix $\mathbf{A}$ (17.77) of the system (17.70) and (17.71) is often severely ill-conditioned and the system of linear algebraic equations (17.70) and (17.71) cannot be solved by direct methods, such as the least-squares method, producing a highly unstable solution, which increases dramatically as the number of boundary collocation points $S$ increases. Several regularization procedures have been proposed to remedy the instability and accuracy loss in the solution of such ill-conditioned matrix equations (see, e.g., Hansen 1998). However, we only consider the Tikhonov regularization (TR) method (see, e.g., Tikhonov and Arsenin (1986)), since it is simple and noniterative and provides an explicit solution. Namely, the TR procedure consists of seeking a solution, which minimizes a criterion made up of the sum of two summands. The first one is a possibly weighted least-square term, while the second one is a quadratic penalty term on the solution, that is

$$\min\{||\mathbf{A}\mathbf{f}-\mathbf{g}||_2^2+\lambda||\mathbf{I}^{\mathrm{dS}}\mathbf{f}||_2^2\}, \tag{17.83}$$

where $||(\cdot)||_2$ denotes the Euclidean norm, while for the zeroth order TR method, $\mathbf{I}^{\mathrm{dS}}=\mathrm{diag}(1,\ldots,1)\in R^{dS\times dS}$ is the identity matrix. Formally, the TR procedure provides an explicit solution of Eq. (17.77)

$$\mathbf{f}=\mathscr{A}\mathbf{g},\quad \mathscr{A}:=(\mathbf{A}^\top\mathbf{A}+\lambda\mathbf{I})^{-1}\mathbf{A}^\top, \tag{17.84}$$

where the partitioned matrix $\mathscr{A}$ can be expressed in the form (17.77) with the blocks $4\times 4$ $\mathscr{A}_{\alpha,\beta}$ presented as

$$\mathscr{A}_{\alpha,\beta}=(\mathscr{A}^u_{\alpha,\beta}\mathbf{0})+(\mathbf{0}\mathscr{A}^t_{\alpha,\beta}), \tag{17.85}$$

where the $4\times 2$ submatrices $\mathscr{A}^u_{\alpha,\beta}$ and $\mathscr{A}^t_{\alpha,\beta}$, in its turn, can be expressed through the blocks $\mathscr{A}^{1,1}_{\alpha,\beta}$, $\mathscr{A}^{2,1}_{\alpha,\beta}$ and $\mathscr{A}^{1,2}_{\alpha,\beta}$, $\mathscr{A}^{2,2}_{\alpha,\beta}$, respectively, in much the same manner as (17.78).

Substitution of the found solution $\mathbf{f}$ of the matrix Eq. (17.77) into Eqs. (17.72)–(17.74) allows one to present all field variables in an arbitrary point $\mathbf{x}\in\Gamma_i, R^d$ in symbolic matrix notations ($k=0,1$),

$$\mathbf{u}(\mathbf{x})-\overline{\mathbf{u}}(\mathbf{x})\delta_{k0}=\mathscr{G}^{(k)}(\mathscr{A}^u\overline{\mathbf{u}}(\mathbf{x})+\overline{\mathscr{A}^t}\overline{\mathbf{t}}(\mathbf{x})), \tag{17.86}$$

$$\boldsymbol{\varepsilon}(\mathbf{x})-\overline{\boldsymbol{\varepsilon}}(\mathbf{x})\delta_{k0}=\mathscr{E}^{(k)}(\mathscr{A}^u\overline{\mathbf{u}}(\mathbf{x})+\overline{\mathscr{A}^t}\overline{\mathbf{t}}(\mathbf{x})), \tag{17.87}$$

$$\mathbf{t}(\mathbf{x})-\overline{\mathbf{t}}(\mathbf{x})\delta_{k0}=\mathscr{T}^{(k)}(\mathscr{A}^u\overline{\mathbf{u}}(\mathbf{x})+\overline{\mathscr{A}^t}\overline{\mathbf{t}}(\mathbf{x})), \tag{17.88}$$

$$\boldsymbol{\sigma}(\mathbf{x})-\overline{\boldsymbol{\sigma}}(\mathbf{x})\delta_{k0}=\mathscr{D}^{(k)}(\mathscr{A}^u\overline{\mathbf{u}}(\mathbf{x})+\overline{\mathscr{A}^t}\overline{\mathbf{t}}(\mathbf{x})), \tag{17.89}$$

which can be considered as a representation of the boundary inclusion perturbations $\mathscr{L}_i^{\chi}(\mathbf{x}-\mathbf{x}_i,\overline{\boldsymbol{\chi}})$ defined at the pseudo-boundaries either $\hat{\Gamma}_i^{(1)}$ or $\hat{\Gamma}_i^{(0)}$ at $k=1$ or $k=0$, respectively. Here, the blocks $4\times 2$ $\overline{\mathscr{A}}^t_{\alpha,\beta}=(\mathscr{A}^{1,2}_{\alpha,\beta}-\delta_{\alpha,\beta}\boldsymbol{\delta},\mathscr{A}^{2,2}_{\alpha,\beta}-\delta_{\alpha,\beta}\boldsymbol{\delta})^{\top}$ of the partitioned matrix $\overline{\mathscr{A}}^t$ are defined through the blocks $\mathscr{A}^{1,2}_{\alpha,\beta}$, $\mathscr{A}^{2,2}_{\alpha,\beta}$, and $\boldsymbol{\delta}$ is a unite $2\times 2$ matrix.

## 17.6 Some Classical Hypotheses and Approaches

The basic hypotheses of micromechanics were analyzed by Buryachenko (2015) in the form adopted to the use of the volume inclusion perturbators $\mathscr{L}^{\theta}(\mathbf{x}-\mathbf{x}_k,\overline{\boldsymbol{\vartheta}})$. We present in this section the same hypotheses in the forms which are most adopted for the subsequent application of the boundary inclusion perturbators $\mathscr{L}^{\chi}(\mathbf{x}-\mathbf{x}_k,\overline{\boldsymbol{\chi}})$.

In order to approximately solve the exact system (17.69), we now apply the so-called effective field hypothesis (EFH), which is the main approximate hypothesis of many micromechanical methods:

**Hypothesis H1a.** *Each heterogeneity $v_i$ is located in the field* ($\boldsymbol{\vartheta}=\boldsymbol{\varepsilon},\boldsymbol{\sigma}$)

$$\overline{\boldsymbol{\vartheta}}_i(\mathbf{y})\equiv\overline{\boldsymbol{\vartheta}}(\mathbf{x}_i)\ (\mathbf{y}\in v_i), \tag{17.90}$$

*which is homogeneous over the heterogeneity $v_i$.*

For the boundary variables ($\mathbf{s}\in\Gamma_i$), the hypothesis **H1** can be presented in the local coordinate systems connected with $v_i$:

$$\overline{\mathbf{u}}_i(\mathbf{s})\equiv\overline{\boldsymbol{\varepsilon}}(\mathbf{x}_i)(\mathbf{s}-\mathbf{x}_i)\quad \overline{\mathbf{t}}_i(\mathbf{s})\equiv\overline{\boldsymbol{\sigma}}(\mathbf{x}_i)\mathbf{n}(\mathbf{s}), \tag{17.91}$$

where $\mathbf{n}^{\Gamma_i}(\mathbf{s})$ is unit outward normal at $\mathbf{s}\in\Gamma_i$.

In some methods (such as the MEFM), this basic hypothesis **H1a** is complemented by a satellite hypothesis presented in the form of the perturbator rather than the Green's function:

**Hypothesis H1b.** *The boundary inclusion operator $\mathscr{L}^{\theta}_k(\mathbf{x}-\mathbf{x}_k,\boldsymbol{\zeta})$ of perturbation generated by the heterogeneities $v_i$ at the point $\mathbf{x}\notin v_k$ is reduced to the decoupled tensorial multiplications*

$$\mathscr{L}^{\theta}_k(\mathbf{x}-\mathbf{x}_k,\boldsymbol{\zeta})=\mathbf{L}^{\zeta}_k(\mathbf{x}-\mathbf{x}_k)\langle\boldsymbol{\zeta}\rangle_{(k)}. \tag{17.92}$$

For the perturbator $\mathscr{L}^{\theta}_k(\mathbf{x}-\mathbf{x}_k,\boldsymbol{\zeta})$ expressed through the Green's functions, the assumption (17.92) is reduced to the known ones (see, e.g., Buryachenko 2007) with the perturbator factors (17.49) presented in terms of both the internal $\mathbf{S}_i$ and external $\mathbf{S}_i(\mathbf{x})$ (Eshelby, 1957) tensors (see also, for references and details, Buryachenko 2007).

It should be mentioned that the popular formulation of the EFH (hypothesis **H1**) is a combination of the hypotheses **H1a** and **H1b**.

Different methods can be employed to truncate the hierarchies (17.68) and (17.69) (see for references, e.g., Hinch 1977; Buryachenko, 2007). Probably the most formal closing assumption is the following (the corresponding assumption for the fields $\boldsymbol{\vartheta}$ and $\overline{\boldsymbol{\vartheta}}$ are formulated analogously).

**Hypothesis H2a)** *For a sufficiently large n, the systems (17.68) and (17.69) are completed by the equations*

$$\begin{aligned}\langle \mathscr{L}_j^{\chi}(\mathbf{x}-\mathbf{x}_j,\boldsymbol{\chi}) \ \big| \ ;v_1,\mathbf{x}_1;\ldots;v_q,\mathbf{x}_q;\ldots,v_{n+1},\mathbf{x}_{n+1}\rangle_j \\ = \langle \mathscr{L}_j^{\chi}(\mathbf{x}-\mathbf{x}_j,\boldsymbol{\chi})|;v_1,\mathbf{x}_1;\ldots;v_n,\mathbf{x}_n\rangle_j, \\ \langle \mathscr{L}_j^{\chi}(\mathbf{x}-\mathbf{x}_j,\overline{\boldsymbol{\chi}}) \ \big| \ ;v_1,\mathbf{x}_1;\ldots;v_q,\mathbf{x}_q;\ldots;v_{n+1},\mathbf{x}_{n+1}\rangle_j \\ = \langle \mathscr{L}_j^{\chi}(\mathbf{x}-\mathbf{x}_j,\overline{\boldsymbol{\chi}})|;v_1,\mathbf{x}_1;\ldots;v_n,\mathbf{x}_n\rangle_j, \end{aligned} \tag{17.93}$$

*respectively, where the right-hand sides of these equalities don't contain the index* $q \neq j$ $(j = 1,\ldots,n;\ q = 1,\ldots,n+1;\ \mathbf{x} \in R^d)$.

In opposite to Eq. (17.68), the sum in the left-hand side of Eq. (17.69) does not contain a summand with the index $k$. The truncated hierachies of equations (17.68) and (17.69) are solved as the systems of coupled equations. One starts with the last equation of the hierarchy which has the most inclusions held fixed, because this equation does not depend on the previous ones. The obtained field gives the forcing term in the previous equation of the hierarchy. One continues step by step up the hierarchy until the first equations in the systems (17.68) and (17.69).

In the simple case $n = 1$, the closing effective field hypothesis is called "quasi-crystalline approximation" by Lax (1952), which neglects direct interaction between each pair of heterogeneities, although such an interaction takes place through the effective field generated by all surrounding inclusions.

**Hypothesis H2b, "quasi-crystalline" approximation.** *It is supposed that the mean value of the effective field at a point* $\mathbf{x} \in v_i$ *does not depend on the stress field inside surrounding heterogeneities* $v_j \neq v_i$ $(\mathbf{x} \in v_i,\ \mathbf{s} \in \Gamma_i)$:

$$\langle \overline{\boldsymbol{\vartheta}}_i(\mathbf{x})|;v_j,\mathbf{x}_j\rangle = \langle \overline{\boldsymbol{\vartheta}}_i\rangle, \quad \langle \overline{\boldsymbol{\chi}}_i(\mathbf{s})|;v_j,\mathbf{x}_j\rangle = \langle \overline{\boldsymbol{\chi}}_i\rangle. \tag{17.94}$$

To make further progress, the hypothesis of "ellipsoidal symmetry" for the distribution of inclusions attributed to Willis (1977) is widely used:

**Hypothesis 3, H3, "ellipsoidal symmetry."** *The conditional probability density function* $\varphi(v_j,\mathbf{x}_j \ |;v_i,\mathbf{x}_i)$ depends on $\mathbf{x}_j - \mathbf{x}_i$ *only through the combination* $\rho = |(\mathbf{a}_{ij}^0)^{-1}(\mathbf{x}_j - \mathbf{x}_i)|$:

$$\varphi(v_j,\mathbf{x}_j \ |;v_i,\mathbf{x}_i) = h(\rho), \tag{17.95}$$

*where the matrix* $(\mathbf{a}_{ij}^0)^{-1}$ *(which is symmetric in the indexes i and j,* $\mathbf{a}_{ij}^0 = \mathbf{a}_{ji}^0$*) defines the ellipsoid excluded volume* $v_{ij}^0 = \{\mathbf{x}:\ |(\mathbf{a}_{ij}^0)^{-1}\mathbf{x}|^2 < 1\}$.

Analyses of the classical counterparts of renormalizing terms $\langle \mathscr{L}_k^{\theta}(\mathbf{x}-\mathbf{x}_k,\boldsymbol{\zeta})\rangle(\mathbf{x}_k)$ (17.58) and $\langle \mathscr{L}_k^{\chi}(\mathbf{x}-\mathbf{x}_k,\chi)\rangle(\mathbf{x}_k)$ (17.59) are worthy of notice. These counterparts were proposed in terms of Green functions by O'Brian (1979) (see for references and details Buryachenko 2007). In particular, for the polarization tensors $\boldsymbol{\tau},\boldsymbol{\eta}$ in Eq. (17.58), the renormalizing terms can be considered as an asymptotic representation of the hypothesis **H1** at $|\mathbf{x}-\mathbf{x}_k|\to\infty$:

$$\langle \mathscr{L}_k^{\epsilon}(\mathbf{x}-\mathbf{x}_k,\boldsymbol{\tau})\rangle(\mathbf{x}_k)=\mathbf{U}^{(0)}(\mathbf{x}-\mathbf{x}_k)\langle\boldsymbol{\tau}\rangle(\mathbf{x}_k), \tag{17.96}$$

$$\langle \mathscr{L}_k^{\sigma}(\mathbf{x}-\mathbf{x}_k,\boldsymbol{\eta})\rangle(\mathbf{x}_k)=\boldsymbol{\Gamma}^{(0)}(\mathbf{x}-\mathbf{x}_k)\langle\boldsymbol{\eta}\rangle(\mathbf{x}_k). \tag{17.97}$$

An analog of Eq. (17.66) for the interface variable $\boldsymbol{\chi}=(\mathbf{u},\mathbf{t})^{\top}$ was proposed in the problem of slow flow of incompressible fluid ($\nu^{(0)}=0.5$) through assemblages of a random field of fixed solid particles, which is a basic one for processes involving flow through porous media. Because the particles are rigid, there are no velocities within the particle and, hence, the double-layer hydrodynamic potentials vanish for rigid particles $v_k$; $\boldsymbol{\chi}=\mathbf{t}^{\Gamma_k}(\mathbf{s})$ is the force density at the point $\mathbf{s}\in\Gamma_k$ on the surface of the particle $v_k$. Durlofsky et al. (1987) and Brady et al. (1988) proposed an extension of the O'Brian (1979) result into the theory of the fluid mechanics in porous media with a filtration counterpart of (17.97) ($\mathbf{x}\notin v_k$):

$$\langle \mathscr{L}_k^{\chi}(\mathbf{x}-\mathbf{x}_k,\boldsymbol{\chi})\rangle(\mathbf{x}_k)=\mathbf{G}^{(0)}(\mathbf{x}-\mathbf{x}_k)\mathbf{F}^{\Gamma_k}, \tag{17.98}$$

where a drag force $\mathbf{F}^{\Gamma_k}:=n\langle\mathbf{t}\rangle_k$ is a total force exerted by the fluid on the particles.

A fundamental deficiency of Eqs. (17.96)–(17.98) is the dependence of the renormalizing terms $\mathbf{U}^{(0)}(\mathbf{x}-\mathbf{x}_k)\langle\boldsymbol{\tau}\rangle(\mathbf{x}_k)$, $\boldsymbol{\Gamma}^{(0)}(\mathbf{x}-\mathbf{x}_k)\langle\boldsymbol{\eta}\rangle(\mathbf{x}_k)$, and $\mathbf{F}^{\Gamma_k}$, respectively, [obtained in the framework of the asymptotic approximation of the hypothesis **H1b**] only on the statistical averages $\langle\boldsymbol{\tau}\rangle(\mathbf{x}_k)$, $\langle\boldsymbol{\eta}\rangle(\mathbf{x}_k)$, and $\mathbf{F}^{\Gamma_k}$, while the renormalizing terms $\langle \mathscr{L}_k^{\theta}(\mathbf{x}-\mathbf{x}_k,\boldsymbol{\zeta})\rangle(\mathbf{x}_k)$ (17.58) and $\langle \mathscr{L}_k^{\chi}(\mathbf{x}-\mathbf{x}_k,\chi)\rangle(\mathbf{x}_k)$ (17.59) explicitly depend on distributions $\langle\boldsymbol{\zeta}|v_k,\mathbf{x}_k\rangle(\mathbf{y})$ ($\mathbf{y}\in v_k$) and $\langle\boldsymbol{\chi}|v_k,\mathbf{x}_k\rangle(\mathbf{s})$ ($\mathbf{s}\in\Gamma_k$), respectively. Because of this, even in the case of statistically homogeneous media subjected to homogeneous boundary conditions, new effects have been found. The detected difference of renormalizing terms allows us to abandon the hypothesis **H1b** whose accuracy is questionable for inclusions of noncanonical shape.

## 17.7 Solution of GIEs

The solution of the GIEs in terms of the volume inclusion perturbators $\mathscr{L}_k^{\theta}(\mathbf{x}-\mathbf{x}_k,\boldsymbol{\zeta})$ was performed by Buryachenko (2014) for the different selections of the accepted hypotheses **H1**–**H3**. At first, we recast these approaches in terms of stress concentrator factors found by the method of effective field (MEF, see for references and details Buryachenko 2007) as well as by MTM. After that, the versions of the NBM's method were presented for both the volume perturbator factor $\mathbf{L}_q^{\sigma}(\mathbf{x}-\mathbf{x}_q)$ and the interface $\mathbf{L}_q^{t\sigma}(\mathbf{s}-\mathbf{x}_q)$ one.

### 17.7.1 Classical Approaches with Volume Effective Fields

Hypotheses **H1–H3** allow one to obtain the explicit solution using the MEF for the stress distribution (the strain field can be considered in a similar manner) for identical aligned heterogeneities ($v_i = v_j = v_1,\ \mathbf{x} \in v_1$):

$$\langle \overline{\boldsymbol{\sigma}} \rangle_1 = \mathbf{R}_i^{-1}\mathbf{Y}\mathbf{R}_i\langle \boldsymbol{\sigma} \rangle, \tag{17.99}$$

$$\langle \boldsymbol{\sigma} \rangle_1(\mathbf{x}) = \mathbf{B}_i(\mathbf{x})\mathbf{R}_i^{-1}\mathbf{Y}\mathbf{R}_i\langle \boldsymbol{\sigma} \rangle, \tag{17.100}$$

$$\mathbf{M}^* = \mathbf{M}^{(0)} + n^{(1)}\mathbf{Y}\mathbf{R}_i, \tag{17.101}$$

$$\mathbf{Y}^{-1} = \mathbf{I} - n^{(1)}\mathbf{R}_i\mathbf{Q}_i^0, \tag{17.102}$$

where the matrix $\mathbf{Y}$ is determined by the action of the surrounding inclusions, and for the sake of simplicity of the subsequent calculation, it is usually assumed that the shape of "correlation hole" $v_{ij}^0$ does not depend on the inclusion $v_j$: $v_{ij}^0 = v_i^0$ and $\mathbf{Q}_{ij}^0 = \mathbf{Q}_i^0 \equiv \mathbf{Q}(v_i^0)$.

As pointed out by Benveniste (1987), the essential assumption in the Mori and Tanaka (1973) method (MTM) states that each inclusion $v_i$ behaves as an isolated one in the infinite matrix and subject to some effective stress field $\overline{\boldsymbol{\sigma}}_i$ coinciding with the average stress in the matrix

$$\langle \overline{\boldsymbol{\sigma}}_i \rangle = \langle \boldsymbol{\sigma} \rangle^{(0)}. \tag{17.103}$$

Using Eq. (17.103) as the closing assumption and substituting the hypothesis **H2** lead to the next representation for both the statistical average local stresses and effective compliance:

$$\langle \boldsymbol{\sigma} \rangle_i(\mathbf{x}) = \mathbf{B}_i(\mathbf{x})[c^{(0)}\mathbf{I} + c^{(1)}\mathbf{B}_i]^{-1}\langle \boldsymbol{\sigma} \rangle, \tag{17.104}$$

$$\mathbf{M}^* = \mathbf{M}^{(0)} + c^{(1)}\mathbf{R}_i[c^{(0)}\mathbf{I} + c^{(1)}\mathbf{B}_i]^{-1}. \tag{17.105}$$

For the identical ellipsoidal inhomogeneous heterogeneities $v_i$ homothetical to $v_i^0$, equivalences of Eqs. (17.100), (17.101) and (17.104), (17.105), respectively, are demonstrated in, for example, Buryachenko (2007). However, the representations (17.100), (17.101) and (17.104), (17.105), respectively, do not coincide even for the identical aligned isotropic fibers if $v_i$ and $v_i^0$ are not homothetic (in particular, if $v_i$ is not an ellipsoid, see Buryachenko, 2007).

It should be mentioned that the effective compliances (17.101) and (17.102) are traditionally expressed through the averages of the tensors $\mathbf{B}_i(\mathbf{x})$ and $\mathbf{R}_i(\mathbf{x})$ over the inclusion volumes $v_i$. However, these tensors can be also estimated through the averages over the inclusion boundaries $\mathbf{s} \in \Gamma_i$ of the fields $\boldsymbol{\vartheta}(\mathbf{s})$ ($\boldsymbol{\vartheta} = \boldsymbol{\varepsilon}, \boldsymbol{\sigma}$) corresponding to the homogeneous loading $\overline{\boldsymbol{\sigma}} \equiv$const. ($c \to 0$) of a single inclusion $v_i$:

$$\mathbf{B}_i\overline{\boldsymbol{\sigma}} = \frac{1}{\overline{v}_i}\int_{\Gamma_i} \mathbf{t}(\mathbf{s}) \overset{s}{\otimes} \mathbf{s}\, d\mathbf{s}, \tag{17.106}$$

$$\mathbf{R}_i\overline{\boldsymbol{\sigma}} = \int_{\Gamma_i} \boldsymbol{\eta}^s(\mathbf{s}) d\mathbf{s}. \tag{17.107}$$

In such a case, the effective compliances $\mathbf{M}^*$ (17.101) and (17.102) are estimated through the boundary integrals as in Eqs. (17.106) and (17.107). In so doing, the stress concentration tensor $\mathbf{B}_i(\mathbf{x})$ in Eqs. (17.100) and (17.104) is estimated by Eq. (17.88) at $k = 1$.

### 17.7.2 NBM's Method in Terms of the Volume Perturbator Factor

In order to simplify a counterpart of the exact systems (17.69) for the volume effective field $\overline{\boldsymbol{\sigma}}(\mathbf{x})$, we accept the hypotheses **H1a** and **H2**, while the hypotheses **H1b** and **H3** are not used. This leads to the following representation for the mean of the effective fields in the fixed inhomogeneity $\mathbf{x} \in v_i$:

$$\langle \overline{\boldsymbol{\sigma}}_i \rangle(\mathbf{x}) = \langle \boldsymbol{\sigma} \rangle + \int \mathbf{L}_q^{\sigma}(\mathbf{x} - \mathbf{x}_q) \langle \overline{\boldsymbol{\sigma}}_q \rangle(\mathbf{x}_q) [\varphi(v_q, \mathbf{x}_q|; v_i, \mathbf{x}_i) - n^{(q)}] d\mathbf{x}_q. \quad (17.108)$$

This allows one to obtain the explicit solution (called an initial approximation) for identical aligned heterogeneities ($v_i = v_q = v_1,\ \mathbf{x} \in v_1$):

$$\langle \overline{\boldsymbol{\sigma}} \rangle_1(\mathbf{x}) = \widehat{\mathbf{Y}} \langle \boldsymbol{\sigma} \rangle, \quad (17.109)$$

$$\langle \boldsymbol{\sigma} \rangle_1(\mathbf{x}) = [\mathbf{L}_1^{\sigma}(\mathbf{x} - \mathbf{x}_1) + \mathbf{I}] \widehat{\mathbf{Y}} \langle \boldsymbol{\sigma} \rangle, \quad (17.110)$$

$$\mathbf{M}^* = \mathbf{M}^{(0)} + n^{(1)} \mathbf{R}_1 \widehat{\mathbf{Y}}, \quad (17.111)$$

$$\widehat{\mathbf{Y}}^{-1} = \mathbf{I} - \int \langle \mathbf{L}_q^{\sigma}(\mathbf{x} - \mathbf{x}_q) \rangle_{(i)} [\varphi(v_q, \mathbf{x}_q|; v_i, \mathbf{x}_i) - n^{(q)}] d\mathbf{x}_q. \quad (17.112)$$

The average stress concentration factor and the effective compliance in Eqs. (17.109)–(17.112) are expressed through the volume perturbator $\mathbf{L}_q^{\sigma}(\mathbf{x} - \mathbf{x}_q)$, which was estimated by the VIE method (see Buryachenko 2010b) and by the FEA (see for references Buryachenko 2014).

### 17.7.3 NBM's Method in Terms of the Interface Perturbator Factor

In this section, we consider the GIE (17.67) for the interface variables $\boldsymbol{\chi}(\mathbf{s})$ ($\mathbf{s} \in \Gamma$) instead of the volume ones $\boldsymbol{\zeta}(\mathbf{x})$ ($\mathbf{x} \in v$) (17.58). In order to simplify the exact systems for the interface effective fields $\overline{\boldsymbol{\chi}}(\mathbf{s})$ ($\mathbf{s} \in \Gamma_i$) (17.69), we accept the hypotheses **H1a** and **H2**, while the hypotheses **H1b** and **H3** are not used. This leads to the following representation for the mean of the interface effective fields at the boundary $\mathbf{s} \in \Gamma_i$ of the fixed inhomogeneity:

$$\langle\overline{\boldsymbol{\chi}}|v_i,\mathbf{x}_i\rangle(\mathbf{s}) = \langle\boldsymbol{\chi}\rangle(\mathbf{s}) + \int \langle\mathscr{L}_q^{\chi}(\mathbf{s}-\mathbf{x}_q,\overline{\boldsymbol{\chi}})\rangle[\varphi(v_q,\mathbf{x}_q|;v_i,\mathbf{x}_i)-n(\mathbf{x}_q)]d\mathbf{x}_q. \quad (17.113)$$

Equation (17.113) holds true for the general cases of statistically inhomogeneous CM loaded by an arbitrary inhomogeneous remote loading. However, for simplicity of results obtained, one only considers hereafter the statistically homogeneous media loaded by the homogeneous boundary conditions (17.8) (the conditions (17.7) can be analyzed in a similar manner). Even in such a case, the statistical average $\langle\boldsymbol{\chi}\rangle(\mathbf{s})$ ($\mathbf{s}\in\Gamma_i$) is an inhomogeneous one:

$$\langle\boldsymbol{\chi}\rangle(\mathbf{s}) = ([\mathbf{M}^*\langle\boldsymbol{\sigma}\rangle](\mathbf{s}-\mathbf{x}_i),\langle\boldsymbol{\sigma}\rangle\mathbf{n}^{\Gamma_i}(\mathbf{s}))^{\top}, \quad (17.114)$$

explicitly depending on both the placement of $\mathbf{s}$ at the interface $\Gamma_i$ and the effective compliance $\mathbf{M}^*$.

Due to acceptance of the hypothesis **H1a** ($17.91_2$), a tensorial product of Eq. (17.113) on $\mathbf{s}$ ($\mathbf{s}\in\Gamma_i$) and their subsequent averaging over the interface $\Gamma_i$ at $\boldsymbol{\chi}=\mathbf{t}$ leads to ($\mathbf{s}\in\Gamma_i$)

$$\langle\overline{\boldsymbol{\sigma}}_i\rangle = \langle\boldsymbol{\sigma}\rangle + \int \langle\mathbf{s}\overset{s}{\otimes}\mathbf{L}_q^{t\sigma}(\mathbf{s}-\mathbf{x}_q)\rangle_{(i)}\langle\overline{\boldsymbol{\sigma}}_i\rangle[\varphi(v_q,\mathbf{x}_q|;v_i,\mathbf{x}_i)-n(\mathbf{x}_q)]d\mathbf{x}_q, \quad (17.115)$$

where one used the equalities (17.30), (17.57), and $\langle\mathbf{n}^{\Gamma_i}(\mathbf{s})\overset{s}{\otimes}\mathbf{s}\rangle_{(i)} = \mathbf{I}$. Equation (17.115) allows one to obtain the explicit solution for identical aligned heterogeneities ($v_i=v_q=v_1$, $\mathbf{x}\in v_1$):

$$\langle\overline{\boldsymbol{\sigma}}\rangle_1(\mathbf{x}) = \widehat{\mathbf{Y}}\langle\boldsymbol{\sigma}\rangle, \quad (17.116)$$

$$\langle\boldsymbol{\sigma}\rangle_1(\mathbf{x}) = \mathbf{B}_1(\mathbf{x})\widehat{\mathbf{Y}}\langle\boldsymbol{\sigma}\rangle, \quad (17.117)$$

$$\mathbf{M}^* = \mathbf{M}^{(0)} + n^{(1)}\mathbf{R}_1\widehat{\mathbf{Y}}, \quad (17.118)$$

$$\widehat{\mathbf{Y}}^{-1} = \mathbf{I} - \int \langle\mathbf{s}\overset{s}{\otimes}\mathbf{L}_q^{t\sigma}(\mathbf{s}-\mathbf{x}_q)\rangle_{(i)}[\varphi(v_q,\mathbf{x}_q|;v_i,\mathbf{x}_i)-n^{(q)}]d\mathbf{x}_q. \quad (17.119)$$

The representations for both the average stress concentration factor and the effective compliance in Eqs. (17.116)–(17.119) are similar to Eqs. (17.109)–(17.112) with replacement $\langle\mathbf{L}_q^{\sigma}(\mathbf{x}-\mathbf{x}_q)\rangle_{(i)} \to \langle\mathbf{s}\overset{s}{\otimes}\mathbf{L}_q^{t\sigma}(\mathbf{s}-\mathbf{x}_q)\rangle_{(i)}$ used.

It should be mentioned that all equations in Sect. 7.2 and 7.3 were derived for the perturbators expressed in both the general operator form and the boundary integral equations. However, the final results (17.109)–(17.112) and (17.116)–(17.119), respectively, are equivalent for both perturbator representations because both approaches use the same selection of hypotheses **H1a** and **H2b**, while the hypotheses **H1b** and **H3** are not exploited. However, the BIE method has the well-known advantage of reduction of dimension by one that can be crucial for the analyst. From another side, the representations (17.109)–(17.112) can be easily applied to CMs with inhomogeneous inclusions ($\mathbf{M}(\mathbf{x})\not\equiv$ const., $\mathbf{x}\in v^{(1)}$) that

presents a real challenge to the BIE methods. Thus, each method (BIE or FEA) has advantages and disadvantages and it is crucial for the analyst to be aware of their range of applications.

## 17.8 Numerical Results

With the nonessential restriction on space dimensionality $d$ and on the shape of inhomogeneities, we will consider 2-$D$ plane strain problems for composites reinforced by aligned infinite fibers with noncircular cross section schematically presented in Fig. 17.1 and described by the curve

$$\begin{cases} (x-R_1+r_s)^2+(y-R_2+r_s)^2=r_s^2, & \text{for } \{|x|>R_1-r_s\}\cap\{|y|>R_2-r_s\}, \\ (x-R_1+r_s)^2+(y-R_2+r_s)^2=r_s^2, & \text{for } \{|x|>R_1-r_s\}\cap\{|y|>R_2-r_s\}, \end{cases} \tag{17.120}$$

which reduces to a circle and a rectangular in the limiting cases $R_1=R_2=r_s=a$ and $r_s=0$, respectively.

We start our estimation from the evaluation of the stress perturbator $\mathscr{L}_j^{\chi}(\mathbf{s}-\mathbf{x}_j,\overline{\boldsymbol{\chi}})$ (17.57) for one heterogeneity in an infinite matrix. In order to estimate the approximations introduced by discretizations implemented in the MFS in Sect. 17.6 and for the evaluation of the solution (17.77), we compare numerical results with a reference analytical solution for a single-circle inclusion inside the infinite matrix in a plane strain problem subjected to the uniform remote loading $\overline{\boldsymbol{\sigma}}$ =const., and the isotropic constituents with the Young's moduli $E^{(1)}=100$, $E^{(0)}=1$ and Poisson ratios $\nu^{(1)}=0.49$, $\nu^{(0)}=0.45$ (see also Buryachenko 2016). In the following experiments, we consider uniformly spaced collocation points on $\Gamma_i$ and the same number of source points on $\hat{\Gamma}_i^{(1)}$ and $\hat{\Gamma}_i^{(0)}$ when the source sets prescribed by Eqs. (17.75) and (17.76) coincide. We consider a uniform remote tension $\overline{\sigma}_{ij}\equiv\delta_{i1}\delta_{j1}$ =const. generating a homogeneous stress distribution inside circle inclusion $\boldsymbol{\sigma}(\mathbf{x})=\mathbf{B}_i(\mathbf{x})\overline{\boldsymbol{\sigma}}$ ($\mathbf{B}_i(\mathbf{x})\equiv$ const., $\mathbf{x}\in v_i$), which is analytically estimated by means of the Eshelby tensor. The value $B_{i|1111}(\mathbf{x})\equiv 1.4587$ analytically evaluated is compared with their numerical values $B_{i|1111}(\mathbf{x})$ estimated by both the direct (least-squares) method of solution of Eq. (17.77) and the pseudo-inverse TR procedure (17.84) in the vicinity of the inclusion boundary $B_{i|1111}(\mathbf{s})\equiv\lim B_{i|1111}(\mathbf{x})$ ($\mathbf{x}\to\mathbf{s}$, $\mathbf{x}\in v_i$, $\mathbf{s}\in\Gamma_i$). In Fig. 17.2 the curves 1 and 2 are estimated by the direct method and the TR procedure, respectively, for $S=30$, $d=0.6$ (17.76), and $\lambda=10^{-5}$. The errors corresponding to the curves 1 and 2 equal 6.5% and 0.23%, respectively. Increasing the number of source points $S=60$ leads to an increase in the accuracy of the TR procedure (17.84)
(curve 4 with the error 0.00068%) and to osculation of the direct solution (17.77) (curve 3, the error 35%). A subsequent increase of the number of source points, $S=200$ with $d=0.1$, provides the error 0.000016% of the stress distribution $B_{i|1111}(\mathbf{s})$ ($\mathbf{s}\in\Gamma_i$) (17.84), while the approximative osculating solution (17.77)

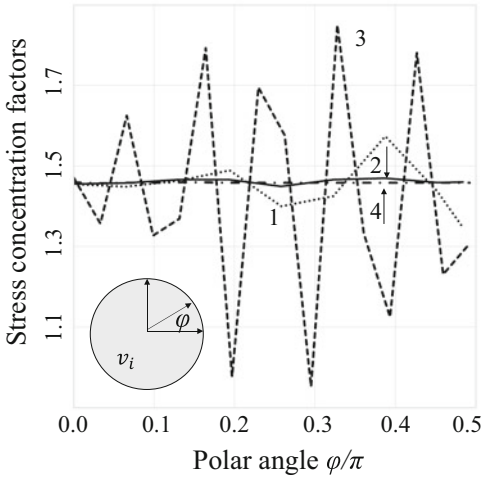


**Fig. 17.2** Stress concentration factor $B_{i|1111}(\mathbf{s})$ vs a polar angle $\varphi/\pi$

takes the negative values ($B_{i|1111}(\mathbf{s}) < 0.$ at some $\mathbf{x} \in \Gamma_i$) and loses a physical meaning. Buryachenko (2016) also demonstrated an advantage of the allocation scheme (17.76) with respect to the set (17.75) for the prolate elliptical heterogeneities with an aspect ratio 10.

An estimation of the perturbator $\mathscr{L}_j^{\chi}(\mathbf{x} - \mathbf{x}_j, \overline{\boldsymbol{\chi}})$ (17.37) makes it possible to turn our attention to the analysis of CM by the substitution of $\mathbf{L}_j^{t\sigma}(\mathbf{s} - \mathbf{x}_j)$ found in Eq. (17.119). A domain $v_i^{\phi}$ (see Sect. 7.3), where $\varphi(v_q, \mathbf{x}_q|; v_i, \mathbf{x}_i) - n^{(q)}$ is not negligible, is discretized by the square mesh $\Omega^{\text{sq}}$ ($p, k \in Z^1$):

$$\Omega^{\text{sq}} := \Big\{(x_1, x_2)^{\top} \mid (p-1)h < x_1 < ph,\ (k-1)h < x_2 < kh\Big\}, \tag{17.121}$$

where $h$ is the discretization step and $x_1, x_2$ are local coordinates with origins at the fiber centers, which will be exploited for stress assignment inside and outside the fiber in Eq. (17.114) and estimated in the postprocessing of FEA. In order to compute the integral in Eq. (17.114), the discretization (17.121) has been applied considering the simple Simpson numerical integration rule on piecewise-constant elements; this choice has been dictated by the simplicity of implementation also for nonregular inclusion shapes even if it does not guarantee a very fast convergence of the results with the discretization step $h$. It should be mentioned that the main reason of the choice of the square mesh (17.121) is its double using for two different problems. At first, this mesh is exploited for the estimation of the effective field $\langle\overline{\boldsymbol{\chi}}\rangle_i(\mathbf{x})$ (17.114). Second, the same mesh (17.121) is used as the location of the moving inclusion centers $\mathbf{x}_q$ in Eq. (17.114). It gives an opportunity the use of the solutions (17.86) and (17.88) for one heterogeneity in a sample in the nodes of just one realization of the mesh (17.121), which is exploited as an "output" mesh for a solution obtained on inhomogeneous sets of collocation and singular points placed

at the boundary $\Gamma_i$ and the pseudo-boundaries $\hat{\Gamma}_i^{(1)}$ and $\hat{\Gamma}_i^{(0)}$, respectively. However, in the case of the immediate use of the inhomogeneous mesh inside and outside a heterogeneity (which is more effective for the estimation of the perturbator factor $\mathscr{L}_q^{\sigma}(\mathbf{x}-\mathbf{x}_q)$), we will need to estimate the stresses in the nodes of a new mesh generated for each location $\mathbf{x}_q$ of the moving inclusion $v_q$. Therefore, the square mesh (17.121) is optimal for the current problem. In so doing, the solutions of Eqs. (17.86) and (17.88) (or alternatively, the matrix Eq. (17.77)) are performed at the collocation points $X_s$.

We are coming now to the analysis of the conditional probability density $\varphi(v_k,\mathbf{x}_k|;\ v_i,\mathbf{x}_i)$. This function is well investigated only for identical spherical (3-*D* and 2-*D* cases) inclusions with a radius $a$ when the pair distribution function $g(\mathbf{x}_i-\mathbf{x}_m)\equiv\varphi(v_i,\mathbf{x}_i|;\ v_m,\mathbf{x}_m)/n^{(k)}$ depending only on $|\mathbf{x}_m-\mathbf{x}_i|$ is called the radial distribution function (RDF). According to the author's best knowledge, a systematic quantitative investigation of the binary correlation function $\varphi(v_k,\mathbf{x}_k|;v_i,\mathbf{x}_i)$ for the noncanonical shape (and even for the nonspherical one) of inclusions is absent. Due to the absence of $\varphi(v_k,\mathbf{x}_k|;v_i,\mathbf{x}_i)$ for nonspherical inclusions $v_q$, $v_i$ ($\mathbf{x}_i=\mathbf{0}$), we will use a well-stirred approximation:

$$\varphi(v_k,\mathbf{x}_k|;v_i,\mathbf{x}_i)=(1-V_i^0(\mathbf{x}_k-\mathbf{x}_i))n^{(k)}. \tag{17.122}$$

A large difference of results is obtained in the framework of the backgrounds (17.99)–(17.102) and (17.116)–(17.119) for composites reinforced by nonellipsoidal inclusions demonstrating essentially inhomogeneous stress distribution inside inclusions even in the framework of the hypothesis **H1a**. In more detail, we analyze the inclusion shape (17.120) with $R_2/R_1=0.2$ and $r_s/R_1=0.1$ (at $c=0$, see Fig. 17.3).

The stress concentrator factors for an isolated inhomogeneity $B_{i|1111}(x_1)$ and $B_{i|2211}(x_2)$ in the cross sections $\mathbf{x}=(x_1/R_1,0)^{\top}$ and $\mathbf{x}=(0,x_2/R_2)^{\top}$ (see Fig. 17.3)

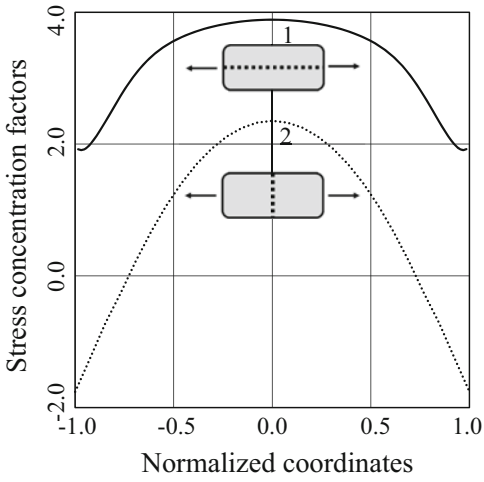


**Fig. 17.3** $B_{i|1111}(x_1)$ (*1*) and $100\cdot B_{i|2211}(x_2)$ (*2*) vs. $x_1/R_1$ and $x_2/R_2$, respectively

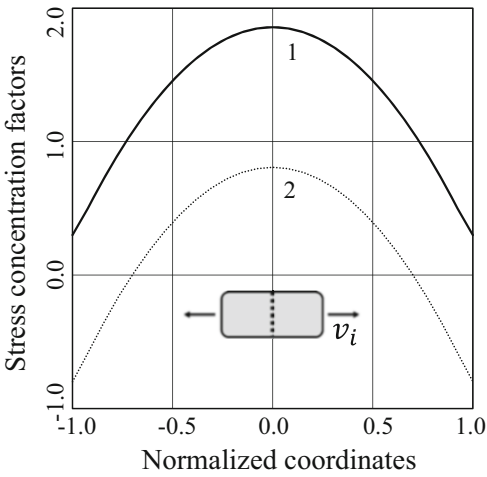


**Fig. 17.4** $100 \cdot B^*_{i|2211}(x_2)$ vs. $x_2/R_2$ estimated by the MEF (17.99)–(17.102) (*1*) and (17.116)–(17.119) (*2*)

grow in both magnitude and variation with decrease of the ratio $R_2/R_1$. For CM, the solution for a single inclusion (see Sect. 17.5 and Fig. 17.3) obtained by the MFS was used in both the known MEF (17.99)–(17.102) and the new approach (NA) (17.116)–(17.119). However, in the new approach (17.116)–(17.119), the hypothesis **H1b** was not used while this hypothesis was exploited in the classical MEF (17.99)–(17.102) with the aspect ratio $v_i^0$ equal to $R_2/R_1$.

The largest difference between the classical (17.99)–(17.102) and new (17.116)–(17.119) approaches is observed for the component $B^*_{i|2211}(x_2)$ in a cross section $\mathbf{x} = (0, x_2/R_2)^\top$ ($c = 0.7$, see Fig. 17.4) where the predicted curves by the new and classical approaches are distinguished by a sign. Normalized effective Young's moduli $E_1^*/E^{(0)}$ and $E_2^*/E^{(0)}$ are presented in Figs. 17.5 and 17.6, respectively, as the functions of the volume concentration $c$ of inclusions at $R_2/R_1 = 0.2$. Curves labeled 1 and 2 are estimated by the new approach (17.116)–(17.119) and the classical one (17.116)–(17.119), respectively, for the $\varphi(v_q, \mathbf{x}_q | v_i, \mathbf{x}_i)$ (17.122) in both Figs. 17.5 and 17.6. The curves labeled 3 are predicted by the MEF for the homogeneous ellipsoidal inclusions $v_i$ and $v_i^0$ with the aspect ratio equal to $R_2/R_1$.

Figures 17.5 and 17.6 are estimated by the new approach (17.112)–(17.119) for the $\varphi(v_q, \mathbf{x}_q | v_i, \mathbf{x}_i)$ (17.122). The curves labeled 2 are predicted by the MEF (17.99)–(17.102) accompanied by the MFS, respectively, which are invariant with respect to the concrete form of $g(r)$, while the curves labeled 3 are evaluated by Eqs. (17.99)–(17.102) for CM reinforced by the elliptical inclusions with the aspect ratio $R_2/R_1$. As can be seen, the estimations carried out by the different methods are essentially different at $c > 0.6$. In so doing, the difference between the curves 1 and 2 in Figs. 17.5 and 17.6 obtained by the NA and the old one, respectively, is not dramatically different, although the local stress distributions can be different, by a sign (see Fig. 17.4).

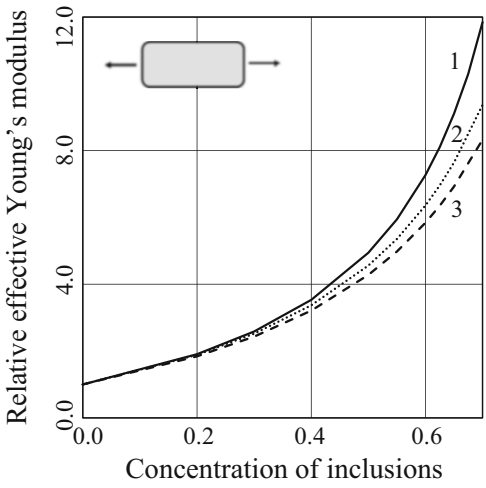


**Fig. 17.5** $E_1^*/E^{(0)}$ vs $c$ estimated by the NA (*1*), MEF for non canonical inclusions (*2*), and by the MEF for canonical inclusions (3)

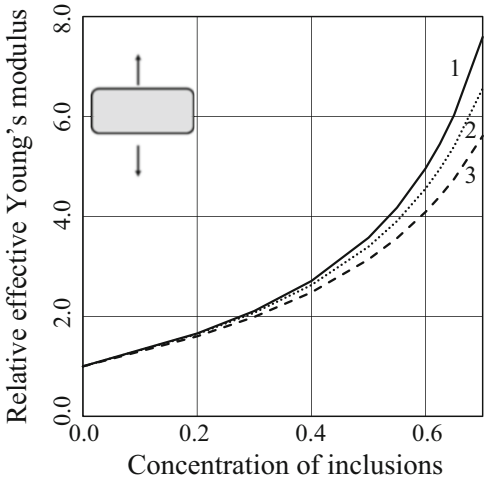


**Fig. 17.6** $E_2^*/E^{(0)}$ vs $c$ estimated by the NA (*1*), MEF for non canonical inclusions (*2*), and by the MEF for canonical inclusions (3)

## 17.9 Conclusion

We obtained a fundamental conclusion that both the effective properties and effective concentration factors in general depend not only average stress distribution inside the referred heterogeneity [describing by the tensor $\mathbf{B}_i$] but also on the stresses in the vicinity of heterogeneity, that is, the extension of $\mathbf{B}_i(\mathbf{x})$ ($\mathbf{x} \in v_i^{\phi}$) is necessary. Then the size of the excluded volume $v_i^0$ as well as the binary correlation function will impact both the effective properties and effective concentration factors even in the framework of hypothesis H2. In so doing, the concentration factors (see Fig. 17.4) are significantly more sensitive values to the choice of the approach (either NA or MEF) than effective properties (see Figs. 17.5 and 17.6, and Buryachenko and

Brun 2013). Thus, we have proposed the new micromechanical model based on the integral Eq. (17.119) for the interface traction, and we have introduced the concepts of both the interface polarization tensors (17.27) and (17.28) and the perturbators expressed through the interface boundary integral (17.57). It opens up the strong possibilities for the systematic exploitation of the BIE methods (and, in particular, the MFS), which have the well-known advantage of reduction of dimension by one that can be crucial for the analysis.

**Acknowledgments** The author acknowledges the support of the US Air Force Office of Scientific Research.

## References

ABAQUS: Theory Manual for Version 6.2-1, Pawtucket, RI: Hibbitt, Karlsson, and Sorenson, Inc. (2001)

Alves, C.J.S.: On the choice of source points in the method of fundamental solutions. Eng. Anal. Bound. Elem. **33**, 1348–1361 (2009)

Alves, C.J.S.,Antunes, P.R.S.: The method of fundamental solutions applied to the calculation of eigenfrequencies and eigenmodes of 2D simplyconnected shapes. Comput. Mater. Continua **2**, 251–66 (2005)

Alves, C.J.S., Silvestre, A.L.: Density results using Stokesltes and a method of fundamental solutions for the Stokes equations. Eng. Anal. Bound. Elem. **28**, 1245–1252 (2004)

Atluri, S.N.: The Meshless Method (MLPG) for Domain & BIE Discretizations. Tech Science Press, Encino, CA (2004)

Balas, J., Sladek, J., Sladek, V.: Stress Analysis by Boundary Element Methods. Elsevier, Amsterdam (1989)

Belytschko, T., Krongauz, Y., Organ, D., Fleming, M., Krysl, P.: Meshless method: An overview and recent developments. Comput. Methods Appl. Mech. Eng. **139**, 3–47 (1996)

Benveniste, Y.: A new approach to application of Mori-Tanaka's theory in composite materials. Mech. Mater. **6**, 147–157 (1987)

Brady, J.F., Phillips, R.J., Lester, J.C., Bossis , J.: Dynamic simulation of hydrodynamically interacting suspensions J. Fluid Mech. **195**, 257–280 (1988)

Brebbia, C.A., Telles, J.C.F., Wrobel, L.C.: Boundary Element Techniques. Springer, Berlin (1984)

Buryachenko V.A.: Micromechanics of Heterogeneous Materials. Springer, New York (2007)

Buryachenko V.A.: On the thermo-elastostatics of heterogeneous materials. I. General integral equation. Acta Mech. **213**, 359–374 (2010a)

Buryachenko, V.A.: On the thermo-elastostatics of heterogeneous materials. II. Analysis and generalization of some basic hypotheses and propositions. Acta Mech. **213**, 359–374 (2010b)

Buryachenko, V.: Solution of general integral equations of micromechanics of heterogeneous materials. J. Solids Struct. **51**, 3823–3843 (2014)

Buryachenko V.: General integral equations of micromechanics of heterogeneous materials. Int. J. Multiscale Comput. Eng., **13**, 11–53 (2015)

Buryachenko, V.A., Brun, M.: Iteration method in linear elasticity of random structure composites containing heterogeneities of noncanonical shape. Int. J. Solids Struct. **50**, 1130–1140 (2013)

Buryachenko, V., Jackson, T., Amadio, G.: Modeling of random bimodal structures of composites (application to solid propellant): I. Simulation of random packs. Comput. Model. Eng. Sci. (CMES) **85**(5), 379–416 (2012)

Chen, H.S., Acrivos, A.: The effective elastic moduli of composite materials containing spherical inclusions at non-dilute concentrations. Int. J. Solids Struct. **14**, 349–364 (1978)
Chen, W., Tanaka, M.: A meshless, integration-free, and boundary-only RBF technique. Comput. Math. Appl. **43**, 379–391 (2002)
Chen, T., Dvorak, G.J., Benveniste, Y.: Stress fields in composites reinforced by coated cylindrically orthotropic fibers Mech. Mater. **9**, 7–32 ( 1990)
Chen, K.H., Chen, J.T., Kao, J.H.: Regularized meshless method for antiplane shear problems with multiple inclusions. Int. J. Numer. Methods Eng. **73**, 1251–1273 (2008)
Cruse, T.A.: An improved boundary-integral equation method for three dimensional elastic stress analysis. Comput. Struct. **4**, 741–754 (1974)
Dong, C.Y., Lo, S.H., Cheung, Y.K.: Stress analysis of inclusion problems of various shapes in an infinite anisotropic elastic medium. Comput. Methods Appl. Mech. Eng. **192**, 683–696 (2003)
Dvorak, G.J.: Micromechanics of Composite Materials. Springer, Dordrecht (2013)
Durlofsky, L., Brady, J.F., Bossis, G.: Dynamic simulation of hydrodynamically interacting particles. J . Fluid Mech. **180**, 21–49 (1987)
Eshelby, J.D.: The determination of the elastic field of an ellipsoidal inclusion, and related problems. Proc. R. Soc. Lond. **A241**, 376–396 (1957)
Fairweather, G., Karageorghis, A.: The method of fundamental solutions for elliptic boundary value problems. Adv. Comput. Math. **9**, 69–95 (1998)
Fasshauer, G.E.: Meshfree methods. In: Rieth, M., Schommers, W. (eds.) Handbook of Theoretical and Computational Nanotechnology, vol. 2, pp. 33–97. American Scientific Publishers, Valencia, CA (2006)
Filatov, A.N., Sharov, L.V.: Integral Inequalities and the Theory of Nonlinear Oscillations. Nauka, Moscow (1979) (In Russian)
Fish, J., Belytschko, T.: A First Course in Finite Elements. Wiley, Chippenham (2007)
Ghosh, S.: Micromechanical analysis and multi-scale modeling using the voronoi cell finite element method. Computational Mechanics and Applied Analysis. CRC, Boca Raton (2011)
Goldberg, M.A., Chen, C.S.: The method of fundamental solutions for potential, Helmholtz and diffusion problems. In: Goldberg, M.A. (ed.) Boundary Integral Methods: Numerical and Mathematical Aspects, pp. 103–176. Pineridge Press, Southampton/Boston (1998)
Hansen, P.C.: Rank-Deficient and Discrete Ill-Posed Problems Numemcal Aspects of Linear Inversin. SIAM, Philadelphia (1998)
Hashin, Z., Shtrikman, S.: On some variational principles in anisotropic and nonhomogeneous elasticity. J. Mech. Phys. Solids **10**, 335–342 (1962)
Hill, R.: Elastic properties of reinforced solids: some theoretical principles. J. Mech. Phys. Solids **11**, 357–372 (1963)
Hill, R.: A self-consistent mechanics of composite materials. J. Mech. Phys. Solids **13**, 212–222 (1965)
Hsiao, G.C., Steinbach, O., Wendland, W.L.: Domain decomposition methods via boundary integral equations. J. Comput. Appl. Math. **125**, 521–537 (2002)
Jayaraman, K., Reifsnider, K.L.: Residual stresses in a composite with continuously varying Young's modulus in the fiber/matrix interphase. J. Comput. Mater. **26**, 770–791 (1992)
Karageorghis, A., Smyrlis, Y.-S.: Matrix decomposition MFS algorithms for elasticity and thermoelasticity problems in axisymmetric domains. J. Comput. Appl. Math. **206**, 774–795 (2007)
Kröner, E.: Berechnung der elastischen Konstanten des Vielkristalls aus den Konstanstanten des Einkristalls. Z. Physik. **151**, 504–518 (1958)
Kupradze, V.D., Aleksidze, M.A.: The method of functional equations for the approximate solution of certain boundary value problems. Z. Vychisl Matimat Fiz. **4**, 683–715 (1964)
Kushch, V.: Micromechanics of Composites: Multipole Expansion Approach. Butterworth-Heinemann, Amsterdam (2013)
Lax, M.: Multiple scattering of waves II. The effective fields dense systems. Phys. Rev. **85**, 621–629 (1952)
Lekhnitskii, A.G.: Theory of Elasticity of an Anisotropic Elastic Body. Holder Day, San Francisco (1963)

Lin, J., Chen, W., Wang, F.: A new investigation into regularization techniques for the method of fundamental solutions. Math. Comput. Simul. **81**, 1144–1152 (2011)
Liu, Y.L., Mukherjee, S., Nishimura, N., Schanz, M., Ye, W., Sutradhar, A., Pan, E., Dumont, N.A., Frangi, A., Saez, A.: Recent advances and emerging applications of the boundary element method. Appl. Mech. Rev. **64**, 031001 (38 pages) (2011)
Marin, L.: A meshless method for solving the Cauchy problem in three-dimensional elastostatics. Comput. Math. Appl. **50**, 73–92 (2005)
Martins, N.F.M., Rebelo, M.: A meshfree method for elasticity problems with interfaces. Appl. Math. Comput. **219**, 10732–10745 (2013)
Milton, G.W.: The theory of composites. Applied and Computational Mathematics, vol. 6. Cambridge University Press, Cambridge (2002)
Mori, T., Tanaka, K.: Average stress in matrix and average elastic energy of materials with misfitting inclusions. Acta Metall. **21**, 571–574 (1973)
Mossotti, O.F.: Discussione analitica sul'influenza che l'azione di un mezzo dielettrico ha sulla distribuzione dell'electricitá alla superficie di piú corpi elettrici disseminati in eso. Mem. Mat. Fis. Soc. Ital. Sci. Modena **24**, 49–74 (1850)
Mukherjee, S., Liu, Y. The boundary element method. Int. J. Comput. Methods **10**, 1350037 (91 pages) (2013)
Mura, T.: Micromechanics of Defects in Solids. Martinus Nijhoff, Dordrecht (1987)
Nemat-Nasser, S., Hori, M.: Micromechanics: Overall Properties of Heterogeneous Materials. Elsevier, North-Holland (1993)
O'Brian R.W.: A method for the calculation of the effective transport properties of suspensions of interacting particles. J. Fluid. Mech. **91**, 17–39 (1979)
Parnell, W.J.: The Eshelby, Hill, moment and concentration tensors for ellipsoidal inhomogeneities in the Newtonian potential problem and linear elastostatics. J. Elast. **125**, 231–294 (2016)
Parton, V.Z., Perlin, P.I.: Integral Equation Method in Elasticity. MIR, Moscow (1982)
Pozrikidis, C.: Introduction to Theoretical and Computational Fluid Dynamics. Oxford University Press, New York (2011)
Russel, W.B., Acrivos, A.: On the effective moduli of composite materials: slender rigid inclusions at dilute concentrations. J. Appl. Math. Phys. (ZAMP), **23**, 434–464 (1972)
Sejnoha, M., Zeman, J.: Micromechanics in Practice. WIT, Southampton (2013)
Shermergor, T.D.: The Elasticity Theory of Microheterogeneous Media. Nauka, Moscow (1977) (in Russian)
Smyrlis, Y.-S.: Mathematical foundation of the MFS for certain elliptic systems in linear elasticity. Numer. Math. **112**, 319–340 (2009)
Tikhonov, A.N., Arsenin, V.Y.: Methods for Solving Ill-Posed Problems. Nauka, Moscow (1986)
Torquato, S.: Random Heterogeneous Materials: Microstructure and Macroscopic Properties. Springer, New York/Berlin (2002)
Torquato, S., Lado, F.: Improved bounds on the effective elastic moduli of random arrays of cylinders. J. Appl. Mech. **59**, 1–6 (1992)
Toselli, A., Widlund, O.: Domain Decomposition Methods. Algorithms and Theory. Springer, Berlin (2005)
Wang, H., Yao, Z.: A new fast boundary element method for large scale analysis of mechanical properties in 3D particle-reinforced composites. Comput. Model. Eng. Sci. **4**, 85–95 (2005)
Willis, J.R.: Bounds and self-consistent estimates for the overall properties of anisotropic composites. J. Mech. Phys. Solids **25**, 185–203 (1977)
Willis, J.R.: Variational principles and bounds for the overall properties of composites. In: Provan J.W. (ed.) Continuum Models of Disordered Systems, pp. 185–215. University of Waterloo Press, Waterloo (1978)
Willis, J.R.: Variational and related methods for the overall properties of composites. Adv. Appl. Mech. **21**, 1–78 (1981)
Yao, Z., Kong, F., Wang, H., Wang, P.: 2D simulation of composite materials using BEM. Eng. Anal. Bound Elem. **28**, 927–935 (2004)

You, L.H., You, X.Y., Zheng, Z.Y.: Thermomechanical analysis of elastic–plastic fibrous composites comprising an inhomogeneous interphase Comput. Mater. Sci. **36**, 440–450 (2006)
Young, D.L, Jane, S.J., Fan, C.M., Murugesan, K., Tsai, C.C.: The method of fundamental solutions for 2D and 3D Stokes flows. J. Comput. Phys. **211**, 1–8 (2006)
Zienkiewicz, O.G., Taylor, R.L.: The Finite Element Method, vols. 1 and 2, 4th edn. McGraw Hill, Berkshire (1994)

# Index





S.A. Meguid, G.J. Weng (eds.), *Micromechanics and Nanomechanics of Composite Solids*, DOI 10.1007/978-3-319-52794-9

**O**



**P**